



NASA SP-55
(Air Force ML-TDR-64-159)

SYMPOSIUM ON THERMAL RADIATION OF SOLIDS

NATIONAL AERONAUTICS AND SPACE ADMINISTRATION

SYMPOSIUM ON THERMAL RADIATION OF SOLIDS

A SYMPOSIUM HELD AT
SAN FRANCISCO, CALIFORNIA, MARCH 4, 5, 6, 1964

SPONSORED BY Research and Technology Division, USAF
National Bureau of Standards
National Aeronautics and Space Administration

EDITED BY S. KATZOFF
National Aeronautics and Space Administration



Scientific and Technical Information Division
NATIONAL AERONAUTICS AND SPACE ADMINISTRATION
1965
Washington, D.C.

Record

The Symposium on Thermal Radiation of Solids was sponsored jointly by the Aeronautical Systems Division, U.S. Air Force; the National Bureau of Standards; and the National Aeronautics and Space Administration. It was held in the Sheraton-Palace Hotel in San Francisco, March 4-6, 1964.

The General Committee consisted of:

Joseph C. Richmond, Chairman—National Bureau of Standards.
John H. Charlesworth—Research and Technology Division, U.S. Air Force.
James J. Gangler—NASA Headquarters.
Gerhardt B. Heller—NASA Marshall Space Flight Center.
Robert A. Winn—Research and Technology Division, U.S. Air Force.

The Program Committee consisted of:

Roger E. Gaumer, Chairman—Lockheed Missiles & Space Company.
Clay P. Butler—U.S. Naval Radiological Defense Laboratory.
William D. Harris—University Extension, University of California, Berkeley.
James F. Haskins—General Dynamics/Astronautics.
Samuel Katzoff—NASA Langley Research Center.
Louis A. McKellar—Lockheed Missiles & Space Company.
Carr B. Neel—NASA Ames Research Center.
Ralph A. Seban—University of California, Berkeley.

Arrangements for facilities and equipment, registration of participants, and distribution of preprints were handled by the University of California on a contract basis. Mr. William D. Harris of the University Extension was in charge of these arrangements. Preprints were prepared at NASA Langley Research Center and were mailed to preregistrants before the Symposium date.

Preface

Spacecraft maintain their thermal balance through radiative processes. Hypersonic aircraft and bodies plunging into planetary atmospheres also depend on radiative processes for part of their temperature control. The expansion of aerospace technology has accordingly brought with it a prodigious development of interest and activity in the field of thermal radiation of solids. In order to provide for a broad interchange of information among workers in this field, a number of symposiums have been held in the last few years in which thermal radiation was either the main topic or a main subtopic. Among these may be cited:

The First Symposium on Surface Effects on Spacecraft Materials, Palo Alto, May 12 and 13, 1959—published as *First Symposium—Surface Effects on Spacecraft Materials*, Francis J. Clauss, editor, John Wiley & Sons, Incorporated, c. 1960.

The NASA Conference on Thermal Radiation Problems in Space Technology, Langley Research Center, September 12 and 13, 1960—not published, but a compilation of summaries of the papers presented was prepared and distributed to the participants.

The Conference on Radiative Transfer from Solid Materials, Boston, December 12 and 13, 1960—published as *Radiative Transfer from Solid Materials*, Henry Blau and Heinz Fischer, editors, The Macmillan Company, 1962.

The Symposium on Measurement of Thermal Radiation Properties of Solids, Dayton, Ohio, September 5–7, 1962—published as *Measurement of Thermal Radiation Properties of Solids*, Joseph C. Richmond, editor, NASA SP-31, 1963.

The present Symposium on Thermal Radiation of Solids was, like the last of the above list,

sponsored jointly by the Research and Technology Division, U.S. Air Force; the National Bureau of Standards; and the National Aeronautics and Space Administration. It was held in San Francisco, March 4–6, 1964.

The Symposium was intended to provide for presentation and discussion of significant developments in the theory of thermal radiation of solids and in our understanding of the important effects of surfaces and interfaces and of surface imperfections on this radiation, of the effects of the space environment on radiation properties, and of the application of this information to the thermal designer's problems. Presentation of data as such—for example, absorptances and emittances of various types of coatings—was not considered a primary purpose of the Symposium; nevertheless, as the reader will observe, an appreciable amount of significant data of this type is contained in some of the papers. Developments in measurement techniques were also not considered basic to the main theme, especially since it was the theme of the preceding Symposium. However, because the subject remains of continuing concern, one session was devoted to it.

Thus, the Symposium was organized into five consecutive sessions along the lines just indicated:

- I. Fundamentals
- II. Surface Effects
- III. Measurement Techniques
- IV. Space Environment Effects
- V. Applications

Sessions I, III, and IV included introductory review papers by either the chairman or invited speakers. Session II was conducted differently from the others in that it took the form of a modified panel discussion with short presentations by the chairman and the panel members, followed by invited comments and then open discussion. In the present Proceedings, how-

ever, this session is arranged similar to the others, although some of the papers are quite brief. The reader should note that although the topics of the five sessions are fairly clearly differentiated, material pertaining to any one may be found in any of the others. A subject index has been added to help the reader locate desired information; in addition, the editor has inserted a few footnotes calling the reader's attention to related papers in the Symposium.

These Proceedings contain all the papers presented orally at the Symposium together with the discussions that followed them, and, in addition, nine papers that were accepted for publication only. Each paper was reviewed by the session chairman and by the editor, and

any apparent technical discrepancies were called to the attention of the author for clarification. As a further aid to the reader, the editor has tried to achieve some degree of uniformity in organization and format of the papers--at least to the extent permitted by the subject matter, and he has also striven for clarity and readability of the text. In this task he has had not only the cooperation of the authors but also extensive help from the Langley Technical Editing Section, the Langley Library (where most of the cited references were checked), and the NASA Headquarters Technical Publications Branch.

S. KATZOFF,
Editor.

Contents

Session I. FUNDAMENTALS

Chairman: Henry H. Blau, Jr.

	Page
1.—A Review of Some Problem Areas in the Theory of Thermal Radiation of Solids..... <i>A. G. Emslie</i>	3
2.—Theoretical and Experimental Studies of the Total Emittance of Metals..... <i>W. J. Parker and G. L. Abbott</i>	11
3.—Far-Infrared Spectra of Solids..... <i>James R. Aronson and Hugh G. McLinden</i>	29
4.—Emissivity and Inter-Reflection Relationships for Infinite Parallel Specular Surfaces..... <i>R. V. Dunkle</i>	39
5.—Numerical Solutions of the Fresnel Equations in the Optical Region..... <i>Herbert B. Holl</i>	45
6.—The Theory of Emissivity of Metals..... <i>Neil Ashby and Klaus Schocken</i>	63
7.—Radiation Heat Transfer Through Scattering and Absorbing Nonisothermal Layers..... <i>Jonathan D. Klein</i>	73
8.—Fundamentals of Thermal Radiation in Ceramic Materials..... <i>R. L. Cox</i>	83
9.—Radiant Emission, Absorption, and Transmission Characteristics of Cavities and Passages..... <i>E. M. Sparrow</i>	103
10.—A Test of Analytical Expressions for the Thermal Emittance of Shallow Cylindrical Cavities..... <i>Francis J. Kelly and Dwight G. Moore</i>	117

Session II. SURFACE EFFECTS

Chairman: Roger E. Gaumer

11.—A Generalized Physical Model of the Role of Surface Effects in Modifying Intrinsic Thermal Radiation Parameters..... <i>Roger E. Gaumer</i>	135
12.—Comments on the Surface Characterization of Real Metals..... <i>David P. DeWitt</i>	141
13.—Influence of Surface Roughness, Surface Damage, and Oxide Films on Emittance..... <i>H. E. Bennett</i>	145
14.—The Effect of Slight Surface Roughness on Emittance..... <i>R. E. Rolling</i>	153
15.—Importance of Surface Films..... <i>Joseph C. Richmond</i>	157
16.—Surface Properties of Metals..... <i>H. H. Blau, Jr. and H. A. Francis</i>	159

	Page
17.—Effect of Surface Texture on Diffuse Spectral Reflectance	
A.—Diffuse Spectral Reflectance of Metal Surfaces.....	165
<i>H. J. Keegan, J. C. Schleter, and V. R. Weidner</i>	
B.—Surface Texture Measurements of Metal Surfaces.....	169
<i>D. B. Spangenberg, A. G. Strang, and J. L. Chamberlin</i>	
18.—The Measurement of Total Surface Area.....	179
<i>J. E. Janssen and R. N. Schmidt</i>	
19.—The Time Variation of the Total Hemispherical Emittance of Polished Platinum Surfaces at High Temperatures.....	183
<i>N. J. Alvares</i>	
20.—Solar Absorptance and Thermal Emittance of Evaporated Metal Films With and Without Surface Coatings.....	189
<i>Georg Hass</i>	
21.—The Effects of Surfaces on the Intrinsic Radiation Properties of Dielectrics.....	197
<i>Jonathan D. Klein</i>	
22.—Light-Scattering Behavior of Pigmented Coatings.....	205
<i>R. L. Cox</i>	
 Session III. MEASUREMENT TECHNIQUES 	
<i>Chairman: Clay P. Butler</i>	
23.—Comment on Measurement Techniques.....	213
<i>Wilson A. Clayton</i>	
24.—Standards, Sources, and Detectors in Radiation Measurements...	217
<i>Ralph Stair and William E. Schneider</i>	
25.—A High-Temperature Circular-Aperture Blackbody Radiation Source.....	233
<i>P. E. Schumacher</i>	
26.—Method and Equipment for Measuring Thermal Emittance of Ceramic Oxides from 1200° to 1800° K.....	241
<i>Howard E. Clark and Dwight G. Moore</i>	
27.—Hemispherical Spectral Emittance of Ablation Chars, Carbon, and Zirconia (to 6,000° F).....	259
<i>R. Gale Wilson</i>	
28.—Emittance Measurements of Solids Above 2000° C.....	277
<i>T. S. Laszlo, R. E. Gannon, and P. J. Sheehan</i>	
29.—Preliminary Studies Toward the Determination of Spectral Absorption Coefficients of Homogenous Dielectric Materials in the Infrared at Elevated Temperatures.....	287
<i>W. Fussell and Ralph Stair</i>	
30.—Directional Solar Absorptance Measurements.....	293
<i>N. J. Douglas</i>	
31.—A Thermal Vacuum Technique for Measuring Solar Absorptance of Satellite Coatings as a Function of Angle of Incidence.....	303
<i>Marla G. Hoke</i>	
32.—The Directional Spectral Emittance of Surfaces Between 200° and 600° C.....	313
<i>W. M. Brandenburg and O. W. Clausen</i>	

33.—Measurement of Emittance of Organic Materials (Electric Wire Insulation).....	Page 321
<i>George W. McIntyre</i>	
34.—Low-Temperature Conductive Losses in Emittance Measurements by the Decay Method.....	325
<i>O. Makarounis</i>	
35.—The Application of Temperature Rate Measurements to the Determination of Thermal Emittances.....	331
<i>William M. Hall</i>	

Session IV. SPACE ENVIRONMENTAL EFFECTS

Chairman: Gerhard B. Heller

36.—Problems and Research Effort in Space Environment Effects.....	339
<i>Gerhard B. Heller</i>	
37.—Solar-Wind Bombardment of a Surface in Space.....	345
<i>G. K. Wehner</i>	
38.—Some Fundamental Aspects of Nuclear Radiation Effects in Spacecraft Thermal Control Materials.....	351
<i>J. E. Gilligan and R. P. Caren</i>	
39.—Nuclear Environmental Effects on Spacecraft Thermal Control..	365
<i>R. A. Breuch and H. E. Pollard</i>	
40.—Development of a Technique for the Correlation of Flight-and Ground-Based Studies of the Ultraviolet Degradation of Polymer Films.....	381
<i>John A. Parker, Carr B. Neel, and Morton A. Golub</i>	
41.—Ultraviolet Irradiation of White Spacecraft Coatings in Vacuum..	391
<i>G. A. Zerlaut, Y. Harada, and E. H. Thompkins</i>	
42.—The Effects of Ultraviolet Radiation on Low α_s/ϵ Surfaces.....	421
<i>R. L. Olson, L. A. McKellar, and J. V. Stewart</i>	
43.—A Study of the Photodegradation of Selected Thermal-Control Surfaces.....	433
<i>George F. Pezdirtz and Robert A. Jewell</i>	
44.—Preliminary Results from a Round Robin Study of Ultraviolet Degradation of Spacecraft Thermal-Control Coatings.....	443
<i>J. C. Arvesen, C. B. Neel, and C. C. Shaw</i>	
45.—The Effects of Micrometeoroids on the Emittance of Solids.....	453
<i>Ronald B. Merrill</i>	
46.—Alteration of Surface Optical Properties by High-Speed Micron-Size Particles.....	473
<i>Michael J. Mirtich and Herman Mark</i>	

Session V. APPLICATIONS

Chairman: Arthur J. Katz

47.—High-Temperature Thermal Optical Property Activities of the U.S. Air Force.....	485
<i>Donald F. Stevison and Merrill L. Minges</i>	
48.—Areas of Research on Surfaces for Thermal Control.....	495
<i>William Snoddy and Edgar Miller</i>	

	Page
49.—Selective Coatings for Vacuum-Stable High-Temperature Solar Absorbers.....	509
<i>R. N. Schmidt and J. E. Janssen</i>	
50.—Surfaces of Controlled Spectral Absorptance.....	525
<i>H. Tabor, H. Weinberger, and J. Harris</i>	
51.—An Experimental Determination of the Absorptances of Cryo-deposited Films by Calorimetric Techniques.....	531
<i>R. P. Caren, A. S. Gilcrest, and C. A. Zierman</i>	
52.—The Study of Low Solar Absorptance Coatings for a Solar Probe Mission.....	535
<i>E. R. Streed and C. M. Beveridge</i>	
53.—Effectiveness of Solar Radiation Shields for Thermal Control of Space Vehicles Subjected to Large Changes in Solar Energy..	549
<i>John C. Arvesen</i>	
54.—Effect of Absorptance-Emittance Ratio in the Storage of Cryogenic Propellants in Space.....	559
<i>C. H. Liebert and R. R. Hibbard</i>	
55.—Thermal Sensor Design for Glide Reentry Vehicles.....	567
<i>F. S. Brunschwig, G. E. Koch, and J. K. Wilhelm</i>	
AUTHOR AND DISCUSSANT INDEX.....	581
SUBJECT INDEX.....	

SESSION I
FUNDAMENTALS

Chairman: HENRY H. BLAU, Jr.
ARTHUR D. LITTLE, INC., CAMBRIDGE, MASS.

1. A Review of Some Problem Areas in the Theory of Thermal Radiation of Solids

A. G. EMSLIE

ARTHUR D. LITTLE, INC., CAMBRIDGE, MASS.

This paper gives a discussion of three problem areas in the field of thermal radiation of solids. The most basic problem is the calculation, from first principles, of the optical constants n and k of homogeneous materials such as metals and dielectrics. If this can be accomplished, all the radiation properties of materials with smooth surfaces can be evaluated by known methods. Another general problem area, involving statistical considerations, includes theories of the radiation characteristics of rough surfaces, of inhomogeneous materials such as powders, and of composite materials such as multiple radiation shields with insulating spacers. The highly nonisotropic thermal properties of such radiation shields cause great difficulties in connection with joints and penetrations. Closely spaced solid objects, as in powders and shields, may involve unusual radiation transfer due to near-field interaction. The third type of theoretical problem is one of computational complexity rather than of principle and has to do with radiation and conduction interchange on a macroscopic scale in complex structures such as space vehicles. When the structure contains many specularly reflecting surfaces the problem is beyond the power of present techniques. New approaches are urgently needed in most of these problem areas.

At the present time, experiment seems to be running well ahead of theory in many areas involving the thermal radiation of solids. New emissometers are being designed and emittances of a great variety of materials are being measured from 4° K to 3000° K. Flux-measuring apparatus has been built and results are accumulating on the radiation transfer through inhomogeneous media such as powders and radiation shields. Finally, large space-simulation chambers are being used to determine the temperature distributions in full-size satellites of highly complex geometry. But the published reports on all these measurements rarely give a comparison between experiment and theory.

The purpose of this paper is to examine the theoretical difficulties in the three areas just mentioned. The first of these difficulties has to do with the fundamental physics of the optical constants of homogeneous materials. The second is concerned with statistical con-

siderations, as in the emittance of rough surfaces or the radiation transfer in inhomogeneous materials such as powders. The third type of difficulty is one of mathematical complexity as in the calculation of satellite temperature distributions.

THE OPTICAL CONSTANTS

Except for the very special case of metals at low temperatures where the anomalous skin effect becomes important, all the radiation properties of smooth-surfaced homogeneous materials can be calculated if one knows the optical constants n and k as functions of wavelength and temperature. The calculation of emissivity, for example, is tedious but presents no problem to a computer.

The real problem is the calculation of the complex refractive index $n-ik$ for an electromagnetic wave passing through the material. The electromagnetic wave in general interacts

with the free electrons, the bound electrons, and the nuclei. The interaction depends strongly on the vibrations of the nuclei, which are determined by the phonon spectrum of the material. The phonons affect the electromagnetic wave in a number of ways. They affect the mean free path and the number of the free electrons. They induce oscillating electric polarization of the medium by shifting the nuclei. They control the line width of the bound electron resonances. These effects are in general quite complex and difficult to calculate. Only in some special cases, such as the far infrared interaction with metals and the infrared spectrum of polar crystals, does theory give results in reasonable agreement with experiment.

Metals

The well-known theory of Hagen and Rubens, based on the d-c conductivity of metals, works quite well at moderate temperatures and long wavelengths. At very low temperatures, however, the electron mean free path becomes longer than the radiation skin depth, and electron collisions with the metal surface then determine the effective electrical conductivity of the surface layer. This effective conductivity is less than the bulk conductivity and therefore makes the reflectivity lower than the value calculated by the Hagen-Rubens formula. This theory of the anomalous skin effect gives results in reasonable agreement with experiment.

At short wavelengths the Hagen-Rubens formula again breaks down because the radiation frequency becomes higher than the collision frequency of the electrons. The general dispersion formula of Drude takes the finite mean free path of the electrons into account and also includes the contribution of the bound electrons to the complex refractive index. Roberts has shown recently (ref. 1) that the observed optical constants of any metal can be fitted by Drude's formula over a wide range of wavelengths if a few bound electron resonance terms and at least two free electron terms are included. It is impossible to obtain good agreement with the optical constants and simultaneously with the d-c conductivity if only one free electron term is included. In terms of the modern

band theory of the electrons, there is no objection to more than one class of free electron in a metal.

A further advantage of including more than one free electron term in Drude's formula is that it appears to provide a good explanation of the mysterious X-point in the spectral emittance curves of metals at different temperatures. Figure 1 shows the typical behavior of the emittance curves of refractory metals at various temperatures. The upward trend with temperature at the longer wavelengths is easily understood since the resistivity increases with temperature, the optical constants therefore become smaller, and the spectral normal emissivity becomes larger, as seen from the formula

$$\epsilon_{\lambda} = \frac{4n}{(n+1)^2 + k^2}$$

The temperature coefficient of the emissivity should be positive for all wavelengths if the free electron density is constant and the electron mean free path decreases steadily with increasing temperature.

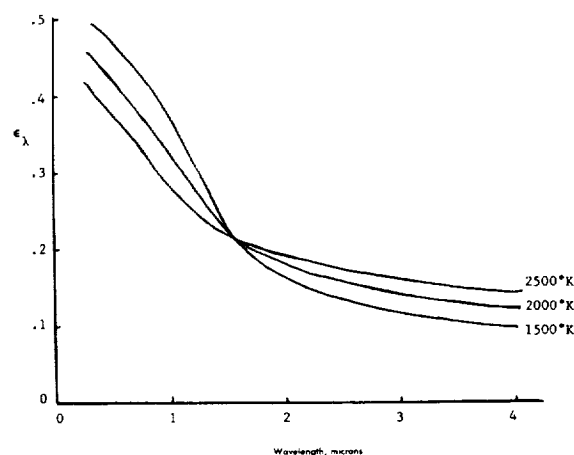


FIGURE 1.—Spectral emissivity of a typical refractory metal.

The change to a negative temperature coefficient of emissivity at short wavelengths can be explained if the second class of electrons has a constant short mean free path and increases in number with increasing temperature. The effect of this is to increase the optical

constants with increasing temperature and thereby lower the emissivity. This second class of electrons contributes only slightly to the d-c conductivity but, on account of the short time between collisions, interacts strongly with short-wavelength radiation.

It should be remarked that Roberts' explanation of the X-point, although quite plausible, is presented only tentatively. Other possibilities exist, such as (1) the long-wavelength tails of optical resonances, which should increase with rising temperature as the resonances broaden, or (2) the interaction of the electromagnetic wave with oscillating electric dipole moments caused by phonon-induced charge separation, which should also increase with temperature. The theory of the optical constants of metals cannot be regarded as complete until the X-point problem is settled.

Nonpolar Insulators

The explanation of the optical constants of nonpolar insulators is very difficult and seems to involve charge separation induced by the phonon spectrum. This problem has been attacked quantum mechanically (ref. 2 and 3) for crystals such as diamond and germanium, with results that agree reasonably well with experiment.

Polar Crystals

Only in the case of polar dielectrics like the metal salts can the optical constants be calculated with reasonable accuracy from first principles. The reason is that the radiation interacts primarily with the known permanent electric dipole moments and excites vibrations only in the optical branch of the phonon spectrum.

Future Work on Optical Constants

From the foregoing discussion it seems likely that, for the most part, one must be content for a considerable time to come with only measured values of the radiation characteristics of solids. Of most value for ultimate comparison with theory, and also for the computation of such characteristics as emissivity and reflectivity, would be the optical constants n and k as functions of wavelength and tem-

perature. It is hoped that more determinations of these constants will be made for the wide range of materials now in use.

INHOMOGENEOUS MEDIA AND STATISTICAL PROBLEMS

Although the optical constants n and k are, in principle, all that one must know in order to solve any radiation problem, in practice difficult statistical considerations usually arise. Real surfaces are invariably far from optically smooth and the emittance depends sensitively on the statistics of the surface contour, as well as on n and k . In other situations the material may be in the form of a powder instead of a homogeneous solid, and statistics again enter into the calculation of the radiation properties.

Rough Surfaces

Calculation of the effect of surface roughness on emittance is a difficult problem which involves the determination of the reflectance for a parallel monochromatic beam of radiation at a given angle of incidence on a medium defined by certain values of n and k and having a surface which is specified statistically. An insight into the problem may be gained along the following lines. The reflection of the beam is a diffraction problem in which the ratio of the wavelength to the scale of the surface irregularities is a controlling factor. If the wavelength is large compared with the irregularities, the reflection from different areas of the surface is highly coherent and the reflection is large and highly specular. When the wavelength is short compared with the irregularities, the reflection is incoherent and therefore weaker and diffuse. One would expect, therefore, that spectral emittance or reflectance should correlate with the degree of diffuseness of the reflected beam at different wavelengths. An experimental test of this expected correlation, for materials of various values of n and k , would help to provide a good background of data with which to establish a comprehensive theory of the effect of roughness.

Another possible approach to the rough-surface problem is to consider the emitted radiation directly. The radiation flux density W in the material is given by (ref. 4)

$$W = \frac{n^4}{n^2 + k^2} \sigma T^4$$

which, for large values of the optical constants, is much larger than the blackbody flux density. In the case of a smooth surface most of this flux undergoes total internal reflection, but it nevertheless gives rise to an exponentially decaying field (evanescent waves) outside the material. If the surface is now roughened, the surface irregularities, immersed in the evanescent wave field, become sources of emitted wavelets in much the same way as dust particles on a totally reflecting prism allow some light to escape. Thus a greater fraction of the internal flux W escapes through the surface and the emittance is accordingly increased.

Inhomogeneous Media

Another important problem with a statistical basis is radiation transfer through inhomogeneous materials such as powder insulation. The medium is characterized by an absorption cross section per unit volume K (cm^{-1}), a scattering cross section per unit volume S (cm^{-1}), and perhaps by an average refractive index N . If these quantities can be determined, the radiation transfer can be calculated by the multibeam method first used by Schuster long ago.

A simple case is that in which the medium scatters the radiation with little absorption, as when light diffuses through a cloud, a layer of snow, or a layer of magnesium oxide particles. Under these conditions the intensity of the incident diffuse beam of light falls off linearly with distance whereas a back-scattered diffuse beam increases linearly, at the same rate, in the opposite direction. The net light flux is independent of distance.

Another case is that in which the medium absorbs and scatters but is kept too cold to re-emit. In this case the intensities of the two diffuse beams vary exponentially with distance in accordance with the well-known equation of Kubelka and Munk (ref. 5).

A third case is that in which the medium is in local temperature equilibrium everywhere with the diffuse radiation. Under steady-state conditions, with no thermal conduction, conserva-

tion of energy again requires that the radiation intensity of the two beams vary linearly with distance in one-dimensional flow. It follows that the fourth power of the temperature of the medium also varies linearly with distance, if the medium is gray. This type of problem was first investigated by H. O. McMahon (ref. 6) for the case of radiative transfer in hot glass, and later elaborated by R. Gardon (ref. 7).

Thus the radiation-transfer problem appears, in general, to be readily soluble when the constants K , S , and N are known. Even the inclusion of thermal conduction presents no particular difficulty. The hard part of the problem is the calculation of the constants themselves.

In the case of widely spaced particles, as in a cloud, the Mie theory of scattering by spheres can be used, with proper attention given to multiple scattering, to derive K and S . But for particles in contact with each other, as in powder, fiber, or foam insulation materials, the Mie theory is unsuitable because the particles interact strongly with each other and scatter in coherent groups. What is needed is a radiation theory analogous to the Bloch theory of the free electrons in solids, in which the normal modes are traveling plane waves modulated in amplitude with the periodicity of the lattice. In the case of radiation through a regular lattice of partially absorbing particles, the Bloch-type functions will be damped spatially. In order to evaluate K , S , and N one could resolve a given plane wave packet into a superposition of these Bloch-type normal modes, from which the rate of decay, the rate of spreading, and the speed of the packet can be calculated.

In the case of a lattice of transparent particles of high refractive index, the Bloch radiation modes would be expected to show strong concentration of energy flow through chains of particles rather than in the spaces between particles. This effect will tend to reduce the scattering constant S and therefore allow the medium to transmit radiation more easily. It is to be noted that the small contact areas between particles do not impede the flow of radiant energy as much as one might suppose because of the strong near-field coupling across the small gap surrounding the actual contact

area. Near-field radiation should also enhance conductive transfer through the particles by removing a significant part of the contact resistance.

The periodic-lattice model of a powder is, of course, only an approximation to the real situation, but the rather small difference in the behavior of the free electrons in a metal at the melting point suggests that the electromagnetic properties of random and periodic distributions of powder particles may also be quite similar.

Radiation Shields

An important special case of an inhomogeneous medium is a stack of metal radiation shields separated by porous insulating spacers. The contacts between shields and spacers may have radiation-enhanced conductance as in the case of powder contacts. Again, if the shields are very closely spaced, near-field interaction can in principle increase the radiation transfer rate even above the blackbody rate (ref. 4).

Difficult theoretical and practical problems arise when structural members or pipes have to penetrate a radiation-shield insulating blanket, owing to the large anisotropy of the effective thermal conductivity of the blanket, which is typically 10^6 times higher in the transverse than in the perpendicular direction. This problem is being investigated at Arthur D. Little, Inc., for the NASA (ref. 8).

PROBLEMS WITH COMPLEX GEOMETRY

A very important type of problem involving the thermal radiation of solids is the accurate calculation of the temperature distribution in highly complex systems such as space vehicles. In a typical case several hundred temperatures may have to be found as a function of the time. This requires the simultaneous solution of several hundred equations, the coefficients of which are the radiative and conductive heat-transfer coefficients between various zones of the vehicle. The calculation of these transfer coefficients is the biggest part of the problem and often proves to be very difficult indeed, especially with regard to the radiative exchange coefficients.

The radiation problem is relatively simple when all surfaces are black. In that case the transfer coefficients are merely the blackbody view areas which are readily computed either by formula or by direct integration.

The problem is somewhat harder when the surfaces are gray diffuse reflectors but can, under the assumption of uniform radiosity over each surface, be reduced to the blackbody case by means of an artifice due to Oppenheim (ref. 9). The method consists of imagining a fictitious floating radiation shield to be placed immediately in front of each surface. The covered surface, which originally had an emissivity of ϵ , is now assumed to be black; and the shield is black on the outward surface but has an emissivity of $\epsilon/(1-\epsilon)$ on the inward surface. This combination emits the same amount of radiation to a 0° black sink as the original surface would by itself. The problem is now solved with the temperatures of the floating shields as extra unknowns. But simple blackbody view areas can now be used for the radiative interchange between the fictitious shields, and the view areas between the shields and the surfaces they cover can be written down at once. Thus the diffuse reflection problem merely requires solving twice as many simultaneous equations as the equivalent blackbody problem.

The radiation-transfer problem becomes very intractable when the reflection from the surfaces is partially specular. In special cases, with only a small number of flat specular surfaces, the method of images can sometimes be used to reduce the problem to that of black or diffusely reflecting surfaces. But in the case of a large number of flat specular surfaces or even a few curved specular surfaces, no practical method of calculation appears to be available at present.

Basically, what is required in the general specular surface problem is a way to calculate the fraction of the radiation emitted by a given surface A that is finally absorbed by each surface of the system, including A itself. Perhaps the only way to do this is to fall back on a Monte Carlo method that simulates on a computer the emission, reflection, and absorption of photons by the various surfaces. The generation of a random number by the computer

selects a point on surface A. Other random numbers select the direction of emission of a group of photons in accordance with the known angular emission function for the surface. The group of photons is projected on the computer until it strikes a surface, whereupon a certain fraction of the photons, determined by the known angular absorptance of the surface, is recorded as absorbed by the surface. The remaining photons are reflected mathematically by the surface and the path is projected to the next surface. This procedure is continued until all photons are absorbed. A new point on surface A is then selected, a new angle of emission is selected, and the performance is repeated. This is done enough times to give good average values of the transfer coefficients from surface A to all surfaces. The same thing is done for emission from all the surfaces. Some checking of the statistics of the procedure will be obtained from the principle of reciprocity which states that the matrix of the transfer coefficients should be symmetrical. Some studies of the Monte Carlo method have already been published, as for example, reference 10.

REFERENCES

1. ROBERTS, S.: Optical Properties of Nickel and Tungsten and Their Interpretation According to Drude's Formula. *Phys. Rev.*, vol. 114, no. 1, Apr. 1, 1959, pp. 104-115.

2. BURSTEIN, E., and OBERLY, JOHN J.: The Infra-red Properties of Diamond, Silicon, and Germanium. Abstracted in *Phys. Rev.*, vol. 78, no. 5, June 1, 1950, pp. 642-643.
3. LAX, MELVIN, and BURSTEIN, ELIAS: Infrared Lattice Absorption in Ionic and Homopolar Crystals. *Phys. Rev.*, vol. 97, no. 1, Jan. 1, 1955, pp. 39-52.
4. EMSLIE, A. G.: Fundamental Limitations of Multilayered Radiation Shields. Aerodynamically Heated Structures, Peter E. Glaser, ed., Prentice-Hall, Inc., 1962, pp. 135-150.
5. KUBELKA, PAUL, and MUNK, FRANZ: A Contribution to the Optics of Paint Finishes. *Z. Tech. Physik*, vol. 12, 1931, pp. 593-601.
6. McMAHON, H. O.: Thermal Radiation From Partially Transparent Reflecting Bodies. *Jour. Optical Soc. of America*, vol. 40, no. 6, June 1950, pp. 376-380.
7. GARDON, ROBERT: The Emissivity of Transparent Materials. *Jour. American Ceramic Soc.*, vol. 39, no. 8, Aug. 1956, pp. 278-287.
8. EMSLIE, A. G.: Radiative Heat Transfer Through Seams and Penetrations in Panels of Multilayer Metal-Foil Insulation. Rep. No. 63270-04-04 (Contract No. NAS5-664), Arthur D. Little, Inc., Apr. 1962.
9. OPPENHEIM, A. K.: Radiation Analysis by the Network Method. *Trans. ASME*, vol. 78, no. 4, May 1956, pp. 725-735.
10. PERLMUTTER, M. and HOWELL, J. R.: Radiant Transfer Through a Gray Gas Between Concentric Cylinders Using Monte Carlo. Paper No. 63-HT-39, ASME, Aug. 1963.

DISCUSSION

JOSEPH RICHMOND, National Bureau of Standards: I would like to ask a question with respect to the equation $W = [n^4/(n^2 + k^2)]\sigma T^4$. If you are considering total radiation, what n do you use, since n is generally a function of wavelength?

EMSLIE: This equation could be used for total radiation only for the "gray" case, where n and k are both independent of wavelength. For the general case, n and k are functions of λ , and σT^4 should be replaced by the blackbody function.

H. E. BENNETT, Michelson Laboratory, U.S. Naval Ordnance Test Station: I think that the technique of calculating the emittance of a material from band theory has real promise, and considerable progress is being made in this direction. However, I would like to point out that there is a factor which is very important and which is usually overlooked, particularly for highly absorbing materials such as metals and semiconductors in the intrinsic region. This factor is the amount of surface damage which the material has suffered; it is especially significant for materials which

have high extinction coefficients. The optical penetration depth is very small, so that all the emission or reflection occurs in the surface layers. Theoretical calculations assume a perfect lattice. When you have surface damage, you no longer have a perfect lattice and the actual optical properties can therefore be very different from the calculated properties. (In this connection, I would like to suggest that perhaps we should talk about emittance rather than emissivity for very smooth surfaces as well as for rough ones.) It is possible to show theoretically that, until one reaches a point at which multiple reflections must be considered, the total hemispherical emittance is independent of surface roughness. The reason the emittance changes for a rough surface is not because of surface roughness (up to the point where multiple reflections must be considered) but because of the surface damage introduced in the process of making the surface rough.

EMSLIE: I think that I would agree with all that you have said about that, but I did not discuss it because it is too complicated to even think about.

G. A. ZERLAUT, IIT Research Institute: I am particularly interested in your comments on Mie scattering. We are working with carefully sized silver halide as a model for scattering studies. This is an extension of Berry's work at Eastman Kodak. We have found, as he did, that the Mie theory does hold down to small center-center separations. In fact, it holds quite closely for carefully sized particles down to about $1\frac{1}{2}$ diameters separation. I think we see the real problem when we start working with a polydisperse system, that is, where we are working with a multiplicity of sizes. The interesting thing here, of course, is that we may be able to determine the multiple scattering with this type of system by the application of computer techniques.

EMSLIE: I would like to ask whether you have any experience with particles that are actually in contact.

ZERLAUT: Not yet, and right now we are attempting to elucidate the concentration effect by working with more and more concentrated solutions and arrays. We have prepared both of these—solutions and arrays in gelatin—and so we obtain both transmittance and reflectance spectra.

EMSLIE: The reason I asked about that was that the evanescent wave that surrounds each particle does not go very far out; it goes out only a fraction of a wavelength, for the peak of the blackbody curve. You could have particles separated by a diameter or two without having too much interaction. It depends upon the size of the particle relative to the wavelength, of course, as to how far this fringing or evanescent wave field extends beyond the surface of the particle.

R. L. Cox, Ling-Temco Vought: We have done some work on coatings for the highly transparent region with particles touching. We have found that a "fudge factor" developed by Blevin and Brown, reported in the *Journal of the Optical Society of America*, does fairly generally account for the proximity effect, and we have been able to predict the back scattering and reflectance within a few percent.

EMSLIE: I wonder what that fudge factor depends on. That is what you have to calculate next.

Cox: The fudge factor in this case is given by a series of curves of reflectance versus proximity. It was obtained for one material, and it works very well for others.

DONALD KOCH, North American Aviation: Did you indicate that the flux inside complex mediums could be much higher than in a normal medium, in which the index is not complex?

EMSLIE: No, I meant that it would be higher than the blackbody flux in a vacuum. This is true even in glass, of course, when there is no k . You then have n^2 times the blackbody flux; for example, if n is 2 you get 4 times the blackbody flux density in the glass.

Koch: The Born and Wolf table (*Principles of Optics*, Pergamon Press, 1959) indicates what the complex index of refraction might be in many complex mediums. The value of k is usually quite a bit larger than n , and this would indicate to me that this factor might quite often be less than 1.

EMSLIE: If k were much bigger than n , this could be true, unless n itself were very big. If n were very big, even when k is bigger, the n^4 in the numerator can still predominate. The actual number you come out with depends on the actual values of both n and k .

Koch: I remember some k values as much as 2 or 3, with n very close to 1.

EMSLIE: But there will be other situations. One can have all kinds of values for mediums other than metals, in which n could be large and k small—as in glass.

DONALD BURKHARD, P.E.C. Research Associates: Some work we have done at P.E.C. is relevant to questions raised this morning. Our work is described in the paper by Ashby and Schocken in this symposium. I would therefore like to describe that part of our work which relates to the basic assumptions underlying Kirchhoff's law (that emissivity is equal to absorptivity) and the Stefan-Boltzmann law ($H = \epsilon \sigma T^4$). Both of these hold for equilibrium conditions but are commonly applied to nonequilibrium situations. For example, the Stefan-Boltzmann law is used to calculate heat loss from a satellite to outer space which is at a much lower temperature than the satellite. This is a nonequilibrium situation, and the usual law is not valid.

We believe that we now know how to calculate radiative heat transfer under such nonequilibrium conditions. Physically, the basic thing which is not taken into account in the application of the usual Stefan-Boltzmann σT^4 law is that the radiation field external to the emitting solid, if it is at a lower temperature than the solid, does not stimulate as much radiation in the emitting body as would be stimulated if the body were in a radiation field at a temperature equal to the temperature of the emitting solid. One obtains a correction to the σT^4 law which involves a function of the ratio of the temperature of the enveloping radiation field to the temperature of the emitting solid. When T of the radiation field is quite a bit smaller than the T of the solid, the heat flux radiated from the solid is about 7 percent less than that predicted by the Stefan-Boltzmann law.

EMSLIE: That is a very interesting bit of work. I suppose that in the type of problem I mentioned previously, concerned with radiation exchange within a satellite, where the temperature differences are not very big—perhaps 20° at 300° K—this effect would not be large.

BURKHARD: If one has a body at room temperature radiating to absolute zero, the usual σT^4 law predicts a rate of heat loss about 7 percent greater than will actually occur. Thus, one should expect space probes to run hotter than previously estimated. We are currently carrying out calculations for smaller temperature differences and various geometries. The basic concept is interesting because it involves a completely new approach to the problem of radiative heat transfer.

2. Theoretical and Experimental Studies of the Total Emittance of Metals

W. J. PARKER AND G. L. ABBOTT

U.S. NAVAL RADIOLOGICAL DEFENSE LABORATORY, SAN FRANCISCO, CALIF.

Equations are presented for the spectral emissivity of metals as a function of angle and plane of polarization based on the Drude free-electron model taking electronic relaxation into account. These equations are integrated to obtain more general expressions than now exist for the total normal and total hemispherical emissivity of metals. Total emittance measurements have been made on tungsten, tantalum, niobium, and molybdenum. These are compared with the theoretical emissivity equations, and a qualitative, but not a quantitative, agreement is found between them. It is necessary to take other factors into account in order to explain the observed emittance data.

There are two theoretical equations developed by Foote (ref. 1) and by Davisson and Weeks (ref. 2) which relate the total normal and the total hemispherical emittance of metals to their electrical resistivity. In the derivation of these equations, it was assumed that the mean free time between collisions of the electron and the lattice is small compared with the period of the electromagnetic wave. This assumption is not completely valid for metals throughout most of the wavelength region in which they emit thermal radiation. In this article a general expression for the spectral emissivity is written down and integrated over all wavelengths and angles to obtain equations for the total normal and the total hemispherical emittance which take the relaxation time of the electron into account.

The total hemispherical emittance and the total normal emittance were measured on clean specular surfaces of tungsten, tantalum, niobium, and molybdenum over a temperature range of 1000° to 3000° K (depending on the material); and the electrical resistivities of the metals were also measured over the same temperature range. The total hemispherical

emittance was obtained from the measured power dissipation within the uniform temperature region of an electrically heated ribbon specimen. The temperature was measured with tungsten/tungsten, 26-percent rhenium thermocouples which had been specially calibrated. The total normal emittance was determined with a radiation thermopile. The ratio of total hemispherical emittance to total normal emittance was also calculated directly from the angular distribution obtained by rotating the ribbon within the field of view of the thermopile. The data so obtained have been compared with the results predicted by the theoretical equations referred to above.

Direct measurements of the normal spectral emittance out to 5 μ are now being made on the refractory metals by using three metal ribbons to form a closed tube of triangular cross section. The radiation from a small rectangular hole in one of the ribbons is compared with the radiation from the surface adjacent to it with a Perkin-Elmer double-pass monochrometer as in the method used by De Vos (ref. 3). These measurements will be made for wavelengths up to 25 μ as a function of angle for

both planes of polarization. The spectral emittance data will be compared with the results predicted by the theoretical spectral emissivity equations. The data will also be integrated with respect to wavelength to determine the total emittance, which can then be compared with the total emittance values already measured directly.

The study of emissivity can provide additional insight into the microscopic phenomena occurring in solids, particularly near their surfaces. While the spectral emissivity is capable of providing a more detailed picture, the total emittance, particularly the total hemispherical emittance, in many cases can be determined much more readily and more accurately. Any complete theory of emissivity must be able to predict the total emissivity and its variation with temperature. Furthermore, from an engineering point of view it is the total hemispherical emittance which is usually of primary concern in matters that involve radiant heat transfer.

SYMBOLS

a	Relaxation parameter, $1.31 \times 10^{11} \tau T = y/x$
C_1	Planck's first radiation constant
C_2	Planck's second radiation constant
c	Velocity of light
D	Complex dielectric constant
D'	Real part of dielectric constant
D''	Imaginary part of dielectric constant
e	Electronic charge
i	$\sqrt{-1}$
J	Spectral intensity given by the Planck distribution, radiant power per unit area per unit wavelength interval
j	$[(1+y^2)^{1/2} - y]^{1/2}$
m	Mass of the electron
N	Number of free electrons per unit volume
T	Absolute temperature
x	$C_2/\lambda T$
y	$\omega \tau$
Z_n	Defined by the equation $\epsilon_n = 2/(1 + Z_n)$
Z_p	Defined by the equation $\epsilon_p = 2/(1 + Z_p)$
ϵ_H	Total hemispherical emissivity
ϵ_h	Spectral hemispherical emissivity (including both planes of polarization)
ϵ_N	Total normal emissivity
ϵ_n	Spectral emissivity (electric vector normal to the plane of emergence); ϵ_n is a function of θ
ϵ_{nh}	Spectral hemispherical emissivity (electric vector normal to the plane of emergence)

ϵ_o	Normal spectral emissivity (including both planes of polarization)
ϵ_p	Spectral emissivity (electric vector in the plane of emergence); ϵ_p is a function of θ
ϵ_{ph}	Spectral hemispherical emissivity (electric vector parallel to the plane of emergence)
θ	Angle of incidence or emergence of radiation
λ	Wavelength
ρ	Electrical resistivity
σ	Stefan-Boltzmann constant
τ	Electronic relaxation time
ω	Angular frequency of the electromagnetic wave

BACKGROUND

The thermal radiation from a solid surface can best be described in terms of its absolute temperature and its emittance. If the surface is black, that is, if it absorbs all of the energy impinging upon it, it will radiate in accordance with the following laws of blackbody radiation.

(1) Stefan-Boltzmann law: The total radiant power emitted per unit area is given by $H = \sigma T^4$ where σ is the Stefan-Boltzmann constant and T is the absolute temperature.

(2) Planck's law: The spectral distribution of the radiation in radiant power per unit area per unit wavelength interval is given by

$$J = C_1 \lambda^{-5} [\exp(C_2/\lambda T) - 1]^{-1}$$

where C_1 and C_2 are Planck's first and second radiation constants and λ is the wavelength.

(3) Lambert's cosine law: The intensity of the radiation is proportional to the cosine of the angle of emergence. From this law it follows that the total normal and the spectral normal intensities in units of radiant power per unit area per steradian and radiant power per unit area per unit wavelength interval per steradian are equal to H/π and J/π , respectively.

(4) The intensity of the radiation at any angle is independent of the plane of polarization.

Emittance is the property of a real surface; it is the ratio of the rate of emission of radiant energy from the surface to the rate of emission from a blackbody radiator at the same temperature under the same conditions. Emissivity is a fundamental property of a material and is numerically equal to the emittance of a specimen of the material that has an optically smooth surface and is sufficiently thick to be opaque. It is further assumed that the surface is

free from contamination and that the crystalline structure, and its defects adjacent to the surface are the same as those of the interior. The emittance and emissivity can be either normal, angular, or hemispherical, depending upon whether the comparison with the black surface is of the intensity radiated normal to the surface, of that emitted at some other angle, or of the power radiated over all angles. They can also be either spectral or total, depending upon whether the comparison is made with monochromatic radiation or whether it includes the radiation at all wavelengths. These parameters will in general be different for each plane of polarization, except for normal emergence.

General expressions will be developed in this article which relate the spectral emissivity to the complex dielectric constant. These equations will be written down specifically for metals, making use of the complex dielectric constant which takes the electronic relaxation time into account. An equation for the total normal emissivity will be obtained by integrating the intensity at normal emergence over all wavelengths and dividing it by the normal blackbody intensity. An expression for the total hemispherical emissivity will be found by integrating over all angles for each plane of polarization as well as over the entire wavelength range.

SPECTRAL EMISSIVITY

Consider, first, a homogeneous and opaque solid at a uniform temperature T with a perfectly specular surface. Blackbody conditions exist in the interior of the solid and blackbody radiation impinges on its inner surface. A fraction R of this radiation is internally reflected and a fraction $\epsilon = 1 - R$ escapes, where ϵ is the emissivity.

In texts on optics or electromagnetic theory (ref. 4) the reflectivities are given by

$$R_n = \frac{\sin^2(\theta - \phi)}{\sin^2(\theta + \phi)}$$

and

$$R_p = \frac{\tan^2(\theta - \phi)}{\tan^2(\theta + \phi)}$$

where R_n is the reflectivity for radiation whose

electric vector is normal to the plane of incidence, R_p is the reflectivity for radiation whose electric vector lies in the plane of incidence, θ is the angle of incidence, and ϕ is the angle of refraction. According to Snell's law, $\sin \theta = n \sin \phi$, where n is the index of refraction, which is equal to the square root of the dielectric constant D for insulators. The reflectivities in terms of the angle of incidence are given by

$$R_n = \frac{|\cos \theta - (D - \sin^2 \theta)^{1/2}|^2}{|\cos \theta + (D - \sin^2 \theta)^{1/2}|^2} \quad (1)$$

and

$$R_p = \frac{|D \cos \theta - (D - \sin^2 \theta)^{1/2}|^2}{|D \cos \theta + (D - \sin^2 \theta)^{1/2}|^2} \quad (2)$$

These expressions are satisfactory for an absorbing medium if the dielectric constant is considered to be complex so that $D = D' + iD''$.

Since $\epsilon = 1 - R$, some algebraic manipulation of equations (1) and (2) leads to the following expressions for the emissivity for radiation polarized normal and parallel respectively to the plane of emergence:

$$\epsilon_n = \frac{2}{1 + Z_n} \quad \epsilon_p = \frac{2}{1 + Z_p} \quad (3)$$

where Z_n and Z_p are given by

$$Z_n = \frac{[(D' - \sin^2 \theta)^2 + D''^2]^{1/2} + \cos^2 \theta}{\sqrt{2} \cos \theta [(D' - \sin^2 \theta)^2 + D''^2]^{1/2} + D' - \sin^2 \theta} \quad (4)$$

$$Z_p = \frac{[(D' - \sin^2 \theta)^2 + D''^2]^{1/2} + (D'^2 + D''^2) \cos^2 \theta}{\left[\sqrt{2} \cos \theta [(D' - \sin^2 \theta)^2 + D''^2]^{1/2} (D'^2 + D''^2) + (D'^2 - \sin^2 \theta)(D'^2 - D''^2) + 2D'D'' \right]^{1/2}} \quad (5)$$

In this article the classical contribution of the free electrons to the emissivity of metals is considered. The effect of the bound electrons, the internal photoelectric effect, and the anomalous skin effect will not be treated. The spectral emissivity equations taking the electronic relaxation time of the free electrons into account are developed here.

From Mott and Jones (ref. 5) the dielectric constant of a metal, considering only the free

electrons, is given by

$$D=1-\frac{4\pi Ne^2\tau^2}{m(\omega^2\tau^2+1)}-i\frac{4\pi Ne^2\tau/\omega}{m(\omega^2\tau^2+1)}$$

since $D=n^2-k^2+2ink$, where n is the index of refraction and k is the index of absorption. N is the number of free electrons per unit volume, e is the electronic charge in statcoulombs, τ is the relaxation time, m is the mass of the electron, and ω is the angular frequency. This can be written

$$D=1-\frac{y+i}{1+y^2}\frac{4\pi Ne^2}{m}\frac{\tau}{\omega} \quad (6)$$

where $y=\omega\tau$. Since the electrical resistivity ρ (in statohm-centimeters), is equal to

$$\rho=\frac{m}{Ne^2\tau} \quad (7)$$

and $\omega=(2\pi c)/\lambda$ where λ is the wavelength and c is the velocity of light, then $D=1-[(y+i)/(1+y^2)](2/c)(\lambda/\rho)$. If λ is expressed in centimeters, and ρ in ohm-centimeters, then in

$$D=1-\frac{y+i}{1+y^2}\frac{60\lambda}{\rho} \quad (8)$$

where D is dimensionless, the constant 60 having units of ohms⁻¹. From the preceding equations

$$y=\omega\tau=\frac{2\pi cm}{\lambda\rho Ne^2}=1.1\times 10^{-9}V/S\rho\lambda \quad (9)$$

where V is the atomic volume, S is the effective number of free electrons per atom, and again ρ and λ are in ohm-centimeters and centimeters.

In order that the first term, 1, on the right-hand side of equation (8) and the term $\sin^2\theta$ in equations (4) and (5) be negligible, either $[1/(1+y^2)](60\lambda/\rho)\gg 1$, or $[y/(1+y^2)](60\lambda/\rho)\gg 1$.

About 99 percent of the thermal radiation from a black surface occurs for λT greater than 0.13, so the inequality

$$\rho T\ll\frac{7.8}{1+y^2}\text{ or } \rho T\ll\frac{7.8y}{1+y^2} \quad (10)$$

is a necessary condition if equation (8) is to hold. When y is small the first inequality holds

adequately well for all of the metals. When y is large, the second inequality becomes $\rho T\ll 7.8/y$. Usually V/S is about 10 so that $1/y\approx 10^8\rho\lambda$ and the second inequality simplifies to $T\ll 10,000^\circ\text{ K}$. This temperature is based on the short-wavelength limit at $\lambda T=0.13$. At λT for the maximum of the spectral distribution $T\ll 15,000^\circ\text{ K}$. If these approximations are assumed to hold, $y=D'/D''$ and equations (4) and (5) can be rewritten as

$$Z_n=\frac{(1+y^2)^{1/4}}{\sqrt{2}j}\left[\left(\frac{\rho}{60\lambda}\right)^{1/2}\frac{(1+y^2)^{1/4}}{(\cos\theta)^{-1}}+\left(\frac{60\lambda}{\rho}\right)^{1/2}\frac{(\cos\theta)^{-1}}{(1+y^2)^{1/4}}\right] \quad (11)$$

$$Z_p=\frac{(1+y^2)^{1/4}}{\sqrt{2}j}\left[\left(\frac{\rho}{60\lambda}\right)^{1/2}\frac{(1+y^2)^{1/4}}{\cos\theta}+\left(\frac{60\lambda}{\rho}\right)^{1/2}\frac{\cos\theta}{(1+y^2)^{1/4}}\right] \quad (12)$$

where

$$j=[(1+y^2)^{1/2}-y]^{1/2}\text{ so that } 1/j=[(1+y^2)^{1/2}+y]^{1/2}. \quad (13)$$

Since

$$\left(\frac{\rho}{60\lambda}\right)^{1/2}(1+y^2)^{1/4}\ll\left(\frac{60\lambda}{\rho}\right)^{1/2}\frac{1}{(1+y^2)^{1/4}}$$

except for very large values of y , which are not of concern here, the normal-emergence value of Z , which is the same for both planes of polarization, is given by

$$Z_n=Z_p=\left(\frac{30\lambda}{\rho}\right)^{1/2}[(1+y^2)^{1/2}-y]^{-1/2} \quad (14)$$

and the normal spectral emissivity is given by

$$\epsilon_0=\frac{2}{j\left(\frac{30\lambda}{\rho}\right)^{1/2}+1}=2\sum_{m=1}^{\infty}(-1)^{m+1}j^m\left(\frac{\rho}{30\lambda}\right)^{m/2}. \quad (15)$$

TOTAL EMISSIVITY

The spectral distribution of intensity normal to the surface of a perfectly black radiator in radiant power per unit area per unit wavelength interval per steradian is given by

$$\frac{J}{\pi} = \frac{C_1}{\pi} \frac{1}{\lambda^5} \left[\exp\left(\frac{C_2}{\lambda T}\right) - 1 \right]^{-1}. \quad (16)$$

Integrating equation (16) over all wavelengths gives the radiant power per unit area per steradian:

$$\int_0^\infty \frac{J}{\pi} d\lambda = \frac{C_1}{\pi} \int_0^\infty \frac{1}{\lambda^5} \left[\exp\left(\frac{C_2}{\lambda T}\right) - 1 \right]^{-1} d\lambda = \frac{\sigma T^4}{\pi} \quad (17)$$

where $\sigma = (C_1/15)(\pi/C_2)^4$ is the Stefan-Boltzmann constant.

In order to determine the total normal emissivity it is necessary to multiply the spectral emissivity, equation (15), by the normal Planck distribution, equation (16), integrate over all wavelengths, and divide by $\sigma T^4/\pi$. That is,

$$\begin{aligned} \epsilon_N &= \frac{\pi}{\sigma T^4} \int_0^\infty \frac{\epsilon_{0j} J d\lambda}{\pi} \\ &= \frac{30 C_2^4}{\pi^4 T^4} \sum_{m=1}^\infty \sum_{n=1}^\infty \int_0^\infty (-1)^{m+1} j^m \\ &\quad \left(\frac{\rho}{30\lambda} \right)^{m/2} \frac{1}{\lambda^5} \exp\left(\frac{-nC_2}{\lambda T}\right) d\lambda \end{aligned}$$

By letting $x = C_2/\lambda T$

$$\epsilon_N = \frac{30}{\pi^4} \sum_{m=1}^\infty \sum_{n=1}^\infty \int_0^\infty (-1)^{m+1} j^m \left(\frac{\rho T}{30 C_2} \right)^{m/2} x^{3+(m/2)} \exp(-nx) dx \quad (18)$$

It is useful first to consider the case where the electronic relaxation time can be neglected. In this case $j=1$, and equation (18) becomes

$$\epsilon_N = \frac{30}{\pi^4} \sum_{m=1}^\infty (-1)^{m+1} \left(\frac{\rho T}{30 C_2} \right)^{m/2} \sum_{n=1}^\infty \int_0^\infty x^{3+(m/2)} \exp(-nx) dx \quad (19)$$

$$= \frac{30}{\pi^4} \sum_{m=1}^\infty (-1)^{m+1} \left(\frac{\rho T}{30 C_2} \right)^{m/2} \sum_{n=1}^\infty \frac{\Gamma\left(4 + \frac{m}{2}\right)}{n^{4+(m/2)}} \quad (20)$$

$$= 0.578(\rho T)^{1/2} - 0.178(\rho T) + 0.0584(\rho T)^{3/2} - \dots \quad (21)$$

This result is identical with that of Foote except that it takes into account one more term which is needed at larger values of ρT . The coefficient of the third term for the total normal emissivity was erroneously given as 0.044 in the article by Davisson and Weeks (ref. 2).

As it is given in equation (13), j and its second and third powers make equation (18) unwieldy to integrate. Therefore, the following approximations to j , j^2 , and j^3 , designated as j_* , j_*^2 , and j_*^3 , respectively, were used to simplify the integration.

$$j_* = 0.430 \exp(-1.05y) + 0.330 \exp(-0.245y) + 0.240 \exp(-0.0207y) \quad (22)$$

$$j_*^2 = 0.700 \exp(-1.32y) + 0.240 \exp(-0.31y) + 0.060 \exp(-0.043y) \quad (23)$$

$$j_*^3 = 0.560 \exp(-2.43y) + 0.400 \exp(-0.79y) + 0.040 \exp(-0.125y) \quad (24)$$

The accuracy with which these three expressions approximate j , j^2 , and j^3 over the significant range of y is demonstrated in table I.

From equation (9)

$$y = \omega\tau = \frac{2\pi c}{C_2} \tau T x = ax$$

where $a = 1.31 \times 10^{11} \tau T$ and $x = C_2/\lambda T$. The product τT is independent of wavelength and only mildly variant with temperature for the metals. This quantity, derived by using equation (7), is tabulated in table II. The values listed in this table are bulk properties and may be different at the surface where the radiating properties are controlled.

When $j \neq 1$, the first three terms for the total normal emissivity are then given as:

$$\begin{aligned} \epsilon_N &= \frac{30}{\pi^4} \left(\frac{\rho T}{30 C_2} \right)^{1/2} \sum_{n=1}^\infty \int_0^\infty x^{3.5} \{ 0.43 \exp[-(n \\ &\quad + 1.05a)x] + 0.33 \exp[-(n + 0.245a)x] \\ &\quad + 0.24 \exp[-(n + 0.0207a)x] \} dx \\ &\quad + \frac{30}{\pi^4} \left(\frac{\rho T}{30 C_2} \right) \sum_{n=1}^\infty \int_0^\infty x^4 \{ 0.70 \exp[-(n \\ &\quad + 1.32a)x] + 0.24 \exp[-(n + 0.31a)x] \} dx \end{aligned}$$

TABLE I.—Comparison of j , j_1 , j_2 , and j_3 with Approximate Values Given by Equations (22), (23), and (24)

y	j	j_1	Error, percent	j^2	j_1^2	Error, percent	j^3	j_1^3	Error, percent
0	1	1	0	1	1	0	1	1	0
0.1	0.950	0.949	0.11	0.903	0.907	0.44	0.858	0.857	0.12
.2	.905	.905	0	.820	.823	.37	.742	.728	1.89
.4	.822	.819	.37	.677	.684	1.03	.556	.542	2.52
.6	.751	.751	0	.565	.574	1.59	.425	.417	1.88
.8	.692	.693	.14	.480	.488	1.67	.333	.330	.90
1.0	.642	.642	0	.413	.421	1.93	.265	.266	.38
1.2	.600	.602	.33	.360	.367	1.94	.216	.219	1.39
1.4	.565	.566	.18	.320	.320	0	.181	.184	1.65
1.6	.535	.535	0	.286	.287	.35	.153	.158	3.27
1.8	.510	.508	.39	.260	.259	.38	.133	.135	1.50
2.0	.486	.485	.21	.236	.234	.85	.115	.117	1.74
4.0	.351	.351	0	.123	.119	3.25	.0431	.0420	2.55
6.0	.288	.288	0	.083	.083	0	.0239	.023	.42
8.0	.249	.249	0	.062	.063	1.61	.0154	.0155	.65
10.0	.223	.224	.45	.0499	.050	.20	.0111	.0115	3.60
15.0	.182	.184	1.10	.0333	.033	.90	.0061	.0061	0
20.0	.158	.160	1.27	.025	.025	0	.0039	.0033	15.4
25.0	.141	.143	1.42	.020	.0205	2.5	.0028	.0018	37.7
30.0	.129	.129	0	.0167	.0166	.60	.0022	.0010	54.6

$$\begin{aligned}
& +0.06 \exp [-(n+0.043a)x] dx \\
& + \frac{30}{\pi^4} \left(\frac{\rho T}{30C_2} \right)^{3/2} \sum_{n=1}^{\infty} \int_0^{\infty} x^{4.5} \{ 0.56 \exp [-(n \\
& + 2.43a)x] + 0.40 \exp [-(n+0.79a)x] \\
& + 0.04 \exp [-(n+0.125a)x] \} dx. \quad (25)
\end{aligned}$$

The integrals appearing in equation (25) and their solutions are of the form

$$\int_0^{\infty} x^z \exp [-(n+k)x] dx = \frac{\Gamma(z+1)}{(n+k)^{z+1}}.$$

The quantity

$$\sum_{n=1}^{\infty} \left(\frac{1}{n+k} \right)^{z+1} \div \sum_{n=1}^{\infty} \left(\frac{1}{n} \right)^{z+1} \equiv q_z$$

can be approximated for $z=3.5$, 4.0, and 4.5 by the functions

$$q'_{3.5} = (1+k)^{-4.33}, \quad q'_{4.0} = (1+k)^{-4.85},$$

$$\text{and } q'_{4.5} = (1+k)^{-5.38}.$$

The accuracy of this approximation is demonstrated in table III.

These relationships can be used to evaluate equation (25) in terms of the emissivity in the $y=0$ case. Hence

$$\begin{aligned}
\epsilon_N = & \left[\frac{0.430}{(1+1.05a)^{4.33}} + \frac{0.330}{(1+0.245a)^{4.33}} \right. \\
& + \left. \frac{0.240}{(1+0.0207a)^{4.33}} \right] 0.578(\rho T)^{1/2} \\
& - \left[\frac{0.700}{(1+1.32a)^{4.85}} + \frac{0.240}{(1+0.31a)^{4.85}} \right. \\
& + \left. \frac{0.0600}{(1+0.043a)^{4.85}} \right] 0.178(\rho T) \\
& + \left[\frac{0.560}{(1+2.43a)^{5.38}} + \frac{0.400}{(1+0.79a)^{5.38}} \right. \\
& + \left. \frac{0.0400}{(1+0.125a)^{5.38}} \right] 0.0584(\rho T)^{3/2} \quad (26)
\end{aligned}$$

which can be written

$$\begin{aligned}
\epsilon_N = & 0.578p_1(\rho T)^{1/2} - 0.178p_2(\rho T) \\
& + 0.0584p_3(\rho T)^{3/2} \quad (27)
\end{aligned}$$

TABLE II.—*Relaxation Times and Electrical Resistivities at Room Temperature.*

Metal	τ , sec (10^{-12})*	τT , deg-sec (10^{-12})*	a	ρ , ohm-cm	$(\rho/T)^{1/2}$, (ohm-cm/deg) $^{1/2}$ (10^{-4})*
Lithium.....	8.6	2.3	0.30	9.2	1.77
Sodium.....	31	8.5	1.1	4.7	1.27
Potassium.....	44	12	1.6	6.6	1.5
Rubidium.....	27	7.4	.97	12.5	2.07
Cesium.....	21	5.7	.75	19.9	2.61
Copper.....	27	7.3	.96	1.72	.77
Silver.....	41	11	1.5	1.59	.74
Gold.....	29	7.9	1.0	2.44	.91
Nickel.....	9.8	2.7	.35	7.8	1.63
Cobalt.....	9.2	2.5	.33	9.8	3.34
Iron.....	24	6.6	.87	10.0	1.85
Palladium.....	9.2	2.5	.33	11.0	1.94
Platinum.....	9.0	2.5	.32	10.0	1.85

*Multiply each value in column by this factor.

where the multiplier function p is tabulated in table IV and plotted as a function of a in figure 1. Values of a for several of the metals are listed in table II.

Equation (27) can now be written explicitly for the values of a used in table IV which includes essentially the whole range of a values encountered in metals. For

$$a=0 \quad \epsilon_N = 0.578(\rho T)^{1/2} - 0.178(\rho T) + 0.0584(\rho T)^{3/2}$$

$$a=0.2 \quad \epsilon_N = 0.403(\rho T)^{1/2} - 0.0826(\rho T) + 0.0165(\rho T)^{3/2}$$

$$a=0.5 \quad \epsilon_N = 0.290(\rho T)^{1/2} - 0.0417(\rho T) + 0.00606(\rho T)^{3/2}$$

$$a=1.0 \quad \epsilon_N = 0.212(\rho T)^{1/2} - 0.0219(\rho T)$$

$$a=1.5 \quad \epsilon_N = 0.175(\rho T)^{1/2} - 0.0153(\rho T) + 0.00234(\rho T)^{3/2} + 0.00128(\rho T)^{3/2} \quad (28)$$

These equations are shown graphically in figure 2. The factor $(\rho T)^{1/2}$ is conveniently written as $(\rho/T)^{1/2}T$, where $(\rho/T)^{1/2}$ is only a mild function of temperature and is listed for several of the metals in table II.

In order to get the total hemispherical emissivity we must go back to the equations of spectral emissivity as a function of angle and plane of polarization. From equations (11) and (12) we can write:

$$Z_n = A \left(\frac{B}{\cos \theta} + \frac{\cos \theta}{B} \right)$$

TABLE III.—*Comparison of Approximate Functions*

k	$q_{3.5}$	$q'_{3.5}$	$q_{4.0}$	$q'_{4.0}$	$q_{4.5}$	$q'_{4.5}$
0.02	0.915	0.918	0.907	0.908	0.898	0.899
.05	.805	.810	.787	.789	.767	.769
.10	.659	.662	.627	.629	.598	.598
.20	.452	.454	.411	.412	.374	.374
.50	.173	.173	.140	.140	.113	.113
1.00	.051	.050	.036	.035	.025	.024
2.00	.009	.009	.005	.005	.003	.003

TABLE IV.—Values of the Multiplier Functions p_1 , p_2 , and p_3 for a Range of Values of the Relaxation Parameter a

a	p_1	p_2	p_3
0.0	1.000	1.000	1.000
.2	.697	.464	.283
.5	.501	.234	.104
1.0	.367	.123	.040
1.5	.303	.086	.022

$$Z_p = A \left(B \cos \theta + \frac{1}{B \cos \theta} \right)$$

where

$$A = (2)^{-1/2} [1 - (1 + 1/y^2)^{-1/2}]^{-1/2} = \frac{(1 + y^2)^{1/4}}{\sqrt{2}y}$$

and

$$B = \left(\frac{60\lambda}{\rho} \right)^{1/2} \frac{1}{(1 + y^2)^{1/4}}$$

Hence, from equations (3)

$$\epsilon_n = \frac{2B \cos \theta}{B \cos \theta + AB^2 + A \cos^2 \theta} \quad (29)$$

$$\epsilon_p = \frac{2B \cos \theta}{B \cos \theta + AB^2 \cos^2 \theta + A} \quad (30)$$

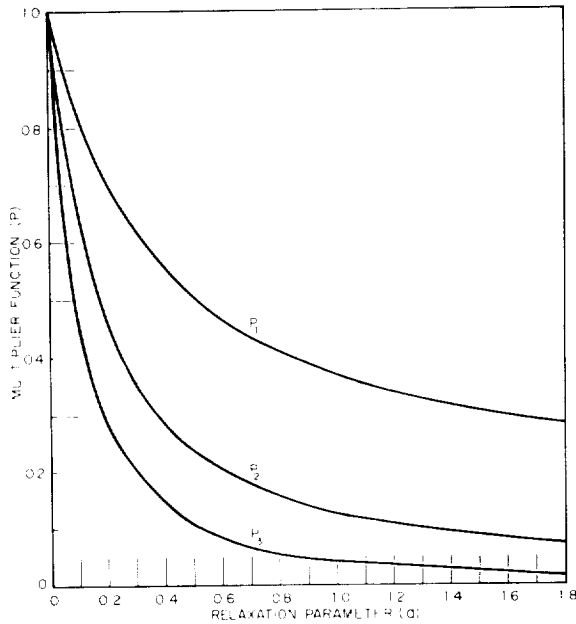


FIGURE 1.—Multiplier functions.

In all cases $B^2 \gg \cos \theta$, so that ϵ_n reduces to

$$\epsilon_n = \frac{2B \cos \theta}{B \cos \theta + AB^2} \quad (31)$$

The spectral hemispherical emissivity is defined by

$$\epsilon_h J \equiv \int_0^{\pi/2} (\epsilon_n + \epsilon_p) \frac{J}{2\pi} \cos \theta \, 2\pi \sin \theta \, d\theta \quad (32)$$

A fraction $1/(2\pi)$ of the radiation from a blackbody appears in a unit solid angle normal to the surface for each plane of polarization. The energy radiated per unit solid angle is proportional to the cosine of the angle for each plane of polarization for radiation from a black surface. Considering each plane separately,

$$\epsilon_h = \frac{\epsilon_{nh}}{2} + \frac{\epsilon_{ph}}{2}$$

where

$$\frac{\epsilon_{nh}}{4B} = \int_0^1 \frac{\cos^2 \theta \, d\cos \theta}{B \cos \theta + AB^2} \quad (33)$$

$$\frac{\epsilon_{ph}}{4B} = \int_0^1 \frac{\cos^2 \theta \, d\cos \theta}{B \cos \theta + AB^2 \cos^2 \theta + A} \quad (34)$$

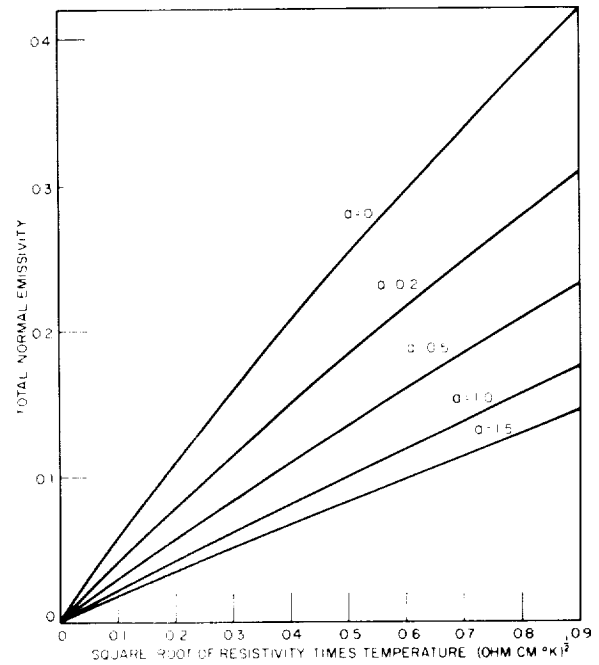


FIGURE 2.—Total normal emissivity.

The integration of equation (33) leads to

$$\frac{\epsilon_{nh}}{4} = \frac{1}{2} - AB + (AB)^2 \log \left(1 + \frac{1}{AB} \right)$$

If the logarithm is expanded,

$$\frac{\epsilon_{nh}}{4} = \frac{1}{3} \frac{1}{AB} - \frac{1}{4} \left(\frac{1}{AB} \right)^2 + \frac{1}{5} \left(\frac{1}{AB} \right)^3 + \dots$$

which is equal to

$$\frac{\epsilon_{nh}}{4} = \frac{j}{3} \left(\frac{\rho}{30\lambda} \right)^{1/2} - \frac{j^2}{4} \left(\frac{\rho}{30\lambda} \right) + \frac{j^3}{5} \left(\frac{\rho}{30\lambda} \right)^{3/2} + \dots \quad (35)$$

The integration of equation (34) yields

$$\begin{aligned} \frac{\epsilon_{ph}}{4} = \frac{1}{AB} - \left(\frac{1}{AB} \right)^2 \left\{ \log B - \frac{1-2A^2}{(4A^2-1)^{1/2}} \right. \\ \left. \left[\tan^{-1} \frac{2AB+1}{(4A^2-1)^{1/2}} - \tan^{-1} \frac{1}{(4A^2-1)^{1/2}} \right] \right\} \\ - \frac{1}{2} \left(\frac{1}{AB} \right)^3 \end{aligned}$$

which is equal to

$$\begin{aligned} \frac{\epsilon_{ph}}{4} = j \left(\frac{\rho}{30\lambda} \right)^{1/2} - j^2 \left(\frac{\rho}{30\lambda} \right) \\ \left\{ \log \left[\left(\frac{60\lambda}{\rho} \right)^{1/2} (1+y^2)^{-1/4} \right] \right. \\ \left. + y \left\{ \tan^{-1} \left[\left(\frac{30\lambda}{\rho} \right)^{1/2} 2j + j^2 \right] \right. \right. \\ \left. \left. - \tan^{-1} j^2 \right\} \right\} - \frac{j^3}{2} \left(\frac{\rho}{30\lambda} \right)^{3/2} + \dots \quad (36) \end{aligned}$$

Before proceeding further, the equation for the total hemispherical emissivity, ϵ_H , will be derived on the assumption that the electronic relaxation time is negligibly small. In this case $y=0$ and $j=1$ so that

$$\frac{\epsilon_{nh}}{4} = \frac{1}{3} \left(\frac{\rho}{30\lambda} \right)^{1/2} - \frac{1}{4} \left(\frac{\rho}{30\lambda} \right) + \frac{1}{5} \left(\frac{\rho}{30\lambda} \right)^{3/2} - \dots \quad (37)$$

$$\frac{\epsilon_{ph}}{4} = \left(\frac{\rho}{30\lambda} \right)^{1/2} - \frac{1}{2} \left(\frac{\rho}{30\lambda} \right) \log \left(\frac{60\lambda}{\rho} \right)$$

$$- \frac{1}{2} \left(\frac{\rho}{30\lambda} \right)^{3/2} + \dots \quad (38)$$

$$\begin{aligned} \epsilon_h = \frac{\epsilon_{nh}}{2} + \frac{\epsilon_{ph}}{2} = \frac{8}{3} \left(\frac{\rho}{30\lambda} \right)^{1/2} - \left(\frac{1}{2} + \log \frac{60\lambda}{\rho} \right) \left(\frac{\rho}{30\lambda} \right) \\ - \frac{3}{5} \left(\frac{\rho}{30\lambda} \right)^{3/2} + \dots \quad (39) \end{aligned}$$

The spectral hemispherical emissivity must be multiplied by the Planck distribution, integrated over all wavelengths, and divided by the total radiation from a blackbody to determine the total hemispherical emissivity. Thus,

$$\epsilon_H = \int_0^\infty \frac{\epsilon_h J d\lambda}{\sigma T^4} = \frac{1}{\sigma T^4} \int_0^\infty \epsilon_h \frac{C_1}{\lambda^5} \sum_{n=1}^\infty \exp \left(-\frac{nC_2}{\lambda T} \right) d\lambda \quad (40)$$

By the previous substitution $x = C_2/\lambda T$,

$$\begin{aligned} \epsilon_h = \frac{8}{3} \left(\frac{\rho T}{30C_2} \right)^{1/2} x^{1/2} - \left(\frac{1}{2} + \log \frac{60C_2}{\rho T} - \log x \right) \frac{\rho T x}{30C_2} \\ - \frac{3}{5} \left(\frac{\rho T}{30C_2} \right)^{3/2} x^{3/2} \end{aligned}$$

or simply

$$\epsilon_h = A_H x^{1/2} - B_H x + C_H x \log x - D_H x^{3/2}$$

where

$$A_H = \frac{8}{3} \left(\frac{\rho T}{30C_2} \right)^{1/2} \quad B_H = \left(\frac{1}{2} + \log \frac{60C_2}{\rho T} \right)$$

$$C_H = \left(\frac{\rho T}{30C_2} \right) \quad D_H = \frac{3}{5} \left(\frac{\rho T}{30C_2} \right)^{3/2}$$

and

$$\begin{aligned} \epsilon_H = \frac{C_1}{\sigma C_2^4} \int_0^\infty (A_H x^{1/2} - B_H x + C_H x \log x \\ - D_H x^{3/2}) x^3 \sum_{n=1}^\infty \exp(-nx) dx \end{aligned}$$

Since

$$\sigma = \frac{\pi^4}{15} \frac{C_1}{C_2^4}$$

$$\begin{aligned} \frac{\pi^4}{15} \epsilon_H = A_H \int_0^\infty x^{3.5} \sum_{n=1}^\infty \exp(-nx) dx \\ - B_H \int_0^\infty x^4 \sum_{n=1}^\infty \exp(-nx) dx \end{aligned}$$

$$+C_H \int_0^\infty x^4 \log x \sum_{n=1}^\infty \exp(-nx) dx$$

$$-D_H \int_0^\infty x^{4.5} \sum_{n=1}^\infty \exp(-nx) dx$$

$$\frac{\pi^4}{15} \epsilon_H = A_H I - B_H II + C_H III - D_H IV$$

The solutions of I, II, and IV are

$$I = \sum_{n=1}^\infty \frac{\Gamma(4.5)}{n^{4.5}} = 12.264$$

$$II = \sum_{n=1}^\infty \frac{4!}{n^5} = 24.885$$

$$IV = \sum_{n=1}^\infty \frac{\Gamma(5.5)}{n^{5.5}} = 53.649$$

If $Z = nx$,

$$III = \sum_{n=1}^\infty \int_0^\infty x^4 \log x \exp(-nx) dx$$

$$= \sum_{n=1}^\infty \frac{1}{n^5} \left[\int_0^\infty Z^4 \log Z \exp(-Z) dZ \right. \\ \left. - \log n \int_0^\infty Z^4 \exp(-Z) dZ \right]$$

Integrating by parts gives

$$\int_0^\infty Z^4 \log Z \exp(-Z) dZ$$

$$= \int_0^\infty \log Z d \int_0^\infty Z^4 \exp(-Z) dZ$$

$$= \log Z \int_0^\infty Z^4 \exp(-Z) dZ \Big|_0^\infty$$

$$- \int_0^\infty \frac{1}{Z} \int_0^\infty Z^4 \exp(-Z) dZ dZ$$

$$= -\log Z \exp(-Z)(Z^4 + 4Z^3 + 12Z^2 + 24Z$$

$$+ 24) \Big|_0^\infty + \int_0^\infty \exp(-Z) (Z^3 + 4Z^2 + 12Z + 24$$

$$+ \frac{24}{Z}) dZ = -24 \log Z \exp(-Z) \Big|_0^\infty + (3!)$$

$$+ 4(2!) + 12(1!) + 24 + 24 \int_0^\infty \frac{1}{Z} \exp(-Z) dZ$$

$$= -24 \log Z \exp(-Z) \Big|_0^\infty$$

$$+ 50 + 24 \log Z \exp(-Z) \Big|_0^\infty$$

$$+ 24 \int_0^\infty \log Z \exp(-Z) dZ$$

$$= 50 + 24(-0.577) = 36.15$$

and

$$\log n \int_0^\infty Z^4 e^{-Z} dZ = 4! \log n = 24 \log n$$

so that

$$III = \sum_{n=1}^\infty \frac{36.2 - 24 \log n}{n^5} = 36.8$$

Finally,

$$\epsilon_H = \frac{15}{\pi^4} (A_H I - B_H II + C_H III - D_H IV)$$

$$= 0.766(\rho T)^{1/2} - (0.309 - 0.0889 \log \rho T) \rho T$$

$$- 0.0175(\rho T)^{3/2} + \dots \quad (41)$$

where it has been assumed that $C_2 = 1.439$.

This result which was obtained by a direct integration of the angular distribution of the spectral emissivity should be compared with the equation of Davisson and Weeks (ref. 2) which was derived by the integration of an artificially constructed function to represent the angular distribution of the spectral emissivity. They found that

$$\epsilon_H = 0.751(\rho T)^{1/2} - 0.632(\rho T) + 0.670(\rho T)^{3/2}$$

$$- 0.607(\rho T)^2 \quad (42)$$

Although this equation gives values that are in good agreement with those given by equation (41) for ρT values up to 0.1, it is not useful at much larger values of ρT because it does not converge rapidly enough. Schmidt and Eckert (ref. 6), also using graphical integration, expressed their result as two binomials, for two ranges of ρT ,

$$0 < \rho T < 0.2 \quad \epsilon_H = 0.751(\rho T)^{1/2} - 0.396 \rho T$$

$$0.2 < \rho T < 0.5 \quad \epsilon_H = 0.698(\rho T)^{1/2} - 0.266 \rho T \quad (43)$$

In treating the general case where $y \neq 0$ the total hemispherical emissivity is again given by

$$\epsilon_H = \frac{1}{\sigma T^4} \int_0^\infty \frac{\epsilon_{ph} + \epsilon_{nh}}{2} J_\lambda d\lambda$$

$$= \frac{15}{\pi^4} \int_0^\infty \frac{\epsilon_{nh} + \epsilon_{ph}}{2} x^3 \sum_{n=1}^\infty \exp(-nx) dx$$

and from equations (35) and (36)

$$\frac{\pi^4}{15} \epsilon_H = \sum_{n=1}^\infty \int_0^\infty \left\{ \frac{8j}{3} \left(\frac{\rho T}{30C_2} \right)^{1/2} x^{1/2} - j^2 \left(\frac{\rho T}{30C_2} \right) x \right.$$

$$\left. \left[\frac{1}{2} + \log 60C_2 - \log \rho T - \log x - \frac{1}{2} \log(1+y^2) \right. \right.$$

$$\left. \left. + y\pi - \frac{y}{j} \left(\frac{\rho T}{30C_2} \right)^{1/2} x^{1/2} - 2y \tan^{-1} j^2 \right] \right.$$

$$\left. - \frac{3}{5} j^3 \left(\frac{\rho T}{30C_2} \right)^{3/2} x^{3/2} \right\} x^3 \exp(-nx) dx \quad (44)$$

where $\tan^{-1} [2(30\lambda/\rho)^{1/2}j + j^2]$ has been expanded to yield $(\pi/2) - (\rho/30\lambda)^{1/2}(1/2j) + \dots$ by assuming in this case that $2(30\lambda/\rho)^{1/2} > j$.

By comparing the first term of equation (44) with the first term of equation (18) it can be seen that the first term of the total hemispherical emissivity will always be 4/3 times that for the total normal emissivity regardless of the relaxation time. The other terms for the total

hemispherical emissivity are calculated by a combination of graphical and analytical techniques similar to those used previously for the total normal emissivity and for the zero relaxation time case for the total hemispherical emissivity.

The results are presented here for the same five values of a as those used for the total normal emissivity.

For $a=0$,

$$\epsilon_H = 0.766(\rho T)^{1/2} - (0.309 - 0.0889 \log \rho T) \rho T - 0.0175(\rho T)^{3/2}$$

For $a=0.2$,

$$\epsilon_H = 0.534(\rho T)^{1/2} - (0.218 - 0.0411 \log \rho T) \rho T + 0.0141(\rho T)^{3/2}$$

For $a=0.5$,

$$\epsilon_H = 0.384(\rho T)^{1/2} - (0.172 - 0.0208 \log \rho T) \rho T + 0.0306(\rho T)^{3/2}$$

For $a=1.0$,

$$\epsilon_H = 0.281(\rho T)^{1/2} - (0.153 - 0.0109 \log \rho T) \rho T + 0.0461(\rho T)^{3/2}$$

For $a=1.5$,

$$\epsilon_H = 0.232(\rho T)^{1/2} - (0.148 - 0.0076 \log \rho T) \rho T + 0.0570(\rho T)^{3/2} \quad (45)$$

These equations are plotted in figure 3.

TOTAL EMITTANCE MEASUREMENTS

Radiation Measurements

The total hemispherical emittance was determined by measuring the temperature and the power dissipation in the uniform temperature region of an electrically heated ribbon specimen. Simultaneously, the angular distribution of radiation from the specimen was measured with a calibrated total-radiation thermopile, from which the total normal emittance was determined. The details of the experimental apparatus and techniques have been described previously (ref. 7 and 8).

Figure 4 is a photograph showing the ribbon support structure and other pertinent components within the vacuum chamber. The total emittances of four refractory metals

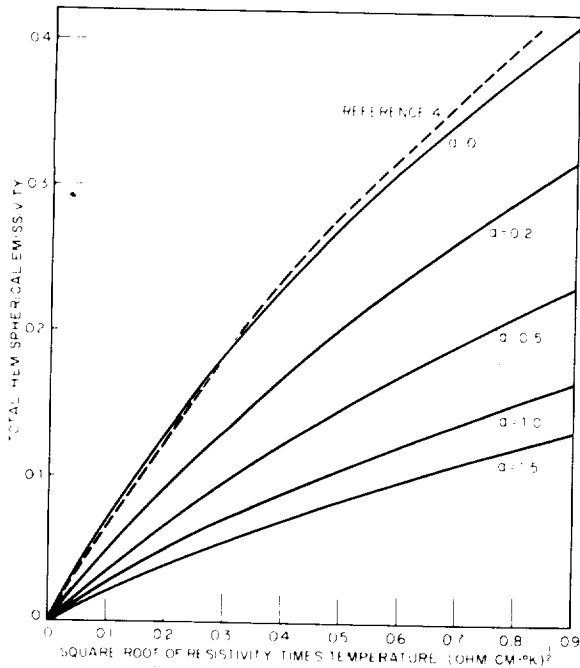


FIGURE 3.—Total hemispherical emissivity.

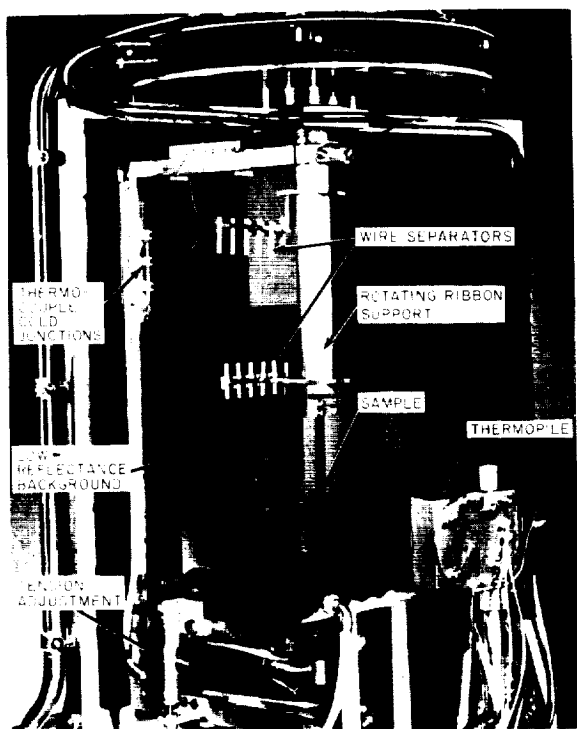


FIGURE 4.—Experimental apparatus.

measured with this technique are presented with a discussion of the problem of temperature determination above 2000° K.

Temperature Determination

The radiant energy emitted by a polished metal surface is proportional to about the fifth power of temperature since, in the equation $H = \epsilon_H \sigma T^4$, the total hemispherical emittance ϵ_H is roughly proportional to the temperature. Accordingly, the temperature is by far the most important variable in any radiation-transfer problem. Unfortunately, its importance is only exceeded by its difficulty of measurement, particularly in the region above 1800° K. Excellent results had been obtained with platinum thermocouples up to 1800° K in previous phases of this project; and it was hoped that refractory-metal thermocouples (tungsten/tungsten, 26-percent rhenium) would provide accurate measurements of temperatures up to 3000° K. Unfortunately, the accuracy and reproducibility were found to be far below that necessary for accurate emittance measurements.

Tungsten/tungsten, 26-percent rhenium thermocouples 0.005 inch in diameter (hereafter designated as W/Re) were obtained from two manufacturers. The first type (referred to as type A) was supplied with a calibration up to 2800° C. The second (referred to as type B) was supplied with a notary-certified calibration up to 2300° C. The type A thermocouple was tried initially on a tantalum ribbon. The wires were attached by drilling 0.005-inch holes in the center of the ribbon about 2 mm apart, inserting the wires through the holes a short distance, and then squeezing the wire by peening the ribbon around the wire with the aid of a punch with rounded nose and a center hole to accommodate the end of the wire. Excess wire was then clipped off. Measured total and spectral emittance values were found to be completely unrealistic. Similar measurements with other ribbons of the same material gave emittances that were not only unrealistic but not reproducible.

The same problem was encountered with type B thermocouples; however, in this case the emittance values at temperatures up to 2000° K appeared at least reasonable, although some nonreproducibility was still noted. Some ribbons were then instrumented with both type A and type B W/Re thermocouples, as well as with a platinum/platinum, 10-percent rhodium thermocouple. Up to 1800° K, type B agreed reasonably well with the platinum thermocouple, whereas type A deviated considerably. Emittances calculated from the platinum-measured temperatures were quite within expectation.

It was evident that a complete calibration of the W/Re thermocouples was necessary before they could be used. A tantalum cylinder $\frac{3}{4}$ inch in diameter and $\frac{1}{2}$ inch deep was instrumented with type A and type B W/Re thermocouples. Two platinum/platinum, 10-percent rhodium thermocouples, one a 0.005-inch working thermocouple and the other a 0.008-inch calibrated standard, were also used. Blackbody holes 0.016 inch in diameter were drilled at various places in the surface. The assembly was placed in the coil of an induction heater and heated in vacuum up to 1800° K. A microoptical pyrometer was used to monitor

the temperature in the blackbody holes. Temperature readings of the pyrometer, the two platinum thermocouples, and the type B W/Re thermocouple agreed well within ± 1 percent over this range, whereas type A deviated as much as 80°C . The platinum thermocouples were then removed, and the comparison was extended to the highest temperature obtainable in the furnace, 2100°K . Type B and the pyrometer remained in agreement to within ± 1 percent whereas type A continued to show large deviations. Although the temperature limit was far below the 3000°K desired, and the thermocouples were not tested in their normal mode of operation (attached to the ribbon), this calibration at least eliminated one of the thermocouples from further consideration.

In order to calibrate the thermocouples in their normal mode of operation, it was necessary to determine the spectral emittance of tantalum as an intermediate step. A tantalum ribbon, 1 cm wide, 6 inches long, and 0.005 inch thick, was folded longitudinally to form a triangular prism with sides approximately $\frac{1}{2}$ cm wide. The length of the prism was about 4 inches. Several 0.005-inch and 0.010-inch holes were drilled into one side to serve as blackbody holes. The prism was instrumented with type B W/Re thermocouples and aged at 2400°K for 15 minutes.

Measurements of true temperature, brightness temperature of the tantalum surface, and thermocouple output voltage were made from 1000°K to 2800°K . The true temperature was obtained by sighting the optical pyrometer

at the blackbody holes; the brightness temperature of the surface was taken adjacent to the holes. The resulting spectral emittance at 0.65 micron is plotted in figure 5. The upper temperature limit was set by the evaporation of the tantalum above 2800°K , which produced sufficient coating on the viewing port to prevent further optical pyrometer observation. A calibration was also obtained for the attached thermocouples, although another check was still necessary for the thermocouples in their normal mode of operation (on a flat strip).

As an added complication, two identical microoptical pyrometers, one recently acquired, the other on hand for 2 years or more, were compared and found to differ by as much as 1 percent in their indicated temperatures. The error was largest in the range of 1800°C to 2200°C . Below this temperature they were nearly identical in calibration. Above this range there was an error but not as serious. These pyrometers have now been recalibrated at the Naval Ordnance Laboratory at Corona, Calif.

Another 6-inch section of the ribbon identical to that which had been formed into the prism was instrumented and aged as before; however, this time the section was used as a flat ribbon. Brightness-temperature measurements, and the calibration data of figure 5 were used to obtain the true temperature, and the thermocouple was again calibrated, with results nearly identical to those of the previous measurement. Hence, a calibration was obtained for type B W/Re thermocouples from 1000°K to 2800°K in their normal mode of operation. The previously mentioned nonreproducibility of emittance data was essentially eliminated by adopting one thermocouple attachment technique, out of the many tried, that gave reproducible results. This technique consisted of inserting the thermocouple wire through the hole in the ribbon, then spreading the end of the wire slightly, and pulling the wire vigorously back into the hole. The wedging was sufficient to hold the wire, and the attachment eliminated the ribbon deformation caused by peening. Results of many measurements confirm the reproducibility of this method. The calibration was within ± 1 percent of

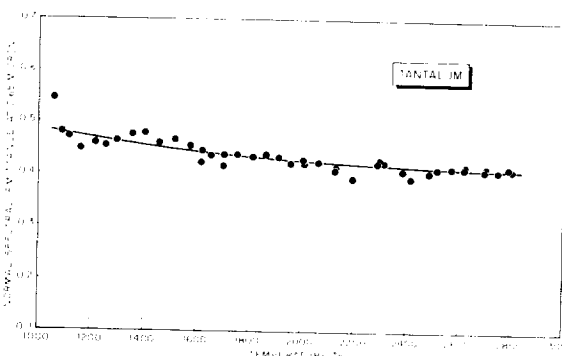


FIGURE 5.—Spectral emittance of tantalum at 0.65μ .

757-044 O-65-3

that supplied with type B thermocouples up to 2150°K . Above this temperature the deviation increased rapidly; it was 90° at 2600°K . In the following description of results, the over-all temperature accuracy is estimated to be within ± 1 percent to 2800°K and ± 1.5 percent from 2800°K to 3000°K . A calibration for the range from 2800°K to 3000°K was obtained by various means of extrapolation. Measurements on tungsten, described in the following section, added confidence to this extrapolation.

Results

TANTALUM

The total hemispherical emittance and the total normal emittance of tantalum, plotted against temperature, are presented in figure 6. The data points for the hemispherical emittance represent measurements from four different samples using both brightness temperature and thermocouple data to determine emittance. At low temperatures tantalum exhibits a gettering action for gases in the vacuum system, with a corresponding increase in the hemispherical emittance, shown by the short dashed line between 1200°K and 1500°K . If the emittance is measured on a fresh unaged tantalum ribbon, it will follow the dashed line to about 1500°K where the gases will be driven off resulting in a sudden drop in the emittance to the solid line. Measurements above this temperature appear quite stable. If, after aging, measurements are made below 1500°K with dispatch, the data will fall on the solid line. However, if a temperature below 1500°K

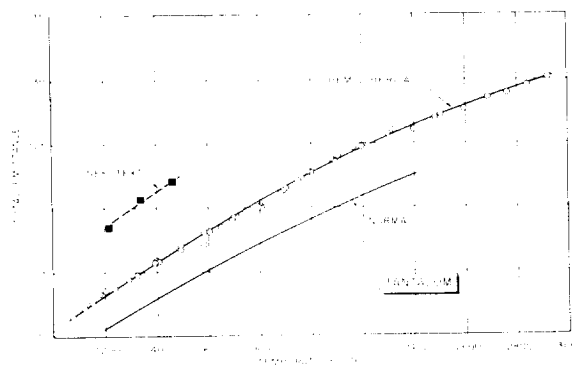


FIGURE 6.—Total emittance of tantalum.

is maintained for an extended period the emittance returns to the dashed line (rate depends on pressure). The gas absorption and liberation can be noted on the vacuum gage connected to the measuring chamber. A separate study of emittances would be advised for those interested in long-term heat-transfer properties below 1500°K .

The total normal emittance shown in figure 6 is calculated from the ratio of total hemispherical to total normal emittance determined from relative angular distribution measurements every 300°K from 1200°K to 2400°K . At the time that angular distribution measurements were being made on tantalum, the thermocouple had not yet had an absolute calibration check so that no total normal emittance values were determined based on absolute normal radiation. The spectral emittance at 0.65 micron is determined with the aid of true and brightness temperatures acquired during the prism thermocouple calibration and plotted against temperature in figure 5.

NIOBIUM

A gettering action similar to that observed with tantalum is exhibited by niobium except that the transition, or outgassing, temperature appears to be 1400°K . This effect can be seen in figure 7, which shows total hemispherical emittance and total normal emittance plotted against temperature up to 2400°K . Evaporation prevented measurements above this tem-

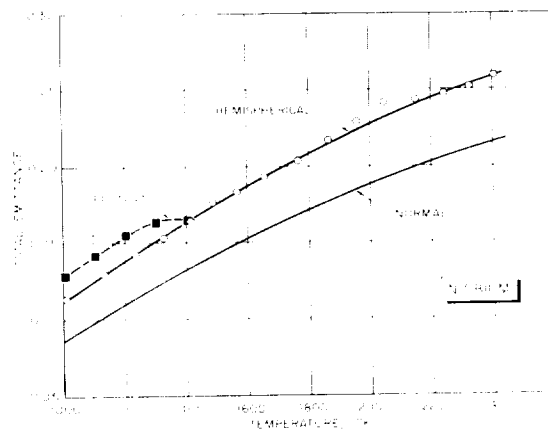


FIGURE 7.—Total emittance of niobium.

perature. The total normal emittance was determined from calibrated thermopile measurements. True temperatures for the niobium measurements were determined with the thermocouples calibrated as previously described.

TUNGSTEN

Considerable effort has been expended by other investigators in studying the thermal-radiation properties of tungsten, with much of the impetus coming from its use by the lighting industry. Consequently, the relation between brightness and true temperature, as determined by Roeser and Wensel and shown in the survey by Gubareff et al. (ref. 9), has been used to obtain the true temperature in this research. Concurrently, however, the calibrated type B W/Re thermocouple was also used.

The total hemispherical emittance, which is quite sensitive to temperature differences, has about ± 5 -percent spread with both temperature-measuring techniques, as can be seen in figure 8. The emittance determined with the brightness temperature (data points indicated by circles) appears generally to be a few percent higher in the middle and upper temperature regions. Considering the problems associated with the thermocouples at high temperatures, and the possible nonequivalence of the tungsten surface used in this investigation and that of Roeser and Wensel, this difference is not surprising. The uncertainty in optical-pyrometer temperatures in the vicinity of 2100°K , pointed out in the

section on temperature determination, could contribute to the wider spread in this region. The reasonable agreement of the results obtained by the two techniques was the basis for using brightness-temperature data to help extrapolate the thermocouple calibration from 2800°K to 3000°K . The tungsten samples used were aged at 2400°K for approximately 30 minutes. The total normal emittance shown in figure 8 was determined with the calibrated thermopile.

MOLYBDENUM

The measurements on molybdenum preceded those on the other metals just discussed, and were made in an earlier apparatus which was originally used for studies of platinum (ref. 10). At first a very high emittance was observed. Although it was quite stable, it was later determined to be due to the formation of molybdenum carbide, Mo_2C , possibly caused by back-streaming of the vapor from the oil diffusion pump. The coating still formed at 10^{-6} torr, but at that pressure it was possible to obtain meaningful emittance measurements provided that they were made rapidly enough.

Figure 9 illustrates the change in emittance with time as well as temperature on a typical specimen. The average time between measurements was about 1 minute. By the time of the fifth measurement there was apparently some increase in emittance due to the coating. After 10 minutes at 1300°K the emittance reached the nearly stable upper curve of emittance versus temperature. The points 1, 2, 3, and 4 are characteristic of the emittance of a polished

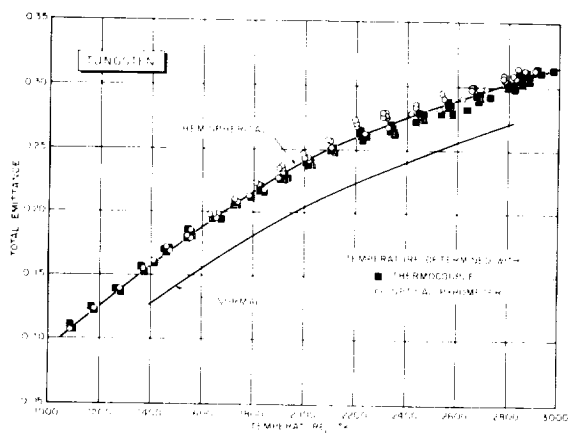


FIGURE 8.—Total emittance of tungsten.

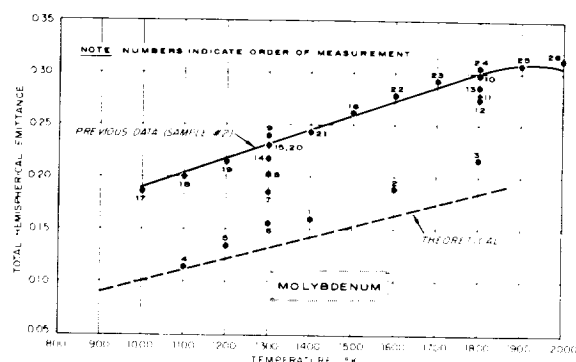


FIGURE 9.—Total emittance of molybdenum.

surface. The points 9 through 26 establish the emittance of a surface with a nearly stabilized coating of molybdenum carbide. The difficulty arising from this coating was one of the reasons for designing the new emittance chamber which was used for the other three metals (ref. 11). The overall accuracy of the total-emittance values quoted for the four metals is ± 5 percent.

ELECTRICAL RESISTIVITY

Because of the importance of the electrical resistivity in the theory of emissivity, the variation of this property with temperature was

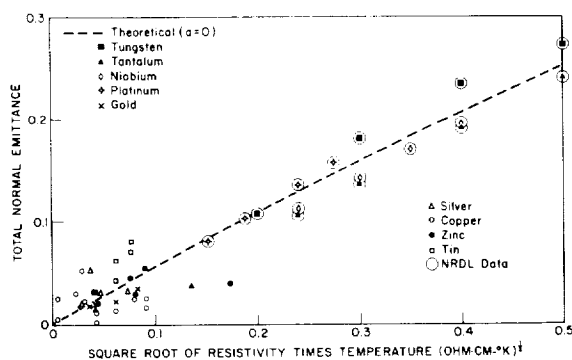


FIGURE 10.—Total normal emittance of various metals.

measured (ref. 7 and 11) for all four metals over the complete temperature range of the emittance measurements. These values were used to determine the abscissas in figures 10 and 11.

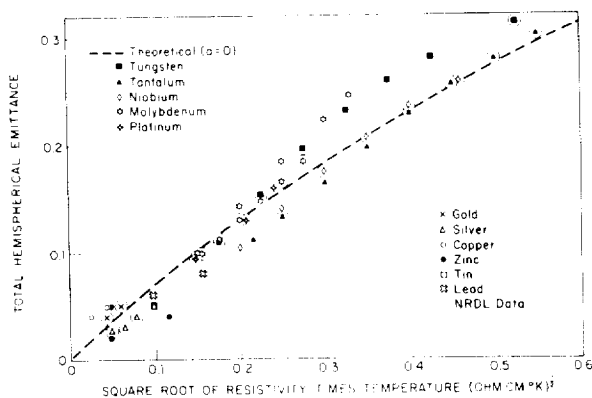


FIGURE 11.—Total hemispherical emittance of various metals.

SPECTRAL EMITTANCE MEASUREMENTS

The previously described experimental apparatus has been modified slightly to facilitate spectral emittance measurements on the refractory metals. The specimen configuration is a long triangular tube formed by clamping three ribbons together at the ends to form a 60° triangular prism. In order to insure that the three edges of the prism remain closed, it is wrapped with fine tungsten wire. A small 1×3 mm rectangular hole in one face of the prism serves as the reference blackbody. A Perkin-Elmer double-pass infrared spectrometer is used, and the external optics allow the blackbody hole and the face of the sample adjacent to the hole to be focused alternately on the entrance slit of the spectrometer. In this way a direct comparison may be made of the radiation from the metallic surface with that of a blackbody at the same temperature. The technique is similar to that used by De Vos in his determination of the normal spectral emittance of tungsten between 0.25 and 2.5 microns (ref. 3).

At present the measurements are being made between 0.6 and 5.00 microns; the long-wavelength limit is determined by the sapphire window in the vacuum chamber and the lithium fluoride prism in the spectrometer, and the short-wavelength limit is determined by the low energy available there. A photomultiplier is used as the detector from the visible to 1 micron, and a thermocouple is used as the detector beyond 1 micron. The present studies are of normal spectral emittance only; however, the angular rotation capabilities of the ribbon mount permit hemispherical spectral emittance measurements to be made. These will be included in future studies in which the wavelength range will be extended to 25 microns and the angular distribution will be determined for each plane of polarization. Since the prism is instrumented with thermocouples and voltage probes, the total hemispherical emittance can be obtained both from the power measurement and from the integral of the spectral emittance over the significant wavelength region and over all angles in both planes of polarization.

Tungsten has been used for the initial study, in order that comparison of the results with the reliable data of De Vos (ref. 3) might provide an evaluation of the performance of the system. Agreement has been within a few percent in the region from 0.6 to 2.5 microns.

DISCUSSION OF DATA

The total normal and total hemispherical emittance data obtained on this project are plotted against the square root of the electrical resistivity multiplied by the absolute temperature in figures 10 and 11. Data from the recent thermal radiation survey of Gubareff et al. (ref. 9) are also included; these data were reported for polished surfaces with no additional characterization. The interesting features are the wide spread of data points, particularly at low values of ρT , and the qualitative agreement with the theoretical (dashed) curves through an extended range of ρT . These curves are taken from figures 2 and 3 for the $a=0$ case. In figure 10 the dashed curve provides about as good a fit as possible for the plotted data. This may seem surprising since it has been shown previously in this article that the finite relaxation time should reduce the total emissivity of all the metals by about 30 to 70 percent as indicated in figures 2 and 3. However, there are some compensating factors which serve to increase the emissivity. The resistivity at the surface will be higher than in the interior due to scattering of the electrons by the interface and by imperfections in the lattice induced by surface preparation. The abscissa in figures 10 and 11 is calculated from the bulk resistivity. The emissivity depends upon an effective value of the resistivity within the penetration depth of the electromagnetic wave, which is of the order of 1000 Å at the peak of the spectral distribution. At very low temperatures the mean free path of the electron may be greater than the penetration depth and the effective resistivity becomes very much higher. This phenomenon is referred to as the anomalous skin effect (ref. 12).

It is only the transition metals which have high values of ρT ; the high values are due to their high melting points and relatively large electrical resistivities. Both of these charac-

teristics depend upon the fact that electrons are both in the incompletely filled d shells of these atoms and in the s shells in the next higher energy level. The transfer of electrons between these shells gives rise to the absorption and emission of radiation in the near infrared and can contribute to the spectral emissivity at short wavelengths and thus to the total emissivity at high temperatures.

The equations developed in this report ignore the effect of the bound electrons which become important at short wavelengths where the effect of the free electrons becomes much less pronounced. Corrections need to be applied to the total emissivity at high temperatures in order to take these electrons properly into account.

Some work has been done elsewhere (ref. 13) in trying to correlate theory and experiment by assuming the existence of different relaxation times for various groups of free electrons in the same metals.

As for the spread of data, which is particularly severe at low values of $(\rho T)^{1/2}$, this is due to several general causes. The extent of the corrections just discussed is different for each metal. The specimens measured may not have been ideal in the sense of complete freedom from thin surface films, imperfections behind the surface, or surface roughness. Emittance measurements are difficult to make and experimental errors can be quite large. Very accurate temperature determinations are required unless the blackbody reference standard is automatically at the same temperature as the specimen. Small percentage errors in reflectance can result in large percentage errors in emittance if the indirect reflectance measurement technique is used.

REFERENCES

1. FOOTE, P. D.: Bull. Nat. Bur. Stand. 11, 607 (1914-1915).
2. DAVISSON, C., and WEEKS, J. R., JR.: The Relation Between the Total Thermal Emissive Power of a Metal and Its Electrical Resistivity. Jour. Optical Soc. of America, vol. 8, no. 5, May 1924, pp. 581-605.
3. DE VOS, J. C.: A New Determination of the Emissivity of Tungsten Ribbon. Physica, vol. 20, no. 10, Oct. 1954, pp. 690-714.
4. STRATTON, JULIUS ADAMS: Electromagnetic Theory. McGraw-Hill Book Co., Inc., 1941, p. 496.

5. MOTT, N. F., and JONES, H.: The Theory of the Properties of Metals and Alloys. Oxford Univ. Press, 1936, p. 112.
6. SCHMIDT, E., and ECKERT, E.: Directional Distribution of Heat Radiation From Surfaces. Forschung. Geb. Ing.-Wes., vol. 6, July-Aug. 1935, pp. 175-183.
7. ABBOTT, G. L.: Total Normal and Total Hemispherical Emittance of Polished Metals, Part III. WADD Tech. Rep. 61-94, U.S. Air Force, Sept. 1963.
8. ABBOTT, G. L.: Total Normal and Total Hemispherical Emittance of Polished Metals. Measurement of Thermal Radiation Properties of Solids, Joseph C. Richmond, ed., NASA SP-31, 1963, pp. 293-306.
9. GUBAREFF, G. G., JANSSEN, J. E., and TORBORG, R. H.: Thermal Radiation Properties Survey. Second ed., Honeywell Res. Center, Minneapolis-Honeywell Regulator Co., 1960.
10. ABBOTT, G. L., ALVARES, N. J., and PARKER, W. J.: Total Normal and Total Hemispherical Emittance of Polished Metals, Part I. WADD Tech. Rep. 61-94, U.S. Air Force, Nov. 1961.
11. ABBOTT, G. L., ALVARES, N. J., and PARKER, W. J.: Total Normal and Total Hemispherical Emittance of Polished Metals, Part II. WADD Tech. Rep. 61-94, U.S. Air Force, Jan. 1963.
12. REUTER, G. E. H., and SONDEHEIMER, E. H.: The Theory of the Anomalous Skin Effect in Metals. Proc. Roy. Soc. (London), ser. A., vol. 195, no. 1042, Dec. 22, 1948, pp. 336-364.
13. ROBERTS, S.: Optical Properties of Nickel and Tungsten and Their Interpretation According to Drude's Formula. Phys. Rev., ser. 2, vol. 114, no. 1, Apr. 1, 1959, pp. 104-115.

DISCUSSION

H. E. BENNETT, Michelson Laboratory, U.S. Naval Ordnance Test Station: I would like to make one comment that may give some hope for the theoretical calculation. The Hagen-Rubens relation is derived by assuming that n and k are equal, which is true only for very long wavelengths. With decreasing wavelength the Hagen-Rubens relation gives higher emittance values, or lower reflectance values, than are obtained by using the exact theory. However, if surface damage is present, the measured emittance is higher, and the measured reflectance is lower than

would be true for an undamaged sample. Therefore, although the Hagen-Rubens relation does not have a good theoretical justification in short-wavelength regions, it frequently fits the experimental data better than does the exact theory.

PARKER: Surface damage is certainly one of the things that should be considered. Several additional factors are involved in this wavelength range, but all of them seem to average out and the data approximately follow the curve based on the assumption that the relaxation time is equal to zero.

3. Far-Infrared Spectra of Solids

JAMES R. ARONSON AND HUGH G. McLINDEN

ARTHUR D. LITTLE, INC., CAMBRIDGE, MASS.

The techniques and experimental results of a study of the far infrared properties of some solids at temperatures down to 6.5° K are presented. The materials studied include sapphire, quartz, strontium fluoride, barium fluoride, germanium, silicon, stainless steel, chromium, an aluminum alloy, and a magnesium alloy.

The radiation properties of solid materials in the far infrared region of the spectrum are important in applications involving low temperatures. The reason is that at low temperatures, the blackbody spectrum shifts to long wavelengths, as can be seen in figure 1. Therefore, the bulk of emitted radiation from a low temperature body in space will take place in a relatively ill-explored spectral region. It is apparent from these curves that, in addition to the long-wavelength shift, the total power is so low that it would be impossible, within the current state of the art, to directly record spectral emissivity at very low temperatures. While total emissivity¹ can be recorded calorimetrically, measurements of the spectral distribution of the emissivity must be obtained indirectly. This can be accomplished most simply by taking advantage of the simple relationship $\epsilon=1-R$ for opaque materials (where ϵ is the emissivity and R is the reflectivity). Unfortunately, when the reflectivity is high, small inaccuracies in its measurement lead to rather large errors in emissivity. When the absorption coefficient k is small, it can be measured directly by transmission methods using different crystal thicknesses, and if the

refractive index n is known, R can be computed from the Fresnel equations; for example, at normal incidence

$$R = \frac{(n-1)^2 + k^2}{(n+1)^2 + k^2}$$

The complicated general formulas for any angle of incidence are given in reference 1.

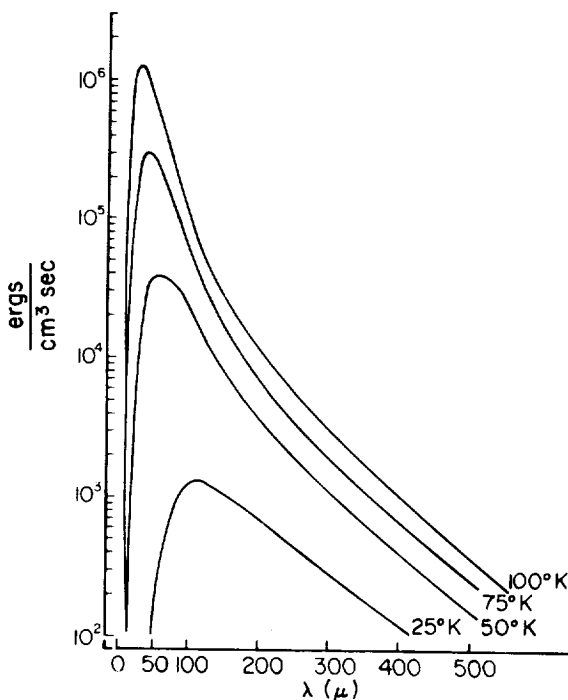


FIGURE 1.—Blackbody radiation spectra.

¹ The terms emissivity and reflectivity will be used in this paper in preference to emittance and reflectance as, for the spectral region in question, the wavelength is so great as to render the surfaces of these homogeneous substances optically smooth.

The present paper describes reflection and transmission measurements on a variety of solids in the far infrared region of the spectrum at temperatures down to 6.5° K. The reflection measurements have been made at 45° incidence. At this angle, the normal reflectivity can be approximated by

$$\frac{R_o + R_r}{2}$$

for any value of n or $k > 1$.

EXPERIMENTAL TECHNIQUES

While far infrared spectroscopy has been a field of study for many years, the inherent difficulties of working in this spectral region have considerably slowed progress and, therefore, relatively few materials have been studied. Some advances have been made in the field in recent years but the principal problem, that of obtaining reasonable amounts of energy, has still to be remedied. This has led spectroscopists to utilize the sensitive but very temperamental Golay pneumatic cell as a detector. Low temperature detectors are beginning to be employed (ref. 2) as they have still greater sensitivities (NEP of approximately 10^{-12} watt/cps^{1/2}). As there are no prism materials for wavelengths beyond about 50 μ (200 cm^{-1}), it is necessary to use gratings in order to scan the spectrum in this region unless one works with an interferometer. A bonus of enhanced resolution is obtained by using gratings instead of prisms and the general rule is that an improvement of a factor of approximately 10 is achieved. Unfortunately, the use of a grating requires heavy filtering in the system. This can be understood quite simply in terms of the grating equation

$$m\lambda = d(\sin i + \sin r)$$

where d is the line spacing, m is the order, i and r are the angles of incidence and diffraction, and λ is the wavelength. At any given position of the grating, the product $m\lambda$ is constant. Therefore, the higher the order, the lower the corresponding wavelength. The effect of this is that the orders pile up at the same angular position and, because of the much greater intensities of short wavelength radiations from

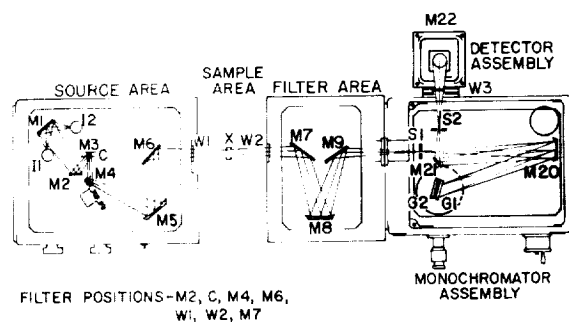


FIGURE 2.—Optical layout—Perkin-Elmer model 201-C spectrophotometer.

blackbody type sources, extremely efficient filtering is necessary. An indication of the seriousness of the problem is given by Lord and McCubbin (ref. 3).

The various types of filters used to remedy this difficulty include transmission filters, reststrahlen crystals, scatter plates, filter gratings, and selective choppers. These techniques are all discussed in detail in comprehensive papers by Lord and McCubbin (ref. 3) and Yoshinaga et al. (ref. 4). In figure 2 the optics of our spectrometer are shown and the filter positions are indicated. Various combinations of filters are installed at these positions, depending on the spectral region to be examined. The spectrometer range from 14.5 to 200 μ (690 to 50 cm^{-1}) is covered in seven sections, each of which requires different optical components. The different regions are indicated in the figure by means of vertical dashed lines. The spectrometer was modified by adding a reflection attachment and a positioner for the Hofman helium research dewar, both of which were designed and built in our laboratories. The dewar has four window positions located 90°

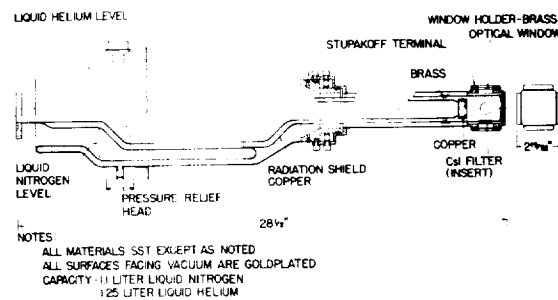


FIGURE 3.—Helium research dewar.

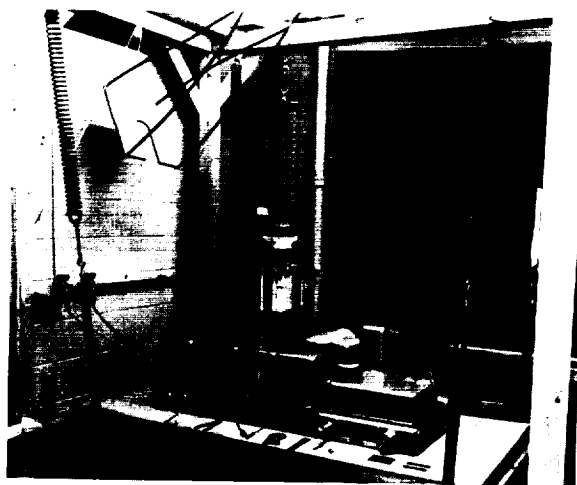


FIGURE 4.—Spectroscopic apparatus.

apart, in which we use 0.8-mm-thick high-density polyethylene. The dewar is shown in figure 3 and the entire apparatus in figure 4. We constructed a small copper crystal holder for use with the low temperature dewar. Crystals of 0.8-inch diameter are mounted in this holder by means of a preloaded copper strap under tension in order that good thermal conductivity will be maintained upon cooling to low temperature.

The temperature of operation is measured by means of a carbon-composition resistor installed at the base of the dewar. Previous measurements with gold-cobalt alloy thermocouples manufactured by the Sigmund Cohn Corporation established that there are no temperature gradients between the bottom of the dewar and the center of a poorly conducting sample (for example, stainless steel). The resistor was calibrated by means of one of these thermocouples, which, although not absolutely calibrated themselves, could measure small deviations from liquid helium temperature as their thermoelectric power is adequately known for use in our method. A thermocouple and the resistor to be calibrated were assembled in close proximity on a long probe which was inserted directly into liquid helium. This established the liquid helium temperature point. A small heater was then placed directly over the resistor-thermocouple assembly which was lowered into the cold helium gas above the

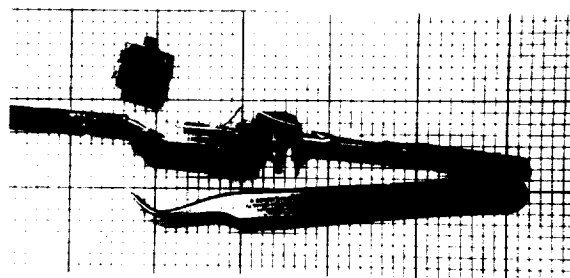


FIGURE 5.—Probe and accessory heater.

liquid while the reference junction of the thermocouple was immersed in the liquid. The probe and accessory heater are shown in figure 5. Measurements of the resistance versus emf at various heat inputs were made. The thermocouple readings were taken as true temperatures referred to liquid helium and a smooth curve was drawn through the measured resistances.

RESULTS

The optical properties of solids in the far infrared region of the spectrum vary from the opaque, highly reflective metals, adequately understood in terms of the Hagen-Rubens theory, to highly transparent materials such as polyethylene and diamond. Most dielectrics and semiconductors lie between these two extremes, and their study gives interesting data relating to lattice dynamics and crystal forces. This type of study is particularly useful at low temperatures where simplifications occur that render these highly complex subjects more tractable.

Our measurements on steel, magnesium, aluminum, and chromium are shown in figures 6 to 9. The aluminum alloy was run at room temperature, using a gold electroplated disk of brass for a background. The results showed the aluminum to have 100 percent reflectivity throughout the spectral region studied, so it was used as our reference standard. As can be seen from these plots, small differences in the reflectivities of these metals exist but, because of the estimated ± 5 percent error limitation, little significance was ascribed to these differences. All of our samples were 0.8-inch disks of a few millimeters thickness. The steel, aluminum, and magnesium were

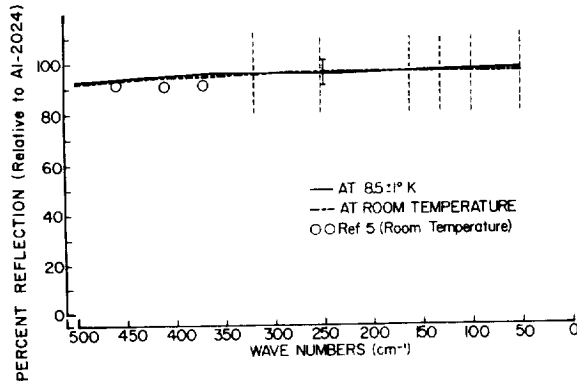


FIGURE 6.—Far infrared reflection spectrum of type 304 stainless steel.

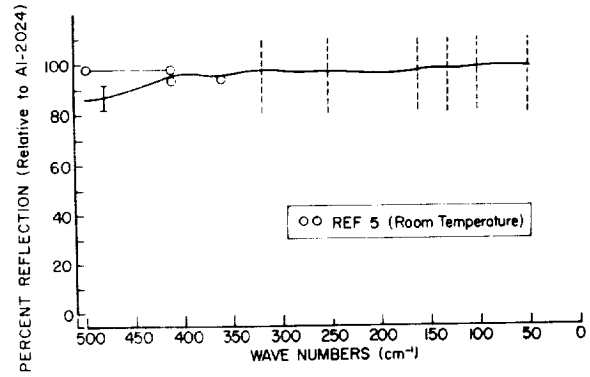


FIGURE 8.—Far infrared reflection spectrum of 2024 aluminum alloy at $8.5^\circ \pm 1^\circ$ K.

cut out of blocks previously studied in the near and intermediate infrared by Blau et al. (ref. 5). Their data are included in the figures for comparison purposes. The small discrepancy can be accounted for by the fact that their data were corrected for the approximately 98 percent known reflectivity of gold. The chromium sample was an electroplated layer on a stainless-steel disk.

According to the Hagen-Rubens theory (ref. 6) when $\omega \ll \rho$, the following simple expressions result:

$$n^2 - k^2 \approx 1 - \frac{\sigma_0}{\kappa_0 \rho}$$

$$nk \approx \frac{\sigma_0}{2\kappa_0 \omega}$$

where σ_0 is the d-c conductivity, ω is the fre-

quency, ρ is the damping coefficient, and κ_0 is the electric permittivity of free space. At very low frequencies, these equations require $n^2 - k^2$ to remain constant while nk grows large. Therefore, $n \approx k$, so that

$$k = \left(\frac{\sigma_0}{2\kappa_0 \omega} \right)^{1/2}$$

For wavelengths of approximately 100μ , k becomes quite large and the reflectivity may be calculated from

$$R \approx 1 - \frac{2}{k}$$

In figures 10 and 11 are shown the far infrared reflection spectra of sapphire and quartz. Both of these materials are oriented so that their optic axes are perpendicular to the plane of the crystal in order to minimize polarization effects.

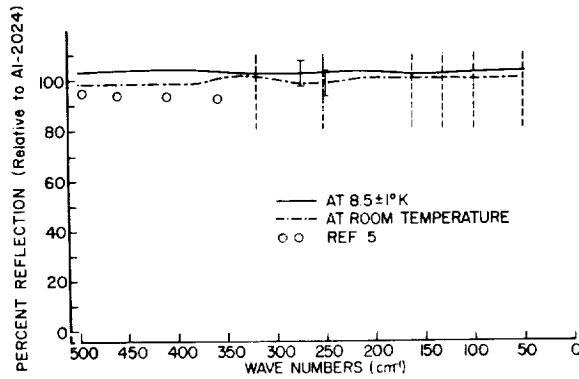


FIGURE 7.—Far infrared reflection spectrum of magnesium alloy.

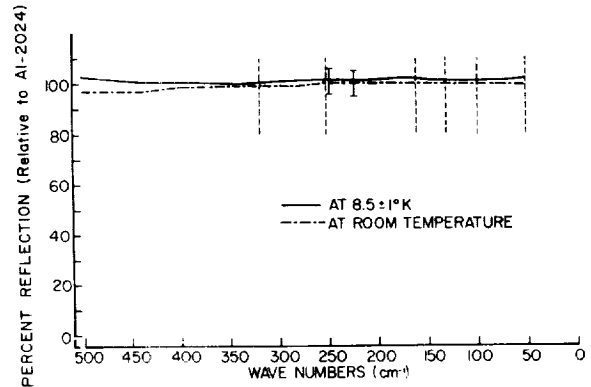


FIGURE 9.—Far infrared reflection spectrum of chromium.

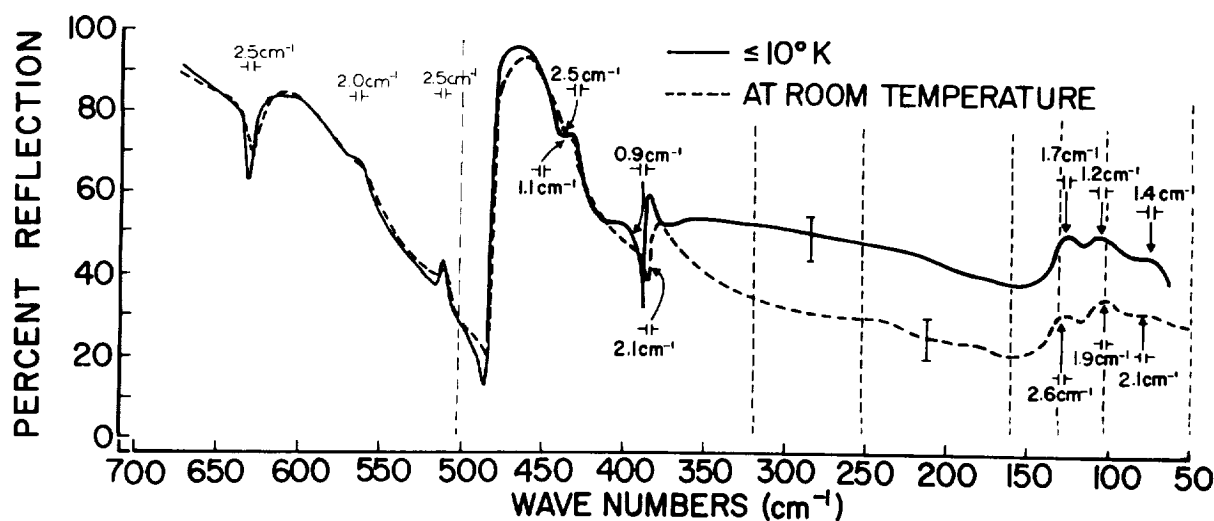


FIGURE 10.—Far infrared reflection spectrum of alumina (Z-cut sapphire).

The overall spectrum of sapphire is quite complex and appears to differ substantially from the values of the absorption maxima of 328 cm^{-1} , 244 cm^{-1} , and 194 cm^{-1} reported by Parodi (ref. 7). Strong (ref. 8) deduced three reflection maxima, at 434 cm^{-1} , 340 to 370

cm^{-1} and 192 cm^{-1} . As can be seen from the figure, we find values close to the first two of these but not the third. There is, of course, a large maximum around 460 cm^{-1} .

Our low temperature results on sapphire show increased sharpness and a high frequency shift

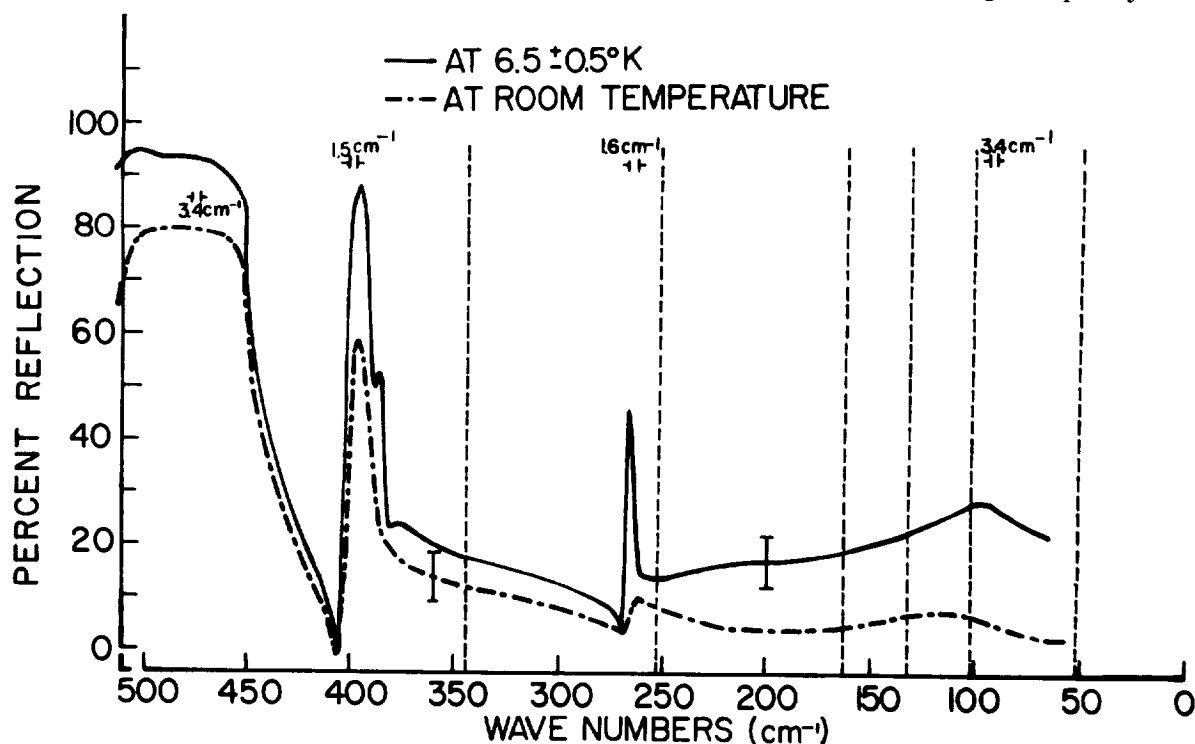


FIGURE 11.—Far infrared reflection spectrum of silica (Z-cut quartz).

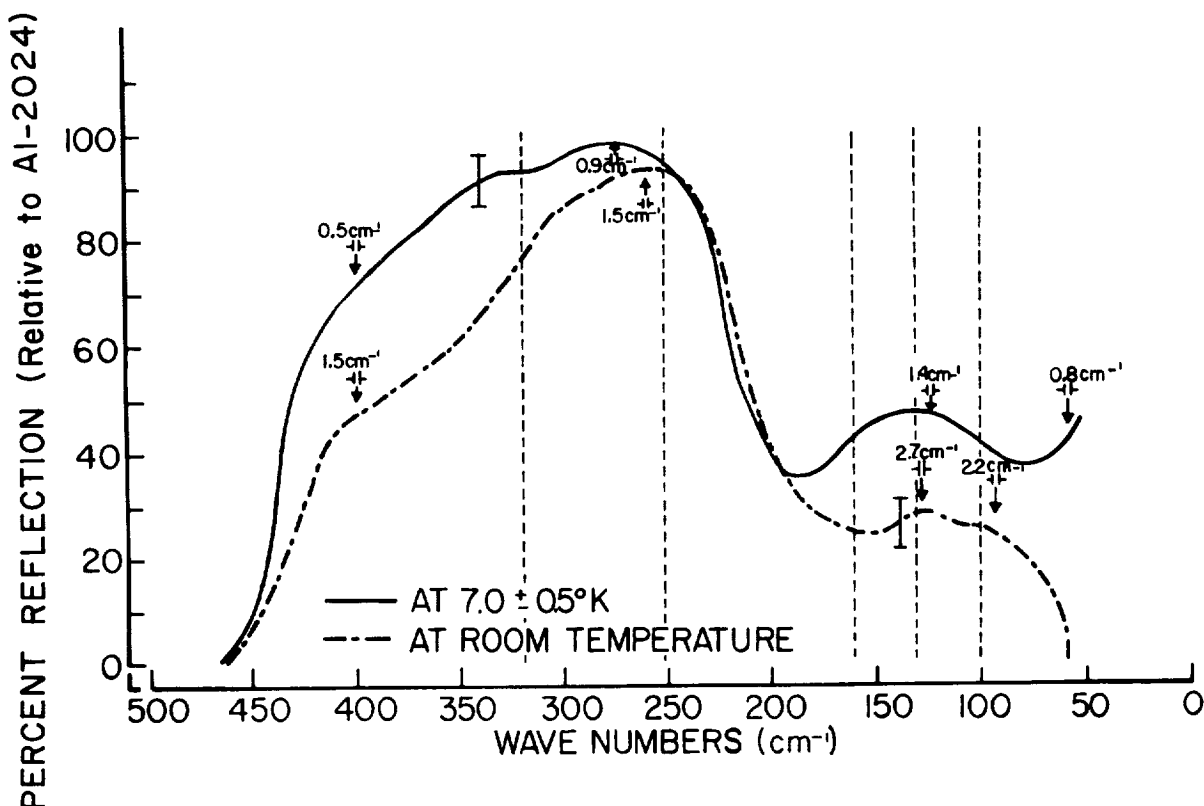


FIGURE 12.—Far infrared reflection spectrum of strontium fluoride.

of most reflection maxima. The disappearance of upper stage transitions (hot bands) which would occur on the low frequency side of a band and the increased force constants involved in a contracted lattice at low temperatures can both be invoked as explanations of these phenomena. The increase in intensities at low temperature is again presumably due to the loss of upper stage transitions, resulting in a greater number of systems existing in the ground states and, hence, available for those particular transitions.

Our long wavelength transmission measurements on sapphire are in accord with Loewenstein (ref. 9), who measured its optical properties between 10 cm^{-1} and 80 cm^{-1} interferometrically. Interference fringes were observed in our thin samples of sapphire in the 70 to 100 cm^{-1} region. They give a value of 3.09 for the refractive index of a crystal with its c -axis parallel to the beam direction. Loewenstein's value for n_{ord} is 3.14 . A crystal oriented with

the c -axis perpendicular to the beam direction gave less regular fringes, which we thought was due to the additional factor of n_{ext} which Loewenstein gave as 3.61 .

Our data on quartz at room temperature agree generally with those of Spitzer (ref. 10) in the region of overlap, but our measurements at greater wavelengths have turned up an additional reflection maximum. The low-temperature spectrum shows considerable interesting detail. The large reflection centered around 480 cm^{-1} appears to split into two rather broad bands. The maximum at 396 cm^{-1} splits into two with the second rather sharp peak appearing at 387 cm^{-1} . The 262 cm^{-1} peak shifts to 267 cm^{-1} and sharpens considerably. All maxima increase in intensity, as is common for essentially ionic materials, and the same explanations can be used as were used for sapphire.

The reflection spectra of strontium fluoride (SrF_2) and barium fluoride (BaF_2) are shown

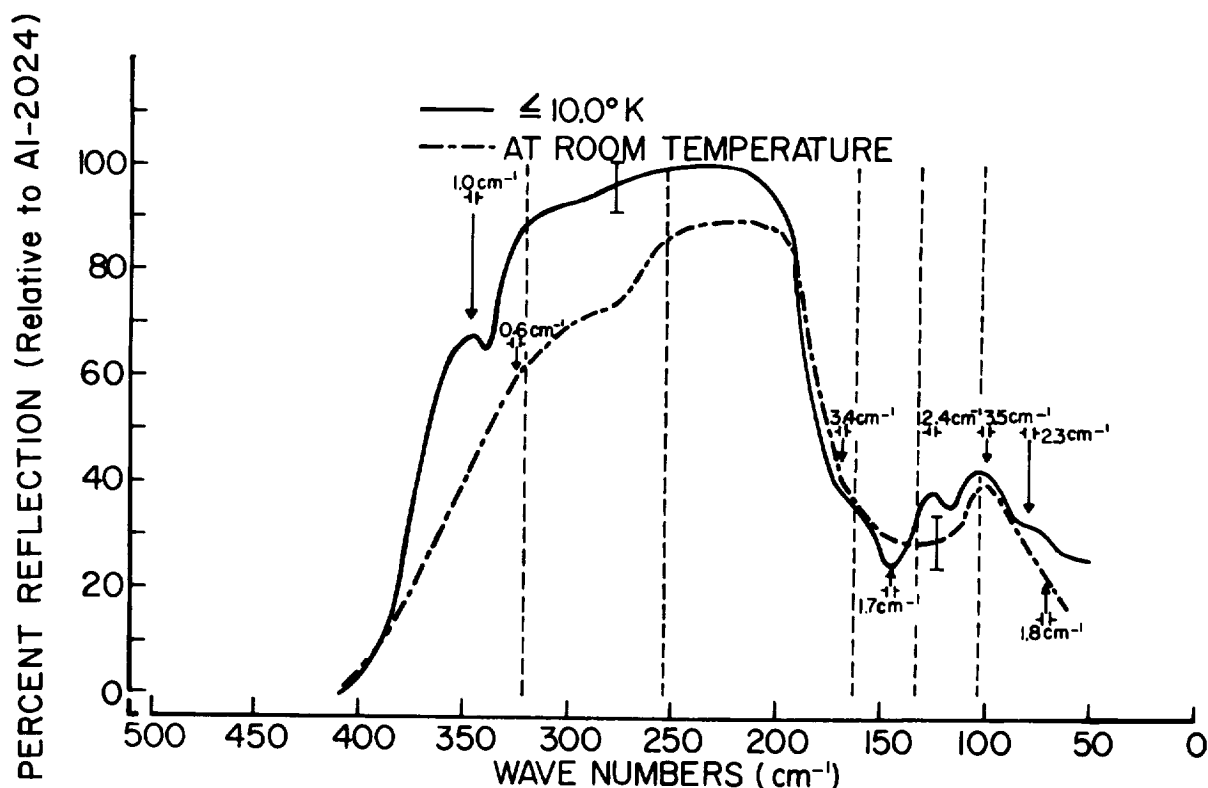


FIGURE 13.—Far infrared reflection spectrum of barium fluoride.

in figures 12 and 13. The room temperature data are in reasonable agreement with the data of Mitsubishi et al. (ref. 11) and of Kaiser et al. (ref. 12). The low temperature data show the usual high frequency shifts, increases in intensity, and some indications of splittings.

We have made transmission measurements on germanium and, by using two different crystal thicknesses and assuming the cancellation of reflection losses, have obtained the k curve shown in figure 14. For covalent materials, there is an intensity decrease on going to low temperatures; but the usual shifts and sharpenings of peaks can be seen. The multiple peaks near 347 cm^{-1} can be accounted for by various combinations of fundamental phonons according to the data of Brockhouse (ref. 13) using the theory of Lax and Burstein (ref. 14).

The absorption at 100 cm^{-1} in germanium has been ascribed to impurities in the lattice (ref. 15), but our measurements show this band in the very pure samples obtained from Knapic

Electrophysics, Incorporated. These samples are claimed by the manufacturer to have about 1.5×10^{14} impurity atoms/cc. The resistivity of this p-type material is 50–56 ohm-cm.

Our low temperature silicon transmission data are shown in figure 15. Room-temperature measurements (not shown) are similar. They were extended out to 75 cm^{-1} and showed the transmission to remain about 50 percent to that point, with some very small variations except for a weak absorption at about 165 cm^{-1} .

By means of interference fringes, we have measured the far infrared refractive index of both germanium and silicon at room temperature and the refractive index of germanium at 7.5° K . The constancy of our fringe spacing over the very small peaks in this region seems to indicate essentially no refractive index change due to absorption, and so we felt justified in using the simple relationship

$$n = \frac{1}{2t\Delta\nu}$$

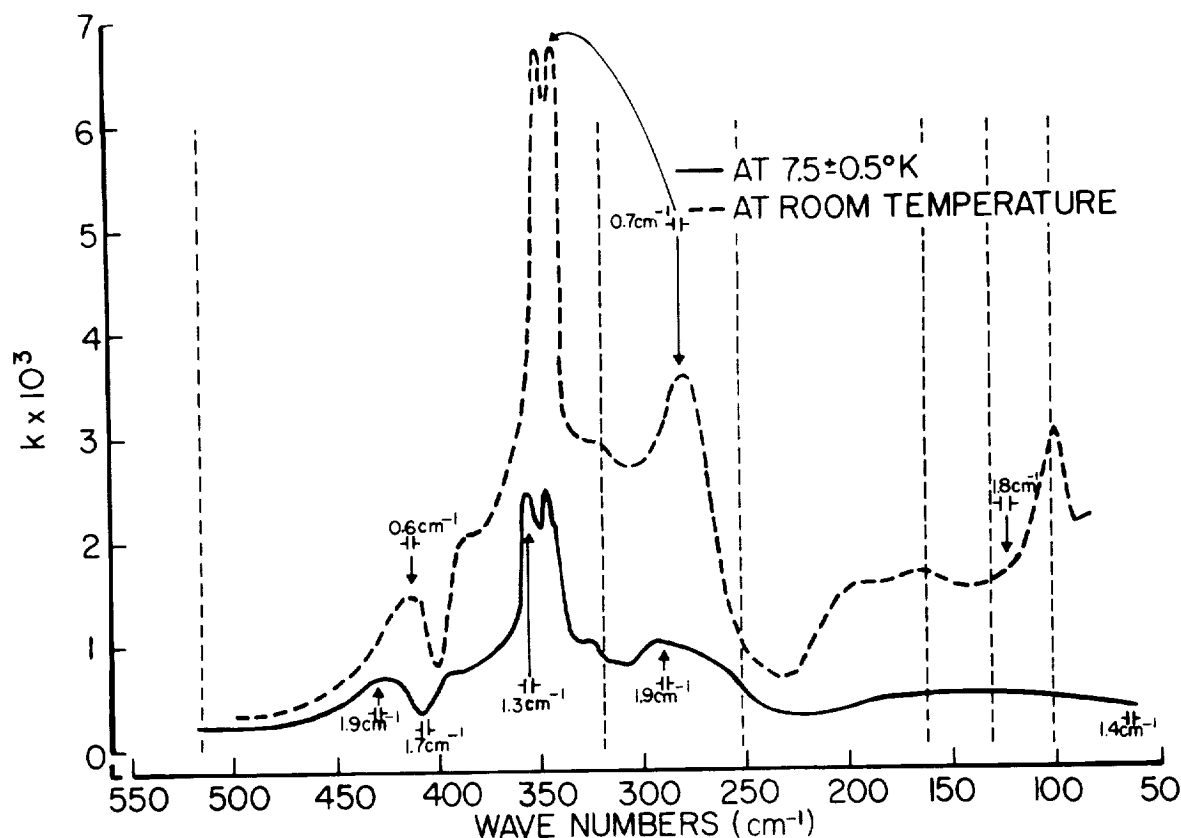


FIGURE 14.—Far infrared absorption of germanium.

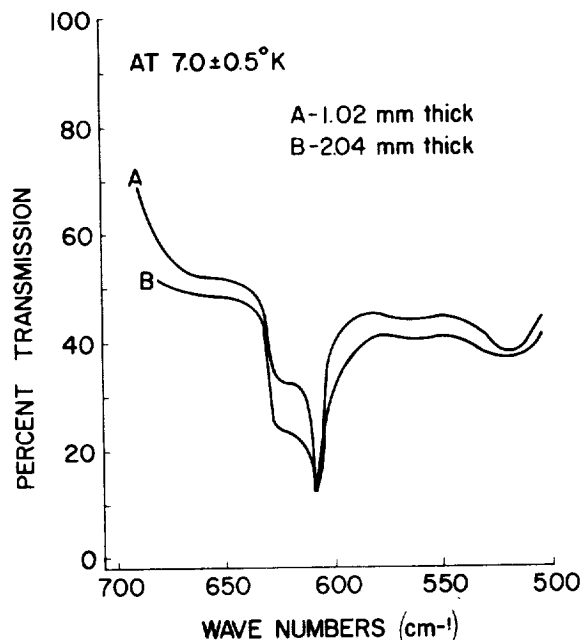


FIGURE 15.—Infrared absorption of silicon.

where t is the crystal thickness and $\Delta\nu$ is the fringe spacing. Our results for germanium at 7.5°K are $n = 3.98 \pm 0.02$ between 150 and 225 cm^{-1} and $n = 3.90 \pm 0.02$ between 250 and 425 cm^{-1} . At room temperature, we obtained $n = 3.98 \pm 0.02$ between 70 and 120 cm^{-1} . For silicon we obtained 3.41 ± 0.03 between 50 and 90 cm^{-1} and between 345 and 385 cm^{-1} . These values are in reasonable agreement with an extrapolation of the results of Simon's work (ref. 16), considering the scatter in his data.

This investigation was sponsored by NASA under contract NAS-8-2537 and by the Air Force Cambridge Research Laboratories under contract AF 19(604)-8504.

REFERENCES

1. SIMON, IVAN: Spectroscopy in Infrared by Reflection and Its Use for Highly Absorbing Substances. *Jour. Optical Soc. of America*, vol. 41, no. 5, May 1951, pp. 336-345.

2. LOW, FRANK J.: Low-Temperature Germanium Bolometer. *Jour. Optical Soc. of America*, vol. 51, no. 11, Nov. 1961, pp. 1300-1304.
3. LORD, R. C., and McCUBBIN, T. K., Jr.: Infrared Spectroscopy From 5 to 200 Microns with a Small Grating Spectrometer. *Jour. Optical Soc. of America*, vol. 47, no. 8, Aug. 1957, pp. 689-697.
4. YOSHINAGA, H., FUJITA, S., MINAMI, S., MITSUISHI, A., OETJEN, R. A., and YAMADA, Y.: Far Infrared Spectrograph for Use From the Prism Spectral Region to About 1-mm Wavelength. *Jour. Optical Soc. of America*, vol. 48, no. 5, May 1958, pp. 315-323.
5. SIMON, I., CHAFFEE, E., and BLAU, H. H., Jr.: Optical Properties of Satellite Surface Materials. Contract DA-19-020-ORD-4857, Arthur D. Little, Inc., Sept. 1961.
6. STRONG, JOHN: Concepts of Classical Optics. W. H. Freeman and Co. (San Francisco), 1958, p. 71.
7. PARODI, MAURICE: Spectroscopie.—Sur la transmission de quelques oxydes dans l'infrarouge lointain. *Comptes Rendus*, t. 205, Nov. 15, 1937, pp. 906-908.
8. STRONG, JOHN: Investigations in the Far Infrared. *Phys. Rev.*, vol. 38, no. 10, Nov. 15, 1931, pp. 1818-1826.
9. LOEWENSTEIN, ERNEST V.: Optical Properties of Sapphire in the Far Infrared. *Jour. Optical Soc. of America*, vol. 51, no. 1, Jan. 1961, pp. 108-112.
10. SPITZER, W. G., and KLEINMAN, D. A.: Infrared Lattice Bands of Quartz. *Phys. Rev.*, vol. 121, no. 5, Mar. 1, 1961, pp. 1324-1335.
11. MITSUISHI, A., YAMADA, Y., and YOSHINAGA, H.: Reflection Measurements on Reststrahlen Crystals in the Far-Infrared Region. *Jour. Optical Soc. of America*, vol. 52, no. 1, Jan. 1962, pp. 14-16.
12. KAISER, W., SPITZER, W. G., KAISER, R. H., and HOWARTH, L. E.: Infrared Properties of CaF_2 , SrF_2 , and BaF_2 . *Phys. Rev.*, vol. 127, no. 6, Sept. 15, 1962, pp. 1950-1954.
13. BROCKHOUSE, B. N.: Lattice Vibrations of Semiconductors by Neutron Spectrometry. *Phys. and Chem. of Solids*, vol. 8, 1959, pp. 400-405.
14. LAX, MELVIN, and BURSTEIN, ELIAS: Infrared Lattice Absorption in Ionic and Homopolar Crystals. *Phys. Rev.*, vol. 97, no. 1, Jan. 1, 1955, pp. 39-52.
15. HADNI, ARMAND: Instrumentation in the Far Infra-Red—Applications to Molecular and Solid State Physics. *Spectrochim. Acta*, vol. 19, no. 5, May 1963, pp. 793-805. (Also, *Comptes Rendus*, t. 255, 1962, p. 1595.)
16. SIMON, IVAN: Optical Constants of Germanium, Silicon, and Pyrite in the Infrared. *Jour. Optical Soc. of America*, vol. 41, no. 10, Oct. 1951, p. 730.

DISCUSSION

FRED VANDERSCHMIDT, Lyon Research Corporation: I notice that all of your reflectance data are referred to Al-2024. May we assume that Al-2024 is uniformly reflective and highly reflecting over this range?

ARONSON: Yes. I did not show a slide of this because it is rather uninteresting. We decided originally to refer everything to gold; but when we measured gold against the Al-2024 we found it so flat and so close to 100 percent that we decided to use the aluminum as a standard, because it would take handling a little better than the gold, which was an electroplated surface. It seemed to be perfectly flat. There are measurements which indicate that gold has 98 percent reflectivity, but they have not been extended into the far infrared. You may have noticed on one slide I showed of the reflectivity of metals that there were some data, obtained by Dr. Blau some time ago, which were very slightly below ours; the difference can be accounted for by the fact that he had corrected for the literature value of 98 percent reflectivity of gold, which is available in the region he studied.

FLORENCE NESH, National Weather Satellite Center: I would like to know the thicknesses of the samples that you used in your transmission studies of the semiconductors.

ARONSON: The thickness ranged between 1 and 2 mm for the semiconductors. I might add that they are the

only materials for which these thicknesses are convenient. For dielectrics such small thicknesses are needed that it becomes more convenient to make reflection measurements unless one uses powder samples.

NESH: Did you do any transmission work with thicker samples?

ARONSON: A run on silicon was tried with a 13-mm piece because the absorption that we found at around 165 wavenumbers was so weak that we were in doubt as to its reality. Dr. Hunt, who is now at the Air Force Cambridge Research Laboratory, had also found something of the sort, but with our thicknesses it did not show up clearly, so we ran this rather thick piece and found that the absorption is real. This pleased some people who had predicted it.

NESH: Did you run it as a transmission measurement on a thick piece using the setup you described?

ARONSON: Yes.

JOSEPH B. BERNSTEIN, Naval Ordnance Laboratory, Corona: In regard to the higher reflectance measurements, where you point out that it is difficult to calculate the emittance from a $(1-r)$ relationship, I might point out that we are doing some work on the direct measurement of emittance at low temperatures out to 45 μ —low temperatures being down to liquid-nitrogen temperatures. We expect to go out even farther, with some sort of device, other than a prism

type, down to liquid-helium temperatures, in the near future; this will permit us to make these emittance measurements directly where the reflectance is better than 90 percent.

ARONSON: Is this intended to be a spectral study?

BERNSTEIN: Yes, it is a spectral study.

ARONSON: Do you have any idea what resolution you might obtain then, when you go to these very low power levels?

BERNSTEIN: No, not at the moment.

ARONSON: This is the problem, I think.

BERNSTEIN: Yes, it is.

DON STIERWALT, Naval Ordnance Laboratory: In answer to that last question, out to about $45\ \mu$ we have a resolution of something on the order of 0.2 to $0.3\ \mu$. For the long wavelengths we have an instrument now that we are planning to use out to $100\ \mu$. We will probably have a resolution of $1\ \mu$ or so. I realize that this is not a high resolution, but for most metals there is no sharp structure anyway; and we are more interested in the emittance itself than in any fine resolution in this structure.

ARONSON: Very true. We wanted our instrumentation not only to study metals but also to study dielectrics and semiconductors, so we wanted higher resolution.

STIERWALT: I might also comment on the germanium and silicon measurements. Again, our direct emittance measurements showed the same lattice band

structures, I think, in perhaps a little bit more detail. The direct emittance measurements have a further advantage in that the measurements are made at normal incidence. Now, in most materials this does not matter much, but in some materials it does make a difference if it is normal incidence or not.

ARONSON: This is very true. One of the big problems with our experimental setup was that we could not conveniently make measurements at normal incidence. However, we can get the normal reflectivity by using 45° incidence and knowing the polarization of our spectrometer and one further fact, namely that, as an approximation, if either n or k is greater than 1, the average of the perpendicular and parallel components of reflectivity at 45° incidence is very close to normal incidence reflectivity.

DON KOCH, North American Aviation: In measuring reflectance on metals, how were the surfaces prepared? Did you use electropolishing techniques and was the structure of the lattice checked by electron diffraction or X-ray diffraction techniques?

ARONSON: They were electropolished, but we did not check the surfaces of the materials. We have a long wavelength in comparison to any surface irregularity. I would say that, on visual examination, they appear highly reflective, although you can see a few surface imperfections; however, because the wavelengths are a hundredfold greater than visual wavelengths, we figured these imperfections were not very important.

4. Emissivity and Inter-Reflection Relationships for Infinite Parallel Specular Surfaces

R. V. DUNKLE

COMMONWEALTH SCIENTIFIC AND INDUSTRIAL RESEARCH ORGANIZATION, VICTORIA, AUSTRALIA

The ratio between the hemispherical and normal emissivity of a smooth isotropic surface has been found by integration of Fresnel's equations. For materials with an absorption index not equal to zero, the equations involve an approximation. The error introduced by this approximation is negligible at large values of n and k and amounts to only about 1.5 percent when $n=1$ and $k=1$.

The ratio of the hemispherical emissivity factor for radiation exchange between infinite parallel smooth isotropic surfaces to the emissivity factor predicted from normal emissivities has been derived in a similar manner and a curve is presented for the general use of radiation exchange between two surfaces with different optical constants.

The reflectivity and emissivity of surfaces vary with wavelength, direction, and plane of polarization of the radiation. Emissivity and reflectivity measurements are often performed at or near normal incidence, and it is frequently necessary to estimate hemispherical properties from values measured normal to the surface. The ratio of the hemispherical emissivity to the normal emissivity can be predicted from electromagnetic theory for smooth isotropic surfaces in terms of the optical constants, that is, the index of refraction n and the absorption index k . Equations and curves for this ratio are reviewed and presented in this paper.

The effect of inter-reflections on radiation exchange between parallel surfaces (or concentric cylinders closely spaced) is also of interest due to the common use of such configurations in structures and radiation shields. The ratio of the hemispherical emissivity factor for specular isotropic surfaces to the emissivity factor computed from normal emissivities is presented herein for the general case of two different materials.

SYMBOLS

F	emissivity factor for infinite parallel surfaces
h	parameter involving values of n and k for evaluation of emissivity factors
k	absorption index
n	refractive index
r	ratio of amplitude of reflected to incident electric vector
ϵ	emissivity
ρ	reflectivity
θ	angle from normal (written as θ if complex)
x	$\cos \theta$

Subscripts

1	first surface
2	second surface
a	first medium or air
b	second medium
n	normal to surface
p	electric vector parallel to plane of incidence or of emission
s	electric vector perpendicular to plane of incidence or of emission
ϵ	emissivity
θ	at angle θ

EMISSIVITIES

The optical constants n and k specify the real and imaginary components of the complex index of refraction:

$$\underline{n} = n(1 - ik) = n - ink \quad (1)$$

It should be noted that the absorption index is frequently defined as the product nk of equation (1); this is a matter of convention and confusion.

Dielectrics.—For a dielectric material, $k=0$, and the emissivity is expressed as a function of angle by the well-known Fresnel equations. Walsh (ref. 1) integrated these equations to find the hemispherical emissivity in terms of the refractive index. The ratio of the hemispherical emissivity to the normal emissivity is given for the two components by the following equations.

Radiation polarized perpendicular to the plane of emission:

$$\frac{\epsilon_s}{\epsilon_n} = \frac{2}{3} + \frac{1}{3n} \quad (2)$$

Radiation polarized parallel to the plane of emission:

$$\frac{\epsilon_p}{\epsilon_n} = \frac{n(n+1)^2(n^2-1)^2}{2(n^2+1)^3} \ln \left(\frac{n+1}{n-1} \right) + \frac{n^2(n+1)(n^2+2n-1)}{(n^2+1)^2(n-1)} - \frac{4n^3(n^4+1)}{(n^2+1)^3(n-1)^2} \ln n \quad (3)$$

The hemispherical emissivity in terms of the two components is given by :

$$\epsilon = \frac{1}{2} (\epsilon_s + \epsilon_p) \quad (4)$$

Metals.—For metals and semiconductors both n and k must be considered. It has been shown theoretically (ref. 2) that if the electrical conductivity controls the reflectivity, as for metals at long wavelengths, $k=1.0$. However, inspection of reported optical constants for metals indicates wide variations for actual metals. When n and k are sufficiently large, the Fresnel equations for reflectivity can be simplified with small error by the approximation that the cosine term within the metal is one. These simplified

Fresnel expressions can then be integrated analytically over the hemisphere (see appendix) to yield the following approximate equations for the two components of the radiation (ref. 3):

Perpendicular component:

$$\epsilon_s = 8n - 8n^2 \ln \left(\frac{1+2n+n^2+n^2k^2}{n^2+n^2k^2} \right) + \frac{8n^2(1-k^2)}{k} \tan^{-1} \frac{k}{1+n+nk^2} \quad (5)$$

Parallel component:

$$\epsilon_p = \frac{8}{n(1+k^2)} - \frac{8 \ln (1+2n+n^2+n^2k^2)}{n^2(1+k^2)^2} + \frac{8(1-k^2)}{n^2k(1+k^2)^2} \tan^{-1} \left(\frac{nk}{1+n} \right) \quad (6)$$

The ratio of the hemispherical to the normal emissivity has been plotted in figure 1 as a function of the index of refraction for $k=0, 1, 2$, and 4. The curve for dielectrics, $k=0$, has been calculated from the exact theory, equations (2), (3), and (4). The curves for $k>0$ have been extended to $n=1$ by numerical integration. The dashed line for $k=1$ represents the approximate curve calculated from equations (5) and (6). For $k=2$ and 4, the difference between numerical integration and the approximate curve was very small and is not

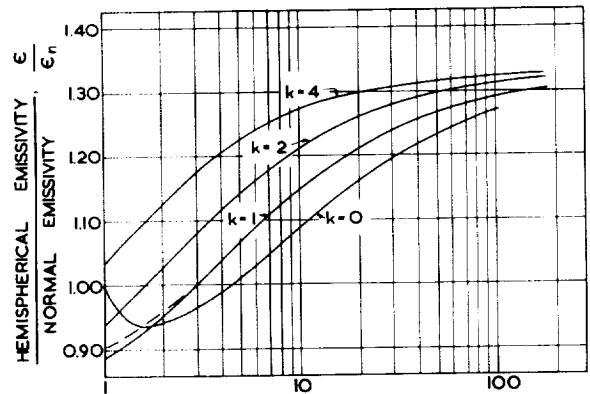


FIGURE 1.—Ratio of hemispherical to normal emissivity as a function of n and k .

shown on the graph. The ratio of hemispherical to normal emissivity is also plotted in figure 2 as a function of the normal emissivity with $k=0, 1, 2$, and 4 . Eckert (ref. 4) has plotted curves of this form and compared them with experimental measurements, but only for $k=0$ and $k=1$.

It should be noted that absorption mechanisms exist other than that due to simple electrical conduction, such as resonance effects of bound electrons, atoms, and molecules. In spectral regions near the resonance points the reflectivity is high and the absorption index large. Crystalline dielectrics exhibit this high absorptivity and reflectivity, commonly called metallic reflection, at infrared wavelengths corresponding to the natural frequencies of elements of the crystal structure.

Figure 3 has been included to illustrate the behavior of materials that are transitional between dielectrics and metals in their optical characteristics. As an example, angular emissivities for a substance with $n=2$ and $k=1$ have been computed and plotted as a function of angle from the normal for the two planes of polarization. The approximate equations for metals (in appendix) with $\cos \theta_b = 1.0$ are also plotted in figure 3 (dashed lines) for comparison. It will be noted that significant errors are involved if the approximate equations are employed in this range of n and k . It is interesting to note that, due to the opposing errors for the emissivities of the two components, the

mean emissivity is nearly the same for the approximate and exact solutions, so that only small errors occur if the hemispherical emissivity is calculated from the approximate equations in this region.

INTER-REFLECTIONS BETWEEN INFINITE PARALLEL SPECULAR SURFACES

Radiation exchange between infinite parallel surfaces can be represented on a unit area basis as the product of an emissivity factor F_e and the difference between the blackbody emissive powers corresponding to the temperatures of the two surfaces:

$$\frac{q}{A} = F_e (\sigma T_1^4 - \sigma T_2^4) \quad (7)$$

where, for diffuse surfaces or at a given angle between specular surfaces, F_e (the emissivity factor) is given by the equation

$$F_e = \frac{\epsilon_1 \epsilon_2}{\epsilon_1 + \epsilon_2 - \epsilon_1 \epsilon_2} \quad (8)$$

The ratio of the hemispherical to the normal emissivity factor (i.e., calculated on the basis of normal emissivities) has been calculated (in appendix) to provide an estimate of the errors which may arise due to neglect of angular variations and polarization effects.

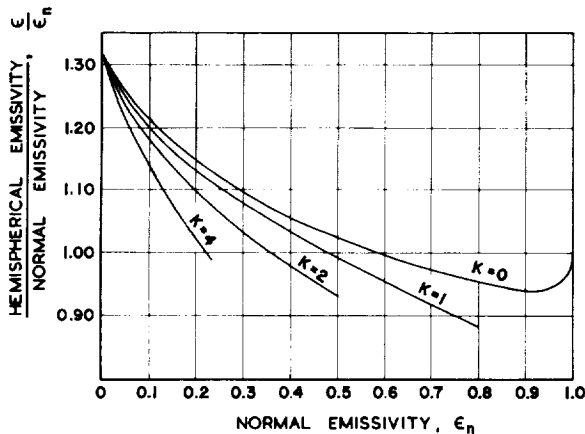


FIGURE 2.—Ratio of hemispherical to normal emissivity as a function of normal emissivity and k .

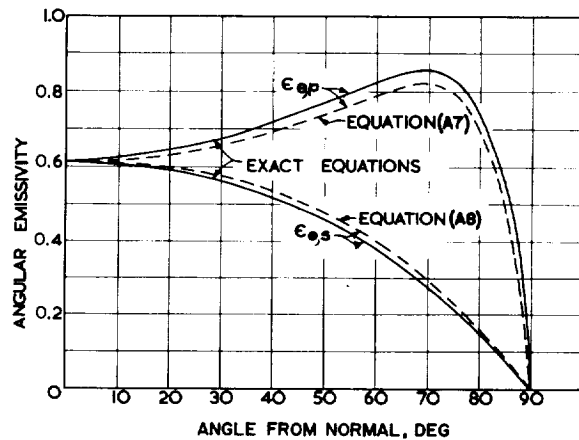


FIGURE 3.—Emissivities for parallel and perpendicular components, as functions of angle from the normal, for a substance with $n=2$ and $k=1$.

Dielectrics

For dielectrics the ratio of the emissivity factor for parallel specular surfaces with the same refractive index to the emissivity factor computed from normal emissivities for the same system is given for the two polarization components by the following equations (details in appendix).

Perpendicular component:

$$\frac{F_{\epsilon s}}{F_{\epsilon n}} = \frac{1+n^2}{2} - \frac{(n^4-1)}{2n} \tan^{-1} \left(\frac{1}{n} \right) \quad (9)$$

Parallel component:

$$\begin{aligned} \frac{F_{\epsilon p}}{F_{\epsilon n}} = & \frac{n^2(n^2+1)}{n^4+1} + \frac{n(n^4-1)^2}{2(n^4+1)^2} \ln \left(\frac{n+1}{n-1} \right) \\ & - \frac{2n^3(n^4-1)}{(n^4+1)^2} \tan^{-1} n \quad (10) \end{aligned}$$

The hemispherical emissivity factor is one-half the sum of the factors for the two components, or

$$F_{\epsilon} = \frac{1}{2}(F_{\epsilon s} + F_{\epsilon p}) \quad (11)$$

Metals

When the value of n is large, the approximation $\cos \theta_b = 1$ can be made for dielectrics as well as for metals, and the equations with this approximation are identical with those for a metal with $k=0$. For this reason, it is found that if one plots the ratio $F_{\epsilon}/F_{\epsilon n}$ against the parameter arrived at for metals (in appendix), namely, $h = \sqrt{n_1 n_2 \left(1 + \frac{n_1 k_1^2 + n_2 k_2^2}{n_1 + n_2} \right)}$, the resulting curve is valid for both dielectrics and metals (fig. 4). This curve holds for any two infinite parallel

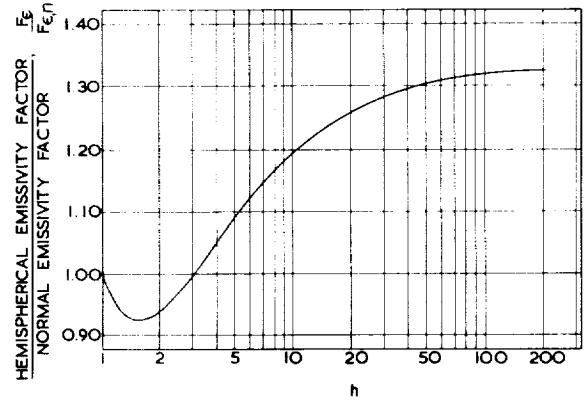


FIGURE 4.—Ratio of hemispherical to normal emissivity factors as a function of h where $h^2 \equiv n_1 n_2 \left(1 + \frac{n_1 k_1^2 + n_2 k_2^2}{n_1 + n_2} \right)$.

metal or dielectric materials radiating to each other provided n is greater than 5. The curve is exact for a dielectric ($k=0$) with any value of n radiating to a second dielectric with the same properties.

$$h^2 \equiv n_1 n_2 \left(1 + \frac{n_1 k_1^2 + n_2 k_2^2}{n_1 + n_2} \right)$$

This curve is also a good approximation for two dielectrics radiating to each other if n_1 and n_2 are not greatly different. This was checked by numerical integrations for the case where $n_1 = 1.5$ and $n_2 = 3.0$ and comparison of the result with the ratio $F_{\epsilon}/F_{\epsilon n}$ as read from figure 4 for $\sqrt{n_1 n_2} = \sqrt{4.5} = 2.121$. The ratio $F_{\epsilon}/F_{\epsilon n}$ from the numerical integrations is 0.952 and from figure 4 is 0.945. This agreement indicates that figure 4 can be used as a good approximation for determining emissivity factors for radiation exchange between different dielectrics as well as for different metals.

APPENDIX: DERIVATIONS OF EQUATIONS

Basic Reflection Laws

The equations in this paper are all derived for reflection and emission at the interface between an isotropic specular surface and air, with the refractive index of air taken as 1.

Fresnel's equations for the ratio of the amplitude of the electric vector of the reflected electromagnetic wave in air to that of the wave incident upon the surface at angle θ_a can be written as follows for the two components of the wave.

Parallel component:

$$r_p = \frac{\sin \theta_a \cos \theta_b - \sin \theta_b \cos \theta_a}{\sin \theta_a \cos \theta_b + \sin \theta_b \cos \theta_a} \quad (A1)$$

Perpendicular component:

$$r_s = \frac{\sin \theta_a \cos \theta_b - \sin \theta_b \cos \theta_a}{\sin \theta_a \cos \theta_b + \sin \theta_b \cos \theta_a} \quad (A2)$$

The angles are related by Snell's law,

$$\frac{\sin \theta_a}{\sin \theta_b} = \underline{n}_l = n(1 - ik) \quad (\text{A3})$$

from which

$$\cos \theta_b = \sqrt{1 - \frac{\sin^2 \theta_a}{n^2(1 - ik)^2}} \quad (\text{A4})$$

For large values of n and k such as are characteristic of metals, $\cos \theta_b = 1.0$ as a first approximation. For dielectrics, $k=0$, and no complex terms are involved. As the energy transported is proportional to the square of the electric vector, the reflectivity for dielectrics is found readily for each component by squaring both sides of equations (A1) and (A2). For absorbing materials this is accomplished by multiplying numerator and denominator by their complex conjugates.

Ratio of Hemispherical Emissivity to Normal Emissivity for Metals

The hemispherical emissivity is related to the angular emissivity by

$$\epsilon = 2 \int_0^{\pi/2} \epsilon_\theta \sin \theta \cos \theta d\theta \quad (\text{A5})$$

and, if the substitution $\cos \theta = x$ is made,

$$\epsilon = 2 \int_0^1 \epsilon_\theta x dx \quad (\text{A6})$$

For metals, with the approximation that $\cos \theta_b = 1.0$, the angular emissivities are, from equations (A1), (A2), and (A3) (using the fact that emissivity = 1 - reflectivity), found to be

Parallel component:

$$\begin{aligned} \epsilon_{\theta p} &= \frac{4n \cos \theta}{(n^2 + n^2 k^2) \cos^2 \theta + 2n \cos \theta + 1} \\ &= \frac{4n\chi}{(n^2 + n^2 k^2) \chi^2 + 2n\chi + 1} \end{aligned} \quad (\text{A7})$$

Perpendicular component:

$$\epsilon_{\theta s} = \frac{4n \cos \theta}{\cos^2 \theta + 2n \cos \theta + n^2 + n^2 k^2} = \frac{4n\chi}{\chi^2 + 2n\chi + n^2 + n^2 k^2} \quad (\text{A8})$$

and the normal emissivity ($\chi = 1$) is

$$\epsilon_n = \frac{4n}{1 + 2n + n^2 + n^2 k^2} \quad (\text{A9})$$

From equations (A6) and (A7),

$$\epsilon_p = \int_0^1 \frac{4n\chi^2 d\chi}{\chi^2 + 2n\chi + n^2 + n^2 k^2}$$

and, upon integration,

$$\epsilon_p = \frac{8}{n(1+k^2)} - \frac{8 \ln(1+2n+n^2+n^2 k^2)}{n^2(1+k^2)^2}$$

$$+ \frac{8(1-k^2)}{n^2 k(1+k^2)^2} \tan^{-1} \left(\frac{nk}{1+n} \right) \quad (\text{A10})$$

which is equation (6) in the text.

Equation (5) in the text for ϵ_n is obtained in a similar manner.

Emissivity Factors for Infinite Parallel Surfaces

DISSIMILAR METALS

At any given angle between specular surfaces the emissivity factor due to multiple inter-reflections at that angle can be written, say for the perpendicular component, as

$$F_{\theta s} = \frac{1}{\frac{1}{\epsilon_{s\theta 1}} + \frac{1}{\epsilon_{s\theta 2}} - 1} \quad (\text{A11})$$

Substituting from equation (A8) gives

$$F_{\theta s} = \frac{4n_1 n_2 \chi}{(n_1 + n_2) \chi^2 + n_2(n_1^2 + n_1^2 k_1^2) + n_1(n_2^2 + n_2^2 k_2^2)} \quad (\text{A12})$$

The hemispherical factor is

$$F_{ss} = 2 \int_0^1 F_{\theta s} \chi d\chi \quad (\text{A13})$$

Substitution of equation (A12) into equation (A13) gives

$$F_{ss} = \frac{8n_1 n_2}{n_1 + n_2} \int_0^1 \frac{\chi^2 d\chi}{\chi^2 + n_1 n_2 \left(1 + \frac{n_1 k_1^2 + n_2 k_2^2}{n_1 + n_2} \right)} \quad (\text{A14})$$

Let

$$n_1 n_2 \left(1 + \frac{n_1 k_1^2 + n_2 k_2^2}{n_1 + n_2} \right) \equiv h^2 \quad (\text{A15})$$

Performing the indicated integration in equation (A14), with this substitution, yields

$$F_{ss} = \frac{8n_1 n_2}{n_1 + n_2} \left[1 - h \tan^{-1} \frac{1}{h} \right] \quad (\text{A16})$$

Similarly,

$$F_{sp} = \frac{8n_1 n_2}{n_1 + n_2} \int_0^1 \frac{\chi^2 d\chi}{h^2 \chi^2 + 1} \quad (\text{A17})$$

which, upon integration, gives

$$F_{sp} = \frac{8n_1 n_2}{n_1 + n_2} \left(\frac{1}{h^2} - \frac{1}{h^3} \tan^{-1} h \right) \quad (\text{A18})$$

The emissivity factor for the normal beam is given by

$$F_{nn} = \frac{4n_1 n_2}{(n_1 + n_2)(1 + h^2)} \quad (\text{A19})$$

and the ratio of the hemispherical emissivity factor to the normal emissivity factor is found to be

$$\frac{F_{\epsilon}}{F_m} = \frac{F_{\epsilon p} + F_{\epsilon s}}{2F_m} = (1 + h^2)$$

$$\left(\frac{1+h^2}{h^2} - \frac{1}{h^3} \tan^{-1} h - h \tan^{-1} \frac{1}{h} \right) \quad (\text{A20})$$

This equation is plotted in figure 4.

DIELECTRICS

The case of a dielectric radiating to a second dielectric of the same properties is quite straightforward, but the case of two different dielectrics is very complicated and has only been solved numerically.

The emissivity factor for the parallel component for radiation exchange between two identical infinite parallel specular surfaces is found by starting with equation (A1) for r_{ps} (with $k=0$ in eq. (A3)), squaring, subtracting from unity in order to get ϵ_{ps} , substituting into equation (A11), and integrating over the hemisphere:

$$F_{\epsilon p} = 4n^2 \int_0^1 \frac{\chi^2 \sqrt{\chi^2 + n^2 - 1}}{(n^4 + 1)\chi^2 + n^2 - 1} d\chi \quad (\text{A21})$$

Performing the indicated integration gives

$$F_{\epsilon p} = \frac{2n^3}{(n^4 + 1)} + \frac{n^3(n^2 - 1)^2(n^2 + 1)}{(n^4 + 1)^2} \ln \left(\frac{n+1}{n-1} \right)$$

SAMUEL SKLAREW, The Marquardt Corp.: I am puzzled by the refractive indexes shown in your first figure. I do not know of any materials with indexes between 10 and 100. Most materials have indexes of around 2 or less, possibly 3, and at the most 4.

DUNKLE: As I recall, if you take the Hagen-Rubens equation for a metal you find that the value of n becomes very large for metals.

$$- \frac{4n^4(n^2 - 1)}{(n^4 + 1)^2} \tan^{-1} n \quad (\text{A22})$$

Likewise, for the perpendicular component,

$$F_{\epsilon s} = 4 \int_0^1 \frac{\chi^2 \sqrt{\chi^2 + n^2 - 1}}{2\chi^2 + n^2 - 1} d\chi \quad (\text{A23})$$

or, on integration,

$$F_{\epsilon s} = n - (n^2 - 1) \tan^{-1} \frac{1}{n} \quad (\text{A24})$$

REFERENCES

1. WALSH, JOHN W. T.: The Reflection Factor of a Polished Glass Surface for Diffused Light. Appendix of Taylor, A. K., and C. J. W. Grieveson: The Transmission Factor of Commercial Window Glasses. Dept. Sci. and Ind. Res.; Illum. Res. Tech. Paper No. 2, 1926.
2. WOOD, R. W.: Physical Optics. MacMillan and Co., Ltd., 1934, p. 547.
3. DUNKLE, R. V.: Thermal Radiation Characteristics of Surfaces. Research in Heat Transfer, Pergamon Press, 1963.
4. ECKERT, E. R. G., and DRAKE, ROBERT N.: Heat and Mass Transfer. McGraw-Hill Book Co., Inc., 1959, p. 380.

DISCUSSION

HENRY BLAU, Arthur D. Little, Inc.: We have measured values as high as 10 or more.

DUNKLE: On what?

BLAU: Tungsten in the infrared.

SKLAREW: Then it is wavelength dependent?

DUNKLE: It is definitely wavelength dependent. These equations are only monochromatic. They still have to be integrated with respect to wavelength to get total values.

5. Numerical Solutions of the Fresnel Equations in the Optical Region¹

HERBERT B. HOLL

U.S. ARMY MISSILE COMMAND, REDSTONE ARSENAL, ALA.

The solutions of the Fresnel equations, which are obtained for approximately 2,500 indices of refraction for normal and oblique incidence, are discussed. Several examples of the graphic illustration of these solutions are given, and the discussion describes in detail the occurrence of reflection characteristics such as the angle of incidence for which (a) the amplitude of the wave oscillating parallel to the plane of incidence is a minimum; (b) the degree of polarization is a maximum; and (c) the two amplitudes of the reflected wave have a difference in phase of 90°. Some examples of the determination of the index of refraction from reflection measurements are also given.

BASIC REFLECTION EQUATIONS

In optics, where the permeability μ_m is unity, the rigorous Fresnel intensity reflection formulas for the bulk material are

$$R_{\perp} = R_1 = \frac{\left(\frac{q}{\alpha_2} - \cos \theta_0\right)^2 + \left(\frac{p}{\alpha_2}\right)^2}{\left(\frac{q}{\alpha_2} + \cos \theta_0\right)^2 + \left(\frac{p}{\alpha_2}\right)^2} \quad (1)$$

$$R_{\parallel} = R_2 = \frac{\left(\frac{q}{\alpha_2} - \cos \theta_0\right)^2 + \left(\frac{p}{\alpha_2}\right)^2}{\left(\frac{q}{\alpha_2} + \cos \theta_0\right)^2 + \left(\frac{p}{\alpha_2}\right)^2} \times \frac{\left(\frac{q}{\alpha_2} - \sin \theta_0 \tan \theta_0\right)^2 + \left(\frac{p}{\alpha_2}\right)^2}{\left(\frac{q}{\alpha_2} + \sin \theta_0 \tan \theta_0\right)^2 + \left(\frac{p}{\alpha_2}\right)^2} \quad (2)$$

where θ_0 is the angle of incidence.

The quantities q and p can be calculated from

$$\left(\frac{q(\theta_0)}{\alpha_2}\right)^2 = \frac{1}{2} \left[\left(\frac{\alpha_1}{\alpha_2}\right)^2 - \left(\frac{\beta_1}{\alpha_2}\right)^2 - \sin^2 \theta_0 \right]$$

$$+ \sqrt{4 \left(\frac{\alpha_1}{\alpha_2}\right)^2 \cdot \left(\frac{\beta_1}{\alpha_2}\right)^2 + \left[\left(\frac{\alpha_1}{\alpha_2}\right)^2 - \left(\frac{\beta_1}{\alpha_2}\right)^2 - \sin^2 \theta_0 \right]^2} \quad (3)$$

$$\left(\frac{p(\theta_0)}{\alpha_2}\right)^2 = \frac{1}{2} \left[-\left(\frac{\alpha_1}{\alpha_2}\right)^2 + \left(\frac{\beta_1}{\alpha_2}\right)^2 + \sin^2 \theta_0 \right] + \sqrt{4 \left(\frac{\alpha_1}{\alpha_2}\right)^2 \cdot \left(\frac{\beta_1}{\alpha_2}\right)^2 + \left[\left(\frac{\alpha_1}{\alpha_2}\right)^2 - \left(\frac{\beta_1}{\alpha_2}\right)^2 - \sin^2 \theta_0 \right]^2} \quad (4)$$

where $\alpha_1/\alpha_2 = n$ and $\beta_1/\alpha_2 = k$, and n and k are the real and imaginary part of the complex index of refraction $N = n - ki$. Given the numerical values R_1 and R_2 , the reflectance R of natural or unpolarized radiation, defined by

$$R = \frac{R_1 + R_2}{2} \quad (5)$$

and the degree of polarization P , expressed by

$$P = \frac{R_1 - R_2}{R_1 + R_2} = \frac{1 - \frac{R_2}{R_1}}{1 + \frac{R_2}{R_1}} \quad (6)$$

¹ See also Papers 4, 20, and 30.

can easily be obtained.

REFLECTION COEFFICIENTS AS FUNCTIONS OF n , k , and θ_0

A general tabulation of numerical wave reflection values would be helpful in optical studies and would greatly reduce duplication of research effort. To my knowledge, these data are not available in reference form; those handbooks which do present data on the index of refraction usually give the reflectance at normal incidence only. If such data, in tabulated or graphical form, were available in sufficient accuracy and interval density, they would be useful in two major types of problems: (1) extracting the numerical values of the reflectance directly from the tables if the index of refraction of the material and the angle of incidence are known; and (2) determining the index of refraction if experimental reflectance data are available. In addition, the data could be of value in studies of wave propagation and wave interaction on material, in studies of laser light, in target determination and discrimination, and in investigation and prediction of behavior of reflecting material and surrounding media.

A recently published report (see ref.) was designed to partially fill this need. It presents the Fresnel reflection-intensity coefficients R_1 and R_2 for the index of refraction $N=n-ki$ for all combinations of $n=0.1(0.1)4.0$, $k=0.0(0.1)6.0$, and angle of incidence $\theta_0=0^\circ(5^\circ)85^\circ$. The selected ranges of the indices of refraction and angle of incidence cover a whole region in sufficient density to permit interpolation.

Since the reflectivity is expressed as a function of a combination of θ_0 , n , and k , there are different ways to illustrate their interdependence. One method we will use is the customary one of plotting the reflection coefficient against the angle of incidence. As an example, figure 1 illustrates the tendencies of the R_1 and R_2 curves, for which the real part of the index of refraction n is held constant and k varied from 0 to 6; figure 2 shows the reflectivity R for natural or unpolarized radiation. Each index of refraction has its own peculiar curve.

Another very useful method is to plot the numerical results of the Fresnel equations ob-

tained for a particular constant angle of incidence θ_0 (such as R , R_1 , R_2 , P or R_2/R_1) against n and k —that is, in the Gaussian plane of complex numbers. This type of graph is also called an Argand diagram. Let us start with the reflection at normal incidence, with which we are most familiar. For a normally impinging wave there is no preferred plane of incidence and $R=R_1=R_2$. The well known equation for this case can easily be developed into the equation

$$\left(n - \frac{1+R}{1-R}\right)^2 + k^2 = \frac{4R}{(1-R)^2} \quad (7)$$

which is the equation for a circle. Figure 3 represents the "isorefectance" curves in the four quadrants of the complex plane. The physical interpretation of the second and third quadrants, where the real refraction index n becomes negative, is beyond the scope of this study. The numerical values of R in the second and third quadrants are the reciprocals of the values at the symmetrically located points in the first and fourth quadrants, and are in the interval $1 \leq R \leq \infty$.

The notation $N=n-ki$ for the index of refraction is arbitrary, but is commonly used in optics. The complex N represents the air-conductor interface, and $k=0$ is the case of air-dielectric interface. This index of refraction also represents the propagation constant of the electromagnetic wave in the second medium relative to vacuum or air. Given the definition $N=n-ki$, the set of complex numbers for N is located in the fourth quadrant of the plot of the complex numbers.

Based on this definition, the first quadrant has a distinct physical significance. If $N=n+ki$, N represents the propagation constant with respect to vacuum or air, and the first quadrant covers the cases in which there is amplification of the amplitudes of the electromagnetic wave. The first and fourth quadrants together make it possible to locate the instance of reflection at the interface of two conducting materials. If N_1 is the index of refraction with respect to air of the first medium and N_2 the index of the second medium, the relative index of refraction $N_{12}=N_2/N_1$ can take on one of two forms, $N_{12}=n_{12}+k_{12}i$ or $N_{12}=n_{12}-k_{12}i$.

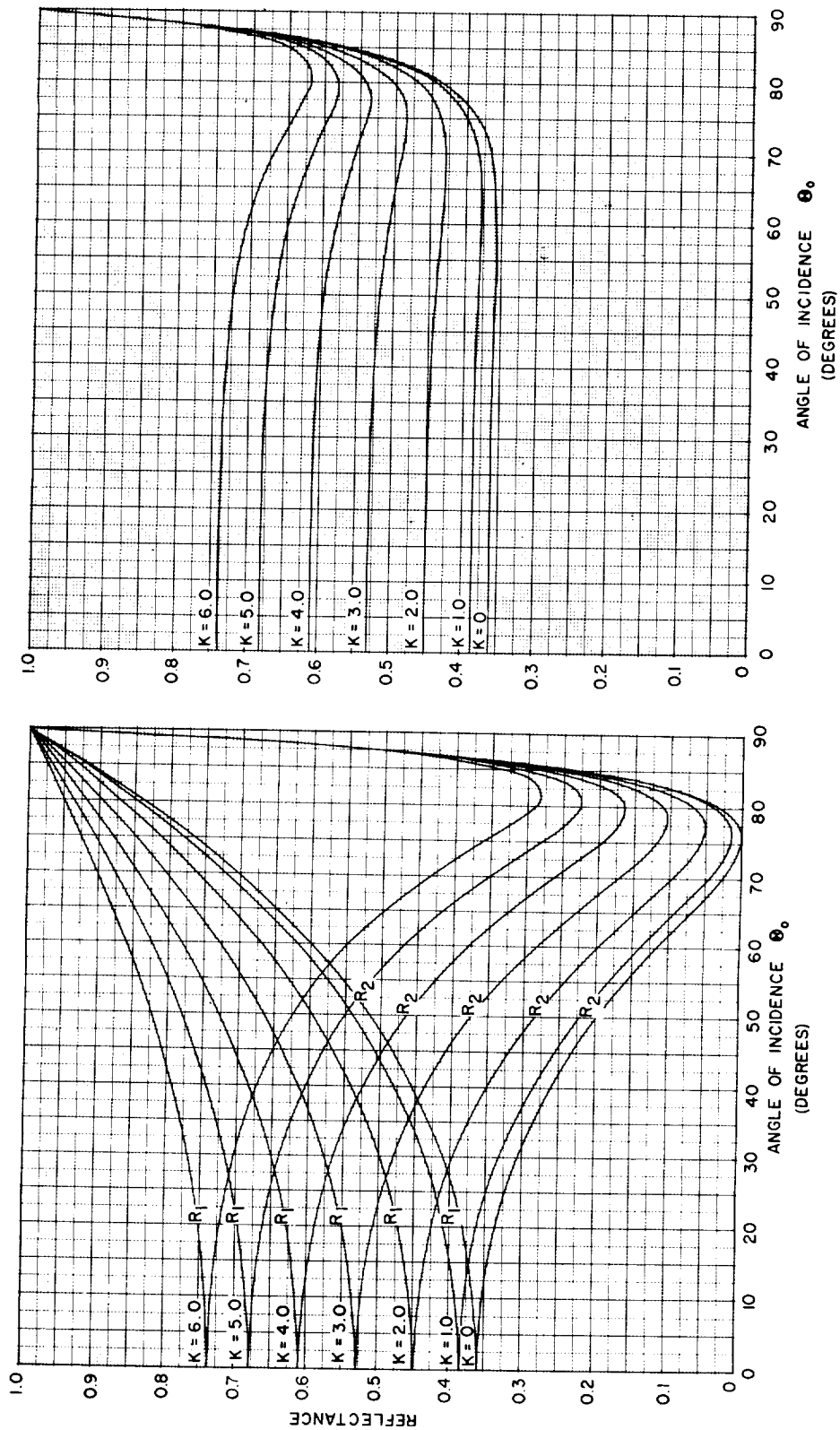


FIGURE 1.—Reflectances R_1 and R_2 for $N = 4.0 - ki$; $k = 0$ (1.0) 6.0.

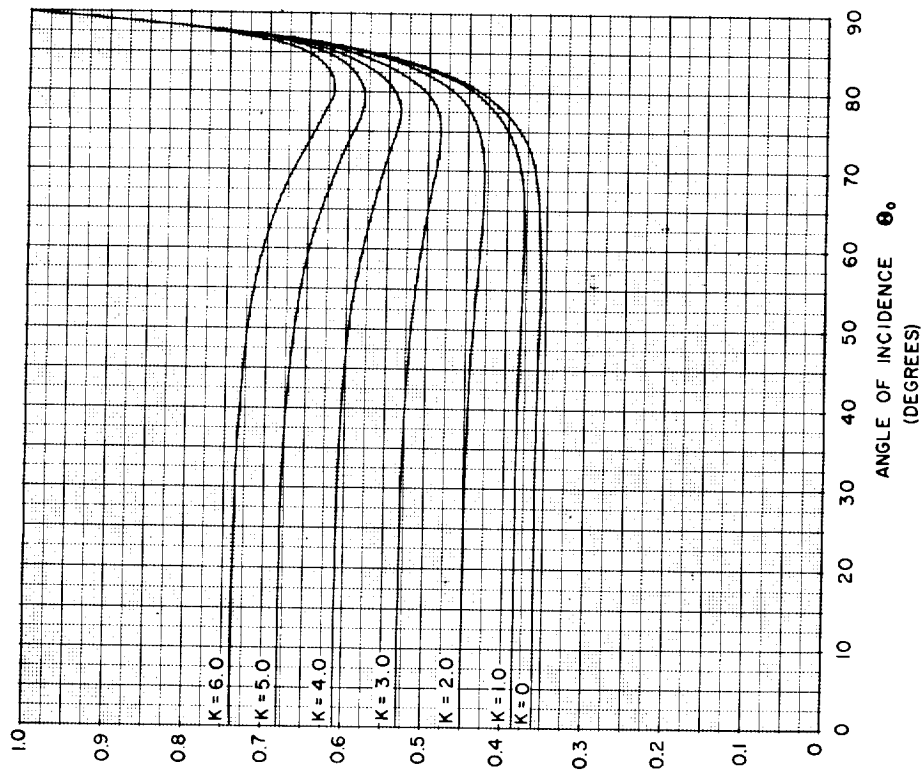


FIGURE 2.—Reflectances $R = \frac{1}{2}(R_1 + R_2)$ for $N = 4.0 - ki$; $k = 0$ (1.0) 6.0.

The first expression holds if the phase of the complex index of the first medium is smaller than that of the second medium. If the indices of refraction of both materials have the same phase, the relative index becomes a real index; it is located on the abscissa axis and resembles the reflection characteristics of dielectrics. It is evident that if n becomes smaller than unity and the angle of incidence is greater than the critical angle of incidence, total reflection theoretically can occur at a metallic interface.

Figure 3 shows that the curves in the first and fourth quadrants are symmetrical with respect to the axis of abscissa. It has been proved that the same symmetry exists in all the *isoreflexion* curves for oblique incidence. Therefore, we have to deal only with the fourth quadrant of the plot, and for convenience we draw the ordinate axis in the opposite direction for the remainder of the discussion.

Figure 4 illustrates the distribution of index of refraction curves in the complex plane for a number of conducting materials. Each curve represents a different metal and shows how its index N changes with the wavelength. The three-digit values at the beginning and end of the curves give the wavelength in millimicrons ($=10^{-7}$ cm). The curves were not smoothed because the values plotted are from various authors and therefore were not obtained under the same test conditions. Figure 5 presents N for the wavelength of the sodium D line, $\lambda=5893\text{\AA}$, and that of a ruby laser light, $\lambda=6943\text{\AA}$.

The isoreflexance curves for R_1 , R_2 , P and R for oblique incidence are given for the angle of incidence $\theta_0=10^\circ$ (10°) 70° (5°) 85° in the reference. Figures 6 to 11 are some examples of these plots.

It will be noted that in figure 1, R_1 and R_2 are equal at $\theta_0=0^\circ$ and $\theta_0=90^\circ$. With increasing angle of incidence, the R_1 curves tend monotonically toward unity. The curves for R_2 , however, first decrease to smaller values until they reach their minimum, which is $R_2=0$ in the case of dielectrics (n real), and $R_2\neq 0$ in the case of conducting materials. Then as the angle of incidence is further increased they also tend monotonically toward $R_2=1$, which they reach for $\theta_0=90^\circ$ if $n>1$.

There exists a remarkable relation between R_1 and R_2 for the angle of incidence $\theta_0=45^\circ$, mathematically expressed as

$$R_1^2=R_2$$

or

$$R_1=\frac{R_2}{R_1} \quad (8)$$

so that the degree of polarization P becomes

$$P=\frac{1-R_1}{1+R_1} \quad (9)$$

This relation is a valuable tool in experimental work for: (1) transforming experimental data that are given in an arbitrary scale into the real reflection coefficients (the conversion factor by which all data have to be multiplied is $x=R_2/R_1^2$ at $\theta_0=45^\circ$); (2) checking the influence of matter located between a radiating source and a reflecting surface; (3) determining properties of the matter itself; and (4) if $R_1^2=R_2$ is observed, use as an aid in locating a transmitter, the radiation from which hits the reflecting surface at an angle of incidence $\theta_0=45^\circ$.

BREWSTER ANGLES

The particular angle θ_0 for which the value of R_2 for dielectrics becomes zero (fig. 1 for $n=4.0$ and $k=0$) is called the Brewster angle; for this angle, $\tan \theta_0=n$ (Brewster's law). This is the only case where the degree of polarization P becomes unity, or 100 percent, because the reflected wave has only one amplitude and that one is polarized perpendicular to the plane of incidence. Furthermore, it follows from Snell's law that the reflected and refracted waves propagate normal to each other. The curves for R_2 of the conductors never reach the value zero regardless of the size of the real angle of incidence. The angle of incidence at which the minimum of R_2 occurs is called the *pseudo Brewster angle*, because here the Brewster law has only a formal meaning and the angle does not have the physical significance it does in the case of dielectrics. As a matter of fact, we observe in this case that (1) only partial polarization occurs, (2) the maximum degree of polarization does not occur for this angle, and (3) the electric

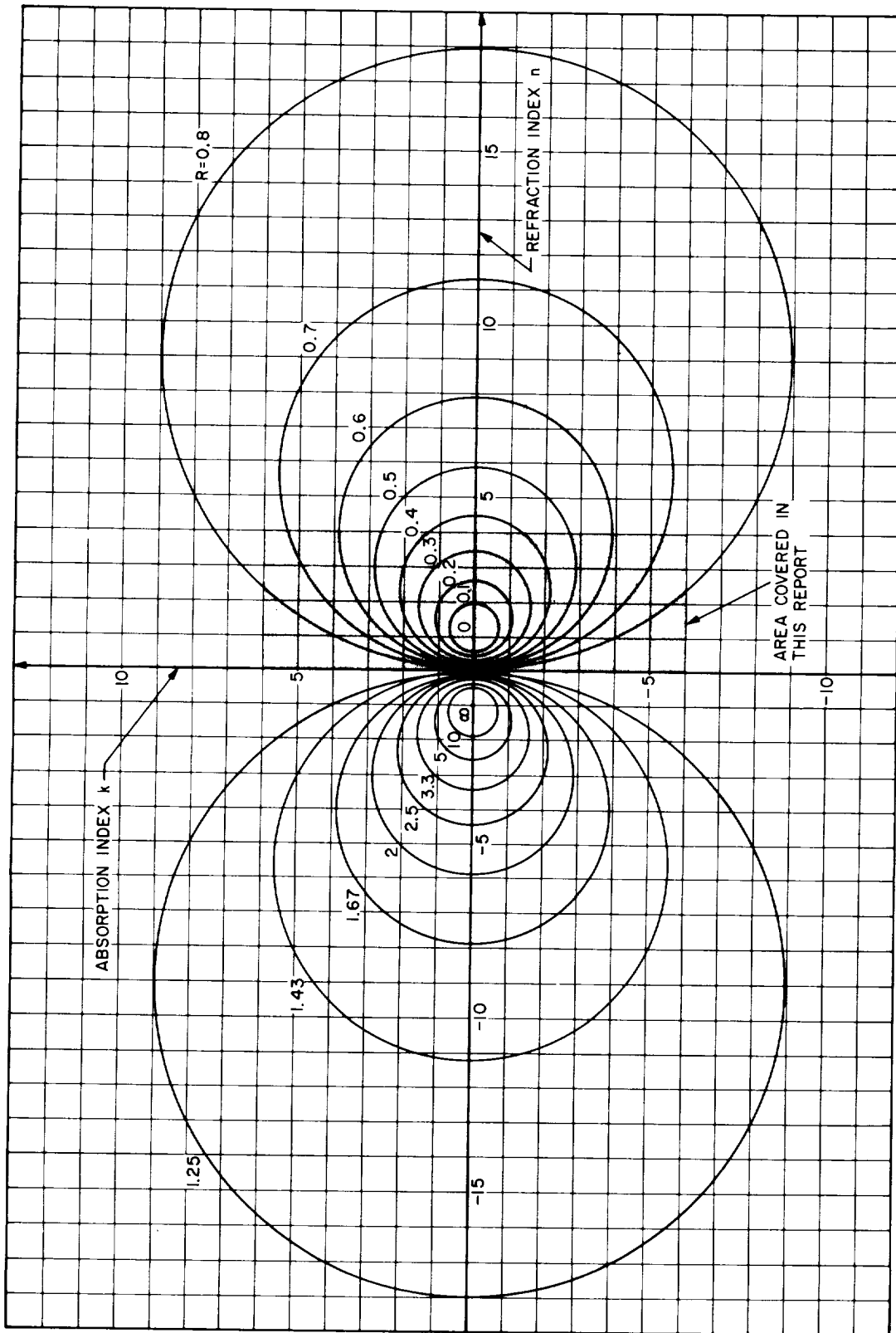


FIGURE 3.—The function $R = [(n-1)^2 + k^2] / [(n+1)^2 + k^2]$. In the first and fourth quadrants, R is physically interpreted as the reflectance at normal incidence.

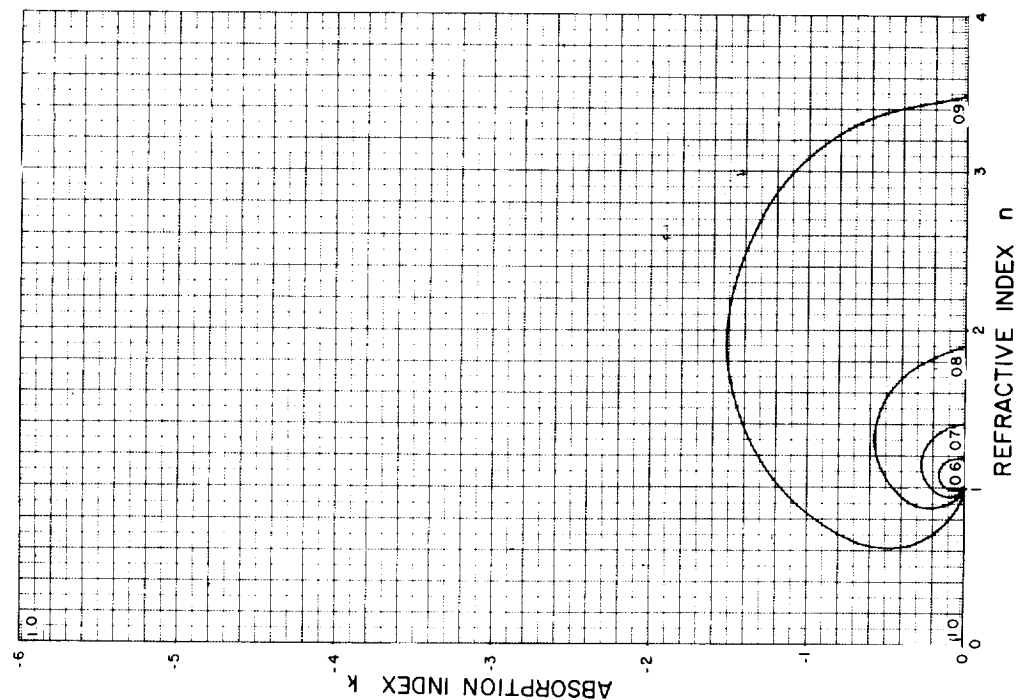


FIGURE 7.—Relation between the reflectance R_1 of electromagnetic radiation and the complex index of refraction $N = n - ki$ for oblique incidence $\theta_0 = 85^\circ$ with respect to the surface normal.

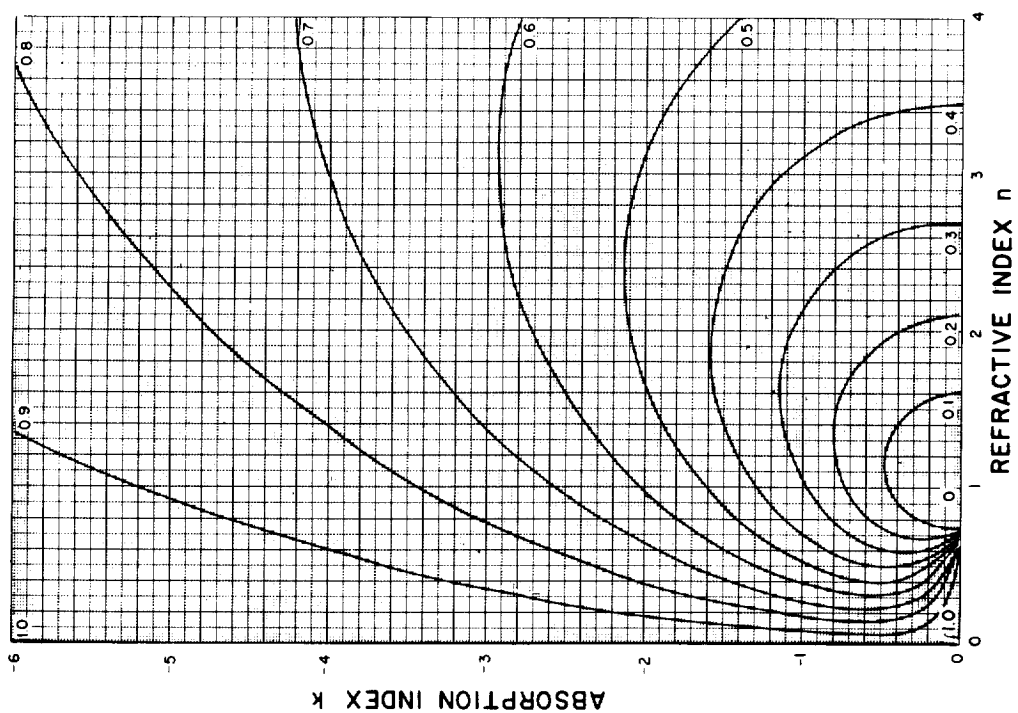


FIGURE 6.—Relation between the reflectance R_1 of electromagnetic radiation and the complex index of refraction $N = n - ki$ for oblique incidence $\theta_0 = 40^\circ$ with respect to the surface normal.

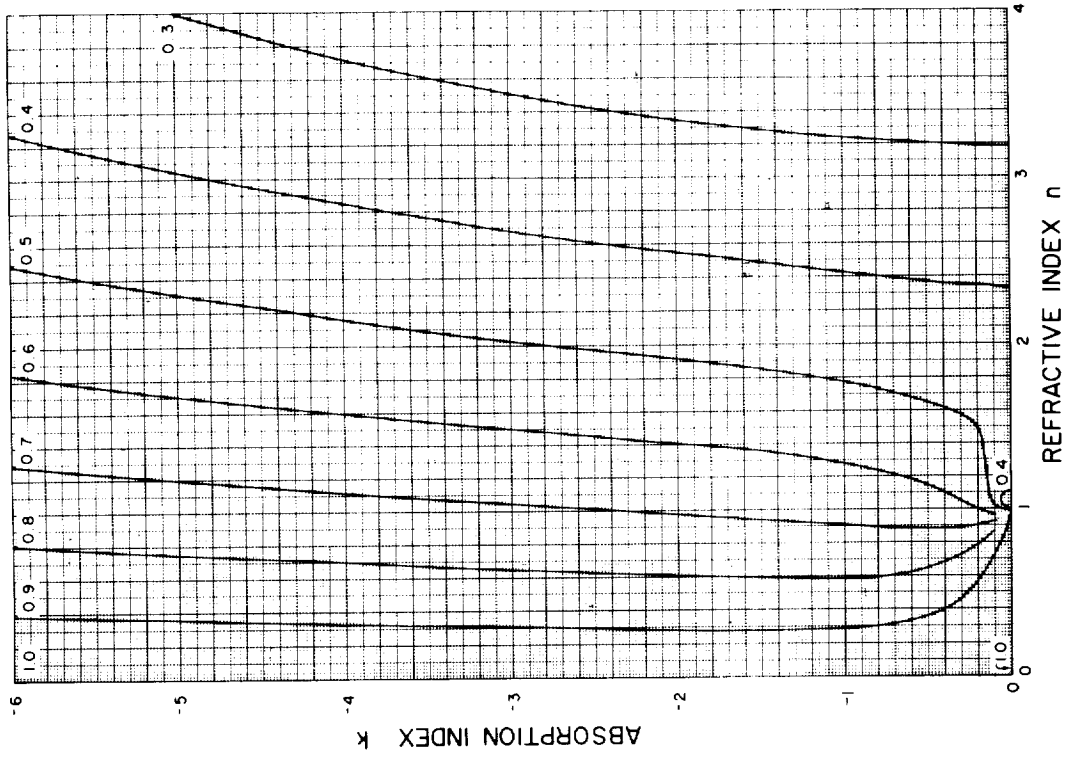


FIGURE 9.—Relation between the reflectance R_2 of electromagnetic radiation and the complex index of refraction $N = n - ki$ for oblique incidence $\theta_0 = 85^\circ$ with respect to the surface normal.

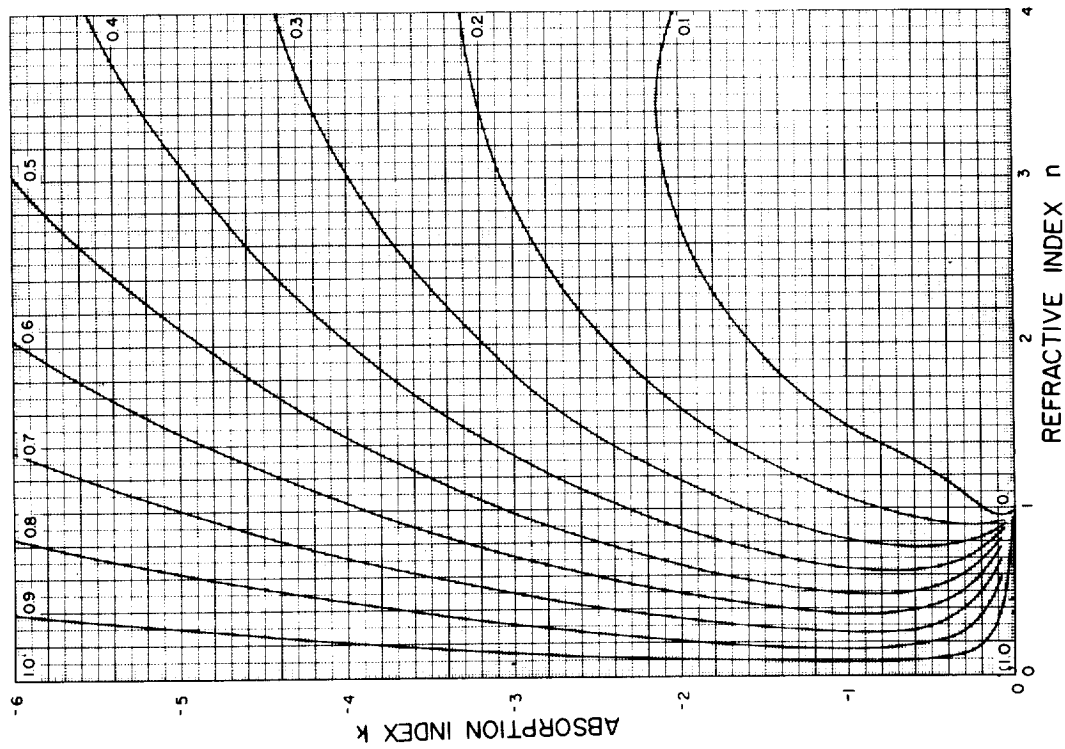


FIGURE 8.—Relation between the reflectance R_2 of electromagnetic radiation and the complex index of refraction $N = n - ki$ for oblique incidence $\theta_0 = 70^\circ$ with respect to the surface normal.

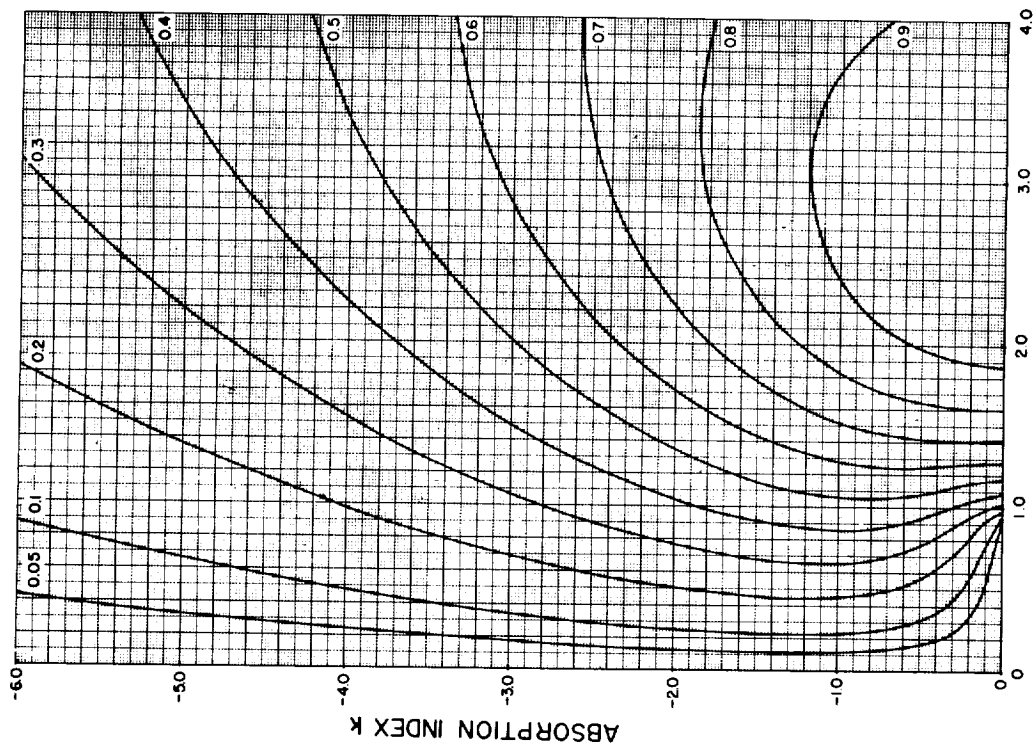


FIGURE 10.—Relation between the degree of polarization $P = (R_1 - R_2) / (R_1 + R_2)$ of electromagnetic radiation and the complex index of refraction $N = n - ki$ for oblique incidence $\theta_0 = 70^\circ$ with respect to the surface normal.

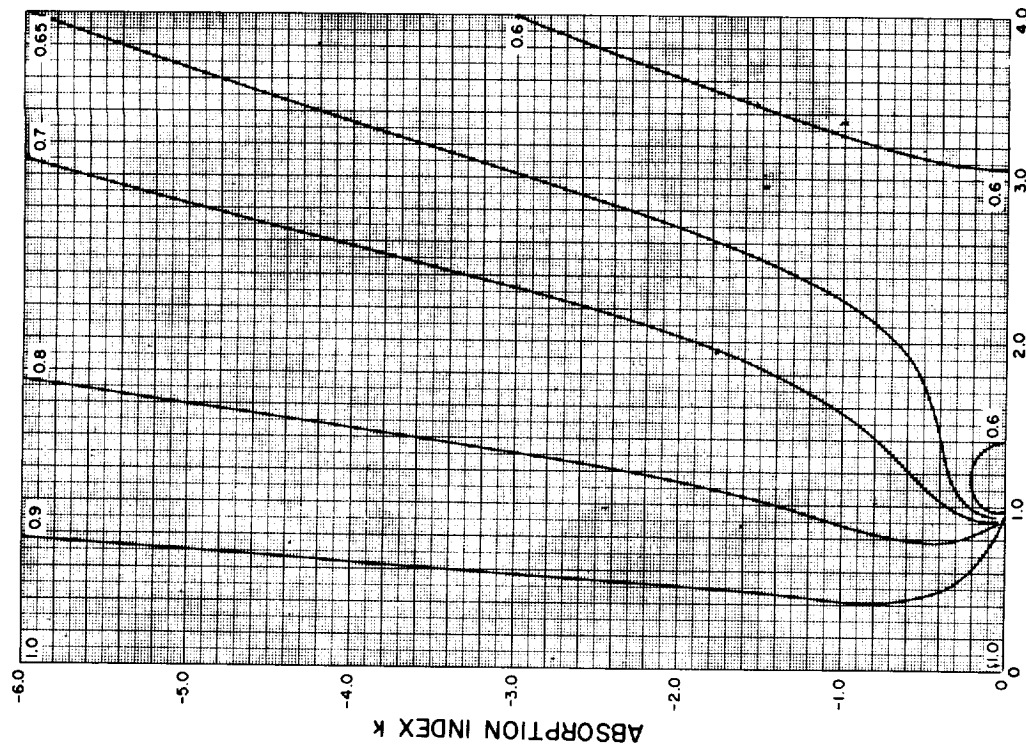


FIGURE 11.—Relation between the reflectance $R = (1/2)(R_1 + R_2)$ of electromagnetic radiation and the complex index of refraction $N = n - ki$ for oblique incidence $\theta_0 = 85^\circ$ with respect to the surface normal.

field vectors of the reflected and refracted radiation are no longer perpendicular to each other.

Along with the reflection, there is also a delay in the phases of the amplitudes. In the case of a conducting material, there is a monotonic decrease in the phase difference from $\delta=180^\circ$ at normal incidence down to $\delta=0^\circ$ at grazing incidence. The geometric picture of the end of the electric (likewise magnetic) field vector will be a circle or an ellipse. The phase shift can be calculated as a function of the index of refraction and the angle of incidence. In experimental work, particularly in optics, that angle of incidence where the difference in phase ($\delta=\delta_{\parallel}-\delta_{\perp}$) after reflection becomes 90° is of special interest, and is called the *principal angle of incidence*. In this case the axes of the vibration ellipse are oriented in the direction of the field components of the \mathbf{E} vector.

Some physics textbooks explain that the principal angle of incidence is the same as the angle at which the reflectance curve of R_2 is a minimum. However, this is generally not true; the assumption is apparently based on mathematical formulations used in metal optics, but are of limited validity even where large values of n and k are concerned. The approximations used in their calculations yield the same angle θ_0 for R_2 =minimum and for $\delta=90^\circ$.

The maximum degree of polarization P (eq. (6)) occurs where R_2/R_1 is a minimum. Contrary to statements appearing in some textbooks, the angle of incidence θ_0 at which the ratio R_2/R_1 is a minimum is not identical to either the pseudo Brewster angle or the principal angle of incidence. The angles of incidence for $(R_2)_{min}$, $(R_2/R_1)_{min}$ or P_{max} , and $\delta=90^\circ$ are distinct, and may differ by angles of between 0° and 45° . As an example, the case $N=n-ki=0.6-0.6i$ is graphically illustrated in figure 12, with the curves representing R_1 , R_2 , R_2/R_1 , P , and δ plotted against θ_n . In order to clarify the distinction, it is proposed here to identify the above-mentioned characteristic angles of incidence as first, second, and third Brewster angles. The following definitions are based on the assumption that

the incoming wave consists of two components with equal amplitudes which oscillate perpendicular to each other, one perpendicular and one parallel to the plane of incidence:

First Brewster angle—pseudo Brewster angle: The angle of incidence θ_0 for which the amplitude $\sqrt{R_2}$ of the wave oscillating parallel to the plane of incidence is a minimum.

Second Brewster angle: The angle of incidence θ_0 for which the ratio of the reflected intensities (R_2/R_1) is a minimum, or, what is the same thing, for which the degree of polarization $P=(R_1-R_2)/(R_1+R_2)$ is a maximum.

Third Brewster angle—principal angle of incidence: The angle of incidence θ_0 at which the two amplitudes of the reflected wave have a difference in phase δ of 90° .

Expressions for the first and second Brewster angles can be obtained by differentiation of expressions based on equations (1) and (2). To do this, however, requires tedious analytical labor and leads to such immense and unwieldy equations that it has to be considered impossible to solve this problem explicitly.

A computer was used to obtain the desired numerical values of $(R_2)_{min}$ and $(R_2/R_1)_{min}$ and the corresponding values of θ_0 for given indices of refraction by successive approximation. Since these data had not been published and are of special interest in experimental work, these numerical values were presented in the reference for the 2400 complex indices. The results of these calculations are presented in figures 13 and 14.

The literature contains a rigorous equation for the principal angle of incidence, or third Brewster angle. This equation can also be written in the following two forms:

$$(n^2+k^2)^2-2\sin^2\theta_0(n^2-k^2)=\sin^4\theta_0\tan^4\theta_0-\sin^4\theta_0 \quad (10)$$

or

$$(n^2-\sin^2\theta_0)^2+(k^2+\sin^2\theta_0)^2+2n^2k^2=\sin^4\theta_0(\tan^4\theta_0+1) \quad (11)$$

For constant angles of incidence, these equations represent Cassinian curves in the Argand diagram. Within the interval of the angle of incidence $0\leq\theta_0\leq90^\circ$, the Cassinian curves

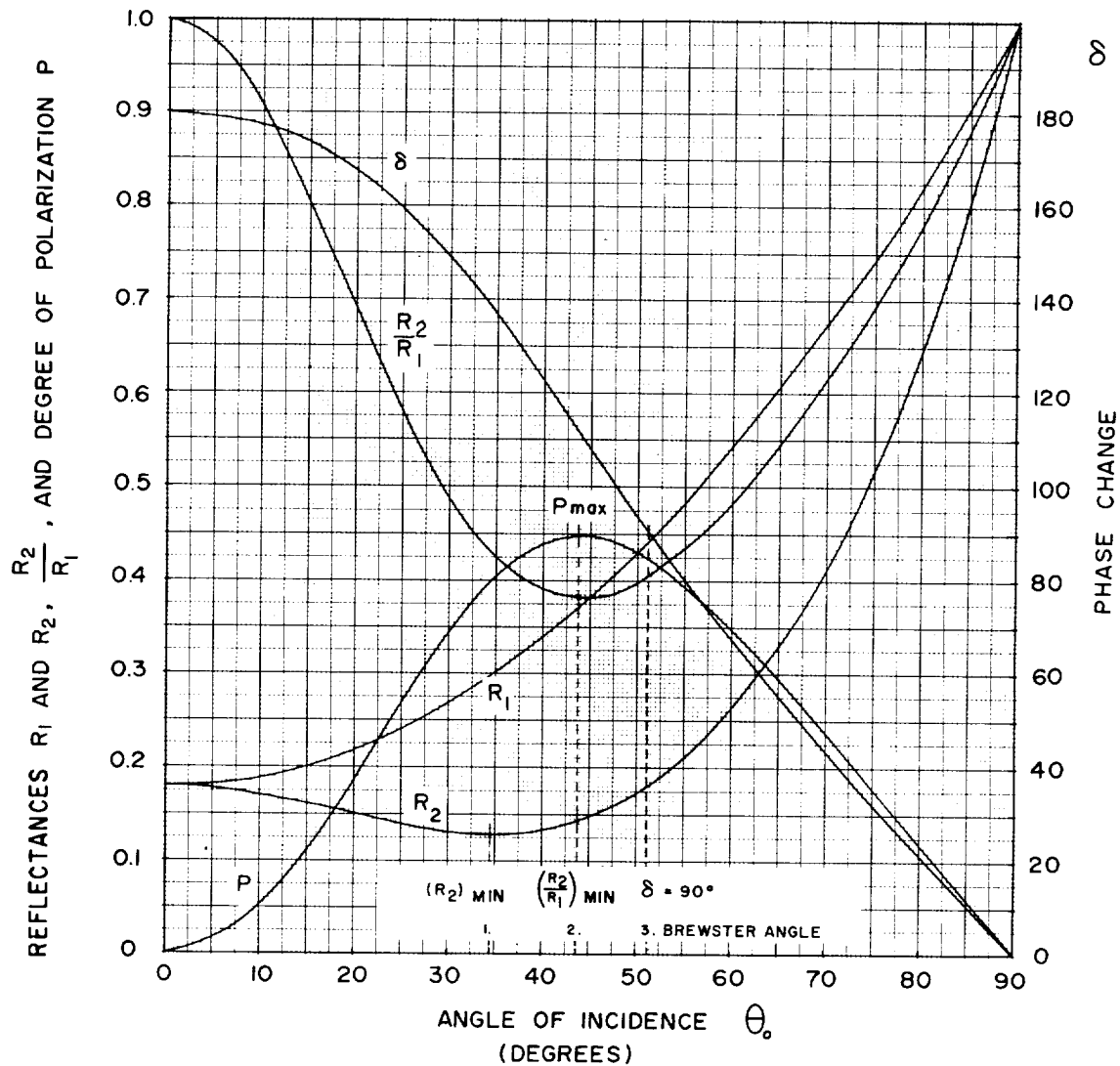


FIGURE 12.—Illustration of the definitions of the first, second, and third Brewster angles of incidence, for $N=0.6-0.6i$.

take on different shapes (fig. 15). We can distinguish three cases:

- (a) $\theta_0=45^\circ$
- (b) $\theta_0>45^\circ$
- (c) $\theta_0<45^\circ$

Case (a) is represented by the lemniscate of Bernoulli with the pole at the origin. In case (b), for values of θ_0 between 45° and $\tan^{-1}\sqrt{2}$, the curves are general lemniscates with their two saddle points on the ordinate axis; for

greater values of θ_0 the curves are Cassinian ovals with their longer axes along the abscissa axis. The curves in (c) are within the lemniscate of Bernoulli, and each branch has two points of intersection with the abscissa axis. This last case is illustrated by a special drawing (fig. 17). It will be observed that the unique relation between the principal angle of incidence and the index of refraction no longer holds for a certain region of small indices. This region of multiple principal angles of incidence is bounded by three curves: (1) the abscissa axis, (2) the envelope of the curves $\theta_0=\text{constant}$,

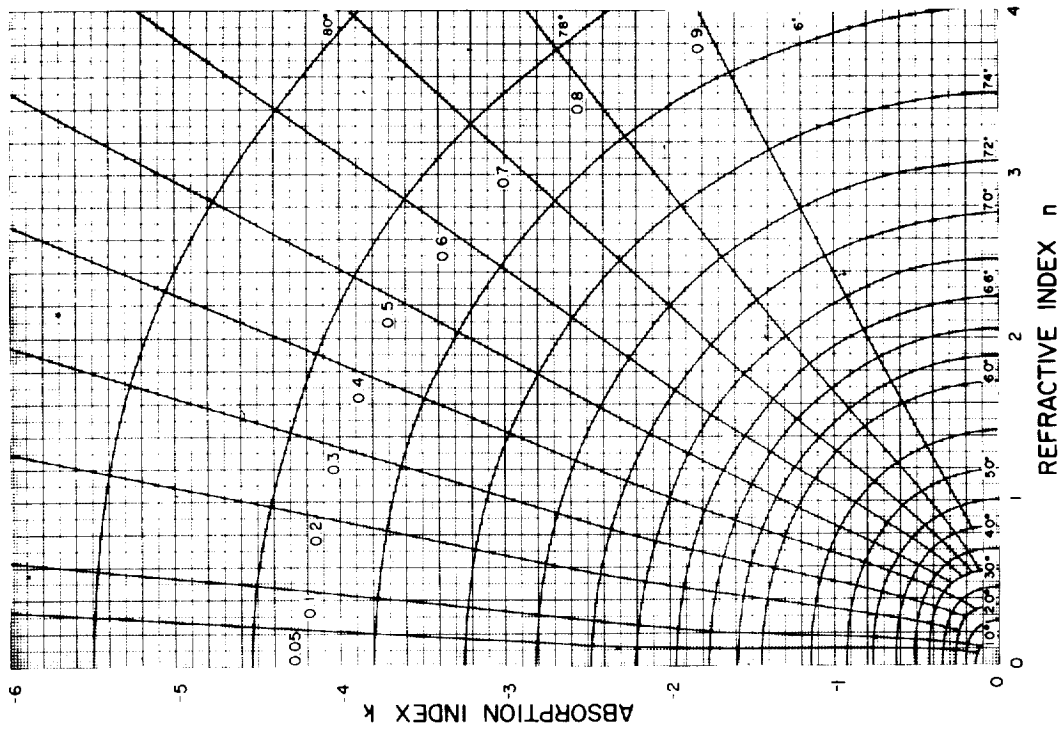


FIGURE 13.—Relation among the first Brewster angle of incidence (where R_1 is a minimum), the reflectance $(R_2)_{\min}$, and the complex index of refraction $N = n - ki$.

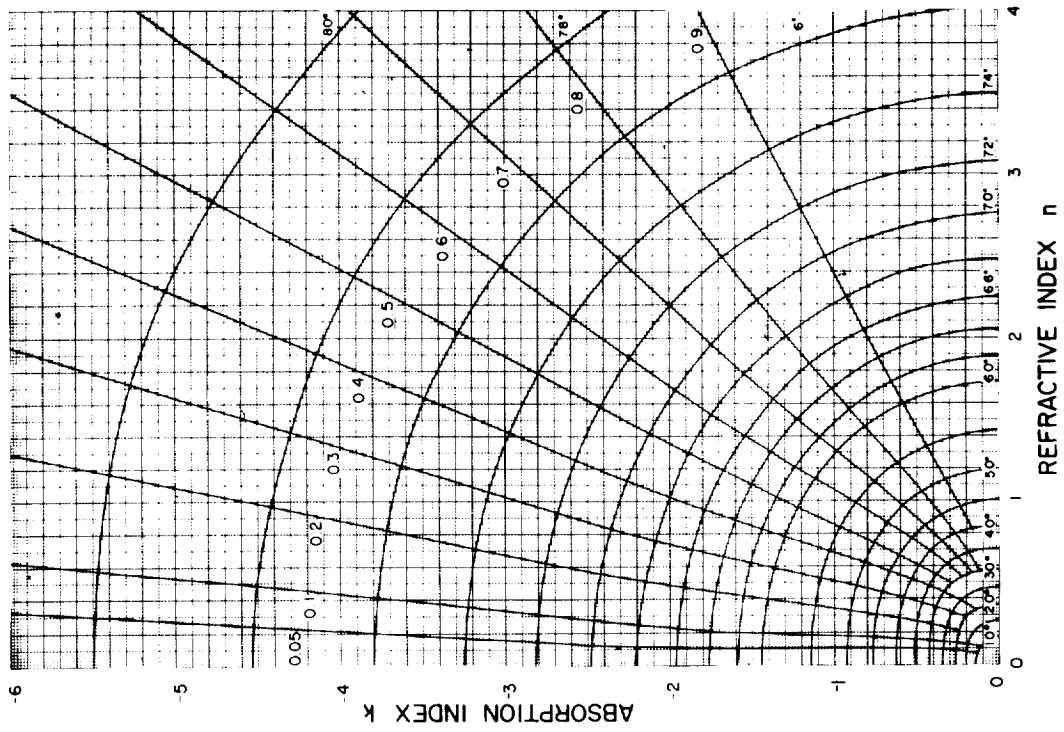


FIGURE 14.—Relation among the second Brewster angle of incidence (where P is a maximum), the degree of polarization P_{\max} , and the complex index of refraction $N = n - ki$.

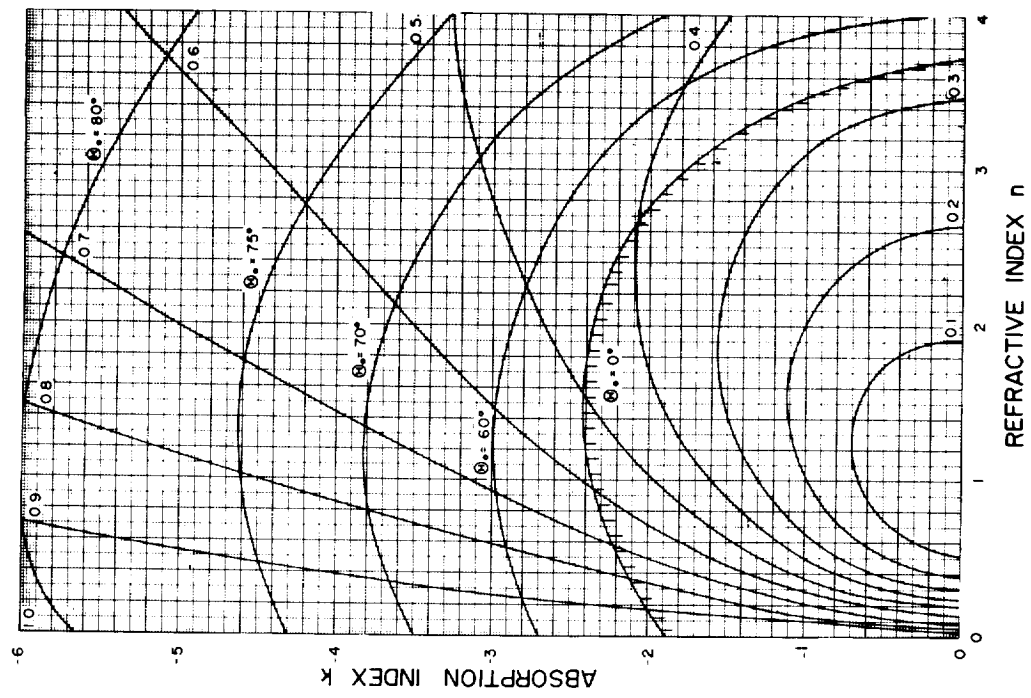


FIGURE 16.—Relation among the angle of incidence θ_0 where the reflectance $R = (1/2)(R_1 + R_2)$ is a minimum, the reflectance R_{\min} , and the complex index of refraction $N = n - ki$.

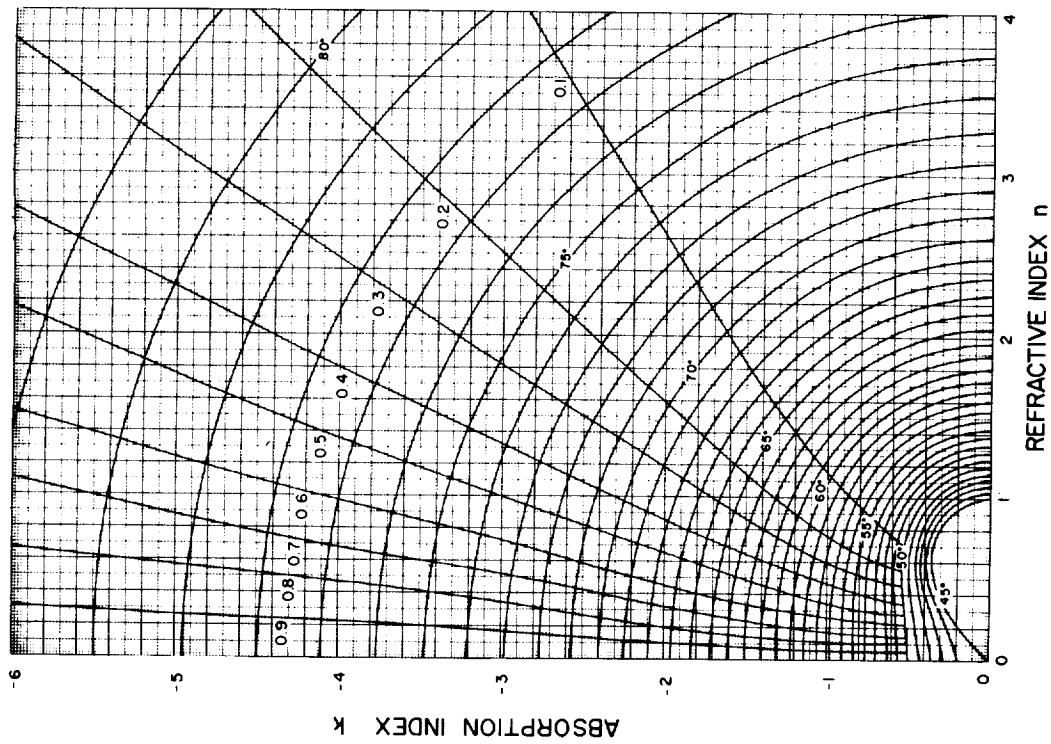


FIGURE 15.—Relation among the third Brewster angle of incidence (equals principal angle of incidence where the phase difference $= 90^\circ$), the reflectance R_3 , and the complex index of refraction $N = n - ki$.

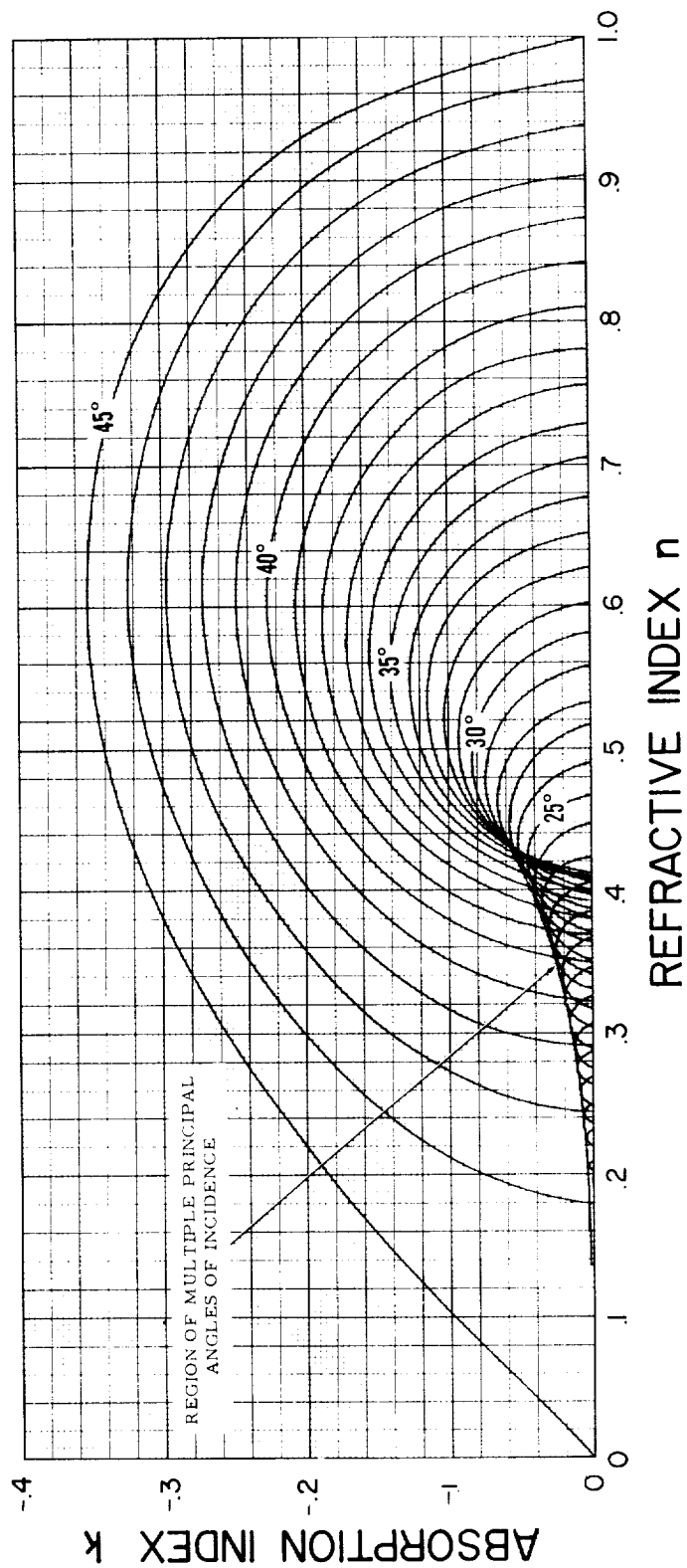


FIGURE 17.—The (third Brewster angle of incidence) equals the (principal angle of incidence), for small values of the index of refraction $N = n - ki$.

and (3) approximately the curve for $\theta_0=33^\circ$. From an inspection of numerical results it was observed that materials with index of refraction located on boundaries (2) and (3) have two principal angles of incidence, and that the materials whose index of refraction falls within the region considered, including the abscissa axis, have three principal angles of incidence. The two points of intersection of the curves $\theta_0=\text{constant}$ with the abscissa axis have a physical interpretation. The point on the right-hand side represents Brewster's law for which $R_2=0$. For the other point we have total reflection, but the two amplitudes of R_1 and R_2 have a difference in phase of 90° . It is supposed that those alkali metals which become transparent in the ultraviolet region have index of refraction curves which cross this region of multiple principal angles of incidence.

With application of the approximation

$$n^2+k^2=\sin^2 \theta_0 \tan^2 \theta_0 \quad (12)$$

used in metal optics, where n^2+k^2 is generally much greater than unity, the curves for constant principal angle of incidence would degenerate into circles and show only fair agreement for large indices, requiring the further restriction $n \sim k$ to obtain accurate results. The precise values and the corresponding values of R_1 and R_2 at these angles of the principal angle of incidence are also given in the reference. Careful inspection of the material presented shows that where N is complex the following relation holds, without exception, for the three Brewster angles for conductors (denoted by θ_1^* , θ_2^* , and θ_3^* , respectively):

$$\theta_1^* < \theta_2^* < \theta_3^*$$

In order to complete the discussion of reflectance curves, let us briefly inspect the case of unpolarized radiation. Figure 2 shows that with increasing k the curves have a more distinct minimum, which approaches $\theta_0=90^\circ$ for very large k values. Figure 16 contains the isorefectance curves of the unpolarized radiation in the complex plane. This particular graph

serves as an illustration only and is not claimed to be as accurate as the other figures. It will be noted that there is an area (the entire area below the curve labeled $\theta_0=0$) for which the minimum reflection occurs at normal incidence, with a small surrounding belt in which the angle of incidence increases very rapidly. Only the curves for $\theta_0=60^\circ$, 70° , 75° , and 80° are represented.

RÉSUMÉ AND APPLICATION

Table I summarizes some characteristics of the perpendicular and parallel components, R_1 and R_2 , of the reflected beam for special angles of incidence.

TABLE I.—*Reflection Characteristics at Special Angles of Incidence*

Material	Angle of incidence θ_0	Reflection characteristics
Dielectrics and conductors	0°	$R_1 = R_2 < 1$
	45°	$R_1 = \frac{R_2}{R_1}$
	90°	$R_1 = R_2 = 1$
Dielectrics	Brewster angle	$R_2 = 0, P = 1$
Conductors	First Brewster angle	$R_2 = \text{minimum}$
	Second Brewster angle	$\frac{R_2}{R_1} = \text{minimum}$ $P = \text{maximum}$
	Third Brewster angle	$\delta = 90^\circ$

Since all the R_1 and R_2 quantities are functions of θ_0 , n , and k , the numerical values of n and k in general can be determined from experimental reflectance data. We can distinguish two major types of data for this purpose: (1) experimental values of the reflectance for arbitrary angles of incidence; and, (2) experimental values of the reflectance for characteristic angles of incidence, or the three Brewster angles.

Figure 18 will serve to explain the treatment of the first type. For the upper part of the

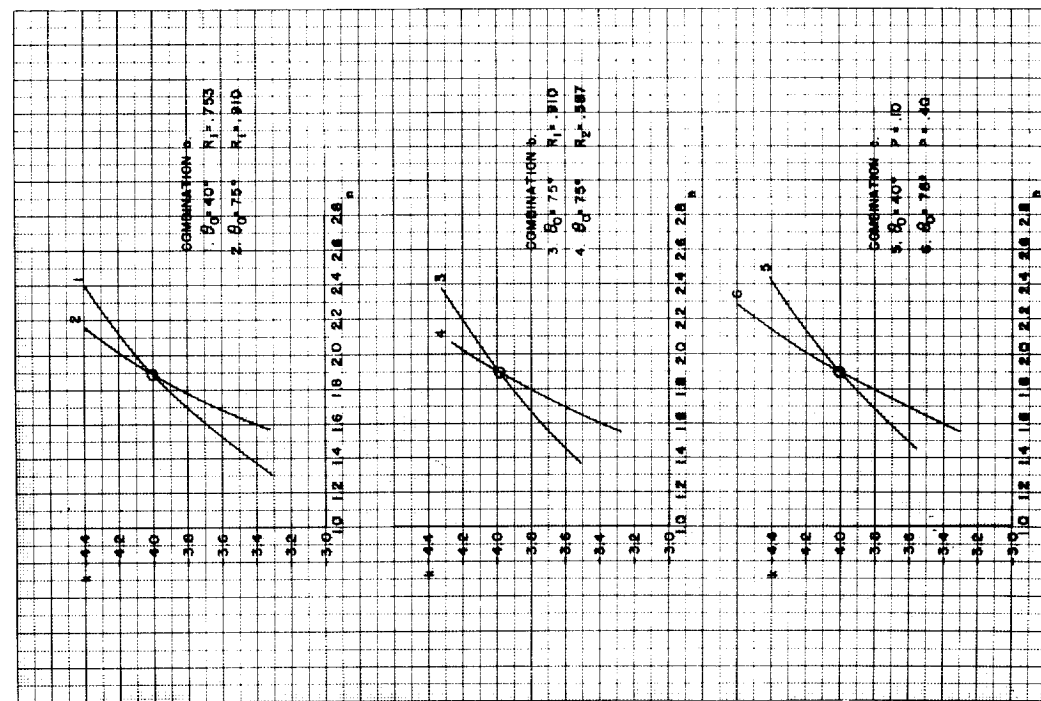


FIGURE 18.—The determination of N from reflection measurements at noncharacteristic angles of incidence.

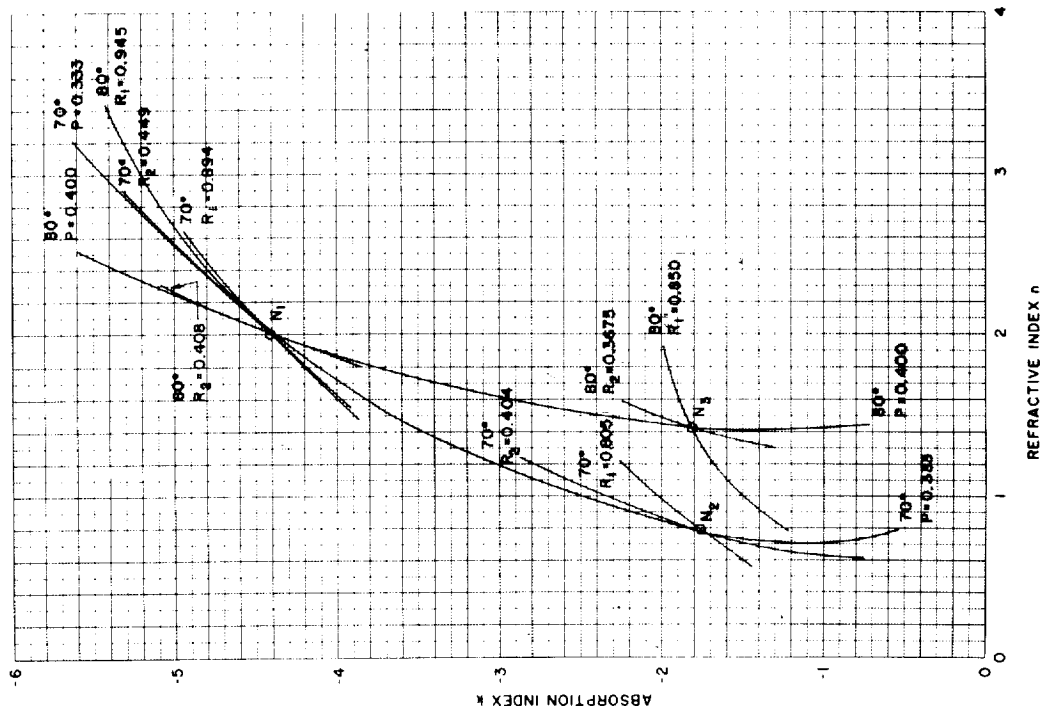


FIGURE 19.—Particular example for the determination of N from experimental reflectances that are in error by a constant factor.

figure, the experimental value $R_1=0.753$ at $\theta_0=40^\circ$ indicates that the index of refraction of the material considered is located on the isorefectance curve $R_1=0.753$ at that angle. The same follows for the experimental data obtained at $\theta_0=75^\circ$, which in this example is $R_1=0.910$. The two isorefectance curves have only one common point, the coordinates of which constitute the index of refraction of the material involved. For the middle part of the figure, the same result is obtained from R_1 and R_2 , which in the case illustrated, were obtained at the same angle, 75° . This method cannot be used for $\theta_0=45^\circ$ because the existence of a unique relation between R_1 and R_2 at this angle ($R_1^2=R_2$) causes the two curves to coincide. The bottom part of the figure illustrates the method that uses only the degrees of polarization at two different angles.

The treatment of the second type makes use of the plots in figures 13, 14, and 15. The curves which appear to emanate more or less radially from the vicinity of the origin on the three graphs are isorefectance or isopolarization curves suitable for identifying the characteristic angles depicted. The relation among the three Brewster angles is unique for each index of refraction (except when the principal angle of incidence $\theta_0 < 45^\circ$). It will be noticed that all isorefectance curves shown in figures 13 to 16 eventually curve back to the abscissa

axis $k=0$ in numerical order by reflectance value.

Experimental data that are in error by a constant factor, if used with the isorefectance curves (for example, fig. 6 to 9) will lead to indices of refraction which are not the true indices of the material considered. As an example, let us inspect experimental data which were obtained at $\theta_0=70^\circ$ and $\theta_0=80^\circ$, and for which, due to unknown influences, the measured intensities were only 90 percent of the expected intensities (fig. 19). The cross points of the isorefectance curves give the index of refraction N_2 for $\theta_0=70^\circ$ and N_3 for $\theta_0=80^\circ$.

However, as long as the deviation is the same for each pair of measured R_1 and R_2 values, the ratio R_2/R_1 , or the degree of polarization, is not affected. The P curves in this example determine the true value for N , designated N_1 on this plot. It should be emphasized that our example was not limited to consideration of the same degree of discrepancy for both angles of incidence, that is, 10 percent of the theoretical data in both cases.

REFERENCE

- HOLL, HERBERT B.: The Reflection of Electromagnetic Radiation (Based on Classical Electrodynamics). Rep. No. RF-TR-63-4, U.S. Army Missile Command, Mar. 15, 1963. Vol. II, appendix, Tables of Radiation Reflection Functions.

6. The Theory of Emissivity of Metals

NEIL ASHBY

P.E.C. RESEARCH ASSOCIATES, INC., BOULDER, COLO.

KLAUS SCHOCKEN

NASA GEORGE C. MARSHALL SPACE FLIGHT CENTER, HUNTSVILLE, ALA.

It is shown that practical situations exist in which the emissivity of a surface is not equal to the absorptivity. The calculations which reveal this fact are based on a second-quantized treatment of the electromagnetic radiation field. To account for the high reflectivity of metals, it is necessary to use a set of basis functions for the radiation field which are exponentially attenuated (but without net absorption) within the metal. On this basis, a perturbation theory formalism is developed with which the emissivity may be calculated as a function of wavelength, angle of emission, polarization, and temperature, whenever the electronic wave functions are known.

Comparatively little progress has been made during the past half-century toward a basic theoretical understanding of the emissivity of solid materials. This is in spite of the enormous amount of research done in solid state physics, and is due primarily to the difficulty of preparing clean surfaces and a consequent shortage of reliable measurements to compare with theory.

The actual state of the solid near the surface is generally unknown. More specifically, neither the identity nor the density of the adsorbed impurities, nor the surface irregularities, are known, and thus we do not know what to use for the electron wave functions near the surface, which are crucial for any theory of emissivity of metals since only the electrons that are near the surface absorb or emit radiation.

In addition to these difficulties, one finds that the published literature on emissivity is based on considerations of thermal equilibrium between a solid and its environment. The emissivity, denoted by e , is generally defined as the ratio of the rate at which energy is emitted by the solid to the rate at which energy

would be emitted by a blackbody at the same temperature. The absorptivity, denoted by α , is defined as the ratio of energy absorbed by a surface to the total energy incident on that surface. Under conditions of thermal equilibrium—in other words, when the radiation incident on a surface is blackbody radiation of the same temperature as the solid—it follows from Kirchhoff's law that

$$\alpha = e \quad (1)$$

This equality also holds for each wavelength.

We wish to point out, however, that this situation holds strictly only for the case of thermal equilibrium. As was first suggested by Einstein (ref. 1) thermal equilibrium between a solid and blackbody radiation is maintained partially by spontaneous emission, and partially by stimulated emission of the emitter. The stimulated emission is proportional to the intensity of radiation falling on the emitter, and therefore if this radiation is not blackbody radiation of the same temperature as the solid, the stimulated emission may be more or less

than that predicted by Kirchhoff's law. This effect is discussed in more detail in a subsequent section.

A second characteristic feature of published treatments of the emissivity of solids is the use of plane waves as basis functions for expansion of the vector potential $\mathbf{A}(\mathbf{r}, t)$ of the electromagnetic field. As was pointed out by Mott and Zener (ref. 2), however, for wavelengths longer than a certain critical wavelength λ_c , which lies in the ultraviolet for most metals, the vector potential inside the metal is not a plane wave but is represented by functions which are exponentially attenuated. This attenuation is due to the electron-electron interactions within the metal; the electrons because of their small mass respond so rapidly to the impinging electromagnetic field that it is prevented from penetrating more than a few thousand Ångströms into the metal. We shall exploit this fact in subsequent sections to indicate how the rate of emission of energy per unit area of a nearly ideal metallic surface may be calculated, when the appropriate electron wave functions are known and when the state of the solid and of its external environment are specified. This analysis is set up so that the dependence of the emissivity on the angle θ between the normal to the surface and the direction of emission, and the dependence on the state of polarization of the emitted radiation, may be calculated. We shall not, however, consider effects due to irregularities in the surface and shall confine ourselves to metals, for which the emissivity is small and may be calculated by appropriate perturbation expansions. In what follows we assume the metal has a perfectly smooth surface at $z=0$ and fills the semi-infinite half-space corresponding to $z<0$.

RADIATION FIELD TREATED CLASSICALLY

Theoretical calculations of the emissivity e of metals as a function of frequency, under conditions of thermal equilibrium, were first made by Hagen and Rubens (ref. 3). Such calculations are based on Kirchhoff's law, which states that the emissivity at a given frequency ν is equal to the absorptivity α at the same frequency. Conservation of energy leads to

the following relation between reflectivity ρ and absorptivity:

$$\alpha + \rho = 1 \quad (2)$$

Reflectivity may be calculated by using a complex index of refraction, $n(1-i\kappa)$, whose imaginary part is closely related to the conductivity σ of the metal, and which describes the absorption of radiation passing through the surface. This procedure leads to the well-known Hagen-Rubens formula for normal emissivity

$$e = \sqrt{\frac{4\nu}{\sigma}} \quad (3)$$

This formula agrees quite well with experiment only at wavelengths longer than 10 microns.

It is possible to carry this procedure quite far by regarding the quantum-mechanically averaged currents and charge densities in the solid as sources of the radiation field. This approach allows the introduction of the effective dielectric "constant" $\epsilon(k, \omega)$ and the effective magnetic permeability $\mu(k, \omega)$, both of which are complex functions of frequency and wave number; then the complex index of refraction is given by

$$n^2(1-i\kappa)^2 = \epsilon\mu \quad (4)$$

These linear response functions, ϵ and μ , have been studied in detail by many authors (refs. 4 and 5), so we shall not describe how they are calculated. They are defined in terms of expectation values of a certain current correlation function which is exceedingly difficult to calculate.

By way of illustration, consider a metal containing n conduction electrons per unit of volume, in which there are a small number n_i per unit volume of randomly distributed impurities. Outside of the metal ($z>0$) the vector potential $\mathbf{A}(\mathbf{r}, t)$ of the radiation field satisfies the wave equation

$$\nabla^2 \mathbf{A} - \frac{1}{c^2} \frac{\partial^2 \mathbf{A}}{\partial t^2} = 0 \quad (5)$$

whereas inside the metal ($z<0$)

$$\nabla^2 \mathbf{A} - \frac{1}{c^2} \frac{\partial^2 \mathbf{A}}{\partial t^2} = \frac{4\pi}{c} \mathbf{j}(\mathbf{r}, t) \quad (6)$$

Here $\mathbf{j}(\mathbf{r}, t)$ is the quantum-mechanically averaged current density. At temperatures such that $kT \ll \mu$, where μ is the Fermi energy of the metal, electron-phonon interactions may

tangential components of \mathbf{E} and \mathbf{H} are continuous across the surface $z=0$, one may calculate the reflectivity and hence the emissivity. The result is:

$$e(\theta) = \frac{4k\beta \cos \theta}{\left[k^4 \cos^4 \theta - 2k^2 \cos^2 \theta \frac{\omega_p^2 k^2}{k^2 c^2 + \Gamma^2} + \frac{\omega_p^4 k^2}{c^2(k^2 c^2 + \Gamma^2)} \right]^{1/2} + 2k\beta \cos \theta + k^2 \cos^2 \theta} \quad (10)$$

where

$$\beta \equiv \frac{1}{\sqrt{2}} \left[\sqrt{k^4 \cos^4 \theta - 2k^2 \cos^2 \theta \frac{\omega_p^2 k^2}{k^2 c^2 + \Gamma^2} + \frac{\omega_p^4 k^2}{c^2(k^2 c^2 + \Gamma^2)}} + k^2 \cos^2 \theta - \frac{\omega_p^2 k^2}{k^2 c^2 + \Gamma^2} \right]^{1/2} \quad (11)$$

be neglected. The result of a lengthy calculation (ref. 5) of the current density \mathbf{j} is

$$\mathbf{j}(\mathbf{k}, \omega) = \frac{n e^2 \omega}{m c (\omega - i\Gamma)} \mathbf{A}(\mathbf{k}, \omega) \quad (7)$$

where

$$\Gamma = \frac{1}{2\pi\hbar} k_f^2 n_i \frac{1}{\left(\frac{\partial \epsilon}{\partial k}\right)_{k_f}} \int_{-1}^1 |v(k_f)|^2 (1 - \cos \theta) d(\cos \theta) \quad (8)$$

Here $\mathbf{j}(\mathbf{k}, \omega)$ is the Fourier transform of the current density:

$$\mathbf{j}(\mathbf{k}, \omega) = \int d\mathbf{r} dt e^{-i\mathbf{k} \cdot \mathbf{r} + i\omega t} \mathbf{j}(\mathbf{r}, t)$$

and similarly for $\mathbf{A}(\mathbf{k}, \omega)$; $\hbar k_f$ is the Fermi momentum of the metal (a spherical Fermi surface is assumed), $v(k)$ is the electron impurity interaction potential, and $\epsilon(k)$ is the single-particle electron energy. The function Γ is related approximately to the static conductivity σ of the metal at low temperatures:

$$\sigma = \frac{n e^2}{m \Gamma} = \frac{\omega_p^2}{4\pi \Gamma} \quad (9)$$

where $\omega_p = \sqrt{4\pi n e^2 / m}$ is the plasma frequency.

These equations may be used to calculate the reflectivity. Consider for example a plane wave of wave-number vector $\mathbf{k} = (-k \sin \theta, 0, -k \cos \theta)$ polarized in a direction parallel to the metallic surface, incident on the surface. By imposing the conditions that the normal and

The appearance of θ in the denominator of equation (10) indicates that Lambert's law is not exactly obeyed. For normal incidence ($\theta=0$), in the limit $kc \ll \Gamma$, equation (10) reduces to the Hagen-Rubens relation. A similar calculation may be performed for emissivity of radiation polarized in the plane of emission. Such calculations are very similar to those of Mott and Zener (ref. 2).

This approach suffers from the defect that calculation of the quantum-mechanically averaged current is excessively difficult. Further, the radiation field is treated only in a gross or statistical sense, and none of the microscopic absorption and emission processes by electrons ever enter into the picture.

BASIS FUNCTIONS FOR AN ATTENUATED RADIATION FIELD

Although the use of a complex index of refraction glosses over the fact that the radiation field is quantized, it has one very satisfactory feature, namely, that the radiation field is damped or attenuated so that it never penetrates far into the metal. In contrast, it is very common to expand the quantized vector potential in a set of plane-wave basis functions which suffer no such damping and which may be emitted or absorbed by electrons far inside the metal.

However, a set of basis functions may be found for the quantized vector potential which are attenuated, so that only electrons near the surface will participate in emission or absorp-

tion. In order to find such a set, we consider those parts of the Hamiltonian of the system which include the kinetic energy of the electrons and the free radiation field. These are

$$H = H' + H_{rad} = \frac{1}{2m} \int d\mathbf{r} \psi^+(\mathbf{r}, t) \left[\frac{\hbar}{i} \nabla + \frac{e}{c} \mathbf{A}(\mathbf{r}, t) \right]^2 \psi(\mathbf{r}, t) + \int \frac{1}{8\pi} d\mathbf{r} \left[\frac{1}{c} \dot{\mathbf{A}}^2 + (\nabla \times \mathbf{A})^2 \right] \quad (12)$$

where $\psi^+(\mathbf{r}, t)$ and $\psi(\mathbf{r}, t)$ are creation and annihilation operators for electrons in the Heisenberg representation, and \mathbf{A} is the vector potential, which is assumed to satisfy

$$\nabla \cdot \mathbf{A} = 0 \quad (13)$$

The right-hand side of equation (12) is rearranged into three contributions:

$$H = H_1 + H_2 + H_3 \quad (14)$$

where

$$H_1 = \frac{1}{2m} \int \psi^+(\mathbf{r}, t) \left(\frac{\hbar}{i} \nabla \right)^2 \psi(\mathbf{r}, t) d\mathbf{r} \quad (15)$$

H_2 is the first-order interaction term between the electrons and the radiation field:

$$H_2 = \int \frac{e\hbar}{2mi} (\psi^+ \nabla \psi - \nabla \psi^+ \psi) \cdot \frac{1}{c} \mathbf{A}(\mathbf{r}, t) d\mathbf{r} \quad (16)$$

and H_3 includes all terms quadratic in \mathbf{A}

$$H_3 = \int \psi^+(\mathbf{r}, t) \psi(\mathbf{r}, t) \frac{e^2}{2mc^2} \mathbf{A}^2(\mathbf{r}, t) d\mathbf{r} + \frac{1}{8\pi} \int d\mathbf{r} \left[\frac{\dot{\mathbf{A}}^2}{c^2} + (\nabla \times \mathbf{A})^2 \right] \quad (17)$$

We suppose that H_1 includes the periodic lattice potential that is used in calculating a set of electronic basis functions. The term H_2 we set aside for the moment; it is the term responsible for absorption and emission.

The term H_3 can be manipulated so as to give a set of basis functions for $\mathbf{A}(\mathbf{r}, t)$ which are exponentially attenuated in the metal. From equation (17) one may derive the equation of motion for the vector potential:

For $z > 0$,

$$\left(\nabla^2 - \frac{1}{c^2} \frac{\partial^2}{\partial t^2} \right) \mathbf{A} = 0 \quad (18)$$

For $z < 0$,

$$\left(\nabla^2 - \frac{1}{c^2} \frac{\partial^2}{\partial t^2} \right) \mathbf{A} = \frac{4\pi e^2}{mc^2} \psi^+(\mathbf{r}, t) \psi(\mathbf{r}, t) \mathbf{A} \quad (19)$$

To a good approximation we may replace $\psi^+(\mathbf{r}, t) \psi(\mathbf{r}, t)$ by its equilibrium expectation value,

$$\psi^+ \psi = n \quad (20)$$

where n is the number of electrons per unit volume. Thus, equation (19) becomes

$z < 0$,

$$\left(\nabla^2 - \frac{1}{c^2} \frac{\partial^2}{\partial t^2} \right) \mathbf{A} = \frac{\omega_p^2}{mc^2} \mathbf{A} \quad (21)$$

That this is a reasonably good approximation is indicated by experiments on the ultraviolet transmissivity of thin metallic films (ref. 6, p. 323). Incident light of frequencies $\omega > \omega_p$ is mainly transmitted through the metal, whereas for frequencies $\omega < \omega_p$, which is the region in which we are primarily interested, incident light is reflected, and not transmitted. This is implied by equation (21), for the wave-number vector \mathbf{k} must satisfy

$$k^2 = \frac{(\omega^2 - \omega_p^2)}{c^2} \quad (22)$$

and hence k is pure imaginary for $\omega < \omega_p$. Physically, this means that we are assuming the electronic relaxation time is very large.

Equations (19) and (21) may be used to obtain a normalized set of basis functions for expansion of $\mathbf{A}(\mathbf{r}, t)$. We require, in addition to equations (19) and (21), that the tangential components of \mathbf{E} and \mathbf{H} and the normal component of \mathbf{B} be continuous across the surface $z=0$, that the normal component of \mathbf{D} be continuous, and that inside the metal

$$\mathbf{D} = \epsilon \mathbf{E} = \left(1 - \frac{\omega_p^2}{\omega^2} \right) \mathbf{E} \quad (23)$$

For the states with polarization parallel to the surface, we find the following results:

$z > 0$,

$$\mathbf{A}_{\parallel k}(\mathbf{r}) = \frac{c}{2\pi} \frac{1}{\gamma + ik \cos \theta} (-\hat{i} \sin \varphi + \hat{j} \cos \varphi) \\ \times [(\gamma + ik \cos \theta) e^{ik_z z} - (\gamma - ik \cos \theta) e^{-ik_z z}] e^{ik_x x} e^{ik_y y} \quad (24)$$

$z < 0$,

$$\mathbf{A}_{\parallel k}(\mathbf{r}) = \frac{c}{\pi} \frac{1}{\gamma + ik \cos \theta} \\ (-\hat{i} \sin \varphi + \hat{j} \cos \varphi) ik \cos \theta e^{z\gamma} e^{ik_x x} e^{ik_y y} \quad (25)$$

where

$$\gamma = \sqrt{\kappa^2 + k^2 \sin^2 \theta} \quad (26)$$

$$\kappa^2 = \frac{1}{c^2} (\omega_p^2 - \omega^2) \quad (27)$$

and where the wave-number vector \mathbf{k} lies in a plane which makes an angle φ with the x -axis, so that

$$k_x = k \sin \theta \cos \varphi \quad k_y = k \sin \theta \sin \varphi \quad (28)$$

For polarizations in the plane of emission, on the other hand, the basis functions are

$z > 0$,

$$\mathbf{A}_{\perp, k}(\mathbf{r}) = \frac{c}{2\pi} \frac{1}{k\gamma + i\kappa^2 \cos \theta} \{ [\cos \theta (\hat{i} \cos \varphi \\ + \hat{j} \sin \varphi) + \hat{k} \sin \theta] \times (\gamma k + i\kappa^2 \cos \theta) e^{-ik_z z} \\ - [-\cos \theta (\hat{i} \cos \varphi + \hat{j} \sin \varphi) + \hat{k} \sin \theta] \\ \times (\gamma k - i\kappa^2 \cos \theta) e^{ik_z z} \} e^{ik_x x} e^{ik_y y} \quad (29)$$

$z < 0$,

$$\mathbf{A}_{\perp, k}(\mathbf{r}) = \frac{c}{\pi} \frac{1}{k\gamma + i\kappa^2 \cos \theta} \times [\gamma (\hat{i} \cos \varphi \\ + \hat{j} \sin \varphi) - i\hat{k} k \sin \theta] \times k \cos \theta e^{z\gamma} e^{ik_x x} e^{ik_y y} \quad (30)$$

This set of functions is complete, and normalized, although it is not an orthogonal set. The lack of orthogonality introduces only negligible errors in our case.

The vector potential is then expanded as follows:

$$\mathbf{A}(\mathbf{r}, t) = \sum_{\lambda} a_{\lambda}(t) \mathbf{A}_{\lambda}(\mathbf{r}) + a_{\lambda}^{\dagger}(t) \mathbf{A}_{\lambda}^*(\mathbf{r})$$

where the index λ denotes all possible values of \mathbf{k} such that $k_z \geq 0$, and all polarizations. The basis functions $\mathbf{A}_{\lambda}(\mathbf{r})$ are as given in

equations (24) to (30), and the operators $a_{\lambda}(t)$, $a_{\lambda}^{\dagger}(t)$ satisfy the commutation relations (ref. 7)

$$a_{\lambda} a_{\mu}^{\dagger} - a_{\mu}^{\dagger} a_{\lambda} = \frac{\hbar}{2\nu_{\lambda}} \delta_{\lambda, \mu} \quad (31)$$

where $\delta_{\lambda, \mu} = 0$ if the two polarizations (γ, μ) are different and $\delta_{\lambda, \mu} = \delta(\mathbf{k}_{\lambda} - \mathbf{k}_{\mu})$ if the two polarizations are the same.

PERTURBATION THEORY

The main thing accomplished up to this point is a choice of photon basis functions that do not penetrate far into the metal. For example, in the case of sodium at long wavelengths, the penetration depth for these basis functions is about 2100 Å and does not change appreciably until the wavelengths of the incident radiation approach the ultraviolet. In this respect, calculations performed with these basis functions will differ markedly from recent calculations by Holstein (ref. 8) and others (ref. 9 and references cited therein) who use plane waves as basis functions.

Calculation of the emissivity is straightforward. We shall give one example. The transition probability W_{fi} for the emission of 1 photon of energy $\hbar\omega$ from the solid, with the solid starting in the state i and ending in the state f , is given by

$$W_{fi} = \frac{2\pi}{\hbar} \delta(E_i - E_f - \hbar\omega) |\langle f | R | i \rangle|^2 \quad (32)$$

where

$$\langle f | R | i \rangle = \langle f | H_1 + H_1 \frac{1}{E_i - H_0 + i\epsilon} H_1 \\ + H_1 \frac{1}{E_i - H_0 + i\epsilon} H_1 \frac{1}{E_i - H_0 + i\epsilon} H_1 + \dots | i \rangle \quad (33)$$

is a well-known perturbation expansion (ref. 9) and H_1 consists of all terms in the Hamiltonian which have not been used to calculate either electronic basis functions or radiation basis functions. The symbol ϵ represents an infinitesimal positive number. In particular, the interaction H_2 of equation (16) is included as a part of H_1 .

Let us suppose that

$$H_1 = H_2 + H_4$$

where we do not specify H_4 in detail, except to say that it could be due to electron-impurity interactions, electron-phonon interactions, or electron-electron interactions.

We take only those terms in equation (33) which are of no higher order than the first in H_4 or H_2

$$\begin{aligned} \langle f|R|i \rangle \approx & \langle f|H_2+H_4|i \rangle + \langle f|H_2 \frac{1}{E_i-H_0+i\epsilon} H_4|i \rangle \\ & + \langle f|H_4 \frac{1}{E_i-H_0+i\epsilon} H_2|i \rangle \quad (34) \end{aligned}$$

The term H_4 by itself can cause no emission of photons, so for our case

$$\langle f|H_4|i \rangle = 0 \quad (35)$$

The term $\langle f|H_2|i \rangle$ gives rise to a finite rate of emission of photons. This is due to the fact that electrons may absorb or emit a photon and "collide" with the surface of the metal to conserve momentum. If plane waves are used for the radiation field, this process is impossible.

To show how this occurs and to illustrate the main features of the perturbation calculation, consider a model of a metal in which the electron wave functions are given by

$$\psi_{p_x p_y p_z} = \sqrt{\frac{4}{(2\pi)^3}} e^{ip_x x} e^{ip_y y} \begin{cases} \sin p_z z, & z < 0 \\ 0, & z > 0 \end{cases} \quad (36)$$

The density of electronic states is $2(dp_x dp_y dp_z)/(2\pi)^3$ per unit volume of the sample, and $p_z \geq 0$. Let us calculate the probability of emission of a photon of frequency ν with polarization parallel to the surface, traveling in the direction (θ, φ) . The final state of the photon field, in the occupation number representation, is given by

$$|n_\nu+1\rangle = \sqrt{\frac{2\nu}{\hbar(n_\nu+1)}} a_{\nu,\parallel}^\dagger |n_\nu\rangle \quad (37)$$

where n_ν is the occupation number of the photons in the initial state. The energy of the radiation field initially will be $n_\nu \hbar \nu$, where $n_\nu = 0, 1, 2, \dots$. If one of the electrons makes a transition from state \mathbf{p} to state \mathbf{q} during this emis-

sion process, a lengthy but straightforward calculation of the matrix element

$$M = \langle f|H_2|i \rangle \quad (38)$$

yields

$$\begin{aligned} |M|^2 = & \frac{e^2 \hbar^2}{m^2} \frac{\hbar(n_\nu+1)}{2\nu} \frac{1}{\pi^4} \frac{k^2 \cos^2 \theta}{\frac{\omega_p^2}{c^2}} (\sin \varphi p_x - \cos \varphi p_y)^2 \\ & \times [\delta(q_x - k_x - p_x) \delta(q_y - k_y - p_y)]^2 \left[\frac{\gamma}{\gamma^2 + (q_z + p_z)^2} \right. \\ & \left. - \frac{\gamma}{\gamma^2 + (q_x - p_x)^2} \right]^2 \quad (39) \end{aligned}$$

This matrix element must be averaged over all possible occupied states \mathbf{p} and all possible unoccupied states \mathbf{q} for the electrons. However, in this form two interesting observations may be made. Firstly, the transition probability is proportional to $n_\nu + 1$. The n_ν corresponds to the stimulated emission; and the 1 is the spontaneous emission.

Secondly, we have two δ -functions squared in the matrix element. A closer look at the square of $\delta(q_x - k_x - p_x)$, for example, shows that the $\delta(0)$ which results can be interpreted as a factor L_x , where L_x is the dimension of the sample in the x -direction. Hence, actually,

$$\begin{aligned} & [\delta(q_x - k_x - p_x) \delta(q_y - k_y - p_y)]^2 \\ & = L_x L_y \delta(q_x - k_x - p_x) \delta(q_y - k_y - p_y) \end{aligned}$$

and, dividing equation (39) by $L_x L_y$, we obtain a definite probability per unit area per unit time for the emission of one photon. The third dimension L_z is not involved because of our choice of basis functions.

A somewhat lengthy calculation of the transition probability per unit area per unit time yields the result:

$$\begin{aligned} \frac{W}{L_x L_y} = & \frac{e^2}{m\pi^3} \frac{n_\nu+1}{\nu} \frac{4k^2 \gamma^2 \cos^2 \theta}{\omega_p^2 (2\pi)^6 \sin \theta} \\ & \times \int_0^\infty dq_z \int_0^\infty dp_z \int_0^\infty \alpha^2 d\alpha \\ & \times \left[\frac{1}{\gamma^2 + (p_z + q_z)^2} - \frac{1}{\gamma^2 + (p_z - q_z)^2} \right]^2 \end{aligned}$$

$$\times \left\{ \left\{ 1 + \exp \beta \left[\frac{\hbar^2}{2m} \right. \right. \right. \\ \times \left. \left. \left(p_z^2 + \delta^2 \frac{m^2}{\hbar^4 k^2 \sin^2 \theta} + \alpha^2 \right) - \mu \right] \right\}^{-1} \\ \left. - \left\{ 1 + \exp -\beta \left[\frac{\hbar^2}{2m} \left(p_z^2 + \delta^2 \frac{m^2}{\hbar^4 k^2 \sin^2 \theta} + \alpha^2 \right) \right. \right. \right. \\ \left. \left. \left. - \mu - \hbar\nu \right] \right\}^{-1} \right\} \quad (40)$$

where $\beta = 1/k_B T$ (T is the electron temperature and k_B is the Boltzmann constant) and

$$\delta = \hbar\nu + \frac{\hbar^2}{2m} (q_z^2 - p_z^2 + k_x^2 + k_y^2)$$

To obtain the emission rate, one then multiplies equation (40) by

$$\hbar\nu\rho_\nu d\nu = \frac{2\pi\hbar\nu^3}{c^3} d(\cos \theta) d\nu \quad (41)$$

Similar calculations may be carried out for radiation with the other polarization. These expressions do not simplify further, but must be evaluated numerically.

Terms of the type $\langle f | H_2 [1/(E_i - H_0 + i\epsilon)] H_1 | i \rangle$ have been considered by Holstein (ref. 8) using plane-wave basis functions. These correspond to an electron colliding with a phonon or impurity in the interior of the metal and diffusing to the surface, where it emits a photon. We have in progress calculations of these matrix elements for a number of special cases using attenuated basis functions, and expect to report in detail on these calculations in the near future.

KIRCHHOFF'S LAW

Let $R_{a,\nu}$ be the rate of absorption of energy of frequency ν per unit area per unit frequency interval per unit solid angle by a solid surface. By means of perturbation-theory calculations such as are illustrated in the previous sections, and using the occupation number representation for the radiation field, it is found that $R_{a,\nu}$ takes the general form:

$$R_{a,\nu} d\nu = n_\nu \overline{|M|^2} \hbar\nu\rho_\nu d\nu \quad (42)$$

where $\overline{|M|^2}$ is some appropriately averaged square of a sum of matrix elements, ρ_ν is a density-of-states factor, and n_ν is the number of photons present in the incident-radiation field. For blackbody radiation at temperature characterized by $\beta_r = (k_B T_r)^{-1}$, the average occupation number n_ν is given by the Planck function

$$n_\nu = n_\nu(\beta_r) = \frac{1}{e^{\beta_r \hbar\nu} - 1} \quad (43)$$

The absorptivity is defined as

$$\alpha = \frac{R_{a,\nu} d\nu}{ch\nu n_\nu \rho_\nu d\nu} = \frac{\overline{|M|^2}}{c} \quad (44)$$

where c is the speed of light.

On the other hand, if we let $R_{e,\nu}$ be the rate of emission of energy of frequency ν per unit area per unit frequency interval per unit solid angle, we find by a similar perturbation-theory calculation,

$$R_{e,\nu} d\nu = (n_\nu + 1) \overline{|M|^2} \hbar\nu\rho_\nu d\nu e^{-\beta_s \hbar\nu} \quad (45)$$

where the factor $e^{-\beta_s \hbar\nu}$ takes into account the fact that for a solid at temperature $T_s = (k_B \beta_s)^{-1}$, there are $e^{-\beta_s \hbar\nu}$ fewer electrons in the upper states capable of emitting photons, as compared with those electrons in lower states capable of absorbing photons. The emissivity of the surface is defined as the ratio of the rate of emission to the rate of emission by a blackbody at the same temperature as the solid, and is thus

$$e = \frac{R_{e,\nu} d\nu}{ch\nu n_\nu(\beta_s) \rho_\nu d\nu} = \frac{(n_\nu + 1) e^{-\beta_s \hbar\nu}}{n_\nu(\beta_s)} \overline{|M|^2} / c \quad (46)$$

Thus,

$$e = \eta \alpha \quad (47)$$

where

$$\eta = \frac{(n_\nu + 1) e^{-\beta_s \hbar\nu}}{n_\nu(\beta_s)} \quad (48)$$

If the temperatures of incident radiation and of the solid are the same, and n_ν is given by the Planck function (eq. (43))

$$\eta = 1$$

and $e = \alpha$, which is just Kirchhoff's law. On

the other hand, if $\beta_s \neq \beta_r$, the factor η may differ considerably from unity. For example, if the temperature of the solid is 2000°K and the radiation temperature is 10°K for a wavelength of about 8 microns, $\eta = 0.63$.

Consider a metallic surface of constant spectral absorptivity α . If the incoming radiation is blackbody radiation with a distribution of occupation numbers given by equation (43), the rate of emission of energy per unit time is given by the emissivity times the emission rate of a blackbody at the temperature T_s of the metal:

$$\begin{aligned} R_e &= \int_0^\infty R_{e,\nu} d\nu = \int_0^\infty [n_r(\beta_r) + 1] e^{-\beta_s h\nu} \alpha c h \nu \rho_\nu d\nu \\ &= \int_0^\infty \alpha c h \nu \rho_\nu d\nu e^{-\beta_s h\nu} / (1 - e^{-\beta_r h\nu}) \end{aligned} \quad (49)$$

where we have integrated over all frequencies to obtain a total emission rate. The integral may be evaluated by expanding the denominator

$$\frac{1}{1 - e^{-\beta_r h\nu}} = \sum_{n=0}^{\infty} e^{-n\beta_r h\nu}$$

and integrating term by term to obtain

$$R_e = \alpha \sigma T_s^4 \frac{90}{\pi^4} F\left(\frac{T_s}{T_r}\right) \quad (50)$$

where

$$F\left(\frac{T_s}{T_r}\right) = \sum_{n=0}^{\infty} \frac{1}{\left(1 + \frac{nT_s}{T_r}\right)^4}$$

The effective emissivity of the surface e_{eff} is defined by

$$\frac{e_{eff}}{\alpha} = \frac{R_e}{\alpha \sigma T_s^4}$$

where σ is the Stefan-Boltzmann constant. This quantity is plotted in figure 1.

For a very hot metallic body in a cold environment, the power radiated is only $90/\pi^4$ or 0.93 of what it would be at thermal equilibrium. Various arguments have previously been advanced (ref. 10) in attempts to prove that even in a nonequilibrium situation, the power radiated by a hot body is the same as it would

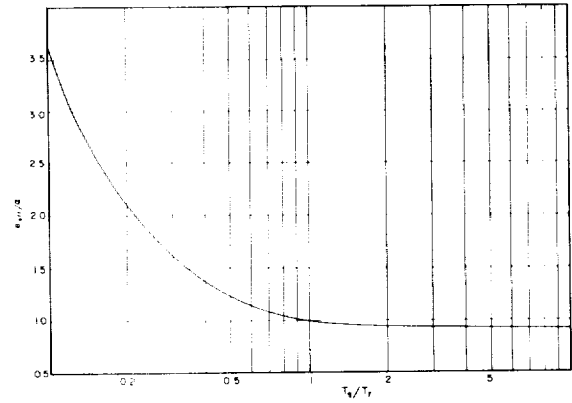


FIGURE 1.—Effect of radiation environment on emissivity of metal. T_s = temperature of solid. T_r = temperature of radiation.

be if the body were in thermal equilibrium with its environment. This may be true for gases and transparent crystals, where the body may be stimulated by radiation which has been emitted from deep within the body itself. For a metal, however, electromagnetic waves of thermal wavelengths are not propagating waves within the metal. The metal must be thought of as a single quantum system which can emit or absorb photons, but none of the photons causing the stimulation can be considered to come from the metal itself. Hence the stimulated emission, for our idealized example, is characteristic only of the environment.

REFERENCES

1. EINSTEIN, A.: *Physik. Z.*, vol. 18, 1917, p. 121.
2. MOTT, N. F., and ZENER, C.: *Optical Properties of Metals*. Cambridge Phil. Soc. Proc., vol. 30, Apr. 30, 1934, pp. 249–270.
3. HAGEN, E., and RUBENS, H.: *Metallic Reflection*. *Ann. Phys.*, vol. 1, no. 2, Feb. 1900, pp. 352–375. See also vol. 8, 1902, p. 1 and vol. 11, 1903, p. 873.
4. DUBOIS, D. F., KIVELSON, M. G., and GELINSKY, V.: *Propagation of Electromagnetic Waves in Plasmas*. AEC Memo. RM-3224-AEC, Rand, Aug. 1962.
5. ASHBY, N.: *Applications of Field Theory to Electrical Conductivity*. Thesis, Harvard Univ., 1961.
6. GIVENS, M. PARKER: *Optical Properties of Metals*. *Solid State Physics*, vol. 6, Frederick Seitz and David Turnbull, eds., Academic Press, Inc. (New York), 1958, pp. 313–352.

7. HEITLER, W.: Quantum Theory of Radiation. 3d ed., The Clarendon Press (Oxford), 1954, p. 41.
8. HOLSTEIN, T.: Westinghouse Res. Labs. Reps. 60-94698-3 R1, R2, R3, M8.*
9. SHOCKEN, KLAUS, ed.: Optical Properties of Satellite Materials—The Theory of Optical and Infrared Properties of Metals. NASA TN D-1523, 1963.
10. SCHWEBER, SILVAN S.: An Introduction to Relativistic Quantum Field Theory. Harper & Row, Pub., Inc. (New York), c. 1961, pp. 320ff.
11. WEINSTEIN, M. A.: On the Validity of Kirchhoff's Law for a Freely Radiating Body. American Jour. Phys., vol. 28, no. 2, Feb. 1960, pp. 123-125.

*Not generally available at the time of publication.

7. Radiation Heat Transfer Through Scattering and Absorbing Nonisothermal Layers¹

JONATHAN D. KLEIN

NASA AMES RESEARCH CENTER, MOFFETT FIELD, CALIF.

Steady-state radiation heat transfer through layers where both scattering and absorption occur within the layers is treated analytically by means of one-dimensional fluxes. The set of simultaneous equations—consisting of a heat-balance equation, an equation for the flux in the direction of heat flow, and an equation for the flux in the opposite direction—has a general solution to which boundary conditions are applied to derive expressions for desired quantities for an arbitrary layer. In this way the transfer through a layer and the emission from it, as well as its temperature distribution, are derived in terms of the absorption and scattering coefficients of the layer, the index of refraction, the lattice conductivity, and the heat applied to it. The treatment includes the effects of surface reflections.

Radiation transfer through nonradiating layers is also treated in order to provide equations for obtaining the absorption and scattering coefficients from optical transmission measurements.

Radiation heat transfer through nonisothermal layers, where both scattering and absorption occur, is a very difficult situation to treat in its full generality. One method is to use electronic data processing machines to arrive at numerical answers for specific situations; however, it is advantageous to obtain analytical expressions since it is usually possible to infer more from such expressions about the mechanisms that occur and the directions to manipulate parameters in order to obtain desired results. It is, however, normally necessary to simplify the situation in order to be able to treat it mathematically. This paper simplifies the actual situation by treating only completely diffuse radiation by a one-dimensional heat-flux calculation and, therefore, neglects any three-dimensional effects. Though this simplification undoubtedly decreases the accuracy of the results, it allows one to handle rather complicated situations and to obtain

useful information about the mechanisms occurring.

SYMBOLS

a	absorption coefficient for diffuse radiation
b	constant equal to $4\sigma'n^2T_0^4$
D	thickness of layer
E	blackbody radiant energy flux
I	radiant energy flux in the direction of the positive X-axis
I_i	incident flux at $x=0$
I_0	forward flux immediately inside interface $x=0$
I_D	forward flux immediately inside interface $x=D$
J	radiant energy flux in the direction of the negative X-axis
J_i	incident flux at $x=D$
J_0	backward flux immediately inside interface $x=0$
J_D	backward flux immediately inside interface $x=D$
k	lattice thermal conductivity
n	index of refraction
s	scattering coefficient for diffuse radiation
T	temperature (absolute)
x	distance from front surface
β	optical constant for nonisothermal case equal to $\sigma/(a+2s)$
β_0	optical constant for isothermal case equal to $\sqrt{a/(a+2s)} = \sigma_0/(a+2s)$

¹ See also Papers 8, 21, and 22.

ϵ	emissivity
η	flux (energy) gradient at surface, $(dE/dx)_{surface}$
κ	material constant representing ratio of radiant transfer to lattice transfer in the center of an optically dense layer and equal to $2b/k(a+2s)$
ρ	diffuse reflectance of a layer
ρ_i	total diffuse reflectance at an interface where the index of refraction is decreasing
ρ_0	total diffuse reflectance at an interface where the index of refraction is increasing
σ	optical constant for nonisothermal case similar to an extinction coefficient equal to $\sigma_0\sqrt{1+\kappa}$
σ_0	isothermal extinction coefficient equal to $\sqrt{a(a+2s)}$
σ'	Stefan-Boltzmann radiation constant
τ	diffuse transmittance of layer

BASIC THEORETICAL ASSUMPTIONS

The theoretical method used in this study is based on a system originally conceived by Schuster (ref. 1 and 2) and added to by Hamaker (ref. 3): the notation used here is essentially that of Hamaker. For the isothermal case the method is equivalent to that developed by Kubelka and Munk and extended by others (ref. 4 to 8). With suitable changes in notation (ref. 3) their set of equations can be transformed into the system discussed here and vice versa. The basic method is that of dividing the flux into two parts: one flowing in a positive direction, and the other in a negative direction. A set of simultaneous differential equations is used to describe these fluxes and the other necessary parameters. Since only a forward and a backward flux are considered, this is a one-dimensional calculation and therefore has as a basic assumption that the incident radiation is diffuse (i.e., the intensity is equal for all angles of incidence) and that the radiation scattered sideways is compensated for by an equal contribution from neighboring parts of the layer (i.e., the area investigated is either small in cross section compared with the total illuminated cross section of the sample or is large compared with the thickness of the sample). This condition is not a severe limitation since many practical heat-transfer problems are concerned with diffuse radiation.

The treatment for the situations where temperature gradients are present suffers from the further limitation that only total radiation

is considered and therefore the fact that the wavelength distribution of blackbody emission changes with temperature is not taken into account. Also, it is assumed that the properties of the material change only gradually. This then implies the assumption that the temperature gradient across the sample which is being measured is small. Practically all the methods of calculation in use today also suffer from this limitation and in practice there are calculation schemes which can alleviate the problem.

ISOTHERMAL LAYERS

General Solutions

The total radiant flux is divided into two parts:

I = the flux in the direction of the positive X-axis

J = the flux in the direction of the negative X-axis

An absorption coefficient a is defined by requiring that $(aI dx)$ be the amount of the radiation absorbed from the flux I on passing through an infinitesimal layer dx ; a scattering coefficient s is similarly defined by requiring that the flux scattered backward from I (and therefore added to J) in an infinitesimal layer dx is $(sI dx)$. On passing through this layer, I will then be diminished by the amount absorbed and the amount scattered, but will be increased by the flux lost by scattering from J or:

$$dI/dx = -(a+s)I + sJ \quad (1)$$

Similarly,

$$dJ/dx = (a+s)J - sI \quad (2)$$

The general solutions of these equations can be found by putting

$$I = C_1 e^{\sigma x} + C_2 e^{-\sigma x} \quad (3)$$

$$J = C_3 e^{\sigma x} + C_4 e^{-\sigma x} \quad (4)$$

only two of the four constants C_1, C_2, C_3, C_4 being arbitrary. The solutions (using the same notation as Hamaker) are then:

$$I = A(1-\beta_0)e^{\sigma_0 x} + B(1+\beta_0)e^{-\sigma_0 x} \quad (5)$$

$$J = A(1 + \beta_0)e^{\sigma_0 x} + B(1 - \beta_0)e^{-\sigma_0 x} \quad (6)$$

where

$$\sigma_0 = \sqrt{a(a + 2s)} \quad (7)$$

$$\beta_0 = \sqrt{a/(a + 2s)} = \sigma_0/(a + 2s) \quad (8)$$

both roots being taken with a positive sign. In these equations A and B are constants to be determined by the boundary conditions.

Specific Solutions

One of the cases for which specific solutions are desired is that of a layer placed in a beam of diffuse radiation where there is reflection from both internal and external surfaces.

At an interface where the index of refraction is increasing, let the reflectivity equal ρ_0 . At an interface where the index of refraction is decreasing, let the reflectivity equal ρ_i . The former parameter can be calculated from the index of refraction by integrating the Fresnel reflection over the solid angle of incidence and dividing by the total radiation. This integration has been carried out by Walsh (ref. 9), and numerical values for the reflectivity as a function of the index of refraction have been calculated and tabulated by Ryde and Cooper (ref. 10). At an interface where the index of refraction is decreasing, the reflectivity can be shown to be $[(n^2 - 1)/n] + (\rho_0/n^2)$ where the additional terms are due to the amount of light that is totally reflected. These terms can be an important, though very often neglected, factor in heat-transfer calculations. For instance, for a material with an index of refraction of 1.5, ρ_i would be 0.595; for a material of index of

refraction 2, ρ_i would be 0.788, both factors being quite significant.

In the following discussion there is assumed to be no incident flux on the back surface $x = D$.

Then the boundary conditions are that at the front surface $x = 0$, part ρ_0 of the incident radiation I_i is reflected back, and part $(1 - \rho_0)$ is transmitted. The flux immediately below this interface I_0 is composed of this flux $(1 - \rho_0)I_i$ plus that flux reflected from the inner surface of $x = 0$ or $\rho_i J_0$, or

at $x = 0$

$$I_0 = (1 - \rho_0)I_i + \rho_i J_0 \quad (9)$$

At the back surface $x = D$, since there is no incident radiation, the only flux is that part ρ_i reflected from the remaining forward flux I_D or

at $x = D$

$$J_D = \rho_i I_D \quad (10)$$

Substituting in these equations for I_0 , J_0 , I_D , and J_D from equations (5) and (6) gives:

$$A(1 - \beta_0) + B(1 + \beta_0) = (1 - \rho_0)I_i + \rho_i A(1 + \beta_0) + \rho_i B(1 - \beta_0) \quad (11)$$

and

$$A(1 + \beta_0)e^{\sigma_0 D} + B(1 - \beta_0)e^{-\sigma_0 D} = \rho_i A(1 - \beta_0)e^{\sigma_0 D} + \rho_i B(1 + \beta_0)e^{-\sigma_0 D} \quad (12)$$

These are the equations to be solved for the constants A and B for these particular boundary conditions. They are (when the exponentials are substituted for by hyperbolic functions):

$$A = \frac{I_i e^{-\sigma_0 D} (1 - \rho_0) [\beta_0 (1 + \rho_i) - (1 - \rho_i)]}{2 \{ [\beta_0^2 (1 + \rho_i)^2 + (1 - \rho_i)^2] \sinh \sigma_0 D + 2 \beta_0 (1 - \rho_i^2) \cosh \sigma_0 D \}} \quad (13)$$

and

$$B = \frac{I_i e^{\sigma_0 D} (1 - \rho_0) [\beta_0 (1 + \rho_i) + (1 - \rho_i)]}{2 \{ [\beta_0^2 (1 + \rho_i)^2 + (1 - \rho_i)^2] \sinh \sigma_0 D + 2 \beta_0 (1 - \rho_i^2) \cosh \sigma_0 D \}} \quad (14)$$

Using these values in equations (5) and (6) gives the following expressions for I_x (the forward flux at x) and J_x (the backward flux at x):

$$I_x = \frac{\left\{ I_i (1 - \rho_0) \{ [\beta_0 (1 + \rho_i) + (1 - \rho_i)] (1 + \beta_0) e^{-\sigma_0 x} e^{\sigma_0 D} + [\beta_0 (1 + \rho_i) - (1 - \rho_i)] (1 - \beta_0) e^{\sigma_0 x} e^{-\sigma_0 D} \} \right\}}{2 \{ [\beta_0^2 (1 + \rho_i)^2 + (1 - \rho_i)^2] \sinh \sigma_0 D + 2 \beta_0 (1 - \rho_i^2) \cosh \sigma_0 D \}} \quad (15)$$

$$J_z = \frac{I_i(1-\rho_0) \{ [\beta_0(1+\rho_i) + (1-\rho_i)](1-\beta_0)e^{-\sigma_0 x} e^{\sigma_0 D} + [\beta_0(1+\rho_i) - (1-\rho_i)](1+\beta_0)e^{\sigma_0 x} e^{-\sigma_0 D} \}}{2 \{ [\beta_0^2(1+\rho_i)^2 + (1-\rho_i)^2] \sinh \sigma_0 D + 2\beta_0(1-\rho_i^2) \cosh \sigma_0 D \}} \quad (16)$$

In practice it is impossible to check these quantities experimentally; what can be checked, however, is the transmission and the reflectivity. To arrive at these quantities the forward flux immediately under the back surface I_D is determined by substituting D for x in equation (15). Then

$$I_D = \frac{I_i 2\beta_0(1-\rho_0)}{[\beta_0^2(1+\rho_i)^2 + (1-\rho_i)^2] \sinh \sigma_0 D + 2\beta_0(1-\rho_i^2) \cosh \sigma_0 D} \quad (17)$$

The transmission τ is then the ratio of the amount of this radiation that gets through the surface $(1-\rho_i)I_D$ to the incident radiation, or

$$\tau = \frac{I_D(1-\rho_i)}{I_i} \quad (18)$$

giving for the transmission

$$\tau = \frac{2\beta_0(1-\rho_0)(1-\rho_i)}{[\beta_0^2(1+\rho_i)^2 + (1-\rho_i)^2] \sinh \sigma_0 D + 2\beta_0(1-\rho_i^2) \cosh \sigma_0 D} \quad (19)$$

The reflectivity ρ can be found similarly if the fraction of incident radiation reflected from the front surface $\rho_0 I_i$ is added to the amount of backward flux that gets through the interface $(1-\rho_i)J_0$. Then

$$\rho = \frac{[(1-\rho_i)^2 - \beta_0^2(1-\rho_i-2\rho_0)(1+\rho_i)] \sinh \sigma_0 D + 2\beta_0(\rho_0+\rho_i)(1-\rho_i) \cosh \sigma_0 D}{[\beta_0^2(1+\rho_i)^2 + (1-\rho_i)^2] \sinh \sigma_0 D + 2\beta_0(1-\rho_i^2) \cosh \sigma_0 D} \quad (20)$$

It is also possible to calculate the absorptivity α of the layer since $\alpha + \rho + \tau = 1$. It is

$$\alpha = \frac{2\beta_0(1-\rho_0)[\beta_0(1+\rho_i) \sinh \sigma_0 D + (1-\rho_i)(\cosh \sigma_0 D - 1)]}{[\beta_0^2(1+\rho_i)^2 + (1-\rho_i)^2] \sinh \sigma_0 D + 2\beta_0(1-\rho_i^2) \cosh \sigma_0 D} \quad (21)$$

This is also the emission of the layer relative to blackbody radiation according to Kirchhoff's law.

Determining Optical Constants From Transmission Measurements

One of the objects of making transmission measurements is to use them to calculate optical constants of the material. In order to do this, equation (19) for the transmission of the material has to be solved for the constants. Cross-multiplying in equation (19) gives:

$$2\beta_0(1-\rho_0)(1-\rho_i) = \tau\beta_0^2(1+\rho_i)^2 \sinh \sigma_0 D + \tau(1-\rho_i)^2 \sinh \sigma_0 D + 2\beta_0\tau(1-\rho_i^2) \cosh \sigma_0 D \quad (22)$$

or, by regrouping the terms,

$$\tau(1-\rho_i)^2 \sinh \sigma_0 D = \beta_0 \{ 2[(1-\rho_0)(1-\rho_i) - \tau(1-\rho_i^2) \cosh \sigma_0 D] - \tau\beta_0(1+\rho_i)^2 \sinh \sigma_0 D \} \quad (23)$$

If two layers of thicknesses D_1 and D_2 and transmissions τ_1 and τ_2 , respectively, are considered, then (dividing by equal quantities)

$$\frac{\tau_1(1-\rho_i)^2 \sinh \sigma_0 D_1}{\tau_2(1-\rho_i)^2 \sinh \sigma_0 D_2} = \frac{2[(1-\rho_0)(1-\rho_i) - \tau_1(1-\rho_i)^2 \cosh \sigma_0 D_1] - \tau_1 \beta_0(1+\rho_i)^2 \sinh \sigma_0 D_1}{2[(1-\rho_0)(1-\rho_i) - \tau_2(1-\rho_i)^2 \cosh \sigma_0 D_2] - \tau_2 \beta_0(1+\rho_i)^2 \sinh \sigma_0 D_2} \quad (24)$$

or (again cross-multiplying),

$$\begin{aligned} & 2\tau_1(1-\rho_0)(1-\rho_i)^3 \sinh \sigma_0 D_1 \\ & - 2\tau_1\tau_2(1+\rho_i)(1-\rho_i)^3 \sinh \sigma_0 D_1 \cosh \sigma_0 D_2 \\ & - \beta_0\tau_1\tau_2(1+\rho_i)^2(1-\rho_i)^2 \sinh \sigma_0 D_1 \sinh \sigma_0 D_2 \\ & = 2\tau_2(1-\rho_0)(1-\rho_i)^3 \sinh \sigma_0 D_2 \\ & - 2\tau_1\tau_2(1+\rho_i)(1-\rho_i)^3 \sinh \sigma_0 D_2 \cosh \sigma_0 D_1 \\ & - \beta_0\tau_1\tau_2(1+\rho_i)^2(1-\rho_i)^2 \sinh \sigma_0 D_1 \sinh \sigma_0 D_2 \end{aligned} \quad (25)$$

All the terms involving β_0 drop out of equation (25) giving (having made use of the identity $\sinh x \cosh y - \cosh x \sinh y \equiv \sinh(x-y)$)

$$\frac{\sinh \sigma_0 D_1}{\tau_2} - \frac{\sinh \sigma_0 D_2}{\tau_1} = \frac{(1+\rho_i)}{(1-\rho_0)} \sinh \sigma_0(D_1 - D_2) \quad (26)$$

or, if sample thicknesses are chosen such that

$$D_1 = 2D_2 \equiv 2D \quad (27)$$

$$\frac{\sinh 2\sigma_0 D}{\tau_2} - \frac{\sinh \sigma_0 D}{\tau_1} = \frac{(1+\rho_i)}{(1-\rho_0)} \sinh \sigma_0 D \quad (28)$$

but

$$\sinh 2x \equiv 2 \sinh x \cosh x \quad (29)$$

and

$$\frac{2 \sinh \sigma_0 D \cosh \sigma_0 D}{\tau_2} - \frac{\sinh \sigma_0 D}{\tau_1} = \frac{(1+\rho_i)}{(1-\rho_0)} \sinh \sigma_0 D \quad (30)$$

and

$$\cosh \sigma_0 D = \frac{\tau_2[\tau_1(1+\rho_i) + (1-\rho_0)]}{2\tau_1(1-\rho_0)} \quad (31)$$

allowing one to calculate σ_0 from two transmission measurements.

Once σ_0 is known, β_0 can be found either by solving equation (19) by the quadratic formula, or with an electronic data processing machine.

It should be noted at this point that these equations are only valid for experimental situations where diffuse radiation is incident on a sample and the total hemispherical transmission is measured. The usual spectrometer experimental setup will not fill these requirements, since narrow angle illumination and

collection is used; however, a microbeam condenser with suitable corrections or an integrating sphere can approximate the proper conditions.

NONISOTHERMAL LAYERS

In order to be useful in heat-transfer calculations, this theory must be extended to nonisothermal situations. This can be done (as is shown by Hamaker as well as Schuster) if in each radiation equation a term is added representing the amount of energy emitted by the infinitesimal region. This is $\epsilon E dx$ where ϵ is the emittance and E is the blackbody radiation at the temperature at x . Making use of Kirchhoff's law, this term becomes $aE dx$ where a is the previously defined absorption coefficient. An additional equation, the heat-balance equation, is now needed expressing the fact that heat is neither accumulated nor produced within the body:

$$\frac{kd^2T}{dx^2} + a(I+J) = 2aE \quad (32)$$

where k is the lattice thermal conductivity. The first term on the left side represents the heat accumulated by conduction; the second term is the heat absorbed from the radiation; and the sum of these equals the heat loss by radiation (the term on the right).

The total blackbody radiation is given by the Stefan-Boltzmann equation:

$$E = \sigma' n^2 T^4 \quad (33)$$

where σ' is the Stefan-Boltzmann radiation constant and T is the absolute temperature. If the temperature is high and the temperature gradient not too large, then E may be represented by

$$E = E_0 + b(T - T_0) \quad (34)$$

where

$$b = 4\sigma' n^2 T_0^3 \quad (35)$$

T_0 is a temperature close to the actual temperature, and E_0 is the corresponding total

radiation. When equation (35) holds, the temperature may be fixed equally as well by E as by T and, since this simplifies matters, E rather than T has been retained in the equations. The set of simultaneous differential equations is then

$$\frac{dI}{dx} = -(a+s)I + sJ + aE \quad (36)$$

$$\frac{dJ}{dx} = (a+s)J - sI - aE \quad (37)$$

$$\frac{k}{b} \frac{d^2 E}{dx^2} + a(I+J) = 2aE \quad (38)$$

Hamaker shows that the complete general solution of these equations is:

$$I = A(1-\beta)e^{\sigma x} + B(1+\beta)e^{-\sigma x} + C(\sigma x - \beta) + F \quad (39)$$

$$J = A(1+\beta)e^{\sigma x} + B(1-\beta)e^{-\sigma x} + C(\sigma x - \beta) + F \quad (40)$$

$$E = -A\kappa e^{\sigma x} - B\kappa e^{-\sigma x} + C\sigma x + F \quad (41)$$

where A , B , C , and F are constants and

$$\sigma = + \left| \sqrt{\frac{2ab}{k} + a(a+2s)} \right| = \sigma_0 \sqrt{(1+\kappa)} \quad (42)$$

$$\beta = \frac{\sigma}{a+2s} \quad (43)$$

$$\kappa = \frac{2b}{k(a+2s)} = \frac{2b\beta}{k\sigma} \quad (44)$$

and the proper n^2 term which does not appear in Hamaker's work has been introduced here.

To illustrate how this theory might be used the particular solutions will be derived for a layer receiving radiation at both surfaces, and where heat is being conducted away from the surfaces. The amount of heat being conducted away from the surface must equal that conducted to the surface in the solid giving one boundary condition at each surface. The other two boundary conditions are supplied by the radiation interchange at the surface. The temperature (particularly at the surfaces) and the emitted fluxes will be solved for.

Immediately below the front surface $x=0$, the forward flux I_0 is equal to that part of the incident flux I_i which is not reflected $((1-\rho_0)I_i)$

plus the amount of the backward flux at this surface J_0 which was reflected $(\rho_0 J_0)$. Therefore

$$I_0 = (1-\rho_0)I_i + \rho_0 J_0 \quad (45)$$

or (substituting from eq. (39) and (40)):

$$A(1-\beta) + B(1+\beta) - C\beta + F = (1-\rho_0)I_i + \rho_0 A(1+\beta) + \rho_0 B(1-\beta) + \rho_0 C\beta + F\rho_0 \quad (46)$$

Similarly, immediately above the back surface $x=D$, the backward flux J_D is composed of the part of the incident flux on this surface J_i which is transmitted $((1-\rho_0)J_i)$ plus the part of the forward flux at this surface which is reflected $(\rho_i I_D)$, and

$$J_D = (1-\rho_0)J_i + \rho_i I_D \quad (47)$$

or

$$A(1+\beta)e^{\sigma D} + B(1-\beta)e^{-\sigma D} + C(\sigma D + \beta) + F = (1-\rho_0)J_i + \rho_i A(1-\beta)e^{\sigma D} + B\rho_i(1+\beta)e^{-\sigma D} + \rho_i C(\sigma D - \beta) + \rho_i F \quad (48)$$

If we define η as the gradient at the surface times b ,

$$\eta = b \left(\frac{dT}{dx} \right)_{\text{surface}} = \left(\frac{dE}{dx} \right)_{\text{surface}} \quad (49)$$

or, if the heat is conducted away by a gas,

$$\eta = \left(\frac{dE}{dx} \right)_{\text{surface}} = \frac{-bQ_g}{k} \quad (50)$$

where Q_g is the heat being conducted (or convected) away by the gas. Then, since (by differentiating eq. (41))

$$\frac{dE}{dx} = -A\kappa\sigma e^{\sigma x} + B\kappa\sigma e^{-\sigma x} + C\sigma \quad (51)$$

the other two boundary conditions are

$$\eta = \left(\frac{dE}{dx} \right)_0 \quad (52)$$

$$\eta = -A\kappa\sigma + B\kappa\sigma + C\sigma \quad (53)$$

and

$$\eta = \left(\frac{dE}{dx} \right)_D \quad (54)$$

$$\eta = -A\kappa\sigma e^{\sigma D} + B\kappa\sigma e^{-\sigma D} + C\sigma \quad (55)$$

The four simultaneous equations (46), (48), (53), and (55) are then solved for the constants A , B , C , and F where it has been found convenient to define a function consisting of the denominator: Let

$$\text{Then } 2(1-\rho_i)(\cosh \sigma D - 1) + [2\beta(1+\rho_i)(1+\kappa) + \kappa\sigma D(1-\rho_i)] \sinh \sigma D \equiv \text{etc} \quad (56)$$

$$A = \frac{(e^{-\sigma D} - 1) \{ \sigma(1-\rho_0)(I_i - J_i) + \eta[2\beta(1+\rho_i) + \sigma D(1-\rho_i)] \}}{2\sigma \text{ etc}} \quad (57)$$

$$B = \frac{(e^{\sigma D} - 1) \{ \sigma(1-\rho_0)(I_i - J_i) + \eta[2\beta(1+\rho_i) + \sigma D(1-\rho_i)] \}}{2\sigma \text{ etc}} \quad (58)$$

$$C = \frac{-2\kappa\sigma(1-\rho_0)(I_i - J_i) \sinh \sigma D + 4\eta[(1-\rho_i)(\cosh \sigma D - 1) + \beta(1+\rho_i)\sinh \sigma D]}{2\sigma \text{ etc}} \quad (59)$$

$$F = \frac{\left\{ \begin{aligned} &2\sigma\eta^2 I_i \{ (1-\rho_i)(\cosh \sigma D - 1) + [\beta(1+\rho_i)(1+\kappa) + \kappa\sigma D(1-\rho_i)] \sinh \sigma D \} \\ &+ 2\sigma\eta^2 J_i \{ (1-\rho_i)(\cosh \sigma D - 1) + \beta(1+\rho_i)(1+\kappa) \sinh \sigma D \} \\ &- 2\sigma\eta D \{ (1-\rho_i)(\cosh \sigma D - 1) + \beta(1+\rho_i) \sinh \sigma D \} \end{aligned} \right\}}{2\sigma \text{ etc}} \quad (60)$$

Introducing these constants into equations (39), (40), and (41) makes it possible now to find the fluxes and temperature at any point in terms of the incident radiant and thermal fluxes. They are

$$I = \frac{\left\{ \begin{aligned} &\sigma(1-\rho_0)(I_i - J_i)[e^{\sigma x}(e^{-\sigma D} - 1)(1-\beta) + (e^{-\sigma D} - 1)(1+\beta)e^{-\sigma x} - 2\kappa(\sigma x - \beta) \sinh \sigma D] \\ &+ \eta \{ [2\beta(1+\rho_i) + \sigma D(1-\rho_i)][e^{\sigma x}(e^{-\sigma D} - 1)(1-\beta) + e^{-\sigma x}(e^{\sigma D} - 1)(1+\beta)] \\ &+ 4(\sigma x - \beta)[\beta(1+\rho_i) \sinh \sigma D + (1-\rho_i)(\cosh \sigma D - 1)] \} \end{aligned} \right\}}{2\sigma \text{ etc}} + F \quad (61)$$

$$J = \frac{\left\{ \begin{aligned} &\sigma(1-\rho_0)(I_i - J_i)[e^{\sigma x}(e^{-\sigma D} - 1)(1+\beta) + e^{-\sigma x}(e^{\sigma D} - 1)(1-\beta) - 2\kappa(\sigma x + \beta) \sinh \sigma D] \\ &+ \eta \{ [2\beta(1+\rho_i) + \sigma D(1-\rho_i)][e^{\sigma x}(e^{-\sigma D} - 1)(1+\beta) + e^{-\sigma x}(e^{\sigma D} - 1)(1-\beta)] \\ &+ 4(\sigma x + \beta)[\beta(1+\rho_i) \sinh \sigma D + (1-\rho_i)(\cosh \sigma D - 1)] \} \end{aligned} \right\}}{2\sigma \text{ etc}} + F \quad (62)$$

$$E = \frac{\left\{ \begin{aligned} &-\kappa\sigma(1-\rho_0)(I_i - J_i)[e^{\sigma x}(e^{-\sigma D} - 1) + e^{-\sigma x}(e^{\sigma D} - 1) + 2\sigma x \sinh \sigma D] \\ &- \eta \{ \kappa[2\beta(1+\rho_i) + \sigma D(1-\rho_i)][e^{\sigma x}(e^{-\sigma D} - 1) + e^{-\sigma x}(e^{\sigma D} - 1)] \\ &- 4\sigma x [\beta(1+\rho_i) \sinh \sigma D + (1-\rho_i)(\cosh \sigma D - 1)] \} \end{aligned} \right\}}{2\sigma \text{ etc}} + F \quad (63)$$

These are again not measurable quantities. The quantities desired are the fluxes emitted at each surface and the temperatures at the surfaces. At the back of the layer $x=D$ the flux emitted in the forward direction (here denoted by I_e) is equal to the fraction of the forward flux immediately under this surface I_D which is not reflected at this surface $(1-\rho_i)I_D$ plus the fraction of the incident radiation on this

surface which is reflected into the forward direction $\rho_0 J_i$, or

$$I_e = (1-\rho_i)I_D + \rho_0 J_i \quad (64)$$

Similarly (where J_e is the flux emitted in the backward direction at the front surface),

$$J_e = (1-\rho_i)J_0 + \rho_0 I_i \quad (65)$$

Finally, the energy equivalent of the temperature at the surfaces is found by substituting $x=0$ and $x=D$ into equation (63). Actually in the constant b , the n^2 term should be the index of refraction of the material in which the particular quantity is measured. In order to keep the notation consistent in this part, the n^2 term will be kept in the constant b but the energy equivalent of temperature measured outside the sample (here denoted by E_{a0} and E_{aD}) will be divided by n^2 , so that the numerical results will be correct. Before the results are set down, it is desirable to define the following functions since most of the equations are symmetrical.

Let

$$f_1 \equiv \frac{2\beta(1-\rho_0)(1+\kappa) \sinh \sigma D}{\text{etc}} \quad (66)$$

$$f_2 \equiv \frac{2(1-\rho_i)(\cosh \sigma D - 1) + [2\beta(\rho_0 + \rho_i)(1+\kappa) + \kappa\sigma D(1-\rho_i)] \sinh \sigma D}{\text{etc}} \quad (67)$$

$$f_3 \equiv \frac{(1-\kappa)(1-\rho_i)(\cosh \sigma D - 1) + [\beta(1+\rho_i)(1+\kappa) + \kappa\sigma D(1-\rho_i)] \sinh \sigma D}{\text{etc}} \quad (68)$$

$$f_4 \equiv \frac{(1+\kappa)[(1-\rho_i)(\cosh \sigma D - 1) + \beta(1+\rho_i) \sinh \sigma D]}{\text{etc}} \quad (69)$$

$$f_5 \equiv \frac{(1-\rho_i)[-2(\cosh \sigma D - 1) + \sigma D \sinh \sigma D]}{\text{etc}} \quad (70)$$

$$f_6 \equiv \frac{[\sigma D(1+\kappa)(1-\rho_i) + 2\beta\kappa(1+\rho_i)](\cosh \sigma D - 1) + \beta\sigma D(1-\rho_i) \sinh \sigma D}{n^2, \text{ etc}} \quad (71)$$

Then the desired terms are (where Q_{-g} is the negative of the heat removed by conduction, and, therefore, $\eta \equiv bQ_{-g}/k$):

$$I_e = f_1 I_i + f_2 J_i + f_3 \kappa Q_{-g} \quad (72)$$

$$J_e = f_2 I_i + f_i J_i - f_5 \kappa Q_{-g} \quad (73)$$

$$E_{a0} = f_3 I_i + f_4 J_i - f_6 \frac{\kappa}{2\beta} Q_{-g} \quad (74)$$

$$E_{aD} = f_4 I_i + f_3 J_i + f_5 \frac{\kappa}{2\beta} Q_{-g} \quad (75)$$

CONCLUSIONS

The previous section illustrates how analytical expressions can be obtained to describe

radiation transfer through scattering and absorbing nonisothermal layers. The actual choice of the independent and dependent variables is arbitrary; for instance, it is also possible to specify the surface temperatures and perhaps assume no incident fluxes, then solve for the emitted fluxes and the surface gradients necessary to maintain the given situation.

Proper boundary conditions for several other cases are given in Hamaker's paper while reference 11 shows some calculations for a semitransparent layer on a metal. The latter paper also discusses the nature of the gradient changes at the interfaces, as well as the considerations that occur when the layer gets thin. Another application is given in reference 12

where radiation heat transfer through powders is treated by using a model of a system of layers through which the radiant transfer has been calculated.

Whereas this simplified system allows one to calculate analytic expressions for radiant transfer in very complex situations, some of the limitations of the method should be noted. Even with perfectly diffuse radiation incident on a sample, the assumption of diffuse radiation right below a surface where the index of refraction is increasing is only an approximation, since the radiation will be brought into a narrower solid angle, as the result of refraction at the interface. It is assumed that the radiation is rapidly rediffused due to scattering.

This treatment is, of course, invalid where the scattering centers are so close together that phase effects must be taken into account and coherent scattering occurs. Also, the method breaks down when the layers become so thin that their properties change; that is, they can no longer be considered to be homogeneous. Illustrations of this would be where the pores might be relatively large compared with the sample layer thickness.

Finally, it should be noted that the absorption and scattering coefficients measured or calculated here from diffuse radiation measurements and calculations are not the same as would be measured by narrow angle measurements. The narrow angle measurements measure changes in the image-forming part of the radiation only. The absorption coefficient defined here will actually be a function of the scattering coefficient, since the scattering coefficient will determine the actual path length through the sample and therefore the total amount of absorption.

ACKNOWLEDGMENT

This work was supported partially by Atomic Energy Commission Contract AT(30-1)-1852 while I was a graduate student and research assistant at Massachusetts Institute of Technology and partially by Air Force Contract AF33(616)-8368 while I was employed by Lexington Laboratories, Incorporated, Cambridge, Massachusetts.

REFERENCES

- SCHUSTER, A.: Radiation Through a Foggy Atmosphere. *The Astrophysical Jour.*, vol. 21, Jan. 1905, pp. 1-22.
- SCHUSTER, A.: Influence of Radiation on Heat-Transmission. *Phil. Mag.*, ser. B, vol. 5, Feb. 1903, pp. 243-257.
- HAMAKER, H. C.: Radiation and Heat Conduction in Light-Scattering Material. *Phillips Res. Repts.*, vol. 2, 1947, pp. 55-67, 103-111, 112-125, 420-425.
- KUBELKA, P., and MUNK, F.: Ein Beitrag zur Optik der Farbenstriche. *Z. Tech. Physik*, vol. 12, 1931, pp. 593-601.
- KUBELKA, PAUL: New Contributions to the Optics of Intensely Light-Scattering Materials. Part I. *Jour. Optical Soc. of America*, vol. 38, no. 5, May 1948, pp. 448-457.
- JUDD, DEANE B.: Optical Specification of Light-Scattering Materials. Res. Paper RP1026, *Jour. Res. Nat. Bur. Standards*, vol. 19, Sept. 1937, pp. 287-317.
- STENIUS, ÅKE S.: Reflectance and Transmittance of Inhomogeneous Diffusing Layers. *Jour. Optical Soc. of America*, vol. 44, no. 10, Oct. 1954, pp. 804-805.
- STENIUS, ÅKE S.: Influence of Optical Geometry and Absorption Coefficient on Diffuse Reflectance Values. *Jour. Optical Soc. of America*, vol. 45, no. 9, Sept. 1955, pp. 727-732.
- WALSH, JOHN W. T.: The Reflection Factor of a Polished Glass Surface for Diffused Light. Appendix of Taylor, A. K., and C. J. W. Grieseson: *The Transmission Factor of Commercial Window Glasses*. Dept. Sci. and Ind. Res.; *Illum. Res. Tech. Paper No. 2*, 1926. p. 10.
- RYDE, J. W., and COOPER, B. S.: Scattering of Light by Turbid Media. Parts I and II. *Proc. Roy. Soc. (London)*, vol. A131, May 1931, pp. 451-475.
- KLEIN, JONATHAN D.: Radiation Heat Transfer to and From Ceramic Coatings on Metals. *American Ceramic Soc. Bull.*, vol. 40, 1961, pp. 366-370.
- KLEIN, JONATHAN D.: Thermal Radiation Characteristics of Transparent, Semi-transparent, and Translucent Materials Under Non-Isothermal Conditions. Sec. Quarterly Prog. Rep. on Air Force Contract No. AF33(616)-8368, Nov. 1961.

8. Fundamentals of Thermal Radiation in Ceramic Materials¹

R. L. COX

LING-TEMCO-VOUGHT ASTRONAUTICS DIVISION, DALLAS, TEXAS

The thermal radiative properties of ceramics that depend on intrinsic optical constants and microstructure are discussed. Surface reflections and volume emission in optically smooth homogeneous materials are first reviewed. Scattering and absorption in heterogeneous materials are then considered, and a correlation is drawn between coefficients predicted from single-particle theory and those utilized by the radiative-transfer equations. The proper inclusion of surface reflections in the radiative transfer equations is discussed, and surface roughness effects in general are examined. Throughout this paper emphasis is placed on interpretation of existing knowledge in a way that will be of value in synthesizing ceramic materials with desired radiative properties.

With the growing emphasis on thermal radiation in aerospace applications, more and more attention is being directed toward developing materials with tailored thermal radiative properties. Demands are such that adequate results can no longer be obtained merely by screening available materials. The approach of synthesis must, therefore, be taken, requiring the full utilization of all available knowledge. Unfortunately, fundamental knowledge of thermal radiation cannot be gathered from a few sources but is widely dispersed among practically all the disciplines of physical science. The thermal radiation specialist is thus faced with the formidable task of assimilating the knowledge that is available to him. The objective of this paper is to bring together existing knowledge in a small but important part of the thermal radiation field and to furnish some interpretation applicable to the tailoring of radiative properties.

Ceramics are chosen as the general topic of this paper because they are valuable in aero-

space thermal radiative applications and because they typify materials in which light-scattering plays an important role in radiative transfer. In general, though, the discussion, or certain aspects of it, applies equally well to other materials, particularly pigmented organic coatings.

In tailoring the radiative properties of a material, two areas of latitude are available. One is in the selection or development of a material with the proper combination of intrinsic optical properties. These are properties of the homogeneous bulk material: the index of refraction and the absorption coefficient. Intrinsic properties of numerous materials have been determined, and physicists are successfully tailoring intrinsic properties for specific applications. The second area of latitude in synthesizing materials with specific properties is in variation of microstructure. Properties that are sensitive both to intrinsic properties and to microstructure will be referred to as induced properties. Included are emittance, reflectance, transmittance, and the optical properties of heterogeneous materials:

¹ See also Papers 7, 21, and 22.

the scattering coefficient and the apparent absorption coefficient. The scope of this paper is limited to induced radiative properties.

The discussion emphasizes the interpretation of the phenomena of interest rather than repeating mathematical derivations which are available elsewhere. The topics discussed will include radiative transfer in homogeneous materials, radiative transfer in heterogeneous materials (with emphasis on the correlation between particle-scattering theory and the radiative transfer equations), and a special case of light-scattering, the interaction of thermal radiation with the surface of a material. Wherever possible, correlation between experiment and theory will be included and attention will be drawn to voids in knowledge.

HOMOGENEOUS MATERIALS

A homogeneous material is defined as one in which there are no discontinuities, such as voids or foreign particles, that would cause appreciable scattering. Examples of homogeneous ceramics are single crystals, such as sapphire, and optical glasses.

The radiative performance of a homogeneous smooth surfaced material can be completely specified by a knowledge of its index of refraction, absorption coefficient, geometry, and the bounding media. Since all materials emit or absorb within their volume, distinction is drawn between surface and bulk interaction between radiation and the material.

Surface Interaction

The equations for reflection of electromagnetic radiation at a smooth surface are well known, and a comprehensive discussion can be found in a textbook on physical optics, such as that by Jenkins and White (ref. 1). This section only states the laws and discusses some of the properties of interest that are predicted for ceramic materials.²

Maxwell's equations of the electromagnetic field have been applied to the boundary between a material and the surrounding medium to derive the laws of reflection for a plane surface, with the following results:

² See also Paper 5.

$$\rho_{\parallel} = \frac{\tan^2(\phi - \theta)}{\tan^2(\phi + \theta)} \quad \rho_{\perp} = \frac{\sin^2(\phi - \theta)}{\sin^2(\phi + \theta)}$$

where

- ϕ angle of incidence
- θ angle of refraction
- ρ_{\parallel} reflectivity for parallel polarized radiation
- ρ_{\perp} reflectivity for perpendicularly polarized radiation

These equations were first derived by Fresnel from the elastic-solid theory and are known as Fresnel's laws of reflection. For unpolarized incident energy the surface reflectivity is:

$$\rho = \frac{1}{2} (\rho_{\parallel} + \rho_{\perp})$$

The angles ϕ and θ are related by Snell's law:

$$\sin \phi = \frac{n}{m} \sin \theta$$

where

- n index of refraction of the material
- m index of refraction of the surrounding medium

In general, the index of refraction of a material is complex, with the imaginary part being proportional to the absorbing characteristics of the material. In Snell's law, the appropriate term then becomes

$$n' = n(1 - ik)$$

where

- k absorption index
- n real part of the refractive index
- n' complex refractive index

The absorption index and absorption coefficient are related as follows:

$$k = \frac{\alpha \lambda}{4\pi n}$$

where

- α absorption coefficient
- λ wavelength

By substitution of the complex index of refraction term into the Fresnel equations, the

importance of the absorption coefficient to surface reflectivity can be assessed. For instance, at a wavelength of $3\ \mu$ and with a value of 1.5 for the real part of the index of refraction, an absorption coefficient of $660\ \text{cm}^{-1}$ is required to increase normal surface reflectivity by 1 percent. Ceramics ordinarily have an absorption coefficient of $0.1\ \text{cm}^{-1}$ or less at wavelengths of high transparency. The absorption coefficient increases at wavelengths approaching an absorption band, but does not reach a value sufficiently high to affect surface reflectivity until well into the band. Then, at wavelengths in the immediate vicinity of the resonant frequency, absorption becomes very strong and a high surface reflectivity results. Simon and McMahon (ref. 2) measured a reflectivity of 80 percent in quartz at a wavelength of $9\ \mu$. Ordinarily, ceramics have absorption bands in the near ultraviolet, the near to intermediate infrared, and the far infrared.

Another interesting observation can be inferred from the surface-reflection equations. This is the prediction of a reflectivity of very nearly zero for an index of refraction equal to that of the surrounding medium and a low value of the absorption coefficient. Since the index of refraction of many ceramics passes through unity as the infrared absorption band is approached, it follows that the emissivity of an opaque specimen will approach unity if the absorption coefficient is not too high. This effect has been frequently observed experimentally. It occurs in quartz at a wavelength of about $7\ \mu$, as is apparent from the measurements of Simon and McMahon.

In the preceding discussion it was assumed that light in the surrounding medium is incident on the material. Fresnel's laws apply equally well for radiation within the material which is incident on the interface, but θ and ϕ must be interchanged. However, one important difference exists for dense-to-rare refractions; a critical angle of incidence (θ_c) is reached. Above this angle all energy is internally reflected.

Other interesting consequences of the laws of reflectivity exist. Most striking is the variation of the polarized components of reflected energy with angle of incidence, as

illustrated by figure 1. Reflectivity for the perpendicularly polarized component ρ_{\perp} increases continuously with increasing angle of incidence to a value of unity at 90° , whereas the reflectivity for the parallel polarized component ρ_{\parallel} first decreases, then increases to unity as the angle is varied from 0 to 90° . The angle at which the minimum is reached for ρ_{\parallel} is called the principal angle of incidence $\bar{\phi}$. It is seen that ρ_{\parallel} is zero at $\bar{\phi}$ for a perfect dielectric (transparent material), and that $\bar{\phi}$ increases as the absorption coefficient, and, consequently, the reflectivity increases. It is evident that reflected energy is partially polarized at all angles other than normal incidence, and that polarization reaches a maximum near $\bar{\phi}$, being complete at $\bar{\phi}$ for the limiting case of a perfect dielectric. Ordinary glass exhibits essentially complete polarization of visible light at $\bar{\phi}$.

By the reciprocity law relating emissivity to reflectivity, the variation of reflectivity with angle predicts a deviation from Lambert's cosine law for the emission of energy. The calculated variation has been found to be in excellent agreement with experimental observations for polished surfaces. The result of

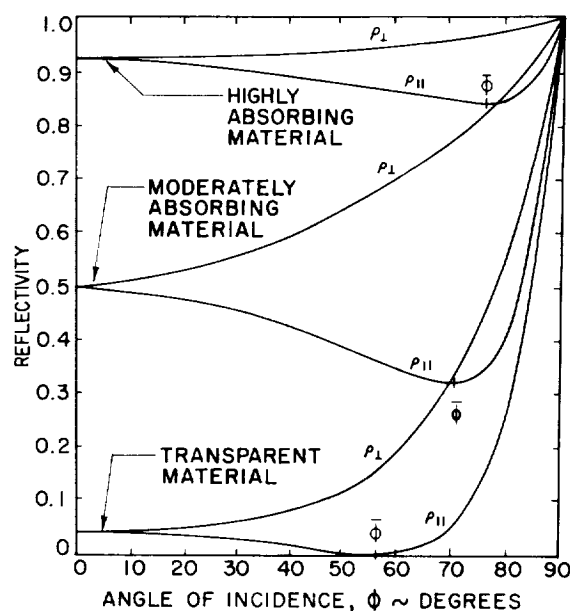


FIGURE 1.—Theoretical reflectivities of polished surfaces for parallel- and perpendicular-polarized components, as a function of angle of incidence.

this deviation from Lambert's cosine law is that the normal emissivity of a homogeneous ceramic is usually about 5 percent higher than its hemispherical emissivity at wavelengths of weak absorption. This trend is reversed, however, at these wavelengths if the ceramic has a very high index of refraction. At wavelengths of strong absorption, hemispherical emissivity exceeds normal emissivity. Optical-constant values at these wavelengths of strong absorption indicate that the calculated excess would be in the range 5 percent to 20 percent.

The spatial relationship between the polarized components of the reflected light is defined by the azimuth angle ψ . It is the angle that the resultant of the amplitudes of the polarized components makes with the perpendicular to the plane of incidence. For unpolarized incident radiation, the reflected azimuth is:

$$\psi = \arctan \sqrt{\frac{\rho_{\parallel}}{\rho_{\perp}}}$$

The value of ψ varies from a maximum of 45° at normal incidence to a minimum near $\phi = \bar{\phi}$, back to 45° at 90° incidence. The azimuth angle at the principal angle of incidence is called the principal azimuth angle $\bar{\psi}$. The value of $\bar{\psi}$ decreases as absorption decreases, and is zero for a perfect dielectric.

Another effect produced by reflection is a change of phase between the incident and reflected energy. For a perfect dielectric, the phase change of the perpendicularly polarized component is 180° at all incidence angles, while the parallel polarized component undergoes a 180° phase change at angles of incidence greater than $\bar{\phi}$. Thus, a phase difference between the polarized components of 180° exists up to the angle $\bar{\phi}$; past this angle the phase difference is zero. Absorbing materials exhibit a continually varying phase difference with angle, from a value of 180° at normal incidence to zero at parallel incidence, passing through a value of 90° at $\bar{\phi}$.

Since the angular distributions of the reflectivities, azimuth angle, and phase difference are determined by n and k , these optical constants can be deduced from observations of the characteristics of reflected or emitted energy.

Measurements of $\bar{\phi}$ and of $\bar{\psi}$ are particularly useful in determining n and k .

Volume Emission

Gardon (ref. 3) demonstrated that the emittance of a smooth sheet of homogeneous material and its angular distribution can be precisely defined from a knowledge of its absorption coefficient and index of refraction. In this analysis, the irradiation of an element on the surface was first computed using the model shown in figure 2. The total irradiation of the surface element δS was obtained by summing the contributions of all the volume elements δV . The contribution of each element was expressed in terms of an elemental volume emissive power, the geometrical fraction of this energy intercepted by δS , and the absorption by the intervening material.

It was shown that a semi-infinite body irradiates δS with a total flux of $n^2 W_{B\lambda}$, where n is the index of refraction of the material and $W_{B\lambda}$ is the blackbody emission at the same temperature according to Planck's law. It was also shown that the angular distribution of

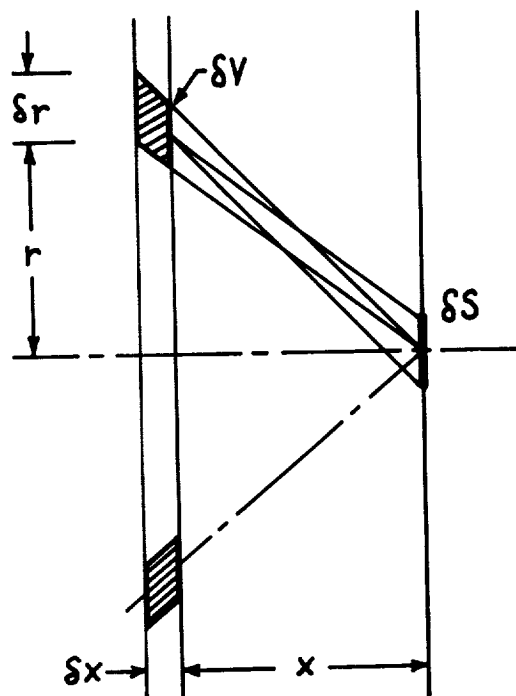


FIGURE 2.--Analytical model for radiative transfer in homogeneous material.

this radiation is a cosine function. For a smooth-surfaced material, the fraction $[1 - (1/n^2)]$ of the internally incident irradiation on δS is outside the critical angle of incidence, and is totally internally reflected. The remainder is transmitted, except for the fraction that is internally reflected in accordance with Fresnel's law for angular surface reflectivity. It is this internal reflectivity that causes the emissivity of a homogeneous semi-infinite body to be less than unity and to conform with the reciprocity law that $1 - \rho_{\lambda\phi} = \epsilon_{\lambda\phi}$ where $\rho_{\lambda\phi}$ and $\epsilon_{\lambda\phi}$ are reflectivity and emissivity, respectively, at wavelength λ and angle ϕ .

Considering sheets of glass, Gardon showed that the value of the product of the absorption coefficient and thickness must be at least 3.5 for the emission to be essentially equal to that from a sheet of infinite thickness. For thinner sheets, some of the emitting elements are absent, and multiple reflections between the faces of the sheet occur. The total irradiation of δS is thus diminished, and its angular intensity distribution is altered from a cosine function. The result is a lowered emittance and a changed angular distribution of emitted energy. It can readily be seen that, if the sheet does not extend infinitely in the direction parallel to the plane of the surface, irradiation of δS , and thus emission, will be reduced further.

The thickness required for opacity of a homogeneous ceramic can be inferred from Gardon's product of the absorption coefficient and the thickness. At wavelengths for which the material is highly transparent, a thickness of greater than 1 foot is often required, compared to a thickness of a few mils in the region bordering an absorption band (where the influence of the absorption coefficient on surface reflectance just begins to become noticeable). At wavelengths close to the resonant frequency, only a few microns are required for opacity.

Computations were made to illustrate the combined roles of volume emission and surface reflectivity in establishing the emittance of a homogeneous ceramic. A hypothetical coating of 10-mil thickness applied to a substrate of 0.5 reflectivity was assumed for this purpose. A wavelength of $3\ \mu$ was selected, and isothermal conditions were assumed. Normal spectral

emittance was calculated to simplify the expressions involved. For these conditions, the one-dimensional treatment cited by Blau (ref. 4) is applicable; accordingly, the following equation was employed:

$$\epsilon_{\lambda N} = \frac{(1 - \rho_{\lambda N})(1 - \rho_s e^{-2\alpha D})}{(1 - \rho_{\lambda N} \rho_s e^{-2\alpha D})}$$

where

- $\epsilon_{\lambda N}$ normal spectral emittance of substrate-coating combination
- $\rho_{\lambda N}$ surface reflectivity of coating from Fresnel equations at normal incidence, $\frac{(n-1)^2 + n^2 k^2}{(n+1)^2 + n^2 k^2}$
- ρ_s substrate reflectivity into coating ($\equiv 0.5$)
- α absorption coefficient
- D coating thickness

Calculations were carried out for real parts of the refractive index of 1.0, 1.5, and 2.0, and for absorption coefficients from 10 to 50,000 cm^{-1} . Results are shown in figure 3. Also shown is the emittance curve for an infinite coating thickness. It is seen that the normal spectral emittance of the coating increases gradually with increasing absorption coefficient until the coating becomes opaque at a value of about 1,000 cm^{-1} . Any further increase in the absorption coefficient decreases emittance, gradually at first, and then rapidly as values greater than 10,000 cm^{-1} are reached. Also of interest is the fact that the maximum emittance attained is only slightly lower than that of an infinitely thick coating of less strongly absorbing material.

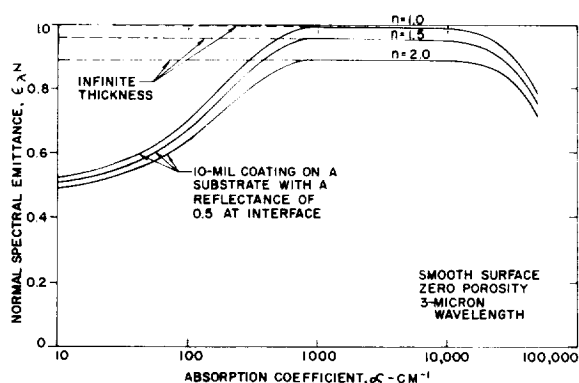


FIGURE 3.—Effect of optical constants on normal emittance.

Of further interest is the fact that the effect of the real part of the refractive index is most pronounced at absorption coefficient values for which the emittance is highest.

Heat transfer through a homogeneous ceramic or emission from a nonisothermal volume within the ceramic is of interest in some applications. Increasing transparency increases the overall heat flow rate for a given set of boundary conditions, and redistributes the internal temperatures. The heat transfer formulation necessary to define internal temperatures must take into account both the true thermal conduction and the three-dimensional radiant flux. Most of the work in this field has been devoted to heat transfer in glass. Gardon (ref. 5) shows the correct formulation of the problem, and presents numerical results for sheets of glass undergoing heating and cooling.

HETEROGENEOUS MATERIALS

Studies of the scattering and absorption of thermal radiation in a heterogeneous material can be categorized in two basic areas: (1) scattering by individual particles, and (2) radiative transfer in a medium containing many scattering centers. The first area concerns the definition of the scattering and absorption coefficients of a single particle from a knowledge of its geometry and physical properties, and the characteristics of the incident radiation.

A comprehensive treatment of the problem of single scattering by independent particles, including the results of numerous investigators, has been published by van de Hulst (ref. 6). The rigorous theory, along with various simplifications, is presented and a good cross-section of the various cases that have been solved is included. (These solutions are exact when the physical situation approaches the theoretical model.) A sufficient number of cases have been solved to enable a variety of scattering situations to be studied without having to resort to additional tedious exact solutions.

The second area concerns the definition of radiative transfer within and from a scattering system. Differential equations describing the radiant flux are formulated in terms of "apparent" absorption and scattering coefficients. A

closed solution is possible for the one-dimensional formulation, and is very useful in specifying the radiant flux (or flux ratios: emittance, reflectance, and transmittance) in many practical scattering systems. The radiative-transfer equations are thus seen to do nothing toward predicting the absorption and scattering coefficients, but predict system performance once these coefficients are known.

The absorption and scattering coefficients employed by the one-dimensional radiative-transfer equations are related to, but not equal to, the coefficients defined by single-particle theory. The scattering coefficient differences are, chiefly, a result of two facts. First, the radiative transfer equations employ a *back-scatter* coefficient, while the single-particle theory defines a total spherical scattering coefficient. This difference can be largely reconciled by integration of the single-particle scattering over the backward hemisphere, which has been done in a few cases. Second, the theory of single scattering by independent particles breaks down when particles are brought into close proximity. The precise conditions implied by the theory are that each particle must have sufficient room to form its own scattering pattern without interference from neighboring particles, and that each particle must be exposed to the original beam of parallel incident light. According to van de Hulst, independent scattering has been estimated to occur as long as particles are separated by a distance of at least three times their radius. This condition often exists in practical ceramic systems.

Multiple scattering, however, occurs in almost all heterogeneous ceramic systems. It is accounted for approximately in the one-dimensional radiative-transfer formulation by employing two oppositely directed fluxes. Limited experimental data exist to correlate back-scattering coefficients from single-particle theory with those required by the radiative-transfer equations. However, as will be seen later, these data indicate that for cases where independent scattering occurs, reasonable quantitative predictions are possible. The differences between apparent absorption coefficient values predicted by single-particle theory and

those required by the radiative-transfer equations are more serious. They arise from the one-dimensional nature of the radiative transfer formulation. Little progress has been made toward quantitatively correlating these absorption coefficient differences, but available experimental data indicate that they are large. The net value of single-particle theory can thus be seen as two-fold: (1) quantitative predictions in conjunction with the radiative-transfer equations are possible for certain practical cases of independent scattering and negligible absorption, and (2) qualitative predictions of trends are possible for other cases.

Particle Scattering

Scattering is fundamentally an interaction of electromagnetic radiation with a particle to produce a redirection of energy. It is always accompanied by some absorption within the particle. If the particle is large compared with the wavelength of incident radiation, reflected and refracted energy can be distinguished from diffracted energy; but for small particles, no such distinction is possible. The theoretical determination of the scattering and absorption characteristics of a particle involves obtaining a solution to the Maxwell equations for the interaction between the "applied" electromagnetic field and the particle. The rigorous formulation is applicable to particles of arbitrary size, and, for spherical particles, is known as the Mie theory. A complete numerical computation is a tedious undertaking, but for several limiting cases excellent approximations can be obtained with greatly reduced effort.

Considering first dielectric particles, the quantity of primary interest for application to radiative transfer in ceramics is a parameter specifying the fraction of the energy incident on a particle that is scattered in a backward direction. A backscatter effectiveness K_B is introduced for this purpose, and is defined in terms of the product of two other coefficients. The first is the scattering efficiency Q_s , which is defined in the usual way as the ratio of total radiation scattered in all directions to that intercepted by the projected area of the particle normal to the beam of incident radiation. The second is the backscatter ratio η , defined as the

fraction of the scattered energy that emerges in the backward hemisphere. In practical ceramic systems, efficiency may range from values much less than unity to values near 6. The backscatter ratio ranges from about 0.5 to less than 0.01 in similar situations. Efficiency and backscatter are affected primarily by the ratio of the particle size to the wavelength of the incident radiation, and by the index of refraction of the particle relative to the index of refraction of the surrounding medium. Particle shape and orientation also influence the efficiency and the backscatter ratio.

In discussing scattering, it will be helpful to employ the particle size factor x and the phase shift factor P , defined as follows:

$$x = \frac{2\pi r}{\lambda}$$

$$P = 2x|m - 1|$$

where

- r radius of particle
- λ wavelength of incident radiation in the medium surrounding the particle
- m ratio of index of refraction of particle to that of surrounding medium

The factor P is useful in correlating scattering efficiency Q_s ; and nondimensional curves of this correlation were formed from information presented by van de Hulst in reference 6. The factor x provides a more illustrative nondimensional correlation of the backscatter ratio η , and curves were computed from scattering intensity diagrams presented by van de Hulst. Figure 4 shows Q_s as a function of m and P , and figure 5 presents η as a function of m and x . The product $K_B = \eta Q_s$ is presented as a function of m and P in figure 6.

INFLUENCE OF PARTICLE SIZE

The effect of particle size (relative to wavelength) is first examined for values of the index of refraction of the particle not significantly greater than that of the surrounding medium. The appropriate curves in figures 4 and 5 are labeled $m \rightarrow 1$ to designate this condition. When the physical dimensions are small relative to wavelength both inside and outside the

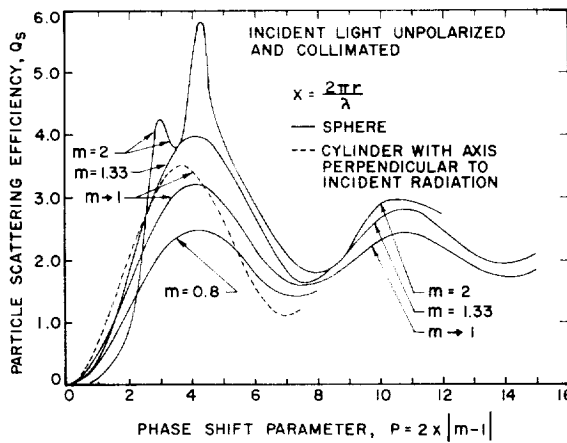


FIGURE 4.—Scattering efficiency of nonabsorbing spherical particles.

particle (that is, when x and the product mx are much less than unity), the domain of Rayleigh scattering is encountered. Rayleigh scattering is thus limited to small values of P on the $m \rightarrow 1$ curve of figure 4 but it is not necessarily limited to values of m close to 1. Scattering is by dipole radiation, and efficiency is very low and proportional to the fourth power of the ratio of particle size to wavelength.

In the Rayleigh domain, an isotropic particle has a backscatter ratio of 0.5 for incident

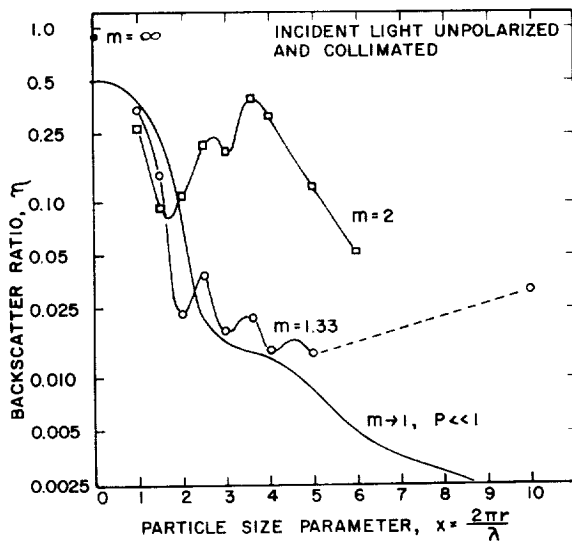


FIGURE 5.—Backscatter ratio for nonabsorbing spherical particles.

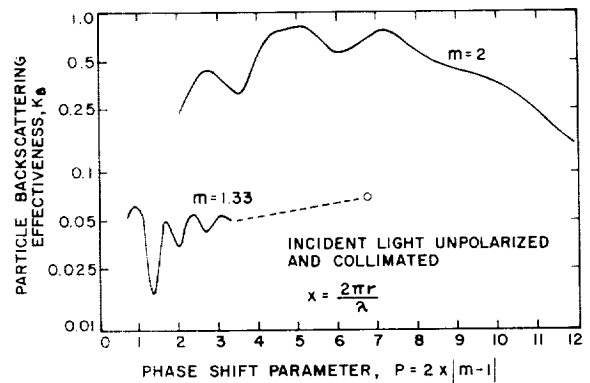


FIGURE 6.—Backscattering effectiveness of nonabsorbing spherical particles.

unpolarized radiation, as shown in figure 5, and scattered energy is fully polarized at 90° to the direction of propagation. As P is increased at values of m close to 1 but remains much less than 1, a transition to the Rayleigh-Gans domain is made. The criteria for Rayleigh-Gans scattering are that $P \ll 1$ and $m \rightarrow 1$, which allow a somewhat larger particle size. Radiation from each volume element of the particle now interferes with that from other elements. Scattering efficiency continues to increase, but the rate of increase is diminished from a fourth-power dependence on particle size to a second-power dependence as the Rayleigh-Gans domain is traversed. Efficiency, however, remains significantly less than unity, as seen in figure 4. As particle size is increased in this domain, the backscatter ratio decreases from 0.5 to a very low value, and approaches zero for large particles. Figure 5 illustrates this trend.

A further increase in particle size places the scattering in the anomalous-diffraction domain. The physical effect now becomes one of interference between transmitted radiation and diffracted radiation. As particle size is increased in this domain, scattering efficiency continues to increase until an efficiency value of about 3 is reached with favorable interference at $P=4.1$. Still larger particle sizes result in unfavorable interference, and efficiency is reduced to about 1.5. As shown in figure 4, this pattern of maxima and minima continues as particle size is further increased, oscillating

about an efficiency value of 2 with a decreasing amplitude. In the upper limit of the anomalous-diffraction domain, interference effects diminish, and the scattered radiation can be separated into two components. The first component is radiation transmitted essentially according to the laws of geometric optics; the second component is radiation diffracted around the particle. Throughout the anomalous-diffraction domain, scattering remains predominantly in the forward direction.

INFLUENCE OF REFRACTIVE INDEX

The preceding discussion of scattering domains shows how increasing the particle size relative to the wavelength affects scattering efficiency and backscattering for the case of the particle refractive index not significantly greater than that of the surrounding medium. It is also interesting to examine how efficiency and backscattering are affected by the refractive index.

First consider the transition in refractive index ratio from $m \rightarrow 1$ to $m \rightarrow \infty$ for a constant small particle size ($x \ll 1$). Scattering efficiency increases with increasing m , and eventually the regime of optical resonance is encountered. Here, scattering efficiency is very high, with a value of about 50 at $m=9$. Although the proper conditions for optical resonance are not closely approached for refractive index values common in ceramics, an indication of the effect does occur; it can be seen as a bump on the Q_s curve of figure 4 at $P=3$ and $m=2$. As m approaches infinity, incident radiation can no longer penetrate the particle; thus resonance does not occur, and a greatly reduced scattering efficiency results. However, the terminal value of Q_s at $m \rightarrow \infty$ is considerably greater than the starting value at $m \rightarrow 1$. As shown in figure 5, the backscatter ratio increases from a value of 0.5 at $m \rightarrow 1$ to a value of 0.9 at $m \rightarrow \infty$, with unspecified intermediate values.

For small values of the phase shift parameter ($P < 1.5$), increasing or decreasing the index of refraction ratio from unity at constant P decreases scattering efficiency, as can be seen from figure 4. Although not readily apparent from figure 5, the backscatter ratio increases with increasing m in this regime.

At values of the phase shift parameter greater than about 2.5, increasing the index-of-refraction ratio produces a marked increase in scattering efficiency, as can be seen in figure 4 for values of m ranging from 0.8 to 2. Figure 5 shows that the index of refraction has an even greater influence on the backscatter ratio as m is increased from 1.33 to 2 at constant P . Demonstrating the influence of index of refraction on overall backscatter effectiveness $K_B = Q_s/\eta$, figure 6 shows that a gain of about an order of magnitude results from increasing m from 1.33 to 2. It is this combined effect that satisfactorily explains the large increase in the reflectance of pigmented white paints with increase in the refractive index of the pigment. The effect is due primarily to increasing the backscatter ratio, rather than scattering efficiency, as is usually supposed.

Figure 6 also allows some other interesting interpretations. One is that maximum backscatter effectiveness K_B occurs at a larger value of P than does spherical scattering efficiency Q_s . For an index-of-refraction ratio of 2, maximum Q_s occurs at $P=4.3$, while maximum K_B occurs at $P=5$. Furthermore, K_B is significantly less sensitive to P than is Q_s . The above values and trends exhibited by K_B , resulting from the combination of a backscatter ratio with the usual spherical scattering efficiency, permit a much improved correlation between single-particle theory and experimental observations with groups of particles, as will be discussed later.

INFLUENCE OF PARTICLE SHAPE AND ORIENTATION

The effects of particle shape and orientation on scattering efficiency and the backscatter ratio have been much less completely studied than have the particle-size and refractive-index effects. The available information indicates that scattering increases with an increase in the ratio of surface area to particle volume, at least in the regions of moderate to small P . Figure 4 shows results for a cylinder oriented perpendicular to the incident light at $m \rightarrow 1$, showing a definite increase in Q_s at $P < 4$. Existing solutions show that for moderately large particles in the Rayleigh-Gans domain ($P \ll 1$), the scattering efficiency of a cylinder

oriented perpendicular to the incident radiation is about 30 percent higher than that of a sphere (compared at equal values of P based on radius). For very small particles, computations for a cloud of randomly oriented long prolate spheroids (approaching a cylinder) show a 20 percent overall increase in net backscatter relative to that from spheres of the same volume.

INFLUENCE OF ABSORPTION

Since all real materials absorb, the proper use of scattering theory must include both direct absorption by the particle and the effect of absorption on the scattering efficiency. Direct absorption is defined in terms of absorption efficiency Q_a , which, analogous to scattering efficiency, is defined as the ratio of incident radiation absorbed to that intercepted by the projected area of the particle normal to the beam of incident radiation. The magnitude of the absorption efficiency is illustrated in figure 7 for the case of a spherical particle and $m \rightarrow 1$. For these conditions, Q_a can be expressed in closed form as:

$$Q_a = 1 + 2 \left[\frac{e^{-2P \tan B}}{2P \tan B} - \frac{1 - e^{-2P \tan B}}{(2P \tan B)^2} \right]$$

The angle B relating Q_a to the absorption characteristics of the particle material is defined as:

$$\tan B = \frac{nk}{n-1} = \frac{r\alpha}{P}$$

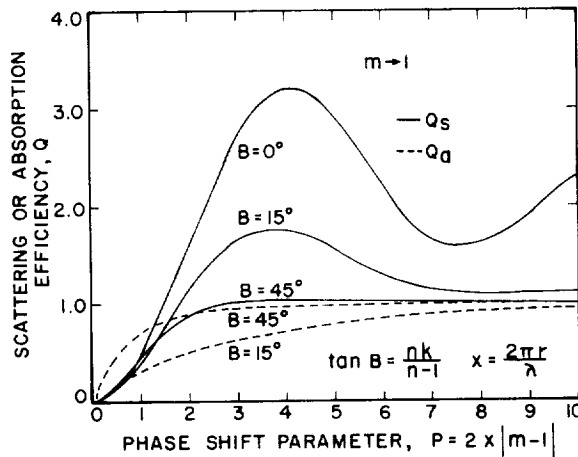


FIGURE 7.—Scattering and absorbing efficiencies of spherical particles.

The influence of absorption on scattering is also shown for $m \rightarrow 1$ in figure 7. The appropriate expression for Q_s is:

$$Q_s = 2 - Q_a - 4e^{-P \tan B} \frac{\cos B}{P} \sin(P - B) - 4e^{-P \tan B} \left(\frac{\cos B}{P} \right)^2 \cos(P - 2B) + 4 \left(\frac{\cos B}{P} \right)^2 \cos 2B$$

For large values of B , absorption greatly reduces scattering efficiency, and it becomes the dominant mode of extinction for small values of P .

The values of the angle B shown in figure 7 correspond to very strong absorption for a ceramic particle at size and wavelength ranges normally encountered. For instance, with a $1\text{-}\mu$ -diameter particle at $P=4$, a value of 15° for B implies an absorption coefficient α of $21,400 \text{ cm}^{-1}$. Since α values of less than 1 cm^{-1} are common at wavelengths of importance in radiant transfer in ceramics, it is desirable to examine absorption effects for these conditions. The equation defining the scattering efficiency curve at $m \rightarrow 1$ shows that for small values of B , Q_s is essentially that for $B=0$. The equation for absorption reduces to:

$$Q_a = \frac{4}{3} P \tan B = \frac{4}{3} r\alpha$$

which is a good approximation as long as $P \tan B < 1$. At these small values of B , scattering is dominant until $P \ll 1$.

Only limited data exist comparing the trends predicted by figure 7 for the case $m \rightarrow 1$ to those obtained by rigorous solution of the Mie formulation for real values of m in the range of interest in ceramics. However, existing results for extinction efficiency ($Q_s + Q_a$) of a sphere with an index of refraction of 1.29 follow very closely the trends inferred at $m \rightarrow 1$ for comparable values of the angle B . In studies with weakly absorbing ceramics, Q_s can be closely approximated by using the appropriate value predicted for nonabsorbing particles. If m is not very far from one, a reasonable approximation to Q_a for a weakly absorbing sphere may be

obtained by multiplying the Q_s for a nonabsorbing sphere by the ratio of Q_a/Q_s predicted by the theory for $m \rightarrow 1$.

Groups of Particles

The discussion of particle scattering showed that the behavior of a single particle can be precisely defined by theory if its geometry, its properties, and the nature of the incident light are all known. From a practical viewpoint, interest here is in the application of theory to the behavior of groups of particles. Existing experimental data show that single-particle theory provides correct predictions when particles are widely separated and multiple scattering does not occur. Under these conditions, the total energy scattered is simply the product of the number of particles and the energy scattered by each. An overall backscatter coefficient is then defined as:

$$S_B = NAK_B = V_p \left(\frac{A}{v_p} \right) K_B$$

where

- N number of particles per unit volume
- A projected area of particle normal to incident energy
- K_B backscattering effectiveness of a particle
- V_p fraction of total volume occupied by particles
- v_p volume of a particle

The units of S_B are the reciprocal of length. An apparent absorption coefficient a is similarly defined by replacing K_B by Q_a .

Some interesting facts are implied by the equation for S_B . One is that, for a given V_p and K_B , maximizing the particle area per unit volume maximizes the backscattering coefficient. Since K_B is influenced by shape, the relationship between particle area and backscattering coefficient is not direct, but, in general, nonspherical particles are most effective. The equation also shows that, for a given V_p and A/v_p , the backscattering coefficient is maximum when the product $K_B(A/v_p)$ is maximum. To see this more clearly, consider spherical particles, where $A/v_p = 0.75/r$. Then S_B is maximum at maximum K_B/r , which

usually does not coincide with maximum K_B . Smaller particles are thus favored, and the tendency is to provide a broader range of particle sizes for a maximum backscattering coefficient than would be inferred by K_B alone.

As long as the conditions of single-particle theory are met, the backscattering coefficient for a layer of unit depth is directly proportional to the concentration of the particles in a nonabsorbing matrix. Bruehlman, Thomas, and Gonick (ref. 7) measured relative reflectances of titania-pigmented organic films, and obtained an indication that the direct proportionality does not hold above concentrations of about 10 percent for the particular degree of dispersion they obtained. If the particles are suspended in a semi-infinite nonabsorbing medium, the reflectivity of a system meeting the conditions of single-particle theory will be independent of particle concentration (that is, the same number of particles will be encountered regardless of dilution, but in the more dilute system light will penetrate to a greater depth). Blevin and Brown (ref. 8) have used this approach to determine the dilution levels at which the backscattering coefficient is no longer directly proportional to concentration. By measuring reflectivities of various pigments and concentrations in both semi-infinite water and air matrices, they found a direct proportionality of the backscattering and absorption coefficients up to concentrations of about 25 percent.

Above the concentration level at which proximity effects become important, the backscattering effectiveness K_B drops off fairly rapidly. Results obtained by Bruehlman, Thomas, and Gonick imply that the backscattering effectiveness at a 45-percent pigment-volume concentration is about 30 percent of the value at low concentrations. Maximum reflectance from a thin layer is obtained at a concentration greater than that for maximum K_B , since the product $K_B V_p$ is involved in the equation for S_B . Bruehlman, Thomas, and Gonick found this concentration to be about 25 percent in their studies with titania paints.

A practical point of interpretation is encountered when applying single-particle theory to highly concentrated scattering systems—at

some concentration the scattering center becomes more correctly the intervening medium than the particle. This is of importance because of the widely different backscattering coefficients that are predicted, depending on the choice of the scattering center. Numerous published data on low concentration particulate systems, such as colloidal dispersions and well-dispersed paint pigments, show that for such a situation particle size most accurately predicts scattering characteristics. In the other extreme of a high density ceramic of porosity less than 10 percent, measurements by Lee and Kingery (ref. 9) show that for this condition correct predictions from theory are obtained when the pore is taken as the scattering center. Data in the transition region are limited. A study by Berry (ref. 10) has shown that the wavelength dependency of scattering by silver bromide particles embedded in a gelatin matrix is correctly predicted by taking the particle as the scattering center at concentrations of 9.5 and 17.2 percent. At a concentration of 64.5 percent, however, his results show that the wavelength dependency of scattering is more accurately predicted by regarding the gelatin matrix as the scattering medium. These limited data in the transition region suggest that it is reasonable to regard the smaller volume fraction as the scattering medium.

The relationship between the apparent absorption coefficient a and the intrinsic-absorption coefficient α of the particle material is important, even in weakly absorbing materials, since the reflectance of an optically thick specimen is directly related to the ratio S_B/a . In the regime where single-particle theory holds, the apparent absorption coefficient is related to the intrinsic-absorption coefficient by the absorption efficiency Q_a , as stated previously. In the limiting case of weakly absorbing particles with $m \rightarrow 1$, in a nonabsorbing matrix, this reduces to the simple volume fraction relationship $a = V_p \alpha$. For cases differing significantly from these conditions the error introduced by such a simplification is appreciable; thus the more general approximation employing Q_a should be used. When the matrix is absorbing and only single scattering occurs, a close approximation to the combined apparent-

absorption coefficient is given by the expression:

$$a = V_p \frac{A}{v_p} Q_a + (1 - V_p) \alpha_m$$

where α_m is the intrinsic absorption coefficient of the matrix material. Again, exact validity is limited to cases where the particles are weakly absorbing with $m \rightarrow 1$. Unfortunately, the limits to which this expression is reasonably valid, even for cases of single scattering without proximity effects, have not been well established. When multiple scattering occurs, the absorption picture is significantly altered. Insufficient experimental data presently exist to draw conclusions as to the effects of multiple scattering on the absorption coefficient.

Reflection from groups of particles in the regime of geometrical optics has been studied apart from single-particle scattering theory. Melamed (ref. 11) analyzed the case of infinitely thick powders composed of diffusely reflecting spherical particles. He derived equations relating powder reflectivity to the particle material intrinsic absorption coefficient, index of refraction, and diameter. In regions of moderate absorption, experimental results correlated well with theoretical predictions. Because of the large particles involved and the analytical requirement of infinite thickness, only a relatively small number of scattering problems in ceramics can make direct application of his results.

Radiative Transfer Equations

In a group of particles conforming to the limiting case of single scattering, all radiant flux that encounters a particle is traveling in the direction of propagation. When multiple scattering occurs, or when the group of particles is bounded by a reflecting medium, a component of radiant flux opposite to the direction of propagation also encounters particles. To allow an analytical specification of radiant transfer in this more complex case, a number of investigators have formulated a system of differential equations defining the transfer process. For the case of an isothermal body, the work of Richmond (ref. 12) is illustrative of the one-dimensional formulation and interpretation. The analytical model employed

is shown in figure 8. An elemental layer of thickness dx and of infinite extent in the plane perpendicular to the axis of propagation is considered. It is assumed that energy is laterally scattered into and out of a unit area at equal rates, and the differential layer is treated as if it were homogeneous. Forward and backward components of the flux are defined as I and J , respectively. Differential equations attributing the changes in this flux as it traverses dx to a backscattering coefficient and an apparent absorption coefficient are written. The simultaneous solution to these equations, with the proper substitution of boundary conditions, then specifies the flux leaving the material as a function of that incident, and thus can be written in terms of emittance, reflectance, and transmittance. The resulting equation for the hemispherical emittance of a coating is:

$$\epsilon = 1 - \left[\rho_e + (1 - \rho_e) \frac{(1 - \beta) A_1 e^{\sigma D} - (1 + \beta) A_3 e^{-\sigma D}}{A_1 A_2 e^{\sigma D} - A_3 A_4 e^{-\sigma D}} \right]$$

where

$$A_1 = (1 + \beta) - \rho_e(1 - \beta)$$

$$A_2 = (1 + \beta) - \rho_i(1 - \beta)$$

$$A_3 = (1 - \beta) - \rho_e(1 + \beta)$$

$$A_4 = (1 - \beta) - \rho_i(1 + \beta)$$

$$\beta = \sqrt{a/(a + 2S_B)}$$

$$\sigma = \sqrt{a(a + 2S_B)}$$

D coating thickness

a apparent absorption coefficient

S_B backscattering coefficient

ρ_e reflectance of the coating-air interface for externally incident diffuse irradiation

ρ_i reflectance of the coating-air interface for internally incident diffuse irradiation

ρ_s reflectance of the substrate for radiation incident from within the coating

The terms a and S_B have the same meaning as before, but because of the effects of proximity, multiple scattering, and diffuse illumination, they are expected, in many cases, to deviate appreciably from single-particle theory predictions for a group of particles. Also, as will be

discussed later, the one-dimensional nature of the derivation limits the direct applicability of the single-particle absorption coefficient. Since the radiative properties of all materials are basically wavelength dependent, the above equation applies to spectral quantities. The equation is equally valid for directional emittance if the proper directional value of ρ_e is incorporated and if the refraction angle of the "incident" illumination is less than 60° (ref. 13).

The proper interpretation of the surface reflectance terms in the radiative-transfer equations is elusive. If the system under consideration is composed of particles dispersed in the surrounding medium (such as fog), surface reflectance does not exist, and scattering commences with the outer layer of particles. On the other hand, if the particles are dispersed in a continuous phase different from the surrounding medium (such as the vehicle of a paint), reflection will occur at the interface between the surface of the continuous phase and the surrounding medium. If this interface is a plane surface, the internal and external reflectivities can be computed by Fresnel's laws of reflection. To allow the internal reflectivities to be computed in this manner, the internal fluxes are usually assumed to be diffuse. The accuracy of this assumption can be very poor, as discussed by Kottler (ref. 14) for the case of opal glass, but the assumption probably is reasonable for intensely scattering materials, such as white paints. The interpretation of the surface-reflection terms for cases intermediate between particles dispersed in the surrounding medium and plane continuous surfaces is more difficult. In particular, a porous ceramic with a mechanically formed surface such as one cut with a diamond wheel presents a surface that is neither smooth and continuous, nor composed of the same scattering geometry as that within the material. An exact definition of surface reflectance is not possible within the present state of knowledge of surface-roughness effects, and accurate determination of the surface-reflection terms requires measurement. Reasonable approximations can probably be made for high-density ceramics by using the Fresnel equations, and for high-porosity ceramics by ignoring surface reflections.

The validity of the radiative-transfer equations is compromised to some extent by the one-dimensional nature of the derivation. Kotler indicates that an experimental dependency of the backscattering coefficient on depth within the material is predicted by the three-dimensional radiative-transfer formulation. He presents experimental values for opal glass that vary considerably with the thickness of the test specimen. For intensely scattering, nearly opaque ceramics, it is expected that the error introduced by using a one-dimensional analysis would not be excessive. Also, as mentioned previously, the direct applicability of the apparent absorption coefficient predicted from single-particle theory is compromised by the one-dimensional nature of the derivation. This results from the fact that the theoretical model accounts only for absorption of radiant flux traveling in a forward or backward direction, whereas, in actuality, absorption also occurs in the laterally scattered flux prior to its being re-scattered out of the elemental slice. Thus an apparent absorption coefficient significantly greater than that predicted by single-particle theory would be expected for the one-dimensional radiative transfer equations. The correlation would be expected to be a complex function of the absorbing and scattering properties of the particles.

It is of primary interest to compare the combined predictions of single-particle theory and the radiative-transfer equations with experiment, since the ability to predict the performance of a light-scattering ceramic is of great value in tailoring its properties. Very little quantitative comparison is available in the literature for systems of interest. The work of Harding, Golding, and Morgan (ref. 15) on anatase-titania-pigmented paints is applicable, however. They tested four particle sizes at three concentration levels up to 25 percent, and inferred a backscattering coefficient from the radiative-transfer equations. By comparing these coefficients with those calculated from single-particle scattering efficiency (spherical scattering), they defined an empirical light-scattering efficiency term E which serves the same function as the present backscatter ratio η . Their values of E ranged from approxi-

mately 0.03 to 0.20, depending on wavelength, particle size, and concentration. These E values agree reasonably well with corresponding η values, especially for the low concentration case (17 percent). For instance, they report an E value of 0.0405 at a mean particle diameter of about 0.35μ and a mean wavelength of about 0.6μ . The index of refraction of anatase titania is 2.52, and the index of refraction of their organic vehicle is about 1.53. The corresponding values of x and m are 2.8 and 1.65, respectively (with x referred to the wavelength of radiation within the vehicle). By interpolating logarithmically in figure 5, a value of $\eta=0.07$ is obtained. The resulting scattering coefficient predicts a reflectance for a 2-mil paint film differing only about 5 percent from the value measured by Harding, Golding, and Morgan. This agreement is considered good because (1) their experimental accuracy may not have greatly exceeded 5 percent, (2) the present comparison was made at a unique wavelength of 0.6μ , while the measurement utilized an amber light filter which transmits over the wavelength range of 0.5 to 0.7μ , (3) Harding, Golding, and Morgan referred their efficiencies E to a universal scattering curve which is only approximate in that it does not fully account for refractive index effects, and (4) Harding, Golding, and Morgan employed an approximate formulation of the one-dimensional radiative-transfer equation in reducing their experimental data. The approximate formula they used does not account for surface reflections.

The net result of these reservations is that the uncertainty in measured E values is probably of magnitude comparable to the difference between E and η , especially in view of the fact that the computed E values are very sensitive to reflectance measurement errors. (For example, a 5-percent error in reflectance produces up to a 70-percent error in E .) These limited data suggest that if the theoretical backscatter ratio η is employed, single-particle theory may be able to predict backscattering coefficients for low concentration dispersions about as accurately as they can be measured. As previously discussed, proximity effects become important at concentrations above about 25 percent, and single-

particle backscattering coefficient predictions would not be expected to hold without modification here. Additional work is needed to more generally correlate theoretical backscattering coefficients with those required by the radiative-transfer equations.

A comparison of the apparent absorption coefficient of the radiative-transfer equations with that predicted by single-particle theory can also be obtained from the data of Harding, Golding, and Morgan. For instance, their data show an experimental value of the apparent absorption coefficient of 16.9 cm^{-1} (normalized to a volume fraction of unity) for the same conditions considered previously. In contrast, the corresponding apparent absorption coefficient predicted by single-particle theory from intrinsic absorption coefficient data is of the order of 0.1 cm^{-1} . This large discrepancy is undoubtedly due, in the main part, to the aforementioned one-dimensional nature of the radiative-transfer equation derivation. Additional work is needed to correlate this fundamental inconsistency before apparent absorption coefficients can be usefully predicted by single-particle theory. Fortunately, in many important systems the dominant mode of attenuation is scattering. In such instances, and when the scattering layer does not approach infinite thickness (for example, a white coating), reasonable reflectance predictions may still be made from single-particle theory by completely ignoring absorption.

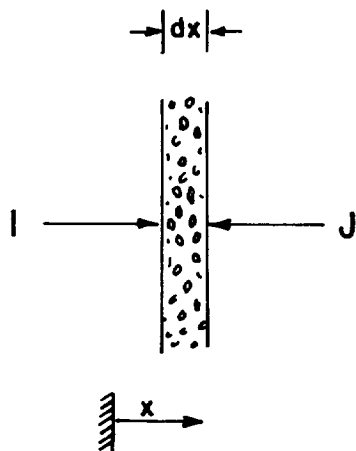


FIGURE 8.—Analytical model for radiative transfer in heterogeneous materials.

The case of combined radiation and conduction heat transfer in ceramics has been formulated one-dimensionally by using the same basic model as that shown in figure 8. To the differential equations expressing radiant flux is added an emission term, and a third equation is written expressing conservation of energy, including thermal conduction. The solution to the resulting system of differential equations, when combined with the appropriate boundary conditions, expresses emission from the non-isothermal specimen and the internal temperature distribution. Hamaker (ref. 16) presents the mathematical treatment in detail, and later studies are reported by Folweiler (ref. 17).

SURFACE ROUGHNESS

Previous discussion has expressed quantitative relationships for the reflectivity of plane surfaces, and has recognized that surface roughness can invalidate the use of these equations. A means of specifying the influence of surface roughness on surface reflectance is, in some cases, of importance equal to or greater than the importance of being able to specify subsurface scattering characteristics. Unfortunately, surface roughness has not been studied to the degree that scattering has, although it is the same basic phenomenon.

In the past, surface-roughness studies have been concentrated in two basic optical regimes: geometrical optics, and diffraction and interference. Work in the geometrical-optics regime considers that roughness produces essentially a blackbody cavity effect, with multiple reflections of rays resulting in an effective increase of the surface emittance. The majority of the applicable studies have been devoted to the analytical, and in some cases experimental, specification of emission from simple geometric shapes of opaque materials. Typical of recent rigorous cavity analyses is that of Sparrow and Jonsson in reference 18. An example of the use of a similar analysis to predict the emittance of a surface is presented by Psarouthakis in reference 19, where good correlation with experimental results was obtained. The specification of the emittance of a highly opaque material of known elemental emissivity requires a knowledge of the exact statistical geometry of

the surface. The interpretation of this statistical information is the fundamental problem that has not been solved. Cox and Forcht (ref. 20) have suggested an interpretation based on a model on which a fraction of the surface is smooth, and the remainder is composed of randomly oriented cavities of some effective diameter-to-depth ratio. Additional theoretical and experimental work is needed to establish a generalized means of relating measurable surface-roughness quantities to some analytical model.

It is notable that nearly all quantitative analyses and experimental observations have been restricted to materials that are opaque in thin sections. Ceramics, however, are often not opaque in sections ranging from a few thousandths to a few hundredths of an inch; and it is not uncommon to find surface irregularities of comparable size in these materials. Theoretical considerations noted in reference 20 indicate that the effect of surface roughness decreases as opacity decreases. Existing measurements, though meager, have also demonstrated that surface effects are of a much reduced magnitude in materials only moderately opaque, and that the extent of the roughness effect is closely related to the ratio of the size of the irregularities to the thickness of the material required for opacity. This peculiarity promises numerous opportunities for practical exploitation, especially in development of ceramics and ceramic coatings with optimum selective radiation properties. For instance, with a coating that is translucent at certain wavelengths but opaque at other wavelengths, roughening the surface would increase emittance in the opaque region but leave it relatively unaffected in the translucent region.

A simple model can be used to illustrate that a definite relationship exists between the degree of opacity of the material and the effect of surface roughness. To simplify the discussion the term "mean free path of a photon" will be employed and designated by the symbol l_m . The mean free path of a photon is defined as the distance of penetration of radiation for an attenuation of intensity to a value of $1/e$ of the initial value. This represents an internal transmission of about 37 percent for a layer of

thickness l_m . Numerically, l_m is the reciprocal of the extinction coefficient of the material and is thus directly related to its opacity. Consider the model shown in figure 9. Radiation leaving element dA_2 is composed of a primary emitted part and a reflected part. The emitted part depends on the internal irradiation of the element and the surface transmittance of the element (to be discussed later). The reflected part includes radiation which is emitted by other elements, such as dA_1 , and makes its way to dA_2 either directly or by single or multiple reflections from still other elements such as dA_3 . This reflected fraction enhances the emitted energy, and the effective emittance of the cavity is, therefore, greater than that of the material of which it is composed.

If l_m is very small (that is, if all internal irradiation incident on the back face of any of the elements of area originates from a depth behind the element which is very much less than the physical dimensions of the cavity) each element will emit the same primary radiation. This case corresponds to highly opaque materials such as metals. Now, if l_m is large compared to the cavity size, the situation is altered for two reasons. First, the internal irradiation of the surface elements on the cavity walls in the above model is considerably altered. For example, with regard to dA_1 , the existence of the surface constitutes the removal of a sizeable portion of the volume that would otherwise contribute to the internal irradiation of dA_1 . Thus, the energy transmitted through dA_1 and emitted is correspondingly reduced, thereby also reducing its component reflected from dA_2 . Second, if the material is a scattering medium (that is, subsurface as well as

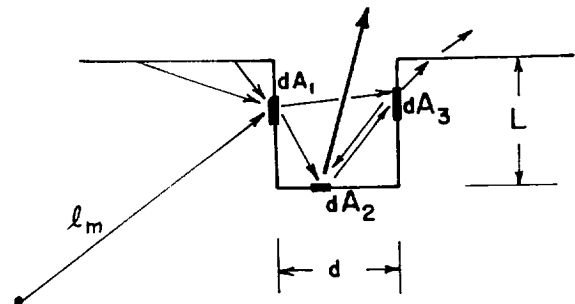


FIGURE 9.—Cavity effect in semitransparent material.

surface reflections occur), the existence of the surface also constitutes the removal of part of the reflecting subsurface, which depletes the total energy that makes its way to dA_2 by way of multiple reflections. Again, the total energy leaving dA_2 is reduced. Thus it can be seen that for large values of l_m compared with the size of the cavity, the effective emittance gain is significantly reduced.

Experimental observations appear to verify this conclusion regarding the relationship between l_m and the cavity effect. As reported by Cox (ref. 21), measurements on polycrystalline zirconia (a scattering material) in the visible have shown that the effect of surface roughness on reflectance is negligible over the roughness range 100 to 400 microinches rms. The mean free path of a photon in this material at these wavelengths is about 0.035 inch, which is about 40 times the measured cavity depth. Data by J. D. Plunkett (now with Denver Research Institute) on polycrystalline alumina have shown similar results. At surface roughnesses ranging from 10 to 200 microinches, he detected no effect of roughness on emittance, while inclusion of voids about 0.033 inch in diameter produced a measurable increase in emittance. As the mean free path of a photon in polycrystalline alumina should be comparable to that in zirconia, it is indicated that a cavity size of the order of magnitude of the mean free path is necessary to produce a significant change in emittance or reflectance.

It is evident, upon examination of previous cavity-analysis problems, and from consideration of the radiative-transfer equations (particularly for homogeneous materials) that quantitative analyses can be conducted to establish a definite theoretical correlation between material opacity and surface roughness effects. Such work has not been accomplished, but will be necessary to allow a correct characterization of surface-roughness effects in ceramics.

Contributions to an understanding of the effects of surface roughness on reflectance for small irregularities have been made by investigators of related wave phenomena, such as the reflection of radar. Davies (ref. 22) obtained a solution for the effect of roughness on the reflection of radar from sea waves by assuming

a perfect conductor, thus eliminating penetration of the electromagnetic wave and reducing the problem to one of diffraction. He employed a statistical specification of height and slope of the irregularities and assumed their geometry to be such that no shadowing occurred. Bennett and Porteus (ref. 23) applied Davies' results to nonperfectly conducting materials in the optical spectrum by assigning a direct proportionality between his results and the reflectance of rough surfaces having less than unit reflectivity (a smooth perfect conductor has a reflectivity of 1). Excellent correlation with this theory was obtained from tests on roughened metallic surfaces.³ Bennett and Porteus found that for irregularity heights considerably smaller than the wavelength of incident radiation, the specular reflectance change at normal incidence due to roughness could be correlated with only the rms roughness value. For larger irregularities, the second statistical function expressing the slope of the irregularities was found to be needed. The magnitude of the roughness effect for very small irregularities was surprising—they reported that a rms roughness of 0.01 wavelength causes an error in specular-reflectance measurement of greater than 1 percent. The work of Twersky on the nonspecular reflection of electromagnetic waves is pertinent to surface-roughness studies. His results with randomly located hemispherical and semicylindrical bosses of perfectly conducting material (ref. 24), especially some predicted variations of the reflectance of polarized and unpolarized radiation with angle, are of interest. One interesting conclusion was that the reflected radiation in the region of the specular angle is an extreme that under certain circumstances is a minimum instead of a maximum.

In summary, previous work in analytical specification of surface-roughness effects has gained success only in the opposing extremes of geometrical optics and diffraction. In these extremes, the limiting cases of materials opaque in thin sections have been successfully studied for a few specialized cases. Since tools for interpreting the influence of surface roughness

³ See also Paper 13.

on the thermal-radiative performance of the material are not generally developed, additional work is needed. The effect of roughness between the regimes of diffraction and of geometrical optics (that is, intermediate sizes of irregularities compared to wavelength) needs considerable investigation, and the influence of the degree of opacity on roughness effects is in severe need of exploration. In short, the problem needs to be studied as vigorously as particle scattering has been studied. In the interim, thermal-radiation property measurements should be accompanied by characterization of the specimen with all information now known to be important: complete statistical information defining the surface geometry (not just rms roughness), and the absorbing, scattering, and refractive properties of the material.

CONCLUDING REMARKS

In discussing the factors affecting thermal-radiative properties of ceramics, a number of areas in which adequate knowledge is lacking have been noted. On the other hand, a great deal is presently known, and an objective of this paper has been to distinguish between these areas of knowns and unknowns. In doing this it is believed that some of the interpretation provided will allow a better use of existing knowledge.

One area where existing knowledge can be better utilized is the application of single-particle scattering theory. Since a fair wealth of published solutions to single-particle scattering theory exists, it should be possible to utilize this information to obtain good predictions of the light-scattering performance of ceramics with moderate to low concentrations of scattering centers. It should then be possible to tailor the performance of these materials for unique applications. Additional research is needed to correlate scattering coefficients predicted by single-particle theory with experimental values for high concentrations of scattering centers. Also, work is needed to further correlate scattering and apparent absorption coefficient values predicted by single-particle theory with values applicable to the one-dimensional radiative-transfer equations.

An encouraging conclusion is that the thermal-radiative performance of homogeneous ceramics can be accurately specified if their optical constants are known and if they are smooth-surfaced. However, since many ceramic applications do not involve smooth-surfaced materials, the influence of surface roughness becomes of major importance. The area of surface-roughness effects represents one of the major gaps in our knowledge of thermal radiation in both homogeneous and heterogeneous ceramics. Of special importance to ceramics is the influence of opacity on surface-roughness effects, but very little definitive information has been obtained here. Research in the area of surface roughness is presently the subject of studies in several laboratories, but additional work is needed. Until means of specifying surface-roughness effects are better developed, the factors known to be of importance in surface characterization must be carefully defined for all new data generated.

REFERENCES

1. JENKINS, FRANCIS A., and WHITE, HARVEY E.: *Fundamentals of Optics*. McGraw-Hill Book Co., Inc. 1957.
2. SIMON, I., and McMAHON, H. O.: Study of the Structure of Quartz, Cristobalite, and Vitreous Silica by Reflection in Infrared. *Jour. Chem. Phys.*, vol. 21, no. 1, Jan. 1953, pp. 23-30.
3. GARDON, ROBERT: The Emissivity of Transparent Materials. *Jour. American Ceramic Soc.*, vol. 39, no. 8, Aug. 1956, pp. 278-287.
4. BLAU, HENRY H., JR.: Measurement of Flux, Emittance, and Related Properties. *Proceedings of an International Symposium on High Temperature Technology*. McGraw-Hill Book Co., Inc., c. 1960, pp. 45-53.
5. GARDON, ROBERT: Calculation of Temperature Distributions in Glass Plates Undergoing Heat-Treatment. *Jour. American Ceramic Soc.*, vol. 41, no. 6, June 1958, pp. 200-209.
6. VAN DE HULST, H. C.: *Light Scattering by Small Particles*. John Wiley & Sons, Inc., 1957.
7. BRUEHLMAN, R. J., THOMAS, L. W., and GONICK, E.: Effect of Particle Size and Pigment Volume Concentration on Hiding Power of Titanium Dioxide. *Official Digest—Federation Societies Paint Tech.*, Feb. 1961, pp. 252-267.
8. BLEVIN, W. R., and BROWN, W. J.: Effect of Particle Separation on the Reflectance of Semi-Infinite Diffusers. *Jour. Optical Soc. of America*, vol. 51, no. 2, Feb. 1961, pp. 129-134.

9. LEE, D. W., and KINGERY, W. D.: Radiation Energy Transfer and Thermal Conductivity of Ceramic Oxides. *Jour. American Ceramic Soc.*, vol. 43, no. 11, Nov. 1960, pp. 594-607.
10. BERRY, C. R.: Turbidity of Monodisperse Suspensions of Ag.Br. *Jour. Optical Soc. of America*, vol. 52, no. 8, Aug. 1962, pp. 888-895.
11. MELAMED, N. T.: Optical Properties of Powders. Part I. Optical Absorption Coefficients and the Absolute Value of the Diffuse Reflectance. Part II. Properties of Luminescent Powders. *Jour. Appl. Phys.*, vol. 34, no. 3, Mar. 1963, pp. 560-570.
12. RICHMOND, J. C.: Relation of Emittance to Other Optical Properties. Paper 67C3-132, *Jour. Res. Nat. Bur. Standards—Sec. C, Eng. and Instrumentation*, vol. 67C, no. 3, July-Sept. 1963, pp. 217-226.
13. KUBELKA, PAUL: New Contributions to the Optics of Intensely Light-Scattering Materials. Part I. *Jour. Optical Soc. of America*, vol. 38, no. 5, May 1948, pp. 448-457.
14. KOTTLER, FRIEDRICH: Turbid Media With Plane-Parallel Surfaces. *Jour. Optical Soc. of America*, vol. 50, no. 5, May 1960, pp. 483-490.
15. HARDING, R. H., GOLDING, B., and MORGAN, R. A.: Optics of Light-Scattering Films. Study of Effects of Pigment Size and Concentration. *Jour. Optical Soc. of America*, vol. 50, no. 5, May 1960, pp. 446-455.
16. HAMAKER, H. C.: Radiation and Heat Conduction in Light-Scattering Material. *Philips Res. Rep.*, vol. 2, 1947, pp. 55-67, 103-125, 420-425.
17. FOLWEILER, R. C.: Thermal Radiation Characteristics of Transparent, Semi-Transparent, and Translucent Materials Under Non-Isothermal Conditions ASD-TDR-62-719, U.S. Air Force, Aug. 1962.
18. SPARROW, E. M., and JONSSON, V. K.: Radiant Emission Characteristics of Diffuse Conical Cavities. *Jour. Optical Soc. of America*, vol. 53, no. 7, July 1963, pp. 816-821.
19. PSAROUTHAKIS, JOHN: Apparent Thermal Emissivity From Surfaces With Multiple V-Shaped Grooves. *AIAA Jour.*, vol. 1, no. 8, Aug. 1963, pp. 1879-1882.
20. COX, R. L., and FORCHT, B. A.: Emittance of Translucent Materials. Rep. No. 00.19, Chance Vought Corp., Dec. 5, 1961.
21. COX, R. L.: A Technique for Measuring Thermal Radiation Properties of Translucent Materials at High Temperature. Measurement of Thermal Radiation Properties of Solids, Joseph C. Richmond, ed. NASA SP-31, 1963, pp. 469-481.
22. DAVIES, H.: The Reflection of Electromagnetic Waves From a Rough Surface. *Proc. Inst. Elec. Eng.*, vol. 101, 1954, pp. 209-214.
23. BENNETT, H. E., and PORTEUS, J. O.: Relation Between Surface Roughness and Specular Reflectance at Normal Incidence. *Jour. Optical Soc. of America*, vol. 51, no. 2, Feb. 1961, pp. 123-129.
24. TWERSKY, VICTOR: On the Nonspecular Reflection of Electromagnetic Waves. *Jour. Appl. Phys.*, vol. 22, no. 6, June 1951, pp. 825-835.

9. Radiant Emission, Absorption, and Transmission Characteristics of Cavities and Passages

E. M. SPARROW

HEAT TRANSFER LABORATORY, DEPARTMENT OF MECHANICAL ENGINEERING
UNIVERSITY OF MINNESOTA, MINNEAPOLIS, MINN.

A systematic study is made of the emission and absorption of thermal radiation by cavities and of the transport of thermal radiation through passages. The conditions under which cavity absorption characteristics can be inferred from cavity emission characteristics (and vice versa) are derived. In particular, it is shown that this reciprocity is valid when the radiation entering the cavity is diffusely distributed across the cavity opening. Available information on cavity-emission and -absorption characteristics is brought together, compared, and generalized. It is demonstrated, for example, that the absorption-emission characteristics of cylindrical-hole cavities and rectangular-groove cavities are essentially identical. Specularly reflecting cavities are found to be more efficient emitters of radiant energy than are diffusely reflecting cavities; this statement also applies to the absorption of diffusely distributed incoming radiation. The transport of thermal radiation through passages which connect isothermal environments is analyzed for both specularly reflecting and diffusely reflecting passage walls. Results are presented for the radiant transport through tapered tubes and tapered (plane-wall) gaps. In general, a passage with specularly reflecting walls is a more efficient transmitter of thermal radiation than is a passage with diffusely reflecting walls.

When thermal radiation is incident upon any nonblack concave surface, the ensuing reflections and re-reflections provide additional opportunities for energy absorption. Consequently, when radiation from an external source enters a cavity, the energy absorbed within the cavity will exceed that which would be absorbed by a plane area of identical absorptance stretched tightly over the cavity opening. This characteristic is often called the cavity effect. For similar reasons, the radiant energy streaming out of a heated cavity will exceed that emitted by a plane area of identical temperature and emittance stretched across the opening of the cavity.

In general, the magnitude of the cavity effect depends on the detailed geometrical configuration of the cavity and on the radiation proper-

ties of its surfaces. Additionally, for the case of the cavity absorber, the extent of the cavity effect also depends on the directional distribution of the incoming radiant energy.

In solving for the emission properties of cavities, it is usual to assume that the surfaces of the cavity are isothermal and also to neglect radiant energy entering the cavity opening from an external source. On the other hand, in determining the absorption characteristics, it is customary to restrict consideration to the radiant energy which enters the cavity opening from an external source; the energy emitted by the cavity walls is not included, that is, the walls may be regarded as being at absolute zero. The emission and absorption properties of cavities are generally represented in terms of an apparent emittance ϵ_a and an apparent

absorptance α_a which are defined as

$$\epsilon_a = \frac{\text{rate of radiant efflux from a cavity}}{\text{rate of efflux from a black-walled cavity}} \quad (1)$$

$$\alpha_a = \frac{\text{rate of absorption of radiant energy in cavity}}{\text{rate of incoming radiant energy}} \quad (2)$$

The respective departures of ϵ_a and α_a from the actual surface emittance ϵ and actual surface absorptance α give the magnitude of the cavity effect.

The present paper aims at establishing certain general characteristics of cavities and then proceeds to bring together, compare, and generalize available quantitative information on cavity absorption and emission. By setting forth and applying a reciprocity theorem, it will be demonstrated that under certain conditions the absorption properties of cavities can be inferred from emission properties and vice versa. As a consequence of the reciprocity theorem, results initially derived for emission can be used for absorption and vice versa. Most of the available information relates to cavities whose surfaces emit and reflect diffusely. However, there are some results which pertain to cavities with specularly reflecting surfaces. Comparison of specularly and diffusely reflecting cavities will be made whenever possible.

Closely related to the emission and absorption properties of cavities is the transmission of radiant energy through passages. The radiant interchange problem for the transmitting passage will be formulated in a general manner for surfaces which are either diffusely or specularly reflecting. The available results for the transmission problem are brought together and discussed.

RECIPROCITY THEOREM FOR CAVITIES

It is of practical interest to determine the relationship between the emission and absorption characteristics of cavities. To this end, consideration is given to a cavity of arbitrary shape such as is pictured in figure 1. At the left is depicted the typical cavity-emission prob-

lem in which the cavity walls are isothermal at temperature T and no external radiation enters through the opening. Suppose that the rate of energy efflux from the cavity under these conditions is Q .

Next, consider this same cavity but with walls at absolute zero (center sketch of fig. 1). The cavity opening is closed by a black surface at temperature T which radiates into the cavity.

When these two physical situations are superposed, there is obtained an isothermal enclosure as shown on the right of figure 1. It is well known that there is no net heat transfer at any surface of an isothermal enclosure regardless of the radiation properties of the surface. In particular, the heat transfer through the cavity opening is zero when the physical situations depicted in the left and center sketches are superposed.

If there is a heat transfer Q out of the cavity for the situation shown in the left-hand sketch, it follows that there must be an identical heat transfer into the cavity for the situation shown in the center sketch. Thus, the cavity with walls at absolute zero absorbs heat at the rate Q from the radiation emitted by the black surface at temperature T stretched across the

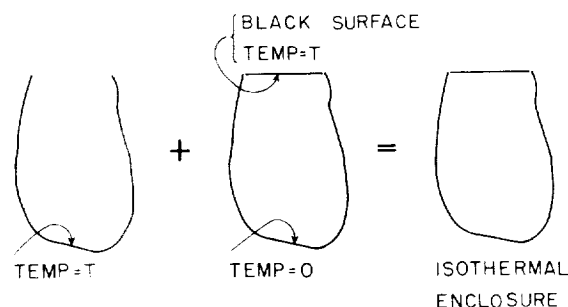


FIGURE 1.—Diagram illustrating superposition of cavity-emission and cavity-absorption problems.

cavity opening. Moreover, the radiation from such a black surface is fully equivalent to the radiation coming from an external source that is uniformly and diffusely distributed as it passes through the opening of the cavity. Consequently, the center sketch of figure 1 represents the cavity-absorption problem for the case of diffuse incoming radiation.

If the area of the cavity opening is A_o , it is readily found from equations (1) and (2) that the apparent emittance and apparent absorptance, respectively, corresponding to the left and center sketches of figure 1 are: $\epsilon_a = Q/A_o\sigma T^4$ and $\alpha_a = Q/A_o\sigma T^4$. From this, there follows the basic result that

$$\alpha_a = \epsilon_a \quad (3)$$

provided that the incoming radiation is diffusely distributed. This conclusion is valid for any cavity configuration.

The foregoing derivation is valid provided that the radiation properties of the cavity walls remain unchanged during the superposition. Inasmuch as $\alpha = \epsilon$ for the isothermal cavity, this same gray body condition must also be fulfilled by the other cavities participating in the superposition. Thus, the relationship $\alpha_a = \epsilon_a$ is restricted to gray cavities.

Another requirement for the equality of α_a and ϵ_a for cavities of arbitrary configuration is that the incoming radiation is diffusely distributed. However, as will be demonstrated later, the equality continues to be valid for the spherical cavity regardless of the directional distribution of the incoming radiation. The author is unaware of other configurations in which the requirement of diffuse incoming radiation can be relaxed without voiding the equality of α_a and ϵ_a .

The discussion of the prior paragraphs has been concerned with total radiation, that is, radiation extending over all wavelengths. A similar derivation can be carried out for monochromatic radiation. The end result of such a derivation is that $\alpha_{\lambda a} = \epsilon_{\lambda a}$, provided that the incoming radiation is diffusely distributed and that $\alpha_\lambda = \epsilon_\lambda$. In accordance with Kirchhoff's law, this latter requirement is generally satisfied by all surfaces.

ANALYSIS OF CAVITY EMITTERS AND ABSORBERS¹

Diffusely Emitting and Reflecting Surfaces

If the surfaces of the cavity are diffuse emitters and diffuse reflectors of radiant energy, then the determination of the emission or the absorption properties of the cavity involves the solution of a linear integral equation. If the location of an area element $dA(x)$ on the cavity wall is specified by the coordinate x , then for the conditions of the cavity-emission problem, a radiant flux balance at a typical location $x = x_i$ yields (for instance, see refs. 1 and 2)

$$B(x_i) = \epsilon\sigma T^4 + \rho \int_x B(x) dF_{dA(x_i)-dA(x)} \quad (4)$$

wherein the integral is extended over all portions of the cavity wall. The symbol B denotes the radiosity, which is the radiant flux leaving a surface element per unit time and area. In general, the radiosity is equal to the sum of the emitted radiant energy (first term on the right of eq. (4)) and the reflected portion of the incident radiation (last term on the right). The surface emittance and reflectance are respectively represented by ϵ and ρ , while $dF_{dA(x_i)-dA(x)}$ is the angle factor for diffuse radiant interchange between area elements $dA(x_i)$ and $dA(x)$. For the condition of gray surfaces, which has generally been adopted in cavity analysis, the radiation properties α , ϵ , and ρ are related by $\alpha = \epsilon = 1 - \rho$.

The net heat flux q_e at a surface location per unit time and area is the difference between the leaving radiant flux B and the incident radiant flux. The latter quantity is represented by the integral appearing on the right-hand side of equation (4). Upon rewriting equation (4), it follows that the incident radiant flux is given by $(B - \epsilon\sigma T^4)/\rho$. Upon subtracting this quantity from B , there is obtained

$$q_e = \frac{[\epsilon\sigma T^4 - (1 - \rho)B]}{\rho} \quad (5a)$$

and, for gray surfaces,

¹ See also Papers 10, 45, and 48.

$$q_e = \frac{[\epsilon(\sigma T^4 - B)]}{(1 - \epsilon)} \quad (5b)$$

in which the subscript e is affixed to denote the cavity-emission problem. In turn, the rate Q_e at which radiant energy streams from the cavity can be determined by integrating the local heat flux, that is,

$$Q_e = \int_x q_e dA(x) \quad (6a)$$

Finally, the apparent emittance ϵ_a follows as

$$\epsilon_a = \frac{Q_e}{A_0 \sigma T^4} \quad (6b)$$

wherein A_0 is the area of the cavity opening.

For the cavity-absorption problem corresponding to a diffusely reflecting cavity with walls at absolute zero, the governing integral equation takes the form

$$B(x_i) = \rho \left[I(x_i) + \int_x B(x) dF_{dA(x_i)-dA(x)} \right] \quad (7)$$

The symbol I represents the distribution along the cavity walls of the radiation which arrives directly from the external source. The rate q_{ab} at which radiant energy is locally absorbed at the cavity walls per unit time and area is derived in a manner analogous to the derivation of equation (5a). The end result of the derivation is

$$q_{ab} = \left[\frac{\alpha}{(1 - \alpha)} \right] B \quad (8)$$

The overall rate Q_{ab} at which radiant energy is absorbed in the cavity as a whole can then be found by integration

$$Q_{ab} = \int_x q_{ab} dA(x) \quad (9a)$$

The apparent absorptance α_a is then

$$\alpha_a = \frac{Q_{ab}}{E} \quad (9b)$$

where E is the rate at which radiant energy enters the cavity.

If the incoming radiation is uniformly and diffusely distributed across the cavity opening,

then

$$I(x_i) = \left(\frac{E}{A_0} \right) F_{dA(x_i)-A_0} \quad (10)$$

where $F_{dA(x_i)-A_0}$ is the angle factor for diffuse interchange between the areas $dA(x_i)$ and A_0 . For this $I(x_i)$ distribution, it can be shown that the results for $q_{ab}/(E/A_0)$ which follow from the solution of equation (7) are identical to the results for $q_e/\sigma T^4$ which follow from the solution of equation (4), provided that $\alpha = \epsilon$. Thus, the apparent emittance ϵ_a and the apparent absorptance α_a are equal, in accordance with the reciprocity theorem. Hence, for the case of diffusely distributed incoming radiation, there is no need for separate solution of equations (4) and (7). However, for an incident energy distribution $I(x_i)$ different from that given by equation (10), the cavity-absorptance problem is, in general, different from the cavity-emission problem and separate solutions must be carried out for each.

It is of interest to discuss briefly the available solution methods for integral equations of the type (4) and (7). So far as the author knows, there are only two cavity configurations which permit exact closed-form solutions of these equations: the spherical shell (ref. 3) and the long circular cylinder whose opening is a longitudinal slit (ref. 4). For other cavity configurations, solutions may be found either by numerical techniques or by approximate analytical procedures.

Among the numerical methods, perhaps the most straightforward is to recast the governing integral equation in finite difference form. In this way, the mathematical problem is reduced to the solution of a set of linear algebraic equations. In particular, if the integral is approximated according to the trapezoid rule, then the resulting finite-difference equations are identical to those derived by applying Hottel's method (ref. 5) or the radiosity method (for example, ref. 1) to an enclosure with finite surfaces. Recently, Perlmutter and Siegel (refs. 6 to 8) have employed a Simpson's rule representation of the integral with a view to achieving greater accuracy. Higher order approximations may also be used without destroying the linearity of the resulting algebraic

equations. The algebraic system thus derived may be solved by standard computer routines.

An alternate numerical technique is that of successive iterations (for instance, ref. 2). In this procedure, one begins by guessing the distribution of the radiosity $B(x)$. With this, the integrals appearing on the right-hand side of equations (4) or (7) can be carried out numerically for a particular value ² of x_i , and a new value of B at x_i is thus obtained. By repeating this operation at all mesh points x_i , there is generated a new distribution function for B which is used in the next cycle of the iteration. The procedure is continued until convergence is achieved.

Three approximate analytical methods which have been used successfully in radiant interchange calculations are: (1) Taylor series expansion, (2) approximation of the angle factor, and (3) variational technique. In the first of these (ref. 8), the radiosity $B(x)$ is expanded in a Taylor series about $x = x_i$:

$$B(x) = B(x_i) + (x - x_i) \left(\frac{dB}{dx} \right)_{x_i} + 0.5(x - x_i)^2 \left(\frac{d^2B}{dx^2} \right)_{x_i} + \dots \quad (11)$$

The substitution of this into the integral term of (4) or (7) reduces the integral equation to a differential equation. The solution of the resulting differential equation, although still requiring numerical techniques, may be easier than that of the original integral equation.

In connection with the second method, it may be noted that the angle factor appearing in equations (4) and (7) may be represented as

$$dF_{dA(x_i)-dA(x)} = K(x, x_i) dx \quad (12)$$

The function $K(x, x_i)$ is the kernel of the integral equation. The basic idea of the method is to approximate the actual kernel with another function which leads to the following property: namely, that if the integral equation is differentiated n times, the integral term of the original integral equation reappears.

Thus, the integral term can be eliminated between the integral equation and its n^{th} derivative, and this leads to an n^{th} order differential equation. The method has been used successfully for situations where the kernel is symmetric, that is, $K(x, y) = K(y, x)$; these include the cylindrical tube (refs. 6 to 10) and the rectangular-groove cavity (ref. 11). As a recent innovation, a correction procedure has been devised (ref. 8) to improve the accuracy of the solutions.

According to the variational method (refs. 8, 10 and 12), consideration is shifted from the integral equation to a corresponding variational expression I (eq. (13) of ref. 12), the basic idea being to find a particular function B which makes I an extremum. The Rayleigh-Ritz procedure provides a systematic way for seeking the extremum condition.

The foregoing summary indicates that a wide range of methods is available for solving the radiant interchange problem for diffusely emitting and reflecting cavities.

Specularly Reflecting Surfaces

For the conditions of the cavity-emission and cavity-absorption problems (that is, prescribed wall temperature), the heat-transfer characteristics of a cavity with specularly reflecting walls can be calculated without recourse to an integral equation. The essential computational feature for the case of specularly reflecting surfaces is the accounting of rays as they reflect and re-reflect within the cavity. In general, the accounting of the rays can be an arduous task for cavities of arbitrary shape, and this may be one reason there is less information available for specularly reflecting cavities than for diffusely reflecting cavities.

There are, however, some situations in which the specular case can be treated without difficulty. When the surfaces of the cavity are plane, the computation can be simplified by making use of a basic property of plane mirrors: namely, that the radiant energy (or light) reflected from a plane mirror appears to come from an image located behind the mirror. The distance between the image and the mirror is identical to the distance between the object and the mirror. In particular, if

² The angle factor $dF_{dA(x_i)-dA(x)}$ generally depends on both x_i and x .

the radiant energy under consideration comes from a diffusely distributed source (that is, diffusely emitting surfaces or diffuse incoming radiation), the above-mentioned images lend themselves to a surprisingly simple computational method (refs. 13 and 14). As demonstrated in these references, the interchange due to specular reflection is computed by applying the angle factors for *diffuse* interchange between the actual surfaces of the cavity and the image surfaces. The image method has been employed in evaluating the absorption and emission characteristics of rectangular-groove cavities (ref. 11) and V-groove cavities (ref. 15).

The computation of the interchange between specularly reflecting non-planar surfaces appears to be a much more formidable undertaking than the corresponding computation for plane surfaces. De Vos (ref. 16) has proposed a method which is *purported* to apply for any directional distribution. However, De Vos' results for the diffuse cavity are themselves in error and this lends uncertainty to the proposed method. The specularly reflecting, diffusely emitting circular-hole cavity has been treated by Krishnan (refs. 17 to 19), but without numerical results.

EMISSION AND ABSORPTION RESULTS FOR CAVITIES

Diffusely Emitting and Reflecting Walls; Diffuse Incoming Radiation

The emission characteristics and the corresponding absorption characteristics for diffusely distributed incoming radiation have been computed for a variety of cavity configurations with gray diffuse walls. For the aforementioned conditions, $\epsilon_a = \alpha_a$. These results were obtained by solving appropriate integral equations of the type (4) or (7). The cavities for which results are available include the cylindrical hole (ref. 2), the rectangular groove (ref. 11), the conical hole (ref. 20), the V-groove (ref. 15), and the spherical shell (ref. 3).

The calculated values of ϵ_a , α_a for the cylindrical-hole and the rectangular-groove cavities have been brought together in figure 2. The former is a cylinder of depth L and radius r , open at one end and closed at the other. The latter is a groove of rectangular profile, with

depth L and width h , whose extension in the direction normal to the plane of the paper is very great. In figure 2, ϵ_a , α_a is plotted against L/r for the cylindrical hole and against L/h for the rectangular groove. Inspection of the figure reveals that when plotted in this way, the values of ϵ_a , α_a are essentially the same for the cylindrical cavity as for the rectangular groove. Thus, h appears to be an appropriate "hydraulic radius," just as it is in fluid mechanics for a parallel-plate channel. The departure of ϵ_a from ϵ (and α_a from α) provides a measure of the cavity effect. It may be seen from figure 2 that the cavity effect is most pronounced for surfaces of relatively low emittance. Additionally, the cavity effect is accentuated in configurations of greater depth; however, ϵ_a approaches a limiting value (less than unity) as the depth increases. It is interesting to note how quickly ϵ_a approaches its limiting value. For instance, for $\epsilon = 0.9$, there is little change beyond L/h or $L/r = 2$; a corresponding statement applies for the $\epsilon = 0.5$ results when L/h or L/r exceeds 5.

The ϵ_a , α_a results for the conical cavity and the V-groove cavity are plotted together in figure 3 as a function of the opening angle θ . The results for these two cavities are also seen to be essentially the same. The cavity effect is most evident for surfaces of low emittance, and this is accentuated at small opening angles, that is, closed-in cavities. The limiting values at $\theta = 0^\circ$ for the cone and the V-groove correspond respectively to those of the cylindrical-hole and the rectangular-groove cavities of infinite depth.

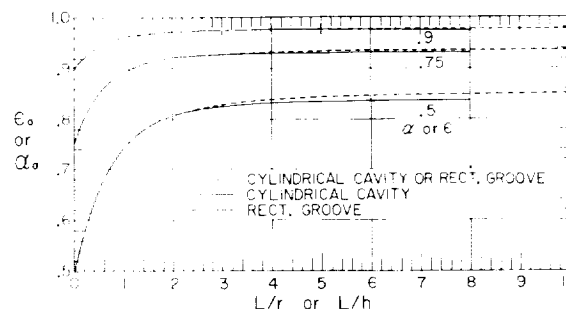


FIGURE 2.—Radiation properties of diffusely emitting and reflecting cylindrical-hole and rectangular-groove cavities; α_a corresponds to diffuse incoming radiation.

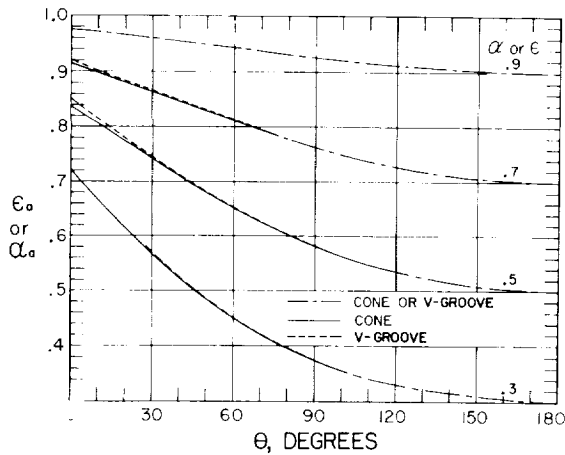


FIGURE 3.—Radiation properties of diffusely emitting and reflecting V-groove and conical cavities; α_a corresponds to diffuse incoming radiation.

Results for the spherical cavity are presented in figure 4. Figure 4 also includes a small sketch which defines the opening angle ϕ^* . The trends evidenced by the figure are essentially the same as those seen in the previous figures. However, the value of α_a applies for any arbitrary spatial distribution of the radiation entering the spherical cavity. Additionally, the following closed-form expressions are available from reference 3.

$$\epsilon_a = \frac{\epsilon}{[1 - 0.5(1 - \alpha)(1 + \cos \phi^*)]} \quad (13a)$$

$$\alpha_a = \frac{\alpha}{[1 - 0.5(1 - \alpha)(1 + \cos \phi^*)]} \quad (13b)$$

Diffusely Emitting and Specularly Reflecting Walls; Diffuse Incoming Radiation

There is less information available for cavities with specularly reflecting walls than for cavities with diffusely reflecting walls. The emission characteristics and the corresponding absorption characteristics for diffusely distributed incoming radiation have been computed for rectangular-groove and V-groove cavities having specularly reflecting, diffusely emitting, gray walls. The cavity reciprocity theorem is applicable for these conditions, so that $\epsilon_a = \alpha_a$. The computations were carried

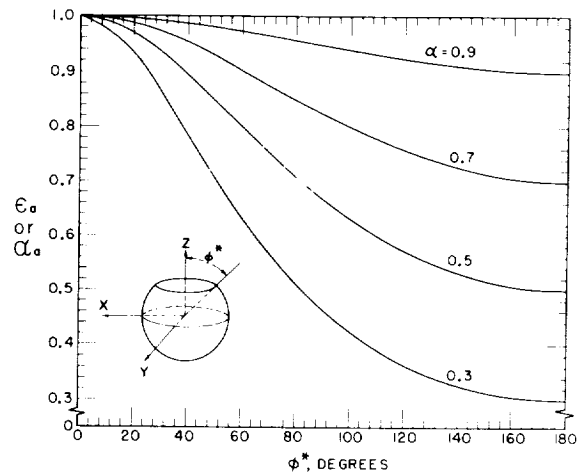


FIGURE 4.—Radiation properties of diffusely emitting and reflecting spherical cavities.

out by applying the previously described image method.

The results for the specularly reflecting, diffusely emitting rectangular-groove cavity are presented in figure 5, where they are compared with corresponding results for a diffusely reflecting and emitting cavity. The abscissa is the cavity depth-to-width ratio, L/h . In-

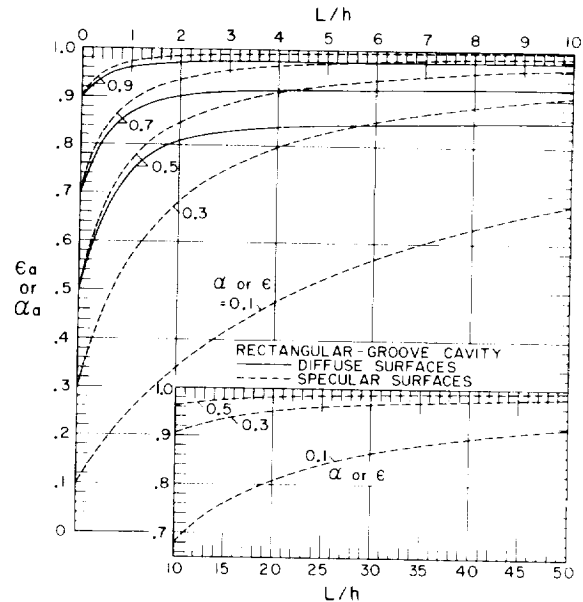


FIGURE 5.—Comparison of specularly reflecting and diffusely reflecting rectangular-groove cavities.

spection of the figure reveals that for the specularly reflecting cavity (dashed lines), ϵ_a and α_a increase monotonically with increasing cavity depth, and ultimately approach unity for sufficiently deep cavities. Thus, a specularly reflecting cavity of sufficient depth can serve as a black-body emitter or absorber. The black-body condition is achieved for relatively small values of L/h when ϵ and α are large; however, for small values of ϵ and α , rather deep cavities are needed to achieve essentially black-body conditions.

This behavior of specularly reflecting cavities is to be contrasted with that of diffusely reflecting cavities (solid lines). For the latter, the ϵ_a , α_a results approach a limiting value less than unity for very deep cavities. In general, a specularly reflecting cavity absorbs and emits more effectively than does a diffusely reflecting cavity having the same values of ϵ or α . The superior performance of the specular cavity is most strongly in evidence for deep cavities and for low surface emittance or absorptance. For instance, for a cavity with $L/h=10$ and $\epsilon=0.5$, the values of ϵ_a (or α_a) are 0.963 and 0.850, respectively, for the specular and diffuse conditions.

Results for the specularly reflecting V-groove cavity are plotted in figure 6 along with corresponding curves for the diffusely reflecting cavity. It may be seen from figure 6 that the ϵ_a , α_a values for the specular cavity increase monotonically as the opening angle θ decreases and approach unity as the angle approaches zero. On the other hand, for the diffuse cavity, the limiting values of ϵ_a , α_a for vanishing θ lie below unity. The specularly reflecting cavity is once again seen to be a more effective emitter and absorber than the diffusely reflecting cavity. This is especially true for cavities having small opening angles θ and walls with low emittance.

Although results are unavailable for cavity configurations other than those just discussed, it is expected that specularly reflecting walls would generally enhance the emitting and absorbing characteristics of the cavity. It would thus appear that the diffusely reflecting cavity provides a lower limit on the values of ϵ_a and α_a .

Absorption of Parallel-Ray Bundles in Cavities

For situations in which the radiant energy entering the cavity is not diffusely distributed across the cavity opening, it appears that the absorption characteristics of the cavity cannot be inferred from the emission characteristics; rather, they must be calculated independently. One nondiffuse distribution which has been studied in some detail is the case in which the radiation enters the cavity as a bundle of parallel rays. For this condition, values of the apparent absorptance have been calculated for the V-groove cavity (ref. 15), the rectangular groove (ref. 11), the long circular cylinder whose opening is a longitudinal slit (ref. 4), and the spherical shell (ref. 3). In the calculations which were made for the first three of these, consideration was given to both specularly and diffusely reflecting cavity walls. For the spherical shell, only diffuse walls were considered (see eq. (13b)).

In summarizing the apparent-absorptance results of references 4, 11, and 15, a blanket statement cannot be made about the relative effectiveness of specularly reflecting walls versus diffusely reflecting walls. For certain angles of inclination of the incoming ray bundle, the diffuse-surface cavity was found to absorb more effectively than the specular-surface cavity. The opposite was true at other angles

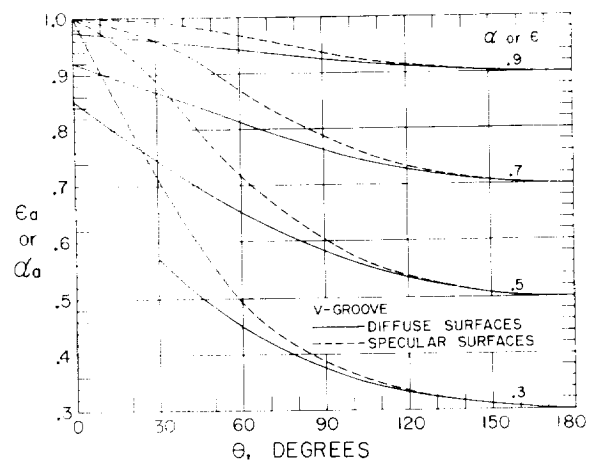


FIGURE 6.—Comparison of specularly reflecting and diffusely reflecting V-groove cavities.

of incidence. The pivotal factor is the number of surface contacts experienced by the specularly reflecting ray bundle before it reemerges from the cavity. The detailed results for the aforementioned configurations require several figures for their presentation and are not included because of space limitations. Interested readers are referred to the original papers.

TRANSMISSION CHARACTERISTICS OF PASSAGES

The transport of thermal radiation through passages which connect isothermal environments is a problem closely related to the absorption and emission of radiant energy by cavities. The physical situation is illustrated in the sketches in figures 7 and 8, which relate to transmission through a tapered (plane-walled) gap and a tapered tube, respectively. The isothermal environments at each end of the passage are represented by temperatures T_1 and T_2 . These environments are taken to be black-body radiators at their respective temperatures.

At the walls of the passage, various thermal boundary conditions may be prescribed. The situation in which the wall is locally adiabatic may be of considerable practical interest, and it is this case which is treated here. For the adiabatic-wall condition, the temperature of

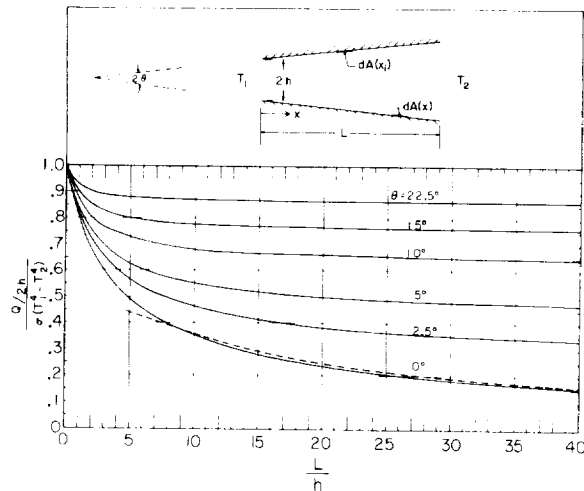


FIGURE 7.—Transport of radiant energy through diffusely emitting and reflecting plane-walled gaps.

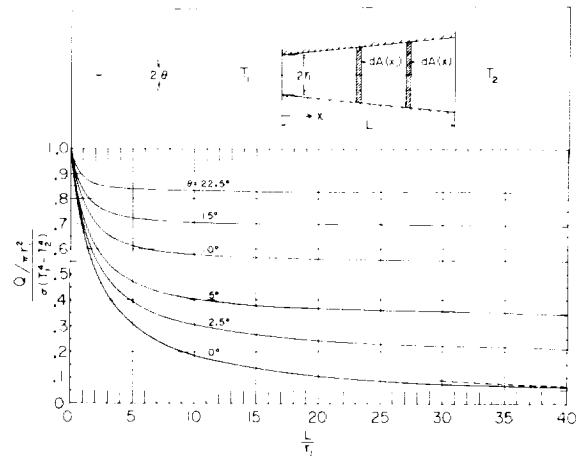


FIGURE 8.—Transport of radiant energy through diffusely emitting and reflecting tapered tubes.

the passage wall varies along the length in a manner which is not known *a priori*. The fact that the wall temperature is unknown requires that the radiant interchange process within the passage be described by integral equations, both for diffusely and for specularly reflecting walls.

The Analysis of Radiant Transport Through Passages

DIFFUSELY EMITTING AND REFLECTING SURFACES

If the walls of the passage are gray, diffuse emitters and reflectors, the local heat flux is related to the local temperature and radiosity as indicated in equation (5b). For the adiabatic condition ($q=0$), it follows that $B=\sigma T^4$ at each surface location. In turn, the local radiosity B is equal to the sum of the emitted radiation plus the reflected portion of the incident radiation. From this, one can readily derive an integral equation which governs the distribution of the temperature as a function of position along the wall of the passage.

$$T^4(x_i) - T_2^4 = (T_1^4 - T_2^4) F_{dA(x_i) - A_1}$$

$$+ \int_0^L [T^4(x) - T_2^4] dF_{dA(x_i) - dA(x)} \quad (14)$$

The coordinates which appear in this equation are those indicated in the sketches in figures 7 and 8. The angle factor $dF_{dA(x_i)-A_1}$ relates to diffuse interchange between $dA(x_i)$ and the area A_1 at the opening of the passage; the angle factor $dF_{dA(x_i)-dA(x)}$ relates to diffuse interchange between the areas $dA(x_i)$ and $dA(x)$.

The net rate of energy throughflow Q from the environment 1 to the environment 2 may be computed as the difference between the radiant energy streaming into and out of the passage opening at 1. For passages with diffusely emitting and reflecting walls, the expression for Q is

$$\frac{Q}{A_1\sigma(T_1^4-T_2^4)} = 1 - \left(\frac{1}{A_1}\right) \int_0^L \left\{ \frac{[T^4(x)-T_2^4]}{[T_1^4-T_2^4]} \right\} F_{dA(x)-A_1} dA(x) \quad (15)$$

Thus, the transport of radiant energy through the passage is found by solving equation (14) for the distribution of $[T^4(x)-T_2^4]/[T_1^4-T_2^4]$ and then integrating this distribution in accordance with equation (15). The solution of equation (14) can be carried out by employing any one of the several numerical or approximate analytical methods which were discussed in connection with diffusely emitting and reflecting cavities. Inspection of equations (14) and (15) reveals that the radiation properties of the passage wall do not appear. Therefore, the radiation transmitted through an adiabatic-walled, gray, diffuse passage is independent of the magnitude of the surface emittance and absorptance.

DIFFUSELY EMITTING, SPECULARLY REFLECTING SURFACES

An integral equation for the radiant interchange in passages having specularly reflecting, diffusely emitting surfaces can also be derived. The pivotal point in the analysis is the fact that all the radiant energy involved in the interchange process originates from diffuse sources: either from the isothermal environments or from the cavity wall. Consequently, the essential role of the specular reflections is to modify the pattern of diffuse interchange.

Indeed, Perlmutter and Siegel (ref. 8) have

demonstrated that for the circular tube, the radiant interchange between a pair of area elements such as $dA(x)$ and $dA(x_i)$ (fig. 8) can be represented in terms of an exchange factor which plays a role similar to that of the diffuse angle factor. An exchange factor was also constructed to describe the radiant interchange between the tube opening area A_1 and the element $dA(x_i)$. For the circular tube, the exchange factors were shown to be infinite series, the typical term of which is a diffuse angle factor multiplied by the surface reflectance raised to an integer exponent. Exchange factors can also be constructed without difficulty for passages whose walls are plane. However, for nonplane configurations other than the circular tube, the construction of exchange factors is a formidable task.

Upon applying the adiabatic condition that the radiant energy incident upon a surface location equals the radiant energy streaming away from that surface location, one can derive

$$T^4(x_i) - T_2^4 = (T_1^4 - T_2^4) E_{dA(x_i)-A_1} + \epsilon \int_0^L [T^4 - T_2^4] dE_{dA(x_i)-dA(x)} \quad (16)$$

where E is the exchange factor. The foregoing applies to a passage with gray, diffusely emitting and specularly reflecting walls. It is interesting to compare equation (16) with that for a fully diffuse passage, equation (14). The form of the two equations is similar, with the exchange factor and the angle factor playing analogous roles. It may be noted, however, that while the transmission through the diffuse cavity is independent of the radiation properties, the same is not true for the specular-diffuse cavity. For the latter, ϵ appears explicitly in the integral equation and ρ is contained in the exchange factors.

The net rate of energy throughflow can be formulated as the difference between the radiant energy passing into and out of the passage at 1; thus

$$\frac{Q}{A_1\sigma(T_1^4-T_2^4)} = 1 - \frac{\epsilon}{A_1} \int_0^L \left[\frac{T^4(x)-T_2^4}{T_1^4-T_2^4} \right] E_{dA(x)-A_1} dA(x) \quad (17)$$

The energy throughflow is calculable from the foregoing equation as soon as solutions of equation (16) have been found. The required solutions may be carried out by choosing among the various numerical and approximate analytical techniques previously discussed, with the reservation that the approximate-kernel and the variational methods are probably not suitable.

Results for Radiant Transport Through Passages

The transmission of radiant energy through tapered (plane-walled) gaps and tapered tubes with gray, diffusely emitting and reflecting walls has been determined in reference 21 by iterative solution of equation (14); this information is plotted in figures 7 and 8, respectively. The results depend on two parameters: the half angle of taper θ and the ratio of the passage length to the dimension of the opening. Inspection of the figures reveals that the energy throughflow decreases with increasing passage length for a given angle of taper. However, the rate of decrease depends quite strongly on the angle of taper. In particular, for passages of moderate and large taper angle, the energy throughflow decreases with increasing length only when the passage is short; for longer passages, further increases in length have very little effect on the throughflow. On the other hand, when the taper angle is small, the energy throughflow is more sensitive to the length of the passage. It is also seen from the figures that for a given opening dimension (either radius r_1 or half-height h) and given length L , the energy throughflow is larger when the taper angle is large. (Note that in preceding figures (figs. 2, 3, 5, and 6) θ is the *total* included angle and h is the total gap spacing.)

For the circular tube and the parallel-walled channel ($\theta=0^\circ$), it is possible to derive closed-form solutions for the energy throughflow for the limiting cases of large L/r_1 and large L/h . These solutions are shown as dashed lines on the figures. For the tube, the limiting solution yields a value of $(8/3)/(L/r_1)$ for the right-hand side of equation (15); while for the parallel-plate channel, the right-hand side is given by $[2 \ln (L/h)-1]/(L/h)$. It is interesting to note that if figures 7 and 8 were plotted on a common coordinate grid, the corresponding curves for the tapered tube and the tapered gap would not coincide.

Radiant transport results for the case of specularly reflecting, diffusely emitting passage walls are available only for the circular tube (ref. 8). This information is presented in table I, in which there is also listed for purposes of comparison results for the diffusely reflecting and emitting circular tube. It is seen from the table that the specularly reflecting tube is a more efficient transmitter of radiant energy than the diffusely reflecting tube. This is especially true when the surfaces of the passage have low emittance, that is, when substantial amounts of energy are transported by the reflection process.

SUMMARY OF VERY RECENT WORK

During the time that has elapsed since the writing of this paper, new information on the radiation characteristics of cavities and passages has become available. In particular, a method of analysis for determining the radiant interchange among curved, specularly reflecting, and diffusely emitting surfaces has been formulated. Application has been made to cylindrical and conical cavities and corresponding results for

TABLE I.—Radiant Transport Through Circular Adiabatic Tubes

$$[(Q/\pi r^2)/\sigma(T_1^4 - T_2^4)]$$

$\frac{L}{r}$	Diffuse reflection	Specular reflection for—				
		$\epsilon=0.1$	$\epsilon=0.2$	$\epsilon=0.4$	$\epsilon=0.6$	$\epsilon=0.8$
10	0.192	0.723	0.588	0.427	0.320	0.246
20	.109	.600	.438	.283	.202	.152
40	.0595	.449	.304	.173	.113	.078

ϵ_a , α_a are now available (ref. 22). A further generalization was carried out to account for the fact that real surfaces are neither pure specular reflectors nor pure diffuse reflectors. For a model wherein the hemispherical reflectance ρ is represented as the sum of specular and diffuse components, radiation characteristics have been computed for cylindrical and conical cavities and for circular-tube passages (ref. 23).

Further study has been performed on the absorption of parallel-ray bundles in cavities. Specifically, solutions have been carried out for a specularly reflecting cylindrical cavity irradiated by an obliquely inclined ray bundle (ref. 24).

The effect of an axial variation in cavity-wall temperature on the apparent emittance was discussed at some length following the presentation of the paper. Numerical information relating to this matter is now available in the literature (ref. 25).

REFERENCES

1. ECKERT, E. R. G., and DRAKE, ROBERT M., Jr.: Heat and Mass Transfer. Second ed., McGraw-Hill Book Co., Inc., 1959.
2. SPARROW, E. M., ALBERS, L. U., and ECKERT, E. R. G.: Thermal Radiation Characteristics of Cylindrical Enclosures. Trans. ASME, Ser. C, Jour. Heat Transfer, vol. 84, no. 1, Feb. 1962, pp. 73-81.
3. SPARROW, E. M., and JONSSON, V. K.: Absorption and Emission Characteristics of Diffuse Spherical Enclosures. Trans. ASME, Ser. C, Jour. Heat Transfer, vol. 84, no. 2, May 1962, pp. 188-189.
4. SPARROW, E. M.: Radiant Absorption Characteristics of Concave Cylindrical Surfaces. Trans. ASME, Ser. C, Jour. Heat Transfer, vol. 84, no. 4, Nov. 1962, pp. 283-293.
5. HOTTEL, HOYT C.: Radiant Heat Transmission. Heat Transmission. William H. McAdams, ed., Third ed., McGraw-Hill Book Co., Inc., 1954, pp. 55-125.
6. PERLMUTTER, M., and SIEGEL, R.: Heat Transfer by Combined Forced Convection and Thermal Radiation in a Heated Tube. Trans. ASME, Ser. C, Jour. Heat Transfer, vol. 84, no. 4, Nov. 1962, pp. 301-311.
7. SIEGEL, R., and PERLMUTTER, M.: Convective and Radiant Heat Transfer for Flow of a Transparent Gas in a Tube with a Gray Wall. Int. Jour. Heat Mass Transfer, vol. 5, 1962, pp. 639-660.
8. PERLMUTTER, M., and SIEGEL, R.: Effect of Specularly Reflecting Gray Surface on Thermal Radiation Through a Tube and From Its Heated Wall. Trans. ASME, Ser. C, Jour. Heat Transfer, vol. 85, no. 1, Feb. 1963, pp. 55-62.
9. BUCKLEY, H.: On the Radiation From the Inside of a Circular Cylinder. Phil. Mag., vol. 4, no. 23, 1927, pp. 753-762.
10. USISKIN, C. M., and SIEGEL, R.: Thermal Radiation From a Cylindrical Enclosure With Specified Wall Heat Flux. Trans. ASME, Ser. C, Jour. Heat Transfer, vol. 82, no. 4, Nov. 1960, pp. 369-374.
11. SPARROW, E. M., and JONSSON, V. K.: Thermal Radiation Absorption in Rectangular-Groove Cavities. J. Applied Mechanics, vol. E30, 1963, pp. 237-244.
12. SPARROW, E. M.: Application of Variational Methods to Radiation Heat-Transfer Calculations. Trans. ASME, Ser. C, Jour. Heat Transfer, vol. 82, no. 4, Nov. 1960, pp. 375-380.
13. ECKERT, E. R. G., and SPARROW, E. M.: Radiative Heat Exchange Between Surfaces With Specular Reflection. Int. Jour. Heat Mass Transfer, vol. 3, 1961, pp. 42-54.
14. SPARROW, E. M., ECKERT, E. R. G., and JONSSON, V. K.: An Enclosure Theory for Radiative Exchange Between Specularly and Diffusely Reflecting Surfaces. Trans. ASME, Ser. C, Jour. Heat Transfer, vol. 84, no. 4, Nov. 1962, pp. 294-300.
15. SPARROW, E. M., and LIN, S. H.: Absorption of Thermal Radiation in V-Groove Cavities. Int. Jour. Heat Mass Transfer, vol. 5, 1962, pp. 1111-1115.
16. DE VOS, J. C.: Evaluation of the Quality of a Black Body. Physica, vol. 20, 1954, pp. 669-689.
17. KRISHNAN, K. S., and SUNDARAM, R.: The Distribution of Temperature Along Electrically Heated Tubes and Coils, I. Theoretical. Proc. Royal Society, ser. A, no. 257, 1960, pp. 302-315.
18. KRISHNAN, K. S.: Effect of Specular Reflexions on the Radiation Flux From a Heated Tube. Nature, vol. 187, no. 4732, (Letters to the Editors) July 9, 1960, p. 135.
19. KRISHNAN, K. S.: Effect of Specular Reflections on the Radiation Flux From a Heated Tube. Nature, vol. 188, no. 4751, (Letters to the Editors) Nov. 19, 1960, pp. 652-653.
20. SPARROW, E. M., and JONSSON, V. K.: Radiant Emission Characteristics of Diffuse Conical Cavities. Jour. Optical Soc. America, vol. 53, 1963, pp. 816-821.
21. SPARROW, E. M., and JONSSON, V. K.: The Transport of Radiant Energy Through Tapered Tubes and Gaps. Trans. ASME, Ser. C, Jour. Heat Transfer, vol. 86, no. 1, Feb. 1964, p. 132.

22. LIN, S. H., and SPARROW, E. M.: Radiant Interchange Among Curved Specularly Reflecting Surfaces—Application to Cylindrical and Conical Cavities. ASME paper 64-WA/HT-5. To be published in Trans. ASME, Ser. C, Jour. Heat Transfer.
23. SPARROW, E. M., and LIN, S. H.: Radiation Heat Transfer at a Surface Having Both Specular and Diffuse Reflectance Components. To be published in Int. Jour. Heat Mass Transfer.
24. LIN, S. H., and SPARROW, E. M.: Absorption Characteristics of a Specularly Reflecting Cylindrical Cavity Irradiated by an Obliquely Inclined Ray Bundle. To be published in Applied Optics.
25. SPARROW, E. M.: Radiant Emission Characteristics of Nonisothermal Cylindrical Cavities. Applied Optics, vol. 4, no. 1, Jan. 1965, pp. 41-43.

DISCUSSION

LES CANOTIN, Aerospace: Are the cavities in which you measure ϵ and α characteristics open-end cavities or are they truncated?

SPARROW: Every cavity has a finite depth, with a surface closing the end of the cavity.

CANOTIN: Have you found any difference between the results for the open and the closed cavities?

SPARROW: I regard a cavity with an open end as a passage, and I am sure that there would be differences between the results for the open- and closed-end cases when the cavity is shallow. However, if the cavity depth is large, there would be very little difference.

DAVID P. DEWITT, National Bureau of Standards: Would you care to comment on the necessity for isothermal conditions, particularly with regard to how serious thermal gradients are in blackbodies?

SPARROW: We made computations for nonisothermal conditions some years ago. However, they have not been published, and I am unable to recall specific results at this time.

H. J. KOSTKOWSKI, National Bureau of Standards: The emittance you are referring to here, I believe, is hemispherical emittance. That is, the radiation that you are considering is the total radiation coming out in 2π steradians. Is that correct?

SPARROW: Yes, it is the total hemispherical emission of the cavity.

KOSTKOWSKI: I think it should be emphasized that these results for cavity measurements with 2π steradians do not, in general, apply to measurements with much smaller solid angles.

SPARROW: In general, I agree with you. The information needed to determine the radiant efflux from specific regions of a cavity is available in many of the papers from which this survey is drawn.

DANIEL COMSTOCK, Arthur D. Little: The results that you have filed away that take into account thermal gradients would be of great interest to all of us, and I would suggest that you publish them.

SPARROW: We did a fair amount of work in generating these results; but I was not certain that there would be sufficient interest to warrant publication.

COMSTOCK: Am I correct in understanding that the tapered tube has an adiabatic wall?

SPARROW: Yes.

COMSTOCK: Then, to some extent diffuse scattering and re-emission are indistinguishable; and this might explain why the transmission down the tube is independent of length. But for a real channel, presumably, quite a lot of the radiation would be lost in going down the tube.

SPARROW: Well, this depends on how well you insulate the tube; but the same general analysis applies.

ARTHUR KATZ, Grumman Aircraft: Have any of the results that you presented been correlated with experimental data? Also, have you considered the sensitivity of the cavity or passage characteristics to the type of surface within the cavity or passage?

SPARROW: Experimental verification will be discussed in the paper by Kelly and Moore. Our choice of parameters was based more on a desire to exhibit trends rather than on a desire to approximate a particular engineering material.

10. A Test of Analytical Expressions for the Thermal Emittance of Shallow Cylindrical Cavities

FRANCIS J. KELLY AND DWIGHT G. MOORE

NATIONAL BUREAU OF STANDARDS, WASHINGTON, D.C.

Analytical expressions for the (approximately axial) thermal emittance of a shallow cylindrical cavity were tested by means of room-temperature reflectance measurements. The measurements were made by placing a paper-lined brass cavity of adjustable depth over the specimen opening of a recording spectrophotometer. Reflectance curves were obtained from 0.40 to 0.75 μ with the plunger positioned to give cavity depth-to-radius ratios of 0, 0.5, 1.0, 1.5, and 2.0. The resulting reflectances were then converted to emittances through use of the relation that, for an opaque material, the emittance is equal to one minus the reflectance.

Two theoretical expressions predicted the emittance of a cavity with a diffusely reflecting wall to within 0.01. A closed-form expression of Gouffé, which forms the basis of a shallow-hole method for measuring the emittance of nonmetals at high temperatures, was in as good agreement with the experimental measurements as a more rigorous expression derived by a different approach.

A specular component in the reflecting behavior of the cavity wall material for light incident at large angles from the normal had a negligible effect on the cavity emittance at a depth-to-radius ratio of 0.5, but its effect became important as the cavity depth was increased.

The problem of determining the thermal emittance of a cavity from a knowledge of the emittance of the wall material and the geometry of the cavity is important both for optical pyrometry and thermal emittance measurements. Most investigators (ref. 1 to 12) have been concerned with deep cavities formed in diffusely reflecting materials. Recently, a method of measuring thermal emittance of polycrystalline ceramics has been proposed in which cylindrical reference cavities of unprecedentedly shallow depth-to-radius (L/R) ratios are used in order to minimize temperature differences between the reference cavity and the surface (ref. 13). The reliability of this method depends on the accuracy of analytical expressions for cavity emittance.

The purpose of the present study was to compare the approximately axial emittances of

cavities predicted by several analytical expressions with those obtained experimentally. The experimental measurements were made by determining the spectral reflectance of an adjustable-depth paper-lined cylindrical brass cavity from 0.40 μ to 0.75 μ and then converting these values to emittance through use of the relation that, for an opaque material, the emittance is equal to one minus the reflectance. Because the incident beam of the spectrophotometer was near normal and the viewing was hemispherical, the reflectance measurement was, in effect, the complement of the normal emittance, which is the property of interest in the shallow-hole method (ref. 13).

The method used for testing the analytical expressions had three distinct advantages over the more direct approach of measuring emittance at high temperatures. First, the prob-

lem of achieving a uniform and accurately known cavity temperature was eliminated; second, it was possible, in a single spectrophotometer run, to determine the cavity spectral emittance as a function of the surface spectral emittance, simply by lining the cavity with a selectively reflecting material; and, third, the spectrophotometer was capable of measuring reflectances to one part in 1000, which is a precision that could not be achieved easily with available thermal-emittance equipment.

It may be desirable here to review some of the phraseology and related concepts associated with the present problem. Emittance is the ratio of the flux per unit area radiated by a specimen to that radiated by a blackbody at the same temperature. It may be "total" (referring to the energy radiated throughout the entire spectrum), "hemispherical" (referring to the energy radiated in all directions), "spectral," or "directional." For a cavity, the area referred to is the area of the opening. A spectrophotometer or radiometer directed toward the opening, however, actually observes some area of the wall (side wall or bottom) of the cavity; and the apparent emittance of this observed area (which is referred to as the emittance of the cavity) exceeds the true emittance of the wall material because the radiation that the instrument observes includes radiation from the remainder of the cavity that is incident on and reflected from the observed area. The cavity emittance thus obtained depends not only on the direction of observation but also on the precise location of the observed area in the cavity. In general, the instrument is directed approximately along the axis and observes an area on the bottom of the cavity.

EXPRESSIONS FOR EMITTANCE OF SHALLOW CYLINDRICAL CAVITIES

Three general methods have been employed for deriving equations to express cavity emittance (ref. 14). The first, which was used by Ribaud (ref. 1 and 2), Gouffé (ref. 3), and Michaud (ref. 4), involves the calculation of the reflectance of the cavity; that is, the fraction of the energy incident through the cavity open-

ing that later leaves the cavity after one or more reflections from the walls. According to Kirchhoff's radiation law, the reflectance of the cavity can then be converted to cavity emittance by subtracting the reflectance from unity.

Of the various expressions derived by this first approach, Gouffé's was of primary interest in the present investigation because of its proposed use in the shallow-hole method (ref. 13). Its derivation is given in the original paper (ref. 3) and also in reference 13 and will not be repeated here. Gouffé, however, was not explicit in his published paper about one of the terms used in his expression (s/S_0 in refs. 3 and 13) and this uncertainty caused some doubt about the validity of his equation for cavity emittance. However, appendix A shows that his s/S_0 term is, in fact, an exact expression for the quantity that is required.

Buckley (ref. 5), Yamauti (ref. 6), Rossmann (ref. 7), Sparrow, Albers and Eckert (ref. 8), and Liebmann (ref. 9) derived their expressions by considering the flux coming from a surface element opposite the opening. This flux includes not only that emitted by the element but also that reflected by the element from other areas of the enclosure. The recent work of Sparrow and coworkers (ref. 8), who used this approach, is especially noteworthy in that it is possible from their analysis to obtain a rigorous evaluation of the apparent emittance of any elemental area on the walls of a cylindrical enclosure. This calculation requires the use of a computer, however, because the integral equation expressing the relations is amenable only to a numerical solution.

The third method, used by De Vos (ref. 10), is based on a calculation of the influence of the hole on the radiation from other surface elements. The derived expression, however, cannot be applied easily to shallow cavities. It should be pointed out that De Vos considers a specularly reflected component in his analysis whereas the equations derived by all other investigators apply rigorously only to materials that are perfect diffusers.

The three expressions that seemed best suited for shallow cavities are those of Gouffé (ref. 3), Buckley (ref. 5), and Sparrow et al. (ref. 8). These may be written in the following forms:

Gouffé:

$$\epsilon_c = \frac{\epsilon \left[1 + (1 - \epsilon) \left(\frac{a}{A} - f \right) \right]}{\epsilon \left(1 - \frac{a}{A} \right) + \frac{a}{A}} \quad (1)$$

where

a/A ratio of area of cavity opening to total area of cavity (opening included),

$\frac{1}{2 \left[1 + \left(\frac{L}{R} \right) \right]}$ for a cylindrical cavity

$f = \frac{1}{1 + \left(\frac{L}{R} \right)^2}$ (see Appendix A for a derivation of this f term, which is the same as Gouffé's s/S_0)

L cavity depth

R cavity radius

ϵ emittance of cavity walls

ϵ_c cavity emittance

Buckley:

where, in addition to symbols used earlier,

$\epsilon_a(x'_0)$ apparent emittance of a point x'_0 on cylindrical wall of cavity

$\epsilon_a(r')$ apparent emittance of a point r' on base of cavity

d diameter of cavity

x'_0, x' dimensionless variable coordinates x_0/d and x/d , respectively, where x_0 and x are distances along cavity wall measured from cavity opening

r radial distance from center point of cavity bottom

r' dimensionless coordinate r/R

Equations (3) and (4) must be solved simultaneously. The mathematical scheme used by Sparrow et al. was a numerical solution accomplished with the aid of a digital computer.

Buckley (ref. 12), Michaud (ref. 4), and Vollmer (ref. 15) made experimental measure-

$$\epsilon_c = 1 + \frac{4\sqrt{\epsilon}(1-\epsilon) \exp\left(-\frac{L}{R}\sqrt{\epsilon}\right)}{(1-\epsilon)^2 - (1+\sqrt{\epsilon})^2 - [(1-\epsilon)^2 - (1-\sqrt{\epsilon})^2] \exp\left[-\frac{2L}{R}\sqrt{\epsilon}\right]} \quad (2)$$

Sparrow et al.:

$$\begin{aligned} \epsilon_a(x'_0) = & \epsilon + (1-\epsilon) \int_0^{L/d} \epsilon_a(x') \\ & \left\{ 1 - |x'_0 - x'| \frac{2(x' - x'_0)^2 + 3}{2[(x' - x'_0)^2 + 1]^{3/2}} \right\} dx' \\ & + 4(1-\epsilon) \left(\frac{L}{d} - x'_0 \right) \int_0^1 \epsilon_a(r') \\ & \frac{\left[4 \left(\frac{L}{d} - x'_0 \right)^2 + 1 - r'^2 \right] r'}{\left\{ \left[4 \left(\frac{L}{d} - x'_0 \right)^2 + 1 + r'^2 \right]^2 - 4r'^2 \right\}^{3/2}} dr' \quad (3) \end{aligned}$$

$$\begin{aligned} \epsilon_a(r') = & \epsilon + 8(1-\epsilon) \int_0^{L/d} \epsilon_a(x') \left(\frac{L}{d} - x' \right) \\ & \frac{4 \left(\frac{L}{d} - x' \right)^2 + 1 - r'^2}{\left\{ \left[4 \left(\frac{L}{d} - x' \right)^2 + 1 + r'^2 \right]^2 - 4r'^2 \right\}^{3/2}} dx' \quad (4) \end{aligned}$$

ments of the emittance of cylindrical cavities. Buckley devised a method for determining the apparent emittance of any point on the wall of a cavity of any given configuration. He used an artificial sky to illuminate a large scale model of the cavity and an illuminometer to measure the resulting brightness on the wall of the scale model. The ratio of the measured brightness at any point on the wall to the brightness of the sky is equal to one minus the apparent emittance at that point. His models had equivalent L/R ratios greater than 8.0 and square, rectangular, and circular cross sections. He shows results for two circular cylinders having wall emittances of 0.15 and 0.265. The theoretical emittances predicted by his two-term solution for an infinitely deep cavity agreed to within 0.02 with the experimentally determined ones. He attributed the difference partially to the effect of specular components in the reflection from the

wall material when illuminated at large angles of incidence.

Michaud used a variable-depth, water-heated "unpolished brass" cavity with a wall emittance of 0.6. His measurements, which were made at 337° K, agreed with the Gouffé equation (eq. 1) to within 2 percent over an L/R range that extended from 0 to 6.0. Vollmer used an aluminum oxide cavity at 1100° K in conjunction with various optical filters. The filters permitted the cavity to be tested at wall emittances of 0.09, 0.13, 0.37, and 0.40. Two L/R ratios were used: 2.988 and 3.966. Vollmer altered Buckley's expressions to conform with his experimental conditions. His tests showed that the measured radiation intensity agreed with the intensities predicted by this altered expression to within 6 percent.

EQUIPMENT AND PROCEDURE

Figure 1 is a photograph of the adjustable cylindrical cavity used for the reflectance measurements. A scale on the plunger shaft permitted the L/R value of the cavity to be set with a precision of approximately 0.5 percent. The cavity was designed so that it could be lined with paper 0.0035-inch thick without obstructing free movement of the plunger. The clearance between the paper-lined cylinder wall and the plunger was about 0.003 inch. The paper was attached to the cylinder wall and to the top of the plunger with a thin uniform layer of rubber cement. Although the area of clear-



FIGURE 1.—Paper-lined cylindrical cavity.

ance between the cavity base and the paper-lined wall is nearly 0.3 percent of the total area of the cavity (for L/R of 0.5), it can be shown that the presence of this clearance area will have only a negligible effect on cavity reflectance.

The cavity opening was the same size as the specimen opening in the General Electric recording spectrophotometer which was used for the reflectance measurements. This instrument is described in reference 16. Basically, it consists of (a) a light source, (b) a double prism assembly for supplying a monochromatic beam, (c) an integrating sphere lined with smoked magnesium oxide with openings for a specimen and a comparison standard, and (d) a radiation and detection system. The instrument operates in the equivalent of a double-beam mode so that the reflected energy from the specimen is compared at each wavelength with that from a reference standard which, in turn, has been calibrated against freshly prepared magnesium oxide. The geometry of the instrument is such that the spectral reflectance is measured under conditions approximating normal illumination and hemispherical viewing, which is the optical equivalent of reflectance for diffuse incident energy and normal viewing; this property, in turn, is the complement of the normal spectral emittance.

Figure 2 shows that the incident beam of the instrument is at an angle of 6° from the normal to the plane of the reflectance-specimen opening. When the depth of the cavity is zero, the beam, which encompasses approximately 25 percent of the area of the specimen opening in the reflectometer, falls on the center of the movable plunger. However, as is evident in figure 2, the beam strikes the cavity base more and more off center as the plunger is lowered. Also, since the incident beam is somewhat divergent, the illuminated area of the cavity base increases slightly as the cavity depth is increased. The effect of these deviations from the conditions assumed in the derivation of the theoretical expressions will be discussed in the following section.

The reflectance measurements were made after first centering the cavity over the specimen opening of the spectrophotometer. Curves of reflectance against wavelength were then

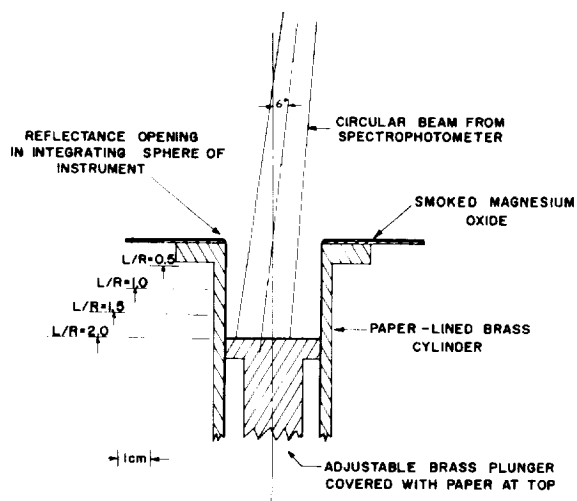


FIGURE 2.—Positioning of cylindrical cavity with respect to incident beam from spectrophotometer. Positions of plunger for various depth-to-radius (L/R) ratios are indicated at left.

obtained from 0.40 to 0.75 for cavity L/R ratios of 0, 0.5, 1.0, 1.5, and 2.0. Two series of determinations were made; one with L/R increasing in steps of 0.5 to the final value of 2.0, and the other with L/R decreasing by the same increments from 2.0 to the final value of 0. In all cases, the duplicate measurements agreed within 0.002. The average reflectance values could be read from the two curves with a precision of ± 0.001 .

The spectrophotometer curves gave the reflectances of the cavities relative to freshly deposited magnesium oxide. The values taken from these curves were then corrected for the reflectance of the magnesium oxide by using the data of Middleton and Sanders (ref. 17). The cavity emittance, $\epsilon_{c,\lambda}$, was obtained from the relation $\epsilon_{c,\lambda} = 1 - \rho_{c,\lambda}$ where $\rho_{c,\lambda}$ was the corresponding spectral reflectance. The spectral emittance of the cavity walls ϵ_λ was measured with $L/R=0$. After the data reduction, it was possible to plot $\epsilon_{c,\lambda}$ against ϵ_λ .

A broad range of ϵ_λ values was obtained by lining the variable-depth cylinder with different selectively reflecting papers. Three different nonglossy papers were used as linings in the initial measurements; one was green (fig. 3), one white, and one black. Goniophotometric measurements were made on each to determine

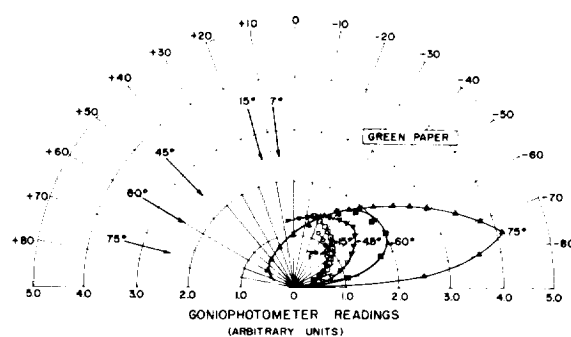


FIGURE 3.—Goniophotometric curves for nonglossy green paper on a brass backing. The curves would be a single circle for a Lambertian diffuser.

the nature of its deviation from a cosine diffuser. The geometry of the instrument used for the measurements was in accordance with ASTM Standard Practice Recommendation E167-60T (ref. 18). The light source in these measurements was a collimated beam from a tungsten lamp.

The goniophotometer data were obtained in arbitrary units rather than in absolute reflectance. In making the measurements, the detector was first placed at the normal or 0° position and the paper specimen illuminated at 75° from the normal. This reading was arbitrarily taken as 1.0; all subsequent measurements were then related to this reading. The measurements gave, in effect, the relative intensities of the reflected flux. If the material were a cosine diffuser these intensities would plot as a circle on polar coordinate paper; if the material were strongly specular, the measured values would plot with a pronounced peak in the direction of mirror reflection.

CORRECTIONS FOR INCIDENT BEAM GEOMETRY

Gouffé's expression applies to a normally incident beam of small cross-sectional area which strikes the center of the cavity bottom. As indicated in figure 2, the incident beam from the spectrophotometer deviated appreciably from this geometry. Both an experiment and a calculation were performed to determine the effect of this deviation on f , the first-reflection fraction in Gouffé's equation. The other terms in

Gouffé's equation are unaffected by the deviation.

The experimental measurements were made by using a 2¼-inch-inside-diameter cavity, lined with black velvet, in which was mounted a movable plunger of ⅝-inch radius, the same size as the specimen opening of the instrument (fig. 4). The top surface of this plunger, the only part of the cavity not lined with black velvet, was covered with one of the three papers mentioned earlier. The velvet was known to be almost completely nonreflecting; hence, the only portion of the incident energy that emerged from the cavity was due to a single reflection from the paper on the top surface of the plunger.

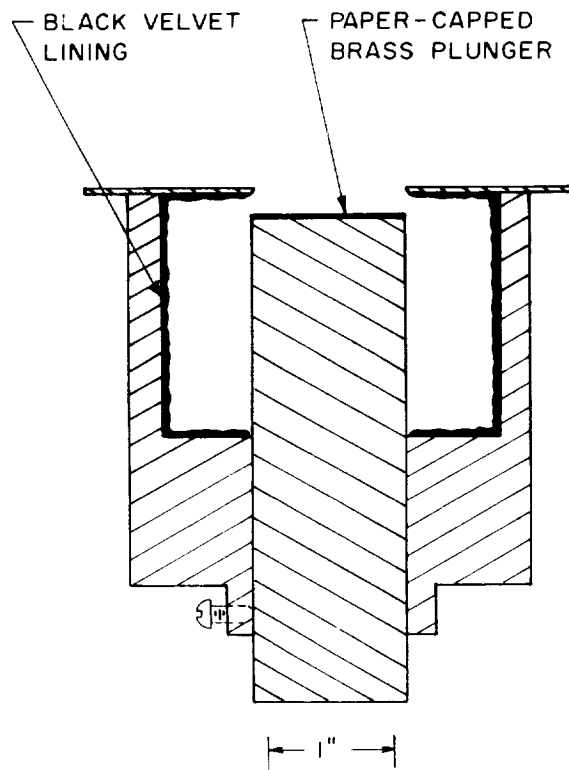


FIGURE 4.—Black-velvet-lined cavity.

Table I compares the f values obtained from these measurements with values computed by the Gouffé expression for center point illumination. Computation showed that a significant error would result, especially at low L/R values, if the f values for center point illumination were

TABLE I.—*Experimental and Computed f Values for Cylindrical Cavities*

Depth-to-radius ratio of cavity	Fraction f of energy reflected from illuminated area of base that emerges from cavity without a second reflection		
	Experimental ^a	Computed for assumed center-point illumination ^b	Computed for actual geometry of incident beam ^c
0.25	0.919	0.941	0.916
.50	.755	.800	.749
1.00	.456	.500	.453
1.50	.289	.308	.285
2.00	.187	.200	.192

^a Measured with a black-velvet-lined cylindrical cavity equipped with an adjustable paper-capped plunger.

^b Computed from expression for f given in equation (1).

^c See Appendix B.

used in equation (1) for computing the cavity emittances.

Theoretical values of f for the geometry of the instrument beam were computed by a graphical method described in appendix B. As shown in table I, there is very good agreement between values as computed in this way for the actual incident beam and those measured with the instrument.

In view of the results given in table I, corrections for incident beam geometry were made by substituting in equation (1) the f values obtained graphically for the f values as computed by the Gouffé expression for center-point illumination. In making these corrections it was assumed that after the second reflection the radiant energy within the cavity is totally isotropic and homogeneous.

EXPERIMENTAL RESULTS FOR CAVITIES LINED WITH NONGLOSSY PAPERS

Figures 5, 6, and 7 show the spectral reflectance curves obtained for white, green, and black nonglossy paper linings at different depth-to-radius ratios of the cavity. Goniophotometric curves for the green paper on the same type of brass backing are shown in figure 3. The goniophotometric curves for the black and white papers were similar to those for the green paper except for somewhat

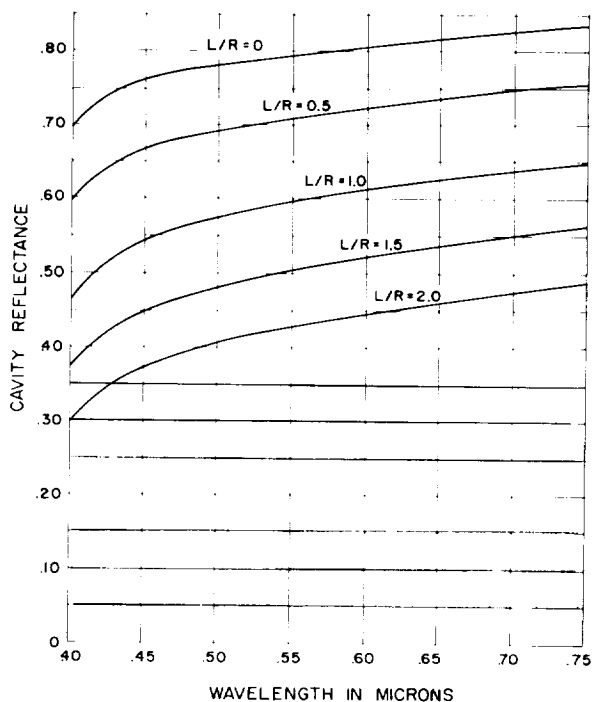


FIGURE 5.—Spectral reflectances of cavities with white paper lining.

stronger specular components at large angles of incidence.

The cavity emittances for different wall emittances are plotted in figure 8 for depth-to-radius ratios of 0, 0.5, 1.0, 1.5, and 2.0. The solid curves are those computed from the Gouffé expression with the f term corrected for the actual beam geometry. The agreement between the experimental points and the values predicted by the Gouffé equation is excellent at an L/R of 0.5, but the agreement becomes progressively poorer as the hole depth increases.

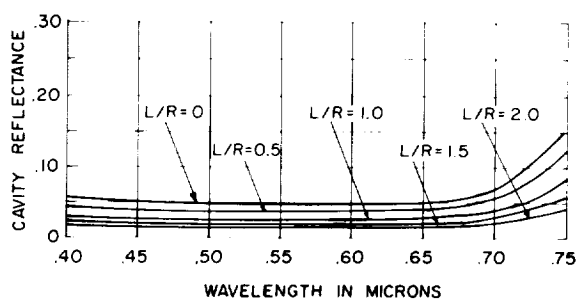


FIGURE 7.—Spectral reflectances of cavities with black paper lining.

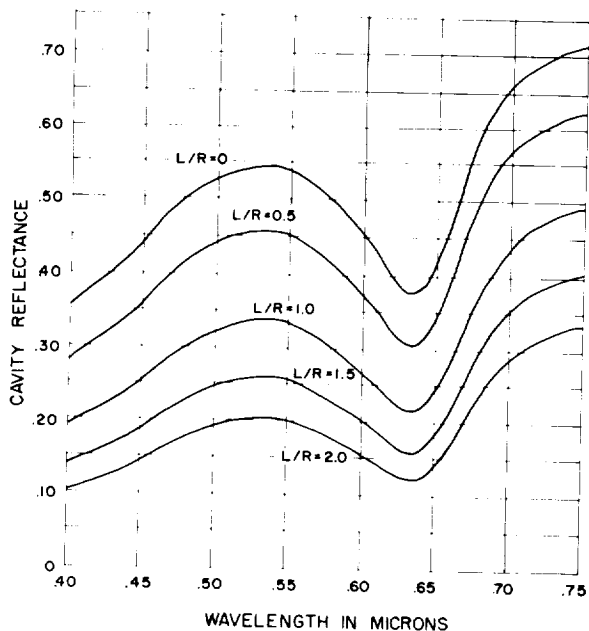


FIGURE 6.—Spectral reflectances of cavities with green paper lining.

The same type of agreement was also observed when the experimental points were plotted without correcting for the reflectance of the magnesium oxide. The principal effect of this correction would be to move the points toward lower emittance for both wall and cavity; the positions of the curves drawn through the points would be changed only slightly by the correction.

EFFECT OF SPECULAR COMPONENTS

All three papers are good diffusers (as shown in fig. 3 for the green paper) under the particular condition of the experiment in which the incident beam strikes the paper at 6° from the normal. This means that the radiant energy is well diffused inside the cavity after the first reflection. The distribution of angles at which this diffused radiation strikes the cylinder walls on the next reflection will

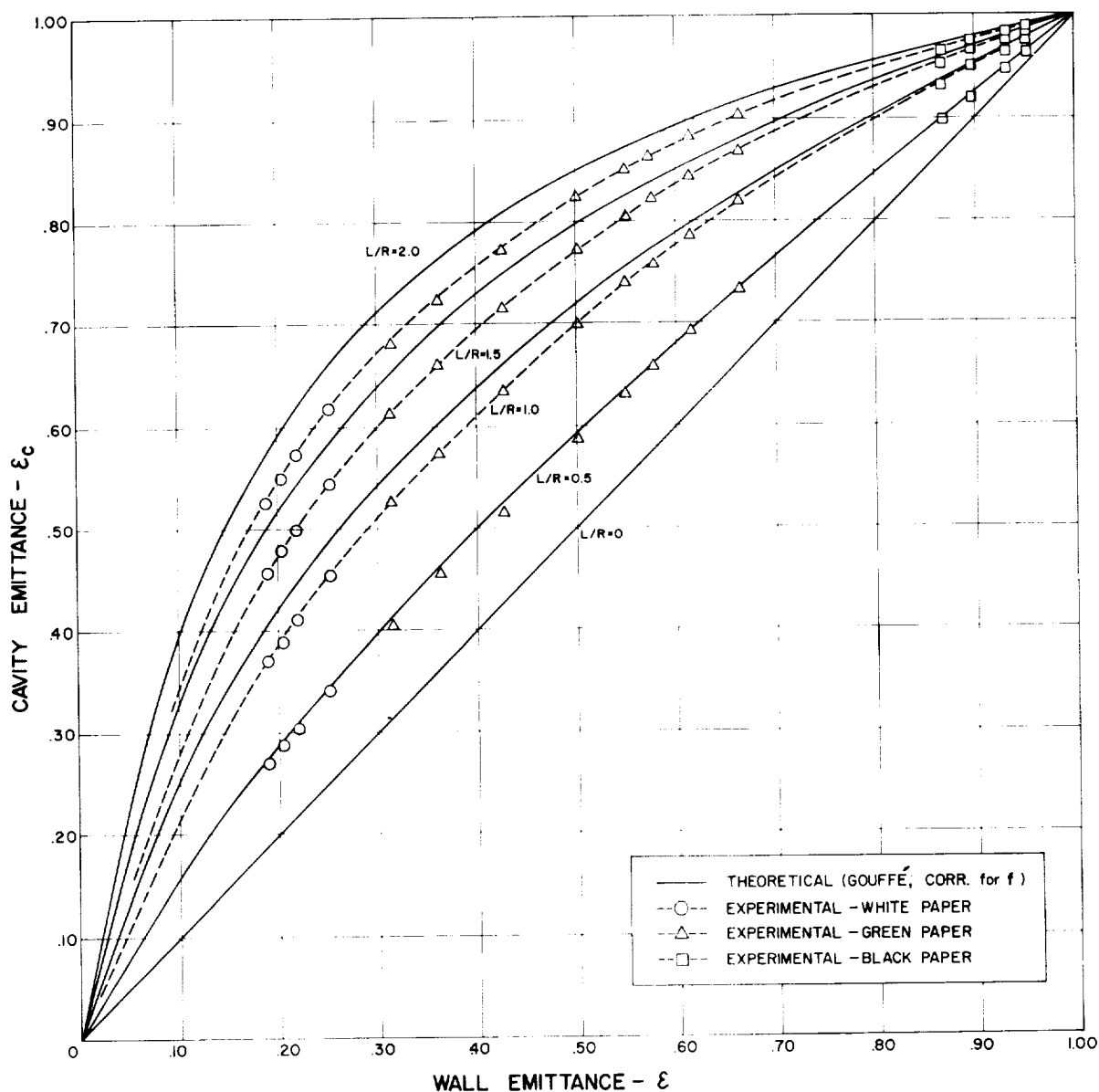


FIGURE 8.—Emittances determined by reflectance technique for cavities lined with three nonglossy papers. Solid lines were computed from Gouffé expression with corrections for beam geometry.

determine to a large extent just how well the experimental measurements will agree with a theory for cavity emittance that assumes that the walls are diffuse reflectors at all angles of incidence.

For a cavity of $L/R=0.5$ (fig. 9a) the energy from the second reflection, because of the small angles of incidence (measured from the normal), will still be almost completely diffuse,

and good agreement with theory should occur. (Figure 9 is constructed for center-point illumination for ease of illustration. Angles of incidence will, on the average, be higher for the experimental beam.) However, in a cavity of $L/R=2.0$ (fig. 9b) a significant part of the diffused radiation from the first reflection will strike the wall at fairly large angles of incidence, and because of the specular component of

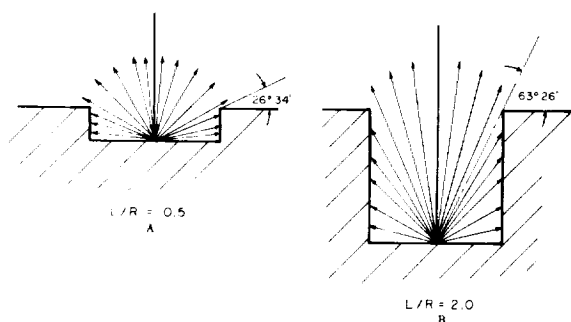


FIGURE 9.—Sketch illustrating angles of incidence at which radiation diffused by a first reflection (center-point illumination) strikes the walls on the second reflection.

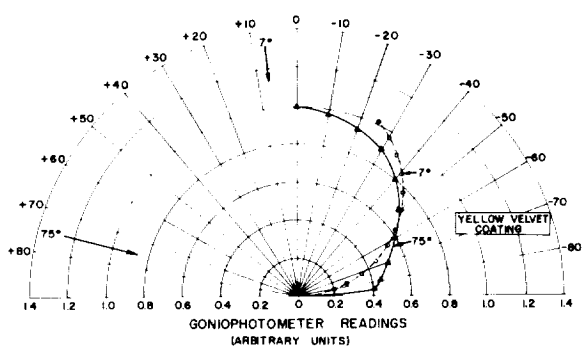


FIGURE 10.—Goniophotometer curves for the yellow "glare-free velvet" coated paper on a brass backing.

reflected energy that is present at these large angles (fig. 3), more of this energy will emerge from the opening than would emerge if the wall were a perfect diffuser. Hence, the measured cavity reflectance should be higher (and the cavity emittance lower) than the values predicted by a theory which is based on a perfectly diffusing wall surface.

Figure 8 shows that the cavity emittances as determined from the reflectance measurements are in good agreement with the Gouffé expression at an L/R of 0.5. The lack of agreement for deeper cavities might be explained then by the presence of specular components at large angles of incidence.

To determine experimentally whether a better agreement with theory could be achieved if the walls of the cavity were lined with a material that was less specular at large angles of inci-

dence than the papers used for the first measurements, a second test was made in which the brass cavity was lined with a recently developed "glare-free velvet" coating.¹ A yellow coating was selected for these measurements and applied at uniform thickness to one surface of a white paper. The coated paper was then used to line the cavity.

The goniophotometric curves for the coated paper on a brass backing are shown in figure 10. It is apparent from these curves that this particular lining is a much better diffuser than the ordinary mat papers used for the earlier measurements. The spectral reflectance curves for the cavity with this yellow lining are given in figure 11. The wall reflectances were converted to emittances and plotted against the corre-

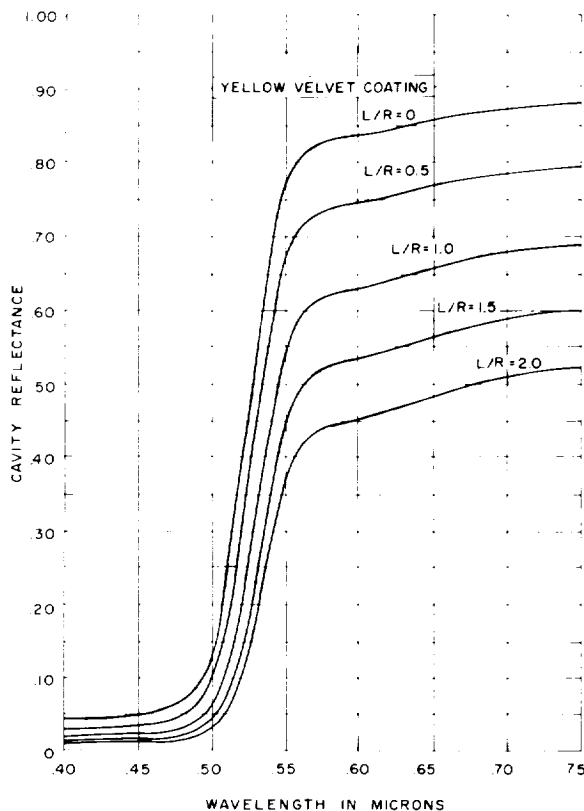


FIGURE 11.—Spectral reflectances of cavities lined with yellow "glare-free velvet" coating.

¹ Available from 3M Reflective Products Division, Minnesota Mining and Manufacturing Co.

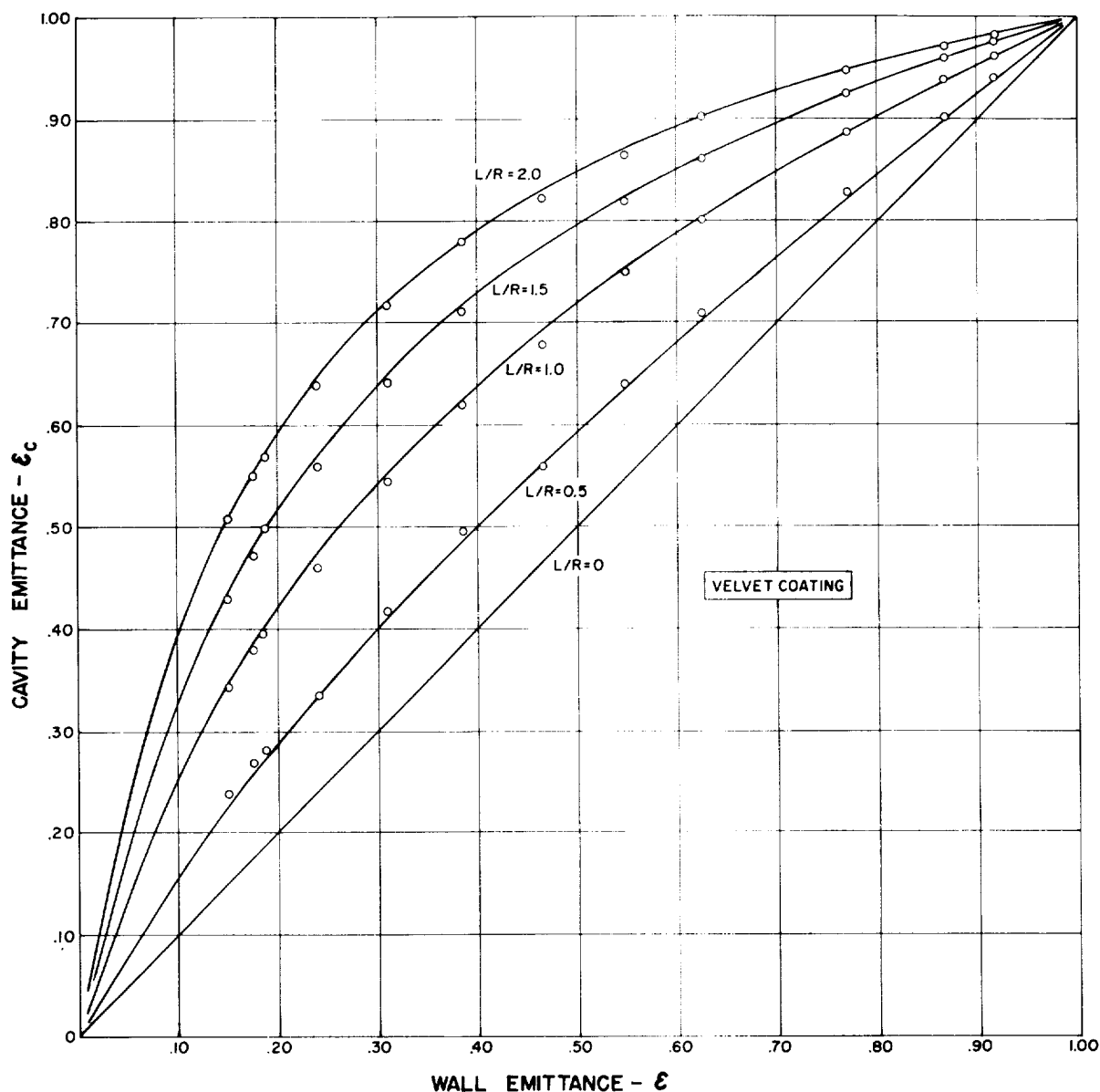


FIGURE 12.—Emittances (circled points) determined by reflectance technique for cavities lined with yellow “glare-free velvet” coating. Solid lines were computed from Gouffé expression with corrections for geometry of incident beam.

sponding cavity emittances by the same procedures used earlier. Figure 12 shows the resulting plot. The fact that the experimental points for this velvet-finish paper are in better agreement with the Gouffé expression than the experimental points obtained from the cavities lined with ordinary mat papers indicates that specular components were affecting the earlier results.

AGREEMENT BETWEEN ANALYTICAL EXPRESSIONS AND EXPERIMENTAL MEASUREMENTS

Table 2 illustrates the degree of conformity between the emittance values predicted by each of the three theoretical derivations and the values obtained experimentally. To obtain the cavity emittances for Sparrow et al.,

TABLE II.—Comparison of Experimental and Theoretical Cavity Emittances

L/R	Wall emittance, ϵ_w	Experimental ^a		Gouffé ^b	Gouffé corr. ^c	Sparrow, <i>et al.</i> ^d	Buckley ^e
		Mat papers	Velvet coating				
0.5	0.20	0.285	0.297	0.269	0.284	-----	0.314
	.40	.492	.507	.481	.498	-----	.544
	.50	.588	.600	.576	.592	0.588	.634
	.75	.803	.813	.795	.805	.805	.837
	.90	.923	.927	.919	.924	.924	.938
1.0	.20	.386	.417	.400	.418	-----	.425
	.40	.610	.633	.618	.638	-----	.659
	.50	.698	.716	.700	.718	.706	.741
	.75	.871	.875	.865	.876	.872	.894
	.90	.951	.951	.949	.953	.951	.961
1.5	.20	.472	.514	.508	.516	-----	.525
	.40	.693	.723	.719	.728	-----	.749
	.50	.770	.793	.788	.796	-----	.817
	.75	.908	.917	.911	.917	-----	.932
	.90	.967	.970	.968	.970	-----	.976
2.0	.20	.546	.590	.584	.590	-----	.613
	.40	.755	.788	.784	.790	-----	.817
	.50	.823	.847	.843	.848	.848	.871
	.75	.936	.942	.939	.942	.942	.955
	.90	.977	.980	.979	.980	.980	.985

^a Interpolated from curves drawn through the data points shown in figs. 8 and 12.

^b Computed for center-point viewing; no correction for beam geometry.

^c Corrected for beam geometry.

^d Corrected for beam geometry through use of curves given in ref. 8.

^e No correction for beam geometry required.

the curves of $\epsilon_a(x')$ against r' in reference 8 were enlarged photographically by a factor of 5. Emittance values were read from these curves with an accuracy of 0.001, and the r' values with an accuracy of 0.01 R . Then these values were used to obtain the average emittance of the area illuminated by the incident beam. The averaging process was very similar to that described in appendix B.

Values included in the same table show the type of agreement with the Gouffé expression with the f value computed for center-point viewing, which is the complement of center-point illumination in the reflectance measurements. This is a condition that could not be duplicated with the spectrophotometer that was used for the measurements. Poor agreement would be expected between experimental values and those computed for center-point viewing, and table II shows that the agreement was relatively poor. However, when the f term in the Gouffé expression was modified to conform with the off-center diverging beam of

the instrument, the agreement was excellent. It should be emphasized that this modification of the f term was not a modification of the Gouffé expression; it was necessitated only to make the Gouffé expression conform with the beam geometry of the instrument used for the measurements.

When this correction was made for the incident beam, excellent agreement resulted between the experimentally determined cavity emittances and those predicted by the Gouffé expression. This same type of agreement with the experimental values was also observed for the expression derived by Sparrow *et al.* Buckley's expression, however, predicted cavity emittances that were higher than the experimental values by as much as 7 percent.

Total normal emittances when computed for the cavity center by the Gouffé and the Sparrow expressions are in excellent agreement in the shallow cavity range. However, for deep holes the Gouffé emittances are lower than those of Sparrow *et al.*; for example, for a wall emittance

of 0.5 and an L/R of 8.0, the Gouffé expression predicts an emittance of 0.966 while the Sparrow analysis gives 0.988.

APPLICATION OF RESULTS TO SHALLOW-HOLE METHOD

Gouffé derives his equation for the emittance of a specimen in which a reference cavity of known geometry has been drilled by introducing into equation (1) for the emittance of a cavity the ratio E , defined as

$$E = \frac{I_s}{I_c} = \frac{\frac{I_s}{I_{BB}}}{\frac{I_c}{I_{BB}}} = \frac{\epsilon_s}{\epsilon_c} \quad (5)$$

where I_s is the normal radiant flux per unit area from a plane (noncavity) surface of a specimen, I_c is the normal radiant flux per unit area from a cavity formed in the specimen material, I_{BB} is the radiant flux per unit area from a blackbody radiator under the same conditions at the same temperature, ϵ_s is the emittance of the specimen, and ϵ_c is the emittance of the cavity. Assuming that the emittance of the cavity wall ϵ is the same as that of the specimen surface ϵ_s , Gouffé combines equation (5) with equation (1) to obtain

$$\epsilon_s = \frac{E \left(1 + \frac{a}{A} - f \right) - \frac{a}{A}}{1 - \frac{a}{A} + E \left(\frac{a}{A} - f \right)} \quad (6)$$

Equation (6) is the expression used in the shallow hole method (ref. 12). Obviously, it can be valid only if equation (1) is valid. Table II shows that the experimental values of cavity emittance are in excellent agreement with those predicted by equation (1), at least for a material that is as good a diffuser as the velvet coating. It would appear then that the shallow-hole method when based on the Gouffé equation can be used with good reliability if the method is restricted to those materials that are diffusely reflecting. Most fine-grained oxide materials fall into this category. However, if the method should be

used for materials that have strong specular components at large angles of incidence (relative to the normal), very appreciable errors could be expected. Such errors could be minimized, however, by maintaining the depth-to-radius ratio of the reference cavity at the lowest value consistent with good measurement precision. A second precaution in the use of equation (6) with the shallow-hole method is that the f term should be corrected by the method outlined in appendix B if an appreciable area of the cavity base is viewed by the radiation detector. This correction may be neglected if the viewed area is at the center of the cavity base and is small compared to the total cross-sectional area of the cavity.

CONCLUSIONS

The results of a study of the emittances of cylindrical cavities with depth-to-radius ratios of 0.5, 1.0, 1.5, and 2.0 have indicated the following:

1. When the wall material was a good diffuse reflector, the theoretically derived expressions of Gouffé and of Sparrow et al. predicted cavity emittance to within 0.01. Emittances predicted by both expressions agreed equally well with the experimentally obtained emittance.
2. If the cavity material had relatively large specular components at large angles of incidence, relative to the normal, the experimental and theoretical emittances still agreed for a depth-to-radius ratio L/R of 0.5. However, the agreement became progressively poorer as the L/R value increased; the emittance difference at $L/R=2.0$ was 0.035.
3. An expression derived by Buckley predicted cavity emittances that were always higher than the experimentally determined values; the maximum deviation was 0.037 for $L/R=0.5$.
4. The Gouffé expression can be used with the shallow-hole method of measuring thermal emittance with good reliability for materials that are good diffuse reflectors.

ACKNOWLEDGMENT

The assistance of the following members of the National Bureau of Standards staff is gratefully acknowledged by the authors: V. R. Weidner, for measuring the spectral reflectance of the cavities and for suggesting the design for the black-velvet-lined cavity; David G. Goebel and Patrick B. Caldwell for obtaining the goniophotometric data; and J. C. Richmond, W. D. Hayes, Jr., and Harry J. Keegan for many helpful criticisms and suggestions during the course of the investigation.

REFERENCES

1. RIBAUD, G., and NIKITINE, S.: Realisation du corps noir au point de fusion du palladium par la méthode du tube. *Ann. Phys.*, vol. 10, ser. 11, 1929, pp. 451-482.
2. RIBAUD, G.: *Traite de pyrometrie optique*. Editions de la Revue d'Optique théorique et instrumentale, Paris, 1931, p. 231.
3. GOUFFÉ, ANDRÉ: Corrections d'ouverture des corps noirs artificiels compte tenu des diffusions multiples internes. *Rev. d'Optique*, vol. 24, no. 1-3, Jan.-Mar. 1945, pp. 1-10.
4. MICHAUD, M.: Facteur d'émission des cavités de formes géométriques simples, *Comp. Rend. Acad. Sc.*, vol. 226, Mar. 22, 1948, pp. 999-1000.
5. BUCKLEY, H.: I. On the Radiation From the Interior of a Reflecting Cylinder. *Phil. Mag.*, vol. 4, Oct. 1927, pp. 753-762. II. On the Radiation From the Inside of a Circular Cylinder. *Phil. Mag.*, vol. 6, Sept. 1928, pp. 447-457. III. On the Radiation From the Inside of a Circular Cylinder. *Phil. Mag.*, vol. 17, Mar. 1934, pp. 576-581.
6. YAMAUTI, Z.: Recherche d'un radiator intégral au moyen d'un corps cylindrique. *Com. Int. des Poids et Mes. Proc. Verb.*, vol. 16, 1933, p. 243.
7. ROSSMANN, M. G.: Radiation From a Hollow Cylinder. *British Jour. Appl. Phys.*, vol. 6, July 1955, pp. 262-264.
8. SPARROW, E. M., ALBERS, L. U., and ECKERT, E. R. G.: Thermal Radiation Characteristics of Cylindrical Enclosures. *Trans. ASME, ser. C, Jour. Heat Trans.*, vol. 84, no. 1, Feb. 1962, pp. 73-81.
9. LIEBMANN, GERHARD: Ein einfacher schwarzer Körper. *Z. Tech. Phys.*, vol. 12, no. 9, 1931, pp. 433-435.
10. DE VOS, J. C.: Evaluation of the Quality of a Blackbody. *Physica*, vol. XX, no. 10, Oct. 1954, pp. 669-689.
11. WILLIAMS, CHARLES S.: Discussion of the Theories of Cavity-Type Sources of Radiant Energy. *Jour. Optical Soc. of America*, vol. 51, no. 5, May 1961, pp. 564-571.
12. BUCKLEY, H.: On the Blackness of Black Bodies and the Illumination of Light Wells. *Jour. Optical Soc. of America*, vol. 18, no. 3, Mar. 1929, pp. 216-222.
13. MOORE, DWIGHT G.: Investigation of Shallow Reference Cavities for High-Temperature Emittance Measurements. *Measurement of Thermal Radiation Properties of Solids*, Joseph C. Richmond, ed., NASA SP-31, 1963, pp. 515-526.
14. RUTGERS, G. A. W.: Temperature Radiation of Solids. *Handbuch der Physik*, Bd. XXVI, Teil 2, no. 9, 1958, pp. 129-170.
15. VOLLMER, J.: Study of Effective Thermal Emittance of Cylindrical Cavities. *Jour. Optical Soc. of America*, vol. 47, no. 10, Oct. 1957, pp. 926-932.
16. GIBSON, KASSON S.: Spectrophotometry (200 to 1,000 Millimicrons). *NBS Circ. 484*, Sept. 15, 1949.
17. MIDDLETON, W. E. KNOWLES, and SANDERS, C. L.: The Absolute Spectral Diffuse Reflectance of Magnesium Oxide. *Jour. Optical Soc. of America*, vol. 41, no. 6, June 1951, pp. 419-424.
18. Tentative Recommended Practice for Goniophotometry of Reflecting Objects and Materials, ASTM Designation: E 167-60T. Pt. 8 of 1961 Book of ASTM Standards Including Tentatives. ASTM (Philadelphia) 1909-1913.
19. SUMPNER, W. E.: The Diffusion of Light. *Proc. Phys. Soc. (London)*, vol. 12, 1892, p. 10.
20. WIEN, W., and LUMMER, O.: Methode zur Prüfung des Strahlungsgesetzes absolut schwarzer Körper. *Ann. Phys.* vol. 56, 1895, p. 451.
21. WALSH, J. W. T.: Radiation From a Perfectly Diffusing Circular Disc. *Proc. Phys. Soc. (London)*, vol. 32, Feb. 1920, pp. 59-70; discussion pp. 70-71.

APPENDIX A.—DERIVATION OF f

Gouffé (ref. 3) derived his expression for the emittance of a cavity through use of a reflectance approach. In his derivation, Gouffé assumes that the radiant flux enters the cavity normally as a beam of small cross-sectional area and that it strikes the base of the cavity at the center point. He then proceeds to compute the fraction of this incident flux that will later leave the cavity after multiple reflections from the walls, which are assumed to be diffusely reflecting.

The f term which appears in equation (1) is the fraction of the reflected flux that is returned through

the opening without a second reflection. This term is the same as the s/S_0 term given by Gouffé. The proof that this expression for f is rigorous for a cylindrical cavity follows:

In figure 13, consider a narrow beam of radiant flux from an external source striking the cavity bottom at a small area at A . This flux will be diffused in accordance with the cosine law so that it will uniformly illuminate the interior of an imaginary sphere of radius r drawn through points ABCD (refs. 19 and 20). Since the sphere is uniformly illuminated the fraction f of the

reflected flux that will emerge through the opening BD without a second reflection is given by the ratio of the area a_s of the spherical segment BCD to the total area of the sphere A_o , or

$$f = \frac{a_s}{A_o},$$

or, with $A_o = 4\pi r^2$ and $a_s = 4\pi r^2 - 2\pi rL$

$$f = \frac{4\pi r^2 - 2\pi rL}{4\pi r^2} = 1 - \frac{L}{2r}$$

It remains to find r in terms of L and R . From figure 13,

$$r^2 = R^2 + (L - r)^2$$

$$r = \frac{R^2 + L^2}{2L}$$

The fraction f then becomes

$$f = 1 - \frac{L}{2\left(\frac{R^2 + L^2}{2L}\right)} = 1 - \frac{L^2}{R^2 + L^2}$$

$$f = \frac{1}{1 + \left(\frac{L}{R}\right)^2}$$

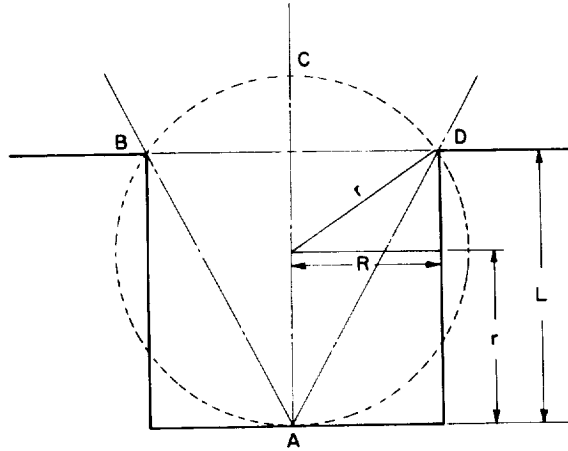


FIGURE 13.—Section through a cylindrical cavity of radius R and depth L .

APPENDIX B.—DETERMINATION OF f FOR AN OFF-CENTER INCIDENT BEAM

Consider a cylindrical cavity with diffusely reflecting walls illuminated by an incident beam of finite size that strikes the bottom of the cavity over any given area. The problem is to find f , the fraction of the energy reflected from the illuminated area that emerges from the cavity without a second reflection.

The f value for a beam striking the bottom at any point between the center and the vertical wall is given by Walsh (ref. 21):

$$f = \frac{1}{2} \left[1 - \frac{\frac{c}{R}}{\left[\left(\frac{c}{R} \right)^2 + 1 \right]^{1/2}} \right] \quad (7)$$

where

$$\frac{c}{R} = \frac{\left(\frac{L}{R} \right)^2 + \left(\frac{r}{R} \right)^2 - 1}{2 \frac{L}{R}}$$

and r is the distance of the point from the center of the cavity bottom.

The average value of f for the illuminated area is needed. This average could not be obtained analytically; hence, a graphical solution was performed. Figure 14 illustrates the method. First, the outline of both the incident beam and the cavity base were plotted to scale. Circles concentric with the base were then inscribed to form circular segments $0.02R$ in width. Next the area of each circular segment, Δa , within the illuminated area was determined and multiplied by the f value computed from equation (7) for the average

radius, r/R , of the segment. The average, \bar{f} , for the illuminated area was then computed from

$$\bar{f} = \frac{\sum f \Delta a}{\sum \Delta a}$$

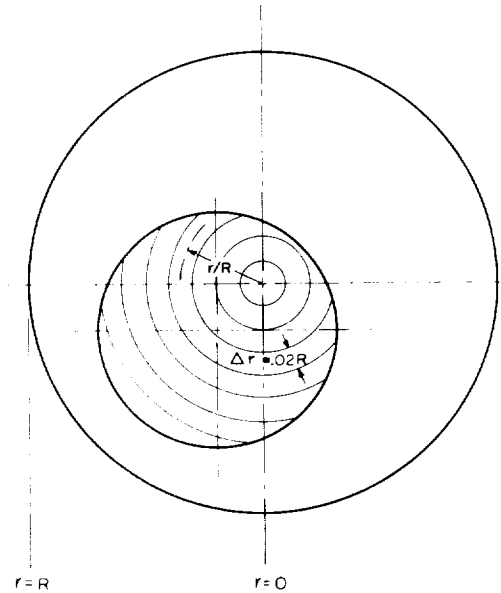


FIGURE 14.—Base of a cylindrical cavity illuminated by an off-center incident beam. (Note: For purposes of illustration circular segments are shown with a larger Δr than was used in the graphical analysis.)

DISCUSSION

E. M. SPARROW, University of Minnesota: In general, the theories were derived for total radiation, whereas you applied them for monochromatic radiation. Would you care to rationalize this difference?

KELLY: To apply the results monochromatically we can use the method of your paper, but replace your local emittance $[B(r)]/\sigma T^4$ by the monochromatic value $[B_\lambda(r)]/[J(\lambda, T)]$ where $J(\lambda, T)$ is the Planck function. The analysis otherwise remains the same.

MICHAEL T. SURH, University of Michigan: Are you able to derive the emittance from the apparent reflectance at the opening?

KELLY: Yes. The spectral, directional emittance is equal to the corresponding spectral directional absorptance of an element df on the imaginary surface of the cavity opening. This follows from a simple generalization of the argument by which von Fragstein² demonstrated the equality of the spectral, directional emittance and absorptance for an element df on the surface of an opaque material.

SURH: How do spherical and cylindrical cavities compare for the same relative cavity depth? I should think that a beam going into the spherical cavity would be more completely absorbed, so the spherical cavity should have the higher emittance. Is that right?

KELLY: I don't remember off-hand how the cylindrical and spherical cavities compare for all depth-to-radius values. However, Professor Sparrow has published the numerical results for cylinders of various depths, and his paper in this Symposium contains an analytical expression for the emittance of a spherical cavity. So the comparison can be made easily.

TIBOR S. LASZLO, Avco Corp.: With regard to the previous question, Gouffé published comparative data for spherical and cylindrical cavities. According to his findings, the cross-over point is at an L/R ratio of about 2. Below this value, the cylindrical cavity has a better effective emittance; above this value, the spherical is better. But I want to repeat a warning which I gave several years ago. In the Gouffé formula there is an error in the expression for s/S . A correction factor has to be applied to reduce the overall surface of both the sphere and the cylinder. The reduction factor corresponds to the area of the cavity opening. If the orifice area is large in relation to the length of the cylinder or to the diameter of the sphere, the correction factor

has to be used. If, however, the orifice is small, the correction factor may be neglected.

KELLY: I do not think that a correction factor, if necessary, can be very large, because the emittances predicted by the Gouffé theory agree well with experiment for shallow cylindrical cavities. Gouffé even gives the correct value for a cavity of $L/R=0$.

ROGER SCHMIDT, Minneapolis-Honeywell Research Center: Maybe it should be pointed out here that you show that specularity reduces the emittance. Possibly there is some confusion arising from the fact that Sparrow's cavity emissivity was hemispherical, whereas your measurements were normal. I wonder if you would clarify this.

KELLY: To obtain the hemispherical data that Professor Sparrow presented today, one must compute the energy loss at each point within the cavity and integrate over the whole cavity. On the other hand, we studied the apparent emissivity of a small area within the cavity. If we had illuminated the cavity over a hemisphere and collected all the radiation reflected from the cavity, I am quite sure we would have obtained Professor Sparrow's values for hemispherical emittance.

One effect of specularity on the normal emittance of the cavity can be seen from this example. If one sends a parallel beam of light normally into a very deep specular cavity, and if the base of the cavity is parallel to the cavity mouth, the reflected light will come right back through the opening, and the cavity reflectance will equal the reflectance of the cavity wall material. However, if the base reflects diffusely, a fraction ρf of the original light will return through the cavity mouth on the first reflection. Here f is the angle factor of the cavity mouth as seen from the base, and ρ is the reflectance of the base. If the angle factor f is very small, very little flux returns out of the mouth of the cavity on the first reflection. So, in this case, the normal emittance would be greater for a diffuse cavity than for a specular cavity.

SPARROW: When the analysis is made for the case in which the incoming radiation is not diffusely distributed but rather is a bundle of parallel rays, under certain circumstances the diffuse cavity is, indeed, a better absorber. Under other circumstances, that depend on the depth of the cavity, the specular cavity is a better absorber. The confusion results from the differences in the assumed conditions. I was talking about diffusely distributed incoming radiation.

KELLY: Our experiment used a bundle of approximately parallel rays falling on a certain area of the cavity bottom. The whole cavity was not illuminated directly by the incoming radiation.

SPARROW: I think your answer was a good one.

² von Fragstein, C.: On the Formulation of Kirchhoff's Law and Its Use for a Suitable Definition of Diffuse Reflection Factors. *Optik*, vol. 12, no. 2, 1955, pp 60-70. Translation available from SLA Translation Center, John Crerar Library, 35 W. 33rd St., Chicago 16, Ill.

SESSION II
SURFACE EFFECTS

CHAIRMAN: ROGER E. GAUMER

LOCKHEED MISSILES & SPACE COMPANY, PALO ALTO, CALIF.

11. A Generalized Physical Model of the Role of Surface Effects in Modifying Intrinsic Thermal Radiation Parameters

ROGER E. GAUMER

LOCKHEED MISSILES & SPACE COMPANY, PALO ALTO, CALIF.

As a basis for discussing thermal radiation characteristics, physical phenomenological models of metallic and dielectric material surfaces are presented. The role and significance of surface topography, of contaminant surface films and infused impurities, and of pore size and separation in dielectrics are reviewed; and the desirability of adequately specifying surfaces is emphasized.

The technical community has recently been confronted with a situation in which it is very difficult to make reliable correlations of experimental data on the thermal radiation properties of any material, regardless of the number of experimental determinations. This situation is only partially due to differences in experimental technique and capability. The apparent discrepancies are in considerable measure attributable to the fact that the materials being measured are not, in fact, the same physical system, with the same physical surface. This discussion will pertain to an approach to the surface effects problem from a physical phenomenological point of view; the engineering heat transfer approach will differ in method, if not in conclusions. Since there is only one true physical reality, different approaches must arrive at the same correct answer.

This discussion will be concerned primarily with two illustrations, one of them a model of a real surface of an electrically conducting material (fig. 1), the other a model of a real surface of a dielectric material (fig. 2). Emphasis will be placed on some of the general problem areas, the physical differences between the electrically

conductive and the dielectric model, wavelength-to-surface scaling parameters and, in general, a discussion of the real physical problems in obtaining and describing a physical system. The objective is to develop sufficient understanding to allow a reliable prediction in advance of the emittance or solar absorptance of the commonly used aerospace materials. There is no intent to go into depth in this

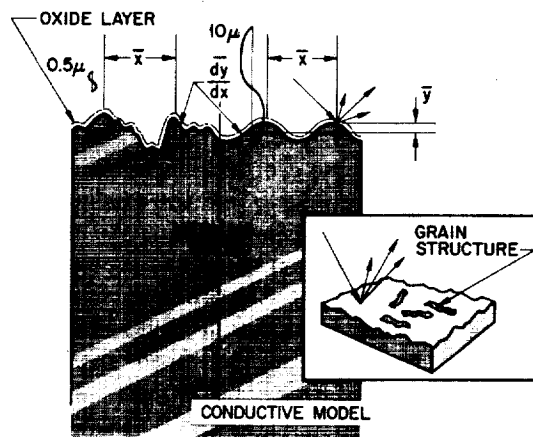


FIGURE 1.—Metallic surface model.

discussion, but rather to present a generalized physical model of the over-all effects of surfaces in modifying intrinsic thermal radiation parameters of materials. If successful, a generalized physical matrix of the important parameters will be evolved here, with many of the details being supplied by the other papers in this session.

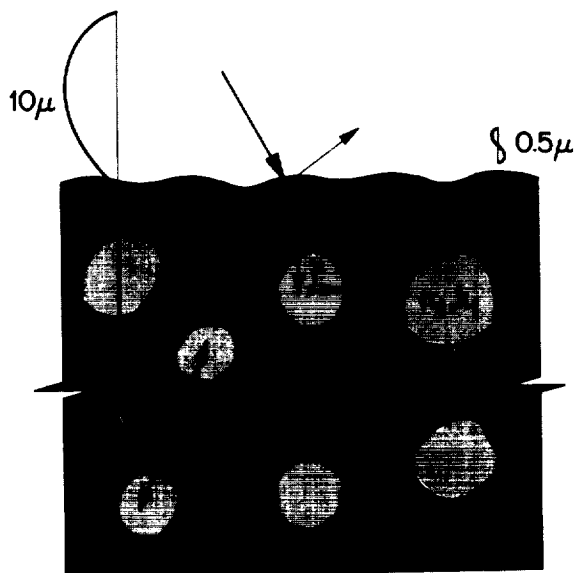


FIGURE 2.—Dielectric surface model.

CONDUCTIVE MODEL

Figure 1 is a generalized model of a metal; no distinction is drawn between the various metallic materials. The model is essentially that of a monatomic, homogeneous, isotropic solid insofar as bulk volume properties are concerned. The wavy lines impinging on the surface are characteristic wavelengths of incident thermal energy, 0.5μ having been chosen as representative of the solar spectrum and 10μ as representative of the room-temperature infrared spectrum. An attempt has been made to demonstrate two aspects of physical reality by describing the surface contour. The contour on the left is representative of surface machining, as indicated by asperities and irregularities. On the right is a typical representation of a

surface that would be produced by sandblasting, hand polishing, or a similar method.

It will be noted that the outermost skin of the surface has been drawn so as to represent the presence of surface layers and contaminants. Realistically these are thin oxide layers, grease, dust and frequently fingerprints. Note that such a thin layer of contaminant is quite effective in modifying characteristic reflection in the solar range but is not important in affecting infrared energy transfer.

The consequences of surface roughness become clear physically from a glance at figure 1. Light of about 0.5μ wavelength (solar energy) probably will be reflected by the indicated surface asperities several times before actual penetration into the volume of the material. Consequently, if a surface is rough in the same dimensional sense as the wavelength of sodium light, there will be multiple internal surface reflections and significantly increased surface absorption. If that same physical surface is considered with respect to a 10μ infrared wavelength, it seems clear that the infrared is unaffected by the relatively minute geometrical surface irregularities.

It is also evident that the angular orientation of regular surface disturbances is important. If for instance, the surface were represented by a 60° V-groove geometry and all the energy were incident 60° to the normal, an equivalent blackbody would be the result. Incident energy oblique to the surface would suffer a very different modification. The physical consequences of this model are that the important characteristics in determining the effect of surface geometry modifications are the average separation of the peaks \bar{x} , the average height of the peaks \bar{y} and the average slope of the irregularities $d\bar{y}/d\bar{x}$. The model should be three-dimensional to be realistic, and the inset in figure 1 attempts to portray the real surface characteristics of waviness and general topographic structure.

The small dark marks in the upper left hand corner of figure 1 are contaminants which in this micro-inch geometry penetrate the surface as a result of mechanical infusion of contaminants, work hardening processes, and machining operations; these must be considered as

impurities. The illustration indicates the possible consequences of grain refining due to cold working or recrystallization.

In order to establish the relative importance of the various physical phenomena it is necessary to consider the effects as a function of the ratio of the wavelength of incident energy to the dimension of a surface disturbance. In other words, one may reasonably expect micro-inch disturbances to influence the reflection or absorption of energy of optical wavelengths but not of infrared. Conversely, only gross microscopic surface phenomena would be expected to alter significantly the infrared reflective characteristics of material. These statements are not adequately confirmed by existing experimental data and should be tested by a suitable set of experiments. One immediate conclusion is that a dielectric material would be expected to influence the infrared wavelengths more strongly, as the average pore size and separation are of this magnitude.

Such phenomena as destructive interference would be exhibited only in the presence of a surface film of the order of $0.1\ \mu$; only in this quarter-wavelength region would interference phenomena be important. In this instance, abundant confirmatory experimental evidence does exist. The deposition of thin contaminant films of smoke or grease on a metallic surface is best detected experimentally in the ultraviolet region—an evident quarter-wavelength phenomenon. In fact, experience to date has been that if degradation does not occur in the ultraviolet, it will not occur at any longer wavelength.

It may be instructive to consider a few of the prevalent notions of a "surface". There is in nature no such thing as a pure surface. A real surface looks a great deal more like that of figure 1 than the straight line that an analyst draws on a clean white sheet of paper. Similarly, there is no such thing as an opaque or a transparent material. The degree of opacity must be specified in terms of absorption coefficient which is not only dependent on wavelength but also dependent on surface condition and geometry. Only by an adequate understanding of the physical nature of real surfaces will it become possible to perform reproducible ex-

periments. One might conjecture that the intrinsic emittance of a metallic conductor is very much less important in determining the effective emittance of a real sample of the metal—for example, aluminum—than is the surface geometry and contamination condition.

DIELECTRIC MODEL

Figure 2 is a generalized physical concept of a dielectric surface model. Again, the dimensions are worthy of note. On the left is a $10\text{-}\mu$ infrared wavelength and on the right a $0.5\text{-}\mu$ solar wavelength. While the penetration depth of solar radiation into metals is usually 100 to 1000 Å the penetration depth of solar radiation into a dielectric is three to four orders of magnitude greater. The average depth for complete optical opacity runs from a few thousandths of an inch for strongly absorbing materials to several inches or feet for relatively transparent, or glassy, substances. In this dielectric model, the spherical dots are representative of pigment or, generally, solid material. The background in figure 2 is representative of the vehicle which holds together this particular aggregate. The medium (vehicle) could be representative of that in any pigment-vehicle paint system. A reasonable extension of this model would be one in which some of the other dots are considered to be metallic in nature, which would lead to a physically adequate model of a semiconductor. In the dielectric, the physical processes that govern the absorption of energy are very different from those for a metallic conductor. It is intuitively obvious that the surface as such is relatively less important in modifying the intrinsic thermal radiative parameters than is the surface of an electrical conductor. Also, the modifying effects of surface films or contaminants are relatively less important. These general observations lead to the conclusion that the bulk structure of a dielectric material is the dominant factor in determining effective radiation parameters.

Again, the absorption of incident energy by a dielectric system is dependent upon several obvious physical parameters. First, as indicated by the black arrows, some of the incident energy will suffer first-surface reflection. The

energy transmitted into the first surface will suffer second-surface reflection dependent upon the nature of the layer and the relative indices of refraction. The energy continuing on in the bulk of the solid is absorbed by the standard optical processes of scattering, back-scattering and true absorption. The degree of absorption is dependent upon the refractive indices of the scatter centers relative to the refractive index of the binder. In a sintered material, the index of refraction and the absorption coefficient for the binder approach unity. Probably the most important parameter in determining absorption within a dielectric is the particle separation. This implies that the basic phenomenon is back-scattering between voids. It is known, however, that the pigment particle size and shape is also important. Undoubtedly the two most important parameters are the particle average radius \bar{r} and the interparticle separation \bar{d} . Additionally, standard processes of manufacture result in the coalescing of foreign material around the scattering centers, and, thus, an additional complicating factor is introduced. The existence of this phenomenon is indicated by the dark border on several of the dots. The infusion of impurities towards the top of the material specimen, which is a natural physical consequence of manufacture, is also indicated in figure 2. Here the impurity effect on thermal radiative parameters is probably percentage-wise less important than in the metallic model.

If an attempt is made to extrapolate the dielectric model to elevated temperatures, a new set of difficulties present themselves. Now the energy content of the body is of such a magnitude that the body itself constitutes a significant source of thermal radiation. The sample is variously transparent or translucent to its own radiation. Electromagnetic energy is not only entering the surface but is also being generated and transmitted within the volume. All of these physical processes are pronouncedly wavelength dependent. The only suitable analytical approach to the solution of this problem is that involving a complete conservation

of energy equation. The elevated-temperature heat balance for a glassy material being externally irradiated is probably best determined experimentally because of the difficulties just mentioned.

CONCLUDING REMARKS

The intent of this paper has been to provide a physical phenomenological model which is useful for determining and evaluating the relative importance of those physical parameters which influence the thermal radiative behavior of real specimens of real materials.

Those parameters which have been identified as possessing considerable importance are:

- Surface geometry and topography
- Contaminant films and infused impurities
- Pore size and separation in dielectrics.

Intermediate between the models of electrical conductors and electrical insulators is probably that of the semiconductor. Much more information is required prior to the formulation of a reliable model. Directional dependence of reflection is an example of an area where more information is required. A significant omission in this paper has been discussion of the optical behavior of radiation originating within the solid at the surface when leaving the sample.

It seems clear that the first and most necessary step in enhancing our knowledge of the governing physical processes of absorption, reflection, and transmission is to develop a suitable means of reproducibly preparing and specifying a surface in terms of those parameters indicated to possess first-order importance. It will be possible to correlate existing experimental information on, say, the total hemispherical emittance of beryllium only when each datum point is accompanied by an adequate specification of the surface geometry and topography, impurity content, thin film, etc. The workers in the field of thermal radiative transfer in solids should devote their immediate attention to establishing suitable techniques for surface preparation, characterization, and specification.

DISCUSSION

TIBOR S. LASZLO, AVCO Corporation: I would like to offer a comment relating to what Dr. Gaumer said at the beginning. We made total emittance measurements on pure alumina samples which differed only in their surface characteristics. A Talysurf instrument was used to measure the differences in surface finish. We found that even in cases where the center line average roughnesses differed by a factor of 10 or even 20, the emittances were the same. Of course, this would bear out the fact that the emittance in this case is not a surface-dependent characteristic but is defined by what

we call volume emittance. For such materials it is sometimes possible to create surfaces with predetermined emittance values without changing other properties. This can be done very easily by selecting a nonmetallic material with satisfactory hardness, refractory properties, and so on, and incorporating a small amount of pigment or coloring material—for instance, chromic oxide in alumina—in such a way that the volume emittance will be very greatly changed without changing the mechanical, physical, and refractory properties.

12. Comments on the Surface Characterization of Real Metals

DAVID P. DEWITT

NATIONAL BUREAU OF STANDARDS, WASHINGTON, D.C.

Radiation properties of metallic specimens have been shown to be very sensitive to methods of preparation, thermal history, and environmental conditions. The magnitude, sensitivity, and complexity are illustrated by an example from the literature. An indication of how a real surface might be characterized is discussed in three general categories: topographical characterization, chemical characterization (species present), and physical (or structural) characterization. Until more systematic methods and techniques for characterization are developed, the experimentalist must assume responsibility for attempting to describe all significant aspects of his physical specimens using conventional laboratory techniques and apparatus.

EXAMPLE OF SURFACE EFFECTS ON EMITTANCE

Radiation properties of metallic specimens have been shown to be very sensitive to methods of preparation, thermal history, and environmental conditions. The magnitude, sensitivity, and complexity of these effects are well illustrated by some recent studies of aluminum surfaces by Reynolds (ref. 1). The measurement technique involved tubular specimens electrically heated in air, with a lateral slit serving as the blackbody cavity opening. Two surfaces were prepared, of roughness 3 μ inch (0.076 μ) and 115 μ inch (2.9 μ), CLA.¹

Figure 1, which compares the normal spectral emittances² of the two specimens at 326° C, indicates primarily the effect of surface roughness. It is easily seen that roughening the

surface increases the emittance at all wavelengths. The effect of the natural oxide layer is more apparent on the rougher specimen, where it gives rise to the prominent peak near 11 μ . The effects of any structural variations among the specimens and bulk aluminum caused by surface preparation technique cannot be discerned from these data.

Figure 2 shows data for these same two specimens for different temperatures. For the 3- μ inch-roughness specimen, heating from 326° C to 532° C caused an increase in emittance at all wavelengths and the appearance of a peak near 11 μ due to the oxide layer formed during heating. Subsequent measurements at 326° C show that the emittance was increased at all wavelengths, with a very pronounced peak near 11 μ . This increase and peak must be attributed to oxidation effects. For the 115- μ inch-roughness specimen the results are similar but more pronounced. Roughening the surface strongly increased the spectral emittance at all wavelengths and accentuated the peak near 11 μ arising from the oxide layer. Subsidiary emittance peaks appeared around 3.5 μ and 6.0 μ as oxidation proceeded. Prolonged heat-

¹ CLA (centerline average) roughness is defined as the average value of the departure of the profile from its center line, whether above or below it, throughout the prescribed sampling length.

² The term *radiance ratio* is used by some workers in the field as equivalent to the term "emittance".

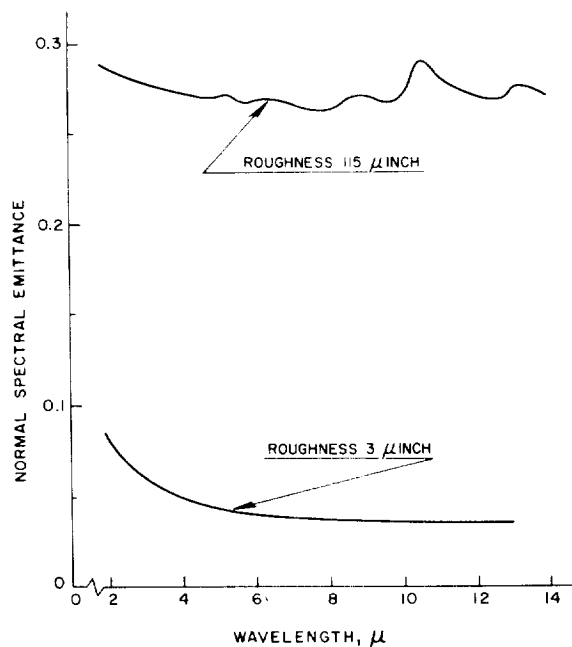


FIGURE 1.—The effect of roughness on normal spectral emittance of aluminum in air at 326° C. (After Reynolds, ref. 1.)

ing at higher temperatures increased the spectral emittance considerably at wavelengths beyond 10 μ .

This example points out the problems involved in understanding the effects of the environment on thermal radiation properties of metals in specific applications. There is further evidence in the literature (ref. 2 and 3) to support this example of extreme dependence of the optical behavior of metals on surface conditions. However, most of this evidence has been collected under unrelated or diversified conditions so that it is not possible to relate observed effects to environmental conditions. It is apparent that the nature of the problem—the identification and control of variables—demands a highly systematic approach to clarify and categorize conditions which give rise to the effects.

CHARACTERIZATION OF REAL SURFACES

Even though the nature of surface conditions and their effects on optical properties are not clearly understood, the differences between real

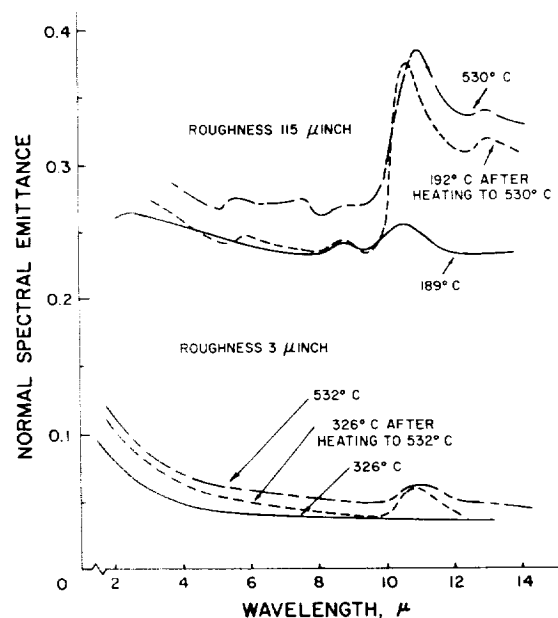


FIGURE 2.—The effects of roughness and oxidation on the normal spectral emittance of aluminum in air. (After Reynolds, ref. 1.)

and ideal surfaces can be distinguished. It seems advantageous to classify these differences under three general headings which give an indication of how a real surface might be characterized; namely, topographical characterization, chemical characterization (species present), and physical (or structural) characterization.

Topographical Characterization

The profiles of real metal surfaces are always shown as irregular patterns of peaks and valleys. Topographical characterization must provide a parametric description of such surface features as roughness type, roughness distribution, and lay³ that affect the optical behavior. Bennett and Porteus (ref. 4, 5, and 6) have shown in a quantitative manner the effect of surface roughness parameters on normal spectral reflectivity. The distinguishing feature of their work was the absence of any effects other than those due to surface topography; consequently

³ Lay refers to the direction of the predominant surface pattern produced by tool marks or grains of the surface ordinarily determined by the production method used.

the results are a significant contribution toward further understanding of topographical characterization. Similar studies that include goniometric measurements need to be made, as it can well be appreciated that the directional characteristics will be very sensitive to surface texture.

Chemical Characterization

The real metal surface unavoidably has a surface film of one type or another. In engineering applications, these films may be greases or other deposits, but normally they are oxides of the base metal. Even if only the natural oxide layer is considered, characterization is difficult. The layer is a mixture of several different chemical species (metal atoms, oxygen ions, and one or more metal ions); the interface between oxides and base metal is not smooth; the rate of oxide growth is dependent upon the base metal surface topography, structure, temperature, and atmospheric conditions. The study of oxide layer growth is a problem of current interest. Numerous reviews and studies (ref. 7, 8, and 9) have been reported, but the mechanism of the oxide layer growth is not completely understood for some metals, for there are many conflicting theories and opinions. It is evident that considerable work is necessary to further our understanding of how to chemically characterize a surface.

Physical or Structural Characterization

The surface characteristics just discussed—topographical and chemical—are easily understood to have important influences on optical behavior. However, the effects caused by physical structure beneath the surface are not so apparent (ref. 10). In the case of a perfectly smooth surface free from surface films, a surface layer several hundred angstroms deep (skin depth of penetration of radiation) is responsible for the optical behavior of the metal. Structural features of this layer, such as adsorbed gas atoms, lattice imperfections, and crystallinity variations, can be expected to have an influence on the optical behavior.

It has been shown that some mechanical polishing processes cause structural changes in layers near the surface (ref. 11). There is

evidence of a layer of supercooled fluid metal that fills the scratches caused by the abrasive (ref. 12). This layer (called the Beilby layer) has no clearly defined interface with the underlying metal (ref. 12 and 13). The outermost regions of this layer appear to be completely noncrystalline, and the structure becomes more crystalline as the depth from the outer surface increases. In some cases the layer will contain oxide. It has also been suggested that the polished layer is unstable and will revert, in time, to the ordinary crystalline state (ref. 14).

Heat-treating, cold-working, various surface preparation treatments, and many other processes can give rise to variations in physical and chemical characteristics between the bulk and surface layers. However, concrete evidence is lacking that these variations can in all cases cause significant changes in the optical behavior of metals.

CONCLUSION

Until systematic methods and techniques for characterization of surfaces are more fully developed, the experimentalist must assume the responsibility for attempting to describe all significant aspects of physical specimens for which data are obtained and reported. Many conventional laboratory techniques and apparatus, such as microphotography, etching techniques, profilometers, and electron microscopy, could be employed to immediate advantage. Certainly for clarity and significance, it is essential that some surface characterization information, no matter how incomplete, accompany numerical values of thermal radiation properties.

REFERENCES

1. REYNOLDS, P. M.: Spectral Emissivity of 99.7% Aluminum Between 200 and 540° C. *British Jour. Appl. Phys.*, vol. 12, no. 3, Mar. 1961, pp. 111-114.
2. CLAUS, FRANCIS J., ed.: *First Symposium—Surface Effects on Spacecraft Materials*. John Wiley & Sons, Inc., c. 1960.
3. RICHMOND, J. C.: Discussion of the Third Session—Thermal Problems Under Orbiting Conditions. *Proc. Fifth Sagamore Ord. Materials Res. Conf.—Materials in Space Environment (Contract ROD-30-115-ORD-947)*, Syracuse Univ. Res. Inst., Sept. 1958, pp. 164-165, 175.

4. BENNETT, H. E., and PORTEUS, J. O.: Relation Between Surface Roughness and Specular Reflectance at Normal Incidence. *Jour. Optical Soc. of America*, vol. 51, no. 2, Feb. 1961, pp. 123-129.
5. BENNETT, H. E.: Specular Reflectance of Aluminized Ground Glass and the Height Distribution of Surface Irregularities. *Jour. Optical Soc. of America*, vol. 53, no. 12, Dec. 1963, pp. 1389-1394.
6. PORTEUS, J. O.: Relation Between the Height Distribution of a Rough Surface and the Reflectance at Normal Incidence. *Jour. Optical Soc. of America*, vol. 53, no. 12, Dec. 1963, pp. 1394-1402.
7. EUBANKS, A. G., MOORE, D. G., and PENNINGTON, W. A.: Effect of Surface Roughness on the Oxidation Rate of Iron. *Jour. Electrochem. Soc.*, vol. 109, no. 5, May 1962, pp. 382-389.
8. GULBRANSEN, E. A., and WYSONG, W. S.: Thin Oxide Films on Tungsten. *Trans. American Inst. Mining and Metallurgical Engineers*, vol. 175, 1948, pp. 611-627.
9. KUBASCHEWSKI, O., and HOPKINS, B. E.: *Oxidation of Metals and Alloys*. Butterworths Scientific Pub. (London), 1953.
10. DONOVAN, T. M., ASHLEY, E. J., and BENNETT, H. E.: Effect of Surface Damage on the Reflectance of Germanium in the 2650-10,000-Å Region. *Jour. Optical Soc. of America*, vol. 53, no. 12, Dec. 1963, pp. 1403-1409.
11. SAMUELS, L. E.: Modern Ideas on the Mechanical Polishing of Metals. *Res. Appl. in Industry*, vol. 13, 1960, p. 344.
12. BEILBY, G.: *Aggregation and Flow of Solids*. MacMillan and Co., Ltd., 1921.
13. FINCH, G. INGLE: The Beilby Layer. *Sci. Progress*, vol. 31, no. 124, Apr. 1937, pp. 609-625.
14. LEES, C. S.: The Structure of Polished Metal Surfaces. *The Structure of Metallic Coatings, Films, and Surfaces*. *Trans. Faraday Soc.* (London), vol. XXXI, 1935, pp. 1102-1106.

13. Influence of Surface Roughness, Surface Damage, and Oxide Films on Emittance

H. E. BENNETT

MICHELSON LABORATORY, CHINA LAKE, CALIF.

A discussion of the effect of surface roughness, surface damage, and surface films on emittance is given. From the results of recent theoretical and experimental investigations of the influence of surface roughness on reflectance, it is concluded that at wavelengths where diffraction effects predominate, the hemispherical emittance is virtually unaffected by surface roughness. Thus, the surface roughness of finished metal surfaces, even those as rough as 60 μ in. rms, will not affect the energy radiated by the material at room temperature. The emittance is, however, strongly affected by disorders in the lattice structure at the surface, often called surface damage, which are introduced in the usual finishing operations. It may also be affected by surface films, although naturally occurring oxide films ordinarily have negligible effect at room temperature and below. Some examples illustrating these points are given.

In order to make accurate radiative transfer calculations, the spectral emittance of the material of which a body is composed must be known. If the spectral emittance is measured directly, formidable temperature-control problems must be overcome. In addition, at room temperature and below, the low signal levels obtained make direct spectral emittance measurements very difficult (ref. 1 and 2). Precise emittance values can, however, be obtained from reflectance measurements (ref. 3) with an uncertainty in the best cases of as little as ± 0.001 . When making emittance measurements, one must consider the effects of surface roughness, surface damage, and the presence of thin surface films. Surprisingly, the hemispherical emittance of surfaces having roughnesses considerably smaller than the wavelength of the light is quite insensitive to surface roughness. The emittance is affected by surface damage and to a lesser extent by the presence of a surface oxide film. Some examples illustrating these points for metals and semiconductors will be given.

DEFINITIONS

Emittance is defined as the ratio of the energy emitted by a material to that which would have been emitted had the material been a blackbody at the same (uniform) temperature. The emittance of a material is thus a function of the kind and thickness of material and also of its surface condition.

The *emissivity* is defined as the *emittance* of an *opaque homogeneous material* with an optically smooth surface which has suffered negligible surface damage. It has been argued (ref. 4) that since it is difficult either to determine the degree of surface damage or to eliminate it, the distinction put forth here is unnecessary. In reply, it should be pointed out that solid state calculations based on band theory yield the emissivity, not the emittance. The presence of surface damage is measurable, and failure to adequately specify sample condition is largely responsible for wide discrepancies both between theory and experiment and between experiments performed in different

laboratories on ostensibly the same materials.

In the case of a stock material used in engineering, it is frequently not possible to specify accurately the history and condition of the surface, and considerable doubt must therefore exist as to the validity of its calculated emittance. Nevertheless, the distinctions presented above have merit, and arguments in favor of them, many of which were ably summarized by Harrison (ref. 5) at the last symposium, are impressive. They will therefore be used in this paper.

EFFECTS OF ROUGHNESS

Kirchhoff's law (ref. 6) states that the total emittance of a body equals its total absorptance. Thus, if its transmittance is zero, the total emittance equals 1 minus the total reflectance, or, if we are considering flat bodies, the hemispherical emittance equals 1 minus the hemispherical reflectance. If the surface is also smooth, so that only specular reflection occurs, there is a unique relation between the angle at which beams of light strike or emerge from the surface of the material and their direction of travel inside the material. Therefore the directional emittance in this case will equal 1 minus the specular reflectance in that direction, and is calculable from Fresnel's equations if the optical constants of the material are known.

If the surface is not smooth, the situation becomes more complicated. The directional emittance is no longer equal to 1 minus the specular reflectance in a given direction, nor is it obvious that it can be calculated from Fresnel's equations. The directional emittance may still be obtained from reflectance measurements, but for surfaces which are quite rough relative to the wavelength it is necessary to measure the light reflected in a given direction from a sample equally irradiated at all angles of incidence, or its optical equivalent, the total reflectance of a sample irradiated from the desired direction.

Fortunately, instruments are available (ref. 7) for making such measurements with reasonable accuracy. Caution should be used, however, in relating the results of such measurements to the reflectance or emittance which a perfectly

smooth surface of the same material would have, since a change in the shape of the curve of directional emittance versus angle may occur as the surface roughness increases. For example, surfaces having gross roughnesses such that all values of the slope of the surface irregularities are equally probable might be expected to obey Lambert's cosine law even though a smooth flat surface of the same material did not. The limited experimental evidence available does indicate that Lambert's law is more closely followed by very rough surfaces than by smooth ones (refs. 8 and 9). Additional quantitative work on the influence of various types of surface roughness on directional emittance is greatly needed.

In addition to possible changes in the ratio of the directional emittance at different angles, for sufficiently rough surfaces a change in the total hemispherical emittance or reflectance would also be expected since light striking the surface would suffer multiple reflections. The hemispherical emittance of a surface having gross surface irregularities compared to the wavelength would then be expected to be larger and the hemispherical reflectance smaller than for a perfectly smooth surface of the same material. As the surface becomes smoother, however, geometrical optics no longer holds exactly, diffraction effects must be considered, and thus the concept of multiple reflections breaks down. In the diffraction region the behavior of the hemispherical emittance has thus been unclear. However, in the limit, as the surface roughness approaches zero, the emittance clearly assumes the value of that for a perfectly smooth surface. Therefore, at some point, as the surface becomes less rough relative to the wavelength, a change in the hemispherical emittance from the multiple-reflection, geometrical-optics value to the smooth-surface value will occur. Although the point at which this change occurs is not known, it will now be shown that in a substantial part of the diffraction region the hemispherical emittance equals the smooth-surface value. This proposition is contrary to generally accepted beliefs about the effect of surface roughness on hemispherical emittance. At first glance it is also contrary to a large amount

of experimental evidence indicating that even slightly rough surfaces in general have higher hemispherical emittances than do smooth ones. However there is good theoretical evidence, substantiated by experiment, for concluding that this observed increase in emittance is a result not of surface roughness but of surface damage introduced in the process of making the surface rough.

The evidence for such a conclusion is based on the effect of surface roughness on specular reflectance in wavelength regions where diffraction effects must be considered. A theory has been proposed which postulates that in this region surface roughness affects only the angular distribution, not the total amount of energy reflected by a surface. If this theory can be shown to be in agreement with experiment, it follows from Kirchhoff's law that, in this diffraction region, the hemispherical emittance is independent of surface roughness.

The effect of surface roughness on the optical properties of materials was apparently first seriously considered by Lord Rayleigh (ref. 10), who published a paper about it in 1901. The solution, however, has only recently been obtained. If the sizes of the irregularities are of the order of the wavelength or larger, the problem becomes one involving geometrical optics. In this case, the facets of the surface behave like small mirrors pointed in various directions, and the statistical properties of the surface must be known in great detail in order to predict the optical behavior. If, however, the surface irregularities are much smaller than the wavelength, one has a diffraction problem.

This problem was solved by Davies (ref. 11), whose work has been extended and experimentally verified by Bennett and Porteus (ref. 12). Their expression for the observed relative reflectance of a rough surface at normal incidence is shown in figure 1. The reflectance of a perfectly smooth, flat surface of the reflecting material is R_0 . The observed specular or coherent reflectance of the rough surface is R , so that the observed relative reflectance at normal incidence is R/R_0 . This observed relative reflectance is expressed in terms of the rms roughness σ , the rms slope m , the wavelength λ , and the half angle of acceptance $\Delta\theta$ of

the optical system which collects the reflected radiation. The second term on the right, which represents the diffusely or incoherently reflected light which is collected by the optical system, is proportional to $(\sigma/\lambda)^4$; hence, it becomes negligible as the wavelength increases, and the observed relative specular reflectance is then given by the first term only, a simple exponential. In figure 2 this exponential expression is represented by the solid line. The circles represent experimental points for aluminized ground glass. The general agreement demonstrates the validity of the theory for small values of σ/λ .

The theory was recently extended by Porteus (ref. 13), who showed that if the surface has a Gaussian height distribution, the exponential term correctly represents the coherent reflectance for all values of σ/λ . However, as σ/λ becomes larger the incoherent term becomes more important and an increasingly exact statistical description of the surface is required, culminating in the limiting case in which geometrical optics applies. The predicted behavior of the coherent term has been experimentally verified (ref. 14), as is shown in figure 3. The circles represent the relative reflectance plotted against σ/λ , of an aluminized sample of ground glass for which the incoherent reflectance was negligible. They fall on the Gaussian curve, represented by the solid line, very accurately, not only for small values of σ/λ , but also up to

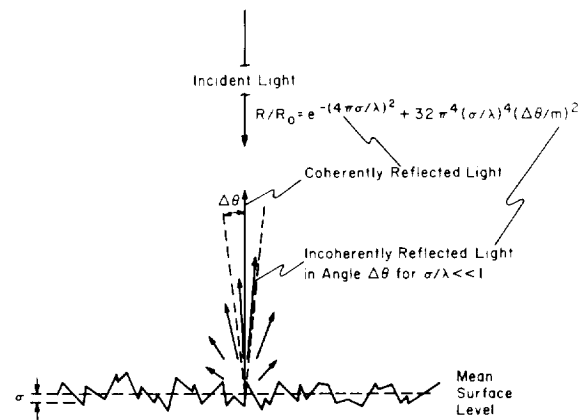


FIGURE 1.—Schematic representation of the reflection of light normally incident on a rough metal surface. The analytical expression for the relative reflectance is shown at the right.

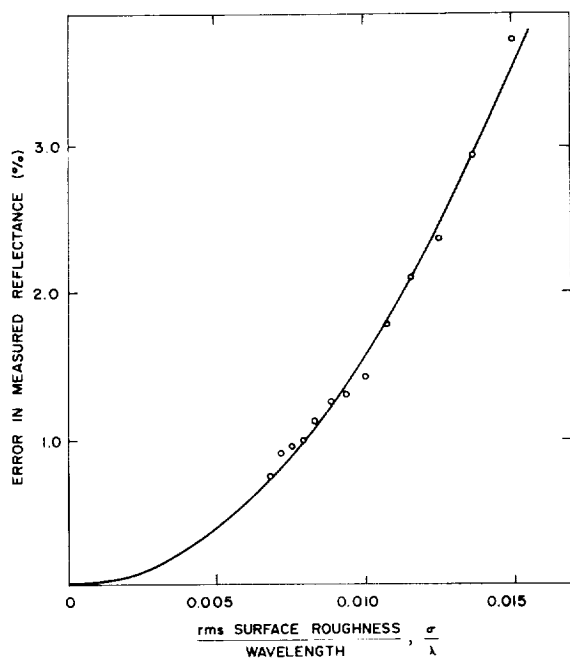


FIGURE 2.—Error made in reflectance measurements when surface roughness is neglected. The circles represent the experimental points. The solid line was calculated from the first term of the equation in figure 1. The agreement between theory and experiment demonstrates the validity of the theory for small values of σ/λ .

the largest value, 0.155, for which specular, or coherent, reflectance could be observed.

At oblique incidence, the theory is complicated by polarization effects, and becomes very difficult to handle unless the s and p components of reflectance are assumed to be equal. If such an assumption is made, the dependence of coherent reflectance on angle of incidence is obtained by substituting $\sigma \cos \psi$ for σ in the exponential, where ψ is the angle of incidence. At large angles of incidence, metals satisfy these assumptions to a good approximation. Experimental reflectance measurements at large angles of incidence on metals having various degrees of surface roughness are in good agreement with this theory (ref. 15, 16, and 17).

The theory predicting the effect of surface roughness on specular reflectance has been shown to be in excellent agreement with experiment in the diffraction region. This theory assumes that there is no change in the total reflectance of the sample as the surface

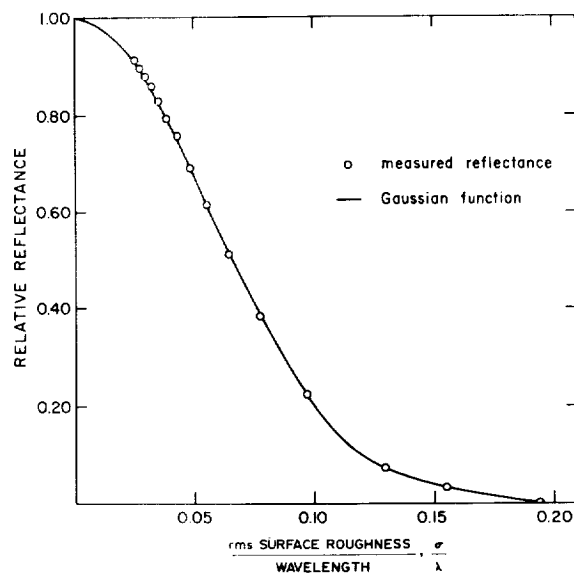


FIGURE 3.—Results of fitting observed reflectance values of a typical aluminized ground-glass surface (circles) to a Gaussian reflectance function (solid line). This demonstrates the validity of the theory for values of σ/λ up to 0.155.

roughness increases, but merely a change in the ratio of coherently to incoherently reflected light. There is thus strong evidence that, in the diffraction region, a change in the total reflectance of a sample with increasing surface roughness does not occur. It follows directly from Kirchhoff's law that no change in total emittance in this region can occur because of surface roughness.

It may be of interest to point out the range of surface roughnesses involved. We have taken an unfavorable case, since the rms slope of the surface irregularities of ground glass is considerably larger than that of a machined or ground metal surface. In this unfavorable case, we have shown that the theory fits the experimental data for values of σ/λ at least as large as 0.15. If one is concerned with the thermal radiation at room temperature or below, the blackbody maximum will occur at a wavelength of 10 μ or more. Thus, since σ/λ may be 0.15, the rms roughness may be as large as 1.5 μ , or 60 $\mu\text{in.}$, an unusually large value for a finished metal surface, and there will still be a negligible effect on the energy radiated by the material at room temperature.

EFFECTS OF SURFACE DAMAGE

The effect of surface damage and resultant lattice distortion on the optical properties of materials has been grossly underestimated, particularly in the case of metals and of semiconductors at wavelengths shorter than that of the absorption edge. In emission or absorption, the surface layers always act to modify the radiation incident on them from inside or outside of the surface. For these materials the extinction coefficient k is usually sufficiently high that the optical penetration depth $\lambda/2\pi k$ is considerably smaller than the depth of the surface damage, and emission or absorption of radiation actually occurs entirely in the disturbed surface layer. The maximum effect of the damage-induced changes in the band structure in this layer will be in the joint density-of-states function for interband transitions, so that the optical properties in the region of intrinsic absorption, which usually occurs in the ultraviolet, visible, and near infrared, will be most strongly affected by surface damage. However, even at longer wavelengths in the free-carrier region some changes will occur.

It has been shown that a minimum amount of surface damage is introduced during sample preparation if etching or electropolishing techniques are used. Recently a technique has been developed (ref. 18) at Michelson Laboratory for producing electropolished samples which are also optically smooth and flat. As an example of the effect of surface damage, figure 4 shows the reflectance at normal incidence in the intrinsic-absorption region of two copper samples cut from the same high-purity ingot. The observed reflectance in both cases was corrected for surface roughness, which was slight, and in each case measurements were made immediately after the polishing was completed to minimize the effect of possible surface films. More or less conventional optical polishing techniques—a pitch lap covered by a silk screen, and bowl feed—were used for the sample whose reflectance is represented by the open circles. Although it was smooth, optically flat, and looked identical to the electropolished sample, its reflectance was considerably lower—by as much as a factor of

two at the shorter wavelengths. Results for the electropolished sample are in good agreement with those of Lowery, Wilkinson and Smare (ref. 19) and also with those reported for evaporated films by Hass (ref. 20). The preliminary values reported here are thus believed to be at least approximately representative of undistorted bulk material.

In the infrared region, the reflectances of the two samples approach the same value, as expected from theory. However, as is shown in figure 5, they do not become equal in the wavelength region where appreciable thermal emission occurs. Although the difference in reflectance is not large, the emittance in this region is sufficiently small that, for example, at $10\ \mu$, the wavelength at which the maximum in the blackbody curve at room temperature occurs, the two emittances differ by over 50 percent. The solid line represents the reflectance predicted for copper in the free-electron region by the Drude-Zener theory (ref. 21). The bulk d-c conductivity, 5.312×10^{17} esu, and an effective electron density of 2 electrons per atom were used in the calculations. The preliminary reflectance values for electropolished copper reported here differ from the theoretical values by less than 0.2 percent in the 3- to $32\text{-}\mu$ wave length region.

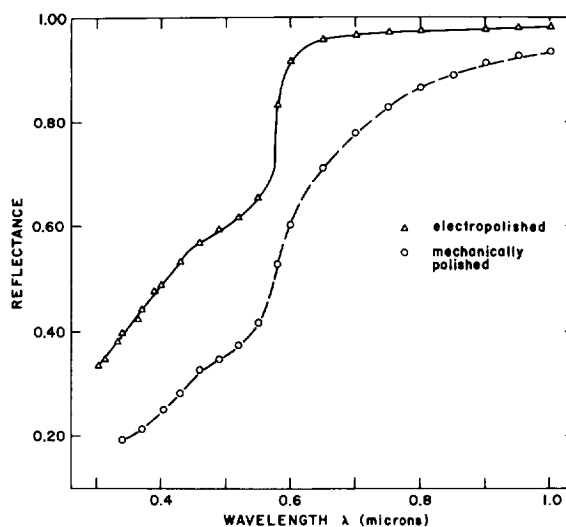


FIGURE 4.—Reflectance of electropolished copper (triangles) and mechanically polished copper (circles) from 0.3 to $1\ \mu$. Both samples were cut from the same high-purity ingot.

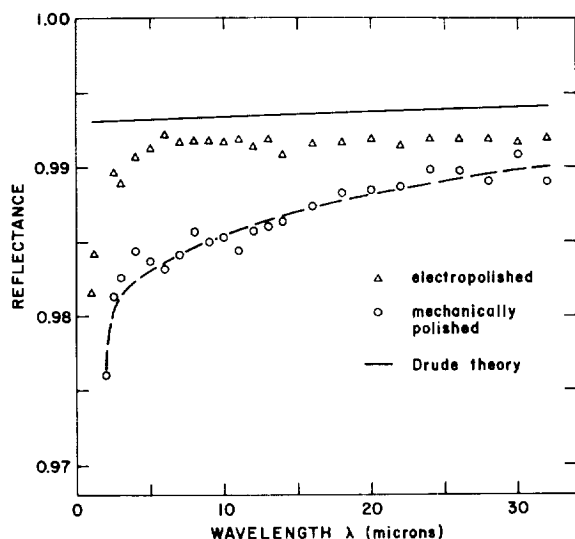


FIGURE 5.—Reflectance of electropolished copper (triangles) and mechanically polished copper (circles) from 1 to 32 μ . The solid line gives the reflectance of copper calculated from the Drude-Zener theory.

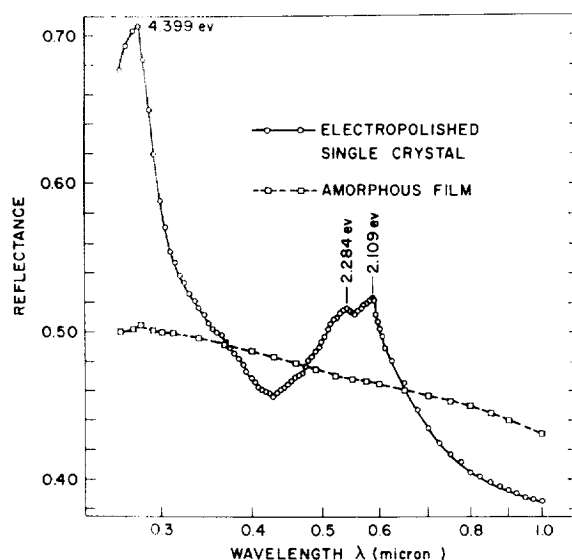


FIGURE 6.—Reflectance of electropolished germanium single crystal and evaporated amorphous germanium in the 0.3- to 1- μ wavelength region. The difference between the two curves illustrates the influence of crystal structure on the optical properties of germanium.

Figure 6 shows the reflectance at normal incidence of an electropolished germanium single crystal, indicated by the solid line, and of an evaporated germanium film which x-ray diffraction measurements showed to be amorphous (ref. 22). The difference between the two reflectance curves, which apparently results only from a difference in the structure of the germanium samples, is particularly striking. When the evaporation conditions are changed so that an epitaxial rather than an amorphous film is formed, the reflectance of the epitaxial film in this wavelength region is virtually identical (ref. 23) to that of the electropolished single crystal.

EFFECTS OF SURFACE FILMS

Little will be said here about the modification of emittance by surface films. It is worth pointing out, however, that although naturally occurring oxide films may strongly affect the emittance of metals at visible and ultraviolet wavelengths, such films often have relatively little effect in the infrared. Figure 7 shows the calculated decrease in the reflectance of aluminum caused by oxide films of various thicknesses (ref. 24). Berning, Hass, and Madden

(ref. 25) have reported that the thickness of the film which forms at room temperature on an aluminized mirror surface is about 22 Å. The decrease in reflectance caused by such a film would be less than 0.2 percent even at 5500 Å. Even much thicker films will have practically no effect on the emittance of aluminum in the infrared region. In some cases, for example TiO_2 on Ti as reported by Hass and Bradford

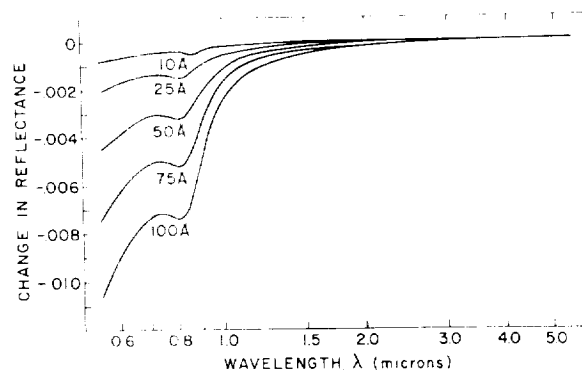


FIGURE 7.—Calculated decrease in reflectance resulting from the formation of oxide layers of various thicknesses on aluminum. The oxide thickness for each curve is shown beneath it.

(ref. 26), the infrared emittance is much more strongly affected by an oxide film than in the case of aluminum. Also, a very small decrease in infrared reflectance may cause an appreciable change in emittance if the reflectance is very high. Nevertheless, for many metals the infrared emittance is not significantly affected by the presence of thin oxide films.

CONCLUSION

To summarize, in determining emittance one must consider surface roughness, surface damage, and the presence of surface films. Surface roughness may cause errors in reflectance measurements, but it does not appreciably change the hemispherical emittance of the sample in the diffraction region. Surface damage may drastically affect the emittance of metals and semiconductors having large extinction coefficients. For this reason, tabulated emittance values for such materials which have undergone such common operations as turning, grinding, or buffing must be regarded, at best, as only approximate. Only if very reproducible methods of sample preparation, such as vacuum deposition under carefully controlled conditions, electropolishing, or vapor decomposition are used is the emittance data at room temperature to be trusted. Fortunately, however, the room temperature emittance of metals in the infrared region is frequently unaffected by the presence of a naturally occurring oxide film.

REFERENCES

1. WEBER, DWIGHT: Spectral Emissivity of Solids in the Infrared at Low Temperatures. *Jour. Optical Soc. of America*, vol. 49, no. 8, Aug. 1959, pp. 815-820.
2. WEBER, DWIGHT: Low-Temperature, Directional, Spectral Emissivity of Translucent Solids. *Jour. Optical Soc. of America*, vol. 50, no. 8, Aug. 1960, pp. 808-810.
3. BENNETT, H. E., and KOEHLER, W. F.: Precision Measurement of Absolute Specular Reflectance With Minimized Systematic Errors. *Jour. Optical Soc. of America*, vol. 50, no. 1, Jan. 1960, pp. 1-6.
4. WEBER, D.: Spectral Emissivity Measurements Near Room Temperature. *Radiative Transfer From Solid Materials*, Henry Blau and Heinz Fischer, eds., The Macmillan Co., c.1962, pp. 157-165.
5. HARRISON, WILLIAM N.: Pitfalls in Thermal Emission Studies. *Measurement of Thermal Radiation Properties of Solids*, Joseph C. Richmond, ed., NASA SP-31, 1963, pp. 3-10.
6. WORTHINGTON, ARCHIE GARFIELD and HALLIDAY, DAVID: *Heat*. John Wiley & Sons, Inc., 1948, pp. 429-433.
7. BENNETT, H. E.: Measurement of Spectral Reflectance at Normal Incidence. *Radiative Transfer From Solid Materials*, Henry Blau and Heinz Fischer, eds., The Macmillan Co., c.1962, pp. 166-180.
8. ECKERT, E. R. G.: Introduction to the Transfer of Heat and Mass. McGraw-Hill Book Co., Inc., 1950, pp. 203, 277.
9. JAKOB, MAX: *Heat Transfer*. Vol. I. John Wiley & Sons, Inc., c.1949, p. 51.
10. RAYLEIGH, (LORD): *Polish. Nature*, vol. LXIV, 1901, pp. 385-388.
11. DAVIES, H.: Reflection of Electromagnetic Waves From Rough Surfaces. *Proc. Inst. Elec. Engineers*, vol. 101, pt. 4, no. 7, Aug. 1954, pp. 209-214.
12. BENNETT, H. E., and PORTEUS, J. O.: Relation Between Surface Roughness and Specular Reflectance at Normal Incidence. *Jour. Optical Soc. of America*, vol. 51, no. 2, Feb. 1961, pp. 123-129.
13. PORTEUS, J. O.: Relation Between the Height Distribution of a Rough Surface and the Reflectance at Normal Incidence. *Jour. Optical Soc. of America*, vol. 53, no. 12, Dec. 1963, pp. 1394-1402.
14. BENNETT, H. E.: Specular Reflectance of Aluminized Ground Glass and the Height Distribution of Surface Irregularities. *Jour. Optical Soc. of America*, vol. 53, no. 12, Dec. 1963, pp. 1389-1394.
15. MIDDLETON, W. E. KNOWLES, and WYSZECKI, GÜNTER: Colors Produced by Reflection at Grazing Incidence From Rough Surfaces. *Jour. Optical Soc. of America*, vol. 47, no. 11, Nov. 1957, pp. 1020-1023.
16. HASUNUMA, HIROSI, and NARA, JIRO: On the Sheen Gloss. *Jour. Phys. Soc. of Japan*, vol. 11, no. 1, Jan. 1956, pp. 69-75.
17. TANAKA, SHUN-ICHI; NOGUCHI, NORIYUKI; WATANABE, MAKATO; and TAKAHASHI, TSUNEHICO: Measurement of Reflection Characteristics of Rough Surfaces by the Use of a Frequency Chart. *Oyo Butsuri (Jour. Appl. Phys. (Japan))*, vol. 31, no. 3, 1962, pp. 216-221.
18. DONOVAN, T. M., and SERAPHIN, B. O.: Undamaged Germanium Surfaces of High Optical Quality. *Jour. Electrochem. Soc.*, vol. 109, no. 9, Sept. 1962, pp. 877-879.
19. LOWERY, H., WILKINSON, H., and SMARE, D. L.: An Experimental Investigation on the Influence of the Polished Surface on the Optical Constants of Copper as Determined by the Method of

- Drude. Phil. Mag. and Jour. Sci., seventh ser., vol. XXII, no. CXLIX, Nov. 1936, pp. 769-790.
20. GRAY, DWIGHT E., coordinating ed.: American Institute of Physics Handbook. Second ed., McGraw-Hill Book Co., Inc., 1963, pp. 6-119.
 21. BENNETT, H. E., SILVER, M., and ASHLEY, E. J.: Infrared Reflectance of Aluminum Evaporated in Ultra-High Vacuum. Jour. Optical Soc. of America, vol. 53, no. 9, Sept. 1963, pp. 1089-1095.
 22. DONOVAN, T. M., ASHLEY, E. J., and BENNETT, H. E.: Effect of Surface Damage on the Reflectance of Germanium in the 2650-10 000-A Region. Jour. Optical Soc. of America, vol. 53, no. 12, Dec. 1963, pp. 1403-1409.
 23. DONOVAN, T. M., and ASHLEY, E. J.: Reflectance of Evaporated Germanium Films. Jour. Optical Soc. of America, vol. 54, no. 9, Sept. 1964, pp. 1141-1144.
 24. BENNETT, H. E., BENNETT, JEAN M., and ASHLEY, E. J.: Infrared Reflectance of Evaporated Aluminum Films. Jour. Optical Soc. of America, vol. 52, no. 11, Nov. 1962, pp. 1245-1250.
 25. BERNING, P. H., HASS, G., and MADDEN, R. P.: Reflectance-Increasing Coatings for the Vacuum Ultraviolet and Their Applications. Jour. Optical Soc. of America, vol. 50, no. 6, June 1960, pp. 586-597.
 26. HASS, GEORG, and BRADFORD, ALAN P.: Optical Properties and Oxidation of Evaporated Titanium Films. Jour. Optical Soc. of America, vol. 47, no. 2, Feb. 1957, pp. 125-129.

DISCUSSION

LEOPOLD CANN, Research and Advanced Technology Division—Aerojet General Corporation: I have been suspicious of the possible effect of surface crystal damage on emissivity determinations for several years. I used the electropolishing method in the preparation of *dark mirrors* on high temperature alpha/epsilon determinations for the Air Force in 1961. My congratulations are extended to Dr. Bennett for effectively demonstrating such a relationship. In surface preparation it should be noted that the oils used in machining and forming stainless steel and other metallic substrates are often based upon sulfur. Conventional degreasing with trichloroethylene may not remove them but electropolishing will.

Again, sandblasting also results in crystal damage and inclusions, and should never be a final surface treatment. I previously encountered some of the problems caused by substrate stress in the magnetic coating of memory devices. Stress was shown to have a marked effect on magnetic qualities, and electropolishing was very effective in removing damaged crystal layers and inclusions. The effect of stress

on the optical qualities of films is revealed by the fact that even the rate of deposition of a thin film will modify the refractive index of the material. Also, the conditions of measuring emissivity will often cause fluctuations because of thermal stress relief.

In conclusion, I feel that the effects of crystal damage and substrate stress on optical properties offer a fine field for further investigation.

ROGER E. GAUMER, Lockheed Missiles and Space Company: Mr. Cann's comment is valid; that is a subject that we have not touched on. I might comment that there exist a considerable number of sophisticated techniques for obtaining smooth and reproducible surfaces, none of which, to my knowledge, is applicable to the construction of space trucks or satellites. The dollar costs are prohibitive because we are building very large, very unsophisticated things in general, and the Vanguard-type techniques simply are not applicable. However, an investigation of the kind that you mentioned will probably be most useful in leading to a fundamental understanding of what is going on.

14. The Effect of Slight Surface Roughness on Emittance¹

R. E. ROLLING

LOCKHEED MISSILES & SPACE COMPANY, PALO ALTO, CALIF.

Further discussion is given of the emittance of slightly rough surfaces. A published example is cited to show that even where the theory does not agree with the measurements, it does correctly indicate the trends. The case in which the surface is more than slightly rough is also discussed.

These comments pertain to one of the conclusions reached by Dr. Bennett; namely, that the hemispherical emittance of a specimen does not appear to be changed in magnitude by surface roughness. It should be emphasized that his observation is based upon results obtained with samples that are only slightly rough. In this case it is unlikely that multiple reflections will occur at the surface; although, if multiple reflections are present, they must cause a change in the gross radiation properties of the surface. The surfaces examined by Dr. Bennett had roughnesses, as I recall, in the range 0.1 to 1.0 micron rms and would have small average slopes between hills and valleys. This is precisely the region where the theoretical approach of Davies, as further treated by Porteus, would be applicable. In spite of the limitations of this theory, it is interesting to note that for many practical roughened surfaces the treatment will indicate trends in radiation properties.

For example, let us consider some results recently published in the *ASME Journal of Heat Transfer* (ref. 1). Figure 1 presents the data for the specular reflection of blackbody energy from the surface of roughened nickel

samples. The samples were roughened in the range 0.14 to 0.86 micron rms and exposed to blackbody energy at temperatures from 125° F to 680° F. The abscissa $\sigma_m T \cos \theta$ contains the blackbody temperature in order that it might more nearly represent the ratio of roughness height to wavelength. The ordinate is found by integration of the product of the spectral specular reflectance, as determined by Davies, and the blackbody spectrum. This integration is shown at the top of the figure. The figure then represents an attempt at correlating data by using a theory that assumes no interreflections are taking place at the surface. The dashed line represents the theoretically predicted results for the surfaces and temperatures reported in the paper.

The differences in magnitude between the theoretical predictions and the experimental observations are quite large. A number of reasons can be postulated as probable causes for the large discrepancy. First, the surface roughnesses were determined by surface probe profilometry which, for small surface roughness, can be considerably in error. Bennett and Porteus report in an earlier work that, in the range of roughnesses used in reference 1, it is possible that profilometry may produce values of σ_m that are too low by a factor of 1½ to 2. Correcting for this error would shift the experimental results toward larger values of

¹ This paper is a prepared comment on the preceding paper *Influence of Surface Roughness, Surface Damage, and Oxide Films on Emittance* by H. E. Bennett.

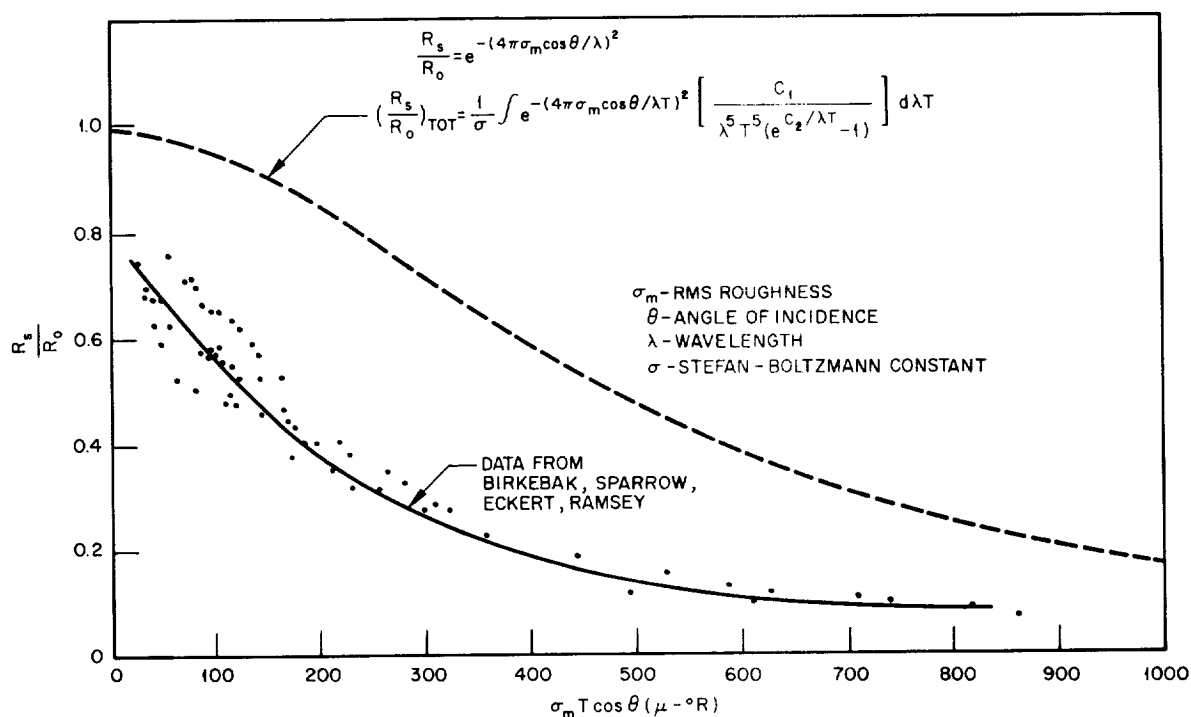


FIGURE 1.—Total specular reflectance of roughened nickel samples.

$\sigma_m T \cos \theta$ and bring the prediction closer to the observations. A second source of error is the solid angle subtended by the detector and the imaging technique used in the optics. I cannot comment with confidence on the effects of these with regard to the data of reference 1, since I have no detailed knowledge of the apparatus other than that reported in the paper. However, it is probable that the detector collected energy other than that which was reflected in a purely specular manner from the surface. Accounting for this source of error would further change the correlation of experimental results. A third possible explanation for the large disparity is that the samples were roughened with grinding techniques, which invariably result in surface strain that changes the basic optical constants of the roughened surface. Here again, a precise assessment of this effect on the data cannot be made but it is likely to have occurred.

In spite of the extent of, or reasons for, the large disparity in absolute magnitude between the experimental and theoretical results, the

correlation does show that the surfaces used follow the behavior predicted by the diffraction theory. The applicability of the theory to such results is indeed encouraging.

Assuming that the diffraction theory applies for predictions of radiation properties of slightly rough surfaces leaves us with the necessity of finding a reasonable basis for the prediction of radiation properties of surfaces that are not in this category, that is, for surfaces that are so rough that a number of interreflections occur. Dr. Chang Lin Tien, of the University of California at Berkeley, suggests that the best approach for this case may be that proposed by Dr. Rice at the Symposium for Electromagnetic Energy held at New York University in 1960. Dr. Rice presented solutions for the reflection of electromagnetic energy from a rough sea using Maxwell's equations and the complex boundary conditions of rough surfaces having a Gaussian distribution. Extending this approach to the interaction of radiant energy with rough metallic surfaces appears promising since the solution allows for inter-

reflections. Theoretical results obtained from Maxwell's equations do not predict the same value of hemispherical emittance as for a smooth surface, which is the result given by the simplified diffraction theory. I wish that progress on this study could be presented at this time, but a good deal of work remains to be done.

Finally, I would like to make some remarks concerning the manner in which experimental results are reported in current literature. The limited number of papers available on surface effects tend toward oversimplification in reporting the properties of the experimental surfaces used. In many cases the only information included as sample description is reference to the material and root-mean-square roughness. Experimental observations of the radiation properties of a surface are determined by optical

properties, surface profile, mechanical structure, chemical structure, instrumentation techniques, and inherent errors. In view of this multitude of variables it is obvious that considerable effort should be put into complete reporting of the experiment and samples so that another investigator can properly assess the results in terms of other observations. The contents of present reports do not permit such evaluation and tend to detract from otherwise valuable contributions to the study of surface effects.

REFERENCE

1. BIRKEBAK, R. C., SPARROW, E. M., ECKERT, E. R. G., and RAMSEY, J. W.: Effect of Surface Roughness on the Total Hemispherical and Specular Reflectance of Metallic Surfaces. A.S.M.E. Jour. Heat Transfer, vol. 86, ser. C, no. 2, May 1964, pp. 193-199.

15. Importance of Surface Films

JOSEPH C. RICHMOND

NATIONAL BUREAU OF STANDARDS, WASHINGTON, D.C.

The effects of surface conditions, such as roughness and the presence of films, on thermal radiation properties are briefly outlined, and an example is cited where oxide films formed on heating in a good laboratory vacuum (about 10^{-5} torr) markedly affected the total hemispherical emittance of a specimen of sandblasted Inconel.

Reflection and refraction occur at an interface as a result of the abrupt change in the speed of electromagnetic radiation in passing across the interface. The physical laws relating the fraction of the incident flux that is reflected and the angles of reflection and refraction to the indices of refraction of the materials on the two sides of an optically smooth interface and to the angle of incidence and the amount and direction of polarization of the incident radiation are well known and need not be elaborated here.

In the specific case of a specimen in vacuum (or air), the reflectance at the specimen-vacuum interface determines how much of the externally incident radiation will be refracted into the specimen, where it can be absorbed or transmitted, and how much of the internally incident flux will be refracted through the interface and thus emitted. Hence the reflectance at the vacuum-specimen interface exerts a strong influence on all of the thermal radiation properties of the specimen.

When the interface is not optically smooth, multiple reflection and destructive interference occur, both of which tend to reduce the reflectance. While the general effect of roughness is known in a qualitative way, no rigorous

equations have been derived which quantitatively relate roughness to reflectance.

A surface film, of index of refraction less than that of the specimen, will reduce reflectance, and a film of index of refraction higher than that of the specimen will increase reflectance. When films are present, interference effects can also occur, which may greatly increase absorptance. These effects are related to both index of refraction and thickness.

Thus we see that to properly characterize the surface of a specimen we need to describe the departures of its surface from an ideal optically smooth surface, and also the thickness and index of refraction of any surface film that may be present.

Changes in both surface contour and the nature of the surface film can occur as a result of test conditions. As an example, about 5 years ago we showed results (ref. 1) that were obtained on a sandblasted specimen of Inconel, on which the total hemispherical emittance was measured at a pressure of about 10^{-5} torr (fig. 1). Since the atmosphere in the test chamber was air, the oxygen partial pressure was on the order of 2×10^{-6} torr.

Heating at temperatures up to about 500°C resulted in a permanent decrease in emittance.

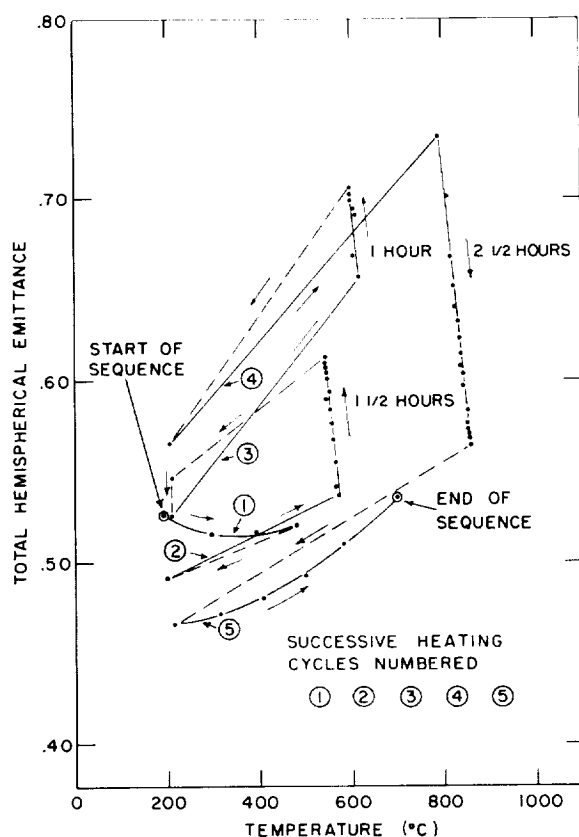


FIGURE 1.—Total hemispherical emittance of a sandblasted Inconel specimen during successive heating cycles in a vacuum with an oxygen partial pressure of the order of 2×10^{-6} torr.

This was believed to be due to removal of adsorbed films, although the exact nature of the films was not determined.

Heating the specimen at temperatures of about 600° and 700° C resulted in both cases in an appreciable increase in emittance with time. This was due to the formation of an

oxide layer which formed on the specimen even at this low oxygen pressure.

At temperatures on the order of 800° C, the emittance decreased appreciably with time—from about 0.72 to about 0.55 in 2½ hours. This effect was caused primarily by removal of the oxide layer. Chromic oxides dissociate in vacuum at temperatures above about 780° C. At temperatures of 800° C and above, chromium volatilizes appreciably and at the same time there is a smoothing effect on the surface of the specimen somewhat similar to that produced by electropolishing. Both peaks and valleys were rounded off, to produce a bright surface that had a much higher reflectance than the initial sandblasted surface.¹

Our experience with Inconel is presented to emphasize that it is not enough to know the surface roughness and the films present on the specimen before a test is started. We must also know how these change during a test in order to interpret our results properly. But most important of all, if our data are to be really useful, we must be certain that the surface condition of the specimen during test is truly representative of the material as it is used. This is perhaps the most frequently neglected and the most critically important aspect of surface characterization.

REFERENCE

1. RICHMOND, JOSEPH C., and HARRISON, WILLIAM N.: Equipment and Procedures for Evaluation of Total Hemispherical Emittance. American Ceramic Soc. Bull., vol. 39, no. 11, Nov. 15, 1960, pp. 668-673.

¹ See also Paper 19.

16. Surface Properties of Metals

H. H. BLAU, JR., AND H. A. FRANCIS

ARTHUR D. LITTLE, INC., CAMBRIDGE, MASS.

Data are presented to show the effect of surface oxidation, caused by heating in air, on the spectral emittance (2 to 14 μ) of stainless steel. Also presented are the spectral emittance data for platinum and Inconel surfaces coated with silicon monoxide 1000 Å thick and then heated in air. A method is described for obtaining aluminum surfaces with periodic distributions of ridges (two-dimensional roughness) or of hillocks (three-dimensional roughness) with periodicities of several hundred angstroms.

Development of mathematical models to aid our understanding of the interaction of radiation and matter—particularly metallic conductors—has been a subject of considerable interest for many years. Its origins are found in the early 1900's in the surprisingly successful work of Hagen and Rubens and of Drude who attempted to explain metallic reflection and absorption in terms of the interaction of a classical electromagnetic wave with free, or conduction, electrons. Today, using more sophisticated quantum mechanical theories such as that of Holstein, it is possible to almost completely specify the optical properties of certain pure metals in terms of measurable solid state parameters. Conversely, a considerable body of information on the solid state can be derived from optical measurements.

Unfortunately, such information is of very restricted value to the engineer or scientist concerned with problems such as space vehicle thermal control. Our ability to predict from first principles is limited to a few very pure metals, carefully prepared so as to have smooth, flat surfaces free of chemical contamination and physical disordering. The influence of the material surface is particularly significant not only with regard to the very pure specimen of interest to the solid state physicist but also with regard to materials of engineering importance.

This is easily understood in terms of the strong absorption characteristics of metals. Extinction coefficients are large so that the penetration depth for optical radiation is limited to very small distances—of the order of a few hundred angstroms. Consequently, emission and reflection processes are surface phenomena and are almost completely controlled by the chemical, physical and topographical nature of a thin surface layer at most a few thousand angstroms in thickness. This note will briefly examine some of the effects of chemical and topographical surface properties.

CHEMICAL EFFECTS

Changes in the chemical nature of a surface can significantly alter emittance or reflectance properties, essentially by altering the emitting or reflecting material. Such effects are most significant at high temperatures, where reaction rates are large, but can be important at low temperatures as well. Oxidation reactions are most frequently encountered.

Figure 1 rather dramatically illustrates the effects of surface oxidation. It is a graph of spectral emittance as a function of wavelength from 2 to 14 μ for stainless steel. The lower curve is for a sample heated in air for 3 hours at 600° C, and the upper curve is for a sample heated in air for 6 hours at 1000° C. The

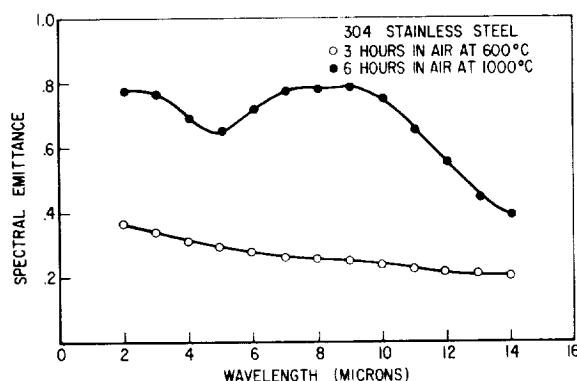


FIGURE 1.—Spectral emittance of oxidized stainless steel.

emittance values differ by a factor of about 2 because of oxide formation. The oxide layer in this case is rather thick.

Figure 2 shows the influence of thinner surface films. Silicon-monoxide films, about 1000 Å thick, were vacuum-deposited on platinum and Inconel substrates. The specimens were then heated (the platinum to 600° C and the Inconel to 1000° C), and the spectral emittances measured. The maxima at about 10 microns are due to intrinsic absorption in the oxide layer. In the case of the Inconel, the structure in the short-wavelength region is probably due to chemical effects in the silicon-monoxide metal interface. The SiO coating did not completely protect the substrate from oxidation. These effects are reasonably representative of what can be encountered, even with rather well protected systems.

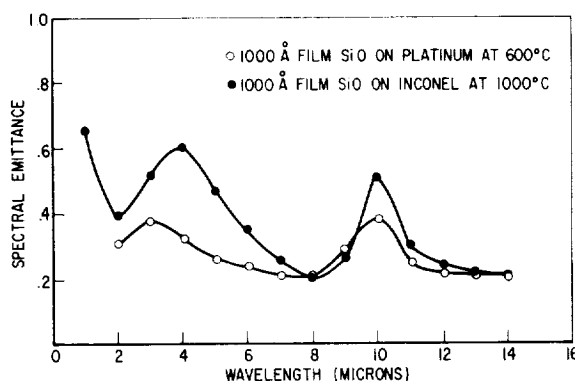


FIGURE 2.—Spectral emittance of silicon monoxide coated platinum and Inconel.

TOPOGRAPHICAL EFFECTS

Surface topography is one of the most important and least understood factors affecting the thermal properties of solid materials, be they metals, dielectrics, or semiconductors. In general, with highly absorbing materials, an increase in surface roughness leads to an increase in emittance—the familiar cavity effect discussed in Professor Sparrow's paper. With highly transparent materials, the effect is quite different; roughening the surface increases surface scattering so that a previously transparent material can become a rather effective reflector.

The problem of surface topography is at least twofold. First, we must devise means of characterizing material surfaces; then we must develop mathematical formalisms that will permit us to express optical properties in terms of the parameters describing surface geometry.

Dr. Bennett and his associates at the Michelson Laboratory have made significant contributions to this subject, relating surface parameters to normal spectral reflectivity. In effect, they have developed an optical method for determining certain surface parameters or, if these parameters are known, for determining their effect on normal spectral reflectance.

Dr. Bennett's work is, however, only a first step, since we are generally concerned with the three-dimensional character of radiation. Ideally we would like a full description of optical properties in terms of surface statistics. Practically, however, we may well have to settle for far less. In Dr. Emslie's paper, he suggested that spectral emittance or reflectance might correlate with the optical diffuseness of a surface. In effect, he suggested an optical rather than a geometrical approach to specification of surface topography, which is certainly an interesting possibility.

A considerable body of experimental data will be required to help establish such correlations. Such data should be obtained under accurately known experimental conditions for specimens with carefully measured surface finishes.

The paper by Keegan, Schleter, and Weidner, taken together with the paper on the measurement of surface properties by Spangenberg,

Strang, and Chamberlin, is an example of the type of study that is required.

In closing, I am going to describe some preliminary work of a related nature that we are conducting which deals with preparation of metal surfaces with controlled surface topography.

Several years ago, Paul Doherty and Richard Davis (ref. 1) of our metallurgy group discovered that very thin amorphous oxide films formed on electropolished aluminum single crystals exhibit highly regular submicron topographies at the free surface while the metal-oxide interface is essentially smooth and flat. These topographies thus represent a corresponding periodic variation in oxide thickness between about 20 and 70 Å. On the (110) surface, this topography is much like that of a diffraction grating and consists of corrugations parallel to the (100) direction. The corrugation spacing may be accurately varied between about 300 and 500 Å which, incidentally, is about ten times finer than can be produced by conventional grating ruling techniques. On the (111) surface, the topography consists of a close-packed array of hillocks with separation on the order of the corrugation spacing.

To account for these ordered topographies, Doherty and Davis proposed that the monolayer of oxide in contact with the metal is a two-dimensional crystal with long-range order corresponding to the substrate orientation. The approximately 0.5 percent difference in atomic spacing between the monolayer and the metal results in a vernier relationship between them. Since the rate-limiting step for oxide growth is cation transport across the oxide metal interface, the periodic variation in interface structure due to the vernier causes a corresponding variation in oxide thickness.

Considerable insight into the physics and physical chemistry of oxide formation was derived from careful study of the nature of the amorphous oxide. The oxide can, however, be used for a more prosaic purpose; it can serve as a *mask* through which, by the chemical action of certain acid reagents, a geometrically characterizable topography may be initiated

in the metal on an extremely fine scale and coarsened to almost any degree desirable. Pits bounded by certain crystallographic planes form in the aluminum at the regions of thinnest oxide and then enlarge to impingement, resulting in a faceted topography which subsequently coarsens with time. This effect is illustrated in figure 3 for the (110) surface. The photograph in the upper left of the figure is a replica of the free surface of the original oxide layer and consists of very regular, closely spaced corrugations. The photograph in the upper right is the same surface after immersion in acid reagent for 3 minutes. A good deal of regularity has been preserved, with the pattern now etched into the metal rather than contained on the oxide layer. With further etching (photographs at lower left and right), the regularity degrades rapidly.

A more attractive situation is illustrated in figure 4, which shows similar photographs for the (111) surface. The pattern here is that of hillocks mentioned previously. The photograph in the upper left is the pattern etched into the metal after immersion in acid reagent for 3 minutes. The peak-to-valley depth here is about 200 Å. The photographs at upper right and lower left and right correspond to 1-hour, 1½-hour, and 2-hour exposures to the reagent, respectively. A high degree of regularity is maintained while the peak-to-valley separation is increased from 250 Å, or 1 microinch, to approximately 5000 Å, or 20 microinches.

The surfaces shown in figures 3 and 4 show considerably more order than surfaces prepared by etching polycrystalline materials or by sandblasting. We hope that study of the emission or reflection properties of such surfaces will assist in developing a better understanding of the optical effects of surface topography.

REFERENCE

1. DOHERTY, P. E., and DAVIS, R. S.: Direct Observation of the Oxidation of Aluminum Single-Crystal Surfaces. Jour. Appl. Phys., vol. 34, no. 3, Mar. 1963, pp. 619-628.

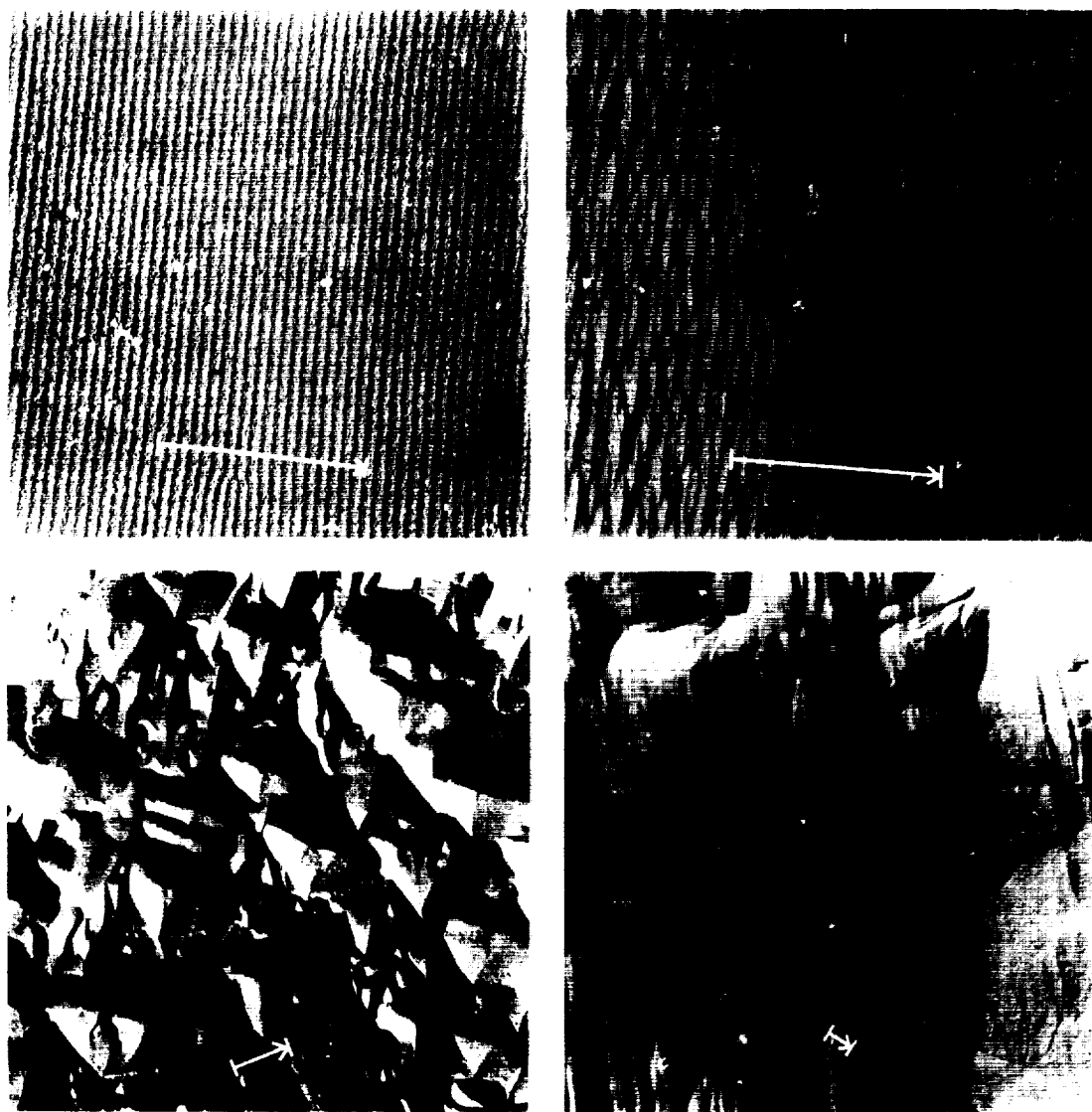


FIGURE 3.—Development of etch topography on the aluminum (110) surface. Arrows indicate 1- μ scale.

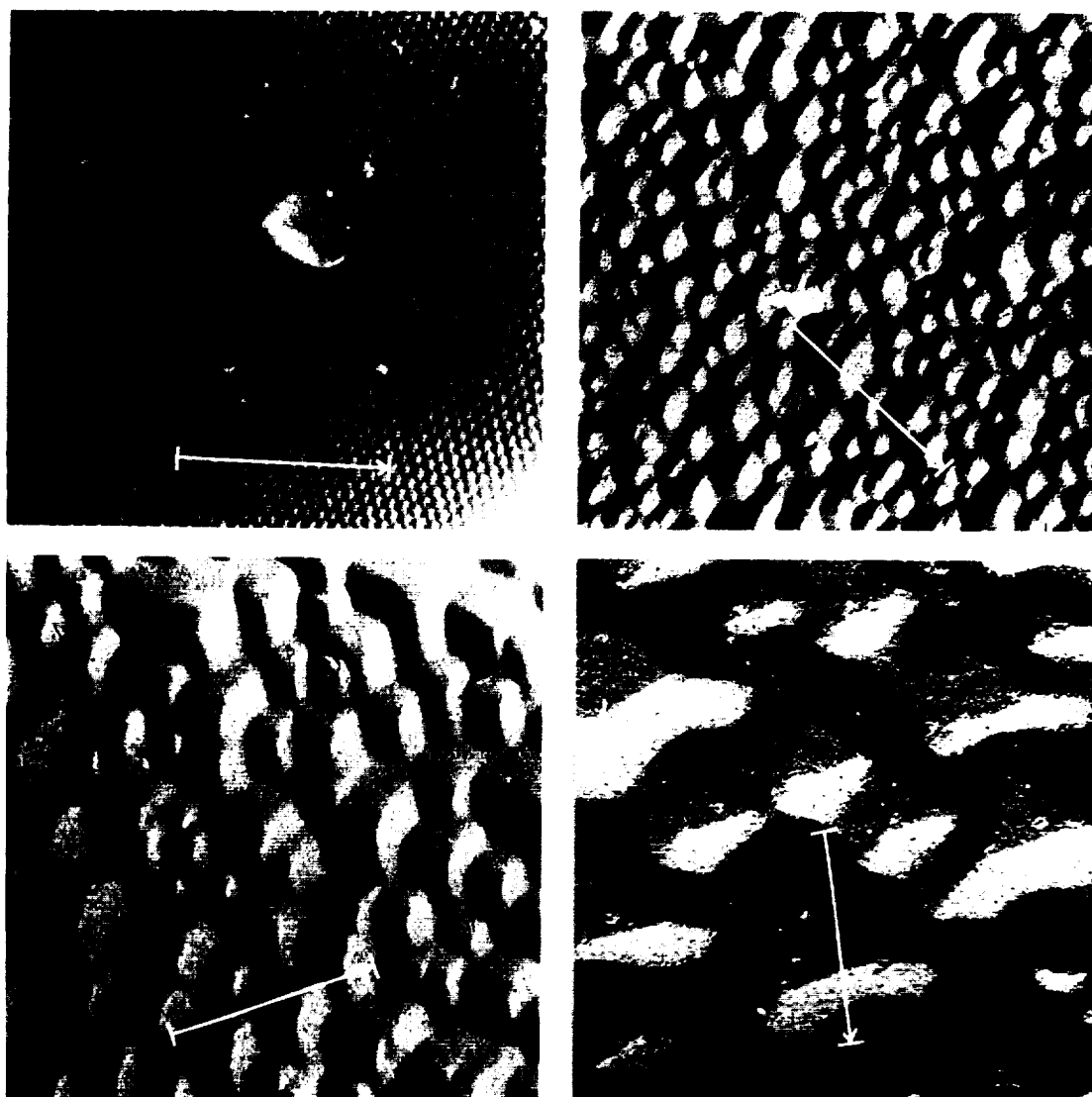


FIGURE 4.—Development of etch topography on the aluminum (111) surface. Arrows indicate 1- μ scale.

17. Effect of Surface Texture on Diffuse Spectral Reflectance

A. Diffuse Spectral Reflectance of Metal Surfaces

H. J. KEEGAN, J. C. SCHLETER, AND V. R. WEIDNER

NATIONAL BUREAU OF STANDARDS, WASHINGTON, D.C.

B. Surface Texture Measurements of Metal Surfaces

D. B. SPANGENBERG, A. G. STRANG, AND J. L. CHAMBERLIN

NATIONAL BUREAU OF STANDARDS, WASHINGTON, D.C.

Part A describes an attempt to correlate the effect of surface finish (texture) on the diffuse spectral directional reflectance of metals; measurements were made over the wavelength range from 0.2 to 2.1 μ for samples of sintered beryllium, steel gage blocks, steels machine-lapped with various types and sizes of abrasives, polished and sandblasted aluminum, platinum, and a chemically polished beryllium block.

Part B describes surface-texture measurements made on most of the same surfaces by interferometry. Several conventional parameters describing these surfaces were determined by stylus and interferometric techniques. Interferograms of the surfaces are included.

A. Diffuse Spectral Reflectance of Metal Surfaces¹

In June 1963, the Flight Reentry Programs Office of the NASA Langley Research Center requested the NBS Spectrophotometry Unit of the Photometry and Colorimetry Section to measure the diffuse spectral directional reflectances of eight samples of sintered pressed beryllium over the wavelength range from 0.26 to 2.1 μ . Each beryllium block had one face polished, and the polished faces had different degrees of finish.

This study led to the investigation of other metals and a wider range of roughness; and the surface finishes were evaluated by several techniques, including microinterferometry.

Microinterferograms of 22 of these metal surfaces are included in part B of this paper.

It was considered of particular interest to study the effect of the lay of the finish on the surface reflectance. In the field of color, the effect of the texture of woven dyed cloth on its spectral directional diffuse reflectance is well known and has been extensively investigated. Nutting (ref. 1) found that representative colorimetric specifications could be correlated with visual estimates by averaging the spectral directional diffuse reflectance measurements of each sample at two angles, one with the lay of the weave at 45° and the other with the lay oriented 90° from the first measurement. This method was used at NBS and correlated with other visual methods (ref. 2). A few studies have been made in other laboratories of the

¹Supported in part by the Advanced Research Projects Agency, Department of Defense.

effect of lay of finish (direction of polishing) on the specular spectral reflectance (refs. 3, 4, and 5), and of the effect of electropolishing on specular reflectance (ref. 6). A study has also been made of the effect of lay on diffuse spectral reflectance of buffed silver surfaces as measured with the General Electric recording spectrophotometer for the visible spectrum only (ref. 7).

SPECIMENS AND TESTS

Test Specimens

The specimens studied were:

- (1) Eight sintered beryllium samples, pressed and polished by manual lapping (no. 1, 2, 3, 4, 6, 7, 8, and 9a)
- (2) One sintered beryllium sample chemically polished (no. 9b)
- (3) Six commercial gage blocks made of steel
- (4) Ten NBS steel samples, machine lapped
- (5) One polished aluminum sample
- (6) One sandblasted aluminum sample
- (7) One polished platinum sample
- (8) One sandblasted platinum sample

Measurements

Measurements of diffuse spectral directional reflectance were made for the following conditions of irradiation and reception:

- (1) 6° incidence, diffuse viewing (specular component included), 0.4 to 1.08 μ , on a GE spectrophotometer (ref. 8)
- (2) 6° incidence, diffuse viewing (specular component included), on a Cary model 14M spectrophotometer (ref. 9) equipped with a model 1411 diffuse reflectance integrating sphere attachment: 0.26 to 0.4 μ , hydrogen source, Dumont K1306 photomultiplier; and 0.36 to 0.7 μ , tungsten source, K1306 photomultiplier
- (3) Diffuse illumination, 6° viewing, on same equipment as described in (2): 0.36 to 0.7 μ , tungsten source, Hamamatsu R136 photomultiplier; and 0.6 to 2.1 μ , tungsten source, lead sulfide photocell

Reference Standards

For the visible and near infrared measurements, 0.4 to 1.08 μ , the reference standard used was freshly prepared magnesium oxide made by burning magnesium metal chips in air and depositing the MgO smoke on troughs 1 mm deep (ref. 10). All integrating spheres were also smoked with MgO. Working standards used were NBS V1-G3 Vitrolite standard (see ref. 11), a rhodium mirror used for some earlier measurements, and the diffuse side of a sample of Corning Thermometer White glass TW1-B1.

The same reference standards were used in the ultraviolet, visible, and infrared measurements, 0.26 to 2.1 microns.

RESULTS

Presentation of Results

The results of these studies of the diffuse spectral reflectance of surfaces of metals are presented in figures 1 to 9 as follows:

Aluminum:	Figure
Machine lapped	1
Sandblasted	1
Platinum:	
Machine lapped	1
Sandblasted	1
Beryllium:	
Sample no. 1, hand lapped (about 4 micro-inches)	2
Sample no. 8, hand lapped (about 20 micro-inches)	3
Sample no. 9a, hand lapped (about 20 microinches), in visible spectrum only	4
Sample no. 9b, chemically polished	4
Steel:	
5 commercial gage blocks	5
Machine lapped, various sizes of grit	6
Machine lapped, polished and depolished ..	7
Rhodium-plated nickel:	
Ruled roughness (20 μ in., arithmetic average)	8
Ruled roughness (125 μ in., arithmetic average)	9

Discussion of Results

ALUMINUM

The diffuse spectral reflectance in the ultraviolet, visible, and infrared (0.26 to 2.1 μ) of

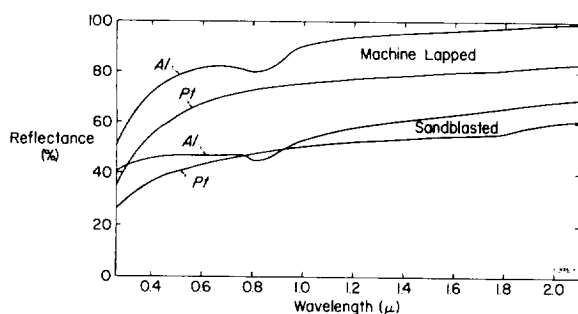


FIGURE 1.—Diffuse spectral reflectances (0.26 to 2.1μ) of machine-lapped and sandblasted samples of aluminum and of platinum. Each curve represents determinations at four orientations. There was no appreciable effect of orientation.

two samples of aluminum, one with a machine-lapped finish and the other with a sandblasted finish, are shown in figure 1. Only a single curve is shown for each sample, since there was no observable separation of the curves obtained over the entire spectral range at four orientations of each sample (0° , 90° , 180° , 270° , and a repeat measurement at 360° between a fiducial mark on the sample and the vertical slit axis of the instrument), that is, the reflectance of the highly polished surface of aluminum and that of the highly depolished surface of aluminum were independent of angle of orientation of the sample. Spectrally the difference between the two reflectance curves varied from 0.10 at 0.26μ to 0.38 at 0.9μ and beyond.

PLATINUM

Diffuse spectral directional reflectance curves of polished and sandblasted platinum, similar to those for aluminum, are also shown in figure 1. These two curves are essentially parallel except in the ultraviolet.

BERYLLIUM

Figures 2, 3, and 4 show the diffuse spectral directional reflectance of sintered beryllium. Figures 2 and 3 are curves for hand-lapped finishes, at eight orientations each (0° , 45° , 90° , 135° , 180° , 225° , 270° , 315° , and a repeat measurement at 360° between a fiducial mark on the sample and the vertical slit axis of the instrument). The most polished sample (fig. 2) showed no variation with orientation of the

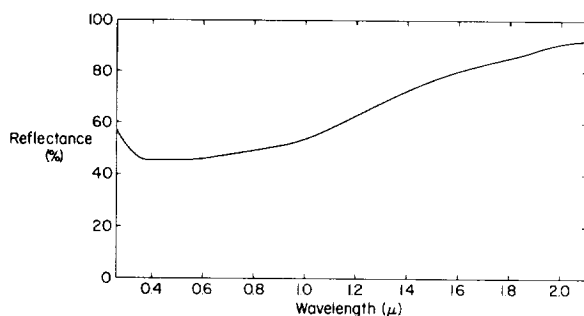


FIGURE 2.—Diffuse spectral reflectance (0.26 to 2.1μ) of surface of beryllium sample 1, hand-lapped to about 4 microinches. The curve represents determinations at eight orientations of the sample.

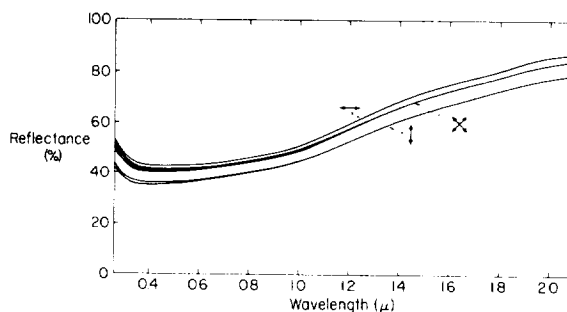


FIGURE 3.—Diffuse spectral reflectance (0.26 to 2.1μ) of surface of beryllium sample 8, hand-lapped to about 20 microinches, at eight orientations. The horizontal lay of finish (texture) yields highest reflectance throughout the spectrum and the vertical lay of finish yields lowest reflectance. The four 45° orientations are in the middle but nearer to the horizontal. (Note: For the vertical lay of the finish, the projection of the incident beam on the surface is parallel to the lay.) The arrows indicate the direction of the lay of the finish relative to the vertical slit axis of the instrument.

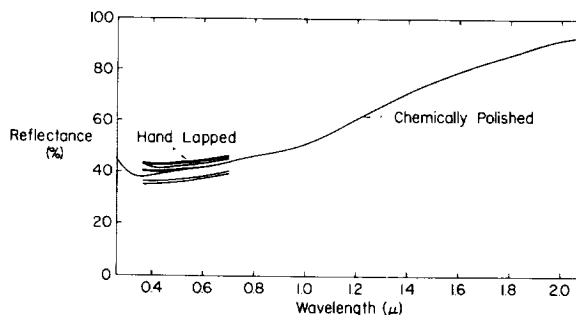


FIGURE 4.—Diffuse spectral reflectances of beryllium samples 9a and 9b, for eight orientations each. The curves for the hand-lapped surface (9a) are shown only for the visible spectral region (0.36 to 0.7μ). The curve for this surface after subsequent chemical polishing (9b) is shown for the range of 0.26 to 2.1μ .

sample. The least polished sample (fig. 3) showed approximately 8 percent variation of reflectance with orientation.

Figure 4 shows the variation of diffuse spectral reflectance for a hand-lapped beryllium specimen, similar to the one shown in figure 3, for the visible spectral region, and for the same sample after chemical polishing, over the full spectral range (0.26 to 2.1 μ). The hand-lapped surface showed an appreciable effect of orientation, but the chemically polished surface showed no variation in reflectance with orientation.

STEEL

Figures 5, 6, and 7 show diffuse spectral directional reflectance of steel specimens with various finishes.

Figure 5 shows data for commercial steel gage blocks. Curves 2 and 4 are for eight orientations each, curves 1 and 3 are for two orientations each, and curve 5 is for six orientations. (The number of orientations was restricted because of the configuration of the gage block relative to the opening of the sphere.) The variations in diffuse spectral reflectance are due to differences in the types of steel used and possibly to oxide surface films.

In figure 6 are curves of diffuse spectral directional reflectance of nearly identical samples of steel with different finishes—a commercial gage block finish, a high polish obtained

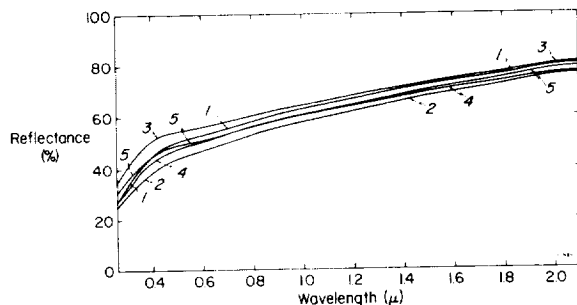


FIGURE 5.—Diffuse spectral reflectances (0.26 to 2.1 μ) of steel gage blocks with commercial finishes. The variation in reflectance is due to differences in the steels used in the manufacture of the blocks and to oxide surface films.

- | | |
|---------------------|-------------------------|
| 1. Webber 5 min M-4 | 4. Van Keuren 0.250 in. |
| 2. Webber 30 min | 222. |
| NBS-2. | 5. Pratt and Whitney |
| 3. NPL 9 sec no. 5 | 0.500 in. Triangle. |

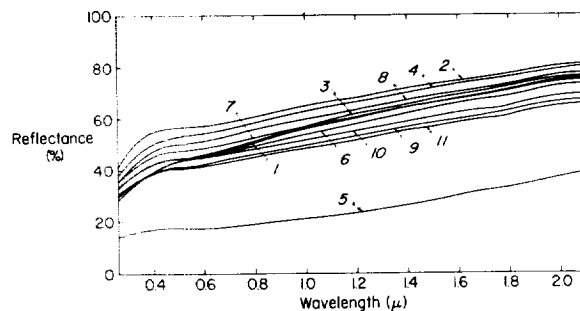


FIGURE 6.—Diffuse spectral reflectances (0.26 to 2.1 μ) of nearly identical steel samples with different finishes, for one orientation each. The finishes include a commercial finish, possibly with an oxide surface film, a high polish obtained with aluminum oxide on a pitch polisher, and a range of finishes obtained with different grades of diamond grit ($\frac{1}{4}$ to 60 μ) on cast iron. The lowest curve is for a surface that was heat damaged during finishing.

- | | |
|--|------------------------------|
| 1. No. 31: commercial finish | 6. No. 54: 6 μ diamond |
| 2. No. 17: aluminum oxide | 7. No. 40: 14 μ diamond |
| 3. No. 20: $\frac{1}{4}$ μ diamond | 8. No. 86: 20 μ diamond |
| 4. No. 35: 1 μ diamond | 9. No. 85: 30 μ diamond |
| 5. No. 77: 3 μ diamond | 10. No. 24: 45 μ diamond |
| | 11. No. 61: 60 μ diamond |

from aluminum oxide on a pitch polisher, and a range of finishes obtained with various grades of diamond grit from $\frac{1}{4}$ to 60 μ on cast iron. These curves are for a single orientation which is representative of the average reflectance for the eight orientations of the sample. The range of the measurements varied from approximately ± 0.2 percent, for the specimen finished with the $\frac{1}{4}$ - μ diamond grit, to approximately ± 1.0

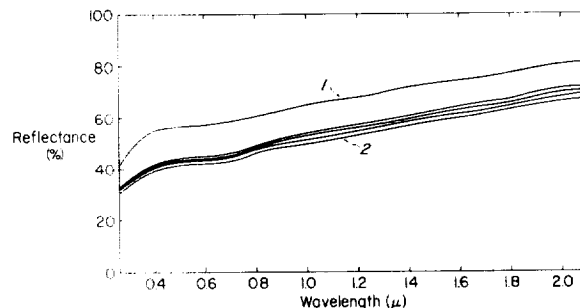


FIGURE 7.—Diffuse spectral reflectances (0.26 to 2.1 μ) of two of the specimens (2 and 10) shown in figure 6 for eight orientations.

1. Pitch polisher with aluminum oxide (Linde A)
2. Cast iron lap with 45 μ diamond

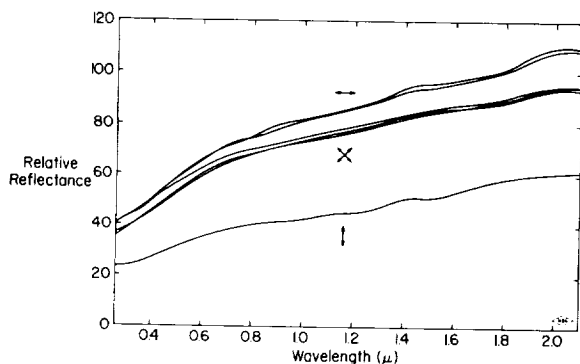


FIGURE 8.—Diffuse spectral reflectance (0.26 to 2.1 μ) of a rhodium-plated nickel ruled roughness specimen of 20-microinch AA surface roughness, for six orientations. The arrows indicate the direction of the lay of the finish relative to the vertical slit axis of the instrument.

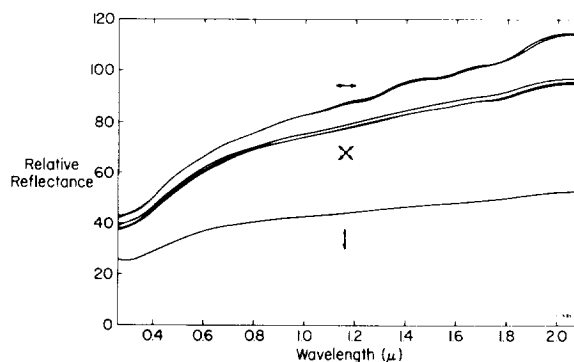


FIGURE 9.—Diffuse spectral reflectance (0.26 to 2.1 μ) of a rhodium-plated nickel ruled roughness specimen of 125-microinch AA surface roughness, for six orientations. The arrows indicate the direction of the lay of the finish relative to the vertical slit axis of the instrument.

percent, for the specimen finished with the 60- μ diamond grit, from the average values indicated in figure 6. Curve 5 is for a surface that was found to be heat damaged when removed from the block.

Curves for two of the specimens, no. 2 and 10 of figure 6, are shown in figure 7 for eight orientations.

RHODIUM-PLATED NICKEL

Curves for ruled roughness specimens of rhodium-plated nickel of 20 and 125 microinches AA (arithmetic average) for six orientations of the rulings are shown in figures 8 and 9. The reflectance, relative to MgO, at orientations of 90° and 270° exceeded 100 percent at wavelengths greater than about 1.8 μ . This is believed to be due to a focusing effect of the

regular rulings of the Caliblock, the geometry of the integrating sphere, and the setting of the 100 percent curve relative to the diffusing MgO surface.

CORRELATION WITH SURFACE TEXTURE

Study of these spectrophotometric curves and of the corresponding 24 microinterferograms shown by Spangenberg, Strang, and Chamberlin in part B of this paper showed a possibility of a correlation between diffuse spectral directional reflectance and the surface texture (roughness) as therein evaluated. However, considerably more work on more accurately prepared specimens must be done before definite conclusions may be reached.

B. Surface Texture Measurements of Metal Surfaces²

Control of surface texture is usually based on a single roughness parameter of the surface. When such single parameter control is used, it is also necessary to specify the manufacturing process. The relationship between the control parameter and the resultant surface texture, for the defined process, is known either by experience or previous tests. No single parameter can, however, fully describe a surface. For

this correlation study, the surface textures of the finely finished specimens used were evaluated by measuring several conventional parameters.

SPECIMENS

Three sets of specimens were measured. These consisted of a set of specially prepared sintered beryllium specimens, a set of specially prepared tool steel specimens, and a set of commercially finished steel specimens.

² See also Paper 27.

Six specimens of sintered beryllium were finished by a hand-polishing process similar to metallurgical polishing. These specimens were polished in one direction, so that there was a predominant lay to the surface texture of all but the finest finished specimen.

Ten specimens of gage block tool steel were finished by a lapping process. Specimen 17 was finished on pitch using a fine aluminum oxide abrasive (Linde A). All others were finished on a cast iron lap using various powdered diamond abrasives. These specimens were randomly finished and had no predominant lay.

Six commercially finished gage block steel specimens were also measured. These surfaces represent commercial machine lapping processes. Specimen 1 had a predominant lay; all others were randomly finished.

In addition, measurements on a commercial precision reference specimen (Caliblock) were also used in this study. This specimen is an electrolytic replica of ruled regular triangular wave patterns having apex angles of 150°. It had two patches with different peak-to-valley heights.

MEASURED PARAMETERS

The parameters measured are those in accord with the M system. This system is based on a *mean line* about which various roughness parameters are measured.

Although by no means complete, the following definitions should be sufficient for understanding the terminology used. Figure 10 graphically illustrates these parameters. A complete physical interpretation of the significance of these and other parameters is contained in references 12, 13, and 14.

Mean line (center line): A mean line is a line parallel to the general direction of the measured surface profile and positioned such that the sums of the areas contained between it and those parts of the profile that lie on each side of it are equal.

Crest and root lines: For these measurements the crest and root lines were determined by the 10-point system, in which the crest line and root line are located parallel to the mean line and through the average height of the

five extreme peaks and the average depth of the five extreme valleys of the profile, respectively.

Peak-to-valley height R : The peak-to-valley height is the distance between the crest and root lines.

Leveling depth R_u : The leveling depth is the distance between the crest and mean lines.

Mean depth R_m : The mean depth is the distance between the root and mean lines.

Roughness height R_a : The roughness height is the arithmetic average deviation of the profile measured perpendicular to the mean line, and is given by

$$R_a = \frac{1}{L} \int_0^L |y| dx$$

Roughness width A_r : The roughness width is the average horizontal spacing between successive peaks of the predominant surface pattern.

Filling-out factor k : The filling-out factor is the ratio of the mean depth R_m to the peak-to-valley height R . Thus,

$$k = \frac{R_m}{R}$$

Profile angle factor j : The profile angle factor is the ratio of the peak-to-valley height R to the roughness width A_r . Thus,

$$j = \frac{R}{A_r}$$

Shape factor l : The shape factor is the ratio of the roughness height R_a to the leveling depth R_u . Thus:

$$l = \frac{R_a}{R_u}$$

Both stylus and interferometric methods were used for the examination of the specimens. Interferometric methods were used for all surfaces too fine for the stylus to penetrate to the full depth of the texture.

A Taylor, Taylor, and Hobson Talysurf, model 3 modified, was used for the stylus measurements (ref. 15). This instrument has a stylus with a tip radius of approximately 100 microinches which contacts the specimen with

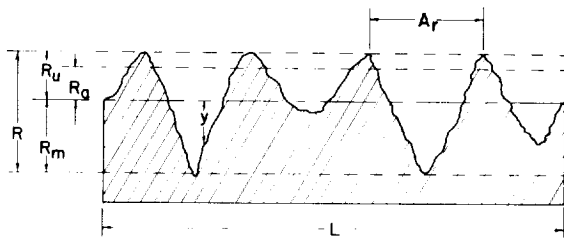


FIGURE 10.—Basic surface measures.

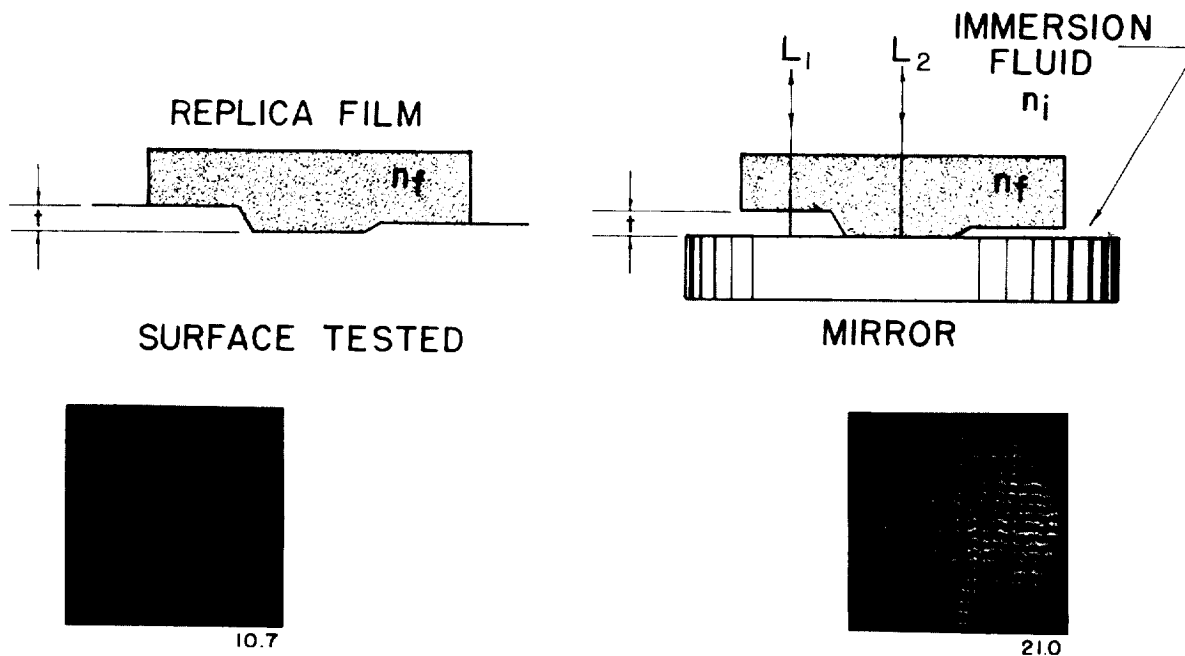
$$R_a = \frac{1}{L} \int_0^L |y| dx \quad j = \frac{R}{A_r}$$

$$k = \frac{R_m}{R} \quad l = \frac{R_a}{R_u}$$

a static force of 30 milligrams. This low measuring force of the stylus permits the tracing of all hard materials without visibly marking them. The undulations of the specimen are measured relative to a straight datum and are graphed (profilogram) as the stylus is drawn over the surface. The desired parameters can be determined from this profilogram.

A Hilger and Watts surface microinterferometer, model TN 200, was used for the interferometric examination of the surfaces. This instrument is an interference microscope as proposed by Linnik (ref. 16). Photographs made of the interference patterns (microinterferograms) can be interpreted in the same manner as profilograms. All measurements were made using the mercury green spectral line (21.4-microinch wavelength).

To extend the usefulness of this instrument, the Zehender method of fringe demagnification λ_2 was used (ref. 17). Interferometric examination of rough surfaces, where the fringes are deflected to such an extent that they can not be resolved, can be performed by the technique. A transparent film replica of the surface is measured interferometrically while immersed in a fluid. The amount of demagnification is determined by the refractive indices of the replica and the fluid. Figure 11 graphically demonstrates this method. The microinterferograms shown are of the same specimen as measured directly and as measured by the Zehender method. Immersion fluids used were

FIGURE 11.—The Zehender method. $OPD = 2R(n_f - n_i)$ $\lambda_s = \frac{\lambda}{(n_f - n_i)}$

air, water, and oil, which gave, respectively, approximate demagnification ratios of 1/2, 2/11, and 1/11.

RESULTS

Several profilograms and microinterferograms were made at random positions in the area of the specimen used for the spectral reflectance measurements. On those surfaces having lay, measurements were made both parallel and perpendicular to the direction of the lay. The measured parameters for the specimens are tabulated in tables I, II, and

III. The reported values are based on four random traces having traversing lengths of 0.030 inch.

Representative microinterferograms of the surfaces tested are presented in figures 12, 13, 14, and 15. The field size shown represents 0.0165 inch. The fringe spacing in microinches is given under each microinterferogram. This represents the half wavelength of the mercury green spectral line in the various immersion fluids used.

Profilograms and microinterferograms of the precision roughness specimen are presented for comparison in figure 16.

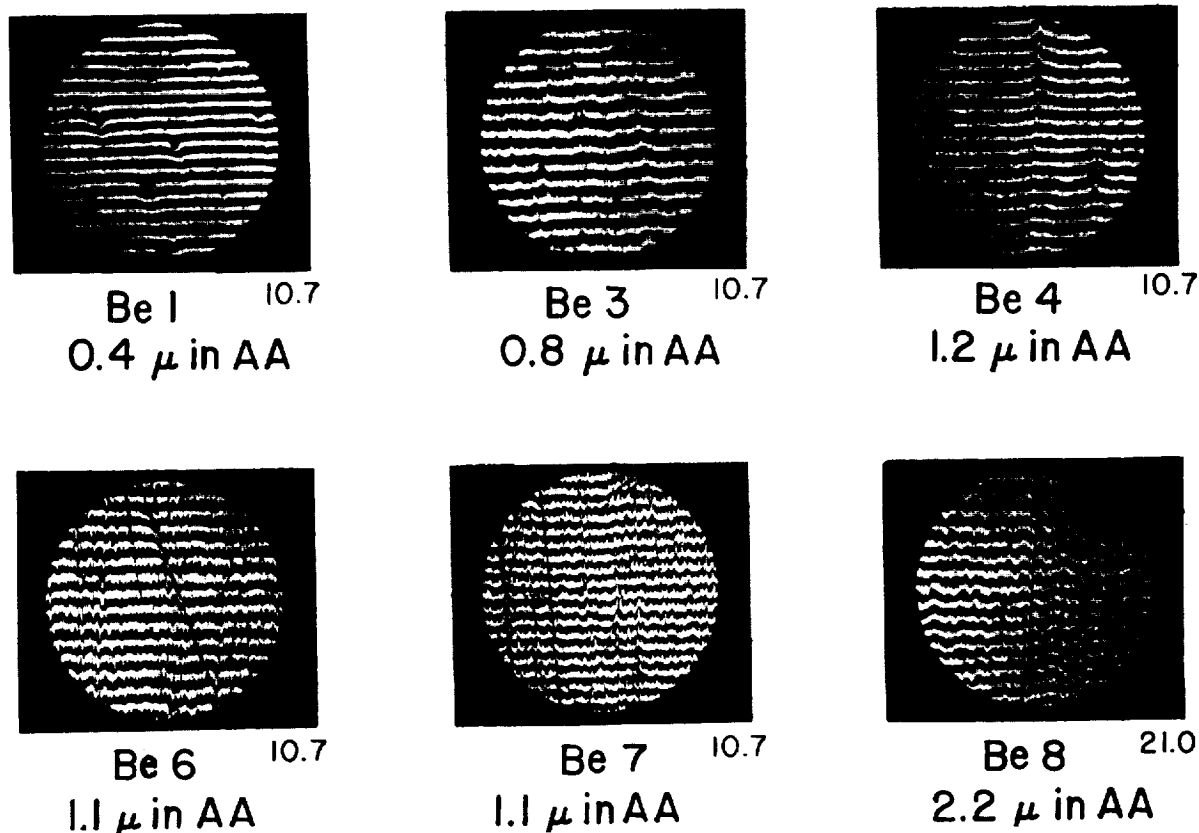


FIGURE 12.—Microinterferograms of sintered beryllium specimens. Field size shown represents 0.0165-in. Fringe spacing in microinch is given below each microinterferogram.

TABLE I.—*Beryllium Specimens*

Sample	Lay	Roughness height R_a , μ in. AA	Peak to valley height R_v , μ in.	Leveling depth R_w , μ in.	Mean depth R_m , μ in.	Roughness width A_r , μ in.	Filling out factor R_m/R	Profile angle factor R/A_r	Shape factor R_s/R_s
Be 1.....	Random	0.4	2.5	1.0	1.5	+	0.60	-----	0.4
Be 3.....	\perp	0.8	6.7	3.7	3.0	2300	.45	0.003	.2
	\parallel	1.0	4.5	1.6	2.9	5500	.65	.0008	.62
Be 4.....	\perp	1.2	6.3	1.9	4.4	2600	.70	.002	.63
	\parallel	1.0	4.7	2.1	2.6	15000	.55	.0003	.48
Be 6.....	\perp	1.1	7.4	2.2	5.2	600	.70	.012	.50
	\parallel	1.1	7.9	3.7	4.2	1600	.53	.005	.30
Be 7.....	\perp	1.1	9.3	2.9	6.4	600	.69	.016	.38
	\parallel	0.7	5.4	1.3	4.1	2200	.76	.002	.5
Be 8.....	\perp	2.2	15.0	6.6	8.4	700	.56	.021	.33
	\parallel	2.2	11.9	6.0	5.9	2000	.50	.006	.37

+ Not applicable.

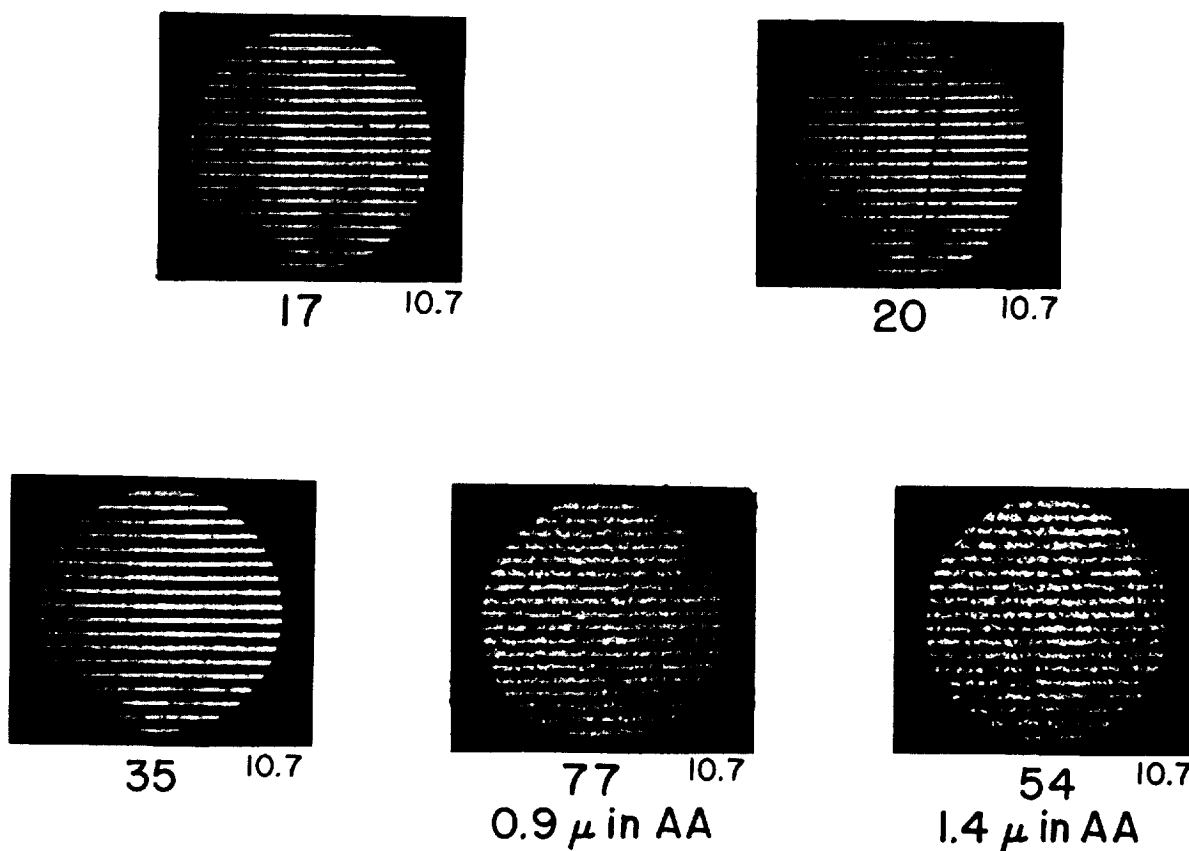


FIGURE 13.—Microinterferograms of prepared steel specimens. Field size shown represents 0.0165-in. Fringe spacing in microinch is given below each microinterferogram.

TABLE II.—*Prepared Steel Specimens*

Sample	Grit	Roughness height R , μ in. AA	Peak-to-valley height R_v , μ in.	Leveling depth R_w , μ in.	Mean depth R_m , μ in.	Roughness width A , μ in.	Filling out factor R_m/R	Profile angle factor R/A	Shape factor R_v/R_m
17	Linde A	—	—	—	—	+	-----	-----	-----
20	$\frac{1}{4}\mu$	—	—	—	—	+	-----	-----	-----
35	1μ	—	0.3	—	—	1400	-----	0.0002	-----
77	3μ	0.9	5.8	1.6	4.2	700	0.72	.008	0.6
54	6μ	1.4	8.7	3.2	5.5	500	.63	.017	.44
40	14μ	3.9	18.0	6.6	11.4	600	.63	.030	.59
86	20μ	5.0	25.5	12.1	13.4	700	.53	.036	.41
85	30μ	13.3	81.5	38.2	43.3	700	.53	.116	.35
24	45μ	15.5	96.0	34.5	61.5	800	.64	.120	.45
61	60μ	15.6	87.0	38.5	48.5	900	.56	.098	.41

— Below measurement capabilities.
+ Not applicable.

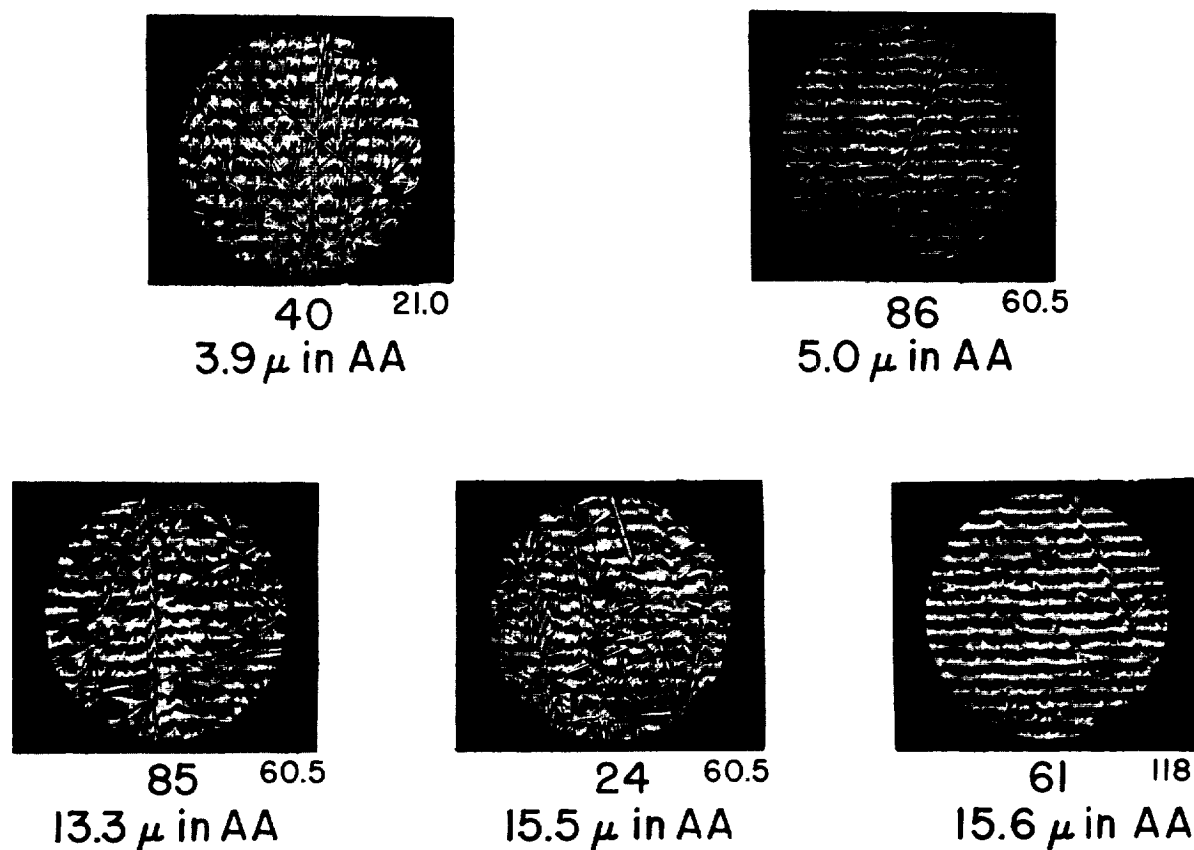


FIGURE 14.—Microinterferograms of prepared steel specimens. Field size shown represents 0.0165-in. Fringe spacing in microinch is given below each microinterferogram.

TABLE III.—Commercial Steel Specimens^a

Sample	Roughness height R_a , μ in. AA	Peak-to-valley heights R_v , μ in.	Leveling depth R_z , μ in.	Mean depth R_m , μ in.	Roughness width A , μ in.	Filling out factor, R_m/R	Profile angle factor R/A	Shape factor R_v/R_a
1	0.7	3.0	n	n	200	n	0.015	-----
2	—	—	—	—	1	-----	-----	-----
3	0.6	3.0	n	n	1000	n	0.003	-----
4	0.5	2.5	n	n	700	n	0.004	-----
5	0.8	3.0	1.1	1.9	500	0.63	0.006	0.7
31	1.9	8.4	1.3	7.1	600	0.85	0.014	1.5
Caliblock								
20	20	80	40	40	600	0.5	0.13	0.5
125	120	480	240	240	3600	0.5	0.13	0.5

^a n Not determined.

— Below measurement capabilities.

+ Beyond measurement capabilities.

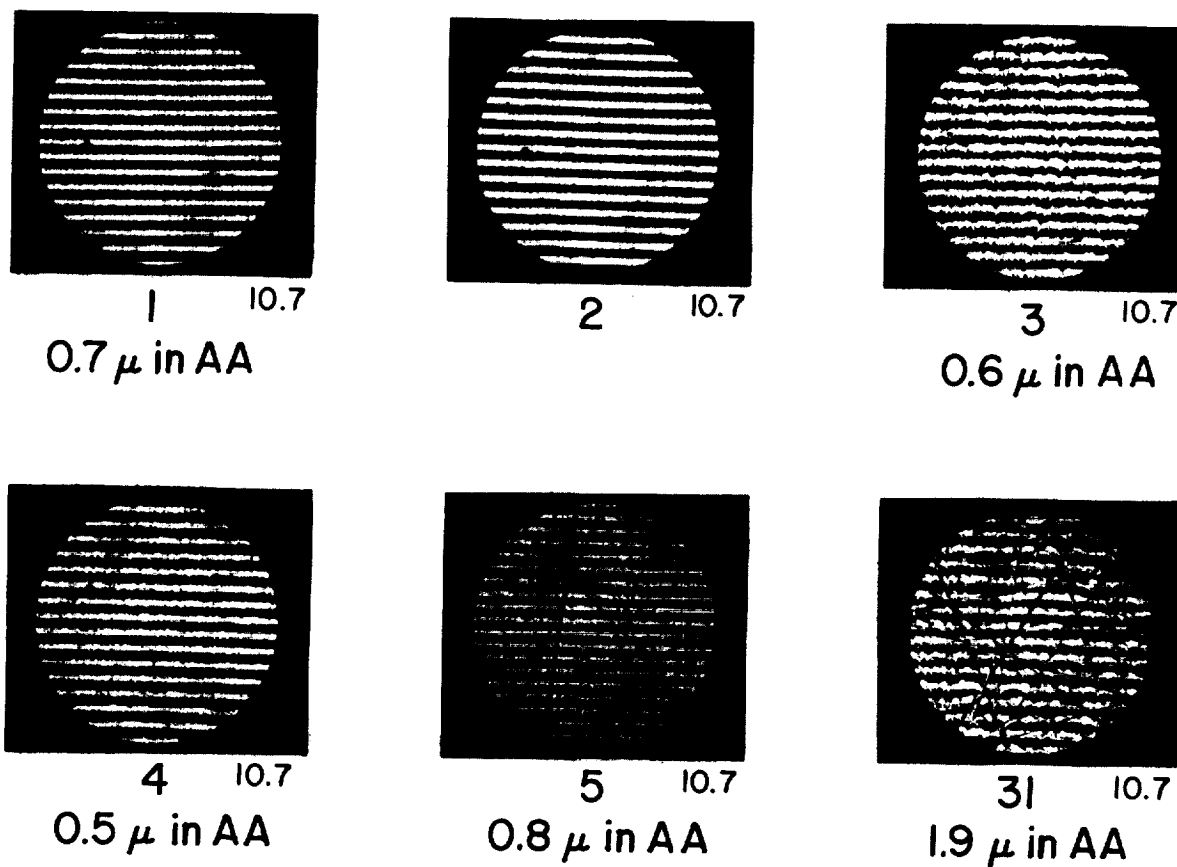


FIGURE 15.—Microinterferograms of commercial steel specimens. Fringe size shown represents 0.165-in. Fringe spacing in microinch is given below each microinterferogram.

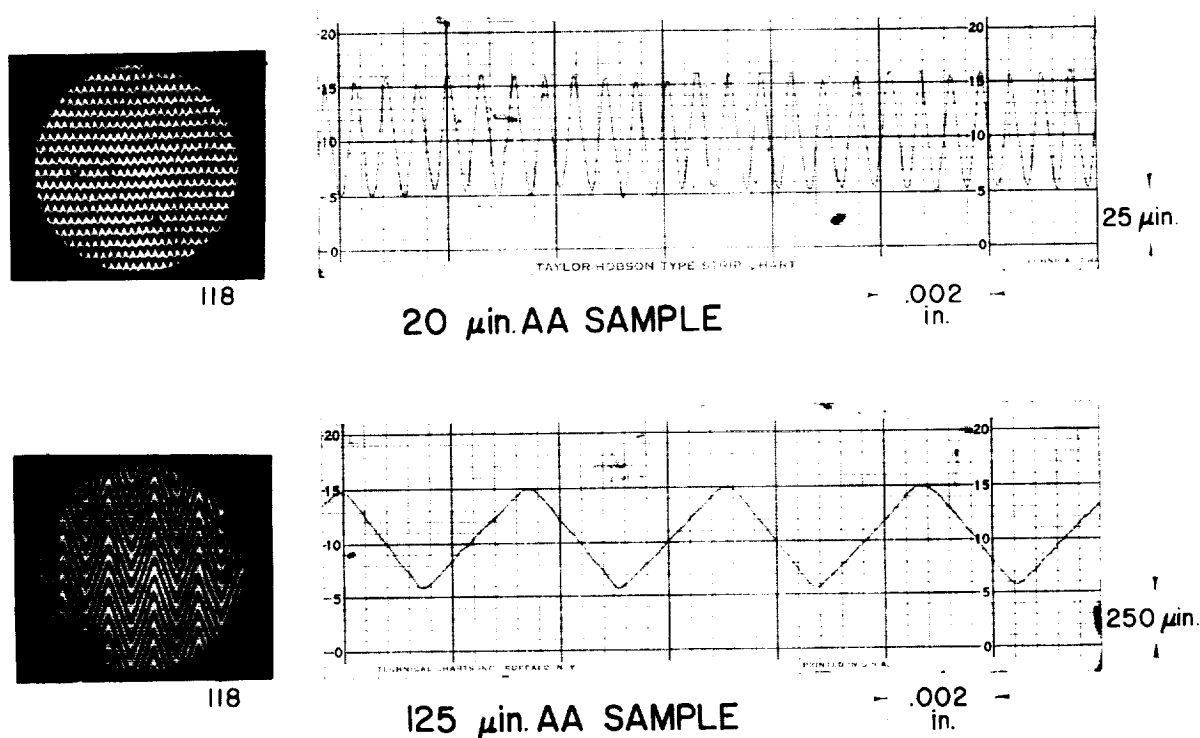


FIGURE 16.—Profilograms and microinterferograms of the two sample areas of the precision roughness specimen.

REFERENCES

1. NUTTING, R. D.: Interpretation of Data Obtained with Spectrophotometers of the Polarizing Type. *Textile Research*, vol. V, no. 9, pp. 391-400, July 1935.
2. REIMANN, GENEVIEVE, JUDD, DEANE B., and KEEGAN, HARRY J.: Spectrophotometric and Colorimetric Determination of the Colors of the TCCA Standard Color Cards. *Jour. Optical Soc. of America*, vol. 36, no. 3, Mar. 1946, pp. 128-159.
3. BENNETT, H. E., and PORTEUS, J. O.: Relation Between Surface Roughness and Specular Reflectance at Normal Incidence. *Jour. Optical Soc. of America*, vol. 51, no. 2, Feb. 1961, pp. 123-129.
4. BENNETT, H. E.: Specular Reflectance of Aluminized Ground Glass and the Height Distribution of Surface Irregularities. *Jour. Optical Soc. of America*, vol. 53, no. 12, Dec. 1963, pp. 1389-1394.
5. PORTEUS, J. O.: Relation Between the Height Distribution of a Rough Surface and the Reflectance at Normal Incidence. *Jour. Optical Soc. of America*, vol. 53, no. 12, Dec. 1963, pp. 1394-1402.
6. DONOVAN, T. M., ASHLEY, E. J., and BENNETT, H. E.: Effect of Surface Damage on the Reflectance of Germanium in the 2650-10 000-Å Region. *Jour. Optical Soc. of America*, vol. 53, no. 12, Dec. 1963, pp. 1403-1407.
7. OLSON, O. H., and PONTARELLI, D. A.: Asymmetry of an Integrating Sphere. *Appl. Optics*, vol. 2, no. 6, June 1963, pp. 631-633.
8. GIBSON, KASSON S., and KEEGAN, HARRY J.: Calibration and Operation of the General Electric Recording Spectrophotometer of the National Bureau of Standards. *Jour. Optical Soc. of America*, vol. 28, no. 10, Oct. 1938, pp. 372-385.
9. KEEGAN, HARRY J., SCHLETER, JOHN C., and JUDD, DEANE B.: Glass Filters for Checking Performance of Spectrophotometer-Integrator Systems of Color Measurement. *Res. Paper 66A3-154*, *Jour. Res. Nat. Bur. Standards*, vol. 66A, no. 3, May-June 1962, pp. 203-221.
10. ANON: Preparation and Colorimetric Properties of a Magnesium-Oxide Reflectance Standard. *NBS Letter Circular LC-547*, U.S. Dept. Commerce, Mar. 17, 1939.
11. KEEGAN, HARRY J., and GIBSON, KASSON S.: On the Use of Working Standards of Didymium and Vitrolite Glasses for Spectrophotometric Measurements. *Proc. Twenty-Ninth Annual Meeting*

- of O.S.A., Jour. Optical Soc. of America, vol. 34, no. 12, Dec. 1944, p. 770.
12. OLSEN, K. V.: The Standardization of Surface Roughness, Brüel and Kjoer Technical Review No. 3, 1961.
 13. American Standard B46.1-1962. Surface Texture.
 14. British Standard 1134-1961. The Assessment of Surface Texture.
 15. REASON, R. E., HOPKINS, M. R., and GARROD, R. I.: Report on the Measurements of Surface Finish by Stylus Method. Taylor-Hobson Research Dept., 1944.
 16. LINNIK, W.: Ein Apparat für Mikroskopisch-interferometrische Untersuchung Reflectierende Objecte. Compt. Rend. Acad. Science USSR S. 21 Bericht: A. Instr. 54, 1934, p. 462.
 17. ZEHENDER, E.: An Interference Method for Examining Rough Surfaces. Z. VDI, vol. 94, no. 14-15, 1952, p. 456.

DISCUSSION

J. T. NEU, General Dynamics Astronautics: Mr. Keegan, you indicated that the Cary and the GE spectrophotometers were unsatisfactory for making reflectance measurements. Why is this?

KEEGAN: The Cary model 14 spectrophotometer was designed and built for the measurement of spectral transmittance of solutions such as those prepared by chemists. To measure reflectance on the Cary 14 spectrophotometer an attachment must be purchased for diffuse reflection measurements and the instrument must be partially dismantled to install this attachment. Because the 100-percent curve is set from two diffusing standards, and because of the baffles in the integrating sphere, the results obtained for specular specimens depend upon the mode of illumination of the specimen.

The GE recording spectrophotometer accurately measures spectral directional reflectance of diffusing samples and samples that are nearly perfect mirrors so that the specular component may be excluded from the measurement. For semiglossy samples

and nonplane surfaces the excluded measurement is in question because of the size of the specular cup. This instrument comes equipped with an integrating for measurements of transmittance and reflectance. It was designed and built for the measurement and specification of colored materials. Does this answer your question?

NEU: No. Is it not possible that the problem is with the integrating sphere that you attach to the spectrophotometer—rather than the spectrophotometer? I consider the spectrophotometer to be an excellent instrument.

KEEGAN: Yes, it is good for diffuse reflectance if it has the proper integrating sphere.

NEU: That is the point! It is not the instrument, it is the device that you fasten to it.

KEEGAN: I rely on the Cary 14 for transmittance and diffuse reflectance measurements. It is the present reflectance attachment that does not measure specular reflectance accurately.

18. The Measurement of Total Surface Area

J. E. JANSSEN AND R. N. SCHMIDT

RESEARCH CENTER, HONEYWELL, INC., MINNEAPOLIS, MINN.

If the geometry of a surface could be adequately described, it might be possible to publish radiation properties for smooth surfaces and calculate the effect of variations in surface roughness. A method employing a radioisotope tracer technique for measuring total surface area is described. A monomolecular layer of carbon-14 tagged surficant is employed. It appears that a knowledge of the total surface area along with profilometer measurements might provide sufficient data to construct a reasonably accurate model of the surface.

Anyone who searches the literature for thermal radiation properties will find a great deal of data on materials and surfaces that are poorly described. Descriptions such as "iron," "oxidized iron," "steel," and "aluminum," are common. Information as to the surface roughness, thickness of oxide layer, and chemical composition of the material is frequently lacking.

The demands for better data imposed by our space programs have resulted in much better descriptions of the materials in recent years. However, the engineer is always faced with the problem that the data available are for a particular surface condition, whereas he may need information on a slightly different surface. It would be desirable if the true emissivity of a material could be specified, and if from this the emittance of a surface with a particular roughness could then be calculated. Emissivity is equivalent to emittance only for an optically smooth opaque surface (ref. 1).

Such an approach is very simple in the case of electrical resistance. The volume resistivity of a material can be easily determined, and the resistance of a particular conductor made of this material can then be computed from the resistivity and the easily measured geometrical parameters.

In the case of thermal radiation, the geometry of surface roughness is much more difficult to

determine. Conventional profilometers give an indication of the average height of the roughness but reveal little about the distribution of the peaks and valleys or the slopes of their sides. Recently a radioactive-tracer technique has been used to study the influence of surface roughness on the magnetic properties of thin films (ref. 2). Basically, the technique consists of treating the surface to be measured with a radioactive surficant in such a way as to achieve a monomolecular layer of the surficant. Under this condition the radioactivity of the surface will be a direct function of the total surface area. A rough surface can then be compared with a smooth surface of the same projected area to give a total surface area ratio.

SURFACE AREA MEASUREMENT

The technique presented here has been described in a paper by Kivel, Albers, Olsen, and Johnson (ref. 3). Surfaces to be measured were immersed in aqueous solutions of 1.0×10^{-4} to 2.0×10^{-3} molar HMAB (hexadecyl-1- C^{14} trimethylammonium bromide, available from Nuclear Chicago Corp.). The samples were then vertically withdrawn at a uniform rate of 2 mm/min by means of a small motor. The radioactivity was then measured with a Tracerlab model FD-1 gas flow counter. When the radioactivity of a surface was plotted against

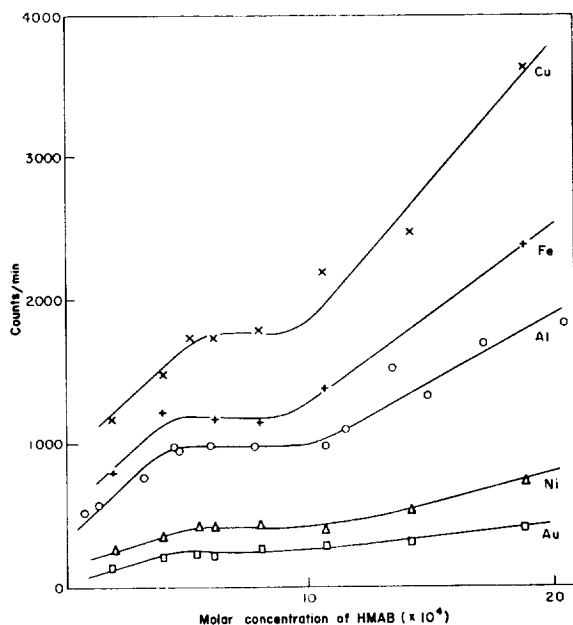


FIGURE 1.—Adsorption isotherms for hexadecyl-1- C^{14} trimethylammonium bromide (HMAB) on metals, at $20^\circ C$.

the concentration of HMAB, it was found that the curve exhibited a plateau. This plateau has been assumed to indicate the existence of a monomolecular layer. Figure 1 shows the data for several metals and figure 2 for two organic surfaces.

Fire-polished glass is optically smooth and makes a good reference surface; but it is conceivable that spectral data could be obtained by using surfaces with known roughness dimensions as references.

ROUGHNESS GEOMETRY

The values of total surface area might be used in the following way. Profilometer measurements of a surface give the mean height of the peaks. Knowing the surface area would enable one to calculate the slope of the sides of the peaks if, for example, V-grooves could be assumed. The slope and height then establish a model for the surface geometry.

Other geometries can be visualized. Cylindrical grooves or spherical depressions might be more realistic for some surfaces. The saw-tooth surface shown in figure 3 might have

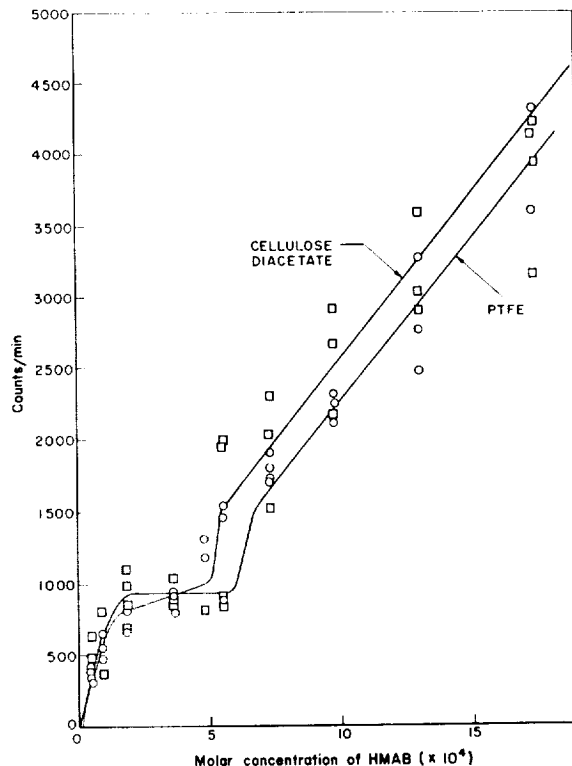


FIGURE 2.—Adsorption isotherms for hexadecyl-1- C^{14} trimethylammonium bromide (HMAB) on two organic surfaces, at $20^\circ C$.

small flats on the peaks and in the valleys. Some experimentation would be required to determine which model gives the best results under specific conditions.

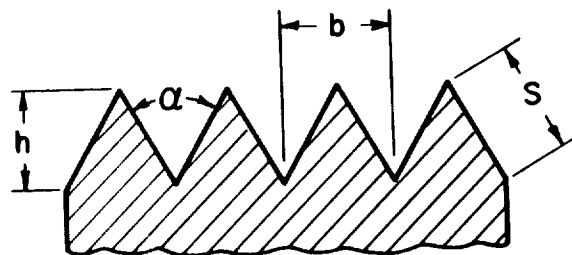


FIGURE 3.—Relationship of total area A_T to nominal area A . L is the number of grooves in the given area:

$$A_T = 2SL$$

$$A = bL$$

$$\frac{A_T}{A} = \frac{2S}{b} = \csc \frac{\alpha}{2}$$

It would be necessary to make a distinction between metals and dielectrics. Smooth metal surfaces are highly specular and the sides of the grooves or pits would have to be treated as specular surfaces. Dielectrics are diffuse by nature and have much lower absorption coefficients. Very small scale roughness probably has a negligible effect on dielectrics. For roughness with significant dimensions it would be necessary to treat the surface elements as diffuse surfaces.

CONCLUSION

The method discussed is admittedly not the complete solution to the problem of reducing surface roughness effects to a rational basis. It would appear, however, that this technique for measuring total surface area is a tool that

can be used to obtain one more item of information about surfaces. If a rough surface can be adequately described, it should be possible to compute the effect of surface roughness and thus eliminate surface geometry as an unknown parameter.

REFERENCES

1. GUBAREFF, G. G., JANSSEN, J. E., and TORBORG, R. H.: *Thermal Radiation Properties Survey*. Second ed., Research Center, Honeywell, Inc., 1960.
2. PROSEN, R. J., HOLMEN, J. O., GRAN, B. E., and CEBULLA, T. J.: Stratification in Thin Permalloy Films. *Jour. Appl. Phys.*, suppl. to vol. 33, no. 3, Mar. 1962, pp. 1150-1151.
3. KIVEL, J., ALBERS, F. C., OLSEN, D. A., and JOHNSON, R. E.: Surface Areas by Adsorption of a Quaternary Ammonium Halide From Aqueous Solution. *Jour. Phys. Chem.*, vol. 67, no. 6, June 1963, pp. 1235-1238.

DISCUSSION

KARL A. SENSE, Astropower Laboratory, Douglas Aircraft Company: How do you know that the radiation that comes off the radioactive material is not intercepted by the wall of the crevice in which it is located, so that it is not registered on the detector?

SCHMIDT: I wish mainly to describe our experience with the technique, rather than to advocate it. Nevertheless, this is an interesting point, and we have thought about it. However, we have not actually used the technique for the measurement of roughness for correlating thermo-physical properties, so I hesitate to give you an answer. I do know that the radioactivity of the material is very weak so it can be handled with little danger. There are some drawbacks to the technique because the molecule is a long chain and it attaches to the surface at one end; that is, the head sticks to the surface and the tail sticks out. Accordingly, the nature of the surface coverage would not be obvious if the surface has sharp irregularities that are of molecular dimensions. I am sure that an error in the measurement would result if the surface roughness had an overlapping configuration. The size of the molecule of the surfactant is also important. A smaller molecule could go into the smaller fissures or pores, whereas the larger molecule could not. The HMAB molecule takes up an area of approximately 20 \AA^2 , which should be satisfactory for very small roughnesses.

Incidentally, some people in Australia are using a compound very similar to HMAB but not radioactive. Its presence is determined by ultraviolet absorption. A paper on the technique has been published recently in one of the physics journals.

SENSE: I would be hesitant to use this method myself.

There is a well known method that Brunauer, Emmett, and Teller established the basis for many years ago, which uses gases like krypton or xenon for monolayer adsorption. From straightforward physical chemical measurements, one can determine the surface area quite accurately with the Brunauer-Emmett-Teller method. For example, Cannon, in a recent publication in *Nature* describes his work on surface roughness using the BET method with xenon.

SCHMIDT: A point we must keep in mind is that we are not measuring total surface area for the sake of measuring total surface area or for the sake of determining area available for chemical reactions but to use it to correlate gross radiation properties with the radiation properties of smooth surfaces. The area measurement made by the nuclear radiation method may be more useful than the methods you consider to be more accurate because those methods include surface areas under overlapping configurations of roughness. Underlying surface areas do not contribute in a direct ratio to the gross thermal radiation properties except where they can be viewed. If they can be viewed for thermal radiation they can also be viewed for nuclear radiation because the mechanisms involved are quite similar.

One final comment is that Dr. Kivel, who developed this method, discussed in his paper an alternative method for determining total surface area. This alternative technique uses the same method for producing a monolayer of HMAB on the surface. The HMAB is washed off, however, and the radioactivity of the wash gives a direct indication of the total surface area including the surface under overlapping configurations of roughness.

19. The Time Variation of the Total Hemispherical Emittance of Polished Platinum Surfaces at High Temperatures

N. J. ALVARES

U.S. NAVAL RADIOLOGICAL DEFENSE LABORATORY, SAN FRANCISCO, CALIF.

Platinum strips were maintained at temperatures up to 1700° K for extended periods, during which repeated measurements of total emittance were made, together with photomicrographs of the surface. The photomicrographs show the gradual appearance and increasing definition of crystal grain boundaries during the extended heating. The simultaneous increase in emittance was very slight. A small decrease of emittance during the first few minutes is ascribed to a thermal-polishing mechanism.

The surfaces of polished metals held at high temperatures for fairly long periods of time eventually lose their specular characteristics because of thermal etching and/or recrystallization. Thermal etching is probably similar to any other etching process, which is the physical removal of material from the surface of the bulk metal in order to reveal its underlying crystalline structure. Thermal etching may involve selective evaporation from the grain boundaries of the crystals. Recrystallization, on the other hand, results from the release of accumulated mechanical energy. The energy imparted to the metal during cold working and polishing is reduced by the migration of dislocations and vacancies from sites of high local strain to the grain boundaries (ref. 1). Both of these phenomena are directly influenced by the temperature and by the amount of cold working.

In order to determine the effect of thermal etching or recrystallization on the total hemispherical emittance, an apparatus was devised which would simultaneously photograph the surface, and measure the emittance as a function of time at high temperature. Thin platinum ribbons were heated electrically in a vacuum of about 10^{-5} torr. The emittance was de-

termined from the electrical power dissipated per unit area in the constant temperature region at the center of the ribbon (ref. 2). The temperature at the center of the ribbon was measured by a platinum/platinum, 10-percent rhodium thermocouple, and the potential drop across the uniform center portion of the ribbon was measured by two voltage leads attached to the ribbon on either side of the center portion.

Changes of the platinum surface were recorded by time-lapse photography. The photo-optical system consisted of a 16-mm Cine Kodak motion picture camera modified by a system of a-c solenoids connected to a mechanical shuttering device that provided precise timing of the repetition rate, which could be varied from one frame per second to one frame per 30 seconds. The camera was coupled to a telemicroscope which magnified the surface by a factor of 40 to 1. Since the telemicroscope had an objective lens with a focal length of 48 mm, the ribbon had to be very close to the window of the vacuum chamber. The entire vacuum chamber was water cooled and a fan was used to cool the window. In order to take photomicrographs having good definition, it was necessary to illuminate the ribbon surface normally, as illustrated in figure 1.

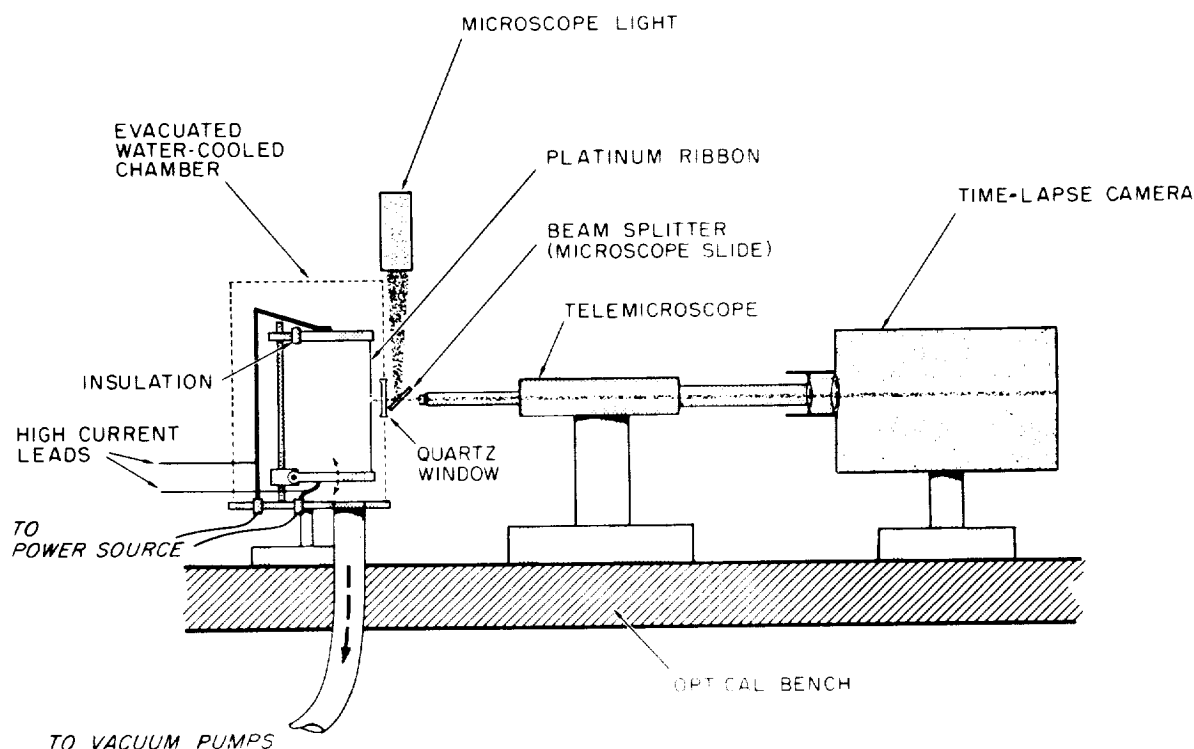


FIGURE 1.—Schematic diagram of apparatus for determining the time variation of emittance and surface appearance.

In the setup shown schematically in figure 1 and by the photograph in figure 2, the power was supplied to the specimen from a voltage-regulated a-c source, and the potential drop between the voltage probes was measured by an a-c voltmeter with an accuracy of 0.25 percent of full scale. The current was monitored by an a-c ammeter of the same accuracy. The emf from the thermocouple was measured with a potentiometer, and the brightness temperature was measured by a micro-optical pyrometer.

The power to the ribbon and the time-lapse camera were turned on simultaneously and the repetition rate of the camera was set at one frame every 30 seconds. When the specimen reached the desired thermocouple temperature, the values of the emittance parameters were recorded. Measurements at this temperature were continued for a period of several hundred minutes, and emittance data were recorded every 15 minutes. During this time, the emf of the thermocouple was held constant by

controlling the power to the ribbon. The accuracy of the electrical power dissipation determination is $\pm \frac{1}{2}$ percent, since it is derived from the previously mentioned current and voltage measurements. Even though the thermocouple voltage could be read quite accurately with the potentiometer, it is believed that systematic errors in the thermocouple circuit of this system increased the temperature error to ± 1 percent.

Figure 3 consists of eight selected frames from a 16-mm film record of a platinum ribbon held at various high temperatures for a period of 900 minutes. The temperature was varied from 1200° K to 1600° K and back down to 1200° K in approximately 100° steps of 100 minutes duration each. Plate a shows the polished surface of the specimen at 1200° K. The horizontal striations visible in this view were probably caused by the initial rolling process. The subsequent views show the progressive degradation of the specular quality of the surface by the appearance of grain bound-

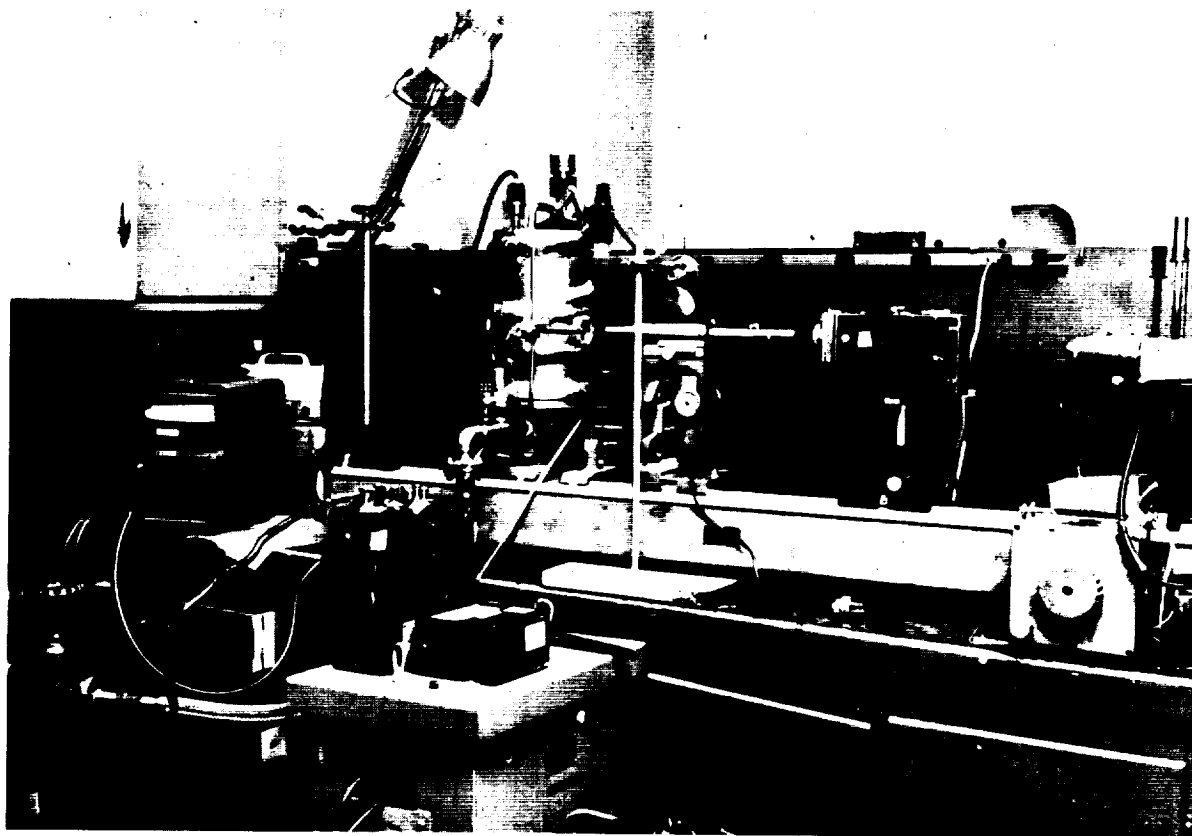


FIGURE 2.—*Photograph of apparatus.*

aries which apparently deepen and become more clearly defined with time. Plate i is a photograph of a reticle placed in the position of the specimen in order to calibrate the system. The distance between the divisions is 100 microns. A chronological record of the temperature and the emittance of another sample is shown in figure 4. The initial decrease in total hemispherical emittance at 1500°K was an unexpected effect. Photomicrographs of the specimens indicate that this decrease could be attributed to a thermal polishing action that smooths the microscratches caused by the lapping wheel.¹ After the temperature was increased to 1700°K the emittance increased perceptibly with time. At 670 minutes the temperature of the specimen was reduced to 1500°K ; the emittance was only about 1.5 to 2.0 percent greater than that for the original

polished state. At 720 minutes the temperature was increased to 1682°K . The rate of increase of the emittance at this temperature is greater than it is at 1500°K , showing that the rate of increase of emittance is related to the temperature of the specimen.

Figure 5 shows photomicrographs of the central areas of two platinum samples. The photomicrographs illustrate the "as received" surfaces (plates a and d), the lapped surfaces (plates b and e), and the recrystallized surfaces (plates c and f). Plate g is the reticle calibration for these six photomicrographs. The lapping scratches visible in plates b and e are not apparent on the single crystals of the recrystallized surfaces. As previously noted, the change is ascribed to some thermal-polishing mechanism, which presumably causes the initial decrease in emittance observed during the first few minutes of the measurements. Plate h is the reticle calibration for the photomicrograph

¹ See also Paper 15.

SURFACE EFFECTS

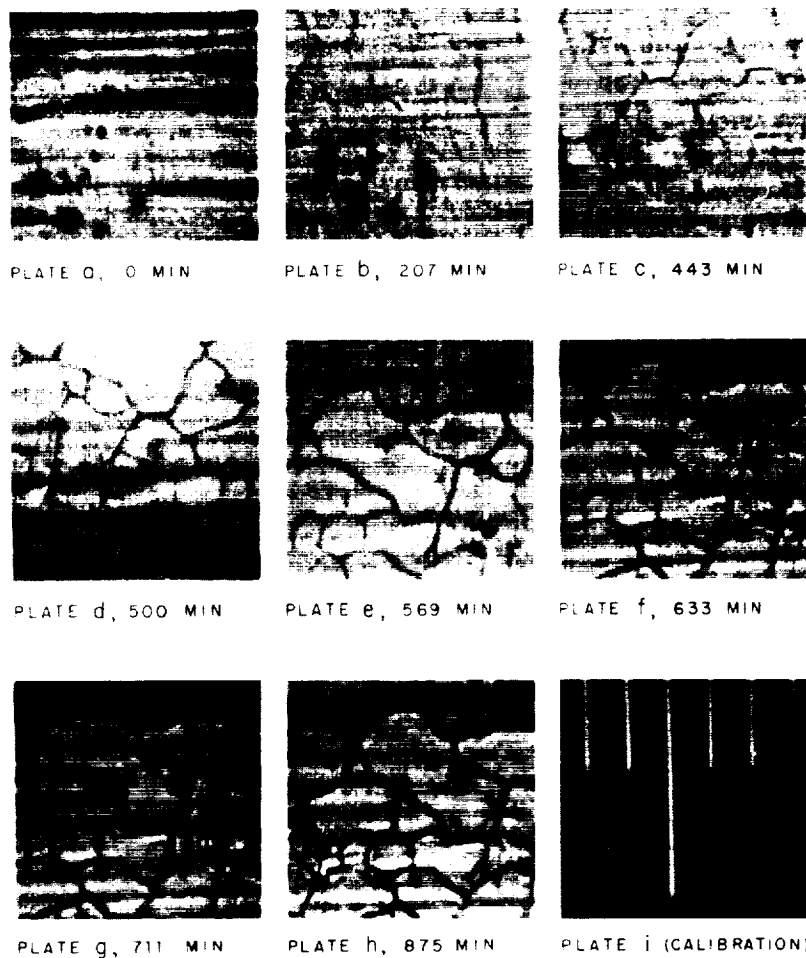


FIGURE 3.—Time lapse photographs of platinum sample showing the change of the surface microstructure from the initially polished state, plate a, to the final state at 900 min, plate h. Plate i is a photograph of the reticle used to calibrate the system, where 1 division equals 100 microns.

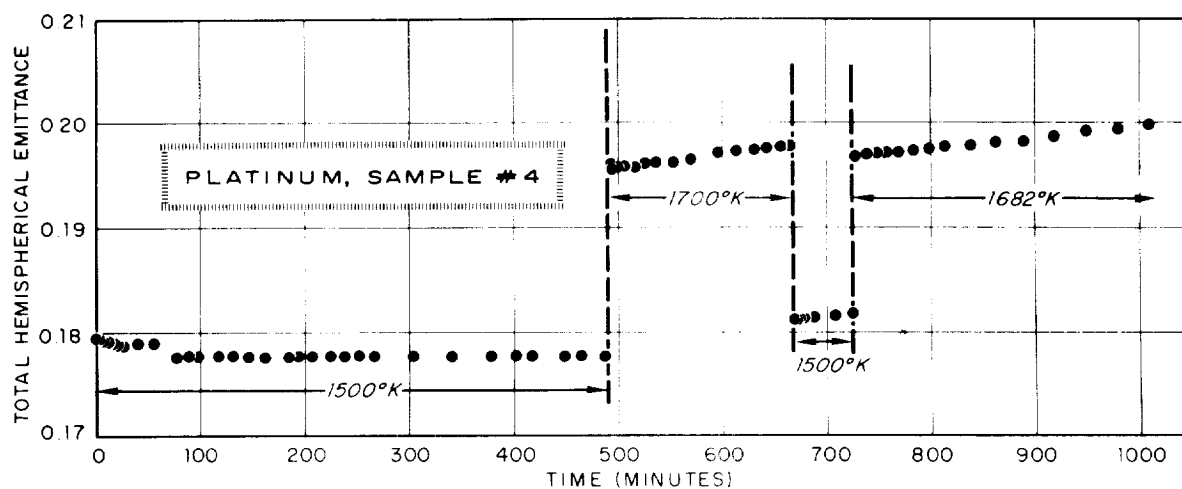


FIGURE 4.—Variation of emittance of platinum during a test run.

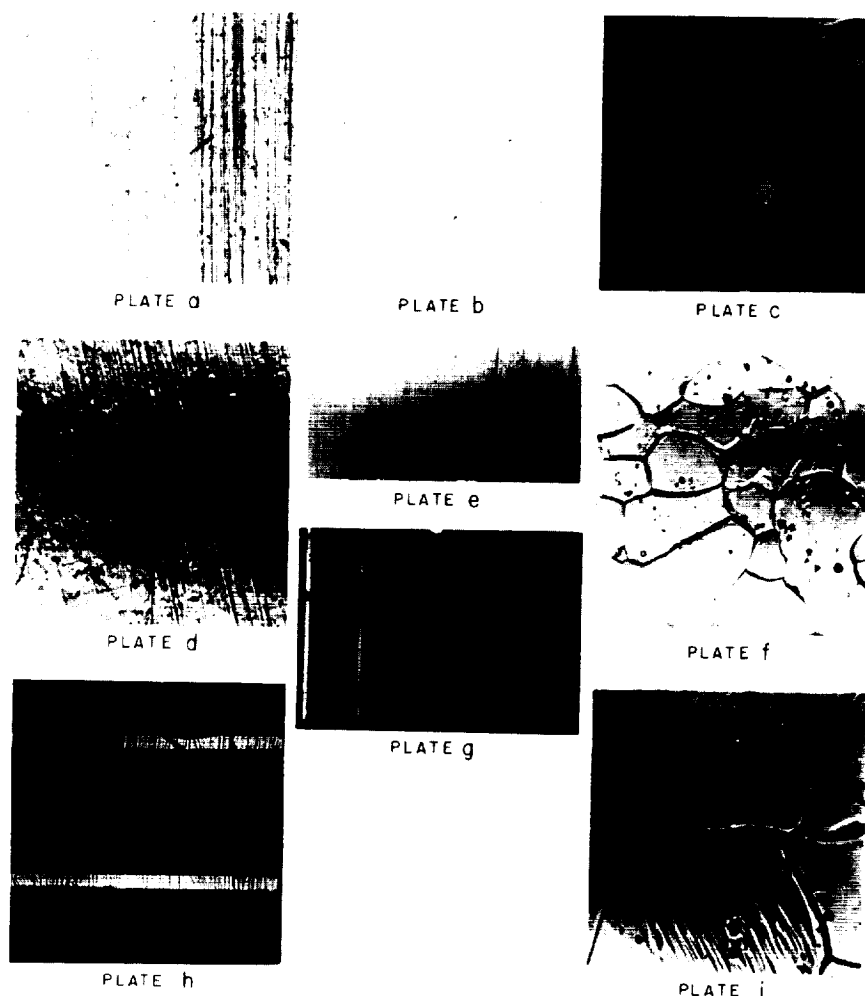


FIGURE 5.—Photomicrographs of two platinum samples. Plates a, b, and c chronologically show the as received, polished, and post run conditions of sample 4; and plates d, e, and f show the as received, polished, and post run conditions of sample 5. Plate g is the calibration for plates a through f, where the distance between any two adjacent lines is $100\ \mu$. Plate h is the calibration for plate i which shows a section of sample 5 at almost three times the magnification of the other photomicrographs.

of plate i, which has nearly three times the magnification of the other plates and which illustrates the "slip planes" in a single crystal which could possibly increase the emittance.

The grain boundaries that appear so dramatically on the surface of the platinum specimen apparently do not have a dramatic effect on the emittance of the surface over reasonably long periods of time at high temperatures. The mechanism by which these boundaries appear has as yet not been resolved. However, the

slight emittance increase with time can be attributed to the gradual deepening of the grain boundaries.

REFERENCES

1. VAN BUREN, H. G.: Imperfections in Crystals. Interscience Publ., Inc. (New York), 1960, pp. 229-239.
2. ABBOTT, G. L., ALVARES, N. J., and PARKER, W. J.: Total Normal and Total Hemispherical Emittance of Polished Metals. WADD Tech. Rep. 61-94, U.S. Air Force, Nov. 1961, and WADD Tech. Rep. 61-94, pt. II, U.S. Air Force, Jan. 1963.

20. Solar Absorptance and Thermal Emittance of Evaporated Metal Films With and Without Surface Coatings¹

GEORG HASS²

U.S. ARMY ENGINEER RESEARCH AND DEVELOPMENT LABORATORIES, FORT BELVOIR, VA.

This paper describes and discusses the techniques used in preparing thin evaporated metal films with and without superimposed dielectric coatings. In particular, the effects of evaporation rate and of oxygen pressure on the characteristics of silicon oxide films are reviewed. Theoretical angular reflectance characteristics of metals, as determined by the optical constants, are also reviewed.

METAL FILMS WITHOUT SURFACE COATINGS

Effect of Deposition Technique

This paper will summarize the current status of several kinds of evaporated, opaque metal films and of several evaporated dielectric films applied over the opaque metal films. The coatings to be described are of interest because they are potentially capable of providing a wide range of ratios of solar absorptance to thermal emittance. The metal films of interest are aluminum, silver, gold, copper, rhodium, and platinum. The quantitative optical properties to be presented apply only for films that have been prepared with great care. In general, these films were prepared by using relatively high rates of vapor deposition, in the range of 200 to 1000 Å/sec, and were prepared in a vacuum in the range of 10^{-5} to 10^{-6} torr. For the lower melting temperature metals, tungsten evaporation (that is, evaporation from a directly heated tungsten source) was used, and for rhodium and platinum an electron gun technique was used.

From reflectance data published by Hass and Hadley in the second edition of the *American Institute of Physics Handbook*, and from the results of new reflectance measurements on aluminum by Bennett et al., on gold by Harris and Fowler, and on platinum and rhodium by Hass and Ramsey, the values for total normal solar absorptance and thermal emittance were determined or estimated:

TABLE I.—Normal Solar Absorptance α_n and Normal Thermal Emittance ϵ_n

Film material	$\alpha_n, \%$		ϵ_n at 27° C, %
	Outside atmosphere	At sea level	
Al	7.8	8.2	1.14
Ag	5.0	2.1	~1.0
Au	19.2	14.7	1.08
Cu	17.2	13.1	~1.0
Rh	18.0	18.1	~1.9
Pt	24.0	23.4	~3.2

Gold, silver, and copper, which have much lower reflectance in the near ultraviolet than at longer wavelengths, show considerably lower solar absorptance at sea level than in outer space.

¹ See also Paper 16.

² This paper was presented by Milton Schach, NASA Goddard Space Flight Center.

The low emittance and absorptance values of aluminum listed in table I can be obtained only with films produced under optimum conditions. The most important factors affecting the reflectance of evaporated aluminum are: rate of deposition, pressure during the evaporation, vapor incidence angle, and purity of the aluminum. To produce aluminum films of highest reflectance at pressures of 10^{-6} to 10^{-5} torr, an extremely high deposition rate is an absolute necessity. Opaque coatings should be deposited in about 1 sec. In addition, the aluminum used should be of highest purity, and the deposition should be performed at vapor incidence angles not greater than 30° . If aluminum is not evaporated under optimum conditions but is deposited at lower rates and higher pressures, the resulting films are contaminated with oxygen and show higher absorptance and emittance values. Films deposited at a rate of 10 to 20 Å/sec at a pressure of 1 to 3×10^{-5} torr show a total normal emittance of 1.7 to 2.0 percent and a normal solar absorptance of about 9 percent.

In the literature, the effect of oxidation during aging on the absorptance and emittance of aluminum is very frequently overrated. The oxide film on evaporated aluminum grows in air to an ultimate thickness of about 30 to 40 Å. The calculated reflectance decrease from such a 40-Å thick oxide film on aluminum is less than 0.1 percent for all wavelengths longer than 1μ , and only 0.3 percent at $500 \text{ m}\mu$. Therefore, the ϵ_n value for aluminum listed in table I should be unaffected by aging, and the normal solar absorptance should be increased by about 0.2 percent.

Theoretical Effects of Optical Constants³

The optical constants listed in the second edition of the *American Institute of Physics Handbook* were used to calculate the effect of angle of incidence on the reflectance of evaporated metal films at various wavelengths and to determine their hemispherical emittance. Figures 1 and 2 show the reflectance of aluminum and silver as a function of angle of incidence for two wavelengths, one in the visible

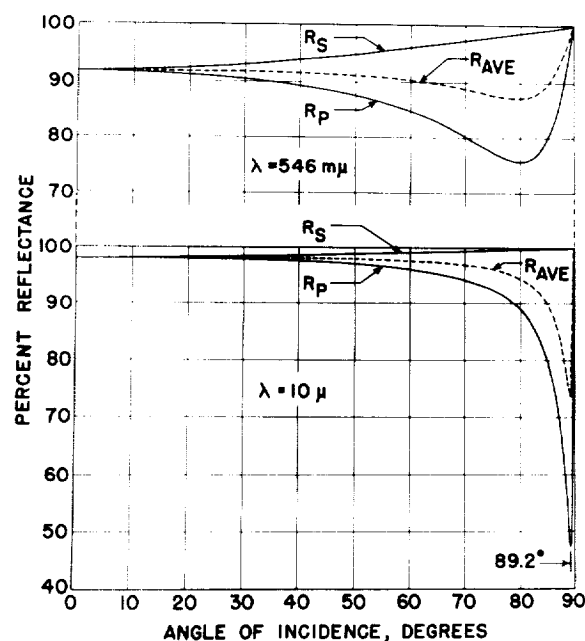


FIGURE 1.—Angular reflectance characteristics of aluminum in the visible and in the infrared.

and one in the infrared at 10μ . For most metallic reflecting coatings used in the infrared and visible, it is possible to make an assessment of their reflectance behavior as a function of angle of incidence rather simply by using certain approximations in the formulas for the reflectances of the parallel (p) and perpendicular (s) components. Such approximations

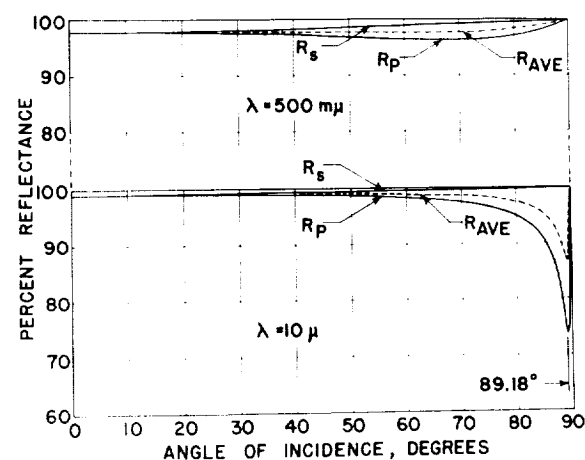


FIGURE 2.—Angular reflectance characteristics of silver in the visible and in the infrared.

³ See also Paper 5.

can be applied when the optical constants are such that $(n^2 + k^2) \gg 1$, which is true for most metals in the visible and infrared.

The angular variation of the reflectance follows a certain pattern in all cases: the reflectance of the perpendicular component R_p increases steadily from the normal incidence value up to 100 percent at grazing incidence, while the reflectance of the parallel component R_p first decreases to a minimum and then rises rapidly to 100 percent at 90° angle of incidence.

The essential features of the reflectance curves are given by three quantities:

- (1) Reflectance at normal incidence, where

$$R_p = R_s = \frac{(n-1)^2 + k^2}{(n+1)^2 + k^2}$$

- (2) Angle at which R_p reaches a minimum,

$$\theta \text{ for } R_{p, \min} = \cos^{-1} \sqrt{\frac{\sqrt{1 + \frac{4}{n^2 + k^2}} - 1}{\sqrt{1 + \frac{4}{n^2 + k^2}} + 1}}$$

- (3) Value of R_p at the minimum,

$$R_{p, \min} = \left[\frac{\frac{k}{n}}{1 + \sqrt{1 + \frac{k^2}{n^2}}} \right]^2$$

The values of $(n^2 + k^2)$ and the ratio k/n are the dominating factors for predicting the reflectance behavior of a metal. The angle of incidence for minimum R_p moves closer to 90° with increasing values of $(n^2 + k^2)$, as shown in table II.

TABLE II.—Effect of Optical Constants on Angle of $R_{p, \min}$

Film material	Wavelength, μ	$(n^2 + k^2)$	θ for $R_{p, \min}$, deg
Ag.....	0.5	8.2	70
	10	4900	89.18
Al.....	0.546	36	80
	10	5200	89.20

TABLE III.—Effect of Optical Constants on Variation of R_p With Angle

Film material	Wave-length, μ	k/n	$R_{p,0}$, %	$R_{p, \min}$, %
Ag.....	0.5	57	97.9	96.3
	10	6.5	99.1	73.4
Al.....	0.546	7.3	91.6	75.6
	10	2.7	98.5	47.0

In the infrared, where most of the low temperature thermal radiation is emitted, the angle of $R_{p, \min}$ for highly reflecting metal lies between 89° and 90°, and the reflectance minimum is so narrow that its reflectance value cannot be measured with any accuracy. It can, however, be calculated from the optical constants.

The ratio k/n has the greatest effect on the decrease of R_p with angle of incidence. If k/n is low, R_p drops to a very low value, and if k/n is very high, R_p drops very little. This can be seen in table III. In the infrared, where n and k become very large and k/n approaches unity for all metals, R_p drops to a minimum of 17 percent at close to grazing incidence. Radiation emitted in this wavelength region and at this angle must, therefore, be strongly polarized.

For most practical applications, knowledge of the hemispherical emittance is required. For all metals with very high reflectance in the infrared the ϵ/ϵ_n ratio lies, in agreement with calculations by Dunkle, between 1.25 and 1.30.⁴ This results in the following hemispherical emittance values for the best evaporated films of the indicated metals:

Metal	Al	Ag	Au	Cu	Rh	Pt
ϵ at 27° C, percent	1.5	~1.3	1.4	~1.3	~2.4	~4.1

METAL FILMS WITH SURFACE COATINGS

Transparent Coatings

Because of its high reflectance and its good adherence to most substrates, evaporated aluminum is the most frequently used film material

⁴ See Paper 4.

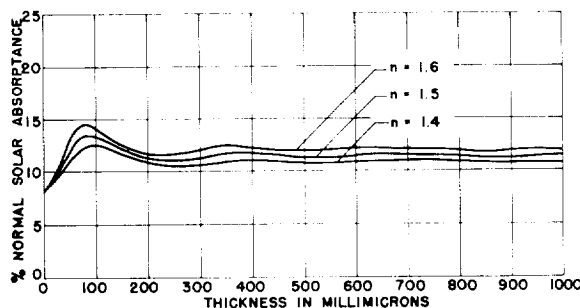


FIGURE 3.—Calculated normal solar absorptance of aluminum coated with nonabsorbing films of various indices of refraction as a function of film thickness.

for producing highly reflecting surfaces. Surface coatings are needed to change the α/ϵ ratio of evaporated aluminum films and to protect aluminum front surface mirrors used as solar energy collectors or as reflectors in solar simulators. Figure 3 shows the calculated total normal solar absorptance of evaporated aluminum coated with protective layers of various film thicknesses and various indices of refraction. The calculations were made for films that are nonabsorbing in the solar region. The curves show that for thicker surface layers the solar absorptance becomes essentially independent of film thickness. An increase of the refractive index of the protective layer from 1.4 to 1.6 increases the solar absorptance from 10.7 percent to about 12.0 percent. There is nothing critical about the thickness of the protective layers that have to be applied on aluminum mirrors which are to be used as solar energy collectors, and rather thick surface films can be deposited to obtain maximum protection.

Silicon Oxide and Aluminum Oxide Coatings

The most suitable protective layers for aluminum are silicon oxide films produced by evaporating silicon monoxide (SiO) slowly in the presence of oxygen, and films of SiO₂ and Al₂O₃ evaporated by electron bombardment. High-vacuum evaporation of SiO is still the most frequently used technique for producing protective coatings on evaporated aluminum. The optical properties of such coatings and the reflectance characteristics of protected alumi-

num mirrors depend strongly, however, upon the conditions under which the SiO is evaporated. High deposition rates at low pressures result in films of true SiO, which show rather strong absorptance in the near ultraviolet and shorter wavelength region of the visible. To produce films with negligible absorptance in the visible and near ultraviolet, low deposition rates at rather high pressures of oxygen must be used (deposition rate $< 4 \text{ \AA/sec}$ at $8\text{--}10 \times 10^{-5}$ torr of oxygen.)

Figure 4 shows the effect of SiO evaporation conditions on the visible and ultraviolet reflectance of silicon oxide protected aluminum mirrors. All three protective coatings are effectively $\lambda/2$ wavelength thick at $550 \text{ m}\mu$ to produce highest reflectance in the visible. The bottom curve shows the reflectance of aluminum coated with SiO at low pressure and a high deposition rate. This true SiO coating causes high absorptance for all wavelengths shorter than $500 \text{ m}\mu$ and therefore results in a surface with high solar absorptance. The top curve shows the reflectance of aluminum coated with strongly oxidized SiO prepared by slow evaporation at a rather high pressure of oxygen. This coating causes no absorptance in the visible and near ultraviolet down to $300 \text{ m}\mu$ and results in a solar absorptance value that agrees with the calculated one shown in figure 3 for $n = 1.55$.

Figure 5 shows the reflectances of aluminum coated with true SiO and with strongly oxidized SiO plotted on a chart with a distorted wavelength scale that allows the determination of the solar absorptance by graphical integration

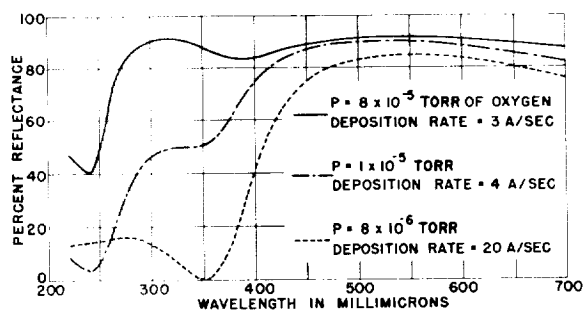


FIGURE 4.—Effect of silicon monoxide evaporation conditions on the visible and ultraviolet reflectance of "SiO"-protected aluminum mirrors. Protective coatings effectively $\lambda/2$ thick at $\lambda = 550 \text{ m}\mu$.

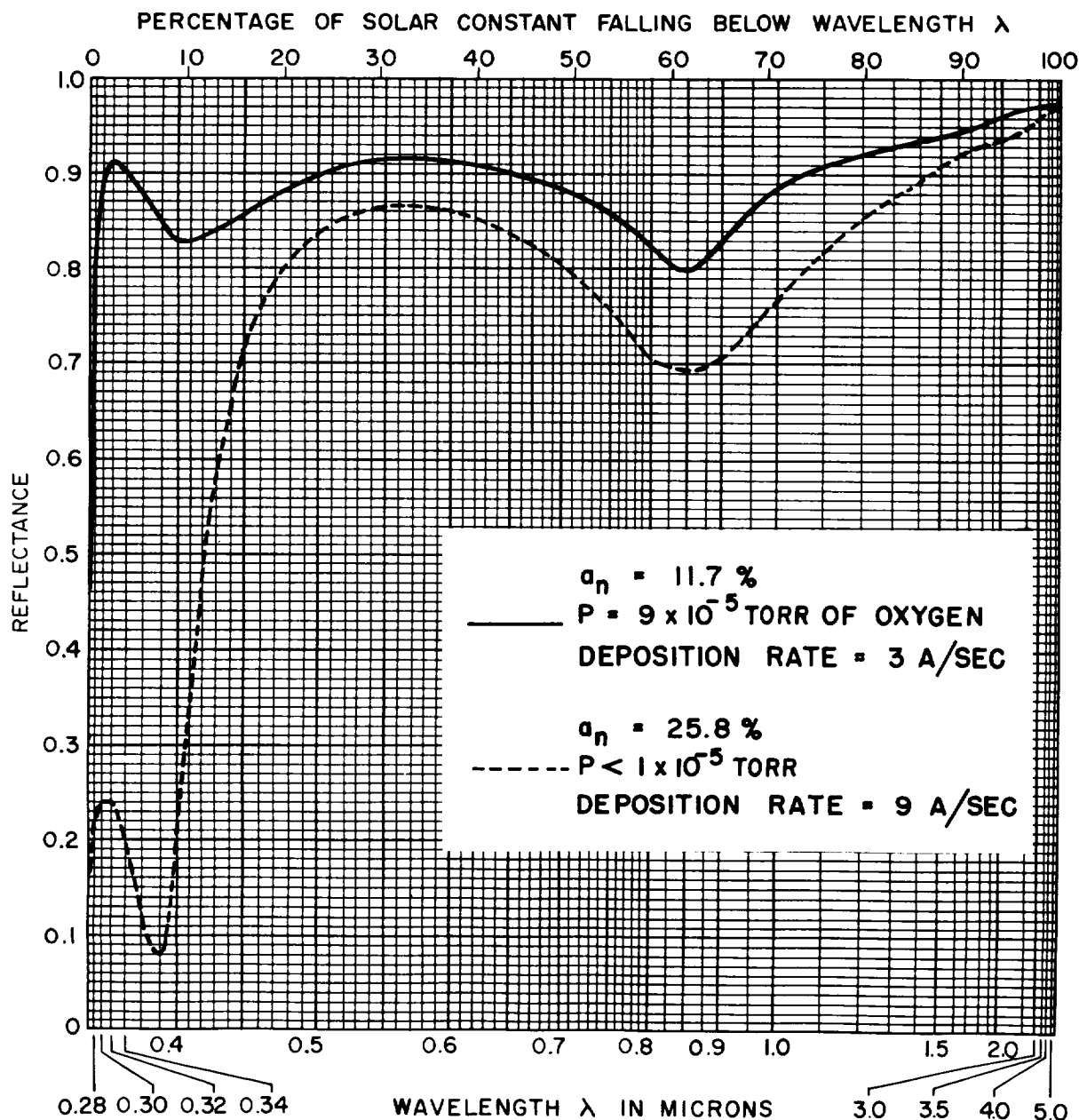


FIGURE 5.—Chart for the graphical determination of normal solar absorptance from reflectance measurements. Reflectance curves of aluminum coated with silicon monoxide under various evaporation conditions are included to illustrate the technique.

with a planimeter. It shows the great difference between the solar absorptances of aluminum coated with true SiO and with strongly oxidized SiO ($\alpha_n = 25.8$ and 11.7 percent, respectively).

In the infrared, silicon oxide films have strong absorption bands in the 9 - to 10 - μ and

the 20 - to 25 - μ regions. The thermal emittance of silicon oxide coated aluminum, therefore, increases steadily with increasing thickness of the surface film, while its solar absorptance remains almost constant if strongly oxidized SiO is used. This is shown in table IV. By the use of strongly oxidized SiO films as surface

TABLE IV.—Normal Solar Absorptance and Thermal Emittance of Evaporated Aluminum Coated With Strongly Oxidized Silicon Monoxide

Thickness of SiO ₂ , μ	ϵ_n at 27° C, %	α_n , %
0.43	5.0	11.6
.61	8.1	11.9
.70	10.1	11.8
0.88	16.8	11.9
1.1	24.2	11.8
1.4	35.5	12.0
2.8	61.0	12.1

coatings, the α/ϵ ratio of evaporated aluminum can be changed from a maximum value of about 6 to values of less than 0.2.

More than 30 satellites up to 36 inches in diameter, including all Vanguards, Injuns, Explorers XVI and XVII, and all satellites of the Naval Research Laboratory, have been coated with aluminum and silicon oxide for controlling their temperatures in orbit. One of these satellites reported temperature data for a time period of almost 3 years. The data indicated that the coating showed practically no change and that the satellite temperature remained in the desired range throughout this time period.

A sketch of the 72-inch evaporator and the arrangement used for coating satellites is shown in figure 6. The satellite is rotated simultaneously about two axes to expose all of its surface uniformly to the incident vapor of the evaporated material. After the satellite is cleaned by a high voltage d-c glow discharge and before the evaporation is started, a mask is placed between the evaporation sources and the sphere to limit the angle of vapor incidence to less than 30° in order to prevent roughening of the surface by the film deposition. A glass plate fastened to the mask allows monitoring of the film thicknesses during the deposition by reflectance measurements with monochromatic light.

Coatings of Al+SiO₂ and Al+Al₂O₃ are also suitable for producing protected front surface mirrors and for preparing films with a great variety of α/ϵ values, since SiO₂ and Al₂O₃ coatings evaporated by electron bombardment are free of absorptance in the solar region and

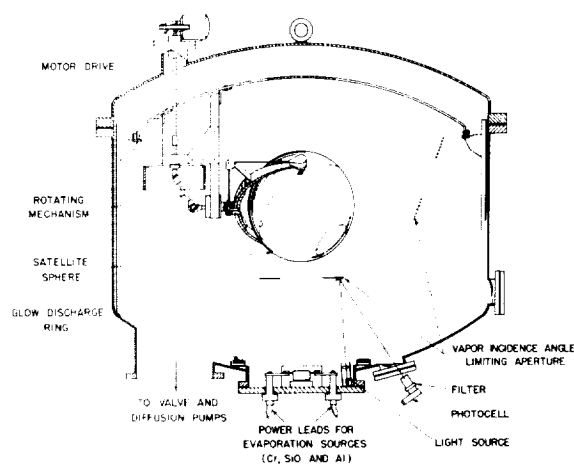


FIGURE 6.—Sketch of 72-inch evaporator, showing arrangement for coating satellites.

show strong absorption bands in the infrared. Figure 7 shows the visible and ultraviolet reflectance of evaporated aluminum coated with a 0.78- μ thick protective layer of SiO₂. The surface film introduces only interference but no absorption effects. Since SiO₂ films have a rather low index of refraction the normal solar absorptance of such a mirror is about 10.9 percent; it is almost completely independent of the thickness of the SiO₂ film. Because SiO₂ has strong absorption bands in the infrared, the thermal emittance of Al+SiO₂ surfaces can be adjusted by the thickness of the SiO₂ film to any desired value between 2 percent and about 70 percent.

The Al+Al₂O₃ surfaces exhibit a similar behavior. Figure 8 shows the infrared reflectance of evaporated aluminum coated with 0.5-, 1.0-,

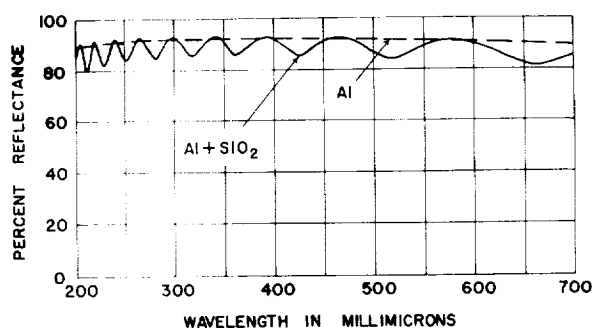


FIGURE 7.—Reflectance of aluminum coated with an evaporated silica film (thickness=7800 Å) as a function of wavelength from 200 to 700 $m\mu$.

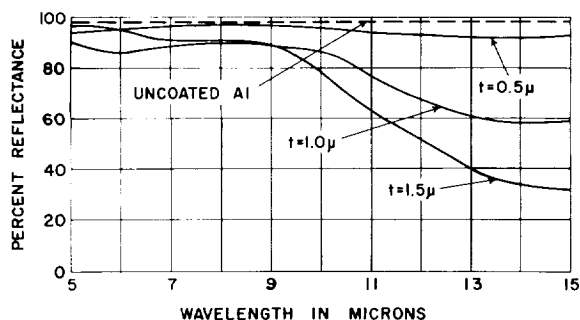


FIGURE 8.—Infrared reflectance of aluminum coated with 0.5-, 1.0-, and 1.5- μ thick films of alumina, from 5 to 15 μ .

and 1.5- μ thick films of Al_2O_3 . It can be seen that increasing the Al_2O_3 thickness greatly decreases the infrared reflectance of Al_2O_3 coated aluminum, and thus increases its thermal emittance without changing its solar absorptance, which measured about 12 percent of all coatings.

SPECIAL APPLICATIONS

There are many other interesting space applications of evaporated film combinations, such

as coatings for studying erosion effects in outer space and surface films for producing high solar absorptance and low thermal emittance.

Evaporated aluminum coated with about 0.8 μ of SiO_2 and 100 Å of germanium shows a solar absorptance of about 40 percent and an α/ϵ ratio of about 3. If the 100 Å of Ge is removed, the solar absorptance decreases to about 10.9 percent and the α/ϵ value drops to about 0.8. Such a surface is, therefore, very temperature sensitive to erosion of the germanium film and should be useful for studying erosion effects caused by micrometeoroids and sputtering in outer space.

Evaporated SiO_2 and Al_2O_3 can also be used in combination with opaque and semitransparent films of rhodium and platinum for producing temperature resistant surfaces with low visible and high infrared reflectance. A coating consisting of opaque Pt+ SiO_2 +semitransparent Pt+ SiO_2 shows a solar absorptance of more than 80 percent and a thermal emittance of about 5 percent and may, therefore, be quite suitable for use on certain types of solar energy converters.⁵

⁵ See also Papers 49 and 50.

21. The Effects of Surfaces on the Intrinsic Radiation Properties of Dielectrics

JONATHAN D. KLEIN

NASA AMES RESEARCH CENTER, MOFFETT FIELD, CALIF.

The effects of both external and internal surfaces on the radiation properties of dielectrics are discussed. External surfaces affect the emitted and transmitted radiation while internal surfaces (scattering centers) affect the heat transferred by radiation in addition. Gradient changes at surfaces due to changes in optical properties, and gradients in optically thin layers are also discussed.

EFFECTS OF EXTERNAL SURFACES OF HOMOGENEOUS DIELECTRICS

The actual absorption and emission of radiation occur within the body of a dielectric. Nevertheless, the surfaces are extremely important in determining the radiation properties. In the center of an infinitely large isothermal dielectric solid, the flux is $n^2\sigma T^4$; where n is the index of refraction, σ is the Stefan-Boltzmann radiation constant, and T is the temperature. When this flux impinges on a surface where the index of refraction decreases to 1, some of the flux is reflected. The fraction $1-(1/n^2)$ impinges at angles greater than the critical angle and is hence totally reflected. Of the remainder, $1/n^2$, some is reflected due to Fresnel reflection so that less than $1/n^2$ of the total flux impinging on the surface is transmitted through it. This effect can be large for even a moderate index of refraction.

If the body is not infinitely large, then it has a second surface somewhere. If this second surface is close to the first one, in terms of the mean free path of the radiation considered, its main effect is to remove part of the radiating material and decrease the flux below that of a large body. This situation can be handled theoretically by calculating

the radiation from each volume element and its attenuation on passing through the body and then integrating over the volume.

EFFECTS OF SCATTERING CENTERS ON EMISSION AND TRANSMISSION

Scattering centers are surfaces within the dielectric. One of their effects is very similar to that of the second surface: they decrease the volume of radiating material. Only the amount of radiation that is emitted from within one mean free path for scattering can reach the surface. Similarly, the absorption is decreased because some of the radiation is scattered back out of the sample before it can be absorbed. The emissivity of a large body is then a function of the ratio of the absorption coefficient to the scattering coefficient (though not a linear one), but does not depend on their absolute values. The emissivity approaches 1 as the absorption coefficient gets very large relative to the scattering coefficient, and it approaches zero as the scattering coefficient gets very large relative to the absorption coefficient.

If the material is not infinitely thick, however, the interaction between the scattering and absorption coefficient is not so simple. Then not only the ratio of the coefficients, but

their absolute values (which will determine the optical thickness) will be important.

To illustrate this effect of thickness consider a sample of glass with bubbles in it. Assume that the mean free path is such that it is just optically thick. Its emissivity will be somewhat less than 1, depending on the ratio of the absorption coefficient to the scattering coefficient. Now, if the sample is heated so that the bubbles start to dissolve, the *emittance* will decrease since the sample is no longer optically thick even though the ratio of the absorption coefficient to the scattering coefficient, and, therefore, the *emissivity* (which is only defined for an optically thick material), increases. This example illustrates that in measuring the *emissivity* of a dielectric it is very important to use a sample that is optically thick.

Another effect of scattering centers is illustrated in the first two figures. Figure 1 represents diffuse radiation impinging on the surface of a dielectric which has no scattering centers. This radiation is refracted at the surface into a beam of narrower solid angle, but with no loss other than the Fresnel reflection. It then comes to the second surface, and, since the angular dependence has not changed, it is again refracted out into the same pattern that it had when it went in (again neglecting Fresnel reflection), and there will be no total reflection.

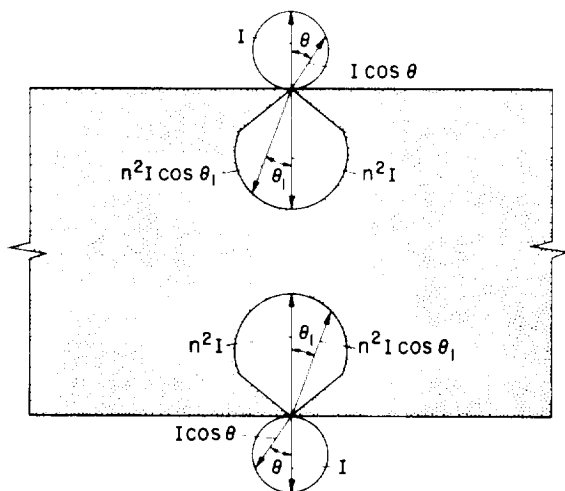


FIGURE 1.—Radiation transmission through a homogeneous dielectric.

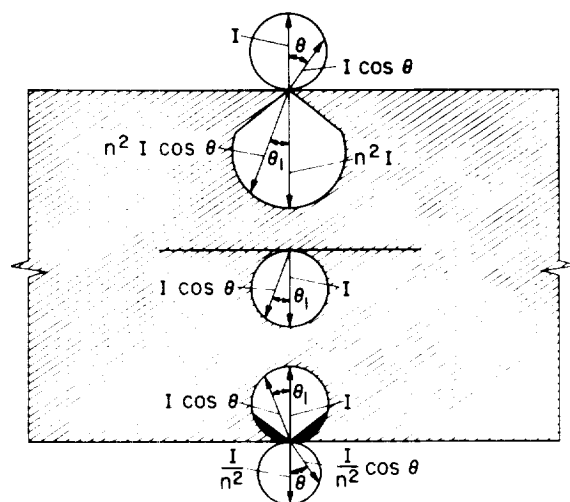


FIGURE 2.—Radiation transmission through a dielectric with diffusing scattering centers.

The situation in figure 2 is similar, except that here there are hypothetical scattering centers which diffuse the radiation only in the forward hemisphere (i.e., without any backscatter). At the first surface the effects are the same, but now, as the radiation penetrates the body, it is diffused into its original angular dependence (with no loss). When this radiation strikes the second surface part of it is in the totally reflecting region and is reflected back; only the fraction $1/n^2$ will pass through. Thus, simply scattering the radiation into a diffuse distribution causes the fraction $1 - (1/n^2)$ of the radiation to be lost. In an actual case backscattering and absorption would also be present.

EFFECTS OF SCATTERING CENTERS ON HEAT TRANSFER BY RADIATION

Scattering centers will also alter the radiation heat transfer through dielectrics. Many workers (see, for example, ref. 1) have shown that if the properties of a material (such as the extinction coefficient and the temperature) do not change significantly in a distance of many mean free paths, an effective conductivity due to radiation (analogous to the lattice conductivity) can be used in heat transfer calculations. This radiation conductivity is equal to a geometrical factor ($16/3$ for nonscattering materials

when diffuse radiation is taken into account) times the blackbody flux at the temperature in question divided by that temperature (since this flux is $n^2\sigma T^4$ the term in question is normally written $n^2\sigma T^3$, showing that the term is the blackbody flux divided by the temperature, which will have an advantage to be shown below) times a mean free path (which is the reciprocal of the extinction coefficient).

The blackbody flux can be shown, by means of the second law of thermodynamics (ref. 2), to be always equal to $\sigma n^2 T^4$; that is, it depends *only* on the index of refraction of the material in question and on its temperature and is not influenced by scattering centers. Note that the *actual flux* in a body in question does not necessarily remain constant when scattering centers are added, but that the *blackbody flux* (which can be shown to be the same as the flux in an optically thick isothermal piece of the body) always does.

The main effect of scattering on heat transfer by radiation, therefore, since it does not affect the flux term of the relation, is due to its effect on the mean free path. This effect is twofold: first, the mean free path is decreased considerably by scattering, and, second, since the mean free path is often determined predominantly by scattering, the temperature dependence is changed considerably.

Most pure single-crystal oxides and glasses are transparent in some region of the infrared as well as the visible. However, when sintered polycrystalline ceramic materials or glasses with pores are investigated, they appear to be quite opaque to all radiation. The difference between the two cases is due mainly to scattering. Even a small percentage of pores will cause enough scattering to lower drastically the mean free path (the reciprocal of the extinction coefficient). The extinction coefficient is the sum of the absorption coefficient and the scattering coefficient, so that any scattering mechanism will add to the extinction coefficient. In fact, if the scattering coefficient is large enough, it will be the predominant mechanism of extinction; in some cases, the absorption coefficient is insignificant with respect to it.

As an example, in a glass at high temperature the mean free path is of the order of 5 cm. This

means that in the fining end of a continuous glass-melting tank, where the bubble spacing is considerably more than 5 cm, the mean free path is limited by absorption and the scattering centers have very little effect on the radiation conductivity. On the other hand, in the raw material end, the extinction due to scattering is very large and the effects of scattering predominate over absorption in limiting the radiation conductivity.

In cases where the mean free path is limited predominantly by scattering, the temperature dependence will be determined by the scattering coefficient. This can be a large effect. For a single crystal and for glasses (without scattering centers), conductivity due to radiation is likely to increase at some rate larger than the third power of temperature, usually as high as the sixth or seventh. The flux law accounts for a third-power effect, and, at the same time, the blackbody spectrum shifts into a region where the material is more transparent. (The spectra of most ceramics and glasses show a transparent region in the visible range and an opaque region in the infrared. The cutoff varies in ceramics from 2 to 10 microns and is close to 2.5 microns for most glasses.) However, the wavelength dependence of the scattering coefficient is entirely different. In the region of interest (about 1 to 10 microns) the scattering coefficient decreases slowly while the absorption coefficient increases abruptly at the edge of the absorption band. Therefore, where scattering is the predominant mechanism of extinction, the shift in the blackbody spectrum to shorter wavelengths as the temperature increases will have very little effect on the mean free path and, therefore, on the heat transfer due to radiation. The temperature dependence of the latter will then be close to T^3 instead of T^6 or T^7 , and the effective conductivity due to radiation will also be much lower at any temperature.

SURFACES AS TRANSITION REGIONS BETWEEN MATERIALS WITH DIFFERENT OPTICAL PROPERTIES

As already noted, it is possible to use the concept of an effective thermal conductivity due to radiation, analogous to lattice thermal

conductivity, in analyzing radiant heat transfer, and this conductivity can be shown to be equal at a particular temperature to the product of the mean free path, the blackbody flux (at that temperature), and a geometrical factor (16/3) divided by the temperature. In such a discussion it is assumed that the properties of the material change *only gradually* within the distance of several mean free paths.

In some cases, however, it is necessary to deal with situations where the properties change drastically within a distance of one or a few mean free paths. Such a situation exists at the boundary surface of the material or when dealing with transfer through a slab of transparent material which is less than one mean free path in thickness. In the center of a thick layer of a semitransparent material the temperature gradient is, therefore, approximately constant, part being due to lattice conduction and part to radiant conduction; at the surfaces, however, radiant energy must be converted to lattice vibrations or vice versa to meet the new condition found at the interface. Near the surface, then, one would expect neither a constant temperature gradient nor a constant ratio of radiant heat transfer to lattice transfer. The boundary is, therefore, a region where the gradient changes to adjust for the transition from the properties of one material to the properties of the material adjacent to it. To describe this situation, one would like to know not only how the gradients in the centers of two materials differ, but also how the gradients change when going from the center of one material to its surface that is in contact with a material of different properties.

To elucidate this, two layers of different materials in contact with each other in steady state and with heat flowing through them are considered. The constant κ is defined as the ratio of the heat transfer by radiation U : the heat transfer by lattice conduction V in the center linear region of a thick layer. It is noted that the total amount of heat transfer Q is the same in both layers. (In the following equations, the subscript 1 will refer to values in the first material and 2 to those in the second material.)

$$Q_1 = Q_2 \quad (1)$$

Also, Q is always equal to the sum of the heat transfer by radiation U and the heat transfer by lattice conduction V

$$Q = U + V \quad (2)$$

At any point, V is proportional to the lattice thermal conductivity of the solid k times the temperature gradient at that point, since this is the definition of thermal conductivity

$$V = -k \frac{dT}{dx} \quad (3)$$

Since κ is the ratio of U to V in the center of the layer, U is then proportional to κ times the thermal conductivity times the temperature gradient in the center, or

$$U_c = \kappa V_c = -\kappa k \left(\frac{dT}{dx} \right)_c \quad (4)$$

where the subscript c refers to values in the center linear region of a thick layer. From equation (4), Q may be written as the product of the gradient in the center and a total effective conductivity in the center, or

$$Q = -(1 + \kappa)k \left(\frac{dT}{dx} \right)_c \quad (5)$$

Furthermore, for two layers in series with each other (from eq. (1) and (5)),

$$(1 + \kappa_1)k_1 \left(\frac{dT}{dx} \right)_{c1} = (1 + \kappa_2)k_2 \left(\frac{dT}{dx} \right)_{c2} \quad (6)$$

or

$$\left(\frac{dT}{dx} \right)_{c1} = \frac{(1 + \kappa_2)k_2}{(1 + \kappa_1)k_1} \left(\frac{dT}{dx} \right)_{c2} \quad (7)$$

Thus, the ratio of the temperature gradients at the centers of two layers in contact is inversely proportional to the ratio of the total effective conductivities of the layers which is, of course, exactly analogous to the case of opaque materials, where κ is zero.

We note that U , V , and T (where it is defined) are all continuous functions. Then at the interface, in order for V to be continuous

$$k_1 \left(\frac{dT}{dx} \right)_{s1} = k_2 \left(\frac{dT}{dx} \right)_{s2} \quad (8)$$

where the subscript s refers to values at the surface of the material, or

$$\frac{\left(\frac{dT}{dx} \right)_{s1}}{\left(\frac{dT}{dx} \right)_{s2}} = \frac{k_2}{k_1} \quad (9)$$

that is, the ratio of the temperature gradients at the interface between two materials is inversely proportional to the ratio of the lattice conductivities of the solids.

Finally, one would like to find the direction in which the gradient changes in going from the center of a layer to its surface that is in contact with a dissimilar material. It will be seen that the direction of the change depends on the relative values of the constant κ in the two materials. Thus, let the surface be assumed to be in contact with a material that has a larger value of κ

$$\kappa_1 < \kappa_2 \quad (10)$$

Since κ in the second material is larger, U/V in the center of the second material is larger (because $\kappa = U/V$), and U/V at the interface will be the same for both materials and will have a value intermediate between the values at the centers of the two materials, that is

$$\left(\frac{U}{V} \right)_{c1} < \left(\frac{U}{V} \right)_{s1} \quad (11)$$

Substituting $U = Q - V$ gives

$$\frac{Q - V_{c1}}{V_{c1}} < \frac{Q - V_{s1}}{V_{s1}} \quad (12)$$

or

$$\frac{Q}{V_{c1}} - 1 < \frac{Q}{V_{s1}} - 1 \quad (13)$$

and

$$V_{s1} < V_{c1} \quad (14)$$

Thus, since $V = -k(dT/dx)$ and k has the same value in the center and at the surface

$$\left(\frac{dT}{dx} \right)_{s1} < \left(\frac{dT}{dx} \right)_{c1} \quad (15)$$

It has been shown then that when going from a material of low κ to one of higher κ , the gradient in the center of the first material is larger than the gradient at its surface. This reflects the fact that some of the lattice conduction must be converted at the surface to radiant conduction in order to match the new conditions found in the second material. In the case of heat transfer to a material in which κ is smaller, the gradient will change in the opposite direction.

Figure 3 has been drawn to illustrate the preceding relations. It represents transfer from a hot wall through a vacuum to a glass, then through the glass (where the path length is assumed to be many mean free paths long) to a refractory wall. It has been assumed that the total conductivity of the refractory is larger than that of the glass, but that a large portion of the conductivity in the glass is due to radiation whereas in the refractory practically none of it is. The temperature decreases from left to right. Then, since the total conductivity of the refractory is larger than that of the glass, according to equation (7) the gradient in the center of the glass is steeper than that at the center of the refractory. The gradient at the hot surface of the glass is less than that at the center of the glass because the value of κ is less in the glass than it is in the vacuum, where κ is infinite (i.e., all the transfer in the vacuum is

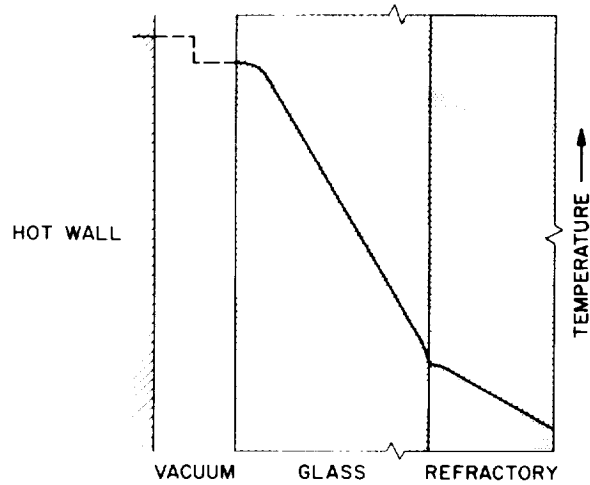


FIGURE 3.—Temperature gradients in heat transfer from hot wall through a vacuum to a glass layer and a refractory wall.

by radiation). For the same reason the gradient increases from the surface to the center of the refractory. On the other hand, at the cooler surface of the glass (the surface adjacent to the refractory), the gradient increases toward the surface since the new material has a lower value of κ . Finally, the ratio of the gradients at the glass-refractory interface is k_R/k_G where k_R , the lattice conductivity of the refractory, is considerably larger than k_G , the lattice conductivity of the glass.

It is possible to understand the gradient changes at boundaries more easily by realizing that they are regions where radiant conduction is being converted to lattice conduction or vice versa. For instance, at the boundary where the glass abuts the vacuum, all the incoming heat transfer is due to radiation. Therefore, the gradient in the glass at this interface must be zero, since there is no lattice conduction right at the interface. As the radiant energy is converted to lattice vibrations in the glass, however, the gradient steepens (since the gradient and the amount of heat conducted by the lattice are always proportional) and, finally, after several mean free paths, an equilibrium between radiant and lattice transfer is reached and the slope becomes constant. At the next boundary more radiant conduction must be converted to lattice conduction (since virtually all the transfer in the refractory is due to lattice conduction), and the gradient, therefore, becomes steeper again.

In an optically thick layer, the boundary region extends over only a small portion of the thickness. Therefore, its effects on the overall heat transfer are small, and it is mainly important when considering radiation being emitted, since this comes from the boundary region. When the layer in question is thin, however, the boundary region can extend a significant distance into the layer, and the linear region may disappear if the layer is thin enough. In this case the gradients and the heat transfer are not at all what one might expect from measurements on a thick piece of the material.

Such a situation is illustrated in figure 4, where the solid line depicts the gradients to be expected in a glass coating on a hot metal where a gas is conducting the heat from the free

surface. The dashed line represents the gradient (for the same amount of total heat transferred) that would be present in an optically thick piece of the glass. For a thin layer, as shown by the solid line, boundary effects predominate, and the gradient is practically constant through the layer and approximately equal to the gradient at the metal surface times the ratio of the thermal conductivity of the metal to the lattice conductivity of the coating. Therefore, in a thin layer, the lattice conductivity alone determines the gradient present. This is of importance in such applications as tempering of glass sheets where the gradients present are of primary importance. On the other hand, if one wants to know the amount of heat transferred one finds that it is no longer a function of the properties of the layer itself, but is now also a function of the surface that is radiating (the metal) and the region it is radiating into (the gas). The optical thickness of the layer has become so small that its effect on heat transfer by radiation is negligible.

The most important thing to be seen from this discussion of thin layers is that here we have lost the use of two important material properties: emissivity as a measure of the emissive power of the sample, and an effective thermal conductivity (due to radiation) as a measure of the heat transferred by radiation through the body. For the first property, it can be seen that the emissive power of thin layers is really a function

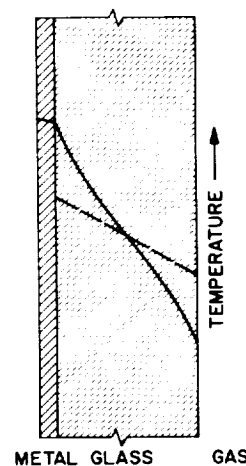


FIGURE 4.—Temperature gradients in heat transfer from a metal through a thin glass layer to a gas.

of the optical constants of the backing material. Heat transfer through an optically thin layer (or at least that part due to radiation) is mainly a function of the emissive power of the material radiating on one side of the layer and of the absorption characteristics of the material on the other side and, perhaps, to a slight extent on the absorption and scattering coefficients of the layer in question.

CONCLUSION

In considering the effects of surfaces on the radiation properties of dielectrics, it is useful to differentiate between external surfaces and internal surfaces or scattering centers. The external surfaces will play a major role for small optical thicknesses—that is, for relatively transparent substances where there is little absorption and few scattering centers. In these materials, the Fresnel reflections at the surfaces partially determine the character and to some extent the amount of radiation.

For large optical thicknesses (optically dense materials) internal surfaces or scattering centers, if they are present, essentially determine the radiation properties, while the external surfaces affect the character of the radiation by refraction, polarization, and diffusion. Also, at

external surfaces there must be a transition from a region of one set of optical properties to that of another.

The concept of *emissivity* becomes less useful for semitransparent dielectrics where thermal gradients are present, since then the *emissive power* depends on the thermal conductivity and the temperature gradient as well as the optical properties.

In general, one finds that the concept of an *effective thermal conductivity* is useful when dealing with radiation through large optical thicknesses, although it is less useful when dealing with small optical thicknesses. For the latter cases, where the dimensions of the sample are less than one or a few mean free paths, different methods of calculations are more fruitful. The approach that is generally most useful here is that of making a heat balance, that is, considering the heat gained or lost from each region, either by lattice conduction or radiation, and writing equations for their interactions.

REFERENCES

1. CONDON, E. U.: Heat Transfer. Part 5, Chapter 5, in Handbook of Physics, E. U. Condon and Hugh Odishaw, eds. McGraw-Hill Book Co., Inc., 1958.
2. DRUDE, PAUL: The Theory of Optics. Dover Publications, Inc., N.Y.

22. Light-Scattering Behavior of Pigmented Coatings¹

R. L. COX

LING-TEMCO-VOUGHT ASTRONAUTICS DIVISION, DALLAS, TEXAS

Finely milled glass pigment particles (sizes ranging from about 0.3μ to about 1.3μ) were lightly sintered to form coatings. Porosity, particle size, and particle shape were evaluated by using an electron microscope, and reflectance measurements were made over the wavelength range of 0.2 to 2.0μ . Results are compared with theory. It is shown that single-particle scattering theory affords reasonable quantitative predictions of the reflectance of thin, intensely scattering, coatings when an empirical correction factor is employed to account for proximity effects at high particle concentrations.

This paper presents an example of the application, examination, and light-scattering behavior of pigmented coatings. In particular, it concerns a very high porosity sintered glass coating that has been studied at LTV-Astronautics Division. (This work is described in detail in the paper *Sintered Ceramic Coatings for Thermal Control*, presented at the Third Aerospace Finishing Symposium of the American Electroplaters Society, held at Dallas, Texas, January 16 and 17, 1964.) Specimens were prepared from sheet glass (in this study, Pittsburgh 3235 borosilicate) by first ball milling the glass to a very fine particle size (mostly sub-micron), suspending the particles in a volatile alcohol, and then spraying the suspension onto a substrate by using an artist's air brush. Then, after evaporation of the alcohol, the coating was sintered (for the particular glass studied, at a temperature of 1050°F). It was possible to apply a 2- to 3-mil-thick coating in this manner. To build up greater thicknesses the process was repeated. In the present studies, the coating was actually sintered onto an intermediate glassy sublayer which, in turn, had been diffused into a molybdenum substrate. Excellent adherence, coupled with some brittle-

ness, was obtained by using this process. As an indication of the coating strength, some bulk specimens of the coating material were made, about $\frac{1}{8}$ -inch thick, and it was found that the sintered piece could be broken by hand only with difficulty. The porosity of such a specimen was determined by density measurements to be about 47 percent.

Electron microscope studies of the coating material were made to enable a correlation between experimental and theoretical performance. Porosity, particle size, and particle shape were evaluated by using the electron microscope technique. Figure 1 shows two photomicrographs, one at a magnification of 6,000 and the other at a magnification of 25,000. Preparation of lightly sintered specimens for such examination is not quite straightforward. Some special technique is required to get a good replica, with vacuum impregnation of the specimen with a resin being an essential step. Examination of the photomicrographs reveals particle sizes varying from about a quarter micron to greater than one micron. The smoother areas are the particles, while the raised and rougher areas are the pores or separating cracks. A fairly modest amount of sintering and a high degree of porosity are indicated by these photomicrographs.

¹ See also Paper 27.

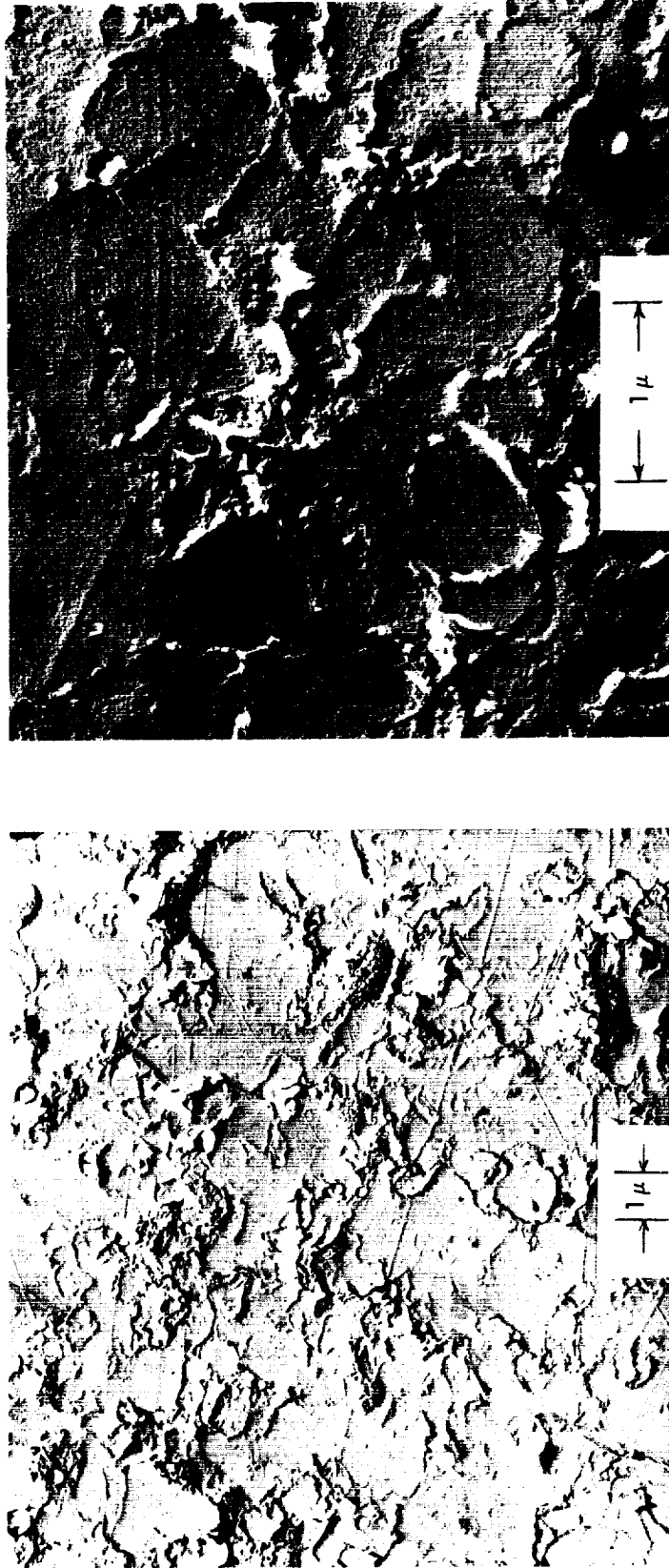


FIGURE 1.—Electron photomicrographs of sintered glass specimen.

To enable a better quantitative interpretation of the photomicrographs, they were traced, as shown by figure 2, which is a tracing of the 25,000 magnification photomicrograph of figure 1. The light areas in figure 2 are the particles and the dark areas are the pores. By somewhat crude graphical analysis of this tracing, porosity was determined to be 53 percent, which compares well with the 47 percent determined from density measurements. The particle size distribution is, roughly, 9 percent at a nominal equivalent-sphere diameter of 0.3 micron, 16 percent at 0.4 micron, 44 percent at 0.8 micron, and 31 percent at 1.3 microns.

The porosity and particle sizes determined from electron photomicrographs were used

to predict backscattering coefficients. The detailed procedure for such a theoretical analysis is discussed in the Session I paper *Fundamentals of Thermal Radiation in Ceramic Materials*. Briefly, the analysis involves a calculation of single-particle spherical scattering efficiency from inputs of particle geometry, radiation wavelength, particle optical constants, and published solutions to the Mie scattering theory. Next, additional published theoretical data on the angular distribution of scattered radiation is used to correct the spherical scattering efficiency to a backscattering effectiveness. Then an overall backscattering coefficient is computed as a simple additive function, summing up all the contributions

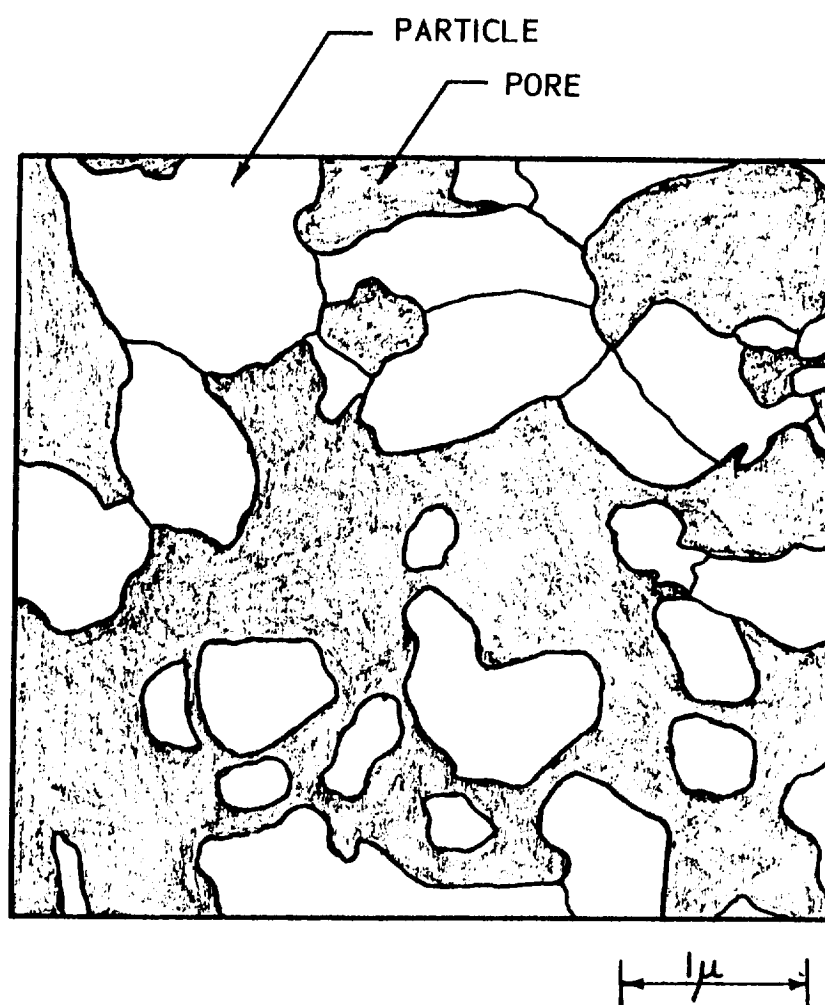


FIGURE 2.— Interpretation of the 25,000 \times magnification electron photomicrograph of figure 1.

of all particles in a unit volume. For particle concentrations above about 25 percent, proximity effects lower the scattering efficiencies below those predicted by single-particle theory, and a correction has to be applied. An empirical scattering coefficient ratio, inferred from the study of Blevin and Brown (Blevin, W. R., and Brown, W. J.: *Effect of Particle Separation on the Reflectance of Semi-Infinite Diffusers*. Jour. Optical Soc. of America, vol. 51, no. 2, Feb. 1961, pp. 129-134), was employed for this purpose in the present work. The ratio was determined to be 0.32 for a particle concentration of 50 percent.

Apparent absorption coefficient values are also required to predict the reflectance of a coating which absorbs as well as scatters. At present, values cannot be adequately

predicted by theory for intensely scattering media, and thus experimental determination of these coefficients is necessary. This was accomplished in the present study by measuring the reflectance of an "infinitely thick" specimen of coating material, and computing the apparent absorption coefficients from this measured reflectance and the theoretical scattering coefficients. The radiative-transfer equations (described in the previously mentioned Session I paper) were employed for this analysis. The measured reflectance data for the "infinitely thick" specimen are presented in figure 3.

The theoretical scattering coefficients and the experimental absorption coefficients were again used with the radiative-transfer equations to predict the reflectance of coatings of 2-, 5-,

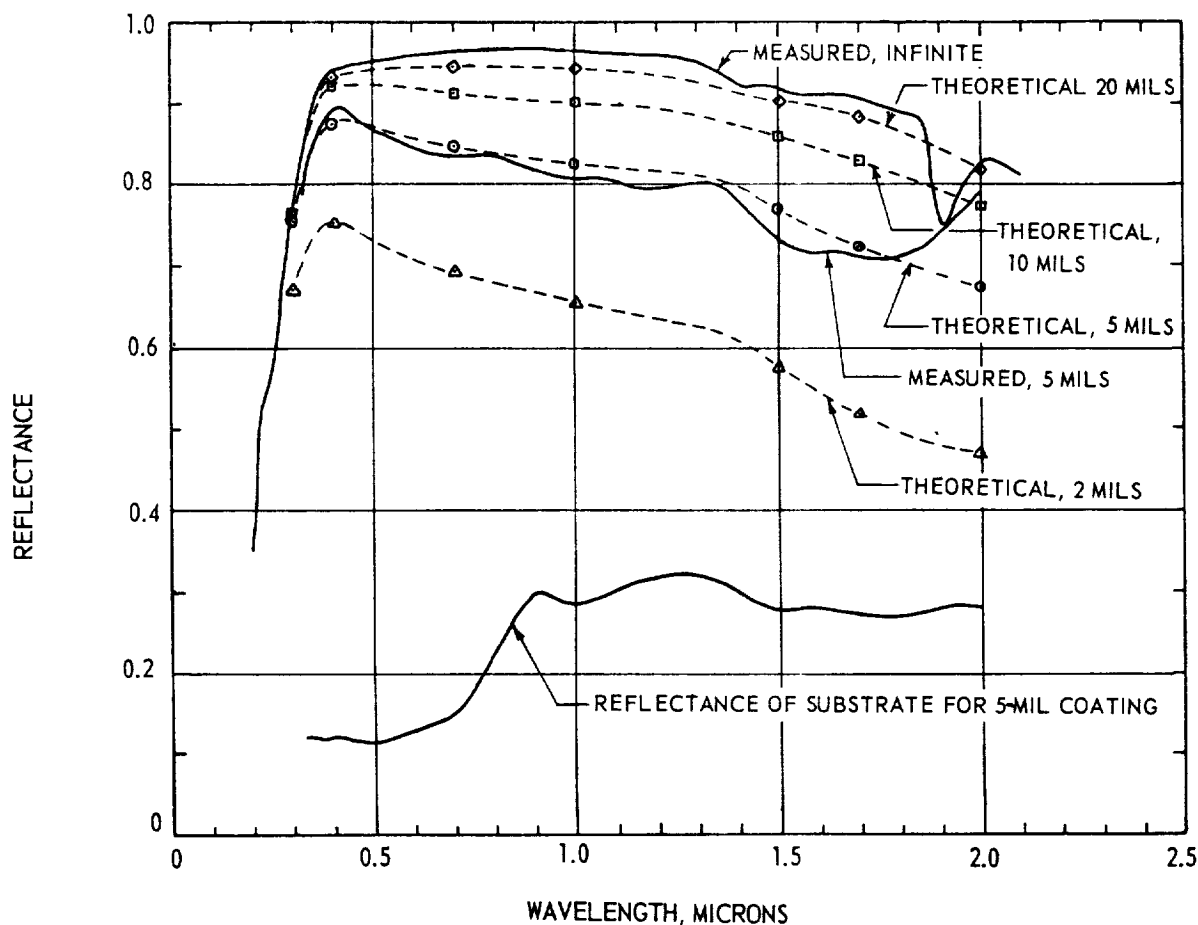


FIGURE 3.—Theoretical and measured reflectances of coating.

10-, and 20-mil thicknesses. For this analysis a black substrate was assumed, which introduces only insignificant errors for the coating thicknesses considered. Results of the analysis are presented in figure 3. Solar absorptances were computed from these reflectance curves, and found to be 0.31, 0.16, 0.10, and 0.07 for the 2-, 5-, 10-, and 20-mil thicknesses, respectively. Figure 3 also shows the measured reflectances of a 5-mil coating and of the substrate employed with the coating. It is interesting to compare the predicted and measured data for the 5-mil coating. The wavelength variation of reflectance predicted by theory is seen to correspond fairly closely with that measured, with both peaking at about 0.4 micron. The divergence of predicted and measured values between 1.7 and 2 microns is the only anomaly and is not understood at present. Quantitatively, the agreement is also good. The solar absorptance computed from the measured curve is 0.17, compared to the predicted 0.16.

As a further test of the accuracy of backscattering coefficient predictions from theory, the assumption of zero absorption in the coating

was made so that only the scattering coefficients would enter into the calculation of reflectance. Such an assumption should be valid at wavelengths where scattering is the dominant mode of attenuation, and for coating thicknesses that do not approach infinity. These conditions are met for the present coating system at wavelengths between 0.4 and 1.7 microns and for thicknesses of 5 mils or less. Computations of reflectance employing this assumption were made for 2-mil and 5-mil coating thicknesses. Resulting values in the range of 0.4 to 1.7 microns agreed almost exactly with those calculated by the complete theory which included the experimental absorption coefficient values.

In summary, one of the most interesting results of this study is the evidence that microstructure data combined with single-particle theory, when properly interpreted for use with the radiative-transfer equations, provides good accuracy in predicted backscattering coefficients. Since scattering is dominant at wavelengths of interest in many pigmented coatings, this provides a quantitative tool for tailoring such coatings.

SESSION III
MEASUREMENT TECHNIQUES

CHAIRMAN: CLAY P. BUTLER

U.S. NAVAL RADIOLOGICAL DEFENSE LABORATORY, SAN FRANCISCO, CALIF.

23. Comment on Measurement Techniques

WILSON A. CLAYTON

THE BOEING COMPANY, SEATTLE, WASH.

A table summarizing the technology of measuring thermal radiation properties is presented and existing inadequacies, particularly with regard to nonopaque materials and angular dependence are pointed out. It is urged that standard measurement techniques with broad applicability be developed and established.

These remarks are directed at the problem of increasing our capability for the measurement of thermal radiation properties. No topic in this symposium is of more practical importance. Nearly all the urgently needed properties must be obtained from new measurements. Data requirements may be best satisfied by development of measurement techniques with broad capability.

Three factors predict a continuing widespread participation in data generation. They are the incompleteness of the body of reliable data, continuing development of new materials, and the necessity to compensate by experiment for lack of prediction and correlation capability. Present inability to define material and surface condition in a manner meaningful for thermal radiation properties often requires that measurements include environmental simulation to insure that properties are valid for the intended application. Under these circumstances data must be generated by measurements that satisfy the required combination of thermal and environmental boundary conditions.

Technique development to meet these many specific boundary conditions is usually concentrated on the adaption of known limited capability techniques for specific material-property-environment combinations. Progress toward methods with broad applicability has lagged in the face of an expanding need for thermal

radiation properties. This is a result of considering data generation primarily in terms of satisfying immediate design or material development requirements.

Technique development should be directed toward general applicability whenever possible. The resulting methods would fill gaps in existing measurement capability and at the same time more efficiently satisfy specialized requirements.

A summary of established basic thermal radiation property measurement techniques is presented in the attached table. An interesting fact about this table is that it was prepared nearly three years ago by the Aerospace Industries Association and is still essentially correct. The same basic deficiencies, noted by their absence in table I, remain. Most of the deficiencies are in the areas of measurements on the general case of nonopaque materials and the analytically exact determination of angular dependence. These problems have not gone unchallenged. Additional capability for determination of angular dependence by a calorimetric method and techniques for certain types of transparent materials are presented in this session. A high-temperature method for opaque materials utilizing hemispherical incidence with hemispherical viewing, a category not included in table I, is also presented. However, capability in these areas is still limited and is likely to remain so unless technique develop-

TABLE I.—*Thermal Radiation Property Measurement Methods*

	Calorimetric	Reflectance: angular incidence, hemispherical viewing	Reflectance: hemispherical incidence, angular viewing	Emittance by blackbody comparison
Metals and opaque dielectrics				
Temperature range	Cryogenic to 2000° F	Ambient	Ambient to 1100° F	300° F to 5000° F
Property derived.*	ϵ α_s/ϵ	$\rho_{\lambda\phi}$ ρ_λ $\epsilon, \epsilon_\lambda, \epsilon_\phi, \epsilon_{\lambda\phi}$ $\alpha_\lambda, \alpha_{\lambda\phi}, \alpha_s, \alpha_s/\epsilon$	$\rho_{\lambda\phi}$ ρ_λ $\epsilon, \epsilon_\lambda, \epsilon_\phi, \epsilon_{\lambda\phi}$ $\alpha_\lambda, \alpha_{\lambda\phi}, \alpha_s, \alpha_s/\epsilon$	$\epsilon_{\lambda\phi}$ $\epsilon, \epsilon_\lambda, \epsilon_\phi$ $\alpha_\lambda, \alpha_{\lambda\phi}, \alpha_s/\epsilon$ $\rho_\lambda, \rho_{\lambda\phi}$
Remarks.	Most accurate for low emittance specimens.	High percentage error on emittance and absorptance if reflectance is high.	High percentage error on emittance and absorptance if reflectance is high.	High percentage error on reflectance if emittance is high. Classic method, still most widely used.
Examples.	ϵ NBS measurement of power loss in resistance heated strip. NRL measurement of power loss in sphere at low temperature. α_s/ϵ Measure equil. temperature of wafer exposed to simulated solar energy.	National Bureau of Standards ellipsoid.** Gier-Dunkle paraboloid.	Gier-Dunkle Hohlraum integrating sphere.**	Back heated specimen with radiation and temperature measurement on front surface. Radiation detector calibrated against black-body.
Nonopaque dielectrics				
Temperature range		Ambient	Ambient	300° F to 4500° F
Property derived.*		$\rho_{\lambda\phi}$	$\tau_{\lambda n} \rho_{\lambda\phi}$ ρ_λ $\epsilon_n, \epsilon_{\lambda n}, \alpha_{\lambda n}$	$\epsilon_{\lambda n} \tau_{\lambda n}$ ϵ_n, τ_n $\rho_{\lambda n}, \rho_n, \alpha_{\lambda n}$
Remarks.		Apparent reflectance measured.	Limited to short λ by sphere coating. τ on non-scattering materials only. Apparent properties measured.	Same as above. Has additional requirement for isothermal specimen. Apparent properties measured.
Examples.		National Bureau of Standards ellipsoid.	Integrating sphere.	McMahon furnace, Boeing thermal radiation facility.

*Primary measurement is boxed. **Most reliable method.

ment is directed toward general applicability.

General capability embodied in relatively few sound measurement methods offers a real economic and competitive advantage in the satisfaction of engineering data requirements. Capital expenditures on facilities of broad capability are not necessarily greater than expenditures for specific capability and the useful life is extended over a long period of varying data requirements. Improvement in thermal radiation property data will result from elimination of the necessity for application of specialized techniques to borderline cases where required boundary conditions are not adequately established. Application of an experimenter's ingenuity to the problem of measuring properties on transparent materials, for instance, would automatically provide for the special case of opaque materials. The environmental boundary conditions made necessary by inability to characterize the sample could be added to basic measurement techniques.

Elimination of duplicate efforts in the development of specialized measurement tech-

niques would free us for efforts toward general capability. A large part of this present duplication of effort is simply repetition of each other's mistakes. Many of the papers in this session demonstrate one solution to this problem—reporting by responsible investigators of detailed error analysis. Another solution is the establishment of initial standard measurement techniques which are fully described in terms of their accuracy and limitations. Efforts on standard methods have been undertaken by the Aerospace Industries Association and the American Society for Testing Materials.

It seems evident that the present approach to satisfaction of immediate data requirements, with little resultant extension of the art of measurement techniques, may not be expedient from the longer term viewpoint. Both our design data requirements and measurement method requirements will be more effectively met by approaching the most general case, as illustrated by transparent materials vs. opaque materials.

.

|

24. Standards, Sources, and Detectors in Radiation Measurements

RALPH STAIR AND WILLIAM E. SCHNEIDER

NATIONAL BUREAU OF STANDARDS, WASHINGTON, D.C.

The NBS standards of total and of spectral irradiance and of spectral radiance are based upon the Stefan-Boltzmann and Planck laws of radiation and, as set up in terms of lamp sources, are in close agreement with each other and with the NBS standard of luminous intensity. Their use in the calibration of various sources requires great skill in the operation of spectroradiometric equipment employing detectors having sensitivities that vary over the detector surface or that vary with wavelength. Examples are given illustrating the wide ranges in sensitivity which may exist over the surface of certain detectors and also the large variation of sensitivity with wavelength of supposedly neutral thermal detectors. General suggestions are made regarding methods for obtaining accurate results in the different types of measurement.

The precise measurement of the radiation from a source requires the use of either a calibrated detector or a calibrated source with which comparison may be made by a transfer operation. At the NBS, the standards of total and of spectral irradiance and of spectral radiance are based upon the radiance from a blackbody as defined by the Stefan-Boltzmann and the Planck laws of radiation.

The Stefan-Boltzmann law is the fundamental law of the blackbody. It relates the total radiant flux W from a unit area of a blackbody to the absolute temperature by the relationship

$$W = \sigma T^4$$

The precise value of the Stefan-Boltzmann constant σ can be derived from other physical constants by the relationship

$$\sigma = \frac{2\pi^5 k^4}{15c^2 h^3}$$

where

- k Boltzmann constant
- c speed of light
- h Planck constant of action

When the NBS standard of total irradiance was set up in 1913 (ref. 1), a value for σ of 5.70×10^{-12} watt/cm²-deg⁴ K was accepted as best representing the extensive experimental radiometric work previously performed with a blackbody. The precision possible in radiometry cannot furnish a hope of improving this value greatly. However, the extensive researches on the physical constants of many investigators through the years have furnished data (ref. 2) which establish the value of σ to possibly five significant figures as follows:

$$c = 2.997925 \times 10^{10} \text{ cm/sec}$$

$$h = 6.6256 \times 10^{-27} \text{ erg-sec}$$

$$k = 1.38054 \times 10^{-16} \text{ erg/deg K}$$

hence,

$$\sigma = 5.6697 \times 10^{-12} \text{ watt/cm}^2\text{-deg}^4 \text{ K}$$

differing but little from the value employed in 1913. Further refinement of this value cannot be expected to affect the results of future radiometric work.

The Planck law of radiation relates the radiance N_λ at a particular wavelength to the absolute temperature T on the International Practical Temperature Scale (IPTS) by the relationship

$$N_\lambda = \frac{c_1 \lambda^{-5}}{e^{c_2/\lambda T} - 1}$$

where c_1 and c_2 are the first and second radiation constants and have the dimensions watt-cm² and cm-deg K, respectively. With

$$c_1 = 2c^2 h = 1.19088 \times 10^{-12} \text{ watt-cm}^2/\text{ster}$$

$$c_2 = 1.4380 \text{ cm-deg K by definition (IPTS, ref. 3)}$$

and wavelength λ in centimeters, N_λ is in watts/cm²-ster-cm wavelength interval.

THE NBS RADIOMETRIC STANDARDS

The Standard of Total Irradiance

The NBS standard of total irradiance as presently issued consists of a carbon-filament lamp operated at a temperature around 1600° to 2200° K. At these temperatures most of the irradiance falls between wavelengths of about 1 and 3 microns. As previously indicated, this standard was set up through comparisons of the irradiances from a group of lamps with the irradiance from a blackbody. For this work the blackbody temperature was usually set at approximately 1400° K and a thermopile heavily coated with lampblack was employed as detector. Such a heavily coated thermopile has been found to be nearly uniform in sensitivity with wavelength between the visible and about 3 microns in the infrared, hence, it will give an acceptably accurate evaluation of an 1800° K lamp filament in terms of a 1400° K blackbody.

Our recent reviews of detectors substantiate the validity of the earlier measurements in this area, so that the carbon-filament lamp standard of total irradiance is an adequate standard for use in the calibration of properly blackened thermal detectors over the range from a few microwatts to several hundred microwatts per cm². To cover higher ranges of irradiance, work is in progress toward setting up a secondary standard yielding an irradiance approximating 100 to 150 mw/cm². There appears to

be little interest in a total irradiance standard having an irradiance lower than a few microwatts per cm². A low intensity standard of spectral irradiance recently set up (ref. 4) and discussed below should fill any existing needs in this area.

Standards of Spectral Radiance

Three standards of spectral radiance have been set up covering the regions of 0.25 to 0.75 micron, 0.5 to 2.6 microns, and 0.25 to 2.6 microns (fig. 1). The first two were set up independently through the use of two blackbodies having temperatures of about 2200° to 2600° K and 1200° to 1400° K. This work has been described in detail elsewhere (ref. 5). One of the setups employed is shown in figure 2.

The experimental work consisted of alternately allowing the radiation from the blackbody (set at a specific temperature) and that from a strip lamp (set at a fixed current) to enter a spectroradiometer after being focused on the entrance slit by the same optical system, and measuring the relative radiances of the two sources at selected wavelengths. For the system illustrated, the wavelength range was 0.25 to 0.75 micron, and a 1P-28 photomultiplier was used as the detector.

A supplementary setup consisting of similar optics and electronics and a 1400° K blackbody covered the spectral range of 0.5 to 2.6 microns. In this case, an Eastman lead sulfide (PbS) cell, supplemented by an RCA 7102 photomultiplier, was employed as detector. Thus, the spectral radiances of two groups of strip lamps were evaluated in terms of those of the two blackbodies at specific temperatures as defined by the Planck law of radiation. Although set up independently, the two standards are in close agreement over the common spectral range of 0.5 to 0.75 micron.

The third standard of spectral radiance simply combines the two spectral ranges by means of a single strip lamp operated at a single current with calibration covering the full range from 0.25 to 2.6 microns.

Standard of Spectral Irradiance

The experimental work connected with setting up the standard of spectral irradiance

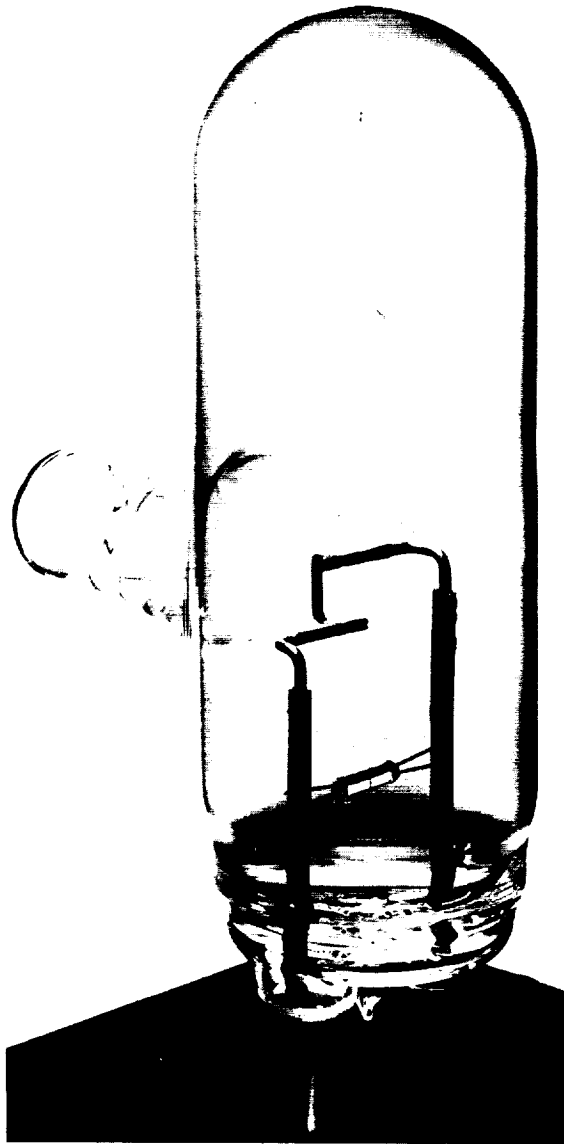


FIGURE 1.—Tungsten-ribbon-strip lamp standard of spectral radiance.

(fig. 3) offered an opportunity to check the agreement between the existing standards of spectral radiance, total irradiance, and luminous intensity. Although consideration was given to setting up this new standard directly against a blackbody, a number of difficulties involved in that procedure led us to set it up through comparisons with the standards of spectral radiance supplemented by measure-

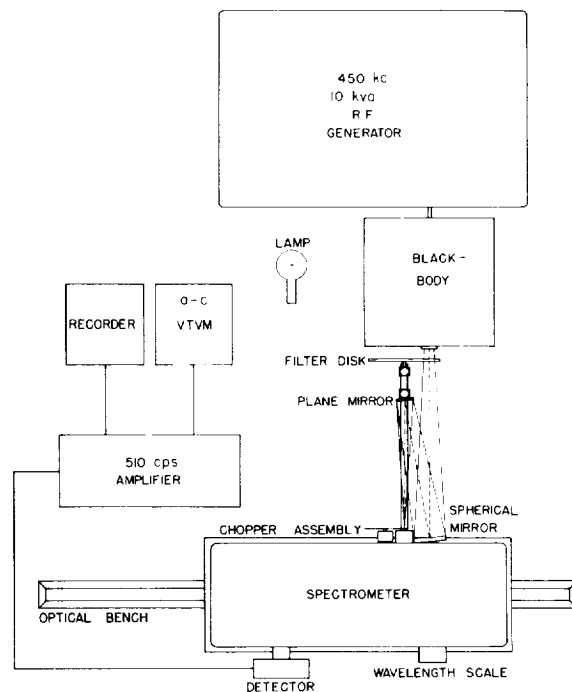


FIGURE 2.—Instrumental setup of blackbody, monochromator, lamp, and associated equipment for the wavelength region of 0.25 to 0.75 micron.

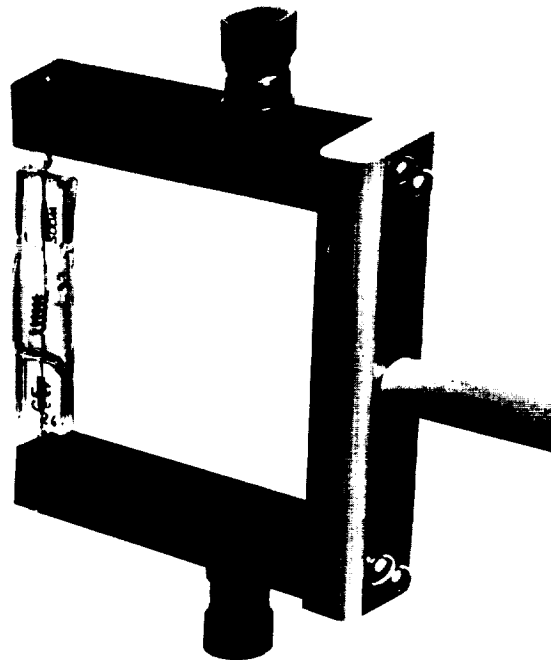


FIGURE 3.—Quartz-iodine lamp standard of spectral irradiance.

ments against the standards of total irradiance and of luminous intensity, all three of which had been established through direct comparisons with the radiances from blackbodies at specific temperatures. This work is described in detail elsewhere (ref. 6). The results indicated close agreement between these standards, in some cases to 1 percent and certainly in all cases to within a few percent. Hence, all the NBS standards in this area are based upon the radiance of the blackbody as defined by the Planck and the Stefan-Boltzmann laws of radiation.

Low Intensity Standard of Spectral Irradiance

To serve the interests of workers in certain fields of extremely low irradiance such as is present in the air glow, and in phosphorescent, fluorescent, biochemical, and associated areas, an extremely low intensity standard of spectral irradiance has been set up (ref. 4). This standard, in effect, combines the NBS standard of spectral radiance with a small aperture which serves as a point source of radiant flux of known spectral intensity. This in combination with one or more convex mirrors set up after the method described by Engstrom (ref. 7) may be readily arranged to supply an irradiance as low as 10^{-16} watt/cm²/nanometer wavelength interval.

SELECTED APPLICATIONS OF SOURCES AND DETECTORS

Sources and detectors will be considered together since they are so closely related for most purposes of this symposium. Furthermore, their consideration is closely linked with the geometrical characteristics of the standards employed. Little difficulty arises from the use of thermal detectors when they are employed with a standard of thermal irradiance or any source of irradiance as long as the flux from the source irradiates the detector uniformly and the detector has a flat response (with wavelength) throughout the spectral interval under investigation. Most sources (including the standard) emit radiant energy

over a wide spectral range, and most thermal detectors available fall far short of having an equally wide spectral range of constant sensitivity. Usually, the thermal detector will have a window cover of selective transmission characteristics. Also, the black coating may vary widely in effective blackness as a function of wavelength. Some information can be deduced from the character, thickness, or measured transmittance or reflectance of similar coatings. But the final answer comes only through a direct measurement of the spectral response of the detector (with its window in place) since the response is affected also by such things as the conductive properties of the coating and receiver elements, the emissivity of the receiver, the reflectance of the receiver metal, and the chopping rate (if the signal is chopped). Hence, the true spectral sensitivity of a specific detector can be obtained only through its individual calibration, and this has not been previously possible since no standard in this area has been available. Work is progressing, however, in a number of laboratories (refs. 6 and 8).

The use of detectors, be they thermal or photoelectric, in conjunction with a spectroradiometer or spectrophotometer of some type, in the measurement of spectral radiance or irradiance, or in comparison of the intensities of two sources, may require a knowledge of the geometrical variations in their sensitivity and relative spectral sensitivity. A spectrometer produces a spectrum, but this spectrum is distorted in a number of ways, especially in a double monochromator. Not only are certain regions of the spectrum more compressed than others, but we have polarization effects, selective absorption, mechanical defects of spectral drive between the two sections of the instrument, imperfect optics, imperfect achromatism, scattered radiation, etc., so that the beam at the exit slit emerges in an uneven pattern covering an area much larger than the first and second defining slits of the instrument. The result may not be too bad if the detector has a uniformly sensitive surface with wavelength and position on its surface. But there is no known commercial detector meeting these specifications.

The New Cavity Detector

The nearest approach to a spectrally "flat" detector is the new cavity or "blackbody" detector recently constructed (ref. 6 and 8), one of which is shown diagrammatically in figure 4. This is constructed in the form of a cone of small angle and coated with carbon or other black on the inside surface. To reduce heat capacity and thereby increase response rate the cone is made of the thinnest gold foil having sufficient strength to insure adequate support under laboratory conditions. Along the outside fold of the foil of the unit illustrated, several wires are connected to serve the double duty of supporting members and thermojunction connectors. Thus, two or more thermojunctions are wired in parallel, resulting in reduced electrical circuit resistance and more rapid thermoelectric response. Increased symmetry and uniformity of response over the conical surface may be obtained by constructing the cone with two or more elements, thereby permitting the attachment of thermal elements at two or more positions around the circumference. However, such construction increases the receiver mass, thereby slowing its response.

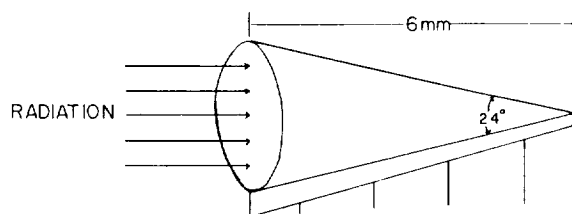


FIGURE 4.—Gold-foil conical cavity detector.

The maximum in flatness of response to be expected from this detector may be approximately calculated (ref. 9 and 10) from a knowledge of its geometry and surface reflectance. Since the cavity shape is not the ideal as a blackbody detector, any spectral variations in reflectance become important. Hence, to insure the greatest degree of spectral flatness, a coating having the most nearly

uniform spectral reflectance (or absorptance) should be employed.

To date, several cavity detectors have been constructed and coated with various blacks. Figure 5 shows a comparison between two of these as a function of wavelength. There are good reasons to believe these are neutral, or uniform in response, from the ultraviolet to about 2 microns. At longer wavelengths, detector 2 is suspected of having a reduced sensitivity because of a higher reflectance of carbon black over camphor black, at least for the respective thicknesses employed on these two detectors. Detector 3 is much better than detector 2 at these longer wavelengths, but there is no assurance from the limited data in this illustration that it, too, does not drop somewhat in sensitivity at the longer wavelengths. However, preliminary comparisons between detector 3 and a surface thermopile heavily coated with Parsons' black indicated equal relative sensitivities between the ultraviolet and about 20 microns. Only additional comparisons with "blacker" surfaces (or with receivers having smaller conical angles or thicker coatings) can decide this point. These investigations are in progress. Meanwhile, detector 3 has the most uniform sensitivity of all detectors (conical or flat) examined in the course of this investigation to date.

Some Commercial and Laboratory Thermal Detectors

Let us now return our attention to the readily available detectors. The usual thermopile or thermocouple consists of a flat surface (usually gold foil) coated with one of the common blacks, such as gold black, carbon black, camphor black, or graphite, in a layer whose thickness is inversely proportional to the "speed" required. The end result is usually an element having selective spectral sensitivity and varying in sensitivity over its surface. The following figures show some of the geometrical variations present in the elements examined. In all cases the thermopile was scanned by a fine line of incandescent lamp flux (set at right angles to the direction of movement) and moved slowly lengthwise with the thermopile or transversely across the element. Figure 6 shows the results

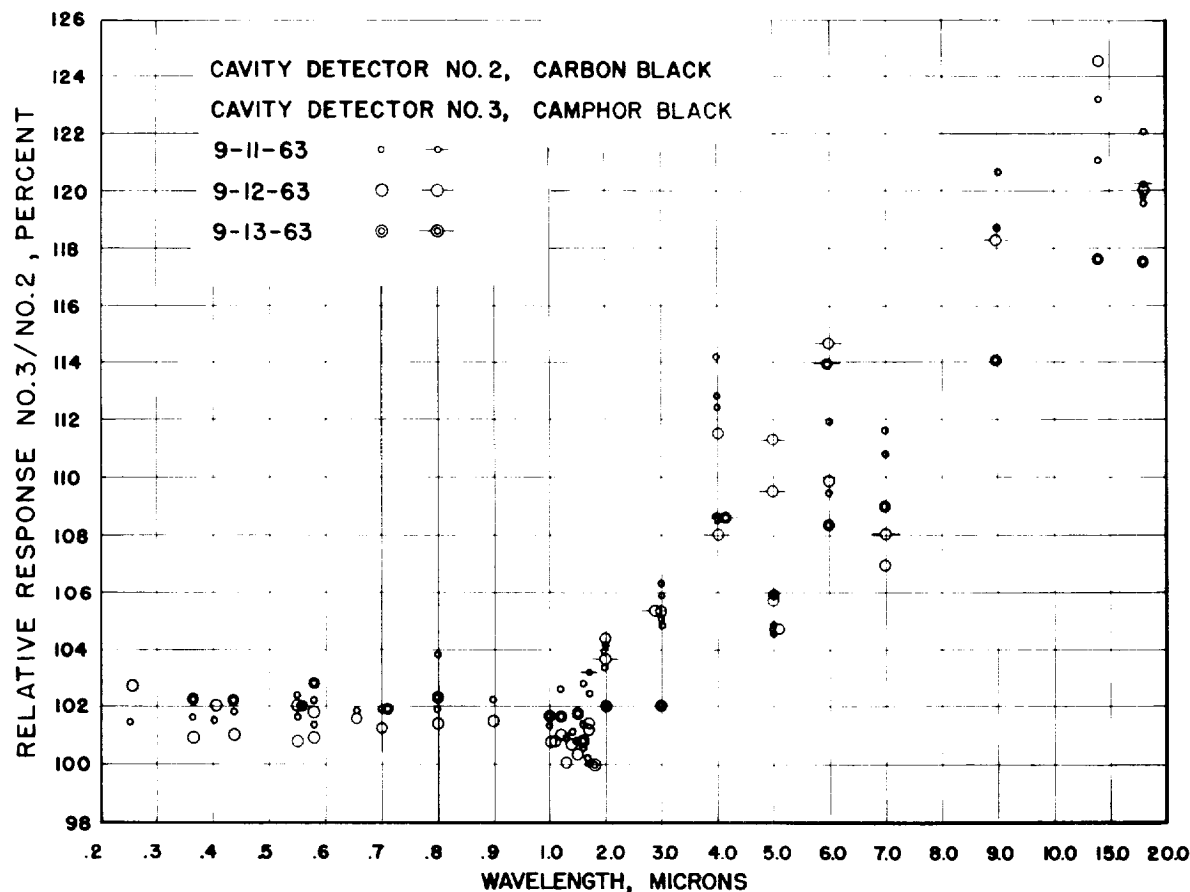


FIGURE 5.—Ratio of spectral sensitivity of cavity detector 3 (camphor black) to that of cavity detector 2 (carbon black).

when a Coblentz 12-junction thermopile was scanned lengthwise. In this illustration, the light beam was chopped at 13 cps and amplified by a Perkin-Elmer 107 amplifier. Eleven peaks of varying sensitivity are noted. The 12th receiver element may have partially separated thermally from the thermoelement. Variations in the degree of thermal contact probably are in part responsible for some of the other variations.

Figure 7 shows the results when the same thermopile is scanned lengthwise, but by measuring the d-c output with a Keithley millimicrovoltmeter. In this case all twelve junctions are represented with corresponding peak responses. Figure 8 shows the results when the same thermopile is scanned crosswise, and with the use of the 13-cycle chopper amplifier. It is noted that somewhere near the two edges, areas of high sensitivity exist. It would

be extremely interesting to study detectors of this type with a point light source if the required sensitivity of amplifying equipment were available. Then each element could be plotted showing its true "valleys and hills" of sensitivity. Such a plot could be expected to show greater contrasts than any pictures available at this time. Figure 9 illustrates the results when this thermopile is scanned crosswise and the d-c output measured. In summary, the results in these four figures show that this thermopile varies significantly in sensitivity over its area, but that the variations are much smaller when it is used as a d-c detector.

Similarly, in figure 10 are shown the variations in lengthwise sensitivity of a Reeder Company thermopile when the signal is chopped at 13 cps. Only noise is produced near one end of this unit. Then follow several peaks and troughs in

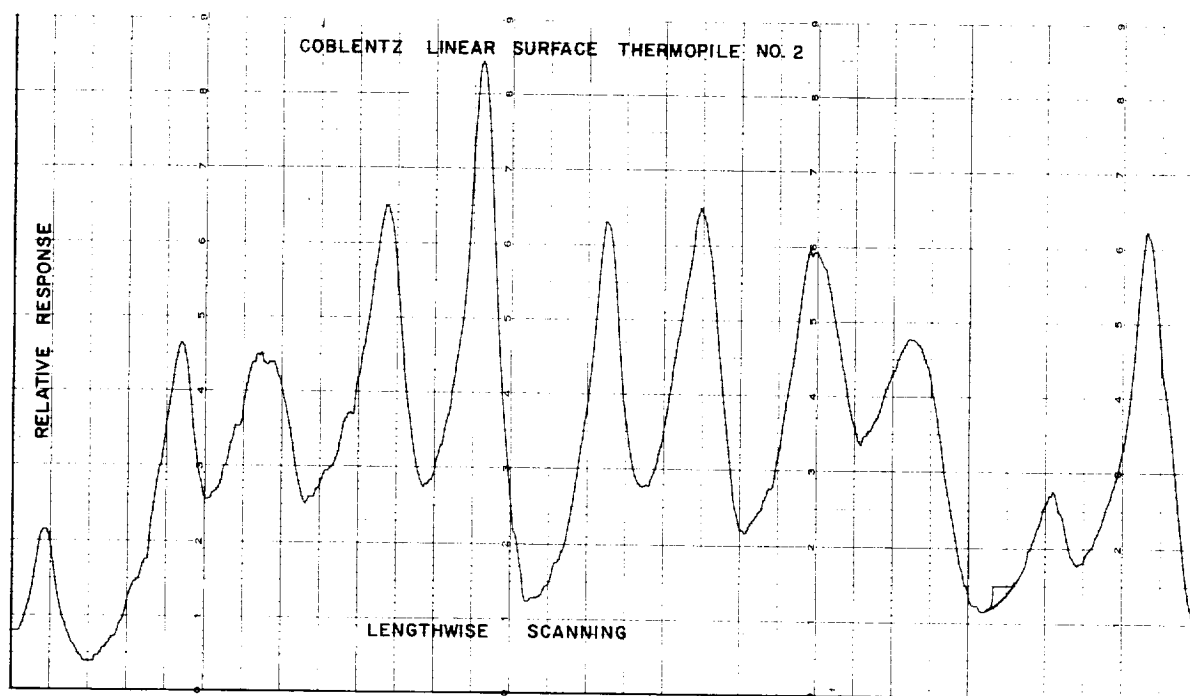


FIGURE 6.—Linear sensitivity of Coblentz thermopile 2 scanned lengthwise (at 13 cps).

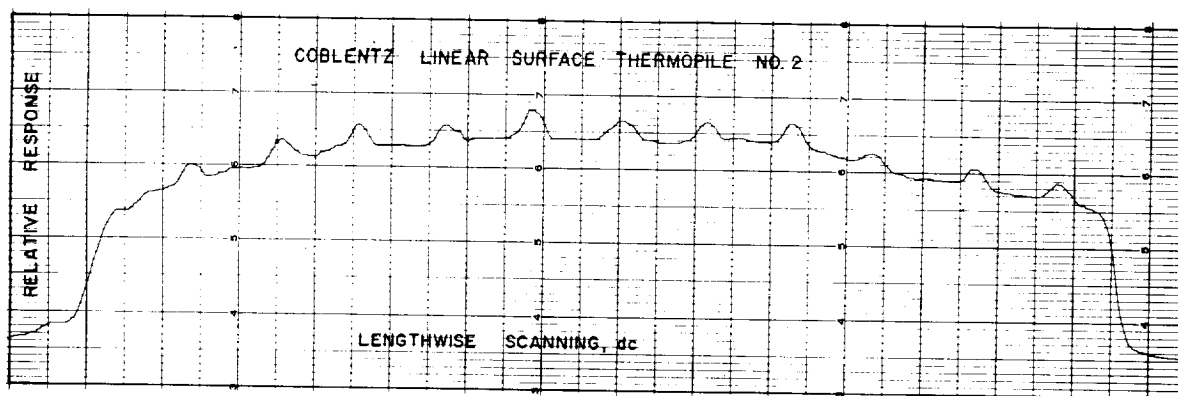


FIGURE 7.—Linear sensitivity of Coblentz thermopile 2 scanned lengthwise (measured by d-c method).

sensitivity. Several of these are negative (below zero). Two are very large, such that the recorder trace is off the scale. The complete explanation for these large negative values is unknown to the authors, but an analysis of similar measurements on other detectors indicates that there is a phase change in the signal resulting from the time lag between the absorption of the light and the resulting build-up of an electric potential in the thermal junction.

Thus, the Perkin-Elmer 107 amplifier picks up a response out of phase with the signal itself. If near 180° out of phase, the signal would be negative, if near 90° , zero, etc. Incidentally, the placing of a narrow shield over the thermopile indicated that this response came solely from the blackened receiver. The number of receivers in this thermopile cannot be determined from this chart. In figure 11 is shown the record obtained when this thermopile is

again scanned lengthwise, but with the d-c output recorded. The resulting tracing is

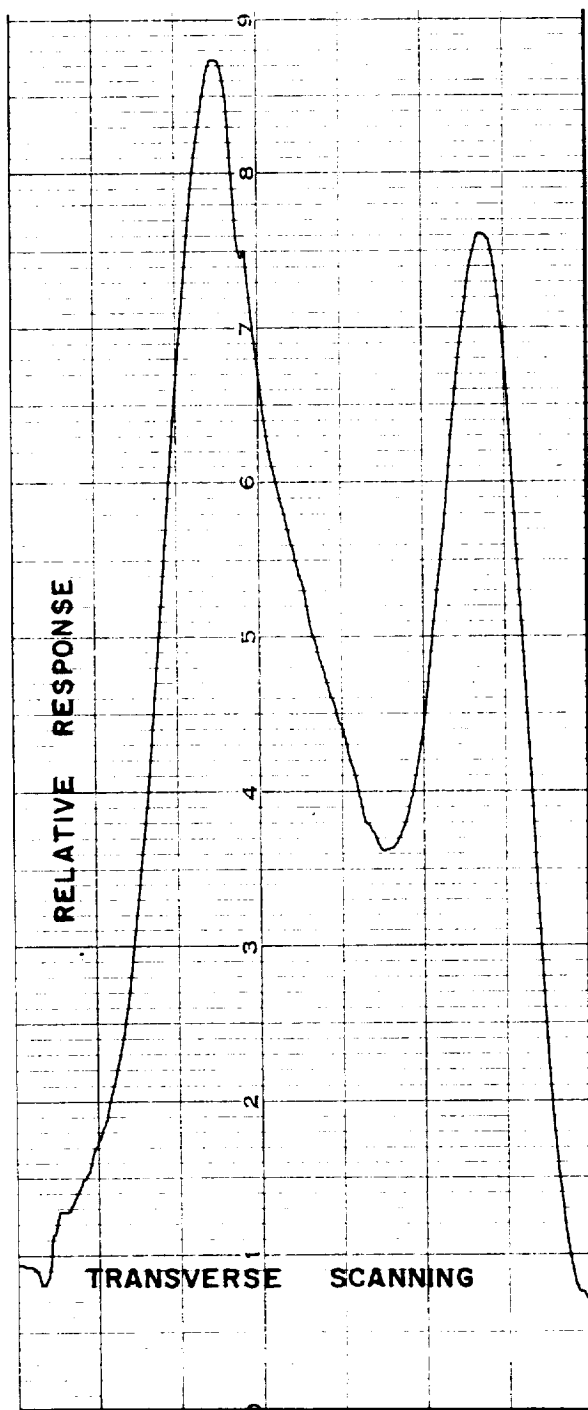


FIGURE 8.—Linear sensitivity of Coblentz thermopile 2 scanned crosswise (at 13 cps).

notably different, there being no recognizable similarity between the two tracings. When the scanning was crosswise, tracings similar to those of figures 8 and 9 were obtained.

Figure 12 shows the recorded response of an Eppley thermopile scanned lengthwise with the signal chopped at 13 cps. Each receiver element of this unit stands out in terms of a definite response since the six elements are physically separated by small distances—not uniform, but definite. A zone of high sensitivity is noted near one end of each receiver element. When scanned in the opposite direction (fig. 13) the pattern is reversed but not exactly since the reverse scanning employs the d-c method with a Keithley millimicrovoltmeter. These differences are small, especially in view of the fact that this is not a fast type of thermopile, the receivers being relatively massive with a response rating near 1 sec. On crosswise scanning (d-c) this thermopile gave a response similar to that shown in figure 9.

The data presented in the previous figures are not specially picked but represent what may be expected as to the geometrical variations in the sensitivity over the surface of represent-

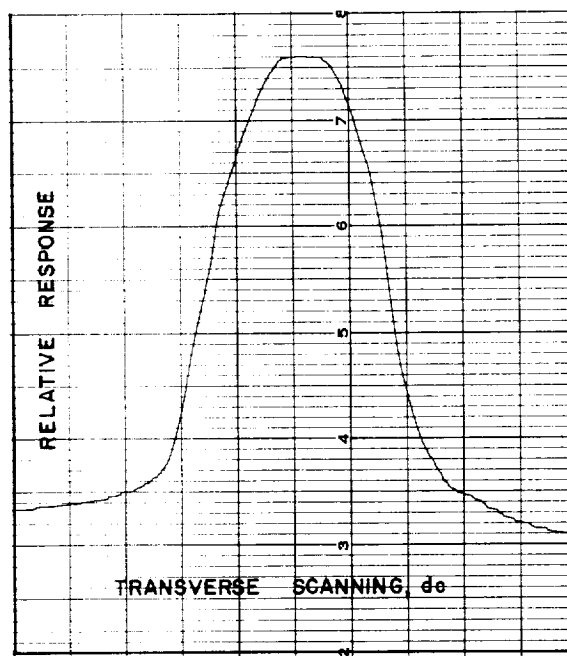


FIGURE 9.—Linear sensitivity of Coblentz thermopile 2 scanned crosswise (measured by d-c method).

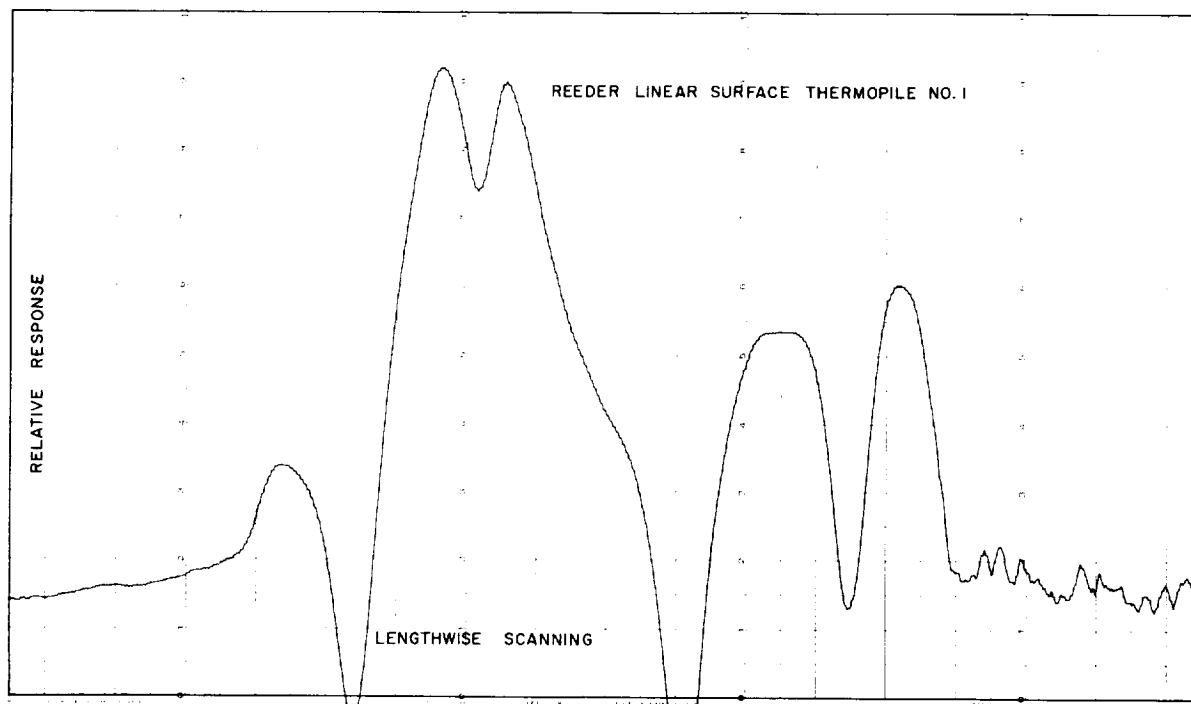


FIGURE 10.—Linear sensitivity of Reeder thermopile 1 scanned lengthwise (at 13 cps).

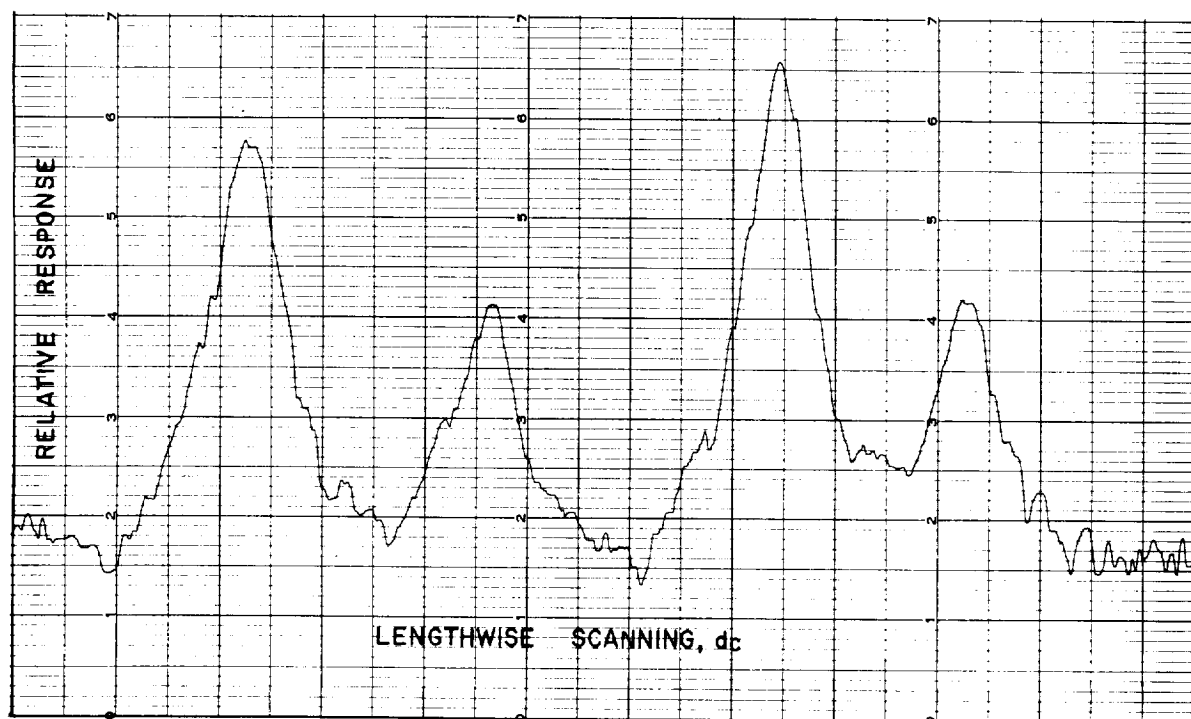


FIGURE 11.—Linear sensitivity of Reeder thermopile 1 scanned lengthwise (measured by d-c method).

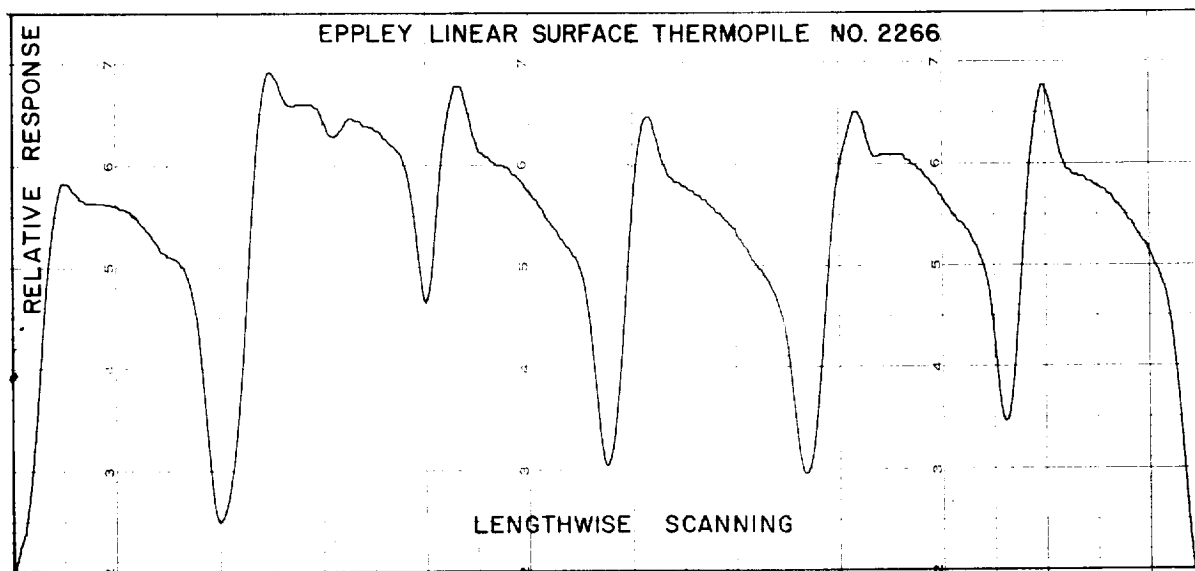


FIGURE 12.—Linear sensitivity of Eppley thermopile 2266 scanned lengthwise (at 13 cps).

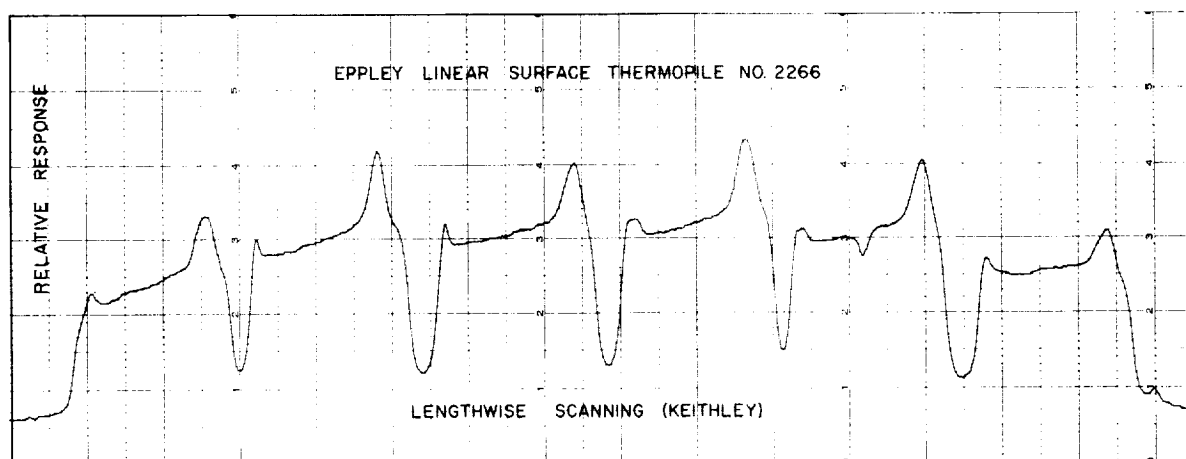


FIGURE 13.—Linear sensitivity of Eppley thermopile 2266 scanned lengthwise (measured by d-c method).

ative thermal detectors of this type. The Golay cell and bolometer may be regarded as having sensitivities more nearly uniform over their surfaces—but most observers are using thermocouples or thermopiles.

A few figures follow which show variations in the spectral sensitivity of available thermal detectors. Bolometers would be expected to have similar responses. Golay cells are yet to be investigated in this respect. These data, and also those illustrated in figure 5, were obtained with a newly developed filter spectro-radiometer shown by block diagram in figure 14.

By means of selected sources, such as low- and high-pressure mercury arcs, incandescent lamps, and glowers, used in conjunction with glass color filters and special multiple unit interference plates, approximately 30 narrow spectral bands of radiant energy are isolated. Data may be taken at a chopping rate of 13 cycles or for d-c output of the thermopiles. The spectral transmittance of a typical filter unit is shown in figure 15.

Figure 16 records a comparison between the spectral sensitivities of the Coblentz thermopile No. 1 and cavity detector No. 2. Since this

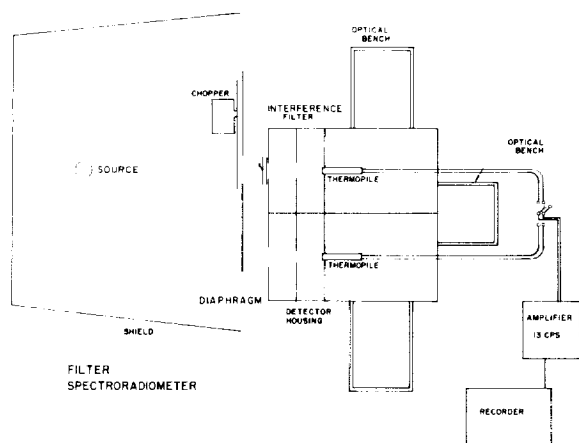


FIGURE 14.—Block diagram of filter spectroradiometer.

curve is flat between 0.6 micron and 3 microns and since that for cavity unit No. 3 vs. cavity unit No. 2 was also flat within this spectral range to 2 microns, it may be assumed that all three receivers are relatively flat between 0.6 and 2.0 microns. At longer wavelengths the Coblentz thermopile and cavity unit No. 2

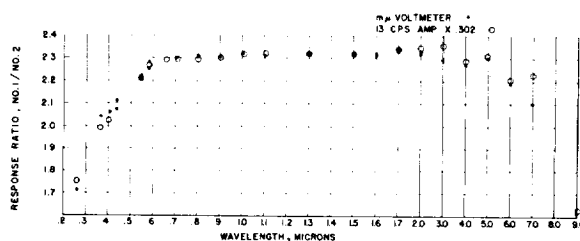


FIGURE 16.—Ratio of spectral sensitivity of Coblentz thermopile 1 to that of cavity detector 2.

appear about equally sensitive, which is reasonable because both are of carbon black. The drop at 7 to 9 microns results from window absorption. The reason for the drop at short wavelengths is undetermined. It is interesting that the data obtained by the two methods (Keithley d-c and Perkin-Elmer chopped at 13 cycles) are in close agreement. Other measurements, especially on thermopiles having thicker coatings, show spectral differences between the two methods, possibly resulting from the fact that the coatings absorb radiation of different wavelengths at different depths, thereby

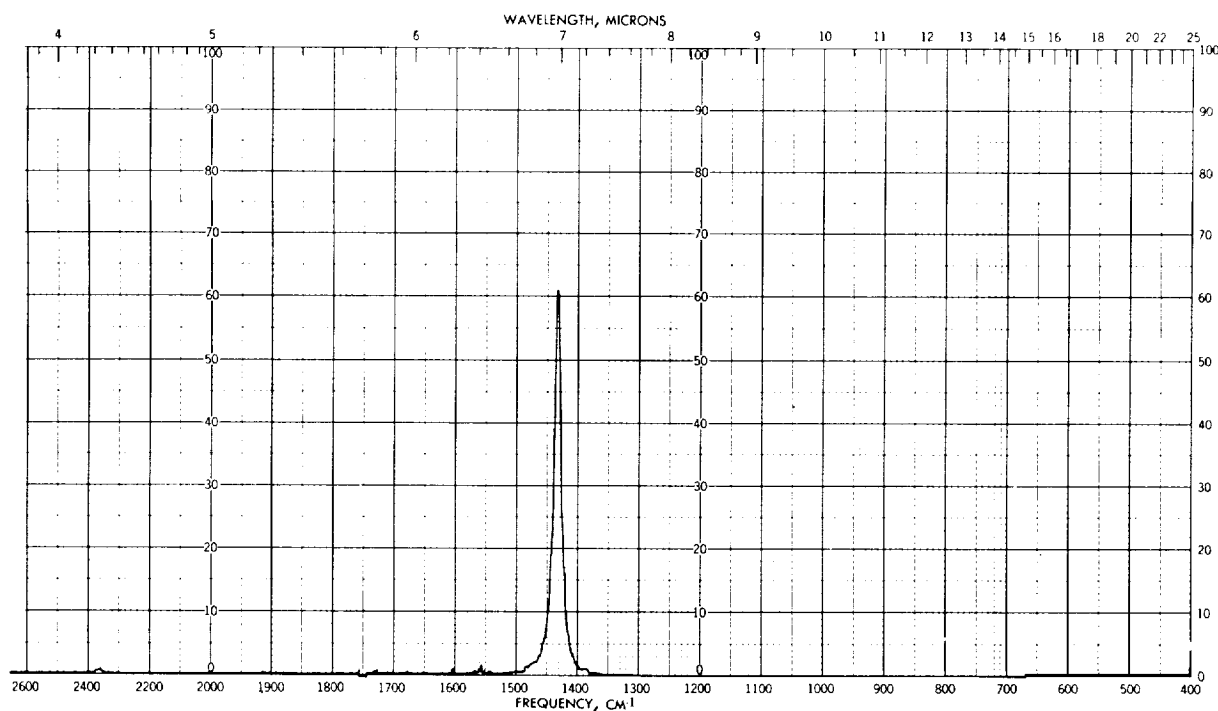


FIGURE 15.—Spectral transmittance of a representative filter.

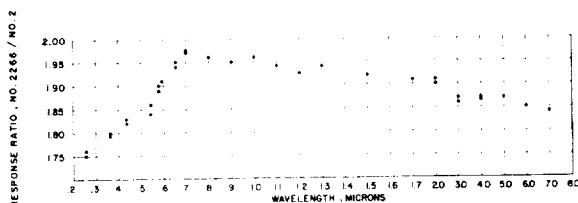


FIGURE 17.—Ratio of spectral sensitivity of Eppley thermopile 2266 to that of cavity detector 2 (13-cps amplifier).

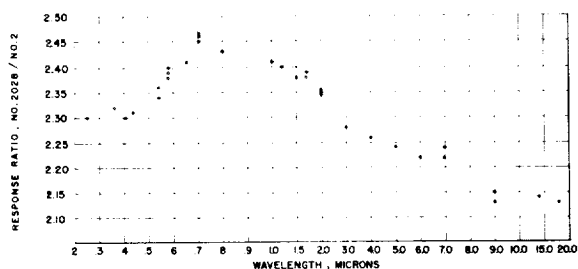


FIGURE 18.—Ratio of spectral sensitivity of Eppley thermopile 2028 to that of cavity detector 2 (13-cps amplifier).

producing phase angle variations with wavelength for the chopped signal.

Figure 17 shows a similar comparison between Eppley thermopile 2266 and cavity detector 2. The Eppley thermopile has a gold black surface and shows a drop in sensitivity at wavelengths both longer and shorter than about 0.7 micron. For wavelengths above about 2 microns the drop is even greater than that recorded for cavity detector 2. Similar data were obtained for Eppley thermopile 2028 (replacement element 2650) having a lampblack surface and no window (fig. 18). Although this thermopile has a coating similar to that of the Coblentz 1 unit, its response drops off at longer wavelengths apparently because the coating is thinner and also because the substrate is gold. For the longer wavelengths, the Coblentz thermopile also has receivers consisting of thin sheets of tin having a lower reflectance than gold.

Photosensitive Detectors

Two types of photosensitive detectors will be considered as representative of what one may encounter in the laboratory—a photomultiplier and a PbS cell. It is realized that others offer

different problems and may be worse or better in certain respects. The two detectors chosen have wide use. For the multiplier type, data are given on an RCA type 1P-28. (Fig. 19). This illustration shows the variations in sensitivity over the cathode surface of a particular tube—one chosen at random from a group of about a dozen having similar characteristics. From this figure it becomes evident that in order to measure radiant flux accurately, the light beam must always fall exactly upon the same position of the cathode in all cases. A movement of the light beam by even a few thousandths of an inch may result in a response change of many percent. A crosswise scanning of the cathode of the same tube in figure 20 shows changes in response across the center of the cathode for blue light and for red light. An appreciable color sensitivity exists. In other tubes much larger color variations have been noted. The third curve (the solid circles)

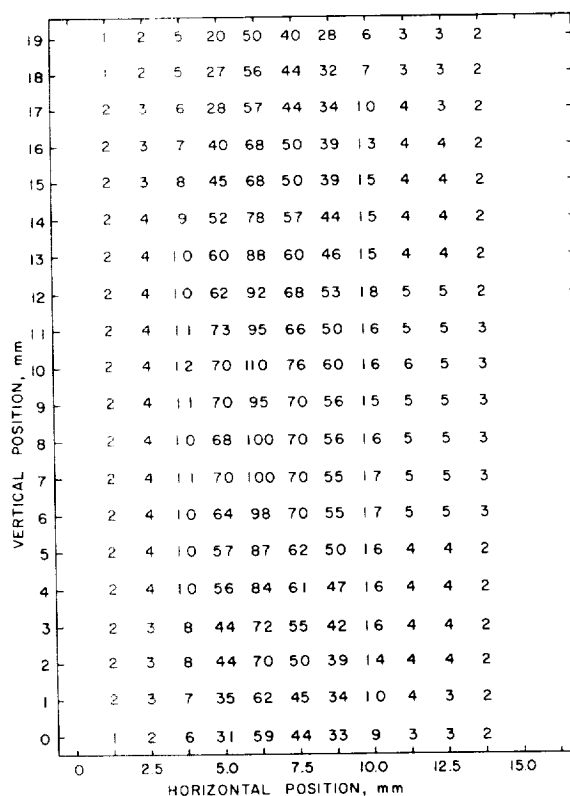


FIGURE 19.—Variation in sensitivity over the surface of a 1P-28 photomultiplier.

shows what may be accomplished with incandescent lamp flux by covering the multiplier

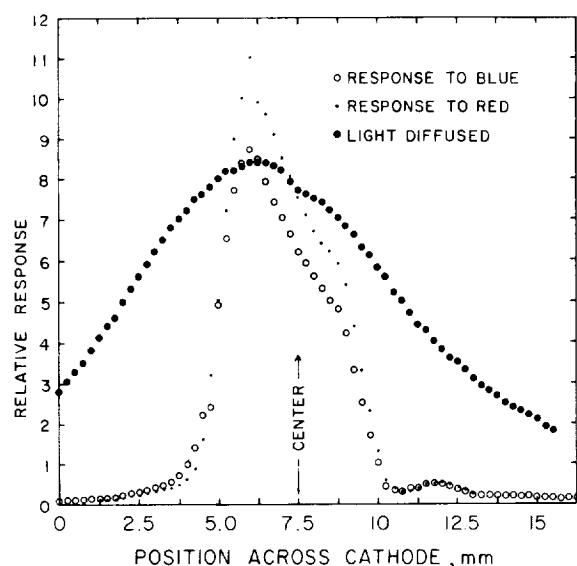


FIGURE 20.—Variation in sensitivity for blue and red light across the cathode of the 1P-28 photomultiplier of figure 19.

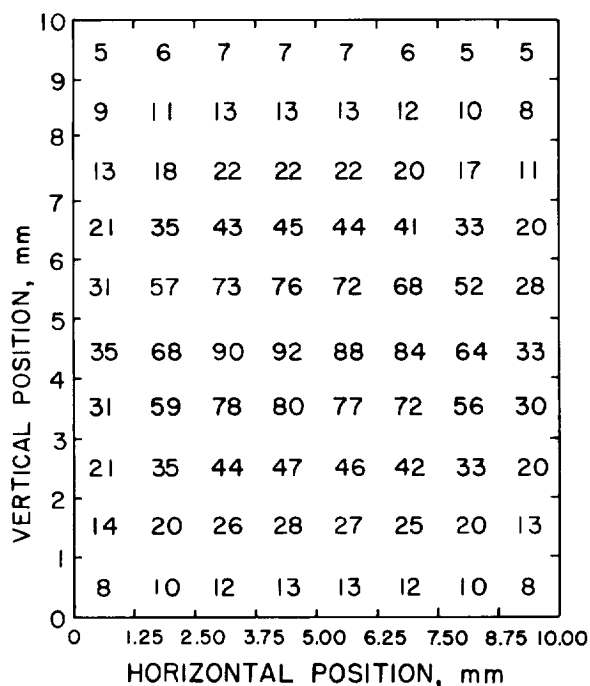


FIGURE 21.—Variation in sensitivity over the surface of an Eastman lead sulfide cell.

with a doubly diffusing fine ground quartz glass plate. A lesser effect may be obtained through roughening (sandblasting) the tube envelope before or after manufacture.

In figure 21 are shown the variations in sensitivity over the surface of a 10 mm x 10 mm Eastman PbS cell when scanned with a small spot of incandescent lamp flux. Highest sensitivity occurs across the center of the element between the electrodes (located at 0- and 10-mm positions). Lower sensitivities exist near the upper and lower edges of the element. A detector of this type should be set up with the spectroradiometer slit along the ridge of highest sensitivity for highest efficiency and highest signal-to-noise ratio. However, for certain purposes a more nearly constant output may be obtained with the cell rotated 90°.

CONCLUDING REMARKS

When consideration is given to the large variations that may exist over the surfaces of detectors, coupled with the nonuniformity of the emergent beam of the spectroradiometer, the direct comparisons of sources spectroradiometrically become very difficult. For example, with one detector, source A may appear to have several times the intensity of source B at the set wavelength, but with a change of detector (or even with a resetting of the original detector) a new measurement may indicate just the opposite—that source B has several times the intensity of source A at the set wavelength. Even with very careful optical adjustments using two similar sources (two lamps of the same type and size) errors of 50 to 100 percent may occur. With sources of unlike size and shape accurate comparisons are impossible by direct radiometric comparisons without auxiliary equipment.

Similarly, when a single source is used, the comparison of two detectors spectroradiometrically poses a like problem. After much effort in this direction, the authors concluded that for thermal detectors having relatively flat responses with wavelength the problem could best be solved through the use of a filter method. Accordingly, the filter spectroradiometer shown in figure 14 employing twenty odd narrow band interference and other type filters was set up

and employed in the comparisons of the thermal detectors described herein. This instrument will be described in greater detail in a coming report.

Accurate comparisons between like sources (two lamps of the same type for example) may be made spectroradiometrically through the use of detectors having surfaces of uniform sensitivity provided each lamp is set to irradiate the spectroradiometer in exactly the same way. This may be simply accomplished through the use of identical auxiliary optics as shown in figure 2 in radiance measurements, but in irradiance work the difficulty is greater. Even the small differences in filament shapes between two lamps of the same type may be sufficient to upset the measurements by many percent. However, in practice the two lamps may be individually set at the optimum position by observing the radiometric deflection and setting each of the lamps (individually) at the position for maximum reading after the detector has been mounted with its position of maximum sensitivity centered on the slit and the wavelength drum of the spectroradiometer has been set for peak response for the particular lamp and detector. With these precautions two like sources may be compared accurately, the same results being obtainable with different detectors.

But when the sources are different—as will usually be the case with an unknown source being measured in terms of a standard—the results will depend greatly upon the experimental setup. With radiance measurements, the results will simply be relative for a particular area of the unknown—as, for example, a limited section of the arc between the electrodes of a xenon arc. Such a result is of little value for most purposes. A more meaningful measurement must include the entire source and will usually require that it be made in terms of irradiance. Since the two sources, the standard and unknown, are of different geometrical shape and area as viewed from the spectroradiometer slit, some optical method must be included to produce like sources as seen from the spectrometer. This can best be accomplished through the use of a diffusing sphere or spheres which are alternately illumi-

nated by the two sources. This is not a new idea, but one which is often by-passed if sufficiently useful information can be had without resorting to its use. For a sphere coating, magnesium oxide offers good reflectance from about 0.25 to 2 microns (ref. 11, 12, and 13) and may be usable to about 11 microns. At wavelengths longer than 2 microns metallic surfaces are probably best. Some of the ceramics appear promising if methods of coating or casting can be worked out. In lieu of spheres for approximate measurements, good diffusing surfaces may be employed and set such that the diffusing surface receives and reflects or transmits the radiant energy in the same manner in the two cases, if sufficient energy is available.

REFERENCES

1. COBLENTZ, W. W.: Measurements on Standards of Radiation in Absolute Value. *Bull. Bur. Standards*, vol. 11, no. 1, Nov. 15, 1914, pp. 87-96.
2. ANON.: NBS Technical New Bulletin, vol. 47, Oct. 1963, p. 10.
3. STIMSON, H. F.: International Practical Temperature Scale of 1948—Text Revision of 1960. *Res. Paper 65A3-96, Jour. Res. Nat. Bur. Standards*, vol. 65A, no. 3, May-June 1961, pp. 139-145.
4. STAIR, RALPH, FUSSELL, WILLIAM B., and SCHNEIDER, WILLIAM E.: A Standard for Extremely Low Values of Spectral Irradiance. *Appl. Optics*, vol. 4, no. 1, Jan. 1965, pp. 85-89.
5. STAIR, RALPH, JOHNSTON, RUSSELL G., and HALBACH, E. W.: Standard of Spectral Radiance for the Region of 0.25 to 2.6 Microns. *Res. Paper 65A-51, Jour. Res. Nat. Bur. Standards*, vol. 64A, no. 4, July-Aug. 1960, pp. 291-296.
6. STAIR, RALPH, SCHNEIDER, WILLIAM E., and JACKSON, JOHN K.: A New Standard of Spectral Irradiance. *Appl. Optics*, vol. 2, no. 11, Nov. 1963, pp. 1151-1154.
7. ENGSTROM, R. W.: Luminous Microflux Standard. *Rev. Sci. Instr.*, vol. 26, no. 6, June 1955, pp. 622-623.
8. EISENMAN, W. L., BATES, R. L., and MERRIAM, J. D.: Black Radiation Detector. *Jour. Optical Soc. of America*, vol. 53, no. 6, June 1963, pp. 729-734.
9. GOUFFÉ, ANDRÉ: Aperture Corrections for Artificial Blackbodies. *Revue d'Optique*, vol. 24, nos. 1-3, Jan.-Mar. 1945, pp. 1-10.
10. SPARROW, E. M., and JONSSON, V. K.: Radiant Emission Characteristics of Diffuse Conical Cavities. *Jour. Optical Soc. of America*, vol. 53, no. 7, July 1963, pp. 816-821.

11. MIDDLETON, W. E. K., and SANDERS, C. L.: An Improved Sphere Paint. *Illuminating Eng.*, vol. 48, no. 5, May 1953, pp. 254-256.
12. McALOREN, J. T.: A Reproducible Magnesium Oxide Standard for Reflectance Measurement From 0.3 to 2.6 μ . *Nature*, vol. 195, no. 4843, Aug. 25, 1962, pp. 797-798.
13. GIER, J. T., DUNKLE, R. V., and BEVANS, J. T.: Measurement of Absolute Spectral Reflectivity From 1.0 to 15 Microns. *Jour. Optical Soc. of America*, vol. 44, no. 7, July 1954, pp. 558-562.

DISCUSSION

THOMAS LIMPERIS, University of Michigan: Perhaps the change in responsivity with wavelength for the a-c and d-c modes might be a thickness effect; for example, at longer wavelengths I would think that the radiation might be absorbed further down into the material and that the recovery time of the detector might be a little longer. Have you reduced the chopping frequencies somewhat to determine whether recovery is toward the d-c level?

SCHNEIDER: No. We are now working on that; we plan to use a variable-frequency-type amplifier and then examine this effect further. That was one of our considerations.

LIMPERIS: What was the band pass of your electronics, operating at 13 cps?

SCHNEIDER: I do not know the exact band pass.

DWIGHT MOORE, National Bureau of Standards: I would like to make a comment on a statement by Clayton, earlier, that the thermal emittance standards were not easy to get from the National Bureau of Standards. This may have been true 3 or 4 years ago, but for the past year, it has been quite easy to obtain these standards from our laboratory. I would guess that some 20 or 25 sets have been sent out over this period. Of course, he might have been referring to the cost—we do charge for them. For a complete set (low-, medium-, and high-emittance standards calibrated from 1 to 15 microns at temperatures of 800°, 1100°, and 1400° K) the price is about \$600, with the exact amount depending on the particular size that is required. Possibly, Mr. Schneider would like to comment on how easy it is to obtain the standards that he referred to in the early part of his talk.

SCHNEIDER: The standards of total irradiance and spectral radiance (the tungsten strip lamps) can be purchased from The Eppley Laboratory, Inc., Newport, Rhode Island. The standard of spectral irradiance can be purchased directly from the National Bureau of Standards. However, there is a delay of about a month.

MICHAEL T. SURH, University of Michigan: In the instructions for the use of standards of spectral radiance or irradiance, it is indicated that the uncertainty of the spectral values that are furnished in the certificate of calibration varies from approximately 8 percent at the shortest wavelength to 3 percent at the longest

wavelength. I wonder if in the future a more detailed statement relating to the accuracy of the standard can be given. I have seen many papers in which the authors claim that they have made radiation measurements with an uncertainty of 1 or 2 percent using a standard which is 3 to 8 percent uncertain. I believe that some of this confusion could be eliminated if the NBS or Eppley would supply data on precision or statistical spread of the values they measure. You mentioned that, in scanning the thermopile lengthwise or vertically, you found some large negative values; I wonder if this is due to the irradiation of the cold junction rather than the hot junction.

SCHNEIDER: I do not think the negative deflections are due to the cold junctions heating up, since we do not observe these deflections with the d-c setup. For one thermopile there was some negative deflection near the edges, which was probably due to the cold junction heating up; but the negative deflections occurring along the length of one of the thermopiles spaced somewhere in the middle of the element are probably not due to cold junctions heating up. However, it has been found that the apparent sensitivity pattern observed changes radically both with change in the chopping frequency and with angular adjustment of the light beam interceptor blade. These results indicate that there is a phase change in the signal resulting from the time lag between the absorption of the light and the resulting buildup of an electric potential in the thermal junctions. Thus, the Perkin-Elmer 107 amplifier picks up a response out of phase with the signal itself.

RICHARD M. JANSSON, Honeywell, Aeronautical Division, Boston: In the past, The Eppley Laboratory has calibrated thermopiles for solar simulation use by comparison with a set of pyrhelimeters. Do you know when your high-intensity standard might be available for more accurate calibrations and what its characteristics will be?

SCHNEIDER: This standard will be a 1000-watt tungsten lamp calibrated for total irradiance. Work on this standard is just beginning. As I mentioned, this standard will have an irradiance of about 100 to 150 mw/cm².

25. A High-Temperature Circular-Aperture Blackbody Radiation Source

P. E. SCHUMACHER

ROCKETDYNE, NORTH AMERICAN AVIATION, INC., CANOGA PARK, CALIF.

A one-quarter inch diameter, circular aperture blackbody radiation source is described. The unit, designed for the field calibration of missile- and air-borne radiometers, is self-contained with the exception of an electrical power source. It is usable in this configuration to temperatures of 2300° C.

The radiation source, which is windowless and, therefore, usable over a broad spectral range, has a short time constant associated with temperature changes, namely, about 1 minute. The source consists of two principal components: an electrically heated blackbody with attached power transformer and a power control—cooling system console. These components are interconnected by hoses and electrical cables to afford flexibility in the placement of the blackbody.

The performance of the system with respect to temperature stability and uniformity is discussed, and the theoretical determination of the effective source emissivity of 0.98 is reviewed briefly.

This system has recently been modified for laboratory operation at higher temperatures. With increased electrical power handling capabilities and cooling system capacity, temperatures of 2800° C have been reached.

Accurate quantitative radiation measurements require calibration of the radiometric instrument used. This, in turn, requires a radiation source whose radiance is a known function of wavelength. A blackbody is, of course, such a source. For optimum accuracy it is desirable to calibrate the radiometer using a source whose radiance approximates that of the target.

The blackbody sources described here are specifically intended for use in the field calibration of missile- and air-borne radiometers used to measure the radiation of missile exhaust plumes. As such the sources were required to be readily movable and as self-contained as possible. Furthermore, since the targets were to be missile exhaust plumes, high-temperature operation of the blackbodies was required. In particular, a temperature capability of 2000° C was necessary. Such sources were

not available commercially when the development of the blackbody described here was undertaken.

DESCRIPTION

Physically the system consists of two principal components: an electrically heated blackbody radiation source with attached power transformer and a power supply-cooling system console. These components are connected by hoses and electrical cables to afford flexibility in the placement of the radiation source. The console houses all necessary appurtenances for the operation of the source except an electrical power source. The system is shown in figures 1 and 2.

Radiation Source

The blackbody source consists of an electrically heated graphite tube about 1/2 inch in

diameter. An integral septum perpendicular to the tube axis is located approximately at its midpoint. The tube is viewed axially so that the septum is the surface seen from the aperture.

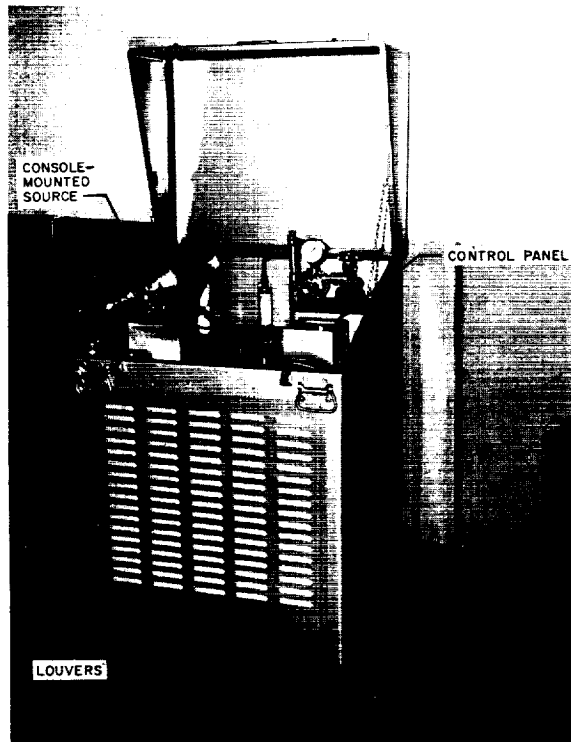


FIGURE 1.—Blackbody system with source mounted on console.

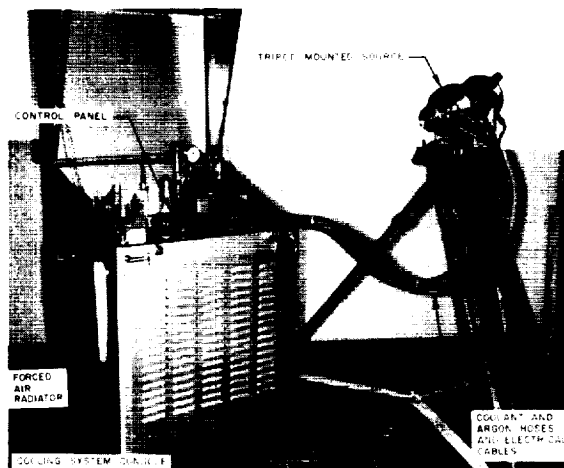


FIGURE 2.—Blackbody system with source mounted on tripod.

A series of concentric grooves machined in its surface increases the source emissivity. The heated tube is surrounded by two radiation shields concentric with it; the inner one is graphite, the outer, goldplated brass. The shields, in turn, are inside a brass housing through which cooling water is circulated. Mechanical and electrical connections are made at the ends of the tube. At the front, a copper flange is screwed onto the graphite and is, in turn, clamped to the housing by a cap. The rear of the tube screws into a copper piston which is soldered to a bellows and thence to the central conductor of the power transformer. This configuration allows thermal expansion of the element. Figure 3 is an exploded view of the source assembly.

To prevent rapid oxidation and subsequent erosion of the element when it is operated at high temperature in air, a flow of argon is directed around the element and allowed to escape via the viewing aperture. The source is flushed thoroughly before heating, and a low flow is maintained during its operation. This provides a nearly inert atmosphere for the heated element even when the viewing aperture is open to the atmosphere. The need for a window with its attendant transmission problems is thus eliminated. Hence, the source can be used over a broad spectral range.

The electrical resistance of the graphite element is low. Thus, very high currents are required to deliver the power necessary to raise

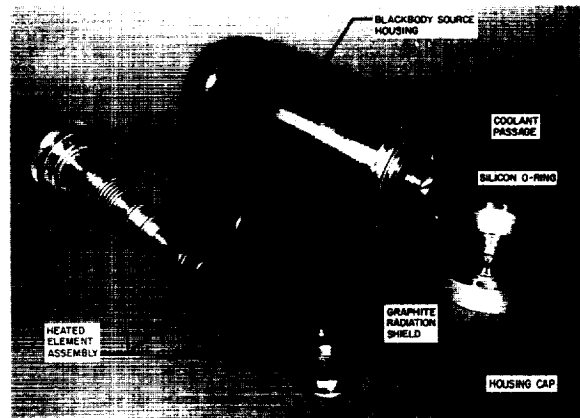


FIGURE 3.—Blackbody-source assembly.

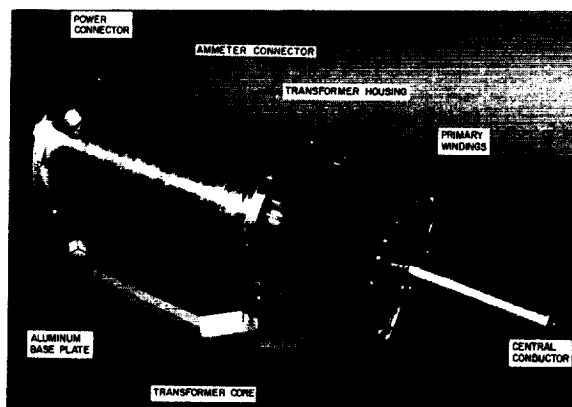


FIGURE 4.—Blackbody-source power transformer.

the element to high temperatures. To minimize the problems of conducting these high currents, the power transformer is mounted contiguous to, and coaxial with, the source. It consists of a toroidal core with a 22-turn primary and a single-turn secondary (as shown in fig. 4). A central conductor, the cylindrical transformer housing and its end plates together with the radiant source housing and the graphite tube form the secondary turn. This concentric arrangement also minimizes stray magnetic fields due to the high current flow.

The entire source-transformer assembly is mounted on an aluminum base plate which can be affixed to a professional motion picture camera tripod or can be used in place on the console brackets in which it is shipped.

The source assembly is connected to the console by flexible hoses and cables. These include coolant supply and return hoses, an inert gas supply hose, an electrical power cable, and an ammeter cable. When the source is mounted on the console, the cables are dropped through an opening in the console deck and stored underneath to prevent interference with the operation of the system. When the source is tripod-mounted, the cables are pulled out the necessary distance. At least 6 feet of separation from the console is possible.

Power Supply—Cooling System Console

The power supply-cooling system console is a $2 \times 2\frac{1}{2} \times 4$ -foot cabinet mounted on wheels for mobility. It houses a variable autotrans-

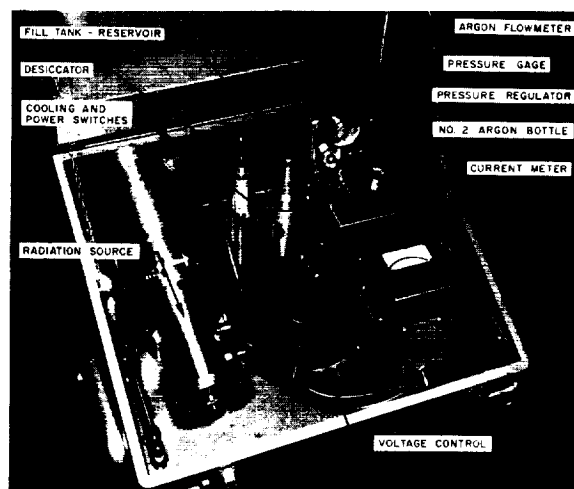


FIGURE 5.—Blackbody control panel.

former for power control, a precision ammeter for monitoring source current, a forced-air radiator and pump for cooling, and an inert gas supply. A hinged cover opens to allow access to the various switches, controls, and meters used in the operation of the source as shown in figure 5.

The radiator is mounted directly in a side panel of the console. The remainder of the panels are louvered to admit cooling air. To facilitate access to the components within the console, the front and back panels are removable. Figure 6 shows the interior of the console with the front panel removed. The operation of the console is discussed in terms of the inert



FIGURE 6.—Console interior, front view.

gas, cooling, and electrical systems for simplicity.

INERT GAS SYSTEM

High-purity argon is used as the inert gas in the present system. To supply the argon, provision has been made for the mounting of a No. 2 cylinder in the console. A schematic of the complete system is shown in figure 7. The function of the components is self-evident and will be mentioned only briefly here. The regulator is used to adjust the argon flow to a suitable rate which is measured with the attached flowmeter. The desiccator serves to remove from the argon any residual moisture which would, of course, cause rapid deterioration of the heated graphite element.

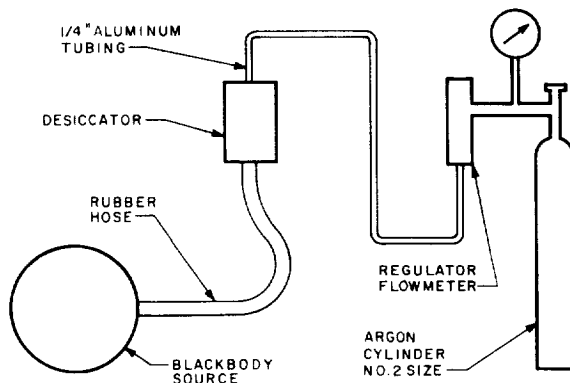


FIGURE 7.—Argon system.

COOLING SYSTEM

Cooling of the radiation source is accomplished by a recirculation system using water as the coolant. The heat gained while passing through the brass housing of the source is rejected to the atmosphere by passing the coolant through a forced-air heat exchanger similar to an automobile radiator. A centrifugal pump circulates the water through the system at a rate of $3\frac{1}{2}$ gallons per minute. The capacity of the radiator at this flow rate is sufficient to keep the coolant well below boiling temperature at sea-level pressure during full-power operation of the source with ambient air temperatures up to 115°F .

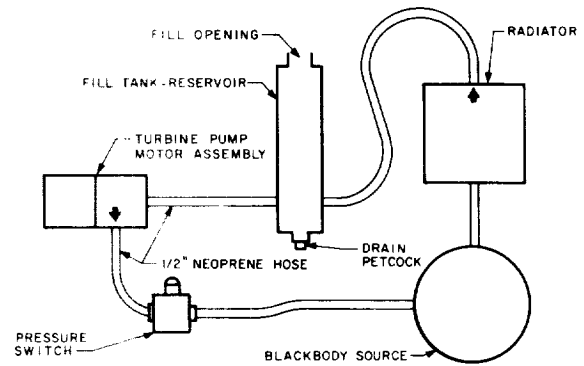


FIGURE 8.—Cooling system.

To prevent destruction of the source if the coolant circulation should stop due to pump failure, for example, a pressure switch is placed at the pump outlet. It is set to actuate at a pressure corresponding to the minimum allowable flow rate and is incorporated in the electrical circuit so that it removes power from the source whenever the pressure drops below this value.

A combination fill tank and reservoir is incorporated in the coolant system near the pump inlet. It remains open to the atmosphere, thus preventing any over-all pressure rise in the system. Figure 8 is a schematic of the cooling system.

ELECTRICAL SYSTEM

To attain maximum temperature, the blackbody system requires a well-regulated supply of electrical power with the following specifications: 60 cycles per second, single phase, 118 volts, 60-ampere capacity. If the voltage at the console is lower than this, due to cable loss, for example, the maximum temperature attainable will be correspondingly lower. If an unregulated power supply is used, the temperature stability of the radiation source will be adversely affected.

The principal components in the electrical system are a 45-ampere, variable autotransformer and a specially fabricated step-down power transformer, discussed in the section describing the source. A relay in the autotransformer output circuit is used to control power delivery to the blackbody. Figure 9 is a

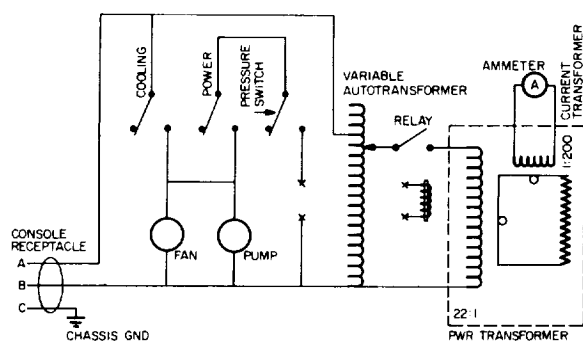


FIGURE 9.—Electrical system.

circuit diagram of the complete system. The heating current is measured by using a 1000:5 current transformer in the secondary circuit together with an ammeter which is mounted on the power supply console.

There are two switches and a continuously variable voltage control on the console control panel. The COOLING switch delivers power to the fan and pump motors. In addition, it delivers voltage to one side of the POWER switch. Thus, both control switches and the aforementioned pressure switch are all in series with the relay actuating coil. Hence, it is almost impossible to apply power to the source without the cooling system operating.

PERFORMANCE

Temperature Characteristics

TEMPERATURE CAPABILITY

As mentioned earlier, the blackbody has a maximum design temperature of 2000° C. In practice, the source can be operated to 2300° C in the configuration described. This temperature is reached with the voltage control set at full scale and a regulated 118 volts supplied to the console. The total power requirement is then 6.5 kilowatts as compared to 5 kilowatts at 2000° C.

TEMPERATURE STABILITY

The temperature of the blackbody is controlled simply by adjusting the voltage input to the power transformer with the variable autotransformer. No temperature sensor and control circuit are used to maintain a constant

temperature in the present model. Hence, the short-time temperature stability of the source is dependent solely on the stability of the supply voltage.

Another factor which affects temperature stability over longer periods is change in the heating element itself. For example, erosion resulting from oxidation of the graphite increases the element resistance and, hence, decreases the temperature under constant-voltage operation. Extended duration tests on a prototype source operating at 2000° C indicated a resistance decrease during the first 150 hours of operation. The change was such as to cause a temperature increase at the rate of 0.5° C per hour during this interval. The change was attributed to further graphitization of the element at the high operating temperatures. After this initial period the temperature remained essentially constant for over 500 hours, the duration of the tests. Thus there was no apparent erosion of the element over this time interval. Figure 10 shows the temperature as a function of the secondary current after 50 and 500 hours of testing.

The ambient temperature of the air in which the blackbody console is operated directly affects the temperature of the watercooled blackbody housing. It is thus a third factor affecting the temperature stability of the radiation source. This follows from the fact that the majority of the heat loss from the high temperature element is to this housing. Thus, for a constant voltage input the element temperature must increase with the housing temperature. That part of the increase due to conduction loss will vary linearly with air temperature while that portion stemming from radiation to the housing will increase at a slower rate. The relatively small amount radiated through the aperture will not be affected. Therefore, the overall change in source temperature with ambient air temperature will be less than linear. Indeed, a large number of temperature measurements made over a period of weeks and at various times of the day indicated no temperature variation when such tests were run in the laboratory, which was air conditioned but did exhibit significant diurnal temperature

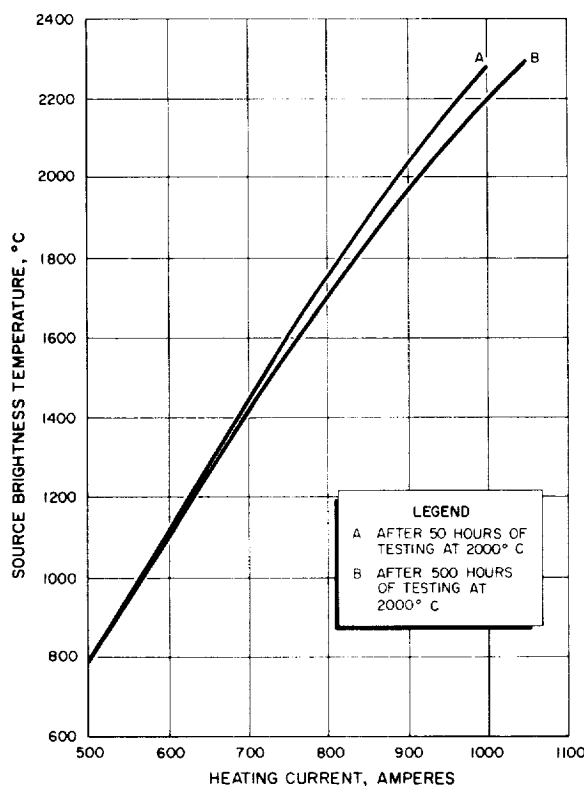


FIGURE 10.—Temperature against heating current for preprototype blackbody source.

fluctuations. This source of temperature instability can, of course, be eliminated by substituting externally supplied cooling water of constant temperature.

RESPONSE TIME

The only components of the blackbody that undergo appreciable temperature changes with voltage changes are the directly heated element itself and the radiation shield. The thermal capacity of these components is quite small so that there is an inherently short time constant associated with temperature changes. (Temperature changes of the source housing, which does possess considerable thermal inertia, are very small compared to the element temperature changes.) Tests have indicated that the source reaches equilibrium temperature within 1 minute for temperature changes as large as 100° C and within several minutes in the case of much larger temperature changes.

TEMPERATURE UNIFORMITY

The temperature measurements referred to heretofore were made by focusing the optical pyrometer on the center of the viewed surface. Measurements over the entire septum surface indicated no variation whatsoever from this temperature.

Emissivity

The construction of the blackbody radiation sources is such that there is a pronounced temperature gradient along the axis of the heated element; hence, the emissivity of the cavity, as such, is not defined. However, if the effective emissivity of the source is defined as the ratio of the radiosity of the viewed surface to that of a blackbody at the same temperature, it serves as a useful measure of the radiation quality of the source.

The feasibility of experimentally determining this emissivity was investigated, and it was concluded that no better than 2 percent accuracy could be obtained with the instrumentation available. Hence, an analytical determination was made by the method of De Vos, as given in reference 1. Perfectly diffuse radiation and reflection from the cavity surfaces was assumed, and the axial temperature distribution of the heated element was estimated from measurements of the brightness temperature at corresponding positions. The resultant estimate of the effective emissivity was 0.98. The details of this calculation are to be found in reference 2.

HIGH TEMPERATURE TESTS

After the 2000° C blackbody sources were fabricated, an interest in similar sources capable of operation at 3000° K developed. The 2300° C limit of the present source is due to its limited electrical power handling capability and to low cooling system capacity. One of the present sources was modified to circumvent these limitations, and a brief series of tests was run to determine whether 3000° K operation could indeed be achieved. These modifications included replacement of the existing power transformer and variable voltage autotransformer with larger units and the use of a

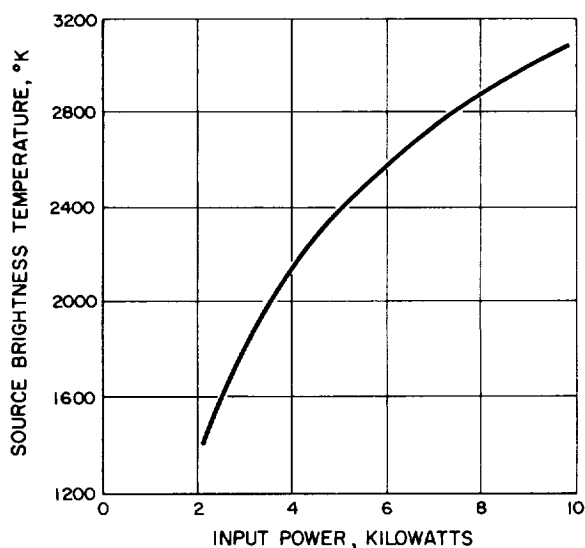


FIGURE 11.—Variation of temperature with input power for modified blackbody source.

laboratory water supply at a high flowrate in place of the recirculating cooling system.

With these modifications 3000° K operation was, in fact, obtained. Figures 11 and 12 show the temperature-power and temperature-current relationships obtained from these tests.

Not enough data are available at the time of this writing to make a definite statement as to the stability of operation at these temperatures. However, since the vapor pressure of graphite is at least 10^{-4} atmospheres at this temperature, it is apparent that erosion due to sublimation of the graphite may be a problem for long duration operation.

CONCLUSIONS

A blackbody radiation source with a $\frac{1}{8}$ -inch circular aperture and an effective emissivity of 0.98 has been developed. It is capable of con-

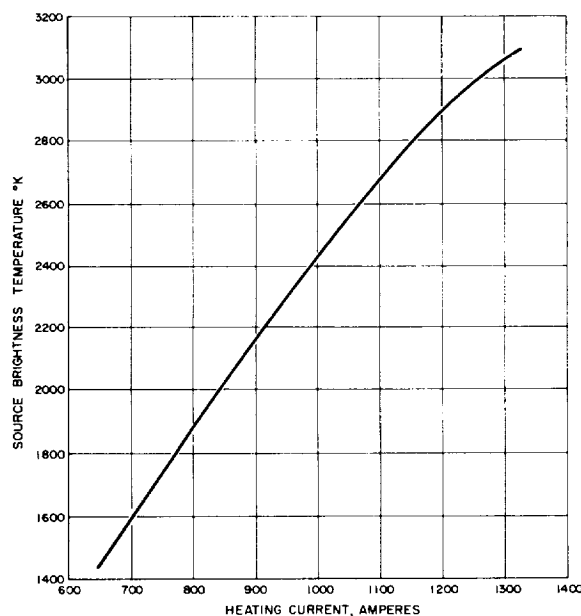


FIGURE 12.—Variation of temperature with heating current for modified blackbody source.

tinuous operation at temperatures in excess of 2000 degrees centigrade. Tests on a modified blackbody have indicated the feasibility of operation at 3000 degrees Kelvin.

ACKNOWLEDGMENT

The work reported here was sponsored by the Advanced Research Projects Agency, Department of Defense, for the Air Force Cambridge Research Laboratories under Contract AF19(604)-8066.

REFERENCES

1. DE VOS, J. C.: Evaluation of the Quality of a Blackbody. *Physica*, vol. 20, 1954, pp. 669-689.
2. SCHUMACHER, P. E.: The Emissivity of the Rocketdyne Circular Aperture Blackbody Radiation Source. Research Report No. 63-3, Rocketdyne, A Division of North American Aviation, Inc., Feb. 1963.

DISCUSSION

ANDREW A. HALACSY, Heat Magnetic Engineering, Mountain View: I have two questions: (1) How was the blackbody joined electrically to the power source; that is, was it a pressure contact or some other type? (2) Where was your current transformer located; was it somehow combined with the main transformer, using the same secondary conductor?

SCHUMACHER: (1) The electrical contact was simply a pressure contact. The graphite element was screwed

into a plate at one end and a piston at the other. Both of these were made of copper. There were approximately 4 threads in contact, and the thread fit was good. (2) The current transformer surrounds the single secondary turn and is located immediately adjacent to the power transformer.

ROY NICHOLS, University of Michigan: I would like to know what sort of temperature errors are associated with this blackbody.

SCHUMACHER: As I mentioned before, the temperatures were brightness temperatures as measured with a disappearing filament-type optical pyrometer. This, in turn, was calibrated by using a tungsten strip lamp calibrated by NBS. I estimate the accuracy as approximately $\pm 6^\circ \text{C}$.

NICHOLS: In other words, it is determined on the basis of a brightness temperature, and, therefore, if the emissivity is less than 1, the temperature is uncertain.

SCHUMACHER: The actual temperature, yes. However, if my emittance calculation is correct, the differ-

ence between brightness temperature and actual temperature at 3000°K is only about 10°C .

KENNEDY, United Technology: You said this source was used to make field calibrations of radiometers. Was this accomplished, and how did it compare with vendor calibrations?

SCHUMACHER: I do not know. The instrument was made for Air Force Cambridge Research Laboratory, and I am not familiar with what field use has been made of it.

26. Method and Equipment for Measuring Thermal Emittance of Ceramic Oxides From 1200° to 1800° K

HOWARD E. CLARK AND DWIGHT G. MOORE

NATIONAL BUREAU OF STANDARDS, WASHINGTON, D.C.

A description is given of the rotating cylinder equipment developed by the National Bureau of Standards for measuring the total normal emittance and normal spectral emittance from 1 to 15 μ of nonmetals as well as metals over the temperature range 1200° to 1800° K. Preliminary data are presented for 11 different ceramic oxide specimens at 1200° K and for platinum at 1400° K. A comparison is made between these data and emittance values obtained by measuring room-temperature spectral reflectance from 0.26 to 2.10 μ for 6 of the 11 ceramic oxides. Possible sources of error are discussed.

Knowledge of the thermal emittance of ceramic oxides at high temperatures is important for many potential space applications and for obtaining an improved understanding of the thermal emission mechanism in solids. Several investigators have made emittance measurements on materials of this type but wide variations in the data are evident.

The purpose of the present study, which is sponsored by the George C. Marshall Space Flight Center of NASA, is to develop equipment and techniques suitable for providing reliable normal spectral and total normal emittance data for nonmetals at temperatures up to 1800° K. A secondary objective is to obtain emittance data of known accuracy on a number of representative nonmetals, especially the ceramic oxides.

Since a number of important changes in the equipment and procedure are yet to be introduced, and because the data and error analysis is still incomplete, the present results are only tentative.

SELECTION OF MEASUREMENT TECHNIQUE

The properties of the ceramic oxides which make high-temperature emittance measure-

ments difficult are their low thermal conductivity and appreciable transmission for radiation in certain spectral regions. The former property makes it difficult to achieve a uniform temperature distribution in a specimen, and the latter gives rise to the phenomenon of volume emission. Thus, if a sample is heated from one side, large temperature gradients will develop, and in those spectral regions where the material is not very opaque, a portion of the radiated energy will originate in volume elements located below the surface, where the temperatures are not the same as the surface temperature. In such a case the radiation does not quite correspond to the surface temperature (in fact, a true temperature cannot be assigned to the radiating material), and too high or too low a value of emittance will be measured, depending on the sign of the gradient. Even when temperature uniformity in the specimen has been approached, serious errors can still arise because of extraneous radiation striking the specimen and being diffusely reflected into the specimen beam. These errors are particularly noticeable in the low-wavelength region where the diffuse reflectance of ceramic specimens often exceeds 0.9. The measurement problems are further complicated if the specimen is not sufficiently thick to be opaque.

When this condition exists, radiation from heated surfaces behind the specimen, for example, the rear wall of a furnace enclosure, will pass through the specimen and reinforce the specimen beam, thus giving a measured emittance that is too high.

A thorough review of methods used by earlier investigators indicated that one of the best approaches for reducing the temperature gradients in a ceramic specimen to workable levels is to move the heated specimen past a water-cooled viewing port. In this way, a freshly heated surface of the material is continuously arriving at the port for measurement. If the movement is rapid, a thermal equilibrium is approached and temperature gradients in the specimen will be reduced to low levels. This technique was first introduced by Féry in 1902 (ref. 1).

In the early applications of the method (ref. 1, 2, and 3), cylindrical specimens were rotated while being heated in a gas flame. The ratio of the radiant flux from the surface to that from a hole placed axially at the center of the specimen was then taken as the emittance. No viewing port was used. In more recent applications, the specimen was rotated in a furnace cavity equipped with a water-cooled viewing port. In the investigations by McMahon (ref. 4), Slomp and Wade (ref. 5), and Olson and Katz (ref. 6), a semicircular disk-shaped specimen was rotated in front of the port so that the detector saw blackbody radiation from the furnace for one-half of the cycle and saw radiation from the specimen for the remaining one-half cycle. McMahon and Olson and Katz arranged for the periodic insertion of a water-cooled shutter behind the specimen. This enabled them to handle materials which were not completely opaque, and at the same time permitted them to determine the transmittance of the specimen. Folweiler (ref. 7) described a rotating cylinder apparatus which incorporated solid cylindrical specimens with a "V" groove positioned around the circumference to serve as a reference blackbody.

Clayton (ref. 8) rotated a disk-shaped specimen in a carbon resistance furnace equipped with separate water-cooled viewing ports for detecting radiation both from the specimen and from the furnace enclosure. The specimen

sighting tube could be alined in two positions. In the first position the region behind the viewed portion was the hot furnace enclosure, and in the second it was a water-cooled baffle. Here, again, the aim was to measure both emittance and transmittance.

A careful consideration of the possible errors and of the expected experimental difficulties inherent in each of these moving specimen methods resulted in our selection of a rotating cylinder method with a separate blackbody. Briefly stated, the method consists of rotating a specimen, 1 inch in diameter and 1 inch high with $\frac{1}{8}$ -inch-thick walls, in a wire-wound furnace equipped with a water-cooled viewing port. Spectral emittance measurements are made with a double-beam spectrophotometer by comparing the radiant flux density from the rotating specimen with that from a blackbody at the same temperature. Errors due to transmitted radiation are avoided by working only with those materials which may be considered opaque at a thickness of $\frac{1}{8}$ inch.

The more important design requirements set forth for the equipment were as follows: (1) a specimen size and shape that could be fabricated easily and at a reasonable cost, (2) a variable-speed capability for the specimen, (3) furnace temperature capabilities of at least 1800° K with an operating life of several hundred hours, (4) temperature uniformity within the blackbodies of at least $\pm 5^\circ$ K and along the specimen axis of at least $\pm 2^\circ$ K, (5) capability of maintaining all furnaces within $\pm 2^\circ$ K of any selected temperature, (6) a method for measuring the temperature of the radiating material to within $\pm 3^\circ$ K, (7) provision for measurement in either air or a controlled atmosphere, (8) reference blackbody sources with an emittance very close to 1.0 at all wavelengths in the range from 1 to 15 μ , (9) provisions for rotating the specimen without wobble in very close proximity to a water-cooled port, (10) a double-beam rather than a single-beam spectrophotometer so as to minimize the effects of atmospheric absorptions, and (11) a system of transfer optics which will provide nearly identical optical paths for each beam and optically equivalent imaging of the two beams on the slits on the spectrophotometer.

ANALYSIS OF PERIODIC HEAT FLOW IN A ROTATING SPECIMEN

A theoretical analysis of periodic heat flow in a specimen rotating before a viewing port, performed as a first phase of the investigation, has been published by Peavy and Eubanks (ref. 9). The analysis showed that at low rotational speeds the surface temperature of a specimen at the center of the viewing port opening will be substantially lower than the temperature of the thermocouple in the specimen cavity. However, this difference will decrease with increasing speed. The speed at which the difference will become negligibly small will depend on system geometry, thermal properties of the specimen material, and a derived average heat flux for the portion of the cycle during which a point on the specimen is being heated by the furnace.

This analytical treatment can be used to compute the rotational speed required to reduce temperature gradients in the specimen to acceptable levels. However, since reliable thermal property data are not presently available for the specimen materials, such computations can be of only limited value and the minimum permissible speeds of rotation were determined experimentally (discussed in the section entitled "Measurement Procedure" and the section entitled "Discussion of Sources of Error in the Spectral Emittance Measurements").

EQUIPMENT

Specimen Furnace

Figure 1 is a schematic drawing of the specimen furnace. The high-temperature alumina core¹ surrounding the specimen is wound with 0.032-inch-diameter platinum-40-percent-rhodium wire. The winding is continuous to the edges of the rectangular opening that was cut into the core to permit entrance of the viewing port. A booster winding of the same wire positioned on the outer alumina core,² as indicated in the figure, is used to compensate for the large heat losses at the center.

¹ Norton RA 139, core 10445. Available from Norton Co., Worcester, Mass.

² Norton RA 98, core 6916.

The viewing port was machined from solid copper, the inner surface of which was curved to the same radius as the specimen. A shield of platinum foil, 0.002 inch thick, surrounds the outer surfaces of the port including the edges that face the specimen, thus helping to thermally isolate the viewing port from the furnace interior. The inner surfaces of the viewing port and the portion of the platinum shield nearest the specimen have been blackened to minimize the possibility of errors from reflected radiation. During operation, the clearance between the viewing port and the specimen is approximately 0.03 in. The opening at the hot end of the port is $\frac{1}{8}$ in. wide by $\frac{1}{2}$ in. high.

The specimen is prepared so as to be cylindrical to within ± 0.002 in. The alumina support tube (fig. 1) is surface ground to this same tolerance. The spindle is driven by a variable-speed motor so that the rotation of the specimen can be adjusted to any speed in the range 1 to 300 rpm.

The design of the furnace shell is such that the furnace may be operated in an inert atmosphere as well as in air. Glass-metal seals are used for power leads and O-ring seals are used for the shell ends as well as for a sodium chloride viewing window. The Teflon thrust bearings are designed to provide a reasonably gas-tight seal at the point where the spindle shaft enters the shell. Although this controlled atmosphere feature has been incorporated into the design, all measurements up to the present time have been made in air with no window. The furnace has been operated at 1800° K for several hours without encountering serious difficulties; however, values of emittance reported in this paper have been determined at lower temperatures.

Blackbody Furnaces

Figure 2 is a schematic of the blackbody furnace. Two furnaces were employed in this system, and they were made to be as nearly identical as possible.

The inner cavity of the furnace is formed of fused alumina bonded with 20 percent by weight of a calcium aluminate cement. This mixture, which sets hydraulically, was mixed with water and vibrated into a greased plaster mold. The

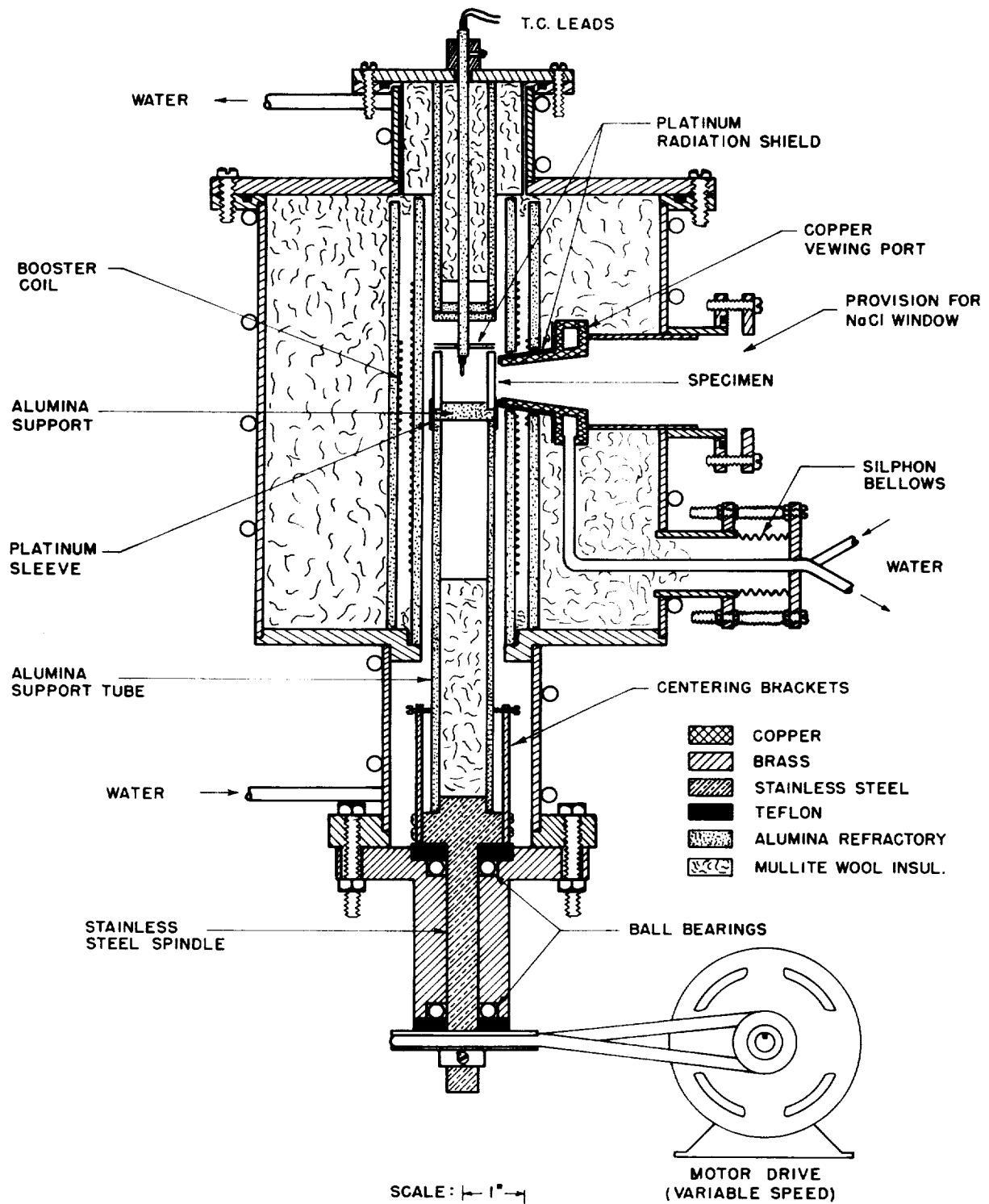


FIGURE 1.—Rotating specimen furnace.

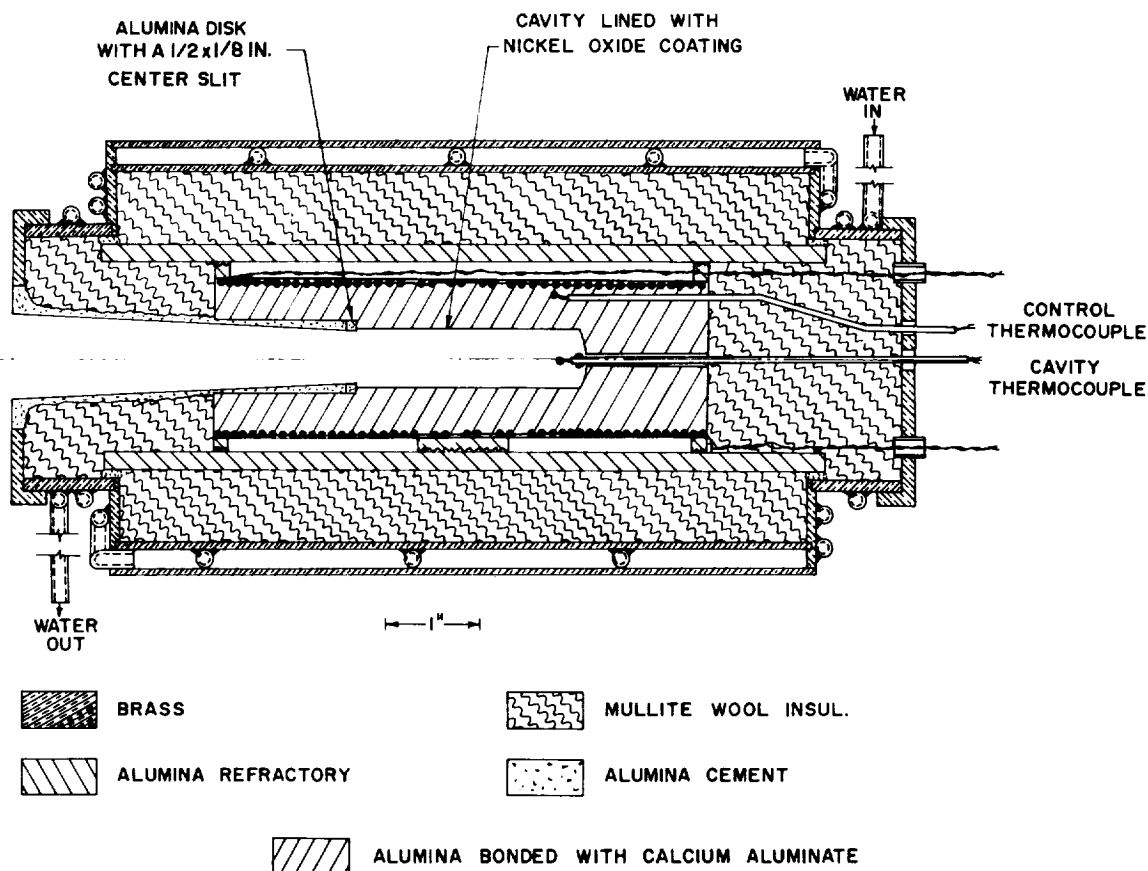


FIGURE 2.—Blackbody furnace.

mold was made by using a Norton alumina core³ as a pattern; a brass mandrel was positioned at the center of the mold to form the outline of the cavity. After 20 hours of curing, the core was removed from the mold, dried in an oven for 24 hours, and then heated to 1925° K for 1 hour. It was later wound with 0.032-in. diameter platinum-40-percent-rhodium resistance wire. Four turns were omitted at the center of the core to compensate for end losses. No power taps were used on the windings.⁴

The alumina core material has a low emittance in the wavelength region 1 to 5 μ . Inas-

³ Norton RA 139, core 10445.

⁴ Power taps were used in an early design. Temperature gradients could be minimized by increasing power to the ends; however, this procedure overloaded the end coils and shortened the operating life of the furnace at 1800° K.

much as the cavity emittance depends, in part, on the emittance of the walls it was necessary to line the cavity with a coating that would have a high emittance at the short as well as the long wavelengths. The coating developed for this purpose consisted of black nickel oxide (Ni_2O_3) bonded with 7.5 percent by weight of clay. This coating was prepared as a coating slip and applied at a thickness of about 0.005 inch to the inner wall surfaces of the cavity by a dipping operation. The core was then heated to 1850° K for 1 hour to bond the coating to the alumina. The spectral emittance of a cylindrical specimen of the core material coated in this way was found to be above 0.875 at all wavelengths from 1 to 15 μ when measured at 1200° K. Hence, the lowest possible cavity emittance at any wavelength from 1 to 15 μ is 0.990. This figure is calculated by the Gouffé

method (ref. 10) assuming isothermal and diffusely reflecting walls.

Temperature Gradients in Furnaces

The power input to the booster coil of the specimen furnace was adjusted at each of the four selected test temperatures (1200°, 1400°, 1600°, and 1800° K) so that no temperature variation was detected from top to bottom on the front face of a rotating alumina specimen when a micro-optical pyrometer was sighted on the rotating specimen through the viewing port. The pyrometer that was used could detect temperature differences as small as 2° K. The problem of radial and circumferential temperature gradients in the specimen has been discussed in the section entitled "Analysis of Periodic Heat Flow in a Rotating Specimen".

Temperature uniformity in the two blackbody furnaces was investigated at each of the four test temperatures by means of a calibrated platinum/platinum-10-percent-rhodium thermocouple inserted into the furnace through the viewing port. The arrangement was such that the bead of the thermocouple could be positioned within $\frac{1}{8}$ inch of the core wall at any point along the length of the cavity. These measurements showed that the maximum nonuniformity occurred at an operating temperature of 1200° K. At this temperature, the back wall of the cavity was as much as 23° K cooler than a 1-in. long isothermal region near the center of the cavity while the front (rear wall of the viewing port) was only 15° K cooler. At increased temperatures the furnaces approach an isothermal condition so that near 1800° K no two points within the cavity have temperatures differing by more than about 6° K. The cavity thermocouple (fig. 2) gave an emf corresponding to the temperature of the isothermal region of the cavity.

In the preliminary measurements used for obtaining the data included in this report, the temperatures of the specimen furnace and the No. 2 blackbody furnace were adjusted manually to within 2° K of the temperature of No. 1 blackbody furnace, which was maintained at constant temperature to $\pm 0.5^\circ$ K by a controller. The manual adjustments were time consuming, and in those cases where the

temperatures changed slightly during measurement the data had to be discarded. In an attempt to eliminate these difficulties, a differential thermocouple temperature control system similar to that described by Harrison et al. (ref. 11) has been incorporated. This system is capable of automatically maintaining a temperature difference of less than 1° K between blackbody No. 1 and either the specimen furnace or blackbody No. 2.

The furnace thermocouples were all made from calibrated wires taken from the same spools. The thermocouples were designed for easy replacement so that new thermocouples could be inserted periodically.

Spectrophotometer and Transfer Optics

A Beckman IR-5A infrared spectrophotometer with a sodium chloride prism has been modified to operate from 1 to 15 μ rather than in the intended 2 to 16 μ range; also, a flip mirror has been incorporated so that the prism could be bypassed when total normal emittances were desired.

The source optics of the IR-5A instrument were removed and replaced with transfer optics as shown schematically in figure 3. The off-axis angle of the spherical mirrors is approximately 5°.

The spectrophotometer is operated in double-beam mode (optical null) for both the spectral and the total normal emittance measurements. However, difficulties have been encountered with the total normal emittance measurements, possibly because of overloading of the detector by the high flux densities encountered in total emittance measurements. Until such time as this condition can be corrected, total normal emittances cannot be measured directly but are computed from the spectral data.

Figure 4 is a photograph of the equipment in operation.

Corrections for Nonlinearity in Instrument

According to the manufacturer's specifications, the spectrophotometer, as delivered, should provide linear response to within 1 percent when operating in double-beam mode. This means, for example, that when the specimen beam is attenuated by 70 percent, the pen

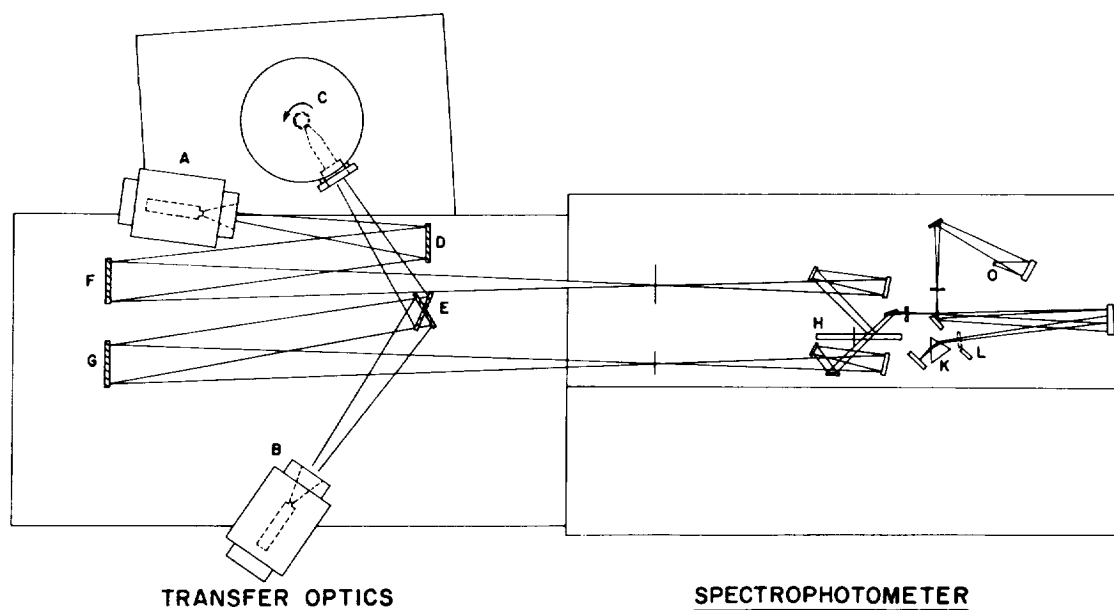


FIGURE 3.—Positioning of equipment and optical paths of two beams.

Transfer optics

- A. Blackbody furnace 1
- B. Blackbody furnace 2
- C. Rotating specimen furnace
- D. Flat front surface mirror
- E. Movable flat mirror
- F. and G. spherical mirrors, 3-in. diam., 18-in. focal length

Spectrophotometer

- H. 10-cps mirror-type chopper
- K. Sodium chloride prism
- L. Movable mirror (for total normal measurements)
- O. Vacuum-type thermocouple detector

should indicate 30.0 ± 3 percent of the original reading. Since the linearity of the instrument may have been disturbed by the previously mentioned modifications, a test of its response was performed.



FIGURE 4.—Equipment in operation.

For this test, both blackbodies were adjusted to $1200 \pm 1^\circ$ K. A sector-disk attenuator was then inserted into the specimen beam and rotated at high speed (greater than 500 rpm). Six disks were used with measured transmission factors of 75.1, 50.0, 25.3, 12.7, and 5.1 percent. The resulting spectral curves, which were found to be reproducible to within the error of measurement, showed that the instrument response was lower than the actual beam attenuation. This lowering was the same at all wavelengths. Wide variations in disk speed above 500 rpm had no effect on the instrument response; accordingly, no appreciable resonance coupling between the chopper and attenuator existed.

Since no method could be devised to restore linearity a correction curve (fig. 5) was prepared. This curve was then used to correct the spectral emittances that were obtained as outlined in the section on measurement procedure. The broken line in figure 5 shows the

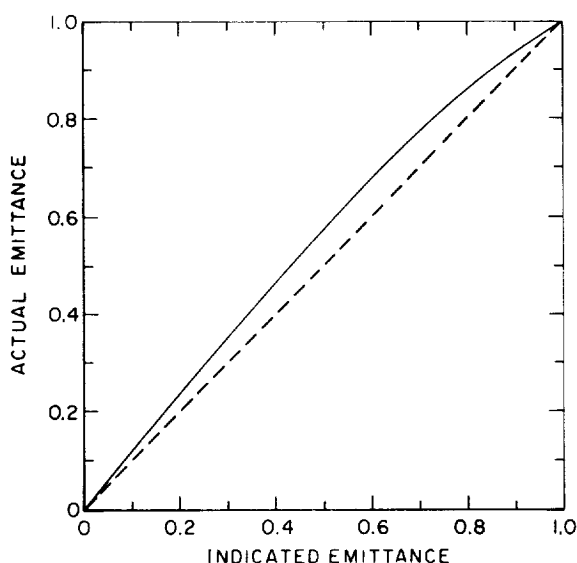


FIGURE 5.—Calibration curve (solid curve) for correcting for lack of instrument linearity. Dashed line shows type of behavior desired of an instrument (linear response).

type of behavior expected from an instrument with completely linear response.

MEASUREMENT PROCEDURE

In making a determination, the specimen was first placed on the top of the refractory pedestal, carefully centered, and then fixed in position with high-temperature alumina cement.⁵ This centering and mounting operation was performed outside the furnace with the aid of a specially prepared jig. After the mounting had been completed, the pedestal was inserted into the furnace from the bottom and carefully positioned radially by adjustment of the bottom flange so that the specimen rotated within about 0.03 inch from the inner face of the viewing port. The top assembly was then inserted and the furnace brought to the desired operating temperature, after which the minimum acceptable speed of rotation of the specimen was determined. This was done by application of the following concept: First assume that the specimen is turning at a relatively slow speed. This will result in a size-

able drop in temperature of an element on the surface of the specimen as it passes the viewing port. Accordingly, the flux entering the spectrophotometer under these conditions will be less than that which would enter if the surface was very nearly at the same temperature as the specimen thermocouple shown in figure 1, so that the measured emittance will be too low. It follows from the heat-transfer analysis of reference 9 that, as the speed of the specimen increases, the temperature drop on passing the viewing port will decrease and the measured emittance will increase up to the point where further speed increase causes no further change. At this speed, the specimen surface temperature will be very nearly the same as that indicated by the specimen thermocouple and the temperature distribution in the system will not be affected appreciably by a further increase in speed.

In keeping with this concept, the minimum acceptable speed for each specimen was determined by measuring the emittance at $1.4\ \mu$ first at a speed of 20 rpm and then at increasing speeds until no further increase in emittance was observed.⁶ The speed at which this maximum value was reached was of the order of 50 rpm for all of the oxide specimens at 1200°K . However, as an added insurance against possible errors from uncertainties in specimen temperature, the operating speed of each specimen was set at 100 rather than 50 rpm.

Once the rotational speed was fixed, the specimen beam was blocked and a "zero line" obtained. Next, mirror E in the transfer optics (fig. 3) was moved into position to focus radiation from blackbody 2 on the entrance slit of the spectrophotometer. The wavelength drive was then started to obtain a "100-percent line",⁷ which indicated the ratio of radiant flux from

⁵ Norton RA 1139, available from Norton Co., Worcester, Mass.

⁶ Difference in temperature between specimen and blackbody has the greatest effect on measured emittance at wavelengths below the energy peak of blackbody radiation. The selected setting of $1.4\ \mu$ is below this peak for the four selected test temperatures.

⁷ Chiefly owing to a lack of perfect optical equivalence in the two beams, neither the zero line nor the 100-percent line was completely flat; it was necessary to correct for this lack of flatness to prevent error.

blackbody 2 to blackbody 1. Ordinarily this line showed only minor deviations from the 100-percent position. However, if the temperature of blackbody 2 was as much as 2° K higher than that of blackbody 1, the 100-percent line would be too high at 1 μ and would gradually reach the 100-percent position at about 3 μ . Conversely, if blackbody 1 was at a higher temperature than blackbody 2, the curve would lie below 100 percent in the range from 1 to 3 μ . This behavior, which is predictable from Planck's radiation law, was used throughout the measurements as an added assurance that good temperature agreement existed between the two furnaces.

After the zero line and the "100-percent line" were obtained, mirror E was shifted to the rotating specimen position and the specimen curve was determined. All three curves were recorded on the same graph. Finally, the (uncorrected) spectral emittance of the specimen was obtained for each wavelength as

$$E_{\lambda} = \frac{S_{\lambda} - Z_{\lambda}}{H_{\lambda} - Z_{\lambda}}$$

where

- E_{λ} normal spectral emittance
- S_{λ} height of recorded specimen curve
- H_{λ} height of 100-percent line
- Z_{λ} height of zero line

As stated in the section entitled "Corrections for Nonlinearity in Instrument", it was necessary to correct the value of E_{λ} thus obtained for the lack of linear response in the instrument. This was done by using the correction curve shown in figure 5. A minimum of three tests were made for each specimen.

PRELIMINARY EMITTANCE MEASUREMENTS

Inasmuch as refinements are still being incorporated into the equipment and also because an error analysis has not been completed, only preliminary data are given at this time. These data were obtained at 1200° K in an air atmosphere, with the exception of a platinum specimen which was measured in air at 1400° K. The measurements are included to indicate the capabilities of the equipment; they should not be interpreted as representing accurate data on well characterized specimens.

Table I identifies the specimens. All were in the form of cylinders of approximately 1-inch outside diameter with smooth surface finishes. The wall thickness of the platinum specimen was approximately $\frac{1}{16}$ in.; that of the sintered ceramic specimens was approximately $\frac{1}{8}$ in.

The spectral curves are shown in figures 6, 7, and 8. Figure 6A is for polished platinum that had been annealed for 1 hour in air at

TABLE I.—Identification of Platinum and Sintered Ceramic Specimens

Code	Material	Description ^a	Number of specimens tested	Porosity, % by volume
P.....	Platinum.....	Commercially pure.....	1	0
AN.....	Alumina.....	Coarse grained furnace tube refractory >95% Al ₂ O ₃	1	45
AD.....	Alumina.....	Fine grained dense; 96% alumina.....	5	11
AL.....	Alumina.....	Fine grained; 99+ % Al ₂ O ₃	3	36
CZ.....	Calcium zirconate.....	Fine grained body 31% CaO; 68% ZrO ₂	1	30
M.....	Magnesium oxide.....	Fine grained magnesia 99.2% MgO.....	2	35
AS.....	Mullite.....	Fine grained body 67% Al ₂ O ₃ ; 30% SiO ₂	1	32
S.....	Silica.....	Fine grained body ^b 95% SiO ₂ ; 4.0% Al ₂ O ₃	1	8
MA.....	Spinel.....	Fine grained body 71% Al ₂ O ₃ ; 28% MgO.....	1	25
T.....	Thoria.....	Fine grained; 99+ % ThO ₂	1	36
ZS.....	Zircon.....	Fine grained body 66% ZrO ₂ ; 32% SiO ₂	2	26
Z.....	Zirconia.....	Fine-grained, lime-stabilized 94% (ZrO ₂ +HfO ₂); 4.5% CaO.....	1	18

^a Compositions are nominal for major constituents in percent by weight.

^b Major crystalline phases—cristobalite and quartz.

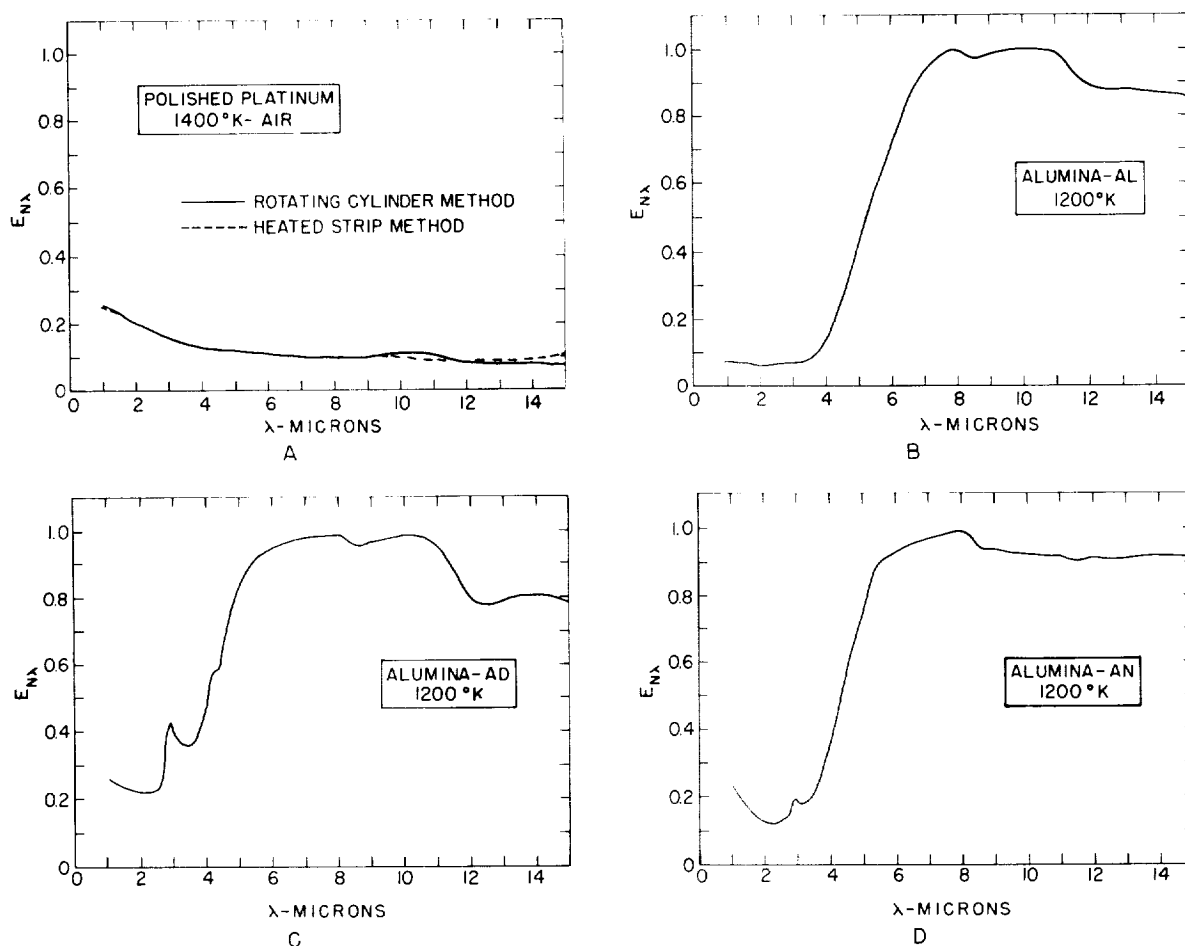


FIGURE 6.— Preliminary spectral emittance curves of polished platinum and three types of sintered alumina.

1525° K prior to testing. The good agreement of the curve determined by the rotating specimen method with that reported by Harrison et al. (ref. 11) for polished platinum as measured by a carefully calibrated heated strip method, indicates that the transfer optics and spectrophotometer are capable of satisfactory operation.

Figures 6B, 6C, and 6D give the curves obtained for three types of sintered alumina. These curves are in fair agreement with data for alumina specimens reported by Blau et al. (ref. 12) and by Slemple and Wade (ref. 5) at wavelengths beyond about 5 μ , but below 5 μ the present measurements give lower values that are more in keeping with those reported by Folweiler (ref. 7). It should be pointed out, however, that such comparisons of emittance measurements are of only limited value unless the

specimens are prepared from the same material, by the same process, and with the same surface finish. Such factors as grain size, porosity, and the presence of impurities are known to have an appreciable effect on emittance.

The absorption peak at 2.9 μ for AD and AN alumina (fig. 6C and 6D) was obtained for all specimens of these materials. A similar absorption band has been noted for flame-sprayed alumina (ref. 13 and 14). It is probably caused by chemically held water in the structure. It was also observed that the intensity of the peak decreased with time of heating at 1200° K, which tends to support this explanation. A similar absorption band was observed for mullite (fig. 8C).

With the exception of the peak at about 4.6 μ for zirconia (fig. 7A) and the low-emittance

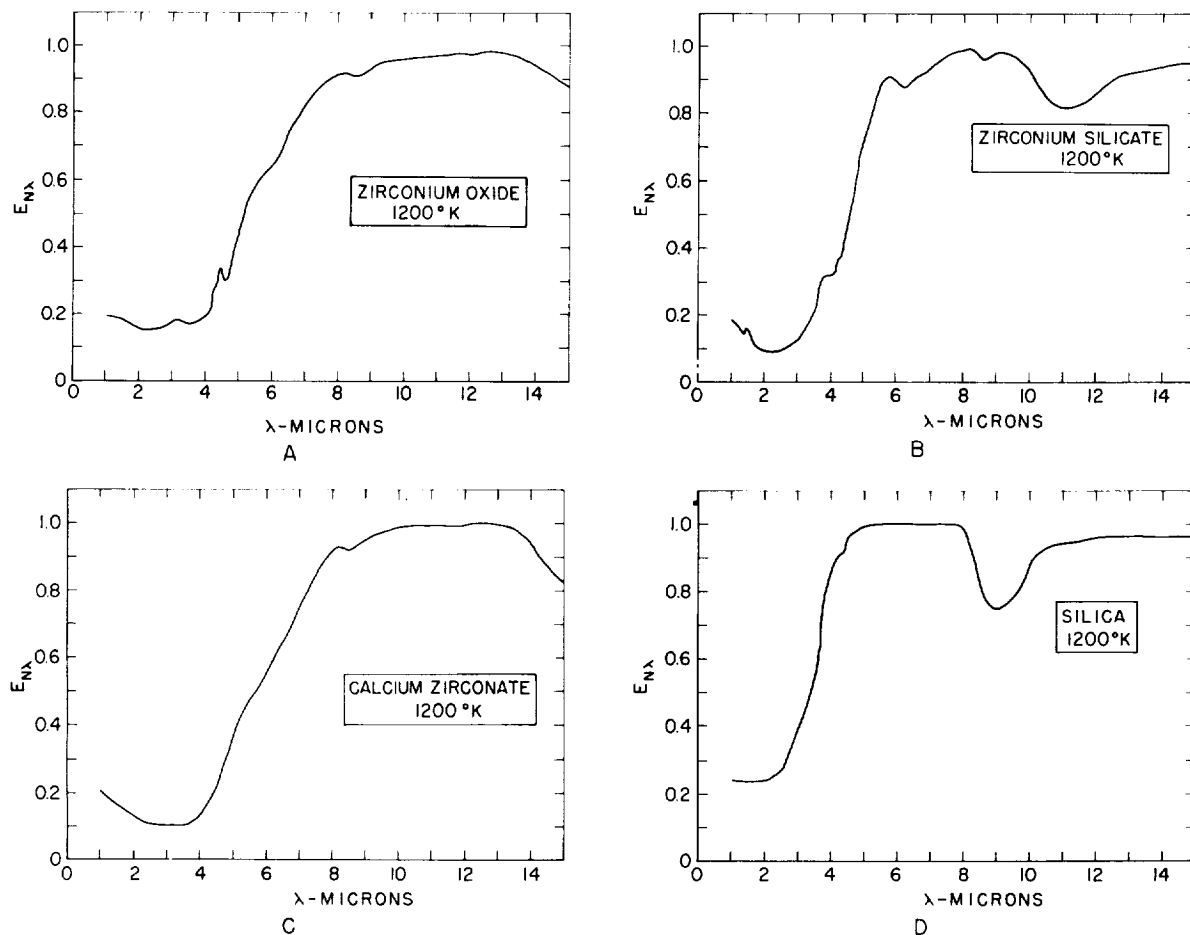


FIGURE 7.—Preliminary spectral emittance curves for sintered ceramic oxide specimens: zirconium oxide and silicate, calcium zirconate, and silica.

band for silica at about $9.0\ \mu$ (fig. 7D), the other deviations are relatively minor and need confirmation by additional measurements, especially at higher test temperatures, before they can be fully accepted. This low emittance band for silica has been observed by other investigators (ref. 15 and 16).

All of the 11 ceramic materials investigated show low emittance at the lower wavelengths and a fairly sharp rise to high emittance at the higher wavelengths. The low-emittance region extends furthest for thorium oxide and magnesium oxide. Thorium oxide does not reach an emittance of 0.9 until the wavelength is approximately $10\ \mu$; the wavelength at which this emittance is attained for magnesium oxide is about $9\ \mu$. The extents of the low-emittance regions should be reflected in the computed

total normal emittances, and table II shows that such is the case. These two oxides gave

TABLE II.—Total Normal Emittances at 1200° K as Computed From Spectral Data

Material	Code	$\epsilon_{t,n}$
Aluminum oxide.....	AL	0.29
Aluminum oxide.....	AD	.52
Aluminum oxide.....	AN	.42
Zirconium oxide.....	Z	.34
Thorium oxide.....	T	.23
Magnesium oxide.....	M	.20
Silica.....	S	.60
Calcium zirconate.....	CZ	.29
Zirconium silicate (zircon)....	ZS	.39
Aluminum silicate (mullite)...	AS	.40
Magnesium aluminate (spinel)...	MA	0.26

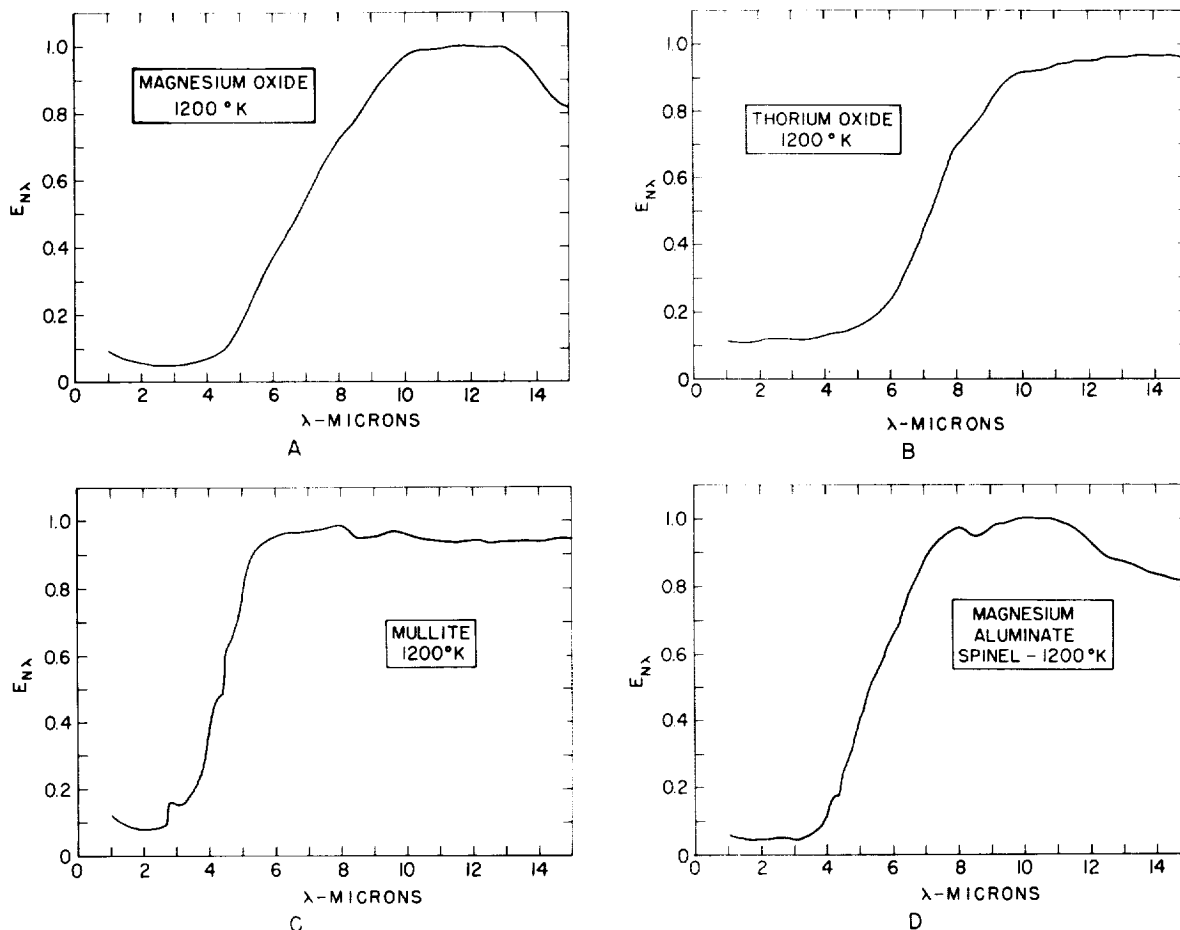


FIGURE 8.— Preliminary spectral emittance curves for sintered ceramic oxide specimens: magnesium oxide and aluminate, thorium oxide, and mullite.

the lowest total normal emittances at 1200° K of all the oxides measured; the silica specimen had the highest.

The selected-ordinate method (ref. 11) with 25 ordinates was used for computing the total normal emittances from the spectral data.

ROOM-TEMPERATURE REFLECTANCE MEASUREMENTS

Because of the many possible sources of error in measuring spectral emittance of ceramic oxide materials, especially in the low-wave length region, it was desirable to test the reliability of the preliminary emittance data by means of spectral reflectance measurements. Spectral reflectance of an opaque material determined under conditions of normal illumination and hemispherical viewing is the com-

plement of normal spectral emittance; hence, reflectances determined in this way can be converted to emittances by subtracting them from unity. Since the spectral emittance varies only slightly with temperature, such measurements should provide a reasonably good check of the emittance data even though the spectral reflectances are obtained at room temperature.

A Cary Model 14M recording spectrophotometer equipped with an integrating sphere was used for these reflectance measurements. Data were obtained over three different ranges (0.26 to 0.4 μ , 0.36 to 0.7 μ , and 0.6 to 2.1 μ) with different source-receiver combinations for each range. The specimens were flat disks, 1½ in. in diameter by ¼ in. thick, prepared of specimen materials AL, M, Z, ZS, CZ, and T (table I). The disks were prepared of the

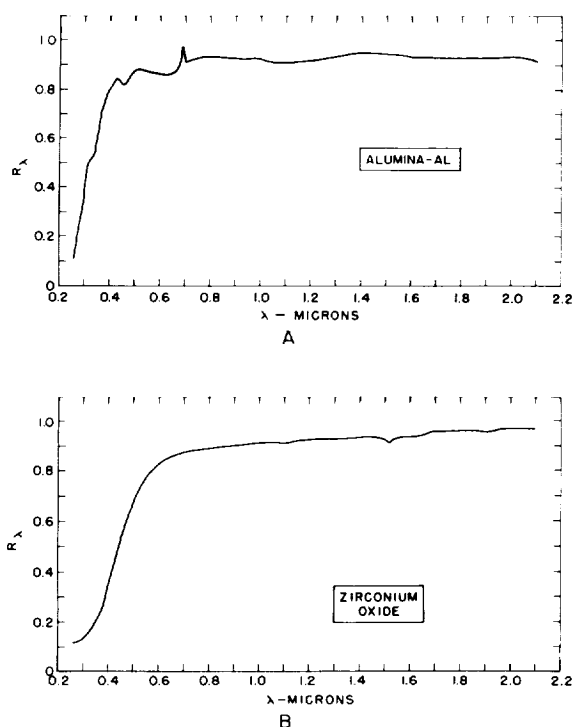


FIGURE 9.—Room-temperature spectral reflectance curves for alumina and zirconium oxide.

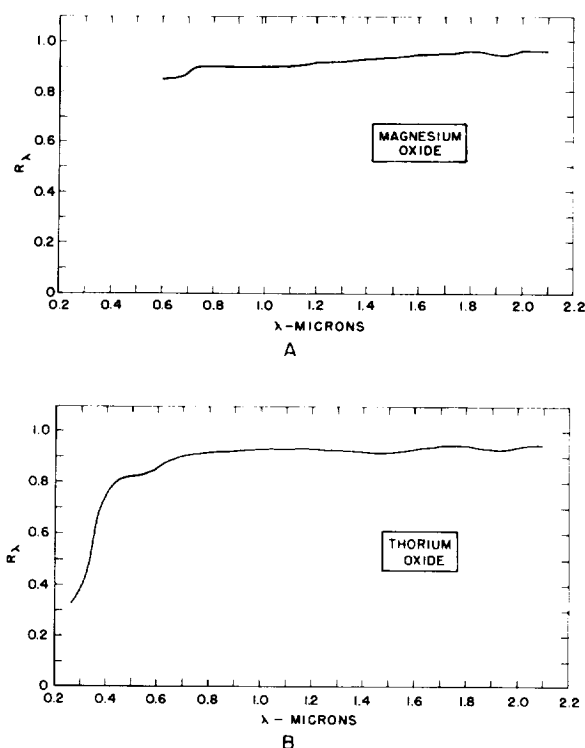


FIGURE 10.—Room-temperature spectral reflectance curves for magnesium oxide and thorium oxide.

same materials and with the same processing as was used for the 1-in.-diameter cylinders.

The measurements were made relative to smoked magnesium oxide and corrected to absolute values by using the data of Middleton and Sanders (ref 17 and 18). However, since the reflectance of magnesium oxide depends on such factors as age of the deposit and hours of exposure to ultraviolet radiation, some selection of their data was required. The values used for this conversion are listed in table III, and the reflectance curves, corrected through use of these data, are shown in figures 9, 10, and 11. The curves in each case were plotted from the average values obtained from two specimens. These values were in good agreement over the entire range except for the two magnesium oxide specimens in the region 0.26 to 0.60 μ where deviations in spectral reflectance of as great as 0.2 were observed. Because of this poor agreement, the average curve for magnesium oxide is not shown below 0.6 μ .

COMPARISON OF EMITTANCE AND REFLECTANCE MEASUREMENTS

Between 1.0 and 2.1 μ it is possible to compare the spectral emittances computed from the reflectance measurements with those obtained with the rotating-cylinder equipment. Table IV shows this comparison at 1.0, 1.5, and 2.0 μ .

Considering both the difference in temperature (900° K) of the samples for the two types of measurements and the uncertainty in converting reflectances from relative to absolute values, the agreement is surprisingly good for the specimens AL, CZ, and M; reasonably good for T and ZS; but poor for Z.

In general, spectral emittance increases only very slowly with increasing temperature; hence, this comparison at the two different test temperatures is of interest. However, until such time as measurements are available at 1200, 1400, 1600, and 1800° K and temperature coefficients are established, it is not possible to obtain a more valid comparison of the two sets

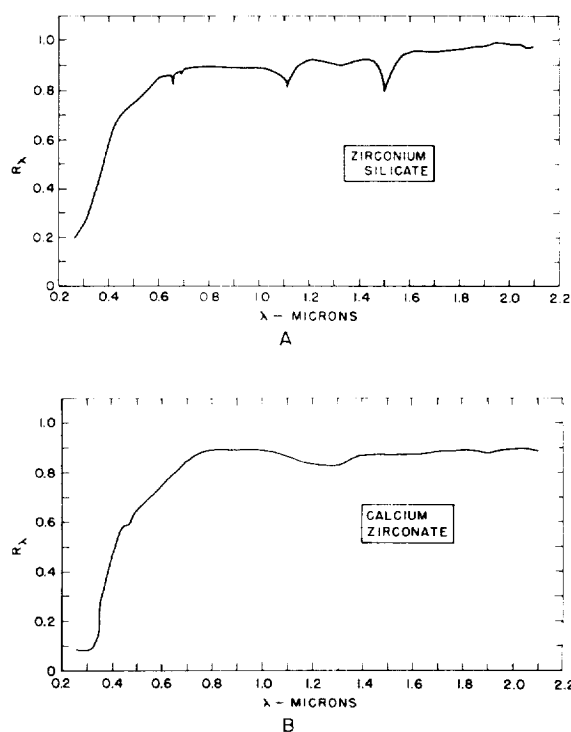


FIGURE 11.—Room-temperature spectral reflectance curves for zirconium silicate and calcium zirconate.

TABLE III.—Spectral Diffuse Reflectances of Smoked Magnesium Oxide

Wavelength, μ	Reflectance
0.20	^a 0.955
.30	.970
.40	.980
.50	.975
.60	.970
.70	.965
.80	.965
.80	^b .965
.90	.960
1.00	.960
1.10	.955
1.20	.955
1.30	.950
1.40	.950
1.50	.945
1.60	.945
1.70	.945
1.80	.940
1.90	.925
2.00	.925
2.10	0.930

^a Values for wavelengths up to 0.8 μ selected from data in reference 17.

^b Values for the infrared are taken from figure 2 of reference 18.

TABLE IV.—Spectral Emittances at 1.0 μ , 1.5 μ , and 2.0 μ

Material	Code	Wavelength, μ	Normal spectral emittance	
			Rotating-cylinder Method (1200° K)	Computed from room-temperature reflectance
Aluminum oxide.....	AL	1.0	0.08	0.08
		1.5	.07	.06
		2.0	.06	.06
Calcium zirconate.....	CZ	1.0	.21	.11
		1.5	.16	.13
		2.0	.13	.11
Magnesium oxide.....	M	1.0	.09	.10
		1.5	.07	.07
		2.0	.06	.04
Thorium oxide.....	T	1.0	.11	.07
		1.5	.11	.09
		2.0	.11	.06
Zirconium oxide.....	Z	1.0	.19	.09
		1.5	.18	.08
		2.0	.16	.03
Zirconium silicate.....	ZS	1.0	.18	.11
		1.5	.16	.21
		2.0	0.09	0.02

of data. The data listed in table IV are nevertheless of value in obtaining an order-of-magnitude comparison.

DISCUSSION OF SOURCES OF ERROR IN THE SPECTRAL EMITTANCE MEASUREMENTS

The most serious sources of error in emittance measurements of this type are (1) lack of optical equivalence in the two beams, (2) reflected flux entering the specimen beam, (3) temperature gradients in the specimen, (4) lack of temperature equality between specimen and blackbody, and (5) radiant flux from the specimen cavity being transmitted through the wall of the specimen and into the specimen beam. Any sizable error from the first of these sources was avoided by establishing the 100-percent line through use of the two blackbodies; the possibility of error from the second source was minimized by maintaining a small clearance between the viewing port and the specimen; and error from the third source was reduced to a low level by rotating the specimen at high speed.

Lack of temperature equality between specimen and blackbody, although potentially a large source of error, was minimized by maintaining the temperatures, as indicated by the blackbody and specimen thermocouples, equal to within $\pm 1^\circ$ K. Even if the temperature of the specimen surface had been as much as 3° K lower than that indicated by the thermocouple at the specimen center, the error in emittance at $1\ \mu$ for $T=1200^\circ$ K would be only 3 percent. Since the precision with which the emittance could be obtained from the recorder chart was 0.005 units, this error would be detectable only when the emittance was above 0.17. At higher temperatures and longer wavelengths the same 3° K uncertainty would, of course, correspond to smaller errors.

The greatest uncertainty that remains is the possibility of transmission of blackbody radiation from the specimen cavity through the wall of the specimen. This radiation, if it were present, would reinforce the emitted flux from the specimen and cause the measured emittance to be high. For example, a specimen with a *true* emittance of 0.15 in the near infrared

would have an apparent emittance of 0.20 if as little as 5 percent of the radiation from the specimen cavity was being transmitted through the wall.

Since the transmittance of the specimen walls could not be measured readily, an effort was made to obtain a qualitative indication of wall transmission at room temperature. This was accomplished by placing each specimen in the beam of a He-Ne laser ($\lambda = 0.6328\ \mu$) with the assumption that if the $\frac{1}{8}$ -in.-thick wall was opaque at $0.63\ \mu$ it would also be opaque in the range of 1.0 to $2.0\ \mu$. The relative flatness of the reflectance and emittance curves (where applicable) in the region 0.6 to $3.0\ \mu$ suggests that this assumption may be reasonably valid. The results of this qualitative type of test indicated that the ZS, T, and Z specimen walls were opaque; the AL walls were nearly opaque; the AD, AN, M, and CZ walls were slightly transmitting; and the S and MA walls were appreciably transmitting.

In view of these results it seems reasonable to believe that the preliminary measurements, with the possible exception of the S and MA specimens, are free of large errors caused by lack of specimen opacity. However, there can be no certainty that such is the case until some reliable method of testing the opacity at each wavelength and temperature has been devised.⁸ Until this is done the possibility must be considered that the spectral emittances measured in the range 1 to $5\ \mu$ may be high by significant amounts.

ACKNOWLEDGMENT

The authors gratefully acknowledge the assistance of the following staff members of the National Bureau of Standards: A. G. Eubanks, who contributed to the solution of some of the early design problems; John C. Schleter, who made the reflectance measurements; and J. C. Richmond and W. N. Harrison, who made valuable suggestions on both method and procedure. (Mr.

⁸ One possible approach for determining if the $\frac{1}{8}$ -in. wall is opaque would be to measure the spectral emittance of a second set of specimens with $\frac{1}{4}$ -in. walls. This is possible with the present equipment. If the measured emittances were the same at both thicknesses, there would then be excellent evidence that the $\frac{1}{8}$ -in. thickness is sufficient.

Eubanks is now with Goddard Space Flight Center, NASA.)

REFERENCES

1. FÉRY, C.: Radiation of Some Oxides. *Annal. Chim. Phys.*, vol. 27, Dec. 1902, pp. 433-548.
2. MICHAUD, M.: Thermal Emissivity of Refractory Materials at High Temperatures. *Silicates ind.*, vol. 19, 1954, pp. 243-250.
3. PATTISON, J. R.: Total Emissivity of Some Refractory Materials Above 900° C. *Trans. Brit. Ceram. Soc.*, vol. 54, no. 11, Nov. 1955, pp. 698-705.
4. McMAHON, HOWARD O.: Thermal Radiation Characteristics of Some Glasses. *Jour. American Ceramic Soc.*, vol. 34, no. 3, 1951, p. 91.
5. SLEMP, WAYNE S., and WADE, WILLIAM R.: A Method for Measuring the Spectral Normal Emittance in Air of a Variety of Materials Having Stable Emittance Characteristics. Measurement of Thermal Radiation Properties of Solids, Joseph C. Richmond, ed., NASA SP-31, 1963, pp. 433-439.
6. OLSON, O. H., and KATZ, SIDNEY: Emissivity, Absorptivity, and High-Temperature Measurements at Armour Research Foundation. First Symposium—Surface Effects on Spacecraft Materials, Francis J. Clauss, ed., John Wiley & Sons, Inc., c. 1960, pp. 164-181.
7. FOLWEILER, R. C.: Thermal Radiation Characteristics of Transparent, Semi-Transparent and Translucent Materials Under Non-Isothermal Conditions. ASD-TDR-62-719, U.S. Air Force, Apr. 1964.
8. CLAYTON, W. A.: A 500° to 4500° F Thermal Radiation Test Facility for Transparent Materials. Measurement of Thermal Radiation Properties of Solids, Joseph C. Richmond, ed., NASA SP-31, 1963, pp. 445-460.
9. PEAVY, B. A., and EUBANKS, A. G.: Periodic Heat Flow in a Hollow Cylinder Rotating in a Furnace With a Viewing Port. Measurement of Thermal Radiation Properties of Solids, Joseph C. Richmond, ed., NASA SP-31, 1963, pp. 553-563.
10. GOUFFÉ, ANDRÉ: Corrections d'ouverture des corps-noirs artificiels compte tenu des diffusions multiples internes. *Rev. d'Optique*, vol. 24, nos. 1-3, Jan.-Mar. 1945, pp. 1-10.
11. HARRISON, WILLIAM N., RICHMOND, JOSEPH C., SHORTEN, FREDERICK J., and JOSEPH, HORACE M.: Standardization of Thermal Emittance Measurements—Part IV. Normal Spectral Emittance, 800-1400° K. WADC-TR-59-510, Pt. IV, U.S. Air Force, Nov. 1963.
12. BLAU, HENRY H., JR., MARSH, JOHN B., MARTIN, WILLIAM S., JASPERSE, JOHN R., and CHAFFEE, ELEANOR: Infrared Spectral Emittance Properties of Solid Materials. AFCRL-TR-60-416, Geophys. Res. Directorate, Air Force Res. Div., Oct. 1960.
13. GRAVINA, ANTHONY, and KATZ, MILTON: Investigation of High Emittance Coating to Extend the Mach Number Range of Application of Structural Materials. WADD Tech. Rep. 60-102, U.S. Air Force, Mar. 1961.
14. EDWARDS, D. K., and RODDICK, R. D.: Basic Studies on the Use and Control of Solar Energy. Rep. 62-27, Univ. of California, July 1962.
15. SCHATZ, ELIHU A., and McCANDLESS, LEE C.: Research for Low and High Emittance Coatings. ASD Tech. Doc. Rep. No. TR 62-443, U.S. Air Force, May 1962, pp. 90-91.
16. CABANNES, F.: Détermination du facteur monochromatique d'émission d'une surface réfractaire à haute température. *Compte rendu du Congrès Technique Céramique 1960, La cuisson des produits céramiques*, D-519.
17. MIDDLETON, W. E. KNOWLES, and SANDERS, C. L.: The Absolute Spectral Diffuse Reflectance of Magnesium Oxide. *Jour. Optical Soc. of America*, vol. 41, no. 6, June 1951, pp. 419-424.
18. SANDERS, C. L., and MIDDLETON, W. E. KNOWLES: The Absolute Spectral Diffuse Reflectance of Magnesium Oxide in the Near Infrared. *Jour. Optical Soc. of America (Letters to the Editor)*, vol. 43, no. 1, Jan. 1953, p. 58.

DISCUSSION

RAYMOND J. PREZECKI, USAF: Have you attempted to explain the minimum at 2 μ and the maximum at 9 μ for the various ceramic materials, and are you planning emittance measurements on nonisothermal materials?

CLARK: No. We have not as yet considered possible theories that might explain the change in emittance of ceramic oxides with wavelength. In answer to your second question, we have no plans for investigating nonisothermal materials. Our emphasis at the moment is on isothermal specimens.

DONALD KOCH, North American Aviation: I understand that many ceramic oxides behave as semicon-

ductors at high temperatures. If this is true, could this effect be used for resistance heating of samples to control the temperature distribution?

CLARK: Yes, this effect can be used for heating purposes. In fact, it is frequently applied in induction heating techniques; but it is of little help to us because many of the materials must be heated to 1800 or 2000° K before they show any appreciable electrical conductivity.

KOCH: If this effect exists, would there not be a considerable difference between the reflectance at room temperature and the reflectance at high temperatures?

CLARK: Yes, there is a considerable difference. In making the comparison between our measured values of emittance and those computed from room-temperature reflectance measurements, we assumed that emittance would change by about 1 percent per 100°. After we get additional data at 1400°, 1600°, and 1800° K, we will have a more exact figure for this temperature coefficient. The important point is simply that this comparison did give us a good order-of-magnitude check.

KARL A. SENSE, Astropower Laboratory, Douglas

Aircraft: Perhaps I can shed some light on the previous question. As you go to higher temperatures, the energy band-gap decreases due to various factors—one of them being the change in the lattice parameter and others being electron-phonon interactions at the band-gap edge. This latter effect has been explained quite well in an article in the *Physical Review* a few years ago. This band-gap decrease results in a shift of the long-wavelength emission limit to longer waves, resulting in a change in the emission spectrum, particularly in the longer wavelength region.

27. Hemispherical Spectral Emittance of Ablation Chars, Carbon, and Zirconia (to 3700° K)¹

R. GALE WILSON

NASA LANGLEY RESEARCH CENTER, LANGLEY AIR FORCE BASE, VA.

The initial results of the application of special optical techniques to high-temperature emittance and reflectance studies of an ablation-material char and certain other refractory materials representative of those present in ablation residues formed during aerospace reentry operations are presented. Spectral hemispherical emittance and reflectance were determined with an image pyrometer integrated with an arc-imaging furnace for carbon, graphite, zirconia, and a phenolic-nylon ablation-material char at wavelengths from 0.37 μ to 0.72 μ for temperatures from 2100° K to 3700° K. The data obtained are compared with those of other investigations to the extent that the existence of comparable data permits.

Surface-roughness properties of the materials studied were determined from measurements made with a light-section microscope. The dependence of the spectral hemispherical emittance of oxidized carbon at a wavelength of 0.65 μ on its surface-roughness properties was investigated experimentally, and the emittance was found to be a linear function of the root-mean-square slope of the surface when the roughness is large compared with wavelength.

At velocities associated with reentry into the Earth's atmosphere from Earth-orbital or outer-space missions, flight vehicles experience aerodynamic heating which produces surface temperatures above the melting or vaporization temperatures of conventional structural materials. Thermal protection systems have been devised in which ablating materials are used effectively to protect the load-carrying structures of these vehicles. Charring ablation materials have been shown to be particularly effective for use in thermal protection systems (ref. 1 and 2) because of their ability to reradiate a significant portion of the heat absorbed. In order to evaluate the radiation-cooling effectiveness of charring ablators, their total hemispherical emittance at performance tempera-

tures must be known. The absorptance of charring ablators in the ultraviolet and visible parts of the spectrum is also important to their performance for certain types of reentry operation, that is, for reentry characterized by significant radiative heating of the vehicle by ultraviolet and visible radiation from shock-heated air (ref. 3).

The objective of the present investigation was to obtain hemispherical spectral emittance, absorptance, and reflectance data at high temperatures on the char of an ablation material and on certain other refractory materials representative of the class of materials present in ablation residues formed during aerospace reentry operations. In order to circumvent some of the problems of radiation measurement and temperature measurement associated with extending the use of conventional methods of measurement to high temperatures, special optical techniques were applied in this investigation. An apparatus consisting of an image pyrometer integrated with a double-ellipsoidal-

¹ This paper is a revised version of that presented at the Symposium. Valuable discussion by Mr. Daniel Comstock of Arthur D. Little, Inc., and Dr. W. W. Lozier of Union Carbide Corp. has been considered in the revision and accordingly omitted from the DISCUSSION. See Paper 28 for description of a related technique.

mirror arc-imaging furnace was used for heating the material samples and for measuring spectral reflectance and temperature. Spectral emittance was calculated from the reflectance measurements. Several filter-detector systems were selected for a range of wavelengths covering the visible spectrum and extending into the near ultraviolet spectrum. Suitable attenuation of the arc irradiation of the sample provided for sample surface temperatures from about 2100° K to 3700° K.

Special consideration was given to surface characterization of the materials studied. Surface-roughness properties were determined from surface-profile measurements made with a light-section microscope, and pore-size spectra were determined for the porous materials by a mercury-intrusion method.

The International System of Units (ref. 4) is used throughout this report excepting μ for μn .

SYMBOLS

A	oscillograph signal for arc light
c_1	first radiation constant, $\text{watts}\cdot\mu^4/\text{m}^2$
c_2	second radiation constant, $\mu\cdot^\circ\text{K}$
E	photomultiplier output for emitted light from sample or standard lamp
h	surface-profile height
i	incident light on element of sample surface
K	combined constant of optical system
k	constant of filter-detector system, per $^\circ\text{K}$
n	summation index
R	photomultiplier output for reflected light from sample
r	reflected light from element of sample surface
T	temperature
W	hemispherical spectral radiant intensity per unit area of sample or standard lamp, $\text{watts}/\text{m}^2\cdot\mu$
Δx	small increment of length along nominal (average) surface of material
Δy	small increment of length perpendicular to nominal surface of material
α	hemispherical absorptance
ϵ	hemispherical emittance
λ	wavelength, μ
ρ	hemispherical reflectance

SUBSCRIPTS

1	higher (temperature) or first (radiation constant)
2	lower (temperature) or second (radiation constant)
a	apparent
L	standard lamp
S	material sample
t	true
λ	spectral

A prime is used to denote values corrected for errors due to rapid cooling.

TEST APPARATUS AND SAMPLES

Apparatus for Measurement of Reflectance and Temperature

IMAGING FURNACE AND PYROMETER

The arc-imaging furnace used in this investigation is described by Glaser in reference 5 and the image pyrometer and its principles of operation are described by Comstock in reference 6. Briefly, the arc-imaging furnace, shown schematically in figure 1, consists of an optical system having two 52-cm-diameter ellipsoidal mirrors located coaxially and facing each other at a distance of approximately 2 m. Their major and minor focal lengths are 104 cm and 20 cm, respectively. An electric-arc radiation source is located at the minor focal point of one mirror and its image is formed at the minor focal point of the other mirror, after two reflections of the arc radiation.

The image pyrometer, illustrated schematically in figure 2, is an instrument designed to obtain radiation measurements in the intermediate image plane where the major focuses of the mirrors coincide and where magnified images of the arc and sample are formed. The image pyrometer consists principally of two light pipes, a chopper, an optical filter, and a photomultiplier. The light pipes are L-shaped, each constructed from platinum tubing enclosing a single filament of quartz. One tube has an aperture facing the sample and the other, an aperture facing the arc. The light pipes are mounted in a common hub, and as it rotates

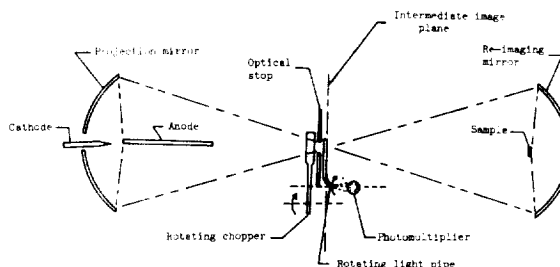


FIGURE 1.—Schematic of arc-imaging furnace with image pyrometer.

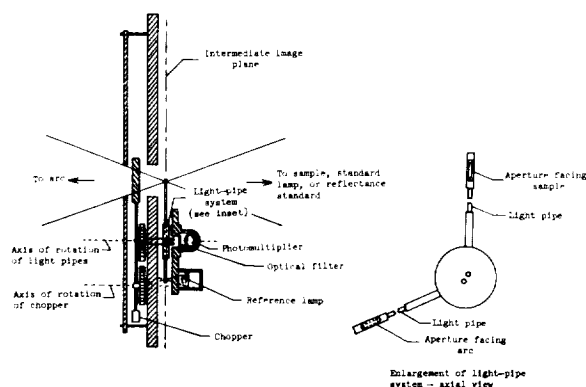


FIGURE 2.—Image pyrometer operating mechanism.

the light pipes scan periodically through the arc and sample images and transmit light from the images to the photomultiplier via the filter. The output of the photomultiplier is amplified and read out on an oscillograph recorder in the form of radiation profiles across the diameters of arc and sample images. The rapidly rotating chopper is synchronized with the light pipes to permit the sample-oriented light pipe to view the sample image alternately with the arc radiation incident on the sample and with the arc radiation briefly obstructed from the sample.

A reduced tracing of a typical oscillogram for carbon ($T_s=3100^\circ\text{K}$; $\lambda=0.72\text{ }\mu$), together with an enlarged view of the central part of the radiation profile, is shown in figure 3. From the radiation measurements on the sample with the chopper alternately open and closed,

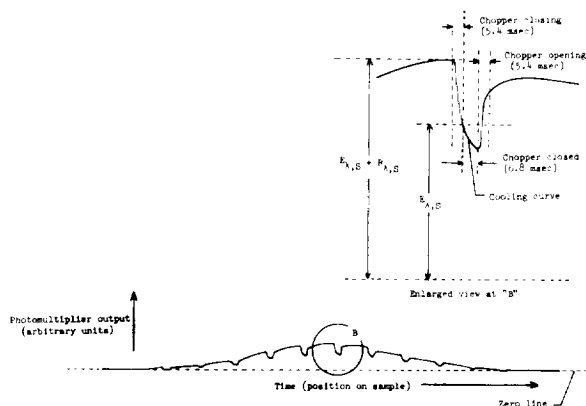


FIGURE 3.—Image pyrometer oscillograph for carbon.

$E_{\lambda,S} + R_{\lambda,S}$ and $E_{\lambda,S}$, respectively, along with measurements on a standard-temperature source and a reflectance standard separately substituted for the sample, the temperature and reflectance of the sample at every point across its irradiated surface can be determined.

OPTICAL FILTERS

A set of five filters was used to make reflectance measurements over a range of wavelengths that included the visible spectrum and extended into the near ultraviolet spectrum. In the set there were two glass filters, one single-film gelatin filter, and two gelatin filters each of which was constructed by superimposing two single gelatin films. The gelatin film in each case was mounted in Canada balsam cement between two thin layers of optically flat glass. Tests were made to assure that the temperature in the filter receptacle of the pyrometer stayed within safe limits for use of the gelatin filters during furnace operation. Table I presents certain properties of the filters and the filter-detector systems.

TABLE I.—Properties of Filters and Detectors

Type of filter	Spectral response curve of photo-multiplier	Half-band width for filter-photo-multiplier system, μ	Effective wave-length, μ
Wratten:			
18A glass -----	S-4	0.040	0.366
45 and 47B -----	S-4	.029	.459
21 and 64 -----	S-4	.021	.560
Corning CS2-59 glass.	S-4	.029	.650
Wratten 70 -----	S-8	.070	.716

TEMPERATURE MODULATION

In order to cover a range of sample temperatures, neutral-density filters were constructed of standard 10- and 20-mesh brass cloth to reduce the intensity of irradiation of the sample. Each wire-cloth filter was mounted on a ring designed to fit the circumference of the mirror at the arc end of the furnace, with a 15-cm hole in the region of the arc. With or without a filter, the temperature distribution across the

diameter of the sample approximates a Gaussian shape, with the temperature decreasing from a maximum value at the center of the sample to about 75 percent of the maximum at a radius of about 0.5 cm, corresponding to the periphery of the arc image. The measurements of reflectance and temperature were obtained in every case in the region of the maximum temperature of the sample, and, except for one particular series of tests whose exception will be explained later, after the sample had attained a steady state. The purpose of this particular method of attenuation of the arc irradiation was to preserve the hemispherical character of the measurements and to avoid shadowing either of the intermediate images. It was believed that this approach to temperature control would yield more reliable and consistent data than those obtainable from measurements during temperature rise of the sample or from measurements made at points other than the maximum-temperature region on the surface of the sample.

Test Samples

Samples of all the materials studied were disks 1.3 cm in diameter and 0.5 cm in thickness. For each reflectance and temperature measurement, one of the disks was mounted in a small steel block, supported in and insulated from the block by four equally spaced spring-loaded zirconia pins which were tapered at the points of contact with the periphery of the sample. Measurements were made on the circular face of the disk which was located in the minor focal plane of the reimaging mirror, with its center on the optical axis of the arc-imaging furnace mirrors.

Apparatus for Measurement of Sample Surface Properties

Inasmuch as the emittance of any material is expected to be variable with surface roughness, it was considered desirable in this investigation to define the microgeometry of the surfaces of the materials for which emittance was determined. A light-section microscope was chosen for making the measurements because it permits measurements on soft materials without destroying or altering the surface and

because it is suitable for the determination of several surface parameters.

One arrangement for use of the light-section method to measure surface roughness is described in reference 7. The optical arrangement of the instrument employed in the present study is shown in figure 4(a). An incandescent lamp illuminates a slit which, by means of an objective, is reproduced on the surface under study as a thin band of light. The band of light illuminates the surface along its contour, and a profile image of the surface may be observed and/or photographed through a microscope whose objective has the same magnification as that of the illuminating objective. Illumination and observation directions form a 90° angle with each other and a 45° angle with the surface being examined. A crosshair, visible in the eyepiece, may be shifted within the field of view by means of a micrometer drum. Because the light band meets the surface at an angle of 45° and is observed at a right angle to this direction, an apparent profile height h_a (fig. 4(b)) is observed instead of the true profile height h_t . Obviously, $h_a = \sqrt{2}h_t$,

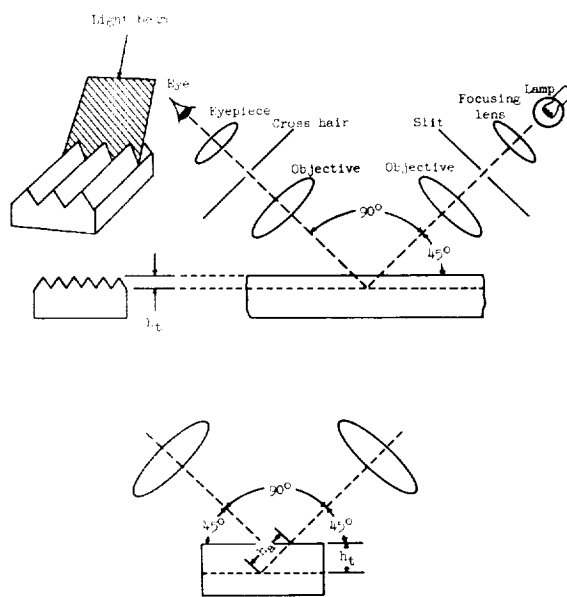


FIGURE 4.—Operation principles of light-section microscope.
(a) Optical arrangement.
(b) Principle of measurement.

but the factor $\sqrt{2}$ is accounted for in the calibration of the crosshair, which makes possible direct reading of the height and longitudinal location of each observed point of the profile. The range of the instrument permits measurements of surface irregularities for which h_z varies from 1 to 400 μ .

Apparatus for Measurement of Sample Porosity

The very porous and precipitous nature of some of the materials studied precluded obtaining meaningful surface-roughness measurements on them with the light-section microscope because of the formation of discontinuous profile images. Since the surface characteristics of porous materials are closely related to their porosity, pore-size spectra were determined for the appropriate materials. A mercury-intrusion method described in reference 8 was employed to make the measurements. Briefly, the method is based on the negative capillarity of mercury; that is, mercury must be forced into a porous material and the pressure required is determined by the surface tension of the mercury, the wetting angle, and the diameter of the smallest pore filled at that pressure. The instrument is designed for forcing mercury into the pores of a sample material at pressures ranging from subatmospheric to 3.5×10^7 newtons/m² and simultaneously indicating the volume of mercury absorbed at any given pressure, thus determining the pore-size spectrum of the sample for pore sizes ranging from 0.035 μ to 100 μ .

TEST METHODS

Method of Reflectance Measurement

In the following discussion, the principles of operation and measurement employed by the image pyrometer given in reference 6 are summarized and the calculations involved are modified for application to measurements covering a range of wavelengths.

To determine the temperature of the sample, it is first necessary to determine its emittance. For an opaque sample,

$$\alpha_\lambda + \rho_\lambda = 1 \quad (1)$$

and from Kirchhoff's law (ref. 9) and equation (1)

$$\epsilon_\lambda = \alpha_\lambda = 1 - \rho_\lambda \quad (2)$$

The image pyrometer measures the spectral reflectance, from which the spectral emittance is calculated by equation (2) and is used in the determination of sample temperature. To accomplish the reflectance measurement, the apparatus measures sequentially the arc light, the emitted plus reflected light from the sample, and the emitted light from the sample. The difference between the last two measurements is the reflected light from the sample, if no cooling of the sample occurs during the brief time taken for the chopper to interrupt the arc irradiation of the sample. The emitted light is measured while the arc radiation is briefly obstructed by the chopper. Interruption by the chopper occurs every 67 msec and the duration of each interruption is about 7 msec as shown in figure 3.

From the foregoing considerations the spectral emittance of the sample may be expressed as

$$\begin{aligned} \epsilon_{\lambda, s} &= 1 - \rho_{\lambda, s} = 1 - \frac{r_{\lambda, s}}{i_{\lambda, s}} \\ &= 1 - K \frac{(E_{\lambda, s} + R_{\lambda, s}) - E_{\lambda, s}}{A_\lambda} \quad (3) \end{aligned}$$

The constant K includes a measure of the fraction of the light from the arc image that is incident on the sample, as well as the pyrometer sensitivity through the sample- and arc-viewing optics. This constant may be determined by replacing the sample with a water-cooled surface of known reflectance. Because the spectral reflectance of freshly deposited magnesium oxide has been extensively studied (e.g., ref. 10 to 12), it was used as a standard for determining the value of K . Its diffuse reflectance throughout the visible spectrum is about 0.97.

The reflectance measurement by the image pyrometer, including specular and diffuse components, is essentially hemispherical, since the re-imaging mirror irradiates the sample and collects reflected and emitted radiation from the sample over a solid angle of about 5.7 (1.8 π) steradians. The emittance determined is

essentially hemispherical, since reflectance measured under conditions of hemispherical illumination and hemispherical viewing is the complement of hemispherical emittance.

Method of Temperature Calculation

Calculation of the sample temperature requires measurement of radiation from a standard-temperature source as well as from the sample itself. A tungsten-strip lamp serves as an accurate standard radiation source. Planck's law or Wien's law may be written for the sample and for the standard lamp. Wien's law is simpler to use and was used here since it agrees within ½ percent with Planck's law for the range of wavelengths and temperatures involved (ref. 13). Wien's law for the sample is

$$W_{\lambda,s} = \epsilon_{\lambda,s} c_1 \lambda^{-5} \exp(-c_2/\lambda T_s) \quad (4)$$

where $W_{\lambda,s}$ is the time rate of emission of radiant energy per unit interval of wavelength throughout 2π steradians per unit area of the sample at absolute temperature T_s . Wien's law for the standard lamp is

$$W_{\lambda,L} = \epsilon_{\lambda,L} c_1 \lambda^{-5} \exp(-c_2/\lambda T_L) \quad (5)$$

Since the viewing optics for measuring emitted radiation is the same for both the sample and the standard lamp, the ratio of the two expressions of Wien's law is equal to the ratio of the oscillograph signals for emitted radiation from sample and lamp $E_{\lambda,s}$ and $E_{\lambda,L}$, respectively. By taking this ratio, the following expression is obtained:

$$\frac{1}{T_L} - \frac{1}{T_s} = \frac{\lambda}{c_2} \ln \frac{\epsilon_{\lambda,L} E_{\lambda,s}}{\epsilon_{\lambda,s} E_{\lambda,L}} \quad (6)$$

Solving equation (6) for T_s gives

$$T_s = \frac{T_L}{1 - k_\lambda T_L \log \frac{\epsilon_{\lambda,L} E_{\lambda,s}}{\epsilon_{\lambda,s} E_{\lambda,L}}} \quad (7)$$

where

$$k_\lambda = \frac{2.302\lambda}{c_2} = \text{Constant incorporating a change from natural to common logarithms and absorbing } \lambda/c_2 \quad (8)$$

The value of λ is a function of the filter and detector system in the pyrometer and is essentially the effective wavelength of response of the image pyrometer. The value of k_λ may be determined by operation of the pyrometer with the standard lamp set successively at two different temperatures, $T_{L,1}$ and $T_{L,2}$. The resultant expression for k_λ is

$$k_\lambda = \frac{T_{L,1} - T_{L,2}}{T_{L,1} T_{L,2} \log \frac{\epsilon_{\lambda,L,2} E_{\lambda,L,1}}{\epsilon_{\lambda,L,1} E_{\lambda,L,2}}} \quad (9)$$

The sample temperature can be determined by substitution of k_λ into equation (7) along with the oscillograph data from the lamp at either temperature.

The physical meaning of effective wavelength of response of the image pyrometer is explained in figure 5. Here the triple product of the ultraviolet-filter transmission curve, the S-4 photomultiplier relative response curve, and the relative spectral radiant intensity curve for the standard lamp determines the combined response (shown in the upper right corner of the figure) of a typical source, filter, and detector system. The effective wavelength is taken as the line dividing the area under the product curve into two equal parts. Values of λ for the five filters determined by this method were

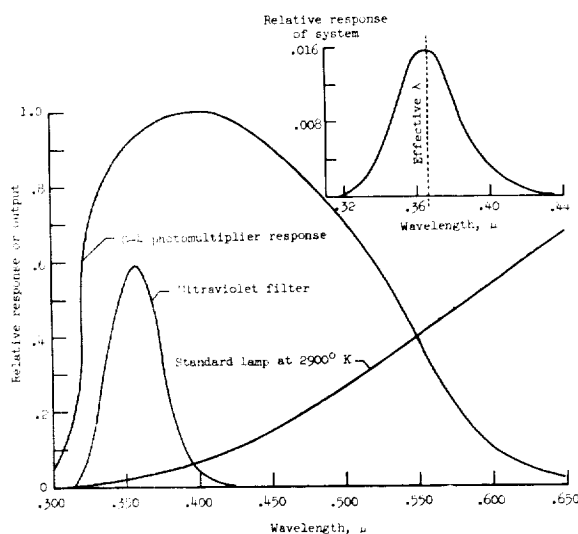


FIGURE 5.—Response of source-filter-detector system plotted against wavelength.

in agreement within 4.5 percent with averaged values calculated by solving equation (8) for λ and making use of the values of k_λ determined by equation (9). The effective wavelengths are only very weak functions of the source temperature for the range of sample temperatures studied and are well defined at the standard-lamp temperature of 2900° K, which is about the midpoint of the range of sample temperatures.

Because of the unavailability of spectral hemispherical emittance data on tungsten-strip lamps at high temperatures, spectral normal emittance data were used in equations (7) and (9). The spectral normal emissivity of tungsten ribbon filament has been the subject of considerable study because of its use as a radiation standard. The data of De Vos (ref. 14) and Larrabee (ref. 15), covering a broad range of wavelengths and temperatures, are considered the most reliable available. The data of De Vos were used in this report because they include a broader temperature range. Normal and hemispherical emittances of tungsten are not equal because tungsten does not emit in accordance with Lambert's cosine law; but studies by Worthing (ref. 16) and by Blau et al. (ref. 17) indicate that hemispherically measured values would not be expected to be more than 6 or 7 percent greater than normally measured values.

Evaluation of Errors

SYSTEMATIC ERRORS

Since several potential sources of error are inherent in methods of measurement of the type applied in this investigation, the most suspected ones are enumerated and evaluated either quantitatively or qualitatively. Errors in temperature measurement would be expected to be due primarily to errors in the experimentally determined emittance values, the use of normal emittance data for the standard lamp in the absence of hemispherical data, and losses due to internal reflections within the envelope of the standard lamp. However, an error of 5 percent in the emittance of the sample or standard lamp would produce an error of less than 1 percent in the temperature. The error due to applying normal emittance data to the

lamp and that due to losses within the lamp tend to compensate for each other.

The possible difference between the geometrical distribution of reflected radiation from the magnesium oxide reflectance standard and that emitted and reflected by the sample might appear to introduce error into the reflectance measurements. However, error due to such a difference would be minimized, on the basis of two considerations: (1) the distribution of illumination and the collection of radiation from the reflectance standard and from the sample are both essentially hemispherical, and (2) the distributions for the reflectance standard and for the generally rough samples studied would be expected to be similar.

Error in the reflectance measurements that might be expected to result from differences in the transmission properties of the two light pipes is eliminated through the calibration constant K , assuming that any such differences remain constant for all the measurements on the sample and reflectance standard at a given wavelength.

In order to eliminate errors in the radiation measurements that might arise from drifts in the electronic equipment, the image pyrometer includes a well regulated reference lamp to permit normalizing all the measurements. The sample-oriented light pipe receives a signal from the reference lamp (fig. 2) once each cycle of rotation, and the accompanying radiation measurements are normalized to the reference lamp oscillogram.

ERRORS DUE TO RAPID COOLING

The most serious problem in measuring reflectance at high temperatures is separating the emitted and reflected radiation. This problem with the arc-imaging furnace arises from the inability to achieve an instantaneous interruption of the incident radiation, with consequent cooling of the sample surface during the brief time required for the edge of the chopper to traverse the aperture at the intermediate image plane. If measurements are made at the end of the chopper-interruption process (just at the instant that the chopper has completely eclipsed the arc), which is the earliest time in the cycle that emitted and

reflected radiation are completely separated, any decrease in the emitted radiance due to cooling will be erroneously classified as reflected radiation. The magnitude of the error is in part dependent upon the thermal conductivity of the sample material, since this property determines the magnitude of the thermal gradient associated with a given amount of radiated flux from the front face of the sample.

Null and Lozier (ref. 18), recognizing that a sample in an arc-imaging furnace provides a plane surface with an essentially uniform temperature over a substantial area, have made use of solutions to the problems of one-dimensional heat conduction normal to the surface of a semi-infinite body subjected to periodic and nonperiodic step-function heat fluxes to evaluate thermal conductivity. The solutions show that, to a first-order approximation, the surface temperature after chopper interruption is directly proportional to the square root of time. Null and Lozier have also mathematically investigated the effect on the cooling curve of the finite time required to interrupt the furnace radiation by means of a mechanical chopper. This analysis showed that if time is measured from the middle of the chopper-interruption process (at the instant when the arc is half eclipsed) and temperature is plotted against the square root of time, the slope of the resulting straight line will be the same as that which would be obtained with a chopper fast enough to provide instantaneous interruption and, thus, to prevent any cooling during the interruption process.

The work of reference 18 provides a basis for investigating the possibility of significant errors inherent in these reflectance measurements due to a combination of high temperatures, high total emittances, rough sample surfaces with high thermal inertia, and finite chopper speed. The approach taken was first to examine the cooling curve for each sample very closely and to calculate the emittance and temperature from oscillograph measurements made at the time corresponding to completed interruption by the chopper. The time on the oscillogram corresponding to completed chopper interruption could be determined quite accurately by magnifying the cooling curve, studying it in

relation to the time scale of the oscillogram, and knowing the time required for the chopper to completely interrupt the radiation and the duration of the interruption.

A typical enlarged cooling curve is shown in figure 3. The photomultiplier output during the time that the chopper is closed is proportional to the spectral radiant intensity per unit area of the sample, which in turn varies linearly with the sample temperature for a small temperature change. Therefore, in accordance with the analysis of reference 18, the photomultiplier output during the time the chopper is closed would be expected to exhibit a square-root-of-time dependence if the temperature drop is sufficiently small. It was found that this was the case, when three or four points on each cooling curve were plotted against the square root of time, with time measured from the half-time point of chopper interruption. By extrapolating the straight line obtained from plotting emitted signal against the square root of time for each sample to the half-time of chopper closure, a new value for the emitted signal corresponding to the beginning of chopper interruption was determined, and thus a corrected emittance and temperature.

To incorporate the corrections into the earlier equations, equations (3) and (7) may be rewritten

$$\epsilon'_{\lambda, s} = \frac{(R'_{\lambda, s} + E'_{\lambda, s}) - E'_{\lambda, s}}{A_{\lambda}} \quad (10)$$

and

$$T'_s = \frac{T_L}{1 - k_{\lambda} T_L \log \frac{\epsilon_{\lambda, L} E'_{\lambda, s}}{\epsilon'_{\lambda, s} E_{\lambda, L}}} \quad (11)$$

where the primed quantities denote extrapolated values. Errors due to rapid cooling were found to be significant in some cases and corrections were made for them.

From the reproducibility of the data and the earlier considerations on systematic errors, it is believed that the emittance values reported herein are generally accurate to 1 or 2 percent; however, for the highest char temperature and the two longest wavelengths, the emittance values may be as much as 3 percent low due

to slight undercorrection for rapid-cooling errors. The undercorrection results because the assumption that the sample spectral radiant intensity per unit area varies linearly with temperature is only a fair approximation for the temperature range over which cooling occurs at the highest temperatures.

Method of Determining Surface Properties

One of the most formidable problem areas in the field of thermal radiation of solids is the development of theory relating the radiative and reflective properties of materials to their surface-roughness properties. Progress toward understanding this problem has been limited to special cases, with suitable assumptions about the statistical character of surfaces, because of the extreme complexity of the generalized problem and the lack of knowledge of the statistics of actual rough surfaces. A good summary of some of the early studies of the problem, including a list of references, is presented in reference 19 (pp. 293-295). Recent work by Bennett and Porteus (ref. 20 and 21), based on a statistical treatment of the reflection of electromagnetic radiation from a rough surface derived by Davies (ref. 22), has revealed certain quantitative relationships between surface character and reflectance properties. In reference 20 a theory is presented which relates the root-mean-square roughness of a plane surface with its specular reflectance at normal incidence, for the case when the roughness is small compared with the wavelength of the radiation. In reference 21 the theory is extended with certain restrictions to shorter wavelengths. The root-mean-square roughness (ref. 23) is the root-mean-square deviation of the surface from the mean surface level. References 21 and 22 seem to be oriented toward the development of a theory to explain surface properties from the reflectance of radiation incident normally and reflected specularly. It is indicated in these references that, for angles of incidence and reflection other than normal and for surfaces with irregularities large compared with the wavelength, the root-mean-square slope is an important factor in determining the reflected radiation.²

² See also papers in Session II.

The primary concern with surface properties in this study was to characterize the surfaces of the materials studied with surface-property data pertinent to the time of reflectance measurement and meaningful with respect to the emissive and reflective properties of the materials. Since arc irradiation of the sample in every case was terminated immediately after the reflectance measurement and the sample quickly cooled to room temperature, the subsequent surface-property measurements were assumed to be reasonably representative of the surface conditions at the time of reflectance measurement. A rather arbitrary method was applied to obtain data which could be expected to be statistically valid. For carbon and zirconia the profile data were obtained for a circular area at the center of the sample surface with a diameter of about 1.3 mm, and profiles were examined across four diameters of the circular area displaced from one another by 45°. Constant increments Δx parallel to the nominal-surface plane and corresponding variable increments Δy perpendicular to that plane were measured to determine the slope $\Delta y/\Delta x$ of each corresponding successive section of profile. Values of Δx were small enough ($12\ \mu$) to follow the profile quite closely. For graphite, Δx increments of $6\ \mu$ were chosen and a circular area of about 0.7 mm diameter was studied. In every case the slopes of 400 increments were evaluated for each sample, and the root-mean-square (rms) slope was calculated by the following equation:

$$\text{rms slope} = \left[\frac{1}{400} \sum_{n=1}^{400} \left(\frac{\Delta y}{\Delta x} \right)_n^2 \right]^{1/2} \quad (12)$$

RESULTS AND DISCUSSION

Measurements on Carbon and Graphite WAVELENGTH AND TEMPERATURE DEPENDENCE

Spectral emittance and reflectance data were obtained on high-purity (less than 6 ppm impurity) spectroscopic grades of carbon and graphite at three temperature levels. To assure that all samples of each material had like surfaces before testing, the surface of each sample disk to be exposed to the furnace

radiation was polished successively with 0, 3/0, and 4/0 grades of Buehler emery polishing paper. This polishing results in a glossy finish. Upon exposure in air to the arc-image thermal flux, this surface was quickly roughened as a result of oxidation.

Each sample was exposed long enough to attain its maximum, steady-state temperature, but not long enough to permit appreciable recession of the surface on which the image pyrometer measurements were being made. Varying arc irradiation level from conditions of no attenuation to that produced by the 20-mesh filter resulted in averaged temperatures of 3230° K, 2530° K, and 2120° K for carbon and 2990° K, 2390° K, and 2120° K for graphite. Figures 6 and 7 present the determined emittances and reflectances plotted against wavelength for each temperature and against temperature for each wavelength. Duplicate measurements were made for each set of conditions, with the exception that triplicate measurements were made on graphite at its highest temperature.

The values of emittance and temperature presented have been corrected for errors due to rapid cooling of the sample during chopper interruption of the arc radiation. Because of the difference between the spectral distributions of the emitted and the reflected radiation, the ratio of the emitted to reflected radiation decreases with decreasing wavelength. Consequently, the error in reflectance measurement

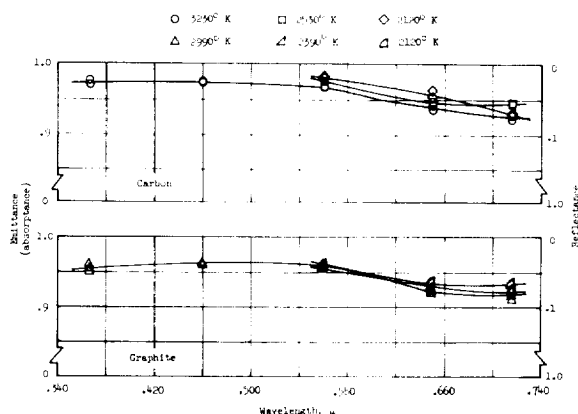


FIGURE 6.—Emittance and reflectance of oxidized carbon and graphite plotted against wavelength.

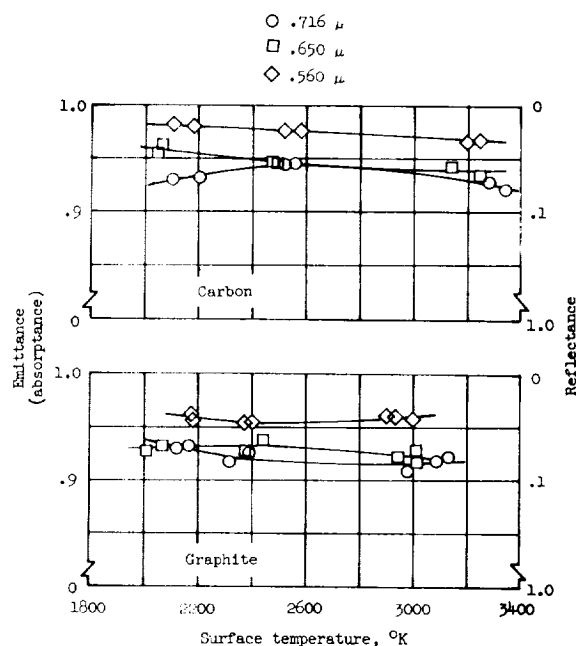


FIGURE 7.—Emittance and reflectance of oxidized carbon and graphite plotted against temperature.

due to rapid cooling is less at shorter wavelengths. Emittance corrections for carbon and graphite were as great as 6 percent at the highest temperature and corresponding longest wavelength and as small as 0.1 percent at the lowest temperature and shortest wavelength. It was determined by using the corrected emittance values that the average temperature drop during chopper closure was about 75° K for carbon at the highest temperature level and about 60° K at the lowest level. Graphite experienced about the same amount of cooling.

The emittance determined at the highest temperature levels is nearly constant for both graphite and carbon from 0.37 μ to 0.56 μ ; it is about 0.97 for carbon and about 0.96 for graphite. Beyond 0.56 μ the emittance decreases for both materials to about 0.92. At lower temperatures the materials also show a decrease in emittance with increasing wavelength and a very slight tendency toward decreasing emittance with increasing temperature. These characteristics have been observed at lower temperatures by a number of other investigators, although considerable discrepancy in the literature exists (ref. 24 and 25).

A similar study on the same grades of carbon and graphite by Null and Lozier (ref. 18) produced values of emittance in close agreement with those obtained in this investigation. Null and Lozier made directional measurements of spectral reflectance at a 45° angle from the normal to the material surface for conditions of hemispherical illumination on roughened and polished samples. Although no data beyond $0.60\ \mu$ are reported in reference 18, it is indicated that a trend toward decreasing emittance for longer wavelengths was observed.

SURFACE-CHARACTER DEPENDENCE

Spectral reflectance measurements at $0.65\ \mu$ similar to those just described were made on carbon samples, with the 20-mesh filter attenuating the irradiation, but the samples were partially protected from oxidation in order to obtain measurements on surfaces having a variety of roughnesses. By forcing a constant stream of helium tangentially across the irradiated surface of each sample and allowing different exposure times for different samples, reflectance measurements were obtained on surfaces ranging from polished to well oxidized. There was no temperature dependence for any of the reflectance data over the range of exposure times from 5 sec to 60 sec, since the final reflectance measurement in every case (corresponding to the maximum temperature for the given exposure time) was always repeated in a 5-sec reexposure under the protective conditions.

The emittance of each carbon sample rose rather abruptly from about 0.70 for a polished surface to about 0.90 upon initial oxidation, and then rose more slowly to 0.97 as further oxidation occurred. Upon making observations of the oxidized carbon samples with the light-section microscope, it was found that the large change in emittance from 0.7 to 0.9 occurred for a corresponding change in roughness that was not measurable with the light-section microscope, that is, a change from a polished surface to a matt surface having a roughness of the order of $1\ \mu$. Surface-profile data were obtained, in accordance with the procedure described previously, on the more severely oxidized carbon samples, which had roughnesses

greater than $1\ \mu$. For these samples it was found that the emittance from about 0.92 to 0.97 was a linear function of the root-mean-square slopes of the surfaces, as can be seen from figure 8 in which each circle represents one test sample.

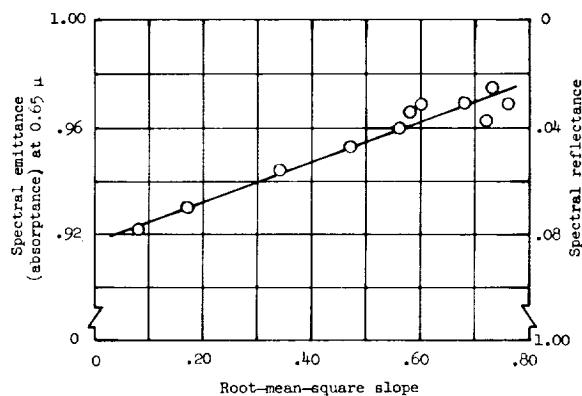


FIGURE 8.—Emittance and reflectance of oxidized carbon plotted against rms slope for constant temperature ($<2000^\circ\text{K}$).

In order to determine whether the average deviation of the surfaces from the mean surface level was a parameter meaningful to the hemispherical spectral emittance of carbon, the arithmetic average deviation was calculated. There was no apparent correlation between this parameter and the emittance. The range of values for the arithmetic average deviation was from 4 to $17\ \mu$.

After root-mean-square slope had been identified as an important surface-roughness parameter for carbon, values of the rms slope were determined for a typical sample of carbon and graphite representing each set of test conditions for earlier measurements in air, that is, for each temperature level represented in figures 6 and 7. These values of rms slope are given in table II, along with emittance data at $0.65\ \mu$ wavelength. The data in table II on carbon are not expected to fit the linear plot in figure 8, since they are slightly dependent on temperature as well as on surface roughness. Likewise the tabular data on graphite are not divorced from temperature dependence.

TABLE II.—*Root-Mean-Square Slopes of Surfaces for Reflectance Measurements in Air*

Material	Temperature, °K	Spectral emittance at $\lambda = 0.65 \mu$	Root-mean-square slope
Carbon.....	3144	0.942	0.47
Carbon.....	2492	.946	.71
Carbon.....	2068	.963	.58
Graphite.....	3018	.918	.78
Graphite.....	2375	.928	1.24
Graphite.....	2067	.933	.92
ZrO ₂ (ground).....	2777	.923	.94
ZrO ₂ (150F-GB).....	2732	.917	1.07
ZrO ₂ (120-150 GB).....	2692	.905	1.06
ZrO ₂ (90-120 GB).....	2680	.920	.86

Measurements on Zirconia

DIAMOND-WHEEL-GROUND SAMPLES

Spectral emittance and reflectance data were obtained on samples machined from calcia-stabilized zirconia (94.57 percent ZrO₂; 3.73 percent CaO). The sample surfaces were ground with a D220-N100-M 1/8 diamond wheel. It has been reported by Cox (ref. 26) that the thickness of zirconia required for opacity to visible radiation varies from about 0.41 cm at room temperature to 0.13 cm at the melting point, which indicates that the thickness of the samples used in this investigation was sufficient to assure the validity of equation (1) for this material. Attenuation of the arc irradiation with the 10-mesh filter produced an arc image that was sufficient to melt only a small spot about 0.3 cm in diameter on the center of the sample surface. Under these conditions the temperature measured would be expected to be very close to the melting point. The temperature values measured at four different wavelengths ranging from 0.46 μ to 0.72 μ averaged 3009° K, with only a 1.5-percent maximum deviation from this value for the eight tests shown in the lower curve of figure 9. The value obtained for the melting point of zirconia is in reasonably close agreement with reported values for calcia-stabilized zirconia of approximately the same chemical composition. These data have been corrected for rapid-cooling errors discussed previously. Emittance corrections were as high as about 7 percent at the longest wavelength and as

low as 0.4 percent for the shortest wavelength. Average temperature drop due to cooling during chopper closure was determined to be about 60° K.

Emittances and temperatures were also determined for diamond-wheel-finished samples of zirconia at a lower temperature level obtained by attenuating the arc irradiation with the 20-mesh filter. The emittance corrections for rapid cooling for these tests varied from about 5 percent to 0.3 percent and average cooling during chopper interruption was about 55° K. The results of these tests are shown as a function of wavelength in the upper curve of figure 9. Few spectral emittance data are available on zirconia at temperatures above 2500° K.

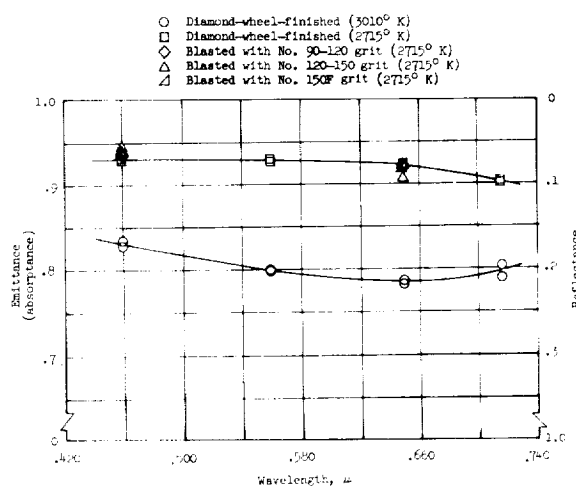


FIGURE 9.—*Emittance and reflectance of zirconia plotted against wavelength.*

Cox (ref. 26) reports measurements at 0.665μ at 2670°K obtained at about 45° with respect to the surface normal. These data are about 10 percent lower than those obtained in the present investigation; however, the accuracy of the measurements in reference 26 is estimated to be only ± 20 percent.

GRIT-BLASTED SAMPLES

Special roughness treatments were given to samples of the diamond-wheel-finished zirconia in an attempt to provide samples with three additional grades of roughness. Samples were grit-blasted with No. 90–120 zirconia grit, No. 120–150 grit, and No. 150F grit. However, because of the porous nature of the zirconia, even the diamond-wheel-ground surface was comparatively rough, and the visual differences in appearance among the three grit-blasted surfaces were not very pronounced. Reflectance was measured, with the 20-mesh filter attenuating the arc irradiation in order to maintain surface temperatures below the melting point at wavelengths of 0.46 and 0.65μ . Reflectance measurements on the three grit-blasted surfaces were essentially the same at each wavelength and did not differ significantly from the values measured on the ground surfaces, as can be seen in figure 9.

Surface profile data were obtained on zirconia samples with the four nominally different roughnesses. Root-mean-square slopes were calculated and are given in table II. Since the rms slopes of the grit-blasted surfaces differ by no more than 14 percent from the slope of the ground surface, the roughness studies on zirconia are inconclusive with regard to the possible existence of any relationship between emittance and rms slope. However, an additional factor not present in the case of carbon is the transmission of zirconia for small thicknesses of the material. Microscope studies indicated that the sizes of the irregularities in the zirconia surfaces were small compared with the thickness reportedly required for opacity. If light transmission is high for such small irregularities, it would appear that the roughness would have little influence on the emittance.³

³ See Paper 8.

POROSITY

As a part of the physical description and identity of the zirconia studied, a pore-size spectrum was determined by the procedure described earlier and it is shown in figure 10. This figure shows the pore volume per unit volume of zirconia for given ranges of pore diameter which vary from 4μ to 100μ .

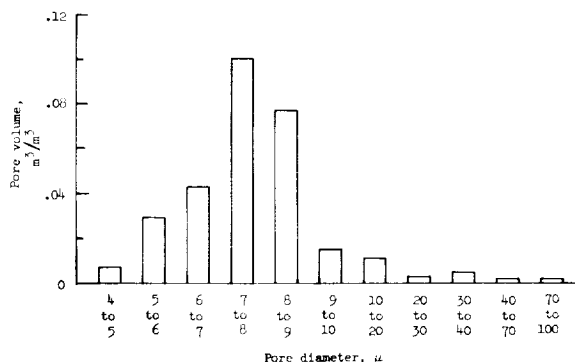


FIGURE 10.—Pore-size spectrum for zirconia.

Measurements on Phenolic-Nylon Ablation Char

WAVELENGTH AND TEMPERATURE DEPENDENCE

The ablation material studied in this program of tests was a phenolic-nylon. The phenolic-nylon was molded from a mixture of 50 percent by weight of nylon powder of 30-mesh average particle size and 50 percent by weight of powdered phenolic resin. The density in molded form was $1.21 \times 10^3 \text{ kg/m}^3$. The phenolic-nylon was heated by two different methods to form char residues. In one method the material was heated in an oven constantly purged with nitrogen at a pressure slightly greater than atmospheric. The oven temperature was controlled to produce an average rate of temperature rise of about 40°K/hr until the material reached 1100°K . The material was maintained at this temperature for 3 hours and then was cooled to room temperature at a rate equal to the temperature-rise rate. The phenolic nylon was charred in cylindrical form and the charred cylinders were subsequently cut into disks for emittance samples. These disks

were given no special surface treatments, since their porosity determined their surface character. (The density of the char was $0.61 \times 10^3 \text{ kg/m}^3$.)

In the other method of forming char, 7.6-cm-diameter disks of the phenolic nylon were exposed to an electric-arc-heated subsonic stream of nitrogen for 165 sec, the time required to produce a char layer about 0.5 centimeter thick. The arc jet, described in reference 2, produced an aerodynamic thermal flux of about 1.13 MW/m^2 on the phenolic-nylon disks. The maximum surface temperature attained by the char layers during their formation was about 2000°K . The density of the chars was $0.34 \times 10^3 \text{ kg/m}^3$. Disks of 1.3-cm diameter were cut from the char layers for emittance samples. The disks were given no special surface preparation, and reflectance measurements were made on the surface that had been exposed to the arc-heated nitrogen stream.

The emittance and reflectance of the chars at different temperatures (averaged) are shown as a function of wavelength in figure 11 and at different wavelengths as a function of surface temperature in figure 12. In general, the emittance of the oven-formed char is very slightly higher than that of the arc-jet-formed char. The slight difference between the emittance characteristics of the two forms of char may be attributable to certain physical differences observed. The oven-formed char appeared to be homogeneous, whereas the arc-

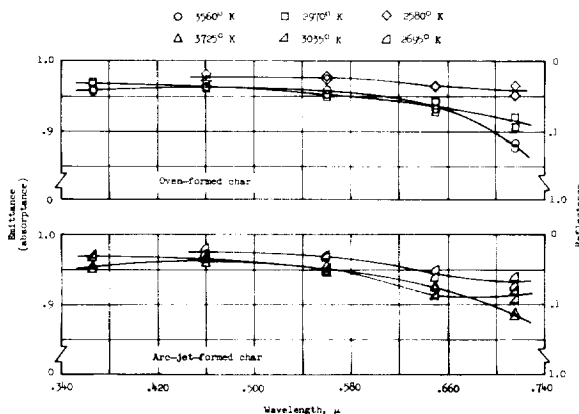


FIGURE 11.—Emittance and reflectance of phenolic-nylon char plotted against wavelength.

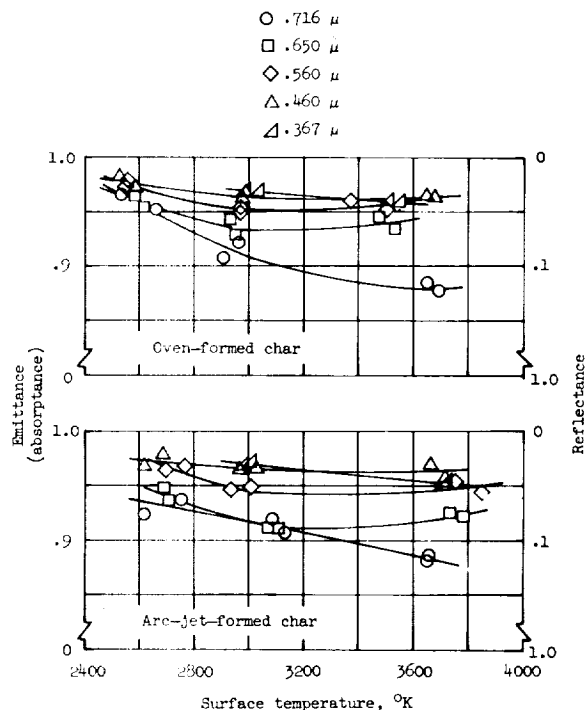


FIGURE 12.—Emittance and reflectance of phenolic-nylon char plotted against temperature.

jet-formed char had a cellular or columnar structure which resulted from the unidirectional flow of gases from the zone of reaction through the char layer during its formation. The densities of the char also were considerably different. The emittance characteristics of both forms of char bear a resemblance to those of carbon and graphite in that the emittance drops in the red region of the spectrum and also tends to drop with increasing temperature. These resemblances are not surprising, inasmuch as the chars themselves are carbonaceous.

The emittance and temperature data on the chars have been corrected for errors due to rapid cooling during chopper interruption of the arc radiation. The errors ranged from as high as 12 percent at the highest temperature and longest wavelength to no more than 0.2 percent for the lowest temperature and shortest wavelength. Cooling during chopper interruption ranged from an average of 150°K at the highest temperature level to 90°K at the lowest level.

POROSITY

Because of the very porous and precipitous nature of the char surfaces it was not possible to obtain continuous profile measurements with the light-section microscope, and it seems likely that it would be difficult to obtain conventional surface parameters by other roughness-measurement techniques. Porosity measurements seemed to be more basic to the physical nature of these materials. Pore spectra on typical char emittance samples obtained after their exposure in the arc-imaging furnace are shown in figures 13 and 14.

Porosimetry studies of the chars indicated the presence of some small pores in the char samples prior to exposure in the arc-imaging furnace which were absent after exposure. It seems likely that internal oxidation of the chars during exposure in the arc-imaging furnace was

responsible for changing the pore spectra, since there was a concomitant reduction in density of about 15 percent.

CONCLUDING REMARKS

Spectral hemispherical reflectance and emittance of carbon, graphite, zirconia, and a phenolic-nylon ablation char were determined with an apparatus consisting of an image pyrometer integrated with an arc-imaging furnace. Measurements on carbon and graphite included the wavelength range for which unidirectional measurements had been made recently by other investigators, but the present investigation was extended to shorter and longer wavelengths. Within the common wavelength range close agreement exists between the two sets of data. The spectral emittance determined at the 3000° K level is nearly constant for both carbon and graphite from wavelengths of 0.37 μ to 0.56 μ —about 0.97 for carbon and 0.96 for graphite. Beyond 0.56 μ the emittance decreases for both materials to about 0.92. At lower temperatures down to 2100° K, the materials also show a decrease in emittance with increasing wavelength and a very slight tendency toward decreasing emittance with increasing temperature.

Phenolic-nylon char was shown to have emittance characteristics in the visible spectrum very similar to those of carbon and graphite. The emittance characteristics of the char were shown to be relatively insensitive to the method of formation of the char, whether it be by an aerodynamic heating method or by a static (oven) heating method.

The emittance of zirconia was found to decrease slowly from the ultraviolet region to the red region of the spectrum and to be a sensitive function of temperature in the temperature region approaching and including the melting point. The temperature of melting measured for zirconia was about 3000° K, which is consistent with reported values for zirconia of similar chemical composition.

Special consideration was given to characterization of the surfaces of the materials studied. Pore-size spectra were determined for the appropriate materials. It was shown that the hemispherical spectral emittance of oxidized

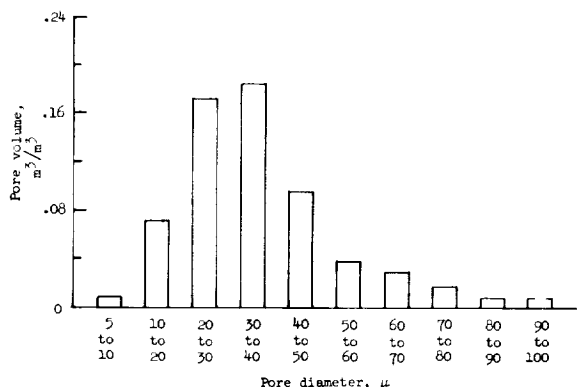


FIGURE 13.—Pore-size spectrum for oven-formed phenolic-nylon char.

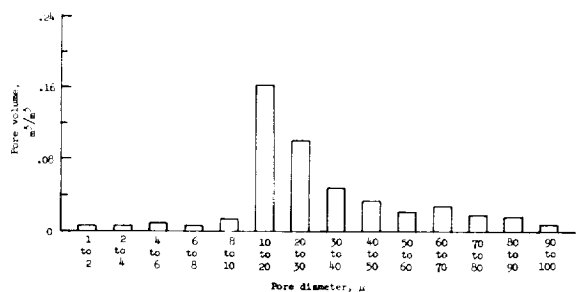


FIGURE 14.—Pore-size spectrum for arc-jet-formed phenolic-nylon char.

carbon at a wavelength of 0.65μ is a linear function of the root-mean-square slope of the surface when the roughness is large compared with wavelength. This result appears to be significant, and it warrants further exploitation of this surface parameter for other materials. It was also shown that changes in surface roughness of carbon which lie in the roughness region of less than approximately 1μ change the emittance much more significantly than changes in the roughness lying in the region above 1μ . The latter result indicates that surface irregularities of magnitude comparable with or smaller than the wavelength influence emittance most strongly, and that polished and nearly polished surfaces should be given special attention in further investigations of the relationship between surface roughness and emittance.

REFERENCES

1. BROOKS, WILLIAM A., JR.; WADLIN, KENNETH L.; SWANN, ROBERT T.; and PETERS, ROGER W.: An Evaluation of Thermal Protection for Apollo. NASA TM X-613, 1961.
2. PETERS, ROGER W.; and WILSON, R. GALE: Experimental Investigation of the Effect of Convective and Radiative Heat Loads on the Performance of Subliming and Charring Ablators. NASA TN D-1355, 1962.
3. CAMM, J. C.; KIVEL, B.; TAYLOR, R. L.; and TEARE, J. D.: Absolute Intensity of Non-Equilibrium Radiation in Air and Stagnation Heating at High Altitudes. *J. Quant. Spectry. & Radiative Transfer*, vol. 1, no.1, Sept. 1961, pp. 53-75.
4. MECHTLY, E. A.: The International System of Units—Physical Constants and Conversion Factors. NASA SP-7012, 1964.
5. GLASER, PETER E.: Imaging-Furnace Developments for High-Temperature Research. *J. Electrochem. Soc.*, vol. 107, no. 3, Mar. 1960, pp. 226-231.
6. COMSTOCK, DANIEL F., JR.: Method for Temperature and Reflectance Determination in an Arc-Imaging Furnace. *Temperature—Its Measurement and Control in Science and Industry*. Reinhold Pub. Corp., c. 1962. pp. 1063-1071.
7. ABBOTT, E. J.; and GOLDSCHMIDT, EDGAR: Surface Quality—A Review of "Technische Oberflächenkunde" by G. Schmaltz. *Mech. Eng.*, vol. 59, no. 11, Nov. 1937, pp. 813-825.
8. WINSLOW, N. M.; and SHAPIRO, J. J.: An Instrument for the Measurement of Pore-Size Distribution by Mercury Penetration. ASTM Bull. 236, Feb. 1959.
9. WEINSTEIN, M. A.: On the Validity of Kirchhoff's Law for a Freely Radiating Body. *Am. J. Phys.*, vol. 28, no. 2, Feb. 1960, pp. 123-125.
10. Anon.: Standard Method of Preparation of a Magnesium Oxide Standard for Spectral Reflectivity. ASTM Designation D 986-50, Pt. 6 of 1961 Book of ASTM Standards Including Tentatives, c. 1961, pp. 225-227.
11. Anon.: Preparation and Colorimetric Properties of a Magnesium-Oxide Reflectance Standard. NBS Letter Circular LC-547, U.S. Dept. Commerce, Mar. 17, 1939.
12. MIDDLETON, W. E. KNOWLES; and SANDERS, C. L.: The Absolute Spectral Diffuse Reflectance of Magnesium Oxide. *J. Opt. Soc. Am.*, vol. 41, no. 6, June 1951, pp. 419-424.
13. HARRISON, THOMAS R.: Radiation Pyrometry and Its Underlying Principles of Radiant Heat Transfer. John Wiley & Sons, Inc., c. 1960.
14. DE VOS, J. C.: A New Determination of the Emissivity of Tungsten Ribbon. *Physica*, vol. 20, no. 10, Oct. 1954, pp. 690-714.
15. LARRABEE, ROBERT D.: Spectral Emissivity of Tungsten. *J. Opt. Soc. Am.*, vol. 49, no. 6, June 1959, pp. 619-625.
16. WORTHING, A. G.: Temperature Radiation Emissivities and Emittances. *Temperature—Its Measurement and Control in Science and Industry*. Reinhold Pub. Corp., 1941, pp. 1164-1187.
17. BLAU, HENRY H., JR.; CHAFFE, ELEANOR; JASPERSE, JOHN R.; and MARTIN, WILLIAM S.: High Temperature Thermal Radiation Properties of Solid Materials. AFRCR-TN-60-165, U.S. Air Force, Mar. 1960.
18. NULL, M. R.; and LOZIER, W. W.: Research and Development on Advanced Graphite Materials. Volume XXI. Carbon Arc Image Furnace Studies on Graphite. WADD-TR-61-72, Vol. XXI, Nov. 1963.
19. BARKAS, W. W. (With appendix by R. F. S. Hearmon): Analysis of Light Scattered From a Surface of Low Gloss Into its Specular and Diffuse Components. *Proc. Phys. Soc.*, vol. 51, 1939, pp. 274-295.
20. BENNETT, H. E.; and PORTEUS, J. O.: Relation Between Surface Roughness and Specular Reflectance at Normal Incidence. *J. Opt. Soc. Am.*, vol. 51, no. 2, Feb. 1961, pp. 123-129.
21. PORTEUS, J. O.: Relation Between the Height Distribution of a Rough Surface and the Reflectance at Normal Incidence. *J. Opt. Soc. Am.*, vol. 53, no. 12, Dec. 1963, pp. 1394-1402.
22. DAVIES, H.: The Reflection of Electromagnetic Waves From a Rough Surface. *Proc. Inst. Elec. Eng.*, vol. 101, 1954, pp. 209-214.
23. Anon.: Surface Texture—Surface Roughness, Waviness and Lay. ASA B46.1-1962, ASME, c. 1962.
24. PLUNKETT, J. D.; and KINGERY, W. D.: The Spectral and Integrated Emissivity of Carbon

- and Graphite. Proceedings of the Fourth Conference on Carbon, Pergamon Press, New York, 1960, pp. 457-472.
25. THORN, R. J.; and WINSLOW, G. H.: Radiation of Thermal Energy From Real Bodies. *Temperature—Its Measurement and Control in Science and Industry*, vol. 3, pt. 1, F. G. Brickwedde, ed., Reinhold Pub. Corp., c. 1962, pp. 421-448.
26. COX, R. L.: A Technique for Measuring Thermal Radiation Properties of Translucent Materials at High Temperature in *Measurement of Thermal Radiation Properties of Solids* (Joseph C. Richmond, ed.) NASA SP-31, 1963, pp. 469-481.

DISCUSSION

DANIEL COMSTOCK, Arthur D. Little, Inc.: I have a comment about equipment of this type or of the type described by Clark and Moore. With increasing temperature the thermal gradient in the material becomes important because of the radiation cooling, particularly in techniques in which we try to measure the emittance by heating the sample at the back side, while observing the radiation at the front side. The gradient can be very high for nonmetals at high temperatures, say, above 2000° K. Techniques such as this one or the one in the Clark-Moore paper eliminate the gradient problem. In such techniques the heat is put

into the face of the material—into the same face from which the heat is subsequently reradiated—so that, to the first order, there is no thermal gradient in the material. That is, if the observation is made fast enough and soon enough after the heat input, the gradient problem is minimized, and there is a very nearly isothermal sample in the region of the front face (although there may also be questions of volume radiation from the sample). As we extend our studies toward the higher temperatures, we must use front-face heating methods such as those described in this and the Clark-Moore paper (rotating cylinder method).

28. Emittance Measurements of Solids Above 2000° C¹

T. S. LASZLO, R. E. GANNON, AND P. J. SHEEHAN

AVCO CORPORATION, WILMINGTON, MASS.

A method of measuring the emittance of solids above 2000° C through the use of a solar furnace has been developed. Two techniques, involving specialized instrumentation, for performing the necessary measurements were investigated. Initial experiments showed that both techniques were suitable and that the specified instruments were adaptable for making the required measurements.

Very few emittance data are available for temperatures above 2000° C, and no satisfactory methods for measurements in this temperature range have been developed. Most methods for measuring emittance at moderate temperatures follow a procedure suggested by the definition of emittance. The radiation emitted by a sample is measured and compared with that emitted by a blackbody maintained at the same temperature as the sample. At higher temperatures, however, this method cannot be applied. Conventional furnaces cannot operate above 1800° C. Induction furnaces can be used to heat materials to much higher temperatures, but reaction between the specimen and the susceptor and/or crucible material is difficult, if not impossible, to avoid.

In 1957 Laszlo (ref. 1) proposed an approach for measuring the emittance of materials above 2000° C, through the use of a solar furnace. Blau (ref. 2) and Comstock (ref. 3) have since attempted with varying degrees of success to use solar and carbon arc image furnaces for emittance measurements based on this approach. The present investigation is concerned with the development of the necessary mathematical equations, instrumentation, and techniques for high-temperature emittance measurements with a calibrated solar furnace.

PROBLEMS IN THE MEASUREMENT OF HIGH TEMPERATURE EMITTANCE

Two basic approaches are generally used in the measurement of emittance. In the first (direct method), the radiant energy emitted by the sample is quantitatively compared with the radiant energy emitted by a blackbody at the same temperature as the sample. In the second (indirect method) the reflectance of the sample is measured and the emittance is calculated from Kirchhoff's law. This method can be used only for opaque bodies or for bodies with known transmittance.

Both methods present considerable experimental difficulties. One of the greatest problems is the measurement of surface temperature. Above the operating range of thermocouples, optical or radiation pyrometers are generally used. Their accurate use, however, requires a prior knowledge of the emittance of the surface.

A further temperature limit is set by the fact that reference blackbody radiators are available only for temperatures below 1500° C. The technique of constructing a reference blackbody cavity directly in the specimen under examination has been used in the past. The requirement of maintaining the same temperature on the specimen surface as in the cavity, however, presents a most difficult task, particularly when the specimen is heated by radiation.

¹ See Paper 27 for description of a related technique.

Controlled heating of a sample to high temperatures also presents difficulties. Beyond the range of electric resistance furnaces, induction heating can be used if the specimen is a susceptor. If it is not, an auxiliary susceptor can be used, for example, graphite or tungsten. In such cases, however, reactions between the sample and susceptor may occur and thus render the results meaningless.

In an image furnace any sample, regardless of its magnetic susceptibility, can be heated to high temperatures without contamination from its surroundings. In a solar furnace, heat fluxes corresponding to a blackbody temperature of approximately 4500° C may be reached under conditions suitable for various measurements (ref. 4). The special characteristics of a calibrated solar furnace also make it possible to measure the surface temperature with an optical pyrometer without previous knowledge of the emissivity.

The use of an image furnace, however, introduces other experimental difficulties. Some of these are: the need to separate the radiation emitted by the surface from that reflected by the surface (this problem also exists with several conventional heating methods), the small size of the radiating area, and the non-uniformity of the heat flux impinging on the specimen. These difficulties have to be overcome when emittance measurements are performed in the solar furnace.

THEORETICAL BASIS OF THE METHOD

A method has been developed for the measurement of the total normal emittance in a solar furnace. The method is based on the well known laws of radiant energy exchange, and it takes advantage of the special heating conditions available in a calibrated solar furnace. The theoretical and experimental approaches of previous investigators, as well as earlier findings and conclusions on high-temperature emittance measurements, were taken into consideration in formulating the method.

Three different radiant energy measurements are required according to this method. The first two measurements are necessary for the determination of the sample temperature during

heating in the solar furnace. The third measurement is required for the calculation of the total normal emittance. First, the energy emitted by the sample at temperature T is measured at a selected wavelength λ . The result of this measurement is expressed according to Planck's law, as

$$J'_\lambda = \epsilon_{\lambda, T} \frac{C_1 \lambda^{-5}}{e^{C_2/\lambda T} - 1} \quad (1)$$

where J'_λ is the radiant intensity at wavelength λ and surface temperature T and $\epsilon_{\lambda, T}$ is the spectral emittance of the surface. C_1 and C_2 are the Planck radiation constants.

In the second step the sum of the emitted and the reflected energy is measured at the same wavelength and temperature and expressed as follows:

$$J''_\lambda = J'_\lambda + \frac{(1 - \epsilon_{\lambda, T}) C_1}{\lambda^5 e^{C_2/\lambda T_s} - 1} \quad (2)$$

where J''_λ is the radiant intensity containing both emitted and reflected components and T_s is the temperature that, by Planck's equation, corresponds to the intensity of the solar radiation (at wavelength λ) impinging on the sample. The commonly used value of 6000° K for the surface temperature of the Sun cannot be used for T_s in equation (2), because atmospheric attenuation and optical losses in the solar furnace make the Sun appear to radiate with a lower intensity. A constant correction factor cannot be used; the losses caused by furnace optical elements are constant, but the atmospheric attenuation is not.

Blau (ref. 2) attempted to overcome this difficulty by using an aluminized water-cooled copper block as a reference standard. Measurements with this standard in place of the unknown specimen permit the calculation of the intensity of the incident radiant energy. This method, however, has a number of shortcomings. The surface finish and the purity of the reflecting aluminum surface cannot be standardized or maintained constant. The reflecting surface is not at ambient temperature in spite of water-cooling; thus, the ambient temperature reflectance value does not strictly apply. A further difficulty is that measurements with the standard and the unknown are

not simultaneous; the incident solar radiation may change while the standard is being replaced by the sample.

Comstock (ref. 3) applied the same principle (ref. 1) to emittance measurements in carbon arc image furnaces. In his calculation he uses a factor K which includes the radiant flux impinging on the sample. This value is determined by using a standard reflecting surface, consisting of a watercooled, magnesia-coated, copper block. This method also has some inherent shortcomings. Magnesium oxide deposited by burning magnesium in air is contaminated with magnesium nitride; it is also slightly hygroscopic (ref. 5). Both these characteristics affect its reflectance. The reflectance is also a function of the coating thickness, at least below 1 mm (ref. 6). If the deposit is thicker, the temperature differential between the cooling water and the front (reflecting) surface is likely to be very high. Thus, the suggested surface reflectance value of 0.95 to 0.97 may not hold.

These difficulties do not arise when the high-temperature emittance measurement is performed in a calibrated solar furnace (ref. 7). In such a furnace the relation between the normal incidence solar radiation and the concentrated flux at the center of the image is precisely known (fig. 1). When the furnace is in use the normal incidence solar radiation is continuously measured with a calibrated pyrheliometer; and the flux at the center of the image is calculated from the normal incidence value recorded at the exact time of the measurement. Since the normal incidence measure-

ment is simultaneous with the measurement of the radiation emitted and reflected by the specimen, errors due to changes in normal incidence solar radiation are eliminated. The concentrated flux calculated from the normal incidence solar radiation measurement is lower than the corresponding flux from a 6000° K blackbody radiator. A correction factor is calculated from the difference, and the spectral radiation at the selected wavelength of a 6000° K blackbody is reduced by this factor. From the Planckian tables the temperature of that blackbody is found which radiates with this reduced intensity at the wavelength of the measurement. This temperature is then considered the apparent temperature of the Sun and is used as T_s in equation (2). Equations (1) and (2) can then be solved simultaneously for $\epsilon_{\lambda T}$ and T .

As a check on the method, the same measurements can be performed at a different wavelength. The resulting $\epsilon_{\lambda T}$ is likely to be somewhat different, but T should be the same. If one set of measurements is performed at the wavelength of the commercially available optical pyrometers, 0.665 μ , another check on T is possible. In this case the brightness temperature can be measured with the optical pyrometer and the true temperature calculated from Planck's law using the known emittance at 0.665 μ .

By a modification of this method it is possible to determine the temperature of the specimen by using an optical pyrometer instead of a monochromator. First, the brightness temperature of the surface is measured when only the emitted radiation is observed. The relation between this value and T is

$$\frac{1}{e^{C_2/\lambda T_a} - 1} = \frac{\epsilon_{\lambda T}}{e^{C_2/\lambda T} - 1} \quad (3)$$

where T_a is the brightness temperature of the emitting surface. Following this the brightness temperature is measured when the sum of the emitted thermal radiation and the reflected solar radiation is observed. The relation between this value and T is

$$\frac{1}{e^{C_2/\lambda T_B} - 1} = \frac{\epsilon_{\lambda T}}{e^{C_2/\lambda T} - 1} + \frac{1 - \epsilon_{\lambda T}}{e^{C_2/\lambda T_s} - 1} \quad (4)$$

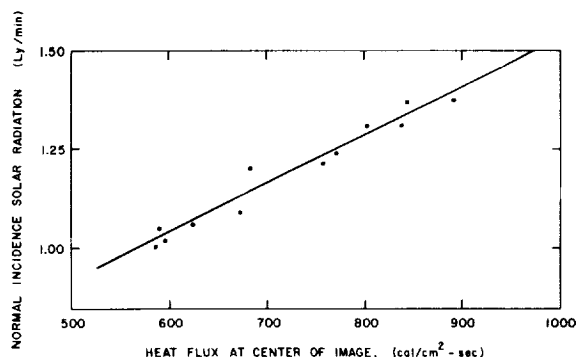


FIGURE 1.—Relationship between peak flux at center of image and normal incidence solar radiation.

where T_B is the brightness temperature when the sum of the emitted and the reflected radiation is observed. From equations (3) and (4) the true temperature can be calculated.

The final step in the determination of total normal emittance is the measurement of the total emitted radiation at temperature T and the calculation of the total emittance from the Stefan-Boltzmann law. During all these measurements only the normal emitted radiant energies are measured and accordingly the result of the calculation is the total normal emittance.

Three assumptions are tacitly included in the preceding considerations. The first is that the samples are opaque; that is, all radiant energy is either reflected or absorbed. In general, this assumption is not justified. In the present work however, such thick samples are used that the opaque condition is approximated. As a further refinement of the method it is planned to use samples of the same materials but of various thickness. Thus, a correlation between thickness and transmissivity may be established and the original form of the Kirchhoff equation (reflectivity plus absorptivity plus transmissivity equals 1) can be applied.

The second assumption is that solar radiation as observed at the surface of the Earth has a blackbody distribution. This is not strictly so because of several atmospheric absorption bands in the spectrum. The correction factor obtained by the described method for the calculation of T_s , therefore, is approximate, since it is not spectrally sensitive. For a more accurate determination of T_s , it is necessary to determine the correction factor at each wavelength for each $J'_{\lambda,T}$ measurement. This can be done by deflecting a small beam of the radiation from the solar furnace mirror into a monochromator. The resulting spectrum compared with the solar spectrum outside the Earth's atmosphere indicates the losses due to atmospheric and mirror attenuation at each wavelength. The loss at the selected wavelength can then be determined quantitatively by a correlation with the normal-incidence concentrated flux relationship (fig. 1).

The third assumption is implied in the application of the Kirchhoff law. The emitted and

reflected energy is measured normal to the sample surface whereas the incident energy lies within a 122° cone, the angular aperture of the solar furnace. As a consequence the sample does not receive solar radiation over a solid angle of 2π steradians, a condition on which Kirchhoff's law is based. It has been shown (ref. 4), however, that the major part of the concentrated flux in a solar furnace comes from the central portion of the paraboloidal concentrator, whereas the peripheral portions contribute very little. Accordingly, the missing 29° annular solid angle of radiation represents only a very small fraction of the total energy impinging on the specimen. It is estimated that the effect of the missing radiation on the reflected energy is negligible. Further, it is possible to evaluate this effect by extrapolation of available data on the correlation between aperture angle and total flux.

INSTRUMENTATION

The high-temperature emittance measurements are performed in a 60-inch-diameter paraboloidal solar furnace. The furnace has a highly sensitive solar tracking mechanism (ref. 8), a movable screen calibrated for flux control (ref. 4), and a pyrheliometer for continuously monitoring the normal incidence solar radiation during all solar furnace measurements (ref. 1). The focal length of the mirror is 25.48 inches, and at its focal point the circle of maximum flux is approximately $\frac{1}{8}$ inch in diameter.

As in most emittance measurements, it was necessary to separate emitted and reflected radiation. In order to accomplish this, two methods were considered. In the first, a rotating sector, similar to the one described by Conn and Braught (ref. 9), was used. As illustrated in the schematic drawing (fig. 2) the rotating sector assembly consists of a rotating collimation tube with a radiation shield, a fixed collimation tube, a rotating disk with two orifices 90° apart, and a spring-loaded rotating disk with one orifice. The two disks and the rotating collimation tube are attached to a drive shaft which is driven at 42 rps by a synchronous motor. The arrangement is such that under normal operating

conditions the detector at the back of the solar furnace views the sample only when the rotating shield and collimator are in front of it. In this way, only the radiation emitted by the sample can reach the detector, but the reflected solar radiation cannot. When the spring-loaded disk is retarded 90°, the detector views the sample while it is being irradiated by solar energy; the radiation thus detected consists of the emitted radiation plus the reflected solar radiation. The values measured by the detector for these two conditions correspond to J'_λ and J''_λ in equations (1) and (2), respectively.

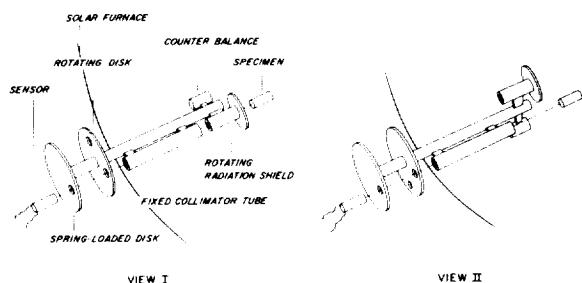


FIGURE 2.—Rotating sector for separation of emitted and reflected radiation. View I: specimen shielded; measures emitted radiation only. View II: specimen exposed; measures emitted and reflected radiation.

The high-speed rotation of the sector, however, presented an immediate problem. As previously stated, the sector rotates at 42 rps, and the sample is viewed once every rotation. From these data and the dimensions of the rotating disk and orifices, it was calculated that the sample is viewed for 0.002 sec during each rotation. Accordingly, the radiation measuring instrumentation (detector, amplifier, and recorder) had to have a correspondingly short response time. A special detector, a thermistor bolometer with a 0.1 mm² manganese-nickel-cobalt oxide flake and a response time of 0.0011 sec, and a correspondingly fast amplifier were obtained. An oscilloscope with an attached Polaroid camera was selected to record the signal from the amplifier.

In the alternate method of separating the emitted and reflected radiation, a cylindrical

sample was rotated about its longitudinal axis, perpendicular to the optical axis of the solar furnace. One radiation detector was placed where it could measure the radiation coming from the irradiated side of the specimen, thus measuring the reflected as well as the emitted radiation. A second detector was placed facing the back of the sample, thus viewing the heated portion as it rotates out of the focal plane. This detector measured only the radiation emitted by the sample.

A special sample holder, shown in figure 3, was used for this method. The samples were supported by two water-cooled shafts which can be adjusted to accommodate samples of various lengths. The shafts, and through them the specimens, were rotated by a variable-speed servomotor.

According to this technique, the radiation measurements are made under equilibrium conditions; thus, the need for a fast response recording system is eliminated. A restriction on the front sensor is the fact that it has to be placed at a certain distance from the sample in order to avoid casting a shadow on it. A small detector is needed, capable of measuring the radiation from a small spot (approximately 1/8 inch in diameter) at a distance of several inches. The sensor used for this measurement was a two-junction bismuth/silver thermopile, 1.25 inch in diameter, with a sensitivity of 0.009 $\mu\text{V}/\mu\text{W}$.

The detectors (the thermistor bolometer and the thermopiles) were calibrated against a blackbody radiation source under simulated operating conditions. This blackbody radiator was constructed from a hollow graphite tube 3/8 inch in diameter and 2 1/2 inches long with a wall thickness of approximately 0.03 inch. A hole, 1/8 inch in diameter to correspond to the high-temperature area of the sample in the solar furnace, was drilled into the wall of the hollow tube. Such tubes have been shown to be blackbody emitters (ref. 10). Power was supplied to the graphite tube, through water-cooled electrodes, by four welding generators. Power settings up to 430 amperes at 13 volts were used to attain temperatures up to 2460° C. The graphite tube was enclosed in a silica sleeve with a suitable sighting hole and pro-

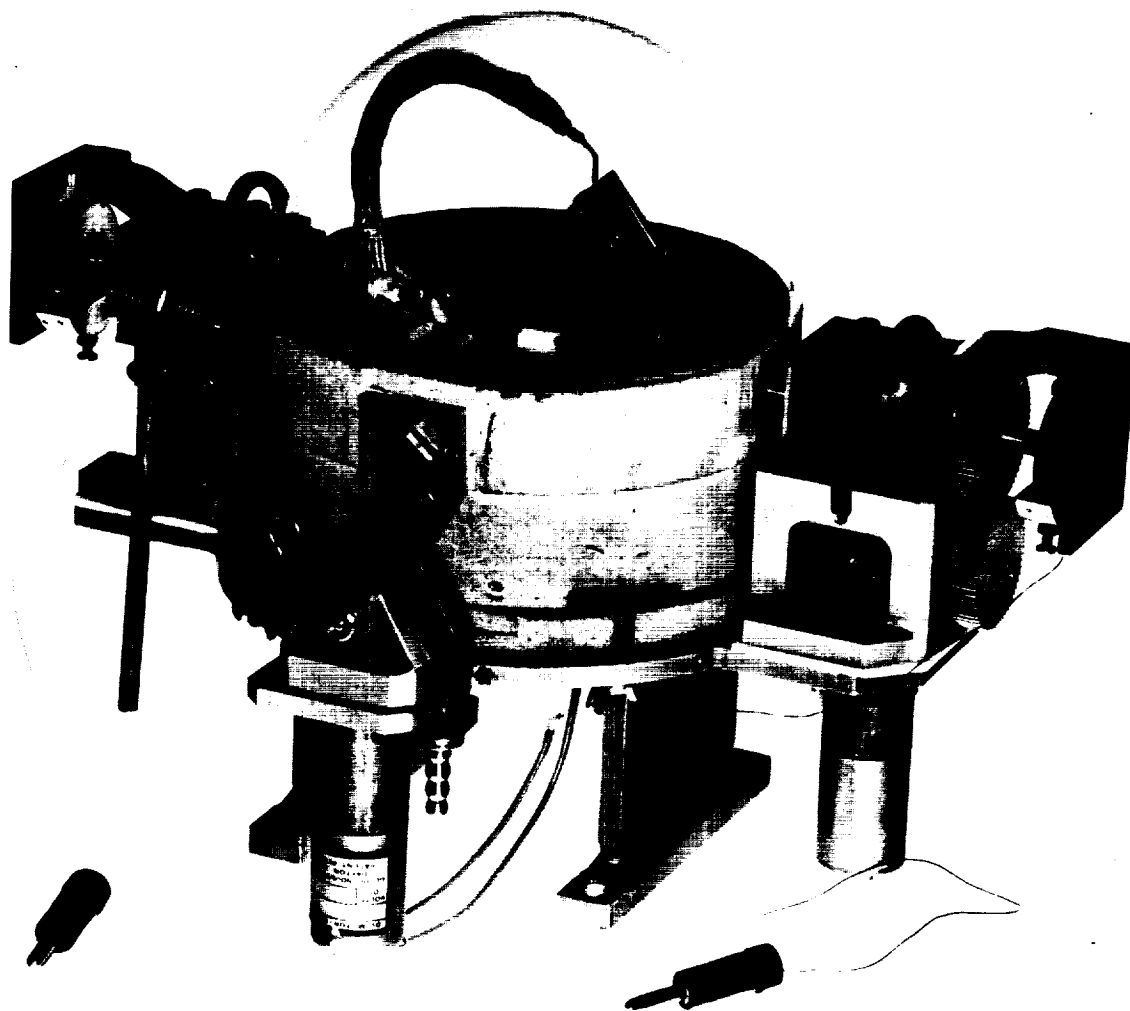


FIGURE 3.—Sample holder for emittance measurements.

tected with radiation shields. During the high-temperature measurements, a flowing argon atmosphere was used to protect the graphite from oxidation. The true temperature of the blackbody cavity was determined by measurements with an optical micropyrometer. The total flux was calculated from this temperature by the Stefan-Boltzmann equation and the spectral flux at selected wavelengths was calculated by Planck's equation.

For calibration of the thermistor bolometer, the rotating sector was mounted in front of the blackbody source and operated as in the solar furnace. The blackbody radiation was therefore chopped and collimated in the same manner

as it was during the emittance measurements. For calibration of the thermopiles, the rotating sector was replaced by the stationary collimator tubes designed for use with the thermopiles.

For spectral measurements a Farrand Uvis monochromator was used. This monochromator has a reflection-type replica grating with 14,000 lines per inch, and a spectral range from 220 $m\mu$ to 700 $m\mu$. Its wavelength dial, readable to 2 $m\mu$ was calibrated against a Jarrell-Ash scanning monochromator and against the spectral lines of a mercury vapor lamp. Its small physical size, approximately 7½ inches \times 7 inches \times 3 inches, makes it suitable for mounting on the back of the solar furnace.

EXPERIMENTAL

Preliminary measurements have shown that both methods of measuring J'_λ and J''_λ are workable.

The effectiveness of the rotating-sector technique with the thermistor bolometer is illustrated in figure 4. Figure 4(a) is an oscilloscope trace of the radiation emitted (J'_λ) by an alumina specimen heated to approximately 1900° C in the solar furnace. The rotating radiation shield and the spring-loaded disk were allowed to rotate in phase with each other. Once during each revolution, when the rotating radiation shield and the spring-loaded disk became aligned with the fixed collimation tube, the detector saw the sample when no solar radiation was impinging on it. Thus, the signal observed on the oscilloscope (fig. 4(a)) represents only the radiation emitted by the sample. When the spring-loaded disk was retarded so that it was out of phase with the rotating radiation shield, the oscilloscope signal represented the sum of the emitted and the reflected radiation, J''_λ . The higher amplitude of the peak in figure 4(b) is thus due to the addition of the reflected solar energy to the radiation emitted by the sample.

In the second technique, one thermopile measures the radiation J''_λ coming from the front of the sample, where it is irradiated by solar energy, and a second thermopile measures the radiation J'_λ emitted by the back of the sample after it rotates away from the irradiated, front position. The effectiveness of this technique has also been demonstrated by actual measurements.

In putting the described methods into practice, however, a number of problems were encountered. Many of these problems have been solved, and others are still being studied.

In order to heat the sample to the desired high temperature, the solar radiation must be concentrated on a small area of the sample. The resulting high-temperature spot usually consists of a $\frac{1}{8}$ -inch-diameter circle of relatively uniform temperature surrounded by an area with a steep temperature gradient down to ambient temperatures. A profile of the temperature across the heated area is shown in figure 5. In order to be certain that only the

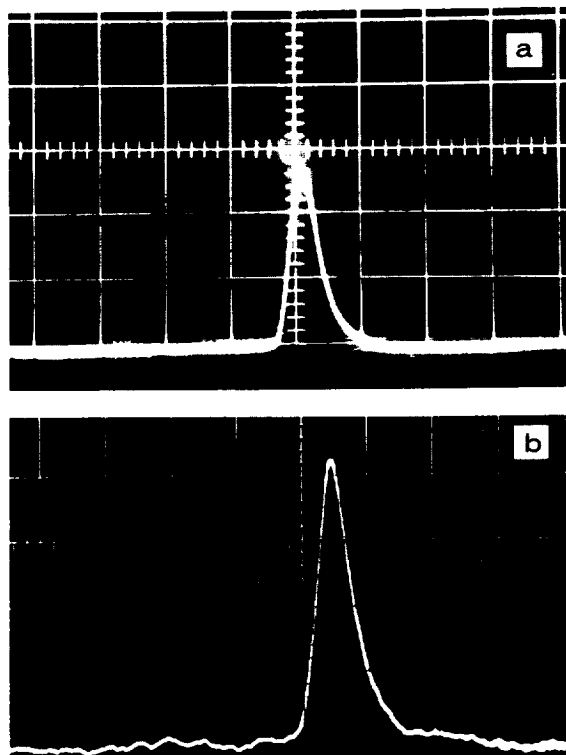


FIGURE 4.—Oscilloscope records of radiant flux. (a).—Emitted radiation. (b).—Emitted plus reflected radiation.

area of uniform temperature was viewed by the detector, precise collimation was necessary.

The rotating radiation shield represents an extension of the fixed collimator tube. Since this shield is not always in front of the sample during measurements, it was necessary to reduce the field of vision of the sensor to such a value that the additional collimating effect of the rotating shield is eliminated. This was accomplished by inserting a $\frac{3}{8}$ -inch orifice into the fixed collimator tube.

In the second method of measuring J' and J'' the collimation of the radiation is also critical. For the thermopile viewing the back of the specimen, a short collimation tube just long enough to eliminate stray radiation is sufficient, since there are no restrictions on how close the thermopile can approach the rear of the sample. In the case of the thermopile viewing the irradiated side of the specimen, measuring J'' , the collimation tube must be placed in the shadow area of the solar furnace

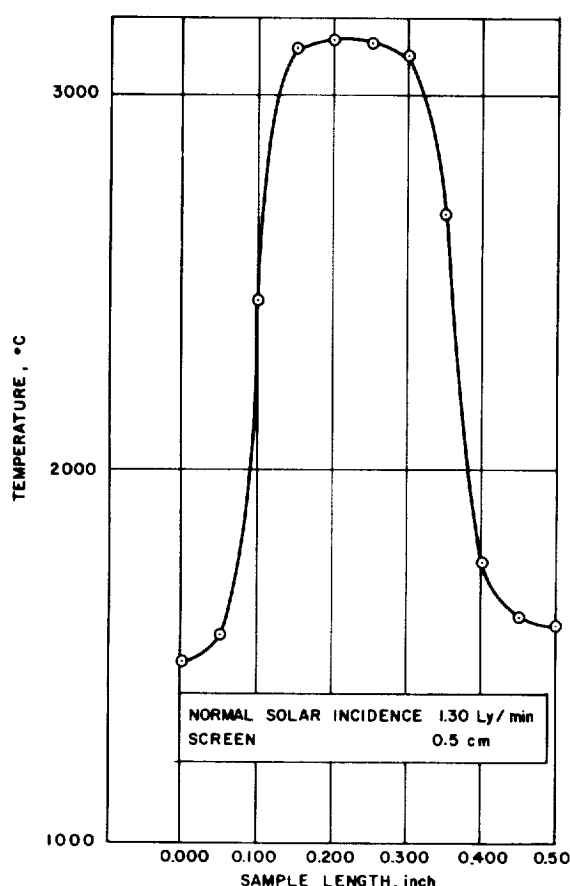


FIGURE 5.—Temperature profile across a heated specimen.

so that it does not shield the specimen or become overheated itself.

The rotating radiation shield in front of the sample acts as a neutral density filter since it reduces the intensity of the solar radiation impinging on the sample without changing its spectral distribution. It was realized that the attenuation of the solar radiation by the rotating shield would reduce the integrated flux (over a finite period of time) to the specimen and thereby limit its maximum attainable temperature. It was also thought that the instantaneous flux, as measured in J''_{λ} , would not be affected since it is measured for a 0.001-sec period when the shield is 90° out of alignment with the sample. Preliminary measurements showed, however, that even when the shield is 90° out of alignment with the sample,

the edge of the shield shades the sample, reducing the incident flux at the instant of the measurement. This shielding effectively reduces the apparent temperature of the Sun and, therefore, the previously established relation between the normal incidence radiation and concentrated flux (fig. 1), used in the calculation of T_s , cannot be applied without suitable corrections.

Consequently, a blackbody radiator, specially designed for heating in the solar furnace (ref. 6), was constructed to determine the necessary correction factor. Optical pyrometer as well as bolometer measurements were made of the blackbody cavity in the solar furnace with and without the rotating sector installed. The differences between the two sets of data were considered to be due to the shadow effect of the rotating sector.

The initial experiments also demonstrated the sensitivity of the bolometer and amplifier to the vibrations caused by the rotating sector. In order to eliminate the effects of such vibrations, elaborate shock-mounting arrangements for the electronic and optical instruments were fabricated. In addition, a swing was constructed and attached to the solar furnace to allow the amplifier to remain in a vertical position regardless of the elevation of the solar furnace.

Although the shock-mounting and swing arrangement reduced the noise level considerably, the signal-to-noise ratio was still too low to allow precise measurements. In order to eliminate this problem a narrow, essentially zero bandwidth filter network was introduced into the circuit and synchronized so that the only signal processed was that coming through at the chopping frequency. Synchronization was accomplished by means of a beam of light reflected from one of the chopper disks. The reflected beam was detected by a light-sensitive silicon diode which triggered the amplifier circuit once during each revolution. In this way only the impulse with the same frequency as the chopped signal was amplified and recorded.

The problem of precisely reading the amplitude of a 0.005-sec pulse on an oscilloscope was eliminated by the construction of an integrating

network with a time constant larger than the repeat time of the rotating sector. The incorporation of this network into the amplifier circuit resulted in the conversion of the chopped signal to a corresponding d-c voltage level which could be displayed on a strip chart recorder.

The suitability of the two methods for measuring emittance at high temperatures can be evaluated by comparing the results obtained by these newly developed methods to those obtained by an already established, conventional method. Such a comparison is necessarily limited to the maximum temperature of the conventional method but the established validity of the new methods should apply also to high temperatures. Accordingly, the total normal emittance of a pure aluminum oxide specimen was measured by a method similar to that described by McMahon (ref. 11). The total normal emittance at 1300° C was found to be 0.35. To eliminate possible discrepancies due to specimen differences, an identical sample was used to measure the emittance in the solar furnace. This was done by the method of alternately observing the radiation emitted at the back of the sample and the sum of the emitted and reflected radiation at the front of the sample. The result of this measurement, performed at a sample temperature of 1290° C, was a total normal emittance value of 0.33.

Work is being continued toward further refinement and establishment of these methods for the measurement of emittance at high temperatures.

ACKNOWLEDGMENTS

The special electronic circuitry was designed and built by John Morreal. The work was sponsored by the Air Force Office of Scientific Research of the Office of Aerospace Research, under Contract No. AF 49(638)-1166.

DISCUSSION

CLAIRE CHAPIN, Purdue University: I was a bit confused about the curve you drew on the board showing the attenuation as being uniform over the wavelength range. What is the mechanism of attenuation, and why is it uniform?

LASZLO: I said that there are a number of reservations. Some of these are discussed in the paper. Of course

REFERENCES

1. LASZLO, TIBOR S.: Temperature and Flux vs. Geometrical Perfection. *Solar Energy*, vol. 1, nos. 2-3, Apr.-July 1957, pp. 78-83.
2. BLAU, HENRY H., JR.: Measurement of Flux, Emittance, and Related Properties. *Proceeding of an International Symposium on High Temperature Technology*. McGraw-Hill Book Co., c. 1960, pp. 45-53.
3. COMSTOCK, DANIEL F., JR.: Method for Temperature and Reflectance Determination in an Arc-Imaging Furnace. *Temperature—Its Measurement and Control in Science and Industry*, Reinhold Publ. Corp. (New York), c. 1962, pp. 1063-1071.
4. LASZLO, TIBOR S.: Solar Furnace in High-Temperature Research. *Science*, vol. 124, no. 3226, Oct. 26, 1956, pp. 797-800.
5. DUNKLE, ROBERT V.: Spectral Reflectance Measurements. *First Symposium—Surface Effects on Spacecraft Materials*, Francis J. Clauss, ed., John Wiley & Sons, Inc., c. 1960, pp. 117-137.
6. TELLEX, PETER A., and WALDRON, JACK R.: Reflectance of Magnesium Oxide. *Jour. Optical Soc. of America*, vol. 45, no. 1, Jan. 1955, pp. 19-22.
7. LASZLO, TIBOR S.: Measurement and Application of High Heat Fluxes in a Solar Furnace. *Solar Energy*, vol. VI, no. 2, Apr.-June 1962, pp. 69-73.
8. LASZLO, TIBOR S., DE DUFOUR, WILLIAM F., and ERDELL, JOSEPH: A Guiding System for Solar Furnaces. *Solar Energy*, vol. II, no. 1, Jan. 1958, pp. 18-20.
9. CONN, WILLI M., and BRAUGHT, GENE: Separation of Incident and Emitted Radiations in a Solar Furnace by Means of Rotating Sectors. *Jour. Optical Soc. of America*, vol. 44, no. 1, Jan. 1954, pp. 45-47.
10. PIRANI, M., and ALTERTHUM, H.: Ueber eine Methode zur Schmelzpunktbestimmung an Hochschmelzenden Metallen. (Determination of the Melting Point of Highly Infusible Metals.) *Z. Elektrochemie*, vol. 29, Jan. 1, 1923, pp. 5-8.
11. MCMAHON, HOWARD O.: Thermal Radiation Characteristics of Some Glasses. *Jour. American Ceramic Soc.*, vol. 34, no. 3, 1951, p. 91.

the attenuation is not uniform. We are all familiar with the ozone absorption band in the ultraviolet and with the water vapor and carbon dioxide bands in the infrared. But if you look at the solar spectrum, you will see that only a small percentage of the total energy is in those portions where these absorptions take place. So, if we neglect these and assume uniform attenuation,

the error is not so large as to make the approximation unusable.

DANIEL COMSTOCK, Arthur D. Little, Inc.: Regarding your reference to magnesium oxide reflectance, it is a little hard to calculate what the front surface temperature of a powder is when the back surface is held at a known temperature on a metal substrate. In the case we are talking about, a smoked magnesium oxide layer with a thickness of, say, 0.1 mm, irradiated with 150 calories/cm²-sec, the temperature of the front surface of a particular particle may be different by 50° C. Also, I am very curious about your blackbody standard. Has it been described in a publication?

LASZLO: It was published about three years ago, and I would be very glad to talk about it, if we had more time. You can find this information in a paper I presented in 1961—at the 18th International Congress of the International Union of Pure and Applied Chemistry, Montreal, Canada. The detailed analytical expression, an extraordinarily difficult one because of the special shape of the blackbody, will be published in the future.

HERSHEL WEINBERGER, National Physical Laboratory of Israel: I do not understand why you need to know the apparent temperature of the Sun after its radiation passed through the Earth's atmosphere. As far as I can understand, you are interested in knowing the value of the radiant flux in the temperature-radiation equation. Why, after having measured the radiation do you have to relate it to the apparent temperature? You are interested only in the intensity of the radiation in the radiation equation. Having already measured this, why is it necessary to calculate the apparent temperature?

LASZLO: The apparent solar temperature is the third unknown in the two equations presented in the paper. We do know the intensity of the concentrated solar radiation and the emitted thermal radiation from the flux measurements. These constitute the left sides of equations (1) and (2). The two equations,

however, contain three unknowns: the emittance of the sample, its temperature, and the apparent temperature of the Sun. Thus, in order to solve the two equations, one unknown has to be determined independently. This approach is the reverse of the conventional one. In most cases the temperature is known and the flux emitted by the radiator is calculated. Here the flux is known from measurements, and the temperature has to be calculated. Since there are two different temperatures in the two equations (sample and solar temperature), one has to be eliminated by experimental methods. Thermocouple measurements cannot be used for obvious reasons; thus, the described process has been developed.

WEINBERGER: I understand. My second question pertains to the diagram you drew on the blackboard. That curve does not represent the solar spectrum. Is it, then, the radiation you receive from the sample?

LASZLO: I am sorry. This is a misunderstanding. That is the solar radiation curve. The top curve represents the spectral distribution of the solar radiation outside the Earth's atmosphere, and the curve underneath corresponds to the solar radiation as received by the specimen after atmospheric and optical attenuations in the solar furnace.

WEINBERGER: Then why are you interested in the solar temperature when you already know the intensity of its radiation? You are interested in the temperature of your sample and not that of the Sun.

LASZLO: I am interested in both because both are required for the calculation of the temperature and emittance of the sample. In the first measurement, with the rotating sector in front of the sample, the emitted radiation is measured. In the second measurement, the emitted plus the reflected radiation is determined. From these two measurements the temperature and the emittance of the sample can be calculated only if the temperature of the body irradiating the sample is known.

29. Preliminary Studies Toward the Determination of Spectral Absorption Coefficients of Homogeneous Dielectric Materials in the Infrared at Elevated Temperatures

W. FUSSELL AND RALPH STAIR

NATIONAL BUREAU OF STANDARDS, WASHINGTON, D.C.

A preliminary determination of the spectral absorption coefficient of potassium bromide was made by measuring the spectral radiance ratios of two samples with different thicknesses mounted against a specular metal surface. The theory of the method, the apparatus used, and the experimental results are described.

The spectral absorption coefficient of a homogeneous dielectric material at an elevated temperature may be determined by measuring the spectral radiance ratios of two different thicknesses of the material mounted against a specular metal surface. (*Radiance ratio* is defined in this paper as the ratio of the radiance of the front surface of a sample, viewed along the perpendicular, to the radiance of a blackbody at the temperature of the sample holder.) This paper will (1) review the theory of the method, (2) describe the double-oven infrared spectroradiometer system used for making the measurements of spectral radiance ratio, and (3) present preliminary results for potassium bromide at a temperature of about 300° C in the wavelength range 4 μ to 13 μ .

SYMBOLS

$K(\lambda)$	normal spectral absorption coefficient, cm^{-1}
t	sample thickness, cm
t_1, t_2	different thicknesses of samples of the same material, cm
$\epsilon'_s(\lambda)$	normal spectral emissivity of an opaque specimen with plane front surface
$\epsilon''_s(\lambda)$	normal spectral radiance ratio of the combination of a plane slab next to an opaque plane substrate

$\epsilon''_{s1}(\lambda)$	$\epsilon''_s(\lambda)$ for a sample of thickness t_1
$\epsilon''_{s2}(\lambda)$	$\epsilon''_s(\lambda)$ for a sample of thickness t_2
λ	wavelength
$\rho_s(\lambda)$	normal spectral surface reflectance
$\rho'_s(\lambda)$	normal spectral reflectivity of an opaque plane surface
$\rho'(\lambda)$	normal spectral reflectance of a plane slab
$\rho''(\lambda)$	normal spectral reflectance of the combination of a plane slab next to an opaque plane substrate
$\tau_s(\lambda)$	normal spectral internal transmittance, $\exp [-K(\lambda)t]$
$\tau'(\lambda)$	normal spectral transmittance of a plane slab

APPARATUS

Basic Elements

The equipment used for measuring the normal spectral radiance ratios is based on the work of Stair and others (ref. 1 and 2) and consists of (1) a reference infrared radiation source (blackbody) whose temperature is accurately known, (2) a second infrared source which consists of a sample of the material under investigation, the back surface of which is heated to approximately the same temperature as the blackbody, and (3) a recording infrared spectroradiometer for comparing the radiance of the sample with that of the blackbody at a particular wavelength. The upper temperature limit of the

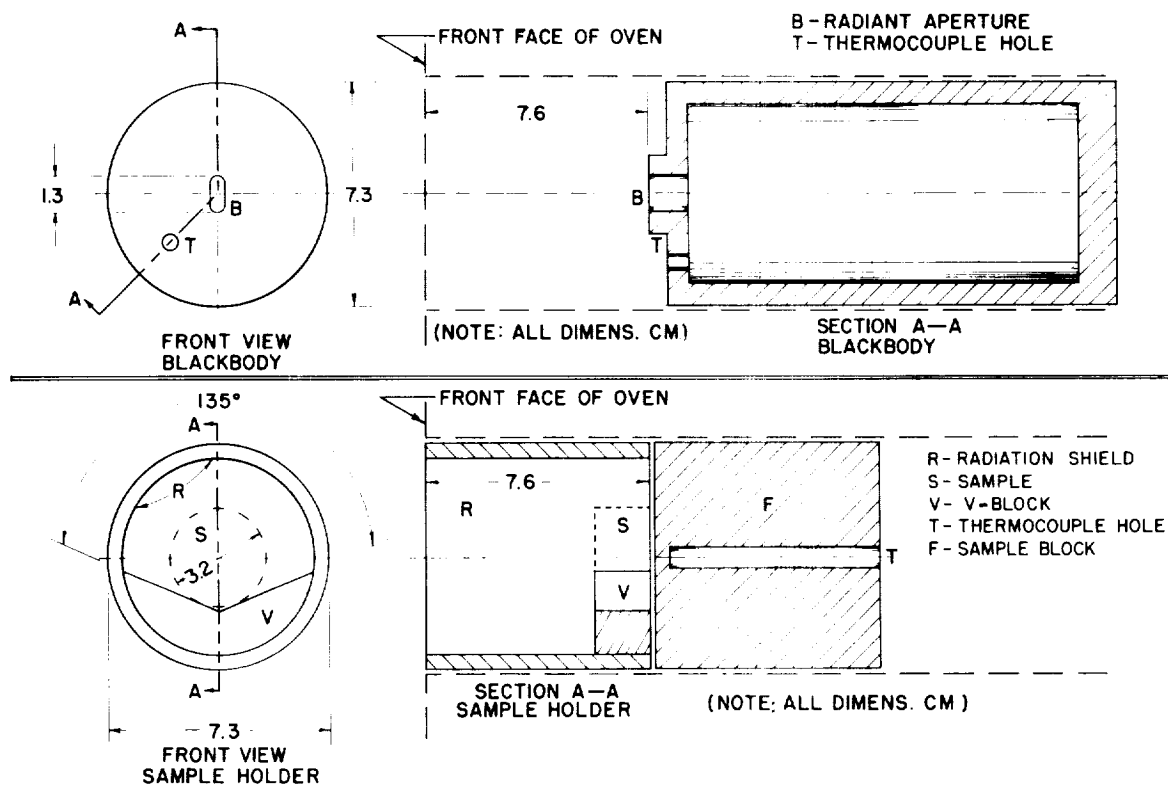


FIGURE 1.—Detail views of the blackbody reference source and the sample holder.

equipment is set by the melting point of the blackbody. The lower temperature limit is set by the Johnson noise generated by the thermocouple radiation detector in the spectroradiometer.

Reference Source and Sample Source

The blackbody reference source is a hollow Inconel cylinder with a narrow slit aperture, which is the radiation source proper, and it is heated by an electric oven which surrounds it. Front and cross-section views of the blackbody are shown in figure 1. The Gouffé analysis (ref. 3) was used to estimate the degree of approximation of the reference source (assumed to be an isothermal cavity) to a blackbody. The analysis indicated the emissivity to be better than 0.9995.

The samples of material whose radiance ratios are to be measured are disks 3.2 cm in diameter and usually 2, 8, and 16 mm in thickness. The sample is held in position during measure-

ment by the sample holder shown in figure 1. The sample holder is in three parts: (1) the V-block, (2) the radiation shield, which supports the V-block, and (3) the sample block, a large solid cylinder which abuts against the sample, V-block, and radiation shield. All surfaces of the sample holder are plated with platinum to reduce their emissivity. The whole sample assembly is placed inside an electric oven which heats it to the point where the sample holder is at the desired temperature.

The blackbody oven and the sample oven are mounted adjacent to each other on a movable carriage so that either source may be placed at the position of the image of the entrance slit of the spectrometer.

Infrared Spectroradiometer and Optical System

The infrared spectroradiometer consists of a Perkin-Elmer Model 99 double-pass Littrow spectrometer with NaCl prism, a Perkin-

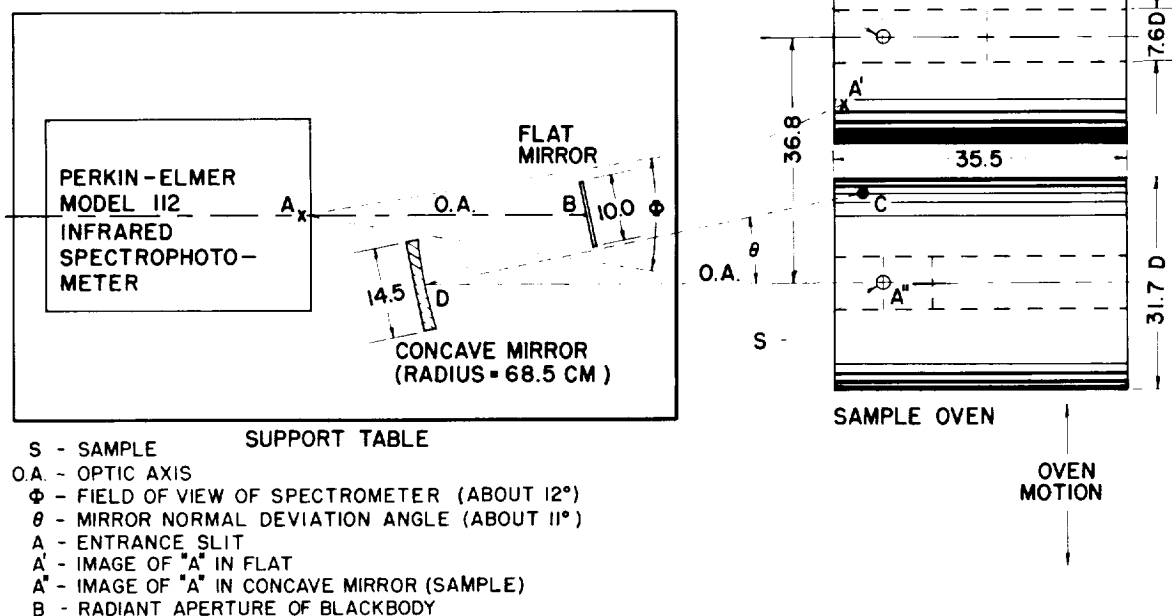
$$\begin{aligned} AB &= 43.8 \\ BD &= 26.3 \\ DA &= 69.9 \end{aligned}$$


FIGURE 2.—*Experimental setup for measurement of the normal spectral radiance ratio of materials in the infrared at elevated temperatures.*

Elmer Model 107 amplifier, a Leeds & Northrup Speedomax G recorder, and associated equipment. The system operates single-beam. The useful wavelength range of the spectrometer is approximately 1 to 15 microns. The effective field of view of the spectrometer is rectangular, diverging approximately 10° horizontally and 13° vertically. The external optical system (fig. 2) consists of two front-surface aluminized mirrors. One is a 10-cm-square plane mirror; the other is a 14.5-cm-diameter spherical mirror of 68.0-cm radius of curvature, which focuses the image of the entrance slit onto the blackbody or the sample surface.

Temperature Measuring and Controlling Equipment

The temperatures of the reference source and sample holder are measured with platinum/platinum-10-percent rhodium thermocouples

calibrated by the Temperature Physics Section of the National Bureau of Standards. The thermocouple voltages are read on a potentiometer. The voltages of the reference-source and sample-holder thermocouples are equalized and held constant to within 4 microvolts by two Leeds & Northrup 10877 control systems, one for each oven.

THEORETICAL BASIS OF METHOD

As is well known (ref. 4 and 5), the normal spectral transmittance $\tau'(\lambda)$ and reflectance $\rho'(\lambda)$ of a specimen with plane parallel faces, composed of a material of spectral absorption coefficient $K(\lambda)$, are related to the normal spectral surface reflectance for one surface $\rho_s(\lambda)$ and the normal spectral internal transmittance $\tau_i(\lambda)$ by the equations

$$\tau'(\lambda) = \tau_i(\lambda)[1 - \rho_s(\lambda)]^2 \{1 - [\tau_i(\lambda)\rho_s(\lambda)]^2\}^{-1} \quad (1)$$

and

$$\rho'(\lambda) = \rho_s(\lambda)[1 + \tau_i(\lambda)\tau'(\lambda)] \quad (2)$$

where $\tau_i(\lambda) = \exp[-K(\lambda)t]$, in which t is the specimen thickness.

Let the specimen be placed next to (but not in optical contact with) an opaque, plane substrate of reflectivity $\rho'_s(\lambda)$ and emissivity $\epsilon'_s(\lambda) = 1 - \rho'_s(\lambda)$. Then it can be shown (see appendix) from equations (1) and (2) that if the specimen-substrate combination is isothermal and if $\rho'(\lambda)$ and $K(\lambda)t$ are much less than one, the normal spectral radiance ratio $\epsilon''_n(\lambda)$ of the specimen-substrate combination is given by the following approximation:

$$\epsilon''_n(\lambda) \approx 1 - \rho'_s(\lambda) + 2K(\lambda)t\rho'_s(\lambda) - 2\rho_s(\lambda)[\epsilon'_s(\lambda)]^2 \quad (3)$$

Let the normal spectral radiance ratios of two specimens of the same material but of different thicknesses, t_1 and t_2 , be denoted $\epsilon''_{n1}(\lambda)$ and $\epsilon''_{n2}(\lambda)$, respectively, both $\epsilon''_{n1}(\lambda)$ and $\epsilon''_{n2}(\lambda)$ applying to the specimens in combination with the same substrate. Then the value of $K(\lambda)$ can be computed from the equation

$$K(\lambda) = [\epsilon''_{n2}(\lambda) - \epsilon''_{n1}(\lambda)][2\rho'_s(\lambda)(t_2 - t_1)]^{-1} \quad (4)$$

which is derived from equation (3).

Hamilton (ref. 6) derives a result from which it can be shown that the most accurate value of the spectral absorption coefficient $K(\lambda)$ of a material can be computed from spectral radiance-ratio measurements made of specimens having thicknesses in the neighborhood of $[2K(\lambda)]^{-1}$, when the measurements apply to specimens placed next to highly reflecting substrates and the surface reflectances are much less than one.

EXPERIMENTAL DATA

To evaluate the spectral absorption coefficient $K(\lambda)$ of a specimen which does not scatter infrared radiant energy appreciably, *three* spectral radiance-ratio measurements are required with the blackbody and sample block heated to the desired temperature:

- (1) Ratio of the spectral radiance of the sample block (specimen removed) to

the radiance of the approximate blackbody. This ratio is the normal spectral emissivity $\epsilon'_n(\lambda)$ of the platinum-plated sample block, and is used to evaluate the reflectivity of the sample block, $\rho'_s(\lambda) = 1 - \epsilon'_n(\lambda)$, for substitution in equation (4).

- (2) Ratio of the spectral radiance of the specimen of thickness t_1 to that of the blackbody. This ratio is $\epsilon''_{n1}(\lambda)$ of equation (4).
- (3) A similar ratio for a specimen of the same material of thickness t_2 . This ratio is $\epsilon''_{n2}(\lambda)$ of equation (4)

Figure 3 shows the results of preliminary determinations of the spectral absorption coefficient of *KBr* between 5.5 and 13 microns. The two sample thicknesses used were 8 mm and 16 mm, and the sample holder temperature was approximately 300° C. The measured values of the preceding three radiance ratios are shown together with the values of spectral absorption coefficient computed from equation (4). Since the uncertainty in the values of radiance ratio found in these preliminary measurements is about 0.02, the uncertainty of the computed values of spectral absorption coefficient is also about 0.02 for $\rho'_s(\lambda) = 0.9$ and $t_2 - t_1 = 0.8$ cm. Corrections for the temperature gradients undoubtedly present in the specimens during observation have not been applied. It remains to be seen whether the uncertainty of radiance-ratio measurements by this method can be reduced sufficiently to yield values of spectral absorption coefficients with acceptable (20 percent uncertainty) accuracy.

REFERENCES

1. STAIR, RALPH; JOHNSTON, RUSSELL G.; and HALBACH, E. W.: Standard of Spectral Radiance for the Region of 0.25 to 2.6 Microns. Res. Paper 65A4-51, Jour. Res. Nat. Bur. Standards, vol. 64A, no. 4, July-Aug. 1960, pp. 291-296.
2. MAKI, ARTHUR G.; STAIR, RALPH; and JOHNSTON, RUSSELL G.: Apparatus for the Measurement of the Normal Spectral Emissivity in the Infrared. Paper 64C2-29, Jour. Res. Nat. Bur. Standards, vol. 64C, no. 2, Apr.-June 1960, pp. 99-102.
3. GOUFFÉ, ANDRÉ: Corrections d'ouverture des corps noirs artificiels compte tenu des diffusion multiples internes. (Aperture Corrections for Arti-

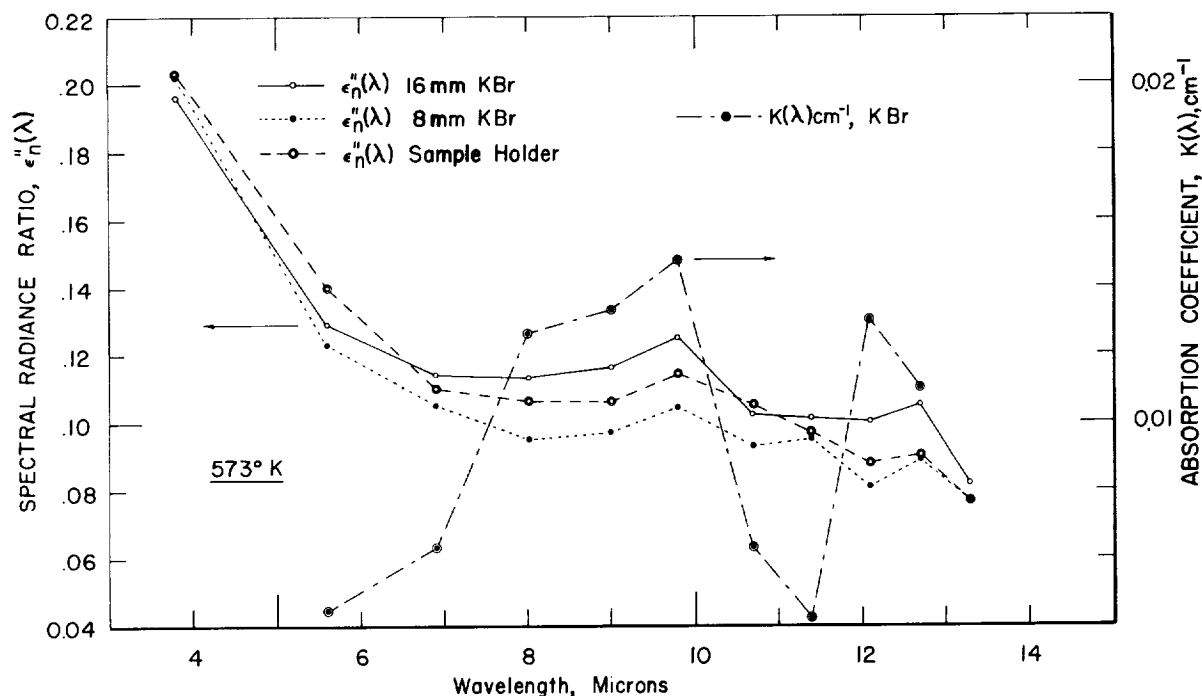


FIGURE 3.—Spectral radiance-ratio spectra of 8- and 16-mm thick samples of potassium bromide at 300° C and preliminary spectral absorption coefficient spectrum of potassium bromide at 300° C, in the wavelength region 4 to 14 microns.

- ficial Black Bodies, Accounting for Multiple Internal Diffusion.) *Revue d'Optique*, vol. 24, nos. 1-3, Jan.-Mar. 1945, pp. 1-10.
4. McMAHON, H. O.: Thermal Radiation From Partially Transparent Reflecting Bodies. *Jour. Optical Soc. of America*, vol. 40, no. 6, June 1950, pp. 376-380.
5. GARDON, ROBERT: The Emissivity of Transparent Materials. *Jour. American Ceramic Soc.*, vol. 39, no. 8, Aug. 1956, pp. 278-287.
6. HAMILTON, R. H.: Photo-Electric Photometry. An Analysis of Errors at High and at Low Absorption. *Ind. and Eng. Chem. (Analyt. Ed.)*, vol. 16, Feb. 17, 1944, pp. 123-126.

APPENDIX: DERIVATION OF EQUATION (3)

Equation (3) may be derived from equations (1) and (2) as follows: Let the specimen with plane parallel faces be placed upon an opaque plane substrate of normal spectral reflectivity $\rho'_s(\lambda)$ and emissivity $\epsilon'_s(\lambda)$ where

$$1 = \rho'_s(\lambda) + \epsilon'_s(\lambda).$$

Then the normal spectral reflectivity of the specimen-substrate combination $\rho''(\lambda)$ is given by

$$\rho''(\lambda) = \rho'(\lambda) + \rho'_s(\lambda)[\tau'(\lambda)]^2[1 - \rho'_s(\lambda)\rho'(\lambda)]^{-1}. \quad (\text{A1})$$

The normal spectral radiance ratio $\epsilon''_n(\lambda)$ of the specimen-substrate combination is equal to the normal spectral emissivity under isothermal conditions. According to Kirchhoff's law, the sum of the normal spectral emissivity and reflectivity is equal to 1; that is,

$$\epsilon''_n(\lambda) = 1 - \rho''(\lambda). \quad (\text{A2})$$

Since $\rho'(\lambda)$ and $\rho_s(\lambda)$ are by assumption much less than 1, the factors $[1 - \rho'_s(\lambda)\rho'(\lambda)]^{-1}$ and $[1 - [\tau_i(\lambda)\rho_s(\lambda)]^2]^{-1}$ in equations (A1) and (1), respectively, can be expanded as convergent power series in $\rho'_s(\lambda)\rho'(\lambda)$ and $[\tau_i(\lambda)\rho_s(\lambda)]^2$, respectively. To first order in $\rho_s(\lambda)$; therefore,

$$\tau'(\lambda) = \tau_i(\lambda)[1 - 2\rho_s(\lambda)] \quad (\text{A3})$$

$$\rho'(\lambda) = \rho_s(\lambda)\{1 + [\tau_i(\lambda)]^2\} \quad (\text{A4})$$

and

$$\rho''(\lambda) = \rho'(\lambda) + \rho'_s(\lambda)[\tau_i(\lambda)]^2[1 - 4\rho_s(\lambda) + \rho'_s(\lambda)\rho'(\lambda)]. \quad (\text{A5})$$

Since $\tau_i(\lambda)$ is approximately equal to $1 - K(\lambda)t$ if the product $K(\lambda)t$ is much less than one, $\epsilon''_n(\lambda)$ is approximately given by

$$\epsilon_n''(\lambda) \approx 1 - 2\rho_s(\lambda)[1 - K(\lambda)t] - \rho_s'(\lambda)[1 - 2K(\lambda)t] \\ \{1 - 4\rho_s(\lambda) + 2\rho_s'(\lambda)\rho_s(\lambda)[1 - K(\lambda)t]\}. \quad (\text{A6})$$

Finally, it is clear that the product $\rho_s(\lambda)K(\lambda)t$ can be ignored to first order of approximation, and so equation (A6) reduces to the approximation

$$\epsilon_n''(\lambda) \approx 1 - \rho_s'(\lambda) - 2\rho_s(\lambda) + 2K(\lambda)t\rho_s'(\lambda) \\ + 4\rho_s(\lambda)\rho_s'(\lambda) - 2\rho_s(\lambda)(\rho_s'(\lambda))^2 \quad (\text{A7})$$

which is the same as equation (3) (with $\epsilon_n'(\lambda)$ replaced by $1 - \rho_s(\lambda)$).

DISCUSSION

RONALD BASCHIERE, General American Transportation Corp.: We are doing some work now for the Air Force on the prediction of temperature distributions through glass materials, so I am very interested in your paper. With regard to measuring radiation coming from your samples, do you correct for the fact that the energy coming from the samples is not only reflected energy but also a combination of the energy that is emitted directly from within the samples and energy that has undergone reflections within the samples? How do you separate these components?

FUSSELL: This is taken into account mathematically. That is why we had to measure two samples to get

the absorption coefficient, and why we could not use just one measurement. Actually, what we did was to take the difference between the results from the 8- and 16-mm thicknesses and compute the absorption coefficient in this manner.

BASCHIERE: I am particularly interested in, for instance, whether you have applied the McMahon correction for the apparent values of radiation as opposed to those that are measured?

FUSSELL: Yes, these have been taken into account.

BASCHIERE: I see. And your measurements are with normal samples?

FUSSELL: Yes, they are normal—not hemispherical.

30. Directional Solar Absorptance Measurements

N. J. DOUGLAS

LOCKHEED MISSILES & SPACE COMPANY, PALO ALTO, CALIF.

A method is presented for determining the solar absorptance of thermal control surfaces as a function of angle of incidence from a knowledge of both the ratio of solar absorptance to the thermal emittance (α_s/ϵ) and the emittance alone. A device which measures (α_s/ϵ) and ϵ of a test disk suspended within an evacuated black cryogenic environment and irradiated by a solar simulator is described. Solar absorptance measurements for incidence angles up to 85° can be accomplished with an uncertainty in the order of 4 to 8 percent. The results associated with directional solar absorptance measurements in the room temperature region for a Mylar-aluminum laminate sample are reported.

Data describing the solar absorptance as a function of incidence angle are necessary to permit accurate thermal design of spacecraft, since Lambert's law is usually an oversimplification of the actual angular absorptance characteristics of surfaces. Previous investigators have shown a definite correlation between absorptance and incidence angle (ref. 1 and 2) but have utilized reflectance measuring techniques which could possibly have inherent sources of error caused by polarization effects, angular selectivity of detectors, specularly, etc. Fresnel's equations in conjunction with electromagnetic theory can be used to provide quantitative information concerning homogeneous isotropic materials with smooth surfaces; but in practice, the theoretical approaches have only limited applicability to the thin, rough, organic coatings that may be used.

SYMBOLS

A	area, ft ²
C_p	specific heat, Btu/lb-°R
E	incident electric vector
I	incident radiation, Btu/ft ² -hr
M	mass, lb
R	reflected electric vector
S	solar constant
T	absolute temperature, °R

k	extinction coefficient
n	index of refraction
\bar{n}	complex index of refraction
r	radius, ft
α	absorptance
δ	thickness, ft
ϵ	emittance
η	multiplicative correction factor for absorptance
$\rho_{\lambda r}$	spectral reflectance obtained by reflectance techniques
θ	incidence angle, deg
θ'	refraction angle, deg
σ	Stefan-Boltzmann constant, Btu/ft ² -hr-°R ⁴
τ	time, hr

Subscripts

c	calorimeter
s	solar radiation (extraterrestrial)
t	test radiation (carbon-arc radiation or sea-level sunlight)
r	derived by reflection-optics studies
w	wall; or wall-temperature radiation

THEORY OF METHOD

In space probe and orbital missions beyond planetary atmospheric influence, radiation constitutes the primary mode of thermal energy transfer experienced by a space vehicle. The thermal energy balance on a suspended test disk in simulated space conditions, namely, within a black cryogenic vacuum chamber and irradiated by a solar simulator, assuming

negligible conduction heat losses, can be expressed as follows:

$$I_t \alpha_t (2r\delta \sin \theta + \pi r^2 \cos \theta) + (\sigma T_w^4) \alpha_w A \\ = \sigma A \epsilon T^4 + MC_p \frac{dT}{d\tau} \quad (1)$$

By assuming

$$\alpha_w \approx \epsilon \text{ (Kirchhoff's law)} \\ T^4 \gg T_w^4$$

Then, at thermal equilibrium

$$\frac{\alpha_t}{\epsilon} = \frac{\sigma A T^4}{(2r\delta \sin \theta + \pi r^2 \cos \theta) I_t} \quad (2)$$

The value of I_t can be determined from the steady-state temperature of a calorimeter irradiated at normal incidence. The calorimeter construction is identical to that of the test disk, and it has an α_t/ϵ value of 1. For the calorimeter, then, equation (2) reduces simply (with $\theta=0$) to

$$I_t = \frac{\sigma A T_c^4}{\pi r^2}$$

Substituting this result into equation (2) gives

$$\alpha_t = \frac{\epsilon T^4}{\left(\frac{2\delta}{\pi r} \sin \theta + \cos \theta\right) T_c^4} \quad (3)$$

The solar absorptance, α_s , can be obtained from α_t by use of a multiplicative correction factor η_r based upon a comparison of the test radiation spectrum with the extraterrestrial solar spectrum (ref. 3). The marked attenuation of ultraviolet radiation in the sea-level sunlight could produce discrepancies for ultraviolet absorbers in the order of 10 percent (ref. 4) unless such a correction is made. The correction is defined as follows:

$$\eta_r = \alpha_s / \alpha_t \quad (4)$$

where the subscript r indicates that the ratio is determined experimentally by reflection optics. The derivation of η_r is shown in appendix A.

Under ideal conditions, it is possible to predict theoretically the angular dependency of solar absorptance for specular surfaces from a knowledge of the optical constants. From Fresnel's equations

$$\frac{R_{\lambda \perp}}{E_{\lambda \perp}} = \frac{-\sin(\theta - \theta')}{\sin(\theta + \theta')} \quad (5)$$

$$\frac{R_{\lambda \parallel}}{E_{\lambda \parallel}} = \frac{\tan(\theta - \theta')}{\tan(\theta + \theta')} \quad (6)$$

where R and E are the amplitudes of the reflected and incident electric vectors, respectively. The solar absorptance can be derived (as in appendix B) as

$$\alpha_s = 1 - \frac{1}{2} \left[\frac{(n_s - \cos \theta)^2 + n_s^2 k_s^2}{(n_s + \cos \theta)^2 + n_s^2 k_s^2} + \frac{\left(n_s - \frac{1}{\cos \theta}\right)^2 + n_s^2 k_s^2}{\left(n_s + \frac{1}{\cos \theta}\right)^2 + n_s^2 k_s^2} \right] \quad (7)$$

by assuming

$$n_s^2 + n_s^2 k_s^2 \gg 1$$

where

- n_s index of refraction of the test material for solar radiation
- k_s extinction coefficient or attenuation index of the test material for solar radiation
- $n_s k_s$ absorption coefficient of the test material for solar radiation

APPARATUS

A stainless-steel, cylindrical-type vacuum chamber, mounted horizontally and maintained at a pressure of approximately 10^{-6} mm Hg by oil diffusion and cryogenic pumping, provides an evacuated environment for the test disk (fig. 1). The view factor from the sample to the sapphire windows located at the chamber end plates is less than $\frac{1}{2}$ percent.

Two concentric, double-walled, liquid, nitrogen-cooled, cylindrical, copper pots, painted black on the inside, are symmetrically positioned inside the vacuum chamber. The pots slide on Teflon studs, which insure complete environmental enclosure when the pots are overlapping, yet, upon separation, enable rapid sample changing through a vacuum-lock valve. The arrangement of Nichrome heater wire in the chamber neck energized by a power supply effectively preheats the test disk in order to



FIGURE 1.—Angular solar absorptance apparatus.

expedite the attainment of steady-state conditions for materials with high α_s/ϵ ratios.

A heliostat consisting of a rigid frame supporting a yoke-mounted, motor-driven mirror projects the solar radiation toward a mirror that

continuously rotates so as to irradiate both faces of the test disk alternately on a time-share basis (through two separate optical systems). The radiation losses are minimized by using sapphire windows and front-surface-aluminized

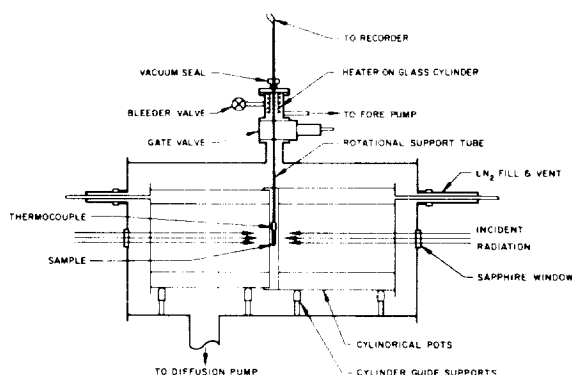


FIGURE 2.—Schematic of angular solar absorptance apparatus.

plane mirrors (fig. 2). The intensity of the carbon-arc or terrestrial solar radiation is monitored by an asymptotic calorimeter or a 180° pyrhelimeter, respectively, in order to insure satisfactory stability during the test runs.

The sample consists of a 1-inch-diameter, 0.030-inch-thick copper disk coated with the test material (fig. 3). Two thermocouple wires at approximately 50° separation are peened into the isothermal substrate. The thermocouple wires supporting the suspended sample are enclosed in a stainless-steel sheath which can be rotated through 360° . The thermocouple output (in millivolts) and pyrhelimeter readings are directly obtained by a Pye precision null-type potentiometer.

This construction provides a simulated space environment allowing directional solar absorptance measurements on candidate thermal control surfaces without requiring reflectance methods.

EXPERIMENTAL PROCEDURE

The operational technique used to establish the angular α , of a sample is to first calibrate the pyrhelimeter by means of a spectrally flat, optically black calorimeter disk having a known α_t/ϵ ratio (equal to 1) and a geometry identical to that of the unknown sample. The pyrhelimeter is standardized by measuring both the equilibrium temperature of the calorimeter and the pyrhelimeter output when both are irradiated by various source inten-

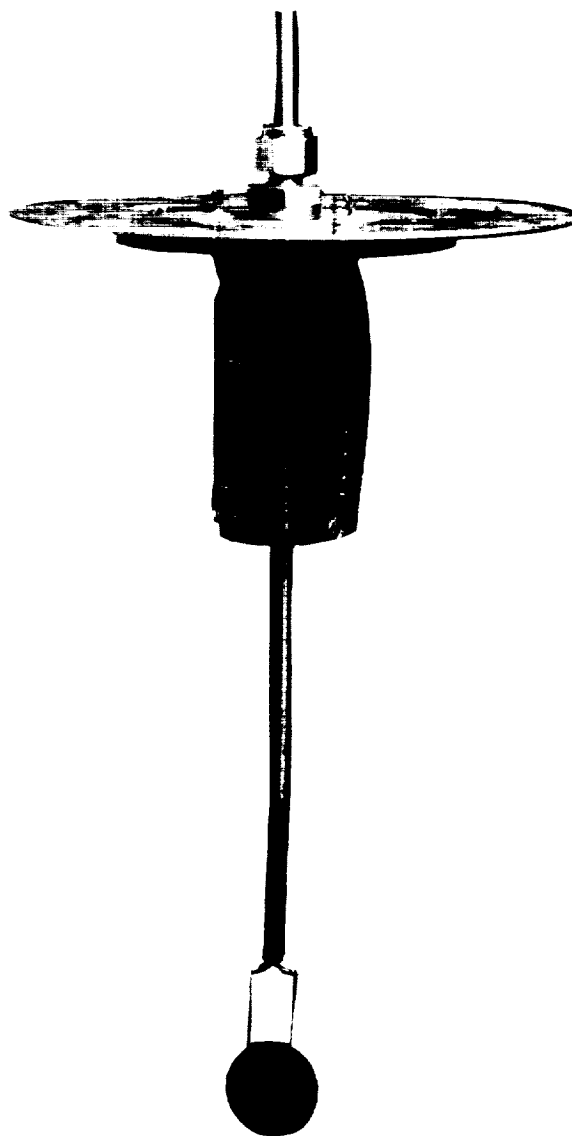


FIGURE 3.—Sample support.

sities. The test sample is then subjected to similar conditions, with the pyrhelimeter-measured intensity simultaneously recorded upon attainment of steady-state conditions at various angles of incidence. The two sapphire window ports are then covered so that the transient cooling curve is obtained. From this curve and specific-heat measurements made by calorimetric methods, the hemispherical emittance can be calculated from the integrated form of equation (1) by assuming

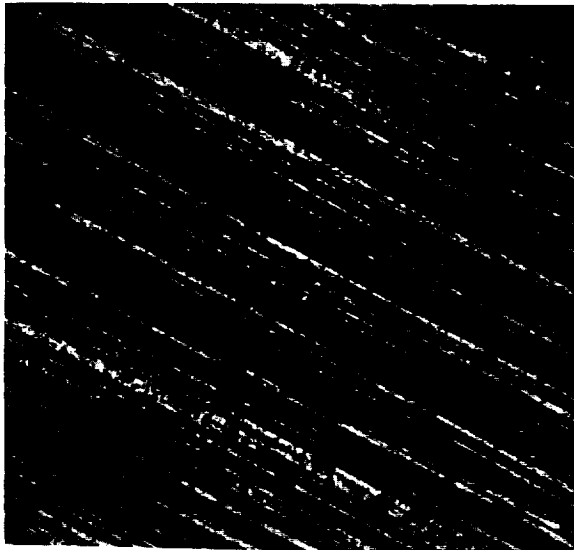
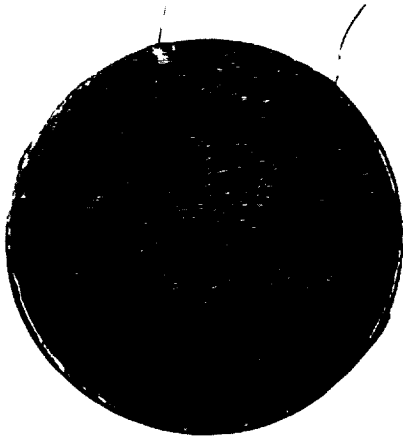


FIGURE 4.—Test sample of Mylar-aluminum laminate. (a) 1-in. diameter test disk, showing thermocouple leads; $2\times$. (b) Photomicrograph showing the striations in the surface; axis of rotation is vertical; $130\times$.

$$I_t = 0$$

$$\alpha_w \cong \epsilon$$

$$T^4 \gg T_w^4$$

so that

$$\epsilon = \frac{MC_p}{3\sigma A \Delta \tau} \left(\frac{1}{T_2^3} - \frac{1}{T_1^3} \right) \quad (8)$$

where T_1 and T_2 are two different temperatures along the cooling curve and $\Delta \tau$ is the corresponding time difference. When this procedure is followed, α_s can be determined for various angular positions by using equations (3), (4), and (8) to obtain

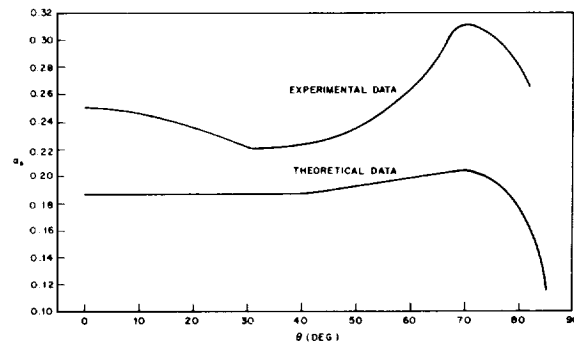


FIGURE 5.—Comparison of theoretical with experimental solar absorptance for Mylar-aluminum laminate.

$$\alpha_s = \frac{\eta_r \epsilon T^4}{\left(\frac{2\delta}{\pi r} \sin \theta + \cos \theta \right) T_c^4} \quad (9)$$

RESULTS

The Mylar-aluminum laminate sample that was tested is not quite isotropic; the striations on the surface are shown in figure 4. The angular dependency of the solar absorptance, as exemplified by the shape of the curve in figure 5, is assumed to have a direct correlation to the anisotropic nature of the surface. The fluctuations in solar absorptance as θ varies can be primarily attributed to interreflections and irradiation of, in effect, only one side of a groove when θ approaches the grazing angle (ref. 5). The fact that the experimentally measured α_s (fig. 5) is higher than the theoretical curve is believed to be related to the surface roughness. The theoretical curve for solar absorptance is based upon equation (7) with $n_s = 0.75$ and $k_s = 4.8$ (ref. 6).

An analysis of the possible error in the determination of α_s as a function of angle was made. The following relation, derived from equation (9), was used:

$$\left(\frac{\Delta \alpha_s}{\alpha_s} \right)^2 = \left(\frac{\Delta \eta_r}{\eta_r} \right)^2 + \left(\frac{\Delta \epsilon}{\epsilon} \right)^2 + 16 \left(\frac{\Delta T}{T} \right)^2 + 16 \left(\frac{\Delta T_c}{T_c} \right)^2 \quad (10)$$

At room temperature, the mean error was found to be in the order of 7 percent. In this analysis it is assumed that:

θ , δ , and r are known exactly.

The uncertainty in the determination of

T or T_c is $\pm 5^\circ$ F from 32° F to 530° F. The primary sources of uncertainty in η_r are the errors in the solar spectrum and test radiation spectrum, assumed to be in the order of 2 percent each.

The emittance can be evaluated to approximately 3 percent.

The spectrum of the test radiation approximates the extraterrestrial solar spectrum so that η_r is assumed independent of θ . The error in $\alpha(\theta)$ for the edge area at the grazing angle can cause perturbation in the shape of the curve in the order of 4 percent.

In arriving at the resultant uncertainty in α_s , consideration has been given to the errors introduced by the following miscellaneous assumptions, but all appear to be negligible compared to the discrepancies listed in equation (10).

$$\alpha_w \approx \epsilon$$

$$T_w^4 \gg T_v^4$$

Reflection from the chamber walls is negligible

$$\alpha_i/\epsilon = \alpha_t/\epsilon = 1 \text{ for the calorimeter}$$

Gaseous conduction is negligible

Thermocouple conduction losses are negligible

View factor to the chamber windows is negligible

CONCLUSION

The limited scope of this program did not permit a more basic theoretical study of the phenomena involved. In view of the differences noted between the experimental and theoretical results on Mylar-aluminum laminate, it is apparent that further experimental studies should be made toward explanation of the results. The results of such a study would make it possible to estimate the behavior of

candidate thermal control surfaces under various orientations and would permit optimum selection of materials for design of space vehicle systems.

ACKNOWLEDGMENTS

The author wishes to express his thanks to R. E. Gaumer, G. R. Cunningham, L. A. McKellar, and R. E. Rolling for their helpful suggestions, and to J. L. Myers for his assistance in the construction of the test apparatus.

REFERENCES

1. NEEL, CARR B.: Measurement of Thermal-Radiation Characteristics of Temperature-Control Surfaces During Flight in Space. NASA paper presented at Ninth National Aerospace Instrumentation Symposium (San Francisco), May 8, 1963.
2. BRANDENBERG, W. M.: The Reflectivity of Solids at Grazing Angles in Measurement of Thermal Radiation Properties of Solids, Joseph C. Richmond, ed. NASA SP-31, 1963, pp. 75-82.
3. GAUMER, R. E.; STREED, E. R.; and VAJTA, T. F.: Methods for Experimental Determination of the Extra-Terrestrial Solar Absorptance of Spacecraft Materials in Measurement of Thermal Radiation Properties of Solids, Joseph C. Richmond, ed. NASA SP-31, 1963, pp. 135-146.
4. OLSON, O. HARRY, and MORRIS, JAMES C.: Determination of Emissivity and Reflectivity Data on Aircraft Structural Materials. WADC Tech. Rep. 56-222, Pt. II, Suppl. I, ASTIA Doc. No. 202494, U.S. Air Force, Oct. 1958.
5. DUNKLE, R. V.; EDWARDS, D. K.; GIER, J. T.; NELSON, K. E.; and RODDICK, R. D.: Heated Cavity Reflectometer for Angular Reflectance Measurements in Progress in International Research on Thermodynamic and Transport Properties, Joseph F. Masi and Donald H. Tsai, ed. ASME, c. 1962, pp. 541-562.
6. SCHULZ, L. G., and TANGHERLINI, F. R.: Optical Constants of Silver, Gold, Copper, and Aluminum. II. The Index of Refraction n . Jour. Optical Soc. of America, vol. 44, no. 5, May 1954, pp. 362-368.

APPENDIX A: DERIVATION OF MULTIPLICATIVE CORRECTION FACTOR

The desired parameter is given by:

$$\alpha_s(\theta) = \frac{1}{S} \int_0^\infty \alpha_\lambda(\theta) S_\lambda d\lambda \quad (A1)$$

The quantity measured by the device is

$$\alpha_t(\theta) = \frac{1}{t} \int_0^\infty \alpha_\lambda(\theta) t_\lambda d\lambda \quad (A2)$$

where

S the solar constant (S_λ is the solar spectral irradiance)

t the normalized test irradiance (t_λ is the normalized test spectral irradiance), the relation between the measured quantity and the desired quantity is assumed to be simply

$$\alpha_s(\theta) = \eta \alpha_t(\theta) \quad (A3)$$

where η , the multiplicative factor, is assumed to be independent of the incidence angle and given by

$$\eta = \frac{t \int_0^\infty \alpha_\lambda(\theta) S_\lambda d\lambda}{\int_0^\infty \alpha_\lambda(\theta) t_\lambda d\lambda} \quad (\text{A4})$$

From reflectance techniques,

$$\rho_{\lambda r} = 1 - \alpha_{\lambda r} \quad (\text{A5})$$

where $\rho_{\lambda r}$ is the spectral reflectance obtained by reflectance techniques.

In general, two types of errors arise, ϵ_0 which is wavelength independent and ϵ_λ which is wavelength dependent.

$$\alpha_{\lambda r}(\theta) = (1 + \epsilon_0)(1 + \epsilon_\lambda)\alpha_\lambda(\theta) \quad (\text{A6})$$

assuming $\epsilon_\lambda \cong 0$

$$\eta \cong \eta_r = \frac{t \int_0^\infty \alpha_{\lambda r} S_\lambda d\lambda}{\int_0^\infty \alpha_{\lambda r} t_\lambda d\lambda} \quad (\text{A7})$$

Therefore

$$\alpha_s(\theta) \cong \eta_r \alpha_t(\theta) \quad (\text{A8})$$

where

$$\eta_r = \alpha_{rr}/\alpha_{tr}.$$

APPENDIX B: DERIVATION OF THEORETICAL ANGULAR SOLAR ABSORPTANCE

From Fresnel's equations,

$$\frac{R_\perp}{E_\perp} = \frac{-\sin(\theta - \theta')}{\sin(\theta + \theta')} = \frac{\frac{\sin \theta'}{\cos \theta'} - \frac{\sin \theta}{\cos \theta}}{\frac{\sin \theta'}{\cos \theta'} + \frac{\sin \theta}{\cos \theta}} \quad (\text{B1})$$

From Snell's law, assuming the sample is in a vacuum,

$$\sin \theta' = \frac{\sin \theta}{\bar{n}} \quad (\text{B2})$$

$$\cos \theta' = \frac{\sqrt{\bar{n}^2 - \sin^2 \theta}}{\bar{n}} \quad (\text{B3})$$

where

- \bar{n} complex index of refraction
- R amplitude of reflected electric vector
- E amplitude of incident electric vector
- \perp component perpendicular to the plane of incidence
- \parallel component parallel to the plane of incidence
- θ angle of incidence
- θ' angle of refraction

$$\frac{R_\perp}{E_\perp} = \frac{\cos \theta - \sqrt{\bar{n}^2 - \sin^2 \theta}}{\cos \theta + \sqrt{\bar{n}^2 - \sin^2 \theta}} \quad (\text{B4})$$

Substituting

$$\bar{n} = n(1 - ik)$$

where k is the extinction coefficient

$$\begin{aligned} \rho_\perp = & \frac{\cos^2 \theta - \cos \theta \sqrt{n^2 - 2in^2k - n^2k^2 - \sin^2 \theta}}{\cos^2 \theta + \cos \theta \sqrt{n^2 - 2in^2k - n^2k^2 - \sin^2 \theta}} \\ & - \frac{\cos \theta \sqrt{n^2 + 2in^2k - n^2k^2 - \sin^2 \theta}}{\cos \theta \sqrt{n^2 + 2in^2k - n^2k^2 - \sin^2 \theta}} \\ & + \frac{\sqrt{(n^2 - 2in^2k - n^2k^2 - \sin^2 \theta)(n^2 + 2in^2k - n^2k^2 - \sin^2 \theta)}}{\sqrt{(n^2 - 2in^2k - n^2k^2 - \sin^2 \theta)(n^2 + 2in^2k - n^2k^2 - \sin^2 \theta)}} \end{aligned} \quad (\text{B5})$$

where ρ_\perp is the reflectance for the perpendicular component,

$$\rho_\perp = \frac{E_\perp}{E_\perp^*} \frac{R_\perp^*}{E_\perp}$$

with * denoting the complex conjugate.

Assuming $n^2 + n^2k^2 \gg 1$, where $|\bar{n}^2| = n^2 + n^2k^2$

$$\rho_\perp = \frac{\cos^2 \theta - 2n \cos \theta + n^2 \sqrt{k^4 + 2k^2 + 1}}{\cos^2 \theta + 2n \cos \theta + n^2 \sqrt{k^4 + 2k^2 + 1}} \quad (\text{B6})$$

$$\rho_\perp = \frac{(n - \cos \theta)^2 + n^2k^2}{(n + \cos \theta)^2 + n^2k^2} \quad (\text{B7})$$

For the parallel component

$$\frac{R_\parallel}{E_\parallel} = \frac{\tan(\theta - \theta')}{\tan(\theta + \theta')} = \frac{(\sin \theta \cos \theta' - \cos \theta \sin \theta')(\cos \theta \cos \theta' - \sin \theta \sin \theta')}{(\cos \theta \cos \theta' + \sin \theta \sin \theta')(\sin \theta \cos \theta' + \cos \theta \sin \theta')} \quad (\text{B8})$$

From equations (B2) and (B3):

$$\frac{R_\parallel}{E_\parallel} = \frac{\frac{1}{\cos \theta} - \frac{\sqrt{\bar{n}^2 - \sin^2 \theta}}{\bar{n}^2 \cos^2 \theta}}{\frac{1}{\cos \theta} + \frac{\sqrt{\bar{n}^2 - \sin^2 \theta}}{\bar{n}^2 \cos^2 \theta}} \quad (\text{B9})$$

Multiplying by its complex conjugate gives

$$\rho_{\parallel} = \frac{1}{\cos^2 \theta} - \frac{\sqrt{n^2 + 2in^2k - n^2k^2 - \sin^2 \theta}}{(n^2 + 2in^2k - n^2k^2) \cos^3 \theta} - \frac{\sqrt{n^2 - 2in^2k - n^2k^2 - \sin^2 \theta}}{(n^2 - 2in^2k - n^2k^2) \cos^3 \theta} + \frac{\sqrt{(n^2 - 2in^2k - n^2k^2 - \sin^2 \theta)(n^2 + 2in^2k - n^2k^2 - \sin^2 \theta)}}{(n^4 + 2n^4k^2 - n^4k^4) \cos^4 \theta}$$

$$\rho_{\parallel} = \frac{1}{\cos^2 \theta} + \frac{\sqrt{n^2 + 2in^2k - n^2k^2 - \sin^2 \theta}}{(n^2 + 2in^2k - n^2k^2) \cos^3 \theta} + \frac{\sqrt{n^2 - 2in^2k - n^2k^2 - \sin^2 \theta}}{(n^2 - 2in^2k - n^2k^2) \cos^3 \theta} + \frac{\sqrt{(n^2 - 2in^2k - n^2k^2 - \sin^2 \theta)(n^2 + 2in^2k - n^2k^2 - \sin^2 \theta)}}{(n^4 + 2n^4k^2 + n^4k^4) \cos^4 \theta}$$
(B10)

$$\rho_{\parallel} = \frac{1}{\cos^2 \theta} - \frac{2}{n \cos^3 \theta (1+k^2)} + \frac{n^2(k^2+1)}{n^4(k^2+1)^2 \cos^4 \theta}$$

$$\rho_{\parallel} = \frac{1}{\cos^2 \theta} + \frac{2}{n \cos^3 \theta (1+k^2)} + \frac{n^2(k^2+1)}{n^4(k^2+1)^2 \cos^4 \theta}$$
(B11)

$$\rho_{\parallel} = \frac{\left(n - \frac{1}{\cos \theta}\right)^2 + n^2k^2}{\left(n + \frac{1}{\cos \theta}\right)^2 + n^2k^2}$$
(B12)

$$\alpha = 1 - \rho = 1 - \frac{1}{2} \left[\frac{(n - \cos \theta)^2 + n^2k^2}{(n + \cos \theta)^2 + n^2k^2} + \frac{\left(n - \frac{1}{\cos \theta}\right)^2 + n^2k^2}{\left(n + \frac{1}{\cos \theta}\right)^2 + n^2k^2} \right]$$
(B13)

where:

$$\rho = \frac{1}{2}(\rho_{\perp} + \rho_{\parallel})$$
(B14)

DISCUSSION

WERNER BRANDENBERG, General Dynamics/Astronautics: I would like to know how you obtained the index of refraction and the extinction coefficient to determine your theoretical curve for the solar absorptance.

DOUGLAS: Let me first say what should be done. By taking the values of n and k , which vary with wavelength, and averaging them (weighting according to the solar spectrum), one can arrive at an n_s and k_s in the same manner that one arrives at values for α_s . I did this to a first approximation for the test material and arrived at the resulting values for n and k .

JACK J. TRIOLO, NASA Goddard Space Flight Center: Was there any attempt to correct for the edge effects at high angles of incidence? Even if it were the same material, the absorptance of the edge would be that for the complementary angle of incidence.

DOUGLAS: The first term in the first equation included a $\sin \theta$ term. This was the projected area of the edge. The ratio of the projected edge area, which in our case is $2r\delta \sin \theta$, to the area of the face ($\pi r^2 \cos \theta$), even when θ is large, such as 80° , will not exceed about 30 percent. Of course, if the edge area were neglected, it would be a serious mistake.

TRILOLO: We had the same setup except that the sample was square, and, as I remember, the projected area of our edge at $\theta = 75^\circ$ was a large percentage of the projected area of the front face.

DOUGLAS: How thick were your samples?

TRILOLO: One-sixteenth of an inch.

DOUGLAS: If you roughly calculate the ratio of projected edge area to face area with our 30-mil-thick, 1-inch diameter samples, I think you will find that even at 80° this is not a major problem area compared with the change in absorptance.

JERRY T. BEVANS, Space Technology Laboratories, Inc.: Can you make a comparison between the accuracy of this method and an analogous measurement spectrally with an integrating sphere?

DOUGLAS: I would say that for the average sample the integrating sphere would perhaps be more accurate and also faster, but this device has a number of advantages. I think that an important purpose of this device is to check on values obtained by the integrating sphere. Also, samples that are transparent or made of some type of mesh or fabric, and materials that have unusual geometric shapes (such as prisms) if they are not too large, can be measured in the α_s device. Another important feature is that the weak temperature dependence of absorptance can be measured by varying the source intensity. So, with these considerations, I think that it has certain advantages over the integrating sphere. Also, an integrating sphere has certain inherent errors due to polarization, the angular selectivity of the detectors, and specularity of certain samples.

BEVANS: I question some of your reasons. With regard to certain types of integrating spheres, I agree with you completely; however, for one specific type, I would disagree heartily. The other point, regarding the actual operating temperature, is as follows: In your device, you have an equilibrium temperature determined by the irradiation and by α_s and ϵ ; but in spacecraft the temperature also depends upon its surroundings or, in essence, on the heat flux through it as well as on just the equilibrium condition.

LOUIS MCKELLAR, Lockheed Missiles & Space Company: The equilibrium temperature of the sample can easily be varied by varying the intensity when you are using a carbon arc. Thus, you can get a controlled temperature independent of α_s/ϵ with this device and still measure α_s/ϵ .

LIONEL BAILIN, Lockheed Missiles & Space Company: I would like to pose this thought—that Fresnel's equations, which are derived essentially for the specular condition, are fine when you use your equipment for specular measurements. In systems which are more diffusely reflecting, there will be a certain error, which

may be the difference which Douglas has shown between the theoretical and the observed curves.

DOUGLAS: I have to agree. There are many limitations to this theory, and it is an oversimplification of the actual case, but it does give some indication of what the magnitude of the absorptance should be.

31. A Thermal Vacuum Technique for Measuring Solar Absorptance of Satellite Coatings as a Function of Angle of Incidence

MARLA G. HOKE

NASA GODDARD SPACE FLIGHT CENTER, GREENBELT, MARYLAND

An experimental technique for measuring the solar absorptance of a satellite coating as a function of angle of incidence has been developed. A thermal vacuum method is used to measure the equilibrium temperature of a coated sample that may be turned so that it makes any desired angle to the incident beam. The sample is turned by means of a rotational apparatus installed in the vacuum chamber. Preliminary measurements of the directional solar absorptance of the following materials have been made: evaporated aluminum, evaporated gold, aluminum leafing paint, zinc sulfide paint, and Parson's black paint. The hemispherical solar absorptance of evaporated aluminum is calculated.

A fundamental problem in the analysis and design of temperature-controlled spacecraft is the prediction of the equilibrium temperature of the satellite in orbit. In order to solve the radiation balance equation for the equilibrium temperature of a satellite, the solar absorptance of the spacecraft surface is usually required. The surfaces of the craft usually do not lie perpendicular to the incident solar radiation; therefore, it is of fundamental importance to know the solar absorptance of a coating as a function of angle of incidence.

In the technique to be described herein, the angular solar absorptance of a coating is determined from the equilibrium temperature of the sample coating suspended in an evacuated chamber and illuminated by a source whose spectral distribution is similar to that of the sun. A rotating-frame apparatus allows the sample, placed in the frame, to be turned to different angles with respect to the incident illumination. Since a gear coupling was employed to rotate the frame, a calibration technique, which used the optical method of superposition of reflected and incident parallel

beams, was devised in order to determine the true angular position of the sample.

Directional solar absorptances of the following materials were measured: evaporated aluminum, evaporated gold, aluminum leafing paint, zinc sulfide paint, and Parson's black paint. The results for evaporated aluminum appear to agree well with theoretical expectations based on the Fresnel equations. The evaporated aluminum data were used to illustrate the calculation of the surface-average solar absorptance for a sphere.

ROTATIONAL APPARATUS

Design and Alinement of Sample Holders and Support Shafts

The apparatus designed for this experiment consists of two sample holders and the hardware necessary for adapting the system for installation through the existing vacuum system base plate.

The sample holders are $\frac{1}{4}$ -inch stainless steel rods welded into a trapezoid shape (fig. 1). Each frame is connected to its supporting

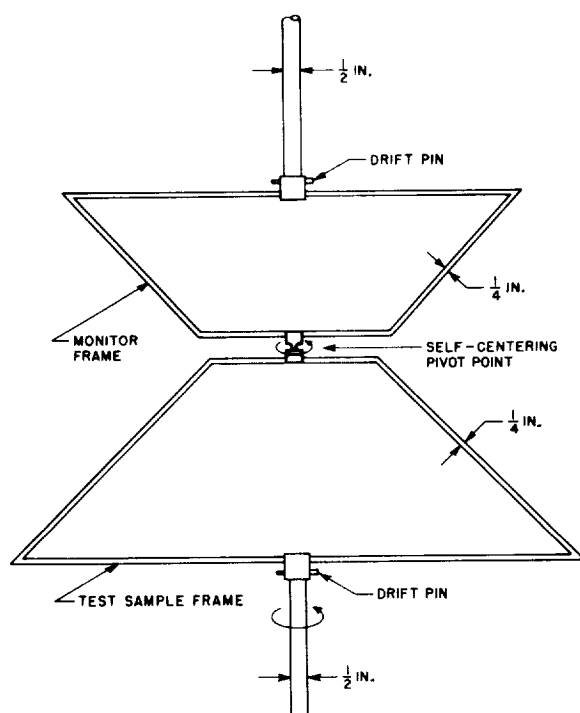


FIGURE 1.—Connection and rotation detail of frames.

shaft with a drift pin which permits removal of each frame while changing samples without disturbing the angle calibration. The upper frame, which remains in a fixed position in the vacuum chamber, holds the monitor sample, which monitors the relative intensity of the incident light. The lower frame, which holds the test sample, rotates about a self-centering pivot point.

The test sample used with this experiment is a 1.5-inch-diameter by 0.062-inch-thick copper sheet covered with the test coating. The monitor is a 1.25-inch-square by 0.005-inch-thick beryllium copper sheet coated with a black paint (carbon black, Cat-O-Lac black, Parson's black). In the center of the back face of each sample a copper-constantan thermocouple junction is imbedded. Four fiberglass strings are attached to each sample for mounting purposes. Figure 2 shows the position of the samples when mounted in the frames. Four screw-down washers on each frame secure the sample strings. The two thermocouple wires pass through

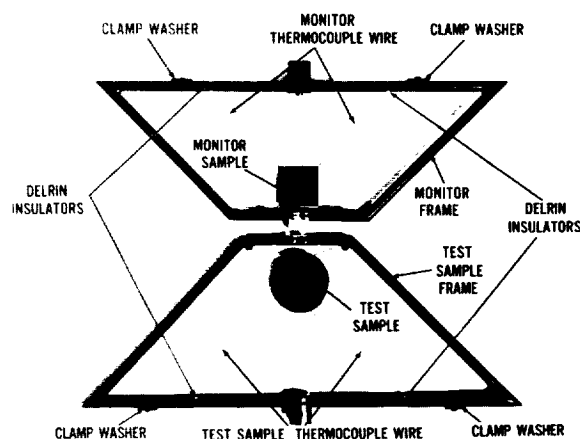


FIGURE 2.—Monitor and test-sample frames with samples mounted in testing position.

Delrin¹-insulated holes in the frames so that they do not tangle during the rotation of the sample.

The frames were painted with Cat-O-Lac black paint (solar absorptance of 0.95) in order to minimize reflections from the frames to the samples. The trapezoid design was the result of an attempt to minimize diffuse radiation emitted from the frames to the samples. If the frame surfaces emit according to Lambert's law, it can be shown geometrically that the rate of radiation from a trapezoid-shaped *monitor frame* to the *test sample* will be approximately 10 percent less than the rate of radiation from a rectangular-shaped monitor frame to the test sample. Since the test-sample frame is also trapezoidal in shape, the 10-percent reduction in radiation rate also applies when considering the rate of radiation from the *test-sample frame* to the *monitor sample*.

The assembled apparatus as it appears in the high-vacuum chamber is sketched in figure 3. The axis of the shafts was established by dropping a plumb line from the top plate of the shroud. The shafts are made of aluminum for greater thermal conductivity as compared to stainless steel, and they are in thermal contact

¹ Delrin: an acetyl resin compound of low thermal conductivity and excellent strength; available through E. I. DuPont de Nemours and Company, Wilmington, Delaware.

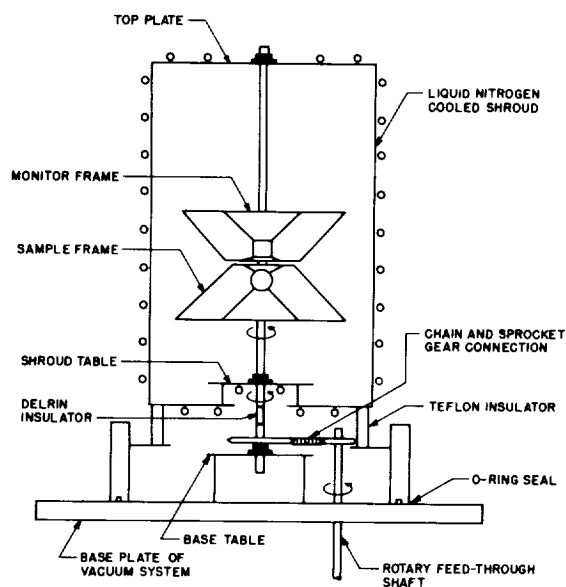


FIGURE 3.—Cross section of the shroud with rotation apparatus installed.

with the liquid-nitrogen-cooled shroud at its top plate and its table. A Delrin insulator was inserted in the aluminum shaft below the shroud table to eliminate heat conduction from the shroud table through the base table to the base plate, since the shroud is thermally insulated from the base plate as shown. Bearings at the shroud table and the base table facilitate the rotation of the lower frame. A chain and sprocket gear arrangement with a 4 to 1 ratio couples the main shaft with the rotary feed-through shaft. A 180° turn of the rotary feed-through shaft then produces a 45° turn of the sample.

Calibration of Sample Holder

In order to know the angular displacement of the sample with respect to the incident light as the rotary feed-through shaft is turned, an optical method of calibrating the system was devised, in which plane reflecting surfaces fixed to the sample frame were made to reflect a narrow-slit light beam back on itself.

A 2.5-inch-diameter lucite disk with three plane, mirrored faces was used as the reflection optics. As shown in figure 4, face 1 was machined parallel to the screw hole center line

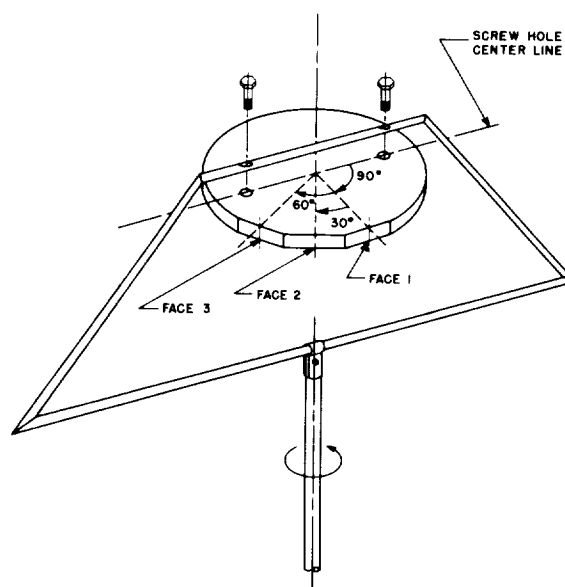


FIGURE 4.—Lucite reflecting disk mounted in rotating frame.

(plane of frame) so that when the disk is mounted in the sample frame, face 1 is parallel to the plane of the frame. Face 2 is then 30° and face 3 is 60° from the plane of the frame. As the shaft connected to the sample frame is rotated, one face comes into perpendicularity with an incident beam at 0°, 30°, and 60°.

An 8-inch collimator was modified to allow light from a high-intensity lamp to enter a 1/2-inch-diameter hole in a diaphragm located at the focal point of its objective. The objective beam was reduced from a 2.5-inch-diameter beam to a 1/16-inch by 1/2-inch vertical slit beam to eliminate the paraxial rays of the objective. The collimator was fastened to an adjustable table and was carefully leveled.

An initial step in the actual calibration involved establishing an axis perpendicular to the vacuum chamber port window. This step involves movement of the collimator table until the beam from the objective slit is reflected by the port window back on itself. At this point the collimator and its table are fixed in position. The lucite disk is then positioned in the rotary frame and is placed in the chamber. As the frame is rotated, face 1 becomes perpendicular to the collimator beam. When this position is

located, the 0° angular displacement of the sample frame is determined. Face 2 and face 3, the 30° and 60° faces respectively, are brought into normality by further rotation of the frame. These three angular positions were marked during the first calibration of the system on a brass blank dial located around the rotary feed-through handle. A dividing head instrument was used to determine the true angular distance between the three positions. Angle marks from 0° to 90° were then engraved on the disk relative to the three reference marks.

The final phase of the alinement involves positioning the carbon arc light source so that its collimated beam lies along the already established axis of the collimator beam and the reflected beam from the lucite disk. A diaphragm with a small pinhole was placed in front of the arc crater, and a second diaphragm with a pinhole was placed over the collimator lens of the arc lamp. A small beam of light through the pinholes was established by placing a light source in the arc crater. Movement of the entire arc lamp unit then allowed this beam to pass entirely through the collimator and onto the port of the bell jar, at which point the two beam axes coincided.

PROCEDURE FOR OBTAINING THE SOLAR ABSORPTANCE $\bar{\alpha}(\theta)$

Determination of $\bar{\alpha}/\bar{\epsilon}$

The high-vacuum chamber employed for these tests operates at a base pressure of 2×10^{-7} torr. A liquid-nitrogen-cooled cylindrical shroud, located inside the bell jar, provides cold-wall, high-absorptance surroundings for the samples. The solar simulator is a high-intensity arc lamp which is collimated with an $8\frac{1}{2}$ -inch-diameter quartz lens. Temperatures of the test sample, the monitor sample, and other points within the chamber are monitored by a multipoint recorder. Sample temperatures have also been monitored by using a manually balanced potentiometer bridge.

Thermal vacuum methods measure the $\bar{\alpha}/\bar{\epsilon}$ or $\bar{\epsilon}$ of a satellite coating by the equilibrium temperature or the rate of temperature change of the materials. The method employed for

this experiment is an equilibrium temperature measurement method in which the sample is heated by the solar simulator until equilibrium temperature is reached. This measurement, as opposed to an alternative method, the transient thermal vacuum technique eliminates the error involved in extrapolating the curve of dT/dt against σT^4 to $dT/dt=0$.

After the samples are mounted in their frames and placed in the vacuum system, the chamber is pumped down to 2×10^{-7} torr and the walls of the shroud are cooled to approximately -193° C. The samples are then heated by the solar simulator until the thermocouple sensors indicate that both the monitor and the test sample have reached their equilibrium temperatures. This condition is maintained for as long as 15 to 20 minutes in order to insure that there is no slow variation in the temperature of the test sample. The black monitor sample, which comes to equilibrium faster than the test sample because of its small time constant, has a twofold purpose:

(1) Because of its small time constant, the monitor sample reveals drift in arc intensity before the test sample temperature is affected appreciably, and thus permits a quicker manual readjustment by repositioning the negative carbon in the arc lamp.

(2) The equilibrium temperature of the monitor sample determines the absolute intensity of the beam.

For each angle of incidence to which the test sample is turned, heating is continued until an equilibrium temperature is maintained. At angles of incidence beyond 30° to 45° the projected area of the test sample is so much reduced that the time required to attain equilibrium increases by a factor of two or more over the time required at smaller angles. In order to decrease the time required to reach equilibrium temperature at larger angles, the sample is heated at normal incidence to a temperature near the expected equilibrium temperature and is then rotated to the desired angle for the exact temperature measurement.

The time rate of change of the thermal energy of a sample is equal to the power absorbed by the sample of projected area A_p , plus the power P absorbed from incident thermal radiation

from the walls of the shroud and the quartz window, minus the thermal power radiated from the total surface area A_s of the sample. The heat balance equation is therefore

$$mc \frac{dT}{dt} = A_p \bar{\alpha} I + P - A_s \bar{\epsilon} \sigma T^4 \quad (1)$$

where

- m mass of sample
- I total irradiated power per unit area of solar simulator
- c specific heat of sample substrate
- T temperature
- σ Stefan-Boltzmann constant
- $\bar{\alpha}$ average solar absorptance of illuminated area of sample (this depends on direction of incident illumination)
- $\bar{\epsilon}$ average thermal emittance of sample
- t time

At thermal equilibrium the change in sample temperature with time is zero; therefore equation (1) becomes

$$0 = A_p \bar{\alpha} I + P - A_s \bar{\epsilon} \sigma T^4. \quad (2)$$

If P , the power absorbed from incident thermal radiation from the walls of the vacuum chamber, is assumed to be negligible, equation (2) becomes

$$0 = A_p \bar{\alpha} I - A_s \bar{\epsilon} \sigma T^4,$$

from which

$$\frac{\bar{\alpha}}{\bar{\epsilon}} = \frac{A_s}{A_p} \frac{\sigma T^4}{I}. \quad (3)$$

A complete description of thermal vacuum methods for measuring the absorptance and emittance properties of spacecraft materials and a description of the equipment employed for these measurements at the Goddard Space Flight Center is given by Fussell, Triolo, and Henninger in reference 1.

Calculation of $\bar{\alpha}(\theta)$

The $\bar{\alpha}/\bar{\epsilon}$ of a coating is a function of the angle of incidence of the beam. Hence, equation (3) is written

$$\frac{\bar{\alpha}}{\bar{\epsilon}}(\theta) = \left(\frac{A_s}{A_p} \frac{\sigma T^4}{I} \right)_{\theta, s} = \frac{\bar{\alpha}(\theta)}{\bar{\epsilon}} \quad (4)$$

where the subscript θ, s signifies that the values are for the angle of incidence θ of the test sample. The $[\bar{\alpha}/\bar{\epsilon}](\theta)$ is assumed equal to $\bar{\alpha}(\theta)/\bar{\epsilon}$; that is, we assume the $\bar{\epsilon}$ of a sample is not temperature dependent [$\bar{\epsilon}(T\theta) = \bar{\epsilon}$]. This assumption is not valid; however, at the present time the error in an emittance measurement made by using a thermal vacuum technique would completely obscure the small correction for the change in $\bar{\epsilon}$ with temperature. For normal incidence, equation (4) is written

$$\frac{\bar{\alpha}}{\bar{\epsilon}}(0^\circ) = \left(\frac{A_s}{A_p} \frac{\sigma T^4}{I} \right)_{0^\circ, s} = \frac{\bar{\alpha}(0^\circ)}{\bar{\epsilon}}. \quad (4a)$$

Dividing equation (4) by equation (4a) gives

$$\frac{\bar{\alpha}(\theta)}{\bar{\alpha}(0^\circ)} = \left(\frac{A_{p, 0^\circ}}{A_{p, \theta}} \frac{T_\theta^4}{T_{0^\circ}^4} \frac{I_{0^\circ}}{I_\theta} \right)_s. \quad (4b)$$

A similar set of equations may be written for the monitor sample. However, since the monitor is not rotated from one test to the next, the equation that corresponds to equation (4b) is

$$1 = \left(\frac{T_\theta^4}{T_{0^\circ}^4} \frac{I_{0^\circ}}{I_\theta} \right)_m \quad (5)$$

where the subscripts 0° and θ refer to the values at the times when the test sample is at the angles 0° and θ , and m stands for monitor. Equation (5) gives the intensity ratio

$$\frac{I_{0^\circ}}{I_\theta} = \left(\frac{T_{0^\circ}^4}{T_\theta^4} \right)_m. \quad (5a)$$

Substituting equation (5a) into equation (4b) gives

$$\frac{\bar{\alpha}(\theta)}{\bar{\alpha}(0^\circ)} = \left(\frac{A_{p, 0^\circ}}{A_{p, \theta}} \frac{T_\theta^4}{T_{0^\circ}^4} \right)_s \left(\frac{T_{0^\circ}^4}{T_\theta^4} \right)_m. \quad (6)$$

The projected area of the test sample $A_{p, \theta}$ in equation (6) changes as the sample is rotated to different angles:

$$A_{p, \theta} = A_{p, s} \cos \theta + A_{p, e} \sin \theta$$

where $A_{p, s} \cos \theta$ is the projected area of the sample face at angle θ , and $A_{p, e} \sin \theta$ is the projected area of the sample edge at angle θ .

The final step in determining $\bar{\alpha}(\theta)$, the directional solar absorptance, is to measure $\bar{\alpha}(0^\circ)$ by an independent method. For this measurement an optical method is used which employs a Beckman DK-2 spectrophotometer with an integrating sphere reflectance attachment. The value found by the optical method is used in the following equation:

$$\frac{\bar{\alpha}(\theta)}{\bar{\alpha}(0^\circ)} \bar{\alpha}(0^\circ)_{\text{optical}} = \alpha(\theta) \quad (7)$$

Future measurements will include the change in emittance with temperature of each test coating. A modified Dymec 2010C Data Acquisition System will be used for recording sample temperatures, along with thermocouples calibrated from -200°C to $+100^\circ\text{C}$. These modifications will increase the accuracy of the temperature readings from ± 0.7 percent to ± 0.008 percent. From the general heat balance equation (1) (with $I=0$ and $P=0$) the slope of the cool-down curve of the sample is

$$\frac{dT}{dt} = \frac{A_s \bar{\epsilon}(T) \sigma T^4}{mc(T)}.$$

For a temperature interval ΔT_1 of 5° or less, the emittance at the mean temperature \bar{T}_1 of the interval would be

$$\bar{\epsilon}(\bar{T}_1) = \frac{mc(\bar{T}_1) \Delta T_1}{A_s \sigma \bar{T}_1^4 \Delta t}. \quad (8)$$

The change in the specific heat of the sample substrate with temperature will also be considered.

EXPERIMENTAL RESULTS

The solar absorptances of the five selected coatings as functions of angle from the normal are presented in figures 5 to 9. In most cases, measurements were terminated at $\theta=75^\circ$ because of the large percentage of the illuminated edge area of the test sample at these larger angles. Measurements beyond 75° have been tried with some coatings; however, the results indicate that errors due to irradiation of the edge area were present.

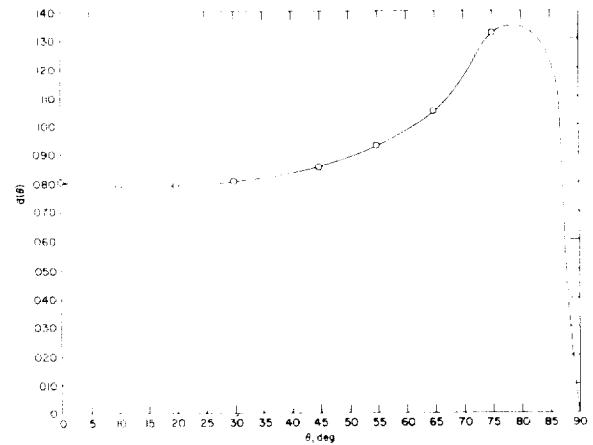


FIGURE 5.—Directional solar absorptance of evaporated aluminum (average of two sets of data).

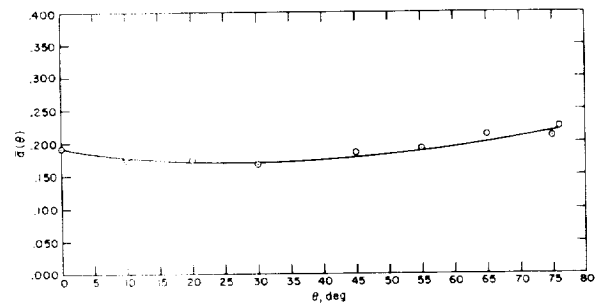


FIGURE 6.—Directional solar absorptance of evaporated gold.

Values of the directional solar absorptance of a coating as presented in figures 5 to 9 are essential for calculating the amount of radiation absorbed by a spherical vehicle. By appropriately integrating over the surface of a hemisphere one obtains (ref. 2) the following expression for the hemispherical solar absorptance:

$$\bar{\alpha}_H = 2 \int_0^{\pi/2} \bar{\alpha}(\theta) \sin \theta \cos \theta d\theta. \quad (9)$$

The data for evaporated aluminum, presented in figure 5, will be used to demonstrate the calculation of $\bar{\alpha}_H$. The extrapolated (dashed) section of the curve in figure 5 was used for values of θ greater than 75° . It can be shown

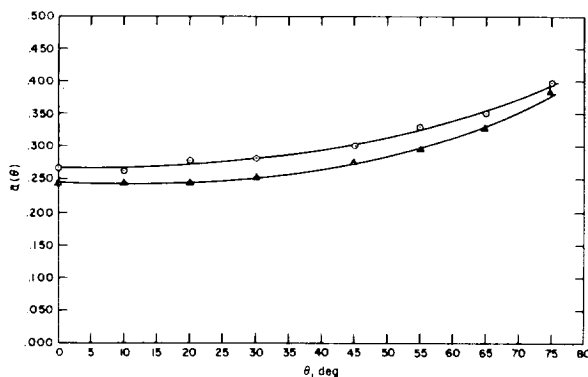


FIGURE 7.—Directional solar absorptance of aluminum leafing paint.

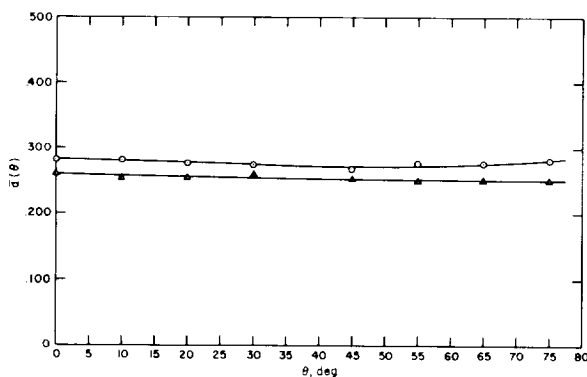


FIGURE 8.—Directional solar absorptance of zinc sulfide paint.

that, whatever the true curve is in this high-angle region, the extrapolated curve in all probable cases is in error by no more than 3 percent.

Figure 10 shows the plot of the integrand of equation 9 from $\theta=0^\circ$ to $\theta=90^\circ$ for the evaporated aluminum. Mechanical integration of the curve yields the value

$$\bar{\alpha}_H = 0.0926$$

which is within 2 percent of the theoretical value obtained by Hass² by using the Fresnel equations of the exact form (ref. 3, chapter 4). For a particular opaque coating with optical con-

² Private communication from G. HASS, USAERDL, Fort Belvoir, Va.

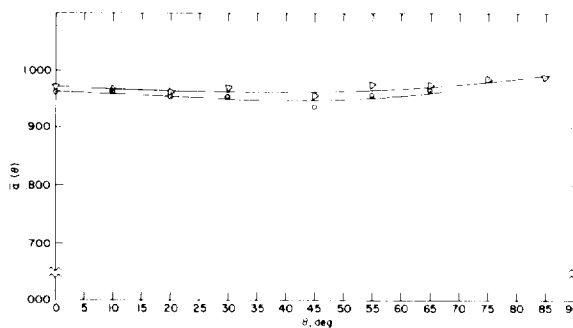


FIGURE 9.—Directional solar absorptance of Parson's black paint.

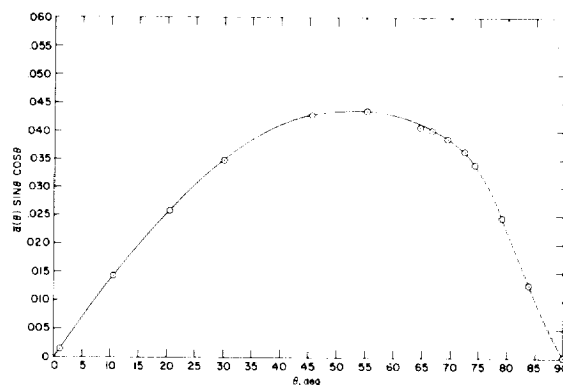


FIGURE 10.—Plot of integrand of equation (9) for evaporated aluminum data (fig. 5).

$$\bar{\alpha}_H = 2 \int_0^{\pi/2} \bar{\alpha}(\theta) \sin \theta \cos \theta \, d\theta.$$

$$\text{Area value under curve} = 0.0463.$$

$$\bar{\alpha}_H = 0.0926.$$

stants $n(\lambda)$ and $k(\lambda)$ the hemispherical solar reflectance \bar{r}_H of the coating is obtained by integrating the Fresnel equations over the solar spectrum and over a hemispherical surface. The hemispherical solar absorptance is then $1 - \bar{r}_H = \bar{\alpha}_H$.

MAJOR ERRORS AFFECTING THE ACCURACY OF $\bar{\alpha}(\theta)$

The errors affecting the accuracy of the $\bar{\alpha}(\theta)$ values have been considered in two groups: those which limit the accuracy of the angular setting of the sample, and those involved in the thermal equilibrium experiment.

Errors in the angular setting of the test sample are random and evolve during the cali-

bration process. First, there exists an error in the accuracy with which the reflected beam from the lucite disk can be superimposed on the incident beam. This error is estimated to be $\Delta\theta_1 = \pm 0.04^\circ$. Second, there is an error $\Delta\theta_2$ in the alinement of the arc lamp for normal incidence. A calculation indicated that $\Delta\theta_2 = \pm 0.19^\circ$. A third error is involved in marking the 0° , 30° , and 60° reference marks and the subsequent engraving of the brass dial; the maximum error is estimated as $\Delta\theta_3 = \pm 0.25^\circ$.

The total random error $\Delta\theta$, combining $\Delta\theta_1$, $\Delta\theta_2$, and $\Delta\theta_3$, is $\Delta\theta = \pm 0.32^\circ$. Since the projected area of the sample A_p is a function of θ , the $\Delta\theta$ error produces an angle-dependent error in A_p . A calculation shows that for normal incidence the error in the A_s/A_p ratio is ± 0.25 percent; at 75° the error increases to ± 3 percent.

The major error that limits the accuracy of the thermal equilibrium experiment is the measurement of the equilibrium temperature of the sample. In the present system, the accuracy of the $\bar{\alpha}/\epsilon$ ratio is ± 2.8 percent. With more accurately calibrated thermocouples this error should be reduced to ± 0.32 percent. This is a random error and cannot be corrected.

As previously mentioned, possible sources of error due to the variation of thermal emittance with temperature of the sample coating and the variation of specific heat with temperature of the sample substrate do exist but are small compared with the temperature measurement error.

A second source of possible error (systematic), neglected in this experiment, is radiation reflected onto the sample from the back of the cylindrical shroud.

The total percentage error in the $\bar{\alpha}(\theta)$ values determined in this experiment is expressed as

$$\Delta\bar{\alpha}(\theta) = \sqrt{(2.8)^2 + (1.5)^2 + \left(\Delta\frac{A_s}{A_p}\right)_\theta^2},$$

where

2.8 = percentage error in equilibrium temperature measurements

1.5 = percentage error in $\bar{\alpha}(0^\circ)$ measurement using the Beckman DK-2 Spectrophotometer for evaporated

aluminum (the error is dependent on the reflectance of the material)

$\left(\Delta\frac{A_s}{A_p}\right)_\theta$ = percentage error in A_s/A_p ratio, which is dependent on θ .

The difference in spectral distribution between the solar simulator and the sun is a source of error for which no correction was made in these measurements. This error is difficult to estimate, but it can be seen that since $\bar{\alpha}(\theta)$ is calculated by taking the ratio of

$$\frac{\bar{\alpha}(\theta)}{\bar{\alpha}(0^\circ)} (\bar{\alpha}(0^\circ)_{\text{optical}}),$$

where $\bar{\alpha}(0^\circ)_{\text{optical}}$ is appropriately weighted for the solar spectrum, less error due to the mismatch is present than if only the $\bar{\alpha}/\epsilon$ of the coating were measured.

CONCLUSIONS

An acceptably accurate method for measuring the solar absorptance of satellite coatings as a function of angle of incidence has been established. This method involves a precise rotational apparatus and an already established reliable method of measuring the $\bar{\alpha}/\epsilon$ of satellite coatings by using a thermal vacuum equilibrium technique.

Directional solar absorptances for five different selected coatings have been measured. The data obtained from these measurements can be used to calculate the hemispherical and cylindrical absorptances of typical spacecraft materials. The hemispherical absorptance of evaporated aluminum, as determined in this way, compares closely with a theoretical value. The continued close agreement of experimental values with theory for single layered samples will justify possible future measurements of complicated layered samples, and their acceptance as being reliable.

FUTURE IMPROVEMENTS AND MODIFICATIONS

Improvements to the present experiment which will be incorporated in future modifications are the following:

1. A direct method for rotating the sample frame which eliminates gear backlash,

gear slippage, and tedious calibration. Such a method would incorporate a Decitrak shaft-position encoder³ coupled to the rotating shaft of the sample frame. This encoder has a resolution of 0.1°.

2. The off-center positioning of the sample frame would minimize any error due to refocusing on the sample of arc light incident on the rear wall of the shroud.
3. An "edgeless" test sample so that errors in the $\bar{\alpha}(\theta)$ values due to edge effects at large angles of incidence will be minimized. A plano-convex sample has

been suggested. Such a sample will make measurements up to 85° feasible.

REFERENCES

1. FUSSELL, W. B., TRIOLO, J. J., and HENNINGER, J. H.: A Dynamic Thermal Vacuum Technique for Measuring the Solar Absorptance and Thermal Emittance of Spacecraft Coatings. NASA TN D-1716, Mar. 1963.
2. DRUMMETER, L. F., JR., and FOWLER, W. B.: Emittance and Absorptance of Pure Aluminum. NRL itr 7360-412, Ser: 10543, U.S. Naval Res. Lab., Nov. 1959.
3. HEAVENS, O. S.: Optical Properties of Thin Solid Films. Academic Press, Inc. (New York), 1955, Chapter 4.

³ Decitrak, Model DE-1-40-B-2-A-CW, made by Theata Instrument Corporation, Saddle Brook, New Jersey.

32. The Directional Spectral Emittance of Surfaces Between 200° and 600° C

W. M. BRANDENBERG AND O. W. CLAUSEN

GENERAL DYNAMICS/ASTRONAUTICS, SAN DIEGO, CALIF.

An apparatus is described for making emittance measurements of flat samples at angles of emission between 15° and 80°, temperatures between 200° and 600° C, and wavelengths between 1 and 25 μ . The samples are placed in a vacuum of approximately 5×10^{-6} mm Hg and are surrounded by a liquid-nitrogen cooled wall to eliminate the effects of extraneous heat sources. For a platinum mirror the angular dependence of the emissivity is compared to that given by the Fresnel equation. Also, the angular dependence of a grooved surface with a black base and highly reflecting side walls was measured and compared to theory. Finally the normal emittance of a black paint as a function of wavelength and temperature was determined.

With the projected increase in the power dissipation rates of future space vehicles comes the likelihood that some surfaces of these space vehicles will have to operate at temperatures as high as 600° C. Many of the space power systems being proposed already have this requirement. It is, therefore, important to measure the emittance characteristics of surfaces at these temperatures; furthermore, the measurements must be made in vacuum in order to avoid oxidation damage. Spectral data are particularly valuable since they allow calculation of the emittance of the coating at a given temperature or the absorptance of the coating for blackbody radiation at some other temperature.

An apparatus is described in the next section for making spectral emittance measurements within the following ranges of the basic parameters:

Wavelength.....	1 μ to 25 μ
Angle of emission.....	25° to 80°
Temperature.....	200° C to 600° C

In order to show the capability of this apparatus the angular dependence of emissivity of a platinum mirror and of a specially grooved surface with highly reflecting sides and black

base were measured. The data for the platinum are then compared with values calculated from the Fresnel equation, and the grooved-surface data are compared with the theory presented in reference 1. In addition, the normal spectral emittance of a black ceramic paint was measured as a function of temperature in order to evaluate its stability and over-all applicability as a black paint for the reference hohlraum. A discussion of the errors associated with the data is also presented in this report.

SYMBOLS

E_s	Energy at detector when viewing the sample
E_b	Energy at detector when viewing the blackbody reference
E_0	Energy at detector when viewing the vacuum chamber walls at 77° K
λ	Wavelength, μ
T_s	Sample temperature, °K
T_b	Cavity or blackbody temperature, °K
δT_s	$T_b - T_s$, °K
ϵ_λ	Emittance of sample at wavelength λ
$i_{s,\lambda}$	Blackbody intensity at temperature T_s and wavelength λ , watts/cm ² - μ
$i_{b,\lambda}$	Blackbody intensity at temperature T_b and wavelength λ , watts/cm ² - μ
c_2	Second radiation constant, 1.4387×10^4 μ -°K
η	Angle between normal to the surface and emitted ray

ϵ_η	Emissivity at angle of emission η
θ	Groove angle
d	Length of groove wall between apex and base (fig. 4)
D	Length of groove wall between apex and top (fig. 4)
n	Index of refraction
k	Extinction coefficient

EXPERIMENTAL APPARATUS

A drawing of the vacuum chamber and the blackbody cavity which were designed for this experiment is shown in figure 1. The sample consists of a cylindrical copper block (2 inches in diameter, $2\frac{1}{4}$ inches long) one face of which is machined into a rectangular sample surface ($\frac{5}{8} \times 2$ inches). Below the sample surface a cavity is milled out which, after being painted with PT 404 black paint (Products Techniques, Inc.), is used as a reference hohlraum. An electric heater made from 0.045-inch-diameter Nichrome wire wound on a $2\frac{5}{8}$ -inch diameter alundum tube surrounds the copper cylinder. A radiation shield made of thin highly polished aluminum covers the heater. A thin gold-plated face plate with two rectangular openings, one for the sample and the other defining the aperture of the cavity, covers the front face of the copper cylinder. To prevent any energy transfer by conduction, this face

plate does not touch the sample surface. Two Chromel-Alumel thermocouples are attached to the copper cylinder, one at the back face of the cavity and the other immediately behind the sample surface. The thermocouples are connected such that the cavity temperature as well as the temperature difference between cavity and sample can be determined. In order to minimize heat losses through the thermocouple wires they are guided through the cavity before being passed through the cavity face plate.

The cavity assembly is mounted to, but thermally insulated from, a shaft which extends through the cover of the vacuum tank. The axis of this shaft lies in the plane of the sample surface, so that by turning the cavity assembly the emittance can be measured as a function of the angle of emission. The vacuum tank has a double wall filled with liquid nitrogen to minimize the effect of extraneous heat sources on the measurements. Foam insulation surrounds this liquid nitrogen jacket. The inside of the tank is coated with a "3M" velvet black paint to prevent radiation originating from the cavity assembly from being reflected back onto the sample. Both the sample beam and the reference beam pass through the same potassium bromide window into the spectrophotometer. To prevent condensation of water the window temperature is kept at 40°C . This is achieved by imbedding the window in a heavy walled copper pipe the temperature of which is controlled by an external electric heater. The chamber is evacuated through a $1\frac{3}{4}$ -inch oil diffusion pump which is baffled by a large nitrogen cold trap. With the tank at room temperature the system reaches a pressure of 5×10^{-5} mm Hg. After the jacket is filled with liquid nitrogen the pressure decreases to approximately 5×10^{-6} mm Hg. The power consumption of the cavity heater was 16, 50, 170, and 380 watts for cavity temperatures of 200° , 400° , 600° , and 800°C , respectively.

The emittance cavity assembly is mounted on the Perkin-Elmer Model 13 spectrophotometer. The optical layout is shown in figure 2. The spectrophotometer is used in single-beam operation. One of the 10-inch-diameter

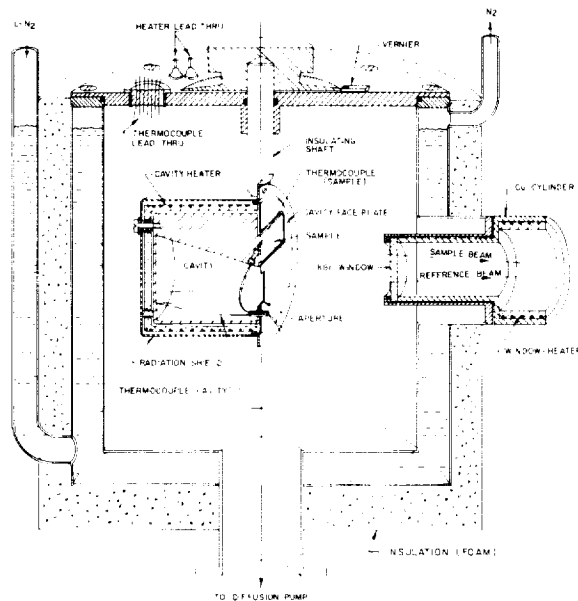


FIGURE 1.—Emittance cavity assembly.

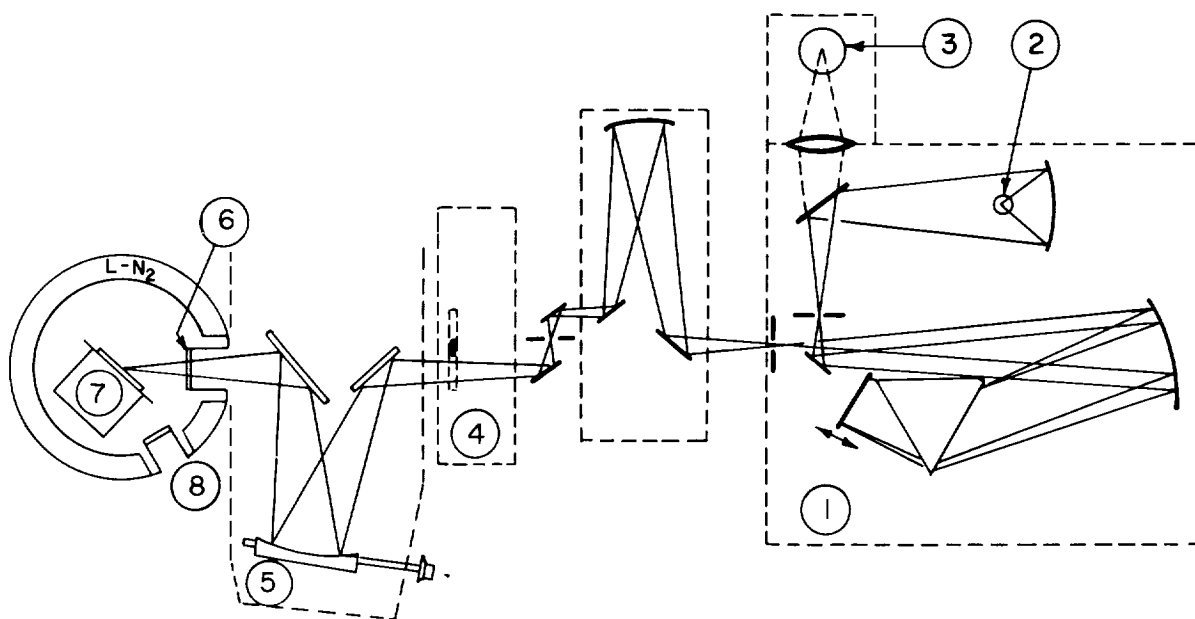


FIGURE 2.—Optical schematic of Perkin-Elmer model 13 spectrophotometer and emittance cavity assembly in single-beam operation.

- | | | | |
|--------------------------|-----------------------|-----------------------------|---------------------|
| 1. Prism monochromator | 3. Mercury vapor lamp | 5. Spherical mirror | 7. Sample, hohlraum |
| 2. Thermocouple detector | 4. Chopper unit | 6. Potassium bromide window | 8. Viewing port |

spherical mirrors can be rotated around a horizontal axis, so that the beam can be moved from the cavity to the sample surface. This feature permits measurements of the reference and sample beam intensities within a relatively small time interval; thus, the effect of long-period temperature fluctuations is eliminated.

PROCEDURE

All measurements were performed with a cesium bromide prism, calibrated for the wavelength region between 1 and 32 μ , and a thermocouple detector with a CsBr window. In order to reduce stray light in the monochromator the filters and diagonals indicated in the following table were used:

Wavelength range, μ	Diagonal	Filter
1 to 4.....	Mirror.....	$\frac{5}{16}$ -inch glass
4 to 12.....	Mirror.....	None
12 to 19.....	Scatter plate.....	None
19 to 24.....	Scatter plate.....	AgCl/AgS
24 to 25.....	Reststrahlen plate	None

The zero point reading was obtained by directing the beam onto the liquid-nitrogen cooled wall. The procedure of determining the emittance was the same for all samples discussed in the next section. After the sample surface had been prepared and the cavity assembly was placed into the vacuum tank a pressure of 10^{-4} mm Hg was established. Then the cavity heater was turned on and the jacket was filled with liquid nitrogen. It took approximately 1½ hours to establish equilibrium for a temperature change of 200° C. The observed deviation from the equilibrium temperature in a time interval of 1 hour was less than $\pm 1.5^\circ$ for cavity temperatures of 200° and 400° C and less than $\pm 1^\circ$ for a cavity temperature of 600° C. The difference between sample and cavity temperature was never greater than 1.1° C. While the cavity assembly was coming to equilibrium, the system was optically aligned and the sample setting for zero emission angle was determined. This was done by projecting the monochromator slit (mercury green line, fig. 2) onto the sample (or a mirror immediately above and coplanar with the sample) and superimposing the incident and

reflected slit image on a screen outside the KBr window. After equilibrium was reached the emittance at a particular angle of emission and wavelength was obtained by taking the following readings:

1. Zero reading, beam from tank wall at liquid-nitrogen temperature,
2. Reference reading, beam from cavity,
3. Sample reading, beam from sample,
4. Reference check, beam from cavity.

The time needed to perform these four steps was less than 2 minutes. Measurements have shown that the temperature changes in the system are negligible within this time interval. The cavity temperature and the temperature differential between sample and cavity were usually read approximately every 8 minutes.

RESULTS

Platinum

The emittances of three different samples were studied. In the first study, the angular dependence of the emissivity of a flat platinum surface was determined at a wavelength of $2\ \mu$ and a temperature of 385°C . The preparation of the sample was as follows: first, the

sample surface of the copper block was highly polished, cleaned, and vacuum plated with aluminum; second, a platinum film was evaporated onto the aluminum surface. Good adherence of the platinum could not be achieved without the intermediate aluminum film. The platinum film, which had less than 0.01 percent of impurity, was found to be opaque at $2\ \mu$. As shown in figure 3, the experimental values are considerably higher than values obtained from the Fresnel equation using the extinction coefficient and index of refraction measured by Eaton and Conn (ref. 2). At an angle of emission of 15° the difference is 32 percent. At the same angle, however, the measurements agree within 3 percent with values obtained at room temperature with an integrating sphere reflectometer (ref. 3) in the same laboratory. Also, the emissivity obtained by extrapolating our experimental values to zero angle of emission agrees to within 1 percent with the value reported by Price (ref. 4).

Grooves

The angular dependence of the emittance of a strongly directional emitting surface was determined. Perlmutter and Howell (ref. 1) have calculated analytically the directional emittance of an infinitely long symmetric groove with specular walls of emissivity zero and a flat black base of emissivity 1 located at an arbitrary depth within the groove. Surfaces made of these grooves could be used when it is desired to achieve high emittance in a particular direction and low emittance in all other directions.

The grooves were milled in a $\frac{1}{8}$ -inch-thick brass plate and had the following dimensions: $\theta=18.23^\circ$, $d=0.222\text{ cm}$, and $D=0.342\text{ cm}$ (fig. 4). Since it was not practical to apply a black coating to the base of the groove, the material behind the base was machined away leaving only a structure of thin parallel rods with triangular cross sections. Next, aluminum was evaporated onto the walls of the grooves, and the sample surface of the copper block was painted with PT 404 flat black paint. Then the grooved plate was mounted $\frac{1}{8}$ -inch from the painted sample surface. The cavity produced by this separation enhanced the blackness of

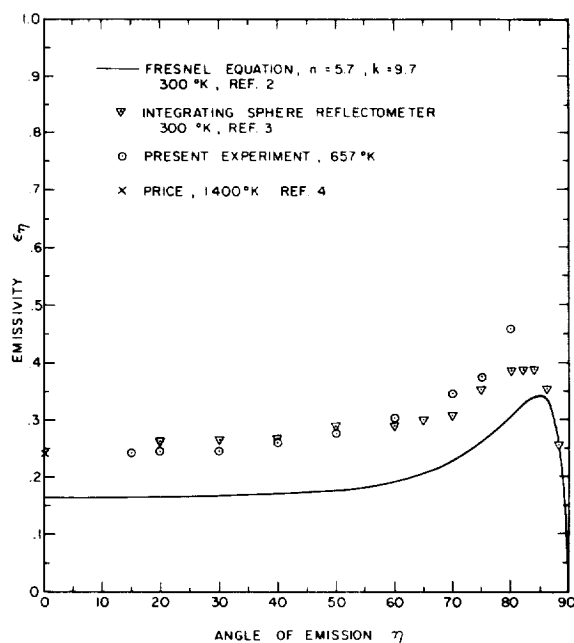


FIGURE 3.—Emissivity of platinum at $2\ \mu$.

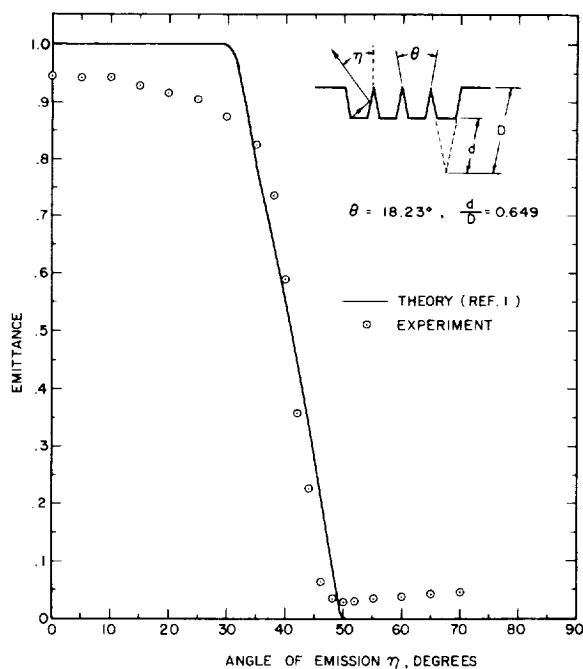


FIGURE 4.—Emittance of strong directional emitter at 8μ .

the base. Measurements were made at 8μ because the emittance of the black paint was highest at this wavelength ($\epsilon_\lambda=0.95$) and the walls could be assumed to be highly specular.

Figure 4 shows the emittance of this surface plotted against angle of emission, and also shows the corresponding theoretical curve from reference 1. Except for the differences that are obviously due to the fact that the theory assumed a completely black base and perfectly reflecting walls, the agreement between theory and experiment is excellent. In addition to slight machining irregularities, the divergence of the sample beam, which is approximately 8° , will introduce some uncertainty in the measurement of the angle.

Flat Black Paint

The emittance of the PT 404 flat black paint at temperatures of 213° , 390° , and 625° C was measured for wavelengths between 1 and 25μ (fig. 5). Since this paint was used to coat the cavity it was important to know that the emittance did not change drastically over the temperature region for which the hohlraum was to operate.

Measurements were also attempted at 800° C. However, after equilibrium was reached part of the PT 404 paint on the sample surface decomposed and a thin deposit formed on the KBr window, reducing the transmission of radiation through the window. With another

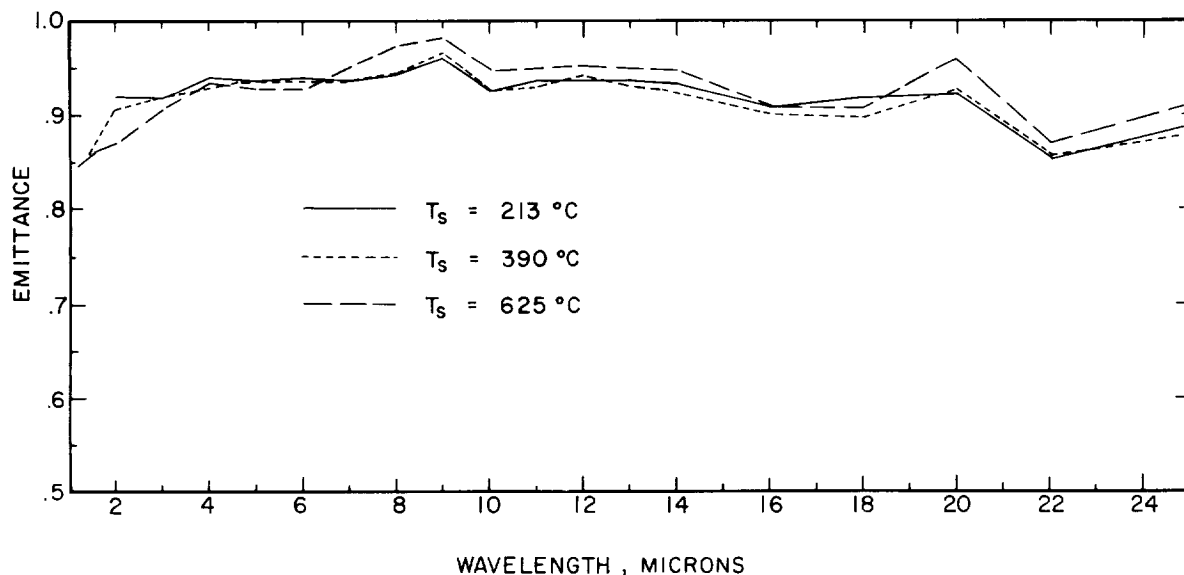


FIGURE 5.—Emittance of PT 404 black paint (Products Technique, Inc.).

coating for the reference cavity (for example, nickel oxide, NiO), emittance measurements up to 800° C can be made safely if the sample surface is stable at that temperature.

Error Analysis

The errors connected with the measurements presented in this report can be classified into three broad categories. First, there are inaccuracies associated with the cavity design; for example, nonblackness of the cavity, temperature differential between cavity and sample face, and temperature drift of the cavity. Second, there are errors resulting from the transfer of the beam between the cavity and the detector, for example, window emission, detector emission, and mirror absorption. Finally, there are errors associated with amplification and recording of the detector signal. The following discussion presents a quantitative assessment of the possible effects of these inaccuracies on the data included in this report.

A sophisticated evaluation of the hohlraum is beyond the scope of this paper. However, a cursory analysis accounting for the cavity geometry and the emittance of the PT 404 black paint indicated that the deviation of the hohlraum emission from that of a blackbody is between 0.02 and 0.4 percent. These bounds were evaluated considering the walls first as perfectly diffuse reflectors and then as perfectly specular reflectors.

If the conventional blackened shutter is used for zero readings another inaccuracy is introduced to the measurements due to self-emission of the KBr window and thermocouple detector. This inaccuracy was eliminated by taking zero readings with the spectrophotometer beam originating from the vacuum chamber wall which was at 77° K. The energy ratio as recorded at the detector is then given by

$$(\text{Energy Ratio})_{\lambda} = \frac{E_{s,\lambda} - E_{0,\lambda}}{E_{b,\lambda} - E_{0,\lambda}}$$

For all measurements presented E_0/E_b was negligibly small compared to E_s/E_b , so that the energy ratio at the detector was considered to be equivalent to E_s/E_b .

Errors due to a temperature differential between the blackbody and the sample surface

can be evaluated from the energy ratio at the detector, which is given approximately by

$$\frac{E_{s,\lambda}}{E_{b,\lambda}} = \frac{\epsilon_{\lambda} i_{s,\lambda}}{i_{b,\lambda}}$$

where ϵ_{λ} is the true emittance. Then

$$\epsilon_{\lambda} = \frac{E_{s,\lambda} i_{b,\lambda}}{E_{b,\lambda} i_{s,\lambda}} = \frac{E_{s,\lambda} e^{c_2/\lambda T_s} - 1}{E_{b,\lambda} e^{c_2/\lambda T_b} - 1}$$

From this expression the relative change of emittance due to a change in sample temperature T_s is obtained.

$$-\frac{\delta \epsilon_{\lambda}}{\epsilon_{\lambda}} = \frac{c_2}{\lambda T_s^2} \frac{e^{c_2/\lambda T_s}}{e^{c_2/\lambda T_s} - 1} \delta T_s$$

Since the relative error is inversely proportional to λT_s^2 , the maximum error for a given δT_s is expected to occur at short wavelength and low temperature. The errors due to the measured cavity-sample temperature differences are summarized in the following table for various temperatures and wavelengths:

$T_s, ^\circ\text{C}$	200		400		600	
λ, μ	2	5	2	5	2	5
$(\delta T_s)_{\text{max}}$	0.4	0.4	0.4	0.4	1.1	1.1
$100 \frac{\delta \epsilon_{\lambda}}{\epsilon_{\lambda}}$	1.31	0.51	0.64	0.26	1.05	0.43

The maximum relative error in ϵ_{λ} was 1.0 percent for platinum and less than 0.5 percent for the grooved surface.

One other potentially serious source of error results from stray light; that is, energy reaching the detector at wavelength bands outside the one being measured. Inaccuracy caused by stray light is dependent to a great extent on the quality of the monochromator and is a strong function of wavelength. A prism-grating monochromator would have been preferable. However, at the time these measurements were made only a single prism monochromator was available. In order to reduce the stray light problem the filter-diagonal mirror arrangement given in the table in the section entitled "Procedure" was

used. With this approach the errors are largest within the 1.0- to 2.0- μ region, but drop off sharply around 3.0 μ . At 4.0 μ the glass plate becomes opaque, filtering out the intense energy at longer wavelengths. The inaccuracy due to stray light is deemed not serious in the important range from 3 μ to 15 μ .

Besides the inaccuracies just discussed, additional effects must be considered in evaluating the over-all measurements; examples are errors due to emission and re-reflection of radiation from the vacuum chamber walls, short term wavelength drift of the monochromator caused by periodic operation of the bedplate heaters, and inaccuracy of the amplification and recording of the detector signal. In general the influence of these items on the measurements can be only qualitatively evaluated. Hence, it is necessary to estimate the influence of these potential errors in order to obtain an over-all accuracy. Based on the arguments and calculations presented in this section it is estimated that the emittance data for the black paint had a maximum associated error of approximately ± 2 percent for all wavelengths and that this error was no more than ± 1 percent for wavelengths greater than 2.5 μ . For the measure-

ments on the platinum surface the estimated over-all error is ± 3 percent; and for the specially grooved surface the estimated error is ± 1 percent.

ACKNOWLEDGMENT

We wish to express our thanks to Messrs. M. Perlmutter and J. R. Howell of NASA Lewis Research Center for providing a numerical solution of their equations (ref. 7) for the particular grooved surface studied in this paper, and to Dr. J. T. Neu of General Dynamics/Astronautics for his many helpful suggestions throughout this program. We also wish to acknowledge General Dynamics/General Atomic's financial support which assisted in the building of the apparatus.

REFERENCES

1. PERLMUTTER, MORRIS, and HOWELL, JOHN R.: A Strongly Directional Emitting and Absorbing Surface. *Trans. ASME, Ser. C—Jour. Heat Transfer*, vol. 85, no. 3, Aug. 1963, pp. 282–283.
2. Eaton and Conn, ed.: *Handbook of Chemistry and Physics*. 38th ed., Chemical Rubber Pub. Co., 1956–1957, p. 2704.
3. BRANDENBERG, W. M.: The Reflectivity of Solids at Grazing Angles. *Measurement of Thermal Radiation Properties of Solids*, Joseph C. Richmond, ed. NASA SP-31, 1963, pp. 75–82.
4. PRICE, DEREK J.: The Emissivity of Hot Metals in the Infra-Red. *Proc. Phys. Soc. (London)*, vol. 59, pt. 1, no. 331, Jan. 1, 1947, pp. 118–131.

DISCUSSION

E. M. SPARROW, Heat Transfer Laboratory, Univ. of Minn.: Whenever an emittance is measured, the question arises as to what is the actual surface temperature of the emitter. You did not give us any indication of how the surface temperature was measured; some information along these lines would be desirable.

BRANDENBERG: First, I would like to say that we measured the temperature at the back of the surface, not the front surface. For the platinum mirror we did not worry too much about the temperature difference because there is good conduction between the substrate and the layer of platinum. For the black paint we made some preliminary calculations, which I did not present here, of the temperature drop due to conduction through the black paint and the total emission from the surface.

SPARROW: Was the temperature difference appreciable?

BRANDENBERG: It was estimated to be somewhat less than 10°.

T. LIMPERIS, Univ. of Mich.: You painted the inside of the tank with a flat, black paint (designated "3M velvet"). I wonder just how black this paint is beyond 10 μ , and, if it is not very black, does this affect

your emittance measurements?

BRANDENBERG: We did measure the emittance of the "3M velvet" black paint. The data are not presented in this paper. If I remember correctly, the reflectance of the paint between 10 and 32 μ was less than 6 percent.

H. E. BENNETT, Michelson Laboratory, U.S. Naval Ordnance Test Station: I wonder if you have made any similar measurements on directional emitters in which the ratio of the roughness to the wavelength was smaller, so that you get into the diffraction range. Such measurements would be quite interesting.

BRANDENBERG: No, we have not made such measurements up to the present time. We will look into this problem in the near future.

RICHARD ZIPIN, Purdue University: You reported data for your grooved surface at only one wavelength. Did you make measurements at any other wavelength? If so, was there an effect?

BRANDENBERG: So far we have not made any measurements at wavelengths other than 8 μ . We chose 8 μ because we could expect that the sidewalls of the grooves were more specular at long wavelengths than at short ones.

33. Measurement of Emittance of Organic Materials (Electric Wire Insulation)

GEORGE W. MCINTYRE

THE BOEING COMPANY, SEATTLE, WASH.

An apparatus and procedure are described for measuring the emittances of organic (or other low-conductance) materials. The method maintains a small sheet of the test material near room temperature by means of a water bath and measures the power input to an adjacent constant-temperature blackbody radiator that radiates only to the test specimen.

This paper describes an apparatus and procedure that were developed for measuring the emittances of organic materials. The work grew out of a program in which electric wire current ratings were to be calculated from the thermal characteristics of the materials involved; and the method has been used successfully for determining emittances of various materials used for wire insulation. However, the method can be used for almost any material available as a thin sheet, and should be of general interest.

In essence, the method maintains the test specimen at a constant temperature (near room temperature) by means of a water bath, and measures the power input to an adjacent constant-temperature blackbody radiator that radiates only to the test specimen. What is determined is thus the room-temperature absorptance of the material for blackbody radiation of a somewhat elevated temperature; and this absorptance is taken as the emittance at the higher temperature. The particular advantage of the method over the methods that measure emittance directly is that the surface temperature of the test material need not be known very accurately, so that the difficult problem of accurately measuring the surface temperature of a sheet of insulation material is avoided.

APPARATUS

Blackbody Emitter

The test setup is shown schematically in figure 1. A large block of aluminum with a blackbody cone cut in one end is suspended inside an insulated box. The blackbody opening is $3\frac{1}{2}$ inches in diameter. This blackbody shape, or emitter, is heated by a standard heater wire strung through ceramic insulating beads and wrapped around the block. Three thermocouples are embedded in the aluminum block, and their average temperature is used as an input to the temperature controller. Provisions are also made to record the temperature indications from the thermocouples, measure the voltage drop across the heater wire, and measure the current through the heater wire.

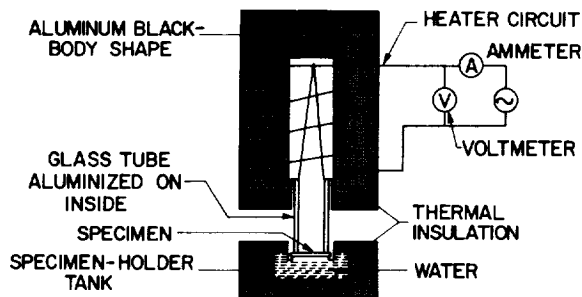


FIGURE 1.—Emissometer.

Power-On Timing Equipment

In order to make an emittance determination on a test specimen, it is necessary to know accurately the heat input to the blackbody emitter at each test temperature. The system used was evolved after a considerable amount of experimentation and study. It was found best, with the equipment available, to measure the electrical power being supplied to the emitter heater and the length of time during which it was being supplied. This is accomplished with a system of relays, timers, and clocks.

The system operates in the following manner. The emitter temperature is selected on the temperature controller and the power is turned on. When the emitter is up to temperature, conditions are allowed to stabilize for one hour. After the stabilizing hour, power to the heater continues to cycle for 1 hour more with the three recording clocks running. These clocks are a *total-time* clock, a *power-off* clock, and a *power-on* clock. The *power-on* clock is a 1-minute-full-scale clock to obtain the seconds *on* accurately. Minutes *on* are determined from the difference between *total* and *off* clocks, which are 1-hour-full-scale clocks.

After the recording hour is over, the timer stops all clocks and the system reverts to the stabilizing hour condition just described. During this hour, data are recorded, clocks reset, a new emitter temperature selected on the controller, and a recycle button pushed to start the sequence again at the new temperature.

Specimen Mounting

The test specimen is mounted on a tank which is filled with water kept at approximately room temperature and circulated to insure that the specimen is maintained as close as possible to water temperature. This tank is so constructed that the water is in direct contact with the back side of the specimen. The tank is held in an insulated box. It is necessary to cool the water since it absorbs heat from the specimen. This is accomplished by circulating air in a copper tube through a dry-ice bath and then through the water.

The air exhaust is then used to drive an impeller which, in turn, drives an impeller on the other end of a vertical shaft which circulates the water in the tank. To control the water temperature, an immersion heater is used, operated by a controller actuated by a thermocouple immersed in the water. A mercury thermometer is provided to measure the water temperature, which is used as the specimen temperature.

SPECIMEN LOCATION

The specimen holder tank is placed under the blackbody emitter and an aluminized glass tube is inserted between the blackbody and the specimen to insure that all the heat radiated from the blackbody arrives at the specimen and vice versa. Unprotected vacuum-deposited aluminum was selected for the reflecting surface to give the highest infrared reflectance over a long service life. Selection was based in part on data given in reference 1.

TEST SPECIMEN

The test specimen is mounted on an aluminum plate to insure good heat transfer from the specimen to the water in the specimen-holder tank.

Procedure

With a specimen in place (Teflon insulated wire with a moderately polished surface) the water circuit is activated first and the water temperature controller is set to approximately room temperature. Room temperature is used for the water temperature as it is desirable to keep the test specimen at as low a temperature as possible in order to promote the largest possible net heat exchange between the emitter and the specimen. With the prevailing humidity in the area of test, temperatures of 10° or 15° F below room temperature usually result in condensation on the test specimen, causing the results to be invalid.

Next, the blackbody emitter circuit is activated, and the system operates as previously described. After the recording hour is completed, the necessary data are recorded. These include times, emitter temperature, voltage and current to the emitter heater, and water

or specimen temperature. Following this, the emitter controller is set to the next higher temperature, clocks are reset, and the apparatus recycled to start the sequence over again with the heating cycle.

This procedure is repeated for each temperature at which the emittance of the test specimen is desired. Data for three temperatures can be obtained in one 8-hour day.

CALCULATIONS

The power q_s delivered to the specimen from the radiator is given by the equation

$$q_s = \sigma A \epsilon (T_1^4 - T_2^4) \text{ Btu/hr} \quad (1)$$

where

- σ Stefan-Boltzmann constant, Btu/hr-ft²-($^{\circ}\text{R}$)⁴
- A area of the specimen exposed to the radiation, ft²
- ϵ emittance of the specimen
- T_1 blackbody temperature, $^{\circ}\text{R}$
- T_2 specimen temperature, $^{\circ}\text{R}$

When the specimen is replaced with a blackbody at the same temperature as the specimen, T_2 , the power q_b delivered to it from the radiator is given by the equation

$$q_b = \sigma A (T_1^4 - T_2^4). \quad (2)$$

The emittance ϵ follows from a comparison of equation (1) with equation (2):

$$\epsilon = \frac{q_s}{q_b}. \quad (3)$$

For this work, the "blackbody" used was the room; that is, the radiator simply radiated through the aluminized cylinder into the room.

The values of q_s and q_b are not the same as the electrical power inputs, because heat is also lost to the insulation. The heat power h lost into the insulation (and thence to the surroundings) is determined by subtracting q_b (which can be calculated directly by means of equation (2)) from the total power input H_b measured when the radiator is radiating into the room:

$$h = H_b - q_b. \quad (4)$$

Calibration curves of q_b and h are plotted against the radiator temperature T_1 . These values of h are still applicable when the specimen is in place. Hence, for the specimen,

$$q_s = H_s - h \quad (5)$$

where H_s is the total power input when the specimen is in place. With q_b and q_s thus determined, the emittance is obtained from equation (3).

An expression for the power input, H , or H_b , is

$$\begin{aligned} H_s \text{ or } H_b &= 3.415 EI \frac{t}{3600} \\ &= 9.486 \times 10^{-4} EIt \text{ Btu/hr} \end{aligned} \quad (6)$$

where

- E potential difference across heater, volts
- I current through heater, amperes
- t time that power to heater is on, sec/hr

The factor 3.415 converts watt-hours to British thermal units.

An analysis of the errors involved with this technique yielded root-mean-square emittance errors of ± 7 percent.

Although the radiation emitted from the conical cavity does not quite have the ideal cosine intensity distribution with angle, the emittance obtained with this apparatus is considered to be hemispherical, since the variation of emittance with angle is small for the types of materials tested.

RESULTS

Values of emittance for Teflon samples were obtained by using the described apparatus and compared to measurements from two other emissometers. Both of the other emissometers were types in which the sample was heated, giving rise to difficulties in measuring sample temperature. In one case, values were as much as double and in the other case they were up to 20 percent higher than the values found by the technique described here. Confidence in the use of values obtained with the new

emissometer came from use of these results in the wire-rating program mentioned in the Introduction. In that program, emittances were used as inputs to the computer which predicted a current rating for the wire being considered. A specimen of the wire was then tested in the laboratory to determine its actual rating under the same conditions. Predictions were within 10 percent of test results, which satisfied the prescribed accuracy requirements of the program. It is therefore concluded that the apparatus has proven to be satisfactorily accurate in the application for which it was developed—namely, the determination of electric wire insulation surface emittance at temperatures up to approximately 600° F. At the present time, the apparatus is being used to provide electric wire insulation surface emittances for use in an extensive wire rating program being carried on at The Boeing Company.

Figure 2 presents emittance data obtained with this apparatus for two types of materials used as electric wire insulation.

CONCLUSIONS

An emissometer has been developed which determines emittance by comparing heat absorption by a specimen with heat absorption

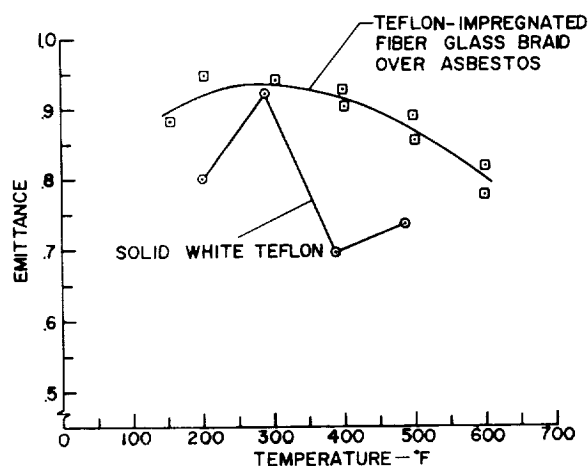


FIGURE 2.—Wire-insulation emittance data.

by a blackbody. This emissometer has proven sufficiently accurate for practical application in determination of emittance of insulating materials (or, in general, materials of low heat conductivity) in the approximate temperature range of 150° to 600° F.

REFERENCE

1. HASS, GEORG: *Filmed Surfaces for Reflecting Optics*, Jour. Optical Soc. America, vol. 45, no. 11, Nov. 1955, pp. 945-952.

DISCUSSION

ANDREW A. HALACSY, Heat Magnetic Engineering: How thick was your sample? I ask this because I suppose your aim was not so much to measure the properties of only the insulation layer, but to measure the properties of the entire system of wire and insulation. Actually, it was the latter that you determined. I wonder if the sample was not too small for your purposes and whether you can get a good average from such a small sample. In this connection, what was the heat loss from the apparatus in percent and how reliable was the measurement of this heat loss? I find sometimes that it is a little tricky to measure.

My suggestion is that you might get even better results if you could devise an apparatus which would be something like this one, but turned inside out—that is, if you could create the heat inside an apparatus and put your specimen around the heat source. Imagine an apparatus in which the heat source is inside and the coil of wire around it. Of course, I do not know whether your purpose was to investigate a single wire or a coil, or whether the wire had a round or oblong cross section. I also wonder what was the temperature

drop, or the gradient, between the surface and the water.

What was the heat loss from the whole apparatus?

McINTYRE: It was on the order of twice the net heat exchange between the emitter and the specimen.

HALACSY: That seems fairly high. Did you measure the total temperature drop between the surface of the specimen and the water?

McINTYRE: No. We could not devise any technique by which to measure it. The main advantage of this method is that the specimen surface temperature need not be known very accurately. We assumed that the specimen surface temperature was the same as the water temperature. We know, of course, that there is a temperature gradient across the specimen. The error is small, however, because the fourth-power law causes the dominant radiation term to be that received from the blackbody cavity. If it were the *sample* that was being heated and was radiating to cold surroundings, it would be essential to know its surface temperature very accurately.

34. Low-Temperature Conductive Losses in Emittance Measurements by the Decay Method

O. MAKAROUNIS

U.S. NAVAL RADIOLOGICAL DEFENSE LABORATORY, SAN FRANCISCO, CALIF.

An analysis of the heat conductive losses along the supporting wires of a specimen and of the air conductive losses in a low-temperature evacuated chamber is presented. Conductive loss corrections for total hemispherical emittance measurements by the decay method, in the temperature range -150°C to 450°C , are also shown.

When low-temperature emittance data are obtained by the temperature decay method, the conductive heat losses along the thermocouple leads or through the residual gas in the vacuum chamber may approach or even exceed the heat loss by radiation. The error introduced by these conductive losses must be measured with precision before valid radiation data can be obtained. The heat lost by the specimen due to radiation varies approximately as the fourth power of the specimen absolute temperature, and since the conductive losses through the air and the leads increase only as the first power of the temperature, they become negligible at the higher temperatures. At temperatures below 100°C , the error in emittance due to conductive losses is appreciable and must be subtracted from the value of the apparent emittance in order to obtain the actual emittance of the surface under investigation.

The heat conducted away from the specimen by the thermocouple wires supporting it was determined experimentally by varying the number of thermocouple leads from three to nine and observing the differences in temperature decay rates. The heat lost from the specimen by air conduction was also determined experimentally by varying the pressure in the chamber and observing the resulting differences in temperature decay rates.

SYMBOLS

a	fraction of existing temperature difference $T_s - T_w$ attained by each air molecule rebounding from specimen
A_s	total emitting area of specimen
C	heat capacity of specimen
l	thermocouple lead length
M	mass of specimen
$P_{\mu b}$	pressure of chamber, microbars (μb)
Q_a	rate of heat loss by air conduction
Q_i	rate of heat loss by conduction along thermocouple wires supporting specimen in chamber
Q_t	total rate of heat loss from specimen
Q_w	rate of heat absorption by specimen from surrounding walls of chamber
Q_r	rate of heat loss from specimen by radiation
\dot{T}_s	observed temperature decay rate of specimen
T_s	absolute temperature of specimen
T_w	absolute temperature of chamber walls
α_s	absorptance of specimen for radiation having spectral distribution of a blackbody at temperature T_w
ϵ_a	emittance correction due to air conduction losses in chamber
ϵ_l	emittance correction due to conductive losses along thermocouple leads supporting specimen in chamber
ϵ_o	observed emittance
ϵ_s	emittance of specimen at temperature T_s
Λ	low-pressure heat conductivity of air, $(2.9 \times 10^{-6} \text{ cal-cm}^{-2}\text{-deg}^{-1}\text{-(}\mu b\text{)}^{-1}\text{-sec}^{-1})$
σ	Stefan-Boltzmann constant $(1.354 \times 10^{-12} \text{ cal-cm}^{-2}\text{-deg}^{-4}\text{-sec}^{-1})$

THEORY OF OPERATION

If a chamber is designed to measure the total hemispherical emittance by the decay method accurately, it should possess the following properties:

- a pressure low enough and sample supports small enough to assure that the primary method of heat transfer is by radiation
- a wall temperature low enough to make the radiation from the inner wall negligible
- an apparent chamber absorptance near 1.0 in the wavelength range which includes essentially all the radiation from the specimen so that negligible energy is reflected from the walls back onto the specimen.

Since these conditions cannot be completely satisfied under laboratory conditions, it is necessary to estimate the error caused by deviations from the ideal conditions. The total rate of heat loss for a specimen at a temperature T_s higher than the wall temperature T_w can be expressed as

$$Q_t = Q_i + Q_r + Q_a - Q_w \quad (1)$$

All heat rates are in calories per second.

The radiation term is

$$Q_r = A_s \epsilon_s \sigma T_s^4 \quad (2)$$

The heat received by the specimen from the surrounding walls is

$$Q_w = \alpha_s A_s \sigma T_w^4 \quad (3)$$

Substituting equations (2) and (3) into equation (1) gives

$$Q_t = \epsilon_s A_s \sigma \left[T_s^4 - \left(\frac{\alpha_s}{\epsilon_s} \right) T_w^4 \right] + Q_i + Q_a$$

The present studies were made with polished silver specimens in order to minimize Q_i and Q_w , and thus to emphasize, relatively, Q_i and Q_a . For such a polished metal surface, it has been shown (ref. 1) that

$$\frac{\alpha_s}{\epsilon_s} \approx \left(\frac{T_w}{T_s} \right)^{1/2}$$

Therefore

$$Q_t = \epsilon_s A_s \sigma \left[T_s^4 - \left(\frac{T_w}{T_s} \right)^{1/2} T_w^4 \right] + Q_i + Q_a \quad (4)$$

The rate of temperature decay is given by

$$\dot{T}_s = \frac{Q_t}{MC}$$

or, from equation (4),

$$\dot{T}_s = \frac{A_s \epsilon_s \sigma \left[T_s^4 - \left(\frac{T_w}{T_s} \right)^{1/2} T_w^4 \right]}{MC} + \frac{Q_i}{MC} + \frac{Q_a}{MC}$$

Solving for the emittance gives

$$\epsilon_s = \frac{MCT}{A_s \sigma \left[T_s^4 - \left(\frac{T_w}{T_s} \right)^{1/2} T_w^4 \right]} - \frac{Q_i}{A_s \sigma \left[T_s^4 - \left(\frac{T_w}{T_s} \right)^{1/2} T_w^4 \right]} - \frac{Q_a}{A_s \sigma \left[T_s^4 - \left(\frac{T_w}{T_s} \right)^{1/2} T_w^4 \right]} \quad (5)$$

or

$$\epsilon_s = \frac{MCT}{A_s \sigma \left[T_s^4 - \left(\frac{T_w}{T_s} \right)^{1/2} T_w^4 \right]} - \epsilon_i - \epsilon_a \quad (6)$$

The lead correction ϵ_i depends on the emitting area of the specimen as well as the length, cross-sectional area, and thermal conductivity of the thermocouple wires supporting it. All data obtained are for a specimen with a total emitting area of 5.99 cm², supported by two 5-mil-diameter chromel and one 5-mil-diameter alumel thermocouple leads, each 4.1 cm long. The correction ϵ_i corresponds to heat conducted away from the specimen to the thermocouple lead terminal posts and heat radiated by the thermocouple leads. At the higher tempera-

tures, that is, above 100° C, ϵ_i consists mainly of radiation losses. The following corrections hold true only at the lower temperatures, that is, below 100° C, where ϵ_i consists mainly of conductive losses.

From equation (5) it is seen that $\epsilon_i \propto \frac{1}{A_s}$ and it can be shown that $\epsilon_i \propto \frac{1}{l}$, where l is the thermocouple lead length. For a new specimen of area A'_s and lead length l' the corrected value of ϵ_i can hence be expressed as

$$\epsilon'_i = \epsilon_i \left(\frac{A_s}{A'_s} \right) \left(\frac{l}{l'} \right).$$

The energy lost by air conduction in a vacuum chamber with a specimen at a temperature T_s different from the wall temperature T_w is related to the number of air molecules hitting the specimen per unit time and to the amount of energy carried away by each molecule. For a vacuum chamber with a wall area considerably larger than the specimen area and a molecular free path longer than the specimen-to-wall distance, the rate of energy loss from the specimen by air conduction can be shown (ref. 2) to be

$$Q_a = a A_s P_w \Lambda \sqrt{\frac{273}{T_w}} (T_s - T_w) \text{ cal/sec.} \quad (7)$$

From equations (5) and (6) the emittance correction for air conduction losses is

$$\epsilon_a = \frac{Q_a}{A_s \sigma \left[T_s^4 - \left(\frac{T_w}{T_s} \right)^{1/2} T_w^4 \right]}. \quad (8)$$

If the thermocouple wire losses are neglected equation (6) can be written as

$$\epsilon_s = \epsilon_o - \epsilon_a.$$

If subscript 1 denotes a certain pressure and subscript 2 denotes a second pressure, where $P_1 < P_2$, then

$$\epsilon_s = \epsilon_{o1} - \epsilon_{a1} = \epsilon_{o2} - \epsilon_{a2}. \quad (9)$$

From equations (7) and (8) it is seen that ϵ_a is proportional to P . Accordingly

$$\epsilon_{a2} = \epsilon_{a1} \frac{P_2}{P_1}. \quad (10)$$

Substituting equation (10) into equation (9) and solving for ϵ_{a1} gives

$$\epsilon_{a1} = \frac{\epsilon_{o2} - \epsilon_{o1}}{\frac{P_2}{P_1} - 1} \quad (11)$$

which is the emittance correction for the air conduction loss with the chamber at pressure P_1 .

EXPERIMENTAL PROCEDURE

For the purpose of measuring the conductive thermal losses of a specimen mounted in an evacuated temperature-controlled chamber, the total hemispherical emittance of the specimen in the chamber had to be first determined by the temperature decay method.

Figure 1 is a schematic drawing of the temperature-controlled chamber employed. Three thermocouple wires, attached to the edge of the specimen, lead through insulators to supports outside the inner chamber. The wires were used for supporting the specimen firmly in the center of the inner chamber in addition

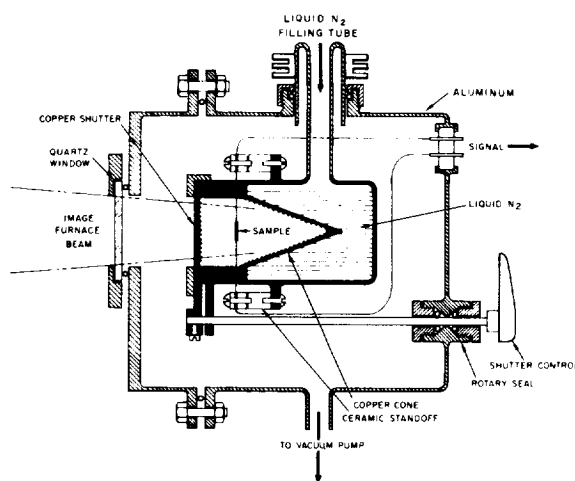


FIGURE 1.—Schematic drawing of low-temperature space chamber.

to monitoring the specimen temperature. Both chambers were evacuated to 1.3×10^{-5} torr and maintained at that pressure during the heating and cooling cycles of the specimen. The inner chamber was conical in shape, and its walls were painted with Parson's Black Lacquer and kept at liquid nitrogen temperature. The conical shape of the chamber was chosen in order to increase the number of reflectances away from the specimen and thereby increase the emittance of the inner chamber to near unity. This condition is the assumption under which equation (6) was derived.

The specimen was located in the long focal plane of an image furnace and could be warmed by irradiating it through a quartz window in the outer chamber and through an aperture in the open end of the conical chamber. Specimen temperatures were monitored by two of the three thermocouple leads supporting it, through an integrating digital voltmeter. Readings were printed out on a digital recorder at time intervals selected by a preset counter using the line frequency as a standard.

The temperature of the specimen was raised by manually opening the shutter of the conical chamber and turning on the arc radiation. When the temperature of the specimen had reached a given level, as monitored by the digital voltmeter, the arc radiation was turned off and the shutter to the inner chamber was closed to allow the specimen to cool.

The rate of decay \dot{T} , of the temperature was determined by dividing the difference of two recorded specimen temperatures by the time interval between them. This value was taken as the rate at a specimen temperature halfway between the two recorded temperatures.

Emittance measurements obtained for a polished silver specimen supported first by nine and then by three thermocouple leads resulted in appreciably higher emittance values for the case of the specimen supported by nine leads. The actual value of ϵ_i , or the error introduced by the three thermocouple leads, is one half the emittance difference thus obtained.

By observing the emittance of the polished silver specimen first at a pressure of 1.3×10^{-5} torr and then at a pressure of 5×10^{-4} torr, in the temperature range from -150° to 450° C,

and substituting these values into equation (11), the air conduction losses ϵ_a of the chamber were determined.

RESULTS AND DISCUSSION

Figure 2 shows the emittance correction for the conduction of the three thermocouple leads supporting the model, plotted against temperature. Figure 3 shows a similar plot of the emittance correction for air conduction at a chamber pressure of 1.3×10^{-5} torr. These corrections are to be subtracted from the observed values of emittance, in accordance with equation (6). As can be seen from the graphs, the emittance error due to the conductive losses becomes very pronounced at low temperatures for very low emittance specimens; it was for this reason that a very low emittance specimen, polished silver, was used to obtain them.

The accuracy of the digital voltmeter and print-out system was estimated to be better than ± 2 percent. With a liquid-nitrogen bath for the reference cold junction, the thermocouple error was found to be less than ± 5 percent at -196° C and the resulting accuracy of the conductive loss corrections, ϵ_i and ϵ_a , is estimated to be better than ± 10 percent of the values shown.

The solid curve in figure 3 is the theoretical curve for ϵ_a determined from equations (7) and

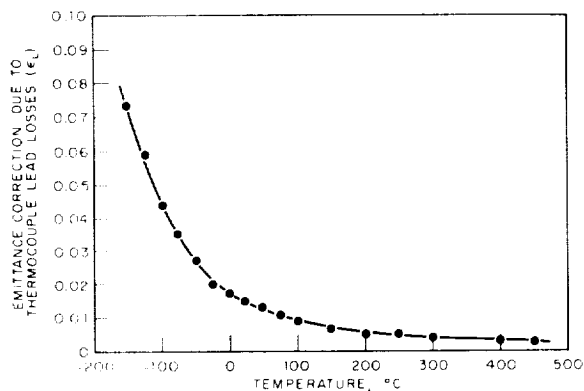


FIGURE 2.—Emittance correction due to conduction of one Alumel and two Chromel wires, 0.005 inch in diameter and 4.1 cm long, when supporting a specimen whose total radiating area is 5.99 cm^2 , with low-temperature ends of wires at 77° K .

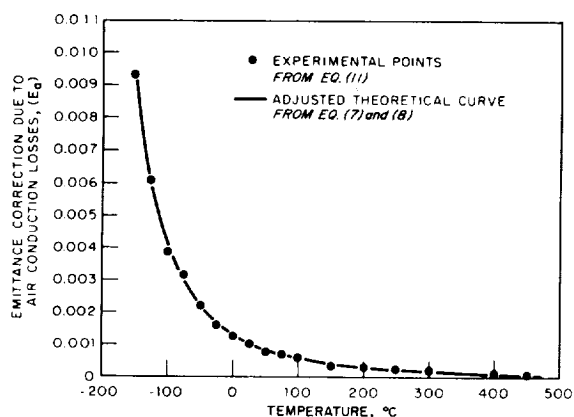


FIGURE 3.—Experimental and theoretical emittance correction due to air conduction losses of chamber kept at a temperature of 77° K and at a pressure of 1.3×10^{-5} torr.

(8) by choosing a value of $0.692 \times 10^{-2} \mu b$ for the product $aP\mu b$ in equation (7). The points shown along this curve are the experimental points obtained through the use of equation (11). If the indicated gage pressure of 1.3×10^{-5} torr (or $1.73 \times 10^{-2} \mu b$) is correct, this product would require a value of 0.40 for a , which is rather low. The pressure gage is located in the wall of the outer chamber and does not read the exact pressure at the center of the chamber where the specimen is suspended. In all probability, the actual pressure at the specimen is lower than what is indicated because of cryogenic pumping by the liquid nitrogen, and therefore a is greater than 0.40. Figure 3 shows that, for the chosen value of $aP\mu b$, the theoretical air conduction losses coincide with the experimental losses.

Figures 4 and 5 are the emittance curves for polished gold and polished silver specimens, corrected for thermocouple and air conduction losses.

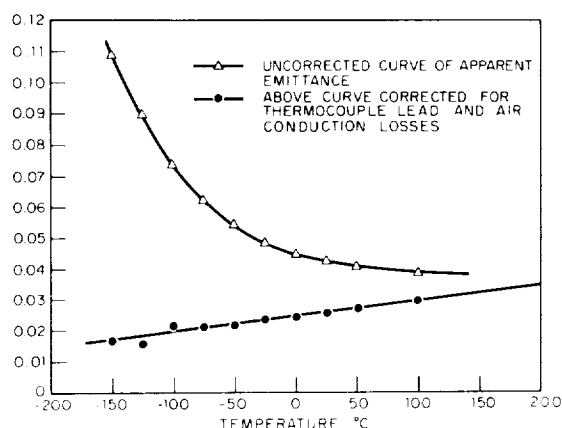


FIGURE 4.—Emittance of polished gold obtained in space chamber, corrected for thermocouple lead and air conduction losses.

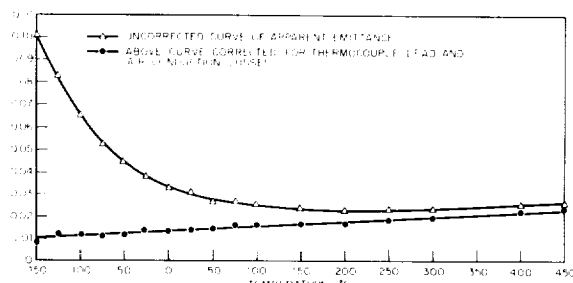


FIGURE 5.—Emittance of polished silver obtained in space chamber, corrected for thermocouple lead and air conduction losses.

REFERENCES

1. ABBOTT, G. L.: Total Normal and Total Hemispherical Emittance of Polished Metals. Measurement of Thermal Radiation Properties of Solids, Joseph C. Richmond, ed., NASA SP-31, 1963, pp. 293-306.
2. DUSHMAN, SAUL: Scientific Foundation of Vacuum Technique. John Wiley & Sons, Inc., c.1949.

DISCUSSION

GARY GORDON, RCA: I was very interested in this method of changing your pressure to estimate your error. It is particularly good since Jeans (Kinetic Theory of Gases) has shown that the accommodation coefficient can vary from less than 0.1 to almost 1. Therefore, there is quite a bit of error. You picked only two pressures. We have measured this heat conduction with various pressures up to about 0.01 or 0.1 torr.

In our experiments, the theory was substantiated that heat conduction is proportional to the pressure. I am glad to see that it has also been checked as a function of temperature.

One comment: In one equation in your paper the thermocouple-lead error is inversely proportional to the length of the leads. I think this relation should be taken with considerable caution since, at some temperatures,

the radiation from the leads, which you did mention, is very important. In a paper presented at the Dayton 1962 meeting,¹ we had an equation for infinitely long thermocouple wires. The solution can be worked out for intermediate lengths; it is expressed in terms of hyperbolic cosines.

MAKAROUNIS: I would like to mention that the thermocouple-lead loss does consist of conducted heat and radiated heat, but it is only at the higher temperatures that radiated heat becomes appreciable compared with the conducted heat. At the lower temperatures the radiated heat is very little. We made some approximate calculations and concluded that at 100° C, about 15 or 20 percent of the total error consists of heat radiated by the wires; whereas, at -100° C, only about 0.1 percent of the total error was heat radiated from the wires.

WILLIAM CLAUSEN, General Dynamics/Astronautics: In regard to the connection of your thermocouple wires to your sample, I would suspect that the manner in which this was done would have a great effect, and I wonder if you could arbitrarily say that your thermocouple-lead loss can be subtracted out directly, as in

your comparison of the nine thermocouple leads with the three. Can you attach nine of exactly the same type?

MAKAROUNIS: Yes, you can because their effect is additive. We attach them by drilling holes in the side of the specimen, inserting the thermocouple leads, and then peening the holes shut. We can just as easily drill pairs of holes at 120° intervals as single holes at 120° intervals.

WILLIAM FULKERSON, Oak Ridge National Laboratory: We have done experiments similar to the one that you have reported; however, your experiments were done at a higher temperature, above 100° C. We have found that you can add the powers from several different thermocouple leads spotwelded to a strip sample. Apparently, you can make a spotweld quite reproducible.

MAKAROUNIS: Well, we tried a spotweld but we did not have much luck with it.

FULKERSON: We do it under a microscope.

MAKAROUNIS: They have a tendency to melt because they are very thin.

FULKERSON: Our wires were also 5 mil, but were made of platinum-rhodium.

¹ Gordon, G. D., and London, A.: *Emittance Measurements at Satellite Temperatures. Measurement of Thermal Radiation Properties of Solids*, Joseph C. Richmond, ed., NASA SP-31, 1963, pp. 147-151.

35. The Application of Temperature Rate Measurements to the Determination of Thermal Emittances

WILLIAM M. HALL

JET PROPULSION LABORATORY, PASADENA, CALIF.

Two calorimetric techniques have been evolved to facilitate accurate measurements of room-temperature hemispherical emittance of spacecraft temperature control surfaces in a reasonably short period of time, without the use of high-precision temperature-control apparatus. One technique makes use of data from several arbitrarily induced heating and cooling curves in an iteration procedure which converges within a 3-hour observation period to a steady-state power-temperature set of values. The other technique uses a heating curve and cooling curve to calculate emittance without the use of the sample heat capacity value. The results are compared with emittances obtained from long-term temperature equilibrium tests for several surfaces of low and medium emittance. Data are given to indicate the accuracy and dispersion of such measurements.

Measurements were made on heated 6- by 6-inch flat samples placed adjacent and parallel to a liquid-nitrogen-cooled flat receiver plate which viewed the sample hemispherically.

A practical need exists for a method of accurately determining the hemispherical emittance of a space-vehicle temperature-control surface that will enable one to identify the variations of this quantity resulting from variations of surface treatment and manufacturing techniques. It is particularly desirable that the method be simple and rapid if many sample surfaces are to be studied.

This paper is concerned with two methods which seem to fulfill this need for determining emittances of sample surfaces at temperatures in the room-temperature range. Both methods use the same apparatus, and differ only in the procedures for running the tests and working up the results. These two procedures, which can be used with a variety of related types of apparatus, constitute the main contribution of the present paper. The apparatus itself is also of interest, but it is not yet considered to be fully developed.

Both methods use the rate of change of temperature of an electrically heated radiating

sample, rather than the equilibrium temperature of the sample. The use of rate measurements for this purpose has been mentioned in references 1, 2, 3, and 4.

Results presented herein for polished aluminum, Dow 7 coated magnesium, and polished gold-plated aluminum will serve to compare the two methods and to indicate the accuracy of each. A brief review of major sources of error is also presented.

SYMBOLS

A	radiating area
C	heat capacity of sample
K	constant for a given experiment; see equation (3)
P_{ab}	heat power absorbed by the sample, $C \frac{dT_s}{dt}$
P_{cond}	power conducted from the sample by wire leads and residual gas
P_e	electrical power input to the sample
P_{rad}	net power radiated from the sample
t	time
T	temperature
ϵ	hemispherical emittance
σ	Stefan-Boltzmann constant

Subscripts

- s* sample
p receiver plate
 1, 2, 3 first, second, or third run, respectively

DETERMINATION OF EMITTANCE FROM TEMPERATURE-TIME MEASUREMENTS

Rate-Equation Method

The heat-balance equation is applied to a flat slab of material to which is attached an electric heating pad, and which is arranged within an enclosure as indicated in figure 1. The heated side of the sample is enclosed in a similarly heated guard box, whose temperature is maintained equal to that of the sample throughout the experiment. The exposed face of the sample is situated parallel to a constant-temperature, blackened cold receiver. The whole apparatus is situated within a vacuum chamber at a pressure of 10^{-7} torr. The balance of heat power for the sample is given by

$$P_e = P_{rad} + P_{abs} + P_{cond} \quad (1)$$

where, for the parallel plate arrangement,

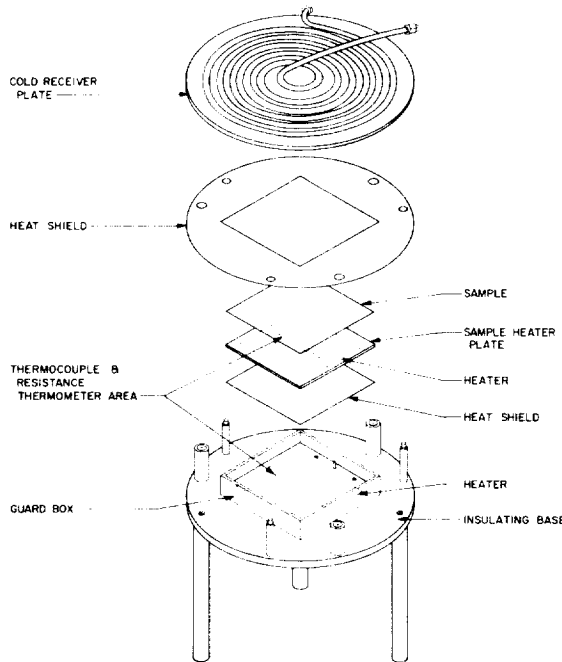


FIGURE 1.—Emittance sample and enclosure.

$$P_{rad} = \frac{\sigma A(T_s^4 - T_p^4)}{\frac{1}{\epsilon_p} + \frac{1}{\epsilon_s} - 1} = K(T_s^4 - T_p^4) \quad (2)$$

The term P_{cond} in equation (1) was neglected in this work, since (1) the leads are shielded from the cold surface, (2) conduction through the leads into the vacuum system terminals results in negligible heat loss from the sample, and (3) residual gas conduction loss to the cold receiver is about 0.03 percent of the sample radiant heat, by the equations of reference 5.

It should also be noted that in the derivation of equation (2) for P_{rad} it is assumed that both sample and receiver surfaces have gray spectral characteristics. This point will be discussed subsequently in the paper.

Equation (1) now becomes

$$P_e = K(T_s^4 - T_p^4) + C \frac{dT_s}{dt} \quad (3)$$

If the temperature-time history of the sample is recorded for two different values of the electrical power input, equation (3) provides two simultaneous equations,

$$\left. \begin{aligned} P_{e,1} &= K(T_s^4 - T_p^4)_1 + C \left(\frac{dT_s}{dt} \right)_1 \\ P_{e,2} &= K(T_s^4 - T_p^4)_2 + C \left(\frac{dT_s}{dt} \right)_2 \end{aligned} \right\} \quad (4)$$

With reasonable care it is possible to have the ranges of T_s in both runs such that fairly accurate values of dT_s/dt can be obtained from both records at the same temperature, which temperature should be close to that for which ϵ_s is desired. At this temperature

$$\left. \begin{aligned} P_{e,1} &= K(T_s^4 - T_p^4) + C \left(\frac{dT_s}{dt} \right)_1 \\ P_{e,2} &= K(T_s^4 - T_p^4) + C \left(\frac{dT_s}{dt} \right)_2 \end{aligned} \right\} \quad (5)$$

where T_s is now the same in both equations. The purpose of having a common T_s is not only to simplify the algebraic manipulation and improve its accuracy, but also to assure that K and C are actually the same constants

in both equations. Solving these simultaneous equations (5) for K gives

$$K = \frac{P_{e,1} - \frac{P_{e,1} - P_{e,2}}{\left(\frac{dT_s}{dt}\right)_1 - \left(\frac{dT_s}{dt}\right)_2} \left(\frac{dT_s}{dt}\right)_1}{T_s^4 - T_p^4} \quad (6)$$

The value of K can be used to solve for the sample emittance (see eq. (2)) if the emittance ϵ_p of the cold plate is known.

In practice, two temperature-time plots are determined, one heating and one cooling, which cover about the same temperature span. Slopes are measured at a common temperature and the values substituted in equation (6). The data reduction is most easily done by the graphic method. Least-squares techniques can also be used (ref. 6).

Iteration Method

With the sample initially in the room-temperature range, the sample heater power is turned up (say, to $P_{e,1}$) to cause a temperature rise. The temperature is read and noted at equal intervals for about 15 data points. The power is turned down (say, to $P_{e,2}$) to cause a temperature fall, and again the temperature history is taken. The least-squares method for determining the best-fit straight line is used to calculate the slopes of these two curves. (In practice, the curves turn out to be very close to straight lines, as the temperature change is restricted to at most 8° F.) At some power between $P_{e,1}$ and $P_{e,2}$, the slope should be zero. This power is estimated simply by a linear interpolation between $P_{e,1}$ and $P_{e,2}$, giving

$$P_{e,3} = P_{e,2} - \frac{\left(\frac{dT_s}{dt}\right)_2}{\left(\frac{dT_s}{dt}\right)_2 - \left(\frac{dT_s}{dt}\right)_1} (P_{e,2} - P_{e,1}). \quad (7)$$

The value $P_{e,3}$ thus obtained represents a first approximation to the power value that would maintain a constant temperature within the desired temperature range. In practice, the sample heater voltage is then adjusted to run at this calculated power level and another

temperature-time plot is obtained. The slope of this third curve is usually less than $\frac{1}{10}$ that of the first curves. The new slope and power values are inserted in an equation similar to equation (7), which will yield a second approximation to the steady-state power. This last power value is then used in equation (3), with $dT_s/dt=0$, to calculate the emittance. The time taken for each temperature curve is 72 minutes.

This technique originated with Mr. Marshall Gram of JPL, who also designed the sample enclosure.

APPARATUS

Figure 1 is an exploded view of the sample and its enclosure. A 6-by-6-by-0.064-inch plate sample is wrung against a similar size aluminum heater plate using Apiezon "T" grease as a bonding agent. A thin-sheet Watlow heater is permanently attached to the underside of the heater plate, where also are located the thermocouples and resistance thermometer elements for measurement and control. The sample-heater plate assembly rests on three plastic pegs to form the closing face of an open rectangular aluminum box. An approximately $\frac{1}{4}$ -inch gap separates it from the box sides. The gap is closed with aluminized Mylar strips to shield the sample edges from the cold plate. The box has a thin-sheet heater, identical to that of the heater plate, fastened to the inside bottom, where are located the box thermocouples and resistance thermometer. A polished aluminum, insulated radiation shield intervenes in the space between the two heaters.

The exposed sample face lies about $\frac{1}{4}$ inch from, and parallel to, the blackened (Parson's black) lower surface of a large copper plate to which is affixed a helical coolant circulation coil. The coil is supplied with liquid nitrogen from a 4-liter reservoir. Filling of the reservoir is accomplished through lines leading into the vacuum chamber and controlled by a signal from a thermistor sealed into an immersion tube in the reservoir. Figure 2 shows the configuration.

The entire unit described is situated within a standard 18-inch bell-jar vacuum system.

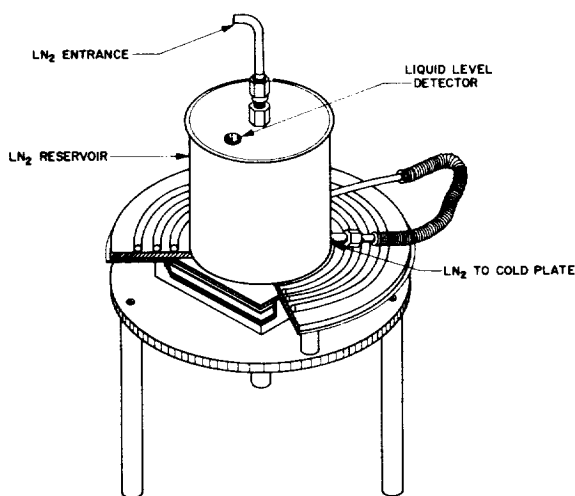


FIGURE 2.—Emittance enclosure assembly.

The system pumps down to about 2×10^{-7} torr when the cold plate is stabilized.

Figure 3 shows the electrical layout. Storage batteries furnish the heater power. In earlier phases of the experimental work, 0.1-percent regulated power supplies were used; but the regulation of these supplies was found insuf-

ficient to be compatible with the sensitivity of the Fluke voltmeters. Power to the sample heater is measured by means of two Fluke Model 825A potentiometric voltmeters, one of which is across an 0.02-percent Leeds and Northrup series resistance to measure current.

EXPERIMENTAL RESULTS

The test surfaces, representative of low- and moderate-emittance surfaces, were used in the equipment just described. For each

TABLE I.—*Buffed 6061-T6 Aluminum*

Iteration method		Rate method	
T, °F	ϵ_s	T, °F	ϵ_s
84.5	0.0490	83.8	0.0506
84.5	.0501	86.0	.0500
		83.8	.0506
Average ϵ_s		0.0495	0.0504
Data spread		2.2%	1.2%
Emittance from a 17-hr constant-temperature run, $\epsilon_s = 0.0501$ at 87.9° F.			

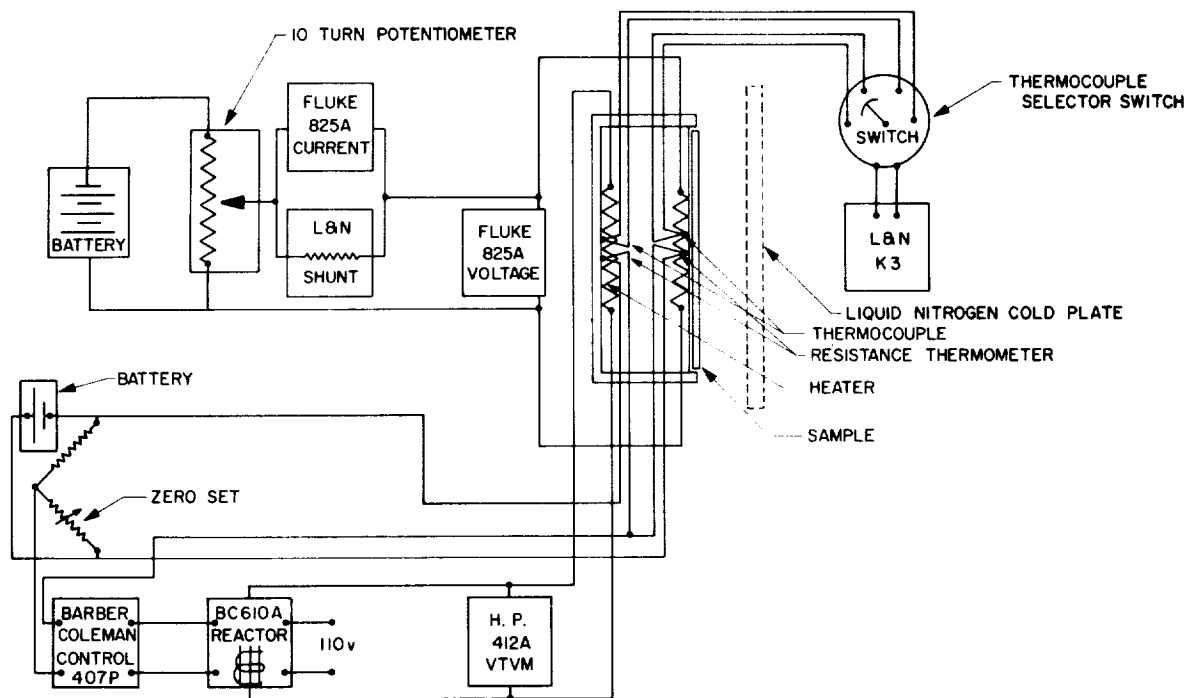


FIGURE 3.—Electrical block diagram.

sample both methods were applied several times in succession without breaking the vacuum, in order to determine the statistical dispersion of the measurements. The surfaces are typical of

those used in the JPL vehicle skins and internal surfaces where heat exchange rates are to be controlled or limited. The results are summarized in tables I, II, and III.

TABLE II.—*Dow 7 Coated Magnesium*

Iteration method		Rate method	
$T, ^\circ\text{F}$	ϵ_s	$T, ^\circ\text{F}$	ϵ_s
84.0	0.248	88.5	0.252
		87.8	.254
Emittance from a 15-hr constant-temperature run, $\epsilon_s = 0.251$ at 84.5°F .			

TABLE III.—*Buffed Gold Plate on Aluminum*

Iteration method		Rate method	
$T, ^\circ\text{F}$	ϵ_s	$T, ^\circ\text{F}$	ϵ_s
79.5	0.0381	82.3	0.0386
82.9	.0389	83.7	.0378
Average ϵ_s	0.0385		0.0382
Data spread	2.1%		2.1%

DISCUSSION OF ERRORS

The statistical dispersions indicated in the three tables are for very limited groups of measurements. Errors arising in the equipment and the techniques have been estimated by the error treatment found in reference 7, with the aid of the functional graphs therein given. In using these graphs, a cold-plate temperature of 77°K and a sample temperature of 300°K were assumed. The major errors and estimates of their magnitudes are given in table IV.

CONCLUSION

Two procedures have been presented for determining the total hemispherical emittances of surfaces in the room-temperature range from measurements of heating power input and rate of change of temperature. An apparatus for making such measurements, which is convenient and uses a minimum of liquid nitrogen, is also described.

TABLE IV.—*Major Errors and Estimates of Their Magnitudes*

Source of error	Error	Resultant emittance error $\delta\epsilon/\epsilon, \%$
1. Temperature measurement, including thermocouple calibration.	$\pm 0.1^\circ\text{F}$	± 0.23
2. Temperature gradients in plane of sample surface.	2.0°F	± 1.3
3. Sample area measurement	$+0.010$ inch of linear dimension.	± 0.33
4. Power measurement:		
a. Instrument reading error	$\pm 0.1\%$	± 0.2
b. Temperature difference between sample and guard box.	$\Delta T \leq 0.5^\circ\text{F}$	± 0.8
c. Gas conduction	0.00016 watts max at 10^{-7} torr (ref. 5).	± 0.03
d. Lead conduction No. 22 AWG copper leads.	0.010 watts max	± 2.5 for $\epsilon = 0.03$
5. Temperature rate measurement	1.3% (graphical)	± 1 for $\epsilon = 0.03$
6. Gray assumption for parallel plate heat exchange.*	1 for gold 7.0 for white paint

*Calculation carried out by applying the equations of reference 7 to the numerical data of reference 8.

Results are given for buffed aluminum, buffed gold-plated aluminum, and Dow 7 coated magnesium surfaces. The dispersions of the emittance values obtained are given, together with a listing of equipment, computational, and intrinsic errors. For the low-emittance surfaces, for which the percentage errors are largest, the maximum error is about 6 percent.

ACKNOWLEDGMENT

The author wishes to express his appreciation to Mr. Stanley E. Peterson of this Laboratory for construction of the liquid-nitrogen system and its controls, and for his many days of help in measurement and data reduction.

REFERENCES

1. GORDON, G. D., and LONDON, A.: Emittance Measurements at Satellite Temperatures. Measurement of Thermal Radiation Properties of Solids, Joseph C. Richmond, ed. NASA SP-31, 1963, pp. 147-151.
2. CAREN, R. P.: Cryogenic Emittance Measurements. Measurement of Thermal Radiation Properties of Solids, Joseph C. Richmond, ed. NASA SP-31, 1963, pp. 45-49.
3. BUTLER, C. P., and JENKINS, R. J.: Space Chamber Emittance Measurements. Measurement of Thermal Radiation Properties of Solids, Joseph C. Richmond, ed. NASA SP-31, 1963, pp. 39-43.
4. BUTLER, C. P., and INN, EDWARD C. Y.: A Method for Measuring Total Hemispherical Emissivity of Metals. First Symposium—Surface Effects on Spacecraft Materials, Francis J. Clauss, ed., John Wiley & Sons, Inc., c. 1960, pp. 195-211.
5. DUSHMAN, SAUL (J. M. Lafferty, ed.): Scientific Foundations of Vacuum Technique. Second ed., John Wiley & Sons, Inc., c. 1962, pp. 43-53.
6. WORTHING, ARCHIE G., and GEFFNER, JOSEPH: Treatment of Experimental Data. John Wiley & Sons, Inc., c. 1943, ch. XI.
7. NELSON, K. E., and BEVANS, J. T.: Errors of the Calorimetric Method of Total Emittance Measurement. Measurement of Thermal Radiation Properties of Solids, Joseph C. Richmond, ed. NASA SP-31, 1963, pp. 55-65.
8. DUNKLE, R. V.: Thermal-Radiation Tables and Applications. Trans. ASME, vol. 76, no. 4, May 1954, pp. 549-552.

SESSION IV
SPACE ENVIRONMENTAL EFFECTS

CHAIRMAN: GERHARD B. HELLER

NASA GEORGE C. MARSHALL SPACE FLIGHT CENTER, HUNTSVILLE, ALA.

36. Problems and Research Effort in Space Environment Effects¹

GERHARD B. HELLER

NASA MARSHALL SPACE FLIGHT CENTER, HUNTSVILLE, ALA.

A very brief review is given of the problem of thermal control of spacecraft and of the problem of the stability of thermal control surfaces to the particle radiation, solar ultraviolet radiation, and micrometeoroids in space. The different aspects of the environment effect problem that are treated by the papers in this session are indicated.

Curves are presented showing equilibrium temperatures of cylindrical spacecraft at distances from the Sun of 0.1 astronomical unit to 30 astronomical units (orbit of Neptune) for α_s/ϵ_T values up to 10.

Papers in the first three sessions of the Symposium indicated that much research has yet to be done to enable us better to understand thermal radiation properties, that we cannot completely define the surface characteristics of real surfaces, and, furthermore, that the precision of a measurement may be irrelevant when the surface being measured cannot be defined. However, in all the matters that have so far been discussed, we have been considering surfaces and measurements in the well-defined and comfortable surroundings of the laboratory. In this session, we leave this familiar environment and go out into space. This means that, if we solve all the problems discussed in the previous sessions, we shall only reach the starting point for the matter that is going to be discussed here. If the right types of surfaces for a space vehicle have been found, if their properties have been properly measured, and, thus, by ground studies, we know exactly what we put up there, then the fun really starts, because none of the surfaces will stay as they were when we put them into orbit, or into deep space. But, lest I overstate this

problem, I can assure you that, of the satellites that have been put into orbit, many have worked well and have remained within acceptable temperature limits. On the other hand, there have been thermal problems and, with the increasing demands of our national space program, the problems are becoming increasingly severe and urgent. Those who have been directly concerned with these problems know that the solutions of the many research questions raised at all sessions of this Symposium have a certain degree of urgency; in fact, many people, including quite a number of those in the audience, would like to have the solutions immediately.

SPACE ENVIRONMENT AND ASSOCIATED PROBLEMS OF THERMAL CONTROL SURFACES

The external thermal environment consists of:

- Solar radiation
- Reflected solar radiation from planetary bodies
- Infrared radiation from planetary bodies

The environmental factors that may affect the

¹ This paper was delivered by Mr Heller, the chairman of Session IV, as an introduction to the session.

surface radiation characteristics are

Cosmic rays
Solar wind
Solar ultraviolet radiation
Micrometeoroids

More information is needed in all of these areas, with regard to both the environment and its effects on solids. This session is mainly concerned with the latter.

Figure 1 shows in graphic form the ranges of interest for the space effort. Solar distances range from 0.1 AU to the distances of the outer planets. The mean temperature of a cylindrical spacecraft is plotted against the ratio α_s/ϵ_T ; this temperature would be close to the mean instrument temperature under conditions of

passive temperature control. The temperature used for defining ϵ_T is the mean temperature of the spacecraft; and since ϵ_T for a given material varies with temperature, α_s/ϵ_T for a given material would plot as a curve on this figure rather than as a vertical line. A vertical line, in effect, would correspond to a range of materials. Temperature curves are shown for a spacecraft at a distance from the Sun of 0.1 AU and at the distances of Mercury, Venus, Earth, Mars, Jupiter and Neptune. At the distance of Earth, spacecraft temperatures in the range of 273° to 333° K, correspond to α_s/ϵ_T values in the neighborhood of 1. This is, of course, a basic reason for the favorable temperature conditions on our planet. Achieving an α_s/ϵ_T ratio of 1 is well within the present state of the art,

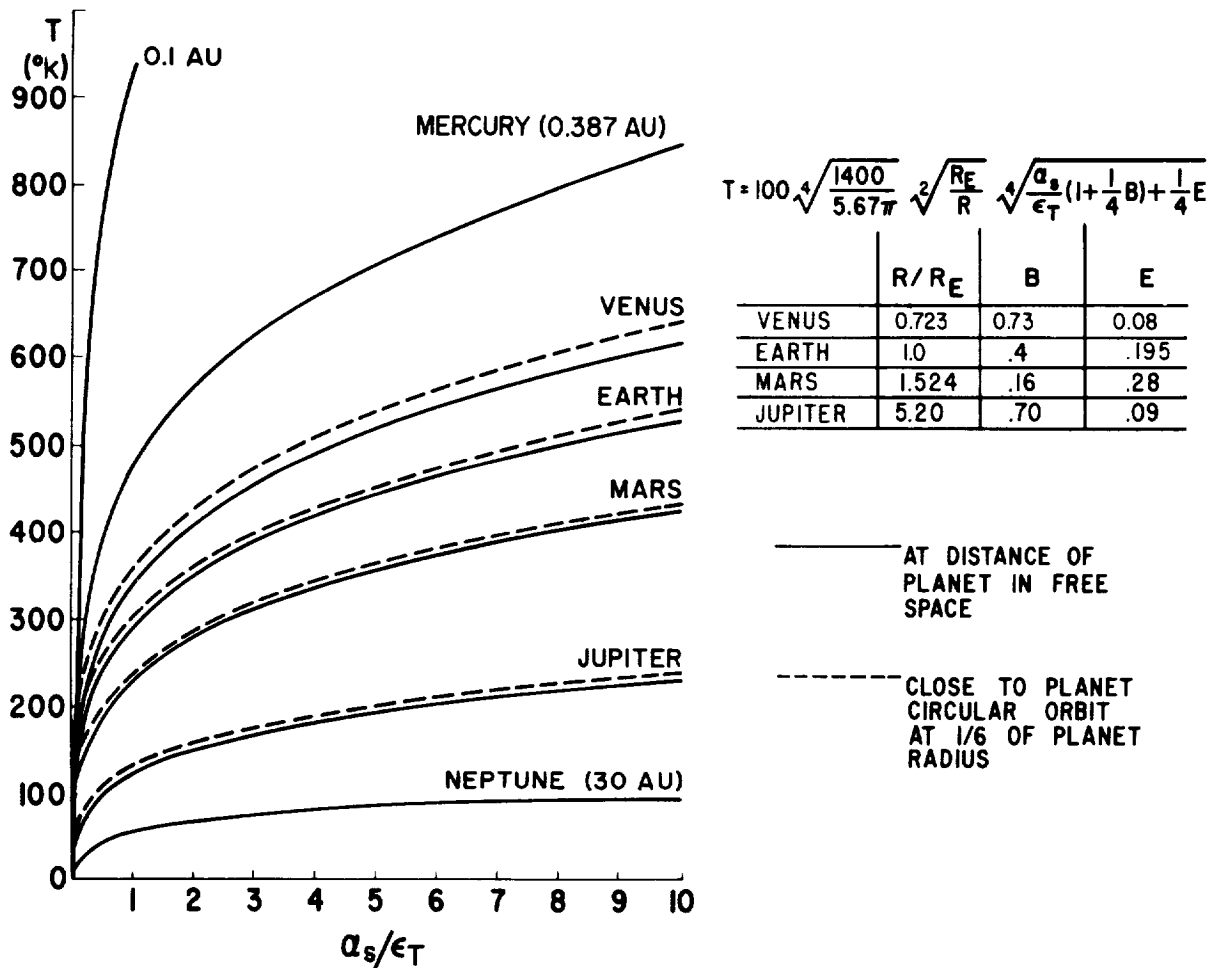


FIGURE 1.—Temperature of cylindrical spacecraft at various distances from the Sun.

provided we can meet the requirement of long-time stability to the space environment. At 0.1 AU, the spacecraft runs too hot, even for very low α_s/ϵ_T values. Present project investigations conducted by NASA aim at probes going to 0.25 AU. Temperatures will fall between those for 0.1 AU and those for the distance of Mercury.

At the distance of Neptune, the spacecraft will be too cold at all α_s/ϵ_T ratios. For these extreme cases, the thermal control problem is much more severe than in the neighborhood of Earth, and the choice of available thermal control surfaces is narrowed down. We also have to consider that a spacecraft must operate when it is close to Earth, and during its entire trajectory through space to the environment of the distant planet. If it is moving away from the Sun, as in a trajectory from Earth to Mars, it could benefit from a gradual degradation of its coating due to the space environment. Such degradation should raise the α_s/ϵ_T ratio to the value required at the distance of Mars; ideally, the increase of α_s with time should exactly compensate for the increase of the solar distance with time along the spacecraft trajectory.

The types of spacecraft surfaces important in our field of thermophysics are:

- a. Functional surfaces, for example, solar cells
- b. Surfaces with surface characteristics that, because of structural or material requirements, are essentially predetermined
- c. Space radiators or solar collectors associated with space power plants
- d. Thermal control surfaces, the specific purpose of which is to raise or lower temperatures to meet spacecraft requirements

A spacecraft may have ten or more different surfaces in categories (a), (b), and (c). The surfaces under (d) are used to counteract their effects and provide acceptable temperatures where needed. Different types of such thermal control surfaces are required on a spacecraft to correct for the undesirable radiation characteristics of the other functional, structural, or

radiative surfaces, which would result in temperatures that are too high or too low. The requirements thus cover an even wider range than is indicated in figure 1, which shows only mean values. These problems, which are already difficult for the neighborhood of Earth, become far more difficult for other regions of the solar system. Because of the thermal control requirements, we need surfaces whose α_s/ϵ_T ratios are higher and lower than the mean values shown in figure 1 by large factors.

Because of these requirements we need surfaces in as large a range of both high and low α_s/ϵ_T values as possible. Furthermore, these surfaces have to operate in space for extended periods of time. In many cases, a solution to the thermal control problem can be found that is adequate for a one- or two-month operation; but we need information with which to predict reliably the operation in space for years.

The papers in this session on *The Effects of the Space Environment on Thermal Control Surfaces* cover the areas of

- Nuclear radiation
- Solar wind
- Solar electromagnetic radiation
- Micrometeoroids

The most important effect for near-Earth operation is that due to the solar electromagnetic radiation, mainly the ultraviolet radiation. Five papers are devoted to this subject, compared with two on micrometeoroids, one on the solar wind, and two on cosmic or nuclear radiation. Most of the effort in various thermophysics laboratories in the country is in the area of ultraviolet degradation.

This problem was important, for example, in the selection of the thermal control surfaces of Explorer I. Paints with organic-type binders were excluded because of possible space environmental effects. The selection had to be made without detailed studies of degradation mechanisms and without development of new space-stable materials. However, the surfaces were selected so that possible environmental effects would be minimized. The metallic surfaces were sand-blasted with a dental abrasive and the required white surfaces were obtained by

coating portions of the metal surface with flame-sprayed alumina. The results of the telemetered temperatures during the 105-day instrument lifetime of the satellite showed that no measurable change due to the space environment occurred in this time period. Since the launching of Explorer I, many spacecraft have been put into orbit or deep space. The thermal control, based on thermophysical principles, has required major analytical and design activity in all of these spacecraft projects. This tremendous effort has contributed to our knowledge, but has also shown in many cases the inadequacy of our fundamental knowledge underlying the various applications.

INTRODUCTION TO THE PAPERS

Cosmic and Nuclear Radiation

It may be useful to consider the present status of our knowledge of the environmental effects. It is generally assumed that the effects due to cosmic and nuclear radiation, solar wind, and micrometeoroids are negligible. However, the only case in which this assumption has been corroborated by extensive research is that of cosmic radiation and nuclear radiation. Considerable effort has been underway for some time on the effects of this hard radiation on materials. However, for the major portion of this research activity, interest has been not in thermophysical properties but in bulk material problems. The papers on this subject are:

Some Fundamental Aspects of Nuclear Radiation Effects in Spacecraft Thermal Control Materials, by J. E. Gilligan and R. P. Caren

Nuclear Environmental Effects on Spacecraft Thermal Control Materials, by R. A. Breuch and H. E. Pollard

Solar Wind

Most of the efforts in the area of solar wind effects were also devoted to other aspects of space research such as sputtering material losses. G. K. Wehner of Litton Industries has recently been studying the effects of simulated solar wind on a white paint used for thermal control of the upper stage of flights SA-8 and

SA-9 of the Saturn I space vehicle. His studies have already shown some interesting and quite unexpected results concerning the effect of the solar wind on white oxide coatings. Early results of research in this area are discussed by Dr. Wehner in his paper *Solar-Wind Bombardment on a Surface in Space*.

Micrometeoroids

The effects of micrometeoroids on thermal control surfaces of space vehicles have been neglected and only a small research effort has gone into this aspect of the space environment. Considerably more research effort is needed to determine both the micrometeoroid flux density and its direction and velocity distribution in near-Earth space and in the solar system. The paper, *The Effects of Micrometeoroids on the Emittance of Solids*, presented by Ronald Merrill covers analytical work done at NASA Marshall Space Flight Center and experimental work done by C. H. Leigh and T. S. Laszlo, of the AVCO Corporation, under a NASA contract during the past three years. The paper shows that there is a still unexplained discrepancy between theoretical and laboratory results on the one hand and preliminary space results on the other. The space results are insufficiently accurate because they were not based on experiments planned for this purpose. More accurate experiments are needed to resolve the problems, especially to understand the mechanisms involved and the correlation with the optical properties of solids. Micrometeoroid effects can be very important for polished surfaces, for surfaces of very high and very low α_s/ϵ_T ratios, and for all surfaces that are exposed in space for long periods of time.

Another effort in this area which has contributed considerably to our knowledge in this field is that by Michael J. Mirtich and Herman Mark at the NASA Lewis Research Center. Their paper is entitled *Alteration of Surface Optical Properties by High-Speed Micron Size Particles*.

Ultraviolet Radiation

Most of the investigations of environmental effects have been in the area of solar electromagnetic radiation effects. In this area, the

effects have been most striking and the early concept that inorganic oxides are stable had to be revised. Because of the pressing needs of our national space effort, most laboratory investigations during the first five years since Explorer I have been of an *ad hoc* nature. Investigations were made to solve specific problems and little time was spent on trying to understand the underlying physical principles. Therefore, if we try to summarize our present state of the art, we find that our knowledge is not very advanced. We still do not understand the interaction of electromagnetic energy quanta with organic and inorganic solids; we still do not know whether there is a wavelength selectivity with respect to ultraviolet-radiation effects; and we do not know the mechanism or mechanisms of relaxation. It is a very complex field, with a multitude of different effects for many different solids. Only in the past two years has the research activity in these areas been increased, and it represents only a modest beginning. The five papers on ultraviolet effects in this session are

Experimental Development of a Technique for the Correlation of Flight- and Ground-Based Studies of the Ultraviolet Degradation of Polymer Films, by John A. Parker, Carr B. Neel, and Morton A. Golub

Ultraviolet Irradiation in Vacuum of White Spacecraft Coatings, by G. A. Zerlaut,

Y. Harada, and E. H. Tompkins
The Effects of Ultraviolet Radiation on Low α_s/ϵ_r Surfaces, by R. L. Olson, L. A. McKellar, and J. V. Stewart
Preliminary Results From a Round-Robin Study of Ultraviolet Degradation of Spacecraft Thermal Control Coatings, by J. C. Arvesen, C. B. Neel, and C. C. Shaw
A Study of the Photodegradation of Selected Thermal Control Surfaces, by G. F. Pezdirtz and R. A. Jewell

These papers describe various aspects of this difficult subject. They also demonstrate clearly that we must consider different physical processes. An attempt is made to solve the problem of the interaction mechanisms for a few specific cases that lend themselves to a theoretical and experimental attack. The results of these papers will hopefully stimulate further research on this subject. The paper on the results of the "Round-Robin" ultraviolet-degradation experiments points out very dramatically how difficult this subject is. The large spread of data obtained by the different investigators using identical ultraviolet lamps and identical thermal control samples shows that more research is needed to clarify the basic phenomena and to determine the effects due to the specific laboratory techniques. A very important aspect is the simultaneous effects of ultraviolet radiation and temperature, vacuum, and other environmental factors.

37. Solar-Wind Bombardment of a Surface in Space¹

G. K. WEHNER

LITTON SYSTEMS, INC., MINNEAPOLIS, MINN.

The solar wind is described and its effects on surfaces are reviewed. Experimental results are given for materials subjected to simulated solar-wind bombardment. Among the effects discussed are sputtering-type erosion, chemical reaction with paint vehicles and reduction of oxide pigments, and production of lunar-surface optical characteristics in a basalt powder.

The surface of any body in space is under bombardment by high- and low-energy elementary particles. The question discussed here concerns the effects that occur on a surface under bombardment by the solar wind, that is, by low-energy protons and α -particles. From astrophysical observations and measurements with Explorer X, Lunik II, and Mariner II, data on flux density, composition, and energies of the particles in the solar wind are now fairly well established. Under a quiet Sun, the data indicate a flux of 2×10^8 protons/cm²-sec with an average velocity of 600 km/sec at Earth orbit distance from the Sun. The protons are accompanied by 15 percent as many α -particles with the same velocities. Under solar storm conditions, the flux and the particle velocities increase to much higher values. Under normal conditions, the bombarding energies are up to 1.85 keV for protons and 7.4 keV for α -particles; under solar-storm conditions, the energies are about 5 keV for protons and 20 keV for α -particles.

These solar-wind bombardment conditions can be simulated in the laboratory and, with much higher flux densities for short bombardment times, measurable sputtering effects and

surface damage can be obtained. With the goal of studying possible modifications of the lunar surface, measurements were performed with mass-separated H^+ , H_2^+ and H_3^+ beams (ref. 1) and in low-pressure H plasmas. It is necessary to distinguish between purely physical effects, such as crystal damage or sputtering, and superimposed chemical reactions between H and compounds such as oxides. Figure 1, for instance, shows the sputtering yields for protons on copper (Cu) in the energy range from 1 to 5 keV. The yields have a rather broad maximum in the range of solar-wind bombardment energies. The sputtering

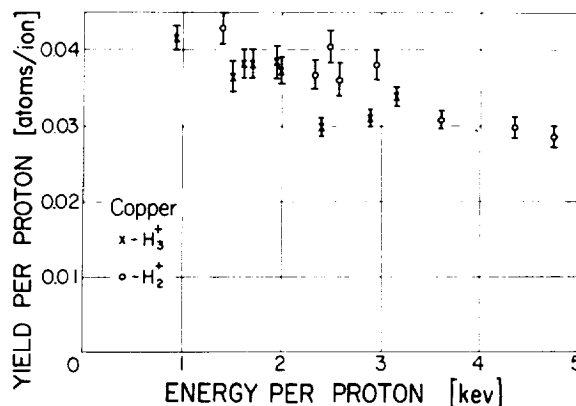


FIGURE 1.—Sputtering yields of copper under proton bombardment (from ref. 1).

¹ This work was partly supported by the National Aeronautics and Space Administration, under Contract NASw-751.

rates are rather small and amount to only about $1 \text{ \AA}/\text{year}$ for Cu and $0.5 \text{ \AA}/\text{year}$ for iron (Fe). For many oxides the rates are roughly in the same range as that for Fe. Thus, the Moon should have lost a layer 17 cm thick in 4.5×10^9 years, or a 1-cm-thick Cu plate would be sputtered away in approximately 10^8 years. Physical sputtering will, therefore, hardly present any erosion problems in space missions. These results have been reported in detail in a recent paper (ref. 2).

More interesting effects arise from the cementing together of powder particles by sputtered atoms, from chemical reactions, or from the bombardment-induced breakup of molecules. Experiments with metal targets and metal-, oxide-, and rock-powder samples demonstrate the leveling and smoothing of macroscopic surface features, the etching of polished surfaces (because differently oriented grains have different sputtering rates), and the cementing together of loose particles into a porous, brittle, fibrous crust.

We have observed that many compounds, such as white oxides, darken under the bombardment because oxygen (O) is more likely to escape in the breakup process resulting in a metal enrichment at the surface. Under noble-gas ion bombardment, black cupric oxide (CuO) is first converted into red cuprous oxide (Cu₂O) and finally becomes covered with a very porous Cu layer. Under H ion bombardment we observed an immediate conversion to metallic Cu. X-ray diffraction analysis shows that the red ferric oxide (Fe₂O₃) changes into ferrihydrous oxide (Fe₃O₄), ferrous oxide (FeO), and Fe under ion bombardment. Very pronounced chemical effects were observed in the case of tin (Sn) bombarded by H ions. Here, the H combines with the tin and forms the volatile tin hydride (SnH₄), which results in much higher apparent sputtering rates.

The controlled ion bombardment of insulator surfaces in a plasma was made possible with a recently developed technique in which a high-frequency voltage provides the necessary neutralization of surface charges at the target (ref. 3). Many of these experimental results are given in a paper on the modification

of the lunar surface by solar-wind bombardment (ref. 4). One interesting result concerns the back reflection properties of surfaces bombarded by the solar wind. This is shown in figure 2, which shows our measurements of the visible light reflected in a direction 60° to the surface normal as a function of the angle of incidence of the incoming light.

A basalt powder, with grain size 2 to 10μ , provides a surface which resembles a Lambert surface. When this basalt powder is bombarded for the equivalent of 10^6 years of solar-wind bombardment, the surface is changed to a very open "fairy castle" structure (ref. 5) with radically different light reflection properties. With a fixed observation (or reflection) angle of 60° , a strong back-reflection peak appears at an incidence angle of 60° , very closely resembling the characteristic back-reflection peak in the corresponding curve for the lunar surface. Figure 3 shows how the surface of basalt powder darkens with bombardment time. The bombardment thus provides an explanation for the low albedo of the lunar surface.

The times involved here for obtaining visible effects are so long that we did not anticipate that spacecraft thermal-control paints would undergo measurable changes in only a few years. However, some exploratory work gave a rather surprising result. Paint samples (ZnO in methyl silicone binder) develop a visible brownish or tan color together with some glossi-

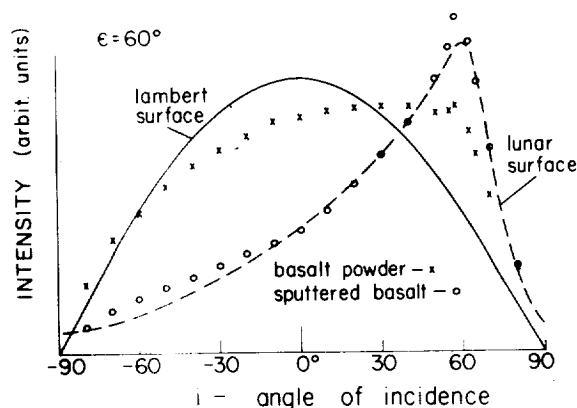


FIGURE 2.—Angular light reflection properties of basalt powder before and after the equivalent of about 10^6 years of solar-wind bombardment.






Sputtering Duration		Normal Albedo
original		~ 0.27
$3\frac{1}{3}$ minutes (100 YR EQUIV.)		0.16
33 minutes (10 ³ YR EQUIV.)		0.07
5 $\frac{1}{2}$ hours (10 ⁴ YR EQUIV.)		0.05
55 hours (10 ⁵ YR EQUIV.)		0.06

FIGURE 3.—Darkening of basalt powder under simulated solar-wind bombardment.

ness at bombardment times equivalent to only 5 years of solar-wind bombardment. Figure 4 shows how the angular light reflection changes. Here, the observation direction was 30° to the surface normal. There is increased specularity of the reflection when the beam impinges at -30° . Measurements (with a Beckman DK2 with integrating sphere) of absorbance in the visible part of the spectrum show a rather pronounced change, as in figure 5.

The hydrogen plasmas used in these studies are strong ultraviolet radiation sources. The effects, however, are not caused by the ultra-

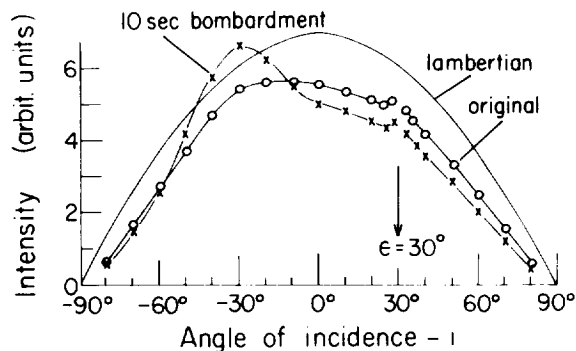


FIGURE 4.—Angular light reflection of a spacecraft paint (zinc oxide in methyl silicone binder) before and after the equivalent of 5 years of solar-wind bombardment. Angle of observation (or reflection), 30° .

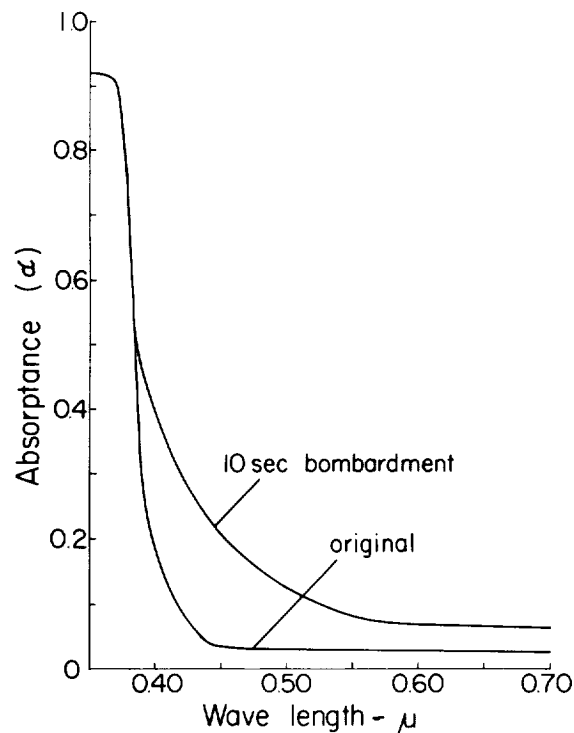


FIGURE 5.—Spectral absorbance of a white paint (zinc oxide in methyl silicone binder) before and after simulated solar-wind bombardment.

violet radiation, as shown in an experiment in which part of the sample was covered with a thin quartz foil. The effects seem to be caused predominantly by chemical reactions of the protons with the binder. In the case of metal surfaces, we are in agreement with recent work by Anderson (ref. 6) who found very little change in thermal radiation properties after the equivalent of a few years of solar-wind bombardment. In the case of more complex materials, such as spacecraft thermal-control coatings, more serious research effort is warranted. We cannot exclude the possibility that serious problems will arise in violent solar storms, in missions closer to the Sun, in missions of long duration, and in ion-engine environments.

REFERENCES

1. KENKNIGHT, C. E., and WEHNER, G. K.: Sputtering of Metals by Hydrogen Ions. *Jour. Appl. Phys.*, vol. 35, no. 2, Feb. 1964, pp. 322-326.
2. WEHNER, G. K., KENKNIGHT, C. E., and ROSEN-

- BERG, D. L.: Sputtering Rates Under Solar-Wind Bombardment. *Planetary and Space Sci.*, vol. 11, no. 8, Aug. 1963, pp. 885-895.
3. ANDERSON, G. S., MAYER, WILLIAM N., and WEHNER, G. K.: Sputtering of Dielectrics by High-Frequency Fields. *Jour. Appl. Phys.*, vol. 33, no. 10, Oct. 1962, pp. 291-292.
4. WEHNER, G. K., KENKNIGHT, C. E., and ROSENBERG, D.: Modification of the Lunar Surface by the Solar-Wind Bombardment. *Planetary and Space Sci.*, vol. 11, no. 11, Nov. 1963, pp. 1257-1261.
5. HAPKE, BRUCE, and VAN HORN, HUGH: Photometric Studies of Complex Surfaces, With Applications to the Moon. *Jour. Geophys. Res.*, vol. 68, no. 15, Aug. 1, 1963, pp. 4545-4570.
6. ANDERSON, DONALD L., and NOTHWANG, GEORGE J.: Effects of Sputtering With Hydrogen Ions on Total Hemispherical Emittance of Several Metallic Surfaces. NASA TN D-1646, 1963.

DISCUSSION

JOSEPH C. RICHMOND, National Bureau of Standards: I am very much interested in this retroreflection phenomenon, both on the lunar surface and on the bombarded basalt specimens. Do you have any explanation for the mechanism that is producing this?

WEHNER: I have here a stereo slide of a sample of an oxide which was bombarded for the equivalent of millions of years. You will find on the surface a very intricate structure which is very similar to what Hapke has investigated and calls the "fairy castle" structure, namely, a formation on the surface resembling dendrites, with deep holes. Only such a surface seems to give this type of reflection; Hapke has simulated this, for instance, with botanical materials—lichens or a forest of closely spaced whiskers.

CLAIRE CHAPIN, Purdue University: I was interested in your remark that you think that the solar wind was pretty well defined. Within what limits do you think you know the solar-wind particle flux and velocity?

WEHNER: I think that from the measurements of Mariner II, especially, which stretch over a long time (three months), it looks as though this is really a fairly constant breeze. I think the energy varies with solar activity from 200 ev to several kilovolts for the protons, but the fluxes may well undergo changes up to an order of magnitude. We should not forget that these measurements were made at the time of a fairly quiet Sun, and it may well be that, in a more active period, these values are higher on the average.

LEONARD JAFFE, Jet Propulsion Laboratory: Can you say more about the paints that you tested? You showed the slides but you did not mention what material it pertained to.

WEHNER: I think these are paints which have actually been developed for space application. These are ZnO and TiO₂ pigments with a silicone vehicle or some other vehicle. I forgot to mention that these pronounced effects are not so much due to physical sputtering as to chemical effects with the vehicle. The pigment itself, like ZnO, does not show these short-time degradations.

FRANCIS J. CAMPBELL, U.S. Naval Research Laboratory: What machine did you say was your source of these particles? And which reference completely describes these experiments?

WEHNER: We have two things here. The measurements we are making with mass-separated H beams are

published in the February 1964 issue of "Journal of Applied Physics". The studies in low-pressure hydrogen plasma have been published in "Planetary and Space Science" in two papers, one last month and one about 5 months ago. We are working here with insulating surfaces, and in working with insulating surfaces, there is the problem of accelerating the ions toward the insulator. This is simple with a metal but not with an insulator. Here we use a special trick which we call our high-frequency bombarding technique. Essentially, we have a metal plate which is covered with this material, and we apply an RF signal to the metal plate—2 megacycles, or something like that. Then one part of the cycle brings in the ions for bombarding the surface; this would soon charge up the surface and stop the bombardment. But, when you do this with high frequency, the other part of the cycle brings in the electrons which neutralize the surface charge. This technique has turned out to be very useful for sputtering insulators, and we can sputter quartz, diamond, and so on, quite readily.

UNIDENTIFIED: I would like to ask what is known of the dependence of these effects on particle velocity. The particles have considerably increased velocities during flares.

WEHNER: When it comes to strictly physical sputtering, and we are beyond the maximum, the effects are bound to get smaller with increasing energy, because then the ion penetrates deeper into the lattice, everything takes place further away from the surface, and the energy is spent in heat or in creating dislocations and so on. The effects that take place close to the surface favor true sputtering. When it comes to chemical effects, I think that the energy is not of so much importance. I think it is mainly just the fact that we have here an ionized hydrogen which is then very active and can cause chemical reactions with the materials.

GENE A. ZERLAUT, IIT Research Institute: I have both a comment and a question. I believe that the specimen is a ZnO-pigmented methyl silicone. The methyl silicone is General Electric's LTV-602. Do you have any idea of whether it is the secondary radiation that might be causing the damage in this type of system?

WEHNER: What do you mean by secondary radiation?

ZERLAUT: In other words, what is the mechanism of

the damage associated with proton bombardment?

WEHNER: I think it is probably a chemical reaction similar to what happens in other oxides; namely, some release of metal atoms. We may actually, in the case of oxides, form some water molecules. The ion coming in combines with oxygen and forms water molecules, and what is left is a metal atom.

ZERLAUT: My question relates to the fact that in the ultraviolet irradiation of elastomeric silicones, one observes less stability than in the resin-type methyl silicones which have less methyl content. As you degrade the elastomeric silicones thermally—toward the basic silicate matrix—you gain in ultraviolet stability.

WEHNER: I fully agree with you. As I mentioned, these are very exploratory results and we must, I

think, find not only how these things behave, but also a little bit more about what is really causing the effects; and this would involve some more penetrating research.

GERHARD B. HELLER, NASA-Marshall Space Flight Center: Thank you, Dr. Wehner. At the beginning of his talk Dr. Wehner mentioned my interest in this, and it might be of interest to you to know why I was interested. This is a paint that has been selected to be used on one of the Saturns as a thermal-control surface, and there was a legitimate question as to whether what happened is really serious, since the intended orbit is below the Van Allen belt. These problems become more serious above the belt; so there is still a problem, but it is not that immediate. I am glad this go-around somehow contributed to this Symposium.

38. Some Fundamental Aspects of Nuclear Radiation Effects in Spacecraft Thermal Control Materials¹

J. E. GILLIGAN² AND R. P. CAREN

RESEARCH LABORATORIES, LOCKHEED MISSILES & SPACE COMPANY, PALO ALTO, CALIF.

The methods and results of an investigation to determine the mechanisms by which solar reflector thermal control systems degrade under individual and combined ultraviolet and nuclear radiations are described. Appropriate optical- and radiation-effects theories are compared with the published results of irradiation experiments in which certain transparent dielectric and semiconductor pigments have been studied. Conclusions are reached regarding the equivalence of ultraviolet- and nuclear-radiation effects, basic mechanisms of induced reflectance changes, and possible means of limiting the degradation caused by these radiations.

At the outset of the investigations reported in this paper, very little was known about the mechanisms responsible for the changes in thermal radiative properties of thermal control systems when subjected to nuclear radiation. While the detailed mechanisms still remain unknown for many of these systems, valuable insight has been gained in determining the fundamental causes of degradation. The paint systems dealt with in this paper are of the solar reflector (white paint) class, and damage (degradation) is defined as increased spectral absorptance in the solar region of the electromagnetic spectrum.

We intend to show how the reflectance spectra of irradiated paint systems can be analyzed by means of theoretical relationships and to show how damage mechanisms can be deduced therefrom. Additionally, it will be shown how these deductions accord with experimental observations. In order to explain the basic causes of degradation, it is necessary to understand (1) the fundamental properties of materials which govern their optical behavior,

(2) the interaction mechanisms of energetic radiation with matter, and (3) the defects which energetic radiations produce and how these may affect optical properties. In the present paper these three topics will be briefly reviewed. Then the effects of radiation on the spectra of several typical paint systems will be described and discussed with regard to possible damage mechanisms.

BACKGROUND THEORY

Optical Properties

The optical properties of solid opaque substances have been treated by many authors (for example, in ref. 1 to 3). The ordinary developments of the theory seek to obtain mathematical expressions for the absorptance and reflectance of electromagnetic radiation as a function of basic material properties. The rigorous Fresnel expression for the specular reflectance R_λ of a plane wave normally incident on a smooth surface of a material with index of refraction n and extinction coefficient k is

$$R_\lambda = \frac{(n_\lambda - 1)^2 + k_\lambda^2}{(n_\lambda + 1)^2 + k_\lambda^2} \quad (1)$$

¹ This work was performed under Air Force Contract AF04(695)-136.

² Now at IIT Research Institute, Chicago, Ill.

The variation of the properties n_λ and k_λ with photon energy (or wavelength) is of immediate importance. The equations that express this dependence of n_λ and k_λ on wavelength are known as dispersion relations.

The complex index of refraction N_λ is given by

$$N_\lambda = n_\lambda - ik_\lambda \quad (2)$$

where n_λ is the real index of refraction and k_λ is the extinction coefficient. The complex index of refraction of a material is related to the microscopic atomic parameters of the material through its relation to the volume polarizability of the material; this relationship is given by

$$N_\lambda^2 = 1 + 4\pi\beta_\lambda \quad (3)$$

where the volume polarizability at a photon frequency ω is given by

$$\beta = \sum_j \frac{Ne^2 f_j}{4\pi m_j} \frac{1}{(\omega_j^2 - \omega^2) + ig_j \omega} \quad (4)$$

where

- β volume polarizability at photon angular frequency ω (wavelength λ)
- N electron density
- e electron charge
- f_j oscillator strength of electrons with characteristic frequency ω_j
- g_j damping constant of electrons with characteristic frequency ω_j
- m_j effective electron mass

From equations (2), (3), and (4), we obtain the dispersion relationships

$$n_\lambda^2 - k_\lambda^2 - 1 = \sum_j \frac{Ne^2 f_j}{m_j} \frac{\omega_j^2 - \omega^2}{(\omega_j^2 - \omega^2)^2 + g_j^2 \omega^2} \quad (5a)$$

$$2n_\lambda k_\lambda = \sum_j \frac{Ne^2 f_j}{m_j} \frac{g_j \omega}{(\omega_j^2 - \omega^2)^2 + g_j^2 \omega^2} \quad (5b)$$

which give n_λ and k_λ as functions of the photon frequency ω .

Thus, the dispersion relations and the physical properties should determine the optical properties of pigments and of vehicles. The reflectance of a pigment-vehicle system, however, depends not only on the optical properties of the components but also on the pigment-vehicle ratio, the sizes and microscopic textures of the pigment particles, and, perhaps, other physical-chemical characteristics of the components. Nevertheless, the dispersion relations are basically valid, and remain useful for qualitatively describing the reflectance and its dependence on wavelength.

Energetic Radiation Interactions

In this section we shall very briefly sketch the important modes by which energetic radiation interacts with matter (ref. 4, 5, and 6). In terms of the damage produced by absorption of energetic radiation, the net immediate effect is the production of free electrons. Gamma (γ) radiation, through the photoelectric effect, Compton scattering, and pair production produces high-energy electrons that release a large number of free electrons along their tracks. Neutrons (n) also produce them indirectly via recoil nuclei that create dense ionization tracks. Ultraviolet radiation also is capable of creating free electrons, by supplying the energy required to raise an electron from the valence band to the conduction band, or to the exciton band from which it may be excited to the conduction band by thermal activation (ref. 3 and 7). Though the mechanisms involved in these processes are very different, it is important to realize the similarity of their end results, namely, the production of free electrons, the fate of which is of prime interest in examining the observed degradation of thermal control materials.

Defect Absorption

For the sake of simplicity, we refer to any radiation-induced condition in a material as a *defect*. Since a real material always contains a certain density of "natural" defects, it is important to determine the effects of changing their concentrations, as by radiation damage. A large number of different types of defects

are known, but it will be of interest to identify only those which can possibly influence solar absorptance. As will become clear subsequently, this is not a simple task; each material differs in the identities of defects responsible for changes in spectral reflectance, R_λ . The defects almost always involve electron deficiencies or excesses, vacancies, interstitials, and combinations of these. The F -center, for example, is an electron trapped at an anion vacancy, but this defect is known as an F' -center when two electrons are so trapped.

An important point is that optical properties, especially in the near infrared, visible, and ultraviolet regions, are sensitive to the local electronic structure and physical state of the crystal. Extensive literature exists describing investigations of the effects of radiation on the optical properties of transparent materials. Alkali halides have been studied in the greatest detail. Silicas and silicates also have received considerable attention. In contrast, very little work has been conducted on other materials, with the exception of certain of the semiconductors. Along with the experimental phases of these studies, much theoretical work has been done to obtain semiquantitative estimates of the effects of defects on optical properties. Unfortunately, most of the theoretical work has dealt principally with simple substances such as the halides. Much of the theoretical work (ref. 8 to 15) nevertheless provides insight into the effects of radiation on the optical properties of more complex materials.

An important theoretical and experimental result of work with alkali halides is the correlation of positions of absorption-band maxima with crystal lattice parameters. Known as Mollwo relationships, these expressions are usually given in the form

$$\nu_m d^n = c \quad (6)$$

where

- ν_m photon frequency at absorption-band maximum
- d crystal interatomic distance
- n constant depending upon the type of defect producing the absorption
- c constant

Ivey (ref. 16) has improved Mollwo's original correlations and has given both calculated and experimental values for ν_m for most of the alkali halides. Still another important expression is the well-known Smakula formula (ref. 2 and 8), which relates optical absorption to the density of defects producing it:

$$N_i f_i = \frac{8.21 \times 10^{18} n W_i}{(n^2 + 2)^2} \quad (7)$$

where

- f_i oscillator strength of i th type defects
- N_i density of i th-type defects, cm^{-3}
- n index of refraction of host medium
- W_i area under absorption curve due to i th-type defects, ev-cm^{-1}

The preceding discussion applies mainly to transparent materials and particularly to the alkali halides. To make use of the theory touched upon here in interpreting radiation effects in solid opaque materials, Fresnel's equation (eq. (1)) and the dispersion equations (eq. (5)) must be applied. As k increases, the index of refraction n goes through a minimum in the neighborhood of an absorption band, and the reflectance passes through a minimum. The extension of the preceding theoretical results to opaque systems thus depends upon how Fresnel's law follows the dispersion relations, and how the parameters in the latter depend upon defect structure.

Related Experimental Results

Before examining data we shall review the general results of many investigators, principally those pertaining to alkali halides and silica structures. Because of the imensity of the data and the large number of important contributors, we have not in the following discussions credited specific authors, but have compiled under appropriate headings a representative bibliography from which we have obtained the bulk of the information presented.

In the silicas (we use this term broadly to designate any system which contains the basic silica structure—quartz, fused silica, silicate glasses, etc.), it is found that under irradiation

several bands develop which are specific to the SiO_2 system, and others which are attributable to impurity atoms. Each band produced has been identified with (assigned to) a particular type of defect. Because of interactions between defects, the assignments are made in many cases by noting how the destruction of one band leads to the formation or enhancement of another. This latter analysis is an extremely important one in explaining the dependence of damage upon the wavelength of damaging and/or bleaching ultraviolet radiation.

With transparent materials a number of common results are obtained. First, the concentration of defects to produce measurable absorption is of the order of 10^{14} cm^{-3} (ref. 10) and the concentration to produce maximum absorption (saturation) is of the order of 10^{18} cm^{-3} . Smakula's formula (eq. (7)) predicts the same range. Second, defects consisting of single electron deficiencies or excesses produce bands at shorter wavelengths than do multiple-type defects. (Compare, for example, the locations of absorption bands in alkali halides due to F - and M -centers (ref. 16).) Third, illumination of X - or γ -irradiated materials with light of wavelengths in the energy region of the induced absorption band will in some materials decrease (bleach) the band intensity; the holes or electrons liberated in the process may become trapped at other defect sites to produce or enhance other bands. Fourth, there exists for each material or system of materials a wavelength above which the incident radiation will cause no damage; this wavelength always lies in the ultraviolet region of the electromagnetic spectrum for dielectric materials and is in the infrared region for many semiconductor materials. Fifth, the rate at which damage is produced under irradiation diminishes exponentially with increasing dose; the concentration of defects thus asymptotically approaches an equilibrium value corresponding to an equilibrium level of optical damage.

EXPERIMENTAL RESULTS

Introductory Remarks

The following list of the immediate results of the studies and then discussion of how

these were obtained by examining the reflectance spectra of irradiated materials should produce a better understanding of the objectives of the experimental work.

(1) In paint systems containing the semiconductor pigments TiO_2 , ZnO , and ZnS (band gaps $\approx 3.2 \text{ eV}$), the pigment alone determines the observed damage; the vehicle influences the amount of damage but does not influence the character of the damage spectra.

(2) In paint systems containing dielectric pigments, the same conclusion can be reached except in the case of inorganic silicate vehicles, where there are effects definitely attributable to vehicle damage.

(3) Degradation of semiconductor pigments is due mainly to photoreduction (oxidation of the volatile anion) and, to a lesser extent, to the formation of color centers.

(4) Degradation of dielectric pigments (and silicate vehicles) is principally due to the formation of color centers.

Conclusions (3) and (4) have been reached principally on the basis of the results of experiments reported in the literature, but they have been verified by work at Lockheed Missiles & Space Company (LMSC) and to a lesser extent by the comparative studies described herein. Conclusion (3) is based on the fact that the fundamental absorption edges of TiO_2 , ZnO , and ZnS lie at wavelengths easily obtained in many types of solar simulating ultraviolet sources. When radiation of wavelength shorter than the edge wavelength is absorbed, an electron is raised from the valence to the conduction band; if this electron was initially on the anion, the anion is oxidized and has a high probability of escaping from the lattice structure (under the influence of thermal energy). As the anions are removed, the cations are reduced eventually to free metal atoms; the effect of this process is to induce free-carrier absorption.

The differences in degradation mechanisms between semiconductor pigments and dielectric pigments now become more apparent. With dielectrics, damage is evidenced principally by short-wave length band absorption. Degradation

tion in the semiconductor pigments involves principally the creation of free carriers, absorption by which results in decreased near-infrared reflectance.

Data Analysis

The data presented here are in the form of spectral absorptance curves, prepared from spectral reflectance data in the wavelength region $0.275\ \mu$ to $1.8\ \mu$ by subtracting the latter from unity. A Cary model 14 double-beam spectrophotometer with an integrating sphere attachment was used to measure reflectance.

The data presented in this section, unless otherwise noted, pertain to samples which have received a nuclear-radiation dose of approximately 10^8R of gamma and 5×10^{14} neutrons ($E \geq 2.9\text{ Mev}$)/ cm^2 , and approximately 200 sun hours of ultraviolet irradiation. The ultraviolet and nuclear irradiations were not concurrent. Some data will be given which pertain to samples exposed simultaneously to nuclear and ultraviolet radiation; in these cases the nuclear doses were the same as above, but the ultraviolet radiation doses exceed 500 sun hours. This information is given for the sake of completeness, but bears little on the qualitative aspects of damage analysis. Except as noted, all data pertain to irradiations conducted in vacuo.

SILICATE PIGMENTS

In figure 1 is shown the spectral absorptance of the system Lithafrax/sodium silicate. (The notation used here is: pigment/vehicle.) Lithafrax has the approximate stoichiometric formula $\text{Li}_2\text{O} \cdot \text{Al}_2\text{O}_3 \cdot 8\text{SiO}_2$. In this figure are shown the spectra of the preirradiation (control) system and of the $n\text{-}\gamma$ and ultraviolet irradiated systems. Figure 2 shows the spectra for the system Ultrox/potassium silicate; Ultrox is ZrSiO_4 . Data for an experimental LiF /sodium silicate system are shown in figure 3. By intercomparing these three figures, one can immediately see the close similarity of ultraviolet and nuclear radiation damage spectra in silicate systems. Of particular importance is figure 3, which shows silicate vehicle damage; we assume here that the LiF does not chemically react with the

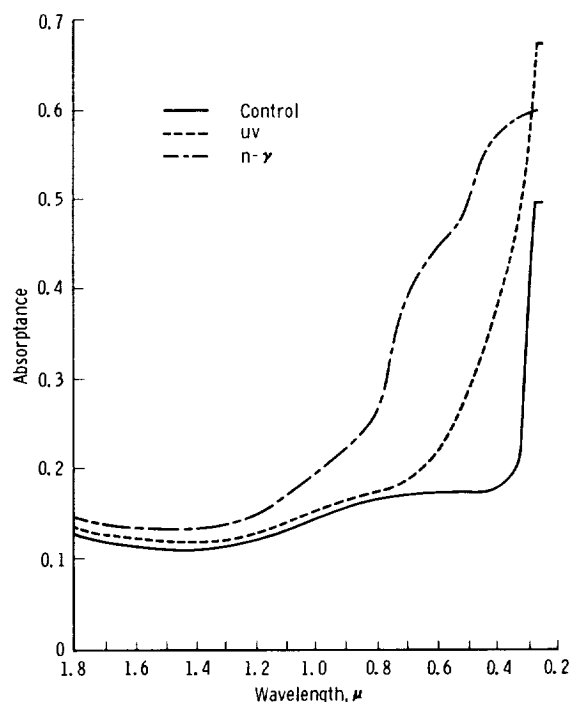


FIGURE 1.—Effects of ultraviolet and nuclear radiation on the Lithafrax/sodium silicate system.

vehicle. The peak in the $n\text{-}\gamma$ spectrum at $0.445\ \mu$ corresponds almost exactly with that reported by Ivey as the M -center absorption band peak (ref. 16 and references cited therein).

Further indication of vehicle damage may be seen in figure 4, which shows the spectra for CaF_2 /sodium silicate. The peak at $0.575\ \mu$ in the $n\text{-}\gamma$ curve does not appear in the uv curve. This effect is interpreted as bleaching. It is apparent from figures 3 and 4 that the pigment damage, which is well documented in the literature, cannot account for the total damage observed, and that the vehicle must also be damaged. Other data, not included, lead to the two conclusions that the change in the spectrum is not qualitatively a function of pigment-vehicle ratio, and that damage to silicate pigments (Lithafrax, Ultrox, etc.) cannot be qualitatively distinguished from silicate vehicle damage. Figure 5 presents data for the Ultrox/aluminum phosphate system. Here again, silicate damage is evidenced in the location of the absorptance band maxima,

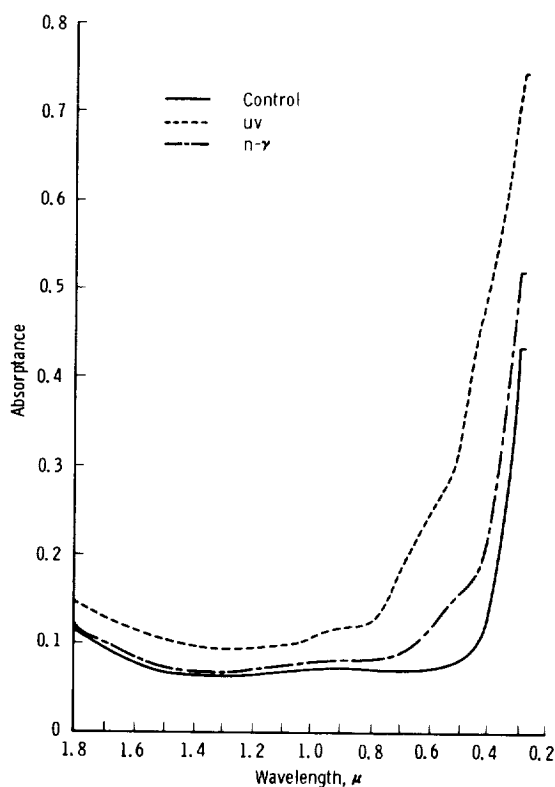


FIGURE 2.—Radiation effects on the Ultrox/potassium silicate system.

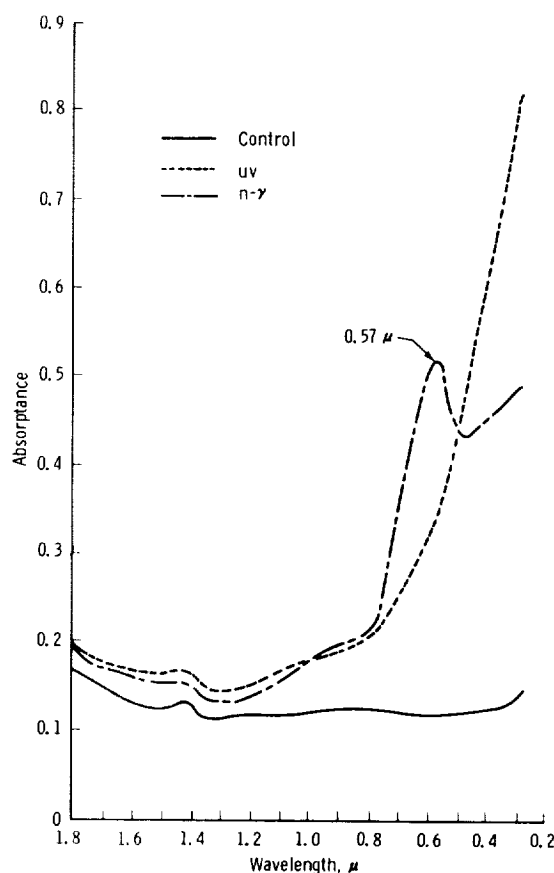


FIGURE 4.—Radiation effects on the calcium fluoride/sodium silicate system.

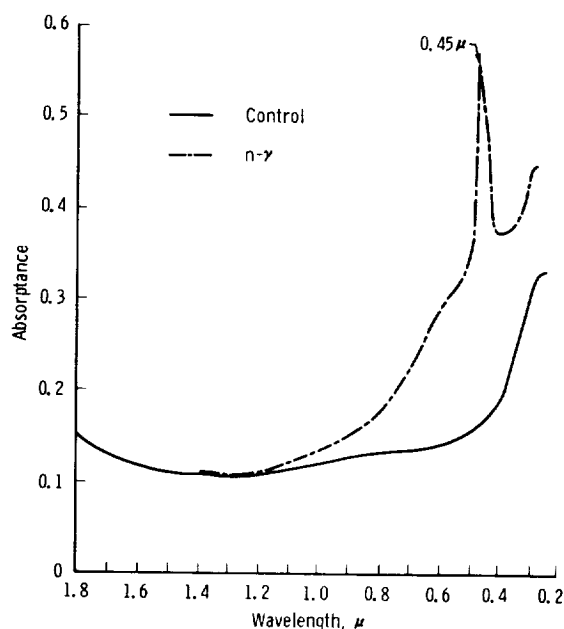


FIGURE 3.—Effect of nuclear radiation on the lithium fluoride/sodium silicate system.

but the differences between the damage effects on the spectra for the silicate- and phosphate-vehicle systems are equally apparent in the curves for both the ultraviolet and the nuclear irradiations.

Our analyses have been made on the basis of the following considerations: First, the spectra shown have been compared with respect to the positions of absorptance peaks. Since the various radiation sources employed differ in their abilities to induce damage in any given band, the bandwidth and, to a minor extent, the peak wavelength of the band will also vary, depending upon irradiation conditions. Second, the wavelength for maximum absorption (extinction) will differ from that for minimum reflectance (ref. 3). Silica systems in general develop, under irradiation, absorption bands at 2.3, 4.1, and 5.5 eV. The 5.5-eV peak will not

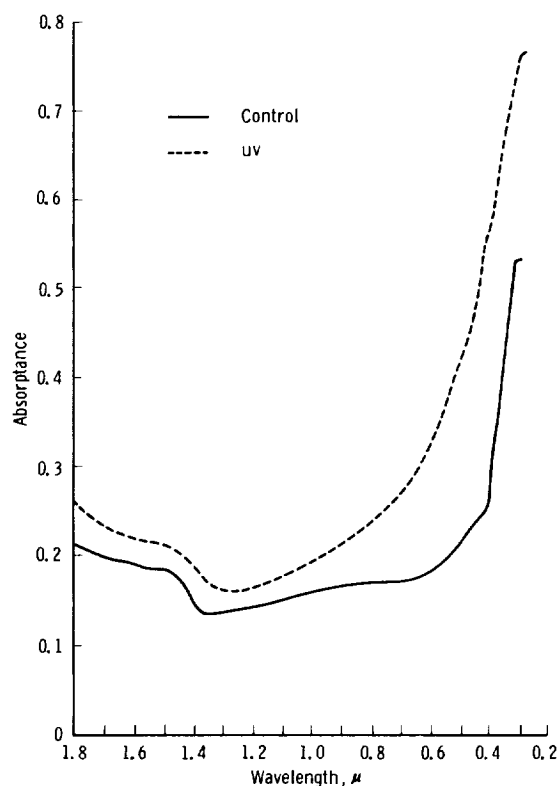


FIGURE 5.—Radiation effects on the Ultrox/aluminum phosphate system.

significantly influence solar absorptance. The 2.3-eV and 4.1-eV peaks are actually observed as apparent absorptance peaks at 2.0 and 3.1 eV. Third, all silicate systems, with the exception of Lithafrax, show the same relative development of the 2.0-eV and 3.1-eV absorptance bands in a nuclear environment. The very large thermal-neutron cross section of lithium may account for the disproportionate (increased) development of the 2.0-eV absorptance band. Figure 6 illustrates the latter point; the regions of absorptance increases are the same for all curves and, with the exception of nuclear irradiated Lithafrax, the damage spectra are quite similar.

Several systematic studies have been reported in which sodium silicate glasses containing various kinds and proportions of impurities have been irradiated (ref. 17 to 20). (A bibliography of radiation effects in silicas and silicates is given at the end of the references.) As

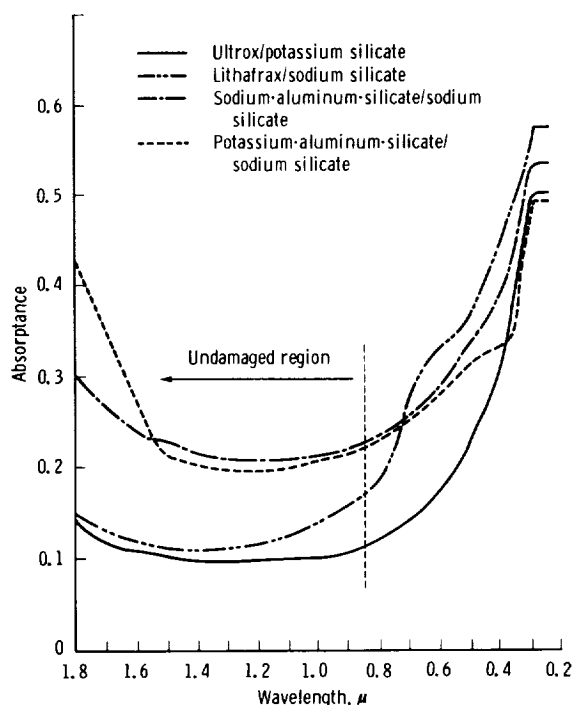


FIGURE 6.—Nuclear radiation effects on systems containing silicate vehicles.

a result, the nature of the defect that gives rise to the 2.3-eV band has been well established as substitutional aluminum impurity (i.e., aluminum atoms occupying normal silicon sites). Some uncertainty exists, however, with regard to the electronic nature of this defect—whether the neighboring oxygen captures a hole or whether the atom exists in the vacancy together with an alkali atom. The latter explanation seems to be favored, particularly in view of the fact that silicate glasses containing aluminum will not develop 2.3-eV bands under irradiation unless a certain proportion of alkali atoms is present (ref. 17). Irrespective of the electronic nature of this defect, the significance of these findings lies in the possibility of purifying the silicate systems to remove as much aluminum impurity as possible and thus achieving much more stable silicate paint systems. The nature of the 4.1-eV band defect still remains obscure, although it apparently also involves an aluminum impurity (probably interstitial) in association with an *F*-center or with an alkali atom.

Further increases in silicate paint system stability are unlikely until the defects responsible for the 4.1-eV band are better identified.

The curves of damage spectra shown in figures 1 to 6 indicate that ultraviolet and nuclear radiation produce the same defects. The differences in optical effects lie chiefly in the relative intensities of the bands produced. The same effects (i.e., the same relative development of the absorption bands) have been found in ultraviolet, X-ray, gamma-ray, and electron irradiation of transparent silicate glasses. (See Silicas and Silicates in the Bibliography.) In the present work this result is not necessarily to be anticipated, for two reasons: first, the neutron-induced damage may be expected to augment the development of one or more bands but with a different *efficiency* for each; second, the changes in reflectance are complex functions of all the bands (eq. (5)).

Other investigators (ref. 21 to 23) have studied the kinetics of radiation-induced color centers. Their analyses indicate that the kinetics can be expressed by the equation

$$\frac{dN_t}{dt} = A - BN_t \quad (8)$$

where

- N_t number of centers per unit volume
- t time
- A constant, depending upon irradiation rate and temperature
- B constant, depending upon temperature

The actual expressions for the growth rate of absorption bands involve much more complicated terms than those given in equation (8). The important results of these studies include the qualitative prediction of rate- and temperature-dependence of optical damage, and the further elucidation of band defect interactions. In the case of inorganic solar reflectors, rate-dependence rarely occurs (i.e., the reciprocity law holds), but considerable temperature-dependence has been observed.

Figure 7 shows damage spectra of materials irradiated at 77° K. The explanation for the greatly increased absorptance in these samples below 0.4 μ is that defects normally unstable or

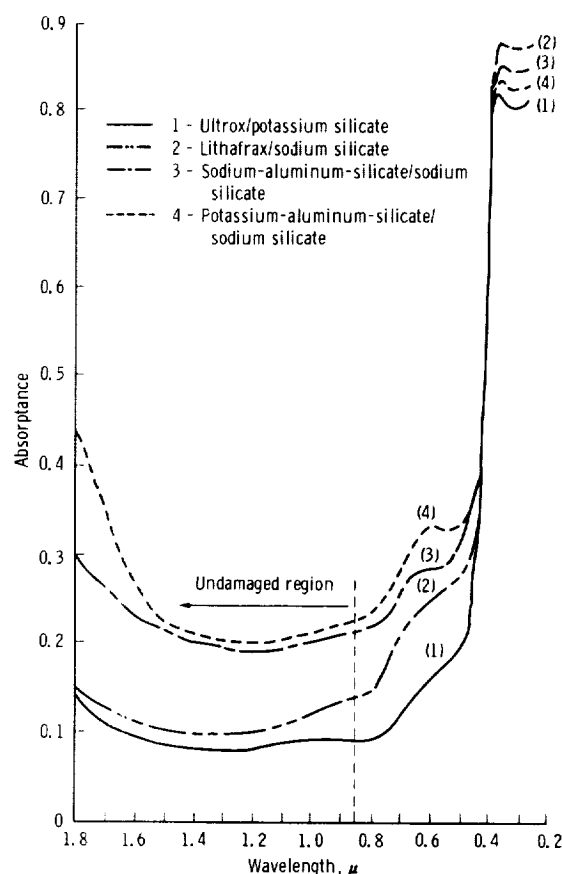


FIGURE 7.—Effects of nuclear irradiation at 77° K on systems containing silicate vehicles. Note the large absorptance increase at 0.4 μ compared with the absorptance spectra of figure 6.

easily bleached at room temperature are not thermally activated at 77° K. The defects normally present in a crystal are greatly increased in number by neutron radiation, and at 77° K these are *frozen in*, thus increasing by one or more orders of magnitude the number of defect sites available for electron or hole capture. The Varley multiple-ionization mechanism (ref. 24 and 25) would quite likely serve to intensify this effect.

From the spectra so far shown plus those referred to, it is evident that ultraviolet and nuclear irradiations produce the same defects and, as we have shown, ultraviolet irradiations cause absorption bands at 2.3 and 4.1 eV, the latter being much more broad and intense. Experiments have shown that when ultraviolet radia-

tion of wavelength longer than 3500 \AA is used, the damage spectrum differs markedly from that observed when radiation of wavelength shorter than about 3000 \AA is used. A simple way of understanding this difference is to note that defects are always formed in pairs—for example, when a vacancy is created, the displaced atom goes into an interstitial site; or when an electron is raised to the conduction band and captured by a vacancy, a positive hole is created at the atom which lost the electron and an F -center is created at the anion vacancy which captures it. When pairs of defect sites are created, each will behave optically according to the new electronic environment in which it exists. Thus, each will tend to capture whatever type(s) of particle will re-establish local electrical neutrality. Wavelength dependence will arise as a result of the different rates at which these defects will capture electrons, holes, excitons, or displaced atoms and the different rates at which they will absorb incident radiation—in this case, solar radiation. Bleaching

experiments in which X- or gamma-irradiated materials are subsequently exposed to ultraviolet and/or visible radiation, in demonstrating the inter-relationships between band defects, have also pointed up the sensitivity of equilibrium band intensity to wavelength and intensity of bleaching radiation. (See Silicas and Silicates in the Bibliography.) Figure 8 compares the spectrum for the Lithafrax/sodium silicate system irradiated concurrently by ultraviolet and nuclear radiations with the spectra produced by each type of radiation separately. These curves show a strong interdependence of the effects of ultraviolet and nuclear radiations and, more importantly, they show that the degradation sustained in separate irradiations cannot be used to predict degradation when the two radiations are concurrent.

SEMICONDUCTOR PIGMENTS

In this section we shall discuss the damage spectra of paint systems consisting of semiconductor pigments in silicate and in silicone vehicles. In both cases the damage spectra, allowing for such vehicle effects as silicate damage and characteristic silicone absorption, will be ascribed to absorption by induced free carriers. The lack of any band structure in the damage spectra of these paint systems may be regarded as an indication of free-carrier absorption. The fact that the band gaps of these pigments (TiO_2 , ZnO , and ZnS) lie at approximately 3.2 eV strongly suggests that these pigments may indeed undergo photoreduction when illuminated by ultraviolet light of corresponding or greater photon energy. Experiments conducted at LMSC and at other laboratories have clearly shown the differences between vacuum and air irradiations of paint systems containing these pigments. In general, these experiments have established the dependence of many electronic properties of TiO_2 , ZnO , and ZnS upon the environment during ultraviolet illumination.

The observations of photoconductivity in these materials, when irradiated with ultraviolet photons with energies equal to or exceeding band-gap energies, and of the dependence of photoconductive current upon the nature and

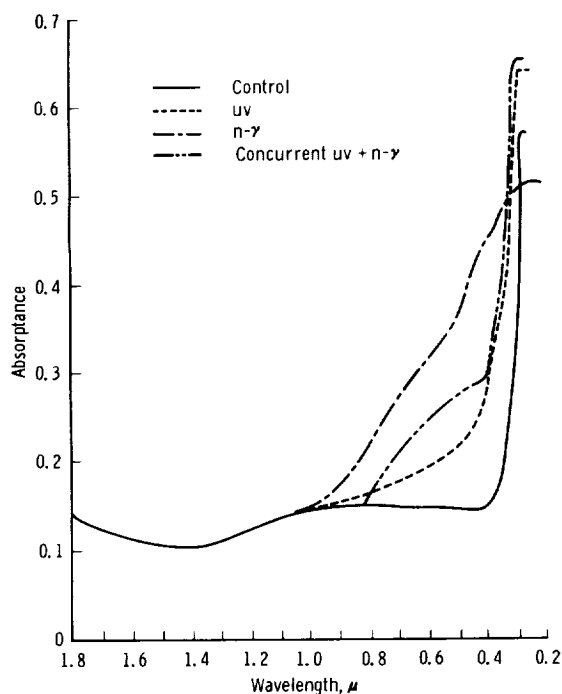


FIGURE 8.—Comparison of the separate effects of ultraviolet and nuclear irradiation with the effect of concurrent irradiation.

pressure of the environment, add further credibility to the arguments for induced free-carrier absorption. Theory predicts that free-carrier absorption will follow the dispersion equations in which ω_k is set equal to zero.

The optical constants would then be obtained from the formulas

$$n^2 - k^2 - \epsilon = \sum_k \frac{Ne^2 f_k}{m_k \epsilon_0} \frac{1}{\omega^2 + g_k^2} \quad (9a)$$

and

$$2nk = \sum_k \frac{Ne^2 f_k}{m_k \epsilon_0} \frac{g_k}{\omega(\omega^2 + g_k^2)} \quad (9b)$$

where

- ϵ material dielectric constant
- ϵ_0 electric permittivity of free space
- m_k effective mass of the k th type carrier
- f_k oscillator strength of k th type carrier

These equations predict decreasing reflectance with increasing frequency.

In a real paint system, however, the optical properties will be given by a combination of equations (5) and (9), that is, by an expression of the form

$$n^2 - k^2 - \epsilon = \sum_j \frac{Ne^2 f_j}{m_j \epsilon_0} \frac{\omega_j^2 - \omega^2}{(\omega_j^2 - \omega^2)^2 + g_j^2 \omega^2} + \sum_k \frac{Ne^2 f_k}{m_k \epsilon_0} \frac{1}{\omega^2 + g_k^2} \quad (10)$$

Since there are a number of unknowns in these equations, it is extremely difficult to obtain other than a qualitative notion of how reflectance will vary with wavelength. However, it should not be surprising to find that the reflectance of a semiconductor paint system with induced free carriers will not in general display damage spectra typical of free-carrier (metallic) absorption. Indeed, as can be seen from figures 9 to 14, absorptance decreases with decreasing wavelength. This can probably be explained by pigment-vehicle interactions, such as those due to geometrical effects and chemical reactions.

Nevertheless, the absence of any induced band structure in the damage spectra is obvious. In the case of the silicone vehicles, we note that the damage spectra contain the original absorptance bands characteristic of the polymethyl-siloxane polymers, thus showing that silicone vehicle damage, if any, does not affect absorptance. On the other hand, the systems with silicate vehicles exhibit damage in the 3.0-eV region. A tentative explanation of these findings is that vehicles with loosely bound oxygen atoms will give them up to the pigment rather easily under irradiation, thus offering the pigment some degree of stability.

Other evidence suggesting induced free-carrier absorption is the fact that semiconductor paint systems when irradiated in air by nuclear radiation often exhibit increased, rather than decreased, reflectance. This increase can be explained as due to the increased importance of the second term of equation (10) in determining the spectral character of the irradiated material, and/or to the possibility that the pigment may, initially, have been slightly reduced and is oxidized in the presence of oxygen during irradiation. This reduces the free-carrier concentration through better pigment stoichiometry.

The similarity of the ultraviolet- and nuclear-radiation-induced spectra of the semiconductor paint systems, as shown in figures 9 to 14, indicates that the damage mechanisms are identical. The explanation follows the same arguments offered previously regarding the formation of defects in pairs. In the semiconductor systems, however, only one of these defects is important in effecting changes in solar absorptance. From these discussions it seems clear that the stability of the semiconductor paint systems could be improved by providing more loosely bound anions, or by making their escape less probable or by both.

CONCLUSIONS

Paint systems containing dielectric pigments will in general sustain reflectance changes due to induced absorption bands, but where the development of these bands depends upon the initial concentration of defects, degradation may be minimized by reducing the number of initial

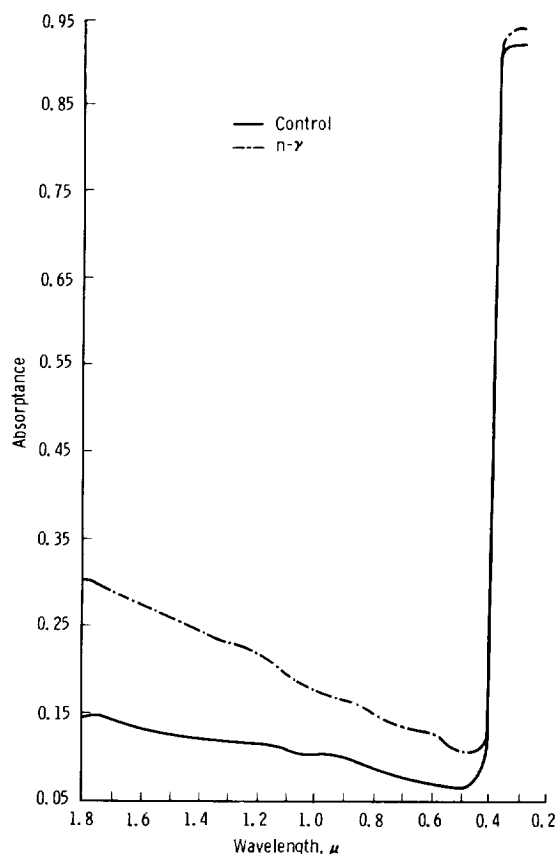


FIGURE 9.—Radiation effects on titania/sodium silicate system.

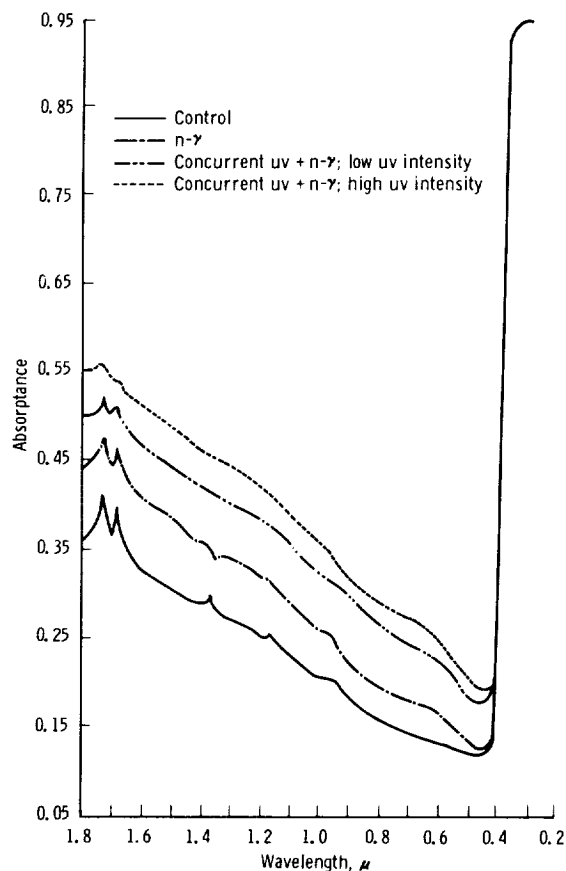


FIGURE 10.—Radiation effects on titania/silicone system.

defects. Thus, in the case of silicate pigments, damage would be lessened by minimizing aluminum impurity. Semiconductor paint systems degrade chiefly because of the photoreduction of the pigment and consequent generation of free carriers. The latter effect could be minimized by reducing the effective loss of volatile anion from the pigment. From theory and from the data given in the figures, we can speculate about the temperature dependence of radiation-induced damage. In the case of ultraviolet radiation, damage would be a monotonically increasing function of the temperature; in other words, damage would be small at cryogenic temperatures and would be severe at high temperatures. Damage due to gamma radiation alone would have roughly the same temperature dependence, except that at

cryogenic temperatures the damage would be slightly greater relative to that caused by ultraviolet radiation. A neutron-gamma radiation environment would produce severe damage at both cryogenic and elevated temperatures.

REFERENCES

1. SEITZ, FREDERICK: *Modern Theory of Solids*. First ed., McGraw-Hill Book Co., Inc., 1940.
2. DEXTER, D. L.: *Theory of the Optical Properties of Imperfections in Nonmetals*. *Solid State Physics*, vol. 6, Frederick Seitz and David Turnbull, eds., Academic Press, Inc. (New York), 1958, pp. 353-411.
3. MOSS, T. S.: *Optical Properties of Semi-Conductors*. Academic Press, Inc. (New York), 1959.
4. SEITZ, F.: On the Disordering of Solids by Action of Fast Massive Particles. *Discussions Faraday Soc.*, no. 5, 1949, pp. 271-282.
5. SNYDER, W. S., and NEUFELD, JACOB: *Disordering*

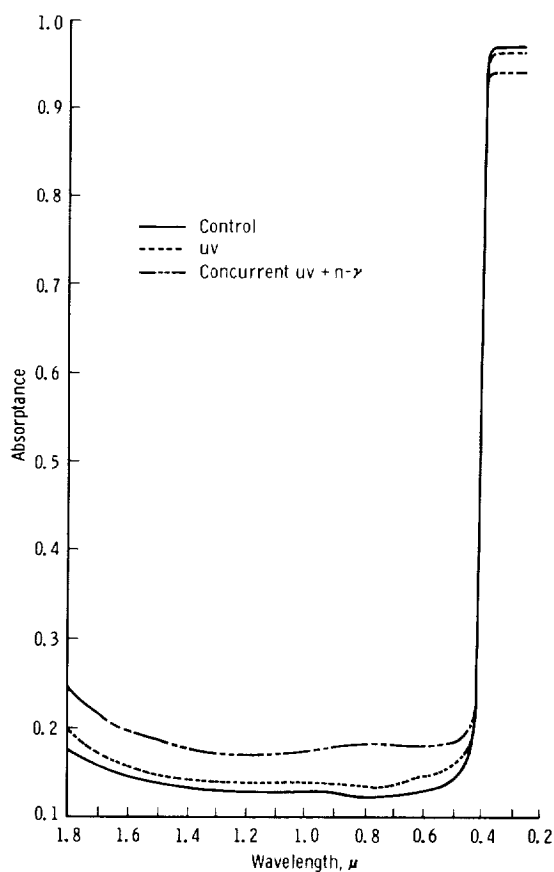


FIGURE 11.—Radiation effects on zinc oxide/sodium silicate system.

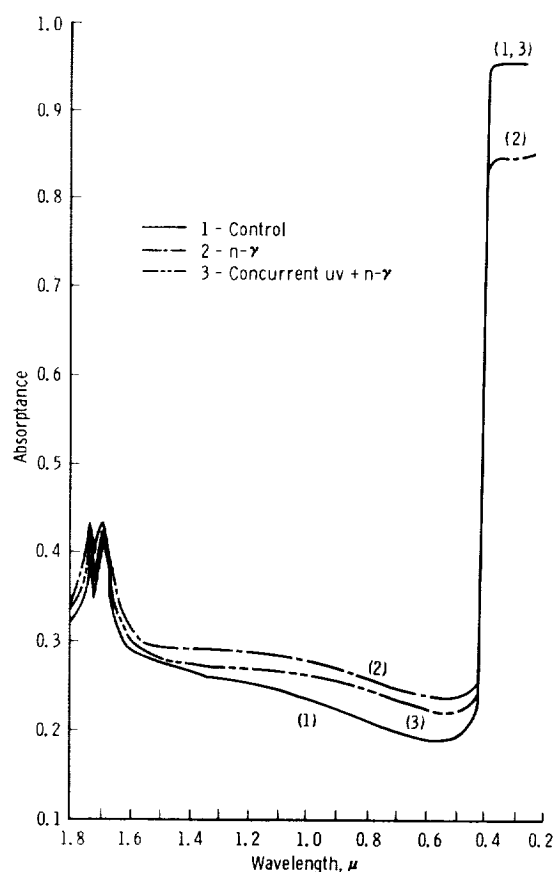


FIGURE 12.—Radiation effects on zinc oxide/silicone system (Dow Corning Q90090 silicone).

- of Solids by Neutron Radiation. *Phys. Rev.*, Second ser., vol. 97, no. 6, Mar. 15, 1955, pp. 1636-1646.
6. EVANS, ROBLEY D.: *The Atomic Nucleus*. McGraw-Hill Book Co., Inc., 1955.
 7. MOTT, N. F., and GURNEY, R. W.: *Electronic Processes in Ionic Crystals*. Oxford Univ. Press, Second ed., 1946.
 8. DEXTER, D. L.: Absorption of Light by Atoms in Solids. *Phys. Rev.*, Second ser., vol. 101, no. 1, Jan. 1, 1956, pp. 48-55.
 9. HUANG, KUN, and RHYS, AVRIL: Theory of Light Absorption and Non-Radiative Transitions in F-Centres. *Proc. Roy. Soc. (London)*, Ser. A, vol. 204, no. 1078, Dec. 22, 1951, pp. 406-423.
 10. SEITZ, FREDERICK: Color Centers in Alkali Halide Crystals. Part I, *Rev. Modern Phys.*, vol. 18, 1946, pp. 384-408. Part II, *Rev. Modern Phys.*, vol. 26, no. 1, Jan. 1954, pp. 7-94.
 11. MITCHELL, E. W. J.: The Effect of Radiation Damage on the Electronic Properties of Solids. *British Jour. Appl. Phys.*, vol. 8, no. 5, May 1957, pp. 179-189.
 12. PEIERLS, R. E.: *Quantum Theory of Solids*. The Clarendon Press (Oxford), 1955.
 13. MONTROLL, ELLIOT W., and POTTS, RENFREY B.: Effect of Defects on Lattice Vibrations. *Phys. Rev.*, Second ser., vol. 100, no. 2, Oct. 15, 1955, pp. 525-543.
 14. LEHOVEC, KURT: Energy of Trapped Electrons in Ionic Solids. *Phys. Rev.*, Second ser., vol. 92, no. 2, Oct. 15, 1953, pp. 253-258.
 15. SLATER, JOHN C.: Interactions of Waves in Crystals. *Rev. Modern Phys.*, vol. 30, no. 1, Jan. 1958, pp. 197-222.
 16. IVEY, HENRY F.: Spectral Location of the Absorption Due to Color Centers in Alkali Halide Crystals. *Phys. Rev.*, Second ser., vol. 72, no. 4, Aug. 15, 1947, pp. 341-343.
 17. HENSLER, J. R., KREIDL, N. J., and LELL, E.: Irradiation Damage to Glass. TID-11034, Bausch and Lomb, Inc., Nov. 1960.

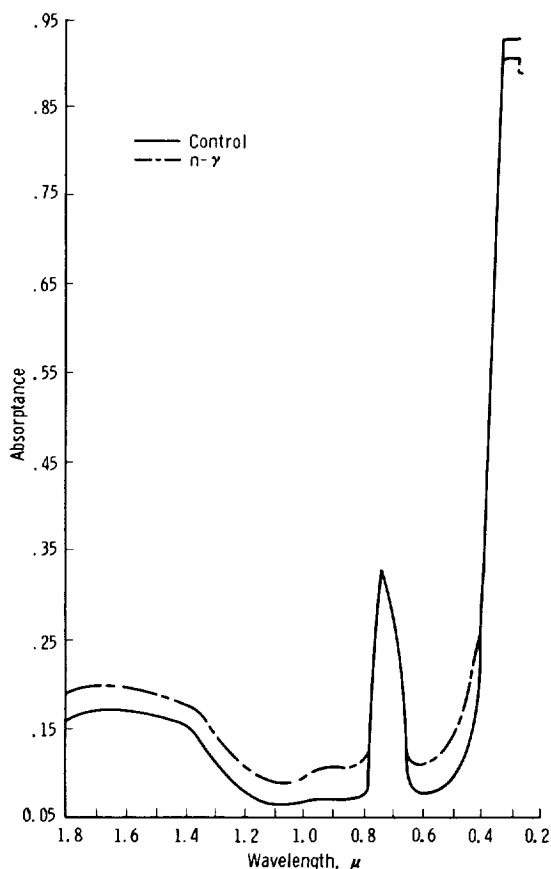


FIGURE 13.—Radiation effects on zinc sulfide/sodium silicate system.

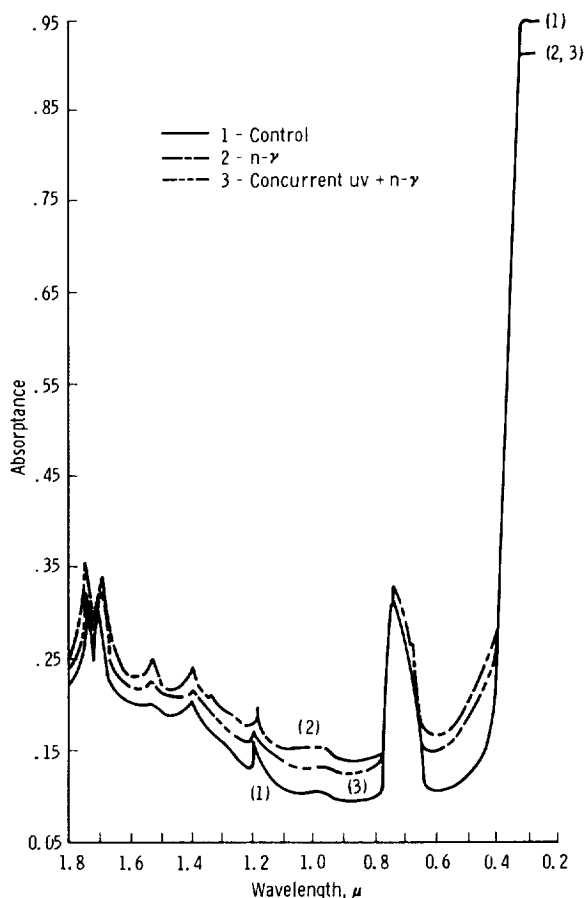


FIGURE 14.—Radiation effects on zinc sulfide/silicone system (Dow Corning 432 silicone).

18. LELL, E.: Synthesized Impurity Centers in Fused Silica. *Jour. American Ceramic Soc.*, vol. 43, no. 8, Aug. 1, 1960, pp. 422-429.
19. COHEN, A. J.: Substitutional and Interstitial Aluminum Impurity in Quartz; Structure and Color-Center Interrelationships. *Phys. and Chem. of Solids*, vol. 13, 1960, pp. 321-325.
20. KATZ, A., and STEVELS, J. M.: The Effects of U.V. and X-Ray Radiation on Silicate Glasses, Fused Silica, and Quartz Crystals. *Philips Research Reports*, vol. 11, 1956, pp. 115-156.
21. LEVY, P. W.: Reactor and Gamma-Ray Induced Coloring of Corning Fused Silica. *Phys. and Chem. of Solids*, vol. 13, 1960, pp. 287-295.
22. LEVY, M., and VARLEY, J. H. O.: Radiation Induced Colour Centres in Fused Quartz. *Proc. Phys. Soc. (London)*, Sec. B, vol. 68, pt. 4, Apr. 1, 1955, pp. 223-233.
23. LEVY, PAUL W.: The Kinetics of Gamma-Ray Induced Coloring of Glass. *Jour. American*

Ceramic Soc., vol. 43, no. 8, Aug. 1, 1960, pp. 389-395.

24. VARLEY, J. H. O.: Radiation Damage in Ionic Solids. *Jour. Inst. of Metals*, vol. 84, Aug. 1956, pp. 103-105.
25. VARLEY, J. H. O.: New Interpretation of Irradiation-Induced Phenomena in Alkali Halides. *Jour. Nuclear Energy*, vol. 1, 1954, pp. 130-143.

BIBLIOGRAPHY

Theory

- BORN, MAX, and HUANG, KUN: *Dynamical Theory of Crystal Lattices*. The Clarendon Press (Oxford), 1954.
- JOOS, GEORG: *Theoretical Physics*. Second ed., Hafner Pub. Co., Inc. (New York), 1950.
- LANDAU, L. D., and LIFSHITZ, E. M.: *Electrodynamics of Continuous Media*. Pergamon Press, 1960.

- KITTEL, CHARLES: Introduction to Solid State Physics. Second ed., John Wiley & Sons, Inc., 1957.
- KRÖGER, F. S., and VINK, H. J.: Relations Between the Concentrations of Imperfections in Crystalline Solids. Solid State Physics, vol. 3, Frederick Seitz and David Turnbull, eds., Academic Press, Inc. (New York), 1956, pp. 307-435.
- McCLURE, DONALD S.: Electronic Spectra of Molecules and Ions in Crystals—Pt. II. Spectra of Ions in Crystals. Solid State Physics, vol. 9, Frederick Seitz and David Turnbull, eds., Academic Press, Inc. (New York), 1959, pp. 399-525.
- GUAN-IN', C.: Possible Shapes of the Reflection Band, and Their Variation as a Function of the Angle of Incidence and State of Polarization, the Dispersion Effect of Reflection Bands. Optics and Spectroscopy, vol. 13, 1962, pp. 299-302.
- GEX, R. C.: Optical Absorption and Reflection of Solids, An Annotated Bibliography, LMSC 3-34-61-4, Feb. 1962.
- PIPER, WILLIAM W.: Some Electrical and Optical Properties of Synthetic Single Crystals of Zinc Sulfide. Phys. Rev., vol. 92, no. 1, Oct. 1, 1953, pp. 23-27.
- HEILAND, G.: Photoconductivity of Zinc Oxide as a Surface Phenomenon. Phys. and Chem. of Solids, vol. 22, 1961, pp. 227-234.
- GRANT, F. A.: Properties of Rutile (Titanium Dioxide). Rev. Modern Phys., vol. 31, no. 3, July 1959, pp. 646-674.
- MEDVED, D. B.: Photodesorption in Zinc Oxide Semiconductor. Jour. Chem. Phys., vol. 28, no. 5, May 1958, pp. 870-873.
- MELNICK, DONALD A.: Zinc Oxide Photoconduction, an Oxygen Adsorption Process. Jour. Chem. Phys., vol. 26, no. 5, May 1957, pp. 1136-1146.
- PIPER, W. W., MARPLE, D. T. F., and JOHNSON, P. D.: Optical Properties of Hexagonal ZnS Single Crystals. Phys. Rev., Second ser., vol. 110, no. 2, Apr. 15, 1958, pp. 323-326.
- VLASENKO, N. A.: Study of the Absorption Spectrum of Zinc Sulfide. Optics and Spectroscopy, vol. 7, no. 4, Oct. 1959, pp. 320-324.

Silicas and Silicates

- NELSON, C. M., and CRAWFORD, J. H., Jr.: Optical Absorption in Irradiated Quartz and Fused Silica. Phys. and Chem. of Solids, vol. 13, 1960, pp. 296-305.
- KURO, KAZUKO: Radiation Induced Optical Absorptions in Crystalline Quartz and Fused Silica. Jour. Phys. Soc. of Japan, vol. 16, no. 1, Jan. 1961, pp. 108-113.
- BYURGANOVSKAYA, G. V., and ORLOV, N. F.: Formation of Color Centers in Sodium Silicate and Quartz Glasses Under the Action of Gamma Radiation. Optics and Spectroscopy, vol. 12, 1962, pp. 151-154. Trans. from Optika i Spektroskopiya, vol. 12, 1962, pp. 278-284.
- MITCHELL, E. W. J., and PAIGE, E. G. S.: The Optical Effects of Radiation Induced Atomic Damage in Quartz. Phil. Mag., ser. 8, vol. 1, no. 12, Dec. 1956, pp. 1085-1115.

Semiconductors

- DIETZ, R. E., HOPFIELD, J. J., and THOMAS, D. G.: Excitons and the Absorption Edge of ZnO. Jour. Appl. Phys., Suppl. to vol. 32, no. 10, Oct. 1961, pp. 2282-2286.
- FILIMINOV, V. N.: Electronic Absorption Bands of ZnO and TiO₂ in the Infrared Region of the Spectrum. Optics and Spectroscopy, vol. 5, 1958, pp. 709-711.
- WEYL, W. A., and FÖRLAND, TORMOD: Photochemistry of Rutile. Ind. and Eng. Chem., vol. 42, 1950, pp. 257-263.
- SOFFER, BERNARD H.: Studies of the Optical and Infrared Absorption Spectra of Rutile Single Crystals. Jour. Chem. Phys., vol. 35, no. 3, Sept. 1961, pp. 940-945.
- MARKHAM, JORDAN J.: Interaction of Normal Modes With Electron Traps. Rev. Modern Phys., vol. 31, no. 4, Oct. 1959, pp. 956-989.
- RABINOWITCH, EUGENE: Electron-Transfer Spectra and Their Photochemical Effects. Rev. Modern Phys., vol. 14, 1942, pp. 112-131.
- GOURARY, B. S., and MARADUDIN, A. A.: Absorption and Emission Spectra of an Electron in a One-Dimensional Deep Trap. Phys. and Chem. of Solids, vol. 13, 1960, pp. 88-104.
- JOHNSON, P. D.: Optical Absorption From Diffuse Reflectance. Jour. Optical Soc. of America, vol. 42, 1952, pp. 978-981.
- O'ROURKE, R. C.: Absorption of Light by Trapped Electrons. Phys. Rev., Second ser., vol. 91, no. 2, July 15, 1953, pp. 265-270.
- EVANS, GEORGE R., and PRICE, WILLIAM E., compilers: The Effects of High Energy Radiation on Infrared Optical Materials. Special Bibliography SB-61-25 (Contract AF 04(647)-564), Lockheed Aircraft Corp., May 1961.
- GEX, ROBERT C., compiler: Ultraviolet and Vacuum Effects on Inorganic Materials—An Annotated Bibliography. Special Bibliography SB-61-19, Missiles and Space Div., Lockheed Aircraft Corp., Apr. 1961.
- GEX, R. C.: Effects of Nuclear Radiation on the Optical, Electrical, and Thermophysical Properties of Solids, An Annotated Bibliography. LMSC 3-34-61-8, Aug. 1961.

39. Nuclear Environmental Effects On Spacecraft Thermal Control Coatings¹

R. A. BREUCH AND H. E. POLLARD

LOCKHEED MISSILES & SPACE COMPANY, PALO ALTO, CALIF.

A total of 250 different standard, developmental, and research thermal-control coatings have been irradiated in vacuum with a nominal integrated dose of 10^{10} ergs/g(C) gamma and 10^{14} fast neutrons/cm². This paper presents a preliminary summary of the effects of nuclear radiation on the optical properties of some selected coating materials. The materials include inorganic (silicate bonded) systems, plasma-sprayed ceramic coatings, chemically polished metals, acrylic- and epoxy-base coatings, silicone dispersion systems (air-cured), and adhesive-applied silicone films. Optical properties before and after irradiation are given. Also presented are plots of total hemispherical emittance measured during irradiation. Effects of accelerated simultaneous nuclear and ultraviolet irradiation on solar-reflector coatings and the effects of sample temperature during irradiation are included.

The optical and mechanical stability of spacecraft thermal-control materials is of prime importance if the thermal integrity of a vehicle is to be maintained throughout a mission. The prime cause of degradation of passive thermal-control materials at normal temperatures in an earth-orbit environment has been proven to be the ultraviolet radiation from the sun. With the development of spacecraft-borne nuclear reactors, radiation from an additional environmental constituent that could degrade optical characteristics of surfaces is present, namely, nuclear fission products. Because little information is available on damage to the optical and mechanical properties of thermal-control materials, a materials-reliability program was established. Standard thermal-control materials were to be irradiated and, if necessary, advanced materials were to be developed and tested.

A total of six irradiations were performed at the Nuclear Aerospace Research Facility (NARF), General Dynamics, Fort Worth.

The reactor used was the NARF swimming-pool-type Ground Test Reactor (GTR). A limited number of exposures were performed with the Lockheed Missiles and Space Company (LMSC) cobalt-60 facility.

APPARATUS

Samples were exposed in vacuum to the various environmental constituents. The vacuum systems were designed for tests within the $32 \times 36 \times 60$ in. irradiation test zone on the north face of the GTR. These systems provided room for the exposure of a large number of static samples at various dose levels; they also provided the necessary volume for the various calorimetric experiments. Aluminum was the primary material used in vacuum-system construction. All vacuum systems contained integral liquid-nitrogen-cooled surfaces to eliminate the contamination of thermal-control coatings by vacuum outgassing and radiation-induced volatilization.

Static exposures were performed in the three initial irradiations, and a satisfactory (10^{-4} torr) vacuum was maintained with a Welch

¹ This work is performed under Air Force Contract AF 04(695)-136.

1397 mechanical pump. The remaining irradiations required high-vacuum conditions because of the nature of the calorimetric experiments. A 4-in. National Research Corporation (NRC) type 121 diffusion pump using Dow Corning (DC) 704 silicone diffusion-pump fluid performed satisfactorily in the radiation environment. A Welch 1397 mechanical pump served as fore pump. Vacuums of 10^{-5} to 10^{-6} torr were maintained with this equipment in conjunction with the liquid-nitrogen-cooled internal surfaces. Vacuum measurements were made with an NRC 501 thermocouple gage; high-vacuum measurements were made with an NRC 507 ionization gage. A nude, dual filament ionization gage constructed from a model 507 gage performed satisfactorily in the final test. This gage provided filament redundancy in case of accidental breakage. An NRC 710-B thermocouple-ionization gage control provided vacuum-gage power and read-out.

Shielding was required to obtain the desired neutron/gamma ratio; water was used to thermalize fast neutrons; boral and cadmium decreased the thermal flux. Diffusion-pump cooling water was routed to the shield to provide the necessary make-up for water which was lost by boiling during reactor operation.

Various experiments were performed during the irradiations. These included static exposures of test specimens at various flux levels, the operation of dynamic total hemispherical emittance calorimeters, simultaneous ultraviolet-nuclear exposures, and the static exposure of test specimens at various temperatures. For the *static* tests, optical properties of the samples were measured only before and after irradiation; in the *dynamic* tests, the progressive degradation of the optical properties could be followed during the irradiation.

Static Panels

The static-exposure panels were aluminum sheets of various dimensions. The test coatings were applied to $\frac{3}{8}$ -in.-diameter aluminum disks, which were attached to these panels with an alumina cement (Sauereisen No. 1); electrical heaters were also attached to the panels. The panels were thermally isolated

from the walls of the irradiation chamber. Their desired temperatures were obtained by applying power to the heaters to properly balance the radiative coupling with the liquid-nitrogen-cooled surfaces. Temperatures were measured with Chromel-Alumel thermocouples and read out on a Leeds and Northrup (LN) Speedomax-H multipoint recorder.

Emittance Calorimeters

The emittance calorimeters were used to measure dynamically the total hemispherical emittance of potential thermal-control surfaces in a nuclear environment. An arrangement of multiple cold-wall chambers within the main chamber permitted the simultaneous study of 16 separate samples (fig. 1, calorimeter design). Total hemispherical emittance is inferred from an energy balance on the electrically heated calorimeter suspended in a vacuum chamber with liquid-nitrogen-cooled black walls.

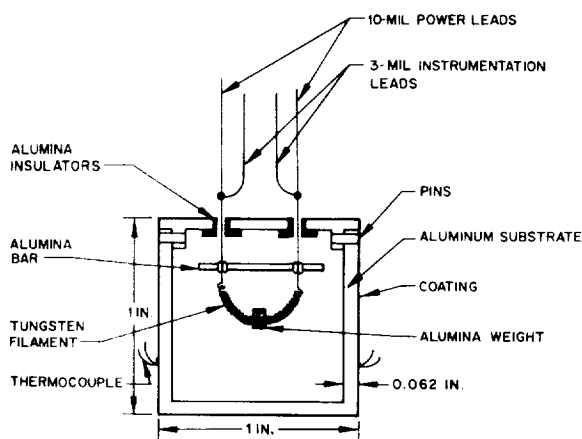


FIGURE 1.—Emittance calorimeter.

The energy balance on the calorimeter at steady state, provided there is sufficient vacuum to make gas conduction and convection negligible, is

$$\epsilon A_s \sigma (T^4 - T_g^4) = P \quad (1)$$

where

ϵ apparent emittance of sample
 A_s surface area of calorimeter
 σ Stefan-Boltzmann constant

T temperature of calorimeter
 T_E temperature of environment
 P net power to the calorimeter

Equation (1) is representative of the radiation heat transfer between the calorimeter and a blackbody with an emittance of unity. The calorimetric environment consisted of a chamber with an emittance of 0.85 and a surface area approximately 50 times that of the calorimeter. The equation for the apparent emittance of the sample as used in equation (1) is

$$\epsilon = \frac{1}{\frac{1}{\epsilon_t} + \left(\frac{A_t}{A_E}\right)\left(\frac{1}{\epsilon_E} - 1\right)} \quad (2)$$

where

ϵ apparent emittance of sample
 ϵ_t true emittance of sample
 ϵ_E emittance of chamber wall
 A_t/A_E ratio of surface area of calorimeter to that of the chamber

The net energy to the calorimeter includes the electrical energy dissipated in the heater, the nuclear-radiation energy absorbed by the calorimeter, and the conductive heat loss along the power and thermocouple leads.

The electrical power dissipated in each calorimeter was determined by measuring the voltage across the resistance heater by means of 3-mil platinum wires attached to the power leads adjacent to the heater. The current was determined by measuring the voltage drop across a calibrated resistor in series with the calorimeter heater. Voltage measurements were made with a Calibration Standards Corporation DC-200AR d-c voltmeter.

The conductive heat loss along the various wires was determined to be one-half percent of the electrical power dissipated within the calorimeter (within 20-percent accuracy) and was considered sufficiently small to be neglected.

Nuclear-radiation heating in the aluminum calorimeters was determined from measurements on one calorimeter with no electrical energy applied so that the only source of heat was nuclear radiation. By assuming a value for the emittance of the surface coating, equation (1) was solved for the nuclear-radiation heating. The resulting heating rate was determined to be 0.0145-watt/megawatt reactor

power for the 15-g calorimeters. Nuclear-radiation heating to the coating and instrumentation leads was neglected.

Two Chromel-Alumel thermocouples were located on the surface of each calorimeter, and temperatures were read out on a LN Speedo-max-G AZAR recorder.

The overall accuracy of the emittance calorimeters is considered to be ± 5 percent of the initial emittance value.

Absorptance Calorimeter

The absorptance calorimeter was designed to determine the combined effect of simultaneous nuclear and ultraviolet radiation on solar-reflector coatings. Figure 2 shows the calorimeter construction. It is essentially a thumb-tack shaped device with the coating to be studied applied to the "head" of the tack. The stem of the calorimeter is coupled to a water-cooled heat sink. Energy from an intense mercury arc is incident upon the coating during nuclear irradiation. It provides both the ultraviolet radiation that induces the coating degradation and the simulated solar-radiation heating by which the degradation is measured.

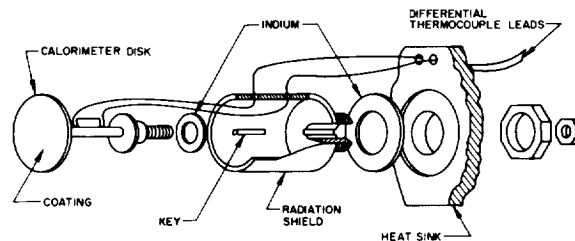


FIGURE 2.—Absorptance calorimeter.

The net energy absorbed by the surface of the tack is a function of the absorptance of the coating, the thermal radiation from the quartz vacuum finger which contains the ultraviolet lamp assembly, the thermal radiation from other portions of the assembled apparatus, and the heat losses from the calorimeter.

A differential thermocouple is attached to the stem of the calorimeter to measure the temperature gradient, which is proportional to the net radiation energy absorbed by the head of the

tack. A concentric aluminum shield thermally isolates the stem. A major portion of the temperature gradient in the stem will be proportional to the absorptance of the coating for the lamp spectrum. If the additional radiation heat inputs to the head are small and well defined and the additional radiation heat losses are small, a change in the absorptance of the coating will effect a proportional change in the temperature gradient along the stem.

The advantages of this absorptance calorimeter are:

- Dynamic measurements of change in absorptance are possible.

- The surface coating is nearly isothermal.

- The temperature of the coating can be controlled by controlling the heat-sink temperature.

- Thermal cycling during exposure is possible.

- The sensitivity can be controlled by proper choice of material and geometry of the calorimeter stem.

The main disadvantage is that it is not feasible to follow the time variation of spectral reflectance, because the necessary photo-detector devices cannot be used in the nuclear-radiation environment of the test chamber. Thus, the time variation of the solar absorptance cannot be determined without further information, or without making some assumptions. In the present work it was assumed that the change in absorptance spectrum at any time during the test was similar, except for a constant factor, to the change in the absorptance spectrum that was measured after the test. On this basis, the increase in solar absorptance at any time during the test could be evaluated by the following method:

Three calorimeters painted with a stable black silicate coating monitored the total output of the high-pressure mercury-arc lamp. Three polished bare aluminum calorimeters monitored the ultraviolet radiation intensity of the lamp. Calorimeters painted with ultraviolet-absorbing coatings (titania-, zinc oxide-, or zinc sulfide-pigmented systems) provided, by their initial readings, their own determinations of their initial ultraviolet irradiation; and subsequent increases in temperature gradient along their

stems (corrected for any radiation intensity changes indicated by the monitors) could be attributed to increased absorptance in the visible and infrared. Comparison of this increase, as measured at any time during the test, with the increase measured just before the test was stopped, gave the fraction of the final degradation achieved up to that time.

Thirty calorimeters were contained in the assembled apparatus; six were the selected controls and twenty-four had thermal-control coatings. The individual calorimeters were fabricated from 2024-T3 aluminum. The coatings were applied to the surface of the 1-in.-diameter tack head, and a differential Chromel-Alumel thermocouple was attached to the 0.125-in.-diameter stem. The calorimeters were individually calibrated in the laboratory by means of known heat fluxes. The base of the stem and the aluminum radiation shield were attached to a copper, water-cooled, heat sink. Indium was used at all calorimeter heat-sink interfaces to obtain maximum interfacial thermal conductance in the vacuum environment. A PEK type C high-pressure, water-cooled mercury arc lamp in a specially designed Suprasil quartz assembly provided an intensity of 15 suns of ultraviolet radiation.² A second lamp in the same assembly provided redundancy. The power supplied to the lamp was 1,000 volts d-c at 1 amp.

Temperature-Dependency Apparatus

Since initial exposures indicated a possible relation between temperature and damage, a temperature-dependency apparatus was integrated into the vacuum cryostat for the final two irradiations. The purpose of this device was to evaluate the effect of sample temperature during nuclear irradiation on optical and mechanical stability.

Temperature increments were obtained by fastening circular copper disks onto a machined brass rod at predetermined locations (fig. 3). Five disks were spaced approximately 1 in.

² A sun is defined as that intensity of the solar radiation in the wavelength region from 2000 to 4000 Å which is incident upon a flat plate perpendicular to the solar vector at a distance of 1 astronomical unit from the sun.

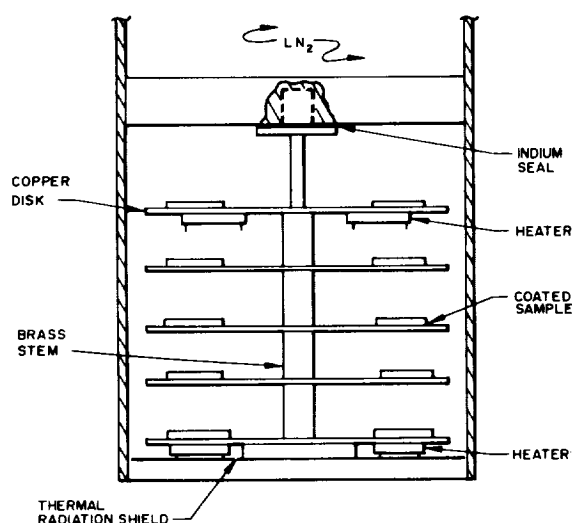


FIGURE 3.—Apparatus for determining effect of temperature.

apart. One end of the brass rod was fastened to a liquid-nitrogen heat sink. Heater assemblies were fastened to the disks at either end of the rod.

With proper choice of rod material, geometrical arrangement, and heater power, selected temperature increments were attained. Twenty 31/32-in.-diameter thermal-control samples were fastened to each disk with an alumina cement. The apparatus was circumferentially enclosed with a liquid-nitrogen-cooled cylinder; the hot end of the apparatus was enclosed by an aluminum thermal-radiation shield.

Reflectance and Emittance Apparatus

The laboratory apparatus used to record directly the sample reflectance from 0.275 to 1.8 μ was the Cary 14M recording spectrophotometer with a Cary 1411 diffuse reflectance attachment.

Solar absorptance was obtained by integrating in 2-percent energy increments the recorded reflectance curves with respect to the extraterrestrial solar distribution.

Infrared spectral reflectance and emittance were obtained by utilizing the heated cavity reflectometer (hohlraum) with a double-beam model 13 Perkin-Elmer spectrophotometer. With this apparatus, rapid measurements of infrared spectral near-normal reflectance with uncertainties of 0.02 reflectance units were

obtained. Values of total hemispherical emittance were estimated from these measurements with suitable accuracy for material-screening and evaluation purposes.

The emissometer portion of the Lion Research Corporation's optical surface comparator³ was also used for rapid emittance measurements.

DOSIMETRY

Dosimeter packets were placed throughout the sample areas in all tests to measure nuclear radiation dose. Each packet contained the following:

Dosimeter	Dose Measured
Nitrous oxide	Gamma, ergs/g(C)
Sulphur	n/cm ² , E>2.9 Mev
Aluminum	n/cm ² , E>8.1 Mev
Cobalt (bare and cadmium-covered)	n/cm ² , E<0.48 ev

The nitrous oxide chemical dosimeter is based upon the reaction $6\text{N}_2\text{O} \rightarrow 5\text{N}_2 + \text{O}_2 + 2\text{NO}_2$. The moles of N_2 and O_2 produced per mole of N_2O are converted to a gamma dose through a calibration curve. Rate effects and dose contributions by neutrons are negligible (less than 0.15 percent in the GTR field). The nitrous oxide dosimeter is, however, temperature sensitive, so that temperature corrections are necessary.

The sulphur and aluminum dosimeters are activated by neutrons of energies greater than particular threshold values, usually in the Mev range. The effective threshold energy for $\text{Al}^{27}(\text{n}, \alpha) \text{Na}^{24}$ is 8.1 Mev, and for the reaction $\text{S}^{32}(\text{n}, \text{p}) \text{P}^{32}$ is 2.9 Mev.

The thermal neutron flux was measured by the cadmium difference technique for neutrons of energy lower than 0.48 ev. The spectrum between 0.48 ev and 2.9 Mev was not measured; estimates of this region were based upon the GTR spectrum.

The absolute accuracy of the dosimetry, in general, is 20 percent; the measurements are reproducible within 5 percent.

EXPERIMENTAL PROCEDURE

Thermal-control samples for static irradiations were prepared on panels (usually alumi-

³ Developed under an LMSC contract sponsored by the Air Force.

num) from which approximately 12 test specimens were obtained. Identical samples allowed the effects of various dose levels to be studied and supplied additional data points. Duplicates also provided redundancy in case of accidental contamination of test surfaces. Two samples of each coating were retained as controls for optical-property measurements.

All vacuum and related experimental apparatus were fabricated at LMSC. For the most part, individual experiments were integrated with the overall equipment in the laboratory to allow calibration and to assure system integrity. All components of the vacuum system were thoroughly leak checked and overall vacuum stability was assured.

Following vacuum and electrical integrity checkout, the equipment was disassembled and transported to the General Dynamics facility.

The equipment was reassembled at the Irradiated Materials Laboratory at the NARF complex with the thermal-control samples and dosimeter packets included. With vacuum integrity achieved, the test apparatus was

transported to the reactor area, where the electrical consoles were placed in the reactor control area and the vacuum chamber was placed upon the north face dolly of the shuttle system. The cable-driven dollies extend from the loading area to the irradiation position. Instrumentation and power leads were connected from the test chamber to the electrical consoles in the reactor control room.

The liquid-nitrogen chambers and fill lines were purged with helium before a continuous flow of liquid nitrogen was established. Purging was to assure that the cryogenic system contained no oxygen, since in the presence of ionizing radiation ozone will be formed from any oxygen present. At liquid nitrogen temperature the ozone is in the solid phase. Since oxygen is present in liquid nitrogen as an impurity, the supply Dewar had to be sampled to determine the maximum possible amount of ozone formed in the cryostat. It was necessary that this amount remain within safe limits during the test.

After vacuum and thermal steady-state con-

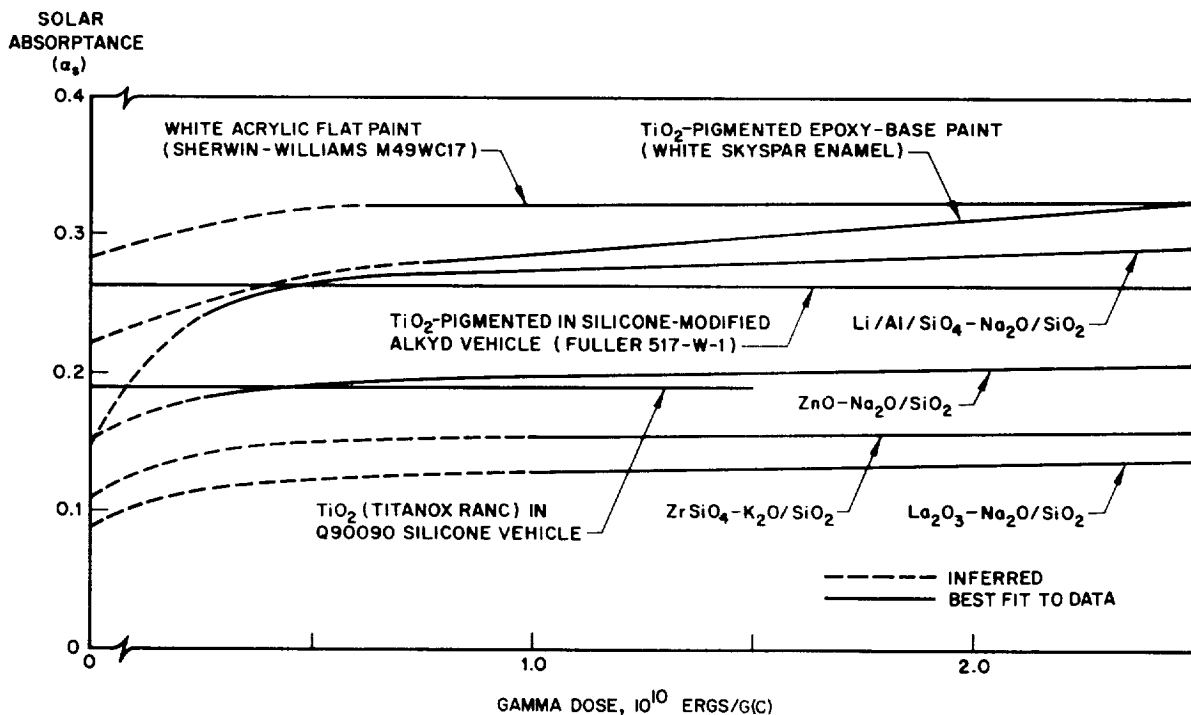


FIGURE 4.—Effect of nuclear radiation in vacuum on the solar absorptance of selected reflector coatings. (Neutron/gamma ratio is approximately 10^9 .)

ditions were verified, an initial data cycle was taken to establish the effective wall temperature for the emittance calorimeters, and to determine the condition of all thermocouples. Power was then supplied to the emittance calorimeters, the temperature-dependency apparatus, and the static panels to attain equilibrium conditions.

The reactor was then sequenced in the following manner: 10 kilowatts for 6 hours, 100 kilowatts for 6 hours, 1 megawatt for 6 hours, and 3 megawatts for the duration of the test for a total of approximately 250 megawatt hours of operation. At the 10-kilowatt reactor power level, the ultraviolet lamp assembly was turned on. Data cycles were taken on all experiments at predetermined time intervals throughout the test. A post-test data cycle was included.

At test termination the apparatus was remotely disconnected and transported to the Irradiated Materials Laboratory. To prevent

sample contamination and possible sample oxidation, the roughing pump was run continuously from the irradiation period to sample removal. Upon removal, the samples were sealed in helium-purged containers for shipment to the LMSC laboratories, where appropriate post-test optical properties were measured.

RESULTS AND DISCUSSION

Initial tests established that optical properties of surface coating materials changed at the nuclear radiation dose levels experienced. The solar absorptances of white coatings (low α_s/ϵ) generally increased appreciably to some saturation level. The curves showing this increase of solar absorptance with dose were similar to those obtained with ultraviolet irradiation, although the saturation values were not the same (compare figs. 4 and 5). Black coatings, leafing and nonleafing aluminum coatings, and metals did not noticeably degrade. Since the degradations of the low- α_s/ϵ materials were

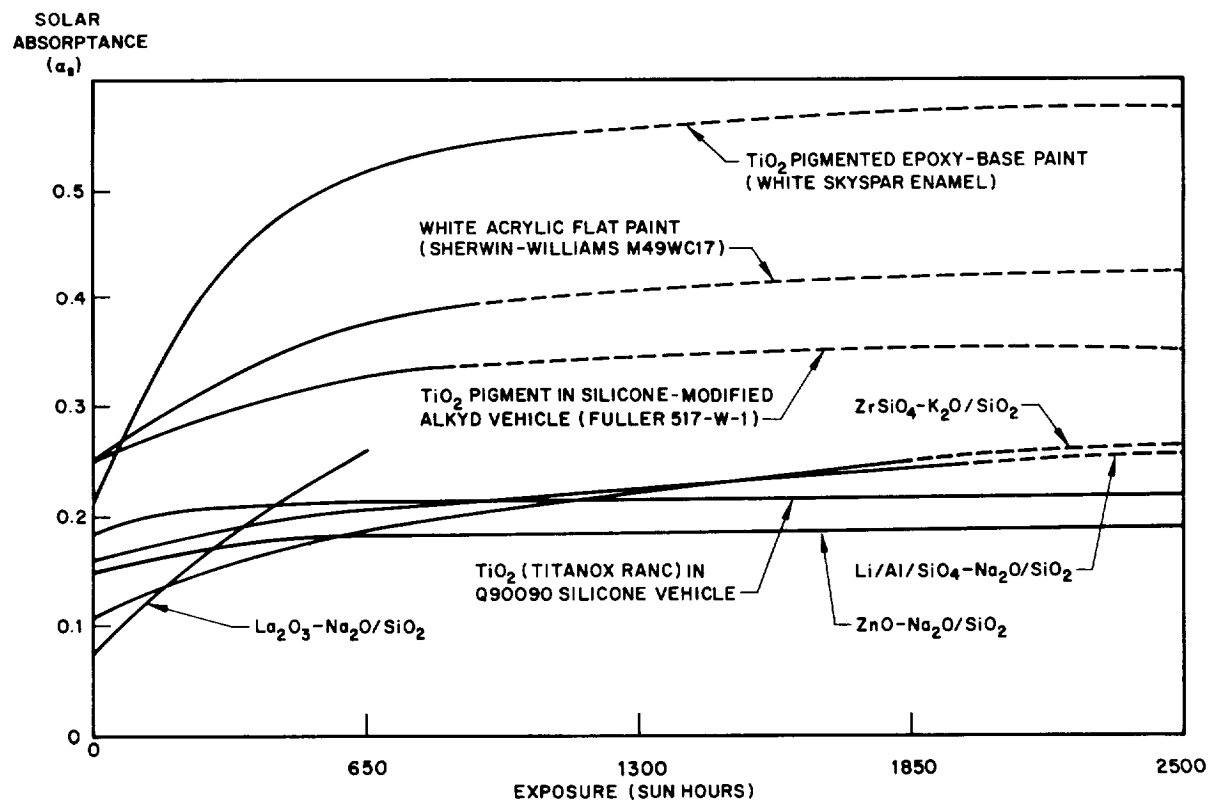


FIGURE 5.—Effect of near-ultraviolet radiation in vacuum on the solar absorptance of selected solar reflector coatings.

determined to be unacceptable for the spacecraft being studied, new materials were developed and additional tests were performed to determine stability to nuclear radiation. Supplemental experiments were added during the static irradiations. These included experiments on temperature dependence and isotope dependence, and dynamic emittance and absorptance experiments.

The initial white coatings tested included standard LMSC coatings which were in use. These included tinted white Kemacryl Lacquer (Sherwin-Williams M49WC17), which is a white acrylic flat paint, room-temperature cured; Fuller Gloss White Silicone Paint (517-W-1) which is a TiO_2 -pigmented silicone-modified alkyd vehicle, cured by baking at 465°F ; white Skypar Enamel (A. Brown A423 color SA9185), which is a TiO_2 -pigmented epoxy-based paint, room-temperature cured; and a $\text{Li}/\text{Al}/\text{SiO}_4$ -pigmented sodium silicate vehicle, cured by baking at 200°C . All but one of these coatings demonstrated unsatisfactory degradation of the optical properties. Figures 4 and 5 show their stability in nuclear and ultraviolet environments, respectively.

It is noted that the best fit of data for the plot of solar absorptance as a function of nuclear radiation dose was obtained by use of gamma dose as abscissa rather than integrated neutron flux. The TiO_2 -pigmented silicone-modified alkyd vehicle indicated some degree of stability in all environments, but required elevated-temperature curing, which is burdensome in production. In addition, optical property degradation was marginal in the ultraviolet-only environment and the initial α_s/ϵ was not low enough to satisfy some thermal requirements. Thus, the development and formulation of special thermal-control coatings with improved resistance to ultraviolet and nuclear degradation and low α_s/ϵ ratios were necessary. Three groups of materials received special attention: (1) inorganic based, both room- and elevated-temperature cured; (2) semi-organic based room-temperature cured; and (3) flame-sprayed inorganic-base materials.

The inorganic, elevated-temperature curing silicate-base coatings were successfully employed for thermal control on several space

vehicles, including Tiros and several Air Force satellites. Laboratory studies resulted in improved inorganic coatings with lower α_s/ϵ ratios, better resistance to ultraviolet radiation, and easier application techniques due to room-temperature curing capability and less stringent requirements for surface preparation.

The effects of the nuclear environment on the solar absorptance of some silicate coatings are shown in table I. The increases in solar absorptance of some selected silicates in an ultraviolet environment are included in figure 5.

In all cases, pre- and post-test emittance measurements indicated that the infrared emittance of these surface coatings is not affected. Pigments used in the silicate coatings included La_2O_3 , $\text{Li}/\text{Al}/\text{SiO}_4$, ZnS , TiO_2 , CaSiO_3 , ZrSiO_4 , SnO_2 , Y_2O_3 , ZnO , $\text{Na}_2\text{O}/\text{Al}_2\text{O}_3/4\text{SiO}_2$, $\text{K}_2\text{O}/\text{Al}_2\text{O}_3/4\text{SiO}_2$, $\text{MgO}/\text{Al}_2\text{O}_3/4\text{SiO}_2$, CaF_2 , LiF , and NaF . The vehicles included $\text{K}_2\text{O}/\text{SiO}_2$ and $\text{Na}_2\text{O}/\text{SiO}_2$.

It is of interest to note that although $\text{Li}/\text{Al}/\text{SiO}_4$ pigmented silicate is relatively stable in an ultraviolet environment, it degrades severely in a nuclear environment. An *isotope-dependence experiment* was performed in an effort to explain the behavior of this pigmented system. Since it is well known that the neutron absorption cross section of Li^6 is large, relative to most isotopes, special coatings were prepared using normal lithium (92.5 percent Li^7 and 7.5 percent Li^6), Li^6 (99.3 ± 0.2 atom percent) and Li^7 (99.9924 atom percent). It would be expected that the Li^7 coating would be much less susceptible to neutron degradation than the Li^6 coating. The results of this experiment are indicated in table II which shows the effect of nuclear radiation in vacuum on Li^6 and Li^7 and normal-lithium-pigmented coatings. It is evident that there is no isotope dependence in optical degradation for these coatings.

The fact that lithium coatings are not isotope dependent and still degrade severely in a nuclear environment while showing ultraviolet stability and the fact that La_2O_3 undergoes catastrophic degradation in an ultraviolet environment while indicating stability in a nuclear environment lead to the following general conclusion: (1) the damage mechanisms in optical surface coatings in a penetrating

TABLE I.—Effect of Nuclear Radiation in Vacuum on Solar Absorptance of Silicate-Based Coatings

Material		α_s		Integrated neutron flux, n/cm ² (10 ¹⁵)**		Gamma dose ergs/g(C) (10 ¹⁶)**
Code	Description*	Initial	Final	E<0.48 ev	E>2.9 Mev	
B-20-5	CaF ₂ —Na ₂ O/SiO ₂ (5 mil)	0.28	0.47	3.2	4.6	2.4
B-23-5	CaF ₂ —Na ₂ O/SiO ₂ (3-mil coating thickness)	.12	.30	2.8	3.8	2.4
C-24-5	CaF ₂ —K ₂ O/SiO ₂	.13	.18	.23	1.3	2.5
A-70-6	LiF—Na ₂ O/SiO ₂ , 24% PVC	.29	.32	.21	.35	.14
A-70-5	LiF—Na ₂ O/SiO ₂ , 24% PVC	.29	.33	.99	1.4	.88
A-94-6	LiF—Na ₂ O/SiO ₂ , 74% PVC	.13	.23	.23	.47	.19
A-94-5	LiF—Na ₂ O/SiO ₂ , 74% PVC	.13	.27	.99	.14	.88
C-23-2	NaF—K ₂ O/SiO ₂ , 80% PVC	.16	.31	.23	1.3	2.5
A-77-4	La ₂ O ₃ —Na ₂ O/SiO ₂	.07	.14	1.3	1.8	1.3
A-77-5	La ₂ O ₃ —Na ₂ O/SiO ₂	.07	.11	.99	1.4	.88
B-56-5	La ₂ O ₃ —Na ₂ O/SiO ₂	.09	.14	2.8	3.8	2.4
C-3-2	La ₂ O ₃ —Na ₂ O/SiO ₂	.07	.10	.23	1.3	2.5
C-4-2	La ₂ O ₃ —K ₂ O/SiO ₂	.05	.14	.23	1.3	2.5
A-89-5	Synthetic Li/Al/SiO ₄ —Na ₂ O/SiO ₂	.12	.23	.99	1.4	.88
A-89-6	Synthetic Li/Al/SiO ₄ —Na ₂ O/SiO ₂	.12	.21	.23	.47	.19
C-19-2	Synthetic Li/Al/SiO ₄ —Na ₂ O/SiO ₂	.14	.32	.23	1.3	2.5
C-37-2	Synthetic Li/Al/SiO ₄ —Na ₂ O/SiO ₂	.11	.24	.23	1.3	2.5
A-80-4	ZnS—Na ₂ O/SiO ₂	.20	.22	1.3	5.6	2.6
A-81-5	ZnS—Na ₂ O/SiO ₂	.17	.20	.99	1.4	.88
A-93-6	ZnS—Na ₂ O/SiO ₂	.18	.18	.23	.47	.19
C-12-2	ZnS—Na ₂ O/SiO ₂	.20	.22	.23	1.3	2.5
C-13-2	ZnS—K ₂ O/SiO ₂	.17	.18	.23	1.3	2.5
A-95-5	TiO ₂ —Na ₂ O/SiO ₂	.15	.20	.99	1.4	.88
A-95-5	TiO ₂ —Na ₂ O/SiO ₂	.15	.21	.23	.47	.19
C-8-2	TiO ₂ —Na ₂ O/SiO ₂	.15	.24	.23	1.3	2.5
C-9-2	TiO ₂ —K ₂ O/SiO ₂	.15	.23	.23	1.3	2.5
C-10-2	TiO ₂ (RANC)—Na ₂ O/SiO ₂	.17	.23	.23	1.3	2.5
C-11-2	TiO ₂ (RANC)—K ₂ O/SiO ₂	.15	.21	.23	1.3	2.5
A-74-6	Li/Al/SiO ₄ —Na ₂ O/SiO ₂ +1% Fe ₂ O ₃ ·NiO	.34	.37	.23	.47	.19
A-74-5	Li/Al/SiO ₄ —Na ₂ O/SiO ₂ +1% Fe ₂ O ₃ ·NiO	.34	.37	.99	1.4	.88
A-74-2	Li/Al/SiO ₄ —Na ₂ O/SiO ₂ +1% Fe ₂ O ₃ ·NiO	.34	.38	<.1	1.5	.97
A-74-4	Li/Al/SiO ₄ —Na ₂ O/SiO ₂ +1% Fe ₂ O ₃ ·NiO	.34	.39	.89	1.5	.97
A-75-6	Li/Al/SiO ₄ —Na ₂ O/SiO ₂ +3% Fe ₂ O ₃ ·NiO	.51	.51	.23	.47	.19
A-75-5	Li/Al/SiO ₄ —Na ₂ O/SiO ₂ +3% Fe ₂ O ₃ ·NiO	.51	.52	.99	1.4	.88
A-76-6	Li/Al/SiO ₂ —Na ₂ O/SiO ₂ +5% Fe ₂ O ₃ ·NiO	.57	.58	.23	.47	.19
A-76-5	Li/Al/SiO ₂ —Na ₂ O/SiO ₂ +5% Fe ₂ O ₃ ·NiO	.57	.59	.99	1.4	.88
A-76-4	Li/Al/SiO ₂ —Na ₂ O/SiO ₂ +5% Fe ₂ O ₃ ·NiO	.57	.59	1.3	1.8	1.3
B-48-5	Li/Al/SiO ₂ —Na ₂ O/SiO ₂ +25% B ₄ C	.89	.89	2.8	3.8	2.4
A-54-3	Li/Al/SiO ₄ (1 part)—ZrSiO ₄ (1 part)—Na ₂ O/SiO ₂	.12	.19	1.1	1.7	1.3
A-54-4	Li/Al/SiO ₄ (1 part)—ZrSiO ₄ (1 part)—Na ₂ O/SiO ₂	.12	.18	1.3	1.8	1.3
A-54-6	Li/Al/SiO ₄ (1 part)—ZrSiO ₄ (1 part)—Na ₂ O/SiO ₂	.12	.16	.30	.49	.19
A-55-1	Li/Al/SiO ₄ (1 part)—ZrSiO ₄ (3 parts)—Na ₂ O/SiO ₂	.08	.16	<.1	1.5	.97
A-55-4	Li/Al/SiO ₄ (1 part)—ZrSiO ₄ (3 parts)—Na ₂ O/SiO ₂	.08	.16	.89	1.5	.97
A-55-5	Li/Al/SiO ₄ (1 part)—ZrSiO ₄ (3 parts)—Na ₂ O/SiO ₂	.08	.16	.99	1.4	.88
A-55-6	Li/Al/SiO ₄ (1 part)—ZrSiO ₄ (3 parts)—Na ₂ O/SiO ₂	.08	.16	.30	.49	.19

TABLE I.—Effect of Nuclear Radiation in Vacuum on Solar Absorptance of Silicate-Based Coatings—Continued

Material		α_s		Integrated neutron flux, n/cm ² (10 ¹⁵)**		Gamma dose, ergs/g(C) (10 ¹⁶)**
Code	Description*	Initial	Final	E<0.48 ev	E>2.9 Mev	
A-56-2	Li/Al/SiO ₄ (3 parts)—ZrSiO ₄ (1 part)— Na ₂ O/SiO ₂	.12	.22	<.1	1.3	.88
A-56-4	Li/Al/SiO ₄ (3 parts)—ZrSiO ₄ (1 part)— Na ₂ O/SiO ₂	.12	.21	.89	1.5	.97
A-56-5	Li/Al/SiO ₄ (3 parts)—ZrSiO ₄ (1 part)— Na ₂ O/SiO ₂	.12	.22	.99	1.4	.88
A-56-6	Li/Al/SiO ₄ (3 parts)—ZrSiO ₄ (1 part)— Na ₂ O/SiO ₂	.12	.19	.21	.35	.14
A-85-6	CaSiO ₃ —Na ₂ O/SiO ₂ (Std PVC)	.15	.16	.23	.47	.19
A-85-5	CaSiO ₃ —Na ₂ O/SiO ₂ (Std PVC)	.15	.19	.99	1.4	.88
A-86-6	ZrSiO ₄ ·CaSiO ₃ —K ₂ O/SiO ₂	.15	.16	.23	.47	.19
A-86-5	ZrSiO ₄ ·CaSiO ₃ —K ₂ O/SiO ₂	.15	.19	.99	1.5	.88
A-87-6	ZrSiO ₄ —K ₂ O/SiO ₂	.11	.13	.23	.47	.19
A-87-5	ZrSiO ₄ —K ₂ O/SiO ₂	.11	.14	.99	1.4	.88
B-38-5	SnO ₂ —Na ₂ O/SiO ₂	.17	.21	2.8	3.8	2.4
C-7-2	Y ₂ O ₃ —Na ₂ O/SiO ₂	.09	.13	.23	1.3	2.5
A-60-6	Na ₂ O·Al ₂ O ₃ ·4SiO ₂ —Na ₂ O/SiO ₂	.17	.24	.21	.35	.14
A-60-5	Na ₂ O·Al ₂ O ₃ ·4SiO ₂ —Na ₂ O/SiO ₂	.17	.26	.99	1.4	.88
A-60-2	Na ₂ O·Al ₂ O ₃ ·4SiO ₂ —Na ₂ O/SiO ₂	.17	.27	<.1	1.5	1.2
A-60-1	Na ₂ O·Al ₂ O ₃ ·4SiO ₂ —Na ₂ O/SiO ₂	.17	.29	<.1	1.7	1.3
A-63-6	K ₂ O·Al ₂ O ₃ ·4SiO ₂ —Na ₂ O/SiO ₂	.17	.25	.30	.49	.19
A-63-5	K ₂ O·Al ₂ O ₃ ·4SiO ₂ —Na ₂ O/SiO ₂	.17	.26	.99	1.4	.88
A-63-2	K ₂ O·Al ₂ O ₃ ·4SiO ₂ —Na ₂ O/SiO ₂	.17	.24	<.1	1.5	1.2
A-63-1	K ₂ O·Al ₂ O ₃ ·4SiO ₂ —Na ₂ O/SiO ₂	.17	.25	<.1	1.7	1.3
A-65-6	MgO·Al ₂ O ₃ ·4SiO ₂ —Na ₂ O/SiO ₂	.16	.24	.30	.49	.19
A-65-5	MgO·Al ₂ O ₃ ·4SiO ₂ —Na ₂ O/SiO ₂	.16	.26	.99	1.4	.88
A-65-2	MgO·Al ₂ O ₃ ·4SiO ₂ —Na ₂ O/SiO ₂	.16	.27	<.1	1.5	1.2
A-65-1	MgO·Al ₂ O ₃ ·4SiO ₂ —Na ₂ O/SiO ₂	.16	.28	<.1	1.7	1.3
A-71-6	ZnO—Na ₂ O/SiO ₂ 75% PVC	.11	.17	.21	.35	.15
A-71-5	ZnO—Na ₂ O/SiO ₂ 75% PVC	.11	.17	.99	1.4	.88
A-72-6	ZnO—Na ₂ O/SiO ₂ 80% PVC	.14	.15	.27	.53	.18
A-72-5	ZnO—Na ₂ O/SiO ₂ 80% PVC	.14	.17	.99	1.4	.88
A-73-6	ZnO—Na ₂ O/SiO ₂ 82% PVC	.12	.18	.27	.53	.18
A-73-5	ZnO—Na ₂ O/SiO ₂ 82% PVC	.12	.18	.99	1.4	.88
C-31-2	ZnO (E.P.714)—Na ₂ O/SiO ₂	.17	.23	.23	1.3	2.5

*PVC=Pigment volume concentration.

**Multiply each value in column by this factor.

radiation environment are of a complex nature and (2) the degradation of inorganic coatings is not dependent on the total energy absorbed in the coating, for if the degradation were dose dependent, one would expect equivalence in ultraviolet and penetrating radiation damage for similar absorbed doses.

It is of interest to note materials A-74 through A-76 in table I. These coatings were white coatings ($\alpha_s \sim 0.15$) "doped" with

various amounts of Fe₂O₃·NiO. Doping at 1-, 2-, and 5-percent levels yields absorptance values of 0.34, 0.51, and 0.57, respectively. Materials ES11, ES12, and ES24 in table V were also doped with black-pigmented silicone and Fe₂O₃·NiO. The purpose of these doping studies was to establish the feasibility of modifying the optical properties of stable low α_s/ϵ materials by adding an inert substance and thus obtaining a wide range of stable α_s/ϵ

TABLE II.—Effect of Nuclear Radiation in Vacuum on Li^6 , Li^7 , and Normal-Lithium-Pigmented Coatings

Material			α_s		Integrated neutron flux, n/cm ²		Gamma dose, ergs/gm (C) (10 ¹⁰)**
Code	Description	PVC* %	Initial	Final	E < 0.48 ev (10 ¹³)**	E > 2.9 Mev (10 ¹⁴)**	
E-44-5	Synthetic Li/Al/SiO ₄ -Na ₂ O/SiO ₂ -----	80	0. 14	0. 22	0. 41	1. 5	0. 45
E-44-2	Synthetic Li/Al/SiO ₄ -Na ₂ O/SiO ₂ -----	80	. 14	. 23	. 82	5. 3	1. 3
E-43-5	Synthetic Li/Al/SiO ₄ -Na ₂ O/SiO ₂ -----	75	. 18	. 26	. 41	1. 5	. 45
E-43-2	Synthetic Li/Al/SiO ₄ -Na ₂ O/SiO ₂ -----	75	. 18	. 27	. 82	5. 3	1. 3
E-49-5	Li/Al/SiO ₄ -Na ₂ O/SiO ₂ -----	82	. 16	. 26	. 41	1. 5	. 45
E-49-2	Li/Al/SiO ₄ -Na ₂ O/SiO ₂ -----	82	. 16	. 28	. 82	5. 3	1. 3
E-46-5	Synthetic Li ⁶ /Al/SiO ₄ -Na ₂ O/SiO ₂ -----	80	. 16	. 22	. 41	1. 5	. 45
E-46-2	Synthetic Li ⁶ /Al/SiO ₄ -Na ₂ O/SiO ₂ -----	80	. 16	. 24	. 82	5. 3	1. 3
E-45-5	Synthetic Li ⁶ /Al/SiO ₄ -Na ₂ O/SiO ₂ -----	75	. 19	. 26	. 41	1. 5	. 45
E-45-2	Synthetic Li ⁶ /Al/SiO ₄ -Na ₂ O/SiO ₂ -----	75	. 19	. 27	. 82	5. 3	1. 3
E-48-5	Synthetic Li ⁷ /Al/SiO ₄ -Na ₂ O/SiO ₂ -----	80	. 14	. 25	. 41	1. 5	. 45
E-48-2	Synthetic Li ⁷ /Al/SiO ₄ -Na ₂ O/SiO ₂ -----	80	. 14	. 25	. 82	5. 3	1. 3
E-47-5	Synthetic Li ⁷ /Al/SiO ₄ -Na ₂ O/SiO ₂ -----	75	. 18	. 25	. 41	1. 5	. 45
E-47-2	Synthetic Li ⁷ /Al/SiO ₄ -Na ₂ O/SiO ₂ -----	75	. 18	. 27	. 82	5. 3	1. 3

*PVC = pigment-volume concentration.

**Multiply each value in column by this factor.

TABLE III.—Effect of Nuclear Radiation in Vacuum on Solar Absorptance of Silicone-Base Coatings

Material			α_s		Integrated neutron flux, n/cm ²		Gamma dose, ergs/g (C) (10 ¹⁰)*
Code	Description		Initial	Final	E < 0.48 ev (10 ¹³)*	E > 2.9 Mev (10 ¹⁴)*	
E-4-2	TiO ₂ (Titanox AMO) pigmented 3% DC 432 Silicone film.		0. 28	0. 28	1. 9	5. 6	1. 3
E-5-2	TiO ₂ (Titanox AMO) pigmented 6% DC 432 Silicone film.		. 22	. 22	1. 9	5. 6	1. 3
E-6-2	TiO ₂ (Titanox AMO) pigmented 12% DC 432 Silicone film.		. 19	. 19	1. 9	5. 6	1. 3
E-7-2	TiO ₂ (Titanox AMO) pigmented 24% DC 432 Silicone film.		. 16	. 16	1. 9	5. 6	1. 3
E-8-2	TiO ₂ (Titanox AMO) pigmented 100% DC 432 Silicone film.		. 23	. 26	1. 9	5. 6	1. 3
E-9-2	TiO ₂ (Titanox AMO) pigmented 200% DC 432 Silicone film.		. 26	. 28	1. 9	5. 6	1. 3
E-10-2	TiO ₂ (Titanox RANC) 100% plus MICA 60% pigmented DC 432 Silicone film.		. 22	. 22	1. 9	5. 6	1. 3
E-12-2	ZnO (Kadox 15) pigmented 6% DC 432 Silicone film.		. 37	. 37	1. 9	5. 6	1. 3
E-13-2	ZnO (Kadox 15) pigmented 100% DC 432 Silicone film.		. 27	. 27	1. 9	5. 6	1. 3
E-14-2	ZnO (SP500) pigmented 200% DC 432 Silicone film.		. 18	. 18	1. 9	5. 6	1. 3
E-15-2	ZnS pigmented 6% DC 432 Silicone film.		. 28	. 28	1. 9	5. 6	1. 3
E-18-2	ZnS pigmented 100% DC 432 Silicone film.		. 19	. 19	1. 9	5. 6	1. 3
E-19-2	SnO ₂ pigmented 24% DC 432 Silicone film.		. 33	. 33	1. 9	5. 6	1. 3
E-21-2	SnO ₂ pigmented 200% DC 432 Silicone film.		. 32	. 32	1. 9	5. 6	1. 3

TABLE III.—Effect of Nuclear Radiation in Vacuum on Solar Absorptance of Silicone-Base Coatings—Continued

Material		α		Integrated neutron flux, n/cm ²		Gamma dose, ergs/g (C) (10 ¹⁰)*
Code	Description	Initial	Final	E < 0.48 ev (10 ¹³)*	E > 2.9 Mev (10 ¹⁴)*	
E-22-2---	Zirconium oxide (Ultrax 500W) pigmented 24% DC 432 Silicone film.	.26	.26	1.9	5.6	1.3
E-24-2---	Zirconium oxide (Ultrax 500W) pigmented 200% DC 432 Silicone film.	.21	.22	1.9	5.6	1.3
E-30-2---	Connecticut hard rubber optical pressure sensitive tape (No. 3).	.15	.15	1.9	5.6	1.3
E-31-2---	TiO ₂ (Titanox RANC) 24% in Q90090 Silicone vehicle.	.21	.22	1.9	5.6	1.3
E-33-2---	TiO ₂ (Titanox RANC) 200% in Q90090 Silicone vehicle.	.20	.20	1.9	5.6	1.3
E-36-2---	TiO ₂ (Titanox RANC) 100% plus mica 10% in Q90090 Silicone vehicle.	.17	.17	.82	5.2	1.3
E-74-2---	TiO ₂ (Titanox AMO) 100% in Q90090 Silicone vehicle.	.18	.20	2.2	4.3	1.7
E-67-2---	TiO ₂ (Titanox AMO) 200% in Q90090 Silicone vehicle.	.16	.17	2.2	4.3	1.7
E-38-2---	ZnO (Kadox 15) 200% in Q90090 Silicone vehicle.	.22	.23	.82	5.2	1.3
E-68-2---	ZnO (Kadox 15) 300% in Q90090 Silicone vehicle.	.30	.30	2.2	4.3	1.7
E-40-2---	ZnO (SP500) 200% in Q90090 Silicone vehicle.	.19	.19	.82	5.2	1.3
E-75-2---	ZnO (Kadox 15) 24% in Q90098 Silicone vehicle.	.31	.31	2.2	4.3	1.7
E-39-2---	ZnO (Kadox 15) 200% in Q90089 Silicone vehicle.	.28	.29	.82	5.2	1.3
E-41-2---	ZnS 100% in Q90090 Silicone vehicle----	.20	.20	.82	5.2	1.3
E-69-2---	SnO ₂ 24% in Q90090 Silicone vehicle----	.35	.35	2.2	4.3	1.7
E-71-2---	SnO ₂ 200% in Q90090 Silicone vehicle----	.30	.30	2.2	4.3	1.7
E-93-2---	Zirconium oxide (Ultrax 500W) in Q90090 Silicone vehicle.	.26	.27	1.2	4.1	1.5

*Multiply each value in column by this factor.

TABLE IV.—Effect of Nuclear Radiation in Vacuum on Solar Absorptance of Arc-Plasma Applied Materials

Material		α		ϵ_H		Integrated neutron flux, n/cm ²		Gamma dose, ergs/gm(C) (10 ¹⁰)*
Code	Description	Initial	Final	Initial	Final	E < 0.48 ev (10 ¹³)*	E > 2.9 Mev (10 ¹⁴)*	
B-1-5-----	Zirconia-----	0.43	0.46	0.74	0.75	3.2	4.6	2.4
B-3-5-----	Alumina-----	.16	.19	.72	.72	3.2	4.6	2.4
B-5-5-----	Titanium carbide-----	.86	.86	.75	.71	2.8	3.8	2.4
B-6-5-----	Titanium nitride-----	.80	.83	.62	.64	2.8	3.8	2.4
B-9-5-----	Li/Al/SiO ₄ -----	.30	.40	.84	.84	3.2	4.6	2.4
B-10-5-----	Zirconia-----	.35	.32	.71	.71	3.2	4.6	2.4
B-12-5-----	Zirconium carbide-----	.81	.80	.63	.61	3.2	4.6	2.4
B-19-5-----	Chromium carbide-----	.78	.77	.54	.54	3.2	4.6	2.4

*Multiply each value in column by this factor.

TABLE V.—Effect of Combined Nuclear and Near-Ultraviolet Radiation in Vacuum on Solar Absorptance

Material		α			Laboratory exposure to near-ultraviolet radiation in vacuum	
Code	Description	Initial	Nuclear exposure * Final	Simultaneous exposure ** Final	α , Final	Sun-hours
ES12-----	TiO ₂ (Titanox RANC) 200%+1% black in Q90090 Silicone vehicle.	0.50	0.50	0.53	----	----
ES11-----	TiO ₂ (Titanox RANC) 200%+0.5% black in Q90090 Silicone vehicle.	.46	.46	.50	----	----
ES1-----	TiO ₂ (Titanox RANC) 300% in Q90090 Silicone vehicle.	.19	.19	.26	----	----
ES20-----	SnO ₂ Pigmented (200%) DC-432 Silicone film.	.34	.34	.42	0.38	640
ES21-----	Zirconium oxide (Ultrax 500W) pigmented DC-432 Silicone film.	.22	.22	.37	.28	640
ES22-----	Connecticut hard rubber optical pressure-sensitive tape (No. 3).	.17	.17	.25	.27	500
ES14-----	SnO ₂ (200%) in Q90090 Silicone vehicle.	.32	.32	.40	.36	500
ES7-----	ZnS (100%) in Q90090 Silicone vehicle.	.26	.26	.32	.32	500
ES2-----	TiO ₂ (Titanox RANC) 100%+3000-mesh mica in Q90090 Silicone vehicle.	.21	.21	.29	.25	500
ES10-----	ZnO (Kadox-15) 200% in Q90090 Silicone vehicle.	.28	.28	.33	.31	400
ES19-----	ZnS pigmented (100%) DC-432 Silicone film.	.20	.20	.27	.25	640
ES24-----	Synthetic zirconium pigment in K ₂ O/SiO ₂ +1% Fe ₂ O ₃ ·NiO.	.47	----	.52	----	----

* 1.5×10^{13} n/cm², E<0.48 ev; 4.3×10^{14} n/cm², E>2.9 Mev; 1.4×10^{15} ergs/g(C) gamma in vacuum.** 7.1×10^{13} n/cm², E<0.48 ev; 4.6×10^{14} n/cm², E>2.9 Mev; 1.1×10^{15} ergs/g(C) gamma; and 920 sun-hours of near-ultraviolet radiation in vacuum.

values from one initially stable low α_s/ϵ system.

Special silicone thermal-control coatings with improved resistance to ultraviolet and nuclear degradation and easier application techniques due to room-temperature curing capability were developed and formulated. These coatings were based on silicone resins made available by DC and on careful control of the pigments. Pigments used included rutile titanium dioxide (Titanium Pigments Co., RANC), anatase TiO₂ (Titanium Pigments Co., AMO), ZnO (New Jersey Zinc, Kadox 15), zinc oxide (SP 500), ZnS (technical grade), SnO₂, and ZrO₂ (Ultrax 500W). The silicone vehicles included DC 432, DC-Q-9-0090, DC-Q-9-0089, and DC-Q-9-0090 modified with acetic acid. The effect of nuclear radiation in vacuum on the solar absorptance of silicone-base coatings is given in table III.

Arc-plasma applied coatings received some attention. The materials included zirconia,

alumina, titanium carbide, titanium nitride, zirconium carbide, and chromium carbide. The effect of nuclear irradiation in vacuum on the solar absorptance and the total hemispherical emittance ϵ_H of these coatings is shown in table IV. These coatings were not recommended for use because the optical properties are not reproducible from one application to the next.

The total hemispherical emittance at 500° K of selected coatings was measured dynamically during nuclear irradiations. Determinations were performed by use of the emittance calorimeters described under Apparatus. The materials tested included White Skyspar Enamel, Fuller Aluminum Silicone (172-A-1), Fuller Aluminum Silicone (172-A-152), ZrSiO₄-Na₂O/SiO₂, Nonleafing Aluminum Acrylic Paint, ZnS-Na₂O/SiO₂, Li/Al/SiO₄-K₂O/SiO₂, La₂O₃-K₂O/SiO₂, and chemically polished aluminum. The results are presented in figure 6.

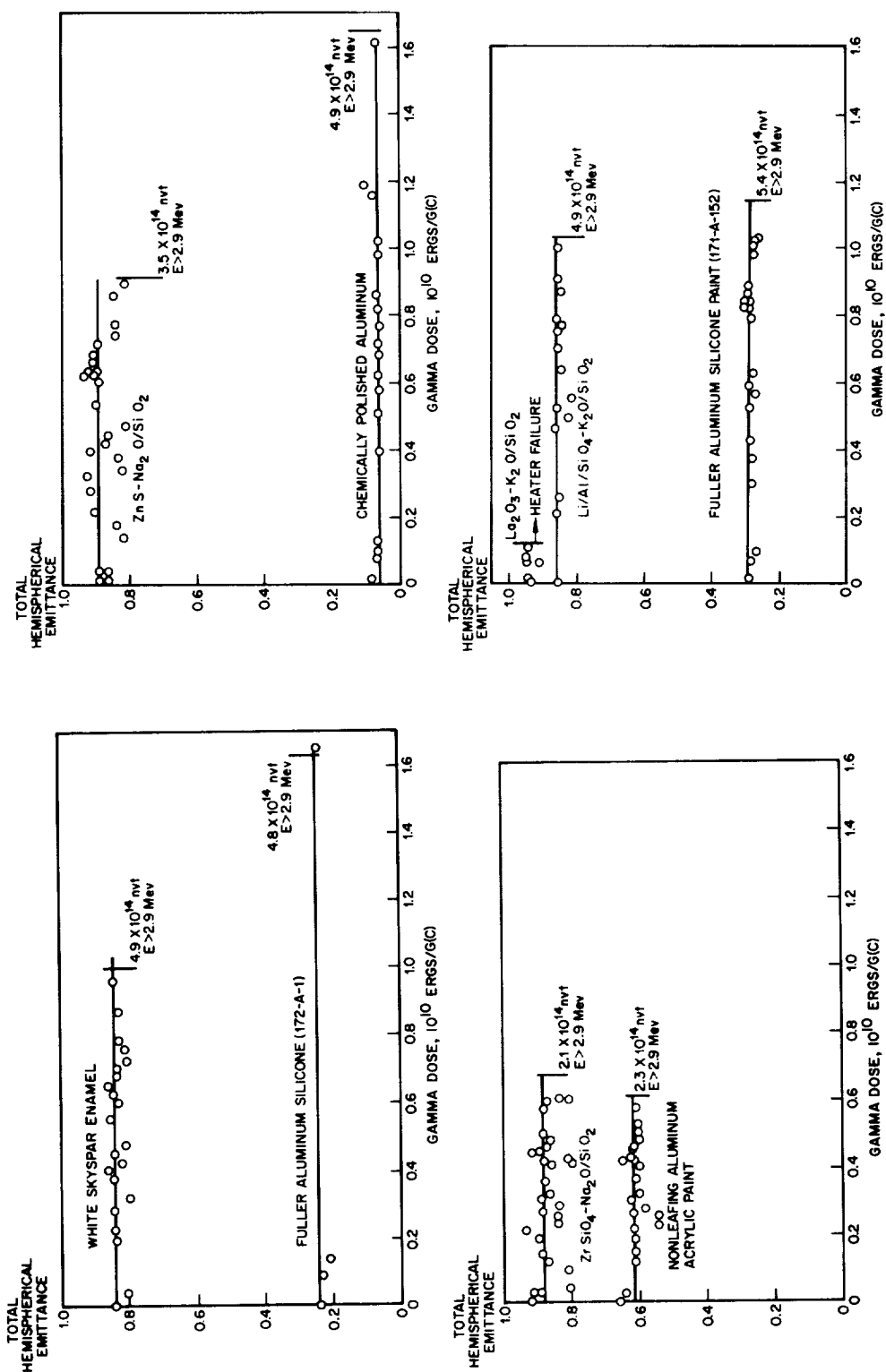


FIGURE 6.—Effect of nuclear dose on total hemispherical emittance.

TABLE VI.—Effect of Sample Temperature During Nuclear Irradiation on the Optical Properties of Thermal-Control Coatings

Material	Temperature During Irradiation, °F \pm 10	α_s		Dose
		Initial	Final	
Skyspar epoxy-based coating--	-100	0.22	0.22	2.2×10^5 ergs/g (C) 0.6×10^{13} n/cm ² , $E < 0.48$ ev 1×10^{14} n/cm ² , $E > 2.9$ Mev in vacuum
	0	.22	.22	
	+100	.22	.23	
	+200	.22	.28	
ZrSiO ₄ -K ₂ O/SiO ₂ -----	70	.11	.13	2.2×10^5 ergs/g (C) 2.26×10^{14} n/cm ² , $E < 0.48$ ev 4.72×10^{14} n/cm ² , $E > 2.9$ Mev in vacuum
	-320	.11	.22	
Na ₂ O·Al ₂ O ₃ ·4SiO ₂ - Na ₂ O/SiO ₂	70	.17	.24	
	-320	.17	.34	

The curves indicate no damage to total hemispherical emittance for both high- and low-emittance coatings. Post-test emittance measurements performed on all static samples also indicate no change in the emittance of any material tested at the nuclear dose levels and temperatures experienced during irradiation.

The effect of simultaneous nuclear and ultraviolet irradiation in vacuum is given in table V. The optical measurements for the combined environmental effects are pre- and post-test optical measurements of the surface coatings on the absorptance calorimeters. Dynamic data obtained during combined environmental testing are still under evaluation. Additional laboratory exposures to near-ultraviolet radiation of the materials listed in table V are also in progress.

The study of the effects of temperature on the optical properties of a thermal control coating during irradiation was confined to the temperature region of -320° F to $+200^\circ$ F. Table VI indicates the results of the behavior of various materials at selected temperatures. Complete reduction of the temperature-dependency data is still in progress. From the temperature-damage data presented, one im-

portant conclusion can be drawn: In reporting radiation damage studies to optical surface coatings, the temperature of the specimen during irradiation should be given.

FUTURE WORK

The following areas should be considered in future work:

- Testing to establish threshold values for unacceptable mechanical and/or optical damage of coatings stable at the dose levels reported herein.
- Correlation of Co-60 radiation damages with reactor radiation damage.
- Study of damage-annealing effects.
- Study of fundamental damage mechanisms.
- High-temperature and cryogenic irradiations of thermal-control materials.
- Study of optical property changes incurred by the synergistic effects of nuclear radiation, ultraviolet radiation, operational temperature, and vacuum.

REFERENCE

1. STRAYHORN, T. R.: The Extra Problem of Nuclear Vehicles—Radiation Heating. *Space Aeronautics*, vol. 39, no. 3, Mar. 1963, p. 111.

40. Development of a Technique for the Correlation of Flight- and Ground-Based Studies of the Ultraviolet Degradation of Polymer Films

JOHN A. PARKER AND CARR B. NEEL

NASA AMES RESEARCH CENTER

MORTON A. GOLUB

STANFORD RESEARCH INSTITUTE, MENLO PARK, CALIF.

The surface temperatures and the environmental stabilities of thermal control surfaces have been observed to change measurably in a near-earth orbit on the first Orbiting Solar Observatory (OSO-I). The changes in surface temperatures caused by in-space ultraviolet degradation do not correlate with predictions from ground-based simulation of environmental conditions. The general behavior of these surfaces has suggested a possible technique for evaluating the accuracy of ground-based simulation experiments, namely, the measurement of surface temperature of a film consisting of a well-behaved polymer system. Films of both polymers and copolymers of vinyl chloride were exposed to ultraviolet radiation in vacuum and were found to exhibit a regular and quantitatively measurable change in solar absorptance with time. The major changes produced by this exposure occurred in the ultraviolet and visible regions. Virtually no change has been observed in the infrared absorption spectra of these films, even after exposure to the equivalent of 72 hours of space solar radiation. In the exposures to simulated conditions of vacuum and ultraviolet radiation, a linear change with time in the ratio of solar absorptance to emittance has been observed to occur after an initial transient period. The regular behavior of these films indicates that a reasonable prediction of the temperature changes which would occur in the real space environment can be made.

To obtain the desired mechanical properties for a flight test, a surface consisting of a pure polyvinyl chloride terpolymer film (VMCH) was cast on a polished aluminum substrate. This material is found to behave almost identically to the pure polyvinyl chloride. Predicted temperature changes of such a surface will be compared with the results obtained on this surface in actual orbital flight of OSO-C. The amount of gamma radiation required to produce a given change in the absorptance equivalent to that produced by a specific amount of ultraviolet radiation has also been determined experimentally. The gamma radiation which would produce the same effect as 30-hour exposure to the solar ultraviolet would require a period of several years of exposure in space, and, hence, would not influence the results of the correlation of the ultraviolet exposure.

Reflective white paints, consisting of inorganic pigments and organic polymeric binders, have been employed as thermal control surfaces for space vehicles. A variety of polymeric

types of binders have been investigated for this purpose. Paints based on acrylics, silicones, phenolics, and epoxy resins have been used (ref. 1). None of these materials is unstable

in vacuum in the range of operating temperatures encountered on a spacecraft. The inorganic pigments (for example, titanium dioxide) are relatively stable to the action of the incident electromagnetic radiation encountered in these applications. All available evidence obtained to date points to an alteration of the molecular structure of the polymeric components produced by the incident ultraviolet radiation as the principal cause of change in the thermal control characteristics of these coatings. About 9 percent of the total energy of incident solar radiation on a satellite in a near-earth orbit lies in the region from 2200 to 4000 Å and only 0.02 percent lies below 2200 Å (ref. 2). The energy of photons in the wavelength region from 2200 to 4000 Å ranges from 5.6 to 3.1 electron volts. These photons have sufficient energy to break carbon-carbon bonds characteristic of organic polymers, the strength of which is of the order of 3 electron volts (69 kcal per mole), and this can initiate molecular damage processes. The specific chemical structure of the polymeric binder determines both the specific wavelengths and the degree of absorption of the incident ultraviolet radiation. The basic chemical constitution of the polymer also determines the course of the ensuing degradation reaction.

The degradation reaction may produce scissions, cross-linking, or functional group alteration. Only when the damage process leads to the production of highly absorbing groups may one expect a significant change in the optical properties of coatings formulated from these polymers.

Because of the different types of mechanisms involved in the degradation of thermal coatings in space, one may question the general validity of laboratory studies of degradation in which thermal coatings are merely subjected to ultraviolet radiation in vacuum—especially when the spectrum is not similar to the solar spectrum. The present study is concerned with means for finding the answer to this question. In particular, it is concerned with finding a coating that might be especially advantageous for use in comparisons of ground degradation with degradation in space (as indicated by the temperature change of a test surface to which the coating is applied).

To correlate quantitatively the effects of a simulated environment with those of an actual orbital flight on the rate of change of temperature of a polymeric film, a basic polymer with the following properties is required:

1. It absorbs photons in the range from 2200 Å to at least 3000 Å and these photons should be effective in generating color-producing groups.
2. Its principal damage reaction is chromophore production so that absorptivity changes in a regular manner with time of exposure. (Under the conditions of exposure, it is analytically convenient not to encounter significant autocatalysis; that is, this reaction should be zero order with respect to the chromophoric reaction.)
3. It undergoes the required chromophoric reaction without significant alteration in the basic mechanical properties of the film; that is, its physical properties should not be affected either by cross-linking or by scissions so that the film can endure a reasonable orbital flight and experience the expected temperature changes while still retaining its mechanical integrity.
4. Its specific color-producing reactions are free from the effects of differences in spectral distribution, that is, the quantum efficiency and both the number and kinds of groups formed should be independent of the wavelength of ultraviolet radiation absorbed (since it is not practical to simulate the solar ultraviolet spectrum accurately in the laboratory).
5. It is sufficiently stable at the operating temperature of the film that thermal degradation does not occur and complicate the interpretation of the ultraviolet damage process.

Information on the photochemical degradation reactions of polyvinyl chloride and copolymers containing a substantial portion of polyvinyl chloride monomer suggests that such polymers could possibly meet the foregoing requirements (ref. 3).

The specific research to be described is concerned with the evaluation of thin films of polymers and copolymers of vinyl chloride as indicator coatings, as well as with approaches

to ground-based simulation which, if successful, could be used ultimately to predict both the expected temperatures and temperature changes with time of exposure to solar radiation. This paper discusses the research to date on the ground-based phase of this program. The results obtained herein will be correlated ultimately with an in-flight test on OSO-C which should provide an evaluation of the simulation technique.

EXPERIMENTAL RESULTS

Titania-Epoxy and Titania-Silicone Coatings Used as Thermal Control Surfaces on the OSO-I Satellite

The surface temperatures attained by TiO_2 -epoxy and TiO_2 -silicone coatings during a typical orbit of the OSO-I are shown in figure 1. It can be seen that the maximum temperature reached by the TiO_2 -epoxy coating is about 15°F , whereas that of the TiO_2 -silicone coating is about 30°F . These temperatures agree with those calculated by the relation given in reference 4 with initial values of α_s/ϵ for these coatings of 0.27 and 0.36.

The increase in solar absorptance of these coatings calculated from the observed increases in surface temperature in the space environment is shown in figure 2. The increase in solar absorptance is given as a function of exposure in equivalent sun hours of ultraviolet irradiation in a near-earth orbit. At the beginning of the exposure, the rate of change in the epoxy

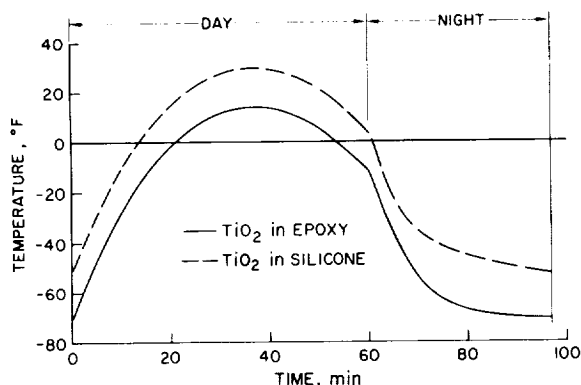


FIGURE 1.—Observed variation in surface temperatures of titania-epoxy and titania-silicone coating in a single orbit of the OSO-I satellite.

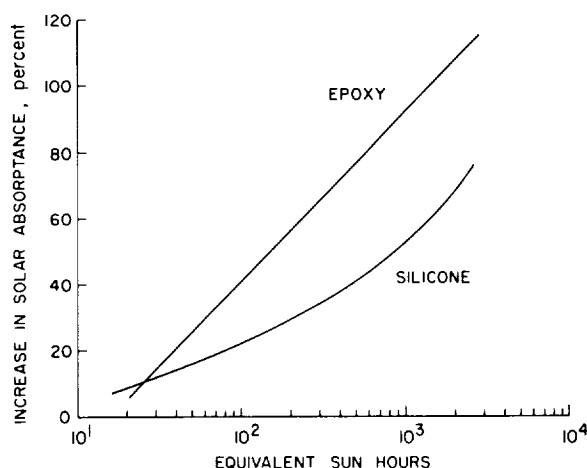


FIGURE 2.—Changes in solar absorptance of titania-epoxy and titania-silicone coatings due to ultraviolet radiation.

is greater than in the silicone coating, but after 1000 equivalent sun hours, the rate of change of the silicone solar absorptance is essentially the same as that for the epoxy coating. These differences in environmental aging characteristics are apparently due to basic differences in the photochemistry of the two polymer binders concerned.

These specific changes in the solar absorptance obtained from in-flight measurements of the temperature have been compared with the changes predicted by ground-based simulation experiments by two different groups of investigators. Unfortunately, the conditions of space cannot be perfectly reproduced in ground-based experiments. Specifically, the temperatures of the films during ultraviolet irradiation and the intensities and spectral distributions of the simulation lamps were not the same as in the space exposure in any of these experiments. In the test run with a General Electric B-H6 lamp, the average film temperature was 185°F and the ultraviolet radiation intensity was 7 times that of the sun at 1 AU (hence, 1 solar constant). With a GE A-H6 lamp, the temperature was 75°F and the ultraviolet radiation intensity was 1 to 10 times that of the sun. The results are compared in figures 3 and 4 with the flight results for which the average in-flight temperature was 0°F when in sunlight. For the exposure time considered, there is apparently better agreement between

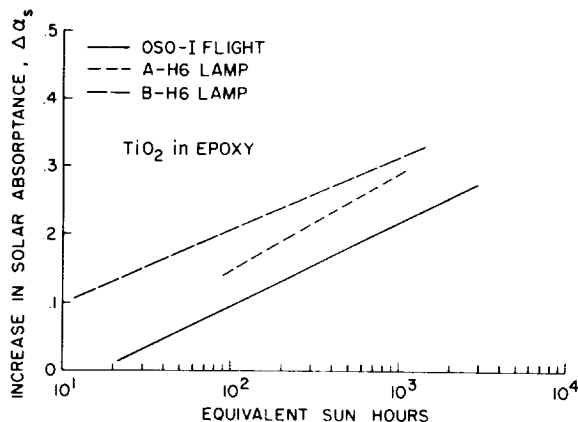


FIGURE 3.—Comparison of predicted increase in solar absorptance of titania-epoxy coating with in-flight results on the OSO-I satellite.

the actual and the predicted values of absorptance change in the case of the silicone (fig. 4) than in the case of the epoxy (fig. 3). The tests suggest that the rate of change of solar absorptance is dependent on the aforementioned test parameters for the polymeric systems in question. These results cannot be interpreted more precisely until the relationships among the rate of chromophore production, temperature, intensity, and wavelength are established.

Some of the difficulties involved in obtaining a simulation match between an ultraviolet mercury-vapor lamp and the actual solar radiation are shown in figure 5. The two curves shown for the General Electric UA-2 mercury-vapor lamp correspond to two different

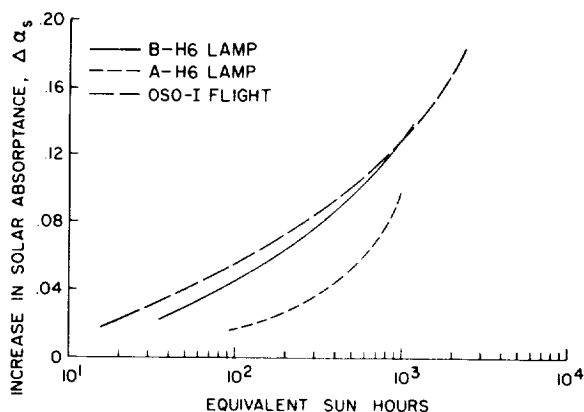


FIGURE 4.—Comparison of predicted increase in solar absorptance of titania-silicone coating with in-flight results on the OSO-I satellite.

distances from the lamp to the detector (or sample). For the upper curve, the integrated intensity (the area under the curve) from 2200 to 4000 Å was made equal to that of sunlight over the same wavelength range. At certain wavelengths, the ordinate (or spectral intensity) of this curve is many times that of the sunlight curve. For the lower UA-2 curve, the integrated intensity was made equal to that of sunlight over the range from 2200 to 3000 Å. The match with the sunlight curve is much better in this case, but is still not close. However, if the photochemical reaction of the coating is significantly dependent on wavelength, that is, if it gives one product at one wavelength and another kind of product at another wavelength, or if synergistic effects occur through combination of wavelengths, it is very unlikely that satisfactory simulation with any lamp source of this kind is possible.

Experimental Polyvinyl Chloride Films for Developing Simulation Techniques

Thin films of pure polyvinyl chloride¹ were cast from dilute solutions in methyl ethyl ketone. After being dried in air, these were water-white transparent films. After further drying at 60° C under vacuum to remove traces of the ketone solvent the films were used in photodegradation studies. Similar films were prepared from an 86:13:1 vinyl chloride vinyl acetate, maleic acid terpolymer (VMCH). These films were cast from solutions containing toluene and methyl Cellosolve, and were dried in a similar manner. The VMCH terpolymer was also studied in combination with a metal substrate. Thin films were cast and

¹ Research conducted since the writing of this paper has shown that the polyvinyl chloride which had previously been considered to be pure actually contained trace amounts of residual solvent which could not be removed by usual outgassing procedures. This solvent (methyl ethyl ketone) acted as an energy transfer agent, leading to rapid changes in optical properties of the film on exposure to short-wavelength radiation. Such behavior, while consistent from film to film, was found to be different from that of perfectly pure polyvinyl chloride. The term "pure polyvinyl chloride" as used in this paper means a film of the pure polymer containing a trace amount of solvent.

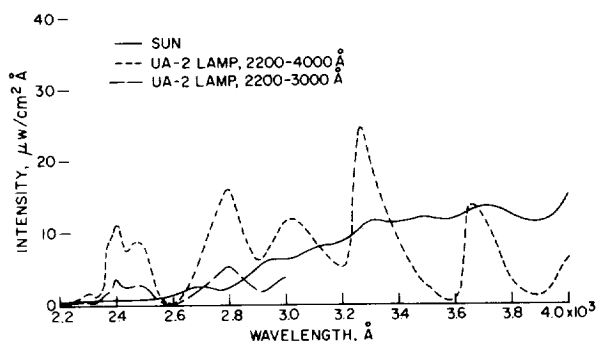


FIGURE 5.—Comparison of the ultraviolet spectrum of a GE UA-2 lamp with the ultraviolet solar spectrum.

affixed to aluminum disks by completing the removal of solvent at 80° C under vacuum. Film thicknesses were calculated to be 7×10^{-4} cm from the weight of film, density of polymer, and surface area. These films were used in the exposure tests to be described.

Environmental Simulation Exposure Conditions

The films were irradiated for periods of time up to 72 hours with the total output of a GE UA-2 lamp (fig. 5) at a distance of 10½ inches from the film surface. Under these conditions, the output of this lamp amounted to an average of one solar constant in the wavelength region from 2000–2700 Å. The power output of the lamp was maintained constant during the entire exposure by monitoring the output with a photocell and adjusting the input power as the lamp output degraded. During the irradiations the vacuum chamber pressure was between 30 and 40 microns. After the irradiations, the films were transferred to a vacuum desiccator where they were kept until spectroscopic measurements were made. The ultraviolet spectra were measured for the films before and after irradiation with a Cary 14 spectrophotometer. The infrared spectra of the films were obtained with a Perkin-Elmer 21 spectrophotometer. The change in reflectance of the terpolymer on the aluminum substrate was determined with a Gier-Dunkle integrating sphere spectrophotometer.

The solar absorptance and emittance were determined by Lockheed Missiles and Space Company in a manner described in reference 1.

Discussion of Results

It was found convenient to present and consider the spectroscopic changes in films in terms of the optical density defined by the equation

$$\text{Optical density} = \log_{10} \frac{I_0}{I}$$

where I_0 is the incident intensity and I is the transmitted intensity. A change in optical density of, say, 1.4 implies that the transmission $T = I/I_0$ is essentially reduced to a level which is $10^{-1.4}$ or about 4 percent of the original transmission value. The method of representing the spectroscopic changes in the films by optical density rather than transmittance or other quantities was selected so that the changes in absorption could be related directly to the increased concentration of the color producing groups. The changes in optical density of the free films of pure polyvinyl chloride with time of exposure to radiation in the wavelength region 2200 to 6000 Å are given in figure 6. The change in optical density, as plotted, is the difference between the optical densities of the polymer film before and after irradiation at the indicated wavelengths. The increase in the optical density and the shift of over-all absorption into the visible region is evident. After a total exposure of 6 hours, the polymer is nearly completely opaque to radiation at 2800 Å.

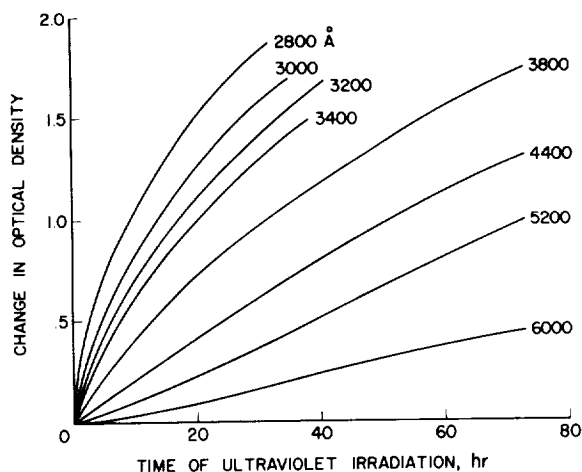


FIGURE 6.—Change in optical density of polyvinyl chloride in the ultraviolet and visible region with time of exposure to a GE UA-2 lamp in vacuum.

The basic chemistry underlying this photochemical change in polyvinyl chloride, based on references 3 and 5, is outlined in figure 7. The first step in this process is assumed to involve absorption of energy by trace impurities in the system in the form of unsaturated end groups, catalyst residue, residual solvent, etc. This energy absorption, followed by energy transfer to the basic polymer, is sufficient to initiate the reaction through the removal of a chlorine atom, leaving a residual radical on the chain as shown. Propagation of the reaction involves the removal of the hydrogen atom immediately adjacent to the radical site to form a molecule of

hydrogen chloride; termination occurs by formation of a π bond from the available pair of electrons. It has been shown by Boyer (ref. 6) that the continued introduction of double bonds by this mechanism is a nonrandom process, the removal of chlorine next to the double-bond site proceeding more easily than the removal of chlorine from an ordinary carbon in the polymer chain. As the process proceeds, a conjugated linear polyene system is developed which absorbs strongly in the ultraviolet and visible region of the spectrum. To date, the exact concentration and extent of the conjugated system are unknown. Photochemical investigations are underway to determine the nature of this structure.

The change in optical density for pure polyvinyl chloride for a number of wavelengths from 2800 to 6000 Å as a function of time of ultraviolet irradiation is shown in figure 8. This figure shows that there is increased opacity at all wavelengths over the ultraviolet and visible regions, and that the region of almost complete opacity (change in optical density in excess of about 2.0), progressively advances to longer wavelengths with increased dose. No difference has been observed in the rate of color formation between the polyvinyl chloride and polyvinyl chloride terpolymers. In the cases of both polymers, no change in the infrared spectrum of the free films has been observed

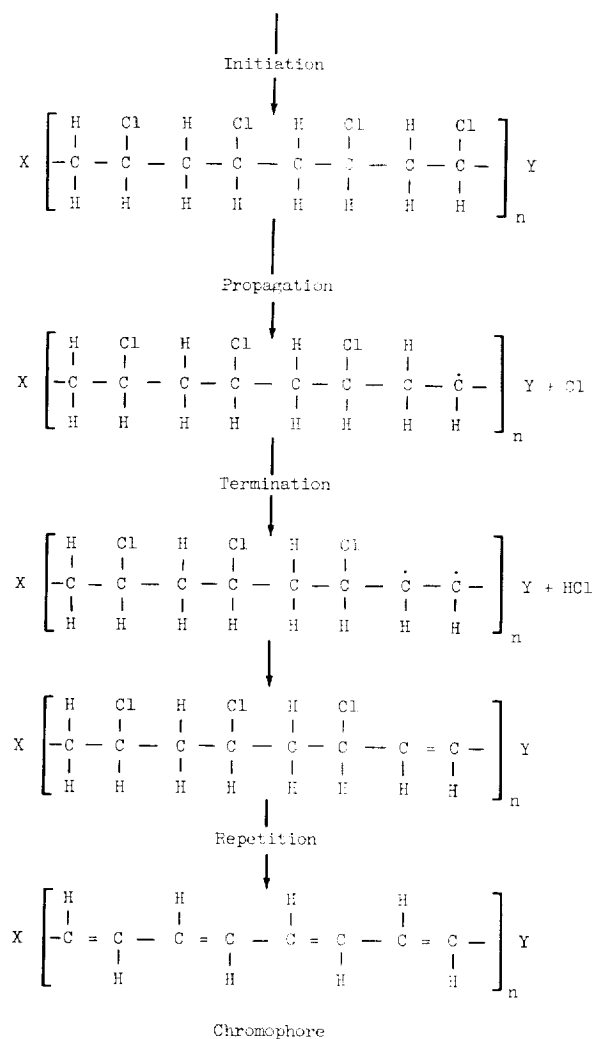


FIGURE 7.—Proposed mechanism of production of chromophores in polyvinyl chloride by radiation.

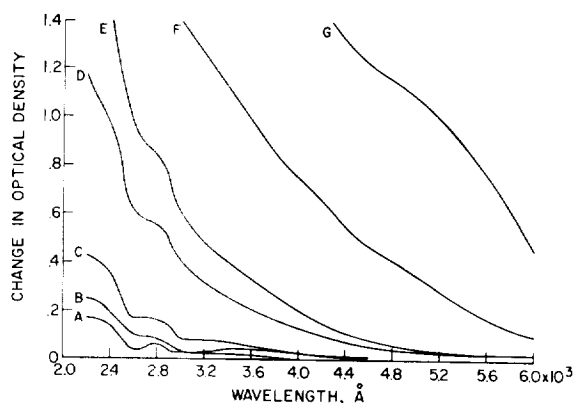


FIGURE 8.—Change in optical density of polyvinyl chloride at various wavelengths from 2800 to 6000 Å as a function of time of exposure to a GE UA-2 lamp. Exposure time, min: A, 15; B, 30; C, 60; D, 180; E, 360; F, 1440; G, 4320.

after exposure to ultraviolet radiation in vacuum for periods up to 72 hours.

As mentioned before, for the proposed flight tests, it is necessary to have a polymer which adheres well to an aluminum metal substrate, and, in addition, is sufficiently flexible not to crack during the expected temperature cycle (similar to fig. 1). The vinyl acetate component of the VMCH terpolymer provides internal plasticization and the maleic acid provides the necessary polar groups for adhesion to the substrate. It is interesting to note that the ultraviolet-induced changes in optical density of this terpolymer are similar to those obtained for pure polyvinyl chloride.

In addition to ultraviolet radiation, the flight-tested surfaces experience collisions with higher energy photons in space. For this reason, the effects on the polyvinyl chloride films of gamma radiation from 10 to 16 MeV were also examined. Figure 9 shows the changes in optical density produced by gamma radiation. The opacity at each wavelength steadily increases with increased gamma radiation, as was observed for ultraviolet radiation. The equivalence in optical density produced at particular wavelengths by ultraviolet and by gamma irradiations can be developed by combining figures 6 and 9, as shown in figure 10. In this figure, the change in optical density at three wavelengths is shown as a function of

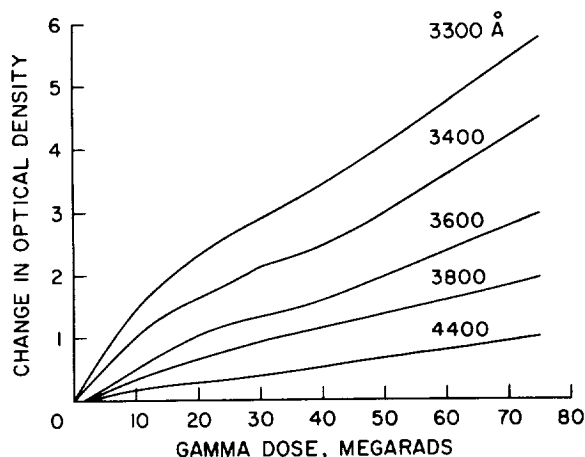


FIGURE 9.—Change in optical density of polyvinyl chloride at various wavelengths as a function of gamma radiation dose.

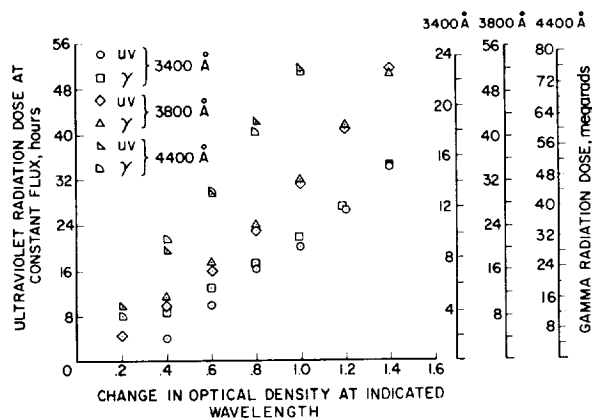


FIGURE 10.—Equivalence of ultraviolet radiation dose to gamma dose for polyvinyl chloride.

both the ultraviolet and the gamma irradiation doses. At each wavelength, a proportionate change in optical density is observed for both kinds of irradiations; however, it should be noted that the relative effectiveness of the ultraviolet and the gamma radiations is different for each wavelength shown. This is not an unexpected result, since it is reasonable to assume that the extent of photochemical reaction may be different at each wavelength, even though, in general, the same kinds of chromophore groups may be formed. It is clear that a total dose of 30 hours of ultraviolet at one solar constant radiation produces a change in optical density in the wavelength region from 3400 to 4400 Å equal to that produced by a dose of about 10 to 50 megarads of gamma irradiation. It might take a period of at least a year to obtain a dose of this magnitude from the high energy particles normally present in the space environment of the OSO satellite.

The temperature rise which occurred during exposure of the VMCH film on aluminum substrate to ultraviolet radiation in vacuum is given in figure 11. It can be seen that there is a rise in temperature from 27° C to about 46° C in 1200 minutes. Since no change in the rate of formation of chromophore was observed in these tests, it appears that the activation energy for the dehydrochlorination of polyvinyl chloride is very small under these conditions. No precautions were taken to control or to correct for the energy emitted from the back face of these composites or to shield this surface;

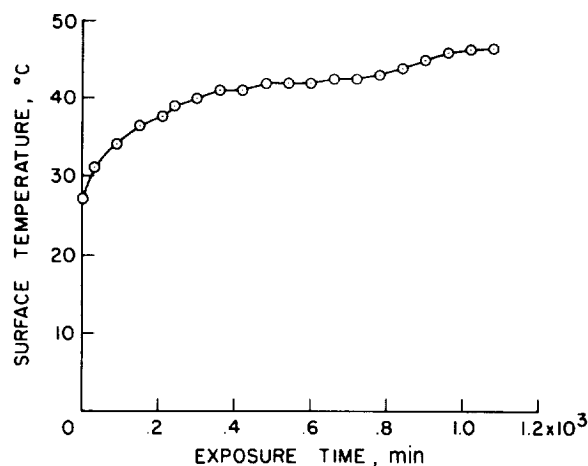


FIGURE 11.—Change in surface temperature of polyvinyl chloride terpolymer (VMCH) on aluminum substrate during irradiation in vacuum at a constant flux with a GE UA-2 lamp.

therefore, this temperature rise does not quantitatively indicate the expected temperature rise on the satellite experiment.

The decrease in spectral reflectance due to 16.5 hours of irradiation with the UA-2 lamp of the VMCH terpolymer cast on an aluminum substrate is given in figure 12. The percent reflectance as a function of wavelength from 3700 to 28,000 Å was determined by the Gier-Dunklehemispherical reflectance spectrophotometer. The shaded area indicates the change in spectral reflectance due to alteration in the film properties. It can be seen that the largest change in reflectance occurs in the visible and

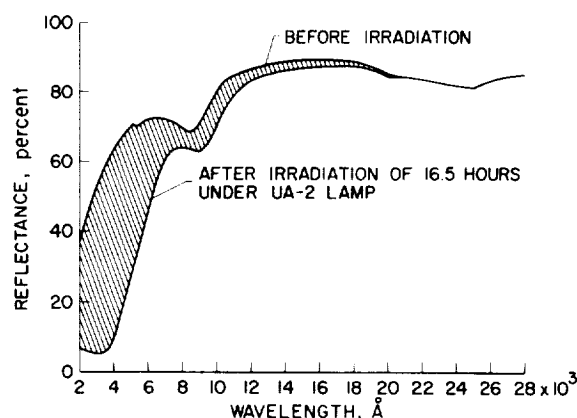


FIGURE 12.—Change in reflectance of polyvinyl chloride terpolymer (VMCH) on aluminum substrate due to irradiation in vacuum with a GE UA-2 lamp.

ultraviolet region below 7000 Å. This corresponds to the region of change in optical density for the free films of this polymer, and suggests that on the aluminum substrate, the production of chromophores in the polymer is still the principal cause of change in optical properties. It can be seen that above 9000 Å there is little change in the absorption with ultraviolet exposure, a result also anticipated from infrared absorption spectra of the free films. This behavior of the reflectance spectra indicates that relatively little change of emittance but a rapid change of the solar absorptance of this system with time of ultraviolet irradiation can be expected. The initial value of solar absorptance of 0.23 changes to 0.45 with 16 hours of irradiation while the emittance remains constant at a value of 0.60.

The change in the ratio of solar absorptance to emittance for the VMCH terpolymer on aluminum substrate after irradiation at 1 solar constant between 2000 and 2700 Å for exposure times up to 1500 minutes is given in figure 13. It can be seen that after an initial relatively rapid rise, the change in the ratio of solar absorptance to emittance continues to rise linearly. The change in α_s/ϵ over the test period is significantly large. The temperature changes calculated for these increases in ratio of solar absorptance to emittance as a function

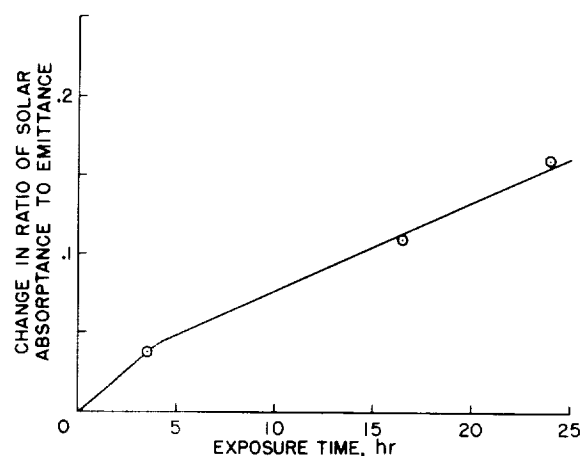


FIGURE 13.—Increase in ratio of solar absorptance to emittance for polyvinyl chloride terpolymer (VMCH) on aluminum substrate due to exposure to a GE UA-2 lamp. Film thickness = 7.6×10^{-4} cm. Radiation intensity = 1 solar constant (2000 Å to 2700 Å).

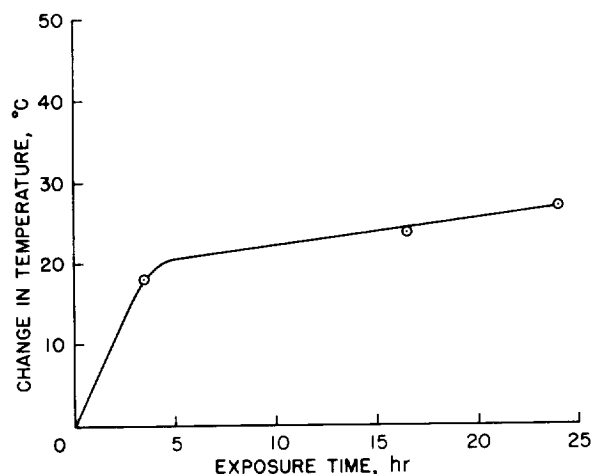


FIGURE 14.—Calculated temperature change in polyvinyl chloride terpolymer (VMCH) on aluminum substrate as a function of exposure time. Film thickness = 7.6×10^{-4} cm.

of exposure time are given in figure 14. These results indicate that a temperature increase of 25° C over a test period of 1500 minutes can be expected.

CONCLUDING REMARKS

The results of this study indicate that polymers of vinyl chloride may be satisfactory comparators for correlating the changes in solar absorptance produced by exposure to ultraviolet radiation in flight and in ground-based tests. These polymeric films meet the criteria for a well-behaved system, in that they undergo a regular change in optical density with time of exposure, and the change in solar absorptance can be measured easily as a change in temperature. Furthermore, the photochemistry occurring in vacuum is free from complicating side effects such as surface erosion and depolymerization characteristic of many polymers.

Because of the extreme sensitivity of the ultraviolet and visible absorption spectra to

the chromophore concentration, these films may find application as accurate ultraviolet dosimeters if it can be shown that the quantum efficiency for the production of these color-forming groups is independent of the wavelength of absorbed photons in the photochemically productive region.

These polymer films will be flown on the OSO-C satellite sometime in 1964, at which time it will be possible to compare the temperature changes predicted by laboratory tests with in-flight measurements directly.

Future plans include improvements in matching the photochemically productive region of the solar spectrum in the laboratory tests and a critical analysis of the kinetics of the chromophore reaction.

REFERENCES

1. McKELLAR, L. A.: Effects of Spacecraft Environments on Thermal Control Materials Characteristics. Spacecraft Thermodynamics Symposium, Galen A. Etemad, ed., Holden-Day, Inc. (San Francisco), c. 1962, pp. 99-128.
2. JOHNSON, FRANCIS S.: Solar Radiation. Space Materials Handbook, Claus G. Goetzl and John B. Singletary, eds., Contract AF 04(647)-673, Lockheed Missiles and Space Co., Jan. 1962, pp. 31-37.
3. WINKLER, D. E.: Mechanism of Polyvinyl Chloride Degradation and Stabilization. Jour. Polymer Sci., vol. XXXV, no. 128, Feb. 1959, pp. 3-16.
4. NEEL, CARR B.: Research on the Stability of Thermal-Control Coatings for Spacecraft. NASA-Ames author; paper presented at Fifth International Symposium on Space Technology and Science, Tokyo, Japan, Sept. 2-7, 1963.
5. OHNISHI, SHUN-ICHI, NAKAJIMA, YOSHIHARU, and NITTA, ISAMU: Mechanism of Discoloration of Irradiated Polyvinyl Chloride. Jour. of App. Polymer Sci., vol. VI, Nov.-Dec. 1962, no. 24, pp. 629-638.
6. BOYER, R. F.: A Statistical Theory of Discoloration for Halogen-Containing Polymers and Copolymers. Jour. of Phys. and Colloid Chem., vol. 51, 1947, pp. 80-106.

DISCUSSION

Since Papers 40, 41, and 42—by Parker, Neel, and Golub; by Zerlaut, Harada, and Tompkins; and by Olson, McKellar, and Stewart—dealt with related topics, discussions of the first two were postponed until after all three papers had been presented.

41. Ultraviolet Irradiation of White Spacecraft Coatings in Vacuum¹

G. A. ZERLAUT, Y. HARADA, AND E. H. TOMPKINS

IIT RESEARCH INSTITUTE, CHICAGO, ILL.

Investigations of stability of materials to simulated space conditions were conducted in conjunction with a developmental program of spacecraft thermal control coatings. Determination of spectral reflectance and solar absorptance before and after exposure showed that none of the materials studied is completely unaffected by ultraviolet irradiation in vacuum. However, zinc oxide and, to a lesser extent, zinc sulfide were found to be unusually stable white pigments and formed relatively stable coatings when dispersed in pure potassium silicate or in experimental methyl silicone polymers. Exposure to 4200 equivalent sun-hours of ultraviolet radiation in vacuum resulted in solar absorptance increases of less than 0.02 for both an experimental silicone and a potassium silicate paint pigmented with zinc oxide.

The principal objective of this research was the development of a white thermal-control coating for spacecraft with exceptional stability to extraterrestrial solar radiation. Emphasis was directed more to the change in value than to the absolute value of solar absorptance. Accordingly, the measurement of spectral reflectance within the solar region was directed more toward reproducibility than toward absolute accuracy.

Conventional or commercial coatings were not studied because they deteriorate rapidly under ultraviolet irradiation in vacuum. Instead, experimental laboratory formulations with known ingredients, purities, and weight ratios were investigated. The work was divided broadly into organic and inorganic coatings. In order to reduce the complexity of the problems involved, pigments and paint vehicles were exposed individually to ultraviolet radiation in vacuum. These screening experiments were the basis for the subsequent choice of potentially stable paint formulations.

Determination of spectral reflectance and solar absorptance before and after exposure showed that no material studied was completely unaffected by ultraviolet irradiation in vacuum. Zinc oxide was found to be an unusually stable white pigment and formed relatively stable coatings when dispersed in pure potassium silicate or in methyl silicone polymers.

The bulk of the research effort was devoted to the development of still more stable pigmented potassium silicate and methyl silicone paints. The effects of soiling and cleaning candidate coatings were studied in an attempt to define the problems anticipated during spacecraft fabrication and during checkout just prior to launch.

The requirement for high stability to the space environment includes not only stability to the solar ultraviolet but also stability to other radiations in space, primarily proton radiation and trapped charged particles in the Van Allen belt. Adequate simulation of solar ultraviolet below 2000 Å, including Lyman alpha as well as the high-energy particulate radiations, is both difficult and expensive.

¹ See also Papers 39, 40, and 52.

Furthermore, of a total solar irradiation of 135 watts per square foot at earth-distance, less than 0.25 watt/ft² is below 2000 Å, whereas about 12 watts/ft² is between 2000 and 4000 Å in the near-ultraviolet. Since the development of stability to high-energy radiations is useless unless stability to the more prevalent near-ultraviolet is assured, space-simulation efforts were confined to the near-ultraviolet region from 2000 to 4000 Å at a vacuum in the range of 10⁻⁷ torr.

SOLAR ABSORPTANCE MEASUREMENT

Solar absorptance was determined indirectly by measurement of spectral reflectance in the wavelength range of 0.3 to 2.7 μ (300 to 2700 mμ). The reflectance data were integrated (weighted with the solar spectral energy distribution (ref. 1)) to yield solar reflectance. Subtraction of the solar reflectance from unity yielded solar absorptance. Comparison of these solar spectral energy data with the data of Nicolet (ref. 2) showed that solar absorptance agreed within 0.005.

A General Electric recording spectrophotometer, which employs approximately normal illumination and diffuse viewing of a sample surface, was used for the visible spectrum, 380 to 700 mμ; and an integrating-sphere reflectometer of our own design was used for both the ultraviolet and infrared regions. The latter incorporates a Perkin-Elmer quartz monochromator as a dispersing system along with appropriate sources and detectors.

Both reflectometers measure reflectance relative to a standard. These are comparison instruments, since the sample and the standard are both in place at all times. Magnesium oxide was used as the standard, and the relative reflectance data obtained were converted to absolute values by using the absolute reflectance data of magnesium oxide published by Middleton (ref. 3 and 4). Reflectance data given in the present paper are limited to values at 440- and 600-mμ wavelength.

Since it was not economical to provide solar absorptance values during the extensive screening operations, for many materials the effect of ultraviolet irradiation was evaluated in terms

of reflectance losses in the visible region. This method is considered satisfactory, since the predominant losses occur in the 400- to 600-mμ wavelength region for most white and transparent materials.

In many cases solar absorptance values are reported as α_1 and α_2 , with the total solar absorptance given by

$$\alpha = \alpha_1 + \alpha_2$$

where α_1 corresponds to that half of the solar spectrum which lies below 700-mμ wavelength, and α_2 corresponds to that half which lies above 700 mμ. By thus splitting α into two components, that region of the spectrum for which the more significant change in absorptance occurs is more readily indicated. For example, some formulations show little change in solar absorptance on irradiation, but their reflectances decrease in the visible region (increase in α_1) and are counterbalanced by a corresponding increase at longer wavelengths (decrease in α_2).

SPACE SIMULATION

Vacuum Chambers

LARGE VACUUM CHAMBER

The vacuum of the space environment is variously quoted at 10⁻⁹ to 10⁻¹⁵ torr, but the attainment of such pressures in the laboratory is time consuming and probably unnecessary for the purposes of this work. At much higher pressures, 10⁻⁶ torr, there is no evidence of oxidative degradation.

These principles guided the design of the space-simulation chamber (fig. 1), which was used in the early screening operations. It consists of a cylindrical chamber 24 inches in diameter and 24 inches high, cooled by refrigerant coils on its outer surface, and capped with a torispherical head in which three GE mercury-arc A-H6 lamps are mounted. The distance from the lamps to the samples, which are mounted on a turntable beneath the lamps, can be adjusted by varying their radial location, to achieve variation of radiation intensity and hence of the acceleration factor. The constancy

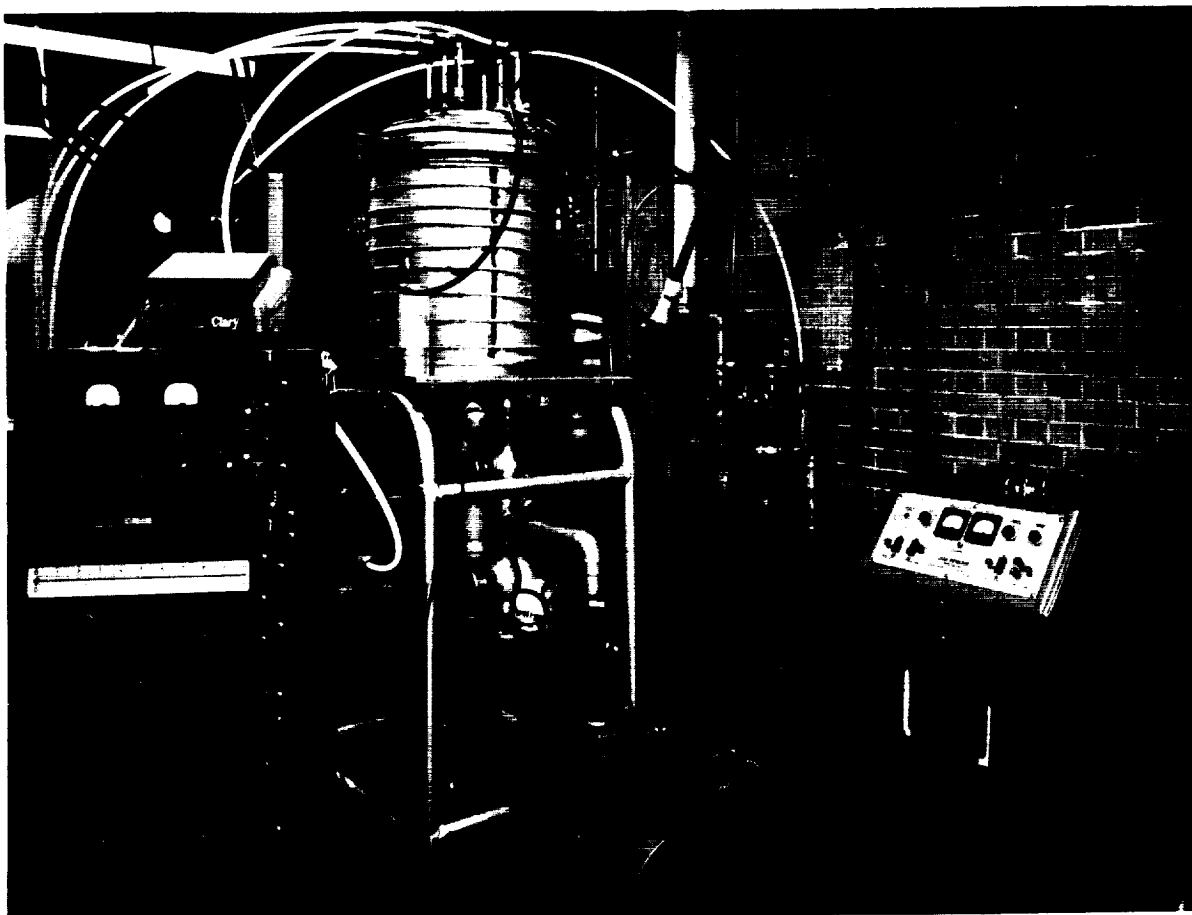


FIGURE 1.—*Diffusion-pumped space-simulation chamber and associated equipment.*

of the radiation is monitored by reflecting a portion from a first-surface mirror, mounted over the center of the turntable, through a quartz window on the head. The absolute intensity is measured before and after each run by using a wide-angle, temperature-compensated thermopile.

Several types of sample turntables are available. The simplest is a 16-inch flat plate, suitable for use when no measurements are to be made in the chamber. Typically, this was used when the reflectances of a number of materials were to be measured before and after irradiation. The turntable assures that all samples receive equivalent exposures at a given radial distance. It is rotated by a 12-point Geneva drive and a 2-rpm fractional horsepower

motor in a welded housing which is open to the atmosphere through ventpipes in order to eliminate the problems associated with operating motors in a vacuum.

The chamber is mounted on a 10-inch oil-diffusion pump, National Research Corporation model H-10-SP, with an approximate pumping speed of 4000 cfm at 10^{-4} torr. In practice, the pump reaches 10^{-6} torr routinely, and all ultraviolet testing was performed at this level or below.

The samples were of many forms: pigmented and clear films, both free and on a substrate; and compacted and loose powders. For uncooled samples, as used in this equipment, the nominal specimen temperatures were 150° F at an intensity of about 3 solar equivalents.

SMALL VACUUM CHAMBER

An ion-pumped space-simulation chamber was constructed and was used for longer-term tests. The system provides a convenient means of obtaining a clean ultrahigh vacuum. The chamber is provided with a quartz window and a liquid-cooled sample table. The table (fig. 2) can be cooled with liquid nitrogen, ice water, or tap water and can accommodate six 1×1 inch specimens. The system (fig. 3) consists of a 400-liter/sec Varian VacIon pump, which is prepumped with both a molecular-sieve sorption pump and a mechanical pump. An A-H6 lamp is mounted over the quartz window, which is shown in place in figure 3. Reproducible equivalent solar factors from 4 to 18 intensities (2000 to 4000 Å), as determined with a temperature-compensated thermopile, were achieved. A plot of intensity against $1/D^2$ (D =distance from the lamp to the sample table) resulted in a straight-line relation.

Solar Simulation

The solar ultraviolet spectrum is given in figure 4. Also shown in this figure is the energy spectrum of a typical A-H6 lamp at comparable total intensity. The wavelengths below 2000 Å contribute less than 0.2 percent of the total solar energy and so can be disregarded without significant error.

The total lamp intensity was measured with a wide-angle temperature-compensated thermopile (obtained from Eppley Laboratories, Inc.), the reading of which was converted to ultraviolet radiation intensity by the equation

$$\frac{\text{thermopile output (millivolts)}}{2 \times \text{thermopile constant}} = \text{cal/cm}^2\text{-min.}$$

The thermopile output was divided by 2 because half of the total energy of the lamp² is assumed to be below 4000 Å. The solar intensity at wavelengths below 4000 Å has been determined to be 13 milliwatts/cm². The radiation intensity in cal/cm²-min was converted to milliwatts/cm²; and by dividing this

² More recent studies have shown that the A-H6 lamps currently used have only one-third of their energy below 4000 Å.

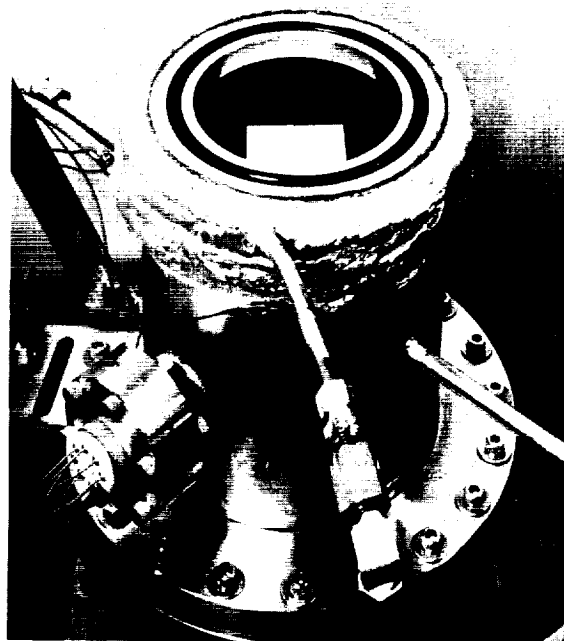


FIGURE 2.—Ion-pumped space-simulation chamber with samples in place.

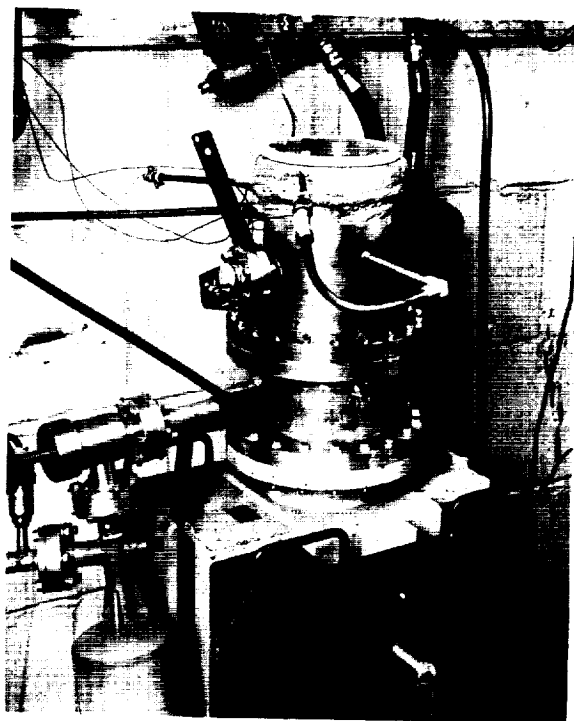


FIGURE 3.—Ion-pumped space-simulation chamber.

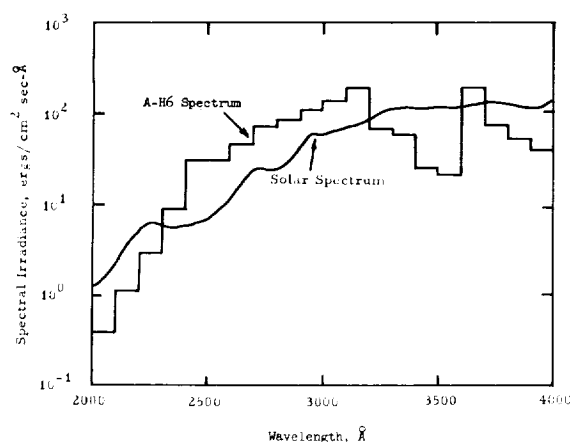


FIGURE 4.—Comparison of the solar spectrum with the spectrum of an A-H6 lamp.

value by 1 solar factor of 13 milliwatts/cm², the number of "suns," or the equivalent solar factor, for a given thermopile output was obtained. Solar factors were determined for various lamp-to-sample distances in the ion-pumped chamber, as follows:

Solar factor	Distance from lamp to sample, inches
5.2	9.00
6.1	6.40
10.3	5.40
12.2	4.75
13.2	4.33
15.9	4.00

The A-H6 lamp is positioned over the samples at a distance corresponding to the solar factor desired. A small recording thermopile is positioned over the lamp and is used to monitor changes in the lamp intensity over periods of time. This information is valuable in assigning an equivalent sun-hour radiation value to a given space-simulation experiment.

Assessment of the damage caused by space-simulation tests could be in error if the spectral output of the ultraviolet source were reduced nonuniformly, for example, if the radiation below about 2800 Å decreased with lamp age at a higher rate than the longer-wavelength ultraviolet. Therefore, attempts were made to

measure the spectral output of several A-H6 lamps before and after operation. A Seya-Namioka vacuum-ultraviolet monochromator, manufactured by Jarrell-Ash, was used.

The results were inconclusive. There appeared to be a disproportionate decrease in peak intensity at 2285 and 2535 Å after 100 hours. The decrease, if interpreted properly, amounted to 20 percent. No such trend was discerned for the lower-wavelength continuum. It was, therefore, concluded that calculations of equivalent sun-hours of exposure (ESH) on the basis of the overall drop in lamp intensity during a given test were reasonably accurate and meaningful.

The criterion for changing lamps was either a 30 percent decrease in the overall lamp intensity, as measured with the recording thermopile, or incipient erratic behavior of the lamp, whichever occurred first.

PIGMENT SCREENING

The prerequisites for selection of pigments were that they be white and of high refractive index and purity. The most important factor in the choice of materials, that is, stability to the space environment, was determined by screening tests and from limited information in the literature. The search for pigment materials was a continuous activity during this research.

For preliminary screening tests, the samples were prepared as compacted powders that were suitable for both solar-simulation exposure and optical measurements. Powders which were not compactable into a cohesive body were placed in aluminum dishes for solar exposure. This procedure precluded optical measurements and permitted only visual observation of color change.

Considerable coloration occurred in most of the pigments, as shown in table I. Representative reflectance values are given for two wavelengths in the visible spectrum, 440 and 600 mμ. For most of the early screening work, reflectance curves in the visible spectrum were sufficient to suggest or preclude additional study.

In general, natural, mined minerals were less affected by ultraviolet irradiation in vacuum

TABLE I.—*Effect of Ultraviolet Irradiation in Vacuum on Optical Properties of Miscellaneous Inorganic Pigments*

Material	Designation and source	Exposure		Reflectance, %	
		ESH*	Solar factor	440 m μ	600 m μ
Al ₂ O ₃ -----	Alucer MC (alpha), Gulton Industries-----	0		100.0	100.0
		180	3	74.0	91.5
Al ₂ O ₃ -----	Alucer MA (gamma), Gulton Industries-----	0		93.5	90.0
		75	1.5	49.5	82.5
Al ₂ O ₃ ·2SiO ₂ ·2H ₂ O-----	Ajax P kaolin, Georgia kaolin-----	0		73.0	84.5
		180	3	46.5	60.0
Al ₂ O ₃ ·2SiO ₂ -----	Ajax SC kaolin, Georgia kaolin-----	0		78.0	87.0
		200	3	65.0	81.0
3Al ₂ O ₃ ·2SiO ₂ +SiO ₂ -----	Molochite, Paper Makers Importing Co-----	0		84.5	86.5
		180	3	75.5	84.5
Sb ₂ O ₃ -----	National Lead Co-----	0		92.5	96.5
		75	1.5	36.5	50.0
CaSiO ₃ -----	Synthetic, Johns-Manville-----	0		86.0	90.0
		75	1.5	58.0	81.0
CaSiO ₃ -----	Wollastonite C-1, Cabot-----	0		92.5	94.5
		75	1.5	81.0	91.5
MgAl ₂ O ₄ -----	Spinel, Linde-----	0		97.5	97.0
		75	1.5	70.0	92.5
MgO-----	Reagent-grade powder, Mallinckrodt-----	0		98.5	98.5
		75	1.5	71.0	92.5
MgSiO ₃ ·nH ₂ O-----	No. 140 Alabama talc, Whittaker, Clark and Daniels-----	0		89.0	92.0
		180	3	62.0	73.5
2MgO·SiO ₂ -----	AlSiMag 243, American Lava-----	0		33.0	59.0
		1036	15	35.5	60.0
Magnesium trisilicate-----	USP, Mallinckrodt-----	0		97.5	99.0
		200	3	18.5	44.5
SiO ₂ -----	Ottawa Special, Ottawa Silica-----	0		88.5	92.5
		75	1.5	77.5	90.0
SiO ₂ -----	Diatomaceous earth, Dicalite WB-5, Great Lakes Carbon-----	0		92.0	93.5
		180	3	87.5	93.0
SnO ₂ -----	CP, Fisher Scientific Co-----	0		88.0	90.0
		300	3	78.5	88.0
ZrO ₂ -----	CP, Titanium Alloy Mfg-----	0		92.5	97.0
		75	1.5	65.5	90.5
ZrO ₂ -----	Cubic, Titanium Alloy Mfg-----	0		88.0	95.5
		180	3	33.0	73.5
ZrSiO ₄ -----	Superpax, Titanium Alloy Mfg-----	0		86.5	92.5
		180	3	65.0	84.5
ZnS-----	Reagent grade, Matheson, Coleman, and Bell-----	0		91.0	94.5
		75	1.5	89.0	94.0

*Equivalent sun-hours.

than synthetic laboratory chemicals. (Exceptions were zinc compounds and tin oxide.) For example, natural wollastonite was superior to synthetic calcium silicate. Calcination of hydrated materials to their anhydrous forms enhanced stability, as evidenced by the kaolins and talc. Calcination at 1000° C for 16 hours of alumina, zirconia, and zircon, however, had

little effect on their stability. Apparently, any loss of adsorbed or absorbed water and the possible strain relief gained by thermal treatment did not change the degradation characteristics of these materials. A marked difference in stability was apparent among different crystal forms of the same material. Metastable gamma alumina and cubic (unstabilized)

zirconia degraded much more severely than their stable counterparts, alpha alumina and monoclinic zirconia. Materials other than zinc oxide which were fairly stable were zinc sulfide, stannic oxide, diatomaceous earth (amorphous silica), and fired kaolin (mullite plus amorphous silica). Although AlSiMag 243 (forsterite) also exhibited good stability (table I), its low initial reflectance precluded further study.

The following materials, which are not listed in table I, were moderately to severely degraded in short exposures to ultraviolet radiation in vacuum: boron nitride, calcium carbonate, calcium fluoride, lanthanum oxide, basic white lead, basic silicate of white lead, hydrated magnesium silicate (talc), titanates of aluminum, lithium, strontium, and zinc, and phosphates of aluminum, calcium, and potassium.

The data in table II show that zinc oxide was clearly the most stable pigment studied, rivaled only by zinc sulfide, tin oxide, and possibly diatomaceous earth (table I). Long-term tests at 1720 ESH revealed a surprisingly high absorptance change in SP 500 zinc oxide. Good stability was exhibited in the same tests

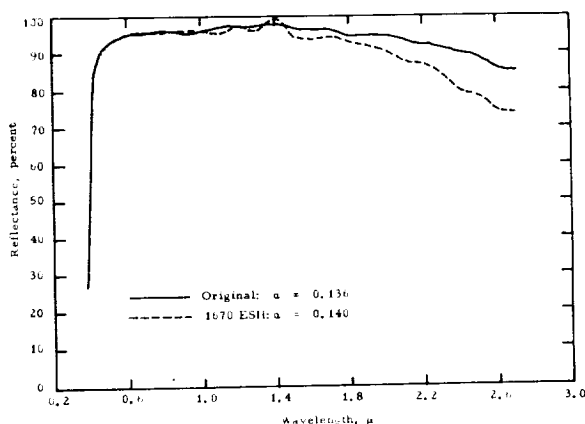


FIGURE 5.—Effect of 1670 equivalent sun hours in vacuum on solar spectral reflectance of SP 500 zinc oxide calcined at 700° C for 16 hours.

by calcined SP 500 (fig. 5) and also by the unfired and fired forms of AZO-55LO zinc oxide.

Improvement of stability, observed in SP 500 and AZO-55LO, may be due to both the smaller surface area of the larger calcined particles and the elimination of defects and may also be due in part to volatilization of contaminants.

TABLE II.—Effect of Ultraviolet Irradiation in Vacuum on Optical Properties of Zinc Oxide Pigments

Manufacturer's designation	Particle size, μ	Purity, %	Exposure		Reflectance, %		Solar absorptance	
			ESH*	Solar factor	440 m μ	600 m μ	α	$\Delta\alpha$
SP 500	0.30	>99.90	0	---	95.0	99.0	---	---
			75	1.5	95.0	99.0	---	---
AZO-66	.20	99.80	0	---	93.0	99.0	---	---
			200	3	91.0	98.0	---	---
USP 12	.30	99.80	0	---	93.5	98.0	---	---
			300	3	92.0	97.5	---	---
AZO-33	.20	99.20	0	---	88.0	95.0	---	---
			300	3	86.5	93.5	---	---
SP 500	---	---	0	---	95.0	99.0	---	---
			3100	10	91.0	98.0	---	---
SP 500	---	---	0	---	93.5	98.0	0.138	---
			1720	10.2	90.5	96.0	.164	0.026
SP 500**	---	---	0	---	92.5	97.5	.133	---
			1720	10.2	91.5	97.5	.140	.007
AZO-55LO	.40	99.20	0	---	86.5	93.5	.198	---
			1720	10.2	83.5	92.0	.213	.015
AZO-55LO**	---	---	0	---	90.0	95.5	.156	---
			1720	10.2	88.5	95.0	.164	.008

*Equivalent sun hours.

**Calcined 16 hr at 700° C.

Lowering of the initial absorptance results mainly from reflectance increases in the infrared region; these increases may be due to enhanced scattering at the longer wavelengths by the larger particles.

MISCELLANEOUS INORGANIC PAINTS

Water-based inorganic binders investigated were: monoaluminum dihydrogen phosphate, colloidal silicas, and alkali silicates. Stability of the binders was studied by their incorporation into paints which were subjected to a simulated space environment. The results revealed the inferior stability of colloidal-silica-bonded coatings. Phosphate-bonded paints generally exhibited optical property changes similar to those of silicate-bonded samples.

As a group, the alkali silicates were preferable to aluminum phosphate from the standpoint of both stability and physical properties.

All paint formulations contained three ingredients: pigment, binder, and enough water to achieve a sprayable consistency. Mixing was accomplished by ball milling with porcelain balls. Spray-painting was done with a Paasche-type AUTF airbrush; limited brush-painting was done with conventional camel-hair brushes. All aluminum pieces were roughened by abrading with No. 60 Aloxite cloth prior to paint application to promote adhesion. Most of the non-zinc oxide paints were irradiated in the oil-diffusion-pumped system with the internally mounted lamps.

Test results for a variety of paints appear in table III. In this group, tin oxide- and zinc sulfide-pigmented coatings were the only materials which exhibited stability approaching that of zinc oxide paints. However, both compositions had a higher solar absorptance than zinc oxide paints.

Diatomaceous earth and fired kaolin were relatively stable in the pigment screening studies. Poor stability was exhibited by the paints incorporating this form of silica, in contrast to the favorable data for the pigment alone. Molochite is a highly calcined aluminum silicate produced from a kaolin low in iron and alkali. It is essentially crystalline mullite plus a small amount of amorphous silica. Fairly low reflectance changes due to ultraviolet

irradiation in vacuum were observed for the various grades of Molochite.

Although the reflectance changes for paints pigmented with zirconia in the short test (75 ESH) indicated fair stability, later experiments revealed that zirconia-pigmented paints were unsatisfactory. Limited tests showed that coatings incorporating zircon were relatively unstable.

Of the non-zinc oxide paints, only three compositions were relatively stable: those containing zinc sulfide, stannic oxide, or Molochite No. 6.

ZINC OXIDE INORGANIC PAINTS

Zinc oxide-potassium silicate paints were formulated and applied in the same manner as described for the other inorganic compositions.

Effect of Coating Thickness on Optical Properties

Studies were conducted to determine the effect of coating thickness on solar absorptance and emittance. Figure 6 graphically illustrates the solar absorptances of SP 500 zinc oxide-PS7 potassium silicate coatings which had a pigment binder weight ratio (PBR) of 4.30 and a solids content of 46.3 percent by weight. The data reveal that minimum solar absorptance was obtained with a coating thickness of about 5 mils. Approximately the same thickness was necessary for minimum solar absorptance of coatings pigmented with calcined SP 500. Minimal solar absorptance is approached at a

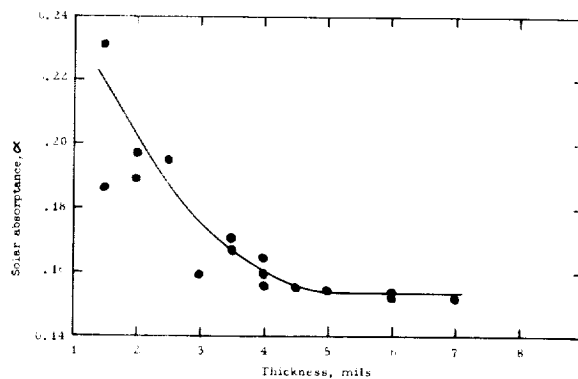


FIGURE 6.—Variation of solar absorptance with thickness in zinc oxide-potassium silicate coatings.

TABLE III.—Effect of Ultraviolet Irradiation in Vacuum on Optical Properties of Miscellaneous Inorganic Coatings

[All samples cured at 140° C for 18 hr]

Sample	Composition*		Exposure		Reflectance, %		Solar absorptance	
	Pigment and source	Solids content, %	ESH**	Solar factor	440 mμ	600 mμ	α	Δα
C2-----	Al ₂ O ₃ ·3H ₂ O C-35, Alcoa-----	63.9	0	----	75.5	75.5	0.345	----
			200	3	64.5	72.5	.371	0.026
C3-----	CaSiO ₃ , Wollastonite-----	62.8	0	----	78.5	83.5	----	----
			180	3	52.5	71.5	----	----
C4-----	La ₂ O ₃ -----	56.9	0	----	92.5	95.0	----	----
			180	3	54.0	77.5	----	----
C5-----	LiAlSi ₄ O ₁₀ , Foote Mineral-----	64.4	0	----	59.0	64.5	----	----
			250	2.5	52.0	62.5	----	----
C7-----	LiAlSiO ₄ , Lithafrax, Carbo- rundum.	64.4	0	----	85.0	86.0	----	----
			2100	10	43.5	60.5	----	----
C8-----	MgAl ₂ O ₄ -----	37.9	0	----	93.5	98.0	----	----
			75	1.5	76.0	94.5	----	----
C9-----	MgSiO ₃ -----	56.9	0	----	92.5	94.5	.130	----
			200	3	66.5	84.0	.219	.089
C11-----	SiO ₂ , fused quartz powder, GE.	62.8	0	----	87.0	87.5	.177	----
			300	3	76.0	85.0	.221	.044
C13-----	SnO ₂ -----	61.7	0	----	77.0	82.5	.264	----
			300	3	76.5	82.0	.278	.014
C17-----	SnO ₂ -----	61.7	0	----	76.5	83.0	----	----
			2100	10	67.0	78.5	----	----
C18-----	ZnS-----	59.0	0	----	85.0	90.5	.220	----
			260	4	81.0	88.5	.231	.011
C19-----	ZnS, XXXN, Chas. Osborne--	56.9	0	----	88.5	88.0	----	----
			250	2.5	86.5	87.5	----	----
C23-----	SiO ₂ , Dicalite WB-5-----	30.4	0	----	90.0	91.5	.136	----
			300	3	77.0	88.5	.173	.037
C25-----	SiO ₂ , Dicalite WB-5-----	26.5	0	----	89.0	91.5	.128	----
			300	3	73.5	88.0	.186	.058
C34-----	Molochite SF-----	56.9	0	----	77.5	81.0	.251	----
			300	3	71.0	79.0	.281	.030
C36-----	Molochite No. 6-----	56.9	0	----	76.5	82.5	.243	----
			300	3	73.5	81.5	.260	.017
C39-----	Molochite No. 6 (HCl leached).	61.7	0	----	74.5	83.5	----	----
			250	2.5	74.5	83.5	----	----
C42-----	Molochite No. 6 (HCl leached).	61.7	0	----	75.0	84.5	----	----
			2100	10	63.5	76.5	----	----
C45-----	ZrO ₂ , CP-----	73.0	0	----	89.0	92.0	----	----
			75	1.5	83.5	90.5	----	----
C46-----	ZrO ₂ , CP-----	72.0	0	----	76.0	86.0	----	----
			75	1.5	71.5	85.0	----	----
C47-----	ZrO ₂ , CP-----	74.8	0	----	88.0	95.5	----	----
			75	1.5	61.5	88.0	----	----
C52-----	ZrO ₂ , CP-----	64.4	0	----	90.5	93.0	.140	----
			200	3	73.5	87.0	.205	.065
C57-----	ZrSiO ₄ , Superpax-----	56.9	0	----	79.0	88.5	.180	----
			200	3	63.0	81.5	.249	.069

*The binder for all paints was PS7 potassium silicate (Sylvania) except for C46 and C47 which were bonded with aluminum acid phosphate and colloidal silica, respectively. The pigment binder ratio (PBR) was 4.30 for all paints, with the following exceptions: C8, 1.50; C18, 3.19; C23, 2.13; C46, 2.80; and C47, 5.33.

**Equivalent sun hours.

thickness of 4 mils. The repeatability of the solar absorptance of a coating thicker than 4 mils is ± 0.01 . Total normal emittance is relatively insensitive to coating thickness. Ten samples which range from 1 to 5 mils exhibited emittance values of 0.94 to 0.98.

Stability to a Simulated Space Environment

PRELIMINARY STUDIES

In all the early studies, zinc oxide paints were clearly more stable than other inorganic coatings. Representative results of the early tests in the oil-diffusion-pumped system are

presented in table IV. Very small reflectance losses, mainly in the 440-m μ region of the visible spectrum, were experienced by all the coatings.

Total normal emittance values were determined for some of the coatings before and after space simulation. The high values, all in excess of 0.90, were virtually unaffected.

A number of silicate-bonded zinc oxide coatings were deliberately soiled by immersion in Duo Seal vacuum-pump oil. This simulates one of the soiling problems which can be expected to occur in satellite evaluation tests. After removal from the oil, the samples were exposed to ambient conditions for 5 hours. The excess oil was then removed with paper

TABLE IV.—Effect of Ultraviolet Irradiation in Vacuum on Optical Properties of Inorganic Zinc Oxide Coatings
[All samples cured at 140° C for 18 hr.]

Sample	Composition ¹			Exposure		Reflectance, %		Solar absorptance	
	Pigment	Solids content, %	PBR ²	ESH ³	Solar factor	440 m μ	600 m μ	α	$\Delta\alpha$
Z5-----	SP 500---	46.3	4.30	0	-----	96.0	98.5	0.132	-----
				200	3	93.5	97.5	.138	0.006
Z8-----	SP 500---	56.9	4.30	0	-----	94.5	98.0	.146	-----
				200	3	90.5	96.0	.150	.004
Z9-----	SP 500---	51.9	2.13	0	-----	88.5	89.5	.258	-----
				200	3	86.5	88.5	.269	.011
Z10-----	SP 500---	46.3	4.30	0	-----	94.0	97.0	.139	-----
				300	3	93.0	98.0	.142	.003
Z27-----	SP 500---	46.3	4.30	0	-----	91.0	94.5	-----	-----
				S-W ⁴	-----	90.5	92.5	-----	-----
				225	2.5	90.5	94.0	-----	-----
Z28-----	SP 500---	49.3	3.58	0	-----	89.0	93.5	-----	-----
				S-W	-----	88.5	90.5	-----	-----
				270	3	87.0	92.0	-----	-----
Z29-----	SP 500---	51.3	3.22	0	-----	89.5	92.5	-----	-----
				S-W	-----	86.0	88.5	-----	-----
				225	2.5	86.5	91.0	-----	-----
Z35-----	SP 500---	64.4	4.30	0	-----	54.0	75.0	-----	-----
				S-W	-----	57.5	77.0	-----	-----
				225	2.5	56.0	76.5	-----	-----
Z39-----	E-P 730--	73.0	4.30	0	-----	52.5	75.0	-----	-----
				S-W	-----	56.5	76.5	-----	-----
				270	3	55.0	76.5	-----	-----
Z42-----	XX 254--	73.0	4.30	0	-----	75.5	89.0	-----	-----
				S-W	-----	78.0	88.5	-----	-----
				270	3	75.0	87.0	-----	-----

¹ The binder for all coatings was PS7. The pigment for Z35 was calcined at 800° C/12 hr.

² Pigment/binder ratio.

³ Equivalent sun hours.

⁴ S-W: After soiling and washing.

towelling. Two cleaning operations followed, the first consisting of wiping with acetone-soaked paper towels and the second consisting of washing with Alconox-tap water and scouring with a nylon brush. Final rinsing with distilled water preceded drying under an airblast and complete drying at 130° C. Moderate care in all the operations prevented any apparent damage to the coatings. The samples were exposed to ultraviolet irradiation in the oil-diffusion-pump vacuum system.

As shown in table IV, a slight decrease in reflectance resulted for most of the soiled and cleaned (S-W) samples. Exceptions to this were some samples of initial reflectance lower than 80 percent at 440 m μ ; these coatings exhibited a slight increase in reflectance. Upon exposure to the simulated space environment the samples which suffered losses on washing bleached slightly. On the other hand, coatings which showed an increased reflectance on washing revealed slight losses after exposure to the simulated space environment. In all cases, the washing appeared to have adequately removed any degradable residual oil.

LONG-TERM TESTS

The longer-term tests were conducted in the ion-pumped vacuum system with an externally mounted ultraviolet lamp. Exposures of 450 to 4170 ESH at solar factors ranging from 8 to 18 suns were used. The limited capacity of the water-cooled shelf in the chamber dictated simple geometries—1-inch squares—for maximum use.

More significant optical changes in the zinc oxide compositions became apparent in the longer tests. Several treatments were found to have little or no effect on stability. Ball-milling of the paint formulations for 6 to 8 hours did not introduce enough impurities to change the degradation characteristics. Physical stresses such as fatigue and thermal shock also had negligible effect on the paint. The lack of heat-curing was not detrimental to stability.

Certain factors were shown to be conducive to solar absorptance changes. Foremost was contamination of the coating, for example, with sebum or acetone residue. Application of a

topcoat over a soiled area was not sufficient to retain stability. It is possible that cleaning might remove any soluble degradable material which may be dissolving in the second coat during respraying. Lowering of the PBR was detrimental to initial solar absorptance and also to stability.

The randomness of some test results suggested the possibility of an aging effect. Samples investigated for curing and storage effects appear in table V. A sample which had been stored for 4 months was cut into three pieces, each of which received different treatments. The data for these samples, Z79, Z80, and Z81, reveal the beneficial effect of washing and the maximization of stability by heating the paint at 500° C. In view of these results, contamination of the paints appears to be possible, since washing presumably extracted some of the degradable components. It is possible that additional washing may have removed even more. The heat treatment was not at a high enough temperature to decompose such materials as potassium carbonate, potassium sulfate, or zinc orthosilicate had they been present as a contributory factor in degradation. It appears that, on storing, the coating collected impurities which had not actually reacted chemically with the paint but instead were held physically in the porous coatings.

Sample Z83 was cured in a carbon dioxide atmosphere by placing it in a closed box with dry ice. The deleterious effect on stability was obvious from the change in absorptance. Poor stability was also exhibited by Z84; a zinc oxide-potassium silicate formulation has a limited, if any, shelf life. Difficulties in remixing and spraying also resulted from storage.

A group of samples (Z87 through Z92) prepared at the same time from the same formulation was irradiated in the same test. As shown in table V, the coatings received various types of cure and storage. Surprisingly, the most stable coating (Z87) was air-cured and stored. Its change in solar absorptance was the smallest noted in any of the extended (>1000 ESH) tests. The desiccator cure appeared to be deleterious to stability, and no difference due to storage in air (Z89),

TABLE V.—Combined Effects of Varying the Curing and Storage Times and of Ultraviolet Irradiation in Vacuum on Optical Properties of Inorganic Zinc Oxide Coatings

[The pigment was SP 500 calcined at 700° C for 16 hr, and the binder was PS7 for all samples. Pigment-binder ratio was maintained at 4.30. Solids content was 56.9% for all samples except Z84 (46.3%).]

Sample	Cure	Treatment	Exposure		Solar absorptance			
			ESH*	Solar factor	α_1	α_2	α	$\Delta\alpha$
** { Z79--- Z80--- Z81---	140° C for 18 hr	Not treated.....	0	-----	0.116	0.079	0.195	-----
			1600	10.2	.152	.079	.231	0.036
	140° C for 18 hr	Washed with detergent and water.	0	-----	.112	.077	.189	-----
			1600	10.2	.135	.075	.209	.020
	140° C for 18 hr	Heated at 500° C for 2 hr.....	0	-----	.111	.077	.188	-----
			1600	10.2	.116	.077	.193	.005
Z83-----	Air-dried....	Cured in CO ₂ atmosphere.....	0	-----	.102	.073	.175	-----
			1780	9.5	.178	.084	.263	.088
Z84-----	140° C for 18 hr	Shelf-life sample. The formu- lation was originally prepared and milled 4 months previous- ly. Vigorous shaking was required to resuspend the pigment.	0	-----	.096	.050	.146	-----
			1780	9.5	.159	.059	.219	.073
Z87-----	Air-dried....	Stored between sheets of vel- lum open to the laboratory environment for 27 days.	0	-----	.099	.059	.157	-----
			1650	9	.103	.056	.159	.002
Z88-----	Air-dried....	Cured and stored in a desiccator containing Drierite (a desic- cant) and Ascarite (a carbon dioxide absorbant) for 27 days.	0	-----	.099	.062	.161	-----
			1650	9	.115	.063	.179	.018
Z89-----	Air-dried....	Cured in a desiccator for 22 hr and stored in air for 26 days.	0	-----	.100	.060	.161	-----
			1650	9	.115	.060	.175	.014
Z90-----	Air-dried....	Cured in a desiccator for 22 hr and stored under Saran wrap for 26 days.	0	-----	.102	.063	.165	-----
			1650	9	.115	.064	.179	.014
Z91-----	140° C for 18 hr	Cured in a desiccator for 22 hr, heated in air at 500° C for 2 hr, and stored in a desic- cator for 25 days.	0	-----	.101	.060	.161	-----
			1650	9	.104	.061	.165	.004
Z92-----	140° C for 18 hr	Cured in a desiccator for 22 hr, heated in air at 500° C for 2 hr, and stored in air for 25 days.	0	-----	.103	.067	.171	-----
			1650	9	.109	.070	.179	.008

* Equivalent sun hours.

** A 1 × 3-in. sample, stored as described in text, was cut into three 1-in. squares—samples Z79, Z80, and Z81.

under Saran Wrap (Z90), or in the desiccator (Z88) was observed. The undesirable effect of the desiccator cure was partially eliminated by heat treatment (Z91 and Z92). The slightly detrimental effect of curing in an atmosphere free of water and carbon dioxide seems paradoxical. However, good stability was exhibited by all coatings in this group.

4170-ESH TEST

The most severe space-simulation test in the program was for 4170 ESH at a solar factor of 10.6 suns, corresponding to nearly 6 months of direct extraterrestrial ultraviolet irradiation. The optical changes plus short histories of the samples appear in table VI. Good stability was exhibited by Z93 (fig. 7) and Z94. The

TABLE VI.—Effect of 4170 Equivalent Sun-Hours of Ultraviolet Irradiation in Vacuum on Optical Properties of Inorganic Zinc Oxide Coatings

[The pigment was SP 500 calcined at 700 °C for 16 hr, and the binder was PS7 for all samples. All samples were cured by air drying.]

Sample	Composition		Treatment	Exposure, ESH**	Solar absorptance			
	PBR*	Solids content %			α_1	α_2	α	$\Delta\alpha$
Z93-----	4.30	56.9	Stored in air, between sheets of vellum, for 37 days.	0	0.102	0.063	0.165	-----
				4170	.120	.059	.179	0.014
Z94-----	5.31	58.5	Stored in air, between sheets of vellum, for 21 days.	0	.096	.051	.147	-----
				4170	.106	.049	.155	.008
Z95-----	4.30	56.9	Stored in air, between sheets of vellum, for 36 days; washed with detergent and water; air-dried for 1 day.	0	.100	.061	.161	-----
				0—washed	.098	.049	.147	-.014
				4170	.122	.050	.172	.025
Z96-----	4.30	56.9	Stored in air, between sheets of vellum, for 24 days; heated at 500° C for 2 hr; stored in air for 13 days.	0	.102	.064	.166	-----
				0—heated	.101	.058	.159	-.007
				4170	.109	.057	.166	.007

*Pigment/binder ratio.

**Equivalent sun-hours.

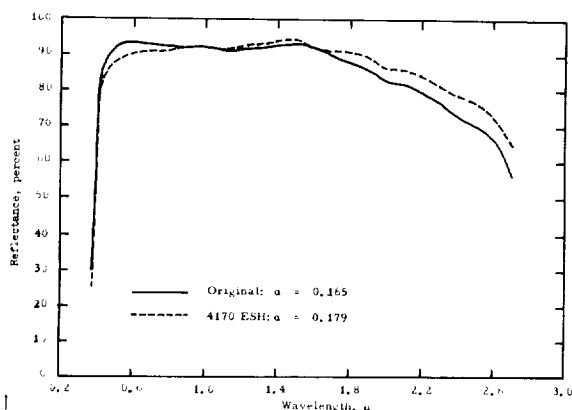


FIGURE 7.—Effect of 4170 equivalent sun-hours in vacuum on solar spectral reflectance of calcined zinc oxide-potassium silicate coating (sample Z93).

comparatively superior behavior of the coating with the high PBR, Z94, indicates the feasibility of increasing pigment concentration. The beneficial effect of a 500° C heat treatment is evidenced by the results for Z96. A limited deleterious effect was imparted by washing.

SCREENING OF ORGANIC AND ORGANO-METALLIC PAINTS

The organic coating vehicles which were considered can be divided into the following

chemical categories: organometallic vehicles with organic "framing" groups, fluorine-containing aliphatic resins, organic polyesters, epoxy resins, and miscellaneous vehicles including commercial resins with undisclosed composition. In this discussion, however, these binders are divided into three categories: commercially available silicones, fluorine-containing aliphatic resins, and a modified silicone-epoxy composition. More than 45 resin films were considered for screening. Nearly 300 pigment-binder combinations were prepared, although only about 50 paints were irradiated in vacuum.

The study of experimental methyl silicone resins comprised a major portion of the non-inorganic phase of the research. For this reason, the methyl silicone resins which were synthesized during the course of the program are discussed separately.

Four silicones were evaluated: General Electric Company's RTV-11 silicone paste, LTV-602 silicone potting compound, and SE551-N silicone gum, and Dow Corning Corporation's 806A silicone resin. The first two materials are polydimethylsiloxane polymers. RTV-11 contains silica, calcium oxide, and calcium carbonate as fillers. It is cured with Thermolite 12, a proprietary catalyst obtained from General

Electric. LTV-602 is a transparent liquid containing no fillers and is cured by addition of SRC-05 catalyst. SE551-N is a low-shrink, methyl-phenyl silicone gum stock which is cured with benzoyl peroxide. Dow Corning 806A resin is also a methyl-phenyl silicone, and requires heating to 480° F to cure. However, addition of tetrabutoxy titanium accelerates the cure at a lower temperature.

Nine fluorine-containing polymers were evaluated. Those which were obtained from E. I. duPont de Nemours and Company were: Teflon TFE Dispersion No. 30, Teflon TFE High Build Clear Finish No. 852-202, Teflon FEP Dispersion No. 120, Viton A, and Viton B. Teflon TFE is polytetrafluoroethylene. Teflon FEP is a copolymer of tetrafluoroethylene and hexafluoropropylene, and Viton is a copolymer of vinylidene fluoride and hexafluoropropylene. The raw polymer of Viton B gum was dissolved in acetone or methyl ethyl ketone. It required about 10 days before the suspended impurities settled and a clear solution was formed.

Kel-F resin No. 800 and Kel-F latex No. KF 8213 were obtained from the Minnesota Mining and Manufacturing Company. The resin and latex are each copolymers of vinylidene fluoride and trifluorochloroethylene. Kel-F No. 8213 was received as an aqueous dispersion. A ketone dispersion was made from it by quenching the aqueous dispersion of the latex with liquid nitrogen, covering the solidified material with acetone, allowing the solid to warm, and decanting the supernatant solution. The process of water removal was repeated without further freezing. The acetone dispersion was then dried over nonreactive drying agents.

The only epoxy resin evaluated was a silicone-epoxy modified acrylic resin known as Leonite 201-S obtained from the Leon Chemical Industries.

Only two clear organic polymer films were irradiated: one specimen of Teflon TFE No. 30 and one of RTV-11 silicone. The data for these two coatings appear in table VII, which also contains data for other representative organic paints. Comparison of the reflectance changes in P-1 and P-3 illustrates the difference between a phenyl and a methyl silicone binder,

although some of the degradation in P-1 at 440 m μ was due to the low PBR. Subsequent silicone paints were formulated at a PBR of about 2.5.

Coating P-4 showed exceptional resistance to degradation; the loss in reflectance at 440 m μ was only 1.0 percent. The PBR of 5 is much higher than is practical, however. This value is in excess of the critical pigment volume concentration (the value above which insufficient binder exists to wet all the particle surfaces in the paint) for this pigment/binder combination.

Coatings P-10, P-12, and P-14 were also pigmented at a very high PBR and their respective critical pigment volume concentrations were probably exceeded, although fairly good adhesion was observed in these paints. Of all the nonsilicone paints, P-14 showed the best resistance to yellowing. This paint was the acetone dispersion of Kel-F 8213 pigmented with SP 500 zinc oxide.

ZINC OXIDE-PIGMENTED METHYL SILICONE PAINTS

Materials

As a result of the pigment and inorganic screening investigations, the pigmentation of silicone-based paints was confined essentially to the use of SP 500 zinc oxide. Rutile titanium dioxide and zinc sulfide were used in several instances for the purpose of comparison.

Except for two phenyl-methyl silicone paints, efforts were devoted primarily to methyl silicone, or polydimethylsiloxane, polymers. The studies were divided into two phases: (1) evaluation of commercially available methyl silicone polymers and (2) synthesis and evaluation of experimental methyl silicone resins.

Paint Formulation

All paints were ground in a porcelain jar mill for about 16 hours at approximately two-thirds critical speed. The formulation data for the silicone paints are given in table VIII in which pigment/binder ratios are given

TABLE VII.—*Effect of Ultraviolet Irradiation in Vacuum on Optical Properties of Several Organic Paints*

Paint	Composition			Exposure		Reflectance, %	
	Pigment	Binder	PBR*	ESH**	Solar factor	440 m μ	600 m μ
-----	-----	RTV-11-----	-----	0	-----	73.5	77.5
-----	-----	Teflon TFE 30-----	-----	108	4	60.5	76.5
-----	-----	-----	-----	0	-----	84.7	80.6
-----	-----	-----	-----	74	4	69.2	74.7
P-1-----	SP 500 ZnO-----	806A-----	0.7	0	-----	89.0	87.5
-----	-----	-----	-----	108	4	56.0	83.5
P-2-----	SP 500 ZnO-----	SE551-N-----	3.4	0	-----	88.5	94.5
-----	-----	-----	-----	500	4	84.0	93.5
P-3-----	SP 500 ZnO-----	RTV-11-----	1.0	0	-----	91.0	92.0
-----	-----	-----	-----	500	4	88.0	91.5
P-4-----	SP 500 ZnO-----	LTV-602-----	5.0	0	-----	91.0	93.5
-----	-----	-----	-----	500	4	90.0	93.5
P-5-----	ZrO ₂ -----	Teflon TFE 30-----	0.66	0	-----	87.8	70.0
-----	-----	-----	-----	74	4	42.0	59.6
P-7-----	SP 500 ZnO-----	Teflon TFE 852-202-----	0.67	0	-----	84.0	91.5
-----	-----	-----	-----	108	4	46.0	74.5
P-8-----	SP 500 ZnO-----	Teflon FEP 120-----	0.4	0	-----	84.2	77.3
-----	-----	-----	-----	314	4	52.4	67.5
P-10-----	SP 500 ZnO-----	Viton B-----	4.0	0	-----	88.5	92.0
-----	-----	-----	-----	500	4	76.5	89.0
P-11-----	SP 500 ZnO-----	Kel-F 800-----	0.5	0	-----	84.0	77.6
-----	-----	-----	-----	108	4	64.8	72.7
P-12-----	ZnS-----	Kel-F 800-----	5.0	0	-----	89.5	92.0
-----	-----	-----	-----	108	4	49.5	78.0
P-13-----	SP 500 ZnO-----	Kel-F 8213-----	1.5	0	-----	87.0	87.5
-----	-----	-----	-----	108	4	52.0	72.5
P-14-----	SP 500 ZnO-----	Kel-F 8213-----	5.0	0	-----	97.0	98.0
-----	-----	(acetone dispersion)	-----	500	4	80.5	95.0
P-19-----	SP 500 ZnO-----	Leonite 201-S-----	0.67	0	-----	86.0	85.0
-----	-----	-----	-----	108	4	71.0	83.0
P-20-----	MgO-----	Leonite 201-S-----	0.44	0	-----	93.5	92.5
-----	-----	-----	-----	108	4	35.0	78.5

*Pigment/binder ratio.

**Equivalent sun hours.

as both weight (PBR) and volume (PVC) ratios.

Synthesis of Experimental Methyl Silicone Resins

A general reaction scheme for methyl silicone resins is given by Rochow and Gilliam (ref. 5). A mixture of mono- and disubstituted silicon halides (or ethoxy esters) is hydrolyzed, and the resultant silanetriols and silanediols are condensed to the resinous product. The composition of the resin is controlled by Me/Si, the

molar ratio of methyl groups to silicon atoms. The Me/Si is essentially the same for both the reactant mixture and the product.

Molecular weights were obtained on a Mechrolab vapor pressure osmometer, model 301A, a "thermoelectric" type of osmometer (ref. 6).

Nine experimental resins were synthesized during the program. The preparations of three are described in the following paragraphs. The procedures for those not included here were similar to the procedures described except for ratios of trifunctional to difunctional reactants.

TABLE VIII.—*Formulation Data for Silicone Paints*

Paint	Ingredients ¹	Parts by weight	PVC, ² %	PBR ³	Solids, percent by volume
S-1.....	Superlith XXXN zinc sulfide.....	107.5	40	2.15	40
	806A resin.....	100.0			
	Toluene.....	37.0			
S-3.....	SP 500 Zinc oxide.....	141.0	20	1.19	40
	XR-6-1057 resin.....	173.0			
	Tetrabutoxy titanium (TBT).....	3.0			
	Toluene.....	108.0			
S-4.....	SP 500 Zinc oxide.....	45.0	25	1.35	26
	R-1 Exptl. resin soln.....	111.0			
S-5.....	SP 500 Zinc oxide.....	93.4	25	1.80	40
	XR-6-0049 resin.....	100.0			
	Xylene.....	38.0			
S-7.....	SP 500 Zinc oxide.....	140.1	20	1.40	40
	LTV-602 Polymer.....	100.0			
	SRC-05 Catalyst.....	0.5			
	Toluene.....	160.0			
S-8.....	SP 500 Zinc oxide.....	112.0	25	1.70	40
	R-2 Exptl. resin soln.....	100.0			
	Toluene.....	67.0			
S-10.....	SP 500 Zinc oxide.....	77.5	25	1.78	40
	R-4 Exptl. resin soln.....	100.0			
	Xylene.....	17.7			
S-11.....	SP 500 Zinc oxide.....	123.6	25	1.63	40
	R-5 Exptl. resin soln.....	104.0			
	Toluene.....	86.0			
S-13.....	SP 500 Zinc oxide.....	240.0	30	2.40	40
	LTV-602 Polymer.....	100.0			
	SRC-05 Catalyst.....	0.5			
	Toluene.....	183.8			
S-15.....	SP 500 Zinc oxide.....	212.0	30	2.12	40
	R-5 Exptl. resin.....	100.0			
	Toluene.....	157.0			
S-16.....	SP 500 Zinc oxide.....	163.0	25	1.63	40
	R-7 Exptl. resin.....	100.0			
	Toluene.....	150.0			
S-17.....	RA-NC rutile.....	140.0	45	2.80	40
	808 Resin.....	100.0			
	Tetrabutoxy titanium (TBT).....	1.0			
	n-Butanol.....	47.0			
	Toluene.....	24.0			
S-18.....	SP 500 Zinc oxide.....	48.0	25	1.45	31
	SR-80 Resin.....	100.0			
S-19.....	SP 500 Zinc oxide.....	268.0	35	2.68	40
	R-5 Exptl. resin.....	100.0			
	Toluene.....	176.0			
S-26.....	SP 500 Zinc oxide.....	373.0	40	3.73	40
	LTV-602 Polymer.....	100.0			
	SRC-05 Catalyst.....	0.5			
	Toluene.....	214.0			
S-27.....	SP 500 Zinc oxide.....	304.0	35	3.04	40
	LTV-602 Polymer.....	100.0			
	SRC-05 Catalyst.....	0.5			
	Toluene.....	197.0			

TABLE VIII.—Formulation Data for Silicone Paints—Continued

Paint	Ingredients ¹	Parts by weight	PVC, ² %	PBR ³	Solids, percent by volume
S-29.....	SP 500 Zinc oxide.....	264.0	35	2.64	40
	R-8 Exptl. resin.....	100.0			
	Tetrabutoxy titanium (TBT).....	1.0			
	Toluene.....	176.0			
S-31.....	SP 500 Zinc oxide.....	316.0	40	3.16	40
	R-8 Exptl. resin.....	100.0			
	Tetrabutoxy titanium (TBT).....	1.0			
	Toluene.....	179.0			
S-32.....	TiPure R-900-1 rutile.....	237.0	35	2.37	40
	LTV-602 Polymer.....	100.0			
	SRC-05 Catalyst.....	0.5			
	Toluene.....	198.5			
S-33.....	SP 500 Zinc oxide.....	316.0	40	3.16	40
	R-9 Exptl. resin.....	100.0			
	Tetrabutoxy titanium (TBT).....	1.0			
	Toluene.....	225.0			

¹ Dow Corning: 806A resin, XR-6-1057 resin, XR-6-0049 resin, and 808 resin. Du Pont: Tetrabutoxy titanium (TBT) and TiPure R-900-1 rutile. General Electric: LTV-602 polymer, SRC-04 catalyst, SRC-05 catalyst, SR-80 resin, and 81932 resin. National Lead: Titanox RA-NC rutile. New Jersey Zinc: SP 500 zinc oxide. Nuodex Products: Silicure Z-775. C. J. Osborn Co.: Superlith XXXN zinc sulfide.

² PVC: pigment volume concentration.

³ PBR: pigment/binder ratio.

EXPERIMENTAL RESIN R-4

A mixture of 0.4 mole (59.2 g) of dimethyldiethoxysilane (90 percent) and 0.48 mole (85.5 g) of methyltriethoxysilane (90 percent) in 150 g of 95 percent ethyl alcohol was added to 400 g of distilled water. To this mixture was added 22 ml of 37 percent hydrochloric acid, and the mixture was refluxed vigorously for 19 hours. A syrupy, viscous, colorless fluid of density greater than that of water resulted. The polymer was washed by decantation until a neutral test to litmus was obtained. Then 70 g of xylene was added, effecting separation of a water phase from an organic phase. The organic layer was washed with distilled water twice and was dried over Drierite after weighing. The resultant solution contained 40 percent resin by volume (47 percent by weight). The Me/Si ratio of the polymer was calculated to be 1.46. The specific gravity of the resin solution was 0.965.

EXPERIMENTAL RESIN R-5

A mixture of 0.3 mole (38.7 g) of dimethyldichlorosilane (99.4 percent) and 0.48 mole (72.0 g) of methyltrichlorosilane (95.0 percent)

in 300 g of anhydrous diethyl ether was added dropwise with agitation, over a period of 40 minutes, to 1000 g of ice. The ether layer was separated and washed once with distilled water. It was then washed with 5 percent solution of sodium bicarbonate, followed by three washings with distilled water. The ether solution was dried over Drierite and evaporated at reduced pressure, leaving a viscous, colorless resin. A resin solution in toluene was made at 67.4 percent solids by volume. The specific gravity of the resin solution was 1.040. Me/Si was calculated to be 1.38.

EXPERIMENTAL RESIN R-9

The basic R-5 methyl silicone resin was prepared according to the procedure outlined above. The resultant stock resin (containing no solvent) was distilled at an average temperature of 100° C and 0.004 mm Hg pressure in an ASCO '50' Rota-Film molecular still. The upper-molecular-weight fraction was collected as R-9. Its molecular weight was found to be 2000, and its specific gravity was 1.180. The resin was decolorized with Darco Activated Carbon G60 (Atlas Powder Co.).

Determination of Optical Properties

The effect of film thickness and PVC on the optical properties of several elastomeric paints is presented in figure 8. The total normal emittance values (at 200° F) of S-12 are presented in close proximity to the points on the graph. The data confirm that thick coatings—approximately 10 mils—are required to approximate the highest reflectance and to avoid the necessity for thickness control. The effect of PVC on solar absorptance was pronounced only at lower film thickness, except for paint S-26, which was pigmented at 40 percent PVC. Little difference in solar absorptance was observed between paints S-12, S-13, and S-27 when applied at a film thickness of about 10 mils. On the other hand, considerably

thinner coatings appear to provide maximum emittance.

Paint S-26, pigmented at 40 percent PVC, possessed an exceptionally low solar absorptance, 0.16, at a thickness of only 7.5 mils. The low absorptance may be attributable to the fact that 40 percent represents a concentration equal to or greater than the critical PVC. Thus, the coating possessed many pigment particles with an air interface and consequently had a higher average refractive index ratio, which resulted in greater scattering due to enhanced porosity throughout the coating. As a consequence of the excessive pigment concentration, the film was powdery and fragile and lacked cohesive strength sufficient to ensure its utility.

The effect of the film thickness of S-33 on its solar absorptance, total normal emittance, and the ratio of the two is presented in figure 9. The vehicle of this paint was the molecularly distilled experimental resin R-9 with an Me/Si ratio of 1.38. It was pigmented with SP 500 zinc oxide at 40 percent PVC.

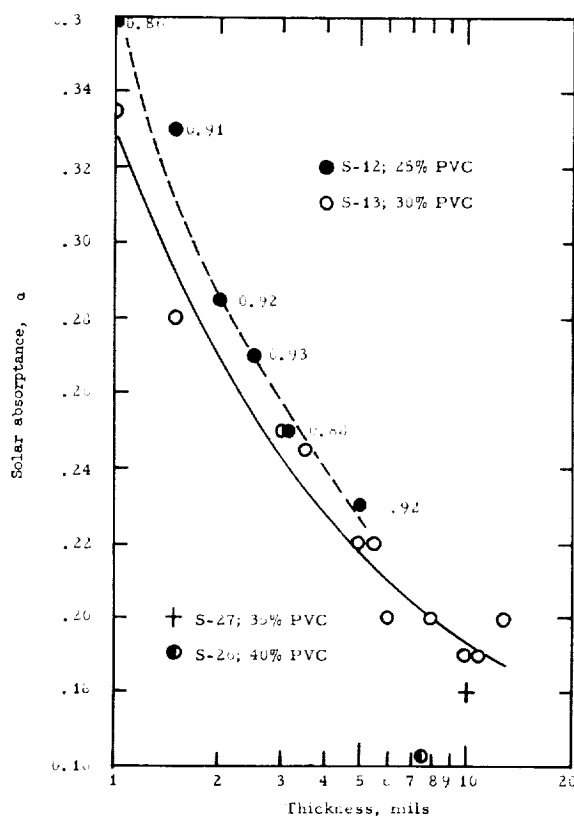


FIGURE 8.—Variation of solar absorptance with thickness in zinc oxide/LTV-602 methyl silicone coatings (paints S-12, S-13, S-26, and S-27). Numbers beside the points are values of total normal emittance for S-12 at 200° F.

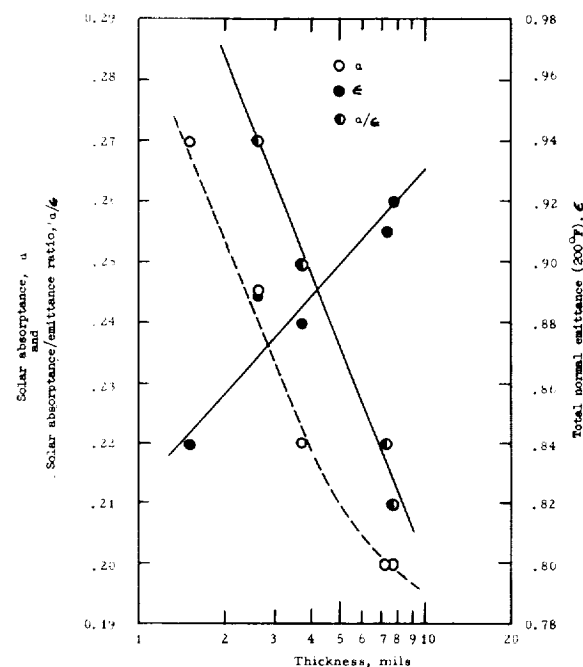


FIGURE 9.—Variation of solar absorptance, solar absorptance/emittance ratio, and total normal emittance with thickness in zinc oxide/R-9 experimental methyl silicone coating (paint S-33).

Stability to a Simulated Space Environment

PRELIMINARY STUDIES

The results of the initial space-simulation tests on several silicone coatings are given in table IX. Coatings S-1, S-3, S-4, and S-5 were irradiated in the oil-diffusion-pumped system; S-7 and S-10 were irradiated in the ion-pumped system. The methyl-phenyl silicone paint S-1 exhibited severe degradation, as evidenced by the loss in reflectance at a wavelength of 440 m μ . Four methyl silicone paints (S-3, S-4, S-5, and S-10) exhibited reflectance changes of 1 percent or less, with several of the changes representing increases. The increases are considered to be a result of experimental errors due, for example, to viewing different measuring positions on the sample before and after exposure.

Although coatings S-3 and S-5 possessed exceptional stability to ultraviolet irradiation in vacuum, their poor physical properties, in comparison with those of S-7 and S-10, precluded their further consideration. They were more difficult to apply, they were brittle, and they checked at moderate temperatures. Subsequent work was therefore confined to the LTV-602 and experimental methyl silicone resins.

EFFECT OF Me/Si

The effect of varying the Me/Si of methyl silicone resins from 1.29 to 1.46 is presented in table X. Examination of the reflectance and solar absorptance changes at various exposures shows that the paints based on resins with lower Me/Si were superior.

The small change in solar absorptance shown for S-4 seems inconsistent with the indicated severe decrease in reflectance at 440-m μ wavelength. This decrease in the visible was counterbalanced by an anomalous increase in reflectance in the near-infrared solar region. Although the anomaly cannot be explained at this time, it is interesting to compare coating S-4 with the inorganic paint Z93 (fig. 7). Resin R-1, the vehicle in S-4, has the lowest Me/Si and possesses a structure which is more like that of the alkali silicates than any of the other experimental resins. Furthermore, S-4, like Z93, showed an increase in near-infrared reflectance on exposure to ultraviolet radiation in vacuum. R-1 was eliminated from further consideration, however, because of its inherent brittleness and failure when torsionally stressed to 90°.

The selection of resin R-5 rather than R-7 for further evaluation and for use as a stock polymer for molecular distillation studies was somewhat arbitrary. The decision was based

TABLE IX.—Effect of Ultraviolet Irradiation in Vacuum on Optical Properties of Several Silicone Paints

Paint No.	Composition			Exposure		Reflectance, %	
	Pigment	Blinder	PVC,* percent	ESH**	Solar factor	440 m μ	600 m μ
S-1.....	ZnS.....	806A.....	40	0		84.4	89.0
				300	3	63.0	87.3
S-4.....	SP 500 ZnO.....	R-1.....	25	0		79.0	81.5
				300	3	79.5	80.5
S-5.....	SP 500 ZnO.....	XR-6-0049.....	25	0		80.5	83.5
				300	3	81.0	84.5
S-7.....	SP 500 ZnO.....	LTV-602.....	20	0		87.5	92.5
				450	10	82.5	90.5
S-10.....	SP 500 ZnO.....	R-4.....	25	0		77.0	87.5
				450	10	77.0	87.0

*Pigment volume concentration.

**Equivalent sun hours.

TABLE X.—*Effect of Ultraviolet Irradiation in Vacuum on Optical Properties of Silicone Paints as a Function of Molar Ratio of Methyl Groups to Silicon Atoms (Me/Si)*

PVC* = 25%

Paint	Composition		Exposure		Reflectance, %		Solar absorptance, α
	Binder	Me/Si	ESH**	Solar factor	440 m μ	600 m μ	
S-4-----	R-1-----	1. 29	0		79. 0	81. 5	-----
			300	3	79. 5	80. 5	-----
			0		83. 0	85. 5	0. 26
			1460	9	71. 0	81. 5	. 27
S-16-----	R-7-----	1. 33	0		80. 5	88. 5	. 26
			615	9	78. 0	87. 0	. 27
			0		81. 5	88. 5	. 27
			1600	11	78. 5	86. 0	. 27
S-11-----	R-5-----	1. 38	0		86. 5	91. 0	. 23
			1460	9	82. 5	88. 5	. 25
S-8-----	R-2-----	1. 46	0		80. 5	92. 0	-----
			450	10	76. 0	91. 5	-----
			0		85. 5	94. 0	. 20
			1460	9	82. 0	91. 0	. 23

*Pigment volume concentration.

**Equivalent sun hours.

on the supposition that an increase in cross-linking and molecular weight probably accompanies molecular distillation. Such an increase, coupled with the fact that the R-7 stock resin was polymerized from a higher ratio of methyl trichlorosilane to dimethyl dichlorosilane, would produce still more brittle, glassy resins.

LTV-602 PAINTS AND EFFECT OF PVC

Paints were formulated from GE's LTV-602 polymer at 20, 25, 30, 35, and 40 percent PVC in order to determine the effect of pigment concentration on stability to a simulated space environment. Experimental resin R-5 was also pigmented at different PVC values. The results of exposure to a simulated space environment are presented in table XI. The data for the LTV-602 paints show the dependence of stability on PVC. Coating S-7 at 20 percent PVC showed an increase in solar absorptance of 0.040 compared with 0.030–0.038 for S-13 at 30 percent PVC and only 0.012 for S-26 at 40 percent PVC. Similarly, coating S-19 at 35 percent PVC exhibited a comparatively smaller increase in solar absorptance than either S-11 or S-15 at 25 and 30 percent PVC, respectively.

The data on LTV-602 in table XI are plotted in figure 10 to show the inverse relation of

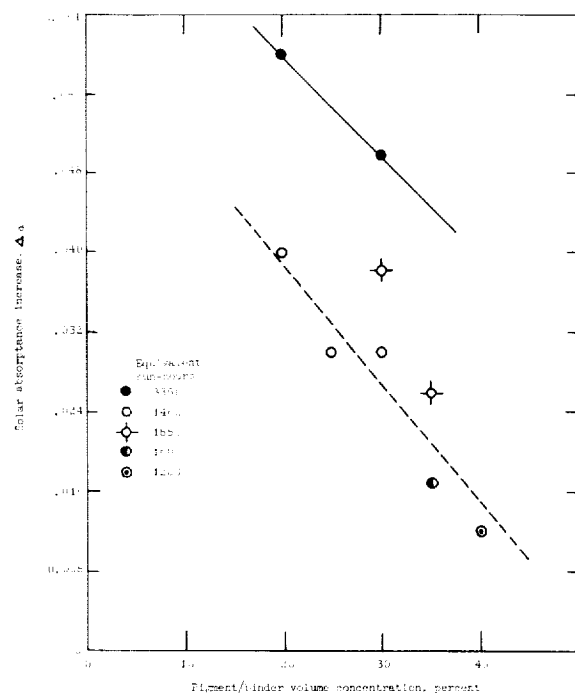


FIGURE 10.—Variation of solar absorptance with pigment volume concentration in zinc oxide/LTV-602 methyl silicone coatings.

solarization to PVC. The dependence of stability on PVC is more easily discerned in less stable systems, such as those based on zinc sulfide- or rutile-pigmented methyl-phenyl silicones. The zinc oxide-methyl silicone and the zinc oxide-silicate systems are, by virtue of their stability, more susceptible to differences caused by soiling, measurement errors, etc.

PAINTS BASED ON DISTILLED RESINS

Zinc oxide paints based on undistilled methyl resins (e.g., R-5) undergo optical flattening and an increase in porosity upon curing. Even though this process may involve thermal erosion on the surface of the organic portion of the resin, the cured films are very stable to the simulated space environment (table XI),

but their porosity and their 300° F curing requirement provide no advantages over the porous potassium silicate paints. It was this porosity and the resultant susceptibility to soiling which prompted molecular distillation experiments with resin R-5. These experiments were aimed at the production of resins of higher molecular weight in the hope that paints based on them would produce glossy, more soil-resistant, and easily cleanable coatings.

The effects of ultraviolet irradiation in vacuum on the paints based on molecularly distilled resins are presented in table XII.

MISCELLANEOUS SILICONE PAINTS

The results of exposure of several miscellaneous silicone paints are presented in table XIII.

TABLE XI.—*Effect of Ultraviolet Irradiation in Vacuum on Optical Properties of Silicone Paints as a Function of Pigment Volume Concentration*

Paint	Composition		Exposure		Solar absorptance			
	Binder	PVC,* %	ESH**	Solar factor	α_1	α_2	α	$\Delta\alpha$
S-7	LTV-602	20	0	-----	-----	-----	0. 220	-----
			1460	9	-----	-----	. 260	0. 040
			0	-----	-----	-----	. 240	-----
			3350	17. 6	-----	-----	. 300	. 060
S-12	LTV-602	25	0	-----	-----	-----	. 230	-----
			1460	9	-----	-----	. 260	. 030
S-13	LTV-602	30	0	-----	-----	-----	. 230	-----
			1460	9	-----	-----	. 260	. 030
			0	-----	0. 115	0. 087	. 202	-----
			1200	8. 7	. 141	. 099	. 240	. 038
S-27	LTV-602	35	0	-----	-----	-----	. 230	-----
			3350	17. 6	-----	-----	. 280	. 050
			0	-----	. 107	. 068	. 175	-----
			1600	10. 2	. 117	. 075	. 192	. 017
S-26	LTV-602	40	0	-----	. 106	. 071	. 176	-----
			1850	10. 1	. 120	. 081	. 201	. 025
			0	-----	. 105	. 056	. 161	-----
S-11	R-5	25	1200	8. 7	. 111	. 062	. 173	. 012
S-15	R-5	30	0	-----	-----	-----	. 230	-----
			1460	9	-----	-----	. 250	. 020
S-19	R-5	35	0	-----	-----	-----	. 230	-----
			1700	10. 7	-----	-----	. 240	. 010
			0	-----	. 125	. 099	. 224	-----
			1200	8. 7	. 126	. 100	. 226	. 002
			0	-----	. 124	. 099	. 223	-----
			1850	10. 1	0. 132	0. 105	0. 237	0. 014

*Pigment volume concentration.

**Equivalent sun-hours.

TABLE XII.—Effect of Ultraviolet Irradiation in Vacuum on Optical Properties of Zinc Oxide-Pigmented Paints Based on Molecularly Distilled Experimental Methyl Silicone Resin R-8

Paint	PVC,* percent	Exposure		Solar absorptance			
		ESH**	Solar factor	α_1	α_2	α	$\Delta\alpha$
S-29-----	35	0	-----	0.128	0.125	0.253	-----
		1000	10.5	.136	.130	.266	0.013
		0	-----	.125	.117	.241	-----
		1600	10.2	.130	.126	.257	.016
S-31-----	40	0	-----	.132	.129	.261	-----
		1600	9	.139	.138	.277	.016
		0	-----	.134	.131	.265	-----
		1780	9.4	.146	.139	.285	.020
S-31 (heated 1 hr at 500° F).	40	0	-----	.134	.126	.260	-----
		1780	9.4	.136	.130	.266	.006

*Pigment volume concentration.

**Equivalent sun-hours.

Paint S-17 was formulated from Dow Corning's 808 methyl-phenyl resin pigmented with Titanox RA-NC, a nonchalking rutile titanium dioxide. This paint was formulated for the round-robin testing program (see the paper in this Symposium by J. C. Arvesen, C. B. Neel, and C. C. Shaw entitled *Preliminary Results From a Round-Robin Study of Ultraviolet Degradation of Spacecraft Thermal-Control Coatings*) and is included here for purposes of comparison.

Paint S-18 was based on General Electric's SR-80 resin, which was reported to be a purely methyl silicone resin containing zinc octoate

catalyst. Unlike the other methyl silicone resins studied, however, the zinc oxide paint (S-18) made from SR-80 degraded severely after exposure to only 1600 ESH—its solar absorptance increased 40 percent. It was concluded that the resin was not purely methyl silicone. Infrared transmission analysis of the resin did not show typical methyl-phenyl structure nor did the absorption spectra match polydimethylsiloxane spectra.

Paint S-32 was pigmented with Du Pont's new TiPure R-900-1. The exceptional reflectance properties of this paint are manifested

TABLE XIII.—Effect of Ultraviolet Irradiation in Vacuum on Optical Properties of Miscellaneous Silicone Paints

Paint	Composition			Exposure		Solar absorptance			
	Binder	Pigment	PVC,* percent	ESH**	Solar factor	α_1	α_2	α	$\Delta\alpha$
S-17-----	808 TBT-----	Titanox RA-NC--	45	0	-----	-----	-----	0.296	-----
				1600	11	-----	-----	.406	0.110
S-18-----	SR-80-----	SP 500 ZnO-----	25	0	-----	-----	-----	.279	-----
				1600	11	-----	-----	.390	.111
S-32-----	LTV-602-----	TiPure R-900-1--	35	0	-----	0.099	0.080	.179	-----
				1650	9	.158	.140	.298	.119
Q-9-0107***--	Proprietary---	r-TiO ₂ -----	25	0	-----	.103	.111	.214	-----
				1480	10.7	.165	.206	.371	.157
Q-9-0108***--	Proprietary---	ZnS-----	15	0	-----	.100	.120	.220	-----
				1530	11.1	.193	.131	.324	.104
Q-9-0106***--	Proprietary---	SP 500 ZnO-----	25	0	-----	.120	.108	.228	-----
				1850	10.1	.144	.117	.261	.033

*Pigment volume concentration.

**Equivalent sun-hours.

***Furnished by Dow Corning Corp.

in the α_1 and α_2 of only 0.099 and 0.080, respectively. Unfortunately, paints prepared from R-900-1 do not offer any other advantage over those pigmented with a standard rutile, since S-32 increased 67 percent in solar absorptance after only 1650 ESH.

Coating Q-9-0106 was formulated by Dow Corning Corporation at our request. Dow Corning's Q-9-0106, Q-9-0107, and Q-9-0108 are all based on a proprietary methyl silicone RTV elastomer and are pigmented with SP 500 zinc oxide, rutile titanium dioxide, and zinc sulfide, respectively. All three coatings air-dried overnight to adherent, soft, resilient films. The large increase in the solar absorptance of Q-9-0108 was attributed in part to the low PVC. Coating Q-9-0106 compared favorably with S-13 in resistance to degradation, although S-13 was tougher and less easily scratched or gouged. However, Q-9-0106 appeared to possess less affinity for dirt than S-13.

4170-EQUIVALENT SUN-HOURS TEST

The results of exposure of four zinc oxide-pigmented methyl silicone paints to 4170 ESH of ultraviolet radiation in vacuum are presented in table XIV.

Paint S-13 increased 0.058 (18 percent) in solar absorptance. Coating S-31 increased 12 percent in solar absorptance, from 0.282 to 0.316, due to degradation. This specimen was applied in a thinner coat than usual; this fact

probably accounts for the unusually high initial solar absorptance.

Paint S-33 was formulated from experimental resin R-9, which was synthesized just prior to the test. The 4170-ESH exposure is the only test to which coating S-33 was subjected. The principal difference between R-9 and the other upgraded resins was the pressure at which it was distilled: 0.004 mm Hg for R-9 and 0.04 mm Hg for the other resins. S-33 increased only 9 percent in solar absorptance.

The S-33 specimen which was heated to 500° F for 1 hour showed the greatest stability to ultraviolet irradiation in vacuum of all the organic and semiorganic paints studied. The increase in solar absorptance of only 0.011, or 4.6 percent, compares favorably with the best zinc oxide pigmented potassium silicate paint, which increased 0.008 in solar absorptance in the same 4170-ESH exposure.

DISCUSSION OF SPACE-SIMULATION EFFECTS

Radiation Intensity

The time-intensity reciprocity of the thermal-control coatings of interest was studied. The effect of ultraviolet intensity on the degradation of three potassium silicate paints pigmented with zinc oxide is presented in table XV. Corresponding samples were: Z69 and Z70, Z73 and Z74, and Z75 and Z76. The uncalcined

TABLE XIV.—Effect of 4170 Equivalent Sun-Hours of Ultraviolet Irradiation in Vacuum on Optical Properties of Silicone Paints

Paint	Binder	Composition			Exposure		Solar absorptance			
		PVC,* %	Cure		ESH**	Solar factor	α_1	α_2	α	$\Delta\alpha$
			hr	at °F						
S-13	LTV-602	30	16	Room	0	----	0.124	0.087	0.211	-----
					4170	10.6	.160	.109	.269	0.058
S-31	R-8	40	1	300	0	----	.145	.137	.282	-----
					4170	10.6	.165	.151	.316	.034
S-33	R-9	40	1	300	0	----	.119	.097	.216	-----
					4170	10.6	.128	.108	.236	.020
			1	300	0	----	.128	.109	.237	-----
			+1	500	4170	10.6	.134	.114	.248	.011

*Pigment volume concentration.

**Equivalent sun-hours.

TABLE XV.—*Effects of Varying the Solar Factor of Ultraviolet Irradiation in Vacuum on Optical Properties of Inorganic Zinc Oxide Coatings*

Sample	Composition*		Exposure		Solar absorptance			
	Pigment	Solids content, percent	ESH***	Solar factor	α_1	α_2	α	$\Delta\alpha$
Z69----	SP 500-----	46.3	0	-----	0.090	0.067	0.156	-----
			3180	10.7	.119	.069	.188	.032
Z70----	SP 500-----	46.3	0	-----	.093	.063	.156	-----
			3300	17.4	.129	.074	.202	.046
Z73----	SP 500**-----	56.9	0	-----	.105	.067	.172	-----
			3180	10.7	.136	.064	.200	.028
Z74----	SP 500**-----	56.9	0	-----	.104	.067	.171	-----
			3300	17.4	.157	.074	.231	.060
Z75----	AZO-55LO**-----	56.9	0	-----	.113	.067	.180	-----
			3180	10.7	.136	.072	.209	.029
Z76----	AZO-55LO**-----	56.9	0	-----	.115	.070	.185	-----
			3300	17.4	.154	.074	.228	.043

*The binder was PS7 and the pigment binder ratio 4.30 for all samples. All samples cured by air drying.

**Pigment calcined 16 hr at 700° C.

***Equivalent sun-hours.

SP 500 pair was formulated and prepared from the same batch. One-inch-square samples of the calcined pairs were obtained by cutting a 1- by 3-inch painted panel. A significant increase in degradation was apparent at the higher solar factor and indicated that irradiation by 17 suns was an unrealistically harsh treatment. The effect of ultraviolet intensity on the degra-

dation of three methyl silicone coatings pigmented with zinc oxide and prepared and cured alike is presented in table XVI.

The data in tables XV and XVI indicate that time-intensity reciprocity is not valid between solar factors of 10.7 and 17.4 intensities for the coatings examined. The question of the validity of photochemical reciprocity, however

TABLE XVI.—*Effects of Varying the Solar Factor and of Ultraviolet Irradiation in Vacuum on Optical Properties of Methyl Silicone Zinc Oxide Paints*

Paint	Composition*		Exposure		Solar absorptance			
	Binder	PVC,** percent	ESH***	Solar factor	α_1	α_2	α	$\Delta\alpha$
S-18----	SR-80-----	25	0	-----	0.130	0.123	0.253	-----
			3180	10.7	.243	.185	.428	0.175
			0	-----	.125	.119	.244	-----
			3300	17.4	.284	.187	.471	.227
S-13----	LTV-602-----	30	0	-----	.113	.086	.199	-----
			3180	10.7	.153	.110	.263	.064
			0	-----	.107	.073	.180	-----
			3300	17.4	.164	.108	.272	.092
S-19----	R-5-----	35	0	-----	.123	.103	.226	-----
			3180	10.7	.131	.108	.239	.013
			0	-----	.123	.102	.225	-----
			3300	17.4	.144	.109	.253	.028

*S-13 was air-cured; all others were cured 1 hr at 300° F.

**Pigment volume concentration.

***Equivalent sun-hours.

was not answered, because the observed increase in degradation may be due in whole or in part to thermal effects or to errors in the measurements of the solar factors at the two intensities. The choice of 10 suns as the factor for later experiments may not be valid either, since no experiments were conducted at 1 solar intensity. Nevertheless, accelerated tests are imperative for obtaining data in a reasonable amount of time.

Exposure Time

Solar absorptance changes of three paints are plotted against the logarithm of exposure (in ESH) in figure 11. The linear relationship between the absorptance change and the logarithm of exposure obeys the classical Hurter-Driffeld equation for photographic materials (ref. 7):

$$A = \gamma(\log E - \log i)$$

where A is the optical density; γ is the slope (the "contrast" in photography); E is the exposure, or product of intensity and time (in joules); and i is the inertia (in joules). Hirt, Schmitt, and Dutton (ref. 8) and Schmitt and Hirt (ref. 9) have discussed this relation for unpigmented and ultraviolet-absorber-containing films.

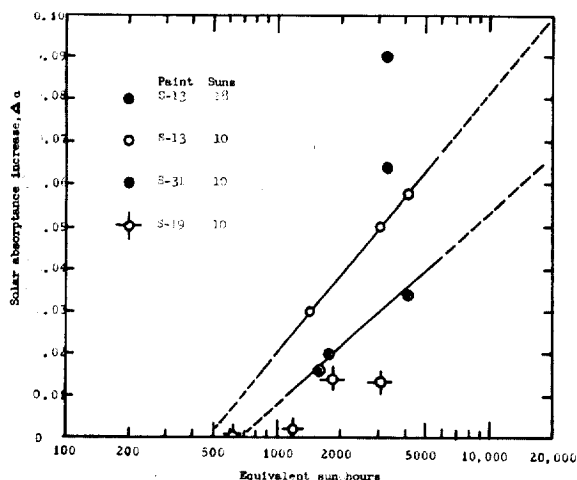


FIGURE 11.—Effect of ultraviolet irradiation in vacuum on solar absorptance of several zinc oxide-methyl silicone paints.

The usefulness of the Hurter-Driffeld relation is that it may permit extrapolation of the curves in order to determine the most extensive damage at long exposures. More work needs to be done on such extrapolation of data. As shown in figure 11, the long-term behavior of the less stable LTV-602-based paint, S-13, is more easily predicted by extrapolation than the behavior of more stable paints—especially S-19, which is one of the most stable coatings studied. The scatter in the data for S-19 precluded drawing a line through the points. As discussed earlier, the effects of contamination are more readily apparent in stable systems and are obscured in degradable systems, where their effects are less important.

Photolysis Mechanisms

PIGMENT

Much has been learned about zinc oxide and other oxides through studies of catalysis and photoconductivity, but rates of separation of photolyzed metal and oxygen are not known. It is conceivable that solar radiation might produce negligible photolysis, even in the high vacuum of space.

The problem of preventing the undesired photolysis is essentially the opposite of trying to make a good photoconductor or semiconductor. Light produces an excited state or nonequilibrium condition which persists for a relatively long time in a photoconductor. During this time atoms in the lattice may diffuse to more stable sites. For example, silver in silver bromide diffuses toward segregated silver metal particles, which grow as photolysis proceeds. If the diffusion of the silver were more restricted, the photolysis would be less efficient. A zinc oxide of high solar stability should therefore be a poor photoconductor, and the diffusion rate of excess zinc (actually interstitial Zn^{+}) should be low.

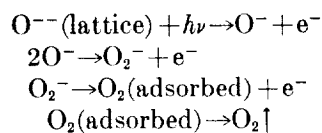
In the following discussion zinc oxide is used as the prime example because it has been studied more than any other metal oxide, but the principles involved apply to magnesium oxide, zirconium dioxide, titanium dioxide, and other oxides suitable for pigments. A con-

sistent picture of zinc oxide behavior has been worked out only in the past few years.

Collins and Thomas (ref. 10) have analyzed the behavior of zinc oxide. It is normally an n-type conductor. When its surface absorbs oxygen, a negative surface layer composed of oxygen ions forms and an electron depletion layer or space charge develops below the surface. Diffusion of photolysis products proceeds in this depleted layer. On the other hand, when the surface is reduced with hydrogen or absorbs zinc atoms, a conductive "enrichment" layer with a high concentration of donors forms near the surface. An enrichment layer having the same characteristics can be produced by photolysis. The light produces hole-electron pairs which break up and diffuse in the surface field. The holes discharge surface oxygen ions and generate oxygen molecules which then evaporate. Further photolysis releases oxygen from the lattice and leaves excess zinc. This zinc remains dissolved in the lattice, at least in the early stages of photolysis, as interstitial Zn^+ ions. These ions are not stable in the presence of oxygen, and they are concentrated in the centers of the crystals. The high free-electron concentrations that are generated by light tend to discharge Zn^+ ions and precipitate zinc metal, but other factors may hinder this reaction. The rate of diffusion of the Zn^+ is particularly important.

There is some evidence that the stability of oxide pigments may depend almost entirely on the binding energy and reaction rate of peroxide-type ions on the surfaces of the pigments. Peroxide is readily detectable on zinc oxide (after exposure to light) by the starch-iodide test.

Since O_2 is observed to be evolved in a vacuum system when zinc oxide is irradiated with ultraviolet the following steps may be postulated for photolysis:



On titania we have not been able to detect peroxide, but Ag^+ reacts (in light) to form AgO . The silver ion probably combines directly with

O^- . In order to make titania more stable, the O_2^- state should be made more stable, or the O_2^- concentration might be increased by adding peroxide additives.

If O_2^- is strongly bonded to the surface of the oxide, photolysis would be inhibited. Perhaps it is significant that zinc does form a peroxide by nonphotolytic reactions. Since hydrogen peroxide is notoriously sensitive to surface catalytic decomposition much about the stability of O_2^- (and HO_2) on surfaces can probably be learned from the observed stabilities of hydrogen peroxide in the presence of various surfaces.

Past work on the photolysis of silver bromide is helpful in analyzing possible mechanisms in pigments. Large single crystals of oxides show less photolysis than powders subjected to the same exposure. In silver halides the silver ions near imperfections or surfaces are more vulnerable to reduction by free electrons generated by light than silver ions at normal lattice sites. These surface or imperfection effects could be important in the photolysis mechanisms of oxides. At one surface, free oxygen may be generated; at another surface less exposed to the light or more favorable for metal separation, the free metal may separate. In other words, light generates electric field and concentration gradients which are equalized by the separation of the elements in the oxide. In fact, an analogous argument can be advanced for the reason why quartz windows are virtually unaffected by ultraviolet irradiation in vacuum but powdered quartz (silica) is severely degraded. A similar argument can be advanced with respect to the relative degradations of magnesium oxide windows and magnesium oxide powder.

In silver bromide the photolysis is sensitized by small islands of silver sulfide, gold, or silver itself. These islands trap electrons, which later reduce silver ions. Trapping is important because it increases the lifetime of chemically active excess carriers. When zinc oxide is made so that small islands of zinc metal remain in the oxide crystals, these crystals might be unusually sensitive to photolysis. This sensitivity could mean that once photolysis produces metal, further photolysis of the satellite coating might be rapid and catastrophic.

When zinc oxide crystals are exposed to zinc vapor at elevated temperatures and cooled rapidly to room temperature, they acquire a red or yellow color due to "dissolved" excess zinc. From conductivity data, Thomas (ref. 11) determined the concentration of excess zinc in equilibrium with zinc metal at temperatures of 450° to 700° C. Data from his plot of solubility (in atoms of excess zinc per cubic centimeter of the crystal) are recorded in table XVII. Photolysis by light in a vacuum can produce the same excess zinc concentrations.

When crystals which have been exposed to zinc vapor are quenched, why does the zinc not segregate? The diffusion coefficient for interstitial excess zinc in the temperature range from 180° to 350° C is given by Thomas as:

$$D = 2.7 \times 10^{-4} \exp(-0.55/kT)$$

where kT is in electron volts. At 300° K, $D = 7.3 \times 10^{-14}$. For a sphere of radius 10^{-5} cm around a zinc metal particle, the concentration gradient might be about 10^{22} atoms of interstitial zinc per cubic centimeter per centimeter in photolyzed material. Such a gradient could exist over a distance of 10^{-5} cm between yellow zinc oxide and the surface of a segregated zinc particle. This condition corresponds to a transfer rate of about 0.02 atom of excess zinc per second to the zinc particle. A zinc particle of 100-Å radius would require about 1.2×10^7 sec, or 140 days, to be built up under these conditions. In other words, if nucleation started, darkening due to metal separation could develop

over a period of months at 300° K. This slow diffusion rate of interstitial zinc may be responsible for the apparent stability of quenched zinc oxide crystals that contain excess zinc.

Particularly significant is the effect of interstitial zinc produced by photolysis on the lifetime of excess carriers generated by light. Although a hole has the same positive charge as interstitial Zn^+ , high polarization effects around an interstitial Zn^+ may favor hole capture and recombination. If this is the case, the stability of zinc oxide in light may stem from this increased recombination after a certain concentration of interstitial Zn^+ is produced by the light. In magnesium oxide, aluminum oxide, and zirconium oxide, which are more easily photolyzed by light, interstitial cations are not readily formed, either because of the compact lattices or because of the large size of the Zr cations. This means that magnesium, aluminum, and zirconium are not as soluble in their oxides as zinc is in zinc oxide. Since there are ways of reducing excess carrier lifetime by adding impurities different from the host cation, the addition of impurities is of interest. Such methods have been tried, but much work remains to be done on correlation with the types and quantities of impurities added.

BINDER

Since the predominant photochemical reactions in a high vacuum are cross-linking and color center formation, large changes in the physical properties of plastic structural members will not occur in a vacuum, particularly in the absence of any accompanying thermal effects. Thus, for polymeric materials which do not undergo catastrophic main-chain cleavage, the predominant physical changes will be discoloration and surface embrittlement as a result of cross-linking. The cross-linking can be considered as self-limiting, since the polymer material acts as a filter which possesses a high extinction coefficient for ultraviolet, particularly for the more damaging, shorter wavelengths.

Thus, the primary concern in the utilization of pigmented organic, semiorganic, and in-

TABLE XVII.—Solubility of Zinc in Zinc Oxide From Saturated Vapor

Temperature, °C	Zinc concentration, atoms/cc
800	3×10^{17}
600	6×10^{16}
500	2×10^{16}
400	5×10^{15}
300	8×10^{14}
162	10^{13}
72	10^{11}

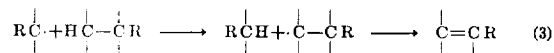
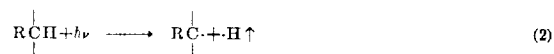
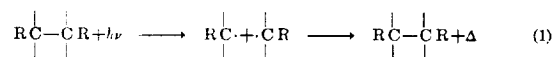
organic coatings for the purposes of spacecraft thermal control is the prevention of color center formation (that is, coloration which increases the solar absorptance). The secondary concern is the prevention of erosion of the surface due to main-chain cleavage, side-chain cleavage, or both.

The aim of photochemical investigation is to determine the mechanisms associated with the chemical change which occurs when a substance absorbs ultraviolet light. The reactions are complex, and the actual change measured is seldom that produced by the primary process of light absorption. Therefore, it is necessary to distinguish between the *primary* effect of ultraviolet and the *secondary* thermal reactions which follow. The frequent production of atoms or radicals in photochemical processes leads to extremely complex secondary reactions.

The basic difficulty in studying the formation of radicals in solids was pointed out by Franck and Rabinowitch (ref. 12), who discussed the cage effect. This effect, often described as the Rabinowitch cage effect, is associated with the framing of a free radical by its surrounding molecules in such a way that free-radical recombination prevails. Such an effect may account for the fact that the gamma irradiation of higher hydrocarbons at 77° K results in the cleavage of C—H rather than of the weaker C—C bonds (refs. 13 and 14). That is, the cage effect may permit the diffusion of hydrogen and simultaneous trapping of the larger carbon radicals, which subsequently recombine.

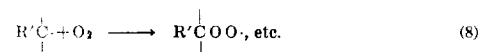
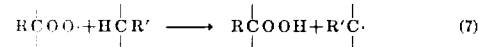
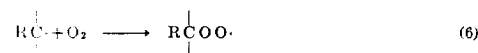
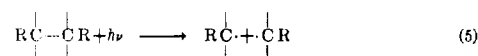
The predominant reaction in the photo-induced decomposition of polymers in the presence of oxygen is oxidative, unless the polymer unzips to yield monomer. The quantum yields in the absence of oxygen are much lower than in its presence, due to the cage effect. When C—C bonds are part of the polymer backbone, they cannot diffuse away rapidly enough and, as a general rule, recombination and cross-linking occur. By contrast, when a C—H bond is broken, the hydrogen atom formed is highly mobile and the statistical probability of recombination is reduced. Thus, the eventual reaction is the production of a molecule of hydrogen and the formation of a new cross-link, representing the combination

of two volatile (hydrogen) fragments and two residual, nonvolatile fragments, respectively. This does not preclude the existence of various chain transfer steps as intermediate reactions, but these do not contribute to the net reaction.



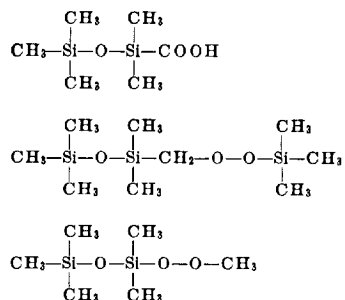
Thus, the creation of stable molecular species is encouraged by: (a) back reaction, (b) cross reaction, and (c) molecular rearrangement. Should the heavier radicals (RC· or ·C—CR in eq. 2 and 3) be sufficiently immobilized, or trapped, the possibility of providing a permanent color center in the absence of oxygen or a similar reactive substance is apparent. Lawton et al. (ref. 15) claim that radical trapping in polymer systems occurs under three conditions: "(a) within the crystallites of the polymer, (b) in the amorphous phase below the glass transition temperature, and (c) in heavily cross-linked polymers, because they may be attached to a network structure in a position in which no other radical is accessible."

In the presence of oxygen, the possibility of chain scission is much greater due to the irreversibility of the reaction with oxygen. Moreover, this reaction is a chain reaction and can therefore be expected to have a higher quantum yield.



Miller (ref. 16) has shown by electron spin resonance that irradiated polyvinyl chloride which has been exposed to air loses radicals at a far greater rate than samples treated similarly in a vacuum. Chapiro (ref. 17) reports a lack

of coloration of the material when it is exposed to air and attributes it to the formation of the peroxy radical. St. Pierre and Dewhurst (ref. 18) found it possible to totally inhibit the formation of C—C cross-links by the introduction of sufficient oxygen. These same authors, in another paper (ref. 19), describe the oxygen termination of free radicals in irradiated siloxane. They found a carboxylic acid and two types of peroxides were formed during radiolysis of hexamethyldisiloxane:



The foregoing analysis provides a general picture of the various possible photochemical reactions and their complexity, against which the results of this program can be evaluated. Upon irradiation with ultraviolet in vacuum, the methyl silicones proved to be among the most resistant materials known. This is not surprising, since short alkyl groups (for example, methyl) are inherently more transparent to extraterrestrial ultraviolet than both longer-chain alkyl and phenyl groups. Finally, the

-Si-O-Si-O backbone possesses a quartzlike structure which is both relatively transparent to ultraviolet and at the same time is thermally resistant.

Binder-Rich Layers (Gloss)

A protective effect of increasing PVC on ultraviolet stability was demonstrated. Yellowing of zinc oxide pigments was shown to be inversely dependent on PVC. Since ultraviolet damage occurs only in the outermost layers (approximately 5μ) of these paints and since some pigment probably settles before the vehicle sets, an unprotected, pigment-deficient (glossy) layer might contribute to the observed degradation.

Accordingly, an experiment was designed to determine the extent of the contribution to degradation of a pigment-poor layer, if present. For the purposes of defining the problem, a moderately degradable paint was chosen rather than one of the more stable coatings. Four 1×3 inch aluminum panels were abraded and coated with paint S-1, a zinc sulfide methylphenyl silicone with a PVC of 40 percent. The coatings were applied at thicknesses in excess of 3 mils, allowed to air-dry for 24 hours, and then baked at 300°F for 16 hours and at 400°F for 2 hours. Two of the coatings were gently scraped with a razor blade in order to remove the top layers; approximately 0.5 mil was removed.

The results after exposure to a simulated space environment are presented below. The

TABLE XVIII.—Effect of Removal of Glossy Layer on Reflectance of Paint S-1

Glossy layer	Exposure, ESII*	Reflectance, percent				
		400 $m\mu$	440 $m\mu$	500 $m\mu$	600 $m\mu$	700 $m\mu$
Present.....	0	72.0	83.9	88.0	87.6	59.0
	315	35.5	50.8	68.6	81.5	59.2
Present.....	0	72.0	82.5	85.0	83.5	58.8
	315	39.0	53.2	68.5	78.2	58.0
Scraped off.....	0	75.0	86.4	89.3	88.7	60.0
	315	51.2	66.2	78.6	85.4	60.0
Scraped off.....	0	73.0	84.1	86.3	84.7	59.5
	315	44.5	59.0	73.0	80.5	58.5

*Equivalent sun-hours.

data (table XVIII) indicate that a pigment-deficient glossy layer was originally present and that it contributed significantly to the degradation of the untreated samples. The higher reflectance of the scraped samples than of the untreated samples before exposure to space simulation is further indication of the existence of a binder-rich layer. Although the existence of a binder-rich layer is not as serious in the more stable zinc oxide-pigmented methyl silicones (e.g., LTV-602), it will be significant when such paints are exposed to 4000 or more ESH.

ACKNOWLEDGMENTS

This work was sponsored by the Jet Propulsion Laboratory of the California Institute of Technology under Contract 950111 (Subcontract under NAS7-100). The authors wish to acknowledge the valuable assistance of Dr. Caroline D. Miller, Mr. Harold L. Rechter, O. Harry Olson, Richard J. Larson, William C. Stepp, Douglas G. Vance, and Dr. Klaus Guenther. The valuable contributions of William F. Carroll, JPL Cognizant Engineer, are gratefully acknowledged.

REFERENCES

1. FORSYTHE, WILLIAM ELMER: Smithsonian Physical Tables. 9th ed., Smithsonian Inst., Wash. D.C., 1954.
2. NICOLET, M.: Chapter XII of Solar Physics and the Atmosphere of the Earth, C. S. White and O. O. Benson, Jr., eds., Univ. New Mexico Press (Albuquerque, New Mexico), 1952.
3. MIDDLETON, W. E. KNOWLES, and SANDERS, C. L.: The Absolute Spectral Diffuse Reflectance of Magnesium Oxide. *Jour. Optical Soc. of America*, vol. 41, no. 6, June 1951, pp. 419-424.
4. SANDERS, C. L., and MIDDLETON, W. E. KNOWLES: The Absolute Spectral Diffuse Reflectance of Magnesium Oxide in the Near Infrared. *Jour. Optical Soc. of America (Letters to the Editor)*, vol. 43, no. 1, Jan. 1953, p. 58.
5. ROCHOW, E. G., and GILLIAM, W. F.: Polymeric Methyl Silicon Oxides. *Jour. American Chem. Soc.*, vol. 63, no. 3, March 1941, p. 798.
6. BRADY, A. P., HUFF, HARRIETTE, and MCBAIN, J. W.: Measurement of Vapor Pressures by Means of Matched Thermistors. *Jour. Physical & Colloid Chemistry*, vol. 55, no. 2, Feb. 1951, pp. 304-311.
7. MEES, C. E. KENNETH: The Theory of the Photographic Process. The Macmillan Co., 1942.
8. HIRT, R. C., SCHMITT, R. G., and DUTTON, W. C.: Solarization Studies on Polyester Resins Using a Heliostat-Spectrometer. *Jour. Solar Energy*, vol. 3, no. 2, April 1959, p. 19.
9. SCHMITT, R. G., and HIRT, R. C.: WADD-TR-60-704, U.S. Air Force, Feb. 1961.
10. COLLINS, R. J., and THOMAS, D. G.: Photoconduction and Surface Effects With Zinc Oxide Crystals. *Phys. Rev.*, vol. 112, no. 2, Oct. 1958, pp. 388-395.
11. THOMAS, D. G.: Interstitial Zinc in Zinc Oxide. *Jour. Phys. Chem. Solids*, vol. 3, nos. 3 & 4, Pergamon Press, 1957, pp. 229-237.
12. FRANCK, J. and RABINOWITCH, E.: Some Remarks About Free Radicals and the Photochemistry of Solutions. *Trans. Faraday Soc.*, vol. 30, no. 152, Jan. 1934, p. 120.
13. NORMAN, IRWIN, and PORTER, GEORGE: Trapped Atoms and Radicals in a Glass "Cage". *Nature*, vol. 174, no. 4428, Sept. 11, 1954, pp. 508-509.
14. SMALLER, B., and MATHESON, M. S.: Paramagnetic Species Produced by γ -Irradiation of Organic Compounds. *Jour. Chem. Phys.*, vol. 28, no. 6, June 1958, pp. 1169-1178.
15. LAWTON, E. J., BALWIT, J. S., and POWELL, R. S.: Effect of Physical State During the Electron Irradiation of Hydrocarbon Polymers. Part I. The Influence of Physical State on Reactions Occurring in Polyethylene During and Following the Irradiation. Part II. Additional Experiments and Discussion Pertaining to Trapped Radicals in Hydrocarbon Polymers. *Jour. Polymer Sci.*, vol. 32, no. 125, Nov. 1958, pp. 257, 277.
16. MILLER, A. A.: Radiation Chemistry of Polyvinyl Chloride. *Jour. Phys. Chem.*, vol. 63, no. 10, Oct. 20, 1959, pp. 1755-1759.
17. CHAPIRO, A.: Action of γ -Rays on Polymers in the Solid State. Part III. Irradiation of Poly (Vinyl Chloride). *Jour. Chim. Phys.*, vol. 53, no. 11-12, Nov. -Dec. 1956, p. 895.
18. ST. PIERRE, L. E., and DEWHURST, H. A.: Oxygen Effects in the Radiation Chemistry of Polyethylene. *Jour. Chem. Phys. (Letters to the Editor)*, vol. 29, no. 1, July 1958, pp. 241-242.
19. ST. PIERRE, L. E., and DEWHURST, H. A.: The Effect of Oxygen on the Radiolysis of Silicones, *Jour. Phys. Chem.*, vol. 64, no. 8, Aug. 17, 1960, pp. 1060-1062.

DISCUSSION

Since Papers 40, 41, and 42—by Parker, Neel, and Golub; by Zerlaut, Harada, and Tompkins; and by Olson, McKellar, and Stewart—dealt with related topics, discussions of the first two papers were postponed until after all three papers had been presented.

42. The Effects of Ultraviolet Radiation on Low α_s/ϵ Surfaces

R. L. OLSON, L. A. MCKELLAR, AND J. V. STEWART

LOCKHEED MISSILES & SPACE COMPANY, PALO ALTO, CALIF.

A primary source of natural environmental damage to spacecraft thermal-control surfaces is solar ultraviolet energy. An experimental investigation of this damage is described. The primary purposes of this work are (1) the evaluation of candidate materials and (2) the prediction of operational behavior for selected materials. Candidate surfaces are exposed in vacuum to near-ultraviolet energy; the effect of these exposures on the materials' normal spectral reflectance is determined. The primary energy source is the A-H6 mercury-argon high-pressure lamp; this is used bare and with filters. Incident fluxes are determined with calibrated phototubes and with thermopiles. Sample ambient pressures are maintained at 10^{-6} to 10^{-7} torr; sample temperatures are varied from 70° F to 500° F. Incident flux densities are varied tenfold.

Both initial damage and damage reversibility (bleaching) are investigated. Efforts are concentrated on white pigment-vehicle binary systems which are candidate low α_s/ϵ spacecraft surfaces. Results demonstrate the dependence of damage upon wavelength of irradiation and upon sample temperature. Materials studied include silicate, silicone, acrylic, and epoxy vehicles, and titania, zinc oxide, zirconium silicate, and lithium-aluminum-silicate pigments. Conclusions are drawn regarding the energetics and kinetics of the damage processes.

Ultraviolet radiation from the sun is a primary cause of damage to thermal control surfaces in an orbital environment. This damage is most severe for surfaces selected to provide a low ratio of solar absorptance α_s to emittance ϵ . An experimental program has been in progress to investigate this damage. This program has as its primary goals (1) the evaluation of candidate materials and (2) the prediction of operational behavior for selected materials. To aid in the achievement of both goals, insight into damage processes is also sought.

Samples of surfaces to be studied are exposed in high vacuum to near-ultraviolet radiation. The exposure time, irradiation flux density and spectral distribution, and sample temperature are varied. In addition, exploratory post-exposure bleaching studies have been performed. Primary criteria for damage in this study are changes in solar absorptance α_s , and in

spectral absorptance α_λ . Room-temperature emittance ϵ has not been observed to be measurably affected.

In order to provide engineering design data, the results of ultraviolet studies are generally interpreted as if simulation of pertinent constituents of the orbital environment were achieved. It must be noted, however, that precise environmental simulation is never achieved in the laboratory. The most notable discrepancy is the spectral dissimilarity between extraterrestrial solar radiation and the output of sources suitable for material screening and development studies. Furthermore, there is evidence that (1) the observed changes in radiative properties may result from several reactions and (2) the dependence of the reactions on irradiance wavelength is likely to be different for each reaction and each material. Therefore, even if one assumes that all significant sources of orbital damage to thermal control surfaces are

found in the laboratory test chamber, a straightforward prediction of behavior in space from laboratory data is not possible. Large uncertainties in predictions of surface stability in orbit result. Both to reduce these uncertainties and to guide material development programs, information on the energetics and mechanisms of ultraviolet damage is desired. The work reported herein, therefore, seeks to investigate the damage processes as well as provide engineering design data.

EXPERIMENTAL EQUIPMENT

Ultraviolet Source

The source of ultraviolet radiation is a 1-kw A-H6 (PEK Laboratories type C) mercury-argon-arc, high-pressure, high-intensity lamp. Approximately 30 percent of this lamp's radiant energy is in the range of 2000 to 4000 Å (ref. 1 and 2). In comparison, roughly 9 percent of the extraterrestrial solar spectrum is believed to lie in the same wavelength range (ref. 3). The lamp is water-cooled and has a quartz water jacket and velocity tube. This assembly is lowered into a quartz envelope extending into the exposure chamber from the top. The lamp assembly can be withdrawn to change lamps without disturbing the vacuum in the system.

Detector and Monitor

The ultraviolet intensity is monitored with calibrated phototubes (RCA 935) that are filtered to detect energy in the 2000- to 4000-Å interval; Corning 7-54 filters are used to pass only near-ultraviolet radiation. In this way only the radiation believed to produce serious damage is monitored routinely. It should be noted that the A-H6 lamp output decreases with time more in the short- than in the long-wavelength regions. Neutral-density filters are used to reduce the flux density incident on the detector, in order to avoid saturation of the phototube. The phototubes have been calibrated by actinometry and with a thermopile. The output of the phototubes is automatically measured and recorded for a few minutes every hour with a recording microammeter. When desired, a Corning 0-54 filter is used to compare the intensity in the 2000- to 3000-Å region with that in the 3000- to 4000-Å region.

Chamber and Vacuum System

The exposure chambers are metal bell jars 14 inches high by 14 inches in diameter mounted on 18-inch base plates. The sample holders are water-cooled copper blocks mounted at different distances from the ultraviolet radiation source. Three exposure chambers are used. In two of these chambers pairs of sample holders are permanently installed at 3.0, 4.6, 7.5, and 11.2 inches from the source. These distances give nominal irradiances of 10, 5, 2, and 1 "suns" of ultraviolet energy. A flux density of one "sun" of near-ultraviolet radiation is herein defined as the flux density of extraterrestrial solar radiation at 1 astronomical unit from the sun, in the wavelength interval from 2000 to 4000 Å. In the other chamber, 24 sample holders are located 3.9 inches from the source for a nominal flux density of 6 "suns." (The "sun" is admittedly an unsatisfactory unit of flux density; it will be used for convenience in comparing data herein with those of other investigators.)

Normally, water is passed through copper tubes soldered to the sample holders. This maintains the specimen temperatures between 65° and 95° F, depending on the tap-water temperature and the ultraviolet irradiance at the sample holders. At the 10-"sun" position, with no cooling except by radiation to the chamber walls and by conduction through the sample holder to the base plate, the steady-state sample temperature is about 500° F. Through controlled use of cooling water and additional conduction paths from the sample holders, specimen temperatures between 90° and 500° F can be achieved. For cryogenic temperatures liquid nitrogen can be passed through the cooling tubes.

Pressures in the range of 10^{-6} to 10^{-7} torr are maintained with electronic high-vacuum pumps using standard vacuum techniques.

Spectral and Reflectance Measurements

Normal spectral reflectance measurements are performed with a Cary model 14 spectrophotometer with integrating sphere attachment. The solar irradiance data of F. S. Johnson (ref. 3) were used as the basis for calculations of

solar absorptance and of 1 "sun" of ultraviolet irradiance.

EXPERIMENTAL RESULTS

In the discussion of experimental results, the solidus (/) is used to separate the pigment from the binder, as TiO_2 /epoxy, titania pigment with an epoxy binder.

Exposure Dependency of Damage

Ultraviolet radiation exposure is herein defined as the product of ultraviolet irradiance of the sample and exposure time. The unit of exposure is sun-hours. Degradation increases with increasing irradiance and with increasing exposure time.

The usual working assumption is that resultant damage does not depend upon the rate of energy deposition; that is, exposure to 1 "sun" for 10 hours will produce the same effect as exposure to 10 "suns" for 1 hour. This assumption serves as a useful first approximation; it has not been verified for the materials under discussion. At least part of the difficulty in attempting to prove or disprove a *rate-dependence* of damage to a given material lies in lamp-to-lamp spectral output variations and temporal spectral shifts of a given lamp output.

Plots of solar absorptance α_s against exposure ("sun-hours") for six materials are given in figure 1. The exposure times were 50 to 275 hours with nominal irradiances of 1, 2, 5, and 10 "suns." The assumption of no rate-dependence is made. Even if this were not true, the comparison of degradation of materials at the same high irradiance should reflect their relative stability for screening purposes.

In general, the solar absorptance increases with exposure but at a decreasing rate and appears to approach a saturation value that is less than unity (usually between 0.2 and 0.6). The materials are described more completely in table I. It should be noted that the three commercial paints are off-the-shelf-materials which were not originally developed for spacecraft use. Their immediate availability, ease of application, and low cost are major reasons for their selection. More importantly, for short-lived vehicles (less than 1-month orbital

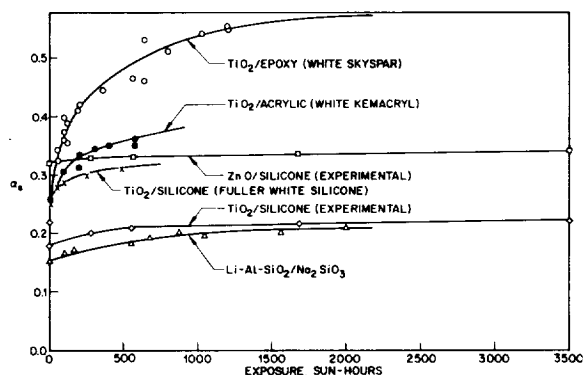


FIGURE 1.—Increase of solar absorptance with exposure to ultraviolet radiation, for six white coatings.

lifetime) or spacecraft surfaces where a certain amount of environmental damage is permissible, these materials have provided successful thermal control.

The data demonstrate the general superiority of silicate and silicone systems to those with organic binders. These data are representative of the data employed for engineering design use (for example, the data of ref. 4).

While the increase in solar absorptance is of practical importance, the spectral changes in absorptance are of interest in the study of processes involved in degradation. Figures 2, 3, 4, 6, 7, and 8 show data representative of the alterations occurring in the spectral absorptance of white engineering surfaces as a result of exposure to the A-H6 lamp. In figure 2, it is seen

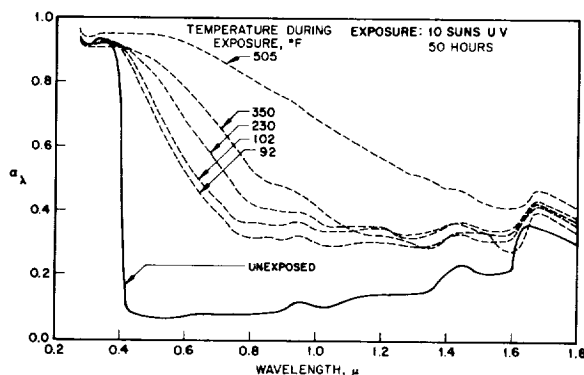


FIGURE 2.—Temperature effect on the change in spectral absorptance induced by ultraviolet radiation. TiO_2 /epoxy coating; ultraviolet radiation intensity, 10 "suns"; exposure time, 50 hours.

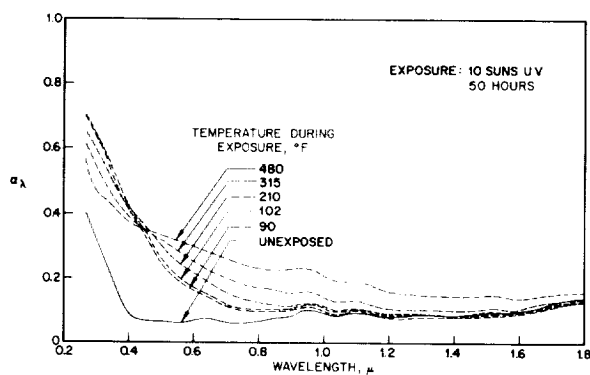


FIGURE 3.—Temperature effect on the change in spectral absorptance induced by ultraviolet radiation. $ZrO_2 \cdot SiO_2 / K_2SiO_3$ coating; ultraviolet radiation intensity, 10 "suns," exposure time, 50 hours.

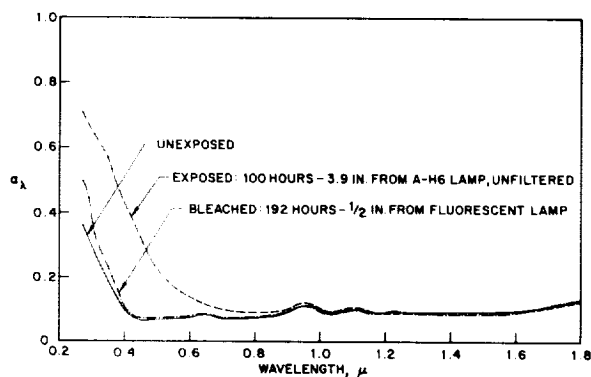


FIGURE 6.—Effect of ultraviolet radiation on spectral absorptance of $ZrO_2 \cdot SiO_2 / K_2SiO_3$ coating and effect of subsequent bleaching.

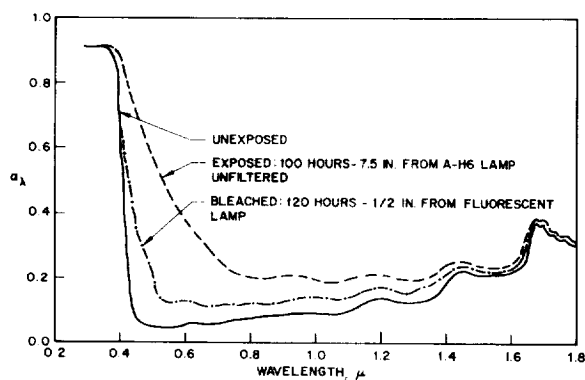


FIGURE 4.—Effect of ultraviolet radiation on spectral absorptance of TiO_2 /epoxy coating and effect of subsequent bleaching.

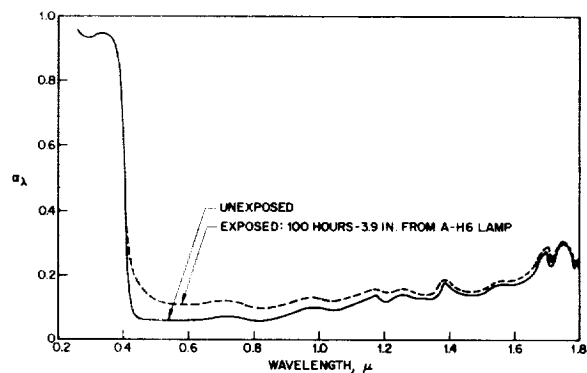


FIGURE 7.—Change in spectral absorptance of LMSC/Dow-Corning experimental TiO_2 /silicone coating induced by ultraviolet radiation.

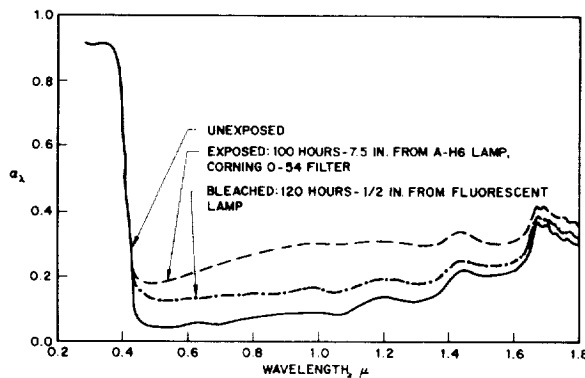


FIGURE 5.—Effect of filtered ultraviolet radiation on spectral absorptance of TiO_2 /epoxy coating and effect of subsequent bleaching.

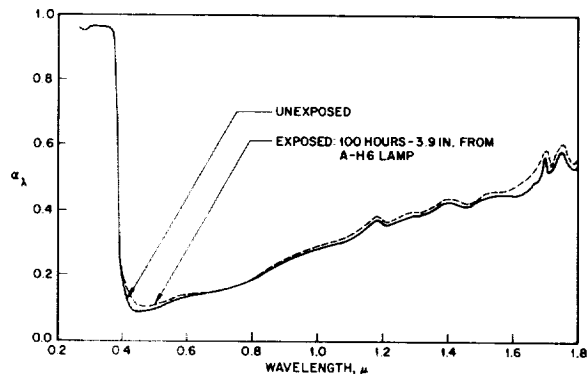


FIGURE 8.—Change in spectral absorptance of LMSC/Dow-Corning experimental ZnO /silicone coating induced by ultraviolet radiation.

TABLE I.—*Materials Investigated*

Pigment/binder	Source	Remarks
TiO ₂ /epoxy: White Skyspar Enamel (A423, color SA9185).	Andrew Brown-----	In LMSC production use on short-lifetime satellites; commercially available.
TiO ₂ /acrylic: tinted white Kemacryl Enamel (M49 WC17).	Sherwin-Williams-----	In LMSC production use; commercially available.
TiO ₂ /silicone: Fuller Gloss White Silicone (517-W-1).	W. P. Fuller-----	In LMSC production use; commercially available.
ZnO/silicone (experimental polymethylvinyl siloxane).	LMSC/Dow-Corning-----	Under development by Dow-Corning and LMSC.
TiO ₂ /silicone (experimental polymethylvinyl siloxane).	LMSC/Dow-Corning-----	Under development by Dow-Corning and LMSC; in limited use on LMSC/USAF satellites.
Li-Al-SiO ₃ /Na ₂ SiO ₃ -----	LMSC-----	Developed by LMSC; in use for special applications on LMSC/USAF satellites.
Synthetic Li-Al-SiO ₃ /K ₂ SiO ₃ -----	LMSC-----	Experimental LMSC paint.
Li-Al-SiO ₃ /K ₂ SiO ₃ -----	LMSC-----	Experimental LMSC paint.
ZrO ₂ ·SiO ₂ /K ₂ SiO ₃ -----	LMSC-----	Experimental LMSC paint.

that irradiation of the TiO₂/epoxy paint produces both an apparent alteration in the ultraviolet absorption edge and a general increase in absorptance. Figure 6 shows that the absorption edge of the ZrO₂·SiO₂/K₂SiO₃ is altered, but the absorptance is otherwise unaffected. Figures 7 and 8 show essentially no effect on the absorption edge of either the experimental TiO₂/silicone or the experimental ZnO/silicone, while a general increase in absorptance occurs throughout the visible and near-infrared spectrum (to 1.8 μ).

Temperature Dependency of Damage

Five samples of white surface coatings were exposed simultaneously to ultraviolet radiation at the same distance from the source. With different cooling paths for each sample holder the samples were maintained at five different temperatures in the range from about 90° F to 500° F during exposure. Spectral reflectance measurements were made after an exposure of 50 hours at a nominal intensity of 10 "suns" of near ultraviolet radiation. An unexposed sample was used as a control coating. Solar absorptances α_s were determined from the reflectance data. These, together with the increase in solar absorptance $\Delta\alpha_s$, are given in

table II. Five different materials were studied in this manner. Plots of the spectral-absorptance data for two of the five materials are shown in figures 2 and 3.

The increase in solar absorptance for a specific ultraviolet exposure, $\Delta\alpha_s$, has been correlated graphically to within ± 10 percent as a function of temperature according to the relationship:

$$\Delta\alpha_s = Ae^{-W/kT}$$

For those cases in which $\Delta\alpha_s$ increases nearly linearly with exposure, it can be shown that W can be considered an effective energy of activation for the temperature dependence of ultraviolet-induced changes in α_s . Specific values of W are related to specific ultraviolet exposures; extrapolation of these specific values to other exposures has not been confirmed. It should be noted that little physical significance can be attached to the value for A . The values of A and W are listed in table III.

The spectral-absorptance curves for the TiO₂/epoxy surface coating are shown in figure 2. An initial large change in absorptance due to exposure to ultraviolet radiation at 92° F is observed. Increasing the temperature at the same exposure causes a general

TABLE II.—Temperature-Dependency Data
(All samples exposed for 50 hours at 10 "suns")

Pigment/blinder	Temperature, ° F	α_s	$\Delta\alpha_s$
Synthetic Li-Al-SiO ₃ /K ₂ SiO ₃ : LMSC experimental paint	Unexposed	0.14	---
	90	.26	0.12
	99	.23	.09
	225	.29	.15
	338	.32	.18
	532	.39	.25
Li-Al-SiO ₃ /K ₂ SiO ₃ : LMSC experimental paint	Unexposed	.13	---
	88	.20	.07
	97	.21	.08
	215	.24	.11
	325	.27	.14
	500	.30	.17
ZrO ₂ ·SiO ₂ /K ₂ SiO ₃ : LMSC experimental paint	Unexposed	.09	---
	90	.19	.10
	102	.19	.10
	210	.21	.11
	315	.21	.12
	480	.26	.17
TiO ₂ /epoxy: White Skyspar enamel (Andrew Brown A423, color SA9185)	Unexposed	.20	---
	92	.50	.30
	101	.53	.33
	230	.58	.38
	350	.62	.42
	505	.78	.58
TiO ₂ /silicone: Fuller Gloss White silicone paint (517-W-1)	Unexposed	.21	---
	88	.34	.13
	101	.34	.13
	227	.42	.21
	362	.41	.20
	520	.52	.31

increase in absorptance with a fairly regular change in shape of the curve. A slight decrease in absorptance in the infrared region is noted. The shape of the curve at 505° F appears not to be an extrapolation from the shapes of the other curves, as if a different process or a different rate of degradation has begun, so extrapolation of the data beyond 500° F would be unwise.

The spectral absorptance curves for the ZrO₂·SiO₂/K₂SiO₃ surface coating in figure 3 show a large initial change in absorptance due to exposure to ultraviolet radiation at 90° F. As the exposure temperature increases, the absorptance increases in the visible and infrared regions of the spectrum but decreases in the

TABLE III.—Parameters Correlating Results of Temperature-Dependency Studies

Pigment/blinder	A	W, eV
Synthetic Li-Al-SiO ₃ /K ₂ SiO ₃ ----	0.78	0.053
Li-Al-SiO ₃ /K ₂ SiO ₃ -----	.50	.049
ZrO ₂ ·SiO ₂ /K ₂ SiO ₃ -----	.33	.032
TiO ₂ /epoxy-----	.78	.024
TiO ₂ /silicone-----	.93	.053

ultraviolet region. The net result is an increase in the solar absorptance with increasing temperature.

Irradiation Wavelength Dependency of Damage

Filters have been used with the A-H6 lamp to study the dependence of damage on photon energy. Pairs of identical specimens were placed side-by-side, at the same distance from the lamp, one specimen with a filter over it and the other one bare. Transmission spectra were obtained for all filters employed. The Corning 0-54 filter was used in these studies (ref. 5). Specific filters were found to have slightly different transmission spectra; this fact was used to advantage in controlling the sample spectral irradiance. Spectral reflectance data for samples before and after exposure were examined.

Often, but not always, exposure of materials to ultraviolet radiation in a vacuum caused the absorption edge to shift to longer wavelengths, as seen in figures 4, 5, 6, 7, and 8; subsequent exposure to visible light in air caused the absorption edge to shift to shorter wavelengths. The first process results in degradation, or an increase in solar absorptance for the material. The reverse process is a bleaching, or decrease in the solar absorptance. The overall energetics for the resulting effects on α_s are illustrated schematically in Figure 9. Such a diagram will apply strictly only if the photo effect is dominant.

The initial state is a white surface of low α_s . If this surface is exposed to photon energies greater than the threshold energy $h\nu_1$, the energy barrier is surpassed, and the process

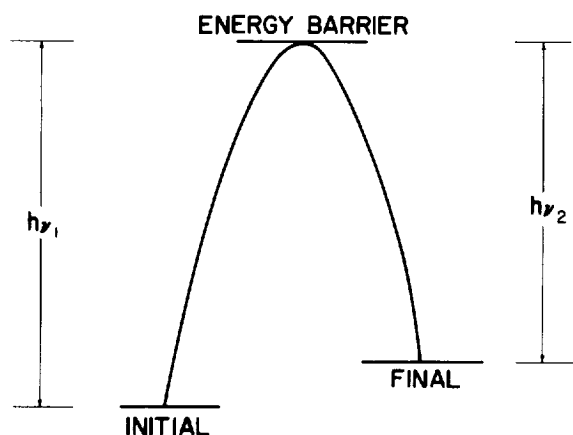


FIGURE 9.—Energetics of degrading and bleaching.

can proceed to the final state. This state is indicated by a shift of the absorption edge to longer wavelengths and an increase in α_s . Since $h\nu_2$, the threshold energy for the reverse process, is less than $h\nu_1$, the threshold energy for the forward process, the reverse process is also possible. However, the rate depends not only on the sufficiency of the photon energy but also on the probability that the photon is absorbed and that all of the reactants are present. Before degradation has occurred no bleaching is possible. As the degradation process proceeds, the rate of bleaching will increase. When the rates of the two processes are equal one would expect that an equilibrium would be reached.

The degradation experiments were done in vacuum and the bleaching experiments in air. This fact may be significant, depending on the processes involved. Optical damage could result from the breaking of oxygen bonds and subsequent removal of oxygen. In such cases the reverse reaction might be slow in a vacuum environment. Even if the photon energy $h\nu_2$ were available, significant bleaching might not occur. However, upon exposure of the degraded surface in air to photon energies greater than $h\nu_2$ and less than $h\nu_1$, the reverse process could proceed with no competition. The initial state would then again be achieved. It may be possible for the reverse process, with return to the initial state, to occur without air (or ambient oxygen) upon exposure to photon energies greater than $h\nu_2$ and less than

$h\nu_1$. It is hoped that this matter will be clarified by future work. Two statements should be made: (1) bleaching in the presence of air has been visually observed without purposeful irradiation with photons of energy $h\nu_2$, and (2) bleaching has been observed to be accelerated by intense irradiation with photons of energy $h\nu_2$.

From the initial exposure studies with different filters, it was possible to determine, within limits, the threshold photon energies necessary to produce movement of the absorption edge. The resulting values are listed in table IV.

TABLE IV.—Threshold Energies for Degrading (Movement of Absorption Edge)

Pigment/binder	$h\nu_1$, eV
Synthetic Li-Al-SiO ₃ /K ₂ SiO ₃ -----	4.3-5.4
Li-Al-SiO ₃ /K ₂ SiO ₃ -----	4.3-4.7
ZrO ₂ -SiO ₂ /K ₂ SiO ₃ -----	4.3-4.7
TiO ₂ /epoxy-----	4.2-4.4

From the subsequent bleaching work it can be shown that the reverse process can be accelerated by photon energies less than 3.9 eV; the lamp employed had a glass envelope, so that the samples were irradiated only by energies less than 3.9 eV. If the photoeffect were truly dominant and the presence of ambient atmospheric oxygen of little importance, $h\nu_2$ would then be established as less than 3.9 eV.

The exact processes of degradation and bleaching are not known at this time. As suggested, removal of oxygen from the pigment, and subsequently from the paint film, may be involved. The process of breaking one chemical bond and making another may be occurring, especially in polymeric materials. The production of electron-hole pairs in dielectrics like the pigments may occur. Subsequent trapping of freed electrons at imperfection sites can result in coloration.

The changes in the spectral-absorptance curve for the ZrO₂-SiO₂/K₂SiO₃ system (fig. 6)

suggest a single reversible process. With photon energies greater than $h\nu_1$ in vacuum, there is a marked increase in absorptance in the ultraviolet region. Photons with energies less than $h\nu_1$ did not cause this increase. In air, photons of energies less than 3.9 eV caused the original changes in the spectral-reflectance curve to be almost completely reversed.

In the TiO_2 /epoxy system photons with energies greater than $h\nu_1$ caused the absorption edge to shift to longer wavelengths (fig. 4). Photons with energies less than $h\nu_1$ did not (fig. 5), but the absorptance increased in the visible and infrared regions of the spectrum more than when photons of energies greater than $h\nu_1$ were present. Both changes were partially reversed upon exposure in air to photons with energies less than 3.9 eV. This more complicated behavior of the TiO_2 /epoxy system indicates that more than a single reversible process is involved. The threshold energy $h\nu_1$ given in the preceding table is for the absorption edge shift.

CONCLUSIONS

Low α_s/ϵ surfaces suffer an increase in α , upon exposure to ultraviolet radiation in vacuum; this damage increases with increase in ultraviolet flux density and with increase in exposure time. The supposition that damage depends upon the total energy absorbed, regardless of the rate of energy deposition, appears to be a valid working assumption for development of rough engineering data. It allows the use of accelerated tests in materials development and evaluation programs. Solar absorptances as a function of exposure in "sun-hours" increase at a decreasing rate and appear to approach a saturation value that is less than unity for all materials studied.

The degradation of samples of white surface coatings increased with increasing temperature

over the temperature range 90° to 500° F. The energies of activation corresponding to the increase in solar absorptance with temperature during exposure for the materials studied are estimated to be in the range from 0.02 to 0.05 eV. However, the spectral absorptance did not increase with increasing temperatures over the entire solar spectrum; in fact, in some regions the absorptance decreased.

For the silicate-pigmented, potassium-silicate-vehicle paints and the titanium-dioxide-pigmented, epoxy-vehicle paints, photon threshold energies for the apparent shift to longer wavelengths of the ultraviolet absorption edge have been found to be about 4.5 eV. This absorption-edge shift is a primary, but not the only, cause for the increase in solar absorptance. Bleaching in air for the same materials occurs with photon energies of less than 3.9 eV.

Further detailed studies are required to identify the first-order damage mechanisms in practical low α_s/ϵ materials. This information is desired both to improve predictions of operational performance based on laboratory data and to guide materials specialists in the development of optimum materials.

REFERENCES

1. CARROLL, W. F.: Development of Stable Temperature Control Surfaces for Spacecraft. Progress Report 1, Tech. Rep. No. 32-340 (Contract No. NAS 7-100), Jet Propulsion Lab., C.I.T., Nov. 20 1962.
2. Anon.: High-Brightness Mercury Arc Lamps, Capillary Tube A-H6 and B-H6. GET-1248I, General Electric Outdoor Lighting Department, Hendersonville, North Carolina, April 1962.
3. JOHNSON, FRANCIS S., ed.: Satellite Environment Handbook. Stanford Univ. Press, 1961.
4. Anon.: Thermophysics Design Handbook. Doc. 8-55-63-3, Lockheed Missiles and Space Co., July 1963.
5. Anon.: Glass Color Filters, Corning Bulletin CF-1, Corning Glass Works, Corning, New York, 1960.

DISCUSSION

Since Papers 40, 41, and 42—by Parker, Neel, and Golub; by Zerlaut, Harada, and Tompkins; and by Olson, McKellar, and Stewart—dealt with related topics, the discussions of the first two were postponed until after all three papers had been presented.

LEOPOLD CANN, Aerojet-General Corporation: Was the zinc oxide used in the pigment prepared by the French process or the American process? In other words, was the material acicular or nonacicular?

Secondly, how pure was the oxide? Most zinc oxide contains a little lead and possibly some cadmium. Such impurities would have quite an effect on the properties of the material.

ZERLAUT: The zinc oxide was New Jersey Zinc Company's SP 500, spectral grade oxide, which costs \$5.00 per pound. It is quite pure—about 99.9 percent—and is manufactured by the French process. It is nonacicular.

PARKER: Is it possible that as a consequence of grinding the zinc oxide pigment, defect sites are created in the zinc oxide, which can in some way catalyze the photochemical reaction of the silicone?

ZERLAUT: We are not ignoring this possibility. However, we doubt this to be the case (if you are referring to the slide which showed a decrease in ultraviolet-stability with length of grind). We attribute this primarily to silica contamination on grinding with a resultant loss in stability.

PARKER: Your change of α_s also increases with the degree of grind. Is this correct?

ZERLAUT: Yes. Zinc oxide paints yellow on grinding—particularly at high shear rates (as would be obtained in a mortar and pestle). We have heard that people who use our formulas have observed mill yellowing. We recommended reducing the ball charge and possibly grinding at a lower speed for a longer time. I understand that these techniques have usually solved their mill-yellowing problems. The yellowing, or discoloration, has been attributed to a spectral shift caused by lattice distortion induced by grinding.

WILLIAM HALL, Jet Propulsion Laboratory: Is there an effect of particle size on the stability of α ? In particular, I am curious about the grinding time. I may misunderstand that grinding curve.

ZERLAUT: It is a question of whether we obtain particle-size reduction by normal grinding or whether we obtain only deagglomeration. Rather high shear rates are required for particle-size reduction. I am talking about the primary particle as opposed to an agglomerate of particles. To answer your question, I would expect smaller particles to scatter ultraviolet more effectively (more deeply, too) and thus to increase the susceptibility of the paint to ultraviolet-induced damage.

BERND LINDER, General Electric Company: Mr. Olson, you indicated that the exposures were run at intensities of 1 to 10 suns. I wonder if any effect of the rate of exposure on $\Delta\alpha$ was found.

OLSON: We have made the assumption that 1 hour at 10 suns is equivalent to 10 hours at 1 sun. This reciprocity has never been completely verified. We are planning to do very carefully controlled experiments to determine whether this assumption really is valid. If it is, we can run accelerated tests with confidence. The present data do not seem to verify this. However, people have been defining one "sun" on the basis of the 2000-Å to 4000-Å interval. Probably, it would be more realistic to consider it from 2000 Å to 3000 Å because of the existence of threshold energies; thus, some are misstating intensity. Whenever the data are examined closely, they can be reinterpreted to indicate that a reciprocal relationship may exist.

Another effect is that due to the temperature. Some-

times, when reciprocity does not seem to hold, the temperature effect may be contributing. These are very stable systems, and I would be very surprised if this equivalence relation did not hold for flux densities of 10 suns, or somewhat less. For paints or for systems that are not so stable, I think there would be a rate effect. We plan to do experiments to verify this. We presently make the assumption of no rate dependence; and, although it seems to be a fairly good assumption, present data really do not precisely substantiate it.

ZERLAUT: Mr. Olson, I think that the secondary thermal effects are very difficult to weigh. Even in zinc oxide systems which we find are quite stable, we observe some influence of intensity. It is particularly difficult to determine these effects for the more stable systems because of scatter in the data; we are dealing with very small changes in α . Furthermore, we have no idea what the effective temperature is in the few microns where the damage occurs. Perhaps Dr. Parker has some comments at this point.

PARKER: I have a comment which pertains to Mr. Olson's quantitative interpretation in matching the lamp spectrum with the solar spectrum. My understanding is that, for 1 sun, the total energy from the A-H6 lamp in the wavelength range between 2000 and 4000 Å was matched with that under the Johnson curve from 2000 to 4000 Å. Now, if we consider the photochemically productive region, we see that there is a five-fold increase in the amount of energy available if we match the 2000- to 3000-Å region. Consequently, we can treat this as otherwise independent of the material only when we know precisely the photochemically productive region, when we know the quantum efficiency, and when we know the cutoff wavelength. It is these three factors—which I think we know for polyvinyl chloride—that we are seeking in examining its properties.

OLSON: I believe I forgot to mention that the A-H6 lamp degrades more in the 2000-Å to 3000-Å region than in the rest of the spectrum. This is why, in reporting our intensity, we can be in error when discussing simulation. The lamp degrades more rapidly in the short-wavelength region than in the longer-wavelength region.

R. D. JOHNSON, Northrop Space Laboratory: Dr. Parker, in figure 10 of your written report, on the equivalence of the gamma and ultraviolet irradiation, were the exposures under similar conditions of temperature, or of vacuum?

PARKER: They were exposed at the same temperature. The dosimetry for the gamma rays is based on the total number of ergs/g(C). The figure shows how we are now comparing the two kinds of radiation; and I think the comparison is very interesting, since it means that I can simulate the effects of gamma irradiation with a brief ultraviolet irradiation. In addition to establishing the equivalence between the gamma irradiation and the ultraviolet irradiation, we have recently examined the effect of the vacuum ultraviolet and we see that a similar equivalence can be established over a considerable wavelength region. Our explanation for this is

that the same primary excited state is involved in all of these energy processes and what one has is the degradation of the higher energy to secondary low-lying energies that excite the same equivalent primary state. As a matter of fact, if I compare my doses—the actual number of electron-volts deposited in the cases of the ultraviolet and the gamma—it appears that the same chemical effects are produced by approximately the same total doses. The temperature and vacuum, however, are held constant.

JOHNSON: What were the temperature and vacuum?

PARKER: The vacuum was around 10 to 40 microns and the temperatures averaged between 25° and 35° C. We really saw no effect of the temperature change here. For the overall rate of change of α , as Olson pointed out, there is an activation energy of maybe 900 calories to 1,000 calories.

I think that our figure 10 is a very interesting plot. The ordinate is the ultraviolet radiation dose at constant flux, in hours, and the abscissa is the change in optical density at each of the wavelengths. We took an average point for each one of these wavelengths and found the gamma radiation dose to produce an equivalent change in optical density; and then with the aid of a Gerber scale we set up these equivalencies at each one of these wavelengths. So one can actually construct an equivalence in this manner.

We also have been able to show that the rate of development of the total opacity envelope is exactly the same in both cases. That is, the total absorbed dose required to increase that envelope is about the same for both the ultraviolet and the gamma radiations. It is not exclusively wavelength dependent (as appears here), but I think that there is pretty good agreement at the three different wavelengths, and the figure shows, for example, that it takes much more gamma radiation to change the film absorption at 4400 Å than it does to change it at 3400 Å. But we think that we have here, possibly, a space dosimeter; that is, when we get this all unravelled, we will be able to count the total effect of both high energy particles and ultraviolet radiation.

GERHARD B. HELLER, NASA Marshall: Could someone comment on the difference between the inorganic systems that we have here and the organic systems with respect to quantum yield and with respect to chemical or physical effects?

ZERLAUT: We have not measured quantum yields. We hope to determine the activation spectrum for simple coatings made from these two systems in the near future. I think you appreciate the fact that when we work with an alkali silicate and a silicone, we are working with two systems that are not greatly different. The silicones apparently degrade through a free-radical photolysis reaction, whereas the mechanisms associated with alkali silicate photolysis are not well understood but probably involve solid state reactions similar to those of the inorganic pigments.

PARKER: We can produce, with gamma radiation, the same change in the visible absorption spectra in a

glass as in the polymer itself. The action of the gamma irradiation of polyvinyl chloride is to produce a conjugated double bond (alternate double bond) system along the polymer chains. In these conjugated double bond structures the π electrons are delocalized, or more loosely held, and hence are more able to absorb the photon energy and be promoted to a higher energy state, that is, an excited state. I think that something very similar occurs when the interstitial defects in a glass are closed and the valence electrons are unpaired. Thus, the basic underlying electronic mechanisms for optical changes in both organic and inorganic materials are in a sense equivalent, I think, although the specific processes are different.

HELLER: Does this mean that the initial absorption of a quantum is the same in these systems, but that what happens afterward, as a prominent change, is different?

PARKER: No, I think I would say it the other way: the initial process by which the quantum is absorbed is different, but the consequence is the same. In other words, in one case there is a recoil effect or a collision effect causing a defect site, and in the other one the molecule is excited and to dissipate this energy it creates free radicals. Thus, the basic quantum processes involved in the two cases are different, but the actual consequences in optical properties are apparently quite equivalent.

LEONARD HASLIM, Lockheed Missiles & Space Company: I think I would prefer to answer the question in this manner: With the inorganic systems, we are primarily dealing, in effect, with pigments, since the inorganic binders act similarly to pigments. With the organic systems, we really have a composite of materials and complex reaction sites—the bulk pigment, the vehicle, the interfacial vehicle-pigment reaction sites—and we also have the contribution of the curing agents. The effect of ultraviolet exposure on organic systems can very well induce competitive reactions with quite unexpected results. For example, we had zinc oxide in a polymethyl siloxane polymer that was proprietarily catalyzed with a nonperoxide system, and we had a very small change in α , as a result of a given ultraviolet exposure. However, when the system (pigmented with the same SP 500 zinc oxide that Mr. Zerlaut used) was peroxide catalyzed, its change in solar absorptance was catastrophic. This change in α was well over 0.3, and the coating surface was blotchy and mottled. Obviously, then, the participation of the vehicle-curing agents in the coating can be rather significant with regard to over-all material stability.

ZERLAUT: I can only comment to this extent: we obtain greater increases in α when using diethylenetriamine as a catalyst for methyl silicones than when using the same amount of General Electric's proprietary SRC-05 amine catalyst. Furthermore, doubling the amount of diethylenetriamine results in catastrophic yellowing of the silicone paints on irradiation. It is difficult to determine whether it is the amine that is itself degrading or whether there is a photosensitization

of the surrounding media with resultant color center formation in the silicone matrix.

PARKER: I thought Mr. Heller's question was directed to the differences between organics and inorganics in my first answer, but you have raised a very important problem that I think has not been resolved in the course of this discussion. Namely, all of these systems undergo indirect effects as a consequence of oxygen in the films. When you begin to irradiate a film, do you pump it down first for many days to be sure that all oxygen is removed before you turn on the light, or do you simply start the irradiation and the outgassing at the same time? And how adequately does either procedure correspond with launch, ascent, and final circulation in an orbit? I think that oxygen can play a dominant role, and it has manifested itself in the case of the triamine catalyst because oxygen plus triamine plus ultraviolet light gives a very black color very quickly. Consequently, we not only need a better understanding of these matters, but we also have to know, for example, the concentration of free oxygen in the film before the vehicle is inserted into the space environment. I think that is an extremely important point regarding this triamine behavior.

ZERLAUT: Many of us use quartz windows in our simulation systems. To my knowledge, no one has reported transmittance losses due to irradiation. This is very interesting since we should be able to grind the quartz and use it as a pigment. We are not able to do so. All attempts to utilize silica as a pigment have met with failure due to severe discoloration on irradiation. However, several reasons may be advanced to account for the lack of ultraviolet stability exhibited by ground quartz and silica. The large surface area of the powder compared to a window (or single crystal); the possibility of a defect structure; or the considerably greater path length of the ultraviolet radiation in a scattering system as compared to the window (or single crystal).

LIONEL BAILIN, Lockheed Missiles & Space Company: Possibly the explanation for this quartz-powder darkening is the grinding. Quartz is not excessively hard, but is rather abrasive. The grinding apparatus and grind media, therefore, might have contributed to surface impurities which could have catalyzed changes in the quartz. So unless quartz is ground with quartz media only, the reasons for any changes are uncertain.

A direct correlation between the effects of ultraviolet and gamma radiations on the organic systems which Dr. Parker talked about and the effects of the radiations on inorganic systems would be highly desirable. However, this may not be possible. I should like to quote one example from some work which we did with lanthanum oxide-pigmented potassium silicate paints. This combination of materials produced a film which was very stable in nuclear environments, such as gamma and neutron radiations. This same paint, placed in an ultraviolet environment, however, degraded radically. If this material were satisfactory in both environments, all would be well for potential correlation of ultraviolet

with nuclear radiation degradation. But there is almost no way of predicting that one kind of radiation multiplied by certain factors is going to have the same effect as another kind has. Such a correlation may exist for pure organic systems, but certainly putting a pigment with a highly active surface into an organic matrix will change the properties of the coating. Each case must be examined separately. Possibly, in the future, general mechanisms will be found that will allow predictions of the behavior of a given pigment/binder system in all radiation environments.

PARKER: There is one further complication in the interpretation of this specific system, relative to our own work with polyvinyl chloride. We have shown that polyvinyl chloride does, indeed, degrade rather rapidly in the presence of ultraviolet and form chromophors. Now, this same ultraviolet radiation used with polyvinyl fluoride causes no change in absorptance. This material is perfectly stable. People tell me that one really need not be concerned about the vacuum ultraviolet, because there is only a very small quantity of energy in this part of the solar spectrum, although the energy per photon is high. However, if a polyvinyl fluoride coating is treated with just a smidgen of vacuum ultraviolet, it does, indeed, degrade catastrophically in the ultraviolet. The problem is that when we talk about simulation in general, we are not talking about a source, a lamp, or a vacuum, but we are talking about the material as well as the environment, because each one has apparently its own unique characteristic, and apparently the material whose behavior is best simulated is the one that changes least.

HELLER: I would again like to ask a general question: We have in the polyvinyl chloride a well behaved system—the curves line up nicely. Now, there are systems that are not well behaved, that are autocatalytic, that do not follow any of these laws. How do we treat those?

PARKER: Polyvinyl chloride, of course, is not a thermal-control coating. I want to make that point perfectly clear from the very outset. Study of polyvinyl chloride does point out certain features which, I believe, once we have identified them in a particular system, will enable us to understand more complicated systems. If, for a particular system, we know what the quantum efficiency is as a function of wavelength, and if we know what the cutoff wavelength is—that is, if we know the region of responsiveness in the photochemical sense—I think we can make predictions about how they will behave; but it depends on having the right approach to the research. Right now we are conducting monochromatic studies in which we count the number of photons of each wavelength and determine the photochemical efficiency by counting the number of double bonds created. This is the approach to setting up the simulation. One must either do this or simulate the Sun perfectly and run the experiment for the length of the mission, which is really a very safe way to do business.

HELLER: If we tried to correlate some of the results

discussed here with the theory discussed in earlier sessions, is there a possibility, for instance, of relating what has been discussed here in terms of color centers with the change of the complex refractive index.

LOUIS McKELLAR, Lockheed Missiles & Space Company: I am talking for some colleagues working at Lockheed, and a consultant, Dr. W. Spicer, of Stanford. I think this can be done in certain materials that are well-known—for example, germanium and silicon, and, possibly, zinc oxide. The complex index of refraction for the pure material probably could be predicted from the band theory. Then defects could be

put into the model, so to speak, to observe the effects that they would have upon the absorption of the material. Then, these theoretical results could be compared with the results of experiments. A similar study could be based on the electronic structure of surface atoms and molecules. This is a very tedious process involving computers for the theoretical portion, and would be done for only one material at a time; but I believe it is within the state of the art. I do not believe that anybody has yet attempted a comprehensive study of this kind on white pigments.

43. A Study of the Photodegradation of Selected Thermal-Control Surfaces

GEORGE F. PEZDIRTZ AND ROBERT A. JEWELL

NASA LANGLEY RESEARCH CENTER, LANGLEY AIR FORCE BASE, VA.

The results of the Langley participation in the Orbiting Solar Observatory II round robin on *Ultraviolet Stability of Thermal-Control Coatings* are presented, as well as some recent studies of the ultraviolet stability of a chemical conversion coating (Alodine 401). A preliminary study of the effects of gamma radiation from cobalt-60 on solar absorptance (α) of several selected white paint-type coatings has shown that the high-energy radiation (electrons and protons) in space can be expected to increase the solar absorptance, but at a slower rate than the ultraviolet radiation from the Sun.

The highly specialized and diverse nature of space vehicles has greatly influenced the development and testing of thermal-control coatings. In general, these coatings have been individually developed or custom-formulated and have been tested in individually developed environmental simulation systems. In an attempt to interrelate the environmental testing of various laboratories representing several government agencies, industry, and research institutes, a round robin on the *Ultraviolet Stability of Thermal-Control Coatings* was established. This round robin, administered by Carr B. Neel of NASA Ames Research Center, included laboratory testing of several coatings identical to those to be flown on the Orbiting Solar Observatory II (S-17) coating-degradation experiment during 1964. Preliminary results of the round robin are reported in the paper by J. C. Arvesen, C. B. Neel, and C. C. Shaw in this symposium. The details of flight results from a related thermal-control experiment (OSO I) have been reported by Neel (ref. 1 and 2). The results of NASA Langley participation in this round robin are discussed in this report, as well as some recent results on the ultraviolet stability of an amorphous aluminum and chromium phosphate chemical conversion coating (Alodine 401), which was used on the Echo II satellite.

In addition to ultraviolet radiation, the high-energy ionizing radiation in space may also

alter the optical properties of thermal-control surfaces. However, the literature is meager on this latter aspect of environmental testing of thermal-control coatings. Most studies of the effect of high-energy ionizing radiation on optical properties of spacecraft materials have been limited to solar cells and solar-cell covers. Accordingly, a brief study of the effects of high-energy ionizing radiation on several paint-type coatings was included in the present work in order to explore the seriousness of this factor. Several organic and inorganic white paints associated with the NASA Ames thermal-control experiments on OSO I and OSO II were sealed under vacuum in Pyrex tubes and exposed to the gamma rays from a cobalt-60 source. Although the flux of gamma rays in space is quite low, the damage from gamma rays is similar to the damage from electrons and protons; thus, the cobalt-60 source offers a convenient means of simulating the effects of the electrons and protons in space.

STABILITY TO ULTRAVIOLET RADIATION

Thermal-Control Coatings

The coatings used in the ultraviolet degradation study and their sources are listed in table I. The first two coatings, titanium dioxide/epoxy and antimony trioxide/potassium silicate (ref.

TABLE I.—Coatings Used in Ultra Violet Degradation Study

Coating		Source
Pigment	Vehicle	
Titanium dioxide	Epoxy ^a resin	Lockheed Missiles & Space Co.
Antimony trioxide	Potassium silicate	Hughes Aircraft Co.
Zinc oxide	Potassium silicate	IIT Research Institute (formerly Armour Research Foundation).
Titanium dioxide	Silicone ^b resin	IIT Research Institute (formerly Armour Research Foundation).
Chromium and aluminum phosphates ^c		G. T. Schjeldahl Co.

^a Skyspar (A-423), manufactured by Andrew Brown Paint Products Co.; the vehicle is Shell Chemical Co. No. 1001 resin, a bisphenol-a-epichlorohydrin resin cured with an amine catalyst.

^b General Electric LTV-602 silicone resin, a dimethyl polysiloxane

resin cured by silanol condensation.

^c Alodine 401-45, a chemical conversion coating on an aluminum substrate, prepared by a dip process of Amchem Products, Inc., using a mixture of chromic and phosphoric acids.

3 and 4), are known to degrade under ultraviolet radiation because of the instability of the vehicle and of the pigment, respectively. The third and fourth coatings, zinc oxide/potassium silicate and titanium dioxide/silicone (refs. 3 and 4), represent stable white coatings. These four paint-type coatings were supplied on aluminum test disks as a part of the round robin. The fifth coating represents a chemical conversion type of surface in which the aluminum substrate contributes significantly to the solar absorptance of the system. These Alodine coatings were received as the outer surface of the 0.74-mil Echo II laminate and were mounted on test disks by means of G. T. 301 polyester adhesive (G. T. Schjeldahl Co.). The laminate consists of two outer layers of 0.18-mil aluminum foil (1080) bonded to a 0.35-mil Mylar C plastic film.

Determination of Solar Absorptance

The solar absorptance α_s is the optical property of most concern in studying the ultraviolet stability of thermal-control surfaces, since it is the property which is usually most sensitive to ultraviolet radiation. The solar absorptance values reported in this paper were determined from measurements of spectral reflectances of the test surfaces over the wavelength range 0.22 to 2.10 microns. A Cary 14 spectrophotometer equipped with a barium sulfate-coated integrating sphere attachment (ref. 5) was used for these measurements. To determine solar absorptance, reflectance values

were read at the center of wavelength increments corresponding to 1-percent increments of the total solar energy, as determined from the spectral distribution given by Johnson (ref. 6). Summations of the readings in the range of 0.29 to 2.02 microns were multiplied by a correction factor to compensate for the fact that only 94 percent of the solar energy is found in the region of summation. This result, subtracted from unity, yields the solar absorptance value.

Ultraviolet-Vacuum Environmental System

The ultraviolet-vacuum environmental system used in these tests is shown schematically in figure 1. The stainless steel front plate is integral with the glycol-water-cooled specimen holder, which can accommodate as many as eight specimens for simultaneous irradiation. The coolant was maintained at 0° C with a refrigerated recirculating bath. The temperatures of the test specimens were monitored periodically throughout the test with copper-Constantan thermocouples mounted in the metal substrates of each coating. (The substrates for the titanium dioxide/epoxy coating, however, were too thin to permit thermocouple mounting. Sample temperatures were assumed to be comparable to the average temperature of the monitored samples.) Some temperature variations among different samples in the same test were noted; they were probably due to differences in sample properties and in thermal contact of the test disks with the cooling plate.

The vacuum chamber was mounted to a 1,200-

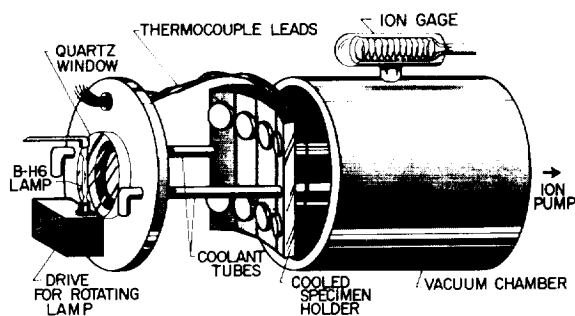


FIGURE 1.—Ultraviolet-vacuum chamber.

liter/sec Ultek ion pump. A silicone rubber O-ring (Dow Corning Silastic 916 compound) was used to seal the quartz window; the remaining seals were Viton (fabricated of Parker Seal Co. V-495-7 compound). The vacuum system was allowed to reach an equilibrium pressure of 1×10^{-6} torr before ultraviolet irradiation was initiated. Chamber pressure was monitored throughout the test and maintained in the range of 1×10^{-6} to 6×10^{-7} torr. After irradiation, sample temperatures were allowed to return to ambient temperature, and the chamber pressure was then brought to atmospheric pressure with argon in an attempt to limit any oxidation effects prior to making reflectance measurements.

High-pressure mercury arc lamps (GE B-H6) were used as the source of ultraviolet radiation in these studies. The lamp manufacturer (ref. 7) and others (ref. 8) have reported that the spectrum of the B-H6 lamp is not completely similar to the solar spectrum. Figure 2 shows the ratio of the lamp intensity (at a distance of 25 cm) to solar intensity (at 1 AU) for different wavelengths in the 0.22- to 0.40-micron region. The average lamp intensity for this wavelength range is approximately 3 times the solar intensity. This figure is based on the geometry of this system and the manufacturer's data for B-H6 lamps (ref. 7). During use and aging of the B-H6 lamps, an uneven milky film is often formed on the surface of the quartz capillary. Decay in intensity with use is not the same for all wavelengths (ref. 8). The lamps were rotated about their axes to reduce intensity nonuniformities arising from inhomogeneities in the quartz envelope and uneven film buildup.

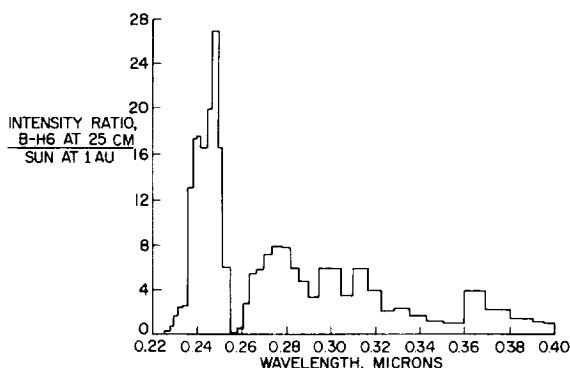


FIGURE 2.—Multiples of solar intensities at selected wavelengths in the ultraviolet for the B-H6 mercury arc lamps at a distance of 25 centimeters.

The relative intensities of the B-H6 lamps were monitored during each run with a Westinghouse SM-200 ultraviolet photometer. The individual lamps were selected and changed as necessary to maintain relative ultraviolet intensities within 15 percent of a nominal intensity of 3 equivalent suns.

Effect of Ultraviolet Radiation

The effects of the ultraviolet irradiation on the spectral absorptance α_λ are shown in figures 3 to 7. These measurements of α_λ were made within 4 hours after the samples were removed from the ultraviolet-vacuum chamber. The solar absorptances of the irradiated coatings were also determined periodically during the subsequent 3 months of exposure to air. The stable coatings, zinc oxide/potassium silicate and titanium dioxide/silicone resin, showed little change in α_s ($\Delta\alpha_s < 0.01$) with air aging after the ultraviolet test. In the cases of the unstable coatings, antimony trioxide/potassium silicate and titanium dioxide/epoxy resin, a bleaching action ($-\Delta\alpha_s > 0.05$) was noted during air aging. This decrease in α_s (bleaching) after exposure to air was greater for the irradiated titanium dioxide/epoxy than for the comparable antimony trioxide/potassium silicate.

A comparison of figures 3 and 4 illustrates the ultraviolet-radiation effects on a stable pigment, titanium dioxide, in stable silicone and in unstable epoxy vehicles. The converse is shown by comparing figures 5 and 6 which illustrate

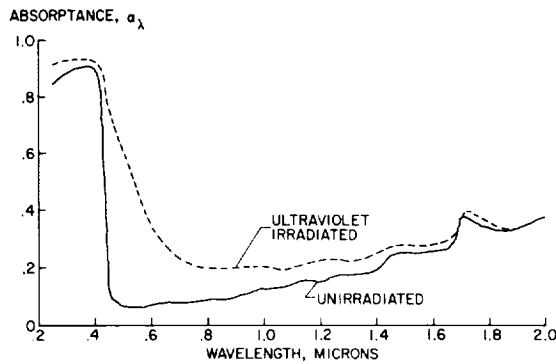


FIGURE 3.—Influence of ultraviolet radiation on spectral absorbance of titanium dioxide/epoxy. 100-hr ultraviolet exposure at 3 times solar intensity. Pressure: 8×10^{-7} torr. Sample temperature not measured.

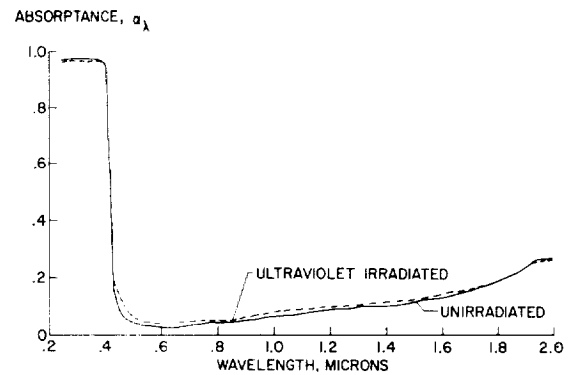


FIGURE 6.—Influence of ultraviolet radiation on spectral absorbance of zinc oxide/potassium silicate. 100-hr ultraviolet exposure at 3 times solar intensity. Pressure: 8×10^{-7} torr. Sample temperature: 15°C .

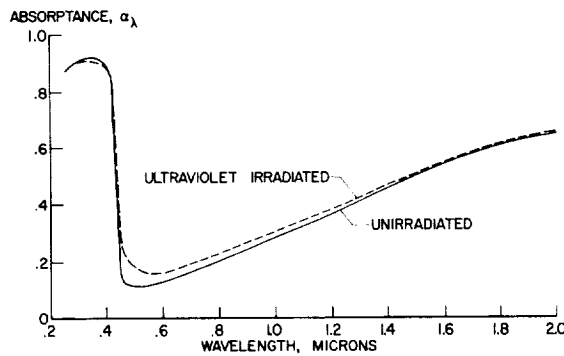


FIGURE 4.—Influence of ultraviolet radiation on spectral absorbance of titanium dioxide/silicone. 100-hr ultraviolet exposure at 3 times solar intensity. Pressure: 8×10^{-7} torr. Sample temperature: 17°C .

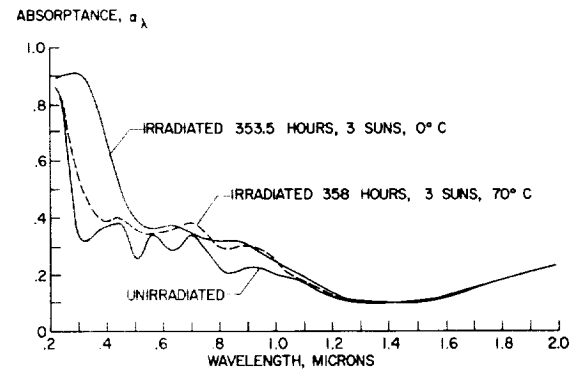


FIGURE 7.—Influence of ultraviolet radiation on spectral absorbance of Alodine 401.

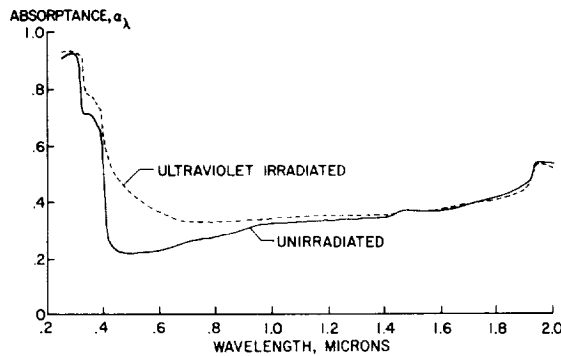


FIGURE 5.—Influence of ultraviolet radiation on spectral absorbance of antimony trioxide/potassium silicate. 100-hr ultraviolet exposure at 3 times solar intensity. Pressure: 8×10^{-7} torr. Sample temperature: 14°C .

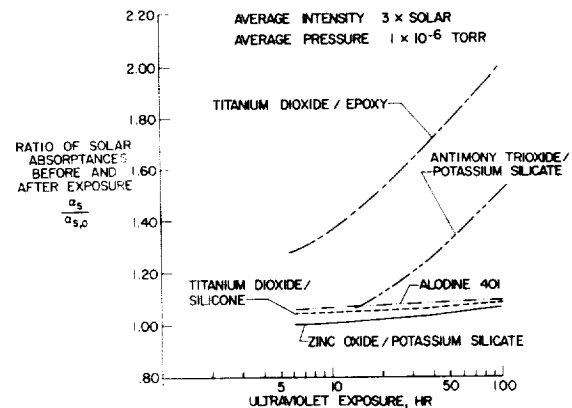


FIGURE 8.—Comparison of effects of ultraviolet radiation on solar absorbances of five coatings.

the ultraviolet-radiation effect on a stable potassium silicate vehicle which contains unstable antimony trioxide pigment in one case and stable zinc oxide pigment in the other.

The effect of ultraviolet radiation on α_s for Alodine 401 irradiated at different temperatures (previously reported in ref. 9) is shown in figure 7. The increase in α_s for the test at 0° C was unexpected and is yet to be adequately explained. It may be due to photochemical reactions with some entrapped water, which would be less volatile at the lower temperature. The ratio α_s/ϵ for the Alodine samples irradiated at 0° C was found to decrease with irradiation time as a result of an increase in thermal emittance ϵ which more than compensated for the increase in α_s . The influence of sample temperature is particularly significant in accelerated testing, where the higher intensities can produce increased temperatures in the sample.

Figure 8 shows the relative change in solar absorptance as a function of total exposure to ultraviolet radiation for the five coatings. The changes in $\alpha_s/\alpha_{s,0}$ for each coating as well as coating thickness and specimen temperature during individual tests are shown in figures 9 to 13. The coating thickness and specimen temperature are shown directly above the corresponding points on the plots of $\alpha_s/\alpha_{s,0}$ against ultraviolet exposure time. Abnormalities in specimen temperature frequently result in abnormal effects in the degradation of the surface. The laboratory exposure times, assumed to be one-third of the effective exposure times (1 AU), are not intended to represent useful lifetimes for satellites. However, they do provide an indication of relative coating stability within reasonable limits of laboratory testings.

Several deviations from a smooth curve relationship were noted in figures 9 to 13; they are attributed in large part to variations in coating thickness and to variations in specimen temperature during exposure. Coating thicknesses of the four paints were measured with a Dermatron, Model 2, eddy current thickness tester and checked with micrometer measurements after all ultraviolet testing and reflectance measurements were completed.

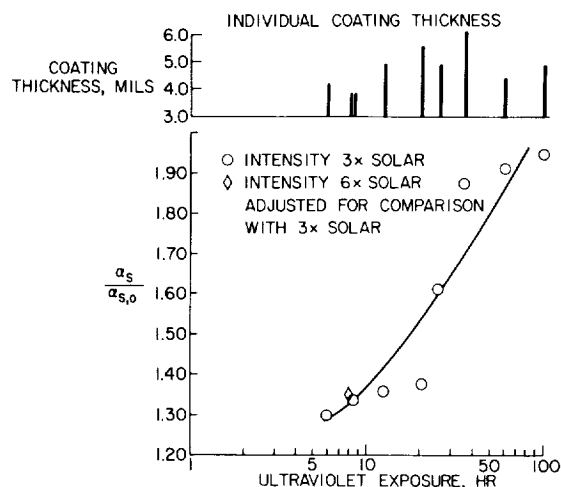


FIGURE 9.—Effect of ultraviolet radiation on solar absorptance of titanium dioxide/epoxy.

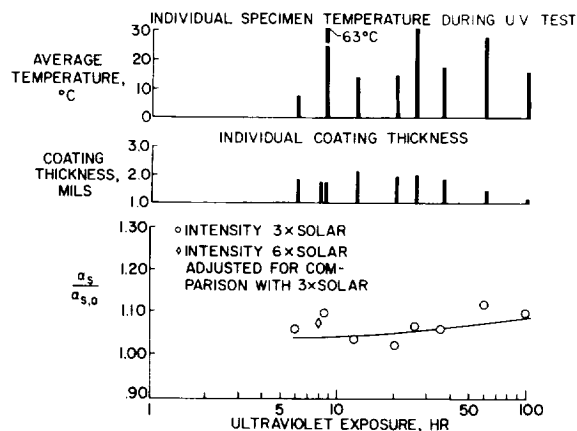


FIGURE 10.—Effect of ultraviolet radiation on solar absorptance of titanium dioxide/silicone.

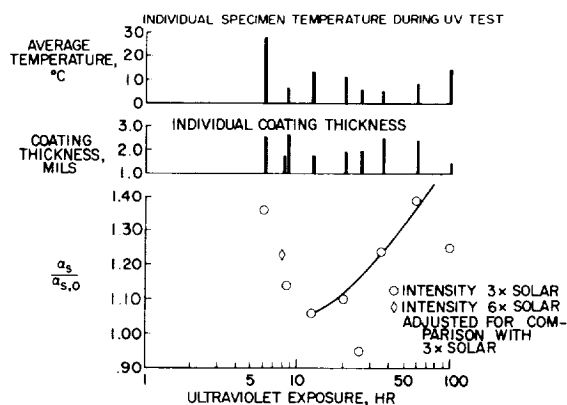


FIGURE 11.—Effect of ultraviolet radiation on solar absorptance of antimony trioxide/potassium silicate.

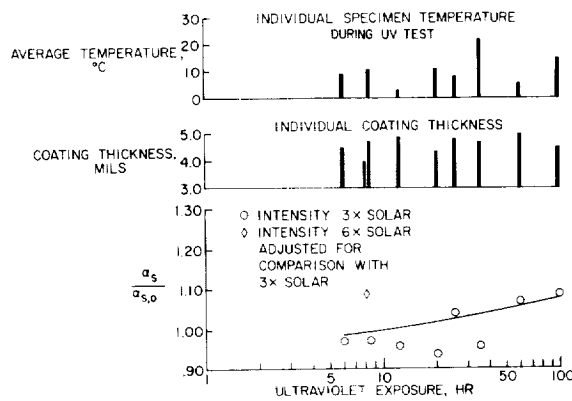


FIGURE 12.—Effect of ultraviolet radiation on solar absorptance of zinc oxide/potassium silicate.

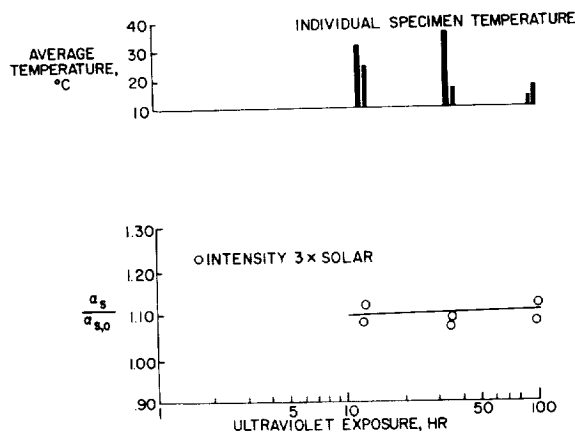


FIGURE 13.—Effect of ultraviolet radiation on solar absorptance of Alodine 401.

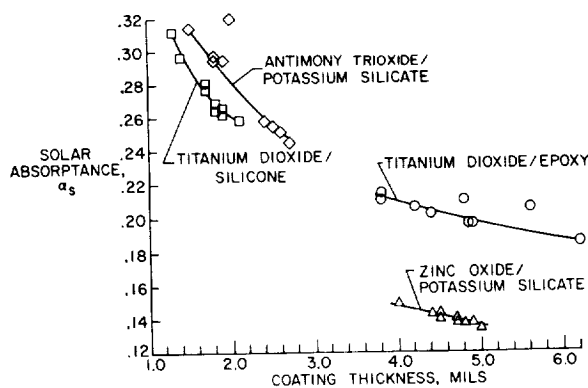


FIGURE 14.—Effect of coating thickness on solar absorptance of irradiated specimens.

Test specimens showed differences in thickness which resulted in different values of the initial solar absorptance $\alpha_{s,0}$ and also, as just noted, may be partially responsible for somewhat erratic results after ultraviolet exposure. The variation in $\alpha_{s,0}$ as a function of thickness for the four paints is illustrated in figure 14. A few specimens showed considerable deviation from the smooth curves shown; generally, the ultraviolet stability of these specimens also deviated from that of their companion specimens.

STABILITY TO GAMMA RADIATION

The stability of thermal control surfaces to high-energy ionizing radiation has been little studied compared to their stability to ultraviolet radiation, although the coloring of glasses, plastics, and alkali halides upon exposure to high-energy ionizing radiation is well known. Gamma radiation from a cobalt-60 source offers a convenient means of simulating the effects rather than the environment (electrons and protons) of space. A brief series of experiments was conducted to determine the extent of change in α , produced by high-energy gamma radiation. The materials used in these tests were coatings associated with the OSO I and OSO II thermal control experiments and were supplied by NASA Ames Research Center (C. B. Neel).

The coating specimens were placed in Pyrex tubes and outgassed for a minimum of 12 hours at 5×10^{-7} torr. After outgassing, the tubes were sealed under vacuum and irradiated, with gamma rays from a cobalt-60 source (A.E.C.L. Gammacell 220, ref. 10) at a dose rate of 1.6 megarad/hour. The ambient temperature in the Gammacell was 47° C. No attempt was made to cool the test specimens. Following irradiation, the Pyrex tubes were opened under argon in an attempt to reduce post-irradiation oxidation effects. The reflectance of each irradiated coating was determined within 1 hour after its Pyrex tube was opened.

The results are summarized in table II. In all cases the solar absorptance increased upon exposure to the 1.33 and 1.17 Mev gamma rays from the cobalt-60 source. A gamma dose of 77 megarads (7.7×10^9 ergs/g(C)) approximates the

TABLE II.—*Effect of Gamma Radiation on Thermal Control Coatings*

Coating		Solar absorptance α_s			
Pigment	Vehicle	Dose, Mrad			
		0	77	0	385
Zinc oxide.....	Silicone plus catalyst.....	0. 17	0. 21	0. 17	0. 21
	Silicone resin.....	. 19	. 22	. 20	. 23
	Potassium silicate.....	. 14	. 18	. 14	. 18
Zinc sulfide.....	Silicone resin.....	. 20	. 23	. 20	. 23
Titanium dioxide.....	Silicone film.....	. 12	. 24	. 13	. 23
	Silicone resin.....	. 25	. 37	. 25	. 43
Zircon.....	Epoxy resin.....	. 20	. 42	. 20	. 47
	Potassium silicate.....	. 09	. 15	. 09	. 15
Zirconium silicate.....	Potassium silicate.....	. 06	. 13	. 07	. 15
Lithium aluminum silicate.....	Sodium silicate.....	. 09	. 35	. 10	. 36
Antimony trioxide.....	Potassium silicate.....	0. 26	0. 36	0. 25	0. 52

surface dose at the end of 12 weeks in the inner Van Allen belt (ref. 11), and a dose of 385 megarads approximates 60 weeks of exposure.

COMPARISON OF EFFECTS OF GAMMA AND ULTRAVIOLET RADIATION

Five white coatings exposed to both types of radiation are listed in table III in decreasing order of stability to these radiations. Only a relative comparison of the effects of gamma and ultraviolet radiations is practical at this time

since a direct comparison would require additional information on specific absorption and specific photon intensities.

A gamma dose of 77 megarads (7.7×10^9 ergs/g(C)) approximates the surface dose at the end of 12 weeks in the intense radiation region of the inner Van Allen belt (ref. 10). The ultraviolet exposures in table III approximate 2 weeks of continuous exposure to sunlight in space. The coatings listed in table III were darkened to approximately the same extent

TABLE III.—*Comparison of Effects of Gamma and Ultraviolet Radiation on Solar Absorptance of Thermal Control Coatings*

Coating		Solar absorptance α_s			
Pigment	Vehicle	Original value, α_{s0}	Increase in α_s		
			Gamma dose		300-ESH • UV exposure
			77 Mrad ^a	385 Mrad ^b	
Zinc oxide.....	Potassium silicate.....	0. 14	0. 04	0. 04	0. 01
Zinc oxide.....	Silicone plus catalyst.....	. 17	. 04	. 04	. 04
Titanium dioxide.....	Silicone resin.....	. 25	. 12	. 18	. 03
Antimony trioxide.....	Potassium silicate.....	. 26	. 10	. 26	. 08
Titanium dioxide.....	Epoxy resin.....	. 20	. 22	. 27	. 19

^a 77 megarads is approximate surface exposure for 12 weeks in inner Van Allen belt.

^b 385 megarads is approximate surface exposure for 60 weeks in inner Van Allen belt.

^c 300 ESH (equivalent sun hours, ultraviolet) approximates ultraviolet exposure for 2 weeks in space at 1 A.U.

by a brief exposure (equivalent to 2 weeks in space) to ultraviolet radiation as they were after a longer exposure to gamma radiation (equivalent to 12 weeks in space). The order of stability for the different coatings was maintained, and coatings stable to ultraviolet were also stable to gamma radiations.

One would not expect the mechanisms of energy absorption for ultraviolet and gamma radiation to be the same. However, the end results as determined from spectral reflectance measurements indicate that the final damage caused by the two types of radiation is quite similar, as shown in figure 15.

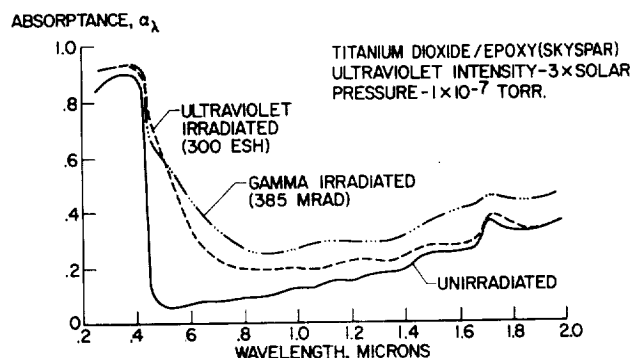


FIGURE 15.—Comparison of effects of gamma and ultraviolet radiation on the spectral absorptance of titanium dioxide/epoxy coating. Ultraviolet intensity: 3 times solar. Pressure: 1×10^{-7} torr.

CONCLUDING REMARKS

The environmental testing of thermal-control coatings is complicated by such variables as coating thickness and sample temperature during testing, both of which may significantly influence the ultimate observable change in solar absorptance during exposure to ultraviolet radiation. The influence of sample temperature is particularly significant in accelerated testing, where the higher intensities can produce increased temperatures unless specifically compensated for by effective cooling.

The change in solar absorptance induced by gamma radiation (used to simulate the effects of electrons and protons) is less than the change

induced by ultraviolet radiation when the comparison is made on the basis of equivalent exposure times in the inner Van Allen belt. More attention should be given to additional studies of the effects of high-energy ionizing radiation on thermal-control coatings. These effects should be considered in the analysis of the results from thermal-control experiments aboard spacecraft, as well as in spacecraft design for long-term missions.

ACKNOWLEDGMENT

The spectral reflectance values reported in this paper were determined by H. D. Burks and P. R. Young.

REFERENCES

1. NEEL, CARR, B.; and ROBINSON, GILBERT G.: Measurement of Thermal-Radiation Properties of Temperature-Control Surfaces in Space. Measurement of Thermal Radiation Properties of Solids, Joseph C. Richmond, ed., NASA SP-31, 1963, pp. 193-207.
2. NEEL, CARR B.: Measurement of Thermal-Radiation Characteristics of Temperature-Control Surfaces During Flight in Space. NASA paper presented at Ninth National Aerospace Instrumentation Symposium (San Francisco), May 8, 1960.
3. ZERLAUT, GENE A.; and HARADA, Y.: Stable White Coatings. Rept. No. ARF 3207-14 (Interim Rept.) (JPL Contract No. 950111—Subcontract NAS7-100), Armour Res. Found., Illinois Inst. Technol., Nov. 13, 1962.
4. TOMPKINS, EDWIN H.: Stable White Coatings. Rept. No. ARF 3207-5 (Interim Rept.) (JPL Contract No. 950111—Subcontract NASw-6), Armour Res. Found., Illinois Inst. Technol., Apr. 13, 1962.
5. MIDDLETON, W. E. K.; and SANDERS, C. L.: An Improved Sphere Paint. Illum. Eng., vol. 48, no. 5, May 1953, pp. 254-256.
6. JOHNSON, FRANCIS S.: The Solar Constant. J. Meteorol., vol. 11, no. 6, Dec. 1954, pp. 431-439.
7. Anon.: High Brightness Mercury Arc Lamps Capillary Type A-H6 and B-H6 Application Data and Accessory Equipment. GET-1248H, Outdoor Lighting Dept., Gen. Elec. Co., Feb. 1961.
8. CARROLL, W. F.: Development of Stable Temperature Control Surfaces for Spacecraft—Progress Report No. 1, Tech. Rept. No. 32-340 (Contract No. NAS 7-100), Jet Propulsion Lab., C.I.T., Nov. 20, 1962.
9. PEZDIRTZ, GEORGE F.; and WAKELYN, NOEL T.: Ultraviolet Stability of Some Modified Metal Phosphates for Thermal-Control Surfaces.

- Materials for Space Vehicle Use. Vol. 3, Soc. Aerospace Mater. Process Engr., No. 1963.
10. RICE, F. G.; and SMYTHE, W. D.: A Cobalt-60 Irradiation Facility. Ind. Eng. Chem., vol. 52, no. 5, May 1960, pp. 47A-49A.
11. SUN, K. H., compiler: A Brief Summary of Space Nuclear Radiations and Effects. Dielectrics in Space Symposium, Westinghouse Res. Lab., June 1963, pp. R-1—R-11.

44. Preliminary Results From a Round-Robin Study of Ultraviolet Degradation of Spacecraft Thermal-Control Coatings

J. C. ARVESEN, C. B. NEEL, AND C. C. SHAW

NASA AMES RESEARCH CENTER, MOFFETT FIELD, CALIF.

Preliminary results are presented from a voluntary round-robin testing program among 16 participating aerospace companies and research laboratories. The study is being conducted on identical samples of four low-solar-absorptance white coatings: rutile titanium dioxide/epoxy, rutile titanium dioxide/silicone, antimony trioxide/potassium silicate, and zinc oxide/potassium silicate. The degradation experienced in the actual spatial environment is known for the first two coatings from an experiment aboard the OSO-I satellite. Results thus far received from 12 of the organizations show considerable variance; however, initial correlations have been attempted on the basis of temperature, pressure, and the intensity and spectral distribution of the source. Results indicate the need for more accurate measurement of thermal radiation properties, improvements in existing environmental simulation capabilities, and a greater understanding of the chemical processes associated with ultraviolet degradation of thermal-control coatings.

In the past, comparisons of laboratory measurements of the rate of degradation of spacecraft thermal-control coatings with the limited data available from flight experiments have shown generally poor agreement (ref. 1). The disagreement is believed to be the result of inadequacy in the laboratory simulation of the space environment and, in particular, of the solar-ultraviolet radiation. The need to resolve the problem of adequate simulation was recognized, and, as a first step, a voluntary round-robin testing program was organized in November 1962 to compare and evaluate existing capabilities for ultraviolet-degradation studies.

Sixteen organizations are participating in this program. Each organization was offered identical samples of four different low α_s/ϵ white thermal-control coatings with various degrees of color stability under ultraviolet irradiation; each organization tested the samples at exposures up to the equivalent of 1,000

sun-hours. Results from 12 organizations had been received at the time of preparation of this paper. The purpose of this paper is to present and compare these results on the rates of coating degradation measured in the various test facilities, and to discuss their significance in a preliminary fashion. The results for two of the coatings were also compared with flight data.

The following organizations participated in the round-robin program:

Air Force Materials Laboratory, Wright-Patterson AFB
American Cyanamid Company
The Boeing Company
Fairchild Stratos Corporation
General Dynamics/Astronautics
General Electric Company
Hughes Aircraft Company
IIT Research Institute
Jet Propulsion Laboratory
Lockheed Missiles & Space Company

Martin Marietta Corporation
McDonnell Aircraft Corporation
NASA Langley Research Center
NASA Marshall Space Flight Center
TRW Space Technology Laboratories
U.S. Naval Research Laboratory

The efforts of those persons directly involved in the tests are appreciated. In particular, the work of Mr. William F. Carroll of the Jet Propulsion Laboratory in establishing the basic ground rules and enlisting participation for the program should be acknowledged. Mr. G. Richard Blair of Hughes Aircraft Company, Mr. Louis A. McKellar of Lockheed Missiles & Space Company, and Mr. Jerry T. Bevans of TRW Space Technology Laboratories also aided in setting up the test requirements.

DESCRIPTION OF COATINGS

Four low α_s/ϵ white thermal-control coatings were chosen for study. The individual coatings were selected on the basis of pigment and binder composition, expected degradation processes, and previous flight and laboratory experience. All samples of a particular coating were prepared at the same time from the same batch and were distributed to the participants in light-tight containers in an effort to minimize variations in the initial undegraded state. The samples were prepared by three of the participants.

The first coating was composed of a rutile titanium-dioxide pigment in an epoxy binder (Andrew Brown Company, Skyspar A423, color SA 9185 untinted) and was chosen for study as an example of a coating with a stable pigment and an unstable binder that degrades noticeably in a short period of time. These coating samples were prepared by Lockheed Missiles & Space Company.

The second coating was formulated and the samples were prepared by the IIT Research Institute (IITRI). The coating consisted of a rutile titanium-dioxide pigment in a more stable silicone binder (IITRI designation: TC-50-19). Previously prepared samples of both this and the epoxy coating were flown aboard the first Orbiting Solar Observatory, OSO-I (ref. 1). Measurements of the rates of degradation of these coatings were made over a

period of 16 months in orbit and, although the coatings were prepared from different material lots than the round-robin samples, the flight data serve as a preliminary basis for evaluating the laboratory-simulation tests.

The third coating was composed of an antimony trioxide pigment in a potassium silicate binder, and was developed especially for the round-robin by Hughes Aircraft Company. In contrast to the titanium dioxide in epoxy, this coating has an unstable pigment in a stable binder. Consequently, its degradation mechanism was expected to be different from that of the epoxy-binder paints.

The last of the four coatings, also prepared by IITRI, was a stable zinc oxide pigment in potassium silicate (IITRI designation: 441-2). The first, third, and fourth coatings are scheduled to be flown aboard the OSO-B2 Satellite near the end of the year.¹ Thus, it is expected that information on their degradation in the actual space environment will be available for correlation with the laboratory results.

TEST PROCEDURE AND EQUIPMENT

Procedure

The test procedures followed by the various organizations were basically the same, although specific simulation equipment and techniques differed considerably. In each organization, the samples were first measured to obtain initial values of solar absorptance. They were then placed in a vacuum chamber and exposed to a source of ultraviolet radiation for various periods of time up to the equivalent of 1,000 hours in space. After irradiation, the samples were removed from the vacuum chamber and their solar absorptances were again measured.

Test Equipment and Conditions

The equipment used by the various participants and the test conditions are listed in table I. The order of listing in this table is not the same as that in the previous list of participating organizations, which was alphabetical.

¹ The OSO-B2 (now designated OSO-2) was successfully launched on Feb. 3, 1965.

TABLE I.—*Test Equipment and Conditions*

No.	Intensity, "UV suns"	Temperature, °C	Lamp type	Vacuum system type	Pressure level, torr
1	3 to 14.4	27	B-H6	Sorption and ion	Below 10^{-6}
	1 to 7		Xenon		
2	1	32	B-H6	Mechanical, diffusion, 10^{-4} sputter ion.	10^{-7} to 10^{-8}
	5	100			
	10	157			
3	10	Not measured	B-H6	Mechanical and diffusion	5×10^{-5} to 7×10^{-6}
4	1 to 11	25	A-H6	Mechanical and ion	3×10^{-6} to 2×10^{-7}
5	2.7	5 to 65	B-H6	Mechanical and ion	10^{-6}
6	5 to 16	35	A-H6	Sorption, mechanical, and ion ...	10^{-7}
7	5	50	A-H6	Mechanical and LN_2 trap	10^{-2} (10 microns)
8	20	150	B-H6	Mechanical and diffusion	10^{-6}
9	15.5	Above 200	A-H6	Mechanical and diffusion	10^{-5}
10	7.1	86	B-H6	Mechanical and diffusion	10^{-5}
11	1	24	Hanovia 54A-10	Mechanical and diffusion	5×10^{-6}
12	1.5	15	UA-3	Mechanical and ion	10^{-5} to 10^{-6}

Oil-diffusion pumps and ion pumps were used about equally in the vacuum systems, along with various types of roughing pumps. These systems produced vacuums in the pressure range from 10^{-5} to 10^{-7} torr. One organization, however, used only a mechanical pump with liquid-nitrogen trapping, which resulted in a relatively high vacuum-chamber pressure of 10 microns of mercury (10^{-2} torr).

In some cases sample temperature was controlled by cooling, and in other cases no cooling was provided. This resulted in variations in sample temperature among the participants from 15°C to over 200°C .

All participants used a mercury lamp to simulate solar ultraviolet radiation. The General Electric B-H6 and A-H6 lamps were most commonly used. In an attempt to investigate the effect of the ultraviolet source on the degra-

dation characteristics of the coatings, one organization also conducted tests with a 2-kw xenon lamp. The spectra of the B-H6 mercury lamp, the xenon lamp, and the Sun in the ultraviolet region from 2000 to 4000 Å are compared (for the same total energy between 2000 and 4000 Å) in figure 1. The spectral distribution of the A-H6 lamp was not shown because it is similar to that of the B-H6 lamp. The spectrum of the B-H6 lamp consists largely of emission bands that may have many times the intensity of the solar continuum at the same wavelengths. The xenon lamp, on the other hand, offers a much better duplication of the solar spectrum below 4000 Å than does the mercury lamp. Because of this closer match, the xenon lamp was expected to provide more realistic coating degradation rates than the mercury lamps.

It was recognized by the round-robin participants that the mercury spectrum gives a poor duplication of solar ultraviolet radiation. However, the assumption was made that if the total irradiation from the lamp below 4000 Å was set equal to the solar irradiation below 4000 Å, the same degradation would occur. This assumption was the basis for calculating the equivalent solar illumination on the samples. Thus, for example, if the total radiation below 4000 Å incident on a sample is 10 times the solar radiation in the same range, the illumination level is designated as 10 "ultraviolet solar constants" or 10 "suns."

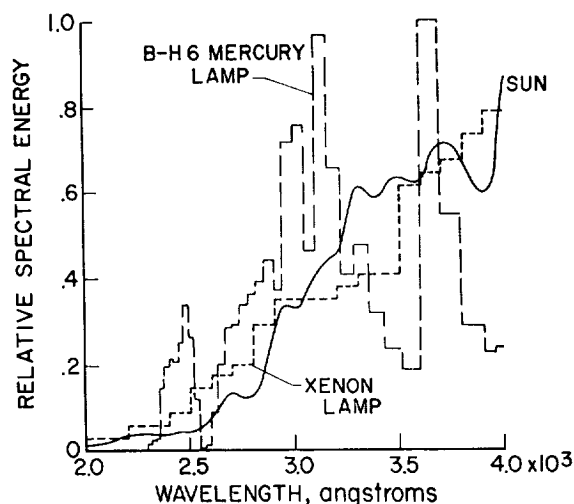


FIGURE 1.—Comparison of ultraviolet spectral distribution of sun and lamps.

The choice of the 4000 Å wavelength as the cutoff point was purely arbitrary. It was thought that 4000 Å represented the upper limit of damaging radiation for nearly all materials of interest. It is known, however, that many materials require higher photon energies, or shorter wavelengths, to cause degradation. Some materials may be particularly sensitive to certain portions of the spectrum. It can be seen from the plots of the B-H6 and solar spectra that below 3200 Å there is considerably more radiation from the mercury lamp than from the Sun. Thus, a sample that is particularly susceptible to

damage below 3200 Å would, in effect, have much more than the equivalent of 1 ultraviolet solar constant incident on its surface when the mercury lamp is used.

Another factor that may influence the degradation rate of some coatings is the possible bleaching resulting from exposure to radiation of longer wavelengths, as mentioned in reference 2. This effect,² which tends to offset the increase in solar absorptance resulting from ultraviolet radiation, apparently is caused by radiation in the visible region. The radiant intensity of the mercury-vapor lamps is well below solar intensity in the visible, and failure of the lamps to simulate the bleaching effect adequately could cause difficulties in simulation of the overall degradation rate.

RESULTS AND DISCUSSION

Initial Values of Solar Absorptance

Solar absorptances of the test coatings, measured before exposure to ultraviolet radiation, are listed in table II. The various instruments used by the participants for the initial and subsequent measurements are also given. The order of listing in this table is the same as in table I. In all cases the solar absorptance of a coating was determined by a reflectance technique. The last two measurements shown were over limited spectral regions and, thus, are not indicative of solar absorptance. Agreement among the remaining measurements is generally within the normal experimental scatter of reflectance measurements. It is apparent that, for coatings with low values of solar absorptance, the deviations, in percent, are quite large. More effort is clearly needed to develop equipment and to refine the techniques for accurately determining the solar absorptance of low α_s/ϵ materials.

Coating Degradation

The results of the coating degradation studies are presented in figures 2, 3, 4, and 5. These figures show the measured change in solar absorptance as a function of "equivalent sun hours." In the studies, it was found that only

² See also Paper 42.

TABLE II.—Initial Solar Absorptance Measurements

Instrument	Initial solar absorptance— α_{λ}			
	Titanium dioxide/epoxy	Titanium dioxide/silicone	Antimony trioxide/potassium silicate	Zinc oxide/potassium silicate
1. Gier-Dunkle integrating sphere.....	0. 21	0. 30	0. 28	0. 14
2. Gier-Dunkle integrating sphere.....	. 22	-----	. 27	-----
3. Gier-Dunkle solar reflectometer.....	. 22	. 27	. 29	. 16
4. Cary 14 integrating sphere.....	. 22	. 31	. 30	. 16
5. Cary 14 integrating sphere.....	. 21	. 27	. 28	. 14
6. G.E. and P.E. integrating sphere.....	. 23	. 30	. 26	. 16
7. Beckman DK-2A integrating sphere.....	. 16	-----	. 25	. 10
8. Beckman DK-2A integrating sphere.....	. 26	. 33	. 27	. 18
9. Beckman DK-2A integrating sphere.....	. 21	. 28	. 26	. 16
10. Bausch and Lomb 505 integrating sphere.....	. 19	. 26	. 25	. 13
*11. Bausch and Lomb 20 integrating sphere.....	. 08	. 11	. 14	. 02
**12. Beckman IR-4 Hohlraum.....	. 14	. 50	. 34	. 17

*4000 Å to 7000 Å only.

**At 1.0 micron.

the solar absorptance of the coatings was altered by exposure to ultraviolet radiation and that the emittance remained relatively unchanged.

In preparing these figures, an attempt was made to separate the effects of what were thought to be two of the most important variables, that is, sample temperature and the radiant intensity of the ultraviolet source. In the figures, temperature is indicated by the color of the curve—five different colors have been used to designate five different temperature ranges. In addition, the curves are drawn with dashes of different lengths, where the length of the dash denotes the radiant intensity used in the test. The shortest dashes indicate an intensity of 1 ultraviolet solar constant, and the longer dashes indicate multiples of the solar constant. In some sets of tests the exposures were made at various different intensities, as indicated by the different lengths of the dashes along the curve. With one exception, mercury-vapor lamps were used in all exposures. The single test with the xenon lamp is indicated on each figure. The tests at a pressure of 10 microns are also indicated.

TITANIUM DIOXIDE/EPOXY COATING

The results of the studies made on the titanium dioxide/epoxy coating are shown in figure

2. Also shown in the figure are the OSO-I flight data for the same type of coating.

The wide spread of the results in figure 2 illustrates the present level of uncertainty in solar-ultraviolet-simulation tests. In view of the poor match of the mercury-vapor-lamp spectrum with the solar ultraviolet spectrum, it is perhaps not surprising to find general disagreement among the laboratory results and the flight data. It is rather surprising, however, that results from two of the tests made with mercury-vapor lamps were in better agreement with the flight results than were the results from the tests with the xenon lamp, which matched the solar spectrum far better than the mercury-vapor lamps. Even for these cases, the time required for the coating to be degraded by a given amount was about one-half to one-third the time required in flight. Results from remaining simulation tests all showed considerably more rapid changes in solar absorptance than were measured in flight, with the exposure time required for a given change in solar absorptance in some cases differing from the flight data by several orders of magnitude.

Although the exact causes of the wide variations in the test results are not immediately evident, the data reveal a number of interesting points. For example, after a large increase in

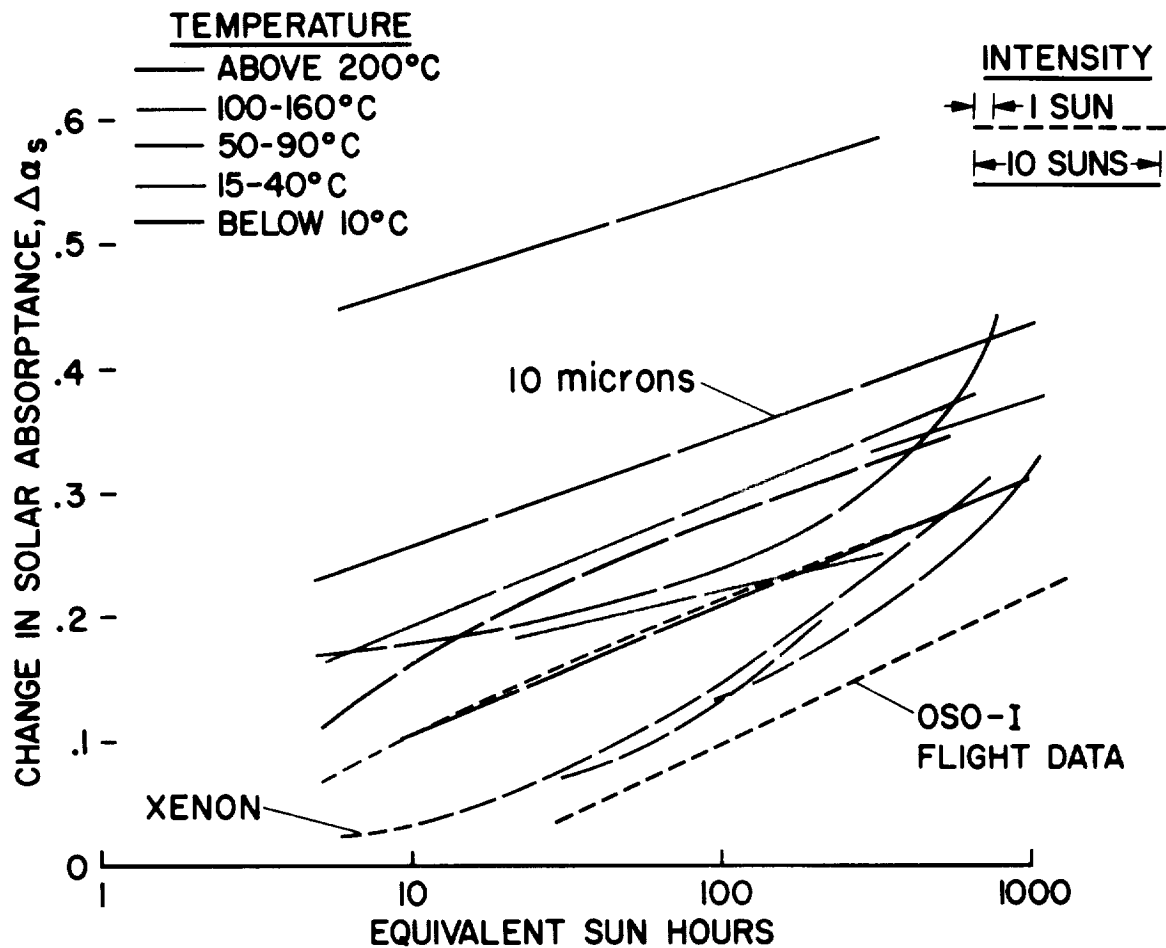


FIGURE 2.—Degradation of titanium dioxide/epoxy coating.

absorptance shortly after the beginning of sample exposure, the rate of increase in absorptance in most cases became roughly equal to the rate obtained in flight. The magnitude of the initial increase in solar absorptance apparently was influenced by both sample temperature and lamp intensity, although it is difficult to separate the relative importance of these two factors. Nevertheless, there appears to be a definite correlation between sample temperature and initial degradation rate, with the higher degradation rates being associated with the higher temperatures. There also appears to be a non-linear correlation of degradation rate with lamp intensity, with the higher intensities producing a relatively higher rate of change of solar absorptance. In tests where the intensity was constant, the change in absorptance with time

was almost linear when plotted on a logarithmic time scale. On the other hand, where the intensity was increased to obtain long equivalent exposures in reasonable lengths of time (increasing lengths of dashes along the line) the corresponding rate of change of solar absorptance increased to an even greater degree.

The curve for the tests made with a chamber pressure of 10 microns is high compared with the other curves for the same temperature level. The higher degradation rate may have been caused by the presence of oxygen or other impurities not present under the higher vacuum conditions of the other tests. Finally, one other possible cause of the higher degradation rates obtained in the laboratory should not be overlooked. This is the effect of bleaching due to visible or longer wavelength radiation in the

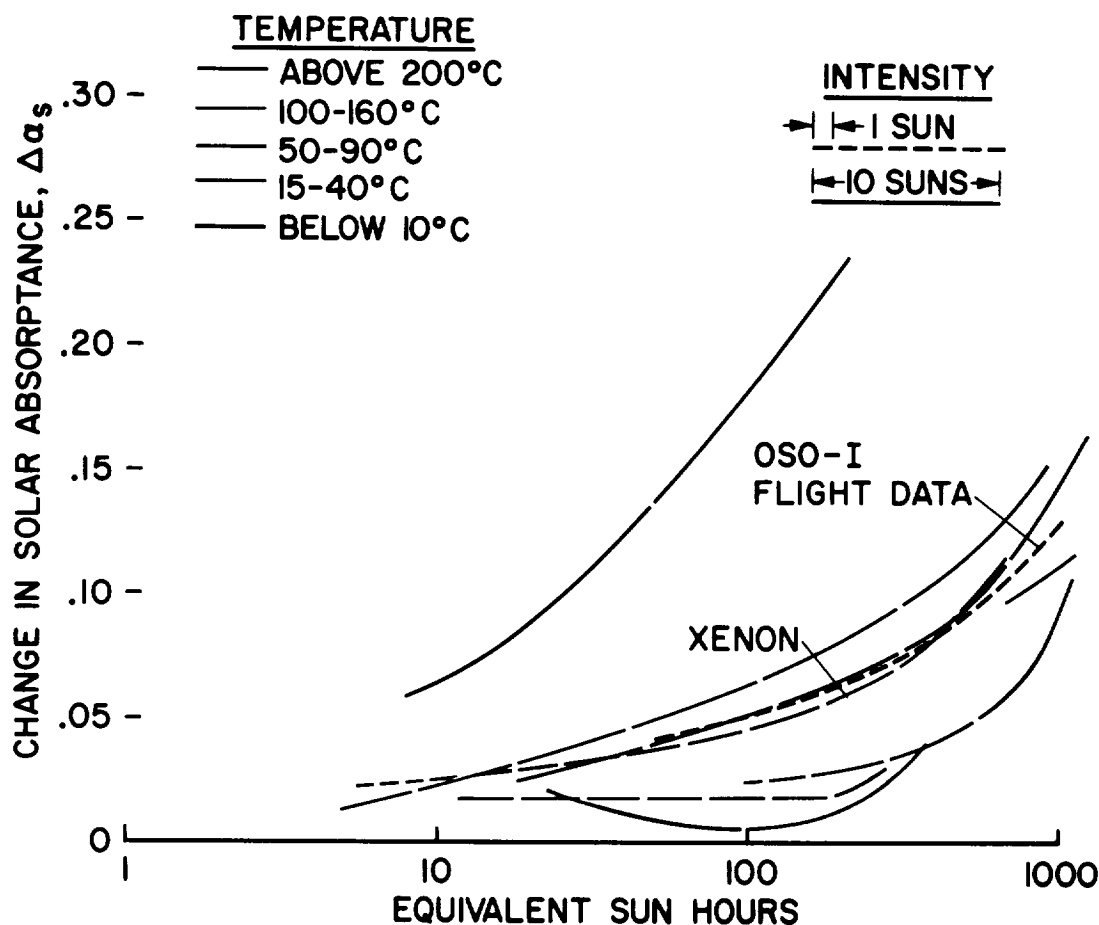


FIGURE 3.—Degradation of titanium dioxide/silicone coating.

solar spectrum which mercury-vapor lamps do not adequately simulate.

TITANIUM DIOXIDE/SILICONE COATING

The results of ultraviolet irradiation on the more stable titanium dioxide in silicone coating are shown in figure 3. Note that the scale for the change in solar absorptance has been expanded to twice that used in figure 2 for the epoxy coating in order to help emphasize differences in the results. This coating apparently is not nearly as sensitive to intensity and temperature variations as the epoxy coating. In fact, with the exception of the high-temperature test, there appears to be no correlation of degradation rate with temperature and only the expected linear correlation with intensity.

The large change in solar absorptance at the high temperature may have been the result of either thermal degradation or an increase in the ultraviolet sensitivity resulting from the excessive temperature. Tests with the xenon lamp at a low sample temperature and with a mercury-vapor lamp at a higher temperature show good agreement with the flight data. In contrast to the tests with the epoxy coating, the laboratory results gave both higher and lower degradation rates than were obtained in flight with the same type of coating. The lack of any apparent trend in the data from the standpoint of temperature or intensity effects suggests that the spread in the curves is the result of differences in other experimental factors.

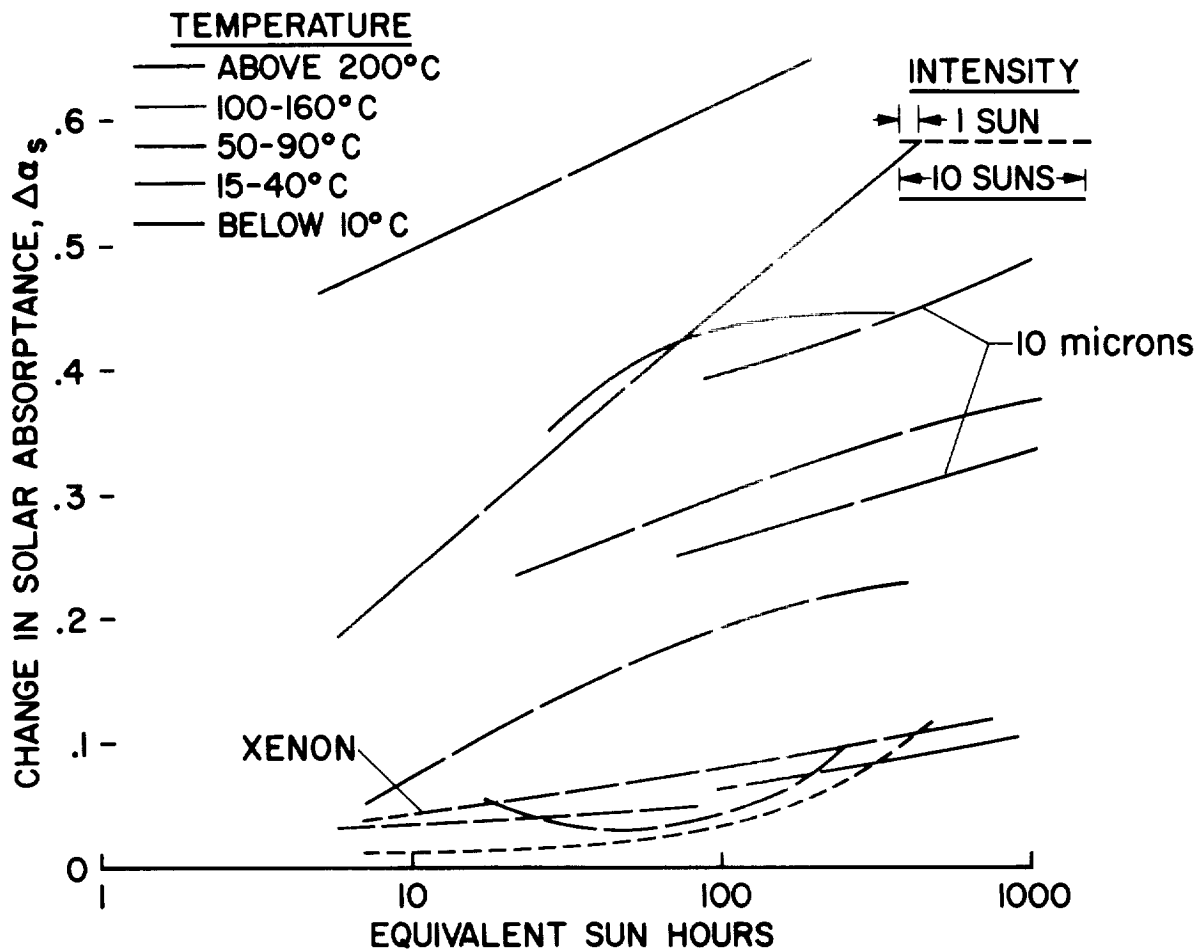


FIGURE 4.—Degradation of antimony trioxide/potassium silicate coating.

ANTIMONY TRIOXIDE/POTASSIUM SILICATE COATING

Results of tests of the antimony trioxide/potassium-silicate coating are shown in figure 4. There is an extreme variation in the degradation rate, even greater than for the titanium dioxide/epoxy coating. For example, the measured values of the change in solar absorptance after 100 equivalent sun hours ranged from less than 0.1 to about 0.65. Since the initial solar absorptance was 0.3, the increase in absorptance of about 0.65 corresponds to the sample becoming a nearly black absorber. The increase in solar absorptance appears to be extremely sensitive to temperature and intensity. As with the epoxy coating, the degradation ap-

peared to increase with increase in sample temperature. Flight data for this coating are not yet available. However, samples of this coating will fly on OSO-B2, so that flight data should be obtained for comparison with these results.

ZINC OXIDE/POTASSIUM SILICATE COATING

Figure 5 shows the data for the zinc oxide pigment in a potassium silicate binder. Excluding the two cases of the excessively high sample temperature and the high chamber pressure, the tests show the coating to be very stable and the degradation to be fairly independent of intensity and temperature. It is interesting that the tests with the xenon lamp

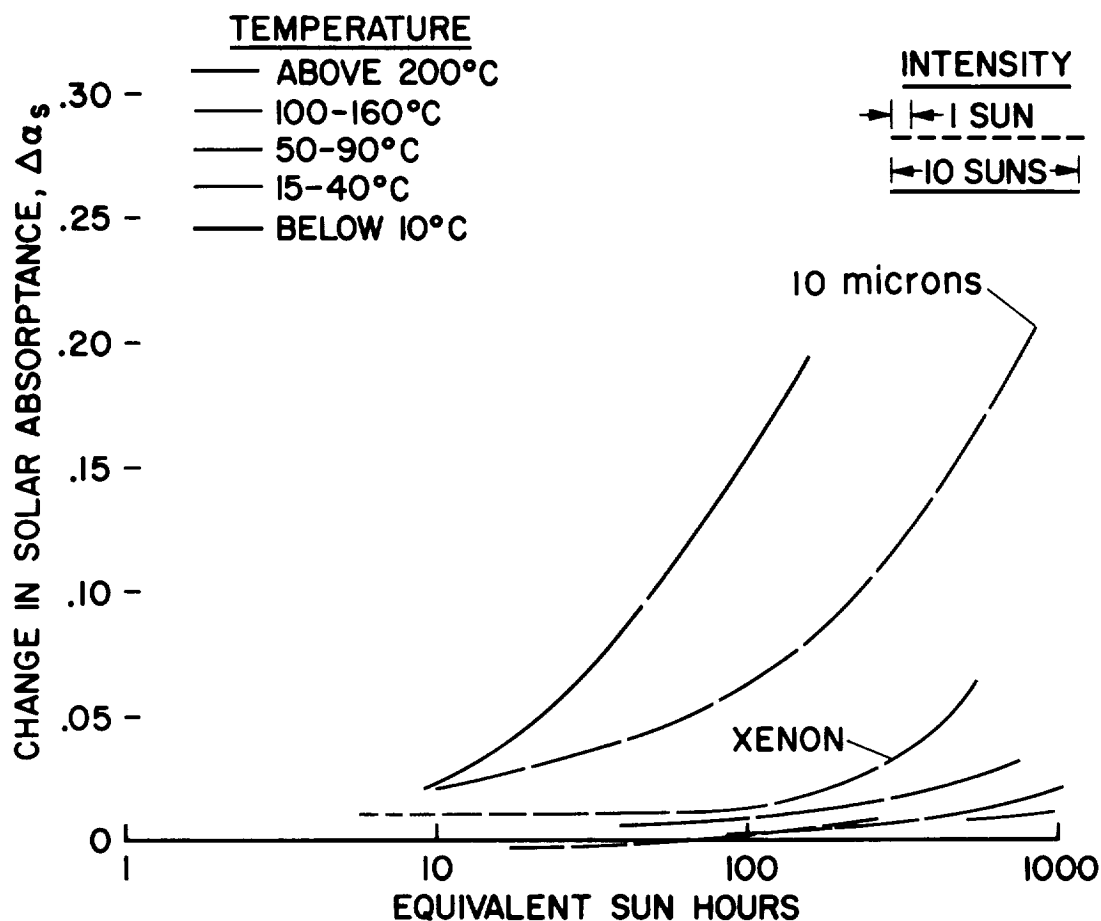


FIGURE 5.—Degradation of zinc oxide/potassium silicate coating.

showed a higher degradation rate than the tests performed with mercury-vapor lamps. Unfortunately, no flight data are yet available for comparison with these results, and it is not known whether the xenon lamp or the mercury-vapor lamp gives the better duplication of the solar degradation of this coating. The difference between the results with the xenon lamp and with the mercury-vapor lamps could be the result of a dependence of degradation upon wavelength for this coating.

As with the previous coatings, the high rate of degradation at 200° C may have been due to increased ultraviolet sensitivity or thermal degradation, or possibly a combination of both factors. The test performed at a pressure of 10 microns also resulted in a high degradation

rate, and these data may reflect the influence of a high oxygen level.

CONCLUDING REMARKS

In reviewing the significance of the limited results obtained through the round-robin tests, a few facts are apparent regarding laboratory simulation of degradation of thermal-control coatings. It is important, for example, in testing some coatings to maintain sample temperatures at a level reasonably near the expected operating temperature. The exposures should be made in an environment in which the pressure does not exceed about 10^{-5} torr. The validity of accelerated testing with lamp intensities many times the solar level is

questionable for some coatings, and further investigation is required into the ramifications of this testing technique.

The question of the importance of the spectral intensity distribution of the ultraviolet lamps has not yet been resolved, although it is hoped that the OSO-B2 flight tests may help in this regard. Without further evidence, it would appear at this time that the solar ultraviolet intensity spectrum should be matched as closely as possible, and that for some coatings it may even be necessary to simulate the visible and near-infrared regions of solar energy. The extent to which these various spectral

distribution requirements must be met is undoubtedly a function of the chemical degradation processes associated with the individual coatings, and before this problem can be completely resolved, more must be learned about the mechanisms of the degradation processes.

REFERENCES

1. NEEL, CARR B.: Research on the Stability of Thermal Control Coatings for Spacecraft. Proc. Fifth International Symposium on Space Technology and Science, Tokyo, Japan, 1963.
2. ZERLAUT, G. A., and HARADA, Y.: Stable White Coatings, IIT Research Institute Rep. no. IITRI-C207-25, 1963.

45. The Effects of Micrometeoroids on the Emittance of Solids

RONALD B. MERRILL

NASA GEORGE C. MARSHALL SPACE FLIGHT CENTER, HUNTSVILLE, ALA.

An analytical model is developed to predict the change in the emittance of a surface caused by particle impact. This model is applied in a representative fashion to determine the change in the emittance due to the space environment. Theoretical results are compared with experimental results obtained by C. H. Leigh of AVCO under a NASA contract in the time period of 1960 to 1962.

Before artificial satellites were placed into orbit, scientists were uncertain what effects various parameters of the space environment would have on them. One such space environment parameter is the presence of a relatively large number of solid particles in space. One usually neglects the effect of the impingement of these particles on the thermal radiative characteristics of surfaces, partly because even erosion- and cratering-sensitive surfaces have not changed enough to significantly affect the temperatures of satellites. However, the nature and magnitude of the effects have really never been determined. In the future this question will become more important because of the postulated increase in particle flux near the lunar surface relative to that in a near-earth orbit, and also because of the anticipated use of thin thermal control coatings and of elements with more critical surfaces, such as lenses and windows.

This paper is restricted to consideration of the change in emittance of a surface due to particle impact as applied, with particular reference to the surfaces exposed, to the space environment. Hence, several topics are discussed only in general terms, mainly for background and for particular information needed in the development of an analytical

model which will be used to predict the change in emittance of solids (specifically metals) in the space environment.

SYMBOLS

A_c	cratered area of surface of interest
A'_c	cratered area for one incident particle
A_T	total area of surface of interest
A_1	area of crater surface (assumed to be semi-ellipsoid)
dA_i	element of area of ellipsoidal crater, where i is 1, 2, 3, . . .
dA_0	element of area of opening of crater
$d\Omega_0$	element of solid angle subtended by dA_0 at dA_1
$d\Omega_i$	element of solid angle subtended by dA_i at dA_{i-1}
E_b	radiative energy flux density emitted from black-body
E_0	radiative energy flux density emitted through crater opening from arbitrary element of area dA_1 lying on crater surface
E_1	radiative energy flux density emitted by crater that is reflected once from dA_1 through crater opening
E_2	radiative energy flux density emitted by crater that is reflected once to dA_1 and thence through crater opening
E_3	radiative energy flux density emitted by surface of crater that is reflected twice and then reflected from dA_1 through crater opening, etc.
G_i	fraction of radiative energy flux from dA_i that passes directly out of crater opening
H	energy of impacting particle

K	ratio of crater volume to kinetic energy of micrometeoroid
m	mass of a micrometeoroid
m_o	cut-off mass (minimum mass of a micrometeoroid)
N	micrometeoroid flux (number of incident particles per square meter per second)
R_{ij}	distance between elemental areas dA_i and dA_j
V	volume
v	velocity of micrometeoroid
W	total radiative energy flux density (energy radiated per second per unit of area)
W_b	radiative energy flux density of blackbody
W_e	total effective radiative flux density of craters (reflected and radiated)
W_n	total radiative energy flux density of cratered surface
W_o	initial radiative flux density of surface
$\Delta\epsilon$	change in emittance
β_i	angle with the perpendicular of the ray from dA_i to dA_{i-1}
β'_i	angle with the perpendicular of the ray from dA_i to dA_{i+1}
β_0	angle with perpendicular of the ray from dA_0 to dA_1
ϵ	emittance
ϵ_c	emittance of crater surface
ϵ_e	effective emittance of crater area
ϵ_n	emittance of surface after cratering
ϵ_0	initial emittance of surface

MICROMETEORIDS IN SPACE

Flashes across the night sky have long proclaimed the existence of meteoroids in space. In fact, an estimate of the number of meteoroids in space was first deduced by counting the number of meteor streaks of a certain intensity in a certain section in the sky and thereby calculating the number that would pass through a square meter per second. This number is called the meteoroid flux and actually is an accumulative number because it is the total number of meteoroids which have a meteor intensity greater than a given minimum value.

The relation of meteor luminosity to meteoroid mass and velocity has been calculated by several investigators (ref. 1 and 2). As a result of these studies, it is possible to plot the flux of meteoroids greater than a given mass, as a function of mass. This plot is a straight line in a log-log coordinate system, and it can be readily extrapolated into the region where meteor trails would not be observable here on the earth. These supposed particles of less than 1-millimeter diameter are called micro-

meteoroids, and from the extrapolated line they are expected to be much more numerous than observable meteoroids.

Observations of the zodiacal light and the scattering of the F-corona of the sun give additional evidence that a comparatively large number of micrometeoroids exists (ref. 3). A measure of the amount of mass accretion of deep-sea sediments has also given an indication that a large number of meteoroids have settled to the earth's surface. Recent satellite data have given additional information.

There are several types of satellite micrometeoroid sensors. One measures the electrical output produced when a particle strikes a sounding board attached to a piezoelectric crystal. The amplitude of the signal generated can be related to the momentum of the particle through a ground-based calibration (performed, however, over a limited particle velocity range). Another type of measurement uses thin-wall pressurized cells. When the wall of a cell is perforated, the event is indicated by the loss of pressure. A calibration of a device of this

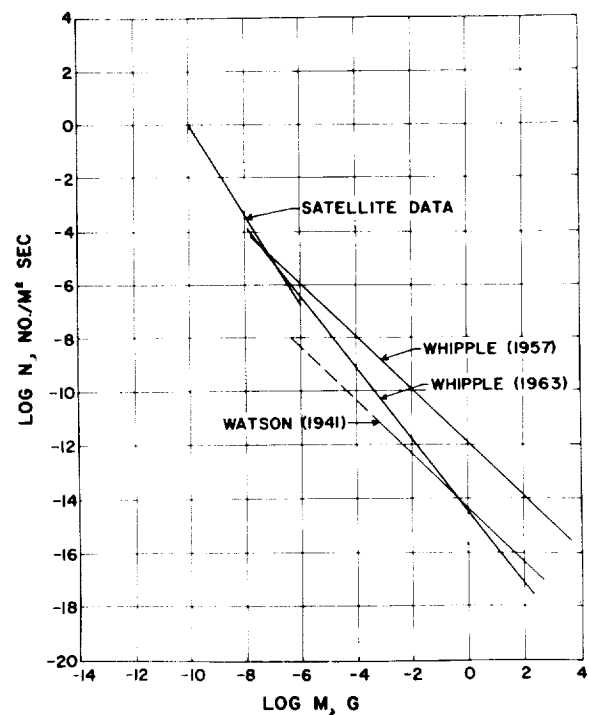


FIGURE 1.—Cumulative micrometeoroid flux against mass.

sort indicates that the thickness of the material which can be perforated is almost a linear function of the energy of the particle. Unfortunately, the cratering hazards deduced from these two types of measurements are not in agreement; the microphone data are high and the perforation data are low. This discrepancy can be explained by various difficulties in calibration or perhaps by the fact that different types of phenomena are being measured. Even the basic assumptions may not be correct. For example, one particular speed (typically 15 or 30 km/sec, depending on the investigator) is usually assumed in all calculations in the reduction of data (ref. 3). An assumed particle density is also used; and if, for example, the average micrometeoroid is less dense, the perforation data would be lower than the microphone data. Plots of some derived flux laws are shown in figure 1.

In the following discussion, a parameter study will be stressed more than any one flux law because there still exists considerable uncertainty regarding the micrometeoroid environment in space.

THE EFFECTS OF MICROMETEOROID IMPACTS ON SURFACES

Micrometeoroid damage to a surface may be classified into three types: (1) perforation, in which the micrometeoroid passes all the way through the material; (2) partial penetration, in which the micrometeoroid does not pass all the way through the material but forms a deep crater with high depth-to-diameter ratio; and (3) removal of surface material accompanied by cratering, with a depth-to-diameter ratio of 0.5 or smaller. Emphasis is placed on the cratering phenomena because perforation would be relatively rare.

The cratering of materials by large particles has been studied extensively. At first, a great deal of confusion existed in trying, even empirically, to describe what was happening, but now a few ideas are generally accepted. The penetration by particles with relatively low velocities is almost a linear function of momentum, and at very high velocities it is a function of energy. This velocity effect is depicted in figure 2; however, the quantitative character-

istics depend on the material of the particle and of the target (ref. 4). At some velocity greater than the transition velocity the craters broaden into a hemispherical shape. This transition region occurs around 2 to 5 km/sec for soft metals, 7 km/sec for aluminum, and higher velocities for the more brittle materials, but is generally under 11 km/sec. Usually the average speed assumed for micrometeoroids in space is equal to, or greater than, 15 km/sec; particles with such speeds would, for most metals, produce hemispherical craters characteristic of the hypervelocity region. Brittle materials have a tendency to shatter around the crater.

The cratering efficiency in the hypervelocity region is measured experimentally, although there have been some attempts to write a descriptive equation. The empirical data can be represented by the equation

$$V=KH$$

relating V , the volume of the crater, and H , the energy of the impacting particle. K is a constant, characteristic of the material. Table I lists several values for K in the hypervelocity region.

One would expect that the inside surface of a crater would be different from the original surface. Figure 3, taken from reference 8, shows a typical hypervelocity impact crater in

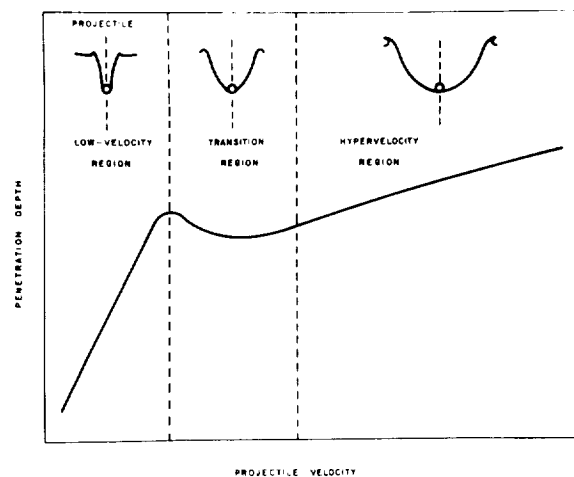


FIGURE 2.—Penetration against velocity for metal-to-metal impacts, with associated crater shapes.

TABLE I.—Crater Volume per Unit Micrometeoroid Kinetic Energy

Material	K, m ³ /joule
Aluminum:	
250-----	13 × 10 ^{-8*}
2014-----	4.5
17ST-----	3.0
75ST-----	2.5
Cadmium-----	13
Copper:	
Soft-----	10
Bar-----	4
	3
Brass-----	2.5
Lead-----	35
Steel:	
1020-----	2.7
4140-----	1.8
	1.1
Titanium-----	1.3

*Multiply each item in column by 10⁻⁴.

a copper plate which was bombarded and then cut and etched. The photograph indicates, by the lack of large craters close to the crater surface, that there is a considerable amount of mechanical working near the surface. This mechanical working does not have to extend very far beneath the surface to affect the emissivity, since, for a metal, most of the electromagnetic energy is emitted at a depth of less than 100 Å. For low velocities, fragments of



FIGURE 3.—Section through typical hypervelocity impact crater (in copper).

the impacting particle may be partially buried in the crater wall. Such fragments, although probably of much smaller size, may also occur for higher velocities.

ANALYTICAL DERIVATION OF THE CHANGE IN EMITTANCE DUE TO CRATERING¹

The emittance of a surface is defined as the ratio of the amount of energy radiated per second by a unit area of surface at a particular temperature to the amount of energy that is radiated per second by a perfect radiator (blackbody) of the same area and at the same temperature:

$$\epsilon = \frac{W}{W_b} \quad (1)$$

Thus, the change in emittance is given by

$$\Delta\epsilon = \epsilon_n - \epsilon_o = \frac{W_n}{W_b} - \frac{W_o}{W_b} \quad (2)$$

where

- ϵ emittance
- $\Delta\epsilon$ change in emittance
- ϵ_n emittance of surface after cratering
- ϵ_o initial emittance of surface
- W total radiative energy flux density (energy radiated per second per unit of area)
- W_b radiative energy flux density of blackbody
- W_n radiative energy flux density of cratered surface
- W_o initial radiative energy flux density of surface

The amount of energy emitted by the cratered sample is given by the sum of the energy emitted by the cratered and uncratered portions:

$$W_n = \frac{(A_T - A_c)\epsilon_o W_b + A_c \epsilon_e W_b}{A_T} \quad (3)$$

where

- A_T total area of surface of interest
- A_c cratered area of surface of interest
- $A_T - A_c$ area not cratered
- ϵ_e effective emittance of cratered area, W_c/W_b

¹ See also Paper 9.

W_c average radiative energy flux density in crater opening

The quantity ϵ_c is the ratio of the radiative energy flux coming out of a crater opening to that of a blackbody of the same area and may be considered as a function of the geometry of the crater and the emittance of the crater surface ϵ_s .

If this expression for W_n is substituted into equation (2), the expression for the change in emittance simplifies to

$$\Delta\epsilon = \frac{A_c}{A_T} (\epsilon_c - \epsilon_o). \quad (4)$$

The problem now reduces to finding an expression for ϵ_c . The calculation involves summing

- the energy per second emitted from the crater surface that passes directly out of the crater opening
- the energy per second emitted and then reflected once before leaving the crater
- the energy per second emitted and then reflected twice before leaving the crater, etc.

and dividing this sum by the energy emitted per second by a blackbody with the same area as that of the crater opening. For the derivation of ϵ_c it is assumed that the whole crater surface is isothermal.

Let

- E_0 radiative energy directly emitted per second per unit area through the crater opening from an arbitrary element of area dA_1 lying on the crater surface (fig. 4)
- E_1 radiative energy per second per unit area radiated directly to dA_1 from the crater surface and reflected from dA_1 through the crater opening
- E_2 radiative energy per second per unit area received at dA_1 , after having been emitted by the crater surface and once reflected by the crater surface, that is reflected through the crater opening
- E_3 radiative energy per second per unit area received at dA_1 , after having been emitted by the crater surface and twice reflected by the crater surface, that is reflected through the crater opening

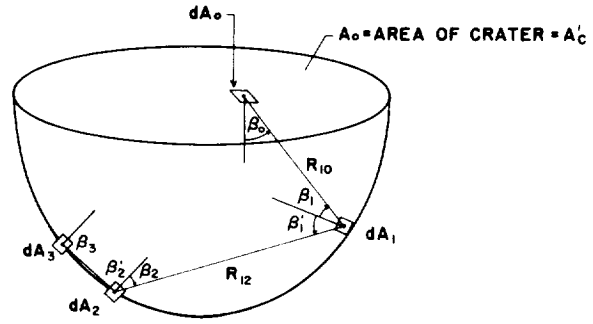


FIGURE 4.—Definitions of terms used in deriving the general expression for the crater emittance.

With this notation, the expression for ϵ_c can be written as:

$$\epsilon_c = \frac{\sum_{i=0}^{\infty} \iint E_i dA_1}{W_b A'_c} = \frac{\iint \sum_{i=0}^{\infty} E_i dA_1}{W_b A'_c}. \quad (5)$$

The energy emitted from dA_1 per second directly into space ($E_0 dA_1$) is (fig. 4)

$$E_0 dA_1 = \iint \frac{\epsilon_s E_b dA_1}{\pi} \cos \beta_1 d\Omega_0 \quad (6)$$

where $[(\epsilon_s E_b dA_1 \cos \beta_1)/\pi]$ is the total energy emitted from dA_1 per second per steradian at some angle β_1 to the normal, $d\Omega_0$ is the solid angle subtended by the element of area dA_o of the crater opening, and the integral is extended over the entire area of the opening. (It is assumed in this analysis that the crater surface is a diffuse emitter—that is, that it emits according to Lambert's law.) The element of solid angle is given by

$$d\Omega_0 = \frac{\cos \beta_0 dA_o}{R_{10}^2}. \quad (7)$$

The energy emitted directly from dA_1 per second into space can then be written as

$$\begin{aligned} E_0 dA_1 &= \epsilon_s E_b dA_1 \iint \frac{\cos \beta_1 \cos \beta_0 dA_o}{\pi R_{10}^2} \\ &= \epsilon_s E_b dA_1 G_1 \end{aligned} \quad (8)$$

where

$$G_1 = \iint \frac{\cos \beta_1 \cos \beta_0 dA_0}{\pi R_{10}^2} = \iint \frac{\cos \beta_1 d\Omega_0}{\pi} \quad (9)$$

The integral G_1 is the fraction of the total emitted energy $\epsilon_c E_b dA_1$ from dA_1 that goes directly out through the crater opening.

The amount of energy radiated directly to dA_1 from the crater wall per second and diffusely reflected from dA_1 through the crater opening is (fig. 4)

$$E_1 dA_1 = \left(\iint \frac{\epsilon_c E_b \cos \beta'_1 d\Omega_2 dA_1}{\pi} \right) (1 - \epsilon_c) G_1 \quad (10)$$

where $\epsilon_c E_b \cos \beta'_1 d\Omega_2 / \pi$ is the incident energy per second per unit of area arriving at dA_1 at an angle to the normal β'_1 in the solid angle $d\Omega_2$. The integral is with respect to $d\Omega_2$, and the integration is over the crater surface. The amount of energy reflected per second from dA_1 is the fraction $(1 - \epsilon_c)$ times this integral, according to Kirchhoff's law, and only G_1 times this amount of reflected energy (assuming a diffuse reflector) leaves through the opening of the crater.

The element of solid angle $d\Omega_2$ can be expressed as follows:

$$d\Omega_2 = \frac{\cos \beta_2 dA_2}{R_{12}^2} \quad (11)$$

Equation (10) may be written as

$$E_1 dA_1 = \epsilon_c (1 - \epsilon_c) E_b \left(\iint \frac{\cos \beta'_1 d\Omega_2}{\pi} \right) G_1 dA_1 \quad (12)$$

The amount of energy received by dA_1 per second after it has been reflected once by the crater wall can be written, with the help of figure 4, as

$$E_2 dA_1 = \iint \left(\iint \frac{\epsilon_c E_b \cos \beta'_2 d\Omega_3}{\pi} \right) (1 - \epsilon_c) \frac{\cos \beta'_1 d\Omega_2}{\pi} (1 - \epsilon_c) G_1 dA_1 \quad (13)$$

where $d\Omega_3$ is the solid angle subtended at dA_2 by an element of crater surface, and the integration is over the crater surface. The quantity

$\iint \epsilon_c E_b \cos \beta'_2 d\Omega_3 / \pi$ is the total energy per second directly emitted and incident on dA_2 ; and the sum total of energy per second reflected once and incident on dA_1 is

$$\iint \left(\iint \frac{\epsilon_c E_b \cos \beta'_2 d\Omega_3}{\pi} \right) (1 - \epsilon_c) \frac{\cos \beta'_1 d\Omega_2}{\pi}$$

By the definition of G_1 it is apparent that

$$\frac{1}{\pi} \iint \cos \beta'_1 d\Omega_2 = 1 - G_1 \quad (14)$$

and, similarly,

$$\frac{1}{\pi} \iint \cos \beta'_2 d\Omega_3 = 1 - G_2 \quad (15)$$

For hemispherical craters it is possible to show that G is independent of the position of the differential element; and G can also be shown to be approximately independent of position for craters that are nearly hemispherical in shape, even if the emittance is fairly large. This fact has been used by other investigators in dealing with reflections from cavities (e.g., ref. 5). Hence, $G_1 = G_2 = G$ and equation (13) can be rewritten as:

$$E_2 dA_1 = \epsilon_c (1 - \epsilon_c)^2 E_b (1 - G)^2 G dA_1 \quad (16)$$

Similar equations hold for three or more reflections. In general, for a total of i reflections, the energy finally reflected from dA_1 out through the opening of the crater is given by

$$E_i dA_1 = \epsilon_c (1 - \epsilon_c)^i E_b (1 - G)^i G dA_1 \quad (17)$$

The equation also holds for $i=0$ (corresponding to the energy emitted directly through the crater opening).

By equation (5) the effective emittance ϵ_e can now be written

$$\epsilon_e = \iint \sum_{i=0}^{\infty} \frac{E_i dA_1}{W_b A'_c} = \epsilon_c \iint \left[\sum_{i=0}^{\infty} (1 - \epsilon_c)^i (1 - G)^i \right] \frac{E_b G dA_1}{A'_c W_b} \quad (18)$$

But $\sum_{i=0}^{\infty} x^i = 1/(1-x)$ and $E_b = W_b$, so that equation (18) becomes

$$\epsilon_e = \frac{1}{A'_c} \iint \frac{\epsilon_c G dA_1}{1 - (1 - \epsilon_c)(1 - G)} \quad (19)$$

where the integration is over the crater surface.

The fraction G of the radiative energy flux that is directly emitted through the crater opening A'_c is called the geometry factor. There are several methods of finding an expression for G , but the simplest seems to be a method described by Sparrow (ref. 6). The function G is defined by equation (9), which is repeated here:

$$G = \iint \frac{\cos \beta_1 \cos \beta_0 dA_0}{\pi R_{10}^2}$$

According to Sparrow,

$$G = l_1 \oint_{\text{rim}} \frac{(z_0 - z_1) dy_0 - (y_0 - y_1) dz_0}{2\pi R_{10}^2} + m_1 \oint_{\text{rim}} \frac{(x_0 - x_1) dz_0 - (z_0 - z_1) dx_0}{2\pi R_{10}^2} + n_1 \oint_{\text{rim}} \frac{(y_0 - y_1) dx_0 - (x_0 - x_1) dy_0}{2\pi R_{10}^2} \quad (20)$$

where l_1 , m_1 and n_1 are the direction cosines of the normal to the elemental area dA_1 ; x_0 , y_0 , z_0 is the variable point on the contour (the rim of the crater); and x_1 , y_1 , z_1 is the location of dA_1 . From figure 5 and from the equation of an ellipse,

$$l_1 = x_1/q$$

$$m_1 = y_1/q$$

$$n_1 = \frac{z_1 - a}{q} = \frac{r_0^2}{pq} \sqrt{1 - \left(\frac{r_1}{r_0}\right)^2}$$

where q is the length of the normal between dA_1 and the axis:

$$q = \sqrt{r_1^2 + (r_0^2/p^2)(r_0^2 - r_1^2)} = \sqrt{r_1^2 + (z_1 - a)^2} \quad (21)$$

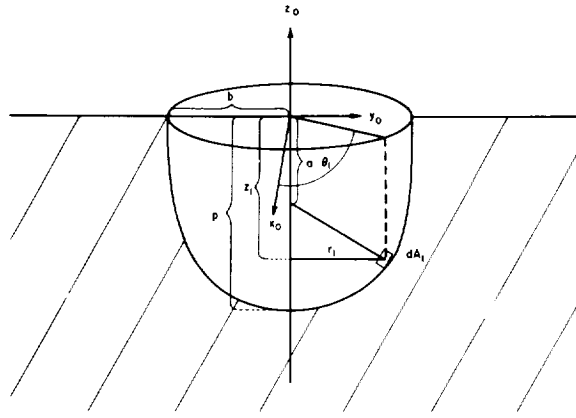


FIGURE 5.—Axes and distances used in the derivation of G .

In cylindrical coordinates,

$$\begin{aligned} x_0 &= r_0 \cos \Theta_0 & x_1 &= r_1 \cos \Theta_1 \\ y_0 &= r_0 \sin \Theta_0 & y_1 &= r_1 \sin \Theta_1 \\ z_0 &= z_0 & z_1 &= z_1 \end{aligned} \quad (22)$$

With the z_0 -axis taken as the axis of the ellipsoid, and with the origin taken in the plane of the opening, $r_0 = b$ and $z_0 = 0$. Then, with Θ_0 taken as the variable of integration, equation (20) becomes

$$G = \left(\frac{1}{2\pi}\right) \oint_{\text{rim}} \left(\frac{b}{R_{10}^2}\right) \{ -l_1 z_1 \cos \Theta_0 - m_1 z_1 \sin \Theta_0 + n_1 [r_1 \cos (\Theta_1 - \Theta_0) - b] \} d\Theta_0. \quad (23)$$

This equation may be reduced to the form

$$G = \frac{1}{2\pi} \oint_{\text{rim}} \frac{b}{R^2} [(A + C) \cos (\Theta_1 - \Theta_0) + B] d\Theta_0 \quad (24)$$

or, with R expressed in terms of the variables,

$$G = \frac{1}{2\pi} \oint_{\text{rim}} b \left\{ \left(\frac{A+C}{E}\right) + \frac{BE - D(A+C)}{E[D + E \cos (\Theta_1 - \Theta_0)]} \right\} d\Theta_0 \quad (25)$$

where A , B , C , D , and E are constants given by:

$$A = \frac{-r_1 z_1 p}{\sqrt{p^2 r_1^2 + b^2(b^2 - r_1^2)}}$$

$$B = \frac{-b^2 \sqrt{b^2 - r_1^2}}{\sqrt{p^2 r_1^2 + b^2(b^2 - r_1^2)}}$$

$$C = \frac{b r_1 \sqrt{b^2 - r_1^2}}{\sqrt{p^2 r_1^2 + b^2(b^2 - r_1^2)}}$$

$$D = (z_1^2 + r_1^2 + b^2)$$

$$E = -2r_1 b$$

$$R_{10}^2 = R^2 = D + E \cos(\theta_1 - \theta_0)$$

In order that this contour integral be positive, it must be integrated clockwise around the opening. The integration can be performed analytically, but some steps become somewhat involved, and particular care must be taken with a many-valued arctan term. The integral is finally obtained in the form

$$G = -b \left[\frac{A+C}{E} + \frac{BE-D(A+C)}{E\sqrt{D^2-E}} \right] \quad (26)$$

or, after expressing A , B , C , D , and E in terms of z_1 , p , and b ,

$$G = \frac{z_1}{2b\sqrt{p^4 + (b^2 - p^2)z_1^2}} \left[(b^2 - p^2) + \frac{2p^4 b^2 + (p^2 - b^2)^2 z_1}{\sqrt{4p^4 b^2 + (p^2 - b^2)^2 z_1^2}} \right]. \quad (27)$$

This expression is inserted in equation (19), which is repeated here for convenience,

$$\epsilon_e = \frac{1}{A_c} \iint \frac{\epsilon_c G dA_1}{1 - (1 - \epsilon_c)(1 - G)} \quad (19)$$

and the effective emittance ϵ_e is obtained by integrating numerically.

The change of emittance per percent area cratered can be written as:

$$\frac{\Delta \epsilon}{100 \left(\frac{A_c}{A_T} \right)} = \frac{\epsilon_e - \epsilon_o}{100} \quad (28)$$

The results of integrating equation (19) numerically are shown in the parameter studies

in figures 6 to 19. The change of emittance per percent area cratered is plotted against the original emittance of the surface, with the emittance of the crater surface as the parameter. The 14 figures of this set are for different ratios of crater depth to crater radius, and cover the range from 0.1 to 3.0. The curved line on each figure goes through the points where $\epsilon_o = \epsilon_c$, that is, where the emittance of the crater wall is the same as that of the original surface.

For a hemisphere, the ratio of crater depth to crater radius is equal to 1, and ϵ_e reduces to the simple expression

$$\epsilon_e = \frac{2\epsilon_c}{1 + \epsilon_c} \quad (29)$$

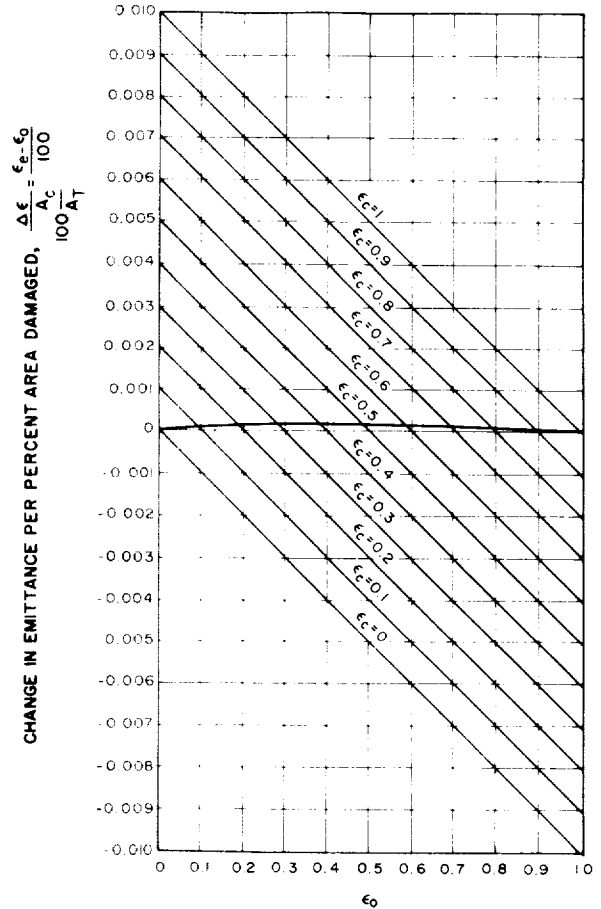


FIGURE 6.— Change in emittance for penetration/radius ratio of 0.1.

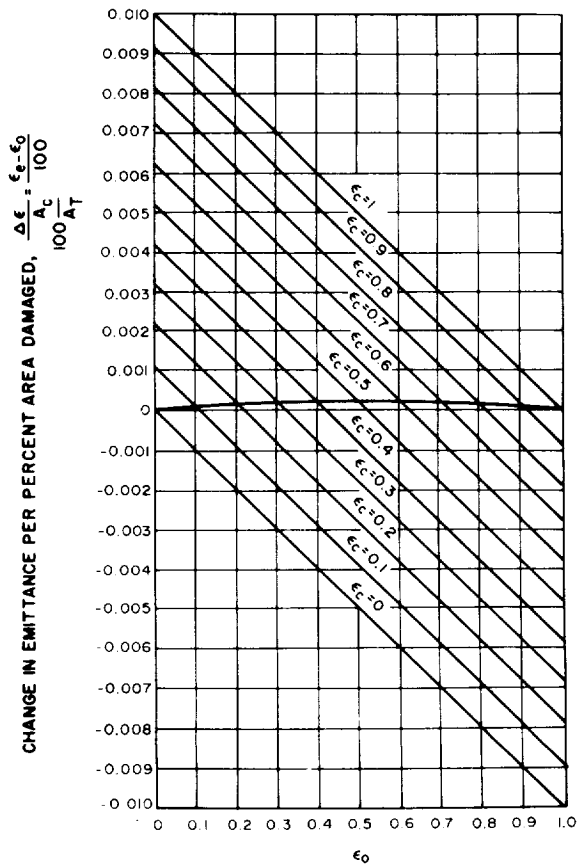


FIGURE 7.—Change in emittance for penetration/radius ratio of 0.2.

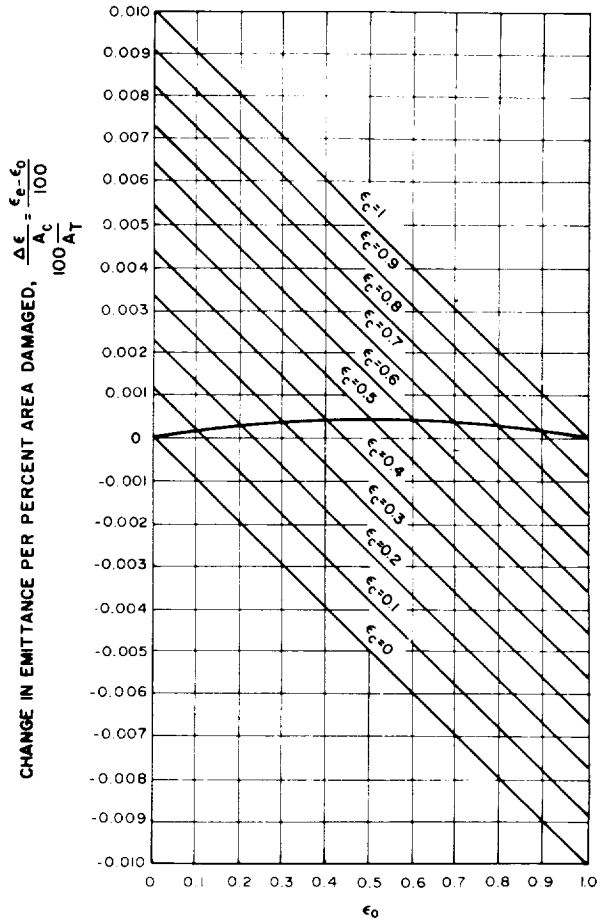


FIGURE 8.—Change in emittance for penetration/radius ratio of 0.3.

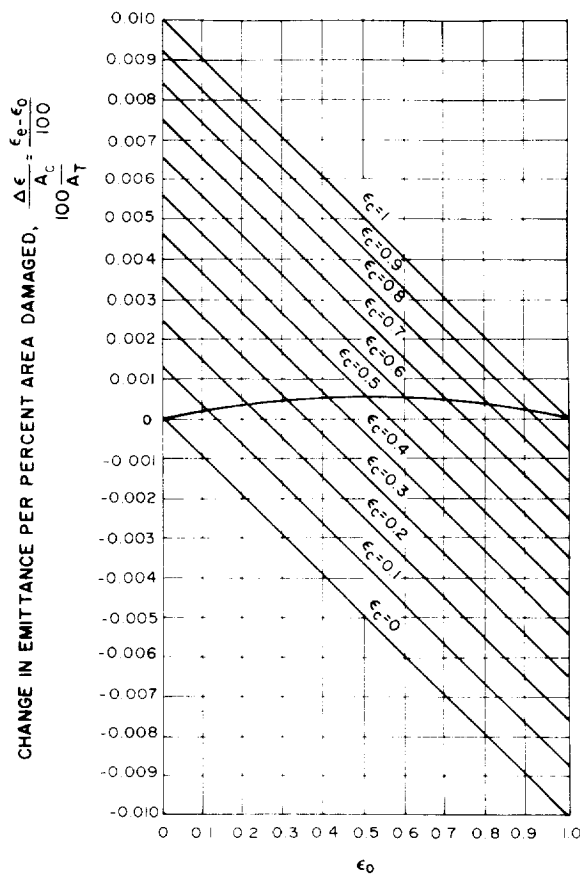


FIGURE 9.—Change in emittance for penetration/radius ratio of 0.4.

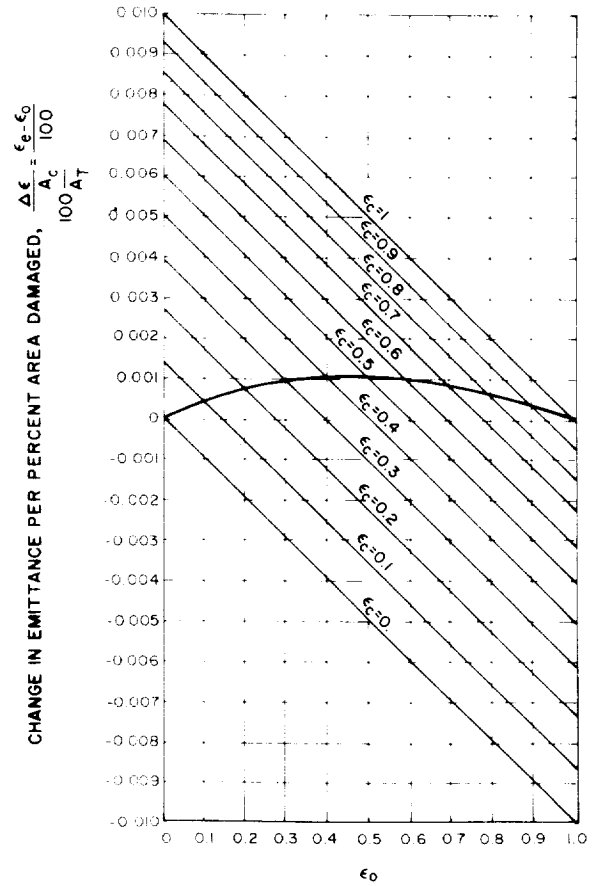


FIGURE 10. Change in emittance for penetration/radius ratio of 0.6.

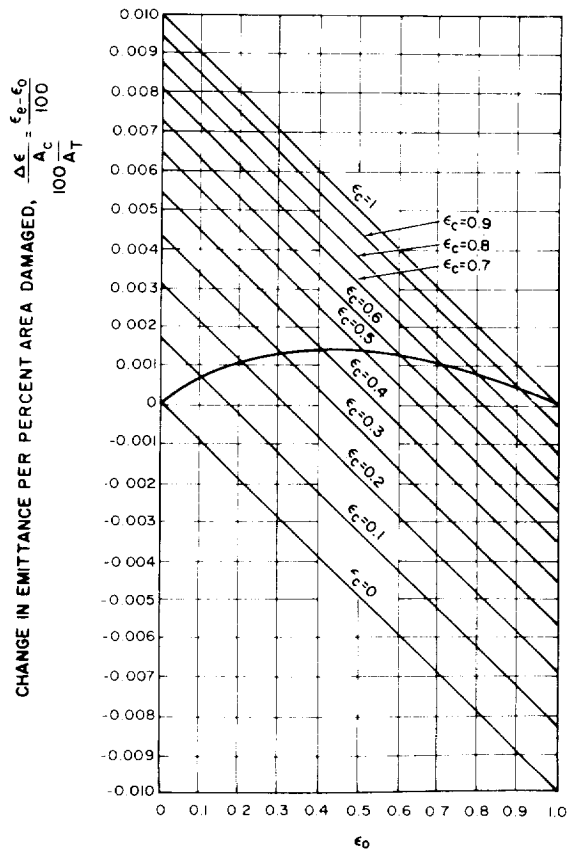


FIGURE 11.—Change in emittance for penetration/radius ratio of 0.8.

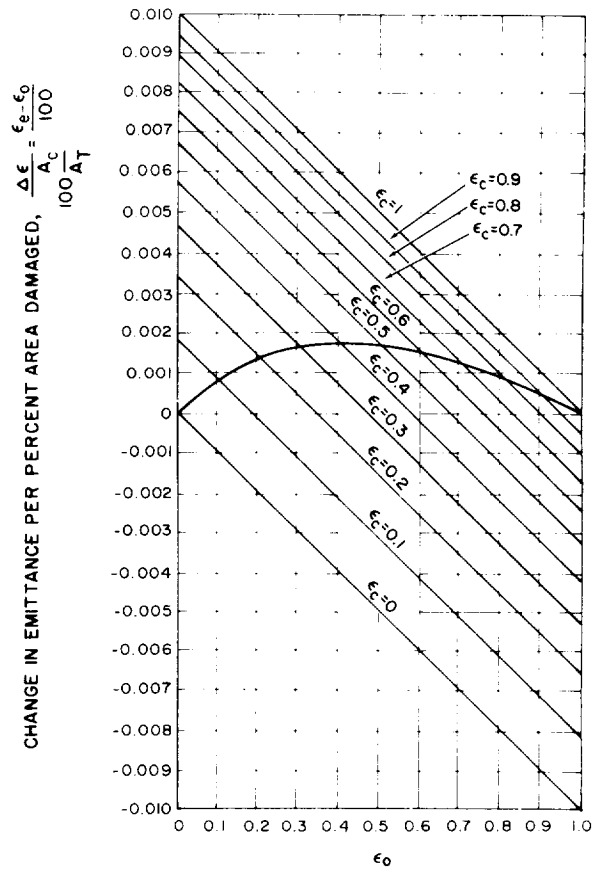


FIGURE 12.—Change in emittance for penetration/radius ratio of 1.0.

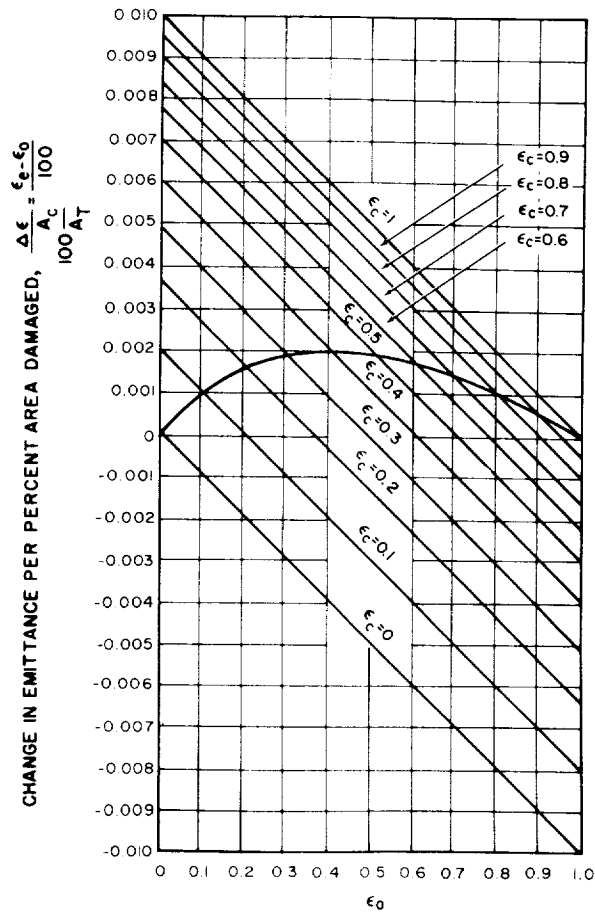


FIGURE 13.—Change in emittance for penetration/radius ratio of 1.2.

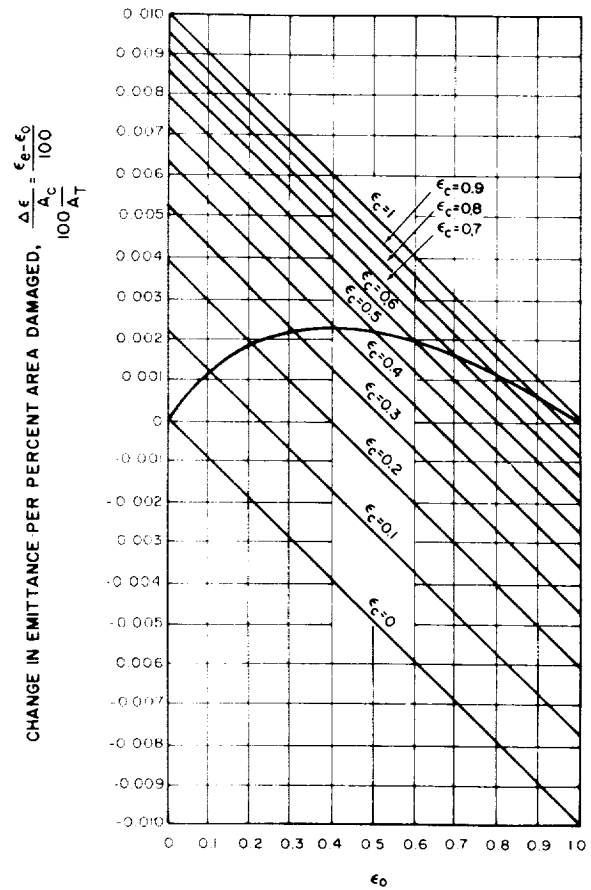


FIGURE 14.—Change in emittance for penetration/radius ratio of 1.4.

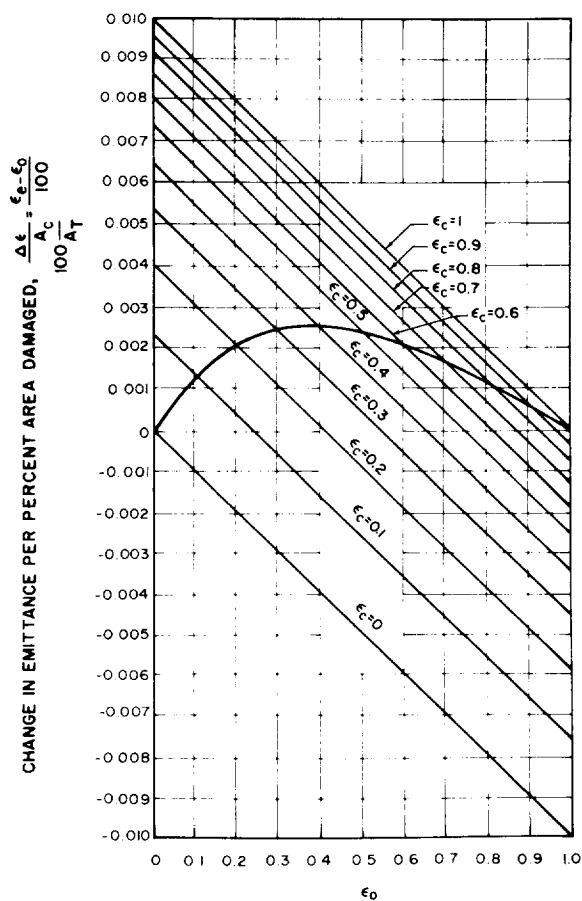


FIGURE 15.—Change in emittance for penetration/radius ratio of 1.6.

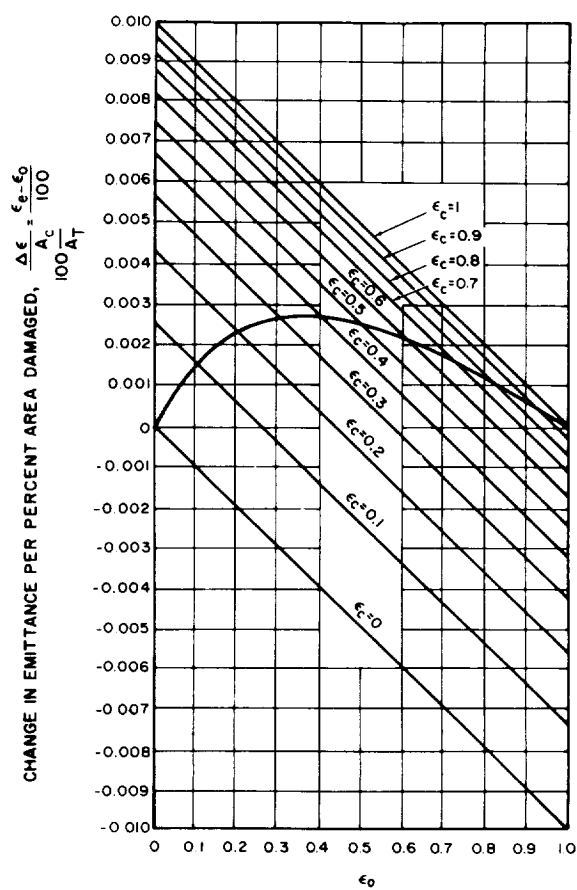


FIGURE 16.—Change in emittance for penetration/radius ratio of 1.8.

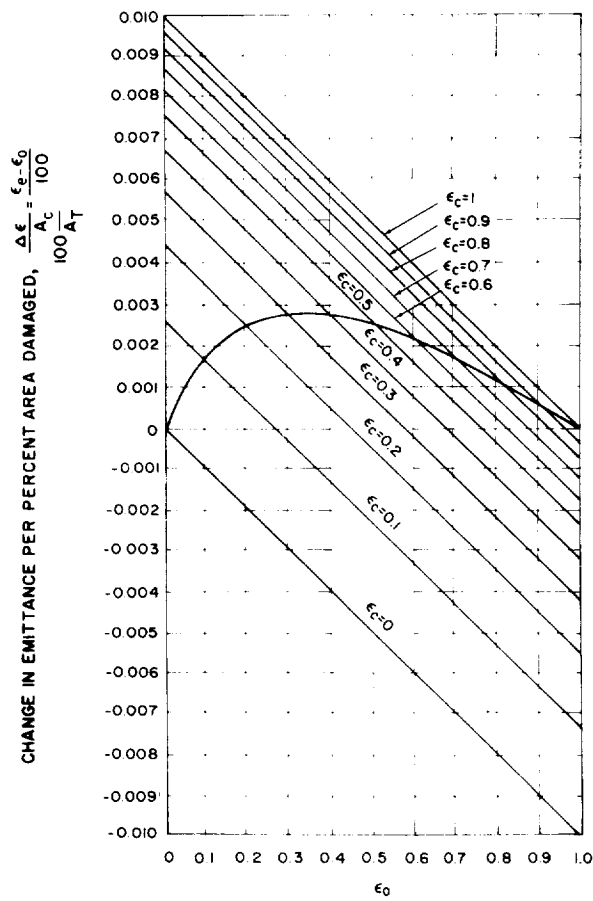


FIGURE 17.—Change in emittance for penetration/radius ratio of 2.0.

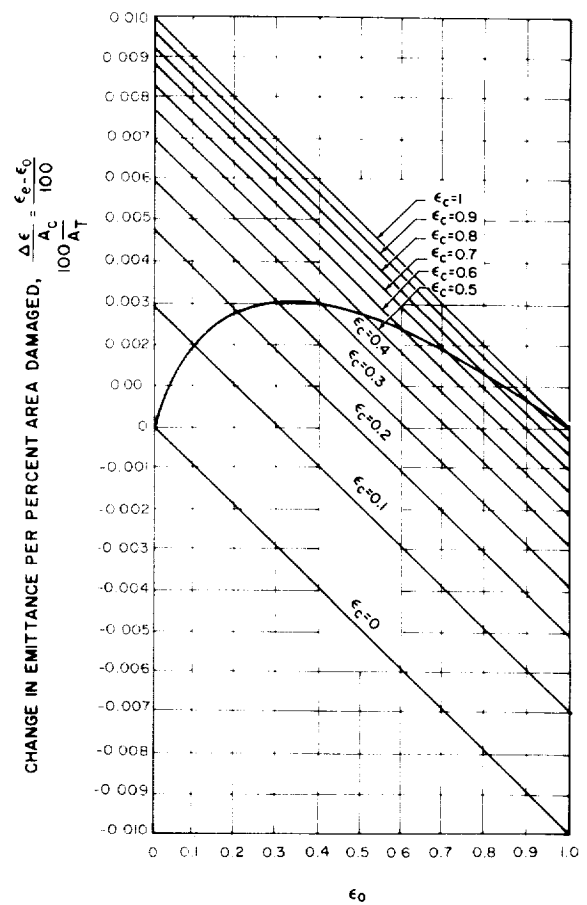


FIGURE 18.—Change in emittance for penetration/radius ratio of 2.5.

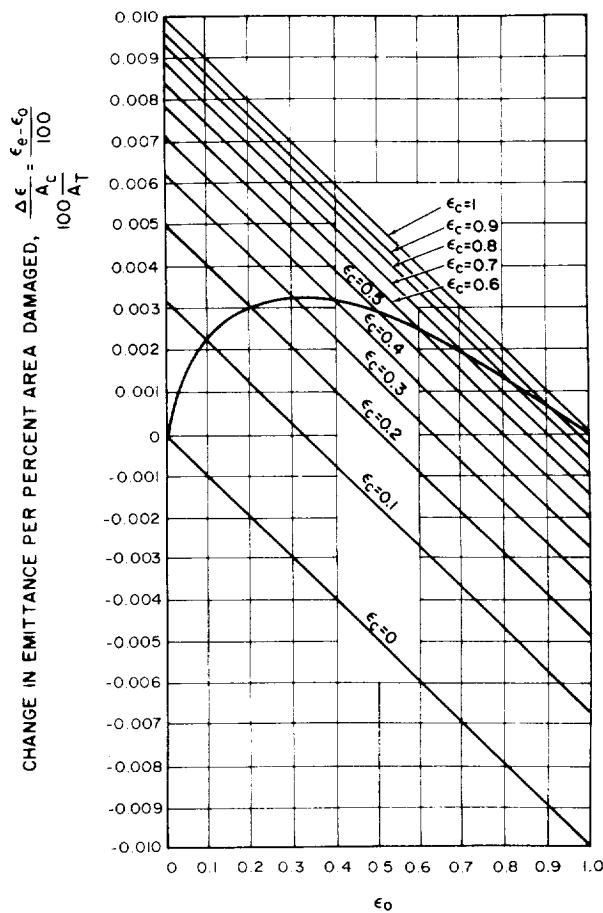


FIGURE 19.—Change in emittance for penetration/radius ratio of 3.0.

Equations (28) and (29) may be combined to give the following equation for the increase in emittance of a (diffuse) hemispherical crater:

$$\Delta \epsilon = \frac{A_c}{A_T} \frac{2\epsilon_c - \epsilon_0(1 - \epsilon_c)}{1 + \epsilon_c}$$

The effective emittance of a hemispherical crater with specularly reflecting walls can also be expressed fairly simply:

$$\epsilon_e = \epsilon_c \left[1 + \sum_{i=1}^{\infty} (1 - \epsilon_c)^i \cos \alpha_i \right] \quad (30)$$

where $\alpha_i = \pi/2(i+1)$. The dotted curve in figure 20 (which is otherwise the same as fig. 12, for hemispherical craters) is for the specu-

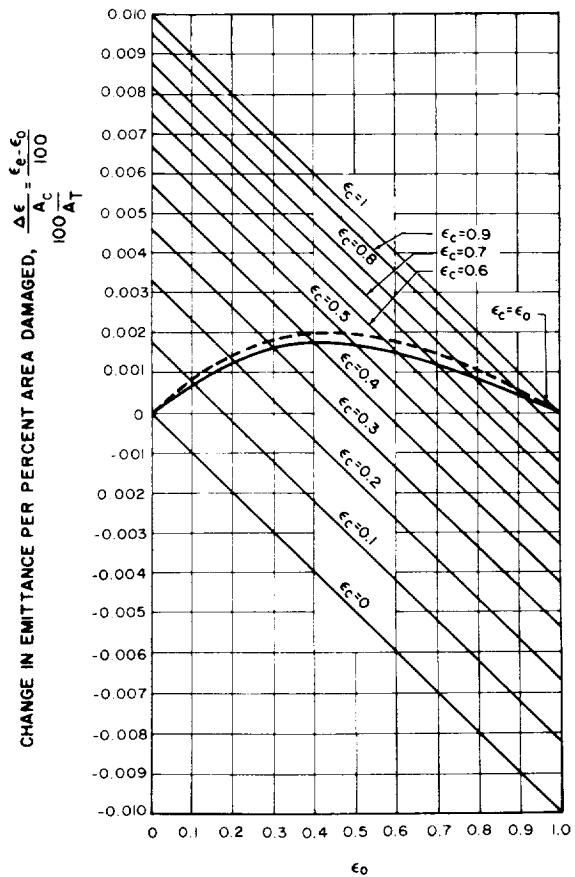


FIGURE 20.—Change in emittance for penetration/radius ratio of 1.0. The dashed curve is for a specularly reflecting crater wall; otherwise the figure is the same as figure 12.

larly reflecting case. It is slightly higher than the curve for the diffusely reflecting case shown by the solid line.

COMPARISON OF THE MATHEMATICAL MODEL WITH LABORATORY DATA

The mathematical model derived in the preceding sections was compared with experimental data obtained by bombarding surfaces with particles. The work was done at AVCO by C. H. Leigh and others (refs. 7, 8, and 9) under contract to the Marshall Space Flight Center. Samples of gold, aluminum, stainless steel (304 and 316), chromium, tungsten, and silver were carefully polished and their reflectances measured over a wavelength range from 2 to 24 microns. The measurements were made with

a heated-cavity-spectrophotometer arrangement, illustrated in figure 21. The samples were then bombarded with spherical zircalloy and tungsten microparticles approximately 100 microns in diameter. The tungsten particles are shown in figure 22. Figures 23 and 24 show the microparticle accelerator or light gas gun and the microparticle carrier, or sabot. The sabot is propelled forward by the expansion of the hydrogen gas down the launch tube and strikes the sabot stripper which separates the particles from the sabot. The particles continue into the sample chamber and strike the

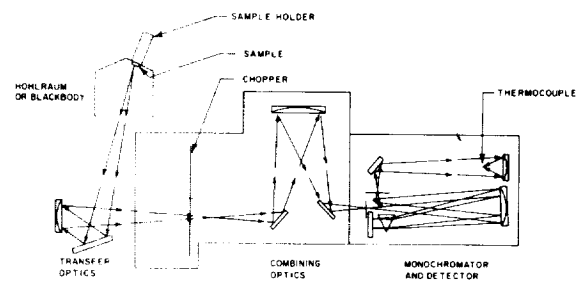


FIGURE 21.—Heated-cavity-spectrophotometer arrangement used (ref. 7) for measuring emittances of surfaces damaged by high-velocity particles.

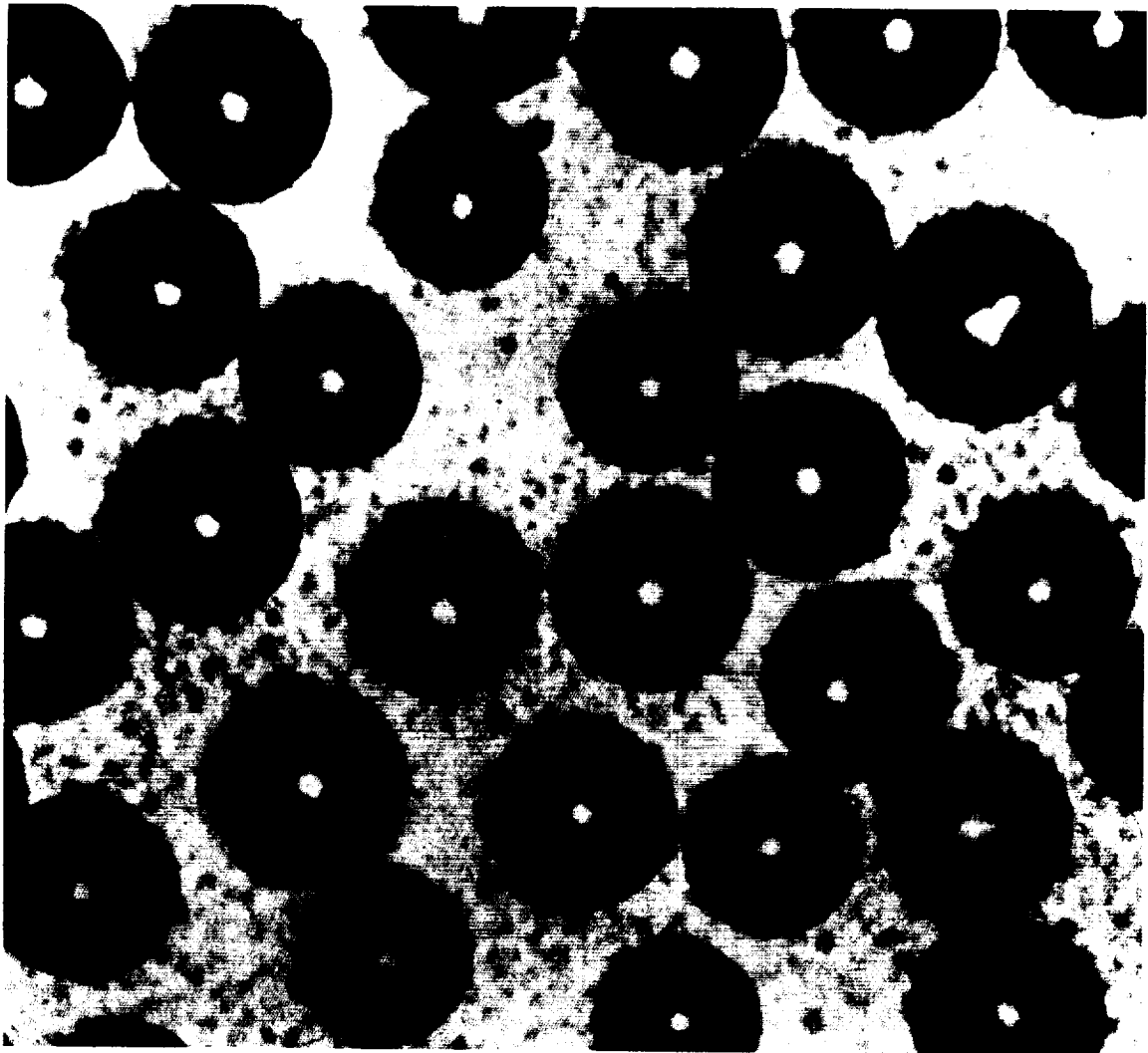


FIGURE 22.—Tungsten projectiles (150X).

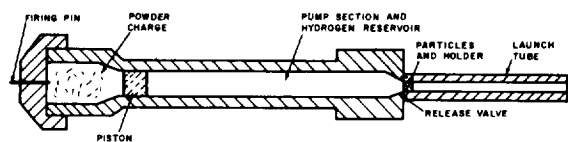


FIGURE 23.—Schematic of high-velocity microparticle accelerator.

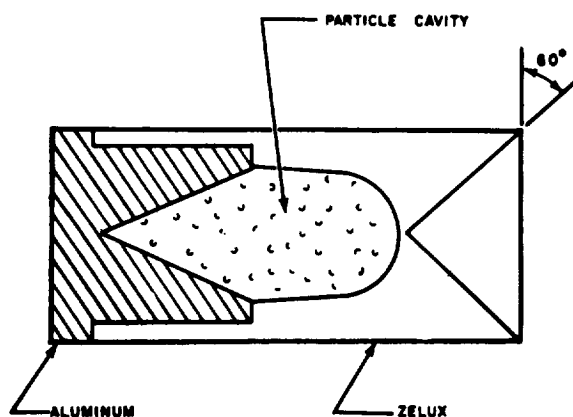


FIGURE 24.—Microparticle sabot.

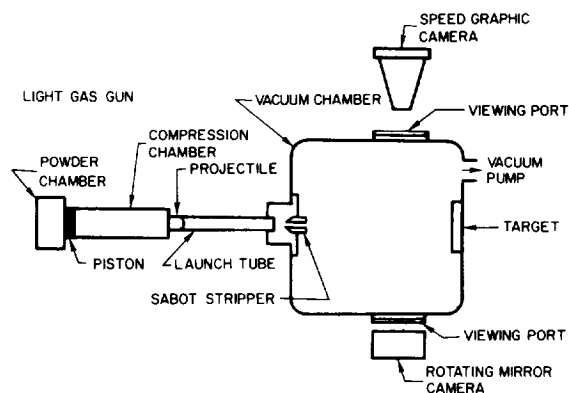


FIGURE 25.—Schematic of microparticle range.

sample. Figure 25 shows the entire range setup with the velocity-measuring cameras. The velocities obtained with this system are of the order of 1.5 km/sec. After the samples were bombarded their reflectances were again measured. A summary of the damage and changes is given in table II.

TABLE II.—Description of Damage to Samples

Material	Measure- ment*	Projectile velocity		Number of craters	Average diameter, μ	Average depth, μ	Depth Diameter	Area damaged, %	Knoop hardness (100-g load)
		ft/sec	m/sec						
Al	R	5,000	1500	549	123	289	2.35	3.41	22
	R	20,000	7000	7,830	54	183	3.39	18.9	----
	α/ϵ	20,000	7000	19,467	27	78	2.87	17.6	----
Au	R	5,000	1500	630	213	241	1.13	9.99	40
	R	17,000	5200	5,526	63	61	0.97	21.47	----
	α/ϵ	20,000	7000	**8,380	53	60	1.13	29.68	----
SS 304	R	5,000	1500	327	111	172	1.55	1.42	219
	R	20,000	7000	3,672	106	179	1.69	17.44	----
	α/ϵ	20,000	7000	6,012	74	124	1.68	19.04	----
Cr	R	5,000	1500	663	130	196	1.51	3.88	697
	R	20,000	7000	3,321	125	239	1.91	21.10	----
	α/ϵ	20,000	7000	**1,764	112	237	2.12	11.40	----
Pt	R	20,000	7000	2,844	182	189	1.04	38.20	120
	α/ϵ	20,000	7000	**4,099	122	127	1.04	34.24	----
SS 316	R	5,000	1500	438	205	186	0.91	6.43	----
W	R	5,000	1500	456	120	----	----	2.27	----
Ag	R	5,000	1500	710	175	306	1.75	7.61	----

*R=reflectance.

**Total number of craters on both sides of α/ϵ specimens.

Table III shows a comparison of computed emittance changes with the measured changes. The particle speeds were less than hypervelocity so that one would expect small fragments of the particles to remain imbedded in the craters. In any case, the emittance of the crater surface, e_c , could not be determined directly. A value of 0.25 for e_c was arbitrarily chosen for purposes of the comparison, and it gave fair agreement for the first three metals in the table. For the last metal in the table, agreement is, of course, impossible since the "measured change" exceeds 1.0.

As was shown earlier, the total number of micrometeoroid particles of mass greater than m passing through a square meter per second is given by

$$N = \alpha m^\beta \quad (31)$$

where α and β are constants, and β is negative. This equation is the usual form of the micrometeoroid flux law. The (positive) number of particles with masses between m and $(m + \Delta m)$ passing through a square meter per second is given by

$$\Delta N = |\alpha \beta m^{\beta-1} \Delta m|. \quad (32)$$

Each particle (in the hypervelocity regime), if it happens to strike a surface, will produce a crater of volume given by

$$V = K \left(\frac{1}{2} m v^2 \right) \quad (33)$$

where K is a constant empirically determined for many materials (table 1) and v is the velocity. Thus, the cratered surface area for one incident particle would be

$$A'_p = \pi \left(\frac{3K}{4\pi} m v^2 \right)^{2/3}. \quad (34)$$

The total crater opening area created per second is found by multiplying equations (32) and (34) and integrating with respect to m

$$\frac{dA_c}{dt} = (A_T - A_c) \int_{m_0}^{\infty} \pi \left(\frac{3}{4\pi} K m v^2 \right)^{2/3} \alpha \beta m^{\beta-1} dm$$

or

$$\frac{dA_c}{dt} = \frac{A_T - A_c}{\beta + \frac{2}{3}} \pi \left(\frac{3}{4\pi} K v^2 \right)^{2/3} \alpha \beta m_0^{\beta+2/3} \quad (35)$$

where $A_T - A_c$ is the uncratered area, m_0 is the cut-off mass, and β is less than $-\frac{2}{3}$.

Equation (35) is a differential equation in A_c and t . Integrating it yields the following equation for the time for the meteoroids to produce the ratio $A_c/(A_T - A_c)$ of cratered to uncratered area

$$t = \log_e \left(1 + \frac{A_c}{A_T - A_c} \right) \frac{\beta + \frac{2}{3}}{\pi \alpha \beta \left(\frac{3}{4\pi} K v^2 \right)^{2/3} m_0^{\beta+2/3}} \quad (36)$$

or, for relatively small values of A_c

$$t \approx \frac{A_c}{A_T - A_c} \frac{\beta + \frac{2}{3}}{\pi \alpha \beta \left(\frac{3}{4\pi} K v^2 \right)^{2/3} m_0^{\beta+2/3}} \quad (37)$$

TABLE III.—Emittance of Cratered Surfaces

Metal	e_c	Depth* radius	Cratered area Total area A_c/A_T	Measured change, $\frac{\Delta e_\lambda}{A_c/A_T}$	Calculated change,** $\frac{\Delta e}{A_c/A_T}$
Gold.....	0.025	2.26	0.100	0.6	0.5
Aluminum 2S.....	.025	4.70	.034	1.0	.75
Stainless steel 316.....	.10	1.82	.064	0.3	.4
Chromium.....	.05	3.02	.039	0.9	.5
Silver.....	.02	3.50	.076	1.1	.55

* Particle speeds, 5000 to 6000 fps = 2 km/s.

** Crater surface emittance e_c assumed to be 0.25.

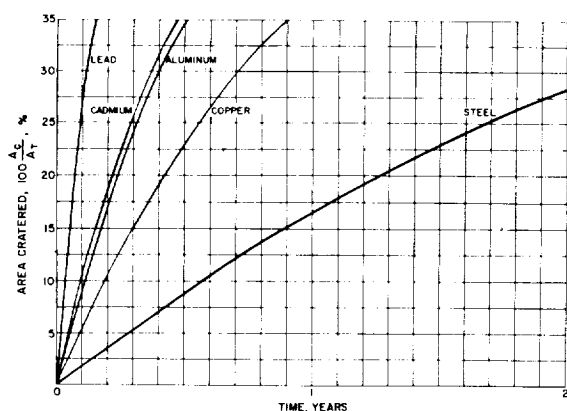


FIGURE 26.—Calculated micrometeoroid erosion as a function of time for five metals. Constants used in the flux law (equation (31)):

$$\alpha = 10^{-21} \text{ cm}^{-2} \text{ sec}^{-1} \text{ g}^{-\beta}$$

$$m_0 = 10^{-11} \text{ g}$$

$$\beta = -1.7.$$

This relation between the exposure time and the proportion of cratered area is plotted in figure 26 for several different metals (different values of K). The constants assumed for the flux law are indicated on the figure. Changes in these constants result in contraction or expansion of the time scale.

RÉSUMÉ AND CONCLUDING REMARKS

In this paper some basic ideas on how the micrometeoroid space environment can affect the thermal radiative characteristics of surfaces have been discussed. Much of what has been said could also be applied to windows and lenses, solar concentrators, or other structures and devices that may be required to operate in the space environment, but the main objective was to describe analytically the change in the emittance of a surface due to particle impact.

An analysis was developed to predict the change of the emittance due to craters of an ellipsoidal shape. One would expect hemispherical craters in the space environment, but in order to compare the results with craters formed by slow particles, which have prolate hemispheroidal craters, a general analysis for any ellipsoidal type of crater was developed. The results are plotted in a parametric fashion in 14 figures. One useful feature of these graphs

is that the surface emittance of the crater can be different from the original surface so that if the substrate were a different material, the change in emittance still can be found. The emittance would probably be expected to be different because of possible contamination of the crater surface by the incident particle and because of work hardening of the material at the crater surface.

The calculated change in emittance due to hemispherical craters is extremely useful in estimating expected changes in the emittance of a surface in the space environment. A simple relationship for this type of crater was derived. For the case of the hemispherical crater, the change in emittance is about the same for a diffusely reflecting as for a specularly reflecting crater surface.

Experimental data and the analytical results for the change in emittance were compared, for an assumed value of crater surface emittance. The experimental data were usually somewhat higher than predicted by the analysis. Perhaps contamination or failure to count all of the craters could explain this difference.

Certainly there still remain further areas of study. For example, because of the large number of very small craters whose dimensions approach the wavelength of the emitted and absorbed electromagnetic radiation, it is necessary to determine the extent to which surface optical properties are affected by craters of this size. The results of such a study could indicate whether the estimated time for changing the emittance by a specified percentage is grossly in error (perhaps by several orders of magnitude). Another important question is the nature of the crater wall. These questions suggest that further experimental and analytical work is necessary.

The micrometeoroid environment as determined by microphone data should, according to the present analysis, result in detectable changes in satellite temperatures within a month. For lower flux laws, such as those predicted from penetration measurements or the Watson flux law, the time scale would be contracted by 10^4 , and there would be no detectable change in temperature for years. When information is available from certain space emissivity experi-

ments, the micrometeoroid flux could, in effect, be calculated from the thermal data and used to predict the change of emittance of materials in space.

REFERENCES

1. JACCHIA, L. G.: Harvard College Observatory Reprint Series II, no. 26, 1945.
2. WHIPPLE, FRED L., and HAWKINS, GERALD S.: Meteors. Encyclopedia of Phys., vol. LII, Astrophysics III: The Solar System, S. Flügge, ed., Springer-Verlag (Berlin), 1959, pp. 519-564.
3. VEDDER, J. F.: Micrometeorites. Ch. 5 of Satellite Environment Handbook, Francis S. Johnson, ed., Stanford Univ. Press, 1961, pp. 91-100.
4. EICHELBERGER, R. J., and GEHRING, J. W.: Effects of Meteoroid Impacts on Space Vehicles. ARS Jour., vol. 32, no. 10, Oct. 1962, pp. 1583-1591.
5. TREUENFELS, ERNEST W.: Emissivity of Isothermal Cavities. Jour. Optical Soc. of America, vol. 53, no. 10, Oct. 1963, pp. 1162-1171.
6. SPARROW, E. M.: A New and Simpler Formulation for Radiative Angle Factors. Trans. ASME, Ser. C—Jour. Heat Transfer, vol. 85, no. 2, May 1963, pp. 81-88.
7. LEIGH, CHARLES H., and WOLNIK, S. J.: Emissivity of Metals After Damage by Particle Impact. AVCO Corp., RAD-SR-61-68, July 21, 1961.
8. LEIGH, CHARLES H.: Spectral Emissivity of Metals After Damage by Particle Impact. AVCO Corp., RAD-TR-62-33, Aug. 13, 1962.
9. LASZLO, T. S., and GANNON, R. E.: Spectral Emissivity of Metals After Damage by Particle Impact. AVCO Corp., RAD-TR-63-39, Sept. 5, 1963.

DISCUSSION

MICHAEL MIRTICH, NASA Lewis Research Center: You indicated that in the hypervelocity region relatively little material from the impinging projectile remains in the crater. Charters and Summers, and also Ralston and Schmidt, using radioactive particles, found that in the hypervelocity region 5 to 8% of the impinging particles lined the craters.

MERRILL: My remark that the crater is mainly free of material from the high-speed particle was based on an article entitled "Effects of Meteoroid Impacts on Space Vehicles," which appeared in the ARS Journal in 1962 (ref. 4).

MIRTICH: What type, size, and speed of particles were used in the experiments that you described?

CHARLES H. LEIGH,² Parametrics, Inc.: The particles had diameters in the range of 50 to 100 microns, with the larger sizes predominating; they were perfectly spherical; and their speeds were 5000 to 6000 feet per second, although in subsequent work speeds up to 23,000 feet per second have been attained by use of a light-gas gun. The speeds of 5000 to 6000 feet per second are generally sufficient to produce the hemispherical craters. Incidentally, your first comment on the residual material lining the crater would be correct. There is a coating left on the inside of the crater, but the major portion of the impacting projectile in the hypervelocity region is vaporized.

MIRTICH: At Lewis we have been accelerating silicon carbide particles ranging from 2 to 14 microns in diameter into the hypervelocity region, and we have

found that our craters are coated with the impacting projectile.

LEIGH: This is quite correct; it is almost always observed with any projectile.

TIBOR S. LASZLO, AVCO Corporation: We made measurements under a NASA Marshall contract of the damage inflicted on metals when micrometeoroids impact it. The studies involved preparing a highly polished metal surface, measuring its α/ϵ value, then simulating the micrometeoroid damage by impacting the surface with minute particles traveling at very high velocities, and, finally, measuring the α/ϵ value again. We found that the change in α/ϵ is a distinct function of the material and of the temperature. For example, in the case of aluminum the α/ϵ value appears to be independent of the temperature within the limits of the experiment. The value for the damaged surface was lower than that of the freshly polished metal. For gold both the polished and damaged surfaces show increasing α/ϵ values with increasing temperatures. Chromium-plated copper appears to be temperature sensitive only in the damaged condition. For all these metals the damage causes a decrease in the α/ϵ value. The α/ϵ value of 304 stainless steel, however, is not only independent of the temperature (or of the intensity of solar radiation), but is also identical for polished and damaged surfaces.

HELLER: As a final remark, it is obvious that more research is needed; especially, experimental work has to be done with impacting particles of higher velocities.

² As mentioned in the text, the experimental work was done by Dr. Leigh, who was then with AVCO Corp.

46. Alteration of Surface Optical Properties by High-Speed Micron-Size Particles

MICHAEL J. MIRTICH AND HERMAN MARK

NASA LEWIS RESEARCH CENTER, CLEVELAND, OHIO

Micron-size particles were accelerated by aerodynamic drag to gas speeds in a 3-inch shock tube to simulate some aspects of micrometeoroid erosion. A streak-camera technique was used to make velocity measurements in the gas-heated, radiating cloud of particles. Good agreement was obtained between measured and theoretically predicted velocities. Integrated density measurements were made by collecting the particles on disk collectors.

Aluminum and aluminum-coated disks were placed in the shock tube and exposed to bombardment by a known number of particles with known velocity, size, and composition. These experiments yielded the following results:

1. Bombardment of polished metallic surfaces by high-speed, micron-size particles causes reduction in average reflectance, $\bar{\rho}$, of the surface. This reduction can be correlated with the kinetic energy of the bombarding particle cloud, H , by an expression of the form

$$\bar{\rho}(H) = \bar{\rho}_i \left[1 - \left(1 - \frac{\bar{\rho}_\infty}{\bar{\rho}_i} \right) (1 - e^{-sH}) \right]$$

where $\bar{\rho}_i$ is the initial average reflectance and $\bar{\rho}_\infty$ is the ultimate average reflectance.

2. This correlation indicates that the measured kinetic energy flux of micrometeoroids in the vicinity of the Earth in the range from 10^{-10} to 10^{-8} g will reduce the reflectance of a polished aluminum surface to half its original value in about 3 years. Although the results of experiments on nine major satellites have provided no information on particles smaller than 10^{-10} g, an extrapolation of the existing data, with the assumption that particles of 10^{-11} g do exist at the extrapolated flux, reduces this damage time to about 7 months. This estimate of degradation of surface reflectance in near-Earth orbit assumes that single-particle kinetic energy, $\frac{1}{2} mV_p^2$, for the laboratory is equal to single-particle kinetic energy in space. Higher space particle kinetic energies will correspond to lower degradation rates.

3. Coatings of 8600 Å aluminum on a $\frac{1}{16}$ -inch-diameter bakelite disk were removed by particle clouds with kinetic energy of less than 2 joules, an amount less by an order of magnitude than the energy required to remove these coatings by evaporation.

One of the hazards encountered by space vehicles, particularly when they are traveling in the vicinity of the Earth, is that of collision with micrometeoroids. The latest data (ref. 1) on space conditions indicate that flux rates become appreciable for particle mass of about 10^{-10} g. (A particle of mass $\geq 10^{-10}$ g hits an area 1 cm square about 10 times per day.) The speeds of these particles, with respect to the Earth, range from about 30,000 to 200,000

ft/sec, and these particles are estimated to have densities between 0.05 and 5 g/cc. The effect on the surface optical properties of materials after prolonged exposure to the high-speed micrometeoroid environment of space is not known. It is, therefore, desirable to simulate this space condition and study the effects in the laboratory. Such a study involves selecting particles of known mass and composition and accelerating these particles to

speeds comparable with those that exist in space. Bombardment of surfaces of interest by these particles causes damage to the surface optical properties, which can be measured and which can therefore be converted into quantitative information concerning the degradation of such surfaces in space.

A facility that can be used in the laboratory to simulate these conditions is the shock tube. The use of aerodynamic drag of a short-duration flow in a shock tube as a means of accelerating small particles to shocked gas speeds was studied both analytically and experimentally at the Lewis Research Center. Although the particle speeds are lower in our present shock tube than those existing in space, they were sufficiently high to make hemispherical craters (particle velocity greater than one-half the sound speed in the target material) in aluminum targets (ref. 2). Various polished aluminum and aluminum-coated disks were placed in the shock tube and exposed to the high-speed particles. Experimental damage to the targets was determined by measuring changes in the optical properties of the various surfaces with a spectral reflectometer. The results of these damage studies are presented herein together with a correlation that permits prediction of time variation of surface reflectance in space.

SYMBOLS

$$b = \frac{3\pi\eta D}{k_m}$$

C_p specific heat of particle

$$C_1 = \frac{2r^2 C_p \rho_p}{3k}$$

D particle diameter, cm

E minimum tungsten radiation energy needed to expose Royal X Pan film (Eastman Kodak Co.), 76×10^{-4} erg/cm²

$$H = \sum_i \frac{1}{2} m_i V_i^2$$

F_d drag force

$$K = \frac{b}{m} = \frac{18\eta}{k_m \rho_p D^2}$$

k thermal conductivity of accelerating gas

k_m Cunningham-Millikan correction factor,

$$1 + \frac{0.16 \times 10^{-4}}{D} \left(\frac{T_g}{T_0} \right) \left(\frac{P_0}{P_g} \right)$$

M Mach number

m particle mass

m_i mass of i th particle

P_0 standard pressure

P_g gas pressure

R distance from particle to lens of streak camera

r particle radius

r_l radius of camera lens

S constant in exponent of equations (6) and (7)

T_0 standard temperature

T_g gas temperature

$T_{p,1}$ temperature of particle in hot gas

$T_{p,2}$ temperature required for particle traveling at velocity V_p to radiate minimum energy needed to expose Royal X Pan film

T_r room temperature

t time

V_g gas velocity

V_i velocity of i th particle

V_p particle velocity

X_p distance from injection point of particle

η viscosity of gas

ρ_p density of particles

$\bar{\rho}$ average reflectance

$\bar{\rho}_f$ final average reflectance

$\bar{\rho}_i$ initial average reflectance

$\bar{\rho}_\infty$ average reflectance after infinite time

σ Stefan-Boltzmann constant

ACCELERATION OF PARTICLES BY SHOCK TUBE FLOWS

An analysis was made to determine the feasibility of accelerating particles in short-duration shock-tube flows. The accelerating force was assumed to be the aerodynamic drag of the high-speed gas acting on spheroidal particles placed in the stream. The results of a typical calculation of the predicted velocity as a function of the distance downstream of injection are shown in figure 1 for silicon carbide, SiC, particles 2 to 20 μ in diameter. The Reynolds number for these particles relative to the gas was sufficiently low during a large part of the accelerating process to warrant use of the well-known Stokes solution for spheres given by the following equation:

$$F_d = b(V_g - V_p) = -m \frac{d(V_g - V_p)}{dt} \quad (1)$$

The semiempirical Cunningham-Millikan correction factor for slip (ref. 3) was added in the b of equation (1), but this factor was generally very close to 1.0.

The solid curves in figure 1 are defined by equations (2) and (3), which are obtained by integrating equation (1):

$$V_p = V_g(1 - e^{-Kt}) \quad (2)$$

$$X_p = V_g t - \frac{V_g}{K}(1 - e^{-Kt}). \quad (3)$$

The temperature of an accelerating particle in the hot gas at time t is

$$T_{p,1} = T_g + (T_r - T_g)e^{-t/C_1}. \quad (4)$$

The temperature required for a particle traveling at velocity V_p to radiate the energy needed to expose the film at the focal plane of the streak camera is given by

$$T_{p,2}^4 = \frac{ER^2 V_p(t)}{2.5\sigma r_i^2 D}. \quad (5)$$

The "visibility curve" of figure 1, obtained by equating $T_{p,1}$ to $T_{p,2}$, connects the points on the three curves (for particle diameters of 2, 5, and 10 microns) where the particles first become visible.

The contact surface in figure 1 signifies the termination of the hot gas flow (i.e., arrival of the cold-gas piston contact surface) which was calculated from the theory of reference 4. This does not terminate the flow altogether,

however, for behind the contact surface is the cold expanded driver gas (He) whose velocity is the same as that of the hot gas (air) for a time. Particles that are not at gas speed on arrival of the contact surface pass through the contact surface and are still accelerated, but at a slower rate, by the cold gas. This condition lasts until termination of the cold flow, usually determined by the arrival of the first expansion wave. When applicable, a calculation was made to obtain the limit of visibility for the heated particles being cooled by the cold driver gas to temperatures below visibility.

EXPERIMENTAL PROCEDURE

The short duration flow in a 3-inch-diameter shock tube was used successfully to accelerate the micron-size particles used in this program. Helium at high pressure was used as the driver gas, and air was used in the low-pressure section. A copper diaphragm separating the chambers was ruptured by an arrowhead plunger. This system was very successful in initiating the flows while preventing any diaphragm particles from tearing loose and interfering with the experiment. An important feature of the experiment is the fact that the gas behind the shock is at a high temperature, and therefore not only accelerates the small particles but also heats them sufficiently to make their trajectories visible on film.

Particles to be injected into the stream were placed on the horizontal surface of a sharp-edged, thin plate located downstream of the diaphragm in the middle of the shock tube, from which they were picked up by the high-speed flows.

Velocity measurements of the gas-heated, radiating cloud of particles were made with 1250 ASA film in a streak camera. Results of one of these velocity measurements are shown in figure 2. The streaks were made by radiation given off by SiC particles in the size range from 2 to 14 μ . The shock Mach number was 6.5, and the initial air pressure was 6.7 mm Hg. The velocity was determined from the speed of the film and the angle of a streak with the horizontal. The speed of the film is very accurately known (to a small fraction of a

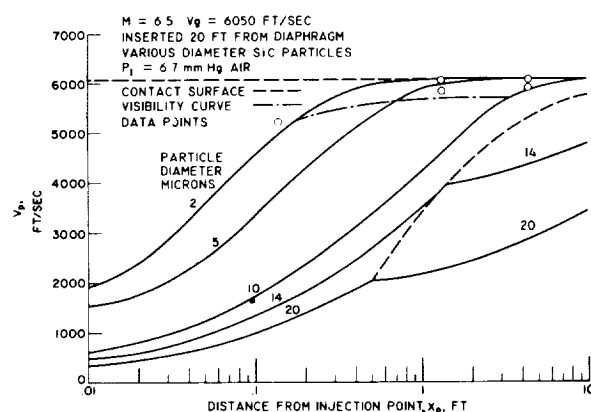


FIGURE 1.—Velocity plotted against position from injection point of silicon carbide particles of various sizes for $M=6.5$, an initial air pressure of 6.7 mm mercury and a gas velocity of 6050 ft/sec.

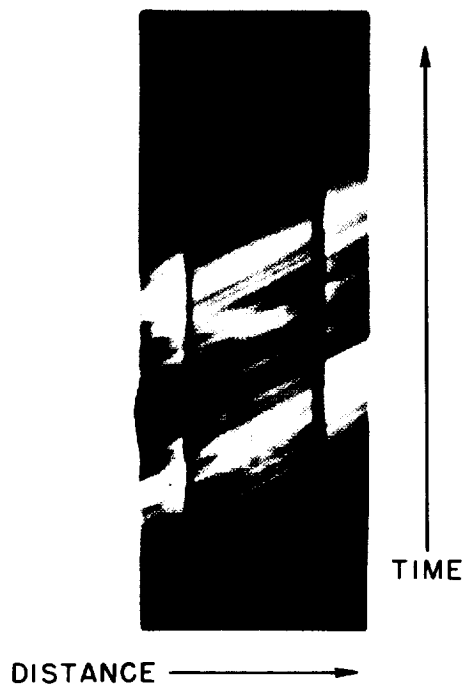


FIGURE 2.—Streaks made by radiation given off by 2- to 14- μ silicon carbide particles at $M=6.5$.

percent) from measurements of the rotational speed of the exposing mirror beam (246 rps), and hence particle speeds are measured to good accuracy. Data obtained in this manner are shown as experimental points in figure 1.

Particle distribution measurements were made by collecting the particles on disk collectors of various diameters, as shown in figure 3. The collectors range in diameter from $\frac{1}{2}$ to $3\frac{1}{16}$ inches and were coated with vacuum grease to insure capture of the particles. The coated disk collectors were weighed on an analytical balance before and after bombardment by the particles. The difference in weight gives the mass of particles collected by each disk, and from this the radial density distribution. When no particles were injected, the weights of the collectors were unchanged, as accurately as could be measured. The mass of particles collected, normalized to the mass of particles collected on the largest disk, is plotted against the diameter of the disk collectors in figure 4. From figure 4 it can be seen that the radial distribution of particles varied only slightly with the Mach number and was independent

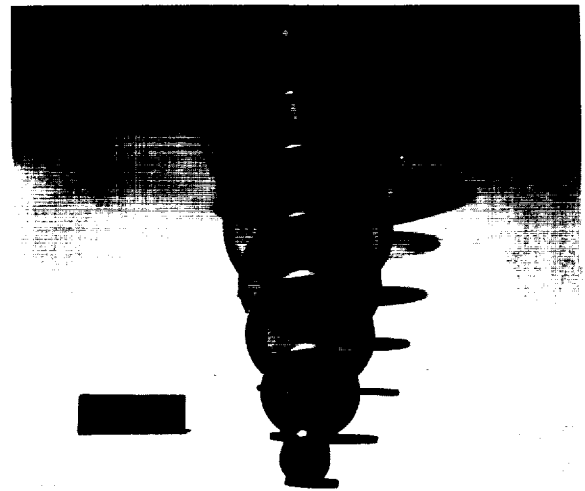


FIGURE 3.—Disk collectors of various sizes ($\frac{1}{2}$ - to $3\frac{1}{16}$ -in. diameter) used to make integrated density measurements.

of the initial total mass of particles placed in the shock tube.

After the velocity, size range, composition, and number of particles striking a given area were determined from the above procedures, aluminum and aluminum-coated disks were placed in the shock tube and exposed to bombardment by the particles. Damage to the targets was considered to be the measured change in the reflectance of the surfaces. This was determined by making reflectance measurements over the wavelength range from 1.5 to 15 μ on the disks before and after bombardment.

DISCUSSION OF RESULTS

A number of experimental investigations (ref. 5 and 6) have shown that the shape of the cavity formed in the target by a hypervelocity projectile is hemispherical, and that the volume of the cavity is proportional to the kinetic energy of the projectile (ref. 7). The theoretical analysis of reference 8 indicates that the crater depth is proportional to a power of the kinetic energy. Hence, we have characterized the exposure to particle bombardment with the quantity $\sum_i \frac{1}{2} m_i V_i^2$. This also allows a possible time-of-exposure scaling factor if kinetic energy flux in a given situation is known.

Six polished aluminum disks $\frac{1}{16}$ inch in diameter were bombarded by SiC particles. Spectral reflectances of these disks before and after exposure are shown in figures 5 to 7.

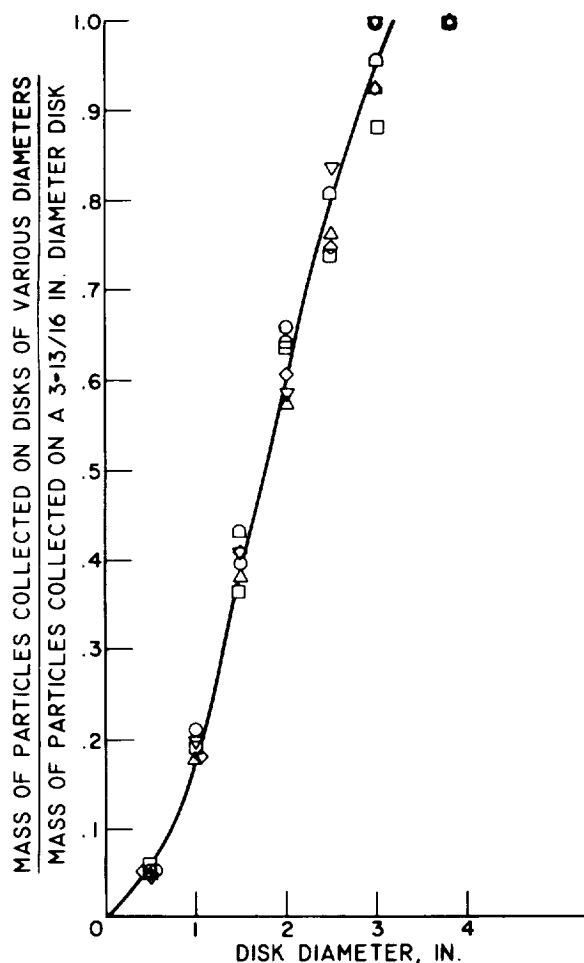


FIGURE 4.—Mass of particles collected on disks of various diameters normalized to total mass collected on the largest disk.

M		Mass of particles placed in shock tube, mg	Mass collected on $\frac{3}{16}$ -in. disk, mg
6.8	△	25	20.1
	○	19.7	16.4
	□	14	11.5
	▽	9.2	6.7
	◇	5.0	3.9
8.02	◐	25	22.5

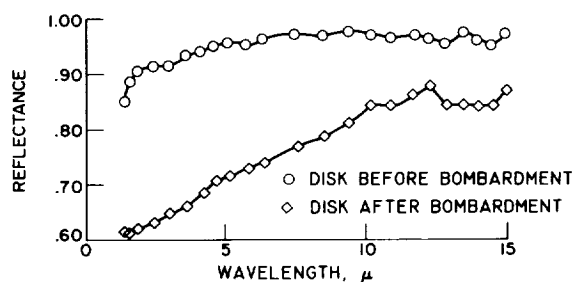


FIGURE 5.—Spectral reflectance of a $\frac{1}{16}$ -in.-diameter aluminum disk before and after bombardment by 0.27 mg of 2- to 14- μ silicon carbide particles at $M=8.4$.

Figure 5 presents the data for a disk exposed to 0.27 mg of SiC accelerated to gas speed at a shock Mach number of 8.4 and shows a considerable reduction in reflectance due to the exposure. Figure 6 shows the reflectance of a similar disk exposed to 0.7 mg of particles also accelerated at a shock Mach number of 8.4. The reflectance in this case was reduced an even greater amount. Figure 7 contains the results for a disk exposed to 0.7 mg of SiC particles accelerated by the gas behind a shock of $M=6.86$. Here, too, the reflectance was considerably reduced. The data on these figures show that in this wave length range (1.5 to 15 μ) there is marked reduction in reflectance with an increase in either particle velocity or number of particles. A sample

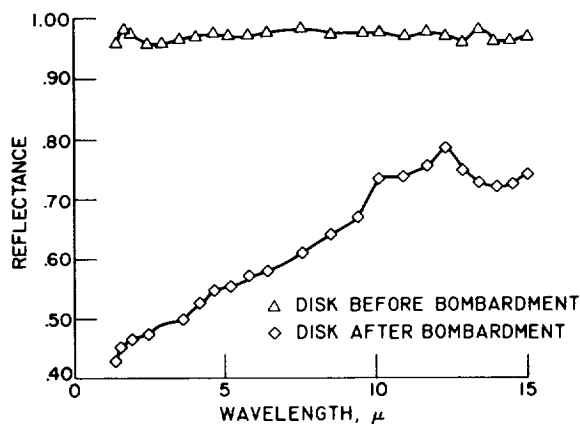


FIGURE 6.—Spectral reflectance of a $\frac{1}{16}$ -in.-diameter aluminum disk before and after bombardment by 0.7 mg of 2- to 14- μ silicon carbide particles at $M=8.4$.

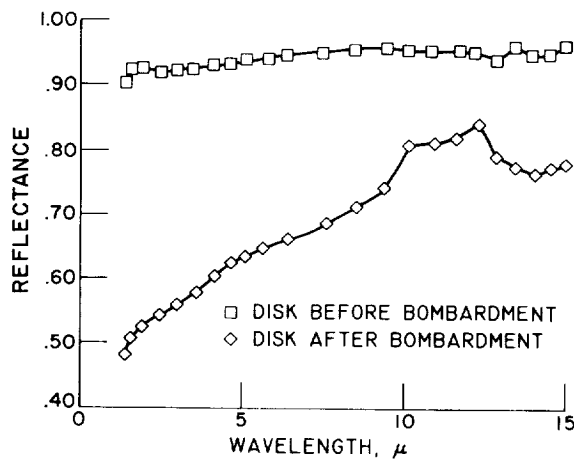


FIGURE 7.—Spectral reflectance of a $\frac{1}{16}$ -in.-diameter aluminum disk before and after bombardment by 0.7 mg of 2- to 14- μ silicon carbide particles at $M=6.86$.

aluminum disk before and after bombardment is shown in figure 8.

The ratio of the final to the initial average reflectance $\bar{\rho}_f/\bar{\rho}_i$ is plotted in figure 9 against the total kinetic energy of the cloud of particles impinging on the disk. It will be noticed that reflectance decreases as kinetic energy increases, and, at an energy of about 1 joule, the ratio $\bar{\rho}_f/\bar{\rho}_i$ has fallen to 0.8. Thus, for the aluminum disk exposed to 1 joule of high-speed particle bombardment, the reflectance has dropped from 0.95 to 0.76. This is equivalent

to an increase in emittance of the disk from 0.05 to 0.24, a factor of approximately 5, in the measured range of wavelengths between 1.5 and 15 μ .

In figure 10 is presented the average cumulative mass distribution of interplanetary dust particles in the vicinity of the Earth as compiled in reference 1. By integration of the measured mass distribution of figure 10 for the particle mass range from 10^{-10} to 10^{-8} g and assignment to the particles of an average velocity of 30 km/sec, as in reference 1, it was found that the $\sum_i \frac{1}{2} m_i V_i^2$ falling on a $\frac{1}{16}$ -inch-diameter disk in one year was equal to 1.5 joules; or the kinetic energy equals 1 joule in about 8 months in space in the vicinity of the Earth. Thus, if the energy coordinate of figure 9 is interpreted as the equivalent time, our laboratory experiment indicates that the damage to optical properties of polished aluminum surfaces is considerable ($\bar{\rho}_f/\bar{\rho}_i=0.8$) at the end of 8 months in a near-Earth orbit.

Assuming surface damage per hit to be proportional to the remaining undamaged area of the surface, it can be shown that the reflectance of a surface exposed to particle bombardment may be expressed as

$$\bar{\rho}(H) = \bar{\rho}_i \left\{ 1 - \left(1 - \frac{\bar{\rho}_\infty}{\bar{\rho}_i} \right) (1 - e^{-SH}) \right\} \quad (6)$$

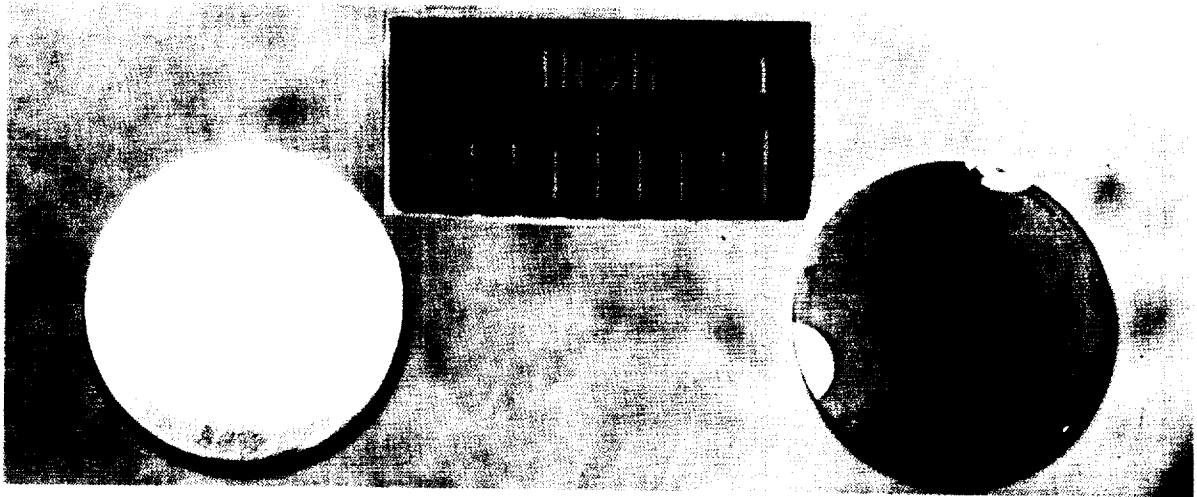


FIGURE 8.—Sample $\frac{1}{16}$ -in.-diameter aluminum disk before and after bombardment by 2- to 14- μ silicon carbide particles. (a) Before bombardment. (b) After bombardment.

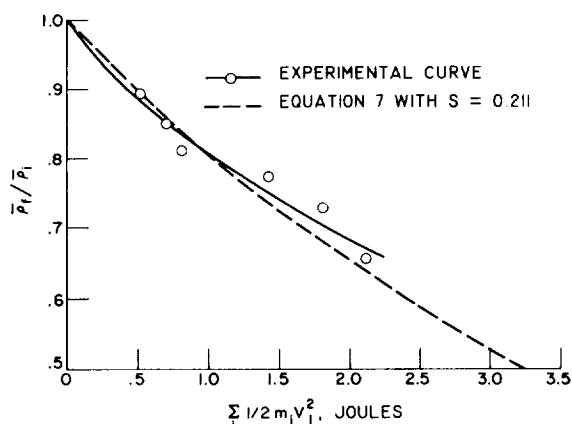


FIGURE 9.—Ratio of final to initial average reflectance $\bar{\rho}_f/\bar{\rho}_i$ plotted against total kinetic energy ($\sum 1/2 m_i V_i^2$) of the cloud of 2- to 14- μ silicon carbide particles impinging on $1\frac{1}{8}$ -in.-diameter aluminum disks.

where $\bar{\rho}_\infty$ is the reflectance of the surface after a very long (infinite time) exposure. If it is assumed that $\bar{\rho}_\infty$ is zero (a blackbody) after a very long time, equation (6) simplifies to

$$\bar{\rho}(H) = \bar{\rho}_i e^{-SH} \quad (7)$$

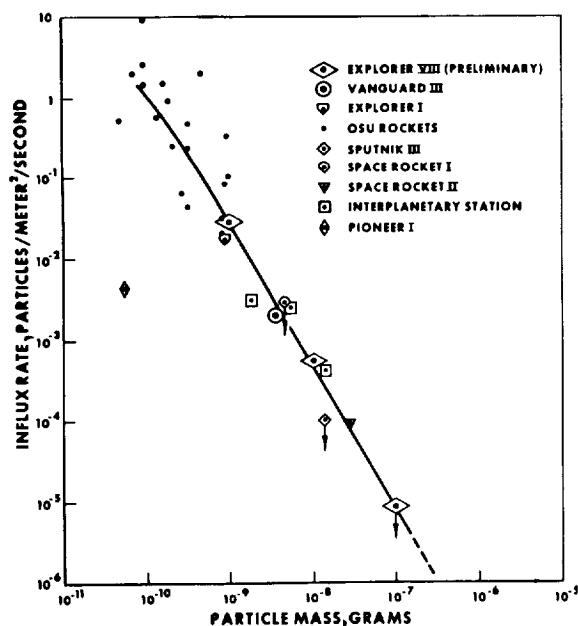


FIGURE 10.—Average cumulative mass distribution of interplanetary dust particles in the vicinity of Earth, established by measurements with microphone systems.

Plotted in figure 9 is equation (7) with $S=0.211$, obtained from the value of $\bar{\rho}(H)/\bar{\rho}_i$ of the experimental curve at 1 joule. Equation (6) indicates that a reduction of the reflectance to one-half the original value would occur in 3 years if $\bar{\rho}_\infty=0.15$. This value is obtained by assuming that the target craters are coated by projectile material (ref. 5) and that the projectile material has a $\bar{\rho}=0.15$, which is a reasonable value for a stony material.

It is important to make clear at this point that the limit of 10^{-10} g at the low end of the mass size range of meteoroids in space corresponds merely to the sensitivity limit of the microphone-type detectors used on the satellites; it does not necessarily represent the minimum meteoroid mass, which is often taken as about 10^{-11} g. It is also possible that particles in the detectable range hitting a surface at extreme glancing angles may cause some surface damage and yet not be detected by the satellite instrumentation. This last group, however, is probably very small since the results of reference 5 indicate that detection would occur for particles above the normal detection limit except for very oblique angles of arrival at the surface.

If the curve in figure 10 is simply extrapolated in order to include particles of mass down to 10^{-11} g, the time equivalence is shortened by a factor of nearly 5. Thus, the estimate of a 3-year life to one-half the original reflectance might be reduced to only 7 months. Such an extrapolation is conservative however, since flux rates probably do not continue to rise as rapidly as in the 10^{-10} to 10^{-8} g range.

To determine the durability of coatings exposed to high-speed particle flows, two $1\frac{1}{8}$ -inch-diameter aluminum-coated bakelite disks were placed in the shock tube. The aluminum had been vacuum deposited on the bakelite disks and the thickness of the coating measured with an interferometer. The aluminum-coated disks were then placed in the shock tube with a special holder designed to insure against removal of the aluminum by the hot gas. Exposure to the shock-tube flows without insertion of particles showed no damage to the coating. The results of the experiment with particles showed that all the

8600-Å-thick aluminum coating was removed when the coated bakelite disk was exposed to 0.9 mg of 2 to 14 μ SiC particles at $M=6.8$, corresponding to a total energy of 1.83 joules. Figure 11 shows the coated bakelite disk before and after exposure. In figure 11(b) unexposed portions of the disk at support points still show the original coating. For another disk with a 4800-Å aluminum coating, all coating was removed with a 0.87-joule (0.27 mg at $M=8.6$) bombardment. Thus, it was shown that typical aluminum coatings (8600 Å or less) on bakelite could be removed entirely from the surface of the bakelite with an exposure to particles of total kinetic energy about an order of magnitude less than the thermal energy required to remove these coatings by evaporation. Calculations of coat-

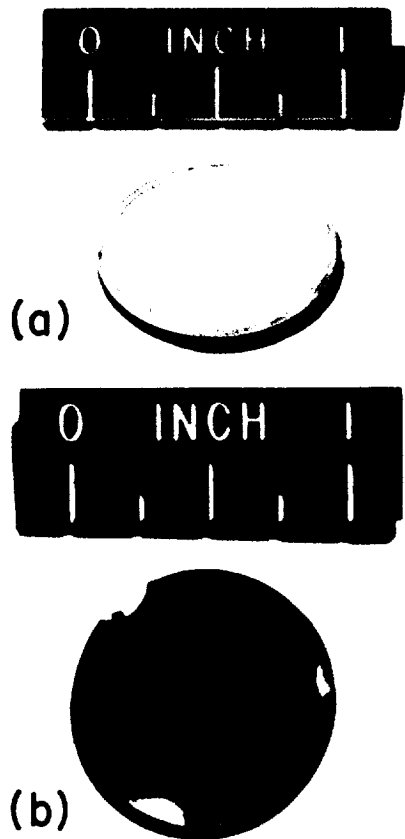


FIGURE 11.—Effect of exposure to particle bombardment on aluminum-coated bakelite disk. Aluminum coating 8600 Å thick; silicon carbide particles, 2 to 14 μ , at $M=6.8$. (a) Before exposure. (b) After exposure.

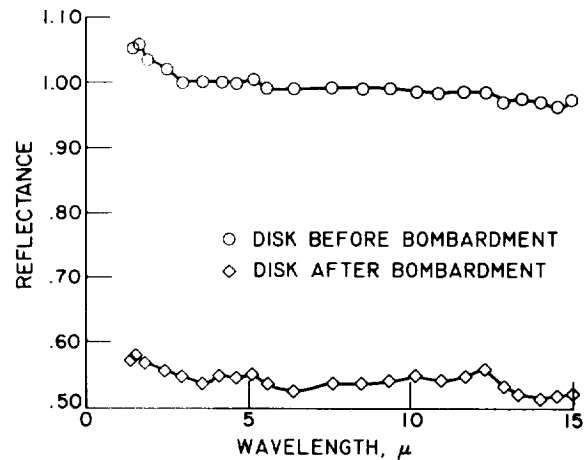


FIGURE 12.—Spectral reflectance of a 15/16-in.-diameter disk of 0.0005-in. Mylar coated on both sides with 2200 Å of aluminum before and after bombardment by 0.7 mg of 2- to 14- μ silicon carbide particles at $M=8.98$.

ing lifetimes made by using heat of vaporization for removal energy would, therefore, give lifetimes that are much too high.

Material similar to that of the Echo I balloon (2200 Å aluminum evaporated on 0.0005-inch Mylar) was also placed in the shock tube and exposed to particle bombardment. For this experiment no real simulation of the support of the material (as in a balloon) could be made. The material was, instead, stretched over a backing plate and exposed in this way to particle bombardment. The reduction in reflectance measured by the spectrophotometer is shown in figure 12. Unfortunately, this cannot be used to determine the life of the balloon reflectance, but it does indicate that micrometeoroids, even if they do not puncture the balloon, will reduce reflectance at a rate that should be noticeable over the life of the satellite.

CONCLUDING REMARKS

Exposure of polished aluminum surfaces to bombardment by a cloud of high-speed particles of known total kinetic energy causes damage that can be fairly well predicted. With a reasonable assumption concerning the reflective properties of stony materials (the material of most meteoroids), a good estimate

of the damage to metal surfaces in interplanetary space near the Earth is also made possible. This requires only that the compiled measurements of meteoroid flux from over a dozen major space vehicles be allowed as correct and that particle kinetic energy for space particles is equal to the laboratory particle kinetic energy. Even considering possible limitations of these data, a useful estimate of damage to surface optical properties in space can be made. The estimates indicate that if changes in surface optical properties of 50 percent are allowable, only missions of over 7 months will be affected. If smaller changes in surface optical properties are not acceptable for satisfactory vehicle performance, missions for less than this time may be affected. The above estimates are conservative if particle kinetic energy for most frequently encountered particles in space is larger than the laboratory particle kinetic energy.

ACKNOWLEDGMENT

The authors wish to thank S. J. Pinali and R. H. Dobshaw whose help with the operation of the shock tube was invaluable. Evelyn Anagnostou developed her own technique for the measurements on the spectral reflectometer and made the measurements for the data presented in this paper.

REFERENCES

1. DUBIN, MAURICE and McCracken, CURTIS W.: Measurements of Distributions of Interplanetary Dust. *The Astronomical Jour.*, vol. 67, no. 5, June 1962, pp. 248-256.
2. KORNHAUSER, MAURY: Prediction of Cratering by Meteoroid Impacts. *Proc. American Astronautical Soc.*, 4th Annual Meeting (New York), Jan. 1958, pp. 33-1 to 33-13.
3. GOLOVIN, M. N., and PUTNAM, A. A.: The Inertial Impaction of Small Particles. AEDC-TN-58-36, ASTIA Doc. No. AD-157135, Arnold Eng. Dev. Center, June 1958.
4. ROSHKO, ANATOL: On Flow Duration in Low-Pressure Shock Tubes. *The Physics of Fluids*, vol. 3, no. 6, Nov.-Dec. 1960, pp. 835-842.
5. SUMMERS, JAMES L.: Investigation of High-Speed Impact: Regions of Impact and Impact at Oblique Angles. NASA TN D-94, 1959.
6. EICHELBERGER, R. J., and GEHRING, J. W.: Effects of Meteoroid Impacts on Space Vehicles. Rep. No. 1155, Ballistic Res. Lab., Aberdeen Proving Ground, Dec. 1961.
7. STANYUKOVICH, K. P.: Elements of the Theory of the Impact of Solid Bodies with High (Cosmic) Velocities in vol. 4 of *Artificial Earth Satellites* (L. V. Kurnosova, ed.). Plenum Press, Inc., 1961, pp. 292-333.
8. RAE, WILLIAM J., and KIRCHNER, HENRY P.: Final Report on a Study of Meteoroid Impact Phenomena. Rep. No. RM-1655-M-4 (Contract No. NAS 3-2121), Cornell Aero. Lab., Inc., Feb. 1963.

SESSION V

APPLICATIONS

CHAIRMAN: ARTHUR J. KATZ

GRUMMAN AIRCRAFT ENGINEERING CORP., BETHPAGE, LONG ISLAND, N.Y.

47. High-Temperature Thermal Optical Property Activities of the U.S. Air Force

DONALD F. STEVISON AND MERRILL L. MINGES

AIR FORCE MATERIALS LABORATORY, WRIGHT-PATTERSON AIR FORCE BASE, OHIO

The importance of high temperature thermal optical property studies in Air Force materials developments is indicated along with a brief discussion of the important physical mechanisms involved in absorption and emission of radiation within solids. The basic experimental and instrumentation problems associated with accurate thermal optical property determinations at high temperatures are considered next. Finally current Air Force efforts are reviewed in the areas of measurement technique developments, analysis of radiative transport phenomena in opaque and semitransparent materials, and new materials developments where radiative characteristics are important.

The design and performance of future space systems will depend to a great extent upon radiant heat transfer characteristics of surfaces exposed to high energy and high temperature environments. Reentry systems following a wide range of trajectories will encounter high heat flux environments and when operating at high temperatures will dissipate large amounts of energy by radiation. In addition, heat transfer from leading edges and rocket nozzles will be a function of the radiation characteristics of their surfaces. In these and other cases the overall system temperature may often be established by surface emittance values. As an example, space radiator size and weight are generally inversely related to surface emittance.

In many cases, reported emittance data are contradictory, or, as with many new coating systems of interest, data are entirely unavailable. Current data obtained by different investigators on the same material have varied by more than 50 percent in some instances. The differences may have been due to poor experimental techniques, improper preparation of samples, inadequate definition of experimental conditions, or poor instrumentation.

Thus, increased attention must be given to the fundamental factors affecting the thermal radiation characteristics of materials. Such parameters as instrumentation characteristics, specimen characteristics, and the interaction of specimen and environment are significant in clarifying discrepancies in reported data and will lead to improvements in the control of emittance and reflectance of new materials being developed for aerospace applications.

ABSORPTION AND EMISSION PROCESSES

In simplest terms the reflection, absorption, emission, and transmission characteristics of solids can be related to excitations of the lattice of the material and its electrons. The excitation interaction results in a net conversion of quantized electromagnetic radiation into quantized vibrations of the lattice (phonons) and the electrons of the material. The extent of the conversion and the relative role of the lattice and the electrons is of course a function of the type of material being considered. For metals it is well known that the outermost electrons of the atoms are relatively free to

move under the influence of an electromagnetic field and thus contribute significantly in radiation absorption-emission processes. With monochromatic infrared or visible radiation impinging upon the surface of a metal these *free electrons* are forced to vibrate at the frequency of the electromagnetic fields associated with the radiation. The lattice may resonate also; however, the free electrons generally predominate in the initial absorption of a portion of the incident energy. The accelerated electrons travel until they interact with neighboring electrons or atoms. Since the electrons are continually being accelerated and decelerated they are continually emitting and absorbing energy. This process of photon to phonon conversion continues through the material until part of the original incident energy is absorbed or transmitted. However, for metals the efficiency of the conversion is so high (high extinction coefficient) that the process is limited to layers near the surface. The transitions discussed above are vibrational in nature; at wavelengths in the visible and ultraviolet electronic transitions in metals appear to become important. Understanding the nature and significance of these "bound electron" contributions is a subject of wide attention at present. At frequencies in the far infrared the electromagnetic energy dispersion characteristics of the free electrons are quite accurately represented by the d-c electrical resistivity. Based on the fact that the free electrons are the predominant means of interaction with the incident radiation in the infrared, it has been possible to relate the infrared spectral reflectance to the d-c resistivity. At shorter wavelengths, for which other contributions such as interactions with different types of bound electrons become significant and the electrons interact with the lattice to a great degree, the correlation breaks down.

The opposite extreme in interaction phenomena between a material and an incident electromagnetic field occurs in the case of dielectrics. Here the electrons are firmly bound in the lattice, and thus there is essentially only one significant mode of radiation absorption and emission—lattice vibrations. In this case, when the monochromatic electromagnetic energy im-

pinges on the surface, the lattice will vibrate if the frequency of the incident radiation is the same as, or a harmonic of, the resonance frequency of the system. Thus energy of a particular frequency will be absorbed or reflected if the energy of the incident photon falls within a resonance band of the solid. For most ceramic materials these resonance bands are quite broad. The bands of oxide materials are generally found in the ultraviolet, visible, and infrared. In the near infrared many ceramics have low absorption coefficients, and thus the thermal optical properties become volume-dependent and are influenced by the degree of porosity and by the grain or particle size. The scattering coefficient (and reflectivity) in this region is sensitive to these volume characteristics. Further in the infrared, absorption bands are encountered. The emittance of the ceramic increases as the absorption coefficient increases and thus the thermal optical properties become more sensitive to surface condition and less dependent on such volume characteristics as porosity. Results of recently sponsored Air Force work in this area will be given in a later section.

Thus the distinctions between the extreme cases of optical properties in metals and in dielectrics become apparent even from a simple qualitative discussion. For semi-conductors and other materials with characteristics intermediate between those of metals and dielectrics the analysis of free-electron, bound-electron, and lattice contributions is more difficult. Many high-temperature materials of interest to the Air Force for heat-shield and rocket-nozzle applications fall in this category—for example, the metallic borides, carbides, and nitrides, and various forms of graphite, both conventional and pyrolytic. In many cases the degree of metallic character of a given material can be accurately determined from electrical and thermal conductivity measurements. The transport of thermal energy through a material, as measured by the thermal conductivity, is obviously by quantized lattice vibrations and electron carriers. If the Lorentz function for a given material is known then the electronic thermal conductivity can be estimated quantitatively from electrical conduc-

tivity measurements. For high temperature metals such as tantalum it has been estimated that about 88 percent of the total thermal energy transport is via electrons (ref. 1). For the metallic carbide TiC, the electronic contribution is around 50 percent while for ceramic oxides it is essentially negligible.

Thus, in studying the optical properties of various materials it appears that useful information may often be neglected because investigators overlook the fact that lattice and electron contributions play similar roles in governing both thermal and optical property characteristics.

HIGH TEMPERATURE RADIATION MEASUREMENTS

Pyrometry

When the temperature of a system under consideration becomes so high that thermocouples become unreliable due to chemical interactions with the system, oxidation, etc., the only reliable methods of measuring the temperature are radiation methods. There are several radiation methods used to measure high temperatures, but consideration here will be limited to optical *single-color* and *two-color*, or ratio, pyrometers.

The optical pyrometer actually measures the brightness temperature of the body or material under consideration. To calculate the true temperature, the mean effective wavelength of the pyrometer must be known along with the spectral emittance of the specimen at the measurement wavelength. The spectral emittance as a function of temperature and surface condition is needed for a true temperature determination; however, this information is not available for many materials of interest. One can overcome this difficulty in some cases if a blackbody is used for comparison; but, at the same time, the critical requirement that the specimen and blackbody have the same temperature may introduce more errors than the initial assumptions concerning emittance.

Two-color pyrometers were developed to eliminate the emittance correction. Such pyrometers measure the ratio of radiant energy emitted by the material at two wavelengths.

If graybody conditions are assumed for the region of the two wavelengths (in particular, if it is assumed that $\epsilon_{\lambda_1} = \epsilon_{\lambda_2}$), the temperature measurement becomes independent of emittance. However, graybody assumptions are generally not valid over a wide spectral range; so the assumption is better if the spectral range is narrow. An optimum must be established since an error analysis reveals that the temperature error is inversely related to the wavelength difference $\lambda_2 - \lambda_1$. Thus, the smaller the wavelength interval, the larger is the error in the temperature measurement.

Fundamentally, two-color pyrometry relies on the principle that the shape of the blackbody radiation curve over any given wavelength interval is a unique function of temperature. Since the overall blackbody radiation curve is highly asymmetric it would be expected that the sensitivity of a two-color pyrometer would depend to a considerable extent on the location of the measurement interval $\lambda_2 - \lambda_1$ in the blackbody spectrum. The position of this interval with respect to wavelength is, of course, fixed for a given instrument. However, as the temperature is changed, the slope of the radiation curve over this interval changes significantly; thus, the pyrometer sensitivity may change significantly with temperature. Quantitatively, this phenomenon may be described by determining the change of the slope of the radiation curve with temperature.

The equation of the blackbody radiation curve is

$$E_b(\lambda, T) = \frac{C_1 \lambda^{-5}}{e^{C_2/\lambda T} - 1} \quad (1)$$

where

$E_b(\lambda, T)$ spectral radiation flux at temperature T

C_1 and C_2 first and second radiation constants, respectively

λ wavelength

The slope of this curve is obtained by taking the derivative of equation (1) with respect to wavelength. Setting the derivative of this slope with respect to temperature equal to zero determines the wavelength of maximum pyrometer sensitivity (ref. 3):

$$\bar{\lambda} = \frac{2410}{T} \quad (2)$$

where

$\bar{\lambda}$ wavelength of maximum sensitivity, microns

T temperature, °K

From Wien's displacement law,

$$\lambda_{max} = \frac{2898}{T} \quad (3)$$

where λ_{max} is the wavelength at the maximum of the blackbody curve. From equations (1) and (2)

$$\bar{\lambda} = 0.832\lambda_{max} \quad (4)$$

High Temperature Emittance Measurement Methods

On the basis of our previous statements concerning the basic radiation emission, absorption, and reflection processes in terms of the basic physics of solids we shall now consider briefly practical measurement techniques for high temperature determination of the corresponding coefficients. In relation to Air Force work the basic methodology can be categorized as indicated in table I.

TABLE I.—High Temperature Emittance Measurement Methods

Measurement method	Heating method
Calorimetric	Resistance heating Encased specimen heater
Rotating specimen	RF Resistance heated furnace
Cavity	RF Torch Arc image furnace Resistance heated furnace

Calorimetric Methods

Total hemispherical emittance can be determined by measuring the steady state rate of heat emission from a specimen and comparing

it with the blackbody emissive power at the same temperature. A calorimetric approach to this measurement is very simple and generally gives good overall accuracy. Furthermore, it eliminates the necessity for a blackbody reference. For this approach the total radiant energy transfer rate is determined by heating the specimen with respect to its surroundings. Convective heat transfer and gas conduction are made negligibly small by placing the specimen in a vacuum. Conduction by the suspension system or temperature sensors is either measured or reduced to negligible proportions. When these conditions are met the steady state heat loss from the specimen is entirely due to radiation. Common calorimetric methods use either a hollow specimen containing an electrical heater or a strip specimen which is resistance heated. The specimens are suspended in a vacuum chamber having cooled, blackened walls. The temperature of the specimen surface is measured with thermocouples or an optical pyrometer. When the system reaches equilibrium, measurements of the potential drop and current establish the power dissipated by the specimen surface. From the total power and the temperature, the total hemispherical emittance can be calculated by the Stefan-Boltzmann relation.

Calorimetric techniques were used by Lockheed Missiles & Space Company to determine the thermal emittance stability of spacecraft radiator coatings (ref. 4). The method permitted measurements to be made at elevated temperatures in a simulated space environment for extended periods of time. The specimens were hollow and were heated to elevated temperatures by electrically heating a tungsten coil placed in the interior. This method of heating caused considerable difficulty due to heater failure at temperatures in the vicinity of 2000° F for specimens which had an emittance of greater than 0.65. Thus the calorimetric method using this heating technique was found to be limited to temperatures below 2000° F for samples with emittance greater than 0.65. An error analysis of this method indicated that the error in the sample surface area computation is less than 0.25 percent when the thermal expansion of the sample at the measurement

temperature is taken into account, that the sample temperature nonuniformity introduces a probable error of 1.0 percent, and that other errors, including thermocouple calibration errors and instrument errors, bring the overall probable error in the emittance values to about 5 percent.

Rotating Specimen Method

Total normal emittance or spectral normal emittance can be measured at high temperatures by rotating a specimen in a high-temperature furnace equipped with a viewing port. The most important experimental requirement for this method is that the specimen be rotated at a sufficiently high speed to reduce temperature gradients and to reduce transients in the surface temperature as it passes the viewing port.

By using a suitable optical system the emitted energies from the rotating specimen and from a blackbody at the same temperature are focused alternately on the entrance slit of a dual-beam monochromator that can cover the spectral range of interest. The output of the monochromator is the ratio of the flux densities in the two beams and is a measure of the spectral normal emittance.

Accuracy of this method is limited by the radiative cooling when the specimen is viewed; however, at high speeds of rotation this effect is relatively unimportant. As the temperature is increased the speed of rotation must be increased to reduce gradients and transients as an incremental area passes the viewing port. Eventually, however, vibration or distortion difficulties may prevent going to higher speeds or higher temperatures. In the apparatus used by Moore (ref. 5; see also Paper 26), the clearance between the specimen and the viewing port had to be less than about 0.04 inch in order to avoid including radiation from the furnace wall. When using Moore's method, sizable errors can occur if the walls of the rotating specimen are not sufficiently thick to be opaque at all wavelengths.

Cavity Techniques

Total normal emittance and spectral normal emittance have been determined by several investigators (refs. 6, 7, and 8) by using a

method in which a small cylindrical specimen, having a blackbody reference cavity drilled into it, is heated to high temperatures by RF induction. The temperature of the specimen is usually measured with a micro-optical pyrometer that views the cavity in the specimen. It is assumed that the cavity fulfills blackbody conditions and is at the same temperature as the specimen surface. As indicated in table I, this basic measurement technique is used with a variety of heating techniques.

Generally, two basic conditions should be met if the cavity is to perform satisfactorily. First, it must be isothermal; second, the walls of the cavity must be diffusely reflecting. Because of these requirements, in practice the basic approach in cavity design for metals is different from that for dielectrics and non-conductors.

For metals the reference cavities used should have large ratios of length to radius. Nearly isothermal conditions can be maintained throughout such a deep cavity because of the high thermal conductivity of the metals and the relative ease of uniformly heating electrical conductors. The inherent specularity of the metal surfaces can be reduced by roughening or machining the cavity walls or by applying a suitable rough dark coating, such as silicon carbide. Extensive emittance measurements of metals have been made by using the cavity technique. Optical aberration may contribute significant errors for reference holes of small diameter (<0.7 mm). When the off-axis angle of the optical system was changed from $3^{\circ}21'$ to $2^{\circ}10'$ a 25-percent error was reduced by a factor of two (ref. 9 and 10). Other mechanisms may contribute to this error, such as improper focus of the detection system and any intervening windows. Even when all measurement errors have been reduced to negligible amounts there will still be uncertainties caused by the failure of real specimens to duplicate the analytical model employed in the derivation of the cavity emittance (as, for example, in the Gouffé theory, ref. 11).

For dielectrics and other nonconductors significant variations in emittance are encountered when using the cavity technique. The reason for these variations arises from the

fact that such materials generally have low thermal conductivity. They are relatively difficult to heat uniformly because of this characteristic and the fact that direct resistance heating is impossible; in most cases direct induction heating is also impossible even at high temperatures. A helpful characteristic of these materials, however, is that they are reasonably good diffuse reflectors, so that a shallow reference cavity can sometimes be used successfully for such materials. (Use of a shallow cavity tends to minimize the difference in temperature between the surface and the bottom of the cavity (ref. 7)). The effective emittance of the shallow cavity can be described explicitly by the expression given by Gouffé (ref. 11). Application of the Gouffé correction to cavities with length-to-radius ratios between 1.0 and 2.0 appears to provide consistent emittance values for these materials.¹

The general results of experimental work utilizing cavity techniques may be summarized as follows: On the one hand, theoretical considerations dictate large length-to-radius ratios; on the other hand, practical considerations limit the volume of the specimen over which the required isothermal conditions can be maintained. Large length-to-radius ratios can be used for metals because of their high thermal conductivities. For nonmetals, shallow cavities dictated by low conductivity may be used successfully because the cavity surfaces are generally more diffuse so that exact analytical corrections can be made for less than ideal cavity geometry.

For dielectrics a more fundamental problem than the various aspects of the practical measurements as discussed above exists. This problem relates to the fact that such materials may have substantial temperature gradients in the proximity of the surface, particularly at higher temperatures, because of volume emission. These diathermancy effects will be discussed in greater detail below.

AIR FORCE MATERIALS EFFORTS

In the area of thermal optical properties at high temperatures the activities of the Air

Force Materials Laboratory are concentrated in two areas: (1) analysis of high temperature measurement techniques and development of standards, (2) measurements and basic analysis of thermal optical properties on newly developed materials which are of interest in Air Force applications.

High-Temperature Techniques and Standards Development

In the temperature interval from 1000° F to 2000° F the National Bureau of Standards has developed low, medium, and high emittance references covering the wavelength range of 1.0 to 15 microns; this work is reported in reference 12. At the present time the temperature interval from 2000° F to 4000° F and the wavelength range of 0.5 to 15 microns is of highest priority in extending the effort. Here the basic problem of selecting and characterizing materials for emittance standards is compounded by uncertainties in measurement techniques. Of particular concern has been the question of whether, at high temperatures (2000° to 4000° F), a direct temperature measurement on the surface of a dielectric is a valid experimental approach. If the material is significantly diathermanous, very large temperature gradients may appear near the surface, thereby introducing large uncertainties in emittance values calculated from surface temperature measurements.

An alternative suggested by J. C. Richmond at the National Bureau of Standards (NBS) has been to measure high-temperature reflectance of such materials rather than to measure the emittance directly. The advantage of this approach is that the reflectance measurement is not a strong function of the specimen temperature. The specimen temperature must be known, of course, but with only relatively fair accuracy. In the high-temperature reflectance measurement the specimen translucency has to be considered only to the extent that the specimen must be thick enough for overall opacity to the incident beam. Temperature gradients in the proximity of the specimen surface do not affect the measurement to any great extent so long as the temperature coefficient of the reflec-

¹ See also Paper 10.

tivity is low for the particular material considered.

With the integrating-sphere arrangement proposed, one of the major problems at high temperatures is to develop a reasonable signal-to-noise ratio for the detection system; in this case the background signal is the thermal emission of the specimen near 4000° F. The problem is effectively resolved by using a gas-phase laser as an illuminating source which has an equivalent temperature of approximately 22,000° F. However, the laser beam is monochromatic, and to obtain spectral reflectance data over a large spectral region it is necessary to use a series of different laser sources or to excite a given unit at different frequencies. The present unit in operation at NBS can be excited at 0.632, 1.15, and 3.39 μ . To obtain the curve of spectral reflectance as a function of wavelength it is necessary to interpolate between the above wavelengths. In order to do this it is planned to accurately measure the room temperature spectral reflectance of the specimens with the NBS ellipsoidal mirror reflectometer (ref. 12); the shape of the reflectance curve so obtained will provide an interpolation base for the wavelengths between the high temperature data points. Such a procedure of course implicitly assumes that phase changes do not occur in the material and that important absorption bands do not appear over the wavelength region of interpolation. Depending on the slope and inflections of the spectral reflectance curve, reflectances at intermediate wavelengths may be required, so that additional laser sources may be needed. For this particular high-temperature work, however, consideration will be limited to the shorter wavelengths below 3.5 μ .

Another problem receiving attention in this project is the investigation of integrating-sphere coatings that will function satisfactorily in vacuum environments over the wavelength interval 0.5 to 3.5 μ .

Also, it is noted that the shortest excitation wavelength of the laser is conveniently near the 0.665- μ optical pyrometer wavelength. Data generated at 0.632 μ will allow very accurate determinations of spectral emittance to be made at the optical pyrometer wavelength.

Future efforts will be directed toward establishing the feasibility and limiting factors, and toward defining resources and time required to extend present emittance and reflectance measurement techniques to 6000° F.

Measurement and Basic Analysis on Materials of Interest for Air Force Applications

RADIATIVE PROPERTIES OF OPAQUE AND TRANSLUCENT MATERIALS

As a first approach to the well recognized but little understood relationship between the thermal-optical properties of a material and its surface and volumetric characteristics the Air Force is sponsoring two rather basic programs. The first concerns analysis of the radiative properties of opaque metallic materials. The second program deals with the more complex problem of the radiative properties of dielectric materials at high temperatures.

At the Lockheed Aerospace Sciences Laboratory, R. E. Rolling and A. I. Funai have been investigating the effects of surface condition on the emittance and reflectance of various metals. Experimental studies are being conducted with copper, platinum, and tungsten specimens having roughness values ranging from 2 to 600 microinches rms. Total hemispherical, total normal, spectral normal, and spectral angular emittances of these specimens are being measured. The objective of the work is the development of analytical expressions which express emittance and reflectance of opaque materials as a function of temperature, wavelength, angle of emission, degree of polarization and roughness.

In the second program, at Lexington Laboratories, J. D. Klein, D. A. Hill, R. C. Folweiler and W. D. Kingery have been investigating both analytically and experimentally the thermal radiation characteristics of transparent and semitransparent materials. The analytical approach has been a rather comprehensive extension of the Hamaker equations to include boundary conditions peculiar to translucent and transparent dielectrics. Of particular significance has been the formulation of equations describing non-isothermal systems

in which substantial temperature gradients exist in the direction of the flux vector. As mentioned earlier these gradients are a direct consequence of volume emission. Equations for emittance and reflectance have been developed for various cases in terms of absorption and scattering coefficients. Experimental values for the coefficients were determined from diffuse transmission measurements for various specimen thicknesses. Initial experimental investigations (ref. 13) were with polycrystalline aluminas and beryllias, Pyroceram, mullite, and sintered glass. Direct spectral emittance measurements over the 1-15 micron range were made on these materials at high temperatures (to 2200° F). Single crystal transmissivity data were also obtained for several materials.

The experimental results of the work showed that below 6 microns the absorption coefficient is sufficiently low that scattering phenomena are of overwhelming importance. Thus, in this region the radiative emission of the various dielectrics is a true volume phenomenon, sensitive to composition and microstructure. At longer wavelengths the absorption coefficient increases greatly, with the result that the emission is more nearly a surface effect. Hence, in this region the optical properties become sensitive to surface condition and roughness.²

To obtain a quantitative indication of the effect of surface temperature gradients on the emittance of various ceramics a non-isothermal emissivity apparatus was developed. The apparatus allows the introduction of a controlled radial temperature gradient in a disc-shaped specimen whose emissive properties are to be measured. Test measurements on aluminum oxide indicate that the energy emitted does strongly depend on the temperature gradient as well as on the surface temperature. With a gradient of about 50° F/inch the emittance at 1830° F is found to be about 22% greater than for the isothermal condition (ref. 14).

Further studies will be conducted on well characterized alumina, magnesia, strontium titanate, fused silica, and Pyroceram. Additional investigations of the effects of specimen

porosity will be emphasized with both isothermal and non-isothermal experimental determinations being made up to 2400° F over the wavelength range of 0.5 to 15 μ .

MATERIALS DEVELOPMENT EFFORTS

In support of Air Force requirements for high-temperature materials a considerable effort has been devoted to the development of oxidation protection coatings for the refractory metals. Numerous intermetallic coatings have been developed that exhibit good thermal stability and oxidation resistance, such as MoSi₂ for molybdenum, tantalum-aluminum (TaAl₃) for tantalum, and (chromium-titanium)-silicon ((Cr-Ti)-Si) and aluminum-silicon-chromium (Al-Si-Cr) slurry coating for columbium. The emittance characteristics of such coatings have not been completely defined; however, it is necessary to have this information along with the degree of oxidation protection and the physical characteristics in order that new and greatly improved high-emittance coatings might be developed.

It has been observed (ref. 15) that emittance curves of intermetallic non-oxide compounds for different stoichiometric proportions of the same elements are always similar. This is not usually the case for the oxides, since oxidation products of intermetallics, even in small amounts, can significantly affect the spectral characteristics of the emitted radiation. Further observations indicate that the method of preparation of the coating—pack cementation or sintering affects the spectral radiation properties. This variation is attributed to differences in the density of the coating rather than to partial transparency effects in the thin coatings. Pack cementation coatings have spectral reflectances that are similar to, but higher than, those of sintered coatings (ref. 15).

A composite material containing 90 mol-percent zirconium diboride (ZrB₂) with 10 mol-percent molybdenum disilicide (MoSi₂) in solid solution has been developed which resists oxidation better than any other non-oxide material known (ref. 16). Good oxidation resistance exists to 3400° F, with reasonable oxidation

² See also Papers 7, 8, and 21.

resistance to 3500° F. The total normal emittance at room temperature of unoxidized samples lies between 0.85 and 0.95. The emittance reaches a maximum of 0.97 at approximately 2500° F and drops to a minimum of 0.3 above 4000° F. Samples given a prior oxidation treatment had room temperature emittances of 0.75 to 0.85. The emittance remained stable at temperatures up to approximately 2700° F (the prior oxidation treatment temperature) at which point the emittance decreased.

CONCLUDING REMARKS

In conclusion, we believe that the fundamental parameters affecting radiant heat transfer in solids and composites have not been given sufficient attention in the past. In many cases, however, this is no fault of the analyst, since the physical phenomena involved are extremely complex and are not properly understood even today. This is particularly true in the case of surface characterization where at high temperatures diathermancy effects become important. Substrate chemistry and physical phase characteristics are involved through volume emission in addition to the effects of microscopic surface irregularities. Through both in-house and contractual efforts, the Air Force is attempting to correlate these fundamental parameters with the observed emittance characteristics of a wide variety of materials. Efforts of this nature are very much needed in this area at present, not only to provide a more complete understanding of the physical phenomena involved but also to provide a rational basis for the development of improved high-temperature materials and composites for practical use.

REFERENCES

1. TYLE, R. P.: Preliminary Measurements on the Thermal and Electrical Conductivities of Molybdenum, Niobium, Tantalum and Tungsten. *J. Less Common Metals*, 3, 1961, pp. 13-18.
2. POWELL, R. W.: Correlation of the Thermal and Electrical Conductivity of Metals, Alloys and Compounds. *Proc. Third Conf. on Thermal Conductivity*, vol. I, 1963, pp. 79-112.
3. KOSTKOWSKI, H. J., WIESE, W. L., STRATTON, T. F., DEBELL, A. G., NUTTER, G. D., and BRENDEN, B. B.: UCLA Summer Seminar, Radiation Thermometry, Aug. 5-16, 1963.
4. GAUMER, R. E., FUNAI, A. I., and STREED, E. R.: Determination of the Thermal Emittance Stability of Spacecraft Radiator Coatings. ASD-TDR-63-429, U.S. Air Force, May 1963.
5. MOORE, DWIGHT G.: Emittance of Materials at Very High Temperatures. Letter Report, July 1, 1964, National Bur. Standards, 1964.
6. BLAU, HENRY H., JR.: Measurement of Flux, Emittance, and Related Properties. *Proceedings of an International Symposium on High Temperature Technology*. McGraw-Hill Book Co., Inc., c. 1960, pp. 45-53.
7. MOORE, DWIGHT G.: Investigation of Shallow Reference Cavities for High Temperature Emittance Measurements. *Measurement of Thermal Radiation Properties of Solids*, Joseph C. Richmond, ed. NASA SP-31, 1963, pp. 515-526.
8. RIETHOF, T. R., and DESANTIS, V. J.: Techniques of Measuring Normal Spectral Emissivity of Conductive Refractory Compounds at High Temperatures. *Measurement of Thermal Radiation Properties of Solids*, Joseph C. Richmond, ed. NASA SP-31, 1963, pp. 565-584.
9. MOORE, DWIGHT G.: Emittance of Materials at Very High Temperatures. Letter Report, Jan. 2, 1963, National Bur. Standards, 1963.
10. MOORE, DWIGHT G.: Equipment for Thermal Emittance Measurements Above 1400° K. NBS Rep. 7857, Jan. 1963.
11. GOUFFÉ, ANDRÉ: Aperture Corrections for Artificial Black Bodies, Accounting for Multiple Internal Diffusion. *Revue D'Optique*, vol. 24, nos. 1-3, Jan.-Mar. 1945, pp. 1-10.
12. HARRISON, W. N., RICHMOND, J. C., *et al.*: Standardization of Thermal Emittance Measurements. WADC Tech. Rep. 59-510, Pts. I, II, III, and IV, U.S. Air Force, Nov. 1963.
13. FOLWEILER, R. C.: Thermal Radiation Characteristics of Transparent, Semi-Transparent and Translucent Materials Under Non-Isothermal Conditions. ASD-TDR-62-719, U.S. Air Force, Apr. 1964.
14. FOLWEILER, R. C.: Thermal Radiation Characteristics of Transparent, Semi-Transparent and Translucent Materials Under Non-Isothermal Conditions. AF Materials Laboratory Report, May 1964.
15. SCHATZ, E. A.: Thermal Radiation Studies of Intermetallic Compounds. Progress Rep. No. 4, June 1-Aug. 15, 1963, American Machine & Foundry Co., 1963.
16. LOGAN, I. M., and NIESSE, J. E.: Process and Design Data on a Boride-Silicide Composition Resistant to Oxidation to 2000° C. ASD-TDR-62-1055, U.S. Air Force, Nov. 1962.

DISCUSSION

ARTHUR KATZ, Grumman Aircraft: Does anyone know of any available compilation of data on composites of substrate material, antioxidation coating, and possibly thermal-control coating that have been investigated

and found useful for application in the aerospace field?

NORMAN ALVARES, NRDL: There is an ASD Refractory Composites Working Group that is particularly concerned with these types of coatings.

48. Areas of Research on Surfaces for Thermal Control

WILLIAM SNODDY AND EDGAR MILLER

NASA MARSHALL SPACE FLIGHT CENTER, HUNTSVILLE, ALA.

Representative current literature was reviewed to determine the state of the art with respect to availability of thermal control surfaces in general, and specifically when certain constraints are imposed. A discussion of the results is given along with tables and graphs. Also discussed briefly are the individual types of coatings that would be desirable for passive thermal control of space vehicles. It is hoped that this paper makes evident some of the many areas of research on thermal control surfaces in which new or additional efforts might yield greatly needed results.

The optical characteristics of the surfaces of a spacecraft (as discussed, for example, in references 1 to 3) are fundamental parameters in determining the spacecraft temperature. Accordingly, a major effort has been made in the last few years to determine the optical properties of various surfaces and even to develop surfaces which have special desired optical characteristics and environmental stability.

The two most important optical properties are the absorptance of the surface with respect to solar radiation α_S and the total hemispherical emittance of the surface in the far infrared ϵ_T (T denotes surface temperature). Of somewhat lesser importance, generally, are the absorptance of the surface to Earth radiation, α_E ; the spectral absorptance and emittance, α_λ and $\epsilon_{T,\lambda}$; the directional absorptance and emittance, α_θ and $\epsilon_{T,\theta}$; and polarization effects.

The first part of this paper concerns α_S and ϵ_T and the work that must be done to assure availability of techniques and on-the-shelf materials which satisfy various specific utilization requirements and have the desired optical characteristics. Figure 1 shows some basic types of surfaces plotted according to their solar absorptance and infrared emittance. The diagonal lines on the graph represent values

of constant α_S/ϵ_T . This ratio is important because the equilibrium temperature of objects in space not near a radiating body (for example, the Earth) and having a fixed position and orientation with no on-board heat generation is a function of only this ratio. These temperatures have been calculated as a function of this ratio and are indicated on the graph for an isothermal sphere and for a flat plate perpendicular to the sunlight and adiabatic on

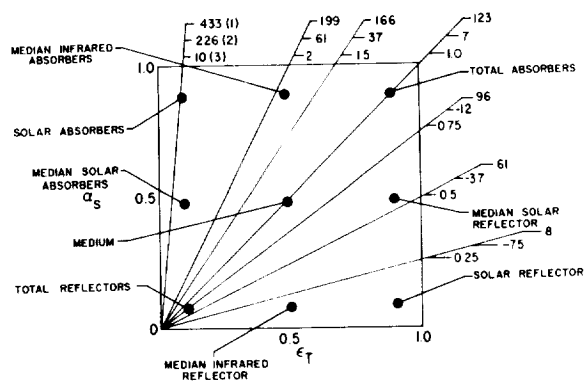


FIGURE 1.—Basic types of surfaces. The three numbers on each line are, respectively, (1) equilibrium temperature ($^{\circ}\text{C}$) for a flat plate perpendicular to the Sun at 1 AU and adiabatic on the back side, (2) equilibrium temperature ($^{\circ}\text{C}$) for an isothermal sphere at 1 AU, and (3) ratio of α_S to ϵ_T .

the back side, both located at a solar distance of 1 AU.

From the figure it can be seen that the "solar absorber" surface ($\alpha_s=1.0$, $\epsilon_T=0.1$) can cause a high equilibrium temperature (433° C for the flat plate); whereas the "solar reflector" type ($\alpha_s=0.25$, $\epsilon_T=1.0$) runs much colder (−75° C for the sphere). The equilibrium temperature with respect to a "total reflector" ($\alpha_s=0.1$, $\epsilon_T=0.1$) is the same as for a "total absorber" ($\alpha_s=0.9$, $\epsilon_T=0.9$); however, this does not mean that a total absorber and a total reflector can be used interchangeably as a thermal control surface. For example, if it were desirable to passively reduce the temperature variations, both in rate and in range, caused by the passages of a satellite through the Earth's shadow, it would be necessary that the absolute values of α_s and ϵ_T be as small as possible. In another case, if the surface is to be used as a radiator of internally generated heat, then ϵ_T should be as large as possible. In many cases, a portion of the spacecraft surface has optical properties which cannot be easily varied, for example, solar cells or various detector surfaces, and in determining the optical characteristics of the remaining surface in order to satisfy thermal requirements, the individual values of α_s and ϵ_T are important. Thus, almost all possible combinations of α_s and ϵ_T are needed at one time or another in the course of thermal design work.

UTILIZATION REQUIREMENTS

Areas of Overall Progress

A literature survey was conducted (ref. 4 to 8) to determine the areas in which the thermal designer will find a limited amount of data for use in his work. In figure 2 the areas where few data were available are shaded, the areas of overall progress (unshaded) seem to include all the basic types of surfaces except the "median infrared reflectors" ($\alpha_s=0.1$, $\epsilon_T=0.5$) and the "median infrared absorbers" ($\alpha_s=0.9$, $\epsilon_T=0.5$). (The surface temperature T is assumed to be in the vicinity of 300° K for the ϵ_T values used here.) A discussion of criteria used in constructing the charts shown in this and the following figures will be given later in the paper.

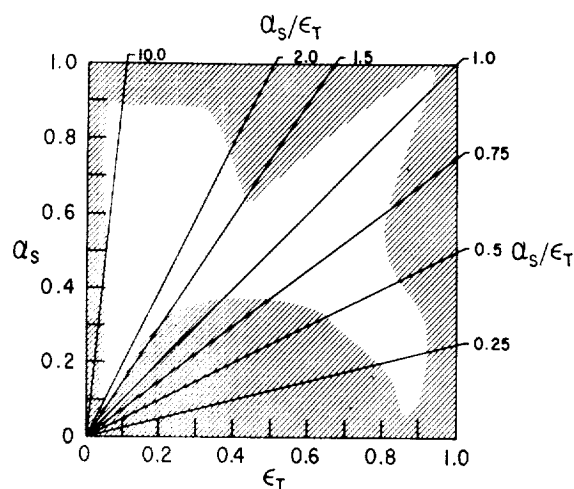


FIGURE 2.—Areas of overall progress (unshaded).

ULTRAVIOLET-STABLE SURFACES

When the question of ultraviolet stability is considered, many of the solar reflectors must be excluded. A chart of the optical characteristics of the ultraviolet-stable surfaces is shown in figure 3.

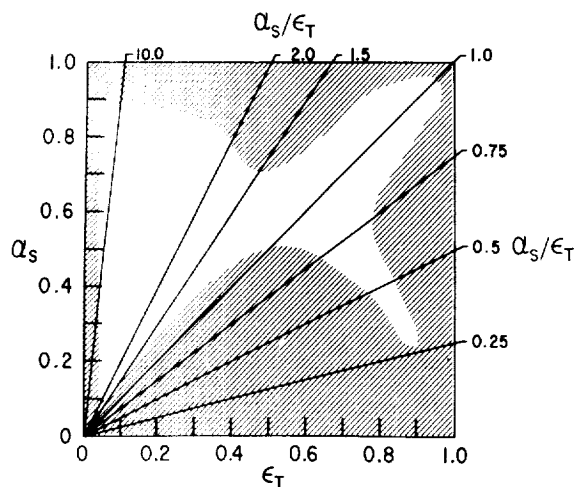


FIGURE 3.—Ultraviolet-stable surfaces (unshaded area).

"THIN" COATINGS

If "thick" coatings (<0.1 mil) are undesirable because of weight or other reasons, figure 2 is modified and becomes as shown in figure 4. On this graph almost the entire area to the

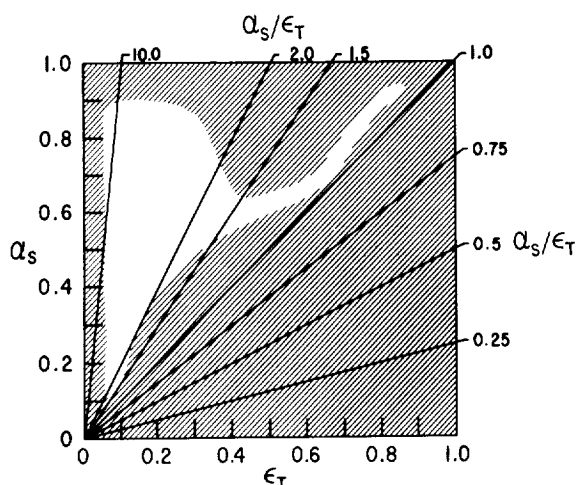


FIGURE 4.—Thin surfaces and electrically conductive surfaces (unshaded area).

right of $\epsilon_T=0.5$ has become shaded, leaving only a very narrow range of α_s and ϵ_T values.

ELECTRICALLY CONDUCTIVE COATINGS

By coincidence, figure 4 also applies if the surface must be electrically conductive. Such a requirement was imposed on Explorer VIII

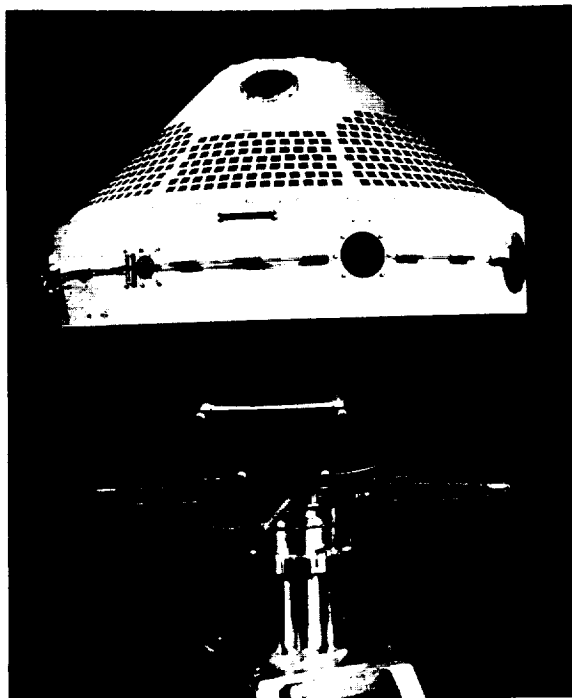


FIGURE 5.—Explorer VIII satellite.

(fig. 5), an ionosphere probe satellite. This satellite measured its immediate ionospheric environment, and it was desirable that the satellite have an equipotential surface. Since there were no known simple means of satisfying the thermal design without using a dielectric paint, it was necessary that this paint be applied in patches, the dimensions of which were less than the expected Debye length for the satellite orbit. It would not have been necessary to apply the paint in patches if the paint had been electrically conducting.

COATINGS FOR LARGE AREAS

If the optical characteristics of large rigid areas are to be controlled, many of the coatings and special bare-surface treatments cannot be used (in particular, those that are prelaunch environmentally unstable or require application techniques presently unavailable on such a large scale). Figure 6 shows the available range under such restrictions. An illustration of such a rigid area is the "dummy payload" flown on Saturn SA-5 (fig. 7). This is an excellent example of a satellite that, while requiring temperature control for the on-board electronics, did not warrant a large-scale thermal design effort. It is for satellites of this type that easily applicable, cheap coatings are especially needed.

A further example of a large surface requiring

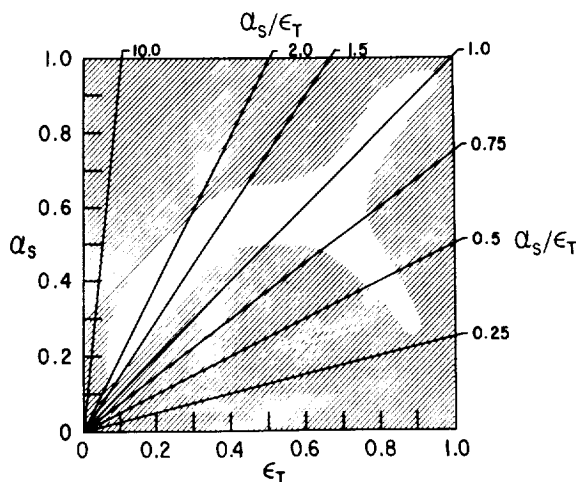


FIGURE 6.—Large-area surfaces (unshaded area).

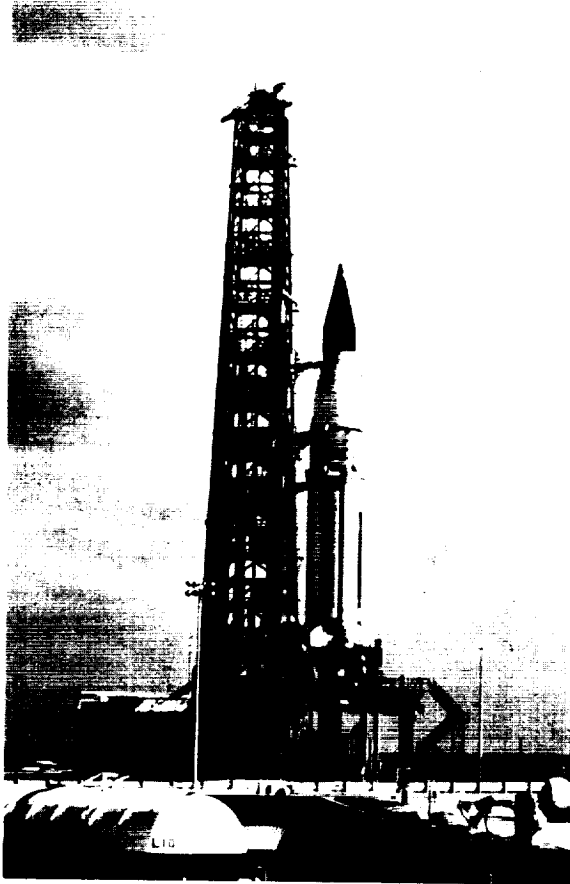


FIGURE 7.—Saturn SA-5 and payload.

thermal control is the meteoroid detector panel of the Meteoroid Detector Satellite to be flown on the Saturn vehicle. The detector panel shown in figure 8 is 96 feet long and 12 feet wide. One full-scale "wing" of the panel is shown in figure 9. It was further desired that the surface be space stable for a year, be "prelaunch stable" or easily repairable, be less than 0.1 mil thick in order that it not have an effect on experimental results (as well as be low in weight), and have an $\alpha_s = \epsilon_T < 0.1$ in order to reduce temperature fluctuations with attitude or during passages through the Earth's shadow. Needless to say, such a coating simply does not exist. The nearest possibility might be vapor-deposited coatings which, at this time, would require a costly and time-consuming process.

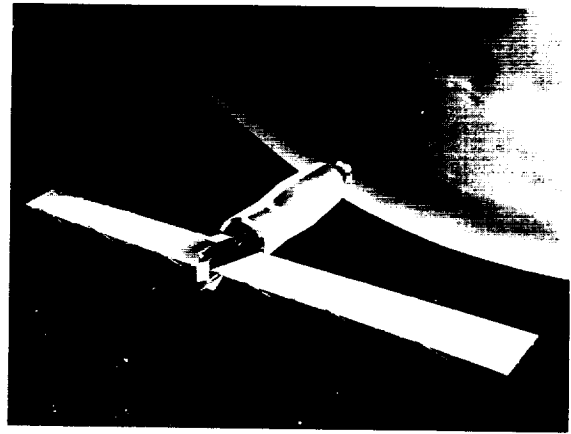


FIGURE 8.—Micrometeoroid Measurement Satellite (full view).

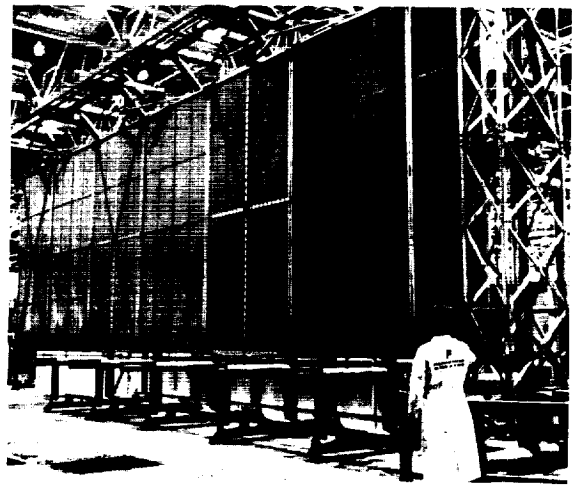


FIGURE 9.—Meteoroid detector panel.

REPARABLE OR PRELAUNCH-STABLE AND ASCENT-STABLE COATINGS

A chart for "prelaunch-stable or repairable" surfaces is shown in figure 10, which also indicates the range of optical properties available with ascent-stable surfaces. Figure 10 is perhaps somewhat more arbitrarily delineated than the other figures, so that particular cases may well fall outside (or inside) the indicated bounds; and the figure might be different for a particular prelaunch handling and environmental situation or for a particular ascent trajectory and vehicle.

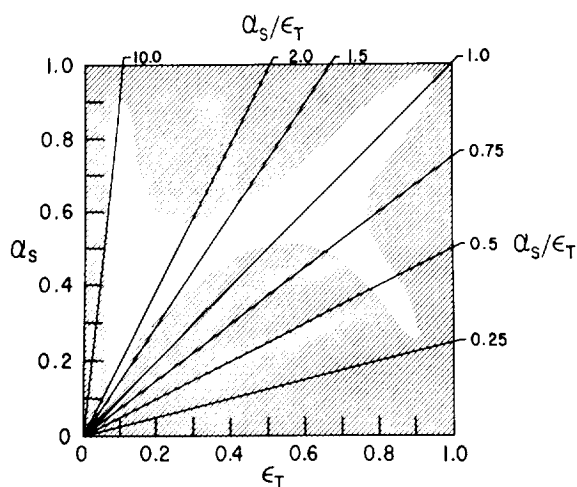


FIGURE 10.—Reparable or prelaunch-stable surfaces and ascent-stable surfaces.

Thermal-Surface Environmental Effect Sensor

A thermal-surface environmental effect sensor has been designed and fabricated at Marshall Space Flight Center (MSFC), to be used for determining effects of the ascent and/or space environments on the optical properties of thermal-control surfaces. The sensors (fig. 11 and 12) consist of 3.175-cm-diameter disks flush with the skin of the Saturn or other vehicle with Kel-F posts for thermal isolation. The optical properties of the disk surfaces are determined in flight by monitoring the temperatures of the disks as a function of time and by solving the thermal design equations backwards to obtain α_s and ϵ_T . The temperatures of four disks flown on Saturn SA-4 (March 28, 1963) are shown as a function of time in figure 13. The purpose of this flight of the sensors was to determine whether the sensors themselves were capable of withstanding the Saturn ascent environment, which consists of aerodynamic heating and shear, vibration, buffeting, and, in this case, exhaust from the retro-rockets. The satisfactory operation of the sensors will make it possible in later flights to determine the effects of both the actual ascent and space environments on thermal control surfaces.

Several attempts have been made by MSFC to put such a sensor into orbit on board satel-

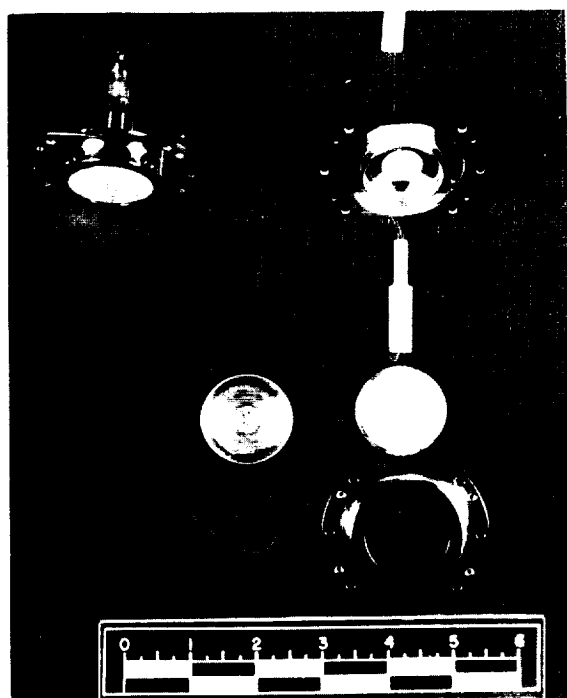


FIGURE 11.—Thermal-surface environmental effect sensor. The scale is graduated in inches.

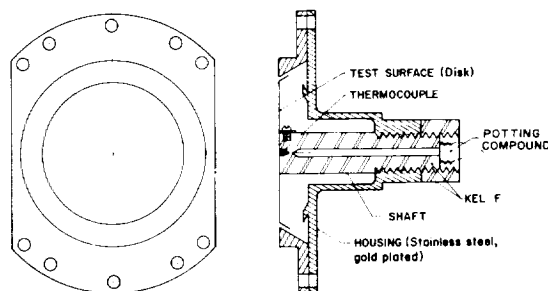


FIGURE 12.—Saturn SA-4 sensors.

lites which were shielded from the ascent environment. The first such attempt (S-46 payload which flew on Juno II AM-19C) on March 23, 1960, failed when orbit was not achieved. A second try with the S-45 payload on AM-19F also failed (February 25, 1961). Success was achieved with Explorer XI (S-15 payload, AM-19E vehicle) which was launched on April 27, 1961.

The surface of interest on this sensor was multilayered and was prepared by Dr. G. Hass

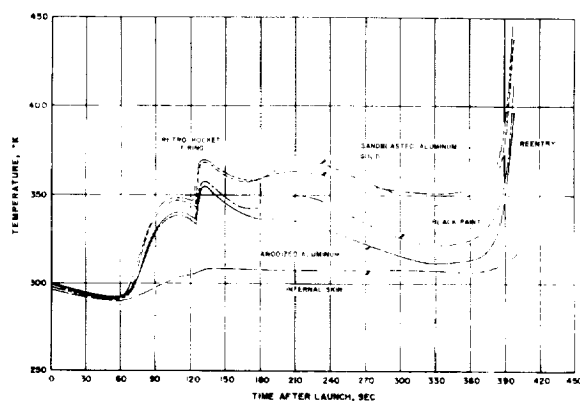


FIGURE 13.—Temperatures from Saturn SA-4 flight of the isolated sensors.

of the Corps of Engineers, Fort Belvoir, Virginia. The surface of the aluminum disk had a 9000-Å layer of SiO, followed by 200 Å of germanium, and topped with 1500 Å of SiO, giving initial α_s and ϵ_T values of 0.71 and 0.12, respectively. A comparison of theoretical and measured temperatures is given in figure 14. From this figure (showing two temperature curves as a function of the time after the satellite egresses from the Earth's shadow), it can be seen that there is good correlation between the theoretical curve and the measured data. From a comparison of data measured on June 19 and October 8, 1961, when the orbital and attitude parameters were about the same, it is apparent that the radiative characteristics of the coating changed very little (no more than 10 percent) during the 3½ months between these two dates (fig. 15).

The determination of the optical properties from sensor data of this type is an extremely tedious process. Since the Explorer XI flight, the data analysis procedure has been improved by (1) an analytically "cleaner" design, (2) higher precision temperature data, and (3) better quality control in fabrication and handling. The next sensor flight planned by MSFC will be on the Meteoroid Detector Satellite to be flown on Saturn SA-9 during 1964.

The utilization requirements which have been discussed in this section are only a few of the many possible restrictions which will be encountered in the selection of thermal control

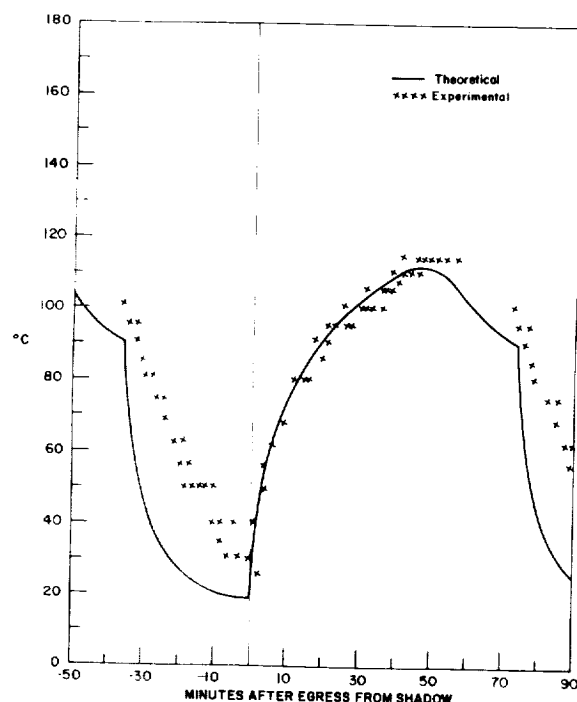


FIGURE 14.—Temperature of sensor for June 19, 1961.

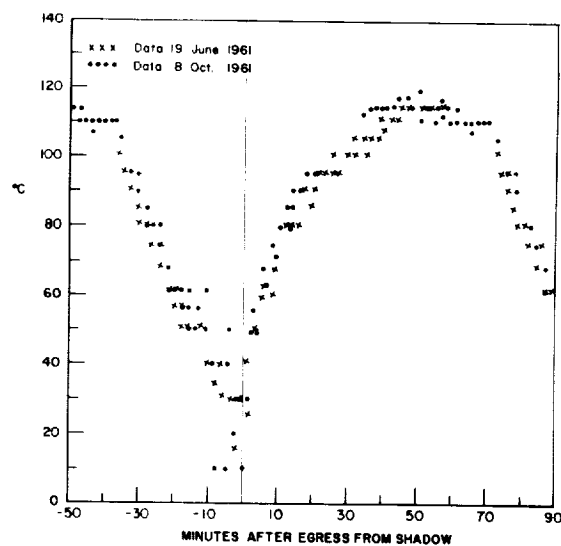


FIGURE 15.—Comparison of temperatures of Explorer XI sensor for June 19, 1961, and Oct. 8, 1961 (when the orbits were thermally similar).

surfaces for future design efforts. It should be pointed out that the intersection of an unshaded area of one of these charts with that of another does not necessarily indicate the upper limit

TABLE I.—*Methods of Obtaining Various Types of Surfaces*

Optical type of surface	α_s	ϵ_T	Polished metals	"As-received" metals	"Sandblasted" metals	Vacuum metallics	Vacuum nonmetallics	Conversion coatings	Plated coatings	Metallic paints	Nonmetallic paints	Vitreous enamel	Inorganic bonded	Transparent conversion	Transparent nonpigmented paints
Total absorber	0.9	0.9						X			X	X	X	X	X
Median IR absorber	0.9	0.5					X	X						X	X
Solar absorber	0.9	0.1				X	X		X						
Median solar absorber	0.5	0.9						X			X	X	X	X	X
Medium	0.5	0.5			X		X	X		X			X	X	X
Median solar absorber	0.5	0.1	X	X	X	X	X		X						
Solar reflector	0.1	0.9						X			X	X	X	X	X
Median IR reflector	0.1	0.5					X	X		X				X	X
Total reflector	0.1	0.1	X	X		X	X		X						

for the possibility of obtaining a surface in a manner which satisfies the conditions of both charts. This is due to the fact that the types of surfaces indicated on the first chart may be different from those used in the second chart.

METHODS FOR OBTAINING SURFACES WITH DESIRED CHARACTERISTICS

For the purpose of discussion it has been found convenient to separate the means of obtaining various surfaces into the following categories:

Bare metals

- (a) Polished
- (b) "As received"
- (c) Sandblasted

Thin films

- (a) Conversion
- (b) Vacuum-deposited
 - (1) Metallic
 - (2) Nonmetallic
- (c) Plated

Pigmented coatings

- (a) Paints
 - (1) Metallic
 - (2) Nonmetallic
- (b) Vitreous enamels
- (c) Inorganic bonded

Transparent coatings

- (a) Conversion coatings
- (b) Nonpigmented paints

Paste-on films

The types of surfaces generally obtained from all but the last of these methods are shown in table I.

In constructing the graphs for the section "Utilization Requirements", ground rules (of the nature of availability criteria) were established and followed in determining which methods could be used to satisfy each of the utilization requirements. These rules are indicated in table II and are discussed in more detail in the following paragraphs along with a brief discussion of each type of surface and some of their individual characteristics. The desirability of surfaces with certain special optical properties is also discussed.

Bare Metals

The optical properties of bare metals are well known from theory and numerous measurements. Yet, when the designer is confronted with the use of these data, he is at once at a loss to correlate this information with the exact surface condition of the metal he is considering.¹

He must consider such fundamental optical properties as solar absorptance α_s , if it is to be exposed to solar radiation, and total hemispherical emittance, ϵ_T . Secondly, he will consider the spectral characteristics of the material, ϵ_T, λ , according to the nature of other radiations

¹ See also Session II papers.

TABLE II.—Rating of Thermal Control Surfaces According to Utilization Requirements

Thermal control surfaces	Utilization requirements*					
	Ultraviolet stable	Thin	Electrically conductive	Large surfaces	Reparable and/or prelaunch stable	Ascent stable
Bare metals:						
(a) Polished.....	Y	Y	Y	Y	S	S
(b) "As-received".....	Y	Y	Y	Y	S	S
(c) Sandblasted.....	Y	Y	Y	Y	S	S
Thin films:						
(a) Conversion.....	S	Y	N	W/R	Y	Y
(b) Vacuum-deposited:						
(1) Metallic.....	Y	Y	Y	N	N	S
(2) Nonmetallic.....	S	Y	N	N	Y	Y
(c) Plated.....	Y	Y	Y	W/R	S	S
Pigmented coatings:						
(a) Paints:						
(1) Metallic.....	S	N	Y	Y	Y	S
(2) Nonmetallic.....	S	N	N	Y	Y	S
(b) Vitreous enamel.....	S	N	N	N	Y	Y
(c) Inorganic bonded.....	S	N	N	W/R	N	Y

*Y = yes; S = selective; W/R = with reservations; N = no.

to which it is to be exposed (such as planetary radiation). Also, he must find the average solar absorptance as a function of aspect angle, α_s , ϵ . Angular dependence of ϵ is also important if various surfaces are exposed to each other.

For accuracy it is necessary to determine how precisely the optical properties are known for a particular surface. For most metals the emittance is low compared to the solar absorptance. Consequently, the ratio can be quite uncertain, depending on the uncertainty in measurement accuracy. For example, aluminum can have an emittance of about 0.03 and α_s of about 0.18, giving an α_s/ϵ_T of 6. If the uncertainty in the emittance measurement is 0.03, then the α_s/ϵ_T has a range from 3 to 6.

Metals have a wide range of surface finishes, from the "as received" to oxidized, to sandblasted, to polished, to vacuum deposited (which will be discussed later). In space applications, the last three have received the most attention. The two primary methods for polishing are mechanical and chemical. Mechanical polishing "work hardens" the surface and usually requires an abrasive which may be

"burnished into" the surface, creating additional uncertainties. Chemical polishing requires a bath and, therefore, needs to be performed prior to assembly. Sandblasting seems to provide the most stable metal surface from the standpoint of handling since the ϵ_T value will be higher and small changes will not affect the α_s/ϵ_T ratio as significantly. Warpage of the metal as a result of sandblasting is a major problem.

In general, metals are considered space stable even for long periods of time. However, the vapor pressure and sputtering rates of some metals preclude their use in long-term applications.

Thus, since much of the exterior surface of most spacecraft is of metal, the optical properties of the bare metal surface are sometimes the ones desired. The consensus that bare metal surfaces are generally space stable, the fact that some coatings would cause a significant weight increase, and the generally low cost in both time and money of using the bare surface make their use for thermal control appear desirable in many cases.

Thin Films

VACUUM DEPOSITED

The vacuum deposited coatings (both metals and dielectrics) represent one of the more expensive methods for obtaining surfaces with specific optical properties. However, a wide range of distinct values of α_s and ϵ_T can be obtained with very close tolerance, and the added weight is negligible.

The expense occurs when it is necessary to coat large rigid areas which require large vacuum chambers and other coating facilities. Handling is also a major problem as is corrosion protection (prelaunch environment) and the repairing of defects or handling scars. Vacuum-deposited metals are particularly subject to these hazards, whereas the dielectrics are much more wear and weather resistant (ref. 9) and, to a certain extent, are cleanable.

CONVERSION COATINGS ²

Almost all metal surfaces form a very thin homogeneous dielectric film. Usually, this film is an oxide of the parent metal and may even be monomolecular in thickness. Conversion coatings, in general, extend the thickness of this film by chemical conversion. The sparse data on such thin coatings show them to exhibit strong absorption in the infrared while retaining varying transparency in the visible region. Application requires a chemical bath with, usually, precleaning and rinsing baths and very close processing control for reliable and repeatable coatings.

There is little information available on the space stability of these coatings. Other considerations such as cost, weight, and handling make these generally rugged coatings look attractive for space applications.

PLATED COATINGS

Plated coatings are normally limited to metals (electrically conductive), but techniques have been developed for plating these coatings on various dielectrics.

As a rule, these coatings are not as highly reflecting in the visible and infrared as are

coatings prepared by vacuum evaporation, but adhesion is usually very good.

Pigmented Coatings

PAINTS

Because of the obvious simplicity and ease of application and the vast experience behind pigmented paints, much effort has gone into developing and testing these coatings for purposes of space-vehicle thermal control. The results of these tests, especially tests of ultraviolet degradation in a vacuum environment, proved that paints were not as stable as once thought. However, research has since produced pigments and vehicles that are relatively stable to ultraviolet in vacuum and to fairly severe ascent environments (ref. 4 and 10).³

A large range of solar absorptance can be obtained because of the availability of many pigments (even low emittance can be obtained by using metallic pigments). However, almost all paints have an α_s/ϵ_T of 1.0 or less; thus, the development of paints having higher ratios would be extremely desirable.

VITREOUS ENAMELS

Very little work has been done with vitreous enamel coatings, probably because of the high temperatures (about 800° to 1250° K) required to fire the coatings. It should be possible to obtain about the same range of optical properties with these coatings as with paints. High-temperature operation, hardness, durability, and cleanability are the major advantages. Disadvantages are also numerous: a thick coating (about 5 to 10 mils) is required for good solar reflectance; the firing temperature is high; the coating is brittle; the coefficients of expansion must be carefully matched; the surface must usually be acid-etched or sand-blasted prior to coating; and the coating is nonreparable.

INORGANIC BONDED COATINGS

Inorganic cements such as aluminum phosphate, potassium silicate, and sodium silicate can be pigmented like a paint and applied to a surface. The results are very porous coatings

² See also Paper 43.

³ See also Session IV papers.

which, as a rule, are oven cured at moderate temperatures (about 420° K). These coatings can be made very white (low α_s) and have high emittance and, hence, a low α_s/ϵ_T ratio. As in paints, a large number of pigments are available to give a wide range of α_s values. Also, resistance to degradation by ultraviolet has been reported (ref. 10) for some combinations of binders and pigments.

Flame and plasma-spray techniques offer excellent possibilities for applying inorganic materials to almost any substrate. These types of coatings were used on some of the first satellites (ref. 1 and 2) and undoubtedly will be used for thermal control coatings in many future cases. Very low α_s/ϵ_T coatings have not been obtained; otherwise, the range of optical properties of flame- and plasma-sprayed coatings exceeds that of paints.

The outstanding disadvantage of these types of coatings is porosity, which makes handling and cleaning difficult.

Transparent Coatings

Transparent coatings, as used here, are coatings which are transparent (nonscattering) over most of the solar energy spectral region (0.2 to 3.5 microns) and opaque to longer wavelengths. Almost no data exist on this type of coating, even though it offers such advantages as being easily applicable and repairable, has good handling properties, and is cleanable.

The α_s is largely determined by the metallic substrate. If a low α_s is desired with a structural skin of, for example, steel, then the metal has to be buffed, electropolished, or even plated to obtain the desired (or the minimum obtainable) values.

CONVERSION COATINGS

Some surface conversion coatings fit into the transparent coating category. The solar absorptance and thermal emittance of these coatings increase with thickness so that good control of these properties can be maintained. The advantages and disadvantages of thin-film conversion coatings as discussed previously apply here also.

NONPIGMENTED PAINTS⁴

Surfaces that strongly reflect solar radiation but exhibit high thermal emittance can be obtained by applying a nonpigmented paint or transparent vehicle directly to a metallic surface. While the solar reflectance and the thermal emittance may not be as high as for some dielectric-particle pigmented paints, coatings with only moderately low α_s/ϵ_T are generally adequate.

Paste-on Films

There are available on the commercial market many adhesive-backed paste-on films. These are usually metallic or metallized plastic films, but similar films could be made for many of the surfaces discussed previously, such as the conversion coatings, paints, etc. The environmental instability of the adhesive seems to be the most severe problem with tapes of this sort (ref. 4).

Special Coatings

DIRECTIONAL SURFACE

It is often the case that the available data on the optical properties consist only of α_s and ϵ_T values calculated from reflectance data taken for nearly normal incidence. These data are often insufficient to permit accurate calculation of the heat balance of a space vehicle. The variation in α_s with incidence angle, for example, has been shown in some cases, using data on representative surfaces, to produce significant deviations from the predicted temperatures (ref. 11). Most real surfaces show considerable differences between the values of normal emittance and of total hemispherical emittance, with the latter value being higher for smooth metal surfaces but lower for most dielectrics.

This directionality of absorptance and emittance may sometimes be of advantage with regard to thermal control. For example, the radiation exchange between surfaces might either be enhanced or attenuated, or orientation to the Sun could be used to help regulate the temperature of a radiator. A mathematical

⁴ See also Paper 40.

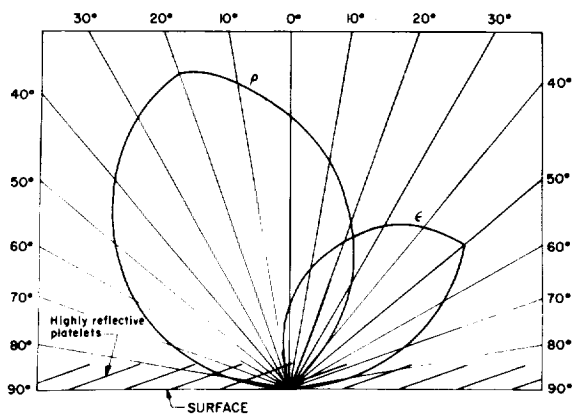


FIGURE 16.—Polar plot of mean density of flux emitted (ϵ) and reflected (ρ) from highly reflective metallic platelets oriented 70° from surface normal. (Refractive index of material between platelets is 1.)

analysis of directional surfaces for the purpose of controlling radiation exchange using asymmetrically grooved surfaces is discussed in reference 12.

Highly reflective metallic platelets, such as leafing aluminum paint pigments or razor blade surfaces, arranged as shown in figure 16, should give very distinct directional properties if the plates are large compared to their spacing.⁵ Filling the space with a dielectric such as a paint vehicle changes the directional characteristics somewhat. If the platelets are inclined at a low angle, the surface will have a lower $\alpha_{s,\theta}$ at near normal angles than at the larger angles. If, with an arrangement such as this, a surface could be made whose $\alpha_{s,\theta}$ is nearly proportional to the secant of the incidence angle, the variation in the amount of energy absorbed by a flat plate due to the variation in projected area would be largely cancelled; giving a constant amount of absorbed energy (fig. 17 and 18).

INTERFERENCE COATINGS⁶

Multilayer coatings can be applied to cause constructive and destructive interference to alter the reflectance of a surface over some wavelength range. Very high α_s/ϵ_r (solar absorbing) coatings have been produced on

⁵ See also Paper 32.

⁶ See also Papers 20, 49, and 50.

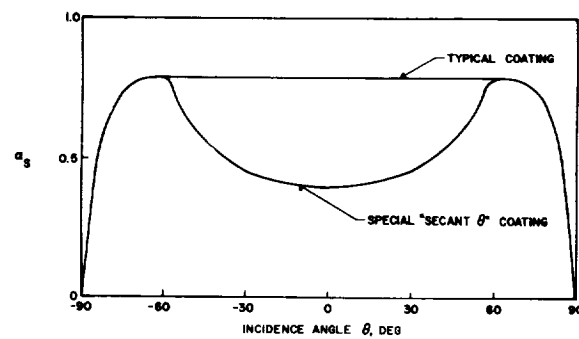


FIGURE 17.—Solar absorptance α_s against aspect angle for "secant θ " coating.

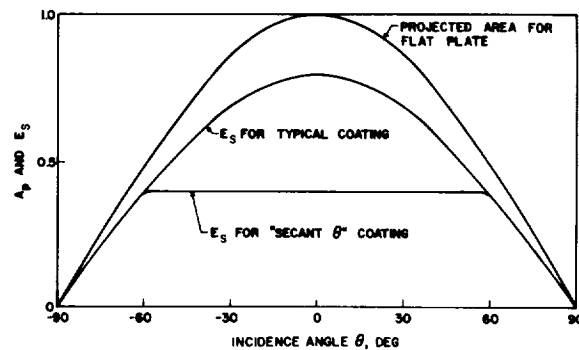


FIGURE 18.—Absorbed solar energy, E_a , and projected area, A_p , against aspect angle for "secant θ " coating.

aluminum substrates using this technique. The same techniques can be employed to obtain very low α_s/ϵ_r coatings for solar collectors and other applications.

Much recent work on infrared filters has so greatly enlarged the overall technology of interference coatings that their use as thermal control coatings merits increased consideration.

NONSPECTRAL COATINGS⁷

A type of surface which would be useful in many applications is a nonspectral or "gray" surface. The spectral absorptance of such surfaces are shown in figure 19. They would have a constant spectral absorptance throughout the solar region (assumed to extend from 0.1 to 3.0 microns) and, perhaps, a different constant absorptance throughout the far infrared (>3.0 microns). Such surfaces would

⁷ See also Papers 49 and 50.

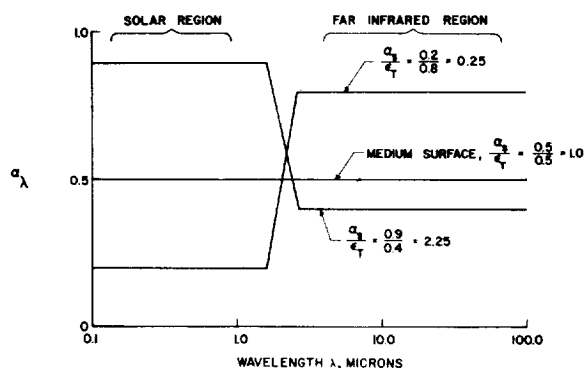


FIGURE 19.—Spectral absorptance curves of some ideal nonspectral surfaces.

be desirable for thermal control of spacecraft because, for example, when the spacecraft are undergoing ground thermal testing, the spectral distribution of any solar simulators would not be critical (within the range of 0.1 to 3.0 microns), so that only the intensity would have to be carefully controlled. This is especially important when the differences between the solar spectrum and the spectra of various "solar simulators" are considered.

It is known that the Earth radiates infrared radiation to space such that the total intensity is about the same as that from a blackbody at 248° K. However, the spectral distribution (typically) is much different, as shown in figure 20 (ref. 13). If a surface is nonspectral (gray) in the far infrared, the absorptance of the surface to the Earth radiation, α_E , is the

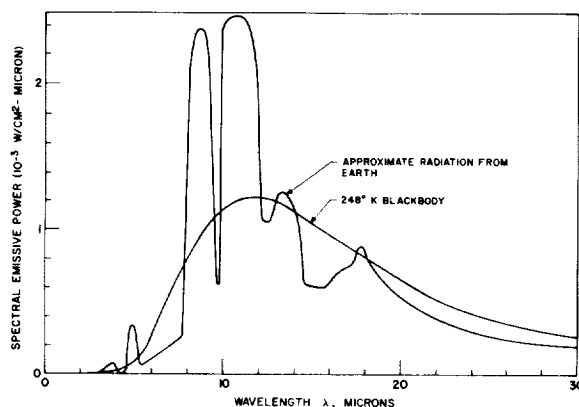


FIGURE 20.—Spectral energy distribution of Earth radiation compared with radiation from 248° K blackbody.

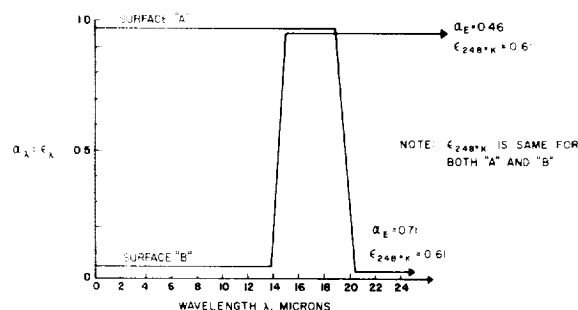


FIGURE 21.—Examples in which absorptance for Earth radiation α_E is different from absorptance for 248° K blackbody radiation.

same as the absorptance to radiation from a 248° K blackbody, $\alpha_{248^\circ \text{K}}$. In most satellite design work it is usually assumed that α_E is equal to ϵ_T , and generally this is a fairly safe assumption. However, in figure 21 are two hypothetical spectral absorptance curves that correspond to α_E values very different from $\epsilon_{248^\circ \text{K}}$ (or $\alpha_{248^\circ \text{K}}$). Even though the $\epsilon_{248^\circ \text{K}}$ values are the same for both surfaces, 0.61, the α_E values are 0.46 in one case and 0.71 in the other.

Thus, the spectral characteristics of thermal control surfaces may be strong tools in spacecraft thermal design work, and additional investigation in this area may be extremely fruitful.

CONTROLLED DEGRADATION

It might be mentioned briefly that the degradation of a surface in space might not necessarily be undesirable for all spacecraft missions. One example might be a one-way trip to Mars in which the increase in the distance from the Sun could cause the temperature of the spacecraft to drop. If the coating degrades due to solar irradiation in a manner as shown in figure 22, the increase in distance would be balanced by an increase in solar absorptance so that the on-board temperature would remain nearly constant. It might be noted that the graph is in "equivalent Earth sun-hours exposures" which is how most ultraviolet degradation data are presented. Thus, even though the time required for the trip is about 6000 hours, the equivalent exposure time is about 3900 hours.

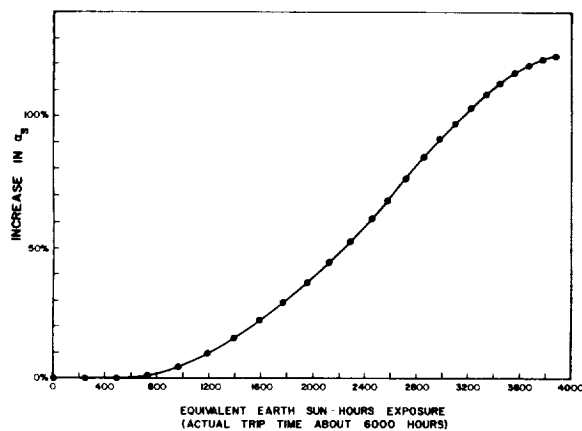


FIGURE 22.—Increase in α_s as a function of exposure to solar radiation required to maintain constant temperature on trip to Mars.

Before coatings of this type can be fully utilized, more theoretical and experimental work must be done in order better to understand the mechanisms of degradation and further describe the degrading environment.

SELF-REGULATING OR INFLIGHT-VARIABLE SURFACES

The desirability of surfaces which have optical properties that can be varied in flight by either passive or active means is obvious. Research in this area has thus far not been very fruitful.

CONCLUSIONS

At first glance, with the exception of the median infrared reflectors and absorbers, there appears to be a large selection of coatings and surfaces with a wide range of optical properties (α_s , ϵ_r , and α_s/ϵ_r). However, definite gaps appear when the following representative utilization requirements are imposed:

1. ultraviolet stable
2. thin
3. electrically conductive
4. applicable to large areas
5. repairable or prelaunch stable
6. ascent stable

These gaps widen severely when two or more constraints are imposed.

To alleviate the restriction in the choice of optical properties available to the designer

due to particular utilization requirements, there is need for further development of coating technology, both in optical properties and in application techniques.

Also, to extend passive coating technology for thermal testing and design, it would be desirable to develop such special surfaces as

1. directional surfaces
2. interference coatings
3. nonspectral coatings
4. controlled-degradation coatings

The development of thermal control surfaces is only in its infancy. Much work must be done before it will be safe to assume that individual "crash" programs will not be necessary to satisfy the thermal design needs for most of the future spacecrafts.

REFERENCES

1. HELLER, GERHARD: Thermal Control of the Explorer Satellites. *ARS Jour.*, vol. 30, no. 4, Apr. 1960, pp. 344-352.
2. HELLER, GERHARD: Thermal Problems of Satellites. *Proc. Fifth Sagamore Ord. Materials Res. Conf.—Materials in Space Environment*, MET 597-596, Contract ROD-30-115-ORD-947, Syracuse Univ. Res. Inst., Sept. 1958, pp. 89-126.
3. HIBBS, A. R.: The Temperature of an Orbiting Missile. *Progress Rep. No. 20-94* (Contract no. DA-04-495-Ord 18), Jet Propulsion Lab., C.I.T., Mar. 28, 1956.
4. GAUMER, ROGER E., and McKELLAR, LOUIS A.: Thermal Radiative Control Surfaces for Spacecraft. LMSD-70414, Lockheed Aircraft Corp., Mar. 1961. (Available from ASTIA as AD 264-127.)
5. MERRILL, RONALD; SNODDY, WILLIAM; and SCHOCKEN, KLAUS: The Results of Emittance Measurements Made in Relation to the Thermal Design of Explorer Spacecraft. *NASA TN D-1116*, 1962.
6. EDWARDS, D. K., and RODDICK, R. D.: Spectral and Directional Thermal Radiation Characteristics of Surfaces for Heat Rejection by Radiation. *Power Systems for Space Flight*, Morris A. Zipkin and Russell N. Edwards, eds., Academic Press (New York), 1963, pp. 427-446.
7. SCHMIDT, R. N.: Effectiveness of Solar Absorber Surfaces. *Power Systems for Space Flight*, 1963.
8. BEVANS, J. T., ET AL.: Final Report—An Investigation of the Thermal Radiation Properties of Certain Spacecraft Materials. *Space Technology Lab.*, 8633-6014-SU-000 (Contract NAS5-1102), Dec. 1962.

9. HOLLAND, L.: Vacuum Deposition of Thin Films. Chapman & Hall Ltd. (London), 1961.
10. ZERLAUT, GENE A., and HARADA, Y.: Stable White Coatings. Rep. No. ARF 3207-14 (Interim Rep.) (Contract no. 950111—Subcontract NAS7-100), Armour Res. Foundation, Illinois Inst. Tech., Nov. 13, 1962.
11. EDWARDS, D. K.: Directional Solar Reflectances in the Space Vehicle Temperature Control Problem. ARS Jour., vol. 31, no. 11, Nov. 1961, pp. 1548-1552.
12. HOWELL, JOHN R., and PERLMUTTER, MORRIS: Directional Behavior of Emitted and Reflected Radiant Energy From a Specular, Gray, Asymmetric Groove. NASA TN D-1874, 1963.
13. JOHNSON, FRANCIS S.: Thermal Radiation From the Earth. Satellite Environment Handbook, ch. 7, Francis S. Johnson, ed., Stanford Univ. Press, 1961, pp. 111-116.

DISCUSSION

ALBERT S. HARON, Martin Company: Do the shaded areas in your plots refer to homogeneous surfaces; and if so, would the use of mosaics increase the useful area?

MILLER: Yes, I think they would. However, I think this is not always the most desirable solution to the coating problem, because this usually ends up with using more than one material, thus doubling or tripling the problems.

ARTHUR KATZ, Grumman Aircraft: You seem to

lump together prelaunch-stable and ascent-stable surfaces. Are you talking about surfaces that will actually feel or see the thermal environment during ascent?

MILLER: Yes, I am. The trend is toward that direction, I think, especially for the larger vehicles.

KATZ: I should think that the requirements would not be the same, since the environments are so different during these two phases of a launching.

49. Selective Coatings for Vacuum-Stable High-Temperature Solar Absorbers

R. N. SCHMIDT AND J. E. JANSSEN

HONEYWELL RESEARCH CENTER, HOPKINS, MINN.

One of the necessary design criteria for a solar thermal-cycle power system aboard a spacecraft is the thermal radiation properties of the surface on which the solar energy is absorbed. A coating which selectively absorbs solar energy but does not radiate infrared energy gives increased absorber efficiency over a nonselective blackbody at lower solar flux concentrations and higher temperatures. An interference coating consisting of multiple layers of alumina and molybdenum on a molybdenum substrate gave a solar absorptance of 0.83 and an emittance of 0.11 at 1000° F. A selective black surface, beryllium plus 1 percent copper alloy anodized in sodium hydroxide, produced a very hard and durable coating with a solar absorptance of 0.91 at room temperature, and a solar absorptance of 0.87 with an emittance of 0.30 at 1000° F.

The sun is a major source of energy for use aboard space vehicles. To date, satellites utilizing solar energy convert the solar energy directly to electrical energy with large arrays of solar cells. However, solar cells are expensive, are subject to damage by radiation, and present increasing reliability and weight problems as the power requirements and the number of solar cells required increase.

A second method for utilizing solar energy is the collection of the energy as heat with subsequent conversion to electrical energy through a thermal cycle. One of the primary questions facing the designer of such a system is the choice of the surface on which the solar energy is to be absorbed. The surface should have a high solar absorptance, but since the surface will necessarily have to operate at an elevated temperature and, in turn, radiate away infrared energy, it should have a low emittance in the infrared region. Fortunately, solar energy is concentrated largely in the short-wavelength region whereas the energy radiated by a surface, even as hot as 1000° C, is con-

centrated in the longer wavelength infrared region. It is possible, therefore, to achieve reasonably high solar absorptance coupled with a low infrared emittance. The question arises, however, as to just where the desired cutoff between solar absorptance and infrared emittance should occur. R. N. Schmidt (ref. 1) has shown that the operating temperature of the absorbing surface and the solar flux intensity have an important bearing on the desired position of this cutoff point.

An ideal selective absorber is defined as a surface which has a spectral absorptance α_λ or emittance ϵ_λ of 1.0 at all wavelengths for which the incident solar monochromatic energy intensity is higher than the monochromatic energy intensity of a blackbody at the absorber surface temperature, and a spectral emittance of zero at all wavelengths for which the solar monochromatic energy intensity is lower than the blackbody intensity. With the solar energy curve assumed to be smooth and continuous, the wavelength for which the monochromatic energy intensities are equal is defined as the cutoff wavelength.

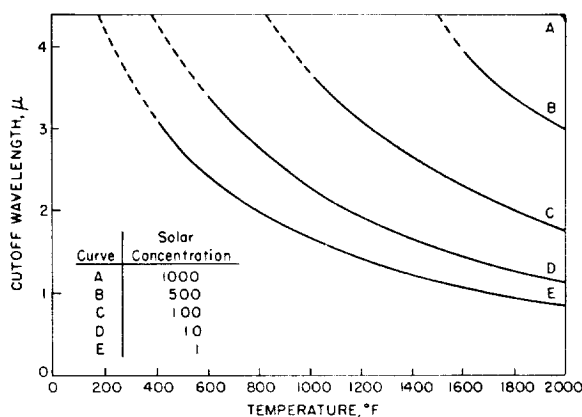


FIGURE 1.—Cutoff wavelength for the ideal solar absorber.

Figure 1 shows the influence of solar concentration and absorber surface temperature on this optimum cutoff wavelength, as presented in reference 1.

The solar absorber effectiveness has been defined (ref. 1) as the ratio of energy absorbed and retained to that absorbed and retained by a perfect absorber under the same conditions. This effectiveness parameter was used to compare the relative merits of solar absorber surfaces. Figure 2 shows the effectiveness of a black surface (α_λ and $\epsilon_\lambda = 1$ for all wavelengths) as a function of temperature for various solar concentrations. It is seen that for a given solar concentration, the need for a selective absorber increases with increasing temperature. The need for a selective absorber cannot be ignored unless the solar concentration is high and the

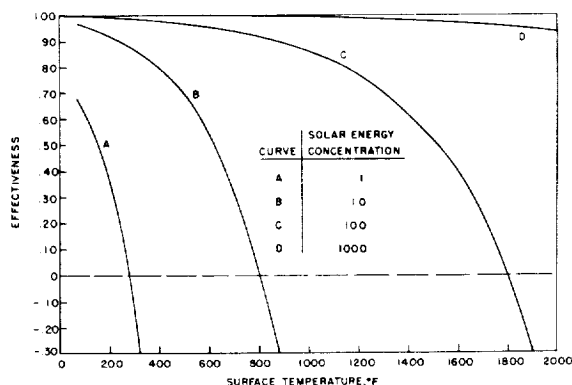


FIGURE 2.—Solar absorber effectiveness of a blackbody.

operating temperature is relatively low. No one surface or coating can satisfy all conditions. A high solar concentration or a low solar concentration with a low absorber temperature requires a relatively long cutoff wavelength. However, if the cutoff wavelength exceeds about 4 microns the selective absorber offers a negligible advantage. On the other hand, at moderate solar concentrations with relatively high absorber temperatures, coatings with cutoff wavelengths in the 1.0- to 2.5-micron region are needed. These are the conditions frequently encountered in the design of a solar thermal power system.

One method for tailoring the optical properties of a surface is the use of thin films on the surface to produce optical interference or reinforcement bands at the desired wavelengths. The Fabry-Perot interference type, in which a dielectric film is deposited on a reflective surface, produces absorption bands. Additional layers of partially transmitting metal films and dielectric films are used to broaden the desired absorption bands and to help achieve cutoff at the desired wavelength. Such a coating is designed to have absorption bands in the solar spectrum region but to be transparent in the infrared; thus, the low emittance of the metal films or substrates can control heat loss in the infrared region. This system will be called an interference film system.

Optical techniques have certain inherent disadvantages. In general, the interference and reinforcement effects are sensitive to the angle of the incident radiation. There would be some loss in the effectiveness of the coatings when used with nonparallel radiation, such as is produced with a concentrating mirror. Also, changes in the index of refraction and film thicknesses may cause the absorption bands to shift with temperature.

A second type of coating not subject to the same problems is a selective black which has high absorptance at short wavelength but is transparent or reflective at longer wavelengths. The transparent type must be deposited over a suitable reflective substrate in order to provide low emittance in the infrared.

One of the major problems to be solved is that of materials selection. In addition to the de-

sired optical properties, which are very restrictive in the case of the selective black and infrared reflector, these coatings must be stable at elevated temperatures in space. Therefore, they must possess very low vapor pressures and must be chemically compatible at elevated temperature so that the films do not diffuse or react. Other desirable properties are good adherence, abrasion resistance, ultraviolet stability, and ease of applications. Martin and Bell (ref. 2) have tabulated some of the more promising metals and oxides stable in a vacuum at temperatures up to 1000° K. In general, the materials used in this study were selected from their list.

SAMPLE PREPARATION

For the multiple-layer interference-type film system, the primary criteria for material selection are as follows: substrate—high reflectance in the infrared, high melting temperature, low vapor pressure, and low electrochemical potential to provide chemical stability with the dielectric layers; dielectric film—high transmission in the infrared, high melting temperature, low vapor pressure, and high electrochemical potential; metal film—high reflectance in the infrared, high melting temperature, low vapor pressure, and low electrochemical potential. For some cases a selective absorption in the solar spectrum is advantageous.

From the list of stable oxides presented by Martin and Bell (ref. 2) Al_2O_3 and Ta_2O_5 were selected for this investigation. Molybdenum was selected for the substrate and semitransparent films because of its low electrochemical potential and vacuum stable properties. Molybdenum also has an absorptance of 0.50 below 1 micron and an emittance of only 0.07 at 1000° F, which makes it a selective material in itself.

Most of the dielectric and metallic films were produced by evaporation. Although the evaporation processes were somewhat difficult because of the low vapor pressures of the materials, successful techniques were available.

Three methods of thin film deposition were used in the preparation of the interference samples: (1) resistive heating evaporation, (2) work-excited electron beam evaporation, and

(3) anodizing. The resistance heated thermal evaporator uses an electrically heated tungsten boat in direct contact with the material to be evaporated. Both Al_2O_3 and Ta_2O_5 were evaporated from a V-shaped tungsten boat. Molybdenum and tantalum films were evaporated with a work-excited electron beam gun. Tantalum oxide films were also produced by anodizing thin tantalum films.

In order to properly apply theoretical analysis and eliminate uncontrolled repetition, it was necessary to deposit reproducible films with predictable optical properties. Electrical resistance measurements were used for monitoring the thickness of metal films, and reflectance measurements were used for monitoring dielectric films.

Glass microscope slides with parallel silver electrodes painted 1 inch apart were used as substrates for the resistance monitor. The resistance between the painted strips was measured during and after evaporation. A correlation of resistance with transmittance for molybdenum is presented in figure 3. It was observed that the resistances of molybdenum films changed appreciably when air was introduced into the vacuum chamber after evaporation. Apparently, the films oxidized in air even at room temperature. This caused the films to become more transparent. Over a period of several days, a transmission increase up to 10 percent was observed. However, this did not greatly impair the use of this system for preparing films of predictable transmittance because film transmission was correlated with resistance after the changes had occurred.

A reflectance monitoring system was designed and installed in the evaporation chamber to measure the thickness of dielectric films. Light from a tungsten lamp, chopped at 750 cps, is projected onto a specularly reflecting monitoring surface located adjacent to the specimen. The light reflected from the monitoring surface is focused through a Gaertner monochromator onto a lead sulfide cell. With this system it is possible to observe the minimum- and maximum-reflectance bands (due to interference or reinforcement, respectively). The light source was not sufficiently intense

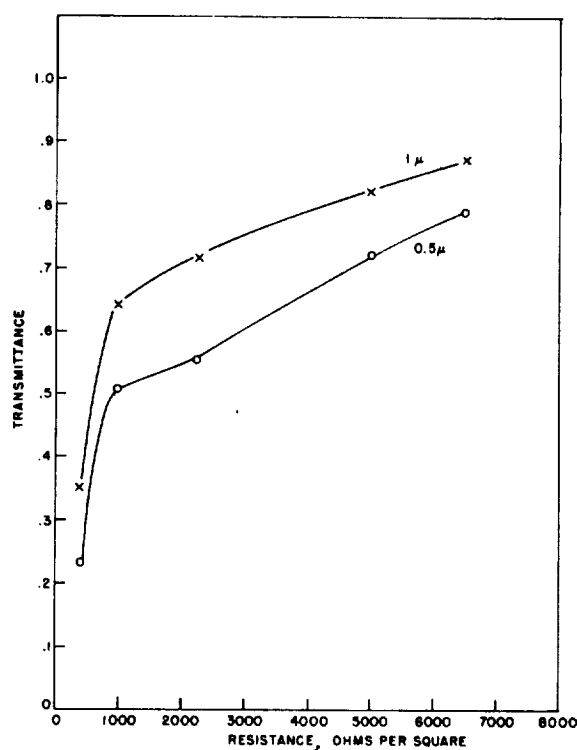


FIGURE 3.—Transmittance against resistance per square for thin molybdenum films.

to permit monitoring films less than about 0.075 micron thick. Therefore, evaporation time was used as an indication of film thickness for thinner films.

Evaporated aluminum on microscope slides was used as the monitoring surface except when monitoring Al_2O_3 film. It was found that Al_2O_3 deposited over an aluminum substrate gave very little interference. Substitution of a molybdenum film on the monitoring surface greatly increased the interference for Al_2O_3 and, hence, the accuracy of film thickness control.

Anodizing was utilized in the preparation of some Ta_2O_5 films. Thin tantalum films evaporated on molybdenum substrates were anodized in an oxalic acid bath (1 part oxalic acid, 2 parts water, 3 parts ethylene glycol by weight) at 69° C. All the exposed molybdenum surfaces were painted with Glyptal paint to insulate the molybdenum from the anodizing bath and thus prevent electrical shorting which interferes with oxidation of the tantalum.

An alloy of beryllium plus 1 percent copper, anodized in sodium hydroxide, was selected (ref. 3) for the investigation of selective blacks. Beryllium has a high reflectance in the infrared, and the copper in the alloy, when anodized, produces a selective high absorption in the solar spectrum.

The beryllium alloy was first hand-polished with 1200 Crystolon lapping compound and degreased in trichloroethylene, then cleaned in Oakite 61A, 6 oz/gal, at 200° F for 5 minutes, and rinsed in cold water. The samples were then anodized in 7.5-percent NaOH at 25° C for 30 to 90 minutes. A steel cathode was used with a current density of 8 amp/ft². The samples were finally sealed in boiling water for 5 minutes. Anodizing time was the only variable in this procedure.

MEASUREMENT APPARATUS

The spectral reflectance was measured with an integrating hemisphere reflectometer (ref. 3 and 4). This instrument measured the near-normal reflectance for hemispherically incident radiation on the specimen. By the reciprocity relationship this reflectance is equal to the hemispherical reflectance for near-normal incident radiation. The wavelength range measured was 0.35 to 20 microns. Measurements in vacuum were made at elevated temperatures at a pressure of 10^{-5} torr or lower.

Solar absorptance was calculated from the spectral reflectance measurements by numerical integration of the reflectance data, weighted by the solar spectral energy distribution (ref. 5).

The instrument used for the total hemispherical emittance measurements is shown in figure 4. The measurement technique and a similar piece of apparatus used for routine low temperature measurements in our laboratory are described in references 6 and 7. The design consisted of a cooled thermopile detector in an evacuated cooled enclosure. The sample was held in a heated sample holder and the detector was suspended from the cover directly over the sample. The enclosure was evacuated to 10^{-5} torr or lower to eliminate free convection and gaseous conduction between the sample and thermopile. The sensor could see only the sample or the cooled wall of the container. The

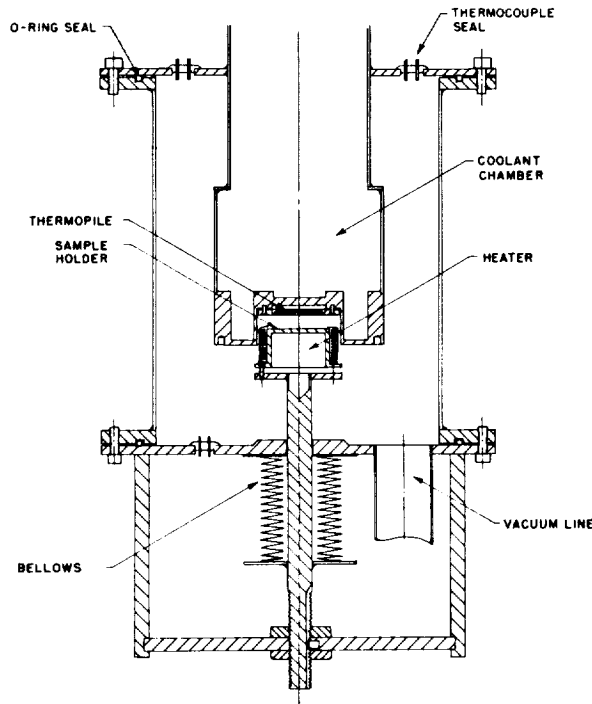


FIGURE 4.—Apparatus for measuring total hemispherical emittance.

apparatus was calibrated by a blackbody measurement. The blackbody consisted of a nickel cylinder with a cone-shaped cavity drilled in one end. The cavity had an opening equal to the sample diameter ($1\frac{1}{8}$ inches) and a depth of $1\frac{1}{4}$ inches. The inner surface of the cone was coated with platinum black. The emittance of the blackbody was assumed to be unity.

The sample emittance is found by comparing the blackbody reference temperature T_r (measured during the calibration) with the sample temperature T_s for the conditions when both resulted in the same detector temperature T_d . The equation for calculating the emittance of the sample was determined from a radiation heat balance on the surface of the detector for the sample measurement and blackbody measurement.

$$\epsilon_s = \frac{F_{dr}}{F_{ds}} \frac{T_r^4 - \epsilon_d T_d^4}{\{[1 + 0.01(1 - \epsilon_s)]T_s^4 - \epsilon_d T_d^4\}} \quad (1)$$

where

- ϵ_s emittance of sample
- ϵ_d emittance of detector
- F_{dr} shape factor from detector to blackbody reference
- F_{ds} shape factor from detector to sample
- T_r temperature of reference
- T_d temperature of detector
- T_s temperature of sample

A calibration curve was determined by varying the blackbody temperature over the necessary temperature range and plotting the temperature to the fourth power against the detector voltage output. The curve presented in figure 5 is the total-hemispherical-emittance calibration curve. The value of T_r^4 was determined from this curve. The sample temperature T_s was determined by the surface thermocouple; and the thermocouple hot junction temperature T_d was determined from the thermopile output and a thermocouple located on the cold junction of the thermopile. The temperature difference between the hot and cold junctions of the thermopile was determined from the standard temperature calibration for the materials used in the thermopile. It was necessary to divide the output voltage by 10 since there were 10 junctions in service. This temperature difference was then added to the measured cold-junction temperature to determine the hot-junction temperature. Equation (1) can be solved most easily for the sample

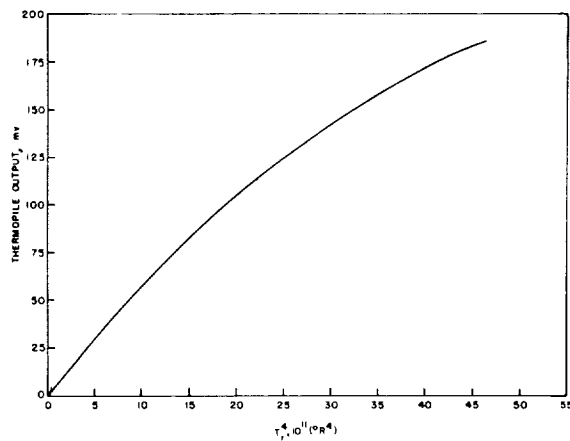


FIGURE 5.—Blackbody calibration curve for hemispherical emittance measurements.

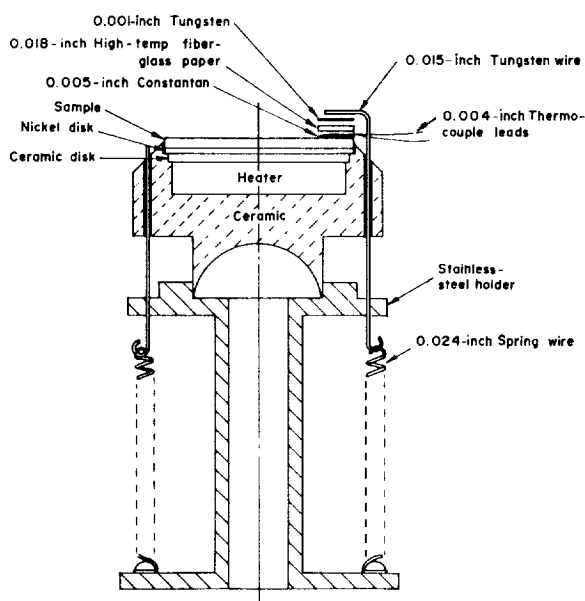


FIGURE 6.—Sample heater and thermocouple installation.

emittance by an iteration method. Since the emittance correction in the denominator of the right side of equation (1) is normally quite small, the first estimate was usually sufficiently accurate.

The maximum uncertainty in total-hemispherical-emittance measurements made with this apparatus at room temperature was less than ± 3 percent, which includes both random and systematic errors. For high-temperature measurements the error was estimated to be less than ± 10 percent. The largest single error was the surface temperature measurement error, which becomes larger as the temperature increases. Figure 6 gives a schematic of a surface thermocouple installation.

RESULTS

Interference Absorbers

ALUMINUM OXIDE FILMS ON A MOLYBDENUM SUBSTRATE

An Al_2O_3 -Mo- Al_2O_3 on Mo sample (No. 36, fig. 7) exhibited high solar absorptance with low infrared emittance—low short-wavelength reflectance but high long-wavelength reflectance. The data for three more alumina-molyb-

denum samples (systems D, E, and F with five, seven, and seven films, respectively) are presented in figures 8, 9, and 10. These systems also exhibit high solar absorptance with low emittance. The larger the number of coatings applied or the further into the infrared region the cutoff is moved, the less steep the cutoff becomes and the less effective is the coating as a solar absorber.

Most of these coatings were prepared with relatively thin Al_2O_3 films of approximately 0.10 micron or less (with primary absorption bands at 0.4 micron or less) and thin molybdenum films having resistances between 1000 and 2000 ohms per square (designated as Ω in the notes on the figures). It was found that this technique of broadening the absorption band worked better than applying several layers with absorption bands at differing wavelengths. Widening the absorption band by that technique generally produced a jumbled reflectance curve with some relatively high reflectance bands in the solar region.

Figure 11 shows the spectral reflectance of sample system D after each film was applied. Note how the application of each additional film moved the cutoff further into the infrared.

The solar absorptances calculated from the vacuum spectral reflectance data are given in table I for room temperature, 500° F, and 1000° F. Most of these samples showed reasonable vacuum stability at 1000° F. The total hemispherical emittances are given in table II for room temperature, 500° F, 750° F, 1000° F, and 1250° F. All of these samples passed the Scotch-tape test for adhesion and had reasonable abrasion resistance.

TANTALUM OXIDE FILMS ON A MOLYBDENUM SUBSTRATE

The spectral reflectance of sample 280 (anodized tantalum on molybdenum) is presented in figure 12. This system was prepared by evaporating a tantalum film, 1000 ohms/sq, onto a molybdenum substrate and anodizing the tantalum film to Ta_2O_5 . This system remained stable up to 500° F in a vacuum, but upon heating to 1000° F a large permanent change occurred in the absorptance. The reflection band in the visible region could be

reduced by applying another molybdenum and tantalum oxide coating. The solar absorptance for this sample is given in table I and the hemispherical emittance is given in table II.

The spectral reflectances of samples 201 and 242, for which the Ta_2O_5 was evaporated directly from a tungsten boat, are presented in figure 13. These results are somewhat similar to the anodized tantalum and Al_2O_3 samples.

Selective Black

Figure 14 shows the effect of subsequent treatment on the spectral reflectance of the

selective black produced by anodizing the alloy beryllium plus 1 percent copper. The solar absorptance dropped from 0.91 to 0.87 upon heating to 1000° F in a vacuum but remained stable thereafter. The infrared emittance, which exceeded 0.60 prior to heating, dropped to 0.30 upon heating to 1000° F and remained stable upon subsequent temperature and pressure cycling. This change is most likely caused by the removal of water from the anodized film.

It was found that the copper content of the anodized surface was of prime importance for

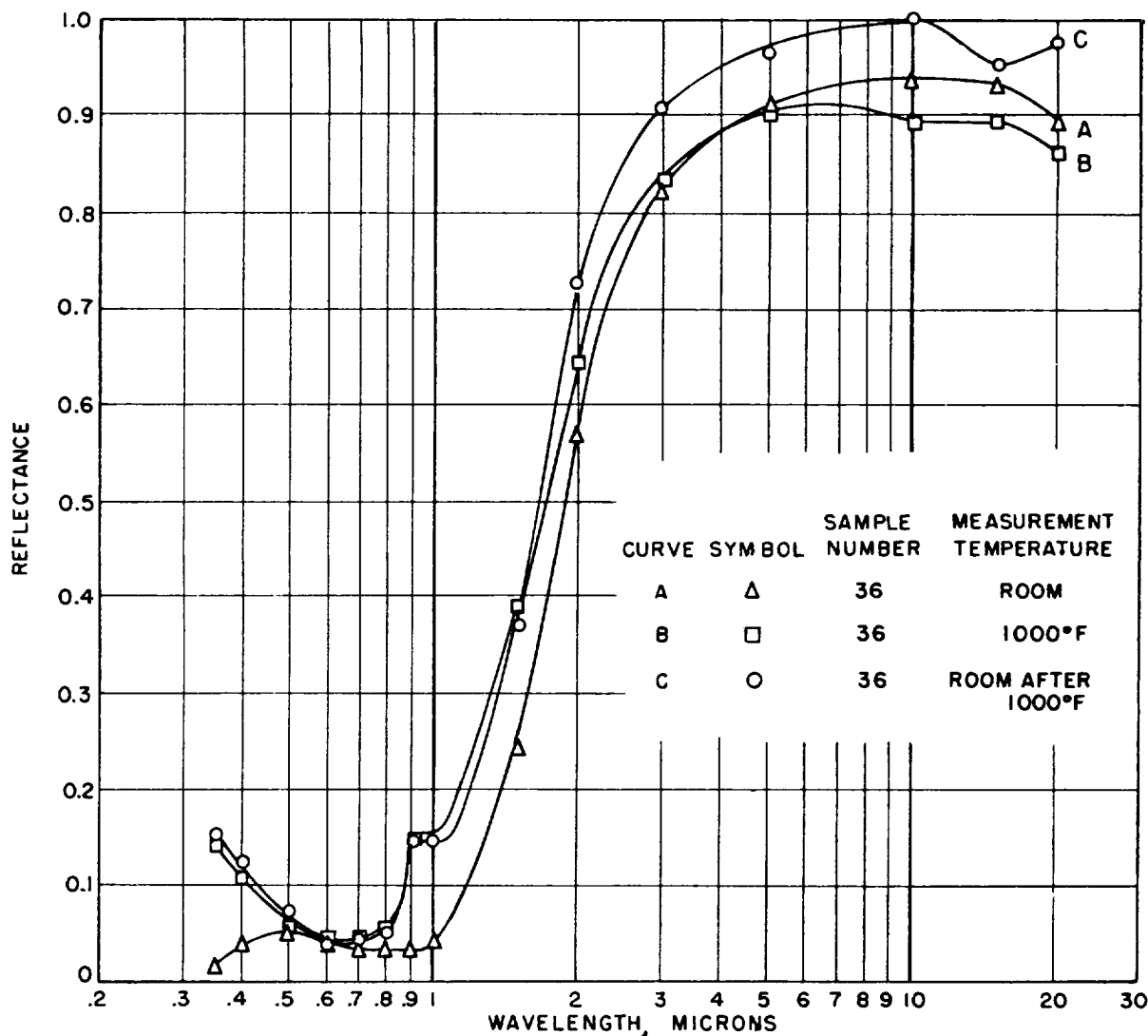


FIGURE 7.—Spectral reflectance of sample 36 (Al_2O_3 -Mo- Al_2O_3 on Mo).

producing a high solar absorptance—even more so than the anodizing time. Some of the samples prepared had been anodized and chemically stripped, which process had apparently depleted the copper content of the sample surface. It was necessary to machine and polish the samples to expose new surface in order to produce a good absorber sample.

The solar absorptances are presented in table I and the emittances in table II. The anodized surfaces of these samples were very hard and smooth.

It was thought that the infrared reflectance of the anodized surface could be raised by applying multiple layers of dielectrics with high and low indexes of refraction in the infrared. Limited attempts on a few samples reduced the solar absorptance more than the emittance. It appears that two dielectric materials with

relatively large differences in index of refraction in the infrared region but small differences in the solar region must be found in order to exploit this effect.

Solar Absorber Effectiveness

The solar absorber effectiveness, as explained in the Introduction, is a single parameter which describes directly the efficiency of the surface in absorbing and retaining solar energy. For example, a surface which has an effectiveness of 0.80 for certain conditions is 80 percent as efficient as a perfect surface under the same conditions. The effectiveness can be calculated from the solar absorptance and emittance. Table III gives the effectivenesses of the samples presented in this discussion for solar concentrations of 1, 10, 100 and 1000, where 1 corresponds to the solar radiation intensity

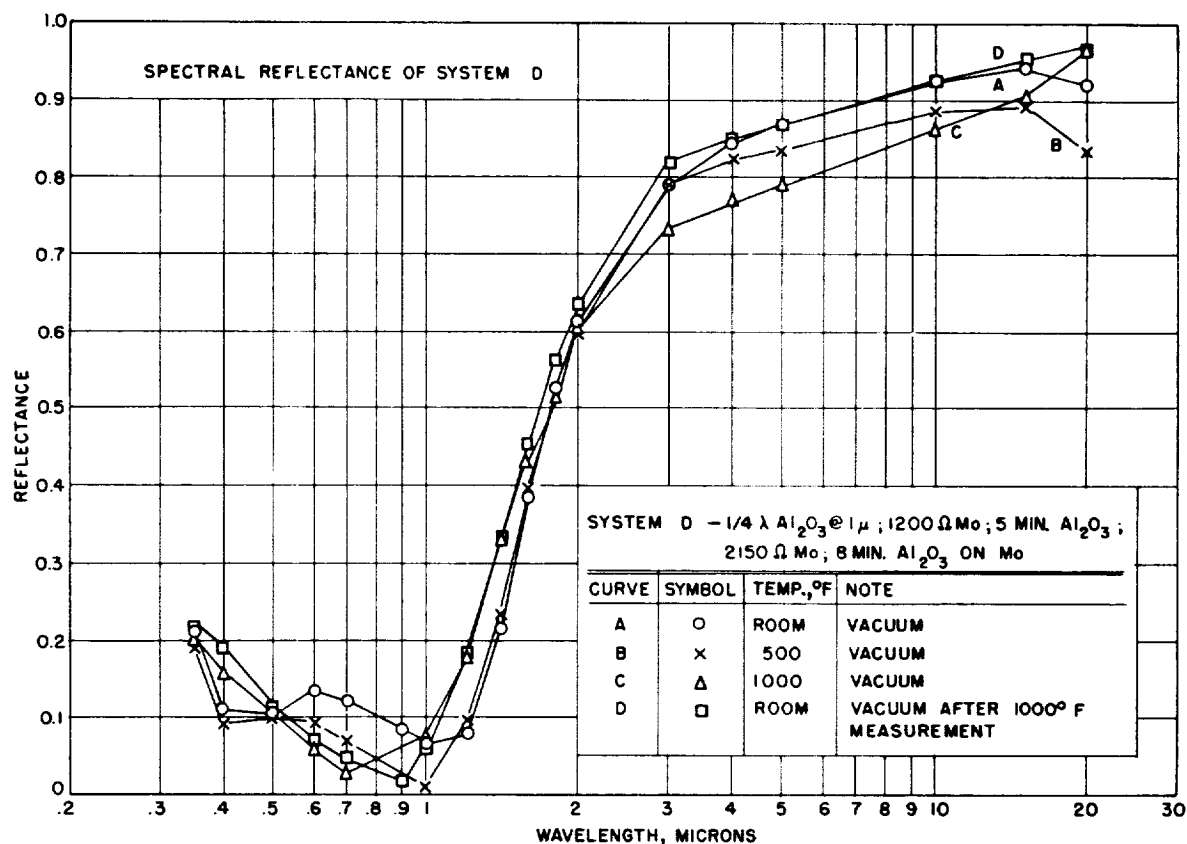


FIGURE 8.—Spectral reflectance of system D. Ω =ohms per square.

TABLE I.—*Solar Absorptance*

Sample	Coating	At temperature, °F		
		Room	500	1000
36	Al ₂ O ₃ -Mo-Al ₂ O ₃ on Mo			0.83
D	Al ₂ O ₃ -Mo-Al ₂ O ₃ -Mo-Al ₂ O ₃ on Mo	0.82	0.85	.83
E	Al ₂ O ₃ -Mo-Al ₂ O ₃ -Mo-Al ₂ O ₃ -Mo-Al ₂ O ₃ on Mo89	.86	.83
F	Al ₂ O ₃ -Mo-Al ₂ O ₃ -Mo-Al ₂ O ₃ -Mo-Al ₂ O ₃ on Mo83	.84	.84
G	Anodized beryllium +1% copper91	.91	.84
280	Ta ₂ O ₅ on Mo	0.83	0.79	0.68

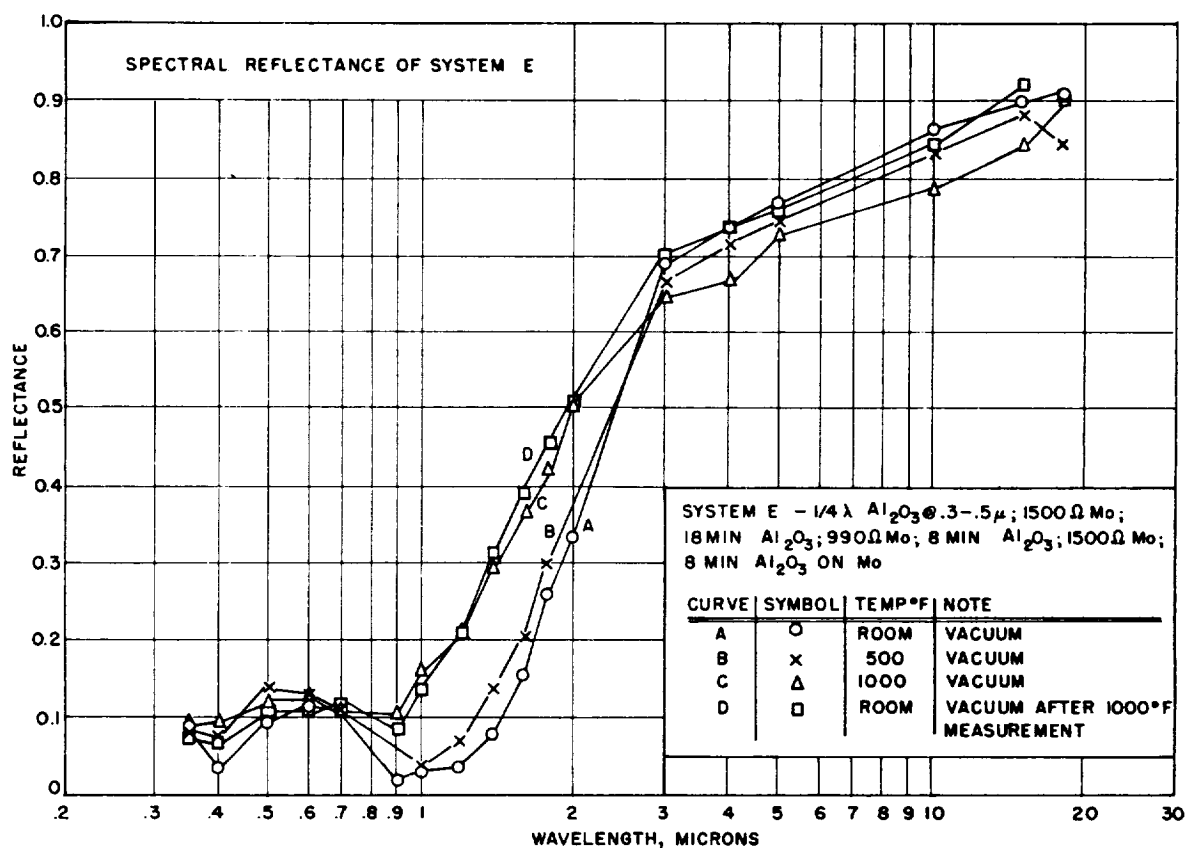


FIGURE 9.—Spectral reflectance of system E. Ω=ohms per square.

just outside the earth's atmosphere (442 Btu/ft²/hr). The effectiveness is also presented as a function of the operating temperature. The effectivenesses of Al₂O₃-Mo interference-type systems range from 0.70 to 0.90 for the high temperatures at solar concentrations of 10 or more, as well as for low temperature at all concentrations. These Al₂O₃-Mo surfaces have effectiveness values higher than that of a blackbody at the high temperatures for solar concentrations of 100 or less. Therefore, these surfaces are potentially useful around 1000° F for solar concentrations of 10 to 100. They are 10 to 15 percent less efficient than a blackbody for concentrations greater than 100 at 1000° F or lower. The surfaces are useful for concentrations less than 10 at lower operating temperatures.

The Ta₂O₅-molybdenum sample (No. 280) and the selective black (system G) show the

same trends as the Al₂O₃-Mo samples. However, there are certain conditions for which each of the samples has an advantage over the others. System G has the highest effectiveness at the lower temperature for higher solar concentrations, whereas sample 280 has the highest effectiveness at 500° F and a solar concentration of unity.

Even though these surfaces are not as efficient as a blackbody for high solar concentrations, the properties of being stable in space, thin, and flat in construction may provide advantages at elevated temperatures in space over present blackbody materials and cavity construction.

Ultraviolet Degradation

Stability to ultraviolet radiation is not expected to be a problem with these types of solar absorbers because most data reported in

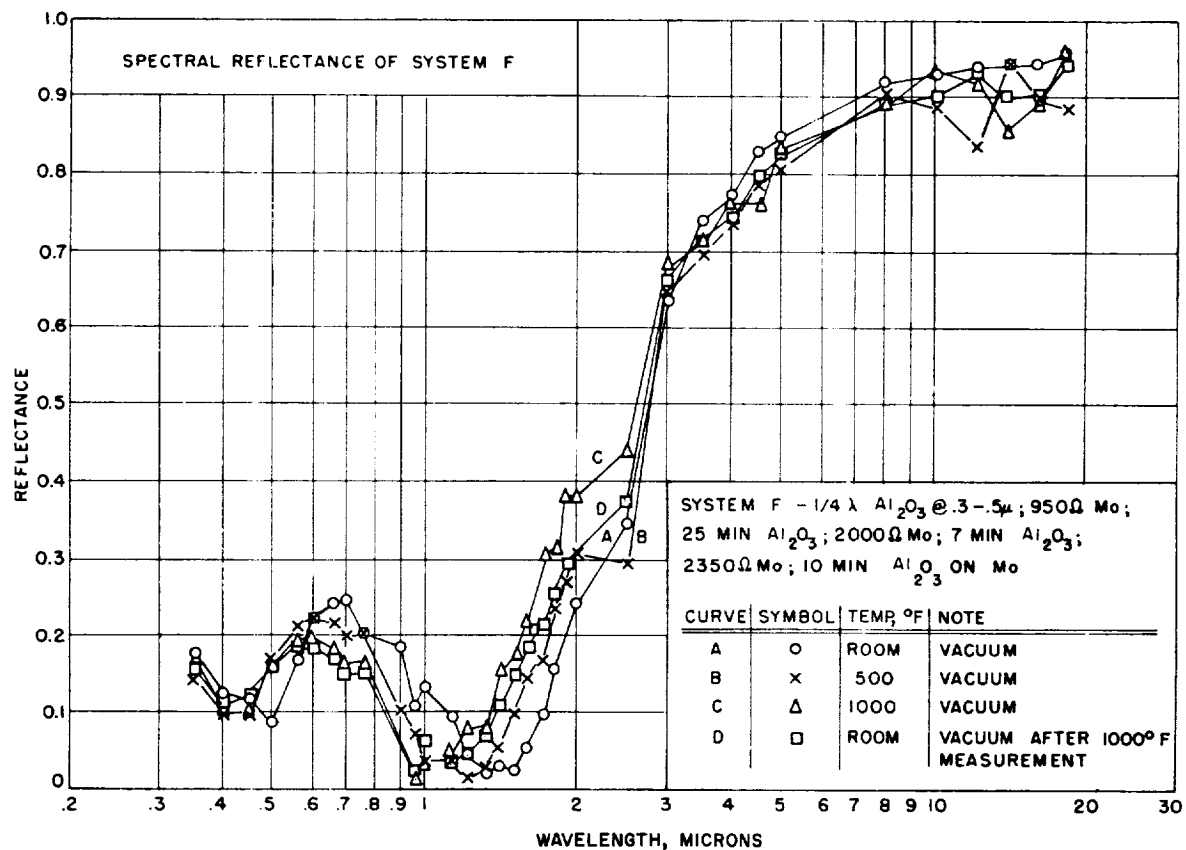


FIGURE 10.—Spectral reflectance of system F. Ω=ohms per square.

the literature and a test performed on anodized aluminum indicate that ultraviolet degradation tends to increase the solar absorptance and causes very little change in the infrared emittance.

CONCLUSIONS

The surfaces described offer advantages as solar absorbers over a blackbody at temperatures around 1000° F for solar concentrations of 100 or less. They are approximately 10 to 15 percent less efficient than a blackbody for concentrations greater than 100 at 1000° F or lower. The surfaces are potentially useful at 1000° F for solar concentrations of 10 or more and for concentrations less than 10 at lower operating temperatures.

It was found that the best way to broaden the absorption band in the solar region was to deposit several layers of a dielectric (or of

dielectrics) having the same (or nearly the same) primary absorption band located at about 0.3 micron or less between thin metal films.

It was found that when anodizing the alloy beryllium plus 1 percent copper, the copper content of the anodized surface was of prime importance for producing a high solar absorptance, even more so than the anodizing time. This suggested interesting possibilities for the general area of doped metal oxides, and further study in this area is recommended.

ACKNOWLEDGMENTS

The authors wish to acknowledge the support for this work by the Air Force Materials Laboratory, Research and Technology Division, Air Force Systems Command (Contract AF33(657)-9164). Also the assistance in the experimental work by Ralph H. Torborg and K. C. Park is greatly appreciated.

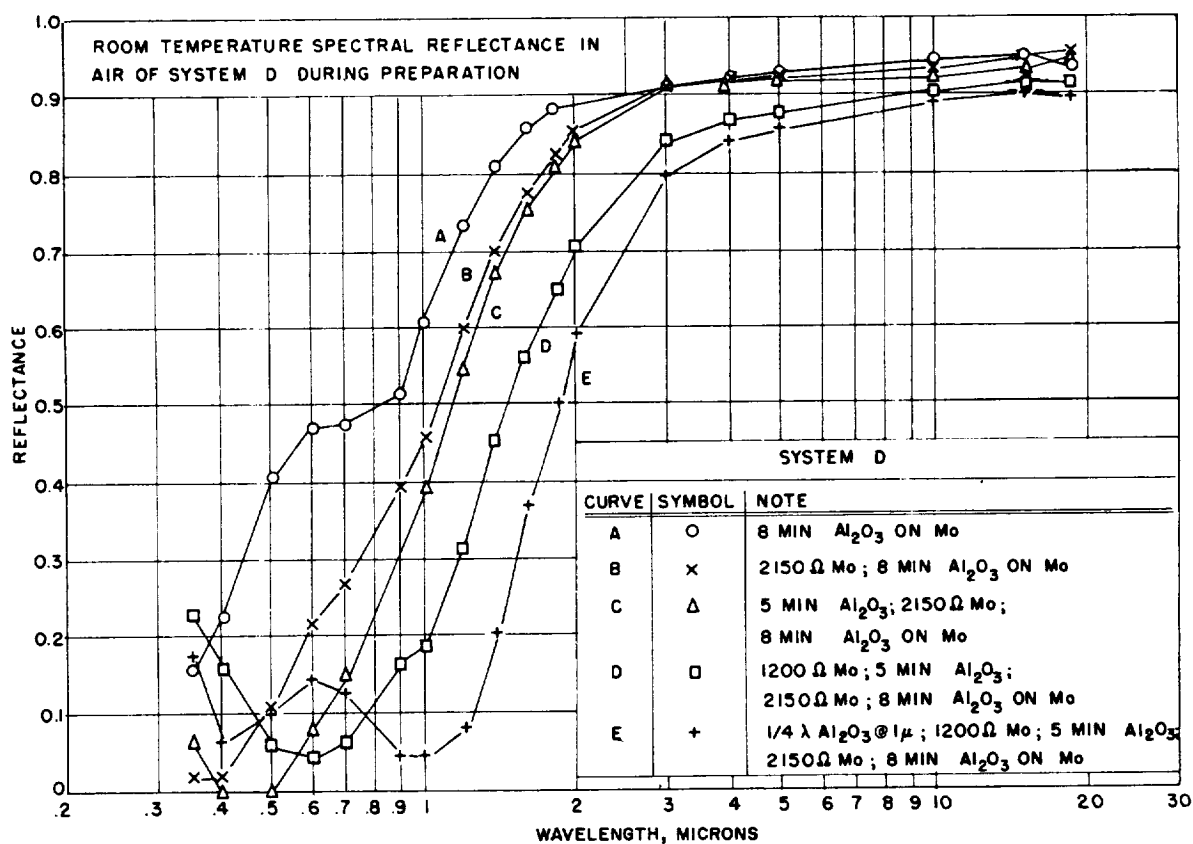


FIGURE 11.—Room temperature spectral reflectance of system D after each stage of preparation.

TABLE II.—*Total Emittance*

Sample	Coating	Tem- pera- ture, °F	ε	Tem- pera- ture, °F	ε	Tem- pera- ture, °F	ε	Tem- pera- ture, °F	ε	Tem- pera- ture, °F	ε
36	Al ₂ O ₃ -Mo-Al ₂ O ₃ on Mo							1000	0.11		
D	Al ₂ O ₃ -Mo-Al ₂ O ₃ -Mo-Al ₂ O ₃ on Mo	71.5	0.060	500	0.085	746	0.095	1014	.12	1253	0.12
E	Al ₂ O ₃ -Mo-Al ₂ O ₃ -Mo-Al ₂ O ₃ -Mo-Al ₂ O ₃ on Mo	70.8	.080	500	.13	748	.16	1034	.14	1262	.12
F	Al ₂ O ₃ -Mo-Al ₂ O ₃ -Mo-Al ₂ O ₃ -Mo-Al ₂ O ₃ on Mo	55.4	.077	487	.16	736	.17	1063	.16	1285	.14
G	Anodized beryllium + 1% copper	89.5	.37	507	.31	752	.28	1010	.27	1260	.28
280	Ta ₂ O ₅ on Mo	82.8	0.051	500	0.058	754	0.067	1014	0.078	1261	0.093

TABLE III.—*Solar Absorber Effectiveness*

Sample	Coating	Temperature, °F.	Solar concentration			
			1.0	10	100	1000
36	Al ₂ O ₃ -Mo-Al ₂ O ₃ on Mo	1000	-1.36	0.73	0.86	0.84
D	Al ₂ O ₃ -Mo-Al ₂ O ₃ -Mo-Al ₂ O ₃ on Mo	Room 500 1000	0.64 0.61 -1.6	.80 .85 .71	.82 .86 .85	.82 .85 .84
E	Al ₂ O ₃ -Mo-Al ₂ O ₃ -Mo-Al ₂ O ₃ -Mo-Al ₂ O ₃ on Mo	Room 500 1000	0.87 0.46 -2.0	.89 .84 .67	.89 .87 .85	.89 .86 .84
F	Al ₂ O ₃ -Mo-Al ₂ O ₃ -Mo-Al ₂ O ₃ -Mo-Al ₂ O ₃ on Mo	Room 500 1000	0.81 0.33 -.245	.83 .81 .64	.83 .85 .86	.83 .84 .85
G	Anodized beryllium + 1% copper	Room 500 1000	0.80 -0.11 -4.86	.90 .84 .42	.91 .91 .84	.91 .91 .85
280	Ta ₂ O ₅ on Mo	Room 500 1000	0.82 0.64 -0.86	.83 .80 0.62	.83 .80 0.71	.83 .79 0.69

REFERENCES

1. SCHMIDT, R. N.: Effectiveness of Solar Absorber Surfaces. J. Am. Rocket Soc., vol. 2, no. 1, Jan.-Feb. 1965.
2. MARTIN, DOUGLAS C., and BELL, RONALD: The Use of Optical Interference to Obtain Selective Energy Absorption. Coatings for the Aerospace Environment. WADD Tech. Rep. 60-773, U.S. Air Force, July 1961, p. 209.
3. JANSSEN, J. E., TORBORG, R. H., LUCK, J. R., and SCHMIDT, R. N.: Normal Spectral Reflectance of Anodized Coatings on Aluminum, Magnesium, Titanium and Beryllium. ASD Tech. Rep. 61-147, U.S. Air Force, Sept. 1961.
4. JANSSEN, J. E., and TORBORG, R. H.: Measurement of Spectral Reflectance Using an Integrating Hemisphere. Measurement of Thermal Radiation Properties of Solids, Joseph C. Richmond, ed., NASA SP-31, 1963, pp. 169-182.
5. FORSYTHE, WILLIAM ELMER: Smithsonian Physical Tables. Ninth rev. ed., Smithsonian Misc. Coll., 1959, p. 722.
6. SCHMIDT, R. N., and JANSSEN, J. E.: Low-Temperature Total Emittance Calorimeter. Measurement of Thermal Radiation Properties of Solids, Joseph C. Richmond, ed., NASA SP-31, 1963, pp. 225-230.
7. JANSSEN, J. E., SCHMIDT, R. N., and TORBORG, R. H.: Emittance Standards. Serial No. 37416, Subcontract No. 28-866, Honeywell Research Center, Dec. 1961.
8. SCHMIDT, R. N., PARK, K. C., TORBORG, R. H., and JANSSEN, J. E.: High Temperature Solar Absorber Coatings. RTD-TDR 63-579, Part I, Nov. 1963.

DISCUSSION

ROGER GILLETTE, Boeing Company: I would like to begin by congratulating you on a very fine piece of work. I think many people have strived to develop a

coating of this type for quite a few years. I have some questions pertaining to your deposition of Al_2O_3 . At what temperature did you deposit the Al_2O_3 , or what

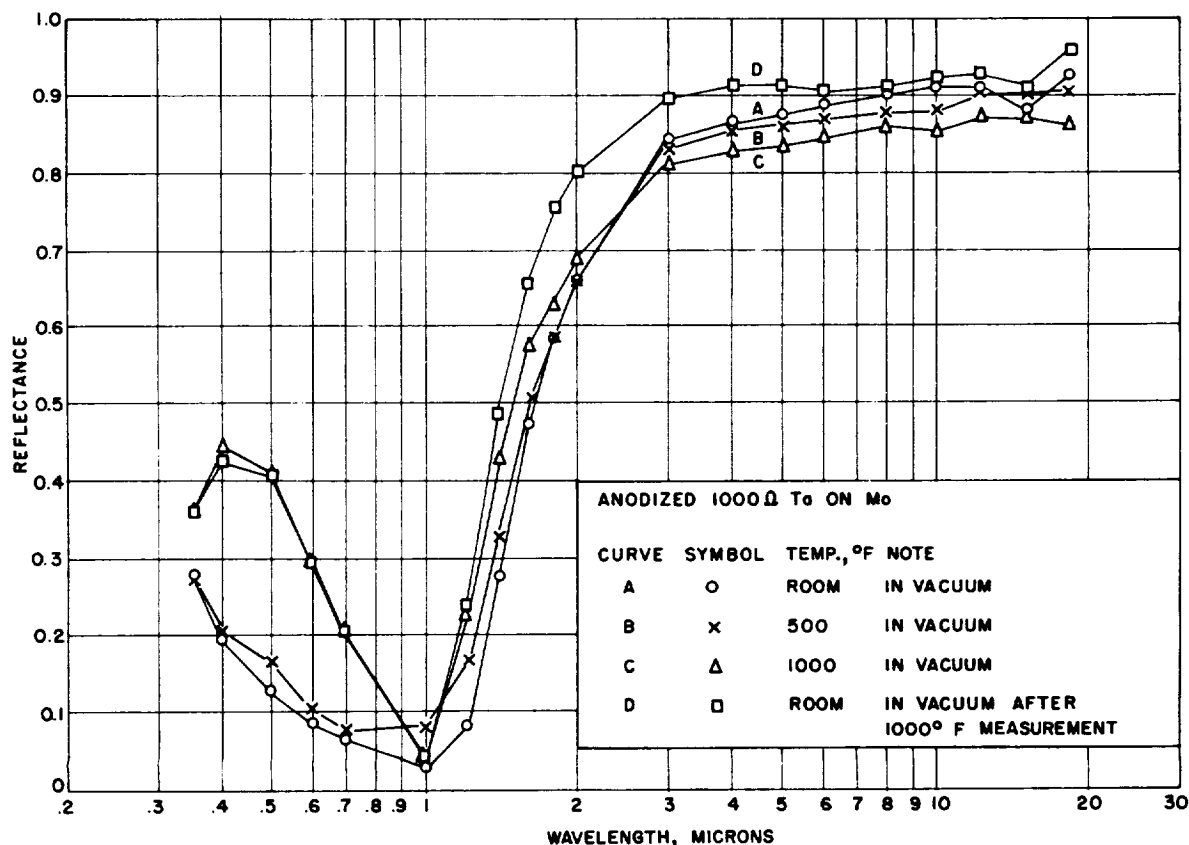


FIGURE 12.—Spectral reflectance of sample 280.

was the temperature of the boat? What was your source of Al_2O_3 , your rate of deposition, and the pressure in the chamber?

SCHMIDT: We just place the Al_2O_3 powder in a tungsten boat, and it evaporates quite easily. The difficulty in evaporating high-temperature dielectrics is usually associated with a heat transfer problem at the electrical leads or supports for the boat. We have had no problem in evaporating Al_2O_3 at pressures of 5×10^{-5} torr and, therefore, have not studied the temperatures associated with the process. It takes about 20 minutes or less to deposit a typical film. Recently, we have found an even easier way to evaporate Al_2O_3 using a work-excited electron beam apparatus that was developed at the Research Center some time ago. It is a very simple apparatus which was expected to be capable of evaporating only electrically conducting materials. A water-cooled pedestal is maintained

at ground potential, and two plates and a filament are maintained at a high d-c potential (approximately 4000 v). A superimposed a-c current heats the filament. We found that almost any material can be evaporated with this apparatus provided it is not a powder. The powders are blown all over the bell jar; however, a powder can be evaporated if it is first pressed into a solid piece. An example of the utility of this apparatus is that a single zirconia film, which took as long as 3 days to evaporate with a tungsten boat, takes only 10 minutes with this electron beam evaporator. In general, it is so easy to evaporate these high temperature oxides that people should not shy away from doing it. However, the deposited film may be different from the material placed in the evaporator. The oxidation state may change, or impurities may result from the evaporation process. All of this

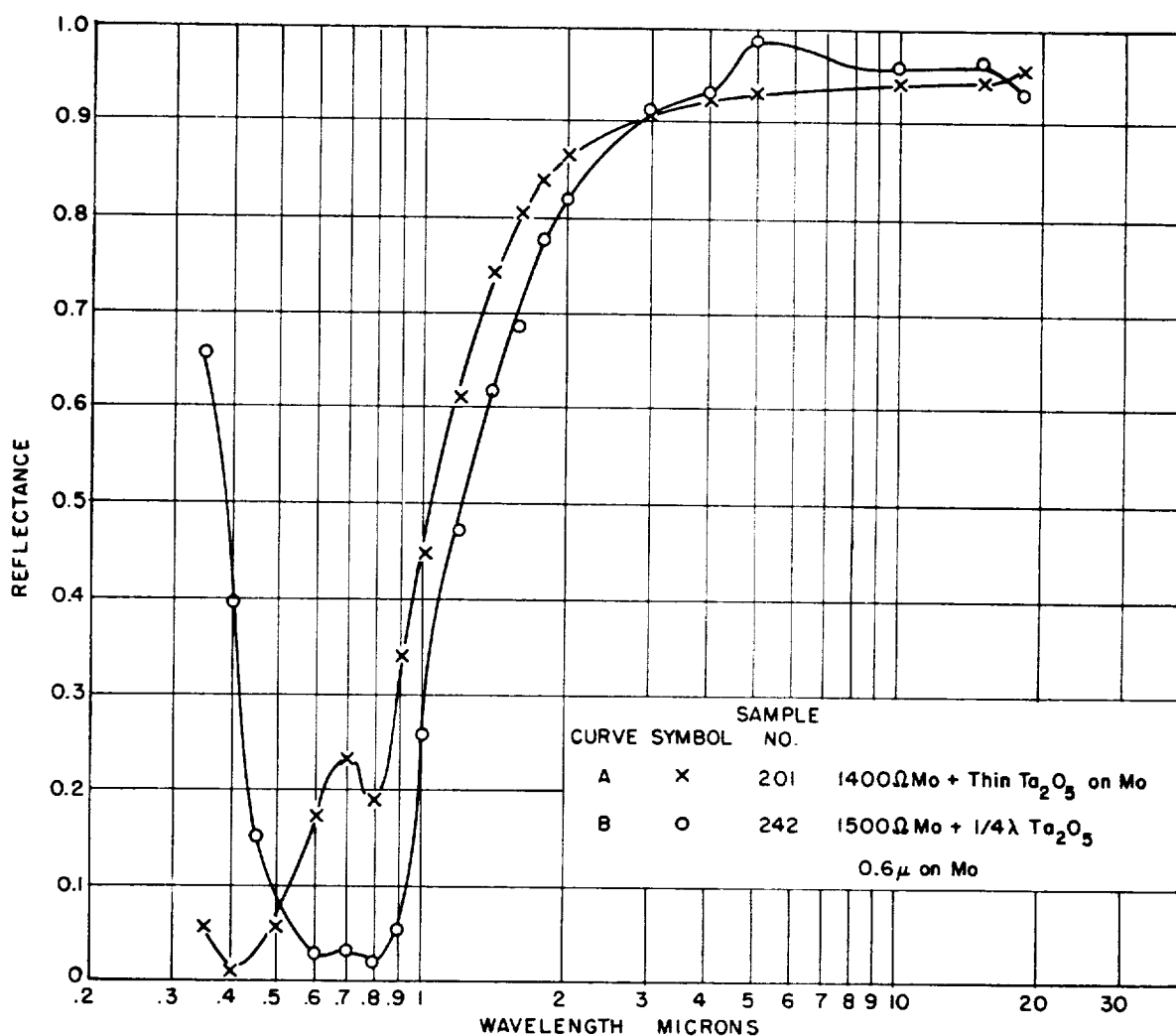


FIGURE 13.—Room temperature spectral reflectance of samples 201 and 242 (evaporated Ta_2O_5 on Mo).

information is covered in more detail in reference 8 of the paper.

GILLETTE: Then you do not actually know what you get?

SCHMIDT: We have not made detailed studies of most of the films we evaporate. However, we were worried about tungsten contamination in the Al_2O_3 films. We made several spectroscopic tests of Al_2O_3 films and were unable to detect the presence of tungsten.

GILLETTE: Is the Al_2O_3 molten, and is it deposited, or is it sublimated directly?

SCHMIDT: The Al_2O_3 is molten when it evaporates; however, we are evaporating many oxides that sublime directly.

BARBARA LIBBERT, Douglas Aircraft: We have been depositing many dielectric films, including Al_2O_3 , and there are some questions I would like to ask you. First of all, we have not been able to reproduce our films; we determine this by measuring the index of refraction after we deposit it. For example, we have found that the rate of deposition does alter the refractive index considerably. Have you determined this? Also, have you looked into the possibility of using stannic oxide

or cerium oxide? These two have similar refractive indexes, as compared to Al_2O_3 , and you might get more reproducible films.

SCHMIDT: This is the first year's work of a 3-year contract that we have with the Air Force Materials Laboratory, and we are looking into all kinds of materials. We are even evaporating combinations of materials. We are doing everything that we can conceive of and have time to do because we realize that developments of this type are often accidents. It is often difficult to reproduce most of the films; however, I would say that Al_2O_3 has worked out very well for us. We seem to be able to reproduce it better than most of the others, and I think that with the proper techniques one should be able to reproduce most films. However, I am sure that evaporation rate does affect the film as does the pressure in the chamber, contaminants in the chamber, and preconditioning of the substrate and material. If one does not pay attention to these variables, he will be in trouble trying to reproduce the films.

LIBBERT: What thicknesses of the dielectrics are you depositing? Are they $\frac{1}{4}\lambda$, $\frac{1}{2}\lambda$, $\frac{3}{4}\lambda$, or what?

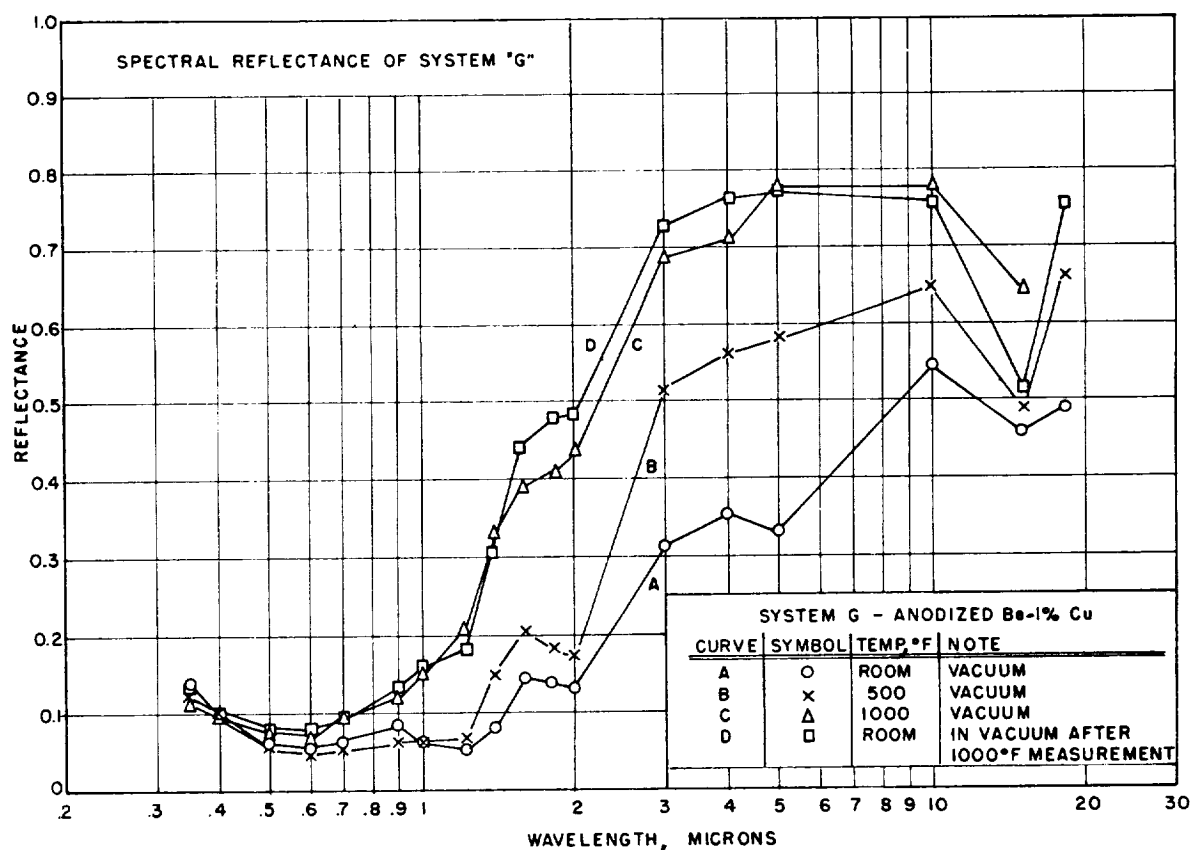


FIGURE 14.—Spectral reflectance of system G.

SCHMIDT: The standard theory that most people use is based on the simple absorption concept. We have been doing a lot of theoretical work and have found that $\frac{1}{4} \lambda$ is not quite what you want; it is more like $\frac{1}{2} \lambda$. It depends, however, on the film material and substrate. We monitored the films that I showed you with a reflectance monitor and note the thickness as $\frac{1}{4} \lambda$ at a designated wavelength. (See the notes on figures 8 to 13.) Although this is not completely

correct, we thought that this would be more generally understood.

LIBBERT: We have done that too, but we have not been able to get $\frac{1}{4} \lambda$ with that kind of method.

SCHMIDT: Recently we started monitoring with a quartz oscillator film-thickness monitor, and we think that this is a much better method which will enable us to control the thickness much more closely.

50. Surfaces of Controlled Spectral Absorptance¹

H. TABOR, H. WEINBERGER, AND J. HARRIS

NATIONAL PHYSICAL LABORATORY OF ISRAEL, JERUSALEM, ISRAEL

Given the optical constants ($n-ik$) of absorbing materials to be applied as interference films on metal surfaces, it is possible to calculate the film thicknesses in two- and three-layer systems required to achieve high absorptance for solar radiation but low thermal emittance. The methods of making such calculations are reviewed and results for nickel-nickel black systems are presented and discussed.

About 10 years ago (ref. 1) we became interested in selective black surfaces for solar energy collectors—that is, surfaces of high absorptance but low emittance. These surfaces were produced by depositing on a metal substrate thin light-absorbing layers that were substantially transparent above about 2μ and thus did not appreciably increase the emittance over the intrinsically low emittance of the substrate.

At a very early stage it was appreciated that the absorptance in the solar spectrum could be enhanced by exploiting destructive interference effects in the layer and that, as we shall see later, it is far easier to get a zero reflectance with an absorbing layer on a metal surface than with a dielectric layer.

The layers were produced by various techniques, such as chemical deposition, oxidation by heating, and electrodeposition. Vacuum deposited layers were avoided as, from a practical point of view, processes were sought that would be applicable for coating large areas.

One of the most successful layers was nickel black produced by electroplating. The deposit is a complex of nickel, zinc, and their sulfides, with a small proportion of additional components probably consisting of oxides and hydroxides. The process is used commercially

for coating solar water heater panels 1×2 m in size.

It had been observed that the optical properties of a metal base-nickel black system could be improved by changing the current density during the plating operation. Analysis showed that the chemical composition of the nickel black coating changed with a change in plating conditions, so that the resulting system consisted of a metal substrate coated with two nickel black films of different optical constants (ref. 2).

These systems had absorptances of about 0.9 and emittances at 100°C in the range of 0.05–0.20, depending mainly upon the nature of the substrate.

The early work, though commercially applicable, was largely empirical, and in the last 3 years a more careful theoretical and experimental study has been conducted. This paper briefly discusses this study.

The study involved the measurement of optical constants of thin absorbing films on absorbing bases (ref. 3) and the computation of the conditions for *blooming*—that is, producing a zero reflectance at at least one wavelength near the peak of the solar spectrum. The reflectance of a base material coated with a multilayer thin-film system may be evaluated from a knowledge of the optical constants and thicknesses of the components. Convenient

¹ See also Papers 20 and 49.

methods of calculation, based on the continuity at an interface of the admittance, defined as the ratio of the magnetic field H to the electric field E of a light beam in a medium, have been variously described (ref. 4, 5, 6, and 7).

For normally incident light the expressions are especially simple and may be outlined as follows:

If $R(x)$ denotes the ratio of the amplitudes of the reflected and incident beams, then the admittance, $N-iK$, which is complex in absorbing media, is given by (ref. 5 and 6)

$$N(x)-iK(x)=\frac{H(x)}{E(x)}=\frac{n(x)-ik(x)}{\mu(x)}\frac{1-R(x)}{1+R(x)} \quad (1)$$

where $n(x)-ik(x)$ is the optical constant at the point x and $\mu(x)$ the magnetic permeability. For nearly all materials, $\mu=1$ at optical frequencies. The magnetic permeability will not, therefore, appear in the following equations. For those instances where the permeability does differ from unity equations similar to those to be presented may be readily derived following the methods of references 5 and 6.

We consider a system of $s-1$ homogeneous films on a substrate s . In the substrate the light consists only of a forward wave in the direction of the incident beam, that is, $R_s=0$, so from equation (1)

$$N_s-iK_s=n_s-ik_s \quad (2)$$

that is, the admittance of the base is equal to its optical constant.

Because of the continuity of the admittance at an interface we have, from equation (1),

$$\begin{aligned} N_{s-1}(0)-iK_{s-1}(0) \\ = (n_{s-1}-ik_{s-1}) \frac{1-R_{s-1}(0)}{1+R_{s-1}(0)} = N_s-iK_s \end{aligned} \quad (3)$$

where we choose the origin of coordinates at the film-substrate interface.

At the entrance boundary of the film, defined as the boundary facing the incident light, we have:

$$R_{s-1}(d_{s-1})=R_{s-1}(0) \exp \frac{4\pi}{\lambda} (k_{s-1}+in_{s-1})d_{s-1} \quad (4)$$

where d_{s-1} is the thickness of the film.

Combining equations (1), (3), and (4), we have for the real and imaginary parts of the admittance at the entrance boundary of the film,

$$\left. \begin{aligned} N_{s-1}(d_{s-1}) &= \frac{n_{s-1}(1-f^2)+2k_{s-1}f \sin g}{1+f^2+2f \cos g} \\ K_{s-1}(d_{s-1}) &= \frac{k_{s-1}(1-f^2)-2n_{s-1}f \sin g}{1+f^2+2f \cos g} \\ f &= \left[\frac{(n_{s-1}-N_s)^2+(k_{s-1}-K_s)^2}{(n_{s-1}+N_s)^2+(k_{s-1}+K_s)^2} \right]^{1/2} \\ &\quad \exp \frac{-4\pi k_{s-1}d_{s-1}}{\lambda} \\ g &= \frac{4\pi n_{s-1}d_{s-1}}{\lambda} \\ &\quad - \tan^{-1} \frac{2(n_{s-1}K_s-N_s k_{s-1})}{n_{s-1}^2-N_s^2+k_{s-1}^2-K_s^2} \end{aligned} \right\} \quad (5)$$

which are equal to the real and imaginary parts of the admittance at the exit boundary of the $s-2$ film. The calculation of the admittance at the entrance boundary of the $s-2$ film follows from equation (5) after making the appropriate change of subscripts:

$$s \rightarrow s-1$$

$$s-1 \rightarrow s-2.$$

The calculations are generally continued as outlined above, with appropriate changes in the subindices of the equations, from layer to layer until the air boundary is reached where equation (3) becomes:

$$\frac{1-R_0}{1+R_0} = N_1(d_1)-iK_1(d_1). \quad (6)$$

The power reflectance of the system is then given by

$$R_0 R_0^* = \frac{[N_1(d_1)-1]^2 + K_1(d_1)^2}{[N_1(d_1)+1]^2 + K_1(d_1)^2} \quad (7)$$

For systems requiring low reflectances (high absorptances) it is not, however, necessary to make extensive numerical experiments with

different film combinations until a satisfactory system is achieved. The design of a system of low reflectance is facilitated by the fact that it is possible to write an expression for the admittances of systems which will be perfectly bloomed by a single outer film.

We observe that for a perfect bloom ($R_0=0$) equations (1) and (6) give us:

$$1 = (n_1 - ik_1) \frac{1 - R_1(d_1)}{1 + R_1(d_1)} \quad (8)$$

from which:

$$R_1(d_1) = \left[\frac{(n_1 - 1)^2 + k_1^2}{(n_1 + 1)^2 + k_1^2} \right]^{1/2} \exp i \tan^{-1} \frac{-2k_1}{n_1^2 + k_1^2 - 1} \quad (9)$$

From equation (4) we find that at the exit boundary of the first film:

$$R_1(0) = R_1(d_1) \exp -\frac{4\pi}{\lambda} (k + in) d_1 \quad (10)$$

Upon substituting for $R_1(0)$ from equations (9) and (10) into equation (3) (for $s=2$) we find that the admittances bloomed by an outer film are given by (ref. 7):

$$\left. \begin{aligned} N_2(d_2) &= \frac{n_1(1-a^2) - 2k_1a \sin b}{1+a^2+2a \cos b} \\ K_2(d_2) &= \frac{k_1(1-a^2) + 2n_1a \sin b}{1+a^2+2a \cos b} \\ a &= \left[\frac{(n_1-1)^2 + k_1^2}{(n_1+1)^2 + k_1^2} \right]^{1/2} \exp \frac{4\pi k_1 d_1}{\lambda} \\ b &= \frac{4\pi n_1 d_1}{\lambda} - \tan^{-1} \frac{2k_1}{n_1^2 + k_1^2 - 1} \end{aligned} \right\} \quad (11)$$

In general the admittance of the intended base alone will not fall within the range of admittances which may be bloomed by the films which are available for use. Numerical experiments with a large number of two-film combinations indicate, however, a high likelihood that the admittances $N_2(d_2) - iK_2(d_2)$ offered by a base-film combination will be bloomed by an outer film of different optical constant and of appropriate thickness. This

result for absorbing films corresponds to a similar analytic result of Schuster (ref. 5) for all-dielectric systems.

Optimum two-film combinations are determined by the graphical solution of equations (5) and (11) for appropriate thicknesses d_1 and d_2 of the two films which give identical values of $N_2(d_2) - iK_2(d_2)$ in the respective equations. In figure 1 the solid line represents the admittance of the combination substrate (nickel base covered with nickel black) as calculated from equation (5), plotted on the N, K plane for a range of values of d_2/λ : This line starts (at $d_2/\lambda=0$, off the diagram) at the admittance of the base, $N=n=1.79$ and $K=k=3.33$; and it moves along a spiral, through various values of N and K , to the point $N=n_2=1.8$, $K=k_2=0.7$, which represents the admittance of a very thick layer of the nickel black. The five dot-dash lines in figure 1 show the results of the calculations from equations (11) of the admittance bloomed by five different assumed coating materials ($n_1=2$; $k_1=0, 0.1, 0.2, 0.3$ and 0.4). All but one of these intersect the solid curve. The fourth dot-dash line ($n_1=2$, $k_1=0.3$), for example, intersects the solid curve at a point where $d_1/\lambda=0.051$ and $d_2/\lambda=0.056$. Thus, blooming can be accomplished at the wavelength λ by depositing on the nickel base ($n=1.79$, $k=3.33$) first a layer of thickness $d_2=0.056\lambda$, $n_2=1.8$, $k_2=0.7$, and then a layer of thickness $d_1=0.051\lambda$, $n_1=2$, $k_1=0.3$.

Examination of figure 1 shows that, where the solid and the dot-dash curves run nearly parallel, the d/λ values move in opposite directions along the two curves. Thus, assuming little or no dispersion, any blooming that occurs will occur at only one wavelength, and there will be a rapid departure from blooming conditions as the wavelength changes from this value. However, if the d/λ values were to move in the *same* direction, one could expect the blooming over a rather wide range of wavelengths.

This desired effect can be obtained by inserting a very thin layer of a metal (high k) between the two moderately absorbing layers. Figure 2 is the chart that results for such a design. The solid line in this case represents

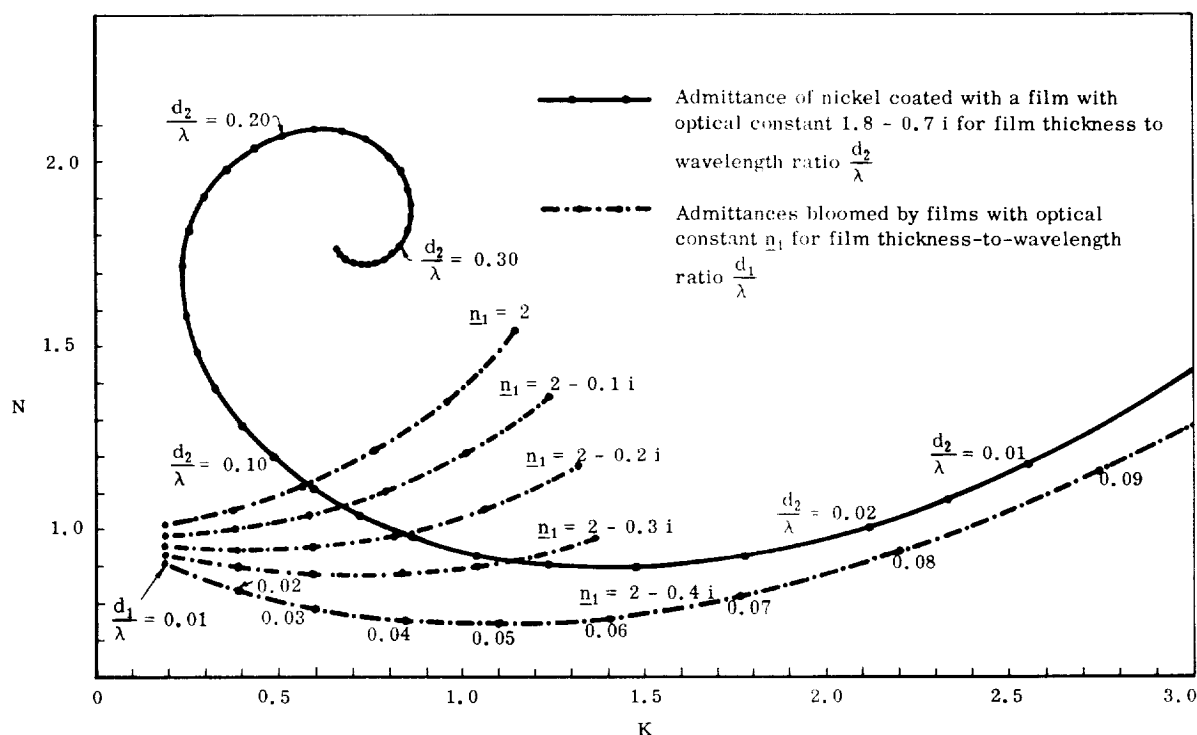


FIGURE 1.—Admittance curves, blooming with two layers.

the admittance of the system: nickel substrate-nickel black-metallic nickel film. The thickness of the metal film is two-thirds that of the nickel black film. The two dot-dash curves are the same as the corresponding two curves of figure 1. It can be seen that for small values of d_2/λ , that is, for long wavelengths, the solid curve tends to cross the intersecting dot-dash curve at right angles. It is also apparent, however, that a dot-dash curve for $n_1=2$, $k_1=0.25$ would nearly coincide with the solid curve for the d_2/λ range between 0.03 and 0.05. Furthermore the d/λ values change in the same sense along the two curves and maintain an approximately constant ratio, giving a near zero reflectance over a range of wavelengths.

Figure 3 shows the difference in the quality of the result when a three-layer system is used instead of a two-layer system. The solar spectrum is also shown, as attenuated by two atmospheres (zenith angle 60°). Note the change in the wavelength scale at $2\ \mu$. The

curve for the two-layer system, taken from an earlier publication, represents about the best that we have done in the past. It shows complete suppression of reflection at about $0.8\ \mu$, and the mean solar absorptance is about 0.90. The emittance at ambient temperatures was computed as 0.05. The three-layer system—with a metallic nickel layer between two nickel-black layers—is the best of a number that we have tried and shows low reflection over the major part of the solar spectrum. The solar absorptance corresponding to this curve is about 0.96. (However, the measured reflectance was essentially specular reflectance; that is, any diffusely reflected radiation was not measured. The real reflectance will hence be slightly higher and the solar absorptance slightly lower—perhaps 0.94.)

The methods discussed herein have been developed specifically for obtaining high α/ϵ surfaces. They are, however, presently being extended for other applications, such as obtaining low α/ϵ surfaces.

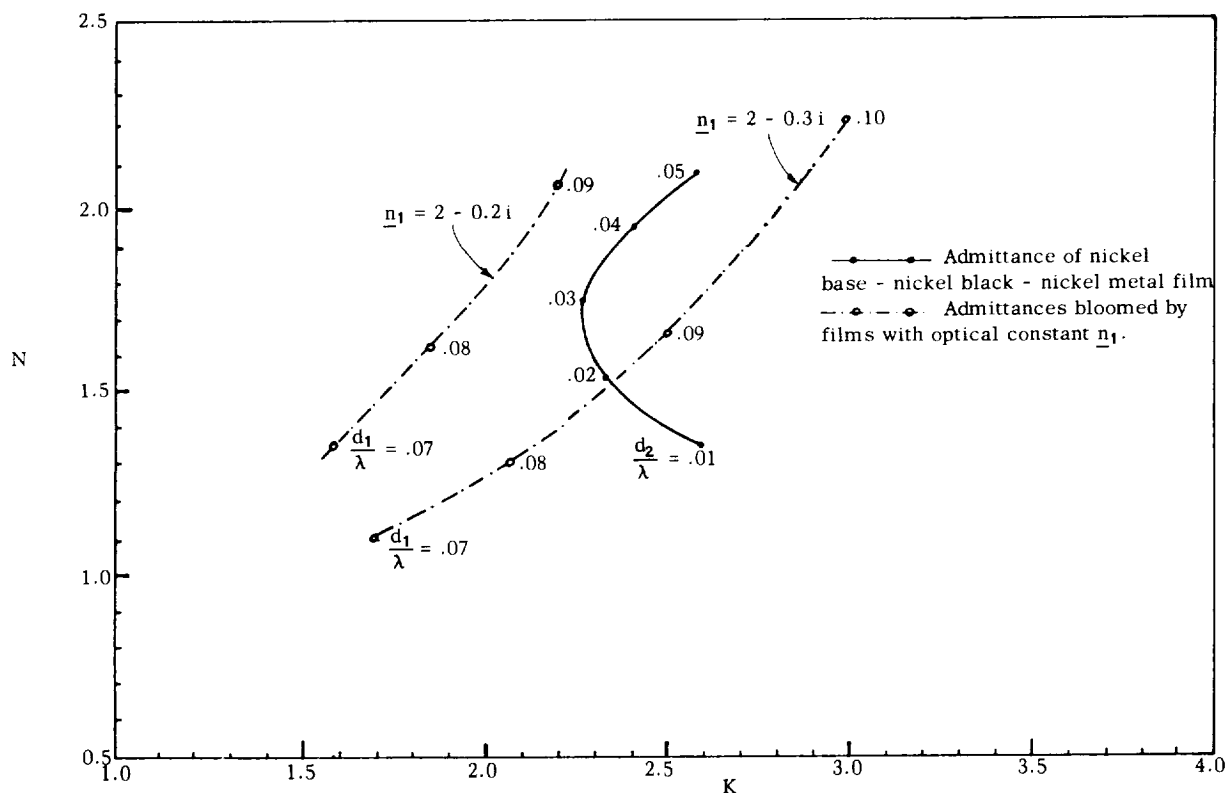


FIGURE 2.—Admittance curves for blooming three-layer systems. ($d_1/d_2 \sim 2.7$ over blooming range.)

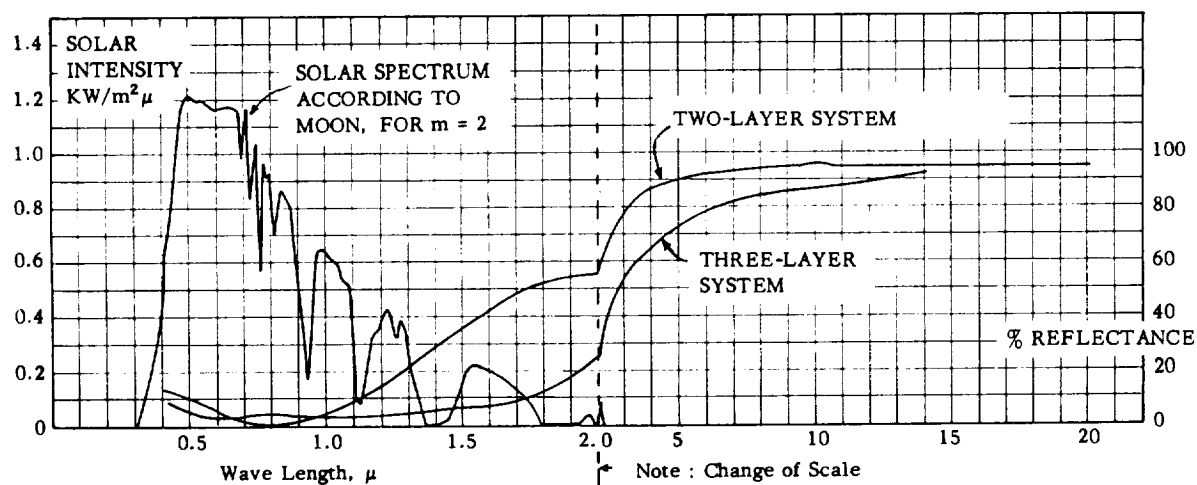


FIGURE 3.—Comparison of two-layer and three-layer systems. Two-layer system is one low-current-density nickel-black layer and one high-current-density nickel-black layer. Three-layer system has intermediate nickel layer between two nickel-black layers. Substrate is nickel.

REFERENCES

1. TABOR, H.: Selective Radiation. I—Wave-Length Discrimination. Bull. Res. Council of Israel, vol. 5A, 1956, pp. 119-128. (Also in Trans. Conf. Use of Solar Energy — The Sci. Basis (Tucson, Ariz.), vol. II, pt. I, sec. A, 1955, pp. 24-29.)
2. TABOR, H., HARRIS, J., WEINBERGER, H., and DORON, B.: Further Studies on Selective Black Coatings. U.N. Conf., New Sources of Energy (Rome), Paper E, 1961.
3. HARRIS, J., and WEINBERGER, H.: A Method for Determination of the Optical Constants of Thin Absorbing Layers. Tech. (Sci.) Note No. 4 (AFCRL-63-918, AD-289426), Nat. Phys. Lab. of Israel, Aug. 1963.
4. SALZBERG, B.: Propagation of Electromagnetic Waves Through a Stratified Medium. I. Jour. Optical Soc. of America, vol. 40, July 1950, pp. 465-470.
5. SCHUSTER, K.: Application of Quadripole Theory to the Problems of the Reduction of Reflectivity, Heightening of Reflectivity and the Interference Filter. Ann. Phys. 6th Ser., vol. 4, no. 6, 1949, pp. 352-356.
6. MACSWAN, A. M.: The Colour of Thin Oxide Films on Metals. Proc. Phys. Soc., vol. 72, pt. 5, Nov. 1958, pp. 742-748.
7. WEINBERGER, HERSHEL: Suppression of Reflection From Metallic Surfaces. Tech. (Sci.) Note 1 (AFCRL-60-7), National Physical Lab. of Israel, Dec. 12, 1960.

51. An Experimental Determination of the Absorptances of Cryodeposited Films Using Calorimetric Techniques¹

R. P. CAREN, A. S. GILCREST, AND C. A. ZIERMAN

LOCKHEED MISSILES & SPACE CO., PALO ALTO, CALIF.

This paper describes an experimental technique for measuring the absorptance of materials for radiation from a low temperature black body radiator. In particular, in the present experiments the absorptances of cryodeposited films of carbon dioxide, nitrogen, and air were measured for 77° K blackbody radiation. The apparatus and instrumentation are described and the experimentally measured absorptances are reported.

In the large space-simulation chambers now being planned, 4° to 20° K cryopumping surfaces will be used to achieve the high pumping speeds required for operation in the 10^{-9} torr range. In a properly designed space-simulation chamber, radiant heat transfer from the chamber cold walls to cryopumping surfaces will be the dominant thermal load on the latter surfaces. As refrigeration in the 4° to 20° K region is quite costly, it is expected that in order to reduce the radiant energy transfer to a minimum the cold wall surfaces viewing the cryosurfaces, and the cryosurfaces themselves will be highly polished metal. However, as cryodeposits build up on the cryopumping surfaces, the absorptance of these surfaces may be greatly increased, thereby creating a need for a much larger refrigeration plant for these surfaces. In order to provide information needed for estimating the maximum heat transfer and refrigeration power required, the present investigation of the absorptances of the various cryodeposits expected on the cryosurfaces were undertaken.

¹ The research reported in this paper was sponsored by the Arnold Engineering Development Center, Air Force Systems Command, under Contract No. AF 40(600)-992.

APPARATUS

The total-hemispherical-radiation calorimeter used in these experiments is shown in figure 1. It consists of a 3-inch-diameter extended-

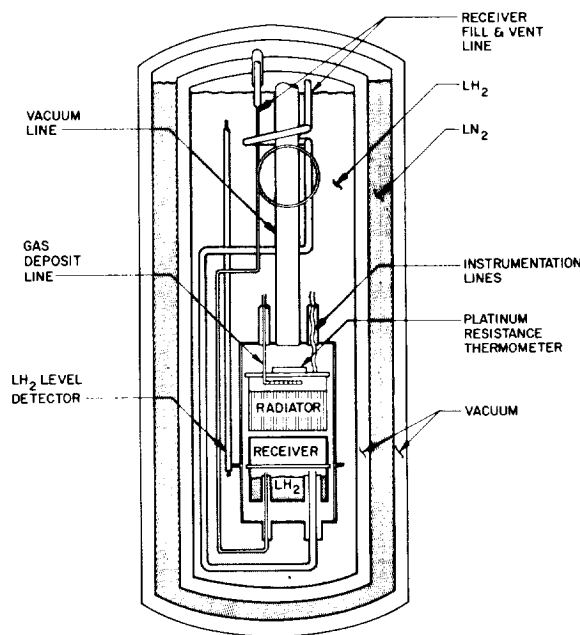


FIGURE 1.—Low-temperature absorptance calorimeter.

surface blackbody radiator and an aluminum receiver cooled to 20° K by thermal contact with a 0.1-liter reservoir containing liquid hydrogen. The rate of boiloff of the hydrogen in the receiver is then used to measure the total energy absorbed by the receiver. The hydrogen reservoir has two lines connected to it—one serves as the hydrogen fill line and the other is connected to the equipment used to measure the hydrogen boiloff rate. The radiator, receiver, and 4-inch lengths of the reservoir fill and boiloff lines are enclosed in a vacuum space whose outer walls are immersed in a liquid-hydrogen bath. The liquid-hydrogen-temperature walls of the vacuum enclosure serve to thermally isolate the receiver from all its surroundings except for the radiator. A Hoke TY445 valve of all stainless steel construction immersed in the liquid hydrogen bath is used to fill the receiver. This valve was checked with a helium mass spectrometer leak detector at liquid hydrogen temperature to insure that it was leak tight. The radiator is thermally grounded to the hydrogen bath through its low heat conducting thin-wall stainless steel supports. The thermal energy conducted down the copper leads to the power resistors and platinum resistance thermometer mounted on the radiator produces an equilibrium temperature of about 70° K in this structure. By supplying power to resistors in the radiator, its temperature can be controlled between 70° and 273° K. The platinum resistance thermometer used was calibrated by the National Bureau of Standards from 10° to 92° K and provided accurate radiator temperature data in the range of interest.

In these experiments the boiloff rates of the hydrogen gas ranged from 0.01 to 0.25 cm³/sec (at NTP). The boiloff was measured with a precision wet-test meter.

The vacuum in the apparatus was maintained with a 4-inch liquid-nitrogen-trapped NRC 4HSP oil diffusion pump backed by a Welch 1402 fore pump. Pressure in the vacuum line going to the apparatus was 10⁻⁶ torr with no hydrogen in the apparatus. With liquid hydrogen in the apparatus the gas pressure in the experimental volume was below 10⁻⁹ torr except during the time the cryofilms were being

deposited. Because residual gas conduction in the experimental volume is unimportant below 10⁻⁶ torr, residual gas conduction is of no consequence in the present apparatus.

The radiator also serves as a means of depositing the films uniformly on the polished aluminum receiver. The gas to be condensed is metered into the apparatus through a 1/8-inch-diameter heated vacuum-jacketed tube. The gas passes out of this tube into a volume 3 inches in diameter by 1/2 inch high in the radiator. This volume is located between the copper plate which forms the back of the radiator and the backface of the brass tubes which make up the blackbody radiator. These tubes have an outside diameter of 3/16 inch, are 1 1/2 inches long, and are tapered to a knife edge at their front surface. The tubes are close packed and soldered into a 3 1/4-inch outside-diameter copper tube which, along with the backplate, defined the outer radiator surface. The depositing gas passes from the volume behind the radiator tubes through the tubes and onto the receiver which directly faces this structure. The gas is metered into the radiator at a rate that produces a pressure in the radiator characteristic of the rarefied gas regime. Since tubes with the characteristic dimensions of the radiator structure have a low conductance for gas at rarefied pressures, the depositing gas passes out of these tubes uniformly over the front surface at the radiator and onto the receiver which faces it. The array of brass tubes is painted with CAT-A-LAC flat-black and because the tubes have a large length-diameter ratio, they form a good blackbody radiator ($\epsilon > 0.98$).

EXPERIMENTAL PROCEDURE

Initially a 3-inch-diameter CAT-A-LAC coated honeycomb blackbody receiver ($\epsilon > 0.99$) was used to calibrate the apparatus. The radiator temperature was varied during this calibration and the analytically predicted high emittances and absorptances of the radiator and receiver were verified by checking the calorimetric boiloff rate against the predicted energy transfer rate. The analytical prediction of the radiant transfer is based on the assumption that both surfaces were perfectly diffuse

radiators. This assumption was verified by varying the radiator-receiver spacing and checking the experimental results against the analytical predictions. The predicted values checked the experimental results to within 3 percent. The experiments involving changes in the radiator temperature were made with liquid nitrogen in the apparatus. The results followed a T^4 dependence to within 3 percent.

After the calibration, the vacuum chamber containing the radiator and receiver was broken open by grinding one of the heli-arc joints, and a polished aluminum receiver was substituted for the blackbody receiver. The receivers were bolted to the receiver reservoir for easy removal.

In measuring the absorptance of a particular surface on the receiver, the boiloff rate from the reservoir is checked from time to time until the apparatus comes to a steady state, which requires about 3 hours, and several steady-state boiloff rate readings, requiring about 6 hours per measurement, are taken. For the measurements with cryodeposits, several boiloff rate readings are taken on the bare aluminum substrate before the gas deposition begins. In order to carry out the deposition, the gas deposit line and the radiator are warmed with electric heaters to 250° K or more and the gas flow is then started. The radiator heater was a carbon resistor and the vacuum-jacketed gas deposit line was heated with a nichrome heater wire wrapped spirally along it. The gas deposit line and radiator must be warm to prevent condensation of the depositing gas within them. After a certain predetermined mass of gas has been deposited, the power to the radiator and gas deposit lines is cut off and these structures are allowed to cool to the desired radiator temperature. Steady-state boiloff rate readings are then taken and the film absorptance determined.

RESULTS

Three cryodeposited films have been investigated, namely, CO₂, N₂, and air. In the case of CO₂, the measured absorptance of the aluminum substrate was 0.078; with a solid CO₂ film thickness of approximately 100 mils the absorptance of the film plus substrate

system was 0.11. For air and N₂ films approximately 50 mils thick similar results were obtained; the total measured absorptance of the substrate plus film was 0.10. The thickness of a film is calculated from the known mass of gas deposited and the density of the corresponding solid at 20° K. The assumption that films cryodeposited in the rarefied gas regime have densities of at least 70 percent of the maximum solid densities at the film temperature has been confirmed in other experiments performed on cryodeposited films in the LMSC Thermophysics Laboratory (ref. 1).

Measurements (ref. 2 and 3) of the infrared transmittance of solid nitrogen and oxygen films at temperatures down to 34.4° K in the wavelength range from 2.5 to 25 μ indicate that these films are almost totally transparent. In this wavelength range, solid oxygen has only one weak absorption band, at 6.4 μ ; and solid nitrogen also has only one weak absorption band, at 4.2 μ . At wavelengths greater than 25 μ , a single absorption band associated with the lattice vibrational frequency should appear in both solids. Thus, for 77° K blackbody radiation, both nitrogen and oxygen, and hence solid air, should be highly transparent. The results of the present experimental measurements indicate that this is indeed the case.

Measurements (ref. 4 and 5) on solid CO₂ in the infrared indicate that, in the wavelength region of interest in the present experiments, the only absorption bands occurring are at 15 and 100 μ . These two bands are so narrow and weak that CO₂ can be considered to be transparent to 77° K blackbody radiation.

REFERENCES

1. CAREN, R. P., GILCREST, A. S., and ZIERMAN, C. A.: Thermal Absorptances of Cryodeposits for Solar and 290° K Blackbody Sources. To be published in *Advances in Cryogenic Engineering*, vol. 9, 1964.
2. SMITH, A. LEE, KELLER, WILLIAM E., and JOHNSTON, HERRICK L.: Infra-Red Spectra of Condensed Oxygen and Nitrogen. *Phys. Rev.*, ser. 2, vol. 79, no. 4, Aug. 15, 1950, p. 728.
3. SMITH, A. LEE, and JOHNSTON, HERRICK L.: The Molecular Spectra of Condensed Oxygen of the O₄ Molecule. *Jour. Chem. Phys.*, vol. 20, no. 12, Dec. 1952, pp. 1972-1973.
4. OSBERG, W. E., and HORNIG, D. F.: The Vibrational

Spectra of Molecules and Complex Ions in Crystals. VI—Carbon Dioxide. *Jour. Chem. Phys.*, vol. 20, no. 9, Sept. 1952, pp. 1345-1347.

5. DAHLKE, W.: Nuclear Vibration Bands of Solid Carbon Dioxide. *Z. Phys.*, vol. 102, nos. 5-6, 1936, pp. 360-372.

DISCUSSION

WILLIAM CLAUSEN, General Dynamics/Astronautics: As you point out, at these low temperatures, radiation heat transfer rates are very low. What provision did you make to assure the temperature equilibrium of your receiver? A large mass thermal capacity can make the equilibrium point difficult to identify.

CAREN: I might point out that in all these experiments, the length of time required to achieve steady state boiloff is on the order of 6 hours. A typical experiment is performed as follows: First the film is deposited. Then about 6 hours are allowed for steady-state conditions to be attained. Then a 6-hour boiloff measurement is taken. This measurement period is followed by another similar measurement period. If these two measurements agree, one can conclude that the measurements were made under steady-state conditions.

CLAUSEN: Did you attempt to measure the temperature of your receiver?

CAREN: No. We just assumed that in this case we had good thermal contact between the receiver and the reservoir. The receiver itself was an aluminum substrate. The liquid-hydrogen container is copper. They are bolted together, and indium metal is used between the two to provide good thermal contact. We had no reason to suspect that the contact was anything but good; and the principal justification for believing that this was the case was the verification of the T^4 dependence of the energy emitted by the radiator and received by the receiver during the calibration of the apparatus. If there had been large departures from the T^4 dependence, one could conclude that there were either heat leaks in the apparatus or that there were nonequilibrium conditions. From the fact that the predicted and measured heat exchange data checked out so well, one can conclude that there were temperature equilibrium conditions in the apparatus.

ROBERT CHAMPETIER, Aerospace Corporation: Can you make any inference on blackness of CAT-A-LAC at wavelengths greater than 15 microns?

² JENKINS, R. J., BUTLER, C. P., and PARKER, W. J.: Total Hemispherical Emittance Measurements Over the Temperature Range 77°K to 300°K. SSD-TDR-62-189, Aug. 6, 1963. (Also available as USNRDL-TR-663.)

CAREN: Butler² at NRDL has, of course, done work on the emittance of paints at low temperatures and his data indicate that, for all the paint systems, at least for all the ones he examined, the emittance does definitely drop off for the longer wavelength radiation. However, one must remember that in our case, in which we used blackbodies with large length-to-diameter ratios, the emittance, to a pretty good approximation, is independent of the emittance of the materials making up the walls. That is, if the emittance of our walls dropped from about 0.86, which might be characteristic of CAT-A-LAC paint for 10-micron radiation, down to 0.5, our bodies will still have emittances on the order of 0.90, so that they are still relatively blackbodies. That is, the temperature dependence of their emittance does not give good direct evidence regarding the emittance of their wall coating. We hope to make some studies in the next few months of the emittances of some paint systems at reduced temperatures in this apparatus. It will be very interesting to see what results we get and what happens to the emittances of these paint systems at reduced temperatures.

CHAMPETIER: I believe that the work so far at NRDL cannot be used to estimate the blackness of metal black or CAT-A-LAC past 60 or 70 microns. I wonder if your work was more certain in that respect.

CAREN: No, because, of course, in order to make measurements of this sort, we would have to have plane surfaces with these paints on them. As I said, we are hoping to get some data on this subject.

ARTHUR KATZ, Grumman Aircraft: Is there any heat leak into the liquid hydrogen reservoir?

CAREN: The lines going from the liquid hydrogen bath to the liquid hydrogen reservoir are purposely several inches long. We control the pressure over the liquid hydrogen bath so that it is approximately the same as the pressure over the boiloff hydrogen reservoir. This guarantees an approximate temperature equality of the two baths, and on the basis of the temperature (pressure) differences of the hydrogen baths in our experiments a calculation of the heat leak down the stainless steel lines to the hydrogen reservoir shows that it is negligible.

52. The Study of Low Solar Absorptance Coatings for a Solar Probe Mission¹

E. R. STREED AND C. M. BEVERIDGE

PHILCO CORPORATION, PALO ALTO, CALIF.

A summary of available information is presented pertinent to the selection, application, and performance of thermal control coatings for use on a flight to 0.3 AU perihelion. Coatings with a solar absorptance of 0.30 or less and a total hemispherical emittance of 0.85 or greater at temperatures up to 500° F are desired. The results of an experimental program to measure the optical properties and to perform simultaneous exposure to simulated solar radiation, temperature, and high vacuum are described.

Reliable thermal design of spacecraft requires intimate knowledge of the initial optical properties of surface materials and their stability in the total space environment. The prelaunch environment is also considered as a source of contamination and resultant change in surface properties. The peculiar environment of temperature, vacuum, ultraviolet radiation, and penetrating radiation has a degrading effect upon the optical and adhesive characteristics of thermal control coatings. Coatings with a low ratio of solar absorptance α_s to infrared emittance ϵ have been developed with relatively predictable performance in the space environment for temperatures up to 150° F. However, under certain conditions, coatings can achieve temperatures as high as 700° F and still require the low α_s/ϵ ratio to minimize the heat load.

A summary of available information and experimental data is presented pertinent to the selection, application, and performance of thermal control coatings for use on a perihelion flight to 0.3 AU with an α_s of about 0.30 or less, and a total hemispherical emittance of 0.85 or greater. A possible trajectory with a total

flight duration of 1 year is shown in figure 1. Exposure to a solar intensity of about nine times the solar intensity near the Earth is expected for periods of about 1 month.

It should be noted that there are order-of-magnitude uncertainties in the amount and distribution of particle and radiation fluxes of certain types. In addition, it is impossible to obtain the various species for simulated individual laboratory tests, let alone provide the combined simulated space environment.

Experimental apparatus to determine the infrared emittance, the solar absorptance, and the stability of thermal control surfaces when exposed to ultraviolet radiation in high vacuum at temperatures up to 500° F is described.

COATING CONSIDERATIONS

Review of Available Information

The choice of suitable and available materials for the prescribed mission and function is based upon laboratory simulation studies, previous or present spacecraft use, data obtained from spacecraft-borne surface stability experiments, and theoretical considerations of inherent material properties. In some instances, specific materials have a high probability of satisfactory

¹ See also Paper 53 and papers in Session IV concerned with degradation caused by ultraviolet radiation.

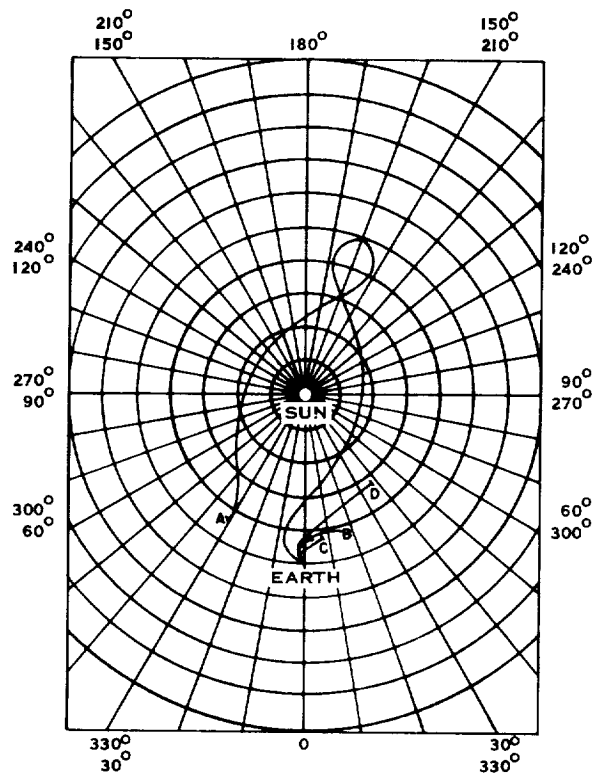


FIGURE 1.—Trajectories of interplanetary probes as viewed from the earth. A, advanced solar probe; B, USSR Sputnik 8; C, Pioneer 5; D, Mariner 2.

performance, but, in other cases, supplemental data are required to insure compatibility with the substrate or long-term stability in the subject environment.

Initially organic spacecraft thermal control coatings with low α_s/ϵ values were specified on the basis of availability, cost, and terrestrial experience. However, vehicles such as polyurethane, epoxy, and polyesters are inherently susceptible to ultraviolet radiation damage, as illustrated in figure 2. The amount of degradation experienced by an actual flight experiment (ref. 1) is plotted in figure 2 for comparison with laboratory data.

New coatings have been developed utilizing silicate and special silicone vehicles which exhibit good ultraviolet radiation damage resistance at moderate temperatures (ref. 2, 3, and 4). However, even these materials require careful selection, as illustrated by the varied performance shown in figure 3 after exposure to the equivalent of 1,000 sun hours (ref. 2).

The α_s performances of other inorganic coatings such as zinc oxide and stannic oxide in special vehicles have been extensively studied for stability against thermal shock, ultraviolet ex-

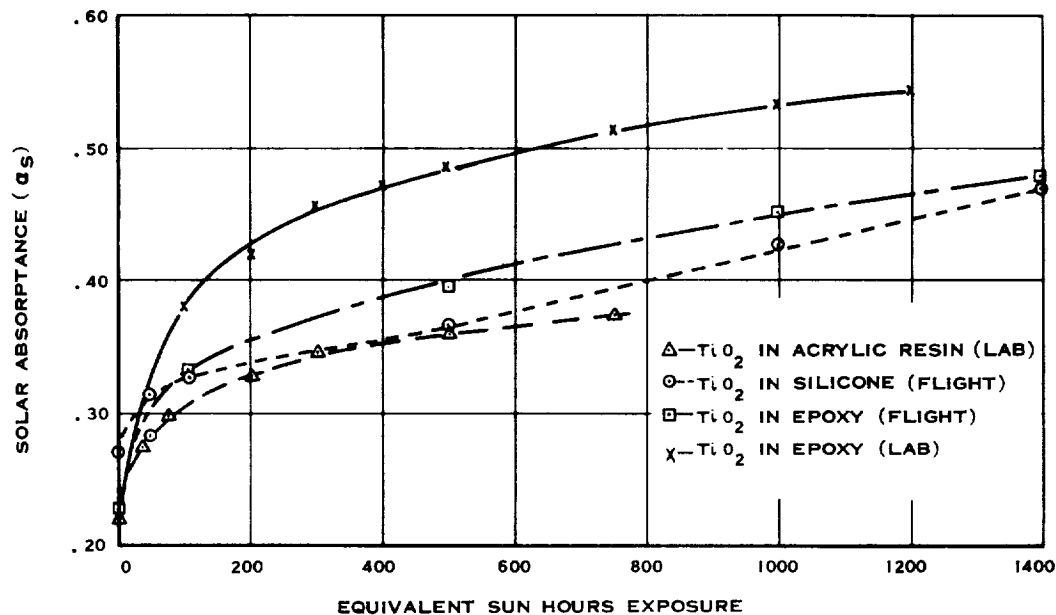


FIGURE 2.—Degradation of several organic thermal-control coatings.

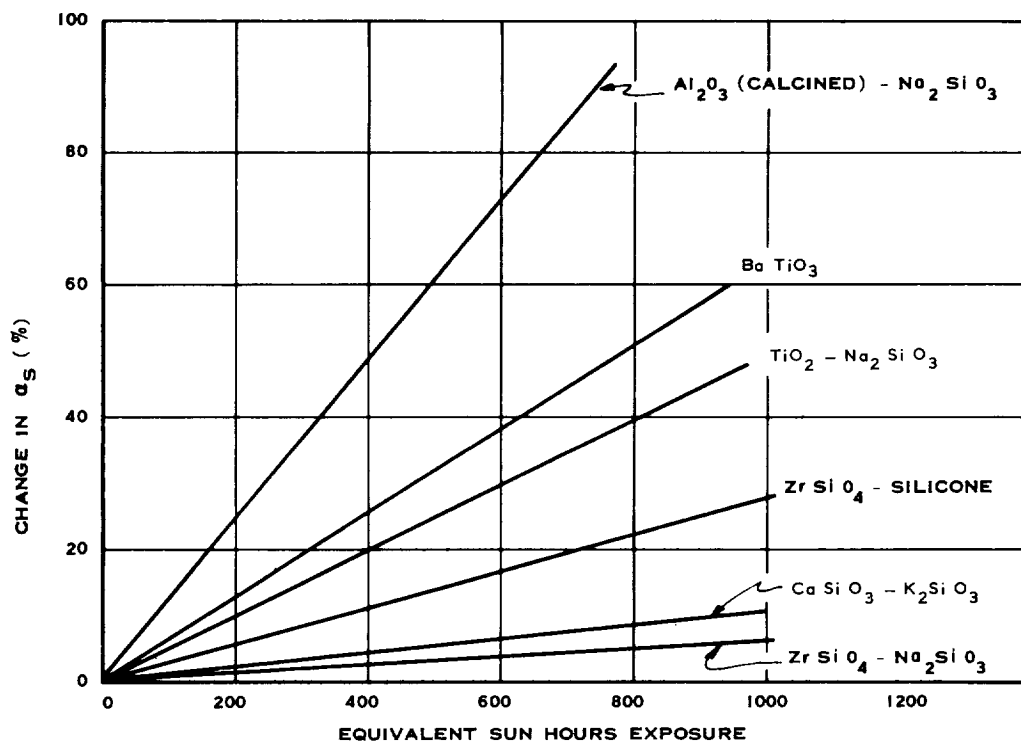


FIGURE 3.—Percentage of change in α_s of various pigments after exposure to the equivalent of 1,000 hours of solar ultraviolet radiation.

posure, abrasion and fatigue (ref. 3.) These studies have resulted in the screening and selection of suitable coating systems for operation in the space environment for extended periods at near ambient temperatures (ref. 5). However, no data were available on the influence of temperatures up to 500° F on the coating optical properties.

Prelaunch Environment

The prelaunch environment includes the manufacturing, assembly, storage, and launch-holding time periods. The effects of impurities or process changes in controlling the α_s/ϵ of white coatings or the effects of such things as rolling marks and thin-film protective coatings on low ϵ coatings can drastically alter their optical properties. Therefore, careful specifications for purity and process control are necessary to insure a reproducible product. The requirements during application of coatings or special cleaning treatments are also exceptionally stringent. Substrate cleanliness, roughness,

and priming must be adequately controlled to obtain proper adhesion. Parameters such as pigment particle size, viscosity, pigment-to-vehicle ratio, curing procedure, and coating thickness contribute to optimum performance. The inorganic coatings are generally porous and relatively rough, which make them susceptible to handling contamination. The silicone coatings can be cleaned without deleterious effects by using careful techniques. Therefore, in some instances, it is necessary to protect the surfaces during assembly, storage, shipment, and prelaunch.

Ascent Environment

All spacecraft components for the subject program are enclosed within a heat shield shroud during ascent. It is assumed that the maximum temperature inside the shroud is 120° F. There will be no deleterious effect on the performance of the suggested thermal control coatings or of any normal coating envisioned for use on spacecraft at this temperature.

Simulation of the other ascent environmental parameters has been performed on a limited basis with no detrimental effect reported to a normally good substrate-coating system.

Penetrating Radiation

The effect of high-energy electrons, protons, or neutrons on the optical properties of materials has not been theoretically or empirically related. Limited experimental data are available from laboratory tests performed primarily with selected materials and radiation for particular material problems or as verification of theoretical concepts. No comprehensive study has been performed that relates intensities, doses, and particle characteristics to changes in the spectral or total absorptance, reflectance, or transmittance properties in the solar or infrared wavelength regions. In the nominal operating temperature range for the subject program, no effects from penetrating radiation on the optical properties of uncoated metals are expected. Inorganic materials such as oxides, ceramics, and glass may discolor depending upon the purity and defect structure of the material. The organic materials are the most susceptible to serious damage in the form of discoloration and degradation of physical properties.

In theories and predictions of changes induced in the properties of solids by high-energy radiation, changes are attributed to structural defects such as (a) vacancies, (b) interstitial atoms, and (c) impurity atoms. Important secondary processes are (a) replacement collisions, (b) thermal and displacement spikes, and (c) ionization effects. Charged particle irradiation always produces primary ionization and usually produces atomic displacements, whereas gamma rays produce only ionization as the first order effect.

Solar flares are considered to be the greatest source of potential damage in the subject environment through the emission of corpuscular radiation. The radiation is believed to be composed of about 90 percent protons and 9 percent gamma rays. Increases in the absorptance of α -alumina (α - Al_2O_3) and silica (SiO_2) have been attributed to just displaced atom phenomena caused by neutron bombardment (ref. 6). The

absorption bands occur in the 0.2- to 0.25- μ region, primarily. A band at 0.465 μ , observed in most crystalline silicas, has been attributed to aluminum impurities and results from ionizing radiation. Annealing of induced defects of this type by heating in air is very gradual over the temperature range from 200° to 1000° C. Alkali halide crystals incurred considerable absorption on irradiation with 350-Mev protons; the coloration began to anneal out at 150° C, and above 250° C the coloration completely disappeared.

Very few quantitative data relating nuclear radiation exposure to changes in α_s or ϵ are available. The penetration of high-energy protons encountered from solar flares should result primarily in a bulk effect. Although prolonged exposure could cause deterioration of the adhesion between coating and substrate, no serious increase of α_s was reported for 10^{13} proton/cm² doses of 700-Mev protons on titanium dioxide (TiO_2), Mylar tape, and aluminum foil (ref. 7). Exposure of common thermal control coatings to 10^7 r of cobalt-60 gamma radiation resulted in negligible increase in the α_s/ϵ values (ref. 7). Comprehensive reviews of available irradiation data for plastics and elastomers (ref. 8) and for metals (ref. 9) are primarily for irradiation in air at room temperature. Experimental studies of ultraviolet-irradiation effects, however, show significant differences between the effects in air and in vacuum. In general, the resistance of materials to high-energy space radiation is assumed to be similar to that shown by experimental data obtained with nuclear radiation (ref. 5). Per unit of absorbed flux density, materials can be ranked in order of resistance to degradation as follows: metals, inorganic materials, organic materials.

Particle Impact

Particle impact can be significant to the extent that the resulting erosion or sputtering of the coating or surface can alter the optical properties by coating removal or changing the surface roughness. Consideration of the effect of meteoroids in interplanetary space flights indicates that surface erosion will be less than 1 Å per year (ref. 10). Sputtering effects could

be more severe.² Estimates that a maximum of 400 Å of aluminum might be removed during exposure to 10 solar flares over a 1-year period have been made (ref. 5). Laboratory simulation of sputtering of thermal control surfaces with argon and xenon ions resulted in negligible effects upon α_s (ref. 11). The thermal control surfaces under consideration will be at least 5 mils in thickness; consequently, no deleterious effects are expected.

Solar Radiation

The effects of solar radiation have been studied primarily from the standpoint of ultraviolet degradation. The chemical structure of many materials is such that the energetic photons in the wavelength range from 2,000 to 3,500 Å (photon energies of 6.2 to 3.5 eV, respectively) can induce chemical changes. These changes in turn result in loss of adhesion or altering of the surface optical properties. The wavelength region below 0.2 μ is potentially capable of producing significant damage, as reported in references 2 and 3, but because the total radiation below 0.2 μ is at least two orders of magnitude lower in intensity than the total radiation in the 0.2- to 0.35- μ region and because most materials show significant absorption in both of these regions, the development and specification of coatings resistant to 0.2- to 0.35- μ radiation is considered the primary objective. Simulation of the solar spectrum to a wavelength of 1.4 μ is desirable to insure that healing, cumulative, or chain reaction effects are included. The degradation of organic materials exposed to ultraviolet radiation has been generally shown to obey a reciprocity expression (ref. 12). The expression applies within certain exposure time restrictions and implies that accelerated testing can provide useful data. Experimental evidence obtained in ultraviolet exposure studies has shown that the changes that occur in air and in vacuum are significantly different. An experimental program and data relating the degradation of promising low α_s/ϵ coatings to ultraviolet exposure at 500° F are presented in the section entitled "Experimental Studies."

² See also Paper 37.

Emittance

Space environmental effects generally do not change emittance values of inorganic coatings except at high temperatures (above 1,000° F). However, as shown in figure 4, the decrease in emittance with temperature for the white coatings can become important at temperatures above 500° F. Although data are not shown for all of the various types of low α_s/ϵ coatings, the downward trend with temperature exhibited in figure 4 is expected. The elevated temperature total normal emittance was calculated from spectral reflectance values obtained from a heated cavity hohlraum apparatus.

Flight-Experiment Data

Probably the best data on synergistic effects are obtained through actual space flight. A silicon oxide coating 1.25 μ (50 microinch) thick on a polished metal substrate has performed satisfactorily on Vanguard II for about 4 years at altitudes varying from 350 to 2,065 nautical miles. A more recent experiment on the S-16 Orbiting Solar Observatory has indicated no serious deterioration of a 500 Å (approx. 20 microinch) coating of silicon oxide in 14 months exposure at an altitude of about 350 nautical miles. Although deterioration of some coatings has occurred in the complete space environment, the extent of degradation of the optical properties has been conservatively predicted by the ultraviolet, vacuum, and temperature simulation tests such as described herein.

EXPERIMENTAL STUDIES

A survey of the literature and of past experience with low α_s/ϵ coatings provided several coatings with simulated space exposure data at nominal room temperatures but no information at elevated temperatures. Therefore, an experimental program was initiated to determine the degradation of five promising coatings when exposed to the intensity equivalent of 10 suns in the 0.2- to 0.4- μ spectral region for 30 days. The samples were maintained at 500° F \pm 25° F in a vacuum of 5×10^{-6} torr or better. Additional studies of a zinc oxide (ZnO) system were performed to determine its degradation as a function of temperature

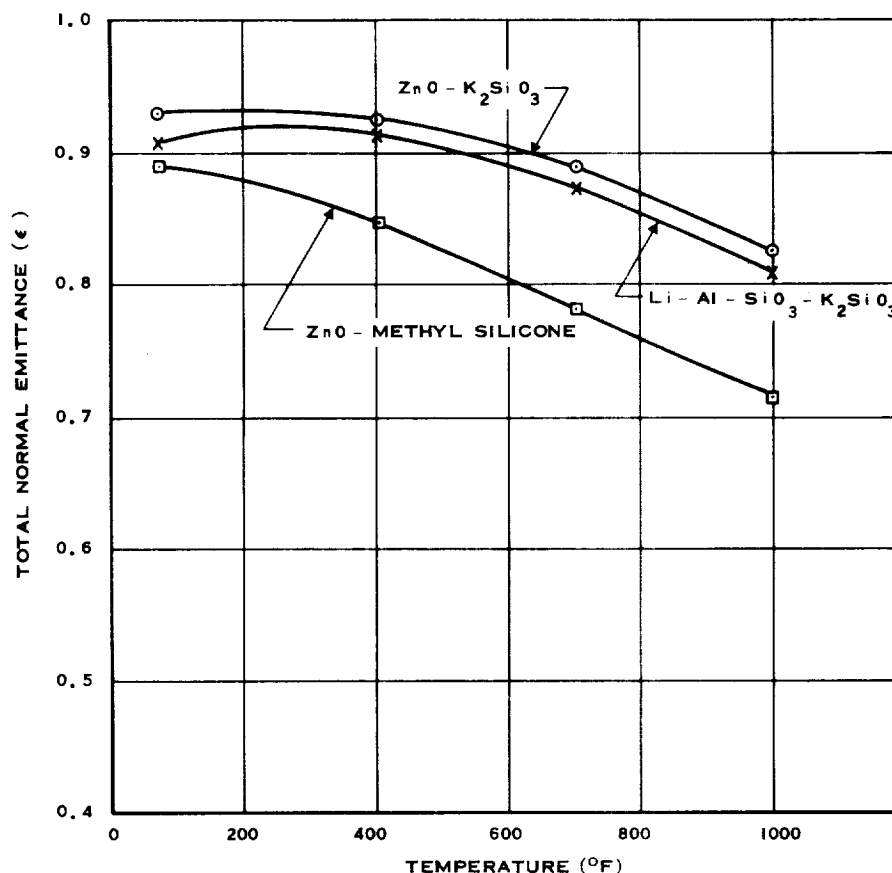


FIGURE 4.—Decrease in emittance with temperature for promising low α_s/ϵ coatings.

and exposure time. Measurements of room temperature α_s and ϵ were made before and after exposure.

Specimen Selection

The promising coating types were selected on the basis of resistance to high temperature, ultraviolet radiation, high-energy particles, and high vacuum. Organic vehicles were immediately excluded on the basis of temperature sensitivity. One silicone vehicle was selected because of its exceptional resistance to ultraviolet radiation. The other coating contained a silicone varnish binder which supposedly evaporated on heating. The three completely inorganic systems were chosen to represent a cross-section of crystalline structure solids available as ultraviolet stable oxides with initially low α_s values. The coatings, sources, and comments on past performance are listed

in table 1. In addition to the ZnO coating, inorganic formulations of calcium silicate (CaSiO_3), zirconium silicate (ZrSiO_4), $\text{ZrSiO}_4\text{-Al}_2\text{O}_3$, and silicone coatings were applied and exposed to ultraviolet radiation for short periods of time.

Specimen Preparation

All coatings were applied to 6061-T6 aluminum sheet. The substrates prepared at Western Development Laboratories (WDL) received a hot alkaline etch with a hot sulphuric acid-sodium dichromate cleaning solution and a 110° C oven drying. Inorganic zinc oxide-potassium silicate ($\text{ZnO-K}_2\text{SiO}_3$) coatings were prepared at WDL in a ball mill. Various ball-to-pigment charge ratios and mixing times were tried, with a 3:2 ratio for 5 hours providing the lowest α_s values.

The coatings were applied with an air brush

TABLE I.—Description, Source and Pertinent Comments on Coatings Exposed to Ultraviolet Radiation at Elevated Temperature

Coating system	Source	Comments
1. 180 g ZnO..... 90 ml K ₂ SiO ₃ 180 ml H ₂ O cured for 1 hour at 500° F.	SP500, New Jersey Zinc Co. PS7, Sylvania Electric Products, Inc.	Prepared at WDL and based upon formulations of ARF (ref. 3).
2. ZnO..... Methyl silicone, 40% PVC (ARF TC-46-20).	SP500, New Jersey Zinc Co. ARF-prepared.....	Samples obtained from ARF. Easy to handle and good ultraviolet resistance (ref. 3).
3. SiO ₂ Silicone varnish.....	Corning #7941 multiform fused silica. Experimental silicone varnish, Dow-Corning.	Obtained from Corning Glass Works. No prior ultraviolet or vacuum ex- posure data available. Coating de- scribed as potentially having good stability (ref. 13).
4. Li ₂ O-Al ₂ O ₃ -SiO ₂ in K ₂ SiO ₃ ...	Trade names of Lithafrax and Kasil 88—obtained by LMSC.	Coating prepared and applied by LMSC. Coating has consistently the lowest initial α , and good adhesion (ref. 5).
5. ZrSiO ₄ in K ₂ SiO ₃	Trade names of zircon and Kasil 88—obtained by LMSC.	Coating prepared and applied by LMSC. Coating has shown good neutron ra- diation resistance (ref. 5).

in a fume hood. The inorganic coatings required from 6 to 10 coats to achieve an opaque coating with a total average thickness of 4 mils. The coatings were dried at 110° C for 2 hours and then fired in a muffle furnace for an additional hour at 500° F (260° C).

Detailed sample preparation for specimens supplied by other sources are proprietary or are described in the respective references.

Space Simulation Exposure Apparatus

The apparatus permits simultaneous exposure of materials to radiant energy in the 0.25- to 1.4- μ region, a vacuum of at least 1×10^{-6} torr, and temperatures to 500° F. The complete apparatus is shown in figure 5. The radiant energy is furnished by a high-pressure, mercury-arc lamp (PEK Labs, type C, which is equivalent to General Electric A-H6) mounted inside a water-cooled quartz finger. The specimens are mounted on individual holders in a radial fashion about the source, as shown in figure 6. The units are mounted inside a stainless steel, water-cooled bell jar having walls coated with a black diffuse coating to reduce reflections. Vacuum is provided with

a 4-inch oil diffusion pump trapped with a liquid nitrogen thimble trap and backed with a 5-cfm mechanical pump. An ionization gage is mounted in the chamber for pressure measurement.

Extensive measurements of the total and spectral radiation emitted by the A-H6 lamps and the B-H6 air-cooled lamps have been reported (ref. 4 and 12). At sample distances of 5 inches, the average measured new lamp intensity was 11.8 ultraviolet suns. Variations of ± 15 percent were found for new lamps. Decreases in total ultraviolet radiation intensity in the 0.25- to 0.40- μ range of up to 75 percent were measured during the useful life of the lamps. Essentially, the same type of apparatus was used for studies at Lockheed Missiles and Space Company (LMSC) and at WDL.

Measurement Techniques

The selection and specification of coatings for use in particular wavelength regions require knowledge of their spectral characteristics. For measuring these characteristics in the solar spectral region from 0.25 to 2.0 μ , a reflectance technique is used. The WDL apparatus

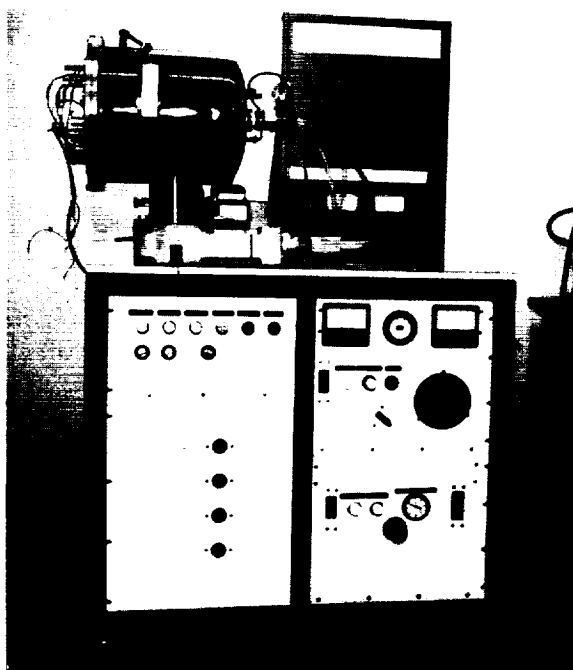


FIGURE 5.—Ultraviolet space simulation exposure apparatus

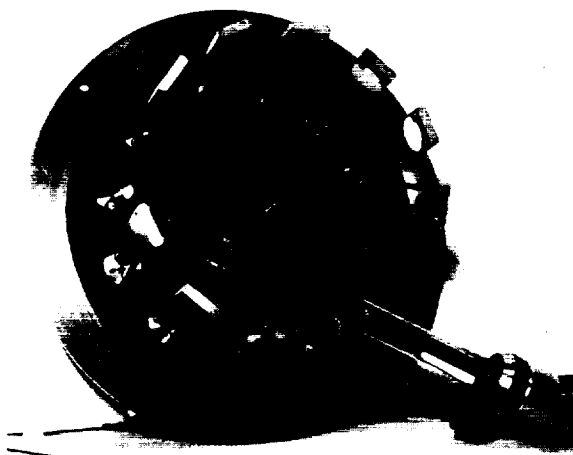


FIGURE 6.—High-pressure mercury lamp, water-cooled lamp holder, and individual temperature-controlled sample holders.

consists of a model 350 Perkin-Elmer spectrophotometer equipped with magnesium oxide-coated integrating spheres, tungsten and hydrogen lamp sources, and photomultiplier and lead sulfide detectors. Measurements are performed

by directional illumination of the specimen and a reflectance standard. The ratio of the reflected radiations is recorded as a function of wavelength. Pertinent data points are picked off of the recording and are computer-integrated with the extraterrestrial solar spectrum to give total solar absorptance.

The measurement apparatus used at LMSC included an integrating sphere reflectance attachment for a Model 14 Cary ratio recording spectrophotometer and a heated cavity reflectometer used in conjunction with a model 13 Perkin-Elmer ratio recording spectrophotometer (ref. 14). The ARF apparatus consists of a General Electric recording spectrophotometer with associated integrating sphere and a total emittance device employing a black-body reference (ref. 15).

Exposure Results

Inexperience with low α_s coatings at elevated temperatures made it desirable to make some preliminary exposures of 50 hours. These tests served to provide additional screening information and to verify that the temperature of the specimen would stabilize at about 500° F with no supplemental heating. Specimens of Rokide "A" (Al_2O_3) and pigmented silicone film material showed serious degradation and were eliminated from further study. Although the multiform, high-purity fused silica was significantly discolored after 50 hours, it was included in the final test to determine if a saturation point would be reached.

The results of a 700-hour exposure at an average ultraviolet intensity of 10.3 suns is shown in table II. The specimen temperature was measured with a Chromel/Alumel thermocouple attached to the specimen holder. A temperature gradient of 15° F was measured through the coating with fine wire thermocouples. Although the sample temperatures varied with lamp intensity and decreased to near room temperature during lamp changes, the temperature values indicated were maintained within $\pm 25^\circ$ F for about 80 percent of the time. The average pressure during the complete exposure time was 4×10^{-7} torr.

The ZnO in methyl silicone showed the least

TABLE II.—Solar Absorptance (α_s) and Emittance (ϵ) of Several Coatings Before (B) and After (A) 700 Hours of Exposure at Approximately 10-Sun Ultraviolet Intensity. (Exposure and Optical Measurements by LMSC.)

Coating		Av. Temp., °F	α_s		ϵ	
Pigment	Binder		B	A	B	A
ZnO.....	K ₂ SiO ₃	495	0.17	0.33	0.95	0.93
Zircon.....	K ₂ SiO ₃	490	.13	.42	.95	.93
Lithafrax.....	K ₂ SiO ₃	495	.12	.32	.93	.89
SiO ₂	Silicone.....	510	.14	.72	.92	.83
ZnO.....	Methyl silicone (ARF TC-46-20).....	505	.18	.27	.91	.88

degradation of α_s ; however, the coating was checked and spalling was commencing at the end of the exposure. The SiO₂ pigmented silicone varnish coating turned dark brown, as substantiated by the α_s value of 0.72. Of the three inorganic systems, the ZnO in K₂SiO₃ and the Lithafrax (Li₂O-Al₂O₃-SiO₂) in K₂SiO₃ gave the lowest exposed α_s values. The values were nearly identical—0.33 and 0.32, respectively; however, the lower initial value for Lithafrax indicates that a faster degradation rate occurred for this coating system. The ZrSiO₄ in K₂SiO₃ coating suffered the second greatest degradation, as evidenced by the exposed α_s value of 0.42. Measurements of the total normal emittance indicated decreases of about 3 percent for four of the coatings and a 10 percent decrease for the badly degraded SiO₂-silicone varnish system.

The over-all performance of the ZnO in K₂SiO₃ coating system appeared to be superior to that of the other coatings, but greater degradation in α_s had occurred than was previously reported for similar exposure times. Therefore, further investigation of the influence of temperature was conducted. Specimens prepared from the same coating batch that was used for the 700-hour 10.3-sun exposure were mounted in individual temperature controlled sample holders. Duplicate specimens were mounted on the back side of the holder to permit exposure to identical temperature and vacuum conditions but no ultraviolet. Different sets of specimens were exposed to 235 equivalent sun hours and 2,300 equivalent sun hours. The α_s values, determined from reflectance

measurements, are shown in figure 7 as a function of temperature and exposure time. The general trend of increasing α_s with temperature is clearly evident. The unirradiated duplicate specimens showed increases of only 0.01 to 0.02 absorptance units, irrespective of specimen temperatures for temperatures between 60° and 350° F.

A comparison with data obtained by Armour Research Foundation (ARF) at about 70° F and by LMSC at 495° F can also be made in figure 7. Although the performance of the ARF coating was not matched for the 2,300-hour exposure, sufficiently good agreement for engineering purposes was achieved.

A comparison of spectral data from 0.25 to 1.6 μ is shown in figures 8 and 9 for unexposed ZnO pigmented K₂SiO₃ and methyl silicone coatings, respectively. The WDL and LMSC data for the K₂SiO₃ coating were measured for the same specimen batch and the ARF data were reported for the same formulation. Although detectable differences are indicated in the region of the absorption band at 0.4 μ , the integrated values of α_s varied by only 4 percent from a nominal value of 0.17. The relatively large variation in the spectral reflectance of the silicone coatings, shown in figure 9, is attributed primarily to formulation. The TC-46-20 specimen is the latest ZnO pigmented methyl silicone formulated by ARF and measured at LMSC. The TC-50-8 specimen is a ZnO pigmented methyl silicone for which ARF spectral and exposure data were available (ref. 3). The Q9-0090 coating is a 20 percent TiO₂ pigmented methyl silicone obtained from

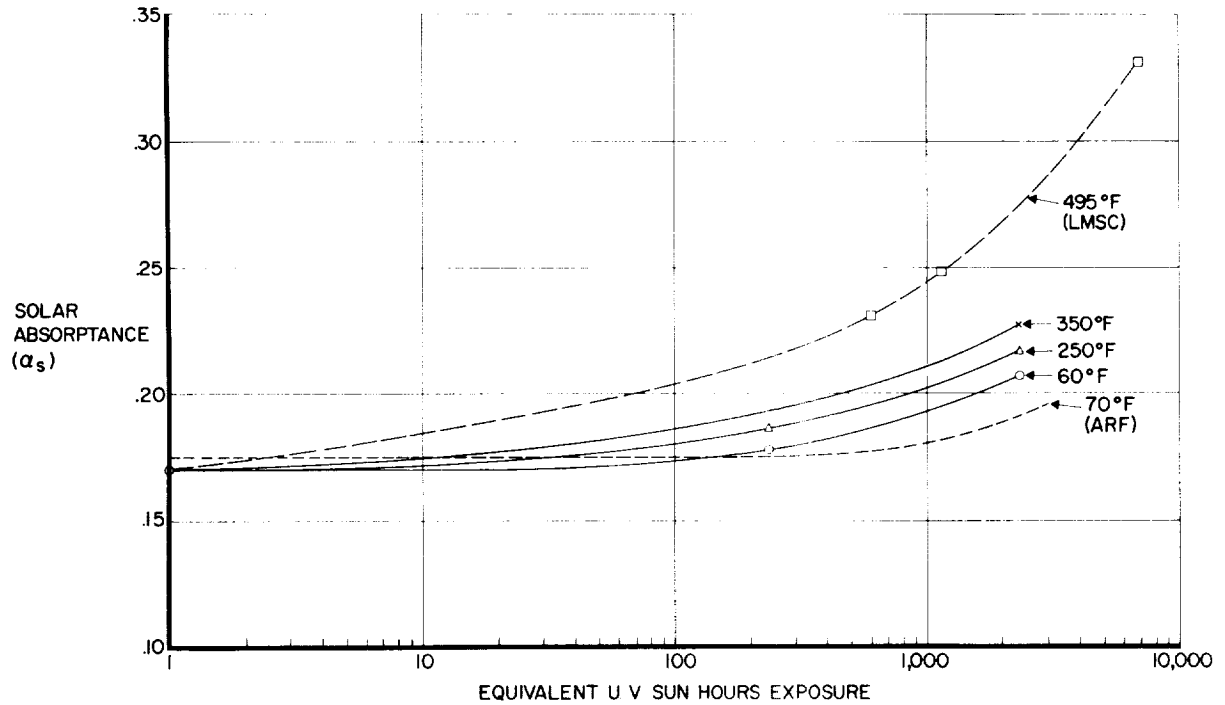


FIGURE 7.—The solar absorbance of zinc oxide pigmented potassium silicate as a function of temperature and exposure time.

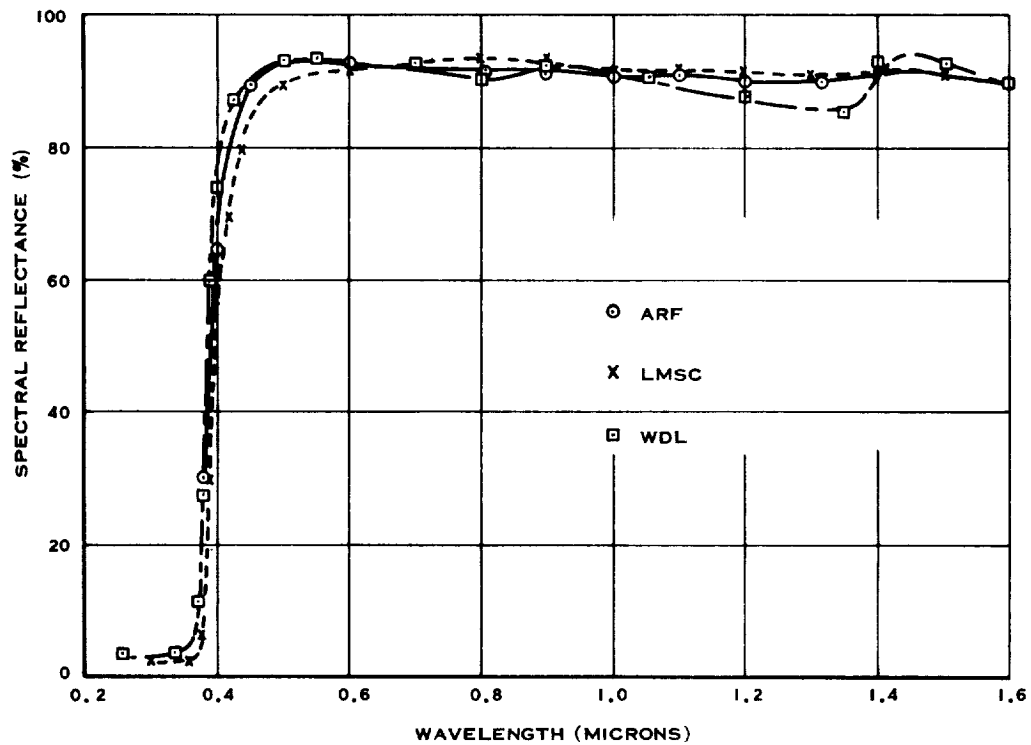


FIGURE 8.—Spectral reflectance of zinc oxide-potassium silicate system before exposure.

Dow-Corning Company and measured at WDL.

The spectral reflectance of the ZnO in K_2SiO_3 as a function of exposure time and temperature is shown in figure 10. The initial degradation begins in the 0.4- to 0.6- μ region and as the temperature and exposure time increases the absorption increases in magnitude and extends to longer wavelengths. The surface becomes tan and for badly degraded materials is a dark brown similar to a scorched white material.

The spectral reflectances of exposed ZnO and TiO_2 pigmented methyl silicone coatings are shown in figure 11. These coatings tended to show greater degradation in the 0.4- to 0.7- μ range and less degradation beyond 0.8 μ than the K_2SiO_3 coatings did. The formulation of additional methyl silicone coatings to investigate the adhesion problem has been hampered by the inability to achieve reproducible results with supposedly similar types of coating vehicles.

CONCLUSIONS

The influence of elevated temperature in increasing the degradation of low α_s/ϵ coatings has illustrated the need for simultaneous simulation of as many environmental factors as possible. Of the three coatings exhibiting the lowest values of α_s/ϵ after exposure, the ZnO pigmented K_2SiO_3 is considered the best. The greatest uncertainty in degradation prediction results from the lack of theoretical models or experimental data on the effects of high-energy particle radiation. However, the ultraviolet radiation effects are considered to cause the greatest potential damage.

ACKNOWLEDGMENTS

The cooperation of L. A. McKellar and R. L. Olson of Lockheed Missiles and Space Company, G. A. Zerlaut of IIT Research Institute (formerly ARF) and C. B. Neel of NASA Ames Research Center in providing samples and data substantially contributed to the study. The efforts of C. J. Strombom made operation of the space simulation chamber successful. Spectral

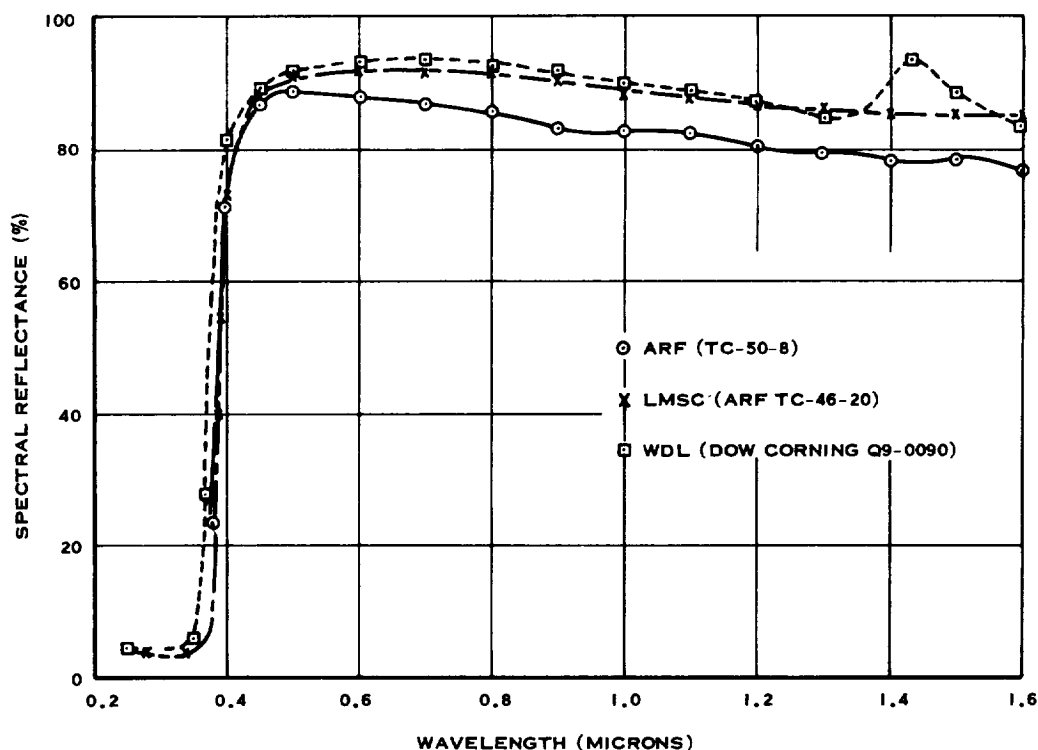


FIGURE 9.—Spectral reflectances of unexposed zinc oxide and titanium dioxide pigmented methyl silicone systems.

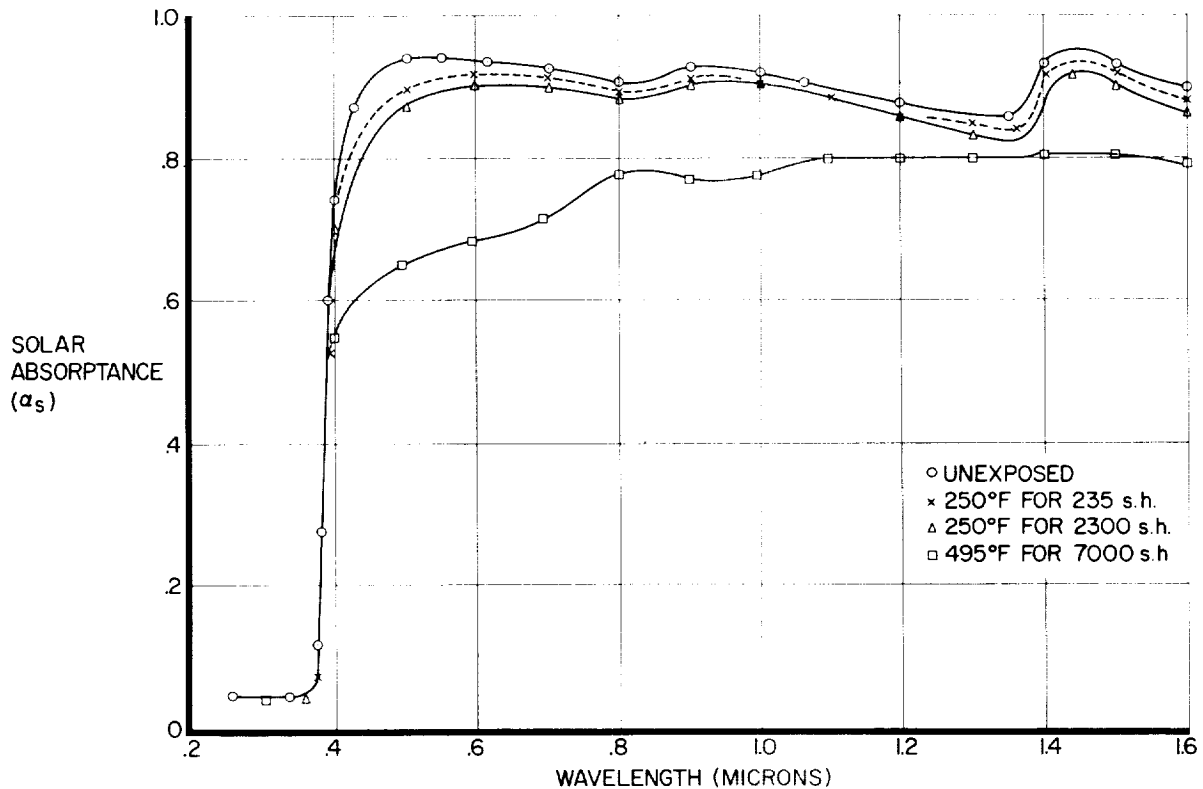


FIGURE 10.—Spectral reflectance of the zinc oxide-potassium silicate systems after exposure.

measurements for determining α_s and the computer data reduction were performed by J. Little and Mrs. L. Patmore, respectively, of WDL.

REFERENCES

1. NEEL, CARR B.: Research on the Stability of Thermal-Control Coatings for Spacecraft. NASA TMX-51, Ames Research Center, 1963.
2. SIBERT, M. E.: Inorganic Surface Coatings for Space Applications. Lockheed Missiles & Space Co. Rep. 3-77-66-12, Astia AD 263335, Aug. 1961.
3. ZERLAUT, GENE A., and HARADA, Y.: Stable White Coatings. Rep. No. ARF 3207-14, JPL Subcontract No. 950111, (Contract NAS7-100), Armour Res. Foundation, Illinois Inst. Tech., Nov. 1962.
4. CARROLL, W. F.: Development of Stable Temperature Control Surfaces for Spacecraft. Prog. Rep. No. 1, Tech. Rep. No. 32-340, (Contract NAS7-100), Jet Propulsion Lab., C.I.T., Nov. 1962.
5. GOETZEL, CLAUS G., and SINGLETARY, JOHN B., eds.: Space Materials Handbook. Contract AF04 (647)-673, Lockheed Missiles & Space Co., Jan. 1962.
6. DIENES, G. J., and VINEYARD, G. H.: Radiation Effects in Solids. Interscience Publ., Inc. (New York), 1957, p. 80.
7. McKELLAR, L. A.: Effects of the Spacecraft Environment on Thermal Control Materials Characteristics in Spacecraft Thermodynamics Symposium, Galen A. Ettemad, ed., Holden-Day, Inc., San Francisco, 1962, pp. 99-128.
8. JAFFE, L. D.: Effects of Space Environment Upon Plastics and Elastomers. (Contract NASw-6), Jet Propulsion Lab. Tech. Rep. No. 32-176, Nov. 1961.
9. ALLEN, J. M.: Environmental Factors Influencing Metals Applications in Space Vehicles. Battelle Memorial Inst., DMIC Rep. 142, (OTS PB 151101), Dec. 1960.
10. JAFFE, L. D., and RITTENHOUSE, JOHN B.: Behavior of Materials in Space Environments. Jet Propulsion Lab., C.I.T., Tech. Rep. No. 32-150, Contract NASw-6, Nov. 1961, p. 72.
11. STEIN, ROBERT P.: Atomic and Molecular Sputtering in, First Symposium—Surface Effects on Spacecraft Materials, Francis J. Clauss, ed. John Wiley & Sons, Inc., 1960, pp. 391-404.
12. SCHMITT, RICHARD G., and HIRT, ROBERT C.: Studies on the Protective Ultraviolet Absorbers in High Vacuum Environment. II. U.S. Air

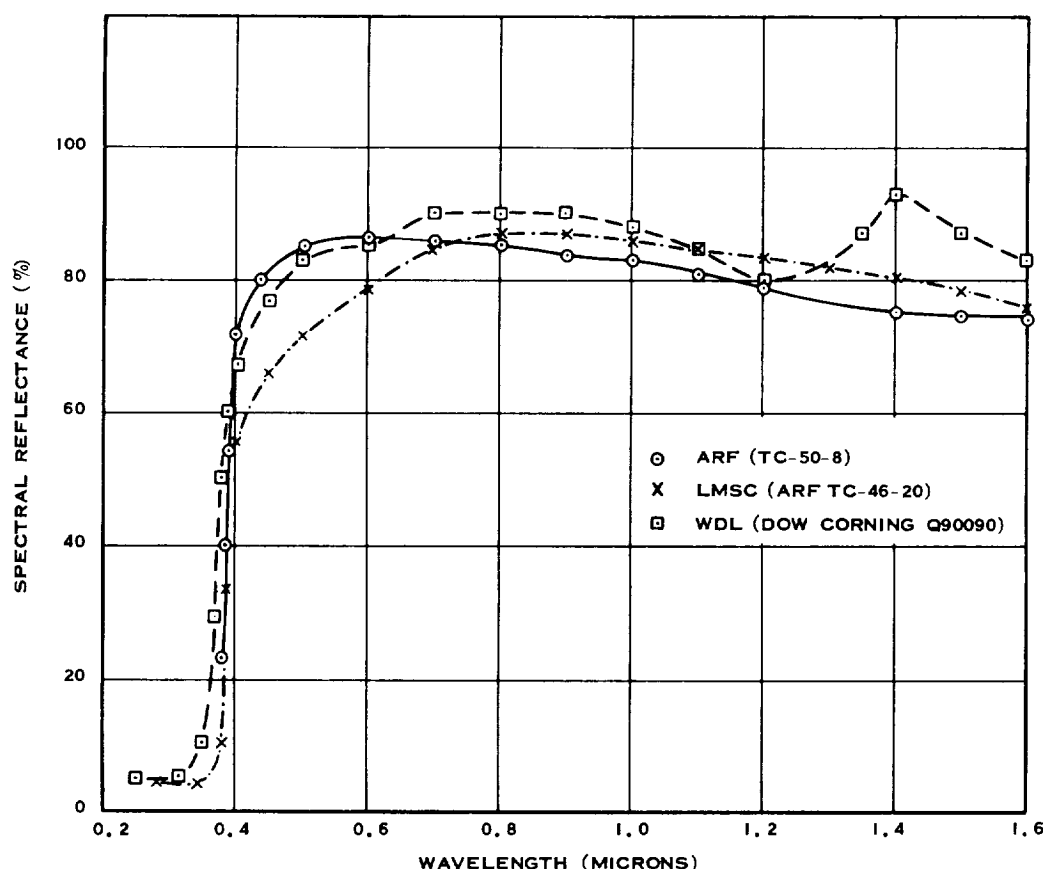


FIGURE 11.—Spectral reflectances of the zinc oxide and titanium dioxide pigmented methyl silicone coatings after exposure.

EXPOSURES: ARF (TC-50-8), 3200 sh at 70° F
 LMSC (ARF TC-46-20), 7200 sh at 500° F
 WDL (Dow Corning Q9-0090), 1400 sh at 475° F

- Force, WADD Tech. Rep. 60-704, Feb. 1961.
13. TANZILLI, R.: Development of a Stable "White" Coating System, AIAA Jour., (Tech. Notes and Comments), vol. 1, no. 4, Apr. 1963, pp. 953-954.
 14. STREED, E. R., McKELLAR, L. A., ROLLING, R., Jr., and SMITH, C. A.: Errors Associated with Hohlraum Radiation Characteristics Determinations in Measurement of Thermal Radiation

Properties of Solids, Joseph C. Richmond, ed
 NASA SP-31, 1963, pp. 237-252.

15. TOMPKINS, EDWIN H.: Stable White Coatings. Interim Rep. ARF 3207-5, JPL Subcontract No. 950111, (Contract NASw-6), Armour Res. Foundation, Illinois Inst. Tech., Apr. 13, 1962, p. 7.

DISCUSSION

ARNOLD HUNTRESS, Dow Corning Corp.: I understand that you mounted samples of several different materials on your sample holders in a single test. Are you concerned about cross-contamination of outgassing materials between samples?

STREED: We did expose samples of different materials in the same chamber simultaneously; however, we restricted such tests to inorganic materials, or to inorganic and silicone materials. We thought that, with

the specimens primarily at elevated temperatures, the outgassing materials would mostly condense on the cold chamber wall, and that if any did stick to the other specimens, it would be for a very short time.

LOUIS McKELLAR, Lockheed: I have two comments, one of which is a partial answer to Mr. Huntress' question. At Lockheed, we generally try to have only samples of the same kind of material in the chamber in any one test. However, we have also run them the

other way—for example, silicone and silicate samples with different pigments in the same chamber at the same time. We have not noticed any measurable difference between the degradation observed for these surfaces and the degradation of the same materials exposed separately. This question is frequently raised; but, at least with the stable systems, we have not noticed any effects attributable to cross-contamination. The other point I wish to make is that the general results that Elmer Streed reported have an impact on the design of space radiators for reactors. For radiators operating at temperatures between 200° and 700° F, the solar absorptance is still important. I understand that Lewis Research Center of NASA is looking for a surface with an α_s/ϵ of 0.1 to 0.2 to operate at 300° to 500° F. Streed's data indicate that at least some of the better coatings that are available from different laboratories cannot be expected to meet this requirement even without considering the penetrating radiation environment that Jack Gilligan talked about; the lowest α_s/ϵ values achieved for stable surfaces at 500° F were greater than 0.30.

ROBERT CHAMPETIER, Aerospace: Did you attempt to evaluate the effect of the diffusion pumps by a comparison with ion pump data?

STREED: The equipment used at Lockheed was an ion pump. On the curve for ZnO and K_2SiO_3 at elevated temperatures, there were three data points. Two of the points were taken by the Lockheed people, the 700-hour actual exposure at 10.3 suns and the 50-hour exposure at 12.7 suns; and the 1200-hour specimen

was exposed in our chamber. There was no inconsistency in the results from the two chambers for this material.

LIONEL BAILIN, Lockheed: I should like to take this opportunity to make an announcement for the Lockheed Research Laboratories. In the last 6 months, two new room-temperature-curing silicate paint systems with synthetic aluminum silicate and synthetic zirconium silicate combined with silicate binders have been developed. These offer some outstanding advantages in adhesion and properties with respect to heating. These materials should behave as well as or better than some of the silicates that were examined in the systems which you described. I think the one that appears the most promising is a zirconium silicate which is relatively simple to prepare and formulate. That particular sample did not get into the test series. Regarding the last question which involved the Vac-ion pump versus the oil diffusion pump, you cannot really distinguish between them. The Lockheed Vac-ion pumps are started with oil pumps, and it is extremely difficult, if not impossible, to keep all oil out of the system. The literature published by Varian and Ultek indicate this. It may be important in eventual comparison of effects in space with effects observed in laboratory simulation studies.

ARTHUR KATZ, Grumman Aircraft: That same point was mentioned last night in a private conversation with Dr. Klein who suggested the possibility of problems associated with roughing pump lubrication oil rather than with diffusion pump oil.

53. Effectiveness of Solar Radiation Shields for Thermal Control of Space Vehicles Subjected to Large Changes in Solar Energy

JOHN C. ARVESEN

NASA AMES RESEARCH CENTER, MOFFETT FIELD, CALIFORNIA

The effectiveness of a solar shield in providing thermal control of a Sun-oriented space vehicle traveling from the Earth to within 9 million miles (≈ 0.1 AU) from the Sun is studied. Experimental temperature changes of the shielded vehicle are compared with predicted values obtained from a previously developed radiative heat-transfer analysis. The capsule tested was conical in shape and the shield was a flat disk. The shield was placed at a given distance from the capsule and completely shaded the capsule from an infrared radiation source. The shield was heated by the source to a predetermined temperature representative of a certain distance from the Sun. The tests were conducted in a 4- by 5-foot vacuum chamber at a pressure level of less than 5×10^{-6} torr. The walls of the chamber were blackened and cooled with liquid nitrogen to simulate the thermal environment of space.

The temperature rise on the capsule resulting from an increase in shield temperature is shown to be a function of the radiation configuration factors between the shield and the capsule, the total hemispherical emittances of the shields and capsules, and the internally generated heat. The necessity of considering the angular absorptance characteristics of the capsule is also discussed. Experimental results indicate that with shields and with constant internal power, the change in capsule temperature can be held to about 10° F for a shield temperature increase of 1000° F. This shield temperature increase corresponds to an approach to within 9 million miles from the Sun with a reasonable shield configuration.

Spacecraft missions in the next decade will be directed toward closer approaches to the Sun than any approaches made up to the present. Programs currently planned include Extended Pioneer, Advanced Pioneer, and solar-probe missions. Temperature control of such vehicles may be especially difficult because of the extremely large variations in solar irradiance associated these missions. At the orbit of Venus, for example, the solar irradiance is approximately 1.9 solar constants (that is, 1.9 times the intensity at the Earth's distance from the Sun). For a mission to Mercury, the irradiance increases to about 6.6 solar constants. A feasibility study has been made (ref. 1)

which concludes that a solar probe which approaches to within 9 million miles from the Sun, or 0.1 AU, will be a probable future mission. For this mission, however, the solar irradiance would reach a level of over 100 solar constants.

Based on the requirements for the solar probe mission described in reference 1, an analysis was made (ref. 2) in which the concept of solar radiation shields was developed as a method of achieving satisfactory temperature control for a Sun-oriented capsule. This study indicated that in going from 1.0 to 0.1 AU, the temperature rise would be no more than 26° and 2° F, respectively, for conical capsules

with single and double radiation shields. This would compare with a temperature rise of hundreds to thousands of degrees, depending on surface properties, for an unshielded capsule. This significant reduction in capsule temperature rise with solar shields was based on an analysis which included some simplifying generalizations and assumptions. It was therefore necessary to substantiate the analytical results with experimentation. The purpose of this paper is to present the results to date of this experimental program and to show how these results compare with those obtained from the analysis of reference 2.

EXPERIMENTAL PROCEDURE

Because of the lack of a suitable source of solar radiation for duplicating the solar irradiance at 0.1 AU (100 solar constants), the solar shields used in the experiments were heated with infrared radiation. However, the resultant temperatures of the shields can be directly related to distance from the Sun with a minimum number of assumptions. The main problem in the analysis of shield-capsule configurations is the prediction of the radiation heat transfer between the shield and capsule and the resultant capsule temperature. Fortunately, this problem can be readily studied experimentally since the source used in heating the shields is immaterial.

Models

Tests were conducted on shield-capsule models having nearly the same geometry as the "solar-probe configuration" studied analytically in reference 2. A schematic drawing of the configuration studied is shown in figure 1 and

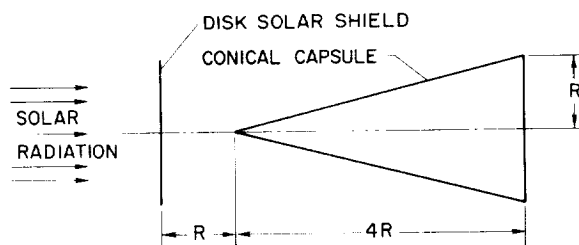


FIGURE 1.—Basic shield and capsule geometry.



FIGURE 2.—Photograph of capsule.

a photograph of a typical capsule model, with thermocouples and power leads attached, is shown in figure 2.

The conical-capsule models were 1 foot in length and 6 inches in diameter, with a resulting semiapex angle of about 14° . They were constructed of $\frac{1}{32}$ -inch-thick aluminum. Heat was generated internally by an electrical resistance heater. Conduction of heat to or from the capsule models through the heater power leads was minimized by the use of guard heaters at the same temperature as the capsule.

The shields were 6 inches in diameter (shield diameter = cone base diameter) and were constructed of $\frac{1}{16}$ -inch-thick aluminum.

In order to evaluate the effect of nondiffuse surface properties on the heat transfer between the shield and capsule, two completely different materials were tested. Figure 3 illustrates the

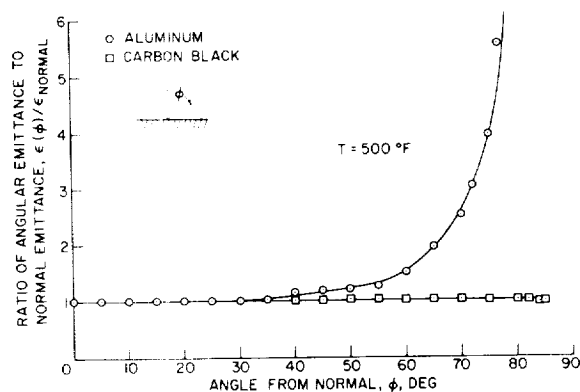


FIGURE 3.—Variation of emittance with viewing angle for carbon-black and aluminum surfaces.

experimentally determined differences in these materials at a temperature of 500° F. For one series of tests, the shield and capsule both had polished aluminum surfaces. The aluminum surface absorbs and emits radiation in a non-diffuse manner, as shown in the figure. (Directionally dependent emittance and absorptance properties are characteristic of polished metals; for example, see ref. 3.) At angles greater than about 50°, the emittance or absorptance of this surface can increase to many times its value at normal incidence.

In the second series of tests (square points), the shield and capsule were coated with a very diffuse carbon-black paint. This surface satisfies the assumption of diffuseness upon which the predicted radiation heat transfer is based.

Test Apparatus

A vacuum chamber 4 feet in diameter and 5 feet in length was used in the tests. Photo-

graphs of this chamber are shown in figure 4. The tests were conducted at a pressure of 5×10^{-6} torr. All convective heat transfer is, therefore, negligible.

A cold-wall assembly, consisting of a double-walled cylinder and two double-walled end sections, is located within the vacuum chamber. This assembly is cooled to -320° F by liquid nitrogen. The interior of the assembly has a black coating with an infrared absorptance of 0.94. The exterior is wrapped with an aluminized Mylar "superinsulation" to reduce the heat input from the vacuum-chamber walls to the cold-wall assembly. The working space within the chamber is 3 feet in diameter and 4 feet long.

The shields are heated to a uniform, predetermined temperature by infrared radiation from a two-element electrical radiative source. The back of this heater is surrounded by a liquid-nitrogen-cooled shroud to eliminate stray

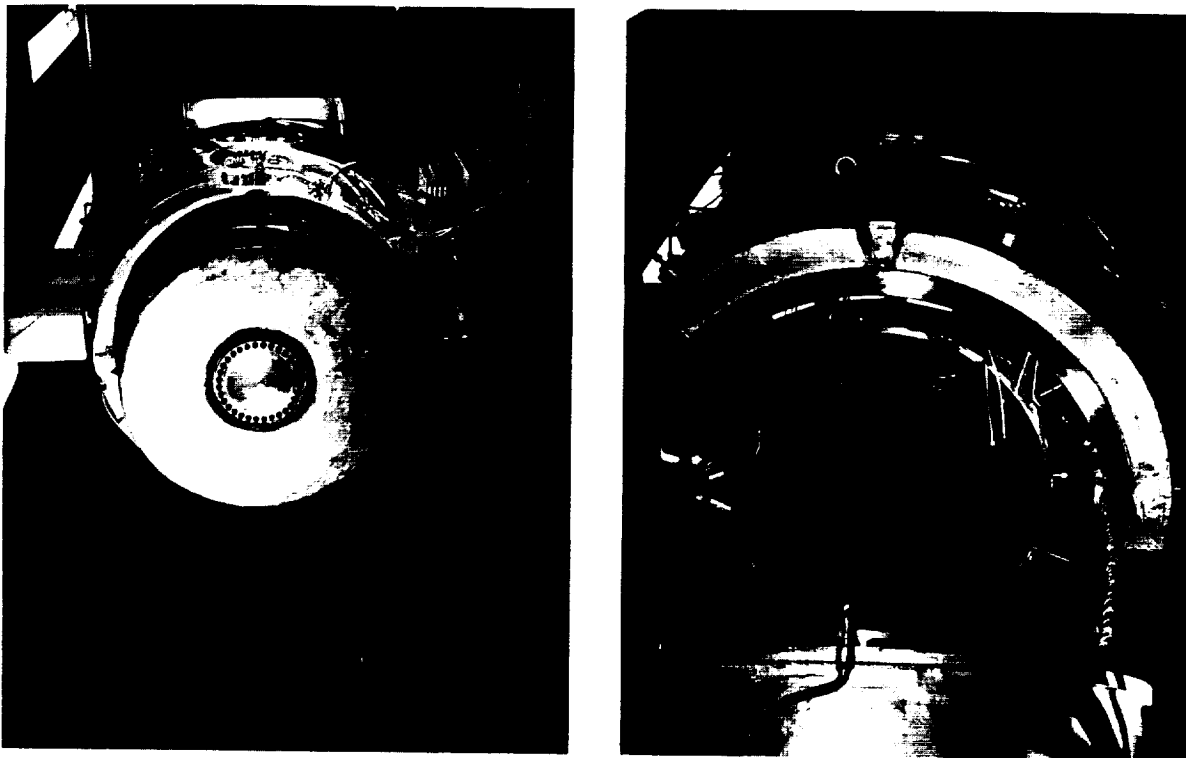


FIGURE 4.—*Photographs of space-environment vacuum chamber.*
(a) *Vacuum chamber.*
(b) *Interior of vacuum chamber; capsule installed.*

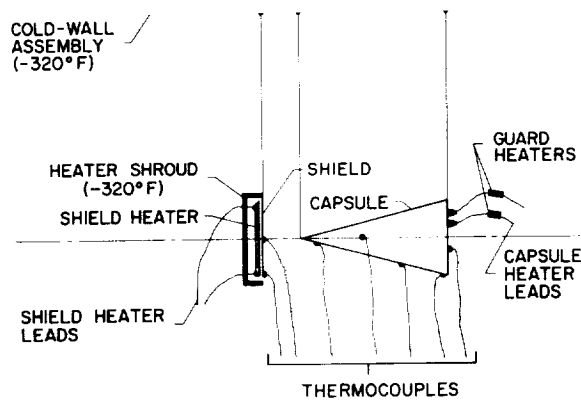


FIGURE 5.—Schematic of experimental test setup.

thermal radiation inside the cold walls due to radiation from the heater. A schematic diagram of a typical experimental test setup is shown in figure 5.

Auxiliary Equipment

Additional equipment was required to monitor the temperatures of the capsule and shield models, to supply and measure the capsule internal heat, and to determine the emittance of the aluminum and carbon-black surfaces of interest.

Temperatures on the models were measured by thermocouples located at various points on their surfaces. The thermocouple readings were recorded on a strip-chart recorder. In order to verify, within a reasonable time, that thermal equilibrium had been established, it was necessary to be able to recognize very small temperature changes. These changes were determined by nulling the thermocouple with a known voltage and amplifying the difference signal.

The electrical power to the resistance heaters within the capsules was supplied by a regulated d-c power supply. The power to the capsule was determined by measuring the voltage across the input terminals and the voltage drop across a known resistance in series with the leads.

Test Procedure

The total hemispherical emittance of each surface material was determined by a heat

balance on the unshielded capsule when heated internally to a uniform (within $\pm 2^\circ\text{F}$) temperature. The technique involved is the same as that presented in reference 4. The shield was then placed at a specified distance from the capsule and the capsule temperature was adjusted by its internal heater to approximately 70° or 80°F . The shield was next heated to a certain temperature and then held constant. The increase in temperature of the capsule was monitored and its temperature at equilibrium recorded. The temperature of the shield was increased in steps up to $\approx 980^\circ\text{F}$ and the corresponding equilibrium capsule temperatures were determined.

ANALYSIS

In this section, those equations from reference 2 which are pertinent for comparison with the experimental results are presented in simplified form. In addition, some discussion is given of those factors or parameters which contribute to the thermal balance of a capsule that is protected by a solar-radiation shield.

Unshielded Vehicles

For a vehicle in space, the only mode of heat transfer to the surroundings is by radiation from the outside skin. This radiation is governed by the Stefan-Boltzmann law, that is,

$$Q_{\text{radiated}} = \epsilon_c A_c \sigma T_c^4 \quad (1)$$

where

ϵ_c capsule emittance

A_c capsule surface area (including the area of the base)

T_c capsule temperature

σ Stefan-Boltzmann constant.

At thermal equilibrium

$$Q_{\text{absorbed}} = Q_{\text{radiated}}. \quad (2)$$

The heat absorbed by a vehicle surface comes from two sources—external radiation and internally generated heat. Thus

$$Q_{\text{absorbed}} = Q_{\text{external}} + Q_{\text{internal}}. \quad (3)$$

The external radiation absorbed when the sun is the only source is

$$Q_{external} = \alpha_s \frac{E}{r^2} A_x \quad (4)$$

where α_s is the solar absorptance of the vehicle surface, E/r^2 is the solar irradiance at a distance r from the Sun (E is the solar constant and r is in AU), and A_x is the projected surface area normal to direct solar radiation.

For the idealized case of uniform surface temperature, the heat balance at thermal equilibrium may be written as

$$\alpha_s \frac{E}{r^2} A_x + Q_i = \epsilon_c A_c \sigma T_c^4 \quad (5)$$

which, when solved for T_c , gives

$$T_c = \left(\frac{\alpha_s \frac{E}{r^2} A_x + Q_i}{\epsilon_c A_c \sigma} \right)^{1/4} = \left(\frac{\alpha_s \frac{E}{r^2} A_x}{\epsilon_c A_c \sigma} + \frac{Q_i}{\epsilon_c A_c \sigma} \right)^{1/4} \quad (6)$$

where $Q_i = Q_{internal}$.

Shielded Vehicles

A simple shield-capsule configuration, such as shown in figure 1, has been chosen to illustrate the degree of temperature control that can be achieved with solar radiation shields. The methods developed in reference 2 to analyze the radiation heat transfer and equilibrium temperatures for shielded capsules are involved and lengthy. Thus, only the pertinent expressions and results from this reference will be presented here.

For purposes of illustration, an expression for the temperature of a single shielded capsule as a function of the temperature of the shield is derived to show the relationships between the radiation heat-transfer parameters. For the configuration chosen, reflections between capsule and shield can be neglected.

For a shield of temperature T_1 , the radiation emitted from the shaded side (side 1b) is

$$Q_{radiated} = \epsilon_{1b} A_1 \sigma T_1^4 \quad (7)$$

The radiation from the shield that is incident upon the capsule is

$$Q_{incident} = F_{1b-c} \epsilon_{1b} A_1 \sigma T_1^4 \quad (8)$$

where F_{1b-c} is a radiation configuration factor defined as the fraction of the total radiation emitted from surface 1b that is incident upon the capsule (for the configuration studied $F_{1b-c} = 0.048$, as determined in ref. 2). The amount of this radiation that is absorbed by the capsule is

$$Q_{absorbed} = \alpha_c F_{1b-c} \epsilon_{1b} A_1 \sigma T_1^4 \quad (9)$$

where α_c is the fraction of the radiation incident upon the capsule that is absorbed. (α_c may be dependent upon the angle of incidence on the capsule of the radiation received from the shield, as shown in fig. 3.) The heat balance on the capsule is then

$$\alpha_c F_{1b-c} \epsilon_{1b} A_1 \sigma T_1^4 + Q_i = \epsilon_c A_c \sigma T_c^4 \quad (10)$$

The temperature of the capsule as a function of the shield temperature is, therefore, given by

$$T_c = \left(\frac{\alpha_c F_{1b-c} \epsilon_{1b} A_1 \sigma T_1^4 + Q_i}{\epsilon_c A_c \sigma} \right)^{1/4} \quad (11)$$

The shield temperature at distance r from the Sun is given by

$$T_1 = \left[\frac{\alpha_s \frac{E}{r^2}}{(\epsilon_{1a} + \epsilon_{1b}) \sigma} \right]^{1/4} \quad (12)$$

where the subscript 1a refers to the sunlit side. Thus, when any practically attainable values for the solar absorptance and emittance of the sunlit side of the shield are specified, equation (12) will relate the shield temperatures in the experiments to particular distances from the Sun. Correspondingly, the capsule temperature T_c can be related to distance from the Sun by equation (11).

CALCULATED RESULTS

The calculated temperatures of unshielded vehicles which approach the Sun are first discussed. The calculated effect of placing a disk shield between the vehicle and the incident solar radiation is next presented. The results of these calculations will be compared with the experimental results in the next section.

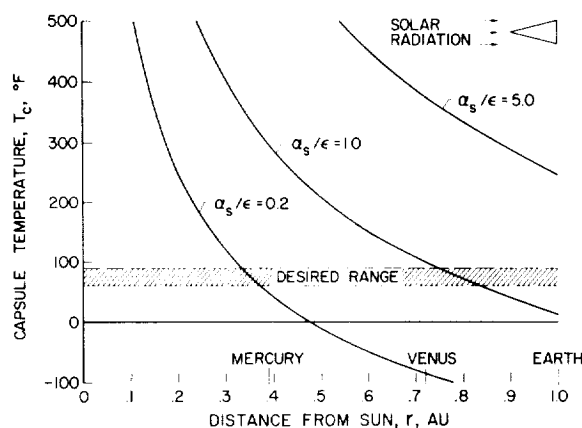


FIGURE 6.—Variation of capsule temperature with distance from the Sun for an unshielded vehicle; no internal heat.

Unshielded Vehicles

The problem of thermal control of an unshielded vehicle during an approach to the Sun is illustrated in figure 6. In this figure, the temperature of a conical capsule (low ratio of A_x/A_c) is given as a function of distance from the Sun for various ratios of solar absorptance to emittance (α_s/ϵ). Also shown in the figure is an arbitrary temperature range of 60° to 90° F within which the vehicle should probably be maintained from an instrumentation and equipment standpoint. Even for the lowest α_s/ϵ ratio of 0.2 (which is near the minimum achievable with engineering materials), the temperature becomes undesirably high when the distance from the Sun is less than 0.33 AU. For all values of α_s/ϵ the temperature of the capsule increases rapidly as the distance from the Sun is decreased.

Shielded Vehicles

Theoretical capsule temperatures as a function of distance from the Sun were calculated from the results of reference 2 and the equations given in the analysis section. These calculations are presented in figure 7 for an aluminum shield and capsule.

The amount of heat that is radiated from the shield back towards the capsule is directly dependent upon the solar absorptance and emittance of the side facing the Sun. Since it

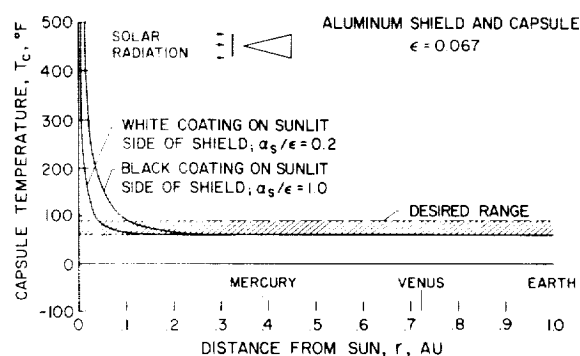


FIGURE 7.—Variation of theoretical capsule temperature with distance from the Sun (predicted by analysis in ref. 2).

may not be possible to expect the properties of the sunlit side of the shield to be stable for any period of time at an intensity level of 100 or more solar constants, the effects of degradation of this surface must be considered. The two curves shown in figure 7 indicate the predicted change in temperature of the shielded capsule for both a low α_s/ϵ white coating on the sunlit side and a coating that has degraded to a black surface. For both of these curves, the capsule is assumed to have a constant internal heat load that maintains its temperature at 60° F at the Earth's distance from the Sun. If the white coating remains stable, the vehicle can approach to within 0.04 AU without exceeding a 30° F rise in temperature. Even if the sunlit side of the shield degrades badly, the vehicle can still approach to within 0.1 AU before overheating. By comparison, an unshielded vehicle at this distance from the Sun would increase in temperature nearly 1000° F if its surface degraded from an α_s/ϵ of 0.2 to an α_s/ϵ of 1.0. Even finer temperature control or a closer approach to the Sun is possible by the use of multiple shields.

The temperature of the shield will increase at a much higher rate than the capsule, as shown in figure 8. Here, the shield temperatures corresponding to the capsule temperatures in figure 7 are shown for the white and black coatings on the sunlit side. The advantage of maintaining a stable white coating is clearly seen. The aluminum shield considered here would vaporize away at about 1000° F, but

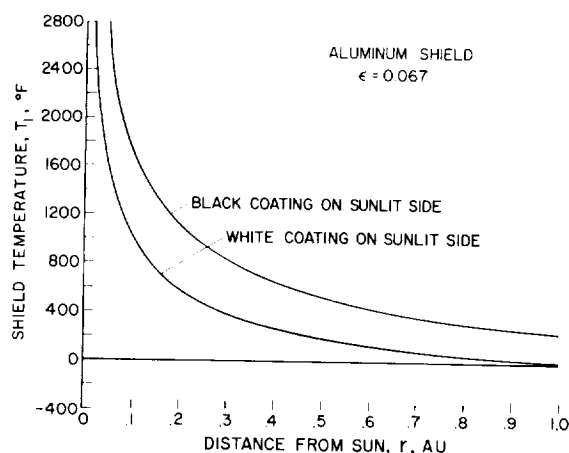


FIGURE 8.—Variation of theoretical shield temperature with distance from the Sun.

materials are available that can be used at much higher temperatures. It should be emphasized that, for given shield properties, the shield temperature may be directly related to distance from the Sun. As will be shown, this fact is utilized in the evaluation of the experimental results in terms of a solar probe mission.

TEST RESULTS AND DISCUSSION

Capsule temperatures as a function of shield temperature were determined experimentally for the two configurations tested. The total hemispherical emittance of each surface material was determined by a heat balance on the unshielded capsule model. This measured emittance was used as the basis for calculating capsule temperatures. These calculated temperatures were then compared with the experimental values.

Black Shield and Black Capsule

Experimentally determined capsule temperatures at various shield temperatures for the shield-capsule model with diffuse, black surfaces are shown in figure 9. As the temperature of the shield was increased from -145°F to 950°F , the temperature of the capsule increased from 73° to 116°F as a result of absorbed radiation from the shield. The experimental and predicted temperature change agreed within 10 percent, indicating that the mathematical techniques of the analysis are satis-

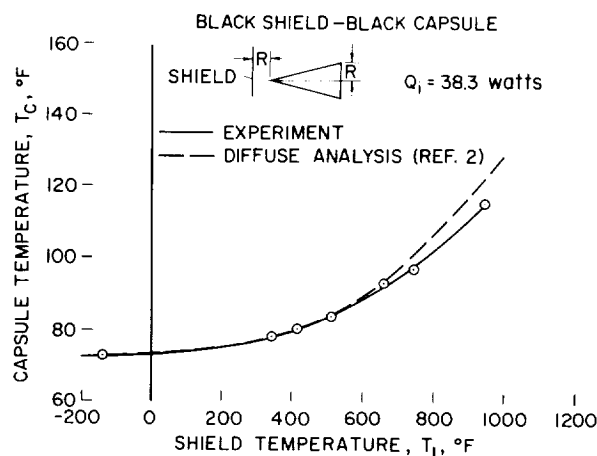


FIGURE 9.—Variation of capsule temperature with shield temperature; black shield and black capsule.

factory and that the assumptions used are justified for the configuration with carbon-black surfaces.

Aluminum Shield and Aluminum Capsule

Results for the aluminum configuration are shown in figure 10. Increasing the shield temperature to 980°F increased the capsule temperature from 81° to 91°F . However, in this case, the calculations predicted only a 4°F increase for the same change in shield temperature. The discrepancy is not excessively large (6°F), although it amounts to

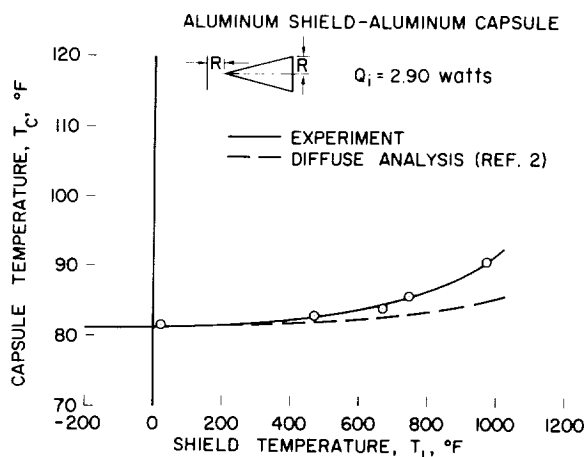


FIGURE 10.—Variation of capsule temperature with shield temperature; aluminum shield and aluminum capsule.

an error of 150 percent in the prediction of the change in capsule temperature.

The calculated radiation configuration factor between the shield and capsule was shown to be correct by the closer agreement between theory and experiment for the diffuse, black configuration. The total hemispherical emittances of the aluminum shield and the aluminum capsule were verified by radiometric measurements to be very nearly the same (as was assumed). It was therefore concluded that the probable cause of the discrepancy was the nondiffuse characteristics of the aluminum surfaces. In the calculations, the absorptance of the aluminum capsule was assumed to equal its measured total hemispherical emittance ($\alpha_c = \epsilon_c = 0.067$). As was shown in figure 3, however, the aluminum surface exhibits a very strong absorptance at high angles of incidence (viewing angle $> 50^\circ$). For the shield-capsule geometry studied, this angular dependence will mean that the actual absorptance of the capsule for radiation from the shield could be much higher than the total hemispherical emittance measured, since the angle of incidence for the capsule is very high. To make a quantitative correction for nondiffuse properties would be very difficult, but it is clear that the deviation in capsule temperature from that predicted is consistent with the differences in angular emittance (or absorptance) noted.

Variation in Capsule Temperature with Distance from the Sun

Experimental values for the change in capsule temperature corresponding to specific changes in shield temperature have now been obtained. These experimental results may be related to an actual solar probe mission when it is assumed that the temperature of the disk shield can be determined (by eq. (12)) with reasonable accuracy for any distance from the Sun. These results are shown in figure 11 for the aluminum shield and capsule. In this figure, the shield is again assumed to have a stable white coating in its sunlit side. The shield temperatures in the experiment were related to certain distances from the Sun, as

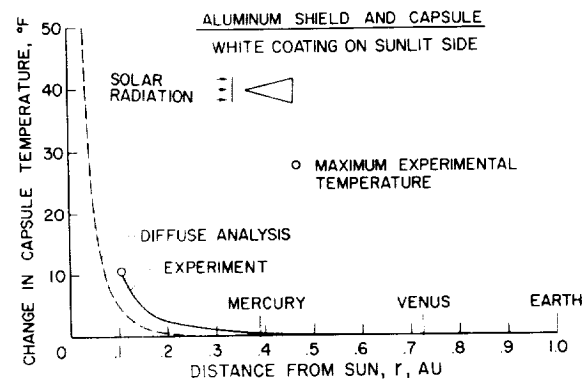


FIGURE 11.—Variation of predicted capsule temperature with distance from the Sun, based on experimentally determined data.

shown in figure 8. The corresponding capsule temperatures are then determined from the shield temperatures by means of the experimental results. Indications are that the configuration studied can approach to within 0.1 astronomical unit without reaching excessively high temperatures. Also, even though the change in capsule temperature is more than twice as high as predicted, the actual rise is well within the allowable range.

CONCLUDING REMARKS

The results of this experimental program have verified that a solar radiation shield is an effective means of minimizing thermal control problems for vehicles traveling very close to the Sun. For vehicles with diffuse surface properties, the change in capsule temperature may be predicted with reasonable accuracy. If the surfaces are not diffuse, a more complete analysis or subsequent experimental testing may be required.

REFERENCES

1. HALL, CHARLES F., NOTHWANG, GEORGE J., and HORNBY, HAROLD: A Feasibility Study of Solar Probes. Paper No. 62-21, Inst. Aerospace Sci., Jan. 1962.
2. NOTHWANG, GEORGE J., ARVESEN, JOHN C., and HAMAKER, FRANK M.: Analysis of Solar-Radiation Shields for Temperature Control of Space Vehicles Subjected to Large Changes in Solar Energy. NASA TN D-1209, 1962.
3. ANDERSON, DONALD L., and NOTHWANG, GEORGE J.:

Effects of Sputtering with Hydrogen Ions on Total Hemispherical Emittance of Several Metallic Surfaces. NASA TN D-1646, 1963.

4. ECKERT, E. R. G., and DRAKE, ROBERT M., JR.: Heat and Mass Transfer. Second ed., McGraw-Hill Book Co., Inc., 1959, p. 377.

DISCUSSION

GARY GORDON, RCA: I think that it should be pointed out that at 1/10 AU, the size of the Sun's disk will make the complete shadow end at about 5 radii beyond your disk. While this does not affect the general principles you have been discussing, I think it would affect the numbers. In particular, I would think that you would put the apex of your spacecraft

away from the shadowing disk rather than towards it.

ARVESEN: We have considered this. However, if the capsule is turned around the low configuration factor between shield and capsule is lost. Increasing the area of the shield will not increase the predicted change in capsule temperature by more than, say, 5° for that last configuration.

54. Effect of Absorptance-Emittance Ratio in the Storage of Cryogenic Propellants in Space¹

C. H. LIEBERT AND R. R. HIBBARD

NASA LEWIS RESEARCH CENTER, CLEVELAND, OHIO

An analysis was performed to determine the effectiveness of spectrally selective surfaces with $\alpha/\epsilon < 1.0$ in reducing the heat transfer through the insulation of cryogenic-propellant tanks located in deep space. The analysis considered the effects of surface coatings with α/ϵ ratios varying from 0.1 to 1.0 applied to the external surfaces of either bulk insulation or multifoil insulation. Results were obtained in terms of the heat-transfer rate to two cryogenic propellants, liquid hydrogen and liquid oxygen, when stored at the Mercury, Earth, and Mars orbital distances from the Sun.

The results show that, with good insulation and correspondingly low heat-transfer rate to the propellant, the α/ϵ ratio is a reasonable criterion of merit for these coatings, but that at larger heat-transfer rates consideration of ϵ (or α) is necessary. It was observed that selective coatings with $\alpha/\epsilon = 0.1$ on a given amount of bulk insulation material can reduce the heat-transfer rate to 40 to 55 percent of the rate with gray coatings. Or, for equivalent rates, a reduction in bulk-insulation-material thickness of about one-half is possible with high-quality selective coatings ($\alpha/\epsilon = 0.1$) as compared with the insulation needed for gray coatings. Larger benefits may be achieved from selective finishes painted on foils, as the analysis shows that the heat-transfer rate for surfaces having an α/ϵ ratio of 0.1 may be only about 10 percent of that for gray surfaces; or, for a given heat-transfer rate, the use of approximately 10 times fewer foils of emittance 0.05 is possible when spectrally selective surfaces are employed.

Cryogenic-propellant systems, in general, give higher specific impulses and greater rocket-vehicle performances than do storable propellants. This is true both for chemical rockets, where, for example, both hydrogen and oxygen may be used (as in the upper stages of the Saturn vehicle) and for nuclear-driven systems, where hydrogen is the only working fluid being considered. However, the equilibrium temperatures of space vehicles having black or gray surfaces are well above those that can be used for storing cryogenics, even at a distance of several astronomical units from the Sun. Therefore, any mission that requires the storage in space of cryogenic propellants also

requires consideration of the rate at which propellants will be lost through vaporization and the types and amounts of insulation needed to keep these losses within bounds.

Smolak, Knoll, and Wallner (ref. 1) have made such a study for a space vehicle using various types and thicknesses of insulation. They show, for example, that the loss of liquid hydrogen can be kept low enough to permit a manned mission to Mars if sufficient numbers of thin low-emittance foils are used. Low-density powders and multiple radiation shields, while yielding low loss rates if used in sufficient thickness or numbers, are less attractive. However, only gray external surfaces, that is, those having $\alpha/\epsilon = 1.0$, were considered in reference 1. Adelberg (ref. 2), Burry (ref. 3),

¹ See also Paper 4.

and Hibbard (ref. 4) have shown that spectrally selective surfaces having $\alpha/\epsilon < 1.0$ can give equilibrium temperatures in sunlight that are well below those obtained with gray surfaces. These lower temperatures suggest that the use of selective coatings on insulated tanks might result in reduced rates of vaporization loss, or might permit the use of lighter insulation with equal losses. Therefore, an analysis was made to determine the advantages of spectrally selective coatings ($\alpha/\epsilon < 1.0$) relative to gray surfaces.

While Smolak et al. made overall heat-balance estimates on a realistic configuration exposed to solar radiation, Earth-reflected radiation, and Earth thermal radiation, the absorption of solar radiation is by far the most important and is the only factor to consider in interplanetary flight. The present study was limited to plane insulated surfaces normal to the solar radiation, and results are given in terms of the heat-transfer rate to two cryogenic propellants of current interest, hydrogen and oxygen, when stored at the Mercury, Earth, and Mars orbital distances from the Sun.

PROCEDURE

Opaque solar reflectors were considered to be applied to the external surfaces of two of the types of insulation studied in reference 1, that is, bulk insulation materials and closely spaced reflective surfaces (foils). These two types of insulation were examined because of their differences in modes of heat transfer. The heat transfer through the bulk insulation was assumed to be entirely by conduction; and the heat transfer through the foils was assumed to be entirely by radiation. Probably neither type of insulation actually transfers heat purely by one mode. However, calculations were made only for these ideal limiting cases, and only heat inputs from solar radiation normal to surfaces characterized by an α/ϵ ratio of 1.0 or less were considered.

If C is the solar flux in terms of power per unit area and if α is the surface absorptance to this flux, the heat absorbed per unit surface area is $C\alpha$; the balance of the flux is reflected away. At equilibrium, the heat absorbed by

the surface minus that reradiated to space is equal to the heat-transfer rate through the insulation. The heat balance for bulk insulation with heat transfer only by conduction may be expressed by the following equation:

$$C(\alpha - \epsilon)\sigma T_1^4 = \frac{k}{x}(T_1 - T_2) \quad (1)$$

where

- C solar flux, w/cm²
- k thermal conductivity of insulation material, w/(cm²)(°K)/cm
- T_1 external surface temperature, °K
- T_2 internal sink temperature, °K
- x thickness of insulation material, cm
- α absorptance of external surface to solar radiation
- ϵ total emittance of external surface
- σ Stefan-Boltzmann constant, w/(cm²)(°K⁴)

For multifoil systems, where the internal heat transfer is by radiation alone, the following equation was used:

$$C(\alpha - \epsilon)\sigma T_1^4 = \frac{\sigma(T_1^4 - T_2^4)}{(N+1)\left(\frac{2}{\epsilon^*} - 1\right)} \quad (2a)$$

where

- N number of foils placed between external surface and surface bounding sink
- ϵ^* emittance (gray) of foils

The denominator of the third term in equation (2a) defines the quality of the insulation.

Let $z \equiv (N+1)\left(\frac{2}{\epsilon^*} - 1\right)$, which is a function of the number and emittance of the foils. Then

$$C(\alpha - \epsilon)\sigma T_1^4 = \frac{\sigma(T_1^4 - T_2^4)}{z} \quad (2b)$$

Solutions of equation (1) for T_1 were calculated by trial and error for assumed values of C , α , ϵ , k/x , and T_2 . Values of T_1 in equation (2b) were obtained directly for various values of C , α , ϵ , z , and T_2 . Solutions of both equations were obtained for: (1) C equal to 0.059, 0.135, and 0.92 w/cm², corresponding to the

solar fluxes at the Mars, Earth, and Mercury orbital distances, (2) α/ϵ ranging from 0.1 to 1.0, and ϵ ranging from 0.1 to 1.0, and (3) T_2 equal to 20° and 90° K, corresponding approximately to the normal boiling points of hydrogen and oxygen. It is not necessary to consider the effects of conductance and thickness for bulk insulation separately, since the parameter k/x describes the overall quality of the insulating blanket. This parameter was varied from 10^{-6} to 10^{-7} w/(cm²)(°K). The parameter z was varied from 20 to 3000. These variations covered a range of heat-transfer rates from about 10^{-2} to 10^{-5} w/cm². Calculations were not performed for rates greater than 10^{-2} w/cm² because these rates are prohibitively high for most storage applications (ref. 1). Calculations were not made for rates less than 10^{-5} w/cm² because the data presented herein can be linearly extrapolated to lower values of heat-transfer rate. Also, calculations for this range are very easily made, as will be shown. After T_1 was determined by solving equations (1) and (2b), the heat-transfer rate through the insulation, in watts per square centimeter, was calculated. The α/ϵ ratio was the principal variable studied, since this ratio is a measure of the spectral selectivity of the surface. The results of these calculations are presented in the following section.

RESULTS

Spectrally Selective Surfaces on Bulk Insulation Materials

Figure 1 presents the variations with α/ϵ of the heat-transfer rate through bulk insulation materials for five values of k/x , several values of ϵ , the three orbital distances from the Sun, and sink temperatures of 20° and 90° K. Figure 1 shows that the rate is always less for spectrally selective surfaces ($\alpha/\epsilon < 1.0$) than for black or gray surfaces ($\alpha/\epsilon = 1.0$).

In addition to the general result that the heat-transfer rate always decreases with decreasing α/ϵ ratio, the independent effect of ϵ (or α) on the rate must be considered, since a given α/ϵ ratio can be achieved with different values of ϵ ; for example, $\alpha/\epsilon = 0.5$ both for $\alpha = 0.25$, $\epsilon = 0.5$ and for $\alpha = 0.125$, $\epsilon = 0.25$. The

heat balance equations (1) and (2b) show that this independent effect will become less significant as the insulation quality improves or as the heat-transfer rate decreases. Consider the terms on the right side of equations (1) and (2b). As lower values of the variable k/x or higher values of the variable z are assumed, the heat-transfer rate will eventually become negligible compared with the heat absorbed and reradiated by the coated surface. For this condition, equation (1) or (2b) may be written approximately as

$$T_1 \cong \left(\frac{C\alpha}{\sigma\epsilon} \right)^{0.25} \quad (3)$$

The validity range of this approximation can be seen, for example, in the Earth curves of figure 1(a), where $C = 0.135$ w/cm² and $T_2 = 20^\circ$ K. For a relatively poor quality of insulation, characterized by $k/x = 10^{-5}$ w/(cm²)(°K) and the fairly substantial heat-transfer rates shown, the calculations show the independent effect of ϵ as indicated by the separate curves drawn for $\epsilon = 1.0$, 0.3, and 0.2. This effect diminishes as the quality of insulation improves, so that at $k/x = 10^{-6}$ w/(cm²)(°K) a narrow band, shown at low values of α/ϵ , comprises the results for all values of ϵ from 0.1 to 1.0. At $k/x = 10^{-7}$ w/(cm²)(°K), a single curve can be drawn for these values of ϵ . In general, all the single-line approximations shown in figure 1 are correct to ± 4 percent or better at $k/x = 10^{-6}$ w/(cm²)(°K) and to ± 1 percent or better at $k/x = 10^{-7}$ w/(cm²)(°K). At $k/x \leq 10^{-7}$ w/(cm²)(°K), surface temperatures can be calculated by equation (3), for the range of ϵ values considered, with inaccuracies no greater than 1 percent.

As previously stated, the use of spectrally selective coatings on the surface of a given amount of bulk insulation material can reduce the heat-transfer rate by amounts that vary primarily with the α/ϵ ratio and only slightly with the individual values of α and ϵ . Selective coatings with $\alpha/\epsilon = 0.1$ reduce the heat-transfer rates to 40 to 55 percent of the values obtained with gray surfaces, where the precise value depends on C , T_2 , and k/x .

Spectral selectivity can also reduce the

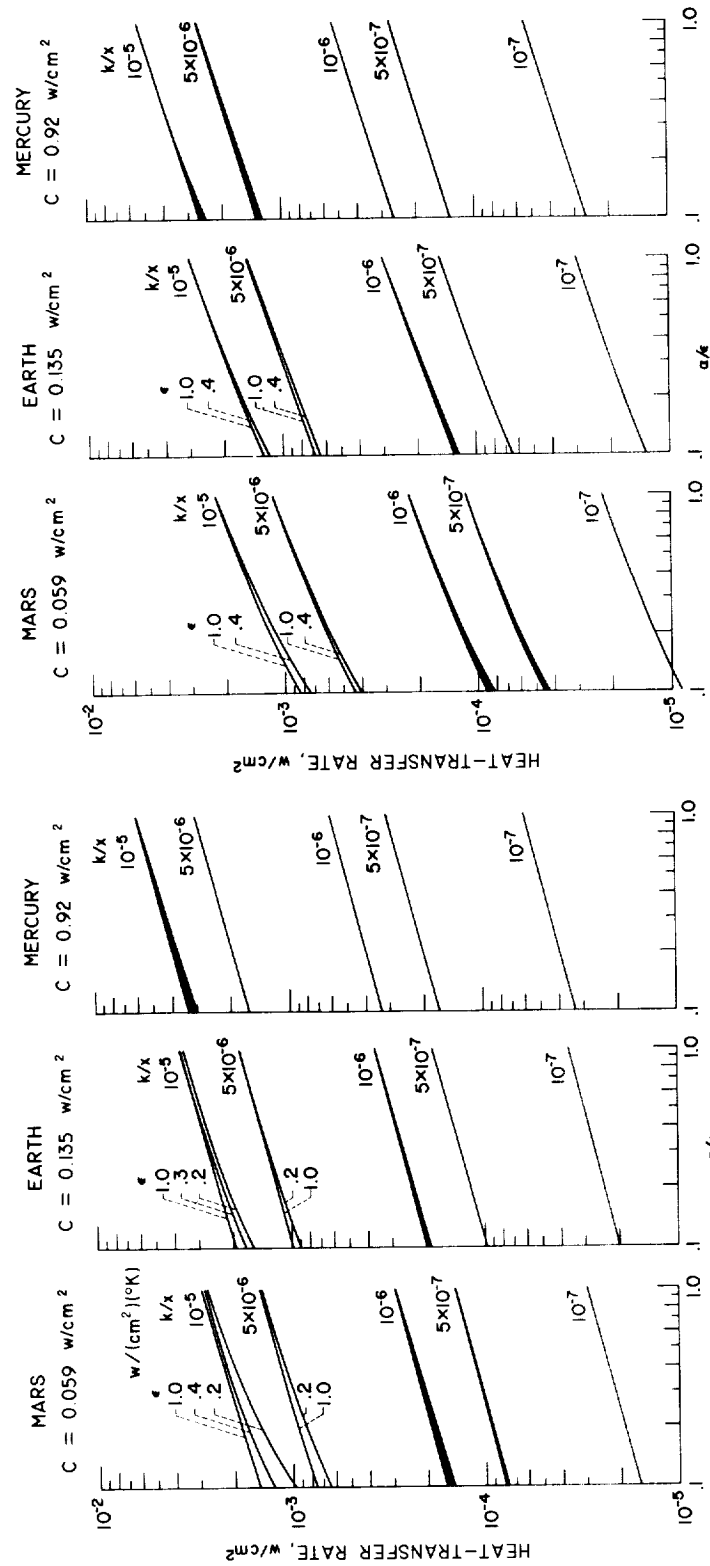


FIGURE 1.—Heat-transfer rate through bulk insulation. Curves for which ϵ is not indicated are for $0.1 < \epsilon < 1.0$.

- (a) Internal sink temperature, 20° K.
 (b) Internal sink temperature, 90° K.

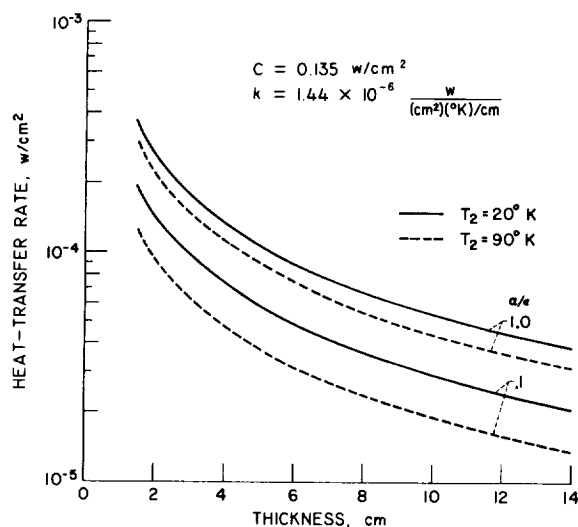


FIGURE 2.—Variation of heat-transfer rate with bulk insulation thickness for selective and gray coatings.

thickness of insulation required to keep the heat-transfer rate at a given value. This effect is shown in figure 2 where the rate at 1 AU is shown as a function of the thickness of a bulk insulation material having a thermal conductivity k of $1.44 \times 10^{-6} \text{ w}/(\text{cm}^2)(^\circ\text{K})/\text{cm}$. This value of k is about the lowest achieved to date for this type of insulation (ref. 1). The curves in figure 2 are for α/ϵ ratios of 0.1 and 1.0 and for heat sinks at 20° and 90° K . This figure shows, for example, that if a heat-transfer rate of $5 \times 10^{-5} \text{ w/cm}^2$ into a liquid-hydrogen tank is permissible, then 10.8 cm of insulation is required with a gray surface and only 5.8 cm with a spectrally selective surface having $\alpha/\epsilon = 0.1$. In general, insulation thicknesses can be reduced by about one-half if surfaces having $\alpha/\epsilon = 0.1$ can be achieved.

Spectrally Selective Surfaces on Multifoils

Figure 3 presents the heat-transfer rate through multilayered foils plotted against α/ϵ , for a range of values of the parameter z and for two values of ϵ . The orbital distances from the Sun and the sink temperatures are the same as those considered for bulk insulation materials. A comparison of heat-transfer rates through the multifoils for α/ϵ values of 0.1 and 1.0 for all values of z shows that the rate can be decreased tenfold when spectrally selective

surfaces are employed and that the rate is almost invariant with sink temperature.

As in the case of spectrally selective surfaces on bulk insulation materials, there is an independent effect of ϵ (or α) on the heat-transfer rate. As figure 3 shows, this effect is not significant for z equal to 100 or more. Thus, for z greater than 100, a single-line approximation may be drawn for heat-transfer rate against α/ϵ over a range of ϵ from 0.1 to 1.0; such a line is correct to within ± 4 percent at $z=100$ and to within ± 1 percent at $z=1000$. For the higher heat-transfer rates ($z=20$), figure 3 shows that the rate is appreciably dependent on ϵ as well as on α/ϵ .

Figure 4 shows the variation of heat-transfer rate with z for selective ($\alpha/\epsilon=0.1$) and non-selective coatings on foils at 1 AU for ϵ between 0.1 and 1.0 and a sink temperature of 20° K . Also shown at the corresponding values of z are the numbers of foils required for an assumed foil emittance (ϵ^*) equal to 0.05. Figure 4 indicates that a selective surface characterized by $\alpha/\epsilon=0.1$ will allow a tenfold decrease in z and approximately a tenfold decrease in the number of foils for equivalent heat-transfer rates (with a corresponding tenfold decrease in foil composite thickness (ref. 1)).

Practical Considerations

The data shown to this point have all been the results of purely analytical considerations and calculations. The data have indicated the benefits that might be derived in coating tank surfaces with spectrally selective finishes; α/ϵ values between 0.1 and 1.0 have been used.

The value of $\alpha/\epsilon=0.1$ used in these calculations as a lower limit is recognized as lower than that which can be obtained with currently available coatings. Snoddy and Miller² indicate that values of α/ϵ between 0.20 and 0.25 are representative of that which can be practically attained. The calculations herein show that coatings of this quality can reduce to about 60 percent the heat-transfer rate through a given thickness of good bulk insulation and reduce to about 20 percent the rate through a multifoil system as compared with gray surfaces ($\alpha/\epsilon=$

² See Paper 48.

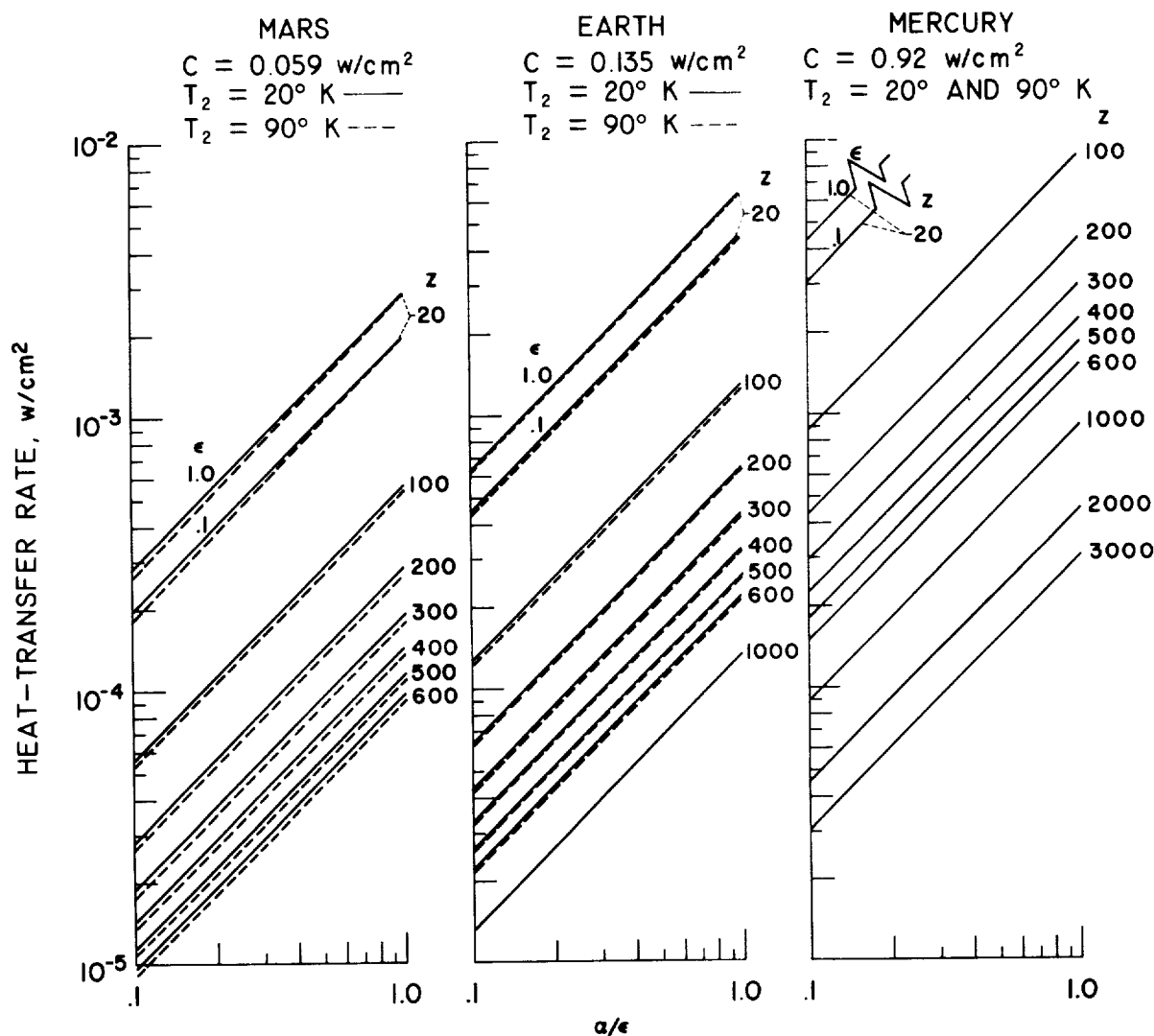


FIGURE 3.—Heat-transfer rate through multifoils. Curves for which ϵ is not indicated are for $0.1 < \epsilon < 1.0$.

1.0). Or, as previously indicated, less insulation can be used for a given heat-transfer rate.

An even greater saving in heat-transfer rate is indicated if the previous comparison is made between the available selective coatings and the uncoated metallic substrates upon which the coatings are likely to be applied. Metallic substrates have α/ϵ values as high as 3.0 or greater. For purposes of rough comparison, assume that α/ϵ is 3.0 for these materials. Then, an approximate extrapolation of the results contained herein indicates that coatings with $\alpha/\epsilon=0.2$ can reduce to about 45 percent

the heat-transfer rate through bulk insulation sealed with the metal discussed or can reduce to about 7 percent the heat-transfer rate through a multifoil system.

CONCLUSIONS

The analysis has shown that the heat transfer through the insulation of cryogenic-propellant tanks located in deep space can be substantially reduced when coatings with low α/ϵ , rather than gray coatings, are applied to the external surface of the insulation.

It was found that the heat-transfer rate into

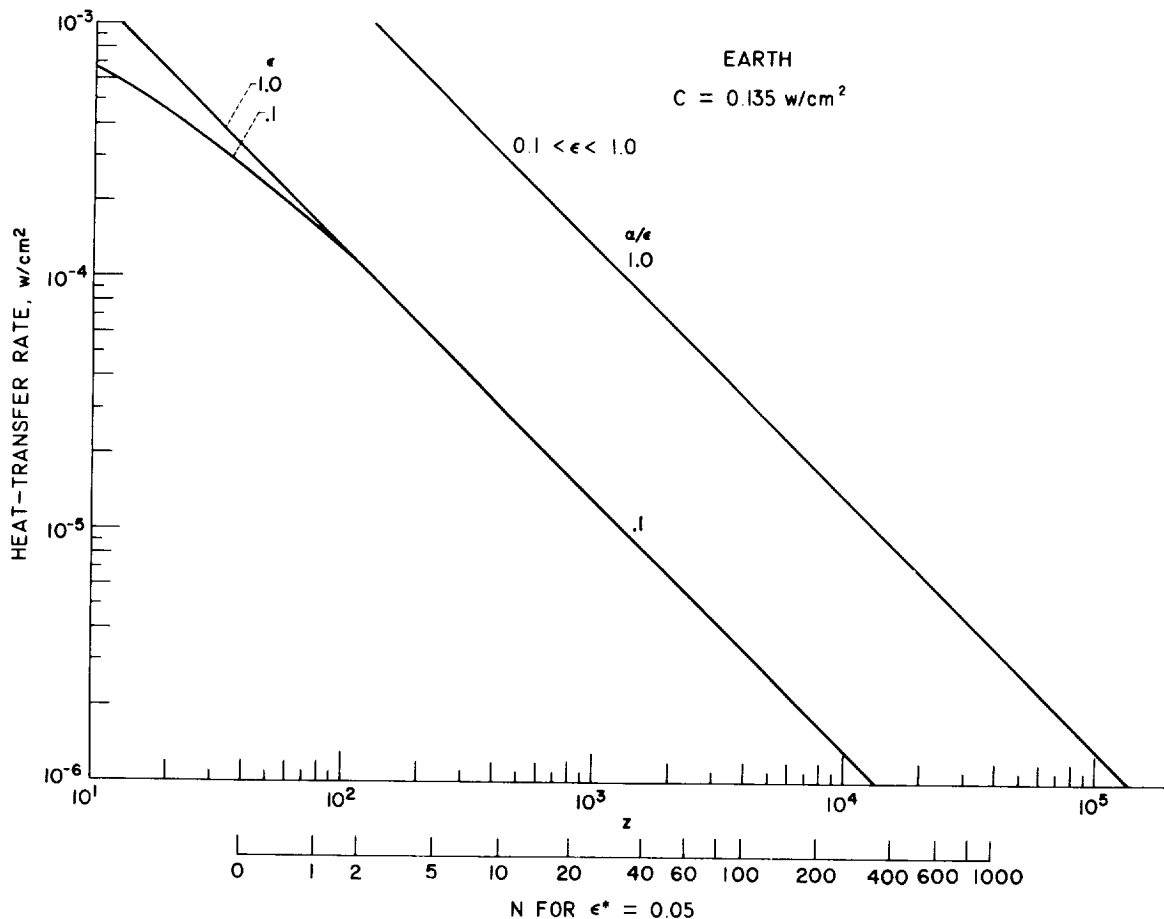


FIGURE 4.—Variation of heat-transfer rate with z and number of foils for selective and gray coatings. Internal sink temperature, 20°K .

stored cryogenic hydrogen or oxygen varies primarily with the α/ϵ ratio and only slightly with the individual values of α or ϵ when sufficiently good insulation is used and low heat-transfer rates are obtained. The heat-transfer rate is also dependent on the distance from the Sun, the ratio of thermal conductivity to thickness for bulk insulation, and the number of foils and their internal emittance for multifoil insulation.

Currently available spectrally selective coatings painted on the external surfaces of insulation materials can reduce to about 60 percent the heat-transfer rate through good bulk insulation and to about 20 percent the rate through a multifoil system, as compared with

the rates when gray paints are used on these insulations.

REFERENCES

1. SMOLAK, GEORGE R., KNOLL, RICHARD H., and WALLNER, LEWIS E.: Analysis of Thermal-Protection Systems for Space-Vehicle Cryogenic-Propellant Tanks. NASA TR R-130, 1962.
2. ADELBERG, M.: Storage of Cryogenic Fluids in Space. Paper 63-278, AIAA, 1963. (See also Space Tech. Labs., Inc., 1962.)
3. BURRY, ROGER: Liquid Propellant Storage in Earth Satellite Orbits. Rocketdyne, North Am. Aviation, Inc., 1960.
4. HIBBARD, R. R.: Equilibrium Temperatures of Ideal Spectrally Selective Surfaces. Solar Energy, vol. V, no. 4, Oct.-Dec. 1961, pp. 129-132.

DISCUSSION

GARY GORDON, RCA: It is easy to calculate the heat transfer through multifoils containing 1000 layers—

the theory is very simple. In our experiments, however, we found that when the number of foils exceeds

some value between 10 and 100, heat transfer by way of the contacts through the foils is predominant and additional foils do not seem to make any difference. I would be interested in knowing whether others have observed this same limitation.

UNIDENTIFIED: We, also, have found that conduction effects take over. I have an additional question. With regard to long term storage of the pro-

pellants in a zero-gravity environment, have you looked into the effects of stratification of the propellants and an increase in the propellant temperature adjacent to the tank wall itself?

LIEBERT: Lewis Research Center is looking into just this sort of thing—boiling and stratification effects at zero gravity. Several groups at Lewis are doing experimental work in this field.

55. Thermal Sensor Design for Glide Reentry Vehicles

F. S. BRUNSCHWIG, G. E. KOCH, AND J. K. WILHELM

THE BOEING COMPANY, SEATTLE, WASH.

Thermal sensors containing thermocouples for the measurement of surface temperature and the impinging heat-flux on glide reentry vehicles such as Asset and the X-20 have been developed. Data for these sensors obtained by heating in plasma, furnace, and rocket exhaust are presented, together with a discussion of the thermal and electrical phenomena involved. Experience with the design of aerodynamic heat-flux sensors has led to the interpretation of the measured temperatures by means of the heat transfer differential equation to obtain the incident aerodynamic heat-flux with better accuracy than direct heat-flux instrumentation. A digital computer program establishes surface temperature and computes aerodynamic heat-flux from temperature data.

During flight tests of a glide reentry vehicle, it is necessary to define quantitatively the structural environment as a function of time during boost and reentry. Two significant quantities requiring measurement are structural surface temperature and the incident aerodynamic heat-flux, which is a function of velocity, air density, altitude, and vehicle attitude. Heat transfer occurs by molecular momentum exchange at the glider surface, with less than 1 percent of the heating being due to radiation from excited molecular species to the surface. Optimized vehicular design results in more than three-quarters of the aerodynamic heating being reradiated from the vehicle surface to free space. The surface temperature to be measured without disturbing the quasi-steady-state isotherms with the measuring instrument is that temperature occurring locally at the surface. This surface temperature is not, in general, at radiation-equilibrium temperature because the surface has not had sufficient time to come to radiation equilibrium.

One design criterion is that the installation of sensors must not perturb the surface temperature. However, there are other factors,

such as material availability, chemical reactions, and physical environment, to be considered. Expected surface temperatures of the Asset and X-20 flight regime are in excess of 3000° F. The high temperatures cause the greatest change in the vehicle material properties. Therefore, the primary range of interest is 2000° F to 4000° F. Materials for sensor usage which will survive these temperatures without melting are subject to recrystallization and chemical reactions (table I). For example, the refractory metals, tungsten (W), molybdenum (Mo), tantalum (Ta), and rhenium (Re), require coatings of silicides or other materials to resist oxidation. The noble metals, platinum (Pt), rhodium (Rh), and iridium (Ir), form low-melting-temperature eutectics with refractory metals and other impurities. The insulating oxides, alumina (Al_2O_3), magnesia (MgO), beryllia (BeO), and zirconia (ZrO_2), react chemically with both noble and refractory metals to form compounds which are structurally unsound. The result is that many sensor designs predicted to give accurate data actually yield unreliable and unrepeatable data. Surface chemical reactions cause emit-

tance changes which alter the sensor response from the original calibration. It is for these reasons that emphasis is placed upon a chemically compatible sensor design of good repeatability, whose output has known thermal errors. These errors can be computed and the sensor output can be reinterpreted by theory to give data of better accuracy than the data from a sensor which purports to measure the actual quantity.

The thermocouple, insulation, and metallic sheath of the sensor are described in this paper. A discussion of sensor assembly procedure and installation on the vehicle surface follows. Calibration of the thermocouple and computation of the thermal effect of assembly installation upon the actual surface temperature to be measured is presented. There is also an error analysis of the computer program which corrects the thermocouple temperature data and computes aerodynamic heat-flux from the temperature data.

SYMBOLS

\dot{q}	incident aerodynamic heat flux
ϵ	surface emittance
σ	Stefan-Boltzmann constant
T	surface temperature
a	disk thickness
ρ	surface density
c_p	specific heat at constant pressure
t	time
k	thermal conductivity
$\nabla^2 = (\partial^2/\partial r^2) + [(1/r)(\partial/\partial r)] + (\partial^2/\partial z^2)$	
r	radial distance
z	depth
c	electrical conductivity
λ	radiation wavelength

NOSE-CAP TEMPERATURE SENSOR

Under design conditions where the surface temperature is above 3800° F, that is, on a re-entry vehicle nose-cap, the simplest sensor design is based on the thermocouple. The installation of the thermocouple on the sensor is shown in figure 1. It consists of tungsten alloy thermocouple wires in a protection tube. The sensor protection tube is inserted through the nose cap to the vehicle surface exposed to the airstream. The surface material and sensor case are shown cut away to exhibit the thermocouple wires.

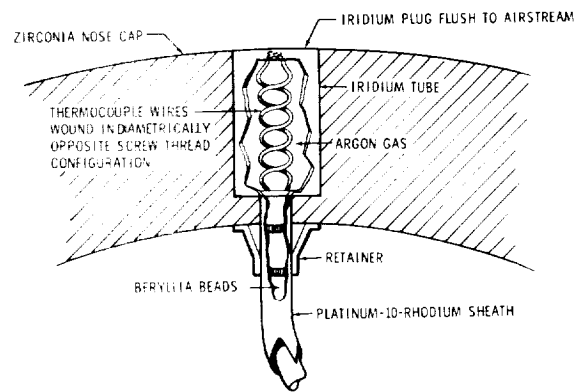


FIGURE 1.—Nose-cap temperature sensor.

High-temperature oxidation rates and chemical reaction rates determine the design materials. P. D. Johnson lists in reference 1 the temperature of reaction onset of metal/metal-oxide systems in vacuum for materials whose melting points are above 2500° F; however, the noble metals are not included. One cannot find a refractory metal which is chemically compatible with zirconia or graphite above 3800° F. The Boeing Company compatibility tests show the refractory-metal/metal-oxide problem to be even more serious in air than in vacuum. The temperatures at which noble-metal/metal-oxide reactions occur are listed in table I. Refractory-metal/metal-oxide reactions are listed in table II. If the nose-cap material is zirconia, iridium is the only metal in contact with zirconia which will survive the 3800° F and hence serve as the thermocouple protection tube or sheath material.

TABLE I.—Reaction Temperatures of Noble-Metal Metal-Oxide Combinations in Air

	Melting point, °F → ↓	Ir 4450	Rh 3630	Pt 3220
ZrO ₂ -----	4830	4100	3600	3200
Al ₂ O ₃ -----	3600	3600	3600	3200
BeO-----	4630	< 4300	3600	3200
MgO-----	5070	-----	-----	< 3000
HfO ₂ -----	5090	> 4300	3200	3200
ThO ₂ -----	5970	< 4300	< 3000	< 3000

TABLE II.—Reaction Temperatures of Refractory-Metal/
Metal-Oxide Combinations in Vacuum

	Melting point, °F→ ↓	W	Mo	Ta
		6810	4760	5410
ZrO ₂ -----	4830	2910	<4000	----
Al ₂ O ₃ -----	3600	3600	----	----
BeO-----	4630	3640	3450	----
MgO-----	5070	3640	2910	3000
HfO ₂ -----	5090	>4300	4300	----
ThO ₂ -----	5970	4000	3450	>4300

Iridium Protection Tube

In order to minimize heat flow along the tubing length, the iridium thermocouple protection tube, shown in figure 1, is as small in diameter and as thin as manufacturing processes permit. The sheath diameter was determined by the minimum weldable diameter of rolled iridium plate manufactured by Engelhard Industries: approximately $\frac{1}{8}$ in. The tube wall thickness of 0.010 in. is the thinnest available.

The oxidation rate of iridium given in reference 2, 50 mg/sq cm/hr at 2700° F, was verified. This rate is equivalent to 0.001 in. of iridium loss per hour on the assembly front surface. Since iridium does not machine well (it work hardens rapidly), the tubes and end plug are welded in an inert atmosphere. Appropriate brazers for attachment of the iridium tube length to a more ductile thermocouple sheathing are given in table III.

Attachment of the iridium case to the nose-cap is also a critical problem. Vibration of

TABLE III.—Appropriate Brazes for Attaching Iridium
Tube to Thermocouple Sheathing

Sheath material	Brazes	Melting temperature, °F
Tantalum-----	Tantalum-30- titanium-----	3450
Platinum-10% rhodium.	Platinum-----	3220
Inconel-----	Paliney-----	2000

the vehicle during boost, and relative motion brought about by vehicular heating require a minimum-stress mounting. For this reason the iridium case on the inside zirconia surface is pivoted from the sensor tip and is free to move at the retainer with any transverse vibration or relative motion. The retainer damps vibratory motion by rubbing against the inside of the nose cap.

Tungsten/Tungsten-Rhenium Thermocouples

Not only the magnitude of thermocouple millivolt indication of temperature is of concern in sensor design, but also the millivolt sensitivity of output with temperature increment. Representative calibration curves of suitable thermocouples, having outputs which are single-valued with a positive slope between 3000° F and 4000° F, are shown in figure 2. Many other combinations have been calibrated to 4000° F (ref. 3), but are unsuitable because their outputs are low or are double-valued functions of temperature. The suitable thermocouples are of two categories—those with graphite in common and those with a refractory metal in common. Both types oxidize and both are brittle.

The refractory-metal thermocouples were chosen over the graphite thermocouples because they are more stable at high temperatures, do not require individual calibration, and may be welded by available techniques.

C. T. Sims et al. (ref. 4) and J. C. Lachman and J. A. McGurty (ref. 5) have shown the

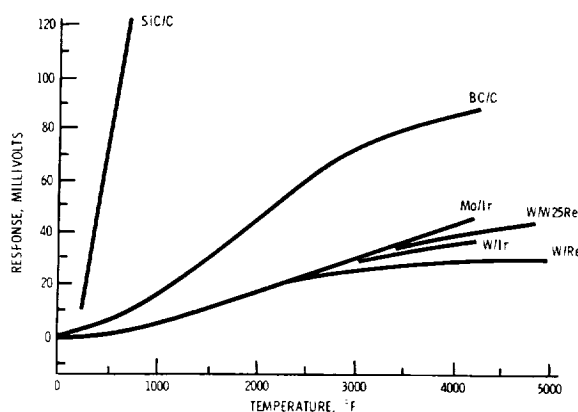


FIGURE 2.—Responses of high-temperature thermocouples.

tungsten/tungsten-25-rhenium thermocouple to have a high, relatively constant temperature sensitivity. Tungsten, however, recrystallizes rapidly above 2000° F. Although the ductile-to-brittle transition temperature (corresponding to this recrystallization of tungsten) is considerably above normal instrument fabrication temperatures, the transition remains a serious problem in swaged construction, which was considered necessary in the present instance for mechanical reasons. In order to alleviate this problem and minimize stress differences due to thermal expansion between sheath materials and thermocouple wires, the wires are formed into coils in the hot test zone. For this geometry, circumferential stresses in the wire result in spiral fractures, producing an acceptable delamination rather than a disastrous break.

Since the alloying of tungsten with rhenium produces a wire with less recrystallization tendency than pure tungsten, other tungsten-rhenium alloys were investigated. Tungsten-5-rhenium, which exhibits recrystallization at about 2800° F, was tried. However, its mechanical properties were unpredictable and it was discarded in favor of the General Electric Company doped tungsten-3-rhenium lamp filament wire (GE-3D). The other leg of the thermocouple was tungsten-25-rhenium made by Chase Brass and Copper. Figure 3 shows results of coiling these three alloys after heating

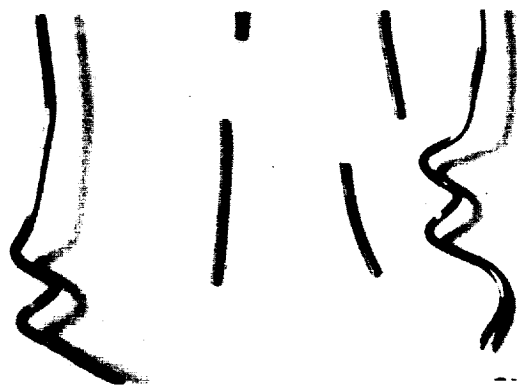


FIGURE 3.—Comparison of ductilities of tungsten-rhenium wires after heating: (a) GE-3D 97-tungsten-3-rhenium, (b) Chase 95-tungsten-5-rhenium, (c) Chase 95-tungsten-5-rhenium, and (d) Chase 75-tungsten-25-rhenium. The wires were furnace heated 4 hours at 3000° F in vacuum and ½ hour at 3300° F in vacuum before coiling on a 0.10-inch-diameter mandrel.

tests. Zysk et al. (ref. 6) showed that the indicated ductility advantage diminishes at higher temperatures and also showed that by proper heat treatment a reliable calibration curve can be obtained (fig. 4). No breakage of wires in swaged construction has occurred up to 3000° F for this thermocouple pair in the configuration of the nose-cap sensor. Care has been required to obtain a reliable junction in the tip when the wires are fused to the iridium, but good reproducibility has been attained.

Calibration of the sensor assembly in a furnace is possible to better than ± 1.7 percent of the Fahrenheit reading up to 3000° F. However, above 3000° F only the wire has been calibrated (to ± 1 percent); the sensor assembly has not been calibrated above 3000° F because of furnace limitations.

Electrical Insulation

Shunting of the thermocouple signal as a result of the low electrical resistance of the insulation at high temperatures is a well known source of error and is considered in detail in this section. Campbell (ref. 7) shows typical variations of resistivity of metal oxides with temperature. By and large, there is an exponential decrease of resistivity of metal oxides with temperature. Above 3000° F, fractions of an inch of insulation provide only a few ohms of resistance.

In the hot region of the sensor assembly the error caused by decrease of resistance of

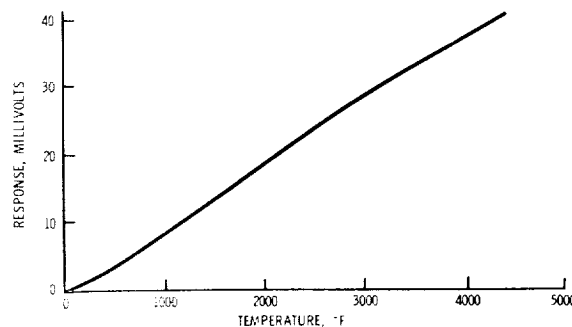


FIGURE 4.—Calibration of tungsten-3-rhenium/tungsten-25-rhenium thermocouple. The calibration curve was obtained in a National Research Corporation furnace. Furnace drift is averaged out on increasing- and decreasing-temperature runs.

electrical insulation above 3000° F was avoided by eliminating insulation other than argon, which exhibits no ionization in this temperature range. Temperatures inside the nose cap will lag the surface cap temperatures; hence, the temperatures inside the nose-cap are not expected to exceed 3000° F. Beryllia beads, presenting minimum electrical contact area and maximum resistance, provide mechanical separation of the thermocouple wires.

In order to determine temperature measurement error, the magnitude of the shunting effect was determined by test. Since beryllia is both expensive and toxic, alumina, which has a resistivity next to that of beryllia, was used in these tests.

RESISTANCE TEST

Twelve-inch lengths of No. 24 tungsten wires, swaged in a platinum-10-rhodium sheath with alumina insulation (similar to the arrangement shown in fig. 1) were baked at 700° F in a vacuum of 10^{-5} torr for 15 hours to eliminate water vapor. The swaged tubing, or sheath, diameter was $\frac{1}{8}$ inch and the tubing wall thickness was 0.010 in. A 5-volt battery was used to determine the resistance between the two wires and between each wire and the sheath; both voltage polarities were used and the results were averaged. Test results given in table IV show the reduction of resistance with increase in temperature.

As an example of the effect of this reduction on the accuracy of temperature readings, with

TABLE IV.—*Temperature effect on sheathed wire insulation resistance*

No. 24 tungsten wires with alumina insulation swaged in $\frac{1}{8}$ -inch-diameter platinum-10-rhodium sheath; length, 1 ft

Temperature, °F	Wire to wire resistance, ohms	Wire 1 to sheath resist- ance, ohms	Wire 2 to sheath resist- ance, ohms
70	809 M	2490 M	3210 M
1352	1.1 M	1.1 M	910 K
1824	47.6 K	58.2 K	78.2 K
2279	2.7 K	3.3 K	3.2 K
2682	320	355	355
3000	106	77	77

an average shunt resistance of 100 ohms at 3000° F and with wire resistances of 0.9 ohm/ft and 1.16 ohm/ft for tungsten-3-rhenium (W3Re) and tungsten-26-rhenium (W26Re), respectively, a 0.5 percent error per foot is introduced for short lengths of lead assembly.

SENSOR ASSEMBLY

The sensor is assembled by stripping back 2 inches of sheath and insulation, slipping on the beryllia beads, then coiling the tungsten wires, and brazing the sheath to the iridium case. Finally, the tungsten wires are prepared for welding to the iridium front plug. They are cut after coiling so that they end halfway through a hole in the iridium plug. The final heliarc weld fills the remaining half of the hole with iridium. The sensor is kept full of argon during the welding in order to prevent oxidation of the tungsten wires. The sensor is inserted into an ultrasonically drilled hole in the zirconia disk (of fig. 1) for test. The retaining ring is then spot-welded on the sheath. The disk is set in a graphite holder mounted on a water-cooled sting which can be moved into a plasma or rocket heating facility to simulate aerodynamic heating. The arrangement allows disk and sensor to reradiate into the laboratory.

Digital Computer Program for Temperature Correction

Heat conduction along the metal tubing and radiation exchange between the front and back faces of the iridium tube cool the sensor-surface during nose-cap heating and heat it during nose-cap cooling. To determine the nose-cap surface temperature, the heat-transfer differential equation for an incremental volume may be used to calculate the magnitude of surface temperature perturbation. This is done on an IBM 7090 electronic data processing system with a thermal difference equation program. The programed model consists of a cylindrical section of zirconia surrounding the sensor assembly with radial thermal contact resistance; the section is mathematically divided into a set of concentric cylindrical annuli. The incident aerodynamic heat flux and the vehicle internal temperature to which the back of the section radiates are programed as functions of time.

The assumed boundary condition at the circumferential edge is that the radial temperature gradient is zero. Radiation exchange inside the sensor void along the iridium tube is computed between different cylindrical annuli and between the end disk and the cylindrical annuli with closed-form precalculated view factors (ref. 8). The physical parameters, thermal conductivity and specific heat, and emittance are programmed as functions of temperature. Thermal contact resistance at the interface between the iridium and the zirconia was assumed to be negligible, not only because the iridium expands in the hole against the zirconia, but also because there is intense radiative heat exchange across the interface at the high temperatures. Resulting surface and internal temperatures are then calculated by the program for boundary conditions of heat flux and internal temperature which are functions of time.

Initial results obtained with the digital computer program aided in the sensor design. The effect of radiation exchange in the void upon thermal gradient in depth is plotted in figure 5. The temperature at the sensor rear is only slightly higher than that of the adjacent zirconia, and was sufficiently low to permit brazing. It was further determined that the magnitude of thermal surface perturbation was quite insensitive to insulating bead material and placement. The calculated tem-

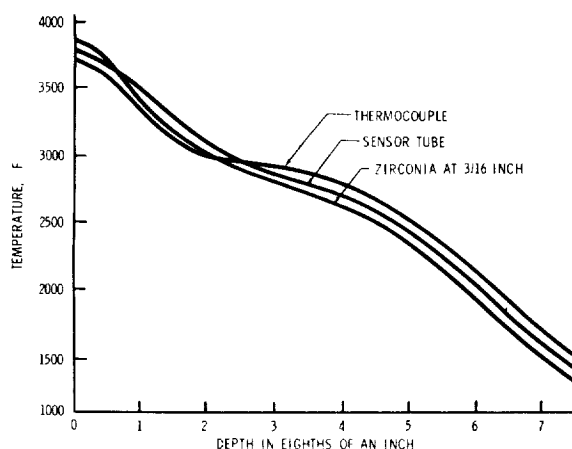


FIGURE 5.—Computed temperature variation along the sensor tube, the thermocouple, and the adjacent zirconia.

perature response of the sensor to a step increase in aerodynamic heat flux is shown in figure 6; the time constant (the time to attain 63 percent of the ultimate temperature rise) is about 3 sec.

The computer program is also used to find the temperature corrections needed to allow for perturbation of the zirconia surface temperature due to the presence of the sensor. A typical radial perturbation is shown in figure 7. The magnitude of the correction difference between sensor temperature and zirconia surface temperature at any time is shown for a surface temperature history in figure 8. The accuracy with which the distortion of the surface isotherms is predictable depends on the uncertainty in system physical properties.

Emittance of Zirconia and Iridium

The accuracy of the computation is limited by the uncertainty of the emittances, as functions of temperature, for zirconia and iridium. Reynolds et al. (ref. 9) find the total emissivity of iridium to be 0.04 at 72° F (fig. 9). Forsythe (ref. 10) reports an emissivity of 0.30 at 3140° F. The emissivity-temperature curve obtained by putting a Hagen-Rubens emissivity curve (ref. 11) through the Fulk and Reynolds low-temperature point lies considerably below Forsythe's high-temperature point. The situation may be resolved by drawing the Hagen-Rubens emittance curve through Forsythe's point. By using this approach, the emittance is 0.1 at 72° F, which is reasonable for unpolished material.

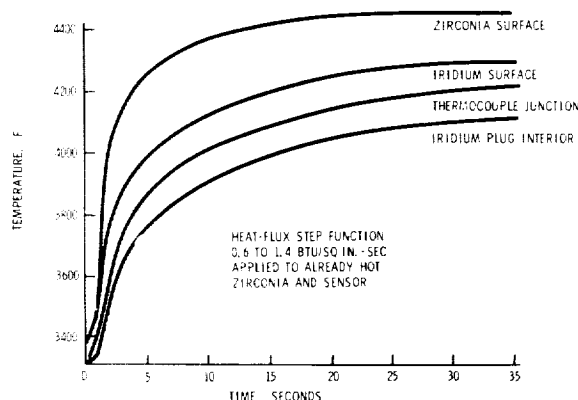


FIGURE 6.—Computed sensor time response.

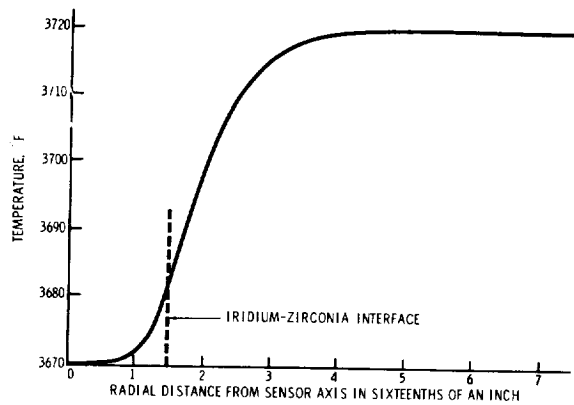


FIGURE 7.—Computed radial surface-temperature perturbation.

There are available considerable data for the emittance of zirconia as a function of temperature. In particular, reference 12, by the Southern Research Institute, is primarily concerned with this subject. A primary finding of this work is that zirconia emittance is dependent upon not only temperature, but also composition, past temperature history, and method of measurement. For the particular composition of zirconia being used for the Boeing nose-cap, the emittance, as a function of temperature, is given with an uncertainty of ± 10 percent by figure 10. This curve, as do curves of references 12 and 13, differs from others (ref. 7) in that there is a significant increase of emittance with temperature at 2300°

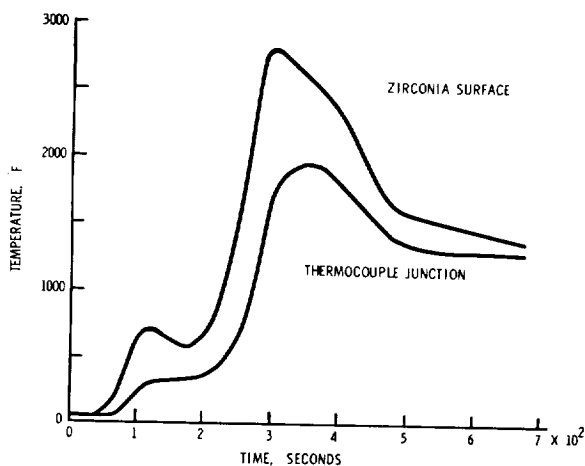


FIGURE 8.—Computed sensor and surface-temperature history.

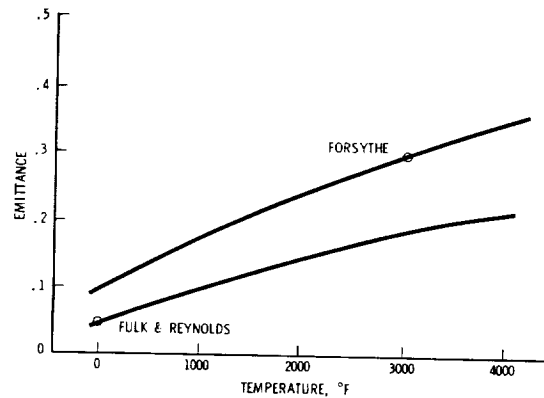


FIGURE 9.—Emittance of iridium. The low-temperature value was obtained by Reynolds et al., reference 9; the high-temperature value, by Forsythe, reference 10. The lines are drawn by using the Hagen-Rubens relation $\epsilon = 36.5(\lambda c)^{1/2} - 670(\lambda c)^{-1} + 6000(\lambda c)^{-3/2}$ for $\lambda = 1.8 \mu$.

F, followed by a second decrease to about 0.6 at melting. Above 2300° F a rise in zirconia surface temperature aids surface cooling by reradiation. The phenomenon, which provides a lowering of maximum nose-cap temperature for given aerodynamic heat flux, is apparently the result of a zirconia phase change at 2300° F.

Temperature Sensor Tests

PLASMA HEATING TEST

In initial nose-cap sensor testing, sensors mounted in zirconia disks were heated by an rf plasma to simulate reentry heat distribution.

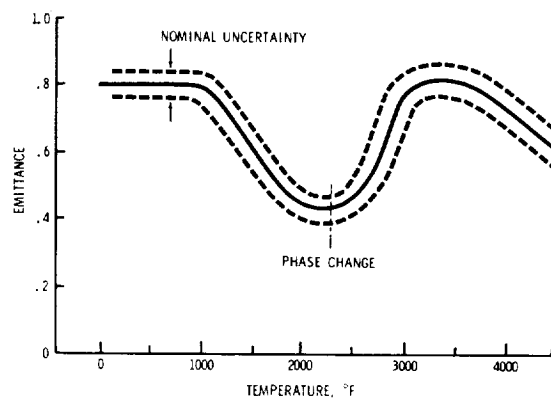


FIGURE 10.—Emittance of zirconia. Data obtained for the Boeing Company.

The installation shown in figure 11 illustrates the symmetrical position of the nose-cap sensor with respect to the small thermocouple which acts as a reference monitor of the zirconia surface temperature. The monitor consists of a fragile iridium/iridium-60-rhodium thermocouple welded to a $\frac{3}{16}$ -inch-diameter, 0.01-in. thick iridium disk. Directly behind the disk is a $\frac{1}{8}$ -inch-deep void backed by an alumina dual-bore tube carrying the thermocouple wires. A digital computer program run predicted the distortion of surface temperature by the monitor thermocouple to be well within a recorded temperature accuracy of ± 3 percent.

When the temperature history of figure 12 was run, the monitor thermocouple failed at the melting point of iridium-60-rhodium, 3800°F . At this time in the temperature history, the indicated temperature of the nose-cap sensor coincided with the indicated temperature of the monitor thermocouple to well within ± 3 percent system error. However, the nose-cap sensor data must, in general, be corrected to find the true zirconia surface temperature. The electrical noise generated by the plasma at the thermocouple surface was a severe problem. Low-frequency electrical noise as high as 200 volts was recorded. It was not until a magnetic

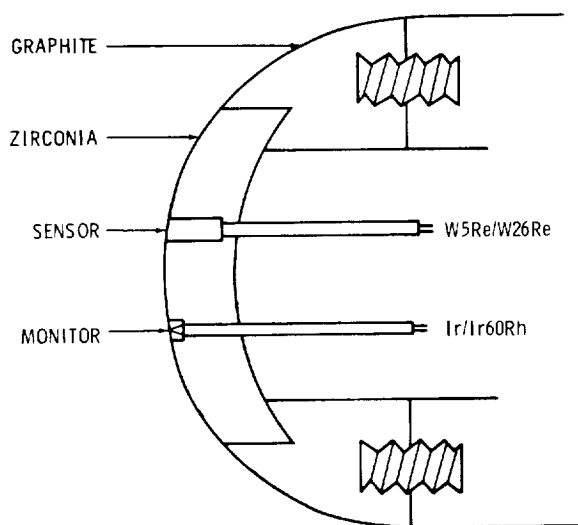


FIGURE 11.—Configuration for plasma test of sensor in 3-inch-diameter zirconia disk.

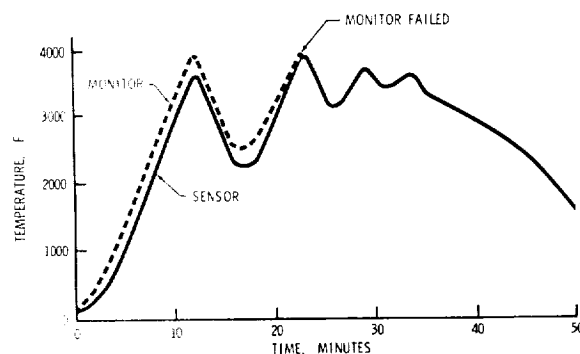


FIGURE 12.—Temperature history of plasma test.

oscillograph was used for recording, with its chassis coupled to the thermocouple sheath, that satisfactory signal discrimination was obtained, and the noise reduced to one-half millivolt.

ROCKET-EXHAUST HEATING TEST

A small rocket engine was used at Boeing to obtain the temperature response of figure 13. The test configuration for the sensor was similar to that of figure 11. The test verified a time constant of less than 3 sec in response to a heat-flux step-function input, as predicted by the digital computer program.

SIMULATED THERMAL REENTRY TEST

A simulated thermal reentry test was made to compare the zirconia surface temperature, as obtained by the computer corrected sensor data, with an external pyrometer reading of zirconia surface temperature. The two

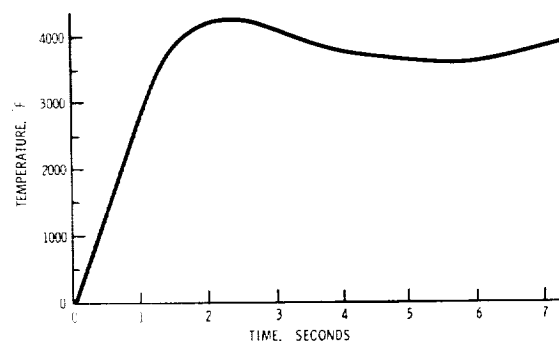


FIGURE 13.—Sensor time response to step increase in heat flux.

methods of obtaining zirconia surface temperature should agree because the volume effect of zirconia emittance (discussed in the section, Nose-Cap Aerodynamic-Heat-Flux Accuracy) is included in the computer program, and the two-color pyrometer temperature reading is nearly independent of zirconia emittance. Because the two-color pyrometer does not yield data below 200° F, surface temperature was initially measured by a platinum/platinum-13-rhodium thermocouple embedded in the zirconia surface near the stagnation point.

The measured sensor temperature is shown by the dashed line in figure 14. A computation of sensor temperature with the digital computer program, using recorded surface and internal nose-cap temperatures, is shown by the dotted line in figure 14. Divergence of the computed sensor temperature from the measured sensor temperature is indicated by separation of the dotted line from the dashed line.

There are three possible explanations for the divergence: (1) In the computer program, too small a value was assumed for the effective radiation area of the sensor sheath inside the nose cap; (2) some water vapor was possibly

trapped in the sensor lead wire insulation during assembly, so that the heated vapor shunted the thermocouple; (3) the zirconia and iridium emittances used in the computation were inaccurate. Since radiation varies with the fourth power of the temperature, even a fairly large inaccuracy in the emittance value can hardly affect the temperature more than a few percent. Hence, either of the first two possibilities or a combination thereof has caused the divergence of computed and measured temperatures.

The simulated reentry test showed that the computer-corrected data of the nose-cap temperature sensor can give zirconia surface temperature during reentry.

Accuracy of Temperature Sensor

For the case where temperature rises at 30° F/sec, the following errors must be considered for nose surface temperature measurement. Percent errors refer to Fahrenheit reading:

- (1) transient—the 3-sec response time of the sensor can result in a ± 2 percent error
- (2) calibration—the calibration contributes no more than ± 1.7 percent
- (3) readout—the electronic amplification and recording can contribute a ± 2.0 percent error
- (4) leakage—the insulation electrical leakage can cause -0.5 percent error
- (5) correction—the computer-calculated correction to the sensor temperature is uncertain by ± 0.7 percent

The root sum square of these uncertainties gives an uncertainty of ± 3.4 percent in temperature measurement of the nose-cap sensor in this case.

AERODYNAMIC HEAT FLUX

Analysis of heat-flux measurement is made by considering a thin surface disk subject to aerodynamic heating \dot{q} . Conservation of energy requires the heat flow differential equation as given here to hold:

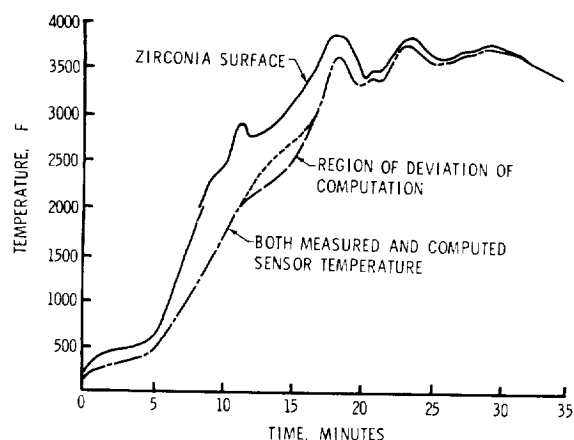


FIGURE 14.—Simulated thermal reentry test. The surface temperature is obtained initially by a platinum/platinum-13-rhodium thermocouple, thereafter by a two-color pyrometer. The measured sensor temperature is indicated by the dashed line; the computed sensor temperature by the dotted line.

$$\dot{q} = \sigma \epsilon T^4 + a \rho c_p \frac{\partial T}{\partial t} - ak \nabla^2 T. \quad (1)$$

The first term on the right-hand side, $\sigma \epsilon T^4$, is the heat-flux reradiated at the disk surface.

The second, $a \rho c_p \frac{\partial T}{\partial t}$, is the local rate of heat accumulation in the disk, and the third term, $-ak \nabla^2 T$, is the net efflux of heat from the volume by radial conduction and through the back face.

Nose-Cap Aerodynamic-Heat-Flux Accuracy

Representative numbers are put into the three terms of equation (1) to find their relative magnitude in the zirconia nose-cap under a condition when heat-flux and hence surface temperature are changing rapidly with time. At the time chosen, a digital computer gives $T(t)$ for the zirconia nose-cap. For example, for

$$\begin{aligned} \dot{q} &= 0.382 \text{ Btu/sq in.-sec as the initial condition, and for the following three assumed zirconia characteristics,} \\ \epsilon &= 0.80 \pm 10 \text{ percent} \\ \rho c_p &= 0.028 \pm 5 \text{ percent Btu/in.}^3 \cdot ^\circ\text{F} \\ k &= 30 \times 10^{-6} \pm 5 \text{ percent Btu/in.-sec.-}^\circ\text{F} \end{aligned}$$

Then 300 sec after the heating begins

$$\begin{aligned} T &= 2765^\circ \text{ F} \\ \frac{\partial T}{\partial t} &= 32^\circ \text{ F/sec} \pm 5 \text{ percent} \\ -\nabla^2 T &= 22,800^\circ \text{ F/in.}^2 \pm 10 \text{ percent.} \end{aligned}$$

Choose the disk thickness of 0.05 in. as being a reasonable dimension in which to measure average temperature.

Substitution of these numbers gives, for the terms in equation (1),

$$\begin{aligned} \sigma \epsilon T^4 &= 0.295 \text{ Btu/sq in.} = \text{sec} \\ a \rho c_p \frac{\partial T}{\partial t} &= 0.045 \\ -ak \nabla^2 T &= 0.035 \end{aligned}$$

When $\dot{q} = 0.382 \text{ Btu/in.}^2 \cdot \text{sec}$ and the surface temperature is 2765° F , the reradiated heat flux is the largest term. If another disk depth

is chosen, both $\frac{\partial T}{\partial t}$ and $\nabla^2 T$ must be recalculated since they increase as the chosen disk thickness is decreased.

In order to calculate heat flux a computer program can reproduce by asymptotic convergence, the temperature curve of a thermocouple instrumentation system. The temperature of the back face of the nose-cap must, of course, be known as a function of time. The system error is assumed ± 3.4 percent of the temperature reading. By considering only the reradiation term of equation (1), the resulting heat-flux error is computed:

$$\begin{aligned} \Delta \dot{q} / \dot{q} &= [(\Delta \sigma / \sigma)^2 + (\Delta \epsilon / \epsilon)^2 + (4 \Delta T / T)^2]^{1/2} \\ &= (0.5^2 + 10^2 + 13.6^2)^{1/2} = 17\%. \end{aligned} \quad (2)$$

Existing information on variation of the Stefan-Boltzmann constant (ref. 14) results in assigning an upper limit of 0.5 percent to this cause for purposes of calculation.

Actually, terms of the following magnitudes have been neglected in the heat-flux error computation:

Item	Unknown by %	Resulting error in heat-flux, %
k -----	5	0.5
ρc_p -----	5	0.5
$\nabla^2 T$ -----	10	1.0

In addition, the heat-flux error has been slightly exaggerated by assuming that the 10-percent error in emittance produces a corresponding 10-percent error in heat-flux. (Actually only a 9-percent error in heat-flux is introduced.) Improving the accuracy with which the emittance of the sensor is known would not improve aerodynamic-heat-flux prediction. This is verified by the test data which show that the thermocouple temperature tends to the zirconia temperature (fig. 12). In order to achieve a temperature at the sensor based upon iridium emittance, a large plate of iridium would be required on the sensor tip; but there is no evidence that iridium surface emittance can be better determined than that of zirconia,

because of possible iridium chemical reactions. The alternative is to determine the emittance of zirconia more accurately. It is hypothesized that this cannot be done independently of the temperature gradient in depth through the zirconia.

The rise in emittance of zirconia at 2500° F can be attributed to radiation in depth. Specimens heated to a surface temperature of 4000° F appear quite glassy after the test, with the individual zirconia grains welded together. An onset of infrared transparency in zirconia at 2500° F could account for the rise in *surface* emittance with temperature.

Data on zirconia emittance in reference 10 were obtained for conditions of minimum temperature gradient rather than for the condition of large temperature gradients under discussion. With such a volume infrared emission, higher accuracy will not be assured by using true zirconia emittance if large temperature gradients exist, so that accuracy can be less under flight conditions. In order to better predict heat flux, failing to reduce emittance variation, improvement of the sensor accuracy is required.

Aerodynamic-Heat-Flux Instrument Errors

Instruments that involve measuring the time rate of change of temperature in a material with known specific heat have been used to measure heat flux. These instruments are known as *slope* or *rate* calorimeters, and are not recommended for time dependent heat conditions.

There is a second class of instruments which record radial temperature gradient on a thin metal skin by distorting the temperature pattern by applying disks with different thermal conductivities against the skin. The Gardon heat-flux meter operates on this principle. A quasi-static solution to equation (1) in radial coordinates can be obtained for the surface temperature $T(r)$ at any time by setting the instrument heat sink temperature and the surface aerodynamic heat flux at the same time (ref. 15). It then develops that the radial temperature gradient is as dependent upon surface emittance as it is on heat flux. Therefore, again with ± 10 -percent emittance un-

certainty, a value of 17 percent is arrived at as the theoretical limit of accuracy for the surface aerodynamic heat flux. Note that now the instrument measurement of radial temperature gradient is dependent upon the temperature gradient in depth, which has been assumed constant. Hence 17 percent is a best theoretical limit.

Aerodynamic-Heat-Flux Measurement on a Metal Surface

Some initial efforts to design a heat-flux meter with the noble metals illustrated surface reactions with erratic heat-flux indications from a pair of thermocouples, reading the radial temperature difference between the noble metal surface ($\epsilon=0.2$) and the blacker molybdenum disilicide ($\epsilon=0.8$). The following reactions occur for noble metals in contact with molybdenum protected with a disilicide coating:

<i>Metal</i>	<i>Melting point, °F</i>	<i>Reaction with MoSi₂ at 2700° F</i>
Pt.....	3220	Pt melts
Rh.....	3630	Rh melts
Ir.....	4450	Ir is embrittled

These vacuum reactions seem to be the result of grain boundary attack of the metal by silicon, forming a lower-melting metal-silicon alloy. In the presence of oxygen, free silicon in the molybdenum disilicide surface will combine with the oxygen to postpone the reactions to 3000° F, which is about the melting point of the molybdenum disilicide.

A second design consists of a conducting bar placed against the metal skin. It is illustrated in figure 15, which also shows the theoretical calibration curve, which exhibits little sensitivity to heat-flux above 10 Btu/sq ft-sec. A laboratory calibration attempt is shown in figure 16. Upon replotting these data (fig. 17), it was observed that emittance changes on the surface were in evidence. The surface emittance is seen to generally decrease with increase in temperature. This is probably caused by the thin disilicide coating, for emittances of disilicide coatings tend to increase with tem-

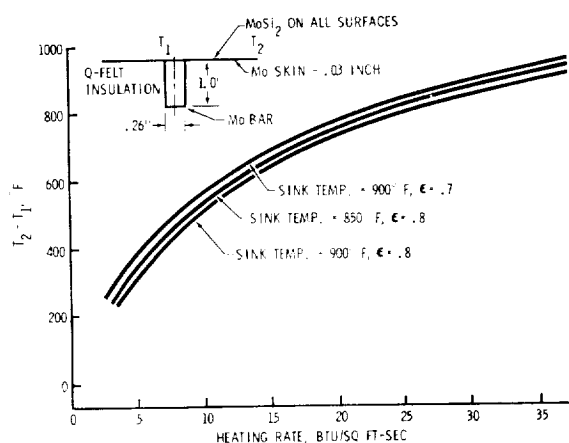


FIGURE 15.—Calculated calibration of heat meter. Curves are obtained by applying the heat-transfer differential equation to the surface of the meter.

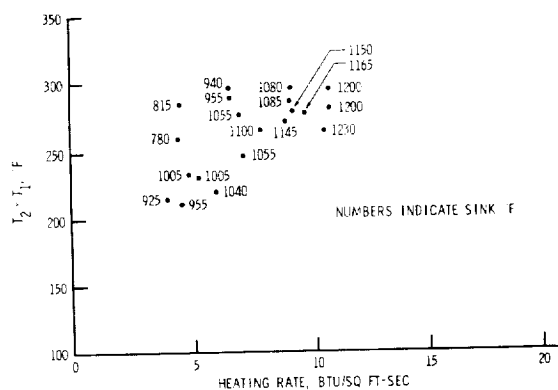


FIGURE 16.—Laboratory calibration of heat meter.

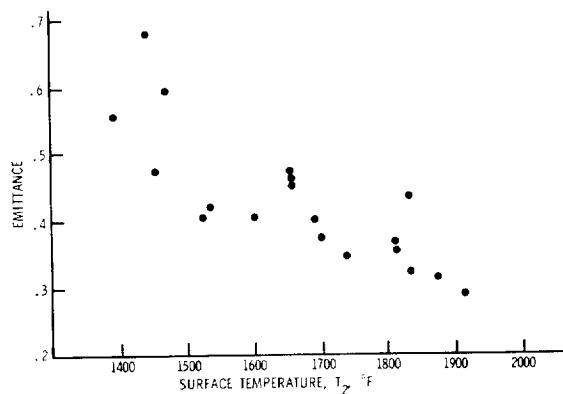


FIGURE 17.—Emittance of heat-meter surface, molybdenum disilicide on molybdenum. Points are calculated from temperature measurements on the heat meter.

perature, so that it is apparently the substrate whose emittance is governing the reradiation. Also, note the large variation of emittance at any one temperature. The explanation of the erratic calibration shown in figure 16 lies there. Two different emittances can be associated with two separate temperature measurements on the same material.

Accuracy Analysis of Measurement of Heat-Flux on a Metal Surface

A mathematical model of a rivet thermocouple installation in a 0.03-in.-thick molybdenum disilicide-coated leading edge (fig. 18) gives the following accuracy prediction: Under radiation equilibrium conditions there is no net efflux or accumulation of heat. The aerodynamic heat flux can be found from the equation $q = \sigma \epsilon T_0^4$ where T_0 is the effective radiation equilibrium temperature and the emittance is assumed known. In practice, the respective differences of thermocouple temperature from skin temperature and of skin temperature from radiation equilibrium temperature can be determined by iteration using equation (1), upon insertion of a sink temperature for the temperature of the thermocouple installation (rivet head) of figure 18. This calculation is carried out in reference 15. Since the metal surface is quite thin, it is quite close to radiation equilibrium temperature, and the correction to the thermocouple reading is of the order of $+80 \pm 2^\circ \text{F}$ for $\epsilon = 0.8$ and $\Delta\epsilon/\epsilon = \pm 10$ percent at an indicated 2700°F surface temperature. With a ± 3 -percent temperature-measurement accuracy, the aerody-

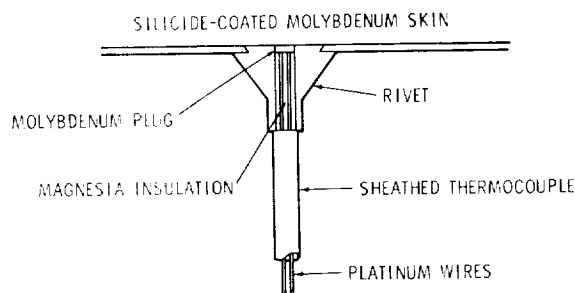


FIGURE 18.—Thermocouple installation on molybdenum skin.

dynamic heat-flux accuracy is, by equation (1), $\Delta\dot{q}/\dot{q} = (0.5^2 + 10^2 + 12^2)^{1/2} = 15.5$ percent.

CONCLUSION

With the presented sensor design, temperature can be measured to ± 3.4 percent of Fahrenheit reading on the nose-caps of glide reentry vehicles. In order to obtain this accuracy during boost and glide reentry, it is necessary to correct sensor readings with a thermal computer program.

In view of the presented emittance data, aerodynamic heat-flux predictions are unlikely to be better than ± 17 percent for glide reentry vehicles. Better prediction of aerodynamic heat flux is dependent upon controlling emittance variations and/or obtaining more accurate surface temperatures.

ACKNOWLEDGMENT

The authors express their thanks to R. W. Boice for his help with nose-cap sensor development, to R. E. Mikkelsen for aid in programming the IBM 7090, and to A. F. Gledhill and J. M. Baresh for heat-meter testing.

REFERENCES

1. JOHNSON, P. D.: Behavior of Refractory Oxides and Metals, Alone and in Combination, in Vacuum at High Temperature. *Jour. American Ceramic Soc.*, vol. 33, no. 5, 1950, pp. 168-171.
2. JAFFEE, ROBERT I.: Refractory Metals. *Proceedings of an International Symposium on High Temperature Technology*. McGraw-Hill Book Co., Inc., c. 1960, pp. 61-75.
3. NADLER, M. R., and KEMPTER, CHARLES P.: Thermocouples for Use in Carbon Atmospheres. *Rev. Sci. Instr.*, vol. 32, no. 1, Jan. 1961, pp. 43-47.
4. SIMS, CHESTER T., GAINES, GORDON B., and JAFFEE, ROBERT I.: Refractory-Metal Thermocouples Containing Rhenium. *Rev. Sci. Instr.*, vol. 30, no. 2, Feb. 1959, pp. 112-115.
5. LACHMAN, J. C., and MCGURTY, J. A.: The Use of Refractory Metals for Ultra High-Temperature Thermocouples. *Temperature—Its Measurement and Control in Science and Industry*, vol. 3, pt. 2, Reinhold Publ. Corp (New York), c. 1962, pp. 177-187.
6. ZYSK, E. D., TOENSHOFF, D. A., and PENTON, J.: Tungsten 3 Rhenium vs. Tungsten 25 Rhenium, A New High Temperature Thermocouple. *Engelhard Ind. Tech. Bull. No. 111*, Mar. 1963, p. 4.
7. CAMPBELL, I. E., ed.: *High-Temperature Technology*. John Wiley & Sons, Inc., c.1956, p. 57.
8. BUSHMAN, ALBERT J., JR., and PITTMAN, CLAUDE M.: Configuration Factors for Exchange of Radiant Energy between Axisymmetrical Sections of Cylinders, Cones, and Their Bases. NASA TN D-944, 1961.
9. REYNOLDS, M. M., CORRUCINI, R. J., FULK, M. M., and BURLEY, R. M.: Radiometry. *American Institute of Physics Handbook*. Dwight E. Gray, coordinating ed., McGraw-Hill Book Co., Inc., 1957, pp. 6-68 to 6-71.
10. FORSYTHE, W. E.: 1919 Report of Standards Committee on Pyrometry. *Jour. Optical Soc. of America*, vol. 4, 1920, pp. 305-336.
11. HAGEN, E., and RUBENS, H.: *Ann. Physik.* vol. 14, 1904, p. 936.
12. The High Temperature Thermal Properties of Several Zirconias, Siliconized Graphite, and Coated Molybdenum. AST/EIR-12890, Supplement I, 1961, pp. 22-35.
13. COX, R. L.: A Technique for Measuring Thermal Radiation Properties of Translucent Materials at High Temperature. *Measurement of Thermal Radiation Properties of Solids*, Joseph C. Richmond, ed., NASA SP-31, 1963, pp. 469-481.
14. GUBAREFF, G. G., JANSSEN, J. E., and TORBORG, R. H.: *Thermal Radiation Properties Survey*. Second ed., Honeywell Res. Center, Minneapolis-Honeywell Regulator Co., 1960, pp. 8-9.
15. BRUNSWIG, FREDERIC S.: Computing Temperature Perturbations on Thin-Skin Panels. *AIAA Jour. (Tech. Notes and Comments)*, vol. 1, no. 9, Sept. 1963, pp. 2163-2164.

AUTHOR AND DISCUSSANT INDEX*

A

Abbott, G. L. 2: 11-28.
 Aerojet-General Corp. 13 D: 152. 42 D: 428.
 Aerospace Corp. 9 D: 115. 52 D: 548.
 Alvares, N. J. 19: 183-7.
 Aronson, James R. 3: 29-38.
 Arthur D. Little, Inc. 1: 3-10. 3: 29-38. 4 D: 44.
 9 D: 115. 16: 159-64. 27 D: 275. 28 D: 286.
 Arvesen, J. C. 44: 443-52. 53: 549-57.
 Ashby, Neil. 6: 63-71.
 AVCO Corp. 10 D: 131. 11 D: 139. 28: 277-86.
 45 D: 472.

B

Bailin, Lionel. 30 D: 301. 42 D: 431. 52 D: 548.
 Baschieri, Ronald. 29 D: 292.
 Bennett, H. E. 1 D: 8. 2 D: 28. 13: 145-52. 32 D: 319.
 Bernstein, Joseph B. 3 D: 37-38.
 Bevans, Jerry T. 30 D: 300.
 Beveridge, C. M. 52: 535-48.
 Blau, H. H., Jr. 4 D: 44. 16: 159-64.
 Boeing Co. 23: 213-5. 33: 321-4. 49 D: 521-523.
 55: 567-79.
 Brandenburg, Werner. 30 D: 300. 32: 313-9.
 Breuch, R. A. 39: 365-79.
 Brunschwig, F. S. 55: 567-79.
 Burkhard, Donald. 1 D: 9.

C

Campbell, Francis J. 37 D: 348.
 Cann, Leopold. 13 D: 152. 42 D: 428.
 Canotin, Les. 9 D: 115.
 Caren, R. P. 38: 351-64. 51: 531-4.
 Chamberlin, J. L. 17B: 169-77.
 Champetier, Robert. 51 D: 534. 52 D: 548.
 Chapin, Claire. 28 D: 285. 37 D: 348.
 Clark, Howard E. 26: 241-58.
 Clausen, O. W. 32: 313-9. 34 D: 330. 51 D: 534.
 Clayton, Wilson A. 23: 213-5.
 Commonwealth Scientific and Industrial Research Organization. 4: 39-44.
 Comstock, Daniel. 9 D: 115. 27 D: 275. 28 D: 286.
 Cox, R. L. 1 D: 9. 8: 83-101. 22: 205-9.

D

DeWitt, David P. 9 D: 115. 12: 141-4.
 Douglas Aircraft Co. 18 D: 181. 26 D: 257. 49 D: 523-524.
 Douglas, N. J. 30: 293-301.

Dow-Corning Corp. 52 D: 547.
 Dunkle, R. V. 4: 39-44.

E

Emslie, A. G. 1: 3-10.

F

Francis, H. A. 16: 159-64.
 Fulkerson, William. 34 D: 330.
 Fussell, W. 29: 287-92.

G

Gannon, R. E. 28: 277-86.
 Gaumer, Roger E. 11: 135-9.
 General American Transportation Company. 29 D: 292.
 General Dynamics/Astronautics. 18 D: 177. 30 D: 300. 32: 313-9. 34 D: 330. 51 D: 534.
 General Electric Company. 42 D: 429.
 Gilcrest, A. S. 51: 531-4.
 Gillette, Roger. 49 D: 521, 523.
 Gilligan, J. E. 38: 351-64.
 Golub, Morton A. 40: 381-9.
 Gordon, Gary. 34 D: 329. 53 D: 557. 54: 565-6.
 Grumman Aircraft. 47 D: 494. 48 D: 508. 51 D: 534. 52 D: 548.

H

Halacsy, Andrew A. 25 D: 239. 33 D: 324.
 Hall, William M. 35: 331-6. 42 D: 429.
 Harada, Y. 41: 391-420.
 Haron, Albert S. 48 D: 508.
 Harris, J. 50: 525-30.
 Haslim, Leonard. 42 D: 430.
 Hass, Georg. 20: 189-95.
 Heat Magnetic Engineering. 25 D: 239. 33 D: 324.
 Heller, Gerhard B. 36: 339-43. 37 D: 349. 42 D: 430-2. 45 D: 472.
 Hibbard, R. R. 54: 559-66.
 Hoke, Marla G. 31: 303-11.
 Holl, Herbert. 5: 45-61.
 Honeywell, Inc. 10 D: 131. 18: 179-81. 24 D: 231.
 49: 509-24.
 Huntress, Arnold. 52 D: 547.

I

IIT Research Institute. 1 D: 9. 37 D: 348-349.
 41: 391-420. 42 D: 428-432.

J

Jaffe, Leonard. 37 D: 348.
 Janssen, J. E. 18: 179-81. 49: 509-24.
 Jansson, Richard M. 24 D: 231.

*Paper numbers are given in *italics*; D following paper number indicates discussion of the paper.

Jet Propulsion Laboratory. 35: 331-36. 42 D: 429.
 Jewell, Robert A. 43: 433-41.
 Johnson, R. D. 42 D: 429-30.

K

Katz, Arthur. 9 D: 115. 47 D: 494. 48 D: 508. 51 D: 534. 52 D: 548.
 Keegan, H. J. 17A: 165-9.
 Kelly, Francis J. 10: 117-131.
 Kennedy. 25 D: 240.
 Klein, Jonathan D. 7: 73-81. 21: 197-203.
 Koch, Donald. 1 D: 9. 3 D: 38. 26 D: 256.
 Koch, G. E. 55: 567-79.
 Kostkowski, H. J. 9 D: 115.

L

Laszlo, T. S. 10 D: 131. 11 D: 139. 28: 277-86. 45 D: 472.
 Leigh, Charles H. 45 D: 472.
 Libbert, Barbara. 49 D: 523-4.
 Liebert, C. H. 54: 559-66.
 Limperis, Thomas. 24 D: 231. 32 D: 319.
 Linder, Bernd. 42 D: 429.
 Ling-Temco-Vought Astronautics Division. 1 D: 9. 8: 83-101. 22: 205-9.
 Litton Systems, Inc. 37: 345-9.
 Lockheed Missiles & Space Co. 11: 135-9. 13 D: 152. 14: 153-5. 30: 293-301. 38: 351-64. 39: 365-79. 42: 421-32. 51: 531-4. 52 D: 547-548.
 Lyon Research Corporation. 3 D: 37.

M

Makarounis, O. 34: 325-30.
 Mark, Herman. 46: 473-81.
 Marquardt Corp. 4 D: 44.
 Martin Company. 48 D: 508.
 McIntyre, George W. 33: 321-4.
 McKellar, L. A. 30 D: 300. 42: 421-32. 52 D: 547.
 McLinden, Hugh G. 3: 29-38.
 Merrill, Ronald B. 45: 453-72.
 Michelson Laboratory. 1 D: 8. 2 D: 28. 13: 145-52. 32 D: 319.
 Michigan, University of. 10 D: 131. 24 D: 231. 25 D: 239.
 Miller, Edgar. 48: 495-508.
 Minges, Merrill L. 47: 485-94.
 Minnesota, University of. 9: 103-115. 10 D: 131. 32 D: 319.
 Mirtich, Michael. 45 D: 472. 46: 473-81.
 Moore, Dwight G. 10: 117-131. 24 D: 231. 26: 241-58.

N

National Aeronautics and Space Administration
 Ames Research Center. 7: 73-81. 21: 195-203. 40: 381-9. 42 D: 428-432. 44: 443-52. 53: 549-57.
 George C. Marshall Space Flight Center. 6: 63-71. 36: 339-43. 37 D: 349. 42 D: 430. 45: 453-72. 48: 495-508.
 Goddard Space Flight Center. 31: 303-11.
 Langley Research Center. 27: 259-75. 43: 433-41.

Lewis Research Center. 45 D: 472. 46: 473-81. 54: 559-66.
 National Bureau of Standards. 1 D: 8. 9 D: 115. 10: 117-31. 12: 141-4. 15: 157-8. 17: 165-77. 24: 217-31. 26: 241-58. 37 D: 348.
 National Physical Laboratory of Israel. 28 D: 286. 50: 525-30.
 National Weather Satellite Center. 3 D: 37.
 Naval Ordnance Laboratory. 3 D: 37-38.
 Neel, Carr B. 40: 381-9. 44: 443-52.
 Nesh, Florence. 3 D: 37.
 Neu, J. T. 17 D: 177.
 Nichols, Roy. 25 D: 239-40.
 North American Aviation, Inc. 1 D: 9. 3 D: 38. 25: 233-40. 26 D: 256.
 Northrop Space Laboratory. 42 D: 429.

O

Oak Ridge National Laboratory. 34 D: 330.
 Olson, R. L. 42: 421-32.

P

Parker, John A. 40: 381-9. 42 D: 429-31.
 Parker, W. J. 2: 11-28.
 P.E.C. Research Associates, Inc. 1 D: 9. 6: 63-71.
 Pezdirtz, George F. 43: 433-41.
 Philco Corp. 52: 535-48.
 Pollard, H. E. 39: 365-79.
 Prezecki, Raymond J. 26 D: 256.
 Purdue University. 28 D: 285. 32 D: 319.

R

RCA. 34 D: 329. 53 D: 557. 54 D: 565.
 Richmond, Joseph C. 1 D: 8. 15: 157-8. 37 D: 348.
 Rolling, R. E. 14: 153-5.

S

Schleter, J. C. 17D: 165-9.
 Schmidt, R. N. 10 D: 131. 18: 179-81. 49: 509-24.
 Schneider, William E. 24: 217-31.
 Schocken, Klaus. 6: 63-71.
 Schumacher, P. E. 25: 233-40.
 Sense, Karl A. 18 D: 181. 26 D: 257.
 Shaw, C. C. 44: 443-52.
 Sheehan, P. J. 28: 277-86.
 Sklarew, Samuel. 4 D: 44.
 Snoddy, William. 48: 495-508.
 Space Technology Laboratories. 30 D: 300.
 Spangenberg, D. B. 17B: 169-77.
 Sparrow, E. M. 9: 103-15. 10 D: 131. 32 D: 319.
 Stair, Ralph. 24: 217-31. 29: 287-92.
 Stanford Research Institute. 40: 381-9.
 Stevison, Donald F. 47: 485-94.
 Stewart, J. V. 42: 421-32.
 Stierwalt, Don. 3 D: 38.
 Strang, A. G. 17B: 169-77.
 Streed, E. R. 52: 535-48.
 Surh, Michael T. 10 D: 131. 24 D: 231.

T

Tabor, H. 50: 525-30.
Tompkins, E. H. 41: 391-420.
Triolo, Jack J. 30 D: 300.

U

U.S. Air Force. 26 D: 256.
U.S. Air Force Materials Laboratory, Wright-Patterson
Air Force Base. 47: 485-94.
U.S. Army
Engineer Research and Development Laboratories,
Fort Belvoir. 20: 189-95.
Missile Command, Redstone Arsenal. 5: 45-61.
U.S. Naval Radiological Defense Laboratory. 2: 11-
28. 19: 183-7. 34: 325-30.
U.S. Naval Research Laboratory. 37 D: 348.
United Technology. 25 D: 240.

V

Vanderschmidt, Fred. 3 D: 37.

W

Wehner, G. K. 37: 345-9.
Weidner, V. R. 17A: 165-9.
Weinberger, Hershel. 28 D: 286. 50: 525-30.
Wilhelm, J. K. 55: 567-79.
Wilson, Gale R. 27: 259-75.

Z

Zerlaut, G. A. 1 D: 9. 37 D: 348-9. 41: 391-420.
42 D: 429-31.
Zierman, C. A. 51: 531-34.
Zipin, Richard. 32 D: 319.

SUBJECT INDEX

A

- Ablation char
 - nylon phenolic
 - arc-jet produced, 271-272
 - emittance, 271
 - oven-produced, 271-272
 - reflectance, 271
- Abrasion resistance, aluminum oxide films, molybdenum substrate, 514
- Absorbers
 - ideal, definition, 509
 - interference
 - aluminum oxide films on molybdenum substrate, 513
 - nickel black on nickel, 528
 - selective, interference film, 195, 510, 525
 - solar, effectiveness, 510
- Absorptance
 - ablation char evaluation, 259
 - aluminum
 - effect of oxidation during aging, 190
 - normal solar, 189
 - shield and capsule, 556
 - substrate, with cryodeposited CO₂ film, 533
 - angular, 293, 303
 - apparent, equal to apparent emittance, 106
 - average, equilibrium temperature method, 306
 - black paint, Cat-O-Lac, 304
 - calorimeter, 367-368
 - cavities, 103
 - change, coatings, UV data, 426
 - change in titania epoxy due to UV radiation, 383
 - coatings, effect of nuclear and UV radiation, 377
 - copper
 - normal solar, 189
 - solar, sea level vs outer space, 189
 - cryodeposited film on aluminum substrate, 533
 - cylindrical, 310
 - definition, 105
 - degradation, thermal coatings, 427
 - different from emittance for same spectrum, 63-72
 - directional
 - evaporated aluminum, 297, 303
 - measuring apparatus, 294-296, 303, 305
 - emittance ratio
 - Alodine 401, 437
 - aluminum/silicon dioxide/germanium coating, 195
 - in storage of cryogenic propellants in space, 559-566
 - polyvinyl chloride exposed to GE UA-2 lamp, 388
 - sensitivity to erosion of germanium film, 195
 - function of angle of incidence, 297, 303-311
 - gold
 - normal solar, 189
 - solar, sea level vs outer space, 189
 - hemispherical
 - calculations from angular, 310
 - solar, aluminum film, 297, 309
 - high solar, coupled with low infrared emittance, 509, 525
 - increase
 - UV exposure of thermal control coatings, 423, 424, 425
 - UV exposure, effect of flux density, 428
 - Lithafrax-potassium silicate coating, 357, 543
 - low, solar probe coatings, 535-548
 - Mylar-aluminum laminate, 298
 - near-UV radiation of reflecting coatings, 371
 - silica-silicone coatings, 543
 - silver, sea level vs outer space, 189
 - solar
 - aluminum oxide films on molybdenum substrate, 514
 - anisotropy of Mylar aluminum laminate, 297
 - calculations for multifilm coatings, 512
 - carbon arc use in measurements, 296
 - changes in thermal control surfaces by UV radiation, 421
 - copper-beryllium alloy, anodized, 515-516
 - defect influence, 353
 - determined from equilibrium temperature, 303
 - determined from spectral reflectance, 454
 - error analysis, 297
 - evaporated metal films, 189-195
 - extinction coefficient, 300
 - graphical integration on special chart, 192
 - heliostat use in measurements, 195
 - hemispheric, Fresnel theory, 309
 - multiplicative correction factor, 298
 - Mylar-aluminum laminate, 297
 - nuclear radiation on plasma arc applied materials, 376
 - reflector coatings, nuclear radiation effects, 370
 - satellite coatings, function of angle of incidence, 308
 - selective black coatings, 517
 - specular surface, angular dependency prediction, 294
 - surface film influence, 157
 - surface types, basic, 495
 - thermal emittance ratio, 189
 - solar angular
 - Fresnel's equations, 299
 - Mylar aluminum laminate, 297
 - Snell's law, 299
 - theoretical derivation, 299
 - solar normal
 - aluminum coated with silicon monoxide, 193
 - determination from reflectance measurements, 193
 - platinum, 189
 - rhodium, 189

Absorptance—Continued

- spectral
 - coatings, UV effect, 423, 424
 - control of, 525-530
 - directional, equal to spectral directional emittance, 131
 - thermal control surfaces, UV effect, 421, 435, 440
 - titania/epoxy, UV effect, 424
 - UV and gamma ray effects on thermal control surfaces, 440
 - zinc oxide/silicone, UV effect, 424
- thermal control coatings
 - effect of thickness, 438
 - rate of change with temperature, UV exposure, 426
- transient thermal vacuum measurement, 306
- zinc oxide
 - methyl silicone coating, 543
 - methyl silicone coating, film thickness, 408
 - methyl silicone paints, UV radiation, 415
 - potassium silicate coating, 543, 544

Absorption

- apparent, coefficient
 - definition, 93
 - equations, 106
 - in single particle theory, 96
 - in tailoring of radiative properties, 84
 - relationship to intrinsic absorption coefficient, 94
- atmospheric, correction in using solar furnace, 280
- bands
 - alumina, flame sprayed, 250
 - ceramics, 85
 - correlation of position with crystal lattice parameters, 353
 - M-center, 355
 - multiple type defects, 354
 - opacity, 87
 - optical characteristics in neighborhood of, 353
 - ozone, UV spectrum, 285
- cavities, 103, 453
- characteristics
 - cavities, rectangular groove, conical hole, V-groove and spherical shell, 108
 - using Maxwell's equations, 89
- coefficient
 - and refraction index value, sintered materials, 138
 - angular distribution, 86
 - as factor in emissivity of opaque specimen, 85
 - at wavelengths of high transparency, 85
 - derivation from single particle theory predictions, 95
 - dielectrics, 181, 197, 287
 - effect on refractive index, 88
 - emittance determination, 86
 - extinction mechanism, 199
 - in description of radiant flux, 88
 - nonisothermal situations, 77
 - potassium bromide, 291
 - powder reflectivity, 94
 - reflectivities of pigments, 93
 - relation to index of refraction, 39-44, 45-62, 84

- sintered glass coating, reflectance, 208
- spectral determination, 289
- tailoring of radiative properties, 83
- thin sample layers, 81
- values in ceramic radiant transfer, 92
- defect, 352
- determination in dielectrics, 138
- direct, definition, 92
- edge shift, after UV exposure, thermal control coatings, 424, 425, 426
- edges for damage control, 354
- effect in thin layers, 203
- efficiency, magnitude, 92
- energetic radiation damage, 352
- free carrier, 360
 - effect on infrared reflectance, 355
- fundamental factors, 485-487
- increased by surface roughness, 136
- lithium pigments, thermal neutrons, 357
- optical, relation to density of defects, 353
- overall rate of radiant energy in cavity, 106
- particle separation of dielectrics, 138
- radiation
 - detector recovery time, 231
 - disturbed surface layer, 149
 - thermopile coating thickness, 227
 - total of surface element, 86
- region of intrinsic optical property effects, 149
- scattering
 - independent, 89
 - influence, 92
 - lateral flux, 96
 - multiple, 94
 - theory, 92
- solar
 - percentage of radiation, atmosphere, 285
 - predictions, aerospace materials, 135
- spectra, radiation effects, 355
- strong, 86
- thickness product in opacity, 87
- total in actual path length scattering, 81
- UV, in total surface area measurement, 181
- Accelerator, microparticle, 468, 475
- Actinometry, phototube calibration technique, 422
- Admittance
 - continuity at interface, 526
 - nickel with nickel-black film, 528
- Adsorption
 - method for measuring surface area, 180
- Aerojet General Corp., 152
- Aerospace Industries Assoc., 215
- Air
 - conduction losses, 325
 - cryodeposited film, absorptance, 531-534
- Air Force Materials Laboratory activities, 485-494
- Albedo, lunar surface, 346
- Alkali halides, radiation effects, 353
- Alodine 401, chemical conversion coating, UV effects, 436
- Alpha particles in solar wind, 345

- Alumel
 - Chromel thermocouples, 366
 - wire in emittance measurements, 328
- Alumina
 - cement, high temperature, 248
 - coarse grained furnace tube, 249
 - cores, 243, 245
 - emittance, not affected by surface roughness, 139
 - fine and coarse-grained, sintered, 249, 250
 - flame-sprayed, absorption band, 250
 - high-temperature core, 243
 - insulation for high-temperature thermocouples, 567
 - molybdenum multilayer coating on molybdenum, 509-524
 - polycrystalline, spectral emittance, 492
 - pure, total emittance, 139
 - sapphire, Z-cut, far infrared reflection, 33
 - spectral reflectance, 253
 - tested in nonisothermal emissivity apparatus, 492
 - volume emittance change with chromic oxide, 139
- Aluminum
 - absorptance
 - normal, solar, 189
 - oxidation during aging, 190
 - adsorption isotherm for HMAB, 20° C, 180
 - alloy 2024, infrared reflection spectrum at 8.5° K, 32
 - alumina film coated, reflectance, 195
 - angular reflectance characteristics, 190
 - anodized, UV degradation, 518-519
 - bombarded by silicon carbide particles, 474-476
 - buffed 6061-T6, temperature rate measurements, 334
 - capsule for solar probe, 555
 - coated bakelite disk, particle bombardment, 480
 - crater volume/unit micrometeoroid kinetic energy, 456
 - diffuse spectral reflectance, 166, 167
 - disk, reflectance before and after bombardment, 477-478
 - dosimeter for neutrons, 369
 - effect of natural oxide layer in rough specimen, 141
 - emittance
 - cratered surface, 470
 - effect of oxide layer formed during heating, 141
 - normal thermal, 189
 - variation with angle, 550
 - evaporated films
 - absorptance, 310
 - absorption-emittance ratio control, 194
 - directional solar absorptance, 303, 308
 - emittance absorption, 192, 195
 - hemispherical emittance, 191
 - oxygen contamination, 190
 - reflectance as function of wavelength, 194
 - reflectance factors, 190
 - silicon dioxide, 195
 - silicon monoxide, 193
 - solar absorptance, 195, 309
 - front surface mirrors, coating protection, 192
 - impurity, substitutional in silicas and silicates, 357
 - in air, roughness and oxidation effects, 142
 - in blackbody emitter, 321
 - in Echo I, 480
 - infrared emittance, oxide films, 151
 - leafing paint, absorptance, 303, 308
 - metallic film, 189
 - micrometeoroid erosion as function of time, 471
 - micrometeoroid velocity, hemispherical cratering, 455
 - mirrors, 192
 - Mylar laminate, 297
 - nonabsorbing film coating, normal solar absorptance, 192
 - normal spectral emittance
 - 326° C, 141
 - 532° C, 141
 - particle impact effects, 538-539
 - periodic, etch figures, 161-162
 - phosphate Ultrox, UV radiation, 357
 - polished, gold-plated, emittance from temperature rates, 331-336
 - radiation properties, sensitivity, 141
 - reflectance
 - decrease by oxide layers, 150
 - low pressure, high deposition rate of silicon oxide coating, 192
 - sandblasted sample, 166
 - shield and capsule for solar probe
 - absorptance, 556
 - temperature variations, 555
 - total hemispheric emittance, 556
 - variation of predicted temperature with distance from sun, 556
 - silicate
 - mullite, total normal emittance, 251
 - synthetic, with silicate binder paint system, 548
 - silicon monoxide coating, reflectance, 193
 - silicon oxide coatings
 - temperature control of satellites in orbit, 194
 - thickness in emittance, 193
 - simulated micrometeoroid erosion, 473-481
 - substrates
 - chemical conversion of thermal control surfaces, 434
 - with interference coatings, 505
 - with cryodeposited CO₂ film, 533
 - surface roughness effects
 - in emittance increase at all wavelengths, 141
 - normal spectral emittance, 141
 - thin films, 161
 - vacuum deposited infrared reflectance, 322
 - variation of emittance with viewing angle, 550
- Amplifier, variable-frequency, detector recovery time, 231
- Anatase-titania paints, theory of backscattering, 96
- Angle of incidence
 - definition, 85
 - directional absorptance, 293, 306
 - solar absorptance, 293, 303-311
- Angle setting
 - error analysis, directional solar absorption measurements, 310
- Dectrak shaft-position encoder, 311

- Angular dependence
 - absorptance and reflectance of special V-groove, etc., surfaces, 136, 505
 - determination of analytically exact measurement deficiencies, 213
 - emissivity, flat platinum surface, 316
 - Antimony trioxide
 - in potassium silicate, UV effects, 433, 434, 436, 444, 450
 - Aperture, solar furnace, angularity effect on emission, 280
 - Apparatus
 - absorptance calorimeter, 367-368
 - angular solar absorptance, measurements, 295, 296, 303
 - blackbody emitter, 321
 - calorimeter, total hemispherical radiation type, 531-532
 - determination of spectral absorption coefficients, 287
 - directional solar absorptance measurement, 294-296
 - double ellipsoid mirror arc imaging furnace, 260
 - emissometer, 321
 - emittance
 - calorimeters, 366
 - spectrophotometer, 314
 - total hemispherical, 512-513
 - experimental spectral emittance (200-600° C) vacuum chamber, 314
 - Gier-Dunkle hemispherical reflectance spectrophotometer, 388
 - goniophotometer, 121
 - heat flux meter, 577
 - integrating hemisphere reflectometer, 512
 - low-temperature space chamber, emittance by decay method, 327
 - quartz oscillator film-thickness monitor, 524
 - reflectance measurements, 260
 - rotational, directional absorptance in vacuum, 303-305
 - specimen porosity, 263
 - spectral reflectance, 512
 - surface properties, 262
 - temperature effect on coatings, 368-369
 - thermal-surface environmental effect sensor, 499
 - UV space simulation exposure, 542
 - Arc lamp, mercury-argon 1 kw UV source, 422
 - Argon
 - antioxidation procedure
 - gamma radiation tests, 438
 - graphite, 234
 - UV vacuum chamber, 435
 - Ascent-stable surfaces, 502
 - Asset vehicle, 567
 - Azimuth angle of polarized reflected rays, 86
- B**
- Backscattering
 - coefficients
 - accuracy of predictions, 96
 - anatase-titania paints, 96
 - depth within material, 96
 - nonabsorbing matrix, 93
 - particle area per unit volume, 93
 - particle concentration, 93
 - porosity and particle size predictions, 207
 - proximity in single-particle predictions, 97
 - reflectivities of pigments, 93
 - dielectric particles, 89
 - effectiveness
 - correction of spherical scattering efficiency, 207
 - definition, 89
 - in phase shift, 91
 - of nonabsorbing spherical particles, 90
 - in pigment volume concentrations, 93
 - increase for cylindrical and long prolate spheroidal particles, 92
 - influence of particle shape and orientation, 89
 - ratio
 - effect of particle shape and orientation, 91
 - nonabsorbing spherical particles, 90
 - nondimensional correlation, 89
 - Rayleigh-Gans domain, 90
 - reflectance, 91
 - refraction index, 91
- Balloon, Echo I, 480
 - Band theory of electrons, 4
 - Barium
 - fluoride, far infrared reflection spectrum, 35
 - sulfate coating, integrating sphere spectrophotometer, 434
 - Basalt powder
 - darkening by solar wind bombardment, 346, 347
 - similarity to Lambert surface, 346
 - sputtered, reflectance similarity to lunar surface, 346
 - Basis functions, attenuated radiation field, 65-67
 - Beckman infrared spectrophotometer, 246
 - Beilby layer
 - definition, 143
 - interface with underlying metal, 143
 - Beryllia insulators for high temperature thermocouples, 567
 - Beryllium
 - copper alloy anodized in sodium hydroxide, 509-524
 - copper substrate, test monitor, directional absorptance measurements, 1304
 - diffuse spectral reflectance, 166-167
 - roughness parameter measurements, 173
 - sintered
 - chemically polished, diffuse spectral reflectance, 166
 - diffuse spectral directional reflectance, 167-168
 - hand-polished, 170
 - microinterferograms, 171
 - pressed, 165
 - BET (Brunauer-Emmett-Teller) method for total surface area, 181
 - Binders, polymeric, UV degradation, 381-389
 - Black
 - camphor vs carbon, reflectance, 221
 - gold
 - thermocouple, 221
 - thermopile surface, 228

- graphite
 - thermocouple coating, 221
 - thermopile coating, 221
 - Blackbody
 - behavior of specular reflecting cavities, 110
 - calibration curve, total hemispherical emittance, 513
 - cavity effect in surface roughness, 97
 - cone, radiation detector, 220
 - cone, radiator, 321
 - deep specular cavity, 110
 - depth, 110
 - design for high temperature, 281, 314
 - flux
 - dependent upon refraction index, 199
 - dielectrics, 199
 - furnace
 - cavity spectral emittance, 245
 - description, 243-246
 - differential thermocouple temperature control, 246
 - nickel oxide black coating, 245
 - graphite
 - argon antioxidant, 234
 - power transformer, 235
 - infrared radiation source reference with known temperature accuracy, 287
 - isothermal environments taken as radiators, 111, 323
 - radiance standards, 217
 - radiation
 - in emittance definition, 118
 - Kirchhoff's law, 76
 - radiation source
 - aluminum cone, 321
 - graphite tube, 233-240
 - Inconel cylinder with slit, 288
 - self-contained field use, 233-240
 - radiator, design, 284
 - solar absorber effectiveness, 510
 - Stefan-Boltzmann law defined, 217
 - temperature in solar furnace calibration, 278
 - thermal gradient effects, 115
 - Blackbody emitter
 - description, 321
 - power-on-timing equipment, 322
 - Bleaching
 - air aging effects, 435
 - gamma irradiated materials, 359
 - titanium oxide/epoxy, spectral absorptance, 424
 - visible light effects, 426, 446
 - Bloch theory of free electrons in solids, 6
 - Blooming over range of wavelengths, 527
 - Bolometer
 - solar furnace calibration, 284
 - surface sensitivity, 226
 - thermister
 - calibration by blackbody radiation, 282
 - short response time, 281
 - Borosilicate glass, 205
 - Boundary region
 - gradient changes, 200
 - heat transfer in thin vs thick layers, 202
 - Brass
 - cavity, 120
 - cloth, neutral-filter, 261
 - crater, 456
 - Brazes, high-temperature thermocouples, 569
 - Brewster angles, 48-59
 - Bridge potentiometer, 306
 - Brunauer-Emmett-Teller method for total surface area, 181
- C**
- Cadmium
 - crater volume, 456
 - micrometeoroid erosion as function of time, 471
 - Calcium
 - fluoride-sodium silicate pigment vehicles, 356
 - silicate in silicone, UV stability, 540
 - zirconate
 - fine grained, 249
 - reflectance, 254
 - spectral emittance, 251, 254
 - total normal emittance, 251
 - Caliblock
 - microinterferograms, 176
 - profilogram, 176
 - Calorimetry
 - absorptance apparatus, 367-368
 - carbon arc monitor, 296
 - cryodeposited films, absorptances, 531-534
 - emittance, 322, 366, 488
 - temperature rate measurements, 331-336
 - Camera, time lapse, 183
 - Camphor-black reflectance, 221
 - Carbon
 - absorptance, solar, 296
 - arc, equilibrium temperature, 300
 - black
 - emittance, 259-275, 550
 - reflectance over camphor black, 221
 - carbon bonds, break, 382
 - high purity, spectroscopic grade, 267
 - image pyrometer, 260
 - phenolic nylon char similarity, 272
 - radiation profile, 261
 - reflectance, 267-270
 - root mean square slope, 269, 270
 - specimen preparation, 267
 - surface profile, 267
 - Carbon dioxide
 - absorption bands, 285
 - cryodeposited film, absorptance, 531-534
 - Cary spectrophotometer, 166, 177, 252, 355
 - Cat-A-Lac blackness, wavelengths greater than 15 microns, 534
 - Cavities
 - absorbers, 103, 105, 108
 - absorption, 105, 110

- Cavities—Continued
 aluminum oxide
 emittance, 120
 optical filters, 120
 black, paper lined, 123
 velvet lined, 122
 blackbody
 depth, 110
 design, 314
 brass, 121
 closed-form solutions, 106
 cylindrical, 117, 119, 120, 122, 128, 130–131
 decrease in opening, 110
 deep, 127
 depth increase, 108, 120
 detector, 221
 ellipsoidal, 460
 emission, 104, 105, 106, 108, 115, 118
 emittance, 108, 110, 117, 118, 119, 120, 124, 126–128, 129, 131
 green, paper-lined, 123
 Gouffé-formula, correction, 131
 hemiellipsoidal, 460
 hemispherical, 460
 Kirchhoff radiation, 118
 nonglossy paper lined, 121, 122–123, 124
 open
 and closed, difference, 115
 depth effect, 115
 end, as passage, 115
 end, truncated, 115
 parallel ray bundle, 110, 131
 plane surface, 107
 radiometer observation, 118
 rectangular groove, 109
 reflectance, 120, 121, 123, 125, 131
 semitransparent material, 98
 shallow cylindrical, 117–131
 shallow hole method, 127
 spectral reflectance, 123
 spectrophotometer observation, 118, 120
 specular, 110, 126, 131
 spherical, 106, 109, 131
 V-grooves, reflecting, 110
 velvet paper-lined, 126
 white paper lined, 123
 yellow “glare-free” velvet coated, 126
Cell, lead sulfide, surface sensitivity, variation, 229
Cellulose diacetate, coated with HMAB, adsorption isotherm, 180
Cementing powder particles by sputtered atoms, 346
Cements
 alumina, high-temperature, 248
 potassium and sodium silicate, 503
Center point viewing of blackbody cavity bottom, 127
Ceramics
 absorption
 bands near UV, 85
 coefficient in radiant transfer, 92
 coefficient, wavelengths of high transparency, 85
 coatings, development, 98
 conduction and radiation heat transfer, 97
 emission, 88
 emittance, 117, 139, 241
 Fresnel's equations, 95
 infrared, 85
 paint, black spectral emittance, 313
 porosity, 95
 powder reflectivity, 94
 reflectance oxides, 257
 scattering by weakly absorbing, 92
 scattering centers on radiation transmission, 199
 surface temperature gradients on emittance, 492
 tailoring scattering properties, 96, 100
 thermal radiative applications, 83
Cesium relaxation times and electrical resistivities, 17
Cesium bromide prism, 315
Chambers, vacuum, 422, 435
Char, ablation
 arc image furnace exposure, 273
 arc-jet formed, 272
 hemispherical spectral emittance, 265–267, 271, 272
 oven produced, phenolic nylon, 271
 reflectance, 271, 272
 surface porosity, 273
 temperature vs emittance, 272
Chromel wire, 328, 366
Chromium
 emittance, cratered surface, 470
 infrared reflection spectra, 32
 microparticle damage, 469
 oxide in alumina, emittance, 139
Cloth reflectance, effect of lay of weave, 165
Cloud, Mie theory of scattering, 6
Coatings
 absorptance
 change, 423
 function angle of incidence, 303
 low, 535–548
 saturation limits, 428
 thickness, 438
 absorptance-emittance ratio, 307
 alumina-molybdenum, 509–524
 aluminum, 192, 433, 492
 aluminum-Ultrox, 357
 antimony trioxide, 444, 450
 ascent environment, 537
 beryllium, 509–524
 bleaching process, 427
 calcium fluoride-sodium silicate pigment vehicles, 356
 chemical conversion, 434
 columbium, 492
 contamination, 537
 curing agents, 430
 degradation, 427, 446–451, 444
 deposition rates, evaporated films, 192
 directional surface, 504–505
 electrically conductive, 497

- electrons, effects, 538
- emittance, 492, 540
- evaporator, 72-inch, 194
- Explorer II, 497
- glass, 202, 205, 207, 208, 209
- graphite, 221
- inorganic, 396, 537
- interference, 505, 514-524
- Lithafrax-potassium silicate, 543
- Lithafrax-sodium silicate, 359
- lithium fluoride-sodium silicate, 356
- magnesium oxide integrating sphere, 230
- Meteoroid Detector Satellite, 498
- mirrors, 192
- molybdenum, 492
- neutron effects, 538
- nickel oxide, black, 245
- nonabsorbing, 192
- nonspectral, 505
- nuclear radiation effects, 358
- organic, 293
- OSO-I flight data, 447-449
- paint, black ceramic, 317, 319
- particle impact, 538-539
- paste-on films, 503
- photodegradation, 433-441
- photomicrographs, 205
- pigmented, 205, 417-418, 501
- platinum and silicon dioxide, 195
- prelaunch environment, 498, 537
- protection thickness, mirrors, 192
- proton effects, 538
- radiation, high energy, 433
- satellite surface absorption, 308-309
- selected, 434
- Saturn, SA-5, 497
- semiconductor pigment vehicles, 360
- scattering efficiency, 208
- silicon monoxide vacuum evaporation, 193
- silica-silicone, 543
- silicon oxide-aluminum, 192-195
- silicon dioxide-germanium, 195
- silicon monoxide, 192
- solar wind, 347
- tantalum, 492
- temperature resistant, 540
- thickness, 227, 437, 440
- titania, OSO-I, 447-448
- titania-silicone pigment vehicles, 361
- transparent, 501
- UV
 - radiation, 435-438
 - resistant, 540
 - stability, 433-438
- vacuum resistant, 540
- Vanguard II, flight data, 539
- vapor deposited, 498
- white, 55
 - solar absorptance, 392
 - stability, 423
 - sun-oriented spacecraft, 554-555
 - UV, 391-420
- zinc oxide
 - curing, 402
 - degradation, 450-451, 539-540
 - solar factor variation, 414
 - UV radiation, 400
- zinc oxide-methyl silicone
 - emittance, 543
 - solar absorptance, 410
- zinc oxide-potassium silicate, 444
- zinc oxide-sodium silicate, 362
 - emittance, 543
- zinc sulfide-sodium silicate vehicles, 363
- zircon-potassium silicate
 - absorptance, 543
 - emittance, 543
- Cobalt
 - dosimeter, 369
 - gold alloy thermocouple, 31
 - relaxation times, 17
 - 60 radiation facility, 365, 433
- Coblentz thermopile, 222, 223, 224, 227
- Cold working, 136-137
- Color centers
 - disappearance, alkali halide crystals, 538
 - formation, semiconductor pigments, 354
 - radiation induced, 358
 - semiorganic coatings, prevention, 417-418
- Collimation
 - apparatus, absorptance calibration, 305-306
 - precision in solar furnaces, 283
 - sensor field of view effect, 283
 - radiation, solar furnaces, 283
- Colloidal dispersions in scattering predictions, 94
- Columbium
 - aluminum-silicon-chromium slurry coating, 492
 - (chromium-titanium) silicon coating, 492
- Compton scattering in free electron release, 352
- Computers, digital, temperature corrections in sensor design, 571-572
- Conduction
 - conversion, radiant and lattice at surfaces, 202
 - emittance corrections, 325
 - lattice, 200, 203
 - true thermal heat transfer formulation, 88
- Conductivity
 - due to radiation dielectrics, 199
 - effective, due to radiation, 198
 - glass vs refractory, radiation, 201

- Conductivity—Continued
 radiation, nonscattering materials, 198
 thermal
 analog of lattice, 199–200
 effective, 203
 semitransparent dielectrics, 203
 thin layers, 202–203
 total effective related to temperature gradients, 200
- Conductors
 Brewster angle, 59
 reflection characteristics, 59, 137
 reflection coefficients, 54
- Constantan-copper thermocouple, 434
- Contaminant, surface, 136
- Cooling, samples, UV radiation, 422, 434
- Copper
 adsorption isotherm for HMAB, 180
 aluminized black, 278
 beryllium alloy anodized, 509–524
 craters, 456
 Drude-Zener theory, 149–150
 emittance, 149, 189, 191
 infrared reflectance, 149
 metal film, 189
 micrometeoroid erosion, 471
 normal solar absorptance, 189
 reduction of oxides by ion bombardment, 346
 reflectance, 149, 150
 relaxation times, 17
 solar absorptance, sea level vs outer space, 189
 specimen base test coatings directional absorptance, 304
 sputtering yields, proton bombardment, 345
- Core, alumina, high-temperature, 243
- Corning
 optical filter, glass, 261
 thermometer white glass, 166
- Cosine diffuser, goniophotometric measurements, 120, 121
- Cosine law, Lambert
 deviation for emission of energy, 85, 86, 265
 rough surface, 146
 smooth surface, 146
- Cosmic rays, surface radiation effect, 340
- Craters
 ellipsoidal, general analysis, 471
 emittance, 456–467
 hemispherical, emittance, specularly reflecting walls, 467
 lining by impinging hypervelocity particle, 472
 small, optical surface properties, 471
- Crest and root lines, surface texture measurement, 170
- Cryogenics
 in large space chambers, 531
 propellants, coatings and insulation for space storage, 559–566
- Cupric oxide reduction by ion bombardment, 346
- Curing agents, thermal control coatings, 430
- Current ratings of electric wires, affected by insulation emittance, 321, 324
- Cylinder temperatures at various distances from sun, 340
- D**
- Debye length, 497
- Decay method, emittance, 325–330
- Defects
 absorption, 352
 concentration, 354
 interstitials, 353
 multiple type, 354
 radiation induced, 352
 silicates, 353
 sites, optical behavior, 359
 substitutional impurity, aluminum, 357
 vacancy material, 353
- Degradation, see also UV, nuclear radiation, γ -radiation, solar wind, and electrons
 desirability, trip to Mars, 506
 organic thermal coatings, 536
 polymer films, flight and ground studies, 381–389
 prediction, 359
 UV
 anodized aluminum, 518–519
 lamps, 435
 solar absorbers, 518–519
- Delrin, 304–305
- Detectors
 blackbody or cavity, 221
 cavity
 camphor black, 221–222
 carbon black, 221–222, 227
 gold-foil, conical, 221
 Coblenz thermopile, 223–224, 226, 227
 cooled thermopile, 512
 Eppley thermopile, 226, 228
 Golay pneumatic cell, 30
 irradiance, 218
 photosensitive, 228–229
 radiation, thermal, 221
 recovery time, 231
 Reeder thermopile, 225
 standards, 217
 thermal radiation
 blackened, calibration, 218
 spectral sensitivity, 220
- Diagonal scatterplate, 315
- Diagonal mirror, monochromator, 315
- Diamond
 optical constants, 5
 wheel-ground zirconia, 270
- Dielectric constant, theory, 13–14
- Dielectrics
 Brewster angle, 59
 emissivity, 40, 42, 44
 external surface effects on radiation, 197
 films, 511
 flux in isothermal solid, 197

- homogeneous
 - spectral absorption coefficient, 287
 - transmission through, 198
- nonopaque, thermal radiation, 214
- perfect, phase change in reflection, 86
- pigment radiation damage, 354
- radiative emission, 492
- radiation scattering, 197
- reflected energy, polarized, 85
- reflection characteristics, 59
- reflection coefficients, 54
- scattering centers on radiation transmission, 198
- surface effects on radiation, 197-203
- UV wavelength limitation, damage control, 354
- Diffraction
 - hemispherical emittance, 146
 - rough surfaces
 - emitters, 319
 - specular reflectance, 148
 - with interference, 97
 - theory, surface optical characteristics, 154-155
- Diffuse incoming radiation, 108-110
- Diffusers, paper, 123
- Directional emitters, 316, 319, 504
- Dissimilar metals, radiation transfer between, 43
- Dosimeters
 - aluminum, 369
 - cobalt, 369
 - nitrous oxide, 369
 - polyvinyl chloride, 389, 430
 - sulphur, 369
- Drag, short-duration flow in shock tube, 474
- Drude
 - dispersion formula, 4
 - free-electron model, 11
- Ductility, tungsten and rhenium wires after heating, 570
- Dust particles, mass distribution near Earth, 479

E

- Eastman, lead sulfide cell, 228, 229
- Echo I, 480
- Edge effects in irradiating disk, 300
- Einstein, thermal equilibrium between solid and black-body radiation, 63
- Electrical conductivity
 - bare metals, 502
 - coatings, 497
 - pigmented coatings, 502
 - thin films, 502
- Electrical resistivity, variation with temperature
 - molybdenum, 11, 26
 - niobium, 11, 26
 - tantalum, 11, 26
 - tungsten, 11, 26
- Electrical wire, current ratings, affected by emittance of insulation, 321, 324
- Electromagnetic energy symposium, 1960, 154
- Electromagnetic radiation
 - second-quantized treatment, 63
 - stability of inorganic pigments, 382
- Electron beam evaporator, 522
- Electron spin resonance, polyvinylchloride, 418-419
- Electron theory
 - correlation with electrical resistivity, 25-26
 - dielectric constant, 13-14
 - hemispherical emissivity, 17
- Electroplating, nickel black, 525
- Electropolishing
 - copper, 149
 - dark mirrors, 152
 - germanium, 150
 - removal of substrate effects, 152
 - removal of sulphur films, 152
 - sample preparation, 149
- Emery polishing paper, 268
- Emission
 - angular, 316, 317
 - cavities, 103, 104, 108, 111
 - conical hole, 108
 - fundamental factors, 485-487
 - glass sheets, 87
 - nonisothermal specimen, 97
 - nonisothermal volume in ceramic, 88
 - opaque materials, 97
 - rectangular groove, 108
 - scattering effect, dielectrics, 197-198
 - solar furnace instrumentation, 281, 282
 - spherical cavity, 109
 - surface layer modification, 149
 - V-groove cavities, 108
- Emissivity
 - absorptivity, unequal to, 63
 - angular
 - parallel components, 41
 - perpendicular components, 41
 - blackbody system, 238, 239
 - ceramic, homogeneous, 86
 - dielectric, 40, 197-198, 203
 - Hagen-Rubens formula, 64
 - hemispherical, 11-28, 86
 - infinite parallel plates, 41-42
 - infinite parallel specular surfaces, 39-41
 - iridium, 572-573
 - metals, 40-41, 42, 63-71, 67-69
 - non-isothermal apparatus, 492
 - normal, 11-28
 - opaque surface, 85, 179
 - optical thickness in measurement, 98
 - platinum surface, 316
 - ratio, hemispherical to normal, 41
 - reflectivity relationship, 5, 85
 - semiconductors, 40-41
 - spectral
 - parallel components, 14
 - perpendicular components, 14
 - zirconia, 572-573

- Emissometer
 - description, 321
 - infrared window, 545
 - silver-bismuth thermopile, 545
 - teflon measurements, 323
- Emittance
 - absorptance ratio
 - cryogenic propellant stored in space, 559-566
 - poly vinyl chloride, 388
 - accuracy of techniques, 335
 - Alodine 401, 437
 - Alumel wire, 328
 - alumina, 139, 250
 - polycrystalline, surface roughness, 99
 - aluminum
 - adsorption ratio, 195
 - cratered surface, 470
 - mullite, 251
 - normal spectral, 141, 142
 - normal thermal, 189
 - oxide, 251
 - oxide films, 194
 - shield and capsule for solar probe, 556
 - silicon oxide, coating thickness, 193
 - surface roughness, 141
 - T6-6061, 334
 - analytical expression, 117
 - angle of emission, as function of, 314
 - apparent, 106, 118
 - average, 306, 307
 - axial, 117
 - black coatings, 520
 - blackbody, 277, 321
 - calcium zirconate, 251, 254
 - calorimetric measurement method, 488
 - carbon, similarity to nylon phenolic char, 272
 - cavities
 - aluminum oxide, 120
 - apparatus, 315
 - artificial sky for illuminating, 119
 - averaging process, 127
 - brass, water-heated, unpolished, 120
 - cylindrical, 108, 119, 128
 - deep, 127
 - derivation of expression, 118
 - Gouffe theory, 129
 - illuminated by incident beam, 127
 - infinite depth, 119
 - measurement method, 488
 - nonglossy paper-lined, 124
 - opening, derived from apparent reflectance, 131
 - predictions, 127
 - shallow, 118, 127
 - spectrophotometer, 118
 - specular components, 119
 - specular reduction, hemispheric and normal measurements, 131
 - spherical and cylindrical, comparison, 131
 - theory, 124
 - thermal experimental equipment, 120-121
 - yellow, glare free, velvet coated, 126
 - ceramics
 - adjusted by added pigment, 139
 - oxides, 241
 - rotating cylinder, 242
 - chromel wire, 328
 - chromium, cratered surface, 470
 - conduction corrections, 325-330
 - copper
 - effect of electropolishing, 149
 - normal thermal, 189
 - cratering, change, 456-457
 - decrease after initial thermal polishing, 185
 - definition, 86, 118, 145
 - dielectrics, optical thickness effect, 198
 - directional
 - equation, 94
 - Fresnel's equations, 146
 - optical constants, 146
 - surface roughness increase, 146
 - effective
 - cavity greater than its material, 98
 - gain reduced by "mean free path of photon," 99
 - surface contamination, 137
 - electrical power dissipation, 183
 - electrical wire insulation, 321
 - emitter, directional, 317
 - energy
 - in determination of optical constants, 86
 - engineering stock material, 146
 - gold
 - buffed, on aluminum, 335
 - cratered surface, 470
 - normal thermal, 189
 - polished, 329
 - graphite, 272, 467, 471
 - grooved surface
 - angular, 316-317
 - directional, 316
 - heat meter surface, molybdenum silicide on molybdenum, 578
 - hemispheric
 - ablation chars, 259-275
 - aluminum film, 191
 - aluminum shield and capsule, 556
 - behavior in diffraction region, 146
 - beryllium, 138
 - blackbody calibration, 513
 - copper film, 191
 - decay method, 326
 - definition, 118
 - evaporated metal films, 190
 - experimental apparatus, 22
 - gold film, 191
 - measurement apparatus, 512
 - molybdenum, 11, 25, 26
 - multiple reflection on rough surfaces, 147
 - niobium, 11, 24, 26
 - platinum, 185

- platinum film, 191
- predictions, 155
- rhodium film, 191
- silver film, 191
- surface roughness, 145, 147, 153
- tantalum, 11, 24, 26
- tungsten, 11, 25, 26
- illuminometer, 119
- Inconel
 - adsorbed film removal, 158
 - oxidation change, 158
- infinite coating thickness, 87
- infrared
 - aluminum oxide film, 151
 - basic surface types, 495
 - low, with high solar absorptance, 509
 - spectrophotometer, difficulty, 246
 - titanium oxide film, 151
- inorganic coatings, 539
- insulating material, 150–600° F, 324
- iridium, 573
- Kirchhoff's law, 146, 148
- Lithafrax-potassium silicate, 543
- magnesium
 - aluminate, 251
 - Dow 7 coated, 335
 - oxide, 251
- measurement methods, review, 241
- metal films, 189–195
- micrometeoroid crater, 457
- micrometeoroid penetration, change, 460–467
- nonmetals, 241
- normal, 87, 120, 127, 131, 251, 252, 280
- nylon phenolic char, 272
- opaque material, 97, 117, 145
- organic materials, 321–324
- oxide films
 - aluminum, 254
 - effect visible wavelengths, 150
 - influence, 145
 - infrared wavelengths, 150
 - silicon, 195
 - surface, 145
- Planck function, 69, 131, 279, 487
- platinum, 183, 184, 186, 187, 189, 316
- polarization in infrared, 191
- predictions, aerospace materials, 135
- pyrheliometer, 279
- radiative transfer calculations, 145
- reduced by specularly, 131
- reflectance comparison, 253
- refractive index effects, 88
- refractory metals, 4
- rotating cylinder furnace method, 241, 242, 243
- rotating sector apparatus, 280, 281
- rotating specimen measurement, 488
- shallow hole method, 118
- silica-silicone coating, 543
- silica, sintered, 251
- silver
 - cratered surface, 470
 - polished, 328, 329
- sintered materials, 251, 252
- solar furnace, 278–280
- solids
 - above 2000° C, 277–286
 - micrometeoroid effects, 453
 - moderate temperatures, 277
- space capsule, carbon black and aluminum surfaces, 550
- spectral
 - ablation char, 265–267, 271
 - aluminum oxide, 254
 - black ceramic paint, 317
 - carbon, 259–275
 - definition, 118
 - directional, 131, 313, 319
 - error sources, 255
 - flat black ceramic paint, 317–318
 - graphite, 267–270
 - magnesium aluminate, 252
 - magnesium oxide, 254
 - platinum, polished, 250
 - radiative transfer calculations, 145
 - sintered calcium zirconate, 251
 - sintered magnesium oxide, 252
 - spectrophotometer, double beam, 242
 - stainless steel, surface oxidation, 159
 - temperature control problems, 145
 - thorium oxide, 254
 - tungsten, 26
 - X-point, 4
 - zircon-potassium silicate coating, 543
 - zirconia, 259–275
 - zirconium silicate, 254
- surfaces
 - cratered, stainless steel, 470
 - damage, 145
 - metallic, chemical effects, 159
 - optically smooth opaque, equal to emissivity, 179
 - roughness, 5, 145
 - roughness vs damage, 147
 - topographical effect, 160–163
 - with predetermined values, 139
- Teflon, 322–324
- temperature
 - at 337° K, 120
 - at 1100° K, 120
 - cycling, variations, 157, 158
 - high, 277–278, 285
 - high, as function of time, 183
 - low, losses from decay method, 325–330
 - measurements, iteration and rate equation methods, 332–333
- thermal
 - absorptance ratio, solar, 189
 - ceramics, polycrystalline, 117
 - low, with high absorptance, 525–530
 - measuring equipment, 243, 247, 248

- Emittance—Continued
 - thermal—Continued
 - predictions, 243
 - pyrometer measurements, 117
 - shallow cylindrical cavities, 117–131
 - time variation determination, 184
 - zinc oxide
 - methyl silicone coating, 408, 543
 - potassium silicate coating, 543
 - zirconium, sintered
 - oxide, 251
 - silicate, 251
 - Emitter, directional, 316, 319, 504
 - Enamels
 - space utilization requirements, 501
 - vitreous surfaces
 - median solar absorbers, 501
 - total absorbers, 501
 - Energy
 - conversion at surfaces, 200
 - electromagnetic symposium, 1960, 154
 - threshold, thermal control coatings, UV radiation, 426, 428
 - Epoxy
 - rutile titania, OSO-1, 444
 - titanium dioxide, OSO-1, 447–448
 - Eppley
 - thermopile, 2266
 - gold black surface, 228
 - lengthwise scan, 224, 226
 - spectral sensitivity, cavity detector, 228
 - Erosion
 - micrometeoroid
 - aluminum, 471
 - cadmium, 471
 - copper, 471
 - lead, 471
 - steel, 471
 - Errors
 - solar absorption
 - angle of incidence, 309–310
 - beam transfer, 318
 - blackbody cavity design, 318
 - detector emission, 318
 - directional absorptance, 309–310
 - equilibrium temperature, 310
 - mirror absorption, 318
 - radiation, stray, 310
 - signal amplification, 318, 319
 - signal recording, 318, 319
 - specimen edge irradiation, 308, 310
 - spectral distribution of power source, 310
 - spectral emittance, 318–319
 - stray light, 318
 - temperature effect, 318
 - thermal equilibrium, 309, 310
 - wavelength, relative effect, 318
 - window emission, 318
 - Etching
 - aluminum, 161
 - thermal, 183
 - thin oxide films, 162
 - Exchange factor, radiant interchange, 112
 - Explorer I, VII, VIII, XI, 479
 - Exposure dependency of UV radiation damage, 423–425
 - Extinction
 - coefficient, 98, 151, 199
 - scattering as predominant mechanism, 199
- F**
- Fabry-Perot, interference-type absorbers, 510
 - Fairy castle, lunar surface structure, 348
 - F-center, definition, 353
 - Films
 - absorptance, gamma vs UV, 430
 - alumina coated, reflectance, 195
 - aluminum, evaporated
 - aluminum oxide coated, 194
 - hemispherical emittance, 191
 - oxygen contamination, 190
 - reflectance factors, 190
 - silicon dioxide coating, 195
 - copper, evaporated, hemispherical emittance, 191
 - dielectric, evaporated on opaque metal films, 189
 - germanium
 - erosion, micrometeoroid, 195
 - on aluminum and silicon dioxide, 195
 - sputtering erosion, outer space, 195
 - germanium, evaporated
 - amorphous, reflectance, 150
 - epitaxial, reflectance, 150
 - gold, evaporated, hemispherical emittance, 191
 - interference, selective absorbers, 510
 - metal
 - aluminum, 189
 - copper, 189
 - gold, 189
 - platinum, 189
 - preparation, 189
 - rhodium, 189
 - silver, 189
 - with surface coatings, 191–192
 - metal, evaporated
 - deposition techniques, 189–190
 - evaporation technique and rate, 190
 - incidence angle effect, 190
 - optical constants, effect, 190
 - pressure and purity effect, 190
 - solar absorptance, 189–195
 - surface coatings, 191–195
 - without surface coatings, 189–191
 - multiple coating
 - alumina and molybdenum, 509–520
 - nickel black and nickel, 525–530
 - platinum and silicon dioxide, 195
 - solar energy converters, 195
 - theory, 510, 526

- oxide
 - aluminum, infrared emittance, 151
 - thin, on aluminum substrate, 162
 - titanium, infrared emittance, 151
 - platinum, evaporated, hemispherical emittance, 191
 - polymer, ultraviolet degradation, 381-389
 - polyvinyl chloride, methyl ethyl ketone residues, 384
 - rhodium, evaporated, hemispherical emittance, 191
 - silica, evaporated
 - aluminum coating, 194
 - reflectance as wavelength function, 194
 - silicon dioxide
 - emittance spectra, 195
 - interference and reflectance spectra, 195
 - silicon monoxide evaporation, 192
 - silver, evaporated hemispherical emittance, 191
 - surface films, effects on optical properties, 135-195
 - surfaces, test condition effects, 157
 - thickness
 - deposition monitoring, 194
 - eddy current tester, 437
 - thin, refraction index modification, 152
 - Filters
 - brass cloth neutral light, 261
 - detector system response, 264
 - electronic, for chopper frequency, 284
 - glass, for infrared, 315
 - infrared, interference coating, 505
 - near-UV pass, 422, 426
 - optical, see Optical filter
 - silver chloride, monochromator, 315
 - silver sulphide, monochromator, 315
 - spectra, 227, 426
 - spectroradiometer, block diagram, 227
 - UV, flux control, 422
 - Finishing Symposium, American Electroplaters Society, 205
 - Flame spraying, 342
 - Free electrons
 - degradation, thermal control surfaces, 352
 - metals, 11, 63, 149
 - release
 - Compton scattering, 352
 - gamma radiation, 352
 - neutrons, 352
 - pair production, 352
 - UV radiation, 352
 - Fresnel equations
 - aluminum, theoretical absorptance, 303
 - ceramics, high porosity and density, 95
 - dielectrics, 40, 203
 - directional emittance, optical constants, 146
 - dispersion, radiation effect, interpretation, 353
 - emissivity
 - experiment vs theory, 313, 316
 - hemispherical to normal ratio, 39
 - hemispherical absorptance calculations, 39
 - metals and semiconductors, 40-41
 - optical region, numerical solutions, 45-61
 - radiation
 - smooth surfaces, 87
 - within materials, 85
 - reflection, 84, 197, 203
 - reflectivities, plane surface, 95
 - specular reflectance, 351
 - surface reflectance, 95
 - thin rough organic coatings, 293
 - Furnaces
 - arc-image
 - carbon arc, emittance measurement, 279
 - contamination freedom, 278
 - description, 260
 - double ellipsoid mirror, 260
 - radiant and reflected energy separation, 278
 - with image pyrometer, 260
 - blackbody
 - cavity, spectral emittance, 245
 - description, 243-246
 - nickel oxide black, 245
 - schematic, 245
 - temperature control system, 246
 - temperature gradients, 246
 - conventional, limitations, 277
 - induction
 - auxiliary susceptor use, 278
 - limitations, 277
 - rotating specimen
 - description, 243
 - temperature control system, 246
 - temperature gradients, 246
 - solar
 - blackbody temperatures attainable, 278
 - calibration techniques, 284
 - corrections, 278, 280
 - emittance measurements, 277, 278-280, 285
 - general specifications, 280
 - instrumentation, 279, 280-282, 284
- G**
- Gage blocks
 - diffuse spectral reflectance, 166
 - Gamma radiation
 - coating absorptance table, 439
 - cobalt-60 cell, 438
 - dose equivalent, 439
 - glass, absorption spectra, 430
 - polyvinyl chloride
 - optical density change, 387
 - ultraviolet equivalence, 387
 - simulation of space, 438
 - stability, surfaces, 438-439
 - test procedure, coatings, 438
 - ultraviolet
 - comparison, 439-440
 - equivalence, 429, 430
 - Gaps
 - plane walled, 111
 - radiant energy transmission, 111

- Gas flow counter, Tracerlab model FD-1, 179
- Gaussian distribution
 - roughness, effect on reflectance, 147
 - temperature across irradiated specimen, 262
- General Dynamics Astronautics Nuclear Aerospace Research Facility, 365
- General-Electric spectrophotometer, recording, 166
- Germanium
 - absorption, far infrared, 36
 - film
 - absorptance-emittance ratio, 195
 - aluminum and silica dioxide base, 195
 - measuring erosion in outer space, 195
 - optical constants, 5
 - optical properties, crystal structure, 150
 - reflectance
 - evaporated amorphous, 150
 - evaporated epitaxial, 150
 - single crystal, electropolished, 150
- Gier-Dunkle spectrophotometer, hemispherical reflectance, 388
- Glass
 - absorption coefficient, emission relation, 87
 - aluminized ground, reflectance, 147, 148
 - borosilicate, 205
 - coloring by high energy radiation, 438
 - diffusing quartz plate, 229
 - emission, thin sheets, 87
 - gamma radiation, absorption spectra, 430
 - heat transfer, 88
 - opacity, long wavelengths, 319
 - opal
 - radiative-transfer formulation, 96
 - reflectivity computation, 95
 - polarization, visible light, 85
 - reference surface, 180
 - scattering centers
 - radiation conductivity, 199
 - radiation transmission, 199
 - sintered coating
 - application, 205
 - density measurements, 205
 - evaluation, electron microscope, 205
 - molybdenum substrate, 205
 - on metal heat transfer, 202
 - particle size, 205
 - photomicrographs, 206-207
 - porosity determination, 205
 - sintered, 205, 208-209
 - standard, working
 - Corning Thermometer White, 166
 - Vitrolite, 166
 - tempering, 202
 - thermal radiation patterns, 199
- Glide reentry vehicle thermal sensor design, 567-579
- Glyptal paint for molybdenum anodizing bath insulation, 512
- Golay cell
 - detector, 30
 - uniform surface sensitivity, 226
- Gold
 - absorptance, normal solar, 189
 - solar, sea level vs outer space, 189
 - adsorption isotherm, HMAB 20° C, 180
 - cobalt alloy thermocouple, 31
 - electrical resistivities, 17
 - emittance
 - cratered surface, 470
 - normal thermal, 189
 - evaporated films
 - absorptance, directional solar, 303, 308
 - hemispherical emittance, 191
 - foil
 - conical cavity detector, 221
 - metal films, 189
 - microparticle damage, 469
 - plate on aluminum, temperature rate measurement, 335
 - polished, emittance measurement, 329
 - reflectance, near ultraviolet, 189
 - relaxation times, 17
- Goniophotometer
 - ASTM Standard Practice Recommendation E 167-60T, 121
 - curves, paper
 - black, 122
 - green, nonglossy, 121
 - white, 122
 - yellow "glare free velvet" coated, 125
 - measurement techniques
 - cosine diffuser deviation, 121
 - reflected flux intensity, 121
 - tungsten lamp source use, 121
- Gouffé
 - blackbody reference source, 288
 - cavity
 - correction, 131, 490
 - emittance derivation, 129
 - spherical and cylindrical, comparison, 131
 - derivation of f , 129
 - diffusely reflecting walls, 129
 - off-center incident beam, 130
 - radiant flux assumptions, 129
- Graphite
 - blackbody
 - argon antioxidant, 234
 - heating, power transformer, 235
 - system, 238
 - coating
 - thermocouple, 221
 - thermopile, 221
 - emittance
 - correction, 268
 - similarity to phenolic nylon char, 272
 - spectral, measurement, 267-270
 - temperature vs wavelength, 268
 - reflectance
 - measurement, 267-270
 - temperature vs wavelength, 268
 - roughness root mean square slope, 270

specimen preparation, 267
 spectroscopic grade, 267
 surface, profile data, 267
 tube, blackbody radiation source, 233-234
 Grating
 reflection type, 282
 Groove
 infinite, emittance, 316
 Gun, light gas, for microparticle range, 468-469

H

Hagen-Rubens emissivity formula
 comparison with data, zirconium and iridium, 572-573
 theory, d-c conductivity of metals, 4, 64
 Halides, alkali, optical properties, radiation effect, 353
 Hamaker equations, transparent materials, radiation characteristics, 491
 Head, dividing, angular measurement, 306
 Heat
 balance equations
 absorptance determinations, 307
 nonisothermal situation, 77
 conduction losses in emittance measurements, 325-330
 flow, rotating specimen, 243
 flux
 aerodynamic, zirconia disk, 576
 image center, solar furnace, 219
 meter, 577-578
 prediction accuracy, 579
 shields
 graphite, 486
 metallic borides, 486
 metallic carbides, 486
 metallic nitrides, 486
 transfer
 approach, surface problems, 135
 boundary region of ceramics, 200
 calculations in ceramics, heat balance, 203
 cavity openings, 104
 dielectric, scattering centers, 198-199
 glass, 88
 homogeneous ceramics, 88
 radiation, 41-42, 73-81, 198-199, 550
 radiation analysis, 200
 rates, 107, 201, 487, 564-565
 thin layers, 202-203
 titanium carbide, 487
 variation, insulation thickness, 563
 Helio-stat in solar absorptance measurements, 295
 Helium oxidation protection, 269
 Hemispherical emittance, see Emittance
 Heterogeneous materials
 absorption, 88
 radiative properties, 83
 optical p transfer, 84, 97
 scattering, thermal radiation, 88
 tailoring radiative properties, 83
 Hilger and Watts microinterferometer, 171

Holders for specimens
 calibration absorptance apparatus, 305-306
 solar furnace, 282
 water cooled, 422
 Homogeneous materials
 analytical model, 86
 definition, 84
 emittance, 86
 radiative transfer, 84
 Hydrogen
 ions, mass separation, 345
 liquid, heat transfer, 559-566
 plasma, UV radiation, 347
 Hypervelocity
 impact crater, copper, 456
 particles in crater lining, 472
 region in cratering, 455

I

Illuminometer, apparent emittance determination, 119
 Image method, absorption and emission, V-grooves, 108
 Image pyrometer, operation summary, 263
 Incidence angle effect on solar absorptance, coatings, 293-301, 303-311
 Inconel
 emittance
 adsorbed film removal, 157
 oxidation, 10^{-3} torr, 157
 oxide film effect, 157
 oxide film removal, 157-158
 thermal polishing, 158
 total hemispherical emittance, vacuum, 157
 Index of refraction
 anatase-titania, 96
 powder reflectivity, 94
 Infrared
 absorptance, thermal coatings, 426
 absorption bands
 carbon dioxide, 285
 water, 285
 double oven spectroradiometer system, 287
 emittance
 aluminum oxide film effect, 151
 basic surfaces, 495
 titanium oxide film effect, 151
 energy transfer
 surface contaminants, 136
 surface roughness, 136
 far-spectra
 alumina (Z-cut sapphire), 33
 aluminum alloy (2024), 32
 barium fluoride, 35
 chromium, 32
 germanium, 36
 magnesium alloy, 32
 silica (Z-cut quartz), 33
 silicon, 36
 stainless steel, 32
 strontium fluoride, 34

Infrared—Continued

near-spectra

- measurement standards, 166
- reflectance, free carrier absorption, 355
- surface damage effects, 149

radiation, planetary bodies, 339

reflectance, 322

- angular, aluminum and silver, 190
- copper, 149
- vacuum-deposited aluminum, 322

reflectivity, microinch surface disturbances, 137

reflectors, 511

spectroscopy, experimental techniques, 30–31

transparency region, ceramics, glass, 199

wavelength relative to pore size in ceramics, 137

Inhomogeneous media, radiation transfer, 6, 73–82, 83–102, 197–203, 205–209

Insulator

- bulk, heat transfer rate, 563
- charge buildup in ion bombardment studies, 348
- electric wire, 321, 324
- electric wire, current ratings, 321

Integrating network, oscilloscope, 285

Integrating sphere spectrometer, 77, 166

Intensity, UV, coating degradation, 450

Interference

- absorbers, Fabry-Perot, 510
- effect on reflectance, 157

Interferometer

- fine surfaces, 170
- fringe demagnification technique, 171

International System of Units, 260

Interplanetary station, 479

Interstitial material defect, 353

Ion

- bombardment, insulator surfaces, 346
- engine, environment effect, 347
- penetration, surfaces, 348

Iridium

- emittance, 572–573
- molybdenum disilicide, reaction, 577
- in sensors, 567–569
- zirconia
 - emittance, 572–573
 - radial surface temperature disturbance, 573

Iron

- adsorption isotherm, HMAB, 20° C, 180
- electrical resistivities, 17
- oxide reduction by ion bombardment, 346
- relaxation times, 17
- sputtering rates, 345

Irradiance

- detector, thermopile, 218
- solar absorptance calculations, 423
- sources and detectors, 220–229
- spectral standards
 - accuracy range, N.B.S., 231
 - blackbody radiance based, 217
 - checking experiments, 219
 - instrumental set-up, 219

low intensity, 218, 220

N.B.S., 217

quartz-iodine lamp, 219

set-up considerations, 219

standard, secondary, 218

UV unit of measurement, 422

Irradiation

absorption spectra change, 355

bleaching experiments, 359

concurrent, UV and nuclear Lithafrax-sodium silicate, 359

damage rate, 354

filter attenuation, 269

nuclear, silicate vehicles, 358

J

Johnson noise, spectroradiometer, 228

Jupiter, spacecraft temperatures at, 340

K

Kinetic theory of gases in determining conduction losses, 329

Kirchhoff's law

diffuse reflection factors, 131

emittance, 263, 277

equality to absorptance, 146

invalid for nonisothermal situation, 63–72

nonisothermal situations, 63–72, 77

radiation

cavity emittance, 118

monochromatic, 105

L

Lambert's law

crater surface emittance, 457

exception, tungsten emittance, 265

rough surface, 146

smooth surface, 146

Lamps

mercury arc

solar intensity data, 435

solar spectrum, 435

ultraviolet intensity degradation with time, 435

mercury-argon arc

degradation, intensity vs wavelength, 429

solar radiation, spectral matching, 429

quartz-iodine, standard, 219

standards, radiation measurements, 217

Lanthanum oxide pigment, stability, 431

Laser, helium-neon, for transmittance measurements, 255

Lattice

crystal parameters, 353

distortion effects, 149

model of powder, 7, 9

Launch vehicles

Saturn

SA-4, 498

SA-5, 498

SA-9, 500

sensors, 499

- Lead
 - micrometeoroid erosion, 471
 - sulfide cell, Eastman, 228, 229
 - Leeds and Northrup thermocouple voltage control system, 289
 - Leveling depth, definition, 170
 - Light pipe, 260
 - Lithafrax
 - formula, 355
 - potassium silicate coating, 543
 - sodium silicate coating
 - nuclear radiation, 355
 - UV-nuclear radiation, 359
 - UV radiation, 355
 - Lithium
 - electrical resistivity, 17
 - relaxation times, 17
 - thermal neutron absorption in pigments containing, 357
 - Lucite
 - reflecting disk for angle calibration, 305
 - Luminous intensity standards, 219
 - Lunar
 - environment, micrometeoroid importance, 453
 - surface, low albedo caused by solar wind, 346
- M**
- Magnesium alloy, far-infrared spectra, 32
 - aluminate (spinel)
 - sintered, spectral emittance curves, 252
 - total emittance, 251
 - Dow 7 coated, emittance determination, 331-336
 - oxide
 - coatings, use problems, 279
 - emittance, total normal, 251
 - fine grained magnesia, 249
 - freshly deposited, cavity reflectance, 121
 - low emittance region, 251
 - reference standard preparation, 166
 - reflectance correction, 123
 - reflectance standard, 166, 263
 - sintered, spectral emittance curves, 252
 - smoked, spectral diffuse reflectances, 254
 - spectral emittance, 254
 - sphere coating, reflectance, 230
 - Mars
 - cryogenic propellant storage, 559-566
 - heat transfer rates, 562, 564
 - spacecraft temperature at, 340
 - space flight, controlled surface degradation, 506-507
 - Materials
 - energetic radiation interaction, 352
 - model
 - homogeneous, isotropic, solid, 136
 - electrically conducting, real surface, 135
 - real
 - infused impurities, 138
 - surface contaminants, 138
 - surface disturbance, 138
 - surface geometry, 138
 - sintered
 - coefficient of absorption, 138
 - refraction index, 138
 - strongly absorbing, average depth, optical opacity, 137
 - M-center absorption band peak, 355
 - Maxwell's equations
 - absorption and scattering characteristics, 89
 - hemispherical emittance prediction, 155
 - rough sea reflections, 154
 - Mean depth, definition, 170
 - Mean free path, radiation scattering in dielectrics, 198
 - Mean line (center line) definition, 170
 - Measurement techniques and deficiencies, 213
 - Memory devices, coated magnetic, 152
 - Mercury intrusion method
 - pore size spectra determination, 260
 - porosity determination method, 263
 - Mercury lamp intensity comparison, 445-446
 - Mercury, mission to, 549
 - Mercury orbital distance from sun
 - cryogenic propellant storage, 559-566
 - heat transfer rate
 - through bulk insulation, 562
 - through multifoils, 564
 - Mercury vapor, spectral lines, 282
 - Metals
 - "as received"
 - medium solar absorber surfaces, 501
 - total reflector surfaces, 501
 - Beilby layer interface, 143
 - dissimilar, emissivity factors, 43
 - doped oxides, 519
 - emissivity
 - factor, comparison to normal, 42
 - radiation environment effect, 70
 - ratio hemispherical to normal, 40, 42
 - theory, 63-71
 - thermal equilibrium, function of frequency, 64
 - emittance, total, 11-28
 - high reflectivity, 63, 65-67
 - interference film thickness calculation, 525-530
 - noble, for high-temperature sensors, 567
 - optical constants, 4-5, 45-62, 190
 - optical properties specification, 159
 - polished
 - medium solar absorber surfaces, 501
 - total reflector surfaces, 501
 - real
 - oxide layer growth mechanisms, 143
 - radiation property sensitivity, 141
 - surface characterization, 141
 - reflectance, behavior prediction, 191
 - refractory
 - metal oxide, combination in vacuum, 569
 - sensors, 567-569
 - spectral emissivity, 4
 - sand blasted surface, 501, 502
 - warpage, 502

- Metals—Continued
 - super-cooled fluid, layer, 143
 - surface
 - heat flux measurement analysis, 578
 - properties, 159–163
 - solar wind bombardment, 347
 - spectral reflectance, 165–169
 - vacuum stable to 1000° K, 511
- Meteoroid Detector Satellite, 498
- Methyl ethyl ketone energy transfer agent, 384
- Methyl silicone
 - resins synthesis, 405–407
 - zinc oxide paints, 414
- Microammeter, recording, automatic, 422
- Microbeam condenser, spectrometer, 77
- Microinterferogram
 - beryllium, sintered, 171
 - Caliblock, roughness specimen, 176
 - interpretations, 171
 - steel, prepared specimens, 173, 174
- Microinterferometer
 - definition, 171
 - surface, Hilger and Watts, 171
- Micrometeoroids
 - crater emittance, 457
 - effect on emittance of surfaces, 457, 470
 - erosion plotted, function of time
 - aluminum, 471
 - aluminum, simulated, 473
 - cadmium, 471
 - copper, 471
 - lead, 471
 - steel, 471
 - flux
 - calculated from thermal data, 472
 - cumulative vs mass, 453–455, 470–471
 - density, 342
 - kinetic energy, crater volume per unit
 - aluminum, 456
 - brass, 456
 - cadmium, 456
 - copper, 456
 - lead, 456
 - steel, 456
 - titanium, 456
 - solids
 - experimental methods, 467
 - mathematical-experimental comparison, 467–471
 - velocity
 - distribution, near Earth, 342
 - hemispherical cratering, 455
 - penetration, metal to metal, 455
 - range near Earth, 473
- Microparticles
 - light gas gun, 469
 - sabot, schematic, 469
 - specimen damage
 - aluminum, 469
 - chromium, 469
 - gold, 469
 - platinum, 469
 - silver, 469
 - stainless steel, 469
 - tungsten, 469
- Microscope, interference, 171
- Microscope, light section,
 - measurement principle, 262
 - optical arrangement, 262
 - surface roughness measurement, 262
- Microstructure, radiative property tailoring, 83
- Mie theory
 - ceramics, 92
 - scattering, 6
 - single particle efficiency, 207
 - spherical particles, 89
- Mirror
 - aluminum
 - oxide film thickness, 150
 - silicon monoxide coated
 - ultraviolet reflectance, 192
 - visible light reflectance, 192
 - surface coating protection, 192
 - dark, electropolishing, 152
 - rhodium reference standard, 152, 166
- Molloy relationships, 353
- Molybdenum
 - alumina films on molybdenum, 509–524
 - disilicide
 - aerodynamic heat-flux measurement, 577–578
 - reaction, rhodium at 2700° F, 577
 - emittance, normal, hemispherical, 11, 25, 26
 - interference absorbers, 514–524
 - molybdenum silicon coating, 492
 - oxidation resistant material, 492
 - silicide coated, thermocouple installation, 578
 - sensor usage, 567
 - thin films, transmittance against resistance, 512
- Monochromator
 - atmospheric absorption, solar furnace, 280
 - double, spectrum distortion, 220
 - prism-grating type, 318
 - quality, experimental error effect, 318
 - scanning, calibration use, 282
 - small, solar furnace use, 282
 - spectral measurements, solar furnace, 282
 - wavelength drift, 319
- Monochromatic radiation, Kirchhoff's law, 105
- Monomolecular layer, radioactive surficant, 179
- Monte Carlo method, specular surface problems, 7–8
- Moon surface
 - solar wind bombardment damage, 345–346
 - sputtering effect loss, 346
- Mullite
 - sintered, spectral emittance, 252, 492
 - total normal emittance, 251
- Multifoils
 - cryogenic insulation in space, 565–566
 - heat transfer rates, 564
 - with low-absorptance coatings, 565–566
- Multiple reflections in rough surface, 146

- Mylar-aluminum laminate
 - Alodine coating, 434
 - angular dependency solar absorptance, 297
 - chemical conversion coating, 434
 - photomicrograph, 297
 - solar absorptance, 297
 - surface anisotropy, solar absorptance, 297
 - thermal shield, 333

N

- Neutrons
 - absorption, lithium pigments, 357
 - effects on coatings, 538
 - in free electron release, 352
- New York University electromagnetic energy symposium, 154
- Nichrome
 - specimen heater in vacuum chamber, 314
- Nickel
 - adsorption isotherm for HMAB, 180
 - black, effect of current density, 525
 - black, electroplating, 525
 - blackbody energy of roughened surface, 153
 - controlled spectral absorptance, 525-530
 - electrical resistivity, 17
 - interference films, 525-530
 - oxide
 - blackbody cavity coating, 317-318
 - blackbody furnace coating, 245
 - relaxation times, 17
 - rhodium plated, diffuse spectral reflectance, 166, 169
 - rough surface
 - profilometry, 153
 - specular reflection, 153
 - surface behavior theory, 154
- Niobium
 - electrical resistivity, 26
 - emittance, effect of absorbed gases, 24
 - hemispherical emittance, 11, 24, 26
 - normal emittance, 11, 24, 26
- Nitrogen
 - absorptance, cryodeposited film, 531-534
 - films, infrared transmittance, 533
 - liquid
 - chamber cooling, 291, 306, 315, 333
 - sample cooling, 422
- Nitrous oxide, dosimeter, 369
- Noise level, reduction in solar furnace, 284
- Nose cap temperature sensor, 568-569
- Nozzles, rocket
 - graphite, 486
 - metallic
 - borides, 486
 - carbides, 486
 - nitrides, 486
- Nuclear radiation damage
 - at 77° K, silicate systems, 358
 - comparison: (1) ultraviolet, (2) gamma, and (3) ultraviolet/gamma radiation, 359
 - comparison with ultraviolet, 358

- pigment-vehicle systems
 - air, 360
 - calcium fluoride/sodium silicate, 356
 - lithium fluoride/sodium silicate, 356
 - Lithafrax/sodium silicate, 355
 - semiconductor in silicate and silicone, 360
 - titania/sodium silicate, 361
 - Ultrox/potassium silicate, 356
- solar absorptance
 - plasma arc materials, 376
 - reflector coatings, 370
 - silicone coatings, 375
- spacecraft thermal control materials, 353-356, 360
- with ultraviolet radiation
 - Lithafrax/sodium silicate, 359
 - solar absorptance of coatings, 377
- Nuclear reactors in spacecraft, 365
- Nylon, phenolic, ablation char
 - arc-jet produced, 271-272
 - emittance, 271
 - oven produced, 271-272
 - reflectance, 271

O

- Opacity
 - depth, transparent materials, 137
 - extinction coefficient, 98
 - films, UV vs gamma radiation, 430
 - surface roughness correlation, 98
- Optical arrangement, microscope, 262
- Optical behavior
 - defect site, 359
 - metals, surface conditions, 142
 - statistical properties of surfaces, 147
 - surface layer effects, 143
- Optical constants
 - absorption, strong, 86
 - aluminum, reflectance, 191
 - determination from emitted energy, 86
 - determination from reflectance measurements, 59
 - directional emittance, 146
 - evaporated metal films, 190-191
 - n and ik refractive index, 3-4
 - n and k functions of wavelength and temperature, 3
 - normal emittance, 87
 - opaque coatings, 309
 - polar dielectrics, 5
 - reflectance relations, 40, 45-62
 - silver, reflectance, 191
 - thin absorbing films, 525
- Optical damage, rate and temperature dependence, radiation, 358
- Optical density
 - polyvinyl chloride, changes
 - function of time of exposure, 386
 - gamma radiation, 387
 - UV radiation, 385
- Optical filters
 - Corning glass, 261
 - gelatin, 261

- Optical filters—Continued
 - reflectance, 261
 - Wratten glass, 261
 - Optical properties
 - Air Force studies, 485-494
 - alkali halides, radiation, 353
 - bombardment by particles, 473-481
 - craters, 471
 - dielectrics, 485-487
 - elastomeric paints, 408
 - electrical resistivity, 14
 - films, substrate stress, 152
 - germanium, 150
 - high-temperature techniques, 490-491
 - induced by microstructure, 83
 - inorganic pigments, 396
 - lattice distortion, 149
 - metals, 485-487
 - multiple film coatings, 525
 - nickel black system, 525
 - opaque materials, 491-492
 - Orbiting Solar Observatory, 381-389
 - paints, organic, 405
 - pigment vehicles, 352
 - region of intrinsic absorption, 149
 - resin paints, UV radiation, 412
 - sapphire, 34
 - semiconductors, 485-487
 - silica radiation, 353
 - silicates, 353
 - silicone paints, 409, 410, 411, 412
 - smooth, electropolished metal, 149
 - standards development, 490-491
 - surface damage, 149
 - surface roughness, 147
 - tailoring radiative properties, 83
 - thermal control materials, 351-352
 - translucent materials, 491-492
 - zinc oxide
 - coatings, 402
 - pigments, 397
 - Optical pyrometry, 25, 117
 - Optical region, Fresnel equations, 39-61
 - Optical resonance in scattering efficiency, 91
 - Optical spectroradiometer system, 289
 - Optical techniques in high-temperature radiation measurements, 259
 - Optical thickness, heat transfer in thin layers, 202
 - Orbit, near-Earth, degradation of surface reflectance, 473-481
 - Orbiting Solar Observatory
 - thermal control surface changes, 381
 - titania epoxy and silicone coatings, 383
 - Organic films, reflectance, titania-pigmented, 93
 - Oscillograph, image pyrometer, carbon, 260
 - OSU rockets, dust particles vicinity of Earth, 479
 - Outgassing
 - coatings, gamma radiation, 438
 - films, UV radiation, 431
 - Oxidation
 - aluminum during aging, 190
 - avoidance by vacuum, 313
 - carbon, 269
 - helium to prevent, 269
 - magnesium, reference standard, 166
 - rates, nose-cap sensors, 568
 - resistance, zirconium diboride, molybdenum disilicide, 492
 - silicon oxide coating-evaporated aluminum, 193
 - Oxides
 - aluminum during heating, 141
 - coating, vacuum stability, 511
 - film surface, emittance, 145
 - hydrogen ion bombardment, reduction, 345
 - inorganic, stability under UV exposure, 343
 - layer growth mechanisms, 143
 - sputtering rates, proton bombardment, 346
 - white, darkening by solar wind, 346
 - Oxygen
 - atmospheric, bleaching effect, 427
 - free, in films, 431
 - infrared transmittance of cryodeposited films, 533
 - liquid, heat transfer, 559-566
 - removal from pigments, UV radiation, 427
 - Ozone
 - absorption band, 285
- P**
- Paint
 - aluminum leafing, absorptance, 308
 - antimony trioxide-potassium silicate, 444
 - carbon
 - black, sun-oriented spacecraft, 551
 - Cat-A-Lac, 532, 534
 - ceramic black, reference blackbody, 313-314
 - dielectric, Explorer VII, 497
 - elastomeric, optical properties, 408
 - metallic, surfaces
 - median infrared reflector, 501
 - medium optical, 501
 - methyl silicone, 391
 - nonmetallic surfaces
 - median solar absorber, 501
 - solar reflector, 501
 - total absorber, 501
 - organic
 - binder degradation, 341
 - UV radiation, 405
 - Parson's black, solar absorptance, 303, 304, 309
 - potassium silicate, 391
 - reflectance, removal of glossy layer, 419
 - resins, distilled, UV exposure, 412
 - rutile titania in epoxy, OSO-I, 444
 - stable molecular species, 418
 - silicone
 - formulation data, 406-407
 - variable molar ratios, 409-413.
 - solar wind effects, 348

- space utilization requirements, 502
- zinc oxide
 - angular reflection, 347
 - methyl silicone, film thickness effect, 408
 - methyl silicone, solar wind, 346-347
 - methyl silicone, UV radiation, 414
 - potassium silicate, 444
- zinc sulfide, solar absorptance, 309
- zirconium silicate-aluminum, room-temperature air-
ing, 548
- Palladium relaxation times and electrical resistivities, 17
- Paper
 - black, spectral reflectances, 123
 - cosine deviation, 121
 - good diffuser, 123
 - green, spectral reflectances, 123
 - mat, cavity lining, 126
 - selectively reflecting, 121
 - velvet finish, 126
 - white, spectral reflectances, 123
 - yellow glare-free velvet coated, 125
- Parallel ray bundles
 - absorptance, 110
 - absorption in cavities, 110
 - in radiation entering cavity, 110
- Particles
 - group scattering, 93-94
 - micrometeoroid, 454, 468
 - shape and orientation, 91, 92
 - single, scattering
 - apparent absorption coefficients, 97
 - backscatter ratio, 96
 - behavior, 83
 - multiple scattering, 93
 - radiative transfer equations, 88, 97
 - reflectance, 97
 - reflectivity, 93
 - scattering systems, 93
 - total spherical scattering coefficient, 88
 - size in paints, 429
 - solar wind, 348
- Passages
 - definition, 115
 - emittance, 112
 - plane wall, radiation exchange factors, 112
 - radiant interchange within, 111
 - throughflow energy rate, 112
 - transmission characteristics, 111
- Peak-to-valley height, 170
- Perkin Elmer
 - spectrometer, 288
 - spectrophotometer, 314
- Periodic etch figures on aluminum, 161-162
- Perturbation theory, emissivity of metals, 67-69
- Phase shift, definition, 89
- Phenolic nylon, ablation char
 - arc-jet formed, 272, 273
 - emittance, 271, 272
 - oven-formed, 272, 273
 - reflectance, 271, 272
 - surface porosity, 273
- Photocell, lead sulfide, 166
- Photochemistry
 - color center formation, 417
 - cross linking, 417
 - mechanisms of change, polyvinyl chloride, 386
- Photodegradation, thermal control surfaces, 433-441
- Photography, time-lapse, 183, 185
- Photolysis
 - alkali silicates, 430
 - zinc oxide, 415-417
- Photometer, UV, lamp intensity, monitor, 435
- Photomicrographs
 - electron, sintered-glass coating, 205, 206
 - Mylar-aluminum laminate, 297
 - platinum ribbon, 183
- Photomultipliers, 166, 228, 229, 260
- Photons, mean free path, 98
- Photoreduction, semiconductor pigment, 354
- Phototube, UV intensity detection, 422
- Plastics, coloring by high-energy radiation, 438
- Pigment
 - addition of, to increase emittance of ceramics, 139
 - contamination, 431
 - dielectric, radiation damage, 354
 - inorganic, UV radiation, 396
 - lithium, neutron absorption, 357
 - semiconductor
 - color centers, 354
 - photoreduction, 354
 - radiation damage, 354
 - vehicles, damage spectra, 359
 - silicate systems, 355-359
 - stability, 360, 435
 - titanium oxide, 354
 - UV irradiation, 537
 - vehicle
 - calcium fluoride-sodium silicate, 356
 - Lithafrax-sodium silicate, 355, 359
 - lithium fluoride-sodium silicate, 355, 356
 - optical properties, 352
 - qualitative description, 352
 - semiconductor, air in nuclear radiation, 360
 - semiconductor, damage spectra, 359
 - titania-silicone, radiation, 361
 - Ultrox-aluminum phosphate, 355, 356, 357
 - zinc oxide-silicone, 362
 - zinc oxide-sodium silicate, 362
 - zinc sulfide-silicone, 363
 - zinc sulfide-sodium silicate, 363
- Pioneer I, distribution dust particles near Earth, 479
- Pipe, platinum in image pyrometer, 260
- Planck's law
 - emittance, 15, 131, 278
 - flux, spectral, 282
 - radiance-absolute temperature, 217
 - semi-infinite body irradiation, 86
 - true temperature, solar furnace, 279
 - vs Wien's law, 264

Planetary probes

- Advanced Solar Probe, 535-536
- Mariner II, 535-536
- Pioneer V, 535-536
- Sputnik 8, 535-536

Plasma

- arc materials, nuclear radiation, 376
- heating test, nose-cap sensor, 574
- hydrogen
 - mass separation of ions, 345
 - UV radiation source, 347

Plastics, high-energy radiation, 438**Platinum**

- absorptance, normal solar, 189
- cause of striations, 184
- commercially pure, 249
- degradation, progressive, 184
- directional spectral emittance, 316-317
- emissivity of flat surface, 316
- emittance, 183, 184, 186, 189, 250
- evaporated film, 191
- grain boundaries, 187
- in temperature sensors, 567
- metal film, 189
- microparticle damage, 469
- mirror-grooved surface, 313
- multiple film coatings, 195
- photography, time lapse, 183, 185
- polishing, 185
- reaction with molybdenum disilicide, 577
- reflectance, diffuse spectral, 166, 167
- relaxation times, 17
- slip planes, 187
- thermocouple, 183, 289
- thin ribbons, 183
- tubing, image pyrometer, 260
- vacuum plating on copper, 316

Polarization

- coherent reflection, 148
- external surface effect, 203
- reflectivity
 - parallel component, 85
 - perpendicular component, 85

Polishing

- beryllium, 166, 170
- chemical, 502
- emery paper, 268
- structural changes, 136, 143, 149
- thermal, platinum, 185
- work hardened surface, 502

Polymers, 360, 381-389**Polyvinyl chloride**

- change in reflectance, 388
- electron spin resonance, 418-419
- films, degradation, 431
- gamma radiation, 387, 430
- impurities, 384
- optical density, 385
- photochemical change, 382, 386
- surface temperature, 388

temperature prediction, 389**UV-gamma radiation, 387****Porosity**

- mercury intrusion method, 263
- phenolic nylon char, 273
- zirconia, 271

Potassium

- bromide absorption coefficient, 290, 314
- relaxation times, 17
- silicate
 - antimony trioxide coating, 444
 - Ultrox, pigment vehicles, 356
 - zinc oxide coating, 444

Powder, periodic lattice model, 7**Power consumption, cavity heater in emittance measurement, 314****Power systems**

- coatings, solar, 509-524
- thermal cycle, solar, 509-524

Prelaunch

- environment, coatings
 - inorganic, 537
 - silicone, 537
- stability
 - bare metals, 502
 - pigmented coatings, 502
 - thin films, 502

Profilograms

- Caliblock, 176
- nickel, rough, 153
- Talysurf, 171

Profilometry, surface roughness, 153**Propellants**

- cryogenic, space storage, 559, 566
- zero-gravity storage, 566

Proton

- copper sputtering, 345
- damage mechanism, 349
- solar wind, 345
- spacecraft coatings, 538

Pumps

- diffusion, 548
- ion, 435
- Vac-ion, 548

Pyrheliometer, 231, 279, 296**Pyroceram, spectral emittance, 492****Pyrometers**

- arc imaging furnace, 260
- blackbody system temperature, 238
- image, 261, 262, 263
- micro-optical, 22, 23, 184, 278, 282, 284
- quartz filament, 260
- single color, 487
- surface temperature limitations, 277
- tubing, platinum, 260
- two-color, 487

Q**Quartz**

- filament, image pyrometer, 260
- foil, proton shield, solar wind bombardment, 347

- glass, ground surface, photomultiplier sensitivity improvement, 229
 - ground, ultraviolet instability, 431
 - infrared reflection spectrum, 33
 - iodine lamp, spectral irradiance standard, 219
 - reflectivity, 85
 - window material in vacuum chamber, 307
 - windows, transmission losses due to ultraviolet radiation, 431
- R**
- Radar reflection, surface roughness effect on reflectance, 99
 - Radiance
 - absolute temperature relationship, 217
 - ratio
 - definition, 287
 - equivalent to emittance, 141
 - normal spectral, experimental set-up, 289
 - spectral
 - calibration accuracy, 231
 - ratio, potassium bromide, 291
 - standards, 217, 218, 219
 - tungsten ribbon strip lamp, 219
 - Radiant interchange
 - angle factor, 107
 - exchange factor, 112
 - multiple scattering, 94
 - parallel specular surfaces, 39-44
 - passages, 111
 - tube opening and element areas, 112
 - variational technique, 107
 - Radiant transport
 - circular tube, 113
 - passage walls, 113
 - Radiation
 - absorptance
 - stray, 305
 - UV effects, 371
 - absorption
 - damage, 352
 - detector recovery time, 231
 - disturbed surface layer, 149
 - scattering media, 74
 - spherical vehicle, 309
 - thermopile coating thickness, 227
 - alkali halides, optical properties, 353
 - balance, orbiting satellite, 303
 - blackbody, 76, 233-240, 321, 532
 - boundary condition
 - dielectrics, 201
 - scattering media, 78
 - carbon, enlarged center, 261
 - cavities
 - conical, 109
 - cylindrical, 103-116, 117-131
 - efflux determination, 115
 - emittance, Kirchhoff's law, 118
 - loss going down tube, 115
 - rectangular groove, 109
 - spherical, 105, 109, 110
 - V-groove, 109
 - wall, distribution, 106
 - ceramics, 98
 - classical calculations, 64-65
 - constant, Stefan-Boltzmann, 197
 - cosmic, thermal control surfaces, 342
 - degradation predictions, 359
 - detectors
 - blackbody cavity cone, 229
 - high-temperature thermopile, 281
 - measurement standards, 217
 - photosensitive, 228-229
 - thermal, 221
 - thermocouple, Johnson noise in spectroradiometer, 288
 - dielectrics
 - effective parameters, 137
 - finite thickness, 197
 - heat transfer influenced by scattering centers, 198-199
 - pigments, damage, 354
 - surface effects, 197-203
 - thin layers, 203
 - transmission, 198
 - diffuse, incoming, 109, 124
 - dose rate, gamma, thermal control coatings, 438
 - electromagnetic, rough surface reflection, 267
 - emission, disturbed surface layers, 149
 - emissivity
 - metals, function of frequency under thermal equilibrium, 64
 - of metal, 70
 - source, 239
 - emittance
 - polarized, infrared, 191
 - solar furnace, 278
 - energetic, interaction with matter, 352
 - error elimination, 265
 - exchange, infinite parallel surfaces, 41-42
 - field, attenuated, basis functions, 65-67
 - Fresnel's laws, application, 42, 45-62, 85, 299
 - gamma
 - free electron release, 352
 - thermal control surfaces, stability, 438-439
 - UV comparison, 439-440
 - glasses, function of temperature, 199
 - graphite tube, blackbody, 281
 - heat transfer
 - dielectrics, 198-199
 - diffuse, 74
 - nonisothermal layers, 74
 - thin layer effects, 202
 - image plane, intermediate, 260
 - infrared
 - blackbody source, 287
 - planetary bodies, 339
 - scattering centers effects, 199
 - solar radiation simulation, 550

Radiation—Continued

kinetics equation, induced color centers, 358

laws

Lambert's cosine, 12

Planck's, 12, 15, 131, 278

Stefan-Boltzmann, 12, 197, 217, 307

mean free path of a photon, 98, 197

metals

sensitivity to environmental conditions, 141

surfaces, solar wind bombardment, 347

missile exhaust plume, 233

monochromatic, 105, 131

nonisothermal layers, 73-81

nuclear

calcium fluoride-sodium silicate system, 356

lithium fluoride-sodium silicate system, 356

Lithafrax-sodium silicate system, 355

semiconductor pigment vehicle systems, 360

silicate vehicles, 357

spacecraft, 341, 538

temperature effects, 358

thermal control surfaces, 342, 351-354, 355, 360

titania-sodium silicate system, 361

-UV, comparison, 358

-UV specimen degradation, 355

-UV spectra, semiconductor pigment vehicles, 360

Ultrox-potassium silicate system, 356

opaque materials, 98

optical damage, 358

organic thermal control coatings, UV, 536

pyrheliometer monitor, 296

pyrometry, 260, 487

radiance standard, 217

rediffused by scattering, 80

reflectance at interface, influence, 157

reflected

rough surfaces, 99, 145-152

surface, root mean square slope, 267

scattering

centers, effects on transmission, 198

heat transfer, 199

semiconductors, pigments, damage, 354

shields

for blackbody, 238

heat transfer with capsule, 550

insulating blanket, 7

porous insulating spacers, 7

powder contacts, 7

space environment vacuum chamber, 551-552

specimen heater vacuum chamber, 314

sun-oriented vehicle protection, 549-557

temperature increase, 549-557

silica, optical properties, 353

silicates

optical properties, 353

vehicle, damage, 360

solar

attenuation by atmosphere, 285

dielectric penetration depth, 137

furnace, 278

incidence measurement, 279

irradiation intensity duplicated by infrared heaters, 550

metals penetration depth, 137

UV, 340, 341, 381-452

solids

complex geometry, 7

high energy changes, 538

inhomogeneous media, 5-7

metals, 4-5

nonpolar insulators, 5

opaque material, 353

optical constants, 5

polar crystals, 5

radiation shields, 7

rough surfaces, 5-6

standard

tungsten strip lamp, 264

Wien's law, 264

temperature calculation, 264

titania-silicone pigment vehicles, 361

titanium oxide, damage, 354

total

blackbody, 77

monochromatic, 131

transfer calculations in spectral emittance, 145

transmission

laws of geometric optics, 91

loss in dielectrics due to scattering centers, 198

through homogeneous dielectrics, 198

UV, 381-452

calcium fluoride-sodium silicate system, 356

exposure dependency, 423-425

free electron release, 352

Lithafrax-sodium silicate system, 355

nuclear, comparison, 358

reversibility of process, 426, 427

temperature effects, 358

Ultrox-aluminum phosphate system, 357

Ultrox-potassium silicate system, 356

zinc oxide

pigment damage, 354, 362

-sodium silicate pigment, 362

zinc sulfide

pigment damage, 354, 363

-sodium silicate pigment, 363

zirconia

melting point, 270

opacity thickness, 270

Radiative properties, tailoring, 83

Radiative transfer

absorption coefficient-single particle theory, 88, 97

backscatter coefficients, 88

coatings, organic, 83

heterogeneous material, 84

homogeneous material, 86

independent scattering, 89

multiple scattering, 88

paints, anatase-titania, 96

particle scattering correlation, 84

- scattering centers, 88
- surface reflectance, 95
- system predictions, 88
- three-dimensional formulation, 96
- Radiator, constant temperature, 321
- Radioactive surficant, measuring total surface area, 179
- Radiometer
 - cavity area observation, 118
 - missile air-borne calibration, 233
 - missile exhaust plume observation, 233
- Radiosity
 - definition, 105
 - expansion in Taylor series, 107
 - local, heat flux in passages, 111
- Ray bundle, parallel
 - absorption, diffuse cavity, 131
 - absorption, specular cavity, 131
- Rayleigh-Gans scattering, 90-91
- Rayleigh-Ritz procedure, 107
- Reactors, General Dynamics Ground Test Reactor (GTR), 365
- Reciprocity theorem in cavities, 104-106, 131
- Recorders
 - Dynec data acquisition, 308
 - multipoint, test monitor, 306
 - strip chart, with oscilloscope, 285
- Recrystallization
 - polished metal surfaces, 183
 - surface consequences, 137
- Reeder thermopile
 - lengthwise scan, 225
 - linear sensitivity, 225
- Reentry heating, sensors, 567-579
- Refining grain, or cold working, 137
- Reflectance
 - absorptance, solar normal, 193
 - admittance, blooming three-layer system, 529
 - aluminum
 - angular characteristics, 190
 - coated film, 195, 297
 - decrease caused by oxide films, 150
 - disk, impact experiments, 477-478
 - evaporated film, 190, 297
 - ground glass, 147
 - low pressure high deposition silicon oxide coating, 192
 - parallel and perpendicular components, 191
 - silicon monoxide coatings, 193
 - angle of incidence, 39-44, 45-62, 191, 293-301, 303-311
 - base coated with multilayer thin film, 525
 - carbon
 - at 3230°, 2530°, 2120° K vs wavelength, 268
 - black vs camphor black, 221
 - roughened by oxidation, 268-269
 - cavities
 - apparent, derivation of emittance, 131
 - diffusing cavity wall, 125
 - emittance conversion, 118
 - emittance, nonglossy paper-lined, 124
 - magnesium oxide, freshly deposited, 121
 - spectrophotometer measurements, 120
 - yellow glare-free, emittance, 126
 - ceramic oxides, 256
 - change of phase: incident and reflected energy, 86
 - coherent
 - angle of incidence, dependency, 148
 - exponential representation, 147
 - incoherent, ratio, 148
 - polarization effects, 148
 - copper
 - Drude-Zener theory, 149, 150
 - electropolished, 149, 150
 - free-electron region, 149
 - near-UV, 189
 - polished, 149
 - degradation, surface, near-Earth orbit, 473-481
 - dielectrics
 - films, thickness monitoring system, 511
 - transparent, 203
 - diffuse, spectral
 - aluminum, 166, 167
 - aluminum, sandblasted, 166
 - beryllium, 166, 167, 168
 - directional, 166
 - Gouffé theory, 129
 - integrating sphere attachment, 166
 - platinum, 166, 167
 - rhodium plated nickel, 166, 169
 - silver, buffed, 166
 - spectrophotometer measurement, 166
 - steel, 166, 168
 - emittance, comparison, 253
 - emittance, measurement, 277
 - films
 - organic, titania, 93
 - surface effects, 150-151
 - thickness, monitoring, 194
 - germanium, amorphous, 150
 - Gier-Dunkle spectrophotometer, 388
 - glass
 - ground, aluminized, 147-148
 - sintered, apparent absorption, 208, 209
 - gold, 189
 - graphite
 - at 2990°, 2930°, 2120° K vs wavelength, 268
 - vs temperature, 268
 - hemispheric, solar, 309
 - image pyrometer, measurement, 263
 - induced property, 83
 - infrared
 - aluminum, angular characteristics, 190
 - aluminum, vacuum deposited, 322
 - copper, 149
 - microscopic surface disturbances, 137
 - near, free carrier absorption, 355
 - silver, angular characteristics, 190
 - interface, influence on radiation, 157

Reflectance—Continued

- magnesium oxide
 - coating, sphere, 230
 - corrections for, 123
 - measurements, corrected to absolute value, 253
 - spectrophotometer curves, 121
- measurement techniques, error sources, 265-267, 293
- metals
 - prediction, 191
 - surfaces, chemical effects, 159
- mirrors, 192
- normal, UV radiation, 422-423
- nylon, phenolic, ablation char, 272
- optically thick specimen, 94
- paints
 - glossy layer removal, 419
 - white pigment, 91
- parallel component
 - aluminum, 191
 - angle of minimum, expression, 191
 - perpendicular components, 190
 - silver, 191
- particle, single-scattering theory, 97
- pigment vehicle system, qualitative description, 352
- polyvinyl chloride, 388
- quartz, 85
- reduction by particle bombardment, 473-481
- roughness, interface relation, 157
- silicon dioxide films, interference spectra, 195
- silicon monoxide coated aluminum mirrors, 192
- silver
 - angular characteristics, 190
 - near-UV, 189
 - parallel, 191
- spectral
 - alumina, 253
 - aluminum disk, eroded by microparticle impacts, 477-478
 - black paper-lined cavities, 123
 - calcium zirconate, 254
 - converted to emittance, 117
 - crystal defects, identification, 353
 - diffuse metal surfaces, 165-169
 - electropolishing, 166
 - emittance data, 252
 - Fresnel's equations, 351
 - green paper-lined cavities, 123
 - image pyrometer, 263
 - laser use, 491
 - magnesium oxide, 253-254
 - measurement apparatus, 512
 - nickel, roughened, 153
 - reflectometer, 512
 - root mean square roughness, 99
 - surface finish lay, 165, 166
 - surface roughness, 148
 - tantalum oxide, molybdenum substrate, 514
 - titanium dioxide-methyl silicone, 545-547
 - walls, hemispherical crater, 467

- white paper-lined cavities, 123
 - woven dyed cloth texture, 165
 - yellow glare-free velvet coated cavities, 125
 - zinc oxide-methyl silicone, 547
 - zinc oxide-potassium silicate, 544, 546
 - zirconium oxide, 253
 - spectrophotometer, precision, 118, 177, 355, 467-468
 - specular, relative, single exponential, 147
 - sphere, integrating, spectrophotometer, 308
 - surface roughness
 - at normal incidence, 147
 - directional emittance, 146
 - measurement error, 148
 - temperature, room measurements, 252
 - thermal polishing, 158
 - thin layer, maximum, 93
 - titania pigmented organic films, 93
 - zero blooming, 525
 - zinc oxide
 - methyl silicone coatings, 547
 - potassium silicate, 4170 sun-hours exposure, 403
 - 1670 sun-hours in vacuum, 397
 - zirconia
 - measurements, 270
 - surface roughness, 99
- Reflected energy, variation of polarized components with angle of incidence, 85
- Reflected light, coherent to incoherent, 148
- Reflection
- angular, solar wind bombardment, paint, 347
 - back, surfaces after solar wind bombardment, 346
 - blackbody energy, specular, 153
 - coefficients
 - angle of incidence, function of, 47
 - differences, conductors and dielectrics, 54
 - index of refraction, function of, 47
 - n and k , functions of, 46-48
 - dielectrics, incident energy absorption, 137
 - diffuse, Kirchhoff's law, 131
 - electromagnetic energy, rough sea, 154
 - emittance, hemispherical changes, 147
 - equations, parallel and perpendicular components, 45
 - Fresnel equations, 75
 - geometrical optics regime, 94
 - incident light on rough metal, 147
 - infrared, solids, 30-36
 - metals, controlled by surface characteristics, 159
 - multiple
 - rough interface, 157
 - surface occurrence, 153
 - nickel, rough, specular, 153
 - oxide paint, solar wind, 347
 - powders, infinitely thick, 94
 - sea, rough, 154
 - solar
 - contaminant layer, 136
 - radiation, planets, 339
 - specular, infinite parallel surfaces, 39, 41-42
 - surface
 - distribution, microinch optical wavelength, 137

- roughness, transparent materials, second, dielectric conditions, 138
 - Reflectivity
 - absorption coefficient, increase with, 85
 - heat transfer calculations, 75
 - parallel and perpendicular components, 13, 39-44, 45-62, 85
 - particle concentration, 93
 - pigment, water and air matrices, 93
 - polished surfaces, 85
 - refractive index, function of, 75
 - spectral, surface roughness, 142
 - Reflectometer, 316, 512
 - Refraction
 - angle in directional emittance, 94
 - dense to rare, critical angle of incidence, 85
 - index
 - absorbing characteristics, relation, 84
 - absorption coefficient, sintered material, 138
 - backscatter ratio, influence on, 91
 - blackbody flux, 199
 - ceramics, 91
 - dielectrics, 138
 - emittance, 88
 - extinction coefficient, solar absorptance, 300
 - film effects, 157
 - Fresnel equations, 84
 - reflectivity, heat transfer, 75
 - scattering, 96
 - tailoring radiative properties, 83
 - thin films, 152
 - white paints, pigmented, 91
 - interface, 157
 - surface effects
 - Relaxation
 - cesium, 17
 - cobalt, 17
 - copper, 17
 - gold, 17
 - iron, 17
 - lithium, 17
 - nickel, 17
 - palladium, 17
 - platinum, 17
 - potassium, 17
 - rubidium, 17
 - silver, 17
 - sodium, 17
 - Resins
 - distilled, 412
 - methyl silicone, synthesis, 405-407
 - Resistance against transmittance, molybdenum films, 512
 - Resistivity, electrical
 - cesium, 17
 - cobalt, 17
 - copper, 17
 - gold, 17
 - iron, 17
 - lithium, 17
 - nickel, 17
 - palladium, 17
 - platinum, 17
 - potassium, 17
 - rubidium, 17
 - silver, 17
 - sodium, 17
 - Resistor, carbon-composition, 31
 - Resonance
 - electron spin, polyvinyl chloride, 418-419
 - in incident radiation, 91
 - Resonant frequency in thickness required for opacity, 87
 - Retroflection, solar wind bombardment, 348
 - Rhenium
 - temperature sensors, 567-569
 - tungsten thermocouples, 569
 - tungsten wires, ductility after heating, 570
 - Rhenium in tungsten thermocouple, 11
 - Rhodium
 - absorptance, normal solar, 189
 - emittance, normal thermal, 189
 - hemispherical emittance, 191
 - metal film, 189
 - mirror, 166
 - platinum thermocouple, 183
 - reaction with molybdenum disilicide, 577
 - sensors, 567
 - thermocouple, 288
 - Rocketdyne, North American Aviation, Inc.
 - high-temperature circular-aperture blackbody radiation source, 233-240
 - Rokide "A", UV radiation, 540
 - Root and crest line, surface texture, 170
 - Rotating sample technique, solar furnace, 281, 283
 - Rubidium
 - electrical resistivity, 17
 - relaxation times, 17
- S**
- Sabot, microparticle, 458, 469
 - Sample preparation
 - copper, optical polishing, 149
 - mounting, vacuum chamber, UV measurement, 422
 - reproducible materials, 151
 - Sandblasting
 - crystal damage, 152
 - metal warpage, 502
 - surface preparation, 341
 - Sapphire
 - as homogeneous material, 84
 - infrared reflection spectrum, 33
 - interferometric determination, optical properties, 34
 - window, vacuum chamber, 294
 - Satellites
 - Explorer, VII, XI, 497, 499
 - Meteoroid Detector, 498
 - micrometeoroid sensors, 454
 - Orbiting Solar Observatory, 381, 539
 - Vanguard II, 539

Scattering

- absorption influence, 92
- anomalous diffraction domain, 90
- center
 - absorption of dielectrics, 197
 - decrease of mean free path of radiation, 197
 - definition, 197
 - dielectrics, coalescing of foreign material, 138
 - dielectrics, diffusing of transmission, 198
 - dielectrics, heat transfer, 198-199
 - emission of dielectrics, 197-198
 - intervening medium, 94
 - optically dense material, 198, 203
- ceramics, powder reflectivity, 94

coefficient

- definition, 74
- dielectrics, 197
- mechanism of extinction, 199
- radiant flux, 88
- reflectance prediction, 96
- single particle, 88
- tailoring of radiative properties, 84
- thin sample layers, 81
- wavelength dependence, 199

coherent, 81, 147

Compton, free electron release, 352

diffusion, 115

dipole radiation, 90

efficiency

- absorbing ceramics, 92
- anomalous diffraction domain, 90
- definition, 92
- empirical, 96
- equations, 92
- nonabsorbing particles, 90
- optical resonance, 91
- particle shape and orientation, 91
- phase shift, 91
- Rayleigh-Gans domain, 90
- reflectance, 91
- refraction index, 91
- single particle, 207

extinction coefficient, 199

gelatin matrix, 94

ground quartz, UV radiation, 431

independent, 89

light

- ceramic performance, 100
- pigmented coatings, 205
- radiative transfer, 83

Maxwell's equations, 89

Mie theory, 6, 207

multiple

- absorption, 94
- heterogeneous ceramics, 88
- single particle theory, 93

nonisothermal layers, 74

predictions, colloidal dispersions, 94

radiation, rediffused, 80

radiative transfer equations, 88, 89

ratio, surface area-particle volume, 91

Rayleigh-Gans, 90

refractive index effects, 96

sideways, 74

silver bromide particles, 94

single, 88, 94

spherical, 91, 207

temperature dependence, 199

thin layers, heat transfer, 203

Scatterplate, in monochromator, 315

Scissions by UV degradation, 382

Semiconductors

angular emissivity, 41

bibliography, pigments, 364

ceramic oxides, 256

emittance, surface damage on; 151

pigment

color centers, 354

photoreduction, 354

radiation damage, 354

pigment vehicle systems, UV and nuclear damage

spectra, 359, 360

Semitransparent material, cavity effect, 98

Sensors

high temperature

aerodynamic heat flux, 576

assembly technique, 571

chemically compatible, 568

computer program, 571-572, 579

electrical insulation, 570

emittance, zirconia and iridium, 572-573

glide reentry vehicles, 567-579

insulating oxides, 567

iridium protection tube, 569

noble metal use, 567-568

nose cap temperature, 568-569

plasma heating test, 574

refractory metal, use, 567-568

rocket exhaust heating test, 574

simulated reentry test, 575

temperature response, aerodynamic heat flux, 572

spacecraft surface temperature

Explorer XI, 499

Saturn, SA-4, 499

Shallow hole method, 118

Shape factor, 170

Silica

aluminum impurity, 357

bibliography, 364

nonisothermal emissivity apparatus, 492

optical properties, radiation effect, 353

-silicone coating, absorptance and emittance, 543

sintered, 1200° K, 251

total normal emittance, 251

UV instability, pigment, 431

Z-cut quartz, infrared spectra, 33

Silicates

absorptance, solar, nuclear effects, 373-374

aluminum, substitutional, 357

bibliography, 364

- coating binder, 423
- damage, pigment vehicles, 355
- Lithafrax pigment vehicles, 355
- lithium pigment vehicles, 355
- nuclear radiation damage, 357
- optical properties, radiation effects, 353
- pigments, 355-359
- radiation damage, 360
- Ultrox pigment vehicles, 355
- Silicon
 - carbide microparticles, aluminum bombardment, 474-476
 - diode, light sensitive, 284
 - dioxide-aluminum, germanium film, 195
 - dioxide films, emittance, 195
 - dioxide films, interference, 195
 - far infrared absorption, 36
 - monoxide coated aluminum, absorptance, emittance, and reflectance, 193
 - monoxide, evaporation in silicon oxide films, 192
 - monoxide, Inconel substrate, spectral emittance, 160
 - monoxide, oxidation during vacuum evaporation, 192
 - monoxide, platinum substrate, spectral emittance, 160
 - oxide-aluminum, reflectance, 192
 - oxide-aluminum, temperature control, satellites, 194
 - oxide coatings, 192-195
- Silicone
 - coating binder, superior to organic, 423
 - Dow Corning Q 90090, 361
 - elastomeric, UV stability, 349
 - methyl-, 349
 - nuclear radiation, coatings, 375
 - OSO-I, coating degradation, 449
 - OSO-I, rutile titania degradation, 444
 - paint, curing catalyst effect, 430
 - paints, formulation, 406-407
 - titania pigment vehicles, 361
 - zinc oxide pigment vehicles, 362
 - zinc sulfide pigment vehicles, 363
- Silver
 - absorptance, solar, sea level vs outer space, 189
 - angular reflectance, infrared, 190
 - angular reflectance, visible light, 190
 - bromide
 - gelatin matrix, 94
 - scattering predictions, 94
 - buffed, spectral reflectance, 166
 - cratered, emittance, 470
 - electrical resistivities, 17
 - film, hemispherical emittance, 191
 - metal film, 189
 - microparticle damage, 469
 - optical constant effects, 191
 - polished, emittance, 328
 - reflectance, near-UV, 189
 - relaxation times, 17
- Single particle theory, see particle theory
- Sintered glass
 - coating, light scattering behavior, 205-209
 - spectral emittance, 492
 - Snakula formula, 353, 354
 - Snell's law, 13, 84, 299
 - Sodium
 - chloride, prism, 288
 - electrical resistivities, 17
 - hydroxide, for anodizing beryllium-copper coating, 512
 - relaxation times, 17
 - silicate-calcium fluoride
 - nuclear radiation, 356
 - UV radiation, 356
 - silicate, cement, 503
 - silicate-Lithafrax
 - concurrent UV-nuclear radiation, 359
 - nuclear radiation, 355
 - UV radiation, 355
 - silicate-lithium fluoride, nuclear radiation, 356
 - silicate-titania, nuclear radiation, 361
 - silicate-Ultrox, radiation, 355
 - silicate-zinc
 - oxide, radiation, 362
 - sulfide, radiation, 363
 - Solar absorbers
 - blackbody effectiveness, 510
 - coatings, vacuum-stable, 509-524, 525-530
 - cutoff wavelength, 510
 - effectiveness, 516-518
 - Solar absorptance
 - angular, 293-311
 - chart for plotting, 193
 - satellite coatings, 303-311
 - Solar energy converters, multiple film coatings, 195, 509-524, 525-530
 - Solar flares, spacecraft radiation damage, 538
 - Solar furnace, for emittance measurements, 277-286
 - Solar Observatory, Orbiting, coating degradation, 539
 - Solar power system, coatings, 509-524
 - Solar probe
 - cone, 549
 - configuration, 550
 - radiation tests, 550-551
 - thermal analysis, 552
 - thermal shield, 554
 - Solar radiation
 - blackbody correction, 279
 - simulation, 550
 - spectral distribution, 286
 - Solar reflection
 - range modification by contamination, 136
 - surface roughness, 136
 - Solar spectrum, attenuation by two atmospheres, 528
 - Solar storms
 - flux density, 345
 - particle energy, 345
 - Solar wind
 - basalt powder darkening, 347
 - cementing effects on particles bombardment, 346, 348
 - chemical effects, 345

- Solar wind—Continued
 - composition, 345
 - crystal surface damage, 345
 - definition, 345
 - lunar surface ion bombardment, 346
 - Mariner II, flux and velocity, 348
 - particle velocity, 348
 - quiet Sun, 345
 - simulated, technique, 348
 - spacecraft damage, 341
 - sputtering effects, 345, 348
 - white oxide coatings, 342
 - white paint, specular absorptance, 347
- Solids, emittance, above 2000° C, 277–286
- Solubility, zinc in zinc oxide from saturated vapor, 417
- Source comparison
 - diffusing sphere use, 230
 - spectroradiometer, 229
- Spacecraft, *see also* Satellites
 - blackbody view area, 7
 - emittance, temperature control surfaces, 331–336
 - emittance, variation with viewing angle, 550
 - shielded, 553
 - specular surfaces and Monte Carlo technique, 7–8
 - thermal control materials, 351–354
 - unshielded, 554
- Space Rocket I, II, 479
- Space simulation chamber, 10⁻⁹ torr, 531
- Space utilization requirements
 - metals
 - "as received," 502
 - polished, 502
 - sandblasted, 502
 - pigmented coatings, 502
 - thin films, 502
- Spectral distribution, solar radiation, 286
- Spectral emissivity of metals, 11–28
- Spectral shift, grinding zinc oxide pigment, 429
- Spectral value, emittance, 313
- Spectrometer
 - integrating sphere, 77
 - Littrow, 288
 - microbeam condenser corrections, 77
 - narrow angle illumination, 77
 - spectrum distortion, 220
- Spectrophotometer
 - Beckman, absorptance, 308
 - Cary, 14M, 166, 177, 252, 355, 422, 434
 - cavity
 - heated, 468
 - observation, 118
 - reflectance, 120
 - double beam
 - equivalent, 120
 - spectral emittance, 242
 - General Electric recording, 120, 166, 177
 - Gier-Dunkle, 388
 - hemispherical viewing, 117
 - incident beam in cavity depth, 120
 - infrared, Beckman, 246, 247, 248
 - magnesium oxide, 121
 - nonlinearity, corrections, 246–248
 - Perkin-Elmer, 315
 - spectral reflectance, 166
 - with transfer optics, 246
- Spectroradiometer
 - double oven infrared, 287
 - filter, black diagram, 226, 227
 - infrared, description, 288–289
 - Johnson noise, 288
 - source comparison difficulty, 229
- Spectroscopy
 - blackbody radiation, 29
 - far infrared
 - alumina, 10° K, 33
 - aluminum, 8.5° K, 32
 - barium fluoride, 10° K, 35
 - carbon-composition resistor, 31
 - chromium, 8.5° K, 32
 - germanium, 7.5° K, 36
 - Hofman helium dewar, 30
 - magnesium alloy, 8.5° K, 32
 - silica, 6.5° K, 33
 - silicon, 7.5° K, 36
 - stainless steel, 8.5° K, 32
 - strontium fluoride, 7° K, 34
- Specular components effect, 123–126
- Specular surfaces, *see* Surfaces
- Spheres
 - cavities, in reciprocity theorem, 105
 - coating, magnesium oxide reflectance, 230
 - diffusing, source comparison use, 230
- Spinel, 249, 251, 252
- Sputnik III, 479
- Sputtering
 - insulators, 348
 - particle velocity, 348
 - powders, cementing effect, 346
 - rates
 - copper, 346
 - crystals, 346
 - iron, 346
 - solar wind effect, 345
 - space vehicle surfaces, 346
- Standards
 - aluminized copper block, reference in solar furnace, 278
 - Corning Thermometer White glass, working, 166
 - detectors, radiation measurements, 217
 - irradiance, spectral and total, 217–219
 - magnesium oxide, reference, 166
 - radiance, spectral, 217–219
 - radiometric, NBS, 218–220
 - reflecting surface, emittance, reference, 279
 - rhodium mirror, working, 166
 - UV measurements, reference, 166
 - Vitrolite glass, working, 166
- Steel
 - commercial, roughness parameters, 175
 - cratered by micrometeoroids, 456

- diffuse spectral directional reflectance, 168
- diffuse spectral reflectance, 166
- emittance, cratered, stainless, 470
- gage block
 - commercially finished, 170
 - diffuse spectral reflectance, 166, 168
 - lapped, 170
- infrared reflection spectrum, T304, 32
- microinterferograms, commercial, 175
- micrometeoroid erosion, 471
- microparticle damage, stainless specimen, 469
- oxide film effect on spectral emittance, 159-160
- prepared
 - microinterferograms, 173, 174
 - parameters, 174
- samples, diffuse spectral reflectances, 166, 168
- vacuum chamber, stainless, 294
- Stefan-Boltzmann
 - blackbody, definition, 217
 - constant, 197, 307
 - heat transfer, unshielded space vehicles, 552
 - Planck laws, NBS radiance standards, 217
 - solar furnace, total normal emittance, 280
 - total flux calculation 282
- Storage, cryogenic propellants in space, 559-566
- Strontium
 - fluoride, far infrared reflection spectrum, 34
 - titanate, nonisothermal emissivity apparatus, 492
- Substrate stress
 - magnetic coated memory devices, 152
 - optical properties of films, 152
 - removal by electropolishing, 152
- Sulphur
 - base oils, surface film caused by, removal, 152
 - dosimeter, 369
- Sun
 - apparent temperature, 284
 - oriented travel, radiation shields, 549-557
 - surface temperature, 278
 - temperature produced on cylindrical spacecraft, 340
 - UV region, comparison mercury and xenon lamps, 445-446
- Surface
 - area, total
 - BET method, 181
 - measurement technique, 179-181
 - roughness geometry, 180
 - to nominal, relation, 180
 - characteristics, absorbers and reflectors
 - median infrared, 501
 - median solar, 501
 - solar, 501
 - total, 501
 - charges, insulators
 - neutralization, ion bombardment, 346
 - removal by RF voltage, 348
 - chemical effects, 159-160
 - cleaning with d-c glow discharge, 194
 - cold working, 137
 - contaminants
 - infrared energy transfer, 136
 - outer skin, 136
 - penetration causes, 136
 - solar range reflection, 136
 - thermal radiative behavior, 138
 - contour
 - hand polishing, 135
 - machining, 136
 - sandblasting, 135
 - conversion of lattice to radiant conduction, 201
 - corrugation, 161
 - damage
 - controlled degradation, 506
 - electropolishing, 149
 - emittance, 145, 147, 468
 - infrared effect, 149
 - micrometeoroid, classifications, 455
 - optical properties, 149
 - solar wind, 345
 - UV, 149
 - visible light, 149
 - zircaloy and tungsten particles, bombardment, 468
 - dielectric
 - model, 136
 - radiation properties, 197-203
 - disturbances, 137
 - effects, modification of thermal radiation properties, 135
 - emittance, cratered surfaces
 - aluminum, 470
 - chromium, 470
 - gold, 470
 - silver, 470
 - stainless steel, 470
 - film
 - absorptance, 157
 - aluminum oxide layer, reflectance, 150
 - destructive interference, 137
 - finish measurements, 139
 - incomplete protection of substrates, 160
 - index of refraction, 157
 - interference, 157
 - mirror, 150, 192
 - oxide, emittance, infrared and UV, 150
 - reflectance, 150-151
 - silicon monoxide, platinum substrate, 160
 - sulphur-base-oils caused, removal, 152
 - thickness, 157
 - types, 143
 - geometry effects, 136-138, 181
 - grain refining, 137
 - gray, 505, 561
 - grooved, angular dependence of emittance, 316-317
 - hillocks, 162
 - HMAB adsorption isotherm, 180
 - Inconel, oxidation in vacuum, 157
 - infinite parallel, heat transfer, 41-42
 - inflight variable, 507
 - insulator, 346
 - interaction with light, 84

Surfaces—Continued

- irregularities, 147
- lay, 142, 165
- layer
 - disturbed, adsorption, 149
 - disturbed, emission, 149
 - polishing, 143
 - structural effects on optical behavior, 143
- lunar
 - simulation, sputtered basalt, 346
 - solar wind bombardment, 346
- metals
 - contaminant detection, 137
 - microinterferograms, 165
 - polished, recrystallization, 183
 - polished, thermal etching, 183
 - real, characterization, 141
 - rough, radiant energy interaction, 154
 - sandblasting, 341
 - solar wind effects, 347
 - texture measurements, 169
- micrometeoroid impact, 455-456
- microscopic measurements, 262
- optical properties
 - behavior of metals, 142
 - craters, 471
 - tailoring, 510
- oxidation of stainless steel, effect on spectral emittance, 159
- penetration, contamination, 136
- phenolic nylon ablation char, 272
- photodegradation, 443-441
- platinum
 - grain boundaries, 187
 - mirror, grooved, 313
 - time lapse photography of changes, 183, 185
- polished, micrometeoroid impact, 342
- porosity
 - determination by mercury intrusion, 260
 - nylon phenolic ablation char, 273
- profiles with light-section microscope, 262
 - carbon, 267
 - graphite, 267
 - zirconia, 267
- profiles by profilometry, 153
- real
 - dielectrics, model, 135
 - differences with ideal, 137, 141, 142
 - electrical conductor, 135
 - metal, oxide layer, 143
- recrystallization, 137
- reflectance
 - diffuse spectral, aluminum, 166
 - diffuse spectral, beryllium, 166
 - diffuse spectral, metal
 - diffuse spectral, platinum, 166
 - film effect, 150-151
 - Fresnel's equation, 351
 - lay effect, 165, 166
 - oxidized carbon, 269
 - radiative transfer equations, 95
 - roughness influence, 95, 97
- reflectance, diffuse spectral
 - aluminum, 166
 - beryllium, 166
 - platinum, 166
 - rhodium plated nickel, 166
- reflection
 - absorption coefficient, 85
 - electromagnetic radiation, 267
 - Maxwell's equations, 84
 - multiple, 153
 - near resonant frequency, 85
 - nickel, rough, 53
- reflectivity, ceramics, emittance, 87
- root mean square slope
 - oxidized carbon, 270
 - reflected radiation, 267
 - roughness, definition, 267, 269
 - zirconium oxide, 270
- roughness
 - alumina, 139
 - aluminum emittance increase, 141
 - angular distribution, 147
 - blackbody cavity effect, 97-98
 - centerline average, 141
 - determination, 153
 - diffraction theory, 154
 - emittance, 5, 99, 145, 146
 - Gaussian distribution, 154
 - geometry, 153, 180-181, 262
 - hemispherical emittance, 147, 153
 - incident light, 147
 - infrared energy transfer, 136
 - Kirchhoff's law, 148
 - known dimension, 180
 - Lambert's cosine law, 146
 - M-system, 170
 - metallic interaction, radiant energy, 154
 - microscopic study, 262
 - multiple reflections, 146
 - nickel samples, 153
 - opacity, correlation, 99
 - periodic, 161
 - profilometers, 153, 179
 - radiative properties, 154
 - Rayleigh, 147
 - reflectance, 95-100, 147
 - root mean square, 155
 - specular reflectance, diffraction region, 148
 - statistical study, 267
 - surface profile measurements, 153, 179, 260
 - surface reflectance, 95, 97, 146, 148
 - thermal radiation, 179
 - total surface area, 180
 - vs damage, emittance, 147
 - zirconia, 99, 271
- second, dielectrics, 138, 197

- selective
 - black, solar absorbers, 525-530
 - black, solar energy collectors, 525-530
 - spectrally, in storage of cryogenic propellants, 563
 - skin, contamination, 136
 - smooth
 - diffraction theory, 155
 - geometric optics, 146
 - isotropic, 39-42
 - Lambert's cosine law, 146
 - solar cells, 341
 - solar collectors, 341
 - space environmental effects, 339
 - space radiators, 341
 - specular
 - absorptance, solar, 294
 - emissivity, 39-41
 - heat transfer, 41-42
 - inter-reflection relationship, 39, 41-42
 - loss, 183
 - optical constants and properties, 39-44, 45-62, 299
 - platinum degradation, 184
 - radiation interchange, 39
 - reflecting, 107-108, 112
 - space vehicles, 7-8
 - stability, 341, 422
 - statistics, optical behavior predictions, 147
 - steel, diffuse spectral reflectance, 166
 - striations
 - aluminized Mylar, 297
 - platinum, 184
 - structural, characterization, 143
 - temperature
 - gradient, 200, 201-202
 - low rotational speed, specimen, 243
 - measurements problems, 277
 - texture
 - filling out factor, 170
 - leveling depth, 170
 - mean center line, 170
 - metals, 165-177
 - parameters, 170
 - peak-to-valley height, 170
 - profile angle, 170
 - root and crest lines, 170
 - roughness height, 170
 - roughness width, 170
 - shape factor, 170
 - thermal control
 - state of the art, 495-508
 - UV stability, 496
 - to-wavelength scaling parameters, 135
 - topography
 - controlled, 163
 - opacity vs transparency, emittance, 160
 - waviness, 136
 - transmission regions between materials, 199-203
 - transparent coatings, 191
 - waviness, 136
 - white, flame-sprayed alumina, 342
 - Surfican, radioactive, 179
 - Susceptor, contamination of specimen at high temperatures, 278
 - Symposia
 - electromagnetic energy, 154
 - finishing, third aerospace, American Electroplaters Society, 205
- T**
- Tailoring ceramic properties, 96, 100
 - Tantalum
 - aluminum coating, 492
 - electrical resistivity variation with temperature, 26
 - hemispherical emittance, 11, 24, 26
 - in sensors, 567
 - normal emittance, 11, 24, 26
 - oxide films, molybdenum substrate, spectral reflectance, 514
 - spectral emittance, 23
 - thermal energy transport by electrons, 487
 - total emittance, 24
 - Tapered gap, thermal radiation transmission, 111
 - Tapered tube, thermal radiation transmission, 111
 - Taylor, Taylor, and Hobson Talysurf, model 3, 170, 171
 - Teflon
 - emittance values, 323
 - insulated wire, 322, 324
 - Temperature
 - accuracy, blackbody system, 237, 238, 240
 - apparent, of sun, 279, 284
 - calculation, radiation measurement, 264-265, 279
 - calibration of high-temperature thermocouples, 22-24, 570
 - control
 - satellites, thin films, 194
 - solar system environment, 341
 - differential, error, cavity and specimen, 318
 - distribution, space vehicles, 7
 - drift error, blackbody cavity, 318
 - effect, coating degradation
 - nuclear radiation, 368, 379
 - UV, 423-429, 437, 450
 - gradient in radiating materials, 201, 202, 246, 283, 284
 - interface of two materials, 201
 - mean, spacecraft, various planetary distances from sun, 340
 - modulation in arc-imaging furnace, with brass cloth, 261
 - optical measurement techniques, 259
 - profile across specimen in solar furnace, 284
 - pyrometer, measurements, 279
 - rate measurements, 331-336
 - iteration method, 333
 - rate-equation method, 332
 - sensor, in reentry vehicle, 575
 - solar, 286
 - solar furnace, 278-280
 - stability, blackbody system, 237

- Temperature—Continued
 thermocouple, blackbody furnace, 246
 uniformity, blackbody system, 238
- Thermal control surfaces
 research areas, 495–508
 space environment effect, 339–342
 UV stability, 496
- Thermal energy balance, test disk, 293–294
- Thermistor bolometer, 283
- Thermocouples
 calibration
 -200 to 100° C, 308, 310
 high temperature, 22–24, 570
 Chromel-Alumel, 314, 366
 copper-constantan, 304, 434
 differential, 246
 gold cobalt alloy, 31
 graphite, 569
 leads, conduction losses, 297, 325
 platinum/platinum-rhodium, 22, 183
 radiation detector, 288
 refractory metals, 569
 rivet installation, 578
 tungsten-rhenium, 11, 22, 23, 570
- Thermopile
 bismuth-silver, 281, 545
 coated with lampblack, 218
 Coblenz, 224, 226, 227
 Eppley, 223, 224, 228
 filter, spectral transmittance, 227
 phototube calibration, 422
 Reeder, 222, 225
 solar furnace, 282, 283
 solar simulation calibration, 231
 temperature measurement, 11, 21
- Thickness
 correction for emittance, 280
 dielectrics, 198
 optical, 203
 temperature gradients, 202
 tester, eddy current, 437
 thin films, 202, 509–524, 525–530
- Thin films
 abrasion resistant, 514
 admittance, 525–530
 alumina, 192
 alumina on molybdenum, 520
 anodized beryllium-copper conversion coatings, 501
 cryodeposited, 531–534
 dielectrics, 511–512
 interference type, 511–512, 525–530
 metal
 evaporated, 189–195
 preparation, 511–512
 reflectance, monitoring, 511
 resistance monitoring, 511
 molybdenum, transmittance vs resistance, 512
 nickel black, 525–530
 nonmetallic, 501
 plated coatings, 501
 reproducibility, 523
 silicon oxide, 192
 tantalum oxide-molybdenum, 514–524
 thickness, 524
 tracer studies, 179
 two- and three-layer systems, 525–530
 UV transmissivity, 66
 vacuum deposited, 501
- Thorium oxide (thoria)
 low emittance, 251
 spectral emittance, 252, 254
 spectral reflectance, 253
 total normal emittance, 251
- Time-temperature measurements, 331–336
- Time variation of total hemispherical emittance,
 polished platinum, 183
- Timing equipment, blackbody emitter, 322
- Tin, ion bombardment, 346
- Titania
 epoxy, absorptance, 383
 OSO-I, 383, 384, 444, 447–448
 -silicone, 361
 -sodium silicate, 361
 solar absorption, 384
- Titanium
 carbide, mechanism of heat conduction, 487
 craters, 456
 dioxide
 -epoxy, OSO-I, 447–448
 -epoxy, paint, 433–434
 -epoxy, spectral absorptance, 423
 -methyl silicone, spectral reflectance, 547
 -silicone, spectral absorptance, 424
 -silicone, UV stability, 434
 emittance, infrared, 150–151
- Transformer, graphite blackbody heating, 235, 239
- Transition measurements, solids, far infrared spectra,
 30–36
- Transition metals, emittance, 26, 27
- Transmission, radiation
 passages, 111
 tube, 111
 tube, independent of length, 115
- Transmission effects of scattering centers in dielectrics,
 197–198
- Transmittance
 against resistance, molybdenum films, 512
 dielectrics, 197
 helium-neon laser for measuring, 255
 infrared, solid nitrogen and oxygen, 532–533
 spectral, filter, 227
- Trichloroethylene in surface preparation, 152
- Tungsten
 boat for preparation of evaporated films, 521–522
 contamination in aluminum oxide film, 523
 electrical resistivity, 26
 emittance, 265
 hemispherical emittance, 11, 25, 26

high-temperature sensors, 567
 lamp, 121, 166
 microparticle damage, 469
 normal emittance, 11, 25, 26
 projectiles, 468
 -rhenium wires, ductility, 570
 sheathed wires, temperature effect, 571
 spectral emittance, 26
 strip lamp, radiation standard, 264
 thermocouples (tungsten-rhenium), 11, 22, 23, 569

U

Ultraviolet, 381-452, 535-548
 absorptance changes, 429
 aluminum phosphate pigment vehicles, 357
 comparison: sun, BH-6 lamp, 445-446
 comparison with gamma radiation, 358, 439-440
 copper, reflectance, 189
 damage, surfaces, 149, 342, 412, 418, 421
 degradation
 antimony trioxide coatings, 450
 coatings, 443, 450
 mechanism, 354, 359
 OSO-I, 444, 449
 rutile titania pigment, 444, 447-448
 surfaces, 341
 thermal control coatings, 435-438, 443, 446-451
 zinc oxide coatings, 450-451
 emittance, effect of oxide films, 150
 exposure control, experimental chamber, 422
 gold, reflectance, 189
 mercury-argon arc lamp, 422-435
 radiation effects
 calcium fluoride-sodium silicate, 356
 comparison with gamma, 358
 distilled resins, 412
 exposure time, 428
 films, polyvinyl, scissions, 382
 hydrogen plasma as source, 347
 inorganic pigments, 396
 Lithafrax-sodium silicate, 355, 359
 low absorptance/emittance surfaces, 421-422
 organic paints, 405
 polyvinyl chloride, 387
 semiconductor pigments, 360
 silicone paints, 409, 411
 temperature effects, 358
 thermal control materials, 421, 422-423
 Ultrox-aluminum phosphates, 356-357
 wavelength dependency, 354, 426-428
 white coatings, 391-420
 zinc oxide pigments, 403, 429
 silver, reflectance, 189
 spectral absorptance of coatings, 436
 stability
 coatings, 502
 inorganic formulation, 343, 540
 metals, 502

thermal control surfaces, 433-438
 thin films, 502
 total energy dependency, 428
 transmissivity, thin films, 66
 vacuum environmental system, 434-435

V

Vacancies, 353
 Vac-ion pumps, 548
 Vacuum chambers
 diffusion, pumped, 393
 emittance measurement apparatus, 314
 high (2×10^{-7} torr), 306
 ion-pumped, 394
 stainless steel, 294
 ultraviolet radiation measurements, 422
 Vacuum ion pump, 1200 liter/sec, 435
 Vacuum plating platinum films on copper, 316
 Vacuum pressure range, ultraviolet radiation measurements, 445
 Vacuum systems
 remote rotating specimen holders, 303-305
 ultraviolet environment, 434-435
 Van Allen belt, exposure dose rate equivalence, 438-439
 Vanguard
 II, coating degradation, 194, 539
 III, mass distribution of planetary dust, 479
 Venus, 340, 549
 Vibration sensitivity of solar furnace instruments, 284
 Volume emission, 86

W

Warpage, sandblasted metals, 502
 Water, from proton bombardment of oxides, 349
 Wien's law vs Planck's law, 264
 Wire
 insulation emittance measurements, 321
 sheathed, temperature effect, 571
 tungsten-rhenium, 571
 Work hardening by mechanical polishing, 136, 143, 149, 502

X

Xenon lamps, 445-446, 451
 X-point in spectral emittance, 4
 X-ray
 bleaching experiment, 359
 diffraction, iron oxides, 346
 X-20 vehicle, 567

Y

Yellowing caused by grinding
 zinc oxide, 429
 silica, 431

Z

- Zinc**, 417
- Zinc oxide**
- absorptance stability, 429
 - curing of inorganic coatings, 402
 - degradation, 391-420, 450-451, 539-540
 - impurities, 428-429
 - methyl silicone paints
 - absorptance, 543
 - emittance, 543
 - solar wind, 346-347
 - spectral reflectance, 547
 - paint, 348
 - photolysis mechanisms, 415-417
 - pigment preparation, 428-429
 - potassium silicate coatings
 - absorptance, 543
 - emittance, 543
 - spectral reflectance, 546
 - UV radiation, 403, 436, 540, 544
 - silicone binder, radiation, 362, 424
 - UV radiation, 397, 400
 - white pigment, stable, 391
- Zinc sulfide**
- absorptance, 503
 - paint, directional solar absorptance, 309
 - radiation damage, 354
 - silicone pigment vehicles, 363
 - sodium silicate, 363
- Zircon** (see also zirconium silicate)
- fine grained, sintered, emittance, 249
 - potassium silicate, emittance, 543
- Zirconia**
- calcia stabilized, 270
 - diamond wheel ground, 270
 - emittance, 265-267, 270, 271, 573
 - mean free path of a photon, 99
 - melting point, 270
 - pins, thermal insulation, 262
 - pore size spectrum, 271
 - reflectance, 270
 - sensor, 567, 573
 - surface profile, 267
 - surface roughness, 271
 - thickness for opacity, 270
- Zirconium**
- dibromide, antioxidant, 492
 - dioxide, absorptance, 424
 - film, electron beam evaporator, 522
 - oxide, emittance, 251, 254
 - oxide, surface roughness, 270
 - oxide, sintered, emittance, 251
 - reflectance, 253
 - silicate-aluminum oxide, UV stability, 540
 - silicate-potassium silicate, emittance, 543
 - silicate, spectral emittance, 254
 - silicate, spectral reflectance, 254